CELLULAR NEUROPATHOLOGY EDITOR'S PICK 2021

EDITED BY: Dirk M. Hermann

PUBLISHED IN: Frontiers in Cellular Neuroscience



frontiers Research Topics



frontiers

Frontiers eBook Copyright Statement

The copyright in the text of individual articles in this eBook is the property of their respective authors or their respective institutions or funders. The copyright in graphics and images within each article may be subject to copyright of other parties. In both cases this is subject to a license granted to Frontiers.

The compilation of articles constituting this eBook is the property of Frontiers.

Each article within this eBook, and the eBook itself, are published under the most recent version of the Creative Commons CC-BY licence. The version current at the date of publication of this eBook is CC-BY 4.0. If the CC-BY licence is updated, the licence granted by Frontiers is automatically updated to the new version.

When exercising any right under the CC-BY licence, Frontiers must be attributed as the original publisher of the article or eBook, as applicable.

Authors have the responsibility of ensuring that any graphics or other materials which are the property of others may be included in the CC-BY licence, but this should be checked before relying on the CC-BY licence to reproduce those materials. Any copyright notices relating to those materials must be complied with.

Copyright and source acknowledgement notices may not be removed and must be displayed in any copy, derivative work or partial copy which includes the elements in question.

All copyright, and all rights therein, are protected by national and international copyright laws. The above represents a summary only. For further information please read Frontiers' Conditions for Website Use and Copyright Statement, and the applicable CC-BY licence.

ISSN 1664-8714
ISBN 978-2-88966-956-1
DOI 10.3389/978-2-88966-956-1

About Frontiers

Frontiers is more than just an open-access publisher of scholarly articles: it is a pioneering approach to the world of academia, radically improving the way scholarly research is managed. The grand vision of Frontiers is a world where all people have an equal opportunity to seek, share and generate knowledge. Frontiers provides immediate and permanent online open access to all its publications, but this alone is not enough to realize our grand goals.

Frontiers Journal Series

The Frontiers Journal Series is a multi-tier and interdisciplinary set of open-access, online journals, promising a paradigm shift from the current review, selection and dissemination processes in academic publishing. All Frontiers journals are driven by researchers for researchers; therefore, they constitute a service to the scholarly community. At the same time, the Frontiers Journal Series operates on a revolutionary invention, the tiered publishing system, initially addressing specific communities of scholars, and gradually climbing up to broader public understanding, thus serving the interests of the lay society, too.

Dedication to Quality

Each Frontiers article is a landmark of the highest quality, thanks to genuinely collaborative interactions between authors and review editors, who include some of the world's best academicians. Research must be certified by peers before entering a stream of knowledge that may eventually reach the public - and shape society; therefore, Frontiers only applies the most rigorous and unbiased reviews.
Frontiers revolutionizes research publishing by freely delivering the most outstanding research, evaluated with no bias from both the academic and social point of view. By applying the most advanced information technologies, Frontiers is catapulting scholarly publishing into a new generation.

What are Frontiers Research Topics?

Frontiers Research Topics are very popular trademarks of the Frontiers Journals Series: they are collections of at least ten articles, all centered on a particular subject. With their unique mix of varied contributions from Original Research to Review Articles, Frontiers Research Topics unify the most influential researchers, the latest key findings and historical advances in a hot research area! Find out more on how to host your own Frontiers Research Topic or contribute to one as an author by contacting the Frontiers Editorial Office: frontiersin.org/about/contact

CELLULAR NEUROPATHOLOGY EDITOR'S PICK 2021

Topic Editor:
Dirk M. Hermann, University of Duisburg-Essen, Germany

Citation: Hermann, D. M., ed. (2021). Cellular Neuropathology Editor's Pick 2021. Lausanne: Frontiers Media SA. doi: 10.3389/978-2-88966-956-1

Table of Contents

06 ***HDAC1 Silence Promotes Neuroprotective Effects of Human Umbilical Cord-Derived Mesenchymal Stem Cells in a Mouse Model of Traumatic Brain Injury* via *PI3K/AKT Pathway***
Ling Xu, Qu Xing, Tuanjie Huang, Jiankang Zhou, Tengfei Liu, Yuanbo Cui Tian Cheng, Yaping Wang, Xinkui Zhou, Bo Yang, Greta Luyuan Yang, Jiewen Zhang, Xingxing Zang, Shanshan Ma and Fangxia Guan

20 ***Neuroprotective Effects of Curcumin on IL-1β-Induced Neuronal Apoptosis and Depression-Like Behaviors Caused by Chronic Stress in Rats***
Cuiqin Fan, Qiqi Song, Peng Wang, Ye Li, Mu Yang and Shu Yan Yu

37 ***Transduction of Adeno-Associated Virus Vectors Targeting Hair Cells and Supporting Cells in the Neonatal Mouse Cochlea***
Xi Gu, Renjie Chai, Luo Guo, Biao Dong, Wenyan Li, Yilai Shu, Xinsheng Huang and Huawei Li

53 ***Silencing of lncRNA PKIA-AS1 Attenuates Spinal Nerve Ligation-Induced Neuropathic Pain Through Epigenetic Downregulation of CDK6 Expression***
Jian-Zhong Hu, Zi-Jie Rong, Miao Li, Ping Li, Li-Yuan Jiang, Zi-Xiang Luo, Chun-Yue Duan, Yong Cao and Hong-Bin Lu

65 ***Long Non-coding RNAs Associated With Neurodegeneration-Linked Genes Are Reduced in Parkinson's Disease Patients***
Maximilianos Elkouris, Georgia Kouroupi, Alexios Vourvoukelis, Nikolaos Papagiannakis, Valeria Kaltezioti, Rebecca Matsas, Leonidas Stefanis, Maria Xilouri and Panagiotis K. Politis

78 ***A Novel Optical Tissue Clearing Protocol for Mouse Skeletal Muscle to Visualize Endplates in Their Tissue Context***
Marion Patrick Ivey Williams, Matteo Rigon, Tatjana Straka, Sarah Janice Hörner, Manfred Thiel, Norbert Gretz, Mathias Hafner, Markus Reischl and Rüdiger Rudolf

90 ***Photobiomodulation and Coenzyme Q_{10} Treatments Attenuate Cognitive Impairment Associated With Model of Transient Global Brain Ischemia in Artificially Aged Mice***
Farzad Salehpour, Fereshteh Farajdokht, Javad Mahmoudi, Marjan Erfani, Mehdi Farhoudi, Pouran Karimi, Seyed Hossein Rasta, Saeed Sadigh-Eteghad, Michael R. Hamblin and Albert Gjedde

107 ***Silencing MicroRNA-134 Alleviates Hippocampal Damage and Occurrence of Spontaneous Seizures After Intraventricular Kainic Acid-Induced Status Epilepticus in Rats***
Xiaoying Gao, Mian Guo, Dawei Meng, Feixiang Sun, Lianyue Guan, Ying Cui, Yan Zhao, Xichun Wang, Xin Gu, Jiahang Sun and Sihua Qi

118 ***Acute and Post-acute Neuromodulation Induces Stroke Recovery by Promoting Survival Signaling, Neurogenesis, and Pyramidal Tract Plasticity***
Ahmet B. Caglayan, Mustafa C. Beker, Berrak Caglayan, Esra Yalcin, Aysun Caglayan, Burak Yulug, Lutfu Hanoglu, Selim Kutlu, Thorsten R. Doeppner, Dirk M. Hermann and Ertugrul Kilic

133 ***From Ganglion Cell to Photoreceptor Layer: Timeline of Deterioration in a Rat Ischemia/Reperfusion Model***
Marina Palmhof, Viktoria Frank, Pascal Rappard, Emely Kortenhorn, Julia Demuth, Nora Biert, Gesa Stute, H. Burkhard Dick and Stephanie C. Joachim

152 ***Wnt Signaling Deregulation in the Aging and Alzheimer's Brain***
Ernest Palomer, Johanna Buechler and Patricia C. Salinas

160 ***Comprehensive Evaluation of White Matter Damage and Neuron Death and Whole-Transcriptome Analysis of Rats With Chronic Cerebral Hypoperfusion***
Wenxian Li, Di Wei, Jianye Liang, Xiaomei Xie, Kangping Song and Li'an Huang

180 ***Epigenetics in Neurodevelopment: Emerging Role of Circular RNA***
Shujuan Meng, Hecheng Zhou, Ziyang Feng, Zihao Xu, Ying Tang and Minghua Wu

192 ***Cellular Prion Protein as a Receptor of Toxic Amyloid-β42 Oligomers is Important for Alzheimer's Disease***
Yuan Zhang, Yanfang Zhao, Lei Zhang, Wanpeng Yu, Yu Wang and Wenguang Chang

201 ***TMEM16A Inhibition Preserves Blood–Brain Barrier Integrity After Ischemic Stroke***
Pin-yi Liu, Zhi Zhang, Yi Liu, Xue-lian Tang, Shu Shu, Xin-yu Bao, Yan Zhang, Yue Gu, Yun Xu and Xiang Cao

214 **In vitro** ***Characterization of Gut Microbiota-Derived Bacterial Strains With Neuroprotective Properties***
Suaad Ahmed, Alessandro Busetti, Parthena Fotiadou, Nisha Vincy Jose, Sarah Reid, Marieta Georgieva, Samantha Brown, Hayley Dunbar, Gloria Beurket-Ascencio, Margaret I. Delday, Anna Ettorre and Imke E. Mulder

231 ***TREM2 Regulates Heat Acclimation-Induced Microglial M2 Polarization Involving the PI3K-Akt Pathway Following EMF Exposure***
Gen-Lin He, Zhen Luo, Ting-Ting Shen, Ze-Ze Wang, Ping Li, Xue Luo, Ju Yang, Yu-Long Tan, Yuan Wang, Peng Gao and Xue-Sen Yang

242 ***The Pomace Extract Taurisolo Protects Rat Brain From Ischemia-Reperfusion Injury***
Dominga Lapi, Mariano Stornaiuolo, Lina Sabatino, Eduardo Sommella, Giancarlo Tenore, Maria Daglia, Rossana Scuri, Martina Di Maro, Antonio Colantuoni and Ettore Novellino

255 ***Treatment With Liraglutide Exerts Neuroprotection After Hypoxic–Ischemic Brain Injury in Neonatal Rats*** **via** ***the PI3K/AKT/GSK3β Pathway***
Shan-shan Zeng, Jun-jie Bai, Huai Jiang, Jin-jin Zhu, Chang-chang Fu, Min-zhi He, Jiang-hu Zhu, Shang-qin Chen, Pei-jun Li, Xiao-qin Fu and Zhen-lang Lin

270 ***Depletion of LncRNA NEAT1 Rescues Mitochondrial Dysfunction Through NEDD4L-Dependent PINK1 Degradation in Animal Models of Alzheimer's Disease***
Zhonghua Huang, Jing Zhao, Wei Wang, Jun Zhou and Jie Zhang

281 ***Peroxisomal Dysfunction in Neurological Diseases and Brain Aging***
Ndidi-Ese Uzor, Louise D. McCullough and Andrey S. Tsvetkov

291 ***Immortalized Dorsal Root Ganglion Neuron Cell Lines***
Rainer Viktor Haberberger, Christine Barry and Dusan Matusica

312 ***SARS-CoV-2 Dissemination Through Peripheral Nerves Explains Multiple Organ Injury***
Matija Fenrich, Stefan Mrdenovic, Marta Balog, Svetlana Tomic, Milorad Zjalic, Alen Roncevic, Dario Mandic, Zeljko Debeljak and Marija Heffer

324 ***Mesenchymal Stromal Cell-Derived Extracellular Vesicles Reduce Neuroinflammation, Promote Neural Cell Proliferation and Improve Oligodendrocyte Maturation in Neonatal Hypoxic-Ischemic Brain Injury***
Nicole Kaminski, Christian Köster, Yanis Mouloud, Verena Börger, Ursula Felderhoff-Müser, Ivo Bendix, Bernd Giebel and Josephine Herz

frontiers in Cellular Neuroscience

ORIGINAL RESEARCH
published: 04 January 2019
doi: 10.3389/fncel.2018.00498

HDAC1 Silence Promotes Neuroprotective Effects of Human Umbilical Cord-Derived Mesenchymal Stem Cells in a Mouse Model of Traumatic Brain Injury *via* PI3K/AKT Pathway

Ling Xu[1,2†], Qu Xing[1†], Tuanjie Huang[1], Jiankang Zhou[1], Tengfei Liu[1], Yuanbo Cui[1,3], Tian Cheng[4], Yaping Wang[1], Xinkui Zhou[1], Bo Yang[4], Greta Luyuan Yang[5], Jiewen Zhang[2], Xingxing Zang[6], Shanshan Ma[1] and Fangxia Guan[1,2,4]**

[1]School of Life Sciences, Zhengzhou University, Zhengzhou, China, [2]Henan Provincial People's Hospital, Zhengzhou, China, [3]Translational Medicine Center, Zhengzhou Central Hospital Affiliated to Zhengzhou University, Zhengzhou, China, [4]The First Affiliated Hospital of Zhengzhou University, Zhengzhou, China, [5]Stuyvesant High School, New York, NY, United States, [6]Department of Microbiology and Immunology, Einstein College of Medicine, Bronx, NY, United States

OPEN ACCESS

Edited by:
Thomas Fath,
Macquarie University, Australia

Reviewed by:
Sabine Wislet,
University of Liege, Belgium
Yaohui Tang,
Shanghai Jiao Tong University, China

***Correspondence:**
Shanshan Ma
mashanshan84@163.com
Fangxia Guan
guanfangxia@126.com

[†]These authors have contributed equally to this work

Received: 26 September 2018
Accepted: 03 December 2018
Published: 04 January 2019

Citation:
Xu L, Xing Q, Huang T, Zhou J, Liu T, Cui Y, Cheng T, Wang Y, Zhou X, Yang B, Yang GL, Zhang J, Zang X, Ma S and Guan F (2019) HDAC1 Silence Promotes Neuroprotective Effects of Human Umbilical Cord-Derived Mesenchymal Stem Cells in a Mouse Model of Traumatic Brain Injury via PI3K/AKT Pathway. Front. Cell. Neurosci. 12:498. doi: 10.3389/fncel.2018.00498

Stem cell transplantation is a promising therapy for traumatic brain injury (TBI), but low efficiency of survival and differentiation of transplanted stem cells limits its clinical application. Histone deacetylase 1 (HDAC1) plays important roles in self-renewal of stem cells as well as the recovery of brain disorders. However, little is known about the effects of HDAC1 on the survival and efficacy of human umbilical cord-derived mesenchymal stem cells (hUC-MSCs) *in vivo*. In this study, our results showed that HDAC1 silence promoted hUC-MSCs engraftment in the hippocampus and increased the neuroprotective effects of hUC-MSCs in TBI mouse model, which was accompanied by improved neurological function, enhanced neurogenesis, decreased neural apoptosis, and reduced oxidative stress in the hippocampus. Further mechanistic studies revealed that the expressions of phosphorylated PTEN (p-PTEN), phosphorylated Akt (p-Akt), and phosphorylated GSK-3β (p-GSK-3β) were upregulated. Intriguingly, the neuroprotective effects of hUC-MSCs with HDAC1 silence on behavioral performance of TBI mice was markedly attenuated by LY294002, an inhibitor of the PI3K/AKT pathway. Taken together, our findings suggest that hUC-MSCs transplantation with HDAC1 silence may provide a potential strategy for treating TBI in the future.

Keywords: histone deacetylase 1, human umbilical cord derived mesenchymal stem cells, traumatic brain injury, neuroprotection, PI3K/AKT

Abbreviations: TBI, traumatic brain injury; HDAC1, histone deacetylase 1; hUC-MSCs, human umbilical cord-derived mesenchymal stem cells; BBB, blood-brain barrier; PI, propidium iodide; MWM, Morris water maze test; FST, forced swim test; NOR, novel object recognition; ROS, reactive oxygen species; TST, tail suspension test; SPT, sucrose preference test.

INTRODUCTION

Traumatic brain injury (TBI) is a common brain disorder with high mortality and disability (Reis et al., 2015). Despite the considerable advances in the treatment and nursing of patients, effective therapy to attenuate the pathological process of TBI remain to be explored extensively. Emerging evidence shows that mesenchymal stem cells (MSCs) transplantation can improve the neurologic function following TBI (Kota et al., 2016), which imply MSCs-based therapy is promising for TBI. Human umbilical cord-derived MSCs (hUC-MSCs) have high self-renewal ability, and multidirectional differentiation potential (Xu et al., 2012). However, many studies reported that only a small fraction of transplanted MSCs could migrate, survive and differentiate into neural-like cells in the injured area, which limits its clinical application (Juliandi et al., 2010; Kang et al., 2016). Therefore, it is imperative to develop new strategies to overcome these problems in preclinical studies.

Histone acetylation modification is involved in the development of many neurological diseases, such as Alzheimer's disease, stroke and cerebral ischemia injury (Benito et al., 2015; Park and Sohrabji, 2016), suggesting that acetylation regulation strategy may be a potential therapeutic avenue to alleviate the neurological dysfunction. It has been demonstrated that histone deacetylase 1 (HDAC1) regulates proliferation and neural differentiation of embryonic stem cells, neural stem cells, tumor stem cells and MSCs (Jacob et al., 2014; Jamaladdin et al., 2014; Cai et al., 2018). More notably, HDAC1 plays a neuroprotective role *in vivo* through enhanced histone acetylation (Lebrun-Julien and Suter, 2015). However, most studies focused on the relationship between HDAC1 and stem cell development *in vitro*, and the regulatory effects of HDAC1 on stem cells *in vivo* are poorly known.

In this study, we found that silencing HDAC1 through siRNA could promote the engraftment of hUC-MSCs in the hippocampus and improve the efficacy of hUC-MSCs transplantation in a TBI mouse model as indicated by improved neurological function, enhanced neurogenesis, decreased neural apoptosis, and reduced oxidative stress in the hippocampus; and, the underlying mechanism of these neuroprotective effects of hUC-MSCs with silenced HDAC1 might involve in the activation of PI3K/AKT pathway.

MATERIALS AND METHODS

Isolation, Culture, and Identification of hUC-MSCs

This study was approved by the Ethics Committees of the Zhengzhou University. hUC-MSCs were isolated, cultured, and identified as previously described (Koh et al., 2008; Wang et al., 2016). After washing cord blood with phosphate buffer solution (PBS), the vessels and umbilical cord membrane were removed. The Wharton's jelly was cut into about 1-cm^3 pieces and cultured in DMEM (Hyclone, Logan, UT, USA) with 10% (v/v) fetal bovine serum (Hyclone), 100 U/ml penicillin and 100 μg/ml streptomycin in a 37°C incubator with 5% CO_2, with media replacement every 3 days. The HDAC1 shRNA and HDAC1 silencing lentivirus (siHDAC1) were designed and synthesized in GenePharm (Shanghai, China) by using lentiviral-vector mediated siRNA targeted HDAC1 silenced expression. The sequence of HDAC1 shRNA is 5′-GCCGGUCAUGUCCA AAGUATT-3′. hUC-MSCs at passage 3 (P3) were plated in 96 well plate for 24 h (2×10^3/well). After transfection at a MOI of 10 for 6 h, cells were rinsed by PBS and maintained in fresh F12-DMEM (10% FBS) for 3 days. HDAC1 expression was detected by Western blotting and quantitative real-time polymerase chain reaction (qRT-PCR).

Animal Model of TBI

This study was approved by the Institutional Animal Care and Use Committee of Zhengzhou University, China. Procedures were conducted in strict accordance with the National Institutes of Health guidelines for the Care and Use of Laboratory Animals. Male C57BL/6 mice (8–12 weeks, 20–25 g) were housed with free access to food and water on a 12-h light/dark cycle in a pathogen-free environment. After anesthesia with 10% chloral hydrate (200 mg/kg), mice were fixed in a stereotaxic frame and the scalp was shaved. Three millimeter craniotomy was performed over the left parietal cortex (1.5 mm to the anterior fontanelle, and 1.5 mm to the sagittal suture), and the exposed dura was kept intact. Modified Feeney's weight-drop model was performed for the present study onto the exposed intact cranial dura to produce a standardized parietal contusion (weighing 20 g, falling from 20 cm height; Liu et al., 2013). After trauma, the skull hole was closed with bone wax, and the scalp was sutured.

Experimental Groups

A total of 120 mice subjected to TBI were randomly divided into four groups: vehicle group, MSCs group, MSCs-siHDAC1 group (MSCs transfected with HDAC1 silencing lentivirus), and LY294002 group. Different treated groups were individually injected into a tail vein. Vehicle group was given 100 μL 0.9% saline. Mice in the MSCs group were injected with 1×10^6 hUC-MSCs suspended in 100 μl 0.9% saline. For the MSCs-siHDAC1 group, mice were injected 1×10^6 hUC-MSCs with HDAC1 silence. For the LY294002 group, 25 mg/kg LY294002 were intraperitoneal administrated 30 min before induction of the TBI model and administered 1×10^6 MSCs-siHDAC1. Mice were intravenously injected with hUC-MSCs at 24 h after operation once a day for 3 days. No mouse died and no aberrant cell growth was observed during the study.

Behavior Tests

Modified Neurologic Severity Score (mNSS)

The neurological functional measurement was evaluated by modified neurologic severity score (mNSS) scoring at 1, 3, 7, 14, 21, and 28 days after treatment by two individuals blinded to the experimental groups. According to this score, the higher the mNSS score, the more severe of TBI deficient. Neurological function was graded on a scale of 0–18 (normal score 0; maximal deficit score 18; Cheng et al., 2015).

Morris Water Maze Test (MWM)

Morris water maze test (MWM; Chengdu Taimeng Tech. Co. Ltd., China) was used to evaluate the spatial learning and memory ability of mice as described previously (Cui et al., 2017). Briefly, mice were continuously trained twice daily for six consecutive days, then the navigation test and probe trial were carried out on the 7th day. The latency to find the hidden platform for the 60 s was recorded. A video tracking system recorded the latency time, frequency of platform crossover, time in each quadrant, and the speed.

Sucrose Preference Test (SPT)

Mice were trained to consume from two 50-ml bottles of 1% sucrose solution for 3 days, then we replaced one bottle of sucrose with water and allowed mice to drink freely from both bottles for 24 h. In the next 3 days, the respective weights of the sucrose solution and water consumed were recorded and refilled each day at the same time in the morning, and mice were allowed to drink freely from both bottles. Sucrose preference was calculated by using the following formula (Tucker et al., 2017): % Sucrose preference = (sucrose intake/total fluid intake) × 100.

Forced Swimming Test (FST)

Mice were placed in a large cylinder (22 cm diameter × 25 cm high) filled with water (13.5 cm high) at a temperature of 23–25°C. Mice movements were recorded for 6 min and mice were placed under a heating lamp to dry upon finishing. Immobility period was defined as motionless floating in the water without struggling and we analyzed immobility time during the last 4 min (Watanabe et al., 2013).

Tail Suspension Test (TST)

Mice were suspended by adhesive tape placed approximately 2 cm from the tip of their tails fixing upside down on the hook so that the mouse was suspended 17 cm above a horizontal surface. The immobility time was recorded for 6 min (Cheng et al., 2016). Mice were immobile only when they hung wholly and passively motionless.

Tissue Preparation

At designated time points, mice were anesthetized and perfused intracardially with 0.9% ice-cold saline. Then, the mice were killed and the brain tissues were collected. The brain tissues were incubated in ice-cold 4% paraformaldehyde (PFA) at 4°C overnight, then transferred into a 30% sucrose solution for 72 h, and sectioned on a cryostat (Leica, Germany) to obtain 20 μm coronal sections. The sections were stored at −80°C until further processing.

Evaluation of Blood-Brain Barrier (BBB) Permeability

Evans blue (EB) extravasation assay was used to evaluate blood-brain barrier (BBB) permeability at 3 days after TBI. Briefly, 2% EB (4 mL/kg) was injected into the tail vein. Animals were anesthetized after 1 h and perfused using saline to remove intravascular EB dye. The brain was removed and homogenized in phosphate-buffered saline. Trichloroacetic acid was then added to the precipitate protein, and the samples were cooled and centrifuged. The resulting supernatant was measured for the absorbance of EB at 620 nm using a spectrophotometer and quantified as microgram of EB per gram of the brain according to a standard curve.

Lesion Volume

After MWM testing, mice were sacrificed and perfused transcardially with PBS followed by 4% PFA. Brains were removed and assessed for lesion volume with cresyl violet (CV) staining and myelin integrity with luxol fast blue (LFB) staining as we reported (Cheng et al., 2015). Using the Measure Tool on ImageJ (Version 1.44), a blinded investigator calculated hemispheric brain volume. Lesion volume was obtained by subtracting the volume of brain tissue remaining in the left (ipsilateral) hemisphere from that of the right (contralateral) hemisphere and expressed as percent volume lost.

Propidium Iodide (PI) Staining

Propidium iodide (PI, Sigma-Aldrich Corporation, St. Louis, MO, USA) staining was performed to assess cell death (Li D. et al., 2016). Briefly, PI (10 mg/ml in saline, 0.4 mg/kg) was administered 1 h before killing by intraperitoneal injection in a total volume of not more than 100 μL. All cortical regions of the brain were chosen from 200× cortical fields from within contused cortex. PI-positive cells were quantitated in the contused cortex in three brain sections and photographed under a DMi8 advanced fluorescence microscope (Leica Microsystems, Germany) using excitation/emission wavelength at 568/585 nm. All images were captured at the same exposure times, contrast settings, and intensity for measurement of fluorescence intensity.

Reactive Oxygen Species (ROS) Staining

The levels of reactive oxygen species (ROS) in the brain were measured by injecting dihydroethidium (HEt), a specific *in situ* marker of superoxide production (Cheng et al., 2016). Two-hundred microliters of 1 mg/ml HEt was intraperitoneal injected and allowed to circulate for 1 h, anesthetized mice were perfused transcardially with PBS and 4% PFA and brains were taken for immunofluorescence. Sections with similar lesion areas were selected, visualized, and photographed under a DMi8 advanced fluorescence microscope (Leica Microsystems, Germany) using excitation/emission filters at 568/585 nm. All images were captured at the same exposure times, contrast settings, and intensity for measurement of fluorescence intensity.

Enzyme-Linked Immunosorbent Assay (ELISA)

Upon anesthesia, the peripheral blood of anesthetized mice was harvested and the serum was stored at −80°C until processing. The protein expression or secretion of BDNF, NGF, inflammatory factors (IL-4, IL-10, IL-1β, and TNF-α) levels and oxidative stress levels (MDA, SOD, GSH, and GSH-Px) were measured using enzyme-linked immunosorbent assay (ELISA) kits (Tsz Biosciences, Boston, MA, USA) according to the manufacturer's instructions.

TABLE 1 | Sequence of primers for quantitative real-time polymerase chain reaction (qRT-PCR).

Gene	Primer (5′-3′)
HDAC1	Forward: 5′-CCAGTATTCGATGGCCTGTT-3′
	Reverse: 5′-AGCAAATTGTGAGTCATGCG-3′
BDNF	Forward: 5′-TCATACTTCGGTTGCATGAAGG-3′
	Reverse: 5′-AGACCTCTCGAACCTGCCC-3′
NSE	Forward: 5′-AGCTCAGGTATCTCCGTGGT-3′
	Reverse: 5′-ACCAGCTCCAAGGATTTATTCTCA-3′
MAP2	Forward: 5′-CTGGACATCAGCCTCACTCA-3′
	Reverse: 5′-AATAGGTGCCCTGTGACCTG-3′
NGF	Forward: 5′-TACAGGCAGAACCGTACACAGATAG-3′
	Reverse: 5′-CAGTGGGCTTCAGGGACAGA-3′
DCX	Forward: 5′-TCCAGTCAGCAAAGGTAAGGA-3′
	Reverse: 5′-CCAAGAGAGAACAGCAAACCA-3′
GAPDH	Forward: 5′-GGTGAAGGTCGGTGTGAAC-3′
	Reverse: 5′-CCTTGACTGTGCCGTTGAA-3′

Quantitative Real-Time Polymerase Chain Reaction (qRT-PCR)

Total RNA of injured cortical tissue from the perilesional area was extracted by using TRIZOL (Invitrogen, Grand Island, NY, USA) according to the manufacturer's protocol. The mRNA expression of BDNF, NGF, NSE, DCX, and MAP2 was measured by qRT-PCR, which was calculated by the $2^{-\Delta\Delta Ct}$ method as previously described (Wang et al., 2018). GAPDH was used as the internal standard. Experiments were carried out in triplicate. The sequence of primers for qRT-PCR are shown in **Table 1**.

Immunofluorescence Staining

Immunofluorescence staining was in accord with previous description (Li D. et al., 2016). After being blocked, coronal sections were incubated with anti-human nuclei antibody (MAB1281, 1:100, Millipore, Oxford, UK), myelin basic protein (MBP; 1:200; Santa Cruz Biotechnology, Dallas, TX, USA), Ki67 (1:200, Bioss, Beijing), DCX (1:200, Proteintech, China), or NeuN (1:200, Proteintech, China) at 4°C overnight and then incubated in Cy3/FITC-conjugated anti-mouse/rabbit anti IgG (1:500, Proteintech, China) for 1 h at room temperature, followed by DAPI (1:2,000, Biotech, China) staining for 10 min. The slides were examined with a DMi8 advanced fluorescence microscope (Leica Microsystems, Germany). Positive-cells were counted with ImageJ software.

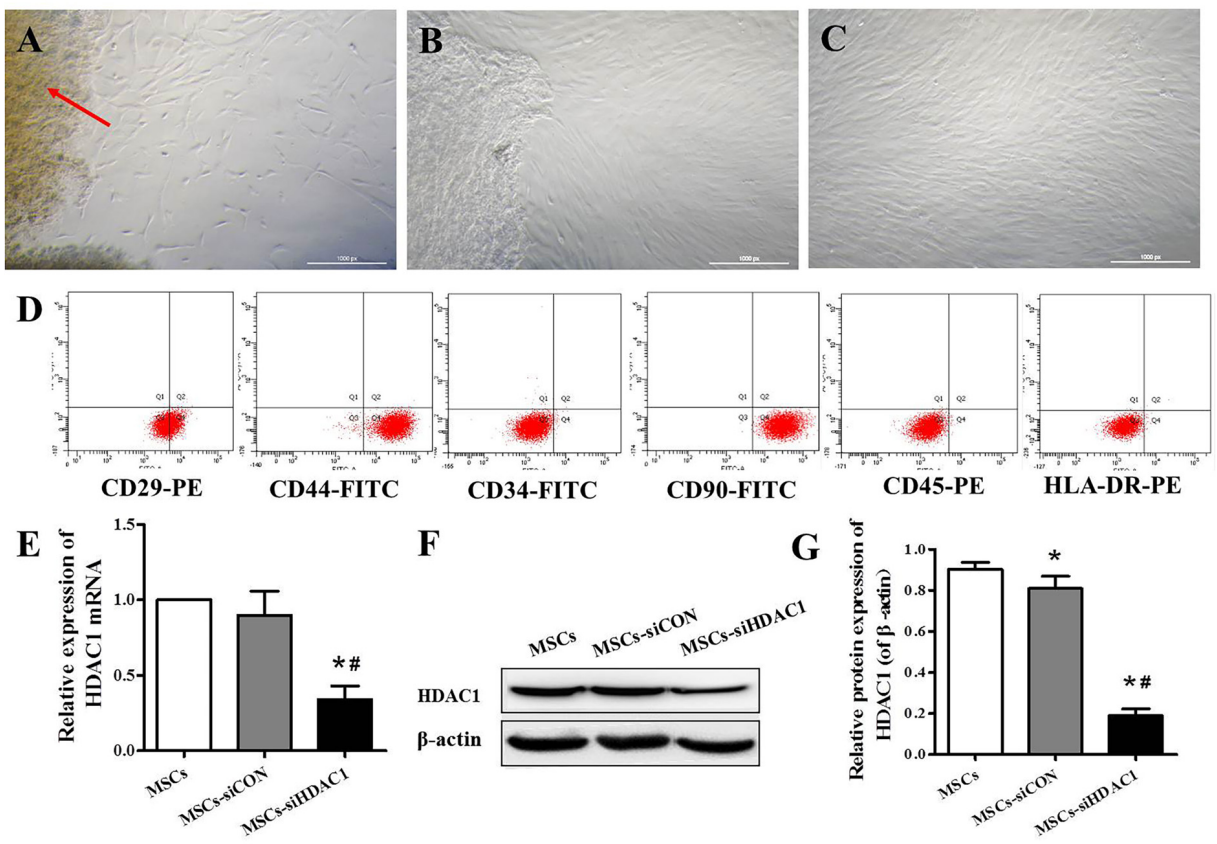


FIGURE 1 | Characterization of human umbilical cord-derived mesenchymal stem cells (hUC-MSCs) and expression of histone deacetylase 1 (HDAC1) in hUC-MSCs. **(A)** Wharton's jelly tissue pieces (red arrow) were plated and cultured to allow primary hUC-MSCs (P0) to grow out. **(B)** MSCs after 2 weeks of primary culture (P0). **(C)** P3 hUC-MSCs, Scale bar = 100 μm. **(D)** Immunophenotypic characterization of hUC-MSCs by flow cytometry. **(E)** Relative HDAC1 mRNA expression by quantitative real-time-PCR (qRT-PCR). **(F)** Representative expression of HDAC1 by Western blotting and **(G)** densitometric analysis of HDAC1 protein. Data are presented as mean ± SEM. $^{*}p < 0.05$ vs. MSCs, $^{\#}p < 0.05$ vs. MSCs-siCON (MSCs transfected with silencing lentivirus control).

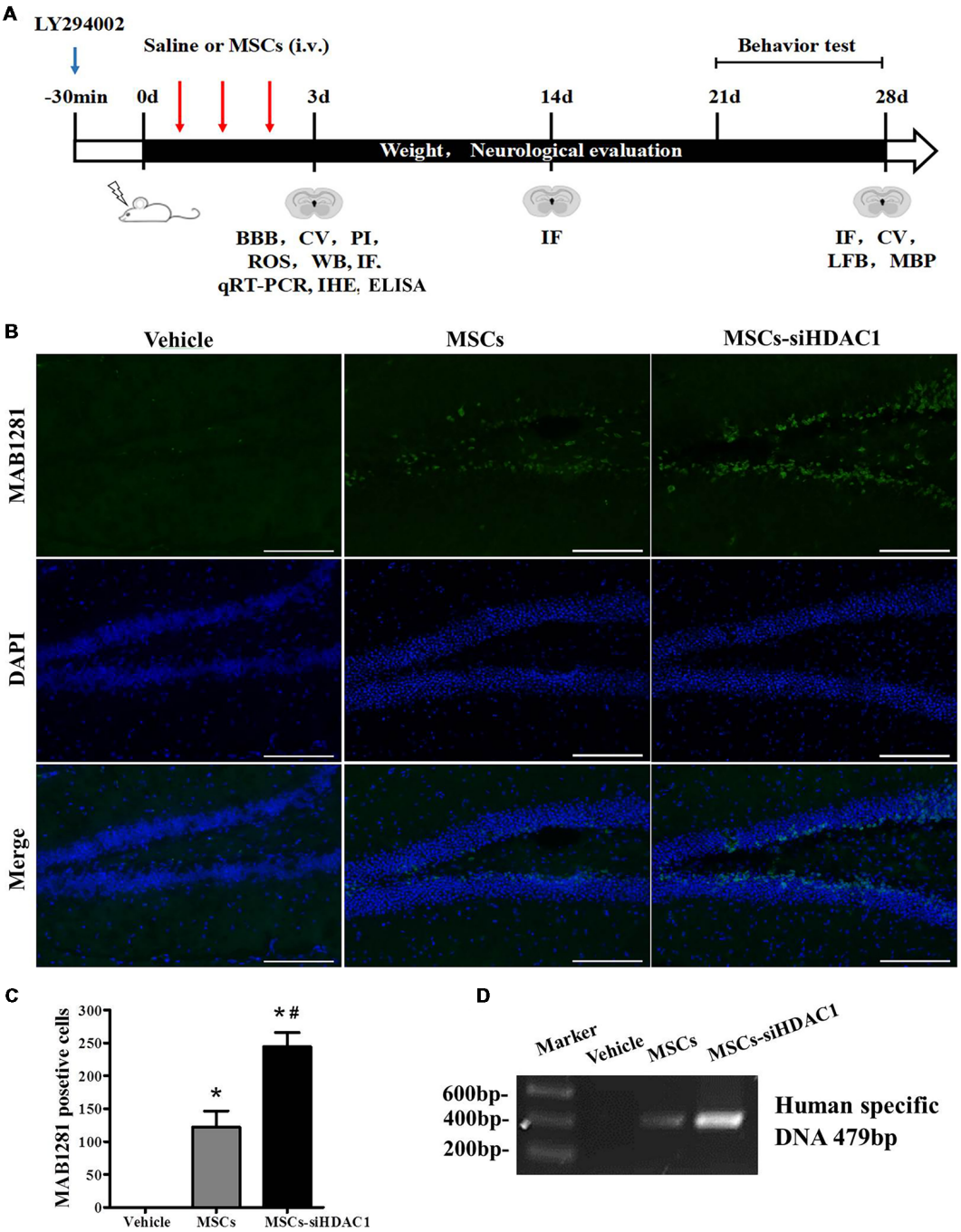


FIGURE 2 | HDAC1 silence enhanced the engraftment of hUC-MSCs in the hippocampus of traumatic brain injury (TBI) mice. **(A)** Overview of experimental design and timeline for experiment. **(B)** Representative immunofluorescent images. **(C)** Quantification analysis of MAB1281^{+} (green) cells in the dentate gyrus of hippocampus, Scale bar = 200 μm. **(D)** Polymerase chain reaction (PCR) results of the human-specific DNA in the hippocampus of TBI mouse. Data were from three mice of each group and three slides of each mouse. Data are presented as mean ± SEM. $^{*}p < 0.05$ vs. Vehicle, $^{\#}p < 0.05$ vs. MSCs.

Western Blotting

Total protein of injured cortical tissue from the perilesional area was harvested. Western blotting was performed (Yu et al., 2013). Equal amounts of protein were separated by SDS-PAGE and transferred to PVDF membrane (Millipore, USA). The membrane was blocked with 5% nonfat milk for 2 h at room temperature and incubated with primary antibodies respectively directed against Bcl2 (1:500, Proteintech, China), Caspase3 (1:500, Proteintech, China), Cleaved Caspase3 (1:500, Proteintech, China), HDAC1 (1:500;

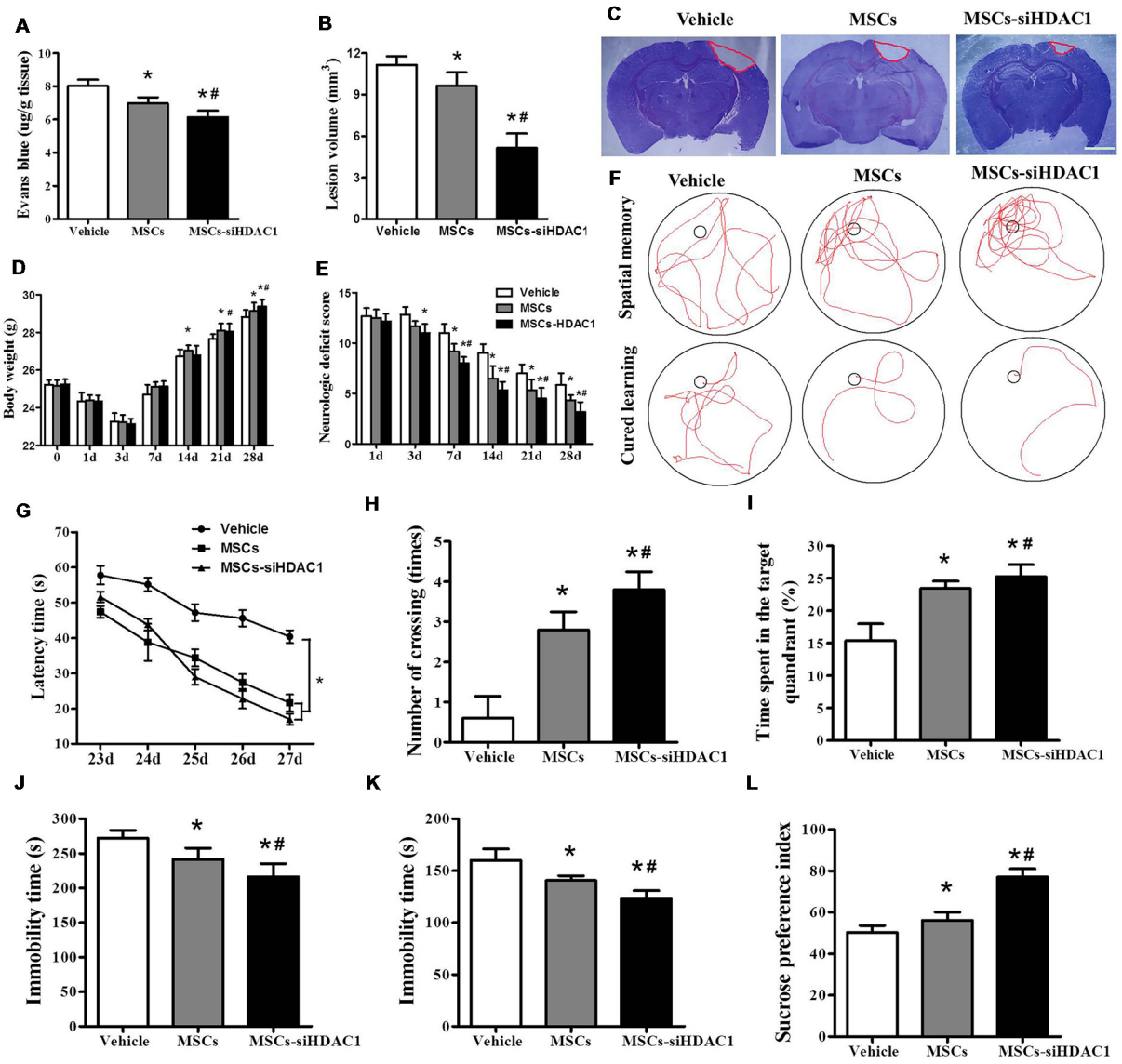


FIGURE 3 | HDAC1-silenced MSCs rescued impaired neural function after TBI. **(A)** Quantitative analysis of extravasated evans blue (EB) dye in the ipsilateral cerebral hemisphere tissue of mice at 3 days after TBI. **(B)** Quantification of lesion volume and **(C)** representative images of cresyl violet (CV) staining, Scale bar = 1 mm. **(D)** Body weight, **(E)** modified neurologic severity score (mNSS) scores. **(F)** Representative tracings from the Morris water maze (MWM) test of the mice. Escape latency **(G)**, platform crossing numbers **(H)**, and time in the target quadrant **(I)** were measured using MWM test. **(J)** Forced swim test (FST), **(K)** tail suspension test (TST), **(L)** Sucrose preference test (SPT). The data were collected from 15 mice in each group and are presented as mean ± SEM. $^{*}p < 0.05$ vs. Vehicle, $^{\#}p < 0.05$ vs. MSCs.

Abcam, Cambridge, England), PTEN (1:500; Sangon Biotech, Shanghai, China), Phospho-PTEN (Ser380/Thr382/Thr383; 1:500; Sangon Biotech, Shanghai, China), AKT-1 (1:500; Sangon Biotech, Shanghai, China), Phospho-AKT1 (Ser473; 1:500; Sangon Biotech, Shanghai, China), GSK-3β (1:500; Proteintech, Wuhan, China), Phospho-GSK-3β (Ser9; 1:500; Cell Signaling Technology, American), or β-actin (1:5,000; Sangon Biotech, Shanghai, China) at 4°C overnight. After the membrane was washed and incubated with horseradish peroxidase-linked secondary antibody (1:3,000; Sangon Biotech, Shanghai, China) for 2 h. The intensity of the resulting protein bands was quantified using ImageJ software.

Statistical Analysis

Data are presented as mean ± SEM by using SPSS 21.0 statistical analysis software. One-way or two-way analysis of variance (ANOVA) was used to compare multiple groups. Differences between two groups were tested with the LSD- t-test. Data shown were representative of at least three independent experiments. A value of $P < 0.05$ was considered to be statistically significant.

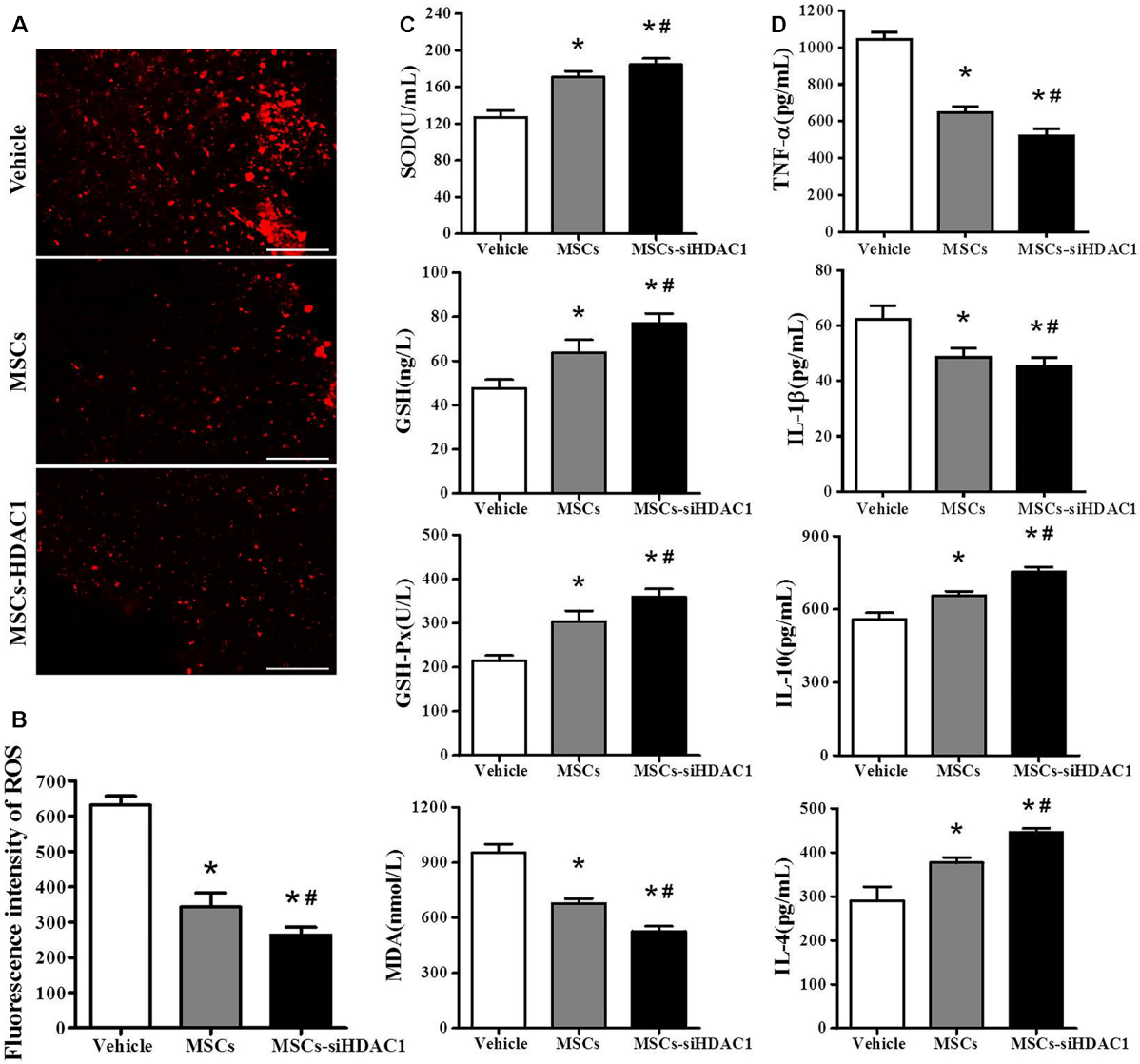


FIGURE 4 | HDAC1-silenced MSCs transplantation attenuated oxidative stress and neuroinflammation in the hippocampus of TBI mice. **(A)** Representative HEt staining on brain sections of different groups at 3 days after TBI. HEt levels in injured cortex. Scale bars = 100 μm. **(B)** Quantification analysis of HEt fluorescence intensity. **(C)** Enzyme-linked immunosorbent assay (ELISA) analysis of SOD, GSH, GSH-Px and MDA at 3 day after TBI. **(D)** ELISA analysis of TNF-α, IL-1β, IL-10, and IL-4 at 3 day after TBI. Data are presented as mean ± SEM. $^{*}p < 0.05$ vs. Vehicle, $^{\#}p < 0.05$ vs. MSCs.

RESULTS

Immunophenotypic Characteristics and Expression of HDAC1 in hUC-MSCs

hUC-MSCs derived from Wharton's jelly, exhibited a fibroblast-like appearance or spindle-shaped morphology at passage 3 (**Figures 1A–C**). Flow cytometry analysis showed that hUC-MSCs were positive for CD29 (99.9%), CD44 (99.1%), and CD90 (99.8%), but negative for CD34 (0.8%), CD45 (1.6%), and HLA-DR (0.2%; **Figure 1D**). To investigate the effects of HDAC1 silence to hUC-MSCs, we generated HDAC1 silenced cells by lentivirus transfection. After transfection at a MOI of 10 for 6 h, the expression of HDAC1 in mRNA and protein level was significantly decreased by about 70%–80% in the MSCs-siHDAC1 group when compared with the MSCs group (**Figures 1E–G**, $p < 0.05$).

HDAC1 Silence Enhanced the Survival and Migration of hUC-MSCs in the Hippocampus of TBI Mice

The complete experimental protocol and timeline were summarized in **Figure 2A**. Previous studies have shown that TBI-induced secondary damage is sufficient to allow MSCs to across the BBB (Cerri et al., 2015). So, the presence of exogenous hUC-MSCs in the hippocampus was measured by using MAB1281 staining (human nuclei antibody) and

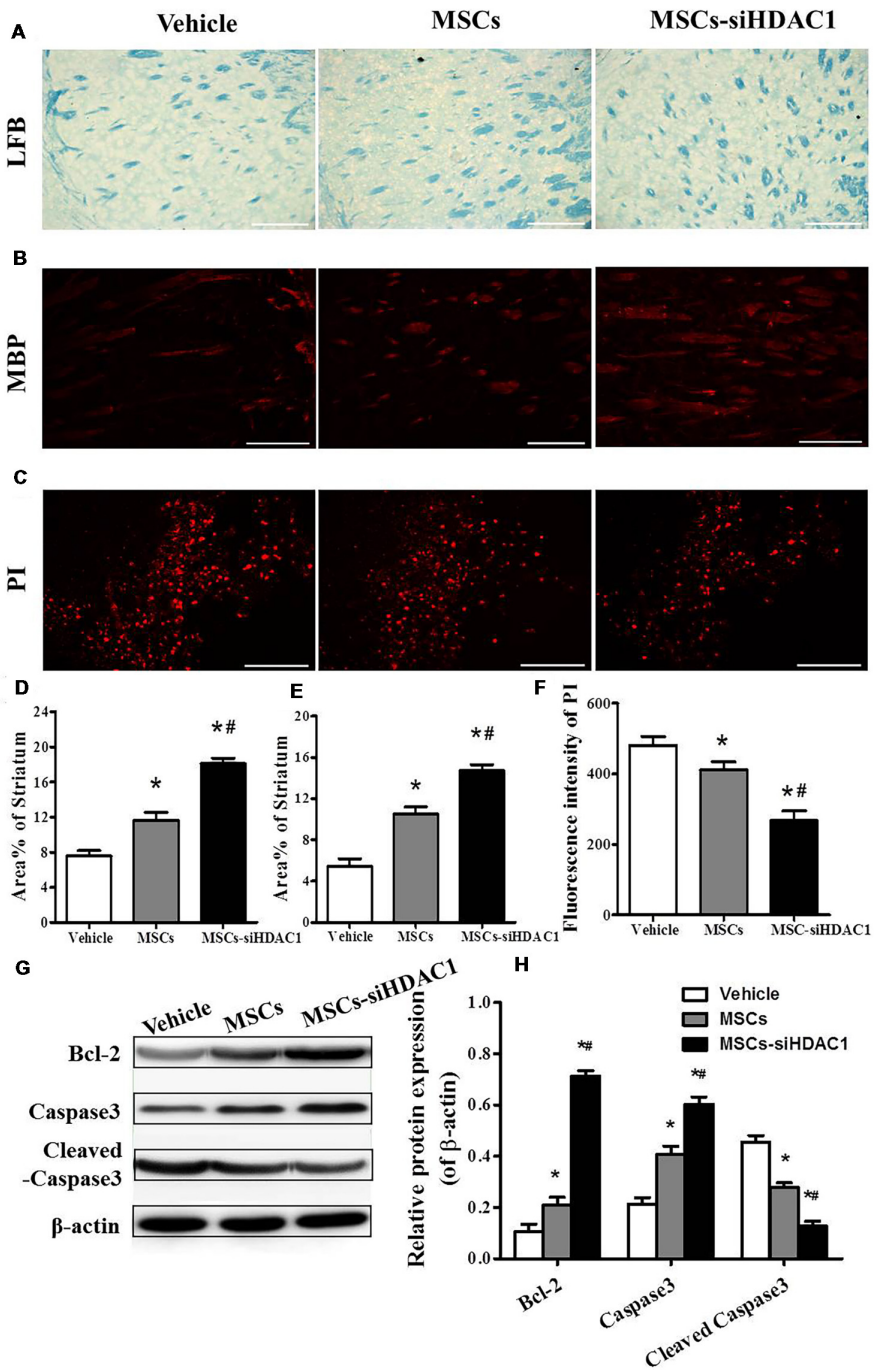


FIGURE 5 | HDAC1-silenced MSCs alleviated white matter injury and reduced cell death after TBI. **(A)** Representative images of luxol fast blue (LFB) staining. Scale bars = 100 μm. **(B)** Myelin basic protein (MBP) staining (red). Scale bars = 200 μm. **(C)** Representative propidium iodide (PI) staining (red) at 3 days after TBI. Scale bars = 100 μm. **(D)** Average area of LFB at 28 days after TBI. **(E)** Average area of MBP. **(F)** Quantitative analysis of PI fluorescence intensity in the injured cortex. **(G)** Western blotting and **(H)** densitometry measurement of Bcl-2, Caspase 3, and Cleaved caspase 3 in the lesion boundary zone of each group at 3 days post-injury. Data are presented as mean ± SEM. $^{*}p < 0.05$ vs. Vehicle, $^{\#}p < 0.05$ vs. MSCs.

PCR for human specific DNA. As shown in **Figures 2B,C**, the number of MAB1281^{+} cells in the MSCs-siHDAC1 group was significantly higher than that in the MSCs group ($p < 0.05$) and Vehicle group ($p < 0.05$) at 7 days after hUC-MSCs transplantation respectively. PCR result was in accordance with immunofluorescence staining with more human DNA in the MSCs-siHDAC1 group (**Figure 2D**). These results indicate that HDAC1 silence enhances the survival and

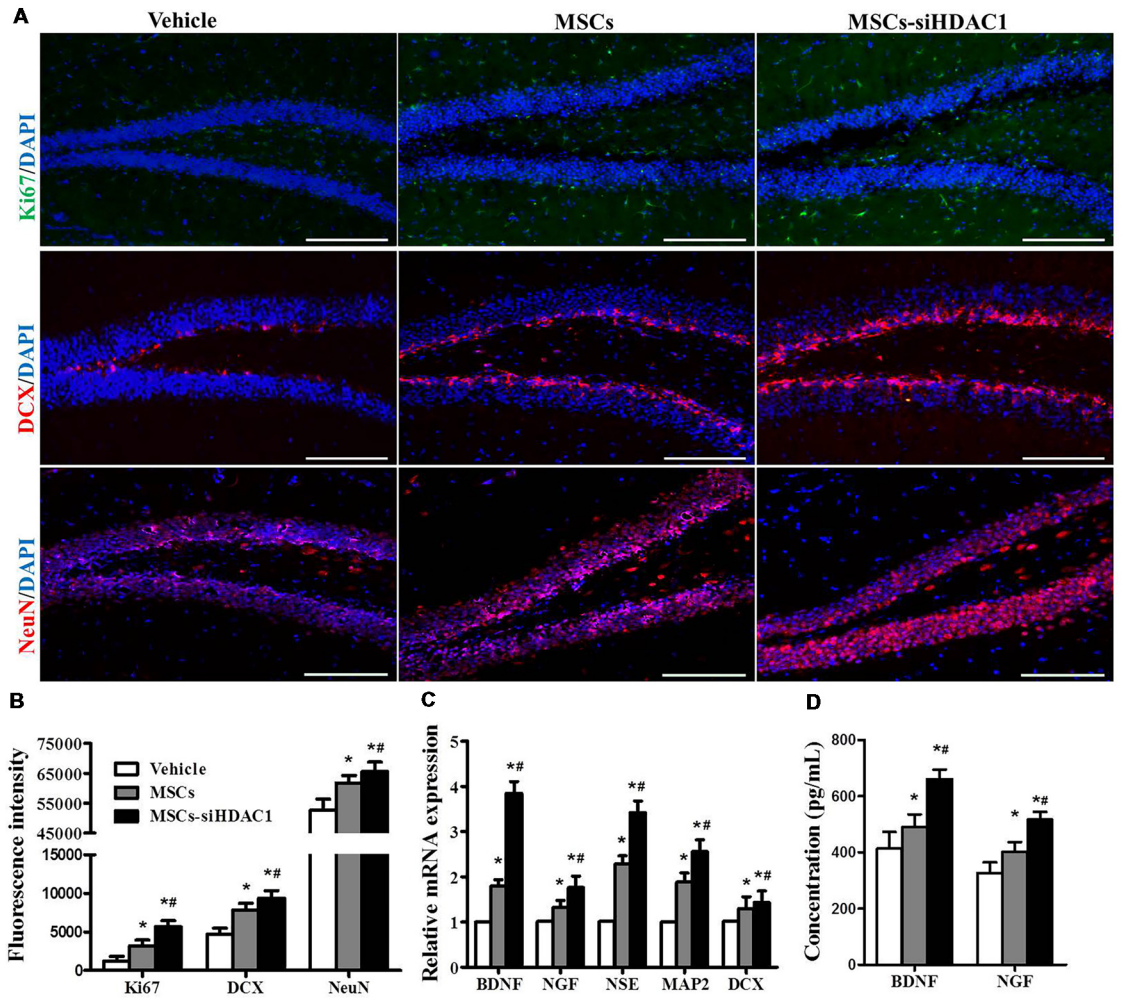


FIGURE 6 | HDAC1-silenced MSCs increased neurogenesis in the hippocampus of TBI mice. **(A)** Representative immunofluorescent images. **(B)** Quantification analysis of fluorescence intensity indicated that Ki67$^+$ (green), DCX$^+$ (red), and NeuN$^+$ (Red) cells in the dentate gyrus of hippocampus in each field, Scale bar = 200 μm. **(C)** Expression of BDNF, NGF, NSE, MAP2 and DCX by qRT-PCR. **(D)** ELISA analysis of BNDF and NGF levels at 28 day after TBI. Data were from three mice of each groups and are presented as mean ± SEM. $^*p < 0.05$ vs. Vehicle, $^\#p < 0.05$ vs. MSCs.

migration of hUC-MSCs in the hippocampus of TBI mice after transplantation via tail vein.

HDAC1-Silenced MSCs Decreased BBB Permeability, Reduced Lesion Volume and Improved Neural Function Recovery After TBI

EB dye cannot pass through an intact BBB; however, following TBI, EB easily permeates a compromised BBB (Cerri et al., 2015; Chen et al., 2018). As shown in **Figure 3A**, MSCs-siHDAC1 group attenuated TBI-induced EB leakage in the ipsilateral hemisphere compared with the vehicle group and MSCs group at day 3-post TBI ($p < 0.05$, **Figure 3A**). In addition, the lesion volume was significantly reduced in MSCs-siHDAC1 group and MSCs group than vehicle group ($p < 0.05$, **Figures 3B,C**). From 14 days after TBI, body weight recovered in all treatment groups. Body weight was highest in the MSCs-siHDAC1 group, but least in the vehicle group compared with the other groups ($p < 0.05$, **Figure 3D**).

The neurological recovery was analyzed by mNSS ($p < 0.05$, **Figure 3E**), MWM (**Figures 3F–I**) and the depressive-like behaviors by sucrose preference test (SPT), forced swimming test (FST) and tail suspension test (TST; **Figures 3J–L**). As expected, the vehicle-infused TBI mice exhibited significant impairments in mNSS and MWM test. However, the mNSS scores were significantly lower in MSCs-siHDAC1 groups on the 3rd to 28th day compared with that of Vehicle and MSCs group ($p < 0.05$, **Figure 3E**). In the MWM test for evaluating spatial learning and memory ability, MSCs-siHDAC1 transplanted mice performed significantly better than other groups (**Figure 3F**), as indicated by significantly shorter latency, more crossing numbers and a higher proportion of time spent in the target quadrant ($p < 0.05$, **Figures 3G–I**).

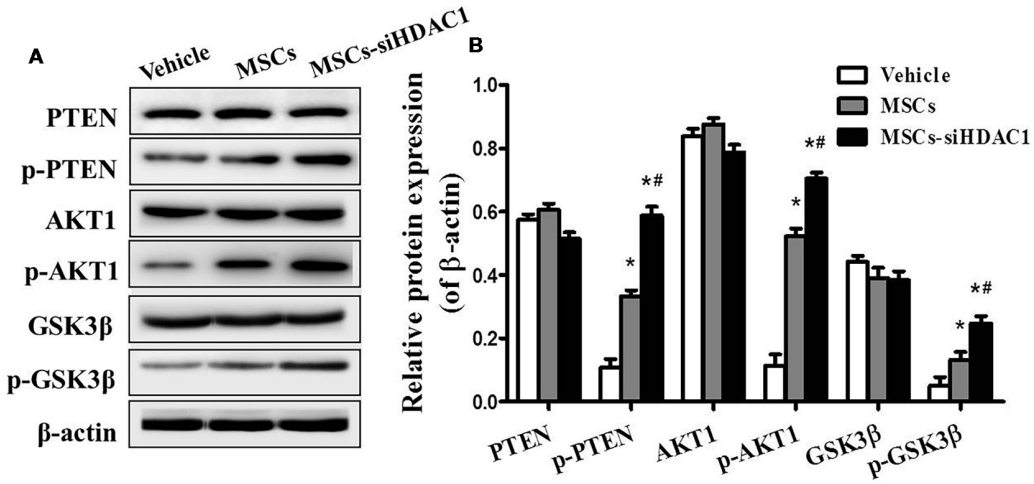


FIGURE 7 | HDAC1-silenced MSCs modulated the protein expression of PI3K/Akt pathway in hippocampus. **(A)** Representative Western blot bands of PTEN, phosphorylated PTEN (p-PTEN), AKT1, phosphorylated AKT1 (p-AKT1), GSK-3β, and phosphorylated GSK-3β (p-GSK-3β) in each group. **(B)** Quantitative protein levels were normalized with β-actin. Data are presented as mean ± SEM. $^{*}p < 0.05$ vs. Vehicle, $^{\#}p < 0.05$ vs. MSCs.

Additionally, MSCs-siHDAC1 treatment significantly decreased the immobility time of FST and TST compared with those in MSCs and Vehicle treated mice ($p < 0.05$, **Figures 3J,K**). Similarly, the sucrose preference index was higher in MSCs-siHDAC1 groups compared with those in MSCs groups ($p < 0.05$, **Figure 3L**). These results indicate that HDAC1-silenced MSCs alleviate BBB permeability and lesion volume, and improve neural function of TBI mice.

HDAC1-Silenced MSCs Attenuated Oxidative Stress and Neuroinflammation of TBI Mice

Previous studies demonstrated that TBI resulted in substantial oxidative stress and neuroinflammatory reaction in the injured sites (Angeloni et al., 2015; Corrigan et al., 2016; Russo and McGavern, 2016). So, we assessed the oxidative stress by HEt staining and ELISA. After mice were injected with Het, ROS was observed as red fluorescence signal around the lesion at 3-day post-TBI (**Figure 4A**). However, the MSCs-siHDAC1 transplanted mice exhibited less ROS production than MSCs group and vehicle groups (**Figure 4B**, $p < 0.05$). The activity of SOD, GSH, and GSH-Px in the MSCs-siHDAC1 group was significantly higher than those of MSCs and Vehicle group, whereas the level of MDA was lower (**Figure 4C**, $p < 0.05$). As shown in **Figure 4D**, the expression level of IL-1β and TNF-α were down-regulated, while, IL-4 and IL-10 were up-regulated in the MSCs-siHDAC1 group (**Figure 4D**, $p < 0.05$). Our findings suggest that HDAC1-silenced MSCs reduce oxidative stress and neuroinflammation of TBI mice.

HDAC1-Silenced MSCs Alleviated Myelin Loss and Reduced Cell Death

It is well known that TBI causes demyelination and neuron death (Gao et al., 2006; Mierzwa et al., 2015). On day 28 after TBI, LFB staining (**Figure 5A**) and MBP staining (**Figure 5B**) were used to label normal myelin in the section. Both LFB and MBP staining procedures showed that the percentage of normal-appearing myelin in the MSCs-siHDAC1 group was significantly higher than that in the Vehicle group and MSCs group respectively ($p < 0.05$, **Figures 5A,B,D,E**). At 3 days after TBI, the cell death in the injured site was measured by PI staining. As shown in **Figures 5C,F**, MSCs-siHDAC1 decreased PI fluorescence intensity compared with that in the Vehicle group and MSCs group ($p < 0.05$), which was further confirmed by the up-regulated expression of Bcl-2 and Caspase3, while down-regulated of cleaved caspase3 in the hippocampus ($p < 0.05$, **Figures 5G,H**).

HDAC1 Silenced MSCs Enhanced the Cell Proliferation Neurogenesis

To further investigate the contribution of MSCs-siHDAC1 to hippocampal neurogenesis, immunofluorescence staining of Ki67 (Acosta et al., 2017; Nuclear proliferation marker), DCX (immature neuronal marker) and NeuN (mature neuronal marker) was performed (Blaya et al., 2015; Neuberger et al., 2017). As shown in **Figures 6A,B**, MSCs-siHDAC1 group displayed increased fluorescence intensity of Ki67, DCX and NeuN, which represented greater number of $Ki67^{+}$, DCX^{+} and $NeuN^{+}$ cells, compared to those in MSCs group and Vehicle group respectively ($p < 0.05$). These results were confirmed by the enhanced mRNA expression of NSE, MAP2, and DCX in the hippocampus ($p < 0.05$, **Figure 6C**). Furthermore, compared with Vehicle group, MSCs and MSCs-siHDAC1 obviously increased BDNF and NGF production, which were detected by qRT-PCR and ELISA ($p < 0.05$, **Figures 6C,D**). So, our findings indicate that MSCs-siHDAC1 treatment enhances hippocampal neurogenesis in TBI mice.

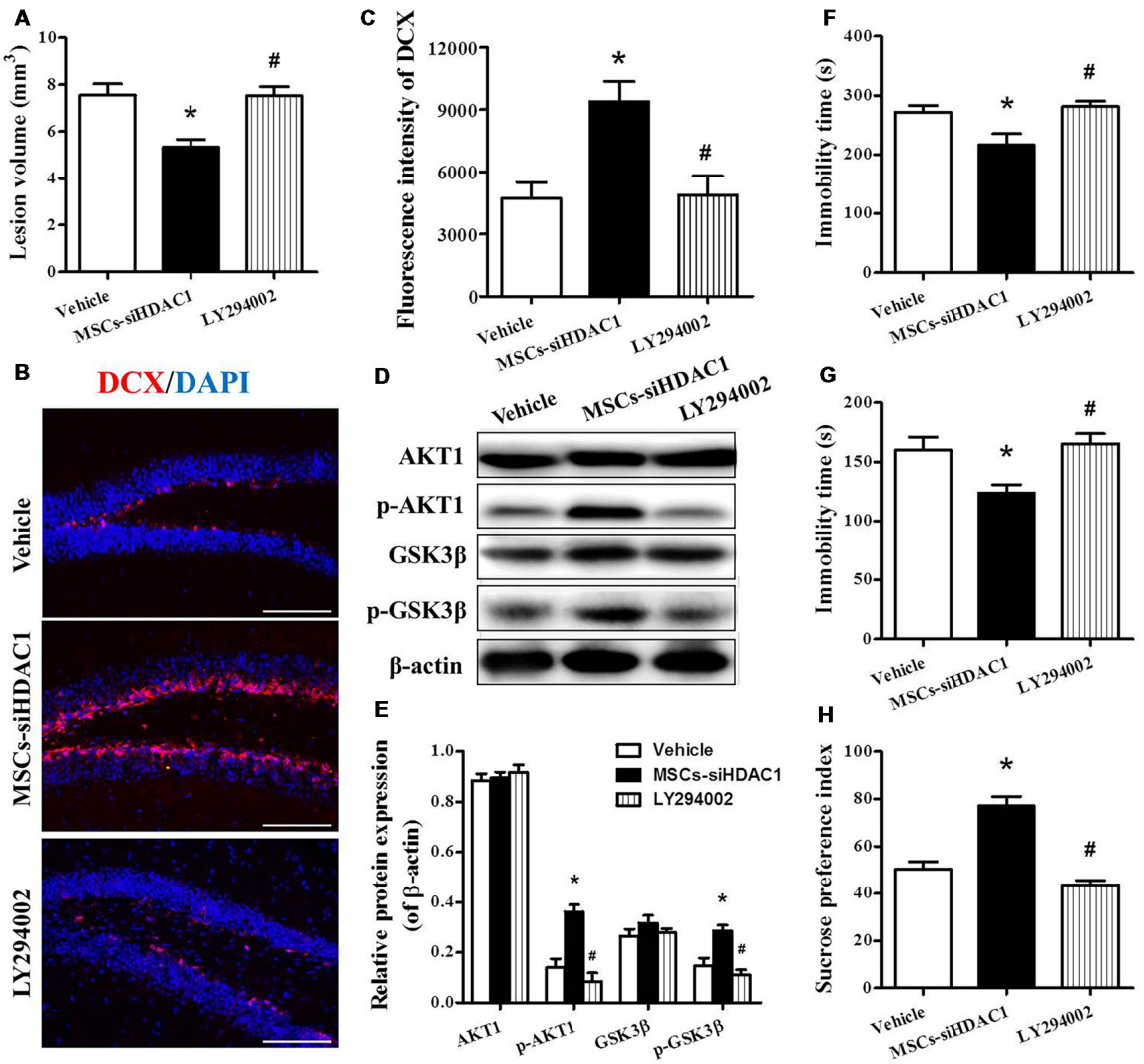


FIGURE 8 | LY294002 abolished the effects of HDAC1-silenced MSCs on neurologic function and the PI3K/AKT pathway of TBI mice. **(A)** Quantification of lesion volume. **(B)** Representative immunofluorescent images. **(C)** Quantification analysis of fluorescence intensity indicated that DCX$^+$ (red) cells in the dentate gyrus of the hippocampus in each field, Scale bar = 200 μm. **(D)** Representative Western blot and **(E)** densitometry measurement of AKT1, p-AKT1, GSK-3β, and p-GSK-3β in each group at 3 days post-TBI, **(F)** TST, **(G)** FST, **(H)** SPT. Data are presented as mean ± SEM. $^*p < 0.05$ vs. Vehicle, $^\#p < 0.05$ vs. MSCs-siHDAC1.

HDAC1 Silenced MSCs Activated the PI3K/AKT Pathway in Hippocampus of TBI Mice

To further study the mechanism underlying the neuroprotective effects of MSCs-siHDAC1 in TBI mice, western blotting was used to examine the protein expression of the PI3K/AKT pathway in the hippocampus at 28 days after TBI. As shown in **Figure 7**, the expression levels of phosphorylated PTEN (p-PTEN), p-AKT and p-GSK-3β were significantly elevated in the hippocampus of TBI mice after infusion with MSCs and MSCs-siHDAC1 ($p < 0.05$), whereas the total PTEN, AKT and GSK-3β expression remained unchanged ($p > 0.05$, **Figure 7B**). To conclude, MSCs and MSCs-siHAC1 both activate PI3K/AKT signaling pathway.

Inhibition of PI3K/AKT Attenuated the Neuroprotective Effect of HDAC1 Silenced MSCs on TBI Mice

In order to clarify whether MSCs-siHDAC1 exerts a neuroprotective effect by activation of PI3K/AKT signaling, LY294002, a specific inhibitor of the PI3K/AKT pathway (Wen et al., 2018), was injected into mice before TBI and stem cell transplantation. As expected, Western blotting revealed that the protein expression of p-AKT and p-GSK-3β were markedly decreased following co-treatment with LY294002 and MSCs-siHDAC1 ($p < 0.05$, **Figures 8D,E**) compared with the MSCs-siHDAC1 treated TBI mice. In addition, LY294002 significantly attenuated the MSCs-siHDAC1 induced lesion volume (**Figure 8A**), neurogenesis (**Figures 8B,C**)

and neurologic function improvement, which appeared as significantly increased immobility time of TST (**Figure 8F**) and FST (**Figure 8G**), and decreased sucrose preference index (**Figure 8H**; $p < 0.05$). Thus, MSCs-siHDAC1 promoted neurologic function recovery of TBI mice by activating the PI3K/AKT pathway.

DISCUSSION

TBI causes extensive neurologic disability and mortality for individuals worldwide. Currently, no available drug is effective for clinical treatment of TBI. In this study, we report that MSC transplantation with HDAC1 silencing provide neuroprotection in a mouse model of TBI, and this neuroprotective effects is likely due to the activation of PI3K/AKT signaling pathway.

Acetylation/deacetylation of histones is an important mechanism to regulate gene expression and chromatin remodeling (Qureshi and Mehler, 2014). Previous studies have revealed that HDAC inhibition provides a statistically significant protection in Alzheimer's disease, cerebral ischemia or ischemia/reperfusion model (Shein and Shohami, 2011; Ganai et al., 2016). Furthermore, HDAC1 regulates stem cell proliferation and neural differentiation *in vitro* (Cho and Cavalli, 2014; Lv et al., 2014). The expression of HDAC1 in neurons is surprisingly lower than that in undifferentiated stem cells (Jacob et al., 2014). Our present study supports the view that HDAC1 silencing could promote the migration and neural differentiation of hUC-MSCs in TBI.

TBI patients often suffer from motor and sensory deficits, cognitive impairments, and neuropsychiatric symptoms such as depression and anxiety (Malkesman et al., 2013). MWM is widely used for evaluating learning and memory abilities (Cui et al., 2017). TST, FST, and SPT are widely used to evaluate the depression degree of animals (Watanabe et al., 2013; Cheng et al., 2016). In the current study, our behavioral results showed that Vehicle treated TBI mice exhibited significant motor and cognitive impairments, but these dysfunctions were remarkably attenuated by MSCs and MSCs-siHDAC1 transplantation, following by lower mNSS scores and immobility time, better cognitive capacity, and higher sucrose preference index, indicating that MSCs, especially HDAC1-silenced MSCs transplantation can reduce the depression s and improve the neurologic function of TBI mice.

TBI markedly disturbed the integrity of the BBB and increased extravasation of EB dye (Li H. et al., 2016). Recent evidence indicates that the intravenously transplanted stem cells cross the BBB, migrate to the brain and improve the cognition in AD mice (Xie et al., 2016; Wang et al., 2018). Our results showed that the human cells and human-specific DNA were presented in the hippocampus of TBI mice about 3 days after MSCs transplantation, which could attenuate TBI-induced EB leakage in the ipsilateral hemisphere (Li H. et al., 2016).

TBI results in oxidative stress and immune activation (Corrigan et al., 2016; Russo and McGavern, 2016). When the rapid accumulation of ROS exceeds the capacity of antioxidant system scavenging, this oxidative stress eventually lead to neuronal cell death (Angeloni et al., 2015). In our study, we found that both MSCs and MSCs-siHDAC1 treatment led to a significant decrease of myelin loss, ROS production and MDA level, and an increased tendency of SOD, GSH, and GSH-Px as well as changes of neuroinflammatory markers including TNF-α, IL-1β, IL-4 and IL-10 when compared with the vehicle group respectively. But, MSCs-siHDAC1 treatment showed better effects than MSCs treatment. These findings implied that MSCs alleviated myelin loss, oxidative stress and neuroinflammation of TBI mice might though HDAC1.

Cell death, neurodegeneration and decreased hippocampal neurogenesis occur after TBI secondary brain injury (Reis et al., 2015). Our data showed that MSCs-siHDAC1 alleviated white matter injury and reduced cell death after TBI. Furthermore, transplanted MSCs-siHDAC1 contributed to functional recovery of TBI, which suggested that several mechanisms may be involved in this process. MSCs-siHDAC1 administration may provide a more favorable microenvironment for the activation of neurogenesis. The expression of Ki67, DCX and NeuN in the MSCs-siHDAC1 group was significantly higher than those in MSCs and Vehicle groups, which accompanied by increased expression of BDNF, NGF, NSE, MAP2, and DCX in the hippocampus. Therefore, MSCs-siHDAC1 transplantation may inhibit cell death and promote neurogenesis in the hippocampus of TBI mice.

PI3K/AKT signaling pathway exerts powerful effects on neuronal survival after injury and plays an important role in the neuroprotection, neuronal apoptosis and neurogenesis (Backman et al., 2001; Park et al., 2008; van Diepen and Eickholt, 2008). Meanwhile, some reports have verified that HDAC inhibition modulates the PTEN/PI3K/AKT axis to combat TBI and neurological diseases characterized by white matter as well as gray matter destruction, such as stroke and neurodegenerative disorders (Liu et al., 2012; Wang et al., 2015). PTEN is a negative regulator of PI3K/AKT signal transduction (Backman et al., 2001; Park et al., 2008; van Diepen and Eickholt, 2008). Inhibition of PTEN activity is currently seen as a persuasive target for increasing regenerative capacities of neurons affected in degenerative conditions, or following an injury to the nervous system (Park et al., 2008). In the early stage after TBI, inhibition of PTEN improved neurological function recovery by decreasing BBB permeability and apoptosis (Wang et al., 2015). Previous studies indicated that HDAC inhibition promoted the cytosolic retention of GSK3β (Zhang et al., 2015), where it may be more likely to inactivate cytoplasmic PTEN (Wang et al., 2015). In this study, we found that phosphorylation of PTEN, AKT, and GSK-3β was significantly elevated in the hippocampus of TBI mice after MSCs and MSCs-siHDAC1 transplantation. Interestingly, these MSCs-siHDAC1-induced changes of the expression of p-PTEN, p-AKT, and p-GSK3β along with recovery neurologic function in TBI mice were markedly attenuated by LY294002. Thus, our data suggest that improved neurological function, enhanced neurogenesis, alleviated neural apoptosis and oxidative stress might be mediated by PI3K/AKT pathway.

CONCLUSION

HDAC1 silencing promotes hUC-MSCs engraftment in the hippocampus and enhances the efficacy of hUC-MSCs in a TBI model by improving neurological function, enhancing neurogenesis and alleviating neural apoptosis and oxidative stress in the hippocampus. The mechanisms underlying these neuroprotective effects involve in the activation of PI3K/AKT signaling pathway. In conclusion, HDAC1 silenced hUC-MSCs transplantation could provide an effective therapy for TBI.

AUTHOR CONTRIBUTIONS

SM and FG conceived and designed the experiments, and revised the final version of the article. BY and TC participated in designing and guiding the experiments. JZha and XZa provided experimental guidance and technical support. LX and QX performed the experiments. LX, QX and TH analyzed the data. SM, LX, YC and FG wrote the manuscript. JZho, TL, YW, XZh and GY prepared reagents and materials and performed part of the experiments. All authors reviewed the manuscript prior to submission.

FUNDING

This study was supported by the National Natural Science Foundation of China (U1404313, 81601078, 81471306), the Innovative Research Team in Science and Technology of the University of Henan Province (15IRTSTHN022), the Plan for Scientific Innovation Talent of Henan Province (154200510008), the Key Research Project of Higher Education of Henan Province (17A310012).

ACKNOWLEDGMENTS

We thank Dr. David Spray in Einstein college of Medicine, USA for his effort in language revision and other suggestions for the project.

REFERENCES

Acosta, S. A., Tajiri, N., Sanberg, P. R., Kaneko, Y., and Borlongan, C. V. (2017). Increased amyloid precursor protein and Tau expression manifests as key secondary cell death in chronic traumatic brain injury. *J. Cell. Physiol.* 232, 665–677. doi: 10.1002/jcp.25629

Angeloni, C., Prata, C., Dalla Sega, F. V., Piperno, R., and Hrelia, S. (2015). Traumatic brain injury and NADPH oxidase: a deep relationship. *Oxid. Med. Cell. Longev.* 2015:370312. doi: 10.1155/2015/370312

Backman, S. A., Stambolic, V., Suzuki, A., Haight, J., Elia, A., Pretorius, J., et al. (2001). Deletion of Pten in mouse brain causes seizures, ataxia and defects in soma size resembling Lhermitte-Duclos disease. *Nat. Genet.* 29, 396–403. doi: 10.1038/ng782

Benito, E., Urbanke, H., Ramachandran, B., Barth, J., Halder, R., Awasthi, A., et al. (2015). HDAC inhibitor-dependent transcriptome and memory reinstatement in cognitive decline models. *J. Clin. Invest.* 125, 3572–3584. doi: 10.1172/jci79942

Blaya, M. O., Tsoulfas, P., Bramlett, H. M., and Dietrich, W. D. (2015). Neural progenitor cell transplantation promotes neuroprotection, enhances hippocampal neurogenesis and improves cognitive outcomes after traumatic brain injury. *Exp. Neurol.* 264, 67–81. doi: 10.1016/j.expneurol.2014.11.014

Cai, M. H., Xu, X. G., Yan, S. L., Sun, Z., Ying, Y., Wang, B. K., et al. (2018). Depletion of HDAC1, 7 and 8 by histone deacetylase inhibition confers elimination of pancreatic cancer stem cells in combination with gemcitabine. *Sci. Rep.* 8:1621. doi: 10.1038/s41598-018-20004-0

Cerri, S., Greco, R., Levandis, G., Ghezzi, C., Mangione, A. S., Fuzzati-Armentero, M. T., et al. (2015). Intracarotid infusion of mesenchymal stem cells in an animal model of Parkinson's disease, focusing on cell distribution and neuroprotective and behavioral effects. *Stem Cells Transl. Med.* 4, 1073–1085. doi: 10.5966/sctm.2015-0023

Chen, S., Ye, J., Chen, X., Shi, J., Wu, W., Lin, W., et al. (2018). Valproic acid attenuates traumatic spinal cord injury-induced inflammation via STAT1 and NF-κB pathway dependent of HDAC3. *J. Neuroinflammation* 15:150. doi: 10.1186/s12974-018-1193-6

Cheng, T., Yang, B., Li, D., Ma, S., Tian, Y., Qu, R., et al. (2015). Wharton's Jelly transplantation improves neurologic function in a rat model of traumatic brain injury. *Cell. Mol. Neurobiol.* 35, 641–649. doi: 10.1007/s10571-015-0159-9

Cheng, T., Wang, W., Li, Q., Han, X., Xing, J., Qi, C., et al. (2016). Cerebroprotection of flavanol (−)-epicatechin after traumatic brain injury via Nrf2-dependent and -independent pathways. *Free Radic. Biol. Med.* 92, 15–28. doi: 10.1016/j.freeradbiomed.2015.12.027

Cho, Y., and Cavalli, V. (2014). HDAC signaling in neuronal development and axon regeneration. *Curr. Opin. Neurobiol.* 27, 118–126. doi: 10.1016/j.conb.2014.03.008

Corrigan, F., Mander, K. A., Leonard, A. V., and Vink, R. (2016). Neurogenic inflammation after traumatic brain injury and its potentiation of classical inflammation. *J. Neuroinflammation* 13:264. doi: 10.1186/s12974-016-0738-9

Cui, Y., Ma, S., Zhang, C., Cao, W., Liu, M., Li, D., et al. (2017). Human umbilical cord mesenchymal stem cells transplantation improves cognitive function in Alzheimer's disease mice by decreasing oxidative stress and promoting hippocampal neurogenesis. *Behav. Brain Res.* 320, 291–301. doi: 10.1016/j.bbr.2016.12.021

Ganai, S. A., Ramadoss, M., and Mahadevan, V. (2016). Histone Deacetylase (HDAC) Inhibitors—emerging roles in neuronal memory, learning, synaptic plasticity and neural regeneration. *Curr. Neuropharmacol.* 14, 55–71. doi: 10.2174/1570159x13666151021111609

Gao, W. M., Chadha, M. S., Kline, A. E., Clark, R. S., Kochanek, P. M., Dixon, C. E., et al. (2006). Immunohistochemical analysis of histone H3 acetylation and methylation—evidence for altered epigenetic signaling following traumatic brain injury in immature rats. *Brain Res.* 1070, 31–34. doi: 10.1016/j.brainres.2005.11.038

Jacob, C., Lötscher, P., Engler, S., Baggiolini, A., Varum Tavares, S., Brügger, V., et al. (2014). HDAC1 and HDAC2 control the specification of neural crest cells into peripheral glia. *J. Neurosci.* 34, 6112–6122. doi: 10.1523/jneurosci.5212-13.2014

Jamaladdin, S., Kelly, R. D., O'Regan, L., Dovey, O. M., Hodson, G. E., Millard, C. J., et al. (2014). Histone deacetylase (HDAC) 1 and 2 are essential for accurate cell division and the pluripotency of embryonic stem cells. *Proc. Natl. Acad. Sci. U S A* 111, 9840–9845. doi: 10.1073/pnas.1321330111

Juliandi, B., Abematsu, M., and Nakashima, K. (2010). Epigenetic regulation in neural stem cell differentiation. *Dev. Growth Differ.* 52, 493–504. doi: 10.1111/j.1440-169X.2010.01175.x

Kang, W. C., Oh, P. C., Lee, K., Ahn, T., and Byun, K. (2016). Increasing injection frequency enhances the survival of injected bone marrow derived mesenchymal stem cells in a critical limb ischemia animal model. *Korean J. Physiol. Pharmacol.* 20, 657–667. doi: 10.4196/kjpp.2016.20.6.657

Koh, S. H., Kim, K. S., Choi, M. R., Jung, K. H., Park, K. S., Chai, Y. G., et al. (2008). Implantation of human umbilical cord-derived mesenchymal stem cells as a neuroprotective therapy for ischemic stroke in rats. *Brain Res.* 1229, 233–248. doi: 10.1016/j.brainres.2008.06.087

Kota, D. J., Prabhakara, K. S., van Brummen, A. J., Bedi, S., Xue, H., DiCarlo, B., et al. (2016). Propranolol and mesenchymal stromal cells combine to treat traumatic brain injury. *Stem Cells Transl. Med.* 5, 33–44. doi: 10.5966/sctm.2015-0065

Lebrun-Julien, F., and Suter, U. (2015). Combined HDAC1 and HDAC2 depletion promotes retinal ganglion cell survival after injury through reduction of p53 target gene expression. *ASN Neuro* 7:1759091415593066. doi: 10.1177/1759091415593066

Li, D., Ma, S., Guo, D., Cheng, T., Li, H., Tian, Y., et al. (2016). Environmental circadian disruption worsens neurologic impairment and inhibits hippocampal neurogenesis in adult rats after traumatic brain injury. *Cell. Mol. Neurobiol.* 36, 1045–1055. doi: 10.1007/s10571-015-0295-2

Li, H., Sun, J., Wang, F., Ding, G., Chen, W., Fang, R., et al. (2016). Sodium butyrate exerts neuroprotective effects by restoring the blood-brain barrier in traumatic brain injury mice. *Brain Res.* 1642, 70–78. doi: 10.1016/j.brainres.2016.03.031

Liu, X. S., Chopp, M., Kassis, H., Jia, L. F., Hozeska-Solgot, A., Zhang, R. L., et al. (2012). Valproic acid increases white matter repair and neurogenesis after stroke. *Neuroscience* 220, 313–321. doi: 10.1016/j.neuroscience.2012.06.012

Liu, S., Shen, G. Y., Deng, S. K., Wang, X. B., Wu, Q. F., and Guo, A. S. (2013). Hyperbaric oxygen therapy improves cognitive functioning after brain injury. *Neural Regen. Res.* 8, 3334–3343. doi: 10.3969/j.issn.1673-5374.2013.35.008

Lv, W., Guo, X., Wang, G., Xu, Y., and Kang, J. (2014). Histone deacetylase 1 and 3 regulate the mesodermal lineage commitment of mouse embryonic stem cells. *PLoS One* 9:e113262. doi: 10.1371/journal.pone.0113262

Malkesman, O., Tucker, L. B., Ozl, J., and McCabe, J. T. (2013). Traumatic brain injury—modeling neuropsychiatric symptoms in rodents. *Front. Neurol.* 4:157. doi: 10.3389/fneur.2013.00157

Mierzwa, A. J., Marion, C. M., Sullivan, G. M., McDaniel, D. P., and Armstrong, R. C. (2015). Components of myelin damage and repair in the progression of white matter pathology after mild traumatic brain injury. *J. Neuropathol. Exp. Neurol.* 74, 218–232. doi: 10.1097/nen.0000000000000165

Neuberger, E. J., Swietek, B., Corrubia, L., Prasanna, A., and Santhakumar, V. (2017). Enhanced dentate neurogenesis after brain injury undermines long-term neurogenic potential and promotes seizure susceptibility. *Stem Cell Rep.* 9, 972–984. doi: 10.1016/j.stemcr.2017.07.015

Park, K. K., Liu, K., Hu, Y., Smith, P. D., Wang, C., Cai, B., et al. (2008). Promoting axon regeneration in the adult CNS by modulation of the PTEN/mTOR pathway. *Science* 322, 963–966. doi: 10.1126/science.1161566

Park, M. J., and Sohrabji, F. (2016). The histone deacetylase inhibitor, sodium butyrate, exhibits neuroprotective effects for ischemic stroke in middle-aged female rats. *J. Neuroinflammation* 13:300. doi: 10.1186/s12974-016-0765-6

Qureshi, I. A., and Mehler, M. F. (2014). An evolving view of epigenetic complexity in the brain. *Philos. Trans. R. Soc. Lond. B Biol. Sci.* 369:20130506. doi: 10.1098/rstb.2013.0506

Reis, C., Wang, Y., Akyol, O., Ho, W. M., Ii, R. A., Stier, G., et al. (2015). What's new in traumatic brain injury: update on tracking, monitoring and treatment. *Int. J. Mol. Sci.* 16, 11903–11965. doi: 10.3390/ijms160611903

Russo, M. V., and McGavern, D. B. (2016). Inflammatory neuroprotection following traumatic brain injury. *Science* 353, 783–785. doi: 10.1126/science.aaf6260

Shein, N. A., and Shohami, E. (2011). Histone deacetylase inhibitors as therapeutic agents for acute central nervous system injuries. *Mol. Med.* 17, 448–456. doi: 10.2119/molmed.2011.00038

Tucker, L. B., Burke, J. F., Fu, A. H., and McCabe, J. T. (2017). Neuropsychiatric symptom modeling in male and female C57BL/6J mice after experimental traumatic brain injury. *J. Neurotrauma* 34, 890–905. doi: 10.1089/neu.2016.4508

van Diepen, M. T., and Eickholt, B. J. (2008). Function of PTEN during the formation and maintenance of neuronal circuits in the brain. *Dev. Neurosci.* 30, 59–64. doi: 10.1159/000109852

Wang, X., Ma, S., Meng, N., Yao, N., Zhang, K., Li, Q., et al. (2016). Resveratrol exerts dosage-dependent effects on the self-renewal and neural differentiation of hUC-MSCs. *Mol. Cells* 39, 418–425. doi: 10.14348/molcells.2016.2345

Wang, X., Ma, S., Yang, B., Huang, T., Meng, N., Xu, L., et al. (2018). Resveratrol promotes hUC-MSCs engraftment and neural repair in a mouse model of Alzheimer's disease. *Behav. Brain Res.* 339, 297–304. doi: 10.1016/j.bbr.2017.10.032

Wang, G., Shi, Y., Jiang, X., Leak, R. K., Hu, X., Wu, Y., et al. (2015). HDAC inhibition prevents white matter injury by modulating microglia/macrophage polarization through the GSK3β/PTEN/Akt axis. *Proc. Natl. Acad. Sci. U S A* 112, 2853–2858. doi: 10.1073/pnas.1501441112

Watanabe, J., Shetty, A. K., Hattiangady, B., Kim, D. K., Foraker, J. E., and Nishida, H. (2013). Administration of TSG-6 improves memory after traumatic brain injury in mice. *Neurobiol. Dis.* 59, 86–99. doi: 10.1016/j.nbd.2013.06.017

Wen, Z., Hou, W., Wu, W., Zhao, Y., Dong, X., Bai, X., et al. (2018). 6'-O-Galloylpaeoniflorin attenuates cerebral ischemia reperfusion-induced neuroinflammation and oxidative stress via PI3K/Akt/Nrf2 activation. *Oxid. Med. Cell. Longev.* 2018:8678267. doi: 10.1155/2018/8678267

Xie, Z. H., Liu, Z., Zhang, X. R., Yang, H., Wei, L. F., Wang, Y., et al. (2016). Wharton's Jelly-derived mesenchymal stem cells alleviate memory deficits and reduce amyloid-β deposition in an APP/PS1 transgenic mouse model. *Clin. Exp. Med.* 16, 89–98. doi: 10.1007/s10238-015-0375-0

Xu, Y., Huang, S., Ma, K., Fu, X., Han, W., and Sheng, Z. (2012). Promising new potential for mesenchymal stem cells derived from human umbilical cord Wharton's jelly: sweat gland cell-like differentiative capacity. *J. Tissue Eng. Regen. Med.* 6, 645–654. doi: 10.1002/term.468

Yu, F., Wang, Z., Tanaka, M., Chiu, C. T., Leeds, P., Zhang, Y., et al. (2013). Posttrauma cotreatment with lithium and valproate: reduction of lesion volume, attenuation of blood-brain barrier disruption and improvement in motor coordination in mice with traumatic brain injury. *J. Neurosurg.* 119, 766–773. doi: 10.3171/2013.6.jns13135

Zhang, S., Taghibiglou, C., Girling, K., Dong, Z., Lin, S. Z., Lee, W., et al. (2015). Critical role of increased pten nuclear translocation in excitotoxic and ischemic neuronal injuries. *J. Neurosci.* 33, 7997–8008. doi: 10.1523/JNEUROSCI.5661-12.2013

Conflict of Interest Statement: The authors declare that the research was conducted in the absence of any commercial or financial relationships that could be construed as a potential conflict of interest.

Copyright © 2019 Xu, Xing, Huang, Zhou, Liu, Cui, Cheng, Wang, Zhou, Yang, Yang, Zhang, Zang, Ma and Guan. This is an open-access article distributed under the terms of the Creative Commons Attribution License (CC BY). The use, distribution or reproduction in other forums is permitted, provided the original author(s) and the copyright owner(s) are credited and that the original publication in this journal is cited, in accordance with accepted academic practice. No use, distribution or reproduction is permitted which does not comply with these terms.

frontiers in Cellular Neuroscience

ORIGINAL RESEARCH
published: 07 January 2019
doi: 10.3389/fncel.2018.00516

Neuroprotective Effects of Curcumin on IL-1β-Induced Neuronal Apoptosis and Depression-Like Behaviors Caused by Chronic Stress in Rats

*Cuiqin Fan[1], Qiqi Song[1], Peng Wang[1], Ye Li[1], Mu Yang[1] and Shu Yan Yu[1,2]**

[1] Department of Physiology, School of Basic Medical Sciences, Shandong University, Jinan, China, [2] Shandong Provincial Key Laboratory of Mental Disorders, School of Basic Medical Sciences, Shandong University, Jinan, China

Depression is suggested to be a neuropsychiatric disease resulting from neuroinflammation within specific brain regions. Curcumin, a potential neuroprotective agent extracted from curcuma loga, exerts antidepressant-like effects in various animal models of depression. However, the underlying mechanisms, in particular whether curcumin may exert neuroprotection through suppression of inflammatory pathway activity in depression remains largely unknown. In the present study, we examined the molecular events of curcumin as related to its capacity for neuroprotection against inflammation-induced neuronal apoptosis and depression-like behaviors in a rat model of depression. Our results show that chronic administration of curcumin (40 mg/kg, i.p., 5 weeks) prior to stress exposure significantly alleviated depression-like behaviors, expression of the proinflammatory cytokine interleukin-1β (IL-1β) and inhibited neuronal apoptosis within neurons of the ventromedial prefrontal cortex (vmPFC). Within the vmPFC of stressed rats, an intracerebral infusion of an RNAi form of IL-1β in adenovirus associated virus (AAV-IL-1β RNAi) significantly ameliorated depression-like behaviors, neuronal apoptosis and reduced phosphorylated-p38 mitogen-activated protein kinase (p-p38 MAPK) expression levels. More important, within the vmPFC of wild type rats, overexpression of IL-1β via intracerebral infusion of AAV-IL-1β induced p38 MAPK phosphorylation and neuronal apoptosis, which could be significantly prevented by chronic treatment of curcumin. Collectively, these findings reveal that curcumin protects against IL-1β-induced neuronal apoptosis, which may be related to the display of depression-like behaviors in stressed rats. Moreover, they provide new insights into the mechanisms and therapeutic potential for curcumin in the treatment of inflammation-related neuronal deterioration in this disorder.

Keywords: interleukin-1β, apoptosis, inflammation, curcumin, depression

OPEN ACCESS

Edited by:
Lavinia Alberi,
SICHH, Switzerland

Reviewed by:
Grzegorz Kreiner,
Institute of Pharmacology (PAS), Poland
Mario Costa,
Italian National Research Council, Italy

***Correspondence:**
Shu Yan Yu
shuyanyu@sdu.edu.cn

Received: *24 September 2018*
Accepted: *12 December 2018*
Published: *07 January 2019*

Citation:
Fan C, Song Q, Wang P, Li Y, Yang M and Yu SY (2019) Neuroprotective Effects of Curcumin on IL-1β-Induced Neuronal Apoptosis and Depression-Like Behaviors Caused by Chronic Stress in Rats. Front. Cell. Neurosci. 12:516. doi: 10.3389/fncel.2018.00516

INTRODUCTION

Depression is one of the most prevalent psychiatric disorders with complex pathogenesis. Previous research has implicated several mechanisms including altered monoaminergic and glutamatergic systems, increased inflammation, HPA axis abnormalities, and decreased neurogenesis and neuroplasticity (Dean and Keshavan, 2017). However, these findings are not present in every

patient, which revealed the diversification of pathophysiology in depression that urgently needed to elucidate. Increasing evidence has accrued which indicates that neuroinflammation plays a critical role in the pathogenesis of various neurological disorders including neurodegenerative diseases (Tan et al., 2013; Tuon et al., 2015), stroke (Zhang N. et al., 2014; Kim et al., 2015) and depression (Dowlati et al., 2010; Alcocer-Gomez et al., 2015). However, the pathophysiological mechanisms involved with these disorders are not fully understood. Recently, results from a number of studies have demonstrated that activation of pro-inflammatory factors, such as interleukin-1β (IL-1β), interleukin-6 (IL-6), and tumor necrosis factor-a (TNF-α) may act as a significant factors in the neuronal damage associated with major depressive disorder (MDD) (Maes et al., 2012; Rawdin et al., 2013). In contrast, antidepressants, such as the classic selective serotonin reuptake inhibitor (SSRI), fluoxetine, exert an anti-inflammatory effect via down-regulating microglial activation (Lee et al., 2015; Du et al., 2016). These results provide new insights into potential avenues of investigation regarding antidepressant therapies through their capacity to provide neuroprotection against the inflammation-induced neuronal deterioration that is associated with depression.

Herbal medicines, with their neuroprotective effects and low levels of side effects, have become attractive pharmacological tools in the treatment of various neurological disorders (Wąsik and Antkiewicz-Michaluk, 2017; Maiti and Dunbar, 2018). Curcumin, a natural polyphenolic compound extract from curcuma longa, has been shown to exert a variety of beneficial effects, including anti-inflammatory, anti-tumor, immunomodulatory and neuroprotective activities (Venigalla et al., 2015; Daverey and Agrawal, 2016, 2018). Recently, the potential antidepressant effects of curcumin have been recognized owing to its effectiveness in preventing the genesis of depression-like behavioral phenotypes in various animal models of depression (Andrade, 2014; Lopresti et al., 2014; Zhang L. et al., 2014). Curcumin was reported to reduce levels of inflammatory markers such as TNF-α, NF-κB, IL-1β, iNOS and COX-2 as induced by doxorubicin in rats (Benzer et al., 2018). However, detailed characterizations of the neuronal mechanisms underlying the antidepressant-like effects of curcumin, in particular whether it exhibits neuroprotective effects via inhibiting the activity of inflammatory processes which can lead to neuronal damage in depression remains largely unknown.

Inflammatory cytokines, especially IL-1β, are considered as important pro-apoptotic factors involved with the progression of neurological disorders (Tsai, 2017). IL-1β may contribute to neurofibrillary pathology in Alzheimer's disease (AD) through activation of the p38 MAPK pathway in cortical neurons (Li et al., 2003), and may also contribute to cortical axon developmental disorders and synaptic deficits through activation of p38 MAPK signaling pathway in septic neonatal rats (Han et al., 2017). The p38 MAPK signaling pathway transduces signals from the cell membrane to the nucleus and, in this way, participates in cell cycle, apoptosis and proliferation (Eriksson et al., 2017). For example, p38 MAPK is crucial for Caspase 3 activation and thus induces neuronal cell apoptosis in the cerebral ischemia-reperfusion injury model (Li and Ai, 2017). However, whether IL-1β up-regulates p38 phosphorylation and thus triggers neuronal apoptosis to promote depression-like behaviors in the chronic unpredictable mild stress (CUMS)-induced animal model requires further investigation.

It should be noted out that not all depressed patients have increased inflammation, previous study reported that the increased inflammation is mainly present in a subgroup of depressed patients who exposure to stress early in childhood or even *in utero*, and these depressed patients is less likely to respond to conventional antidepressants (Pariante, 2017). This shows that many important future questions still exist. What are the epigenetic mechanisms by which chronic stress induce a long-term trajectory of neuroinflammation? How do anti-inflammatories relieve some depressive phenotypes, and whether the anti-inflammatory effects of many herbal medicines serve as the underlying mechanisms of their antidepressant effects?

Therefore, in the present study, we investigated the involvement of inflammation-induced neuronal apoptosis in depression, and whether treatment with curcumin could prevent the neuronal apoptosis and depression-like behaviors induced by inflammation in CUMS-exposed rats. To further explore the underlying mechanisms of the neuroprotective, and thus antidepressant-like effects of curcumin, the regulatory roles of the pro-inflammatory cytokine, IL-1β, upon neuronal apoptosis and expression of apoptosis-related proteins that accompany depression were examined within the vmPFC, a site that represents a critical brain region involved in the pathogenesis of depression in the animal model.

MATERIALS AND METHODS

Animals

Male Wistar rats weighing 240–260 g were obtained from the Experimental Animal Centre of Shandong University. All experiments were approved by the Shandong University Animal Care and Use Committee and were conducted in accordance with the National Institutes of Health Guide for the Care and Use of Laboratory Animals. Rats were allowed to acclimatize to the laboratory environment for 7–8 days prior to use in the experiments. All efforts were made to minimize the pain and numbers of the animals used in these experiments.

Drugs and Treatment

Curcumin (Sigma, St. Louis, MO, United States) was prepared with use of 0.1% dimethyl sulfoxide (DMSO, Sigma, St. Louis, MO, United States) at a concentration of 10 mg/ml. Due to the poor bioavailability of curcumin when applied oral, we chose a 40 mg/kg intraperitoneal injection regimen as based upon previous results (Bhutani et al., 2009). Curcumin or DMSO was administered daily via an intraperitoneal (i.p.) injection at 30 min prior to a stress exposure that continued for 5 weeks. For CUMS depression model assessment, rats

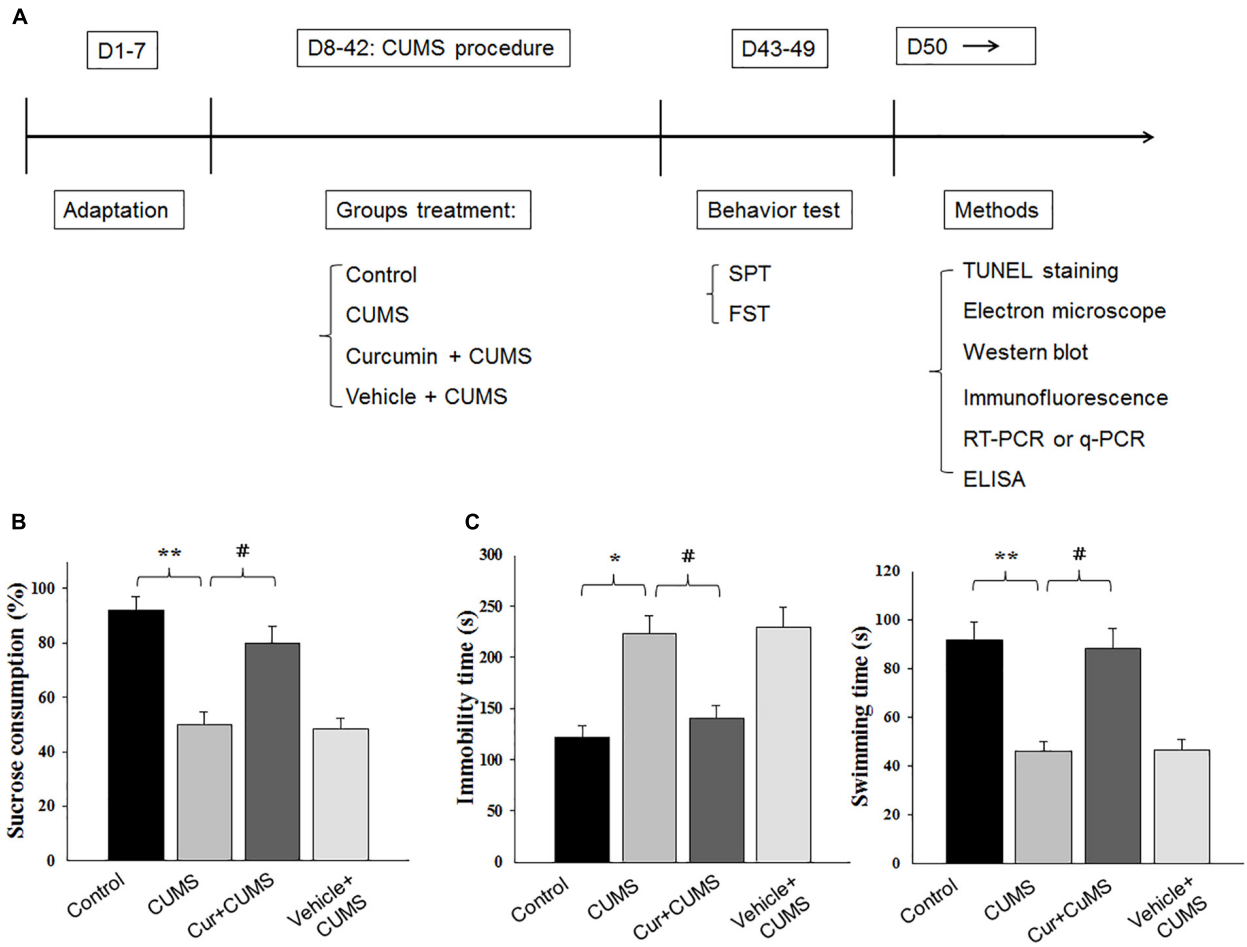


FIGURE 1 | Curcumin rescues CUMS-induced depression-like behaviors in rats. **(A)** Experimental design: schematic figure of the treatment protocol. **(B)** Chronic treatment of curcumin (40 mg/kg) reversed the decreases in percent of sucrose consumption of CUMS-exposed rats. **(C)** Curcumin treatment decreased immobility times and increased swimming times of CUMS-exposed rats in forced swim test. All data are presented as means ± SEM (N = 18/group). $^{*}P < 0.05$, $^{**}P < 0.01$, $^{***}P < 0.001$ CUMS vs. Control group (non-stressed). $\#P < 0.05$, $\#\#P < 0.01$, $\#\#\#P < 0.001$ Cur + CUMS vs. CUMS group (Cur, Curcumin).

were randomly allocated to one of the following four groups (N = 18/group): (a) control (non-stressed group), (b) CUMS, (c) curcumin treatment (40 mg/kg) followed by CUMS, (d) vehicle treatment (0.1% DMSO, 5 ml/kg) followed by CUMS.

CUMS Procedure

The CUMS procedure was performed according to procedures described previously with minor modifications (Mao et al., 2009). Rats in the non-stressed control group were housed in groups of four per cage in the colony room while rats in the stressed-groups were housed individually in a separate colony room and subjected to a daily stress regime over the 5-week period. Unpredictable mild stressors were applied in a variable sequence that included overnight illumination, 24 h food deprivation followed by 24 h water deprivation, 5 min cold swimming (4°C), cage shaking (2 h), physical restraint (2 h), wet bedding (24 h) and 1 min tail pinch (1 cm from the end of the tail). Each of these stressor episodes were applied daily to each rat in a random order (**Figure 1A**).

Stereotaxic Injection of the AAV Virus

For AAV viruses, the HBAAV2/9-r-IL-1β-GFP virus (AAV-IL-1β, Hanbio Biotechnology, Shanghai, China) was used to overexpress IL-1β in the vmPFC and the HBAAV2/9-r-IL-1β shRNAi-GFP virus (AAV-IL-1βi, Hanbio Biotechnology, Shanghai, China) to block IL-1β in the vmPFC. In this series of experiments, rats were randomly allocated to one of the following groups (N = 18/group): (a) wild type (non-stressed and non-injected group), (b) wild type + AAV-control (GFP-Cre construct), (c) wild type + AAV-IL-1β, (d) stressed, (e) stressed + AAV-control (GFP-Cre construct), (f) stressed + AAV-IL-1β RNAi and (g) stressed + AAV- IL-1β RNAi + curcumin. For viral injections, rats were deeply anesthetized with sodium pentobarbital (150 mg/kg, i.p.) and placed in a stereotaxic frame (Stoelting, United States). The vmPFC injection site was determined according to coordinates of the Rat Brain

Atlas (from bregma: AP, +3.24 mm; ML, ±0.5 mm; DV, −4.8 mm). Rats were infused bilaterally with 1–1.5 μl of purified and concentrated AAV virus ($\sim 10^{12}$ infection units per ml) using microinjection pump (Stoelting, United States) at a rate of 150 nl/min. The microelectrode remained in the injection site for at least 5 min after infusion and was then slowly withdrawn. Behavioral experiments or biochemical assays were performed at a minimum of 14 days after viral infusion into the vmPFC. The injection sites were examined after the behavioral tests and only data from rats with correct injection site placements within the vmPFC were included in the analyses.

Behavioral Tests

Behavioral tests were conducted after 5 weeks of CUMS treatment in the following sequence.

Sucrose Preference Test

The sucrose preference test was performed to assess anhedonia in rats as described previously with minor modifications (Mao et al., 2009). In the initial adaption phase, rats were placed individually in cages with two bottles of sucrose solution (1%, w/v) for a 24 h period; one bottle was then replaced with tap water for the second 24 h period. In the test phase, rats were deprived of water and food for 24 h and then permitted 3 h of free access to the two bottles, one filled with 100 ml of 1% sucrose solution and the other 100 ml of tap water. The consumption of the sucrose solution and tap water were measured and the sucrose preference was defined as sucrose consumption/[water consumption + sucrose consumption] × 100% during the 3 h test.

Forced Swim Test

On the day after the sucrose preference test, the forced swim test was conducted to assess "behavioral despair" in rats as described previously (Porsolt et al., 1977; Duman et al., 2007). In the training session, rats were placed individually in a glass cylinder (Temperature: 25°C, height: 80 cm, diameter: 30 cm) filled with 40 cm of water for 15 min of forced swimming. The test session was performed 24 h later. Rats were individually placed in the cylinder for a 5 min period, during which immobility and swimming times were recorded. The immobility time was defined as floating with only small movements necessary to maintain their head above the water.

Electron Microscopy Analysis

Two days after behavioral testing, brain samples from four rats per group were prepared for transmission electron microscopy (TEM). The vmPFC (1 mm × 1 mm × 1 mm) was carefully dissected and primary-fixed in buffered glutaraldehyde 2.5% for a minimum of 4 h at 4°C. The tissue was then post-fixed in 1% buffered osmium tetroxide for 2 h. After an ascending series of graded ethanol dehydrations, the tissue was infiltrated with a mixture of one-half propylene oxide overnight and then embedded in resin. Ultrathin sections (70 nm) were cut and stained with 4% uranyl acetate for 20 min followed by 0.5% lead citrate on copper grids for 5 min. Ultrastructure of the vmPFC was then observed with use of TEM (Philips Tecnai 20 U-Twin, Holland). A minimum of 30 micrographs per rat were randomly selected for analysis.

TUNEL Staining

Two days after behavioral testing, paraffin embedded sections of the vmPFC were sampled to measure TUNEL positive cells with use of the In Situ Cell Death Detection Kit (Roche, Germany) according to the manufacturer's instructions. Briefly, 5 μm sections were dewaxed and rehydrated according to standard protocols consisting of incubating with protease K (10 μg/ml) at room temperature for 15 min. Sections were then incubated with the TUNEL reaction mixture at 37°C for 1 h followed by incubation with 50 μl DAB Substrate (DAKO, Denmark) for 10 min at room temperature. Images were captured using light microscopy (Nikon, Japan). The number of TUNEL positive neurons was counted within three different fields (500 × 500 μm grids) per section and calculations were performed within 12 randomly selected fields per rat. Data were expressed as the ratio of positive cells obtained relative to that of the control group.

Immunofluorescence Assay

Rats were anesthetized with sodium pentobarbital (150 mg/kg, i.p.) and perfused with 4% paraformaldehyde (PFA). Brains were collected and post-fixed overnight at 4°C followed by a graded dehydration. Brain samples were then cut into serial coronal frozen sections (30 μm). Sections were incubated with the primary polyclonal rabbit anti-ionized calcium binding adaptor molecule-1 (Iba-1) (1:500, WAKO, Japan) and rabbit anti-glial fibrillary acidic protein (GFAP) (1:100, Proteintech, United States) followed by the fluorescent-conjugated secondary antibody (goat anti-rabbit IgG, 1:200; Sigma-Aldrich). Images were captured with use of a scanning laser confocal microscope (LSM780, Carl Zeiss, Germany). At least six to eight representative images were taken from each rat for analysis by Image-Pro plus 6.0 software. The number of Iba-1/DAPI double positive cells and GFAP/DAPI double positive cells were determined in each section (N = 6 rats/group). The values were expressed as the ratio of double positive cells relative to that of the control group.

Reverse Transcription PCR

Total RNA was isolated and extracted from samples of the vmPFC using a TRIpure Reagent Kit (Invitrogen, United States) and reverse-transcribed into cDNA with use of the HIScript II Q RT SuperMix Kit for qPCR (+gDNA wiper) (TaKaRa, Japan). Reverse transcription was then conducted using a 2xEasy Taq PCR SuperMix Kit for PAGE (TransGen, China). PCR products were assessed by electrophoresis on a 3% agarose gel and were analyzed using the Gel Image Analysis System (Bio-Rad, United States). Levels of targeted mRNA were normalized to the housekeeping gene GAPDH. Real-time PCR was performed

with use of the Bio-Rad IQ5 Real Time PCR System (Bio-Rad, United States). A relative fold change in expression of the gene was determined using the RQ = 2^{-Ct} method by Bio-Rad IQ5 Software (Bio-Rad, United States). The primers used for PCR amplification were as follows: (F, forward; R, reverse)

IL-1β (F): GGGATGATGACGACCTGC;
(R): CCACTTGTTGGCTTATGTT;
Bcl-2 (F): GGATCCAGGATAACGGAGGC;
(R): ATGCACCCAGAGTGATGCAG;
Bak (F): TCTTCAAACTGCTGGGCCATT;
(R): CTTGTCACCTGCCTGACTGCT;
Caspase3 (F): GGAGCTTGGAACGCGAAGAA;
(R): ACACAAGCCCATTTCAGGGT
Caspase9 (F): CAAGAAGAGCGGTTCCTGGT;
(R): CAGAAACAGCATTGGCGACC;
GAPDH (F): AGTGCCAGCCTCGTCTCATA;
(R): GGTAACCAGGCGTCCGATAC.

Enzyme Linked Immunosorbent Assay (ELISA)

Concentrations of IL-1β, Bcl-2, Bcl-2, Caspase 3 and Caspase 9 were measured with use of cytokine ELISA assays according to the manufacturer's instructions (Abcam Co., United Kingdom). Total protein isolated from vmPFC tissue samples was determined with use of the BCA assay (Thermo Fisher, Waltham, MA, United States). For serum IL-1β detection, all blood samples were obtained via venous collection. Equal amounts of diluted samples were added to each well of the ELISA kits (96 well) coated with the appropriate antibody. Data were displayed as cytokine (pg) vs. total protein (mg) (mean ± SEM). N = 6–8 animals per group.

Western Blot Analysis

Two days after behavioral testing, rats were anesthetized with sodium pentobarbital (150 mg/kg, i.p.), and the vmPFC was carefully dissected. Thirty μg of proteins per lane were electrophoretically separated on SDS-PAGE gels and transferred onto PVDF membranes which were then incubated overnight at 4°C with the appropriate antibodies. Primary antibodies used included polyclonal rabbit anti-p38 MAPK (1:1000, CST-9212S, Cell Signaling Technology, Beverly, MA, United States), anti-phospho-p38 MAPK (1:500, CST-9211S, Cell Signaling Technology, Beverly, MA, United States) and anti-β-actin (1:8000) (SC-47778, Santa Cruz Biotechnology, Santa Cruz, CA, United States). The secondary antibody was horseradish peroxidase-conjugated antibody (1:5000, SC-2030, Santa Cruz Biotechnology, Santa Cruz, CA, United States). The blots were detected using an enhanced chemiluminescence detection kit (GE Healthcare, Buckinghamshire, United Kingdom) and protein band densities were quantified using Image-J software (NIH, Scion Corporation, Frederick, MD, United States). Final data were expressed as a percent difference from that of the control group.

Data Analysis

All statistical procedures were performed on SPSS version 13.0. One-way or two-way analysis of variance (ANOVA) was used to establish differences among groups followed by the Tukey's test for post-hoc comparisons. The data were expressed as mean ± SEM of at least four individual animals. $P < 0.05$ was required for differences to be considered statistically significant.

RESULTS

Curcumin Treatment Rescued Depression-Like Behaviors Induced by CUMS Exposure

The effect of curcumin treatment on sucrose preference in CUMS-exposed rats is presented in **Figure 1**. One-way ANOVA revealed that there was an overall statistically significant difference in the percent of sucrose consumption among the four groups [$F_{(3,68)} = 19.23$, $P < 0.05$] (**Figure 1B**). *Post hoc* analysis indicated that a 5-week period of CUMS exposure significantly reduced the percent of sucrose consumption in rats as compared with that of the non-stressed control group ($P < 0.01$). Chronic pretreatment with curcumin (40 mg/kg daily) significantly increased the percent of sucrose consumption in CUMS-exposed rats ($P < 0.05$). No statistically significant differences were obtained between the vehicle-treated CUMS-exposed and CUMS-exposed control groups with regard to percent of sucrose consumption ($P > 0.05$).

Another method to assess antidepressant-like effects is the forced swim test. As shown in **Figure 1C**, results of the one-way ANOVA revealed an overall significant difference among the four groups with regard to both immobility times [$F_{(3,68)} = 18.12$, $P < 0.05$] and swimming times [$F_{(3,68)} = 15.87$, $P < 0.05$]. *Post hoc* analysis indicated that 5-weeks of CUMS exposure significantly increased immobility times ($P < 0.05$) and decreased swimming times in rats as compared to the non-stressed control group ($P < 0.01$). In contrast, rats pretreated with curcumin showed significantly decreased immobility times and significantly increased swim times as compared to CUMS-exposed control group ($P < 0.05$, for both). Overall, the main findings of both behavioral tests indicating that chronic curcumin treatment of CUMS rats exerted antidepressant-like effects in this animal model of depression.

Curcumin Treatment Reduced CUMS-Induced Glial Activation and IL-1β Overexpression Within the vmPFC

The results of immunofluorescence assay showed that was significantly different among the four groups with regard to the number of Iba-1^+ microglia [$F_{(3,20)} = 17.63$, $P < 0.001$] and GFAP positive astroglia [$F_{(3,20)} = 18.05$, $P < 0.001$] within the vmPFC region (**Figures 2A,B**). *Post hoc* analysis indicated that the 5-weeks of CUMS exposure significantly increased the number of activated vmPFC microglia and

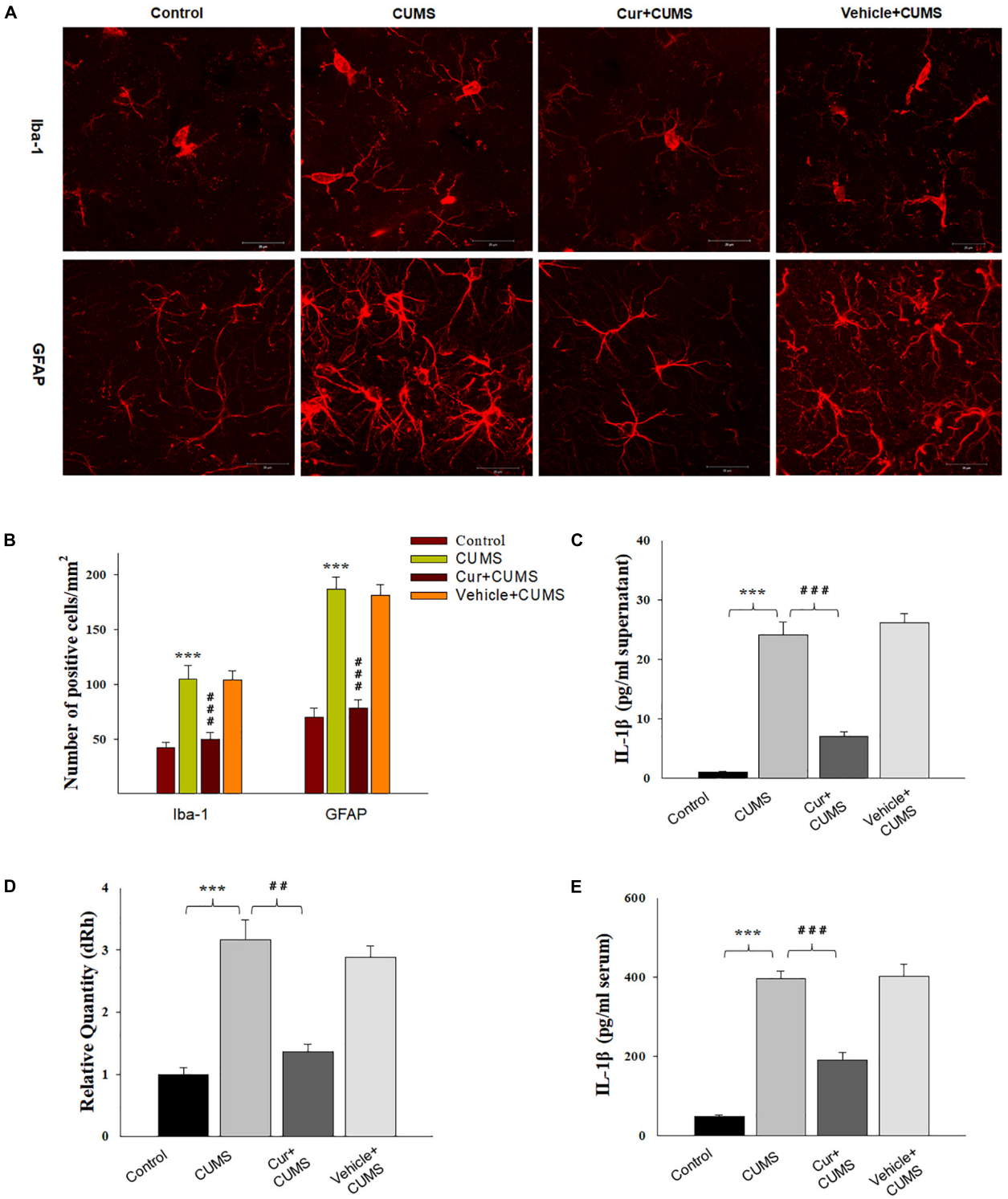


FIGURE 2 | Curcumin attenuated glial activation and IL-1β expression induced by CUMS-exposure. **(A)** CUMS exposure significantly increased the number of Iba1 positive microglial cells (top) and GFAP positive cells (bottom) within the vmPFC. **(B)** Histograms showing the glia activation were significantly attenuated by curcumin pretreatment. **(C)** ELISA assays showed that CUMS exposure increased IL-1β protein expression within the vmPFC, effects which were ameliorated by curcumin. **(D)** Real-time quantitative PCR assays showed that CUMS exposure increased IL-1β mRNA expression within the vmPFC, effects which were ameliorated by curcumin. **(E)** ELISA assays showed that CUMS exposure increased serum IL-1β expression, effects which were ameliorated by curcumin. Data were presented as the means ± SEM (N = 6/group). $^{*}P < 0.05$, $^{**}P < 0.01$, $^{***}P < 0.001$ CUMS vs. Control group; $\#P < 0.05$, $\#\#P < 0.01$, $\#\#\#P < 0.001$ Cur + CUMS vs. CUMS group (Cur, Curcumin).

astroglia as compared to the non-stressed rats ($P < 0.001$, for both). These changes in glia number were significantly reversed by chronic pretreatment with curcumin ($P < 0.001$, for both). As IL-1β is a critical pro-inflammatory factor in brain, we next examined whether curcumin could modulate IL-1β expression within the vmPFC of CUMS-exposed rats. Significant differences were obtained among the four groups with regard to the expression of IL-1β [qPCR: $F_{(3,20)} = 17.16$; $P < 0.001$; ELISA: $F_{(3,20)} = 16.85$; $P < 0.001$] (**Figures 2C,D**). *Post hoc* analysis showed that after 5-weeks exposure to CUMS, the mRNA and protein expression levels of IL-1β within the vmPFC were significantly increased ($P < 0.001$). Moreover, the level of serum IL-1β were significantly different between these groups [$F(3,20) = 17.16$; $P < 0.001$] (**Figure 2E**). *Post hoc* analysis showed that the serum IL-1β level in this depression animal model was significantly increased ($P < 0.001$). These increases were significantly reversed by pre-administration of curcumin.

Curcumin Treatment Attenuated CUMS-Induced Apoptosis in the vmPFC

As shown in **Figure 3A**, one-way ANOVA results of the TUNEL Staining assay revealed that there was an overall statistically significant difference in the density of apoptotic cells among the four groups [$F_{(3,20)} = 16.52$, $P < 0.001$]. TUNEL positive labeled cells were found to be particularly prevalent within the vmPFC of CUMS-exposed rats. Post-hoc analysis indicated that chronic CUMS-exposure significantly increased the density of apoptotic cells within vmPFC regions ($P < 0.001$), while chronic curcumin pretreatment markedly inhibited this massive CUMS-induced loss and apoptosis of neurons in the vmPFC area of CUMS rats (**Figure 3B**). In addition, immunohistochemistry assays showed that NeuN positive labeled cells were also significantly decreased within the vmPFC regions after chronic CUMS-exposure ($P < 0.001$) (**Figures 3A,C**), while curcumin pretreatment markedly inhibited this massive cell loss in the vmPFC area of CUMS-exposed rats ($P < 0.01$).

As nuclear chromatin condensation and margination represent the main changes observed within apoptotic cells, we next examined the neuronal ultrastructure in the vmPFC using TEM. The vmPFC neurons within the CUMS-exposure group showed strong staining of the condensed portion of their chromosomes accompanied with nuclear chromatin margination, aggregation and condensation, all of which indicate apoptotic morphological changes induced by CUMS exposure. In contrast, these apoptotic morphological changes were obviously alleviated by chronic pretreatment with curcumin (**Figure 3D**).

Curcumin Rescued Depression-Like Behaviors Caused by IL-1β Overexpression in vmPFC

As IL-1β is a potential modulator of cell apoptosis, to further explore whether curcumin treatment could alleviate CUMS-induced apoptosis via suppressing IL-1β expression, a AAV-IL-1β virus was constructed (**Figure 4A**) and infused bilaterally into the vmPFC of non-stressed normal wild type rats to overexpress IL-1β, followed by treatment with curcumin for 14 days (**Figure 4B**). After estimating the overexpression efficiency ($P < 0.001$, **Figure 4C**), the behavioral tests were then conducted. Results revealed that significant differences were present regarding the percent of sucrose consumption [$F_{(3,44)} = 16.19$; $P < 0.01$] (**Figure 4D**), immobility times [$F_{(3,44)} = 14.98$; $P < 0.01$] and swimming times [$F_{(3,44)} = 15.47$, $P < 0.01$] among the four groups (**Figure 4E**). *Post hoc* analysis showed that an overexpression of IL-1β within the vmPFC significantly decreased sucrose consumption and increased immobility times as compared with rats receiving an AAV-vector control injection ($P < 0.01$). In contrast, 14-days of curcumin treatment following AAV-IL-1β virus injection significantly reversed these depression-like behaviors induced by overexpression of IL-1β within the vmPFC ($P < 0.01$). These results indicate that curcumin may exert antidepressant-like effects via suppression of the IL-1β pathway.

Curcumin Attenuated Neuronal Apoptosis in vmPFC Caused by IL-1β Overexpression

Therefore, we next investigated whether the overexpression of IL-1β in the vmPFC, which induces neuronal apoptosis, could be prevented by curcumin treatment. One-way ANOVA results from the TUNEL Staining assay showed an overall statistically significant difference in the density of apoptotic cells among these four groups [$F_{(3,20)} = 15.91$, $P < 0.001$] (**Figures 5A,B**). *Post hoc* analysis revealed that IL-1β overexpression significantly increased the density of apoptotic cells within vmPFC regions ($P < 0.001$). Furthermore, a high-density chromatin margination was present under the nuclear membrane in the group treated with an AAV-IL-1β injection as revealed with TEM (**Figure 5C**). Moreover, curcumin treatment dramatically attenuated the apoptotic cells ($P < 0.001$) and apoptotic related morphological changes induced by overexpression of IL-1β. These results indicate that the pro-inflammatory cytokine, IL-1β, likely produced the substantial increases in apoptotic cells within the vmPFC in this animal model of depression, effects which could be ameliorated by curcumin treatment.

Curcumin Attenuated Apoptosis-Related Factors Expression Caused by IL-1β Overexpression

To further substantiate these findings, we examined the effects of IL-1β overexpression on apoptosis-related protein expression levels. Similar to that obtained with morphological results, there was an overall statistically significant difference among the four groups in biochemical markers associated with the apoptotic markers Bcl-2 [RT-PCR: $F_{(3,20)} = 14.83$; $P < 0.01$; ELISA: $F_{(3,20)} = 15.76$; $P < 0.001$], Bak [RT-PCR: $F_{(3,20)} = 15.18$; $P < 0.01$; ELISA: $F_{(3,20)} = 12.63$; $P < 0.001$], Caspase-3 [RT-PCR: $F_{(3,20)} = 15.04$; $P < 0.01$; ELISA: $F_{(3,20)} = 13.96$; $P < 0.001$] and Caspase-9 [RT-PCR: $F_{(3,20)} = 15.21$; $P < 0.01$; ELISA: $F_{(3,20)} = 12.75$; $P < 0.001$]

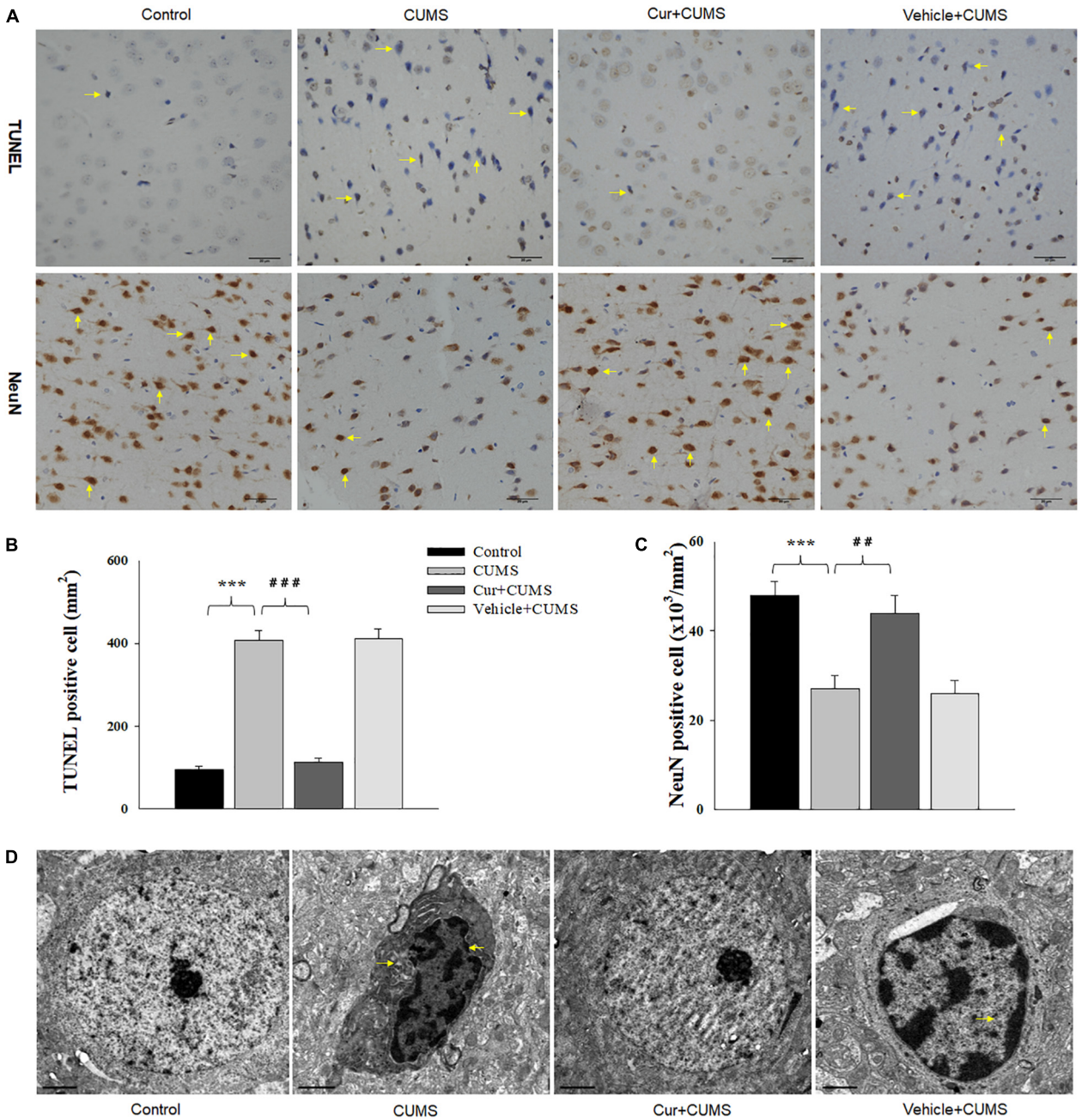


FIGURE 3 | Curcumin ameliorated neuronal apoptosis within the vmPFC as induced by CUMS exposure. **(A)** Curcumin treatment decreased the number of TUNEL positive apoptotic cells (top, indicated by the arrows) and NeuN positive cells (bottom, indicated by the arrows) in the vmPFC of CUMS-exposed rats. Scale bar is 20 μm. **(B)** Histograms showing the increased TUNEL positive cells were significantly attenuated by curcumin pretreatment. **(C)** Histograms showing the decreased NeuN positive cells was significantly attenuated by curcumin pretreatment. **(D)** Representative electron micrograph of vmPFC neuronal ultrastructure. Arrows indicate nuclear chromatin aggregation, condensation and margination. Scale bar is 2 μm. Curcumin significantly ameliorated apoptosis of vmPFC neurons in CUMS-exposed rats. N = 6/group. $^{*}P < 0.05$, $^{**}P < 0.01$, $^{***}P < 0.001$ CUMS vs. Control group (non-stressed). $\#P < 0.05$, $\#\#P < 0.01$, $\#\#\#P < 0.001$ Cur + CUMS vs. CUMS group.

within vmPFC regions (**Figures 6B,C**). *Post hoc* analysis showed that an overexpression of IL-1β within the vmPFC of non-stressed rats significantly decreased mRNA and protein expression of Bcl-2 and increased expression levels of pro-apoptotic proteins. Notably, curcumin treatment dramatically attenuated the apoptotic related morphological and biochemical changes induced by overexpression of IL-1β ($P < 0.01$). More importantly, we found that IL-1β overexpression also produced an overall statistically significant increase in the phosphorylation of P38 MAPK [$F_{(3,20)} = 16.83$, $P < 0.05$]

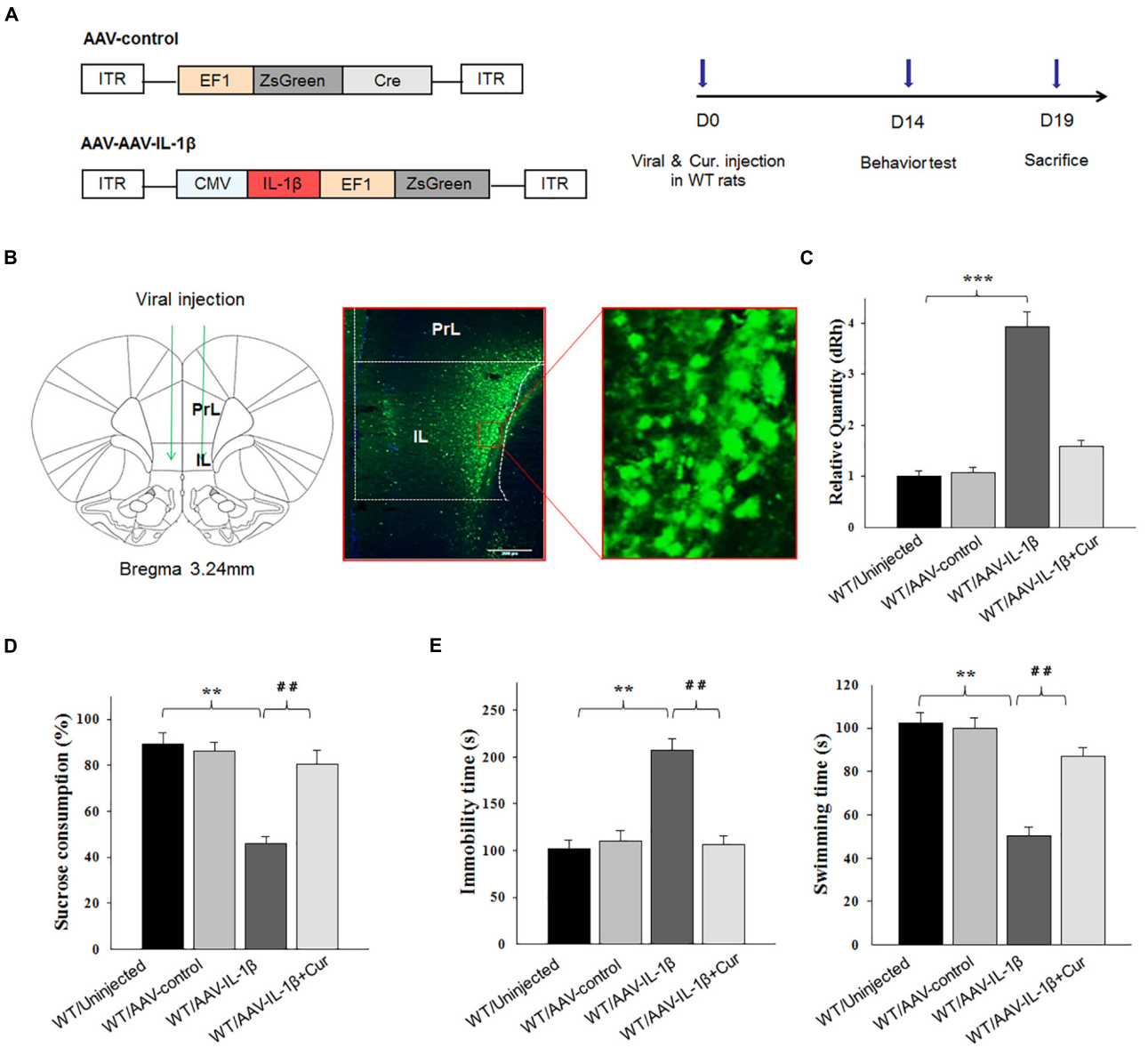


FIGURE 4 | Overexpression of IL-1β within the vmPFC leads to depression-like phenotypes in normal wild type rats. **(A)** Left: Schematics of AAV vectors engineered to overexpress a control construct or IL-1β. ITR, inverted terminal repeats; EF1, ZsGreen promoter; CMV, IL-1β promoter. Right: Experimental paradigm for behavioral biochemical testing of rats infected with the virus. **(B)** Illustration of viral infusion of AAV-IL-1β into the vmPFC. PrL, prelimbic cortex; IL, infralimbic cortex. Scale bar is 100 μm. **(C)** Estimation of βCaMKII overexpression efficiency after viral constructs injection. **(D,E)** Behavioral effects of over expressing viral AAV-IL-1β in the vmPFC. $N = 12$ in all groups. $^{*}P < 0.05$, $^{**}P < 0.01$, $^{***}P < 0.001$ WT + AAV-IL-1β vs. WT rats. $\#P < 0.05$, $\#\#P < 0.01$, $\#\#\#P < 0.001$ WT + AAV-IL-1β + Cur vs. WT + AAV-IL-1β (WT, wild type).

(**Figure 6A**), which proposed that p38 MAPK may act as a critical downstream molecule trigger for apoptotic processes in the vmPFC.

Knocking-Down of IL-1β in vmPFC Rescued Depression-Like Behaviors in Stressed Rats

Next, we used RNA interference (RNAi) to reduce (knock down) IL-1β protein as a means to determine whether a down-regulation or blockade of IL-1β function within the vmPFC would reverse depression phenotypes (**Figure 7A**). Behavioral testing of depression was then performed at 14-days post-infusion of the small interference RNA sequence form of IL-1β in the AAV virus (AAV-IL-1β-RNAi) in vmPFC of stressed rats (**Figures 7B,C**). One-way ANOVA revealed an overall statistically significant difference in behaviors related to depression. Specifically, the percent of sucrose consumption [$F_{(3,44)} = 17.36$; $P < 0.01$] (**Figure 7D**), immobility times [$F_{(3,44)} = 16.79$; $P < 0.01$] and swimming times [$F_{(3,44)} = 15.16$, $P < 0.01$] (**Figure 7E**) all

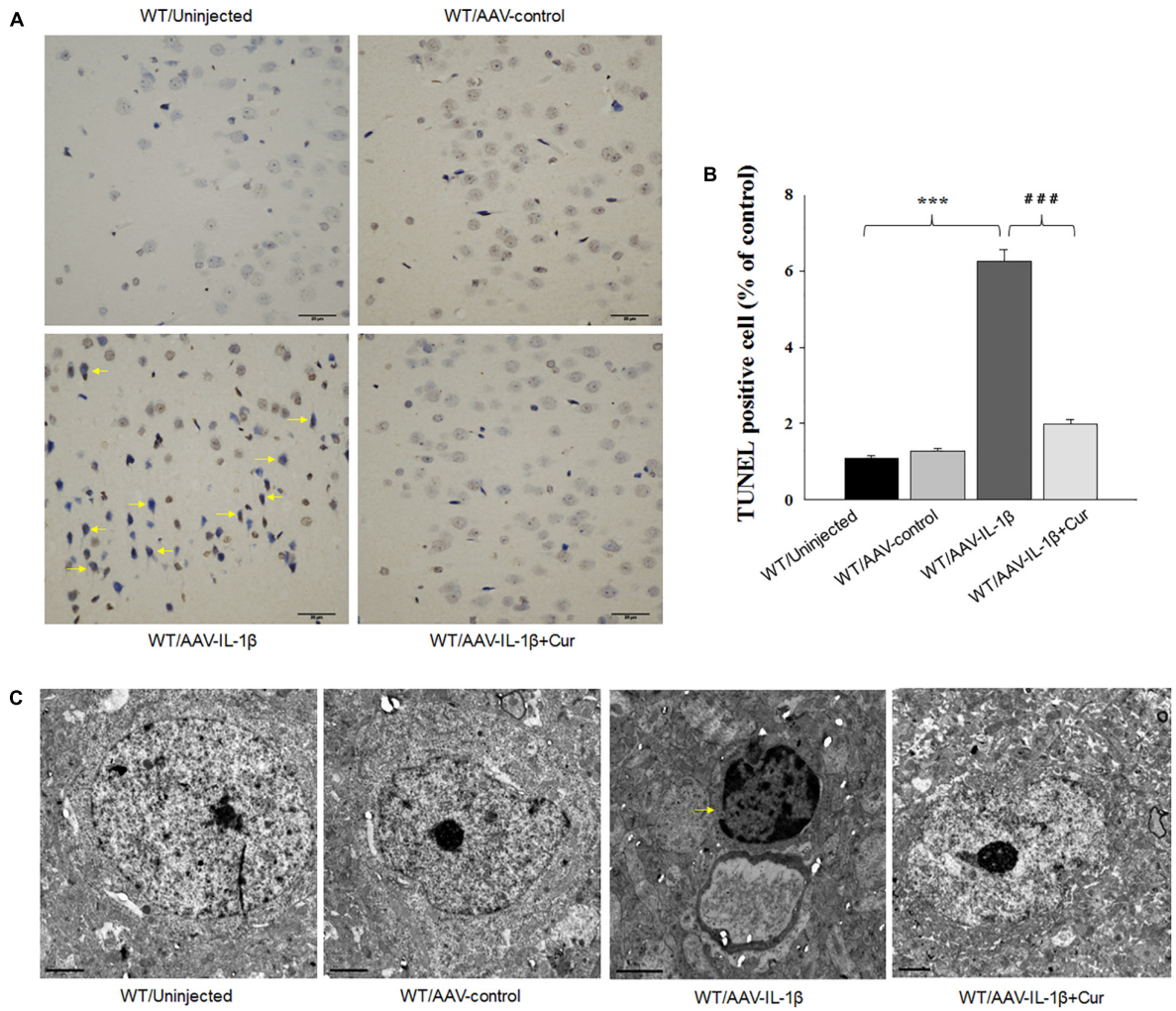


FIGURE 5 | Overexpression of IL-1β within the vmPFC leads to neuronal apoptosis within the vmPFC of normal wild type rats. **(A)** TUNEL positive apoptotic cells (indicated by the arrows) in vmPFC regions infected with AAV-IL-1β. **(B)** Histograms showing the increased TUNEL positive cells caused by AAV-IL-1β infusion were significantly attenuated by curcumin treatment. **(C)** Nuclear chromatin abnormalities in vmPFC neurons infected with AAV-IL-1β. Arrows indicate nuclear chromatin aggregation, condensation and margination. N = 6/group. $^{*}P < 0.05$, $^{**}P < 0.01$, $^{***}P < 0.001$ WT + AAV-IL-1β vs. WT rats. $\#P < 0.05$, $\#\#P < 0.01$, $\#\#\#P < 0.001$ WT + AAV-IL-1β + Cur vs. WT + AAV-IL-1β.

showed significant differences among the four groups. Post-hoc analysis indicated that infused AAV-IL-1β-RNAi to block IL-1β function in stressed rats produced significant increases in the percent of sucrose consumption in the sucrose preference test and also prevented the "behavioral despair" symptoms (increased immobility times and decreased swimming times in stressed rats) in the forced swim test ($P < 0.05$).

Knocking-Down of IL-1β in vmPFC Reduced Neuronal Apoptosis in Stressed Rats

In addition to its effects upon depression-like behaviors, we also found that blockage of the IL-1β pathway also produced substantial effects upon amelioration of neuronal apoptosis [$F_{(3,20)} = 16.39$, $P < 0.001$, **Figures 8A,B**] and nuclear apoptotic morphological changes (**Figure 8C**) within the vmPFC of stressed rats. To corroborate this result, we examined the modulatory effects of IL-1β on the expression of apoptosis-related proteins. As shown in **Figures 9B,C, mRNA** and **protein** expressions of Bcl-2 within the vmPFC differed significantly among the four groups [RT-PCR: $F_{(3,20)} = 15.07$; $P < 0.01$; ELISA: $F_{(3,20)} = 14.91$; $P < 0.001$]. Moreover, one-way ANOVA also revealed that there was an overall statistically significant difference among the four groups with regard to the mRNA and protein expression of pro-apoptosis factors such as Bak [RT-PCR: $F_{(3,20)} = 14.72$; $P < 0.01$; ELISA: $F_{(3,20)} = 12.96$; $P < 0.001$], Caspase-3 [RT-PCR: $F_{(3,20)} = 12.78$; $P < 0.01$; ELISA: $F_{(3,20)} = 13.26$; $P < 0.001$] and Caspase-9 within vmPFC regions [RT-PCR: $F_{(3,20)} = 15.17$; $P < 0.01$; ELISA: $F_{(3,20)} = 12.39$; $P < 0.001$]. *Post hoc* analysis indicated that injection of AAV-IL-1β-RNAi significantly increased the expression of Bcl-2, along with a

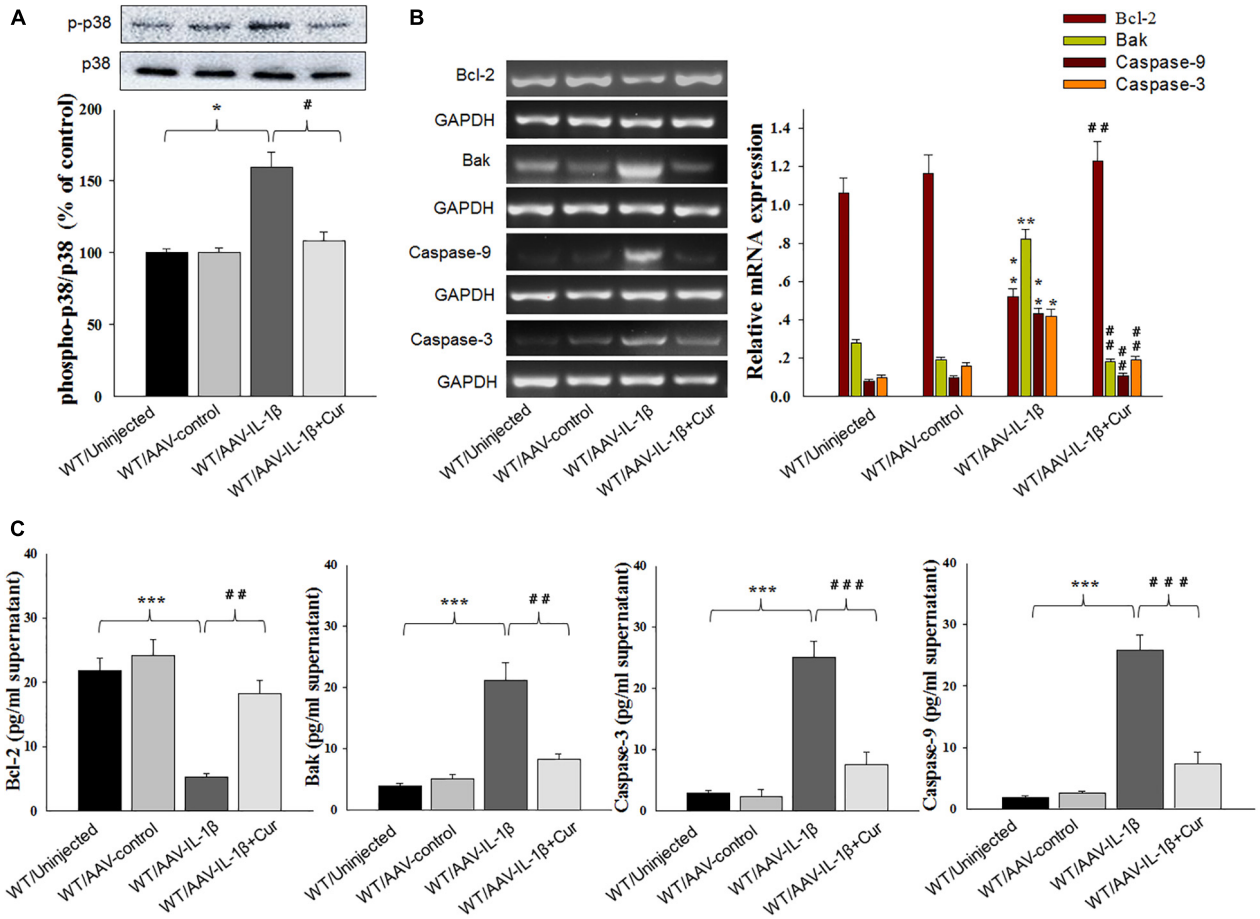


FIGURE 6 | Curcumin attenuated apoptosis-related factors expression caused by IL-1β overexpression. **(A)** Phosphorylation levels of p38 MAPK in the vmPFC infected with the AAV-IL-1β virus. **(B)** RT-PCR assays of expression levels of Bcl-2, Bak, Caspase 3 and Caspase 9 in vmPFC neurons infected with AAV-IL-1β. **(C)** ELISA assays of expression levels of Bcl-2, Bak, Caspase 3 and Caspase 9 in vmPFC neurons infected with AAV-IL-1β. $N = 6$/group. $^{*}P < 0.05$, $^{**}P < 0.01$, $^{***}P < 0.001$ WT + AAV-IL-1β vs. WT rats. $\#P < 0.05$, $\#\#P < 0.01$, $\#\#\#P < 0.001$ WT + AAV-IL-1β + Cur vs. WT + AAV-IL-1β.

decrease in expression levels of Bak, Caspase-3 and Caspse-9 within the vmPFC ($P < 0.01$). In addition, one-way ANOVA analysis of P38 MAPK activity within the vmPFC also showed an overall statistically significant difference among the four groups with regard to phosphorylation levels of p38 MAPK [$F_{(3,20)} = 15.24$; $P < 0.05$] (**Figure 9A**). *Post hoc* analysis indicated that P38 MAPK phosphorylation levels in the vmPFC were significantly reduced in the AAV-IL-1β-RNAi infused stressed groups. When combined with the results obtained from the IL-1β-overexpression experiments, these results provide evidence indicating that suppression of phosphorylated p38 MAPK may contribute to the antidepressant-like behaviors caused by IL-1β knock down.

DISCUSSION

In the present study, we show that curcumin exerts neuroprotective effects against apoptosis-related depression-like behaviors in a CUMS rat model. Moreover, we found that curcumin ameliorated IL-1β-induced neuronal apoptosis via suppressing the P38 pathway within the vmPFC of CUMS exposed rats. Taken together, these findings suggest that: (1) chronic stress-induced inflammation may contribute to neuronal apoptosis and thus promote depression-like symptoms and (2) the neuroprotectant, curcumin, exhibits antidepressant-like effects via suppressing the pathway involved with inflammation-induced apoptosis within the vmPFC, a brain site associated with depression.

The classical antidepressants currently used for the treatment of depression usually induce many side effects and possess low efficacy (Ereshefsky, 2009). Recent evidence has accrued indicating the potential antidepressant effects of curcumin in various animal models of depression; moreover this agent has attracted considerable attention due to its high safety margins (Zhang et al., 2013; Lopresti, 2017) and its ability to function as a multi-target natural compound which may modulate numerous pathways (Zhou et al., 2011). Within our laboratory we have shown that curcumin prevented neuronal plasticity dysregulation induced by chronic stress via its

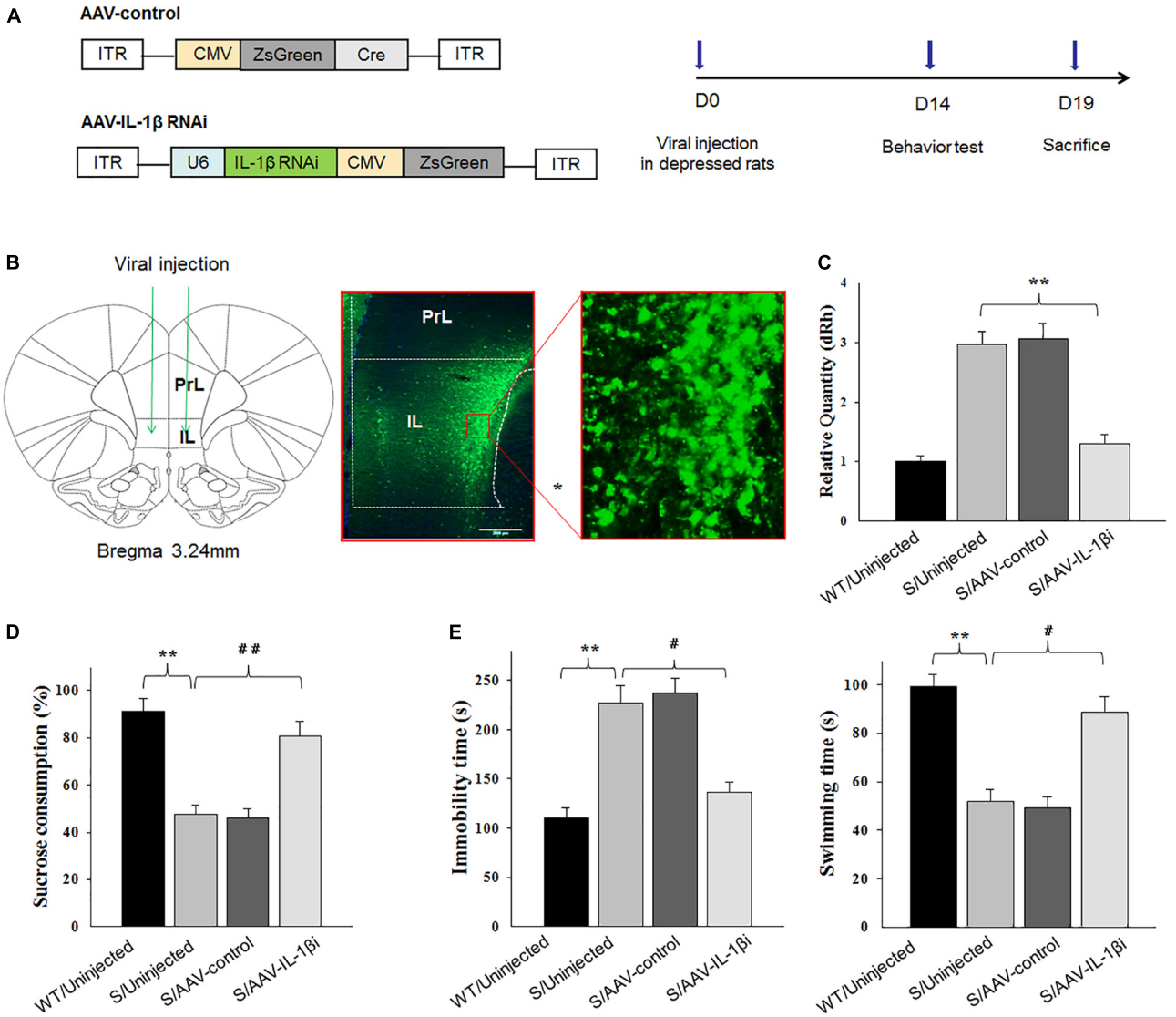


FIGURE 7 | Knocking-down of IL-1β in the vmPFC reduced depression-like phenotypes of stressed rats. In these experiments, prior to virus infusion, rats experienced a 5-week period of CUMS exposure to induce depression-like phenotypes. **(A)** Left: Schematics of AAV vectors engineered to overexpress a control construct or RNAi form of IL-1β. U6, IL-1β shRNA promoter. Right: Experimental paradigm for behavioral testing of rats infected with the virus. **(B)** Illustration of viral infusion of the IL-1β RNAi construct into the vmPFC. Scale bar is 100 μm. **(C)** Estimation of βCaMKII overexpression efficiency after viral constructs injection. **(D,E)** Behavioral effects of expressing AAV-IL-1β RNAi construct within the vmPFC of stressed rats. $N = 12$ in all groups. $^{*}P < 0.05$, $^{**}P < 0.01$, $^{***}P < 0.001$ Stressed rats vs. WT rats. $\#P < 0.05$, $\#\#P < 0.01$, $\#\#\#P < 0.001$ S+AAV-IL-1β RNAi vs. Stressed rats (S, stressed).

neuroprotective ability involving MAPK/ERK-dependent brain-derived neurotrophic factor expression (Zhang L. et al., 2014), as well as by modulating the miR-134 signaling pathway (Fan et al., 2018). Furthermore, curcumin has been reported to prevent the increase of an apoptotic factor (caspase-3) resulting from oxidative-nitrosative stress, as demonstrated in an olfactory bulbectomy induced rat model of depression (Rinwa et al., 2013). However, no evidence exists indicating any anti-apoptotic effects of curcumin as related to its anti-depression effects. In this study, we show that chronic curcumin treatment significantly suppressed neuronal apoptosis induced by inflammation in a CUMS-induced rat model of depression. These findings not only confirm the neuroprotective effect of curcumin in this CUMS-induced depression model but offer new insights into the mechanistic basis for this neuroprotection.

Recent evidence has indicated that depression is associated with structural and functional injury within specific brain regions (Goldwater et al., 2009; Gilabert-Juan et al., 2011; Oh et al., 2012). In the present study, we focused on the vmPFC, a critical brain region believed to be involved with depression. Neuroimaging studies revealed that the activity of vmPFC was reduced in depression (Takahashi et al., 2004). Moreover, alterations in the structure and function were also

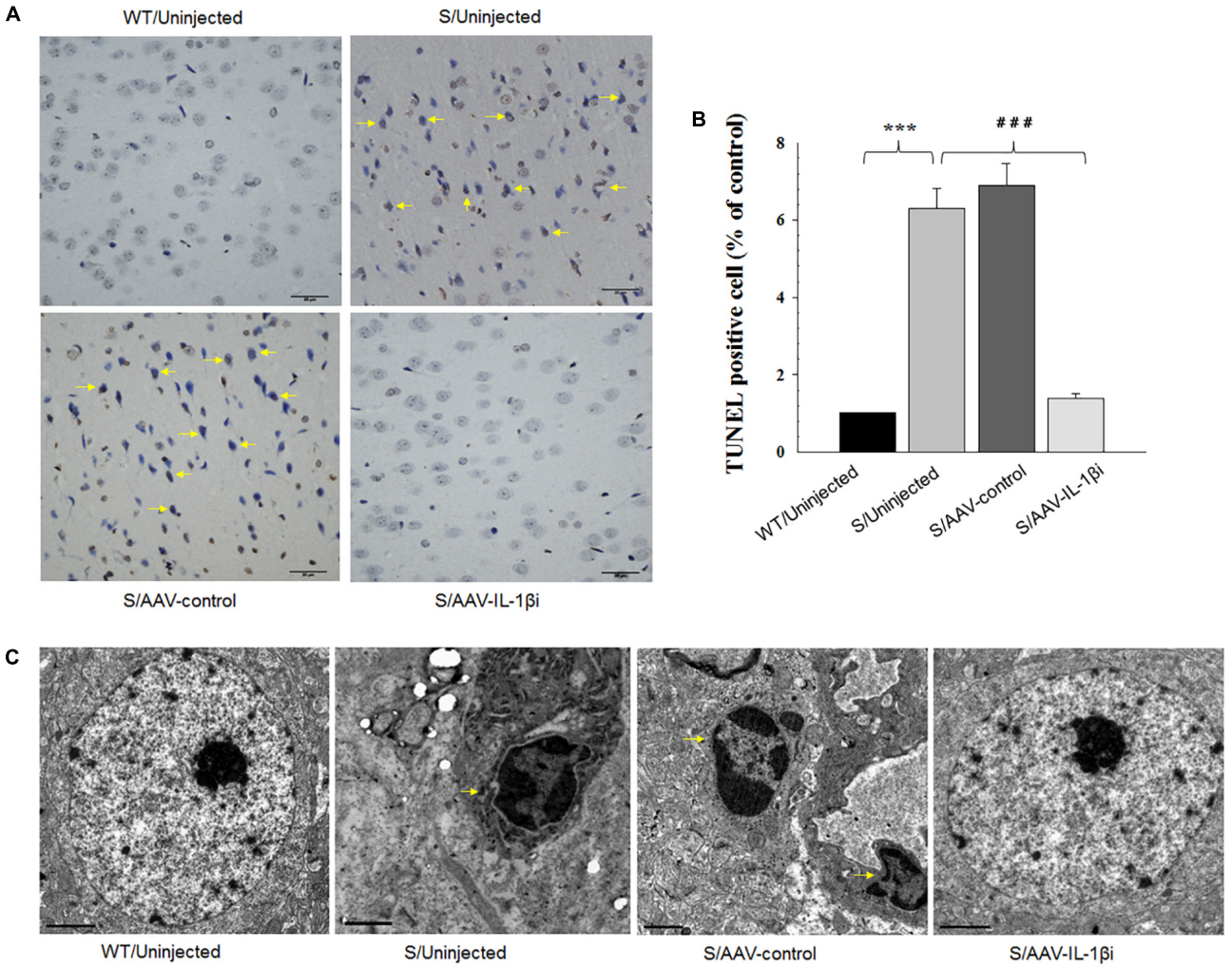


FIGURE 8 | Knocking-down of IL-1β in the vmPFC decreased neuronal apoptosis within the vmPFC of stressed rats. **(A)** TUNEL positive apoptotic cells (indicated by the arrows) in vmPFC regions infected with AAV-IL-1β RNAi construct. **(B)** Histograms showing the decreased TUNEL positive cells caused by AAV-IL-1β RNAi construct infusion. **(C)** nuclear chromatin abnormalities in vmPFC neurons infected with the AAV-IL-1β RNAi construct. Arrows indicate nuclear chromatin aggregation, condensation and margination. N = 6/group. $^{*}P < 0.05$, $^{**}P < 0.01$, $^{***}P < 0.001$ Stressed rats vs. WT rats. $\#P < 0.05$, $\#\#P < 0.01$, $\#\#\#P < 0.001$ S+AAV-IL-1β RNAi vs. Stressed rats.

found within the vmPFC in response to chronic stress in animal models (Cook and Wellman, 2004; Radley et al., 2006; Holmes and Wellman, 2009; McLaughlin et al., 2009). In the present study, our results indicate that CUMS exposure induced neuronal apoptosis in the vmPFC as indicated by significant increases in the number of TUNEL positive apoptotic cells in this area. Because TUNEL assay may also label cells with DNA damage by other means than in the course of apoptosis, for example the necrotic cells, then we further detected the DNA breakage using TEM. Consistently, the apoptotic cells within the vmPFC of stressed rat showed ultrastructural changes involving nuclear damage, presenting as chromatic agglutination, margination and nuclear karyopyknosis. Such morphological results suggest that cell apoptosis, localized to specific brain regions, may be involved in the pathophysiology of depression. Of particular significance, our current results demonstrating a reversal in depression-like behavioral responses by curcumin were found to be accompanied with a significant amelioration of cell apoptosis within the vmPFC of CUMS-exposed rats. We also found that CUMS-exposure induced a significant overexpression of IL-1β which paralleled the neuronal apoptosis observed within the vmPFC, an effect which was alleviated by curcumin. Moreover, our results showed that the levels of interleukin-1β protein in serum of CUMS exposed rats were significantly increased, which suggest that the changes in peripheral cytokines are paralleled with the inflammatory state of the central nervous system. More interestingly, chronic administration of curcumin also attenuated the increased levels of IL-1β in peripheral blood. This is generally consistent with multiple previous studies which found an increased level of IL-1β in peripheral blood of depressed patients (Panighini et al., 2013; Su et al., 2017;

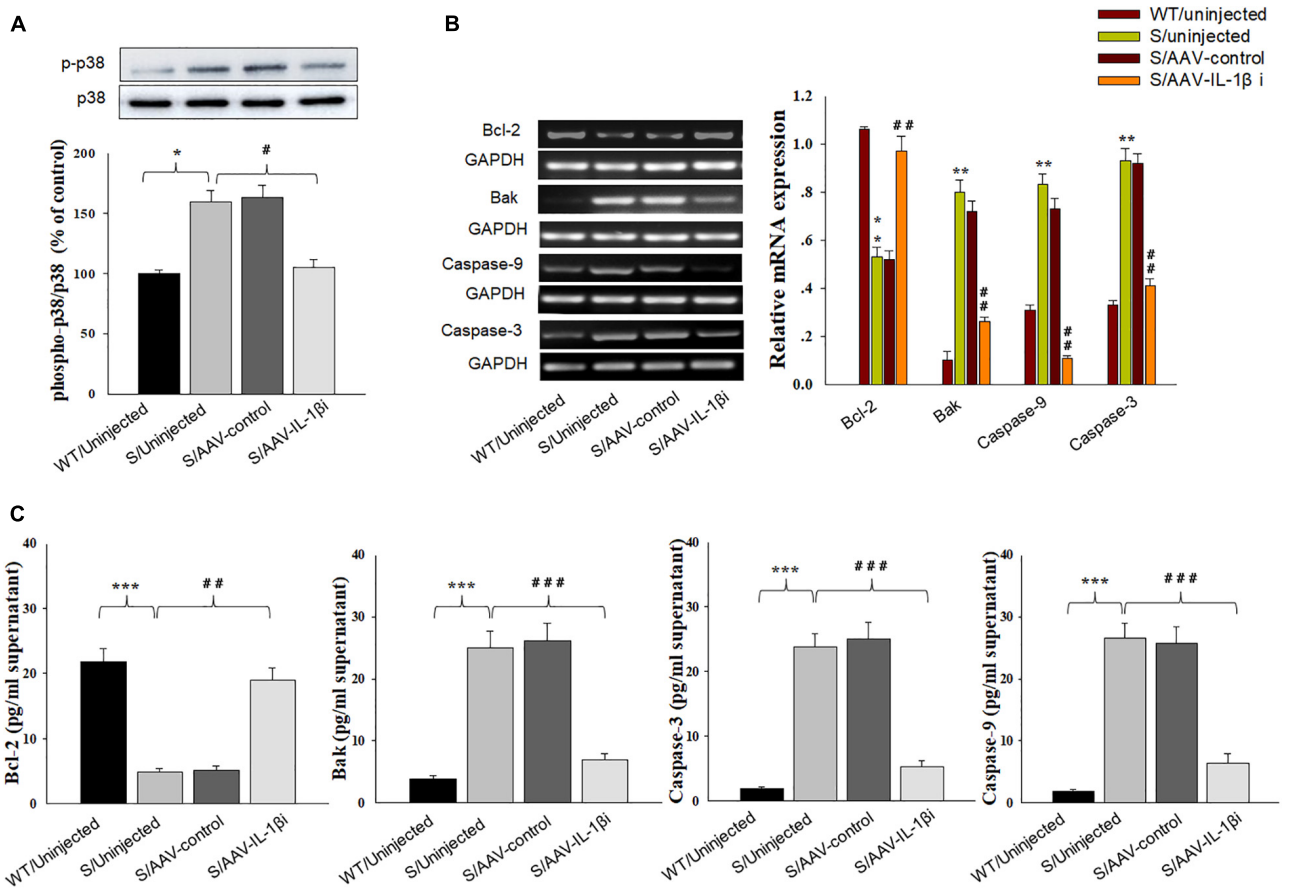


FIGURE 9 | Knocking-down of IL-1β in vmPFC reduced apoptosis-related factors produced by CUMS exposure. **(A)** Phosphorylation levels of p38 MAPK in the vmPFC infected with the AAV-IL-1β RNAi virus. **(B)** RT-PCR assays of expression levels of Bcl-2, Bak, Caspase 3 and Caspase 9 in vmPFC neurons infected with the AAV-IL-1β RNAi construct. **(C)** ELISA assays of expression levels of Bcl-2, Bak, Caspase 3 and Caspase 9 in vmPFC neurons infected with the AAV-IL-1β RNAi construct. N = 6/group. $^{*}P < 0.05$, $^{**}P < 0.01$, $^{***}P < 0.001$ Stressed rats vs. WT rats. $\#P < 0.05$, $\#\#P < 0.01$, $\#\#\#P < 0.001$ S+AAV-IL-1β RNAi vs. Stressed rats.

Zou et al., 2018). It is important to note that the serum IL-1β may possibly led to the damage of blood-brain barrier and enhanced the inflammatory response centrally (Morgenstern and Pettigrew, 1997; Iadecola and Anrather, 2011; Labus et al., 2014). This overexpression of IL-1β may indicate one potential pathway through which neuroinflammatory mechanisms may proceed to produce neuronal apoptosis, eventually leading to depression. Accordingly, the neuroprotective ability of curcumin to regulate neuroinflammatory-induced neuronal apoptosis within the vmPFC indicates some of the underlying mechanisms of curcumin's beneficial effects along with its potential for use as a novel tool in the treatment of depression.

The IL-1-type cytokines are major mediators of neuroinflammation and accumulating evidence suggests that IL-1β is a key contributor to neuronal deterioration in depression (Maes et al., 2012; Fernanda et al., 2017) Levels of IL-1β are increased within the brain in response to chronic stress (Pan et al., 2014) and inhibiting IL-1β reversed stress-induced social avoidance in rats (Ramirez et al., 2015). Accordingly, increased IL-1β expressions may play a critical role in inflammation-induced neuronal apoptosis after chronic stress. In the present study, we found that down-regulation of this IL-1β expression within the vmPFC of stressed rats significantly reversed cell apoptosis along with the display of depression-like behaviors, whereas overexpression of IL-1β within the vmPFC of unstressed rats significantly increased depression-like phenotypes. In order to determine whether curcumin protects against IL-1β-induced neuronal apoptosis, we infused IL-1β-expressing viruses into the vmPFC of unstressed rats to overexpress IL-1β and examined the effects on neuronal apoptosis and depression-like behaviors. The results of this experiment demonstrated that curcumin was effective in reducing the apoptotic and depression-like phenotypes induced by IL-1β overexpression within the vmPFC of rats. Consistent with these results were the findings showing that the downregulation of the pro-apoptotic proteins Bak, Caspase-3 and Caspase-9 and an upregulation of the anti-apoptotic protein Bcl-2 within the vmPFC of stressed rats. Therefore, these findings suggest that an anti-inflammatory strategy may contribute to antidepressant-like effects of curcumin via prevention of inflammation-induced neuronal apoptosis in response to chronic stress. The ensuing issue to address in these investigations involves identifying the

downstream molecular targets of IL-1β in mediating vmPFC neuronal apoptosis in depression.

The MAPK pathway represents an important signal transduction pathway in the regulation of inflammation and apoptosis (Kim and Choi, 2015). It has been reported that p38 MAPK plays a major regulatory role in the crosstalk between the caspase-dependent pathway and apoptosis (Park et al., 2003; Wang et al., 2018). Our present results show that chronic stress significantly increased the expression of IL-1β and phosphorylation levels of p38 MAPK within the mPFC. With an intracerebral injection of AAV-IL-1β-RNAi virus into the vmPFC of stressed rats, as a means to block IL-1β expression and function, a significant reduction in p38 MAPK phosphorylation levels were observed. This effect paralleled the decreases in pro-apoptotic proteins levels suggesting that CUMS-induced neuroinflammation played a critical role in p38 MAPK phosphorylation. More importantly, the decreases in neuronal apoptosis within the vmPFC and depression-like behaviors induced by CUMS were also ameliorated by the injection of IL-1β-RNAi virus. Conversely, an overexpression of IL-1β as accomplished with an infusion of AAV-IL-1β virus into the vmPFC of unstressed rats up-regulated the activity of the p38 MAPK pathway and produced apoptotic phenotypes similar to that induced by chronic stress. However, a 2-week treatment of curcumin following AAV-IL-1β virus infusion significantly prevented the IL-1β/p38 MAPK pathway-induced neuronal apoptosis in the vmPFC along with a downregulation in the pro-apoptotic proteins Bak, Caspase-3 and Caspase-9 and an upregulation of the anti-apoptotic protein Bcl-2. Related results from a previous study have supported these findings as IL-1β has been shown to activate p38 MAPK cascades (Yu et al., 2017) and been shown to induce robust neuronal apoptosis resulting in neuronal injury within the rat hippocampus (Dong et al., 2017). Collating these findings, it seems likely that IL-1β-activated p38 MAPK cascades may participate in the ameliorative effects of curcumin on neuronal apoptosis and depression-like behaviors in our CUMS rats. In this way, IL-1β/p38 MAPK dysregulation may serve as an important trigger involved in the neurobiological and behavioral changes in stressed rats and that the antidepressant mechanisms of curcumin may result from its modulatory neuroprotective effects upon these pathways within localized depression-related sites of the brain. However, detailed molecular mechanisms regarding the means through which chronic stress may regulate IL-1β expression will require further investigation.

This study has some limitations. Firstly, it should be noted out that the nuuroinflammation theory of depression is only one hypothesis among several possibilities underlying the pathophysiological mechanisms. Moreover, only IL-1β was subjected to further investigation and analysis in this depression animal model, and the analysis of other pro-inflammatory factors would also be valuable. Additionally, the present study lacks of direct evidence to confirm the neuroinflammatory response act as a causative factor led to the depressive behaviors in rats. Therefore, whether and how curcumin exerts antidepressant-like effects via suppressing neuroinflammation remains further investigation. Finally, depression is a complex disease involving potential interactions among gene-environment and gene-gender factors. This study failed to consider gender factors, which could also influence the study results.

In summary, the present study revealed a potential novel neuroprotective mechanism whereby curcumin exerts antidepressant-like effects might via preventing inflammation-induced neuronal apoptosis in an animal model of depression. Our current results suggest that curcumin attenuates CUMS-induced neuronal apoptosis by inhibiting the IL-1β/p38 MAPK signaling pathway and regulating apoptosis-related protein expressions. Such findings not only reveal some of the underlying mechanisms for curcumin's beneficial effects but also their potential for use as a therapeutic strategy against inflammation-related neuronal disorders.

AUTHOR CONTRIBUTIONS

CF, QS, PW, and SY contributed to the study design and analyses of data. CF performed the biochemical analysis and intracerebroventricular injections, immunohistochemistry and confocal imaging and Golgi staining experiments with QS. PW performed the synaptic image analysis. YL and MY performed depression model and behavioral tests. SY wrote the first draft. CF and QS participated in the subsequent drafts.

FUNDING

This study was supported by grants to SY from the National Natural Science Foundation of China (NSFC81873796 and NSFC81471371), Shandong Provincial Key Research and Development Plan (2017CXGC1504), the Key Research and Development Foundation of Shandong Province (2018GSF118050), and the Fundamental Research Funds of Shandong University (2018JC008).

REFERENCES

Alcocer-Gomez, E., Ulecia-Moron, C., Marin-Aguilar, F., Rybkina, T., Casas-Barquero, N., Ruiz-Cabello, J., et al. (2015). Stress-induced depressive behaviors require a functional NLRP3 inflammasome. *Mol. Neurobiol.* 53, 4874–4882. doi: 10.1007/s12035-015-9408-7

Andrade, C. (2014). A critical examination of studies on curcumin for depression. *J. Clin. Psychiatry* 75, 1110–1112. doi: 10.4088/JCP.14f09489

Benzer, F., Kandemir, F. M., Kucukler, S., Comakl, S., and Caglayan, C. (2018). Chemoprotective effects of curcumin on doxorubicin-induced nephrotoxicity in wistar rats: by modulating inflammatory cytokines, apoptosis, oxidative stress and oxidative DNA damage. *Arch. Physiol. Biochem.* 5, 1–10. doi: 10.1080/13813455.2017.1422766

Bhutani, M. K., Bishnoi, M., and Kulkarni, S. K. (2009). Anti-depressant like effect of curcumin and its combination with piperine in unpredictable chronic stress-induced behavioral, biochemical and neurochemical changes. *Pharmacol. Biochem. Behav.* 92, 39–43. doi: 10.1016/j.pbb.2008.10.007

Cook, S. C., and Wellman, C. L. (2004). Chronic stress alters dendritic morphology in rat medial prefrontal cortex. *J. Neurobiol.* 60, 236–248. doi: 10.1002/neu.20025

Daverey, A., and Agrawal, S. K. (2016). Curcumin alleviates oxidative stress and mitochondrial dysfunction in astrocytes. *Neuroscience* 333, 92–103. doi: 10.1016/j.neuroscience.2016.07.012

Daverey, A., and Agrawal, S. K. (2018). Pre and post treatment with curcumin and resveratrol protects astrocytes after oxidative stress. *Brain Res.* 1692, 45–55. doi: 10.1016/j.brainres.2018.05.001

Dean, J., and Keshavan, M. (2017). The neurobiology of depression: an integrated view. *Asian J. Psychiatr.* 27, 101–111. doi: 10.1016/j.ajp.2017.01.025

Dong, Y., Kalueff, A. V., and Song, C. (2017). N-methyl-d-aspartate receptor-mediated calcium overload and endoplasmic reticulum stress are involved in interleukin-1beta-induced neuronal apoptosis in rat hippocampus. *J. Neuroimmunol.* 307, 7–13. doi: 10.1016/j.jneuroim.2017.03.005

Dowlati, Y., Herrmann, N., Swardfager, W., Liu, H., Sham, L., Reim, E. K., et al. (2010). A meta analysis of cytokines in major depression. *Biol. Psychiatr.* 67, 446–457. doi: 10.1016/j.biopsych.2009.09.033

Du, R. H., Tan, J., Sun, X. Y., Lu, M., Ding, J. H., and Hu, G. (2016). Fluoxetine inhibits NLRP3 inflammasome activation: implication in depression. *Int. J. Neuropsychopharmacol.* 19:yw037. doi: 10.1093/ijnp/pyw037

Duman, C. H., Schlesinger, L., Kodama, M., Russell, D. S., and Duman, R. S. (2007). A role for MAP kinase signaling in behavioral models of depression and antidepressant treatment. *Biol. Psychiatry* 61, 661–670. doi: 10.1016/j.biopsych.2006.05.047

Ereshefsky, L. (2009). Drug-drug interactions with the use of psychotropic medications: questions and answers. *CNS Spectr.* 14, 1–8.

Eriksson, M., Peña-Martínez, P., Ramakrishnan, R., Chapellier, M., Högberg, C., Glowacki, G., et al. (2017). Agonistic targeting of TLR1/TLR2 induces p38 MAPK-dependent apoptosis and NFκB-dependent differentiation of AML cells. *Blood Adv.* 1, 2046–2057. doi: 10.1182/bloodadvances.2017006148

Fan, C., Zhu, X., Song, Q., Wang, P., Liu, Z., and Yu, S. Y. (2018). MiR-134 modulates chronic stress-induced structural plasticity and depression-like behaviors via downregulation of Limk1/cofilin signaling in rats. *Neuropharmacology* 33, 364–376. doi: 10.1016/j.neuropharm.2018.01.009

Fernanda, N. K., Ana, P. C., Gabriele, G., Alexandre, P. D., Ana Lúcia, S. R., Hugo, P., et al. (2017). NLRP3 inflammasome-driven pathways in depression: clinical and preclinical findings. *Brain Behav. Immun.* 64, 367–383. doi: 10.1016/j.bbi.2017.03.002

Gilabert-Juan, J., Castillo-Gomez, E., Pérez-Rando, M., Moltó, M. D., and Nacher, J. (2011). Chronic stress induces changes in the structure of interneurons and in the expression of molecules related to neuronal structural plasticity and inhibitory neurotransmission in the amygdala of adult mice. *Exp. Neurol.* 232, 33–40. doi: 10.1016/j.expneurol.2011.07.009

Goldwater, D. S., Pavlides, C., Hunter, R. G., Bloss, E. B., Hof, P. R., and McEwen, B. S. (2009). Structural and functional alterations to rat medial prefrontal cortex following chronic restraint stress and recovery. *Neuroscience* 164, 798–808. doi: 10.1016/j.neuroscience.2009.08.053

Han, Q., Lin, Q., Huang, P., Chen, M., Hu, X., Fu, H., et al. (2017). Microglia-derived IL-1β contributes to axon development disorders and synaptic deficit through p38-MAPK signal pathway in septic neonatal rats. *J. Neuroinflammation* 14:52. doi: 10.1186/s12974-017-0805-x

Holmes, A., and Wellman, C. L. (2009). Stress-induced prefrontal reorganization and executive dysfunction in rodents. *Neurosci. Biobehav. Rev.* 33, 773–783. doi: 10.1016/j.neubiorev.2008.11.005

Iadecola, C., and Anrather, J. (2011). The immunology of stroke: from mechanisms to translation. *Nat. Med.* 17, 796–808. doi: 10.1038/nm.2399

Kim, E. K., and Choi, E. J. (2015). Compromised MAPK signaling in human diseases: an update. *Arch. Toxicol.* 89, 867–882. doi: 10.1007/s00204-015-1472-2

Kim, J. Y., Kim, N., Yenari, M. A. (2015). Mechanisms and potential therapeutic applications of microglial activation after brain injury. *CNS Neurosci. Ther.* 21, 309–319. doi: 10.1111/cns.12360

Labus, J., Häcke, S., Lucka, L., and Danker, K. (2014). Interleukin-1β induces an inflammatory response and the breakdown of the endothelial cell layer in an improved human THBMEC-based in vitro blood-brain barrier model. *J. Neurosci. Methods* 228, 35–45. doi: 10.1016/j.jneumeth.2014.03.002

Lee, J. Y., Kang, S. R., and Yune, T. Y. (2015). Fluoxetine prevents oligodendrocyte cell death by inhibiting microglia activation after spinal cord injury. *J. Neurotrauma.* 32, 633–644. doi: 10.1089/neu.2014.3527

Li, D., and Ai, Y. (2017). Hydrogen saline suppresses neuronal cell apoptosis and inhibits the p38 mitogen-activated protein kinase-caspase-3 signaling pathway following cerebral I,schemia-reperfusion injury. *Mol. Med. Rep.* 16, 5321–5325. doi: 10.3892/mmr.2017.7294

Li, Y., Liu, L., Barger, S. W., and Griffin, W. S. J. (2003). Interleukin-1 mediates pathological effects of microglia on tau phosphorylation and on synaptophysin synthesis in cortical neurons through a p38-MAPK pathway. *Neuroscience* 23, 1605–1611. doi: 10.1523/JNEUROSCI.23-05-01605.2003

Lopresti, A. L., Maes, M., Maker, G. L., Hood, S. D., and Drummond, P. D. (2014). Curcumin for the treatment of major depression: a randomised, double-blind, placebo controlled study. *J. Affect. Disord.* 167, 368–375. doi: 10.1016/j.jad.2014.06.001

Lopresti, A. L. (2017). Curcumin for neuropsychiatric disorders: a review of in vitro, animal and human studies. *J. Psychopharmacol.* 31, 287–302. doi: 10.1177/0269881116686883

Maes, M., Song, C., and Yirmiya, R. (2012). Targeting IL-1 in depression. *Expert Opin. Ther. Targets* 16, 1097–1112. doi: 10.1517/14728222.2012.718331

Maiti, P., and Dunbar, G. L. (2018). Use of curcumin, a natural polyphenol for targeting molecular pathways in treating age-related neurodegenerative diseases. *Int. J. Mol. Sci.* 194, E1637. doi: 10.3390/ijms19061637

Mao, Q. Q., Ip, S. P., Ko, K. M., Tsai, S. H., and Che, C. T. (2009). Peony glycosides produce antidepressant-like action in mice exposed to chronic unpredictable mild stress: effects on hypothalamic-pituitary-adrenal function and brain-derived neurotrophic factor. *Prog. Neuropsychopharmacol. Biol. Psychiatry* 33, 1211–1216. doi: 10.1016/j.pnpbp.2009.07.002

McLaughlin, K. J., Baran, S. E., and Conrad, C. D. (2009). Chronic stress- and sex-specific neuromorphological and functional changes in limbic structures. *Mol. Neurobiol.* 40, 166–182. doi: 10.1007/s12035-009-8079-7

Morgenstern, L. B., and Pettigrew, L. C. (1997). Brain protection–human data and potential new therapies. *New Horiz.* 5, 397–405.

Oh, D. H., Son, H., Hwang, S., and Kim, S. H. (2012). Neuropathological abnormalities of astrocytes, GABAergic neurons, and pyramidal neurons in the dorsolateral prefrontal cortices of patients with major depressive disorder. *Eur. Neuropsychopharmacol.* 22, 330–338. doi: 10.1016/j.euroneuro.2011.09.001

Pan, Y., Chen, X. Y., Zhang, Q. Y., and Kong, L. D. (2014). Microglial NLRP3 inflammasome activation mediates IL-1β-related inflammation in prefrontal cortex of depressive rats. *Brain Behav. Immun.* 41, 90–100. doi: 10.1016/j.bbi.2014.04.007

Panighini, A., Duranti, E., Santini, F., Maffei, M., Pizzorusso, T., Funel, N., et al. (2013). Vascular dysfunction in a mouse model of Rett syndrome and effects of curcumin treatment. *PLoS One* 8:e64863. doi: 10.1371/journal.pone.0064863

Pariante, C. M. (2017). Why are depressed patients inflamed? A reflection on 20 years of research on depression, glucocorticoid resistance and inflammation. *Eur. Neuropsychopharmacol.* 27, 554–559. doi: 10.1016/j.euroneuro.2017.04.001

Park, M. T., Choi, J. A., Kim, M. J., Um, H. D., Bae, S., Kang, C. M., et al. (2003). Suppression of extracellular signal-related kinase and activation of p38 MAPK are two critical events leading to caspase-8- and mitochondria-mediated cell death in phytosphingosine-treated human cancer cells. *J. Biol. Chem.* 278, 50624–50634. doi: 10.1074/jbc.M309011200

Porsolt, R. D., Le Pichon, M., and Jalfre, M. (1977). Depression: a new animal model sensitive to antidepressant treatments. *Nature* 266, 730–732. doi: 10.1038/266730a0

Radley, J. J., Rocher, A. B., Miller, M., Janssen, W. G., Liston, C., and Hof, P. R. (2006). Repeated stress induces dendritic spine loss in the rat medial prefrontal cortex. *Cereb. Cortex* 16, 313–320. doi: 10.1093/cercor/bhi104

Ramirez, K., Shea, D. T., McKim, D. B., Reader, B. F., and Sheridan, J. F. (2015). Imipramine attenuates neuroinflammatory signaling and reverses stress-induced social avoidance. *Brain Behav. Immun.* 46, 212–220. doi: 10.1016/j.bbi.2015.01.016

Rawdin, B. J., Mellon, S. H., Dhabhar, F. S., Epel, E. S., Puterman, E., Su, Y., et al. (2013). Dysregulated relationship of inflammation and oxidative stress in major depression. *Brain Behav. Immun.* 31, 143–152. doi: 10.1016/j.bbi.2012.11.011

Rinwa, P., Kumar, A., and Garg, S. (2013). Suppression of neuroinflammatory and apoptotic signaling cascade by curcumin alone and in combination with piperine in rat model of olfactory bulbectomy induced depression. *PLoS One* 8:e61052. doi: 10.1371/journal.pone.0061052

Su, W. J., Zhang, Y., Chen, Y., Gong, H., Lian, Y. J., Peng, W., et al. (2017). NLRP3 gene knockout blocks NF-κB and MAPK signaling pathway in CUMS-induced depression mouse model. *Behav. Brain Res.* 322, 1–8. doi: 10.1016/j.bbr.2017.01.018

Takahashi, H., Koeda, M., Oda, K., Matsuda, T., Matsushima, E., Matsuura, M., et al. (2004). An fMRI study of differential neural response to affective pictures in schizophrenia. *Neuroimage* 22, 1247–1254. doi: 10.1016/j.neuroimage.2004.03.028

Tan, M. S., Yu, J. T., Jiang, T., Zhu, X. C., and Tan, L. (2013). The NLRP3 inflammasome in Alzheimer's disease. *Mol. Neurobiol.* 48, 875–882. doi: 10.1007/s12035-013-8475-x

Tsai, S. J. (2017). Effects of interleukin-1beta polymorphisms on brain function and behavior in healthy and psychiatric disease conditions. *Cytokine Growth Factor Rev.* 37, 89–97. doi: 10.1016/j.cytogfr.2017.06.001

Tuon, T., Souza, P. S., Santos, M. F., Pereira, F. T., Pedroso, G. S., Luciano, T. F., et al. (2015). Physical training regulates mitochondrial parameters and neuroinflammatory mechanisms in an experimental model of Parkinson's disease. *Oxid. Med. Cell. Longev.* 2015:261809. doi: 10.1155/2015/261809

Venigalla, M., Gyengesi, E., and Münch, G. (2015). Curcumin and apigenin-novel and promising therapeutics against chronic neuroinflammation in Alzheimer's disease. *Neural Regen. Res.* 10, 1181–1185. doi: 10.4103/1673-5374.162686

Wang, Y., Xia, C., Lun, Z., Lv, Y., Chen, W., and Li, T. (2018). Crosstalk between p38 MAPK and caspase-9 regulates mitochondria-mediated apoptosis induced by tetra-α-(4-carboxyphenoxy) phthalocyanine zinc photodynamic therapy in LoVo cells. *Oncol. Rep.* 39, 61–70. doi: 10.3892/or.2017.6071

Wasik, A., and Antkiewicz-Michaluk, L. (2017). The mechanism of neuroprotective action of natural compounds. *Pharmacol. Rep.* 69, 851–860. doi: 10.1016/j.pharep.2017.03.018

Yu, J., Berga, S. L., Zou, W., Yook, D. G., Pan, J. C., Andrade, A. A., et al. (2017). IL-1β inhibits connexin 43 and disrupts decidualization of human endometrial stromal cells through erk1/2 and p38 MAP kinase. *Endocrinology* 158, 4270–4285. doi: 10.1210/en.2017-00495

Zhang, L., Luo, J. X., Zhang, M., Yao, W., Ma, X., and Yu, S. Y. (2014). Effects of curcumin on chronic unpredictable mild stress-induced depressive-like behavior and structural plasticity in the lateral amygdala of rats. *Int. J. Neuropsychopharmacol.* 17, 793–806. doi: 10.1017/S1461145713001661

Zhang, J., Wei, H., Lin, M., Chen, C., Wang, C., and Liu, M. (2013). Curcumin protects against ischemic spinal cord injury: The pathway effect. *Neural. Regen. Res.* 8, 3391–3400. doi: 10.3969/j.issn.1673-5374.2013.36.004

Zhang, N., Zhang, X., Liu, X., Wang, H., Xue, J., Yu, J., et al. (2014). Chrysophanol inhibits NALP3 inflammasome activation and ameliorat cerebral ischemia/reperfusion in mice. *Mediat. Inflamm.* 2014:370530. doi: 10.1155/2014/370530

Zhou, H., Beevers, C. S., and Huang, S. (2011). The targets of curcumin. *Curr. Drug Targets* 12, 332–347. doi: 10.2174/138945011794815356

Zou, W., Feng, R., and Yang, Y. (2018). Changes in the serum levels of inflammatory cytokines in antidepressant drug-naïve patients with major depression. *PLoS One* 13:e0197267. doi: 10.1371/journal.pone.0197267

Conflict of Interest Statement: The authors declare that the research was conducted in the absence of any commercial or financial relationships that could be construed as a potential conflict of interest.

Copyright © 2019 Fan, Song, Wang, Li, Yang and Yu. This is an open-access article distributed under the terms of the Creative Commons Attribution License (CC BY). The use, distribution or reproduction in other forums is permitted, provided the original author(s) and the copyright owner(s) are credited and that the original publication in this journal is cited, in accordance with accepted academic practice. No use, distribution or reproduction is permitted which does not comply with these terms.

frontiers in Cellular Neuroscience

ORIGINAL RESEARCH
published: 24 January 2019
doi: 10.3389/fncel.2019.00008

Transduction of Adeno-Associated Virus Vectors Targeting Hair Cells and Supporting Cells in the Neonatal Mouse Cochlea

Xi Gu[1,2], Renjie Chai[3,4,5,6], Luo Guo[7,8], Biao Dong[9], Wenyan Li[7], Yilai Shu[7,8], Xinsheng Huang[1]* and Huawei Li[7,8,10,11,12]**

[1] Department of Otorhinolaryngology-Head and Neck Surgery, Zhongshan Hospital, Fudan University, Shanghai, China, [2] Department of Otolaryngology-Head and Neck Surgery, The First Affiliated Hospital of Fujian Medical University, Fuzhou, China, [3] Key Laboratory for Developmental Genes and Human Disease, Ministry of Education, Institute of Life Sciences, Southeast University, Nanjing, China, [4] Co-innovation Center of Neuroregeneration, Nantong University, Nantong, China, [5] Institute for Stem Cell and Regeneration, Chinese Academy of Sciences, Beijing, China, [6] Jiangsu Province High-Tech Key Laboratory for Bio-Medical Research, Southeast University, Nanjing, China, [7] ENT Institute and Otorhinolaryngology Department, Eye and ENT Hospital, State Key Laboratory of Medical Neurobiology, Fudan University, Shanghai, China, [8] NHC Key Laboratory of Hearing Medicine, Fudan University, Shanghai, China, [9] National Clinical Research Center for Geriatrics, State Key Laboratory of Biotherapy, West China Hospital, Sichuan University and Collaborative Innovation Center for Biotherapy, Chengdu, China, [10] Institutes of Biomedical Sciences, Fudan University, Shanghai, China, [11] Shanghai Engineering Research Center of Cochlear Implant, Shanghai, China, [12] The Institutes of Brain Science and the Collaborative Innovation Center for Brain Science, Fudan University, Shanghai, China

OPEN ACCESS

Edited by:
Josef Bischofberger, Universität Basel, Switzerland

Reviewed by:
Ellen Reisinger, University Medical Center Göttingen, Germany
Shin-ichi Muramatsu, Jichi Medical University, Japan

***Correspondence:**
Yilai Shu
yilai_shu@fudan.edu.cn
Xinsheng Huang
huang.xinsheng@zs-hospital.sh.cn
Huawei Li
hwli@shmu.edu.cn

Received: 20 September 2018
Accepted: 10 January 2019
Published: 24 January 2019

Citation:
Gu X, Chai R, Guo L, Dong B, Li W, Shu Y, Huang X and Li H (2019) Transduction of Adeno-Associated Virus Vectors Targeting Hair Cells and Supporting Cells in the Neonatal Mouse Cochlea. Front. Cell. Neurosci. 13:8. doi: 10.3389/fncel.2019.00008

Adeno-associated virus (AAV) is the preferred vector for gene therapy of hereditary deafness, and different viral serotypes, promoters and transduction pathways can influence the targeting of AAV to different types of cells and the expression levels of numerous exogenous genes. To determine the transduction and expression patterns of AAV with different serotypes or promoters in hair cells and supporting cells in the neonatal mouse cochlea, we examined the expression of enhanced green fluorescent protein (eGFP) for five different types of AAV vectors [serotypes 2, 9, and Anc80L65 with promoter cytomegalovirus (CMV)-beta-Globin and serotypes 2 and 9 with promoter chicken beta-actin (CBA)] in *in vitro* cochlear explant cultures and we tested the transduction of AAV2/2-CBA, AAV2/9-CBA, and AAV2/Anc80L65-CMV by *in vivo* microinjection into the scala media of the cochlea. We found that each AAV vector had its own transduction and expression characteristics in hair cells and supporting cells in different regions of the cochlea. There was a tonotopic gradient for the *in vitro* transduction of AAV2/2-CBA, AAV2/9-CBA, AAV2/2-CMV, and AAV2/9-CMV in outer hair cells (OHCs), with more OHCs expressing eGFP at the base of the cochlea than at the apex. AAV2/2-CBA *in vitro* and AAV2/Anc80L65-CMV *in vivo* induced more supporting cells expressing eGFP at the apex than in the base. We found that AAV vectors with different promoters had different expression efficacies in hair cells and supporting cells of the auditory epithelium. The CMV-beta-Globin promoter could drive the expression of the delivered construct more efficiently in hair cells, while the CBA promoter was more efficient in supporting cells. The *in vitro* and *in vivo* experiments both

demonstrated that AAV2/Anc80L65-CMV was a very promising vector for gene therapy of deafness because of its high transduction rates in hair cells. These results might be useful for selecting the appropriate vectors for gene delivery into different types of inner ear cells and thus improving the effectiveness of gene therapy.

Keywords: adeno-associated virus vectors, gene therapy, cochlea, hair cell, supporting cell, promoter

INTRODUCTION

Noise, ototoxic drugs, infections, autoimmune diseases, and hereditary factors can cause loss of hair cells (HCs) and/or functional deficiency of HCs and supporting cells (SCs). Such changes are usually irreversible and account for a large proportion of all incidences of sensorineural hearing loss. The treatment for hereditary deafness caused by hundreds of different gene mutations has traditionally been hearing aids or cochlear implants, but these rarely achieve the desired effect. Gene therapy is therefore a very promising approach to restoring hearing in patients with hereditary deafness (Akil et al., 2012; Lentz et al., 2013; Yu et al., 2014; Askew et al., 2015; Zuris et al., 2015; Chien et al., 2016; Gao et al., 2018).

Adeno-associated virus (AAV) is the preferred vector for gene therapy in the treatment of sensorineural hearing loss (Li Duan et al., 2002; Lustig and Akil, 2012). Different serotypes, promoters, and transduction pathways can influence the targeting of AAV to different types of cells (Sacheli et al., 2013); for example, AAV2/2 can transduce HCs and SCs *in vitro* (Stone et al., 2005), while introduction of AAV2/2 into the inner ear through the round window can only transduce the spiral limbus, spiral ganglion cells, and the spiral ligament (Jero et al., 2001; Luebke et al., 2001a; Li Duan et al., 2002). Morphologically, gene expression has been shown to be more abundant after injection into the scala media compared to injection into the scala tympani (Shibata et al., 2009), and it has been shown that delivery of AAV1-Kcnq1-GFP into the inner ear through the scala media can induce the expression of target genes in marginal cells of the stria vascularis (Chang et al., 2015). Yu et al. (2014) inoculated modified AAV vectors into the scala media of early postnatal conditional *Gjb2* knockout mice to drive exogenous connexin26 expression. They found extensive virally expressed connexin26 in cells lining the scala media, and the intercellular gap junction network was re-established in the organ of Corti of the mutant mouse cochlea, although auditory brainstem responses (ABRs) did not show significant hearing improvement. Akil et al. (2012) reported the successful restoration of hearing in the *Vglut3* knockout mouse using AAV-mediated gene delivery. They found that cochlear delivery of Vglut3 using AAV1 led to transgene expression only in inner hair cells (IHCs), and within 2 weeks of AAV1-Vglut3 delivery the click ABR thresholds had almost normalized. These findings indicate the successful restoration of hearing by gene replacement in mice, which is an important step toward gene therapy for human deafness.

Deafness results from damage to many different cell types in the inner ear. To cure deafness by restoring the structure and function of the damaged cells, we need more knowledge about the transduction characteristics of AAV vectors so as to choose the most appropriate AAV vectors for specific and accurate transgene expression. To clarify the targeting and expression features of AAV vectors with different serotypes or promoters, we investigated the transduction efficiencies of five different AAV vectors [serotypes 2, 9, and Anc80L65 with the cytomegalovirus (CMV)-beta-Globin promoter and serotypes 2 and 9 with the chicken beta-actin (CBA) promoter] in HCs and SCs in the apical, middle, and basal turns of the cochlea. We also chose AAV2/2-CBA, AAV2/9-CBA, and AAV2/Anc80L65-CMV for our *in vivo* experiments due to their high expression efficacy in SCs *in vitro*. While there have been many studies (Liu et al., 2005; Stone et al., 2005; Bedrosian et al., 2006; Ballana et al., 2008; Konishi et al., 2008; Kilpatrick et al., 2011; Shu et al., 2016; Landegger et al., 2017) comparing the transduction efficiencies of different AAV serotypes in inner ear cells, few studies (Liu et al., 2007; Luebke et al., 2009) have focused on the difference in expression efficacy between promoters. Luebke et al. (2009) found that AAV1/2 using astrocyte-specific promoters [the glial fibrillary acid protein (GFAP) and the brain lipid-binding protein (BLBP)] had the potential to drive SC-specific expression in the adult guinea pig cochlea, but the injection of AAV1/2-GFAP/BLBP-eGFP caused the loss of outer hair cells (OHCs). In their experiments, they did not compare the expression efficacy between the two promoters in SCs. Liu et al. (2007) evaluated the expression of enhanced green fluorescent protein (eGFP) driven by six different promoters, including the CMV IE enhancer and CBA promoter (CAG), the CMV promoter, the neuron-specific enolase promoter, the myosin 7A (Myo7a) promoter, the elongation factor 1α promoter, and the Rous sarcoma virus promoter, but the level of eGFP expression was graded by fluorescent intensity rather than presented as a specific number of eGFP positive ($eGFP^+$) cells. To date, there have been no reports comparing the expression efficacy of AAV vectors with different promoters in SCs. Few studies have directly compared the performance of viral vectors in titer and promoter-matched and controlled conditions as has been done in the present work. In this work, we studied the transduction patterns of AAV vectors with different serotypes, and we present detailed data on transduction efficiencies in different regions of the cochlea. We found that AAV vectors with different promoters (CMV-beta-Globin or CBA) had different expression efficacies in HCs and SCs of the auditory epithelium. We conclude that CMV-beta-Globin is a superior promoter for driving expression of the delivered construct in HCs, while the CBA promoter is superior at driving expression in SCs.

MATERIALS AND METHODS

Animals

We used C57BL/6J wild type mice to examine the transduction efficiency of different types of AAV vectors *in vitro*, and we used ICR wild type mice for the *in vivo* experiments. All animal experiments were approved by the Institutional Animal Care and Use Committee of Fudan University.

Viral Vectors

We tested the transduction efficiency of five different types of AAV vectors that mediated the expression of eGFP. Three of the AAV vectors had the CMV-beta-Globin promoter and the Woodchuck hepatitis virus post-transcriptional regulatory element cassette (original titer given in parentheses), namely AAV2/2-CMV-beta-Globin-eGFP [1×10^{13} viral genomes (VG) per ml], AAV2/9-CMV-beta-Globin-eGFP (1×10^{13} VG/ml) and AAV2/Anc80L65-CMV-beta-Globin-eGFP (2.08×10^{12} VG/ml), and these were purchased from the Biolink Company (Shanghai, China). The other two AAV vectors had the CBA promoter, namely AAV2/2-CBA-eGFP (1×10^{13} VG/ml) and AAV2/9-CBA-eGFP (1×10^{13} VG/ml), and these were kindly given as gifts from Professor Biao Dong of Sichuan University. The AAV2/Anc80L65 plasmid reagents are available through http://www.addgene.com. The CMV-beta-Globin promoter is comprised of a CMV immediate early enhancer and the CMV promoter itself. The intron part of the rabbit beta-Globin gene is in the promoter. The origin of the CBA promoter is from a well-characterized plasmid pscAAV-CBA-eGFP which was used for the packaging of a self-complementary AAV vector. The part we took is the CBA promoter and an intron just behind it which was widely used to enhance the expression of the gene of interest. The eGFP expression was analyzed 7 days after virus incubation *in vitro* and 1 month after virus injection *in vivo*.

All the AAV vectors were generated utilizing the triple-plasmid co-transfection method as previously described (Wang et al., 2014). The AAV vectors from Sichuan University were purified by two rounds of cesium chloride (CsCl) gradient ultracentrifugations (Wang et al., 2014), and the AAV vectors from the Biolink Company were purified using the discontinuous iodixanol density gradient centrifugation procedure (Grieger et al., 2006). Virus titers were measured by quantitative polymerase chain reaction (qPCR) as previously described (Wang et al., 2016). The previous results showed that the full particles in the vectors purified using the CsCl gradient centrifugation procedure were >90% by electronic microscopy (Wang et al., 2016), while the full particles in the vectors purified using the iodixanol gradient centrifugation procedure were >80% (Grieger et al., 2006).

Virus purity of the AAV vectors from Sichuan University was examined by silver staining after separation using a sodium dodecyl sulfate polyacrylamide gel electrophoresis (SDS-PAGE) gel and the purity of VPs of the vectors was >90%. For the purity test of the AAV vectors from the Biolink Company, the protein samples were prestained by Band-Now Pre-Staining Protein Sample Treatment Buffer (Sangon Biotech) during sample treatment prior to electrophoresis and the result of protein purity could be directly observed after SDS-PAGE under an UV transilluminator. The results showed that the purity of vectors from the Biolink Company was >95%.

We obtained two different lots of virus for each AAV vector. To validate the quality and stability of virus, we tested the transduction efficiency of two lots of virus in cochlear explant cultures with the same experimental conditions and compared the transduction efficiencies of AAV vectors in HCs between the two different lots.

In vitro Cochlear Explant Cultures

After being dissected in pre-chilled phosphate buffered saline (PBS, Hyclone), the cochleae of postnatal day 1 (P1) C57BL/6J mice were cultured in DMEM/F12 (Hyclone) with 1% N2 supplement (Life Technologies), 2% B27 supplement (Life Technologies), and 50 μg/ml ampicillin (Sigma) at 37°C with 5% CO_2. The virus was applied after 2 h in culture, and all of the explants were cultured in the nutrient solution with AAV vectors for 48 h. The medium was then changed to a DMEM/F12 mixture without virus, and the explants were cultured for another 5 days. During the culture, the medium was changed every other day.

In vivo AAV Microinjections

P2–3 ICR mice were used for AAV2/2-CBA, AAV2/9-CBA and AAV2/Anc80L65-CMV-beta-Globin injection. Mice were anesthetized with low temperature exposure by placing them on ice, and a skin incision was made behind the right ear of the mouse to expose the otic bulla and the stapedial artery. Glass micropipettes (WPI, Sarasota, FL) held by a Nanoliter Microinjection System (WPI) were used to penetrate into the scala media through the soft cochlear lateral wall. The total injection volume was 0.2 μl per cochlea, and the injection was controlled by a micromanipulator at a speed of 3 nl/s (Shu et al., 2016). The mice were sacrificed at 1 month after AAV injection.

Hearing Tests After AAV Injection

All injected animals survived the surgery. The ABR test was used to measure hearing 1 month after virus injection, and the un-injected ears were used as controls. Tone burst sound stimuli were presented at 4, 8, 16, and 24 kHz to test frequency-specific hearing thresholds as previously described (Huang et al., 2013). The ABR thresholds were analyzed blinded.

Immunohistochemistry

After being cultured for a total of 7 days *in vitro*, the cochleae were fixed with 4% (wt/vol) paraformaldehyde (Sigma) for 30 min at room temperature. All samples were then permeabilized and blocked in PBS containing 1% Triton X-100 (1% PBS-T) and 10% donkey serum for 1 h at room temperature. All primary and secondary antibodies were diluted in 1% PBS-T. To observe the eGFP expression in HCs and SCs of the cochlear sensory epithelium, we used rabbit anti-Myo7a (1:600 dilution, Proteus BioSciences) and goat anti-Sox2 (1:300 dilution, Santa Cruz) primary antibodies to label HCs and SCs, respectively. To compare the transduction rates between different samples in the

same fluorescence condition, all of the *in vitro* samples were analyzed by the cellular eGFP fluorescence itself, while the eGFP fluorescence of *in vivo* samples was enhanced by immunolabeling with chicken anti-eGFP primary antibody (1:1,000 dilution, Abcam). Appropriate Alexa-conjugated secondary antibodies were used for detection, and DAPI was used to label the nuclei (1:1,000 dilution, Sigma).

Cochleae were dissected from the temporal bones at 1 month after AAV2/2-CBA, AAV2/9-CBA, and AAV2/Anc80L65-CMV injection *in vivo*, and the samples were fixed with 4% paraformaldehyde for 60 min at room temperature. After rinsing with PBS three times, we soaked all of the cochleae in 10% EDTA for 3 days for decalcification. The entire basilar membrane was divided into three pieces of equal length designated the basal, middle, and apical turns of the cochlea. Subsequent staining steps followed the same procedures as described above.

Cell Counting and Statistics

A Leica TCS SP8 laser scanning confocal microscope was used to observe the immunohistochemical staining and to collect fluorescent Z-stack images. We used a 40× objective for microscopy, and the z-step size was 1 μm. The maximum intensity projections of optical confocal sections are displayed in the figures. For cell counting, the numbers of $Myo7a^+$ HCs, $Sox2^+$ SCs outside of IHCs, $Myo7a^+/eGFP^+$ cells and $Sox2^+/eGFP^+$ cells were counted in every 200 μm region of the apical, middle, and basal turns of the cochlea using ImageJ software. For *in vitro* experiments, five 200 μm regions were counted to derive a value for each "Apex," "Mid," and "Base" region when calculating the transduction efficiency of AAV vectors in HCs of the three regions, respectively. Four 200 μm regions were counted to calculate the transduction efficiency of AAV vectors in SCs of the three regions, respectively. In some cases, the average transduction efficiency of AAV vectors in SCs of the whole cochlea was calculated by averaging the transduction efficiencies of the three regions. For *in vivo* experiments, at least three samples in each group from three independent experiments were collected. The transduction efficiencies of AAV vectors targeting HCs or SCs were calculated as the ratio of $Myo7a^+/eGFP^+$ cells to $Myo7a^+$ cells or the ratio of $Sox2^+/eGFP^+$ cells to $Sox2^+$ cells, respectively. The results are presented as the mean ± standard deviation, and all statistical analyses were performed with GraphPad Prism 6.0. In the case of abnormal distribution, a non-parametric statistical test (Mann–Whitney *U* test) was applied to analyze the data. In the case of normal distribution and equal variance, unpaired two-tailed Student's *t*-test was applied to determine statistical significance. Unpaired *t*-test with Welch's correction was performed if the data conformed to a normal distribution but equal variance could not be assumed. When multiple comparison tests were applied to compare the transduction efficiencies of AAV vectors between different groups in the three regions of the cochlear, $P < 0.0167$ was considered statistically significant after Bonferroni correction. In other cases, $P < 0.05$ was considered statistically significant.

RESULTS

The Observation of the Culture Explants of the Neonatal Mouse Cochlea After AAV Incubation

After being cultured in the DMEM/F12 medium containing AAV vectors for 48 h, a small number of fibroblasts around the basilar membrane expressed eGFP. With longer culture time, the expression of eGFP in the sensory epithelium of the cochlea gradually increased, and the cells of the basal turn usually expressed eGFP before the other turns. On the fourth day of culture, the IHCs and OHCs presented different fluorescence intensities in different AAV groups.

Results of Validations With Multiple Lots of Each AAV Vector

The transduction efficiencies of AAV2/2-CBA, AAV2/9-CBA, AAV2/2-CMV, AAV2/9-CMV, and AAV2/Anc80L65-CMV with two different lots were presented in **Supplementary Table 1**. The transduction efficiencies in IHCs and OHCs of the apical, middle, and basal turns of the cochlea between two different lots were not statistically significantly different which indicated that the effectiveness of virus from both facilities were stable.

The Transduction Efficiency of AAV Vectors Targeting HCs With Different Working Titers

When the working titer was increased from 1×10^{11} VG/ml to 1×10^{12} VG/ml, the transduction efficiency of AAV2/2-CBA in IHCs and OHCs did not increase statistically significantly in the apical, middle, or basal turn of the cochlea. The percentage of $eGFP^+$ IHCs was no more than 10% throughout the cochlea on average at a titer of 1×10^{12} VG/ml. This suggests that even when the viral titer was very high, AAV2/2 with the CBA promoter still could not efficiently transduce IHCs (**Table 1** and **Supplementary Figure 1**). However, the transduction efficiency of AAV2/9-CBA in IHCs throughout the cochlea and in OHCs of the apical and middle turns increased statistically significantly as the titer increased. The transduction efficiency of AAV2/9-CBA was concentration-dependent in the IHCs and OHCs and there was a greater increase in transduction efficiency in IHCs (∼6-fold) compared to OHCs (∼2-fold) (**Table 1** and **Supplementary Figure 1**).

As the titer increased from 0.5×10^{11} VG/ml to 1×10^{11} VG/ml, the transduction efficiency of AAV2/2-CMV in IHCs in the basal turn of the cochlea increased statistically significantly (∼2-fold). However, the percentage of $eGFP^+$ OHCs did not increase statistically significantly. It is possible that in the case of the lower concentration AAV2/2-CMV preferentially transduced OHCs, and as the concentration increased more IHCs could be transduced (**Table 2** and **Supplementary Figure 2**). The transduction efficiency of AAV2/9-CMV in IHCs and OHCs did not increase statistically significantly as the titer increased (**Table 2** and **Supplementary Figure 2**). There was a

TABLE 1 | The transduction efficiencies of AAV2/2-CBA and AAV2/9-CBA in IHCs, OHCs, and SCs in the conditions of different viral titers.

Serotype	Cell type	Viral titer (VG/ml)	Apex (%)	Mid (%)	Base (%)
AAV2/2	IHCs	1×10^{11}	6.0 ± 3.2	3.9 ± 2.5	11.7 ± 12.7
		1×10^{12}	7.3 ± 5.8	9.1 ± 10.4	3.6 ± 2.1
	OHCs	1×10^{11}	35.1 ± 3.3	47.8 ± 16.4	68.2 ± 17.7
		1×10^{12}	56.2 ± 18.0	62.1 ± 21.7	75.2 ± 9.2
	SCs	1×10^{11}	35.8 ± 10.6	6.9 ± 9.1	4.2 ± 4.1
		5×10^{11}	47.1 ± 7.4	32.5 ± 30.6	24.6 ± 24.7
		1×10^{12}	61.4 ± 21.9	40.8 ± 38.3	7.6 ± 1.4
AAV2/9	IHCs	1×10^{11}	6.9 ± 2.9	4.2 ± 0.9	6.6 ± 1.7
		1×10^{12}	39.0 ± 17.4	41.6 ± 11.0	40.1 ± 14.9
	OHCs	1×10^{11}	4.5 ± 1.1	3.0 ± 1.9	26.2 ± 5.9
		1×10^{12}	25.9 ± 7.0	30.5 ± 12.2	17.9 ± 6.2
	SCs	1×10^{11}	4.3 ± 5.1	0	5.5 ± 11.1
		5×10^{11}	10.2 ± 11.8	19.1 ± 16.4	4.3 ± 5.2
		1×10^{12}	65.1 ± 20.6	53.6 ± 15.1	39.1 ± 11.8

The values were represented as mean ± standard deviation (n = 5 for HCs; n = 4 for SCs).

tonotopic gradient for the transduction efficiency of AAV2/2-CBA, AAV2/9-CBA, AAV2/9-CMV at a titer of 1×10^{11} VG/ml, and AAV2/2-CMV at a titer of 0.5×10^{11} VG/ml, with more OHCs expressing eGFP at the base of the cochlea than at the apex (**Supplementary Figure 5**).

We tested three virus titers, including 0.5×10^{11} VG/ml, 1×10^{11} VG/ml, and 2×10^{11} VG/ml, for the transduction of AAV2/Anc80L65-CMV. The transduction efficiencies of AAV2/Anc80L65-CMV in IHCs and OHCs were clearly concentration-dependent. With the concentration elevated within a narrow range, the percentage of both $eGFP^+$ IHCs and $eGFP^+$ OHCs increased statistically significantly. The transduction efficiencies in IHCs of the apical, middle, and basal turns were 97.8 ± 3.1%, 97.7 ± 3.4%, and 98.3 ± 2.3%, respectively, and the transduction efficiencies in OHCs of the apical, middle and basal turns were 93.1 ± 5.9%, 95.3 ± 1.2%, and 98.2 ± 1.9%, respectively, at a titer of 2×10^{11} VG/ml. Thus, the viral transduction rates of AAV2/Anc80L65-CMV in IHCs and OHCs were consistently high along the base-to-apex axis (**Table 2**, **Supplementary Figure 2**, and **Figure 3**).

Comparison of the Transduction Efficiencies Targeting HCs Between Different Serotypes of AAV Vectors With the Same Promoters

When the promoter was CBA, the differences in transduction efficiencies in IHCs between AAV2/2 and AAV2/9 were not statistically significant, and both of the transduction efficiencies were very low (<10%). However, AAV2/2-CBA had higher transduction efficiency than AAV2/9-CBA in OHCs in the apical (35.1 ± 3.3% vs. 4.5 ± 1.1%), middle (47.8 ± 16.4% vs.

TABLE 2 | The transduction efficiencies of AAV2/2, AAV2/9, and AAV2/Anc80L65 with the CMV-beta-Globin promoter in IHCs, OHCs, and SCs in the conditions of different viral titers.

Serotype	Cell type	Viral titer (VG/ml)	Apex (%)	Mid (%)	Base (%)
AAV2/2	IHCs	0.5×10^{11}	17.9 ± 14.0	20.0 ± 5.0	35.1 ± 16.6
		1×10^{11}	35.9 ± 24.3	45.5 ± 18.8	67.0 ± 6.5
	OHCs	0.5×10^{11}	56.2 ± 11.9	65.8 ± 14.3	81.2 ± 6.2
		1×10^{11}	68.3 ± 19.8	63.8 ± 22.8	76.0 ± 21.6
	SCs	1×10^{11}	14.8 ± 19.6	0	5.0 ± 10.0
		5×10^{11}	18.6 ± 7.4	19.7 ± 13.7	36.4 ± 5.9
		1×10^{12}	7.3 ± 8.6	5.5 ± 6.7	21.2 ± 15.0
AAV2/9	IHCs	0.5×10^{11}	43.7 ± 20.6	36.0 ± 25.2	52.1 ± 21.2
		1×10^{11}	47.9 ± 19.2	58.8 ± 20.0	73.6 ± 6.5
	OHCs	0.5×10^{11}	7.1 ± 9.8	11.4 ± 10.8	17.6 ± 17.9
		1×10^{11}	12.1 ± 11.7	30.1 ± 12.6	53.5 ± 28.1
	SCs	1×10^{11}	0	0	0
		5×10^{11}	5.5 ± 5.8	14.4 ± 17.1	5.6 ± 3.7
		1×10^{12}	3.5 ± 5.7	0	17.4 ± 15.5
AAV2/Anc80L65	IHCs	0.5×10^{11}	28.2 ± 15.5	25.6 ± 11.5	26.0 ± 12.7
		1×10^{11}	76.7 ± 11.8	82.5 ± 6.4	83.8 ± 8.8
		2×10^{11}	97.8 ± 3.1	97.7 ± 3.4	98.3 ± 2.3
	OHCs	0.5×10^{11}	24.3 ± 15.3	27.9 ± 13.0	33.6 ± 12.4
		1×10^{11}	68.9 ± 8.4	75.8 ± 6.6	81.6 ± 8.0
		2×10^{11}	93.1 ± 5.9	95.3 ± 1.2	98.2 ± 1.9
	SCs	1×10^{11}	0	7.1 ± 10.1	0
		2×10^{11}	45.3 ± 19.7	48.4 ± 25.8	15.1 ± 3.5
		5×10^{11}	7.0 ± 14.1	2.6 ± 3.7	21.4 ± 12.3

The values were represented as mean ± standard deviation (n = 5 for HCs; n = 4 for SCs).

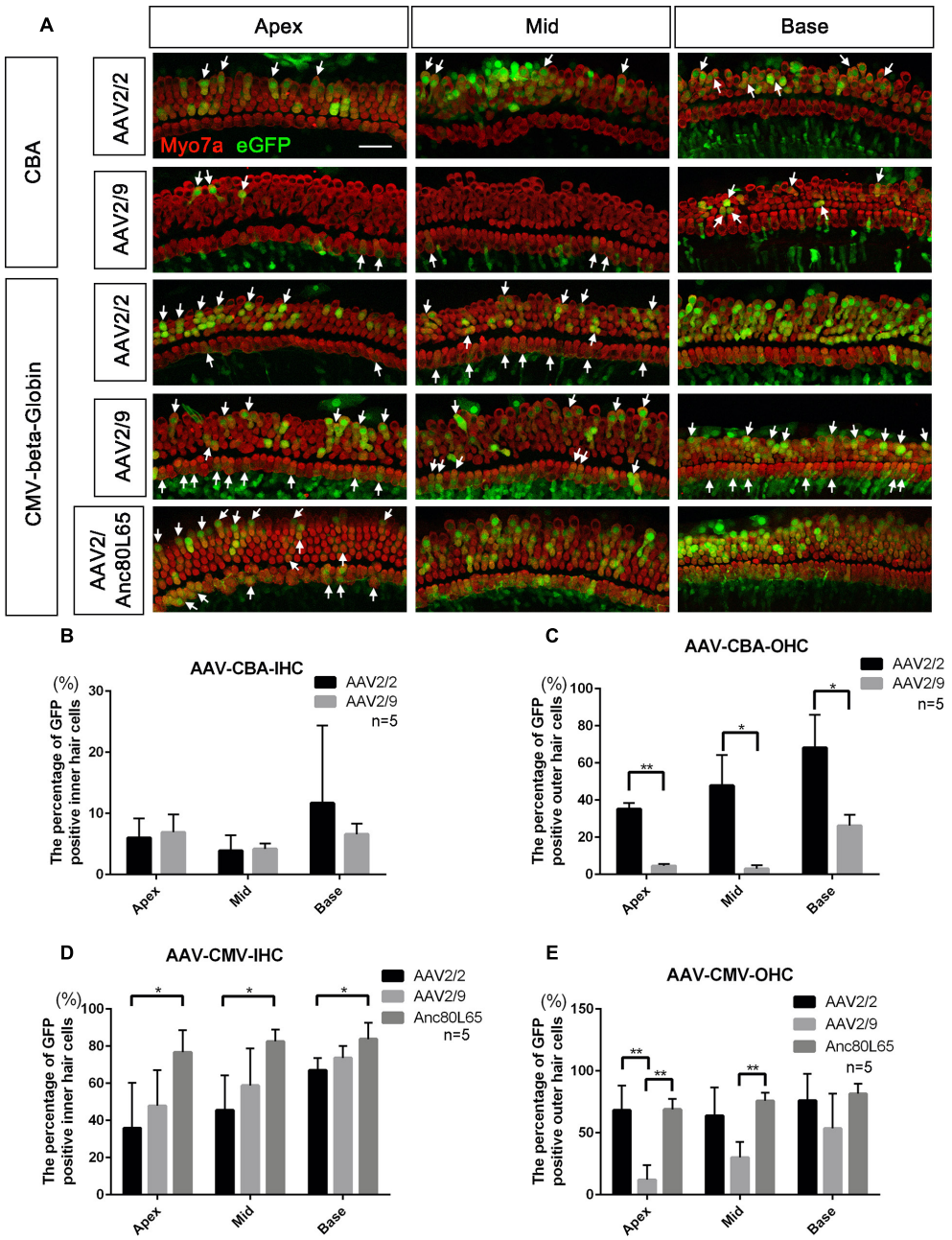


FIGURE 1 | Comparison of the *in vitro* transduction efficiencies in targeting HCs between different serotypes of AAV with the same promoters. **(A)** Representative confocal images of transduction of five AAV vectors (serotypes 2 and 9 with the CBA promoter and serotypes 2, 9, and Anc80L65 with the CMV-beta-Globin promoter) in HCs of the apical, middle, and basal turns of the cochlea. The arrows indicate the eGFP^{+} HCs. **(B)** Comparison of the transduction efficiencies between AAV serotypes 2 and 9 with the CBA promoter in targeting IHCs at a titer of 1×10^{11} VG/ml. **(C)** Comparison of the transduction efficiencies between AAV2/2-CBA and AAV2/9-CBA in targeting OHCs at a titer of 1×10^{11} VG/ml. AAV2/2-CBA clearly transduced more OHCs than AAV2/9-CBA in the apical, middle, and basal turns of the cochlea. **(D)** Comparison of the transduction efficiencies between serotypes Anc80L65, 2, and 9 with the same CMV-beta-Globin promoter in targeting IHCs at a titer of 1×10^{11} VG/ml. Overall, the transduction efficiency of AAV2/Anc80L65 was statistically significantly greater than the transduction efficiency of AAV2/2. There was no statistically significant difference in the percentages of eGFP^{+} IHCs between AAV2/2 and AAV2/9. **(E)** Comparison of transduction efficiencies between the three AAV vectors with the CMV-beta-Globin promoter when targeting OHCs at a titer of 1×10^{11} VG/ml. AAV2/Anc80L65 transduced more OHCs in the apical and middle turns than AAV2/9, while AAV2/2 transduced more OHCs in the apical turn than AAV2/9. $*p < 0.0167$, $**p < 0.0033$, $n = 5$. Scale bar: 20 μm.

3.0 ± 1.9%), and basal (68.2 ± 17.7% vs. 26.2 ± 5.9%) turns of the cochlea (**Table 1** and **Figure 1**). With the CMV-beta-Globin promoter, AAV2/Anc80L65 had the overall highest transduction efficiency among the three serotypes in IHCs, while AAV2/9 had the lowest transduction efficiency in OHCs (**Table 2** and **Figure 1**).

TABLE 3 | Comparison of the expression efficiencies in IHCs and OHCs between AAV2/2-CBA and AAV2/2-CMV-beta-Globin when the viral titer was 1×10^{11} VG/ml.

Promoter	Cell type	Apex (%)	Mid (%)	Base (%)
CBA	IHCs	5.8 ± 2.5	4.8 ± 3.3	12.4 ± 11.9
	OHCs	36.6 ± 1.8	43.6 ± 8.7	67.6 ± 16.2
CMV-beta-Globin	IHCs	34.4 ± 20.7	49.4 ± 16.7	68.4 ± 6.7
	OHCs	70.4 ± 17.3	74.0 ± 15.8	75.4 ± 20.6

The values were represented as mean ± standard deviation (n = 5).

Comparison of the Expression Efficacy in HCs Between AAV Vectors With Different Promoters

When the working titer of virus was 1×10^{11} VG/ml, the expression efficacy of AAV2/2-CMV in the IHCs and OHCs was statistically significantly greater than that of AAV2/2-CBA, with about a 6-fold increase in IHCs and about a 1.5-fold increase in OHCs (**Table 3** and **Figure 2**). Similarly, AAV2/9-CMV had higher expression efficacy than AAV2/9-CBA in HCs, with about an 8-fold increase in IHCs and about a 3-fold increase in OHCs (**Table 4** and **Figure 2**). This indicates that the CMV-beta-Globin promoter is more efficient than the CBA promoter when driving target gene expression in cochlear HCs.

The Transduction Efficiency of AAV Vectors Targeting SCs With Different Working Titers

As the virus titer was increased by 5-fold or 10-fold, the transduction efficiency of AAV2/2-CBA in SCs in the apical, middle, and basal turns did not increase statistically significantly. When the working titer of virus was increased from 5×10^{11} VG/ml to 1×10^{12} VG/ml, the average transduction efficiency of AAV2/9-CBA in SCs of the whole cochlea increased statistically significantly (11.20 ± 2.88% vs. 52.58 ± 12.02%, $p = 0.0048$). Unlike the tonotopic gradient in HCs, AAV2/2-CBA induced more SCs expressing eGFP at the apex of the cochlea than in the base at a titer of 1×10^{11} VG/ml (**Table 1** and **Supplementary Figures 3**, **5**).

As the virus titer was increased, the transduction efficiencies of AAV2/2-CMV and AAV2/9-CMV in SCs in the apical, middle, and basal turns did not increase significantly (**Table 2** and **Supplementary Figure 3**). When compared in the three regions of the cochlea, respectively, the transduction efficiencies of AAV2/Anc80L65-CMV in SCs did not increase statistically significantly with the working titer increased. The average transduction efficiencies of AAV2/Anc80L65-CMV in SCs of the whole cochlea increased significantly (2.35 ± 3.36% vs. 36.24 ± 13.00%, $p = 0.0023$) with the working titer increased from 1×10^{11} VG/ml to 2×10^{11} VG/ml. Surprisingly, the average transduction efficiencies in SCs of the whole cochlea decreased instead of increasing (36.24 ± 13.00% vs. 10.33 ± 4.93%, $p = 0.0098$) when the titer was increased from 2×10^{11} VG/ml to 5×10^{11} VG/ml (**Table 2** and **Supplementary Figure 3**).

Comparison of Transduction Efficiencies Targeting SCs of the Cochlea Between Different Serotypes of AAV Vectors With the Same Promoters

The difference in transduction efficiencies in SCs of the apical, middle, and basal turns between AAV2/2-CBA and AAV2/9-CBA was not statistically significant at a titer of 5×10^{11} VG/ml (**Table 1** and **Supplementary Figure 4**).

When the working titer of AAV2/2-CMV and AAV2/9-CMV was 5×10^{11} VG/ml and the working titer of AAV2/Anc80L65-CMV was 2×10^{11} VG/ml, the transduction efficiencies of the three serotypes in the basal turn ranked from high to low were AAV2/2 > AAV2/Anc80L65 > AAV2/9. AAV2/Anc80L65-CMV transduced 45.3 ± 19.7%, 48.4 ± 25.8%, and 15.1 ± 3.5% of the SCs in the apical, middle, and basal turns of the cochlea, respectively, at a titer of 2×10^{11} VG/ml (**Table 2, Figure 3,** and **Supplementary Figure 4**).

Comparison of Expression Efficacy in SCs of the Cochlea Between AAV Vectors With Different Promoters

AAV2/2-CBA had greater expression efficacy on average than AAV2/2-CMV in SCs of the whole cochlea (36.56 ± 17.70% vs. 11.33 ± 6.51%, $p = 0.0367$), while AAV2/9-CBA induced more SCs of the cochlea on average to express eGFP than AAV2/9-CMV (52.58 ± 12.02% vs. 6.97 ± 6.35%, $p = 0.0005$) at a titer of 1×10^{12} VG/ml (**Figure 4**). This indicates that the CBA promoter is more efficient than the CMV-beta-Globin promoter when driving target gene expression in SCs.

Transduction of AAV2/2-CBA, AAV2/9-CBA, and AAV2/Anc80L65-CMV in Targeting HCs and SCs After *in vivo* Injection

Although the *in vitro* data showed that AAV2/2-CBA had good performance in terms of transduction and gene expression in HCs and SCs, the *in vivo* experiment resulted in few $eGFP^+$ HCs or SCs (data not shown). One month after injection of AAV vectors into the scala media of the inner ear, the organ of Corti was isolated from the cochlea and the transduction efficiencies (the percentages of $eGFP^+$ cells) in HCs and SCs of the apical, middle, and basal turns were calculated separately. For AAV2/9-CBA, the percentages of $eGFP^+$ IHCs in the apical, middle, and basal turns were 39.6 ± 16.3%, 52.7 ± 5.7%, and 78.3 ± 7.2%, respectively, while the average transduction efficiency in OHCs was about 15% in all three turns (**Table 5** and **Figure 5**). After *in vivo* injection, AAV2/Anc80L65-CMV transduced 100% of the IHCs and about 90% of the OHCs. We observed similar levels of Anc80L65 transduction in HCs from the base to the apex in the three injected mice. We also found a tonotopic gradient for the transduction of Anc80L65 in SCs *in vivo*, with more SCs expressing eGFP at the apex than in the base. The

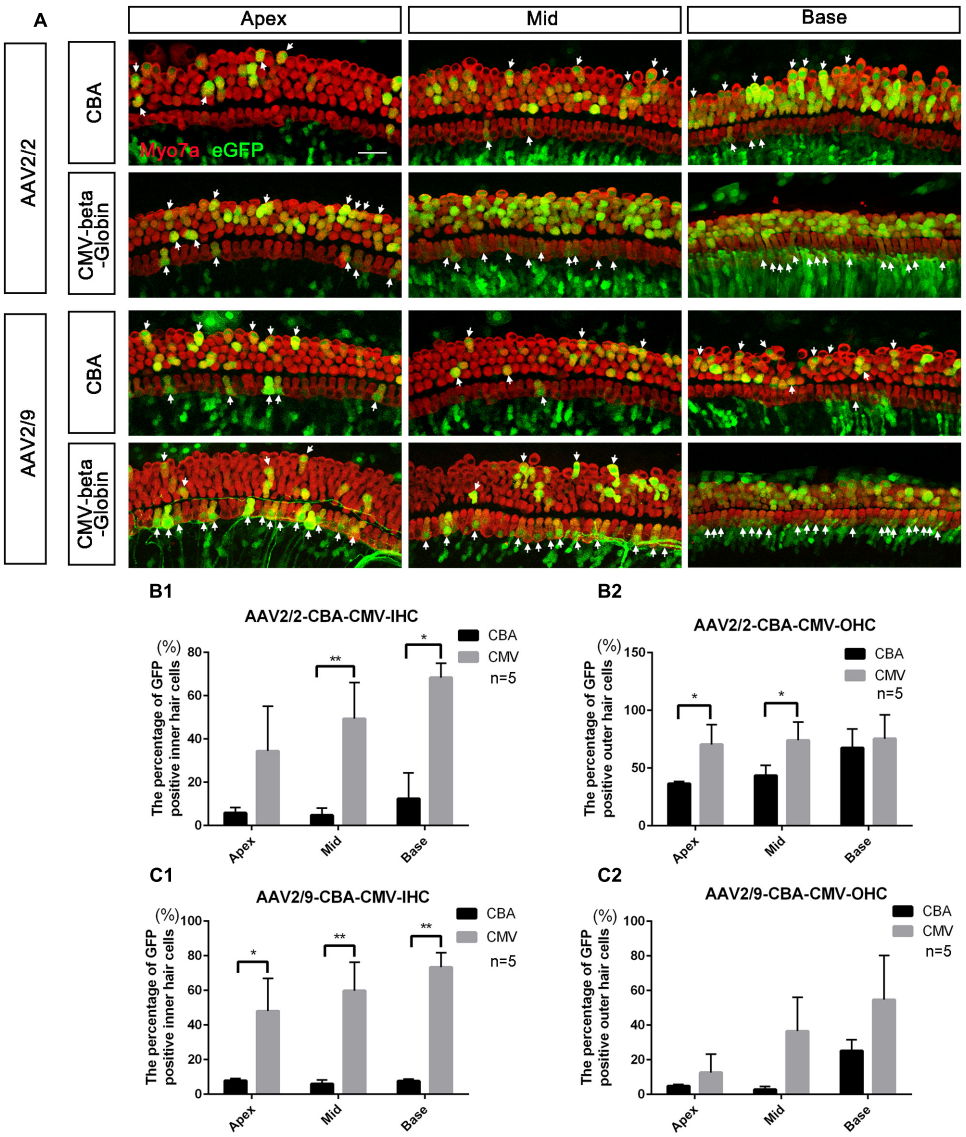


FIGURE 2 | Comparison of the *in vitro* expression efficacy in HCs between AAV vectors with different promoters. **(A)** Representative confocal images of transduction of AAV2/2-CBA, AAV2/2-CMV-beta-Globin, AAV2/9-CBA, and AAV2/9-CMV-beta-Globin in HCs of the apical, middle, and basal turns of the cochlea. The arrows indicate the eGFP^{+} HCs. **(B1)** Comparison of the expression efficiencies between AAV2/2-CBA and AAV2/2-CMV-beta-Globin in IHCs at a titer of 1×10^{11} VG/ml. **(B2)** Comparison of the expression efficiencies between AAV2/2-CBA and AAV2/2-CMV-beta-Globin in OHCs at a titer of 1×10^{11} VG/ml. AAV2/2-CMV-beta-Globin induced more IHCs in the middle and basal turns and more OHCs in the apical and middle turns of the cochlea to express eGFP than AAV2/2-CBA. **(C1)** Comparison of the expression efficiencies between AAV2/9-CBA and AAV2/9-CMV-beta-Globin in IHCs at a titer of 1×10^{11} VG/ml. **(C2)** Comparison of the expression efficiencies between AAV2/9-CBA and AAV2/9-CMV-beta-Globin in OHCs at a titer of 1×10^{11} VG/ml. AAV2/9-CMV-beta-Globin induced more IHCs throughout the cochlea to express eGFP than AAV2/9-CBA. $^{*}p < 0.0167$, $^{**}p < 0.0033$, $n = 5$. Scale bar: 20 μm.

transduction efficiencies of AAV2/Anc80L65-CMV were higher than that of AAV2/9-CBA in IHCs of the middle turn and in OHCs of the three regions of the cochlea. The transduction efficiencies in SCs of the apical, middle, and basal turns were not significantly different between AAV2/Anc80L65-CMV and AAV2/9-CBA. AAV2/Anc80L65-CMV induced more SCs to express eGFP than AAV2/9-CBA on average (24.33 ± 1.83% vs. 17.87 ± 1.88%, $p = 0.0130$) (**Table 5, Figure 6,** and **Supplementary Figure 5**).

AAV2/9-CBA Transduction in the Neonatal Inner Ear Does Not Impair Hearing

One month after injection of AAV2/9-CBA into the neonatal cochlea, we performed ABR tests to compare the hearing thresholds of the injected and un-injected ears. Although the ABR threshold of the injected ears was elevated by about 3, 8, 5, and 10 dB at frequencies of 4, 8, 16, and 24 kHz, respectively, there were no statistically significant differences between the

TABLE 4 | Comparison of the expression efficiencies in IHCs and OHCs between AAV2/9-CBA and AAV2/9-CMV-beta-Globin when the viral titer was 1×10^{11} VG/ml.

Promoter	Cell type	Apex (%)	Mid (%)	Base (%)
CBA	IHCs	7.9 ± 1.2	6.0 ± 2.30	7.6 ± 1.2
	OHCs	4.9 ± 0.9	2.9 ± 1.7	25.2 ± 6.4
CMV-beta-Globin	IHCs	48.0 ± 18.9	59.8 ± 16.4	73.4 ± 8.3
	OHCs	12.6 ± 10.7	36.5 ± 19.5	54.7 ± 25.6

The values were represented as mean ± standard deviation (n = 5).

injected and un-injected ears, which showed that hearing could be preserved after AAV transduction into the inner ear in mice (**Figure 5**).

The exact *p*-values for all experiments were presented in **Supplementary Table 2**.

DISCUSSION

The concept of gene therapy was first proposed by Friedmann and Roblin (1972), and it was initially studied for the treatment of tumors (Chada et al., 2007), cardiovascular diseases (Muller et al., 2007), and central nervous system diseases (Ryan and Federoff, 2007). Research into the use of gene therapy in the field of otology is a recent phenomenon. By transducing exogenous genes or gene editing systems into the specific cells of the mammalian inner ear, it is possible to regulate the expression level of targeted genes in the inner ear cells for the purpose of recovering the structure and function of the auditory organ.

The key to the success of gene therapy is to choose safe and efficient vectors and appropriate pathways for gene transduction. Various viral vectors, including adenovirus (Ad) (Mondain et al., 1998; Stover et al., 2000; Dazert et al., 2001; Jero et al., 2001; Luebke et al., 2001b; Nakaizumi et al., 2004; Rejali et al., 2007; Lin et al., 2011), AAV (Lalwani et al., 1996, 1998, 2002; Kho et al., 2000; Luebke et al., 2001a; Stone et al., 2005; Bedrosian et al., 2006; Liu et al., 2007), herpes simplex virus (HSV) (Derby et al., 1999; Staecker et al., 2007), lentivirus (Han et al., 1999), and retrovirus (Zheng et al., 1998), have been applied to study gene transduction into cells of the inner ear.

Retrovirus, lentivirus, and HSV are not usually used to study gene therapy for sensorineural hearing loss because these viruses do not transduce HCs efficiently, and the expression level of the delivered genes tends to be very low (Sacheli et al., 2013). In contrast, Ad vectors have been widely applied to transduce cells of the cochlea and the vestibule (Raphael et al., 1996; Mondain et al., 1998; Stover et al., 2000; Dazert et al., 2001; Jero et al., 2001; Luebke et al., 2001b), and in mice Ad can transduce spiral ganglion cells and the epithelial layer of the scala tympani and Reissner's membrane (Jero et al., 2001). However, although Ad is capable of transducing inner ear cells, its application in gene therapy for deafness is limited by some properties such as its inability to integrate into the host genome, its transient existence in cells, its strong immunogenicity, and its lack of tissue specificity.

Some characteristics of AAV make it a very attractive tool for transducing genes or gene editing systems (Flotte et al., 1996; Bueler, 1999; Snyder, 1999; Carter and Samulski, 2000; Peel and Klein, 2000; Rabinowitz and Samulski, 2000). AAV is a replication-defective virus containing single-stranded DNA, and it is suitable for the treatment of genetic and chronic diseases because it can transduce both mitotic and post-mitotic cells and because it has the advantages of high safety, weak immunogenicity, a wide host range, stable physical properties, and long-lasting expression. Many studies have demonstrated that AAV is the preferred vector for treating sensorineural hearing loss (Li Duan et al., 2002; Lustig and Akil, 2012). After introducing five different serotypes of AAV vectors into the cochlea of adult mice aged 2–12 months through the scala media, Kilpatrick et al. (2011) found that HCs, SCs, spiral ganglion cells, and the spiral ligament could all be transduced. Among the five serotypes (1, 2, 5, 6, and 8), AAV8 had the highest transduction rate with a higher rate in IHCs and a lower rate in SCs. Askew et al. (2015) incubated AAV-CMV-eGFP reporter vectors containing capsid serotypes 1, 2, 6, 8, or 9 with organotypic mouse cochlear cultures from P0 mice, and quantification of the viral transduction rates for the whole cochlea showed that AAV serotype 2/1 transduced the greatest number of HCs at equivalent viral titers for each serotype. AAV2/1 transduced an average of 58% of the HCs along the length of the cochlea compared to only 14% for AAV2/6, the serotype with the next highest viral transduction rate. They noted a tonotopic gradient of viral transduction, which was most apparent for AAV2/1, with more total HCs expressing eGFP in the base of the cochlea (up to 95%) than at the apex (up to 54%). The rate of viral transduction of IHCs declined sharply from the base to the apex, whereas viral transduction rates in OHCs remained higher along the entire base-to-apex axis. The mechanism behind the basal-apical gradient is not clear. In our work, there was a similar tonotopic gradient for viral transduction with the AAV2/2-CBA, AAV2/9-CBA, AAV2/2-CMV-beta-Globin, and AAV2/9-CMV-beta-Globin vectors with more $eGFP^+$ OHCs in the base of the cochlea compared to the apex. However, the tonotopic gradient for viral transduction of SCs with AAV2/2-CBA *in vitro* and AAV2/Anc80L65-CMV-beta-Globin *in vivo* was different from that of HCs, and more $eGFP^+$ SCs were seen at the apex than in the base of the cochlea. The transduction efficiencies of AAV vectors targeting HCs have not been completely consistent between studies, and this might be due to factors such as the serotype, the promoter, the developmental stage of the inner ear of the experimental animals, and the route of virus introduction.

Anc80L65, a unique AAV capsid, was designed to mimic an ancestral form of several AAV serotypes (1, 2, 6, 8, and 9) in order to minimize the antigenic similarity to naturally circulating AAVs that poses a problem in clinical translation of AAV gene therapies (Zinn et al., 2015). Anc80L65 was shown to be a potent gene transfer agent in liver, retina, and muscle (Zinn et al., 2015), and soon after these initial experiments, Landegger et al. (2017), Pan et al. (2017), and Suzuki et al. (2017) characterized its tropism in the inner ear *in vivo*. After systemic injection, the safety of Anc80L65 was similar in mice and non-human primates.

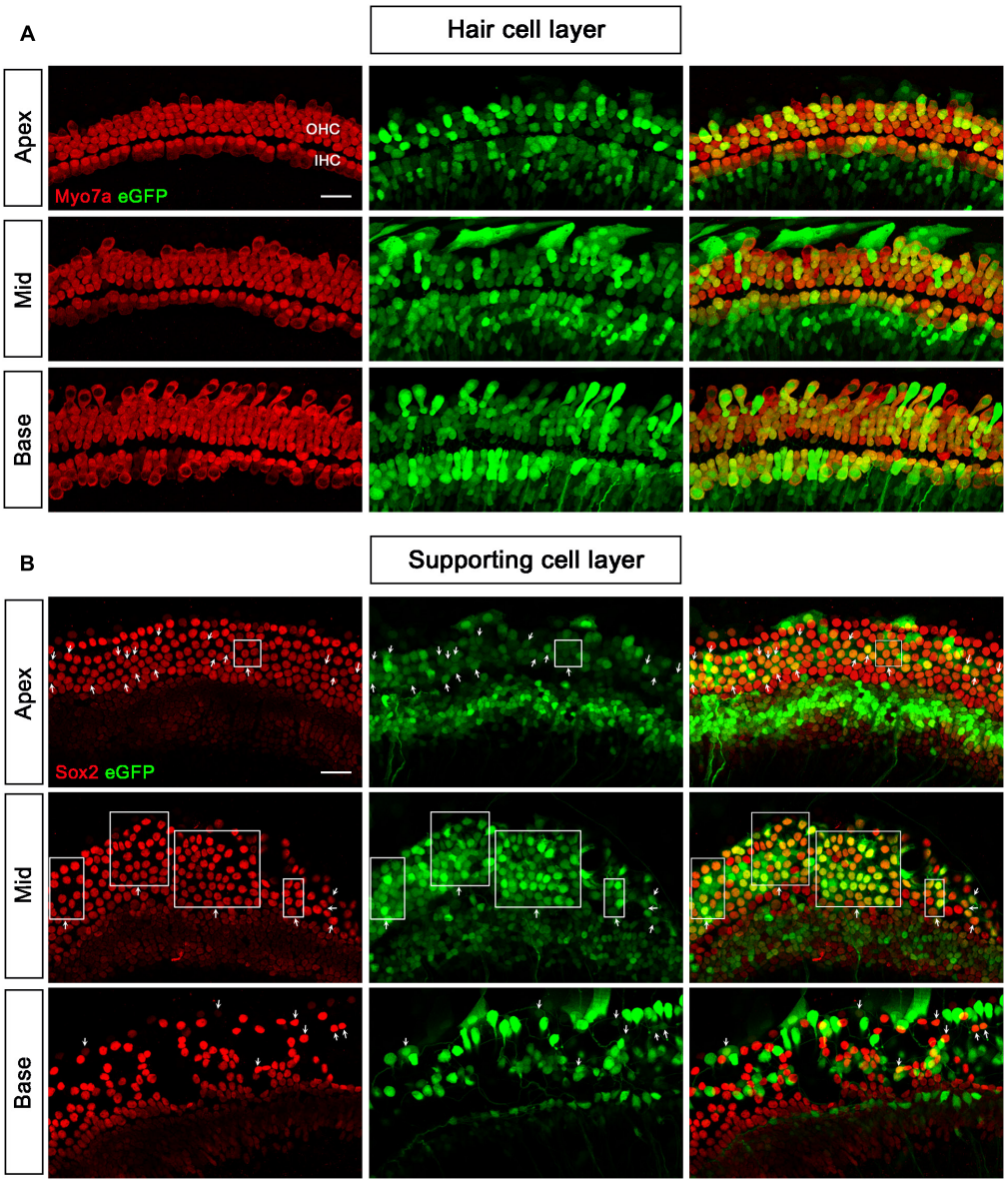


FIGURE 3 | Transduction of AAV2/Anc80L65-CMV-beta-Globin in HCs and SCs at a titer of 2×10^{11} VG/ml. **(A)** In the HC layer, the arrows indicate the Myo7a^{+}/eGFP^{+} HCs. **(B)** In the SC layer, the arrows indicate the Sox2^{+}/eGFP^{+} SCs. The square frames indicate the regions of SCs expressing eGFP.

The pre-existing immunity against circulating AAVs limits the efficacy of conventional AAV vectors, but the antigenicity of Anc80L65 is different from that of circulating AAVs, and this provides a potential benefit in terms of avoiding pre-existing immunity. The low transduction efficiency of conventional AAV vectors in OHCs has hampered the development of gene therapy for treating sensorineural hearing loss, but the highly effective transduction of Anc80L65 in OHCs overcomes this shortcoming and makes it a valuable vector for treating hereditary deafness and balance disorders. Suzuki et al. (2017) demonstrated that Anc80L65 could target almost 100% of IHCs and about half of the OHCs throughout the cochlea of adult mice after injection into the posterior semicircular canal. In our study, Anc80L65 showed consistently and qualitatively greater eGFP expression in IHCs and OHCs compared to other tested AAV vectors *in vitro* as well as *in vivo*. After *in vivo* injection into the scala media, Anc80L65 transduced 100% of the IHCs and about 90% of the OHCs. Although the transduction rate of Anc80L65 in SCs *in vivo* was about 25% on average, it still did not reach the desired level.

In addition to serotypes, promoters also play an important role in transgene expression. Most of the early studies in cochlear gene transduction relied on the human CMV promoter, but improvements in gene transduction systems have greatly increased the number of candidate promoters to choose from. The CAG promoter, which contains the sequences of both the CBA promoter and CMV promoter, shows strong and

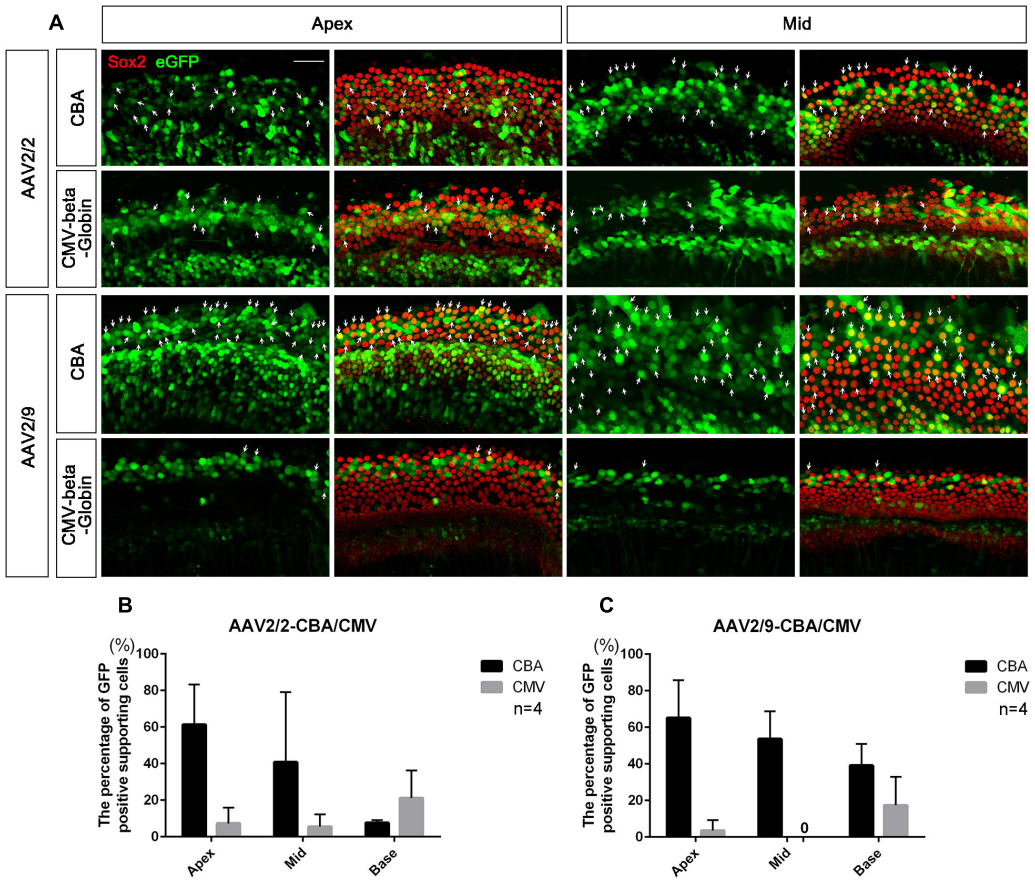


FIGURE 4 | Comparison of the expression efficacy in SCs of the cochlea between AAV vectors with different promoters. **(A)** Representative confocal images of transduction of AAV2/2-CBA, AAV2/2-CMV-beta-Globin, AAV2/9-CBA and AAV2/9-CMV-beta-Globin in targeting SCs of the apical and middle turns of the cochlea *in vitro*. There were many Sox2^{+}/eGFP^{+} SCs (arrows) in the apical and middle turns of the cochlea when transduced with AAV2/9-CBA. **(B)** Comparison of the expression efficiencies between AAV2/2-CBA and AAV2/2-CMV-beta-Globin in SCs of the apical, middle, and basal turns of the cochlea *in vitro* at a working titer of 1×10^{12} VG/ml. AAV2/2-CBA had greater expression efficacy in SCs than AAV2/2-CMV-beta-Globin on average, although there was no statistically significant difference between the expression efficiencies of AAV2/2-CBA and AAV2/2-CMV-beta-Globin in the apical, middle, or basal turn, respectively. **(C)** Comparison of the expression efficiencies between AAV2/9-CBA and AAV2/9-CMV-beta-Globin in SCs of the apical, middle, and basal turns of the cochlea *in vitro* at a working titer of 1×10^{12} VG/ml. AAV2/9-CBA had greater expression efficacy in SCs than AAV2/9-CMV-beta-Globin on average. $n = 4$. Scale bar: 20 μm.

TABLE 5 | Transduction efficiencies of AAV2/9-CBA and AAV2/Anc80L65-CMV-beta-Globin in IHCs, OHCs, and SCs after *in vivo* injection.

Cell type	AAV type	Apex (%)	Mid (%)	Base (%)
IHCs	AAV2/9-CBA	39.6 ± 16.3	52.7 ± 5.7	78.3 ± 7.2
	AAV2/Anc80L65-CMV-beta-Globin	100.0 ± 0.0	100.0 ± 0.0	100.0 ± 0.0
OHCs	AAV2/9-CBA	14.4 ± 0.9	15.0 ± 3.0	15.3 ± 8.1
	AAV2/Anc80L65-CMV-beta-Globin	93.5 ± 7.2	95.6 ± 4.4	81.6 ± 11.4
SCs	AAV2/9-CBA	21.9 ± 2.8	19.4 ± 4.0	12.3 ± 1.2
	AAV2/Anc80L65-CMV-beta-Globin	29.4 ± 1.7	26.1 ± 3.8	17.5 ± 0.7

The values were represented as mean ± standard deviation (n = 3).

constitutive expression activity in many cell types. However, the activity of the CAG promoter is confined to cochlear HCs in mice and guinea pigs with no expression activity in SCs (Liu et al., 2005, 2007; Stone et al., 2005; Bedrosian et al., 2006). Askew et al. (2015) measured the activities of the CMV, CBA, mouse phosphoglycerate kinase 1, and synapsin 1 promoters in cochlear cultures *in vitro* using the AAV2/1 vector for delivery and eGFP expression as the readout of promoter activity. It was found that both the CMV and CBA promoters drove robust eGFP expression in HCs as well as many types of SCs in the cochlea, but there were no specific results for the transduction efficiency of AAV vectors targeting SCs in their study. In cochleae injected via the round window membrane with AAV2/1-CBA-eGFP, 59 ± 2% ($n = 2$) of the IHCs were eGFP^{+}, and with AAV2/1-CMV-eGFP 70 ± 9% were eGFP^{+} ($n = 4$). This indicated that the CMV promoter led to greater expression in IHCs than the CBA promoter, which is consistent with the results of our present study.

Our study demonstrated that AAV vectors with different serotypes had different affinities for IHCs and OHCs. In our *in vitro* experiments, AAV of serotype 2 had high

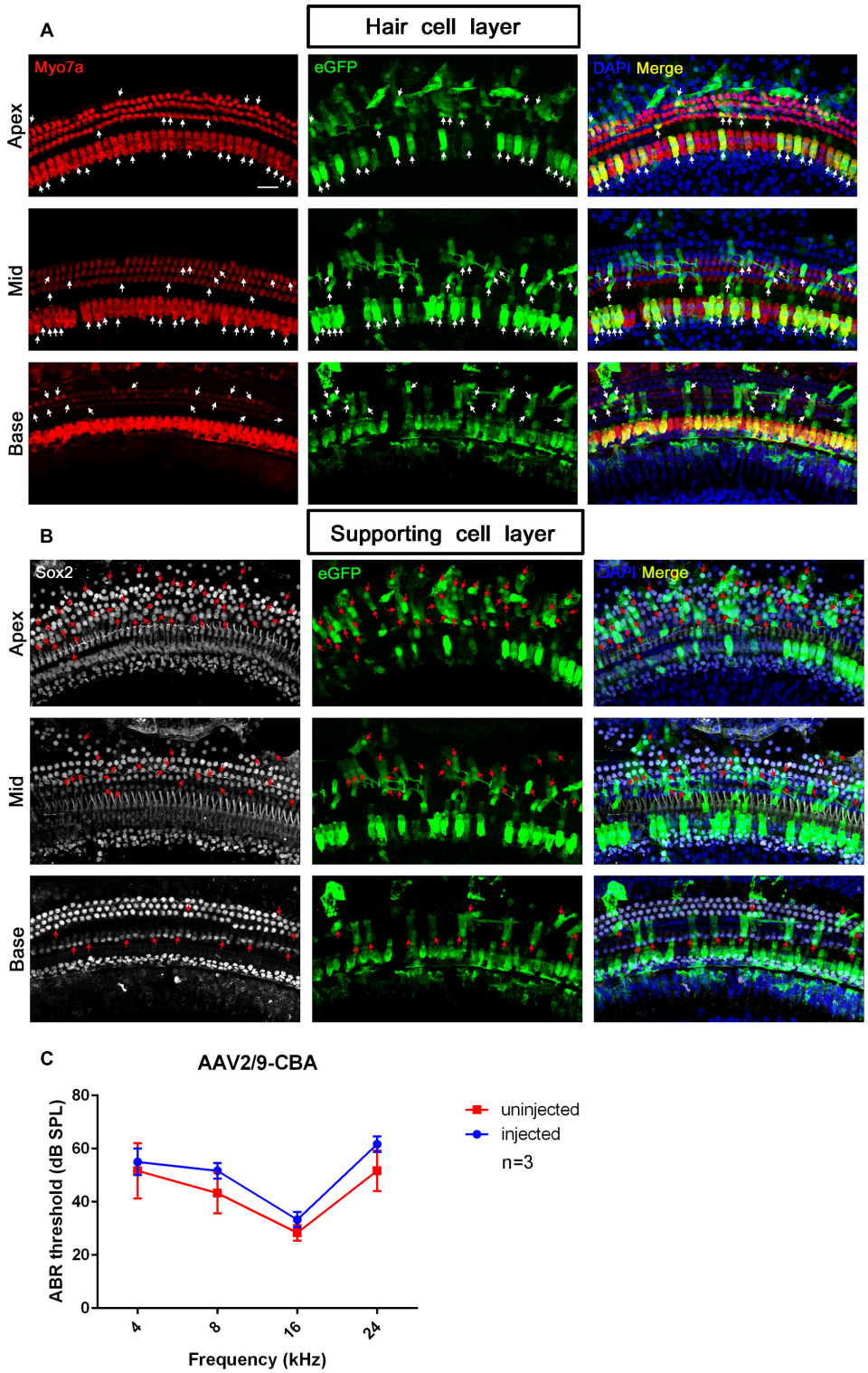


FIGURE 5 | The confocal images and ABR test results of AAV2/9-CBA transduction into the cochlea after *in vivo* injection. **(A)** Transduction of AAV2/9-CBA in HCs of the apical, middle, and basal turns of the cochlea after *in vivo* injection. The white arrows indicate the Myo7a^{+}/eGFP^{+} HCs. **(B)** Transduction of AAV2/9-CBA in SCs of the apical, middle, and basal turns of the cochlea after *in vivo* injection. The transduction efficiency of AAV2/9-CBA in SCs gradually decreased from the apex to the base. The tonotopic gradient with more eGFP^{+} SCs at the apex than in the base was similar to what was seen *in vitro*. The red arrows indicate the Sox2^{+}/eGFP^{+} SCs. **(C)** The ABR thresholds of the injected ears were not statistically significantly different compared to the un-injected control ears 1 month after injection of AAV2/9-CBA into the inner ears ($p > 0.05$, $n = 3$). Scale bar: 20 μm.

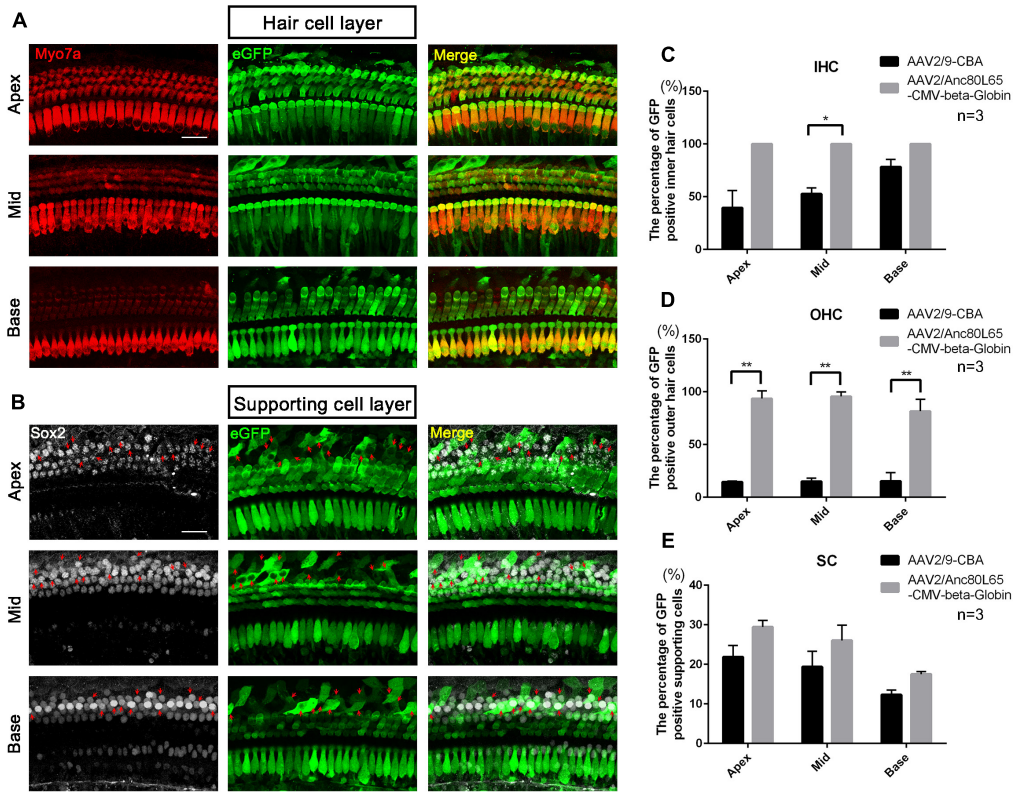


FIGURE 6 | The confocal images of AAV2/Anc80L65-CMV-beta-Globin transduction into the cochlea after *in vivo* injection and comparison of the *in vivo* transduction efficiencies in IHCs, OHCs, and SCs between AAV2/9-CBA and AAV2/Anc80L65-CMV-beta-Globin. **(A)** Transduction of AAV2/Anc80L65-CMV-beta-Globin in HCs of the apical, middle, and basal turns of the cochlea after *in vivo* injection. **(B)** Transduction of AAV2/Anc80L65-CMV-beta-Globin in SCs of the apical, middle, and basal turns of the cochlea after *in vivo* injection. The red arrows indicate the $Sox2^{+}$/$eGFP^{+}$ SCs. **(C)** Comparison of the *in vivo* transduction efficiencies in IHCs between AAV2/9-CBA and AAV2/Anc80L65-CMV-beta-Globin. **(D)** Comparison of the *in vivo* transduction efficiencies in OHCs between AAV2/9-CBA and AAV2/Anc80L65-CMV-beta-Globin. Overall, the *in vivo* transduction efficiency of AAV2/Anc80L65-CMV-beta-Globin in IHCs and OHCs was statistically significantly greater than the transduction efficiency of AAV2/9-CBA. **(E)** Comparison of the *in vivo* transduction efficiencies in SCs between AAV2/9-CBA and AAV2/Anc80L65-CMV-beta-Globin. AAV2/Anc80L65-CMV-beta-Globin induced more SCs to express eGFP than AAV2/9-CBA on average (24.33 ± 1.83% vs. 17.87 ± 1.88%, $p = 0.0130$). *$p < 0.0167$, **$p < 0.0033$, $n = 3$. Scale bar: 20 μm.

transduction efficiency in OHCs, while Anc80L65 could transduce a large portion of both IHCs and OHCs when injected at appropriate concentrations. The transduction efficiency of AAV2/Anc80L65-CMV approached 100% in HCs, which suggests that this is a very promising vector for inner ear gene therapy. We also found that the CMV-beta-Globin promoter had greater expression efficiency than the CBA promoter when driving transgene expression in HCs of the cochlea, whereas the CBA promoter had greater activity than the CMV-beta-Globin promoter in SCs. Thus, if the target of gene therapy is HCs, we can choose AAV vectors with the CMV promoter, but when the therapeutic target is SCs, the CBA promoter might be a better choice. In our work, the AAV vectors with the CMV-beta-Globin promoter contain a WPRE regulatory element which is thought to stabilize the mRNA, but the AAV vectors with the CBA promoter do not contain such an element. Therefore, an additional effect of the WPRE regulatory element on enhancing the eGFP expression cannot be ruled out. There is one more noteworthy issue which is the different sources of the AAV vectors with CBA promoter and CMV-beta-Globin promoter. Although the quality testing reports provided by the two facilities showed that the AAV vectors were of high quality and good stability, an effect of virus preparation from different facilities on the transduction efficiencies should be taken into consideration.

Landegger et al. (2017) used C57BL/6 or CBA/CaJ mice for *in vitro* experiments and the transduction efficiencies of AAV vectors between the two strains were not significantly different. It indicates that the transduction of AAV vectors in HCs and SCs of the cochlea would hardly be affected by the mouse strains which were used to investigate the transduction efficiencies. C57BL/6J is the most widely used inbred strain and the first to have its genome sequenced[1]. This strain is homozygous for *Cdh23*^{ahl}, the age related hearing loss 1 mutation, which on this background results in progressive hearing loss with onset after 10 months of age. ICR may serve as a general purpose strain and is known for susceptibility to induced colon cancer[2]. C57BL/6J mice were previously used for *in vivo* microinjection in our research, but

[1]https://www.jax.org/strain/000664

[2]https://www.jax.org/strain/009122

we found that the survival rate of the post-injection pups was low. There was no morphological or functional difference in the neonatal inner ear between C57BL/6J mice and ICR mice (data not shown). Since ICR mice have better maternity and stronger fertility than C57BL/6J mice, we used ICR mice for the *in vivo* experiments.

Injection of AAV vectors into the scala media was a safe and efficient way to transduce exogenous genes in HCs and SCs of the inner ear, but the low transduction rate of AAV vectors targeting SCs limits their application in treating sensorineural hearing loss caused by defects in SCs. In consideration of the important role of SCs in gene therapy and regenerative medicine, it is critical to find safe and efficient vectors for gene delivery into SCs. In previous studies (Liu et al., 2007; Luebke et al., 2009; Askew et al., 2015; Shu et al., 2016), there were either no detailed results of the transduction rate of AAV vectors in SCs or the transduction efficiency was very low (about 5% on average). We found that AAV2/2 and AAV2/9 with the CBA promoter had much higher expression efficiencies in SCs *in vitro*, which could reach 61.4 ± 21.9% and 65.1 ± 20.6%, respectively, at the apex of the cochlea and that AAV2/9-CBA could transduce 21.9 ± 2.8% of the SCs at the apex after *in vivo* injection. Landegger et al. (2017) found that the pattern of eGFP expression in IHCs and OHCs was similar in long-term culture with both AAV2 and Anc80L65. However, the *in vivo* results indicated that AAV2 could transduce only small numbers of IHCs and that transduction of OHCs was minimal (<5%). In contrast, Anc80L65 transduced nearly 100% of the IHCs and ∼90% of the OHCs after *in vivo* injection. This means that AAV2/2 could transduce HCs with high efficiency *in vitro*, but the transduction efficiency was sharply reduced *in vivo*. We also found a similar phenomenon for AAV2/2-CBA, which could transduce both HCs and SCs efficiently *in vitro* but had poor performance after *in vivo* injection. It is currently unclear why AAVs behave so differently when applied to explanted organs of Corti vs. *in vivo* injection. Even though several AAV vectors can transduce HCs with high efficiency, there are few AAV vectors that have good performance in transducing SCs, and the level of eGFP expression in target cells changes when using the same AAV serotype but with different promoter choice. Thus, when a new AAV vector is being constructed for the transduction of SCs, the promoter will be a very important factor to be considered in addition to the capsid. Although eGFP expression in SCs in our study was greater than previously reported, the total transduction efficiency still did not reach the desired level. In future studies, we would like to investigate the transduction efficiencies of AAV-CBA with different serotypes to determine if any serotypes of AAV-CBA can drive the expression of exogenous genes in SCs with high efficiency *in vivo*. Meanwhile, a systematic study of virus titers for *in vivo* injection will be performed in a follow-up study. All of this work will help to identify appropriate vectors for gene delivery into specific cell types of the inner ear, and such vectors will likely advance the possibility of using gene therapy to treat sensorineural hearing loss and other inner ear deficiencies.

AUTHOR CONTRIBUTIONS

XG was responsible for the study design and implementation, data analysis and manuscript preparation. LG, BD, WL, and RC were responsible for the data collection, statistical analysis, and manuscript preparation. YS, XH, and HL played an important role in study design and guidance and were responsible for the revision of the manuscript. All the authors approved the final version and agreed to be accountable for all aspects of the work in ensuring that questions related to the accuracy or integrity of any part of the work are appropriately investigated and resolved.

FUNDING

This work was supported by grants from the National Natural Science Foundation of China (Grant Nos. 81620108005, 81500801, 81771013, and 81822011), the Qi Hang Foundation Project of Fujian Medical University (Grant No. 2017XQ1052), the Science and Technology Commission of Shanghai Municipality (Grant Nos. 17ZR1448600 and 18410712400), and the Strategic Priority Research Program of the Chinese Academy of Sciences (Grant No. XDA16010302).

SUPPLEMENTARY MATERIAL

The Supplementary Material for this article can be found online at: https://www.frontiersin.org/articles/10.3389/fncel.2019.00008/full#supplementary-material

REFERENCES

Akil, O., Seal, R. P., Burke, K., Wang, C., Alemi, A., During, M., et al. (2012). Restoration of hearing in the VGLUT3 knockout mouse using virally mediated gene therapy. *Neuron* 75, 283–293. doi: 10.1016/j.neuron.2012.05.019

Askew, C., Rochat, C., Pan, B., Asai, Y., Ahmed, H., Child, E., et al. (2015). Tmc gene therapy restores auditory function in deaf mice. *Sci. Transl. Med.* 7:295ra108. doi: 10.1126/scitranslmed.aab1996

Ballana, E., Wang, J., Venail, F., Estivill, X., Puel, J. L., Arbones, M. L., et al. (2008). Efficient and specific transduction of cochlear supporting cells by adeno-associated virus serotype 5. *Neurosci. Lett.* 442, 134–139. doi: 10.1016/j.neulet.2008.06.060

Bedrosian, J. C., Gratton, M. A., Brigande, J. V., Tang, W., Landau, J., and Bennett, J. (2006). In vivo delivery of recombinant viruses to the fetal murine cochlea: transduction characteristics and long-term effects on auditory function. *Mol. Ther.* 14, 328–335. doi: 10.1016/j.ymthe.2006.04.003

Bueler, H. (1999). Adeno-associated viral vectors for gene transfer and gene therapy. *Biol. Chem.* 380, 613–622. doi: 10.1515/BC.1999.078

Carter, P. J., and Samulski, R. J. (2000). Adeno-associated viral vectors as gene delivery vehicles. *Int. J. Mol. Med.* 6, 17–27. doi: 10.3892/ijmm.6.1.17

Chada, S., Menander, K. B., Bocangel, D., Roth, J. A., and Ramesh, R. (2007). Cancer targeting using tumor suppressor genes. *Front. Biosci.* 13:1959–1967. doi: 10.2741/2815

Chang, Q., Wang, J., Li, Q., Kim, Y., Zhou, B., Wang, Y., et al. (2015). Virally mediated Kcnq1 gene replacement therapy in the immature scala media restores hearing in a mouse model of human jervell and lange-nielsen deafness syndrome. *EMBO Mol. Med.* 7, 1077–1086. doi: 10.15252/emmm.201404929

Chien, W. W., Isgrig, K., Roy, S., Belyantseva, I. A., Drummond, M. C., May, L. A., et al. (2016). Gene therapy restores hair cell stereocilia morphology in inner ears of deaf whirler mice. *Mol. Ther.* 24, 17–25. doi: 10.1038/mt.2015.150

Dazert, S., Aletsee, C., Brors, D., Gravel, C., Sendtner, M., and Ryan, A. (2001). In vivo adenoviral transduction of the neonatal rat cochlea and middle ear. *Hear. Res.* 151, 30–40. doi: 10.1016/S0378-5955(00)00189-1

Derby, M. L., Sena-Esteves, M., Breakefield, X. O., and Corey, D. P. (1999). Gene transfer into the mammalian inner ear using HSV-1 and vaccinia virus vectors. *Hear. Res.* 134, 1–8. doi: 10.1016/S0378-5955(99)00045-3

Flotte, T., Carter, B., Conrad, C., Guggino, W., Reynolds, T., Rosenstein, B., et al. (1996). A phase I study of an adeno-associated virus-CFTR gene vector in adult CF patients with mild lung disease. *Hum. Gene Ther.* 7, 1145–1159. doi: 10.1089/hum.1996.7.9-1145

Friedmann, T., and Roblin, R. (1972). Gene therapy for human genetic disease? *Science* 175, 949–955.

Gao, X., Tao, Y., Lamas, V., Huang, M., Yeh, W. H., Pan, B., et al. (2018). Treatment of autosomal dominant hearing loss by in vivo delivery of genome editing agents. *Nature* 553, 217–221. doi: 10.1038/nature25164

Grieger, J. C., Choi, V. W., and Samulski, R. J. (2006). Production and characterization of adeno-associated viral vectors. *Nat. Protoc.* 1, 1412–1428. doi: 10.1038/nprot.2006.207

Han, J. J., Mhatre, A. N., Wareing, M., Pettis, R., Gao, W. Q., Zufferey, R. N., et al. (1999). Transgene expression in the guinea pig cochlea mediated by a lentivirus-derived gene transfer vector. *Hum. Gene Ther.* 10, 1867–1873. doi: 10.1089/10430349950017545

Huang, M., Kantardzhieva, A., Scheffer, D., Liberman, M. C., and Chen, Z. Y. (2013). Hair cell overexpression of Islet1 reduces age-related and noise-induced hearing loss. *J. Neurosci.* 33, 15086–15094. doi: 10.1523/JNEUROSCI.1489-13.2013

Jero, J., Mhatre, A. N., Tseng, C. J., Stern, R. E., Coling, D. E., Goldstein, J. A., et al. (2001). Cochlear gene delivery through an intact round window membrane in mouse. *Hum. Gene Ther.* 12, 539–548. doi: 10.1089/104303401300042465

Kho, S. T., Pettis, R. M., Mhatre, A. N., and Lalwani, A. K. (2000). Safety of adeno-associated virus as cochlear gene transfer vector: analysis of distant spread beyond injected cochleae. *Mol. Ther.* 2, 368–373. doi: 10.1006/mthe.2000.0129

Kilpatrick, L. A., Li, Q., Yang, J., Goddard, J. C., Fekete, D. M., and Lang, H. (2011). Adeno-associated virus-mediated gene delivery into the scala media of the normal and deafened adult mouse ear. *Gene Ther.* 18, 569–578. doi: 10.1038/gt.2010.175

Konishi, M., Kawamoto, K., Izumikawa, M., Kuriyama, H., and Yamashita, T. (2008). Gene transfer into guinea pig cochlea using adeno-associated virus vectors. *J. Gene Med.* 10, 610–618. doi: 10.1002/jgm.1189

Lalwani, A., Walsh, B., Reilly, P., Carvalho, G., Zolotukhin, S., Muzyczka, N., et al. (1998). Long-term in vivo cochlear transgene expression mediated by recombinant adeno-associated virus. *Gene Ther.* 5, 277–281. doi: 10.1038/sj.gt.3300573

Lalwani, A. K., Han, J. J., Castelein, C. M., Carvalho, G. J., and Mhatre, A. N. (2002). In vitro and in vivo assessment of the ability of adeno-associated virus-brain-derived neurotrophic factor to enhance spiral ganglion cell survival following ototoxic insult. *Laryngoscope* 112(8 Pt 1), 1325–1334. doi: 10.1097/00005537-200208000-00001

Lalwani, A. K., Walsh, B. J., Reilly, P. G., Muzyczka, N., and Mhatre, A. N. (1996). Development of in vivo gene therapy for hearing disorders: introduction of adeno-associated virus into the cochlea of the guinea pig. *Gene Ther.* 3, 588–592.

Landegger, L. D., Pan, B., Askew, C., Wassmer, S. J., Gluck, S. D., Galvin, A., et al. (2017). A synthetic AAV vector enables safe and efficient gene transfer to the mammalian inner ear. *Nat. Biotechnol.* 35, 280–284. doi: 10.1038/nbt.3781

Lentz, J. J., Jodelka, F. M., Hinrich, A. J., McCaffrey, K. E., Farris, H. E., Spalitta, M. J., et al. (2013). Rescue of hearing and vestibular function by antisense oligonucleotides in a mouse model of human deafness. *Nat. Med.* 19, 345–350. doi: 10.1038/nm.3106

Li Duan, M., Bordet, T., Mezzina, M., Kahn, A., and Ulfendahl, M. (2002). Adenoviral and adeno-associated viral vector mediated gene transfer in the guinea pig cochlea. *Neuroreport* 13, 1295–1299. doi: 10.1097/00001756-200207190-00016

Lin, V., Golub, J. S., Nguyen, T. B., Hume, C. R., Oesterle, E. C., and Stone, J. S. (2011). Inhibition of Notch activity promotes nonmitotic regeneration of hair cells in the adult mouse utricles. *J. Neurosci.* 31, 15329–15339. doi: 10.1523/JNEUROSCI.2057-11.2011

Liu, Y., Okada, T., Nomoto, T., Ke, X., Kume, A., Ozawa, K., et al. (2007). Promoter effects of adeno-associated viral vector for transgene expression in the cochlea in vivo. *Exp. Mol. Med.* 39, 170–175. doi: 10.1038/emm.2007.19

Liu, Y., Okada, T., Sheykholeslami, K., Shimazaki, K., Nomoto, T., Muramatsu, S., et al. (2005). Specific and efficient transduction of Cochlear inner hair cells with recombinant adeno-associated virus type 3 vector. *Mol. Ther.* 12, 725–733. doi: 10.1016/j.ymthe.2005.03.021

Luebke, A. E., Foster, P. K., Muller, C. D., and Peel, A. L. (2001a). Cochlear function and transgene expression in the guinea pig cochlea, using adenovirus- and adeno-associated virus-directed gene transfer. *Hum. Gene Ther.* 12, 773–781.

Luebke, A. E., Steiger, J. D., Hodges, B. L., and Amalfitano, A. (2001b). A modified adenovirus can transfect cochlear hair cells in vivo without compromising cochlear function. *Gene Ther.* 8, 789–794.

Luebke, A. E., Rova, C., Von Doersten, P. G., and Poulsen, D. J. (2009). Adenoviral and AAV-mediated gene transfer to the inner ear: role of serotype, promoter, and viral load on in vivo and in vitro infection efficiencies. *Adv. Otorhinolaryngol.* 66, 87–98. doi: 10.1159/000218209

Lustig, L. R., and Akil, O. (2012). Cochlear gene therapy. *Curr. Opin. Neurol.* 25, 57–60. doi: 10.1097/WCO.0b013e32834f038c

Mondain, M., Restituito, S., Vincenti, V., Gardiner, Q., Uziel, A., Delabre, A., et al. (1998). Adenovirus-mediated in vivo gene transfer in guinea pig middle ear mucosa. *Hum. Gene Ther.* 9, 1217–1221. doi: 10.1089/hum.1998.9.8-1217

Muller, O. J., Katus, H. A., and Bekeredjian, R. (2007). Targeting the heart with gene therapy-optimized gene delivery methods. *Cardiovasc. Res.* 73, 453–462. doi: 10.1016/j.cardiores.2006.09.021

Nakaizumi, T., Kawamoto, K., Minoda, R., and Raphael, Y. (2004). Adenovirus-mediated expression of brain-derived neurotrophic factor protects spiral ganglion neurons from ototoxic damage. *Audiol. Neurootol.* 9, 135–143. doi: 10.1159/000077264

Pan, B., Askew, C., Galvin, A., Heman-Ackah, S., Asai, Y., Indzhykulian, A. A., et al. (2017). Gene therapy restores auditory and vestibular function in a mouse model of Usher syndrome type 1c. *Nat. Biotechnol.* 35, 264–272. doi: 10.1038/nbt.3801

Peel, A. L., and Klein, R. L. (2000). Adeno-associated virus vectors: activity and applications in the CNS. *J. Neurosci. Methods* 98, 95–104. doi: 10.1016/S0165-0270(00)00183-7

Rabinowitz, J. E., and Samulski, R. J. (2000). Building a better vector: the manipulation of AAV virions. *Virology* 278, 301–308. doi: 10.1006/viro.2000.0707

Raphael, Y., Frisancho, J. C., and Roessler, B. J. (1996). Adenoviral-mediated gene transfer into guinea pig cochlear cells in vivo. *Neurosci. Lett.* 207, 137–141. doi: 10.1016/0304-3940(96)12499-X

Rejali, D., Lee, V. A., Abrashkin, K. A., Humayun, N., Swiderski, D. L., and Raphael, Y. (2007). Cochlear implants and ex vivo BDNF gene therapy protect spiral ganglion neurons. *Hear. Res.* 228, 180–187. doi: 10.1016/j.heares.2007.02.010

Ryan, D. A., and Federoff, H. J. (2007). Translational considerations for CNS gene therapy. *Expert Opin. Biol. Ther.* 7, 305–318. doi: 10.1517/14712598.7.3.305

Sacheli, R., Delacroix, L., Vandenackerveken, P., Nguyen, L., and Malgrange, B. (2013). Gene transfer in inner ear cells: a challenging race. *Gene Ther.* 20, 237–247. doi: 10.1038/gt.2012.51

Shibata, S. B., Di Pasquale, G., Cortez, S. R., Chiorini, J. A., and Raphael, Y. (2009). Gene transfer using bovine adeno-associated virus in the guinea pig cochlea. *Gene Ther.* 16, 990–997. doi: 10.1038/gt.2009.57

Shu, Y., Tao, Y., Wang, Z., Tang, Y., Li, H., Dai, P., et al. (2016). Identification of adeno-associated viral vectors that target neonatal and adult mammalian inner ear cell subtypes. *Hum. Gene Ther.* 27, 687–699. doi: 10.1089/hum.2016.053

Snyder, R. O. (1999). Adeno-associated virus-mediated gene delivery. *J. Gene Med.* 1, 166–175. doi: 10.1002/(SICI)1521-2254(199905/06)1:3<166::AID-JGM34>3.0.CO;2-Z

Staecker, H., Liu, W., Malgrange, B., Lefebvre, P. P., and Van De Water, T. R. (2007). Vector-mediated delivery of bcl-2 prevents degeneration of auditory hair cells and neurons after injury. *ORL J. Otorhinolaryngol. Relat. Spec.* 69, 43–50. doi: 10.1159/000096716

Stone, I. M., Lurie, D. I., Kelley, M. W., and Poulsen, D. J. (2005). Adeno-associated virus-mediated gene transfer to hair cells and support cells of the murine cochlea. *Mol. Ther.* 11, 843–848. doi: 10.1016/j.ymthe.2005.02.005

Stover, T., Yagi, M., and Raphael, Y. (2000). Transduction of the contralateral ear after adenovirus-mediated cochlear gene transfer. *Gene Ther.* 7, 377–383. doi: 10.1038/sj.gt.3301108

Suzuki, J., Hashimoto, K., Xiao, R., Vandenberghe, L. H., and Liberman, M. C. (2017). Cochlear gene therapy with ancestral AAV in adult mice: complete transduction of inner hair cells without cochlear dysfunction. *Sci. Rep.* 7:45524. doi: 10.1038/srep45524

Wang, Q., Dong, B., Firrman, J., Roberts, S., Moore, A. R., Cao, W., et al. (2014). Efficient production of dual recombinant adeno-associated viral vectors for factor VIII delivery. *Hum. Gene Ther. Methods* 25, 261–268. doi: 10.1089/hgtb.2014.093

Wang, Q., Firrman, J., Wu, Z., Pokiniewski, K. A., Valencia, C. A., Wang, H., et al. (2016). High-density recombinant adeno-associated viral particles are competent vectors for in vivo transduction. *Hum. Gene Ther.* 27, 971–981. doi: 10.1089/hum.2016.055

Yu, Q., Wang, Y., Chang, Q., Wang, J., Gong, S., Li, H., et al. (2014). Virally expressed connexin26 restores gap junction function in the cochlea of conditional Gjb2 knockout mice. *Gene Ther.* 21, 71–80. doi: 10.1038/gt.2013.59

Zheng, J. L., Lewis, A. K., and Gao, W. Q. (1998). Establishment of conditionally immortalized rat utricular epithelial cell lines using a retrovirus-mediated gene transfer technique. *Hear. Res.* 117, 13–23. doi: 10.1016/S0378-5955(97)00205-0

Zinn, E., Pacouret, S., Khaychuk, V., Turunen, H. T., Carvalho, L. S., Andres-Mateos, E., et al. (2015). In silico reconstruction of the viral evolutionary lineage yields a potent gene therapy vector. *Cell Rep.* 12, 1056–1068. doi: 10.1016/j.celrep.2015.07.019

Zuris, J. A., Thompson, D. B., Shu, Y., Guilinger, J. P., Bessen, J. L., Hu, J. H., et al. (2015). Cationic lipid-mediated delivery of proteins enables efficient protein-based genome editing in vitro and in vivo. *Nat. Biotechnol.* 33, 73–80. doi: 10.1038/nbt.3081

Conflict of Interest Statement: The authors declare that the research was conducted in the absence of any commercial or financial relationships that could be construed as a potential conflict of interest.

Copyright © 2019 Gu, Chai, Guo, Dong, Li, Shu, Huang and Li. This is an open-access article distributed under the terms of the Creative Commons Attribution License (CC BY). The use, distribution or reproduction in other forums is permitted, provided the original author(s) and the copyright owner(s) are credited and that the original publication in this journal is cited, in accordance with accepted academic practice. No use, distribution or reproduction is permitted which does not comply with these terms.

frontiers in Cellular Neuroscience

ORIGINAL RESEARCH
published: 20 February 2019
doi: 10.3389/fncel.2019.00050

Silencing of lncRNA PKIA-AS1 Attenuates Spinal Nerve Ligation-Induced Neuropathic Pain Through Epigenetic Downregulation of CDK6 Expression

*Jian-Zhong Hu[1,2], Zi-Jie Rong[1,2], Miao Li[1,2], Ping Li[1,2,3], Li-Yuan Jiang[1,2], Zi-Xiang Luo[1,2], Chun-Yue Duan[1,2], Yong Cao[1,2] and Hong-Bin Lu[2,4]**

[1] Department of Spine Surgery, Xiangya Hospital, Central South University, Changsha, China, [2] Key Laboratory of Organ Injury, Aging and Regenerative Medicine of Hunan Province, Xiangya Hospital, Central South University, Changsha, China, [3] Department of Obstetrics, Xiangya Hospital, Central South University, Changsha, China, [4] Department of Sports Medicine, Xiangya Hospital, Central South University, Changsha, China

Neuropathic pain (NP) is among the most intractable comorbidities of spinal cord injury. Dysregulation of non-coding RNAs has also been implicated in the development of neuropathic pain. Here, we identified a novel lncRNA, PKIA-AS1, by using lncRNA array analysis in spinal cord tissue of spinal nerve ligation (SNL) model rats, and investigated the role of PKIA-AS1 in SNL-mediated neuropathic pain. We observed that PKIA-AS1 was significantly upregulated in SNL model rats and that PKIA-AS1 knockdown attenuated neuropathic pain progression. Alternatively, overexpression of PKIA-AS1 was sufficient to induce neuropathic pain-like symptoms in uninjured rats. We also found that PKIA-AS1 mediated SNL-induced neuropathic pain by directly regulating the expression and function of CDK6, which is essential for the initiation and maintenance of neuroinflammation and neuropathic pain. Therefore, our study identifies PKIA-AS1 as a novel therapeutic target for neuroinflammation related neuropathic pain.

Keywords: neuropathic pain, long non-coding RNA, spinal cord injury, neuroinflammation, CDK6

OPEN ACCESS

Edited by:
Thomas Fath,
Macquarie University, Australia

Reviewed by:
Huiyin Tu,
Zhengzhou University, China
Justin Lees,
University of New South Wales, Australia
Alexandre Charlet,
Centre National de la Recherche Scientifique (CNRS), France

***Correspondence:**
Hong-Bin Lu
hongbinlu@hotmail.com

***Received:** 06 September 2018*
***Accepted:** 01 February 2019*
***Published:** 20 February 2019*

Citation:
Hu J-Z, Rong Z-J, Li M, Li P, Jiang L-Y, Luo Z-X, Duan C-Y, Cao Y and Lu H-B (2019) Silencing of lncRNA PKIA-AS1 Attenuates Spinal Nerve Ligation-Induced Neuropathic Pain Through Epigenetic Downregulation of CDK6 Expression. Front. Cell. Neurosci. 13:50. doi: 10.3389/fncel.2019.00050

INTRODUCTION

Neuropathic pain (NP) is among the most intractable comorbidities of spinal cord injury (SCI). It can manifest as multiple forms of chronic pain in areas where skin sensation is lost below the injury plane (Dones and Levi, 2018). The incidence of NP in patients with SCI is increasing annually (Wayne, 2018). There are currently no curative therapies for SCI-associated NP, and clinical management is limited to symptomatic treatment. Further, treatment efficacy is often not ideal, which seriously affects patient quality of life. Indeed, many patients experience depression and anxiety, develop drug addictions, and even contemplate or attempt suicide.

The release of inflammatory cytokines from activated astrocytes and microglia is strongly implicated in the development of neuropathic pain (McKelvey et al., 2015). As inhibition of neuroinflammation by inactivation of astrocytes and microglia can ameliorate pain-related behavior (Walters, 2014). In addition, genetic deletion of cell cycle-related proteins such as

cyclin-dependent kinases (CDKs) has also been shown to reverse pain-related behavior (Gwak and Hulsebosch, 2011). Nociception is an integral component of host defense, but prolonged nociceptive input can drive central neuroinflammation and induce neuroplastic changes within pain pathways (Gwak et al., 2012). It has been suggested that spinal injury can activate nociceptor-mediated host defense responses via neuroinflammatory signaling to produce chronic pain (Coraggio et al., 2018).

Non-coding RNAs (ncRNAs), including microRNAs and long non-coding RNAs (lncRNAs), contribute to diverse biological processes by regulating the expression of mRNA targets at the post-transcriptional level (Bali and Kuner, 2014; Zhou et al., 2017) by targeting several pain pathways (Tan et al., 2015; Plassais et al., 2016; Shao et al., 2018). Dysregulation of non-coding RNAs has also been implicated in the development of neuropathic pain (Liu et al., 2017; Vieira et al., 2018). For example, lncRNA BC168687 is associated with diabetic neuropathic pain (Liu et al., 2018), while lncRNA MRAK009713, NEAT1, and XIST can regulate chronic constriction injury-induced neuropathic pain (Li et al., 2017; Xia et al., 2018; Yan et al., 2018).

Here, we identified a novel lncRNA, PKIA-AS1, by using lncRNA array analysis in spinal cord tissue of spinal nerve ligation (SNL) model rats, and investigated the role of PKIA-AS1 in SNL-mediated neuropathic pain. We observed that PKIA-AS1 was significantly upregulated in SNL model rats and that PKIA-AS1 knockdown attenuated neuropathic pain progression. Alternatively, overexpression of PKIA-AS1 was sufficient to induce neuropathic pain-like symptoms in uninjured rats. We also found that PKIA-AS1 mediated SNL-induced neuropathic pain by directly regulating the expression and function of CDK6, which is essential for the initiation and maintenance of neuroinflammation and neuropathic pain. Therefore, our study identifies PKIA-AS1 as a novel therapeutic target for neuroinflammation related neuropathic pain.

MATERIALS AND METHODS

Animal Model

Male Sprague-Dawley (SD) rats (∼200 g) were obtained from the Experimental Animal Central of Central South University. The animal experiments were approved by the Animal Care and Use Committee of Central South University. Spinal nerve ligation (SNL)-induced neuropathic pain model was established as previous described (Zhang et al., 2013). Briefly, following anesthetized with 1% sodium pentobarbital (40 mg/kg i.p.), the fifth lumbar (L5) spinal nerves were isolated and ligated tightly with 6–0 silk suture. For sham-operated mice, rats received identical surgical procedure without ligation. Mechanical withdrawal threshold (MWT) and thermal withdrawal latency (TWL) were used to validate the SNL model.

Animal Infection

To test the effect of lentivirus shPKIA-AS1 (Lv-shPKIA-AS1, sequence: CCGGGACGACCCTGACCATGGTCGCGATATC TCGAGATATTTGAGGTCAGGGTCGTCAATTTG, Sigma Aldrich), SNL rats were received intrathecal injections of either Lv-shPKIA-AS1 (MOI = 100) or the lentivirus with scramble sequence on the third day after surgery.

To assess the effect of PKIA-AS1 overexpression, rats were received intrathecal injections of either Lv-PKIA-AS1 [multiplicity of infection (MOI) = 100] or the lentivirus with scramble sequence on the fifth day of observation.

To assess the effect of CDK6 overexpression, rats were received intrathecal injections of either Lv-CDK6 (MOI = 100) or the lentivirus with scramble sequence on the third day after surgery. Intrathecal injection process was performed as previously described (Zhang et al., 2013). Briefly, rats were placed in a prone position after anesthesia. After creating a small opening at the intervertebral space between the L4–L6 vertebrae, a sterile PE10 intrathecal catheter was inserted through the opening into the lumbar enlargement. After catheterization, all rats were allowed to recover for two days before being used in other experiments.

Pain Threshold Assessment

Mechanical allodynia was evaluated by paw withdrawal threshold (PWT) using von Frey filaments. Briefly, rats were put into a transparent plastic box (22 cm × 12 cm × 22 cm). The box has a metal mesh floor. The calibrated von Frey filaments (IITC, Woodland Hills, CA, United States) were used to make pressure on the plantar surface of rat hind paw. The investigators recorded the size of the filaments when paw withdrawal. Paw withdrawal latency (PWL) was used to evaluated thermal hyperalgesia by the Plantar Test Instrument (Hargreave's Method). The hind paws were tested alternately at 5-min intervals. The investigators recorded the duration between stimuli and paw withdrawal. The cut-off time was at 30 s. All tests were performed blindly.

LncRNA Microarray Analysis

On the 15th day after spinal nerve ligation (SNL) or sham operation, rats were anesthetized with pentobarbital sodium (150 mg/kg IV) and their spinal cord tissues (L5) were removed and frozen by liquid nitrogen immediately. RNeasy Mini Kit (Qiagen, GmBH, Hilden, Germany) was used to extract total RNA from spinal cord tissues according to the manufacturer's instructions. NanoDrop 2000 spectrophotometer was used to quantify purified total RNA. To analyze lncRNA expression profiles (Arraystar Rat LncRNA Expression Array V2.0), the purified total RNA was sent to Novogene Co. Ltd. (Beijing, China). Differentially expressed lncRNAs were identified through fold change (>2) and P-value (<0.05).

RNA Extraction and qRT-PCR

TRIzol reagent (Invitrogen) was used to extract total RNA from cells or tissues. Maxima First Strand cDNA Synthesis kit (cat no. K1642; Thermo Fisher Scientific, Inc.) was used for reverse transcription according to the manufacturer's protocol. Quantitative PCR amplification was performed with an CFX96 Touch^{TM} Deep Well Real-Time PCR Detection System (Bio-Rad, Hercules, CA, United States). Expression of lncRNAs, PKIA-AS1, IL-1β, IL-6, IL-12, TNFα, and CDK-6 was detected via UltraSYBR Mixture (cat. no. CW2602; CWBio) according to the

manufacturer's protocol. QPCR was performed at the condition: 95.0°C for 3 min, and 39 circles of 95.0°C for 10 s and 60°C for 30 s. Expression of β-actin was used as an endogenous control. Relative gene expression was calculated using $2^{-\Delta\Delta Ct}$ method. The real-time PCR primer sequences are shown in **Supplementary Table S1**.

Western Blot

Radio immunoprecipitation assay (RIPA) lysis buffer (Boster, Wuhan, China) was used to extract protein from spinal cord tissues (L5). BCA Protein assay kit (Thermo Scientific, Waltham, MA, United States) was used to measure protein concentrations. Proteins (60 μg) were separated by 10% SDS/PAG. The membranes were blocked by 5% non-fat milk for 30 min at room temperature and then immunoblotted with the following primary antibodies: CDK6 antibody (cat no. 13331, Rabbit monoclonal, diluted at 1:1000), DNMT1 antibody (cat no. 5032, Rabbit monoclonal, diluted at 1:1000), DNMT3A antibody (cat no. 32578, Rabbit monoclonal, diluted at 1:1000), DNMT3B antibody (cat no. 57868, Rabbit monoclonal, diluted at 1:1000), GAPDH antibody (cat no. 5174, Rabbit monoclonal, diluted at 1:1000). All antibodies were purchased from Cell Signaling Technology. Membranes were then incubated with peroxidase-conjugated secondary antibody, and specific bands were detected with a Bio-Rad (Hercules, CA, United States) imaging system.

Immunofluorescence Assays

Spinal cord tissues were cut into twenty-μm thick sections for immunofluorescence assays. After permeabilized with 0.5% Triton-100, the sections were blocked with BSA for 60 min at 37°C. The sections then were incubated with primary antibody (cat no. ab68428, anti-GFAP, 1:500; cat no. ab15690, anti-Iba-1, 1:200, Abcam, Cambridge, United Kingdom) at 4°C overnight. After that, sections were washed by PBS and secondary antibody was added to incubation at 37°C for 1 h. The coverslips were stained with DAPI (1:1000, Santa Cruz Biotechnology) for 2 min

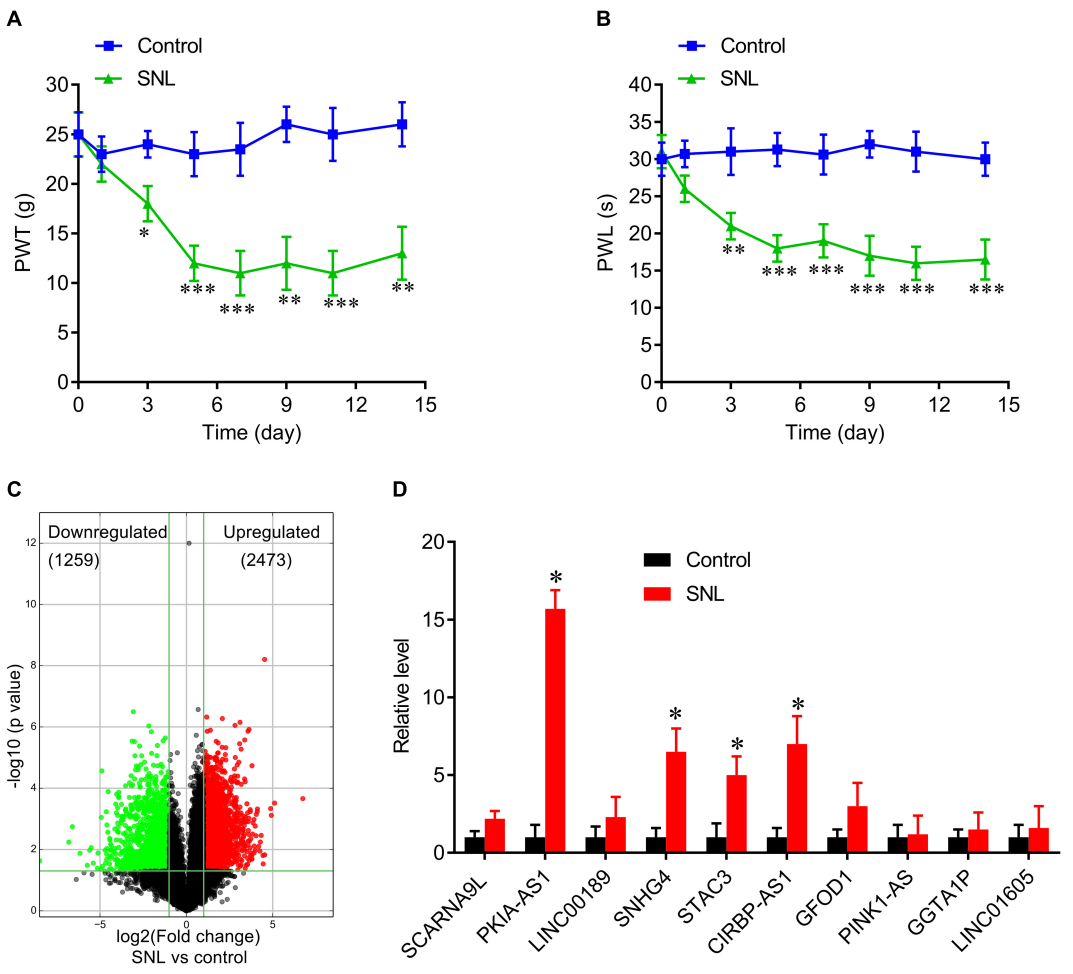


FIGURE 1 | Differentially expressed lncRNAs in spinal cord of SNL rats. **(A,B)** Spinal never ligation induced mechanical hyperalgesia **(A)** and thermal hyperalgesia **(B)** in rats. $N = 8$ for each group, $^{*}P < 0.05$, $^{**}P < 0.01$, $^{***}P < 0.001$ vs. control group. **(C)** Volcano plot shown the downregulated and upregulated lncRNAs. **(D)** Real-time PCR data confirmed the expressions of top 10 upregulated lncRNAs in spinal cord of SNL rats and control group. $^{*}P < 0.05$ vs. control group. SNL, spinal never ligation; PWT, paw withdrawal threshold; PWL, paw withdrawal latency; lncRNA, long non-coding RNA.

at room temperature and mounted. Fluorescence microscope (Nikon ECLIPSE 80i, Nikon Corporation, Tokyo, Japan) was used to immunofluorescence acquire images. ImageJ (version 1.8) was used to quantify the fluorescence intensity on 8 sections per animal at 40× magnification.

Proteomics Analysis

Total proteins were extracted and purified from fresh spinal cord tissues (L5) of Lv-PKIA-AS1 infected mice and the control mice using a ReadyPrep^{TM} Protein Extraction kit (Bioscience) following the procedure recommended by the manufacturer. The proteomics analysis was performed as previously described (Yang et al., 2014). Protein samples were separated by two-dimensional polyacrylamide gel electrophoresis (2-DE). Samples containing 150 μg of protein were diluted to 450 μl with rehydration solution and used for isoelectric focusing. The proteins were electrophoresed in SDS–PAGE and then stained with coomassie brilliant blue dye. Spot-detect and determine the quantity were analyzed by DeCyder software version 6.5 (GE). The statistical significance was assessed by using a one-way ANOVA analysis. Protein spots were selected as the mean ratio was greater than 1.5-fold or less than −1.5-fold.

Cell Culture and Cell Infection

PC12 cells were purchased from the American Type Culture Collection (Manassas, VA, United States). The cells were cultured in DMEM medium (Gibco) supplemented with 10% fetal bovine serum (Invitrogen, Carlsbad, CA, United States) and 1% penicillin/streptomycin in a 5% CO2 incubator at 37°C.

The cells were infected with the lentiviral transduction particles for PKIA-AS1. Briefly, when the cells confluence reached 80–90% in 6-well plates, the cells were infected with lentivirus [multiplicity of infection (MOI) = 50] in the presence of 5 mg/ml polybrene (Sigma-Aldrich, St. Louis, MO, United States) for 48 h.

Luciferase Reporter Assay

To test the promoter activity, CDK6 promoter was cloned into the pGL3-Basic vector using the Fast-Fusion^{TM} Cloning Kit (FulenGen, Guangzhou, China). Luciferase reporter constructs were co-transfected with pRL-TK (Promega) into PC12 cells, followed by infection with Lv-PKIA-AS1. Dual Luciferase Reporter Assay Kit (Promega) was used to measure the luciferase activity according to the manufacturer's instruction.

RNA-Binding Protein Immunoprecipitation Assay

RNA-binding protein immunoprecipitation assay was conducted using Magna RIP Kit (EMD Millipore, Billerica, MA, United States) according to the manufacturer's instruction. After the cells were lysed by RIP lysis buffer, magnetic beads conjugated to human anti-Ago2 antibody (Millipore) or control antibody (normal mouse IgG; Millipore) were added into cell lysate for incubation at 4°C overnight. CDK6 and PKIA-AS1 expression were measured by qRT-PCR.

Quantitative Methylation-Specific PCR

CDK6 promoter (−2000–+150) methylation status was measured by MSP. Genomic DNA (1 μg per sample) extracted by the Qiagen FFPE DNA Kit (Qiagen, CA, United States) was modified with bisulfite using the EZ DNA Methylation-Gold Kit (Zymo, Orange County, CA, United States) according to the manufacturer's instructions. Bisulfate-treated DNA was used to perform quantitative methylation-specific PCR (MSP). The qPCR steps were as following: initial denaturation at 95.0°C for 3 min; 39 cycles of 95.0°C for 10 s and 60°C for 30 s. The primers were as following: methylated-specific primer, forward, 5′-AGGCGGTTGTAGTTTTTGTAGTC-3′, reverse, 5′-ATTATTATTATTACTTTCCCACGCT-3′; unmethylated -specific primer, forward, 5′-GGAGGTGGTTGTAGTTTTTG TAGTT-3′, reverse, 5′-ATTATTATTATTACTTTCCCACACT-3′.

ELISA

Rat IL-1β, IL-6, IL-12, and TNFα ELISA kit was purchased from Cwbiotech (Beijing, China). The lumbar spinal cord segments (L5) were removed and were homogenized in a lysis buffer. ELISA was performed according to manufacturer's protocol.

Statistical Analysis

The experiments repeated at least three times. Data are expressed as means ± SEM. Statistical analyses were processed on GraphPad Prism software (GraphPad Software Inc., La Jolla, CA, United States). Student's *t*-test and one-way ANOVA with Bonferroni test were used to assess the statistical significance of the differences between two groups and multiple groups, respectively. Two-way repeated measure ANOVA with Bonferroni post-test for multiple comparisons at each time point was used to analyze PWT and PWL. P less than 0.05 was considered statistically significant.

RESULTS

Identification of Differentially Expressed lncRNAs in a Rat Spinal Nerve Ligation (SNL) Model of NP

To investigate the role of lncRNAs in neuropathic pain induced by spinal cord injury, we established a SNL rat model (**Figures 1A,B**). Total RNA was extracted from spinal cord tissues of these SNL rats and sham-operated control rats to perform lncRNA array analysis. We successfully identified 1259 downregulated lncRNAs and 2473 upregulated lncRNAs in SNL rats compared to controls (**Figure 1C**). **Table 1** presents the detail information on the top 10 most upregulated and top 10 most downregulated lncRNAs. We then investigated the profiles of the 10 most highly upregulated lncRNAs in the spinal cord of SNL rats by real-time quantitative PCR. These substantially upregulated lncRNAs, included PKIA-AS1 (fold change >15), SNHG4 (fold change >5), STAC3 (fold change >5), and CIRBP-AS1 (fold change >5) (**Figure 1D**). Specific overexpression in the SNL model strongly suggests that these differentially expressed lncRNAs are involve in the pathogenesis of neuropathic pain.

TABLE 1 | The detail information of the top 10 up-regulated and 10 down-regulated lncRNAs.

Upregulated lncRNAs	Fold changes (SNL/control)	*P*-value	Downregulated lncRNAs	Fold changes (SNL/control)	*P*-value
SCARN9L	29.5890184	0.00520449	CTA-363E6.5	−20.526302	0.00627821
PKIA-AS1	28.6970089	0.00230417	MIR99AHG	−13.0203657	0.03423339
LINC00189	9.4945753	0.00784969	LINC01168	−10.8343423	0.00972820
SNHG4	8.536707	0.00093759	TAPT1-AS1	−10.3589502	0.03339935
STAC3	7.0920605	0.01445976	LOC10192705	−9.7866859	0.03897605
CIRBP-AS1	6.8681445	0.02234753	HMGA1P7	−8.943874	0.00490554
GFOD1	6.7029805	0.01379864	SATB2-AS1	−8.616979	0.00299287
PINK1-AS	6.5001638	0.0191133	SIGLEC17P	−8.3775419	4.70013E-05
GGTA1P	5.7075659	0.00586269	MEF2C-AS1	−7.6937744	0.01728860
LINC01605	5.2351126	0.00020316	LANCL1-AS1	−6.4846909	0.01137424

In this study, we focused on the contributions of PKIA-AS1 to SNL-associated NP development as it exhibited the greatest upregulation.

Effects of PKIA-AS1 on Spinal Cord Ligation-Induced Neuropathic Pain

Similar to NP development, expression of PKIA-AS1 increased over time following SNL (**Figure 2A**). Therefore, we investigated whether reducing PKIA-AS1 expression in SNL rats by shRNA knockdown can attenuate SNL induced neuropathic pain. Real-time PCR demonstrated that PKIA-AS1 expression in spinal cord of SNL rats was markedly downregulated 3 days following infection with a lentivirus vector targeting PKIA-AS1 (Lv-PKIA-AS1) compared with the SNL rats infected with control lentivirus ($P < 0.05$, $N = 5$; **Figure 2B**).

The effects of PKIA-AS1 shRNA on both mechanical and thermal hyperalgesia were tested by measuring the paw withdrawal threshold (PWT) and latency (PWL). Animals developed progressive mechanical hyperalgesia following SNL as evidenced by reduced PWT that plateaued on the 7th day after surgery. At 3 days post-surgery, PWT was significantly lower in rats earmarked for Lv-NC and Lv-shPKIA-AS1 infection (SNL+Lv-NC and SNL+Lv-shPKIA-AS1 groups, respectively) compared to sham-operated controls. The PWT of the SNL+Lv-shPKIA-AS1 group rose significantly above that in the SNL+Lv-NC group following infection ($P < 0.05$, $N = 8$ rats per group), indicating reduced hyperalgesia. However, the PWT of the SNL+ Lv-shPKIA-AS1 group remained slightly lower than that of the control group (**Figure 2C**). Similarly, the PWL was significantly shorter in the SNL+Lv-NC, and SNL+ Lv-shPKIA-AS1 groups compared with the control group on the 3th day after surgery, but was significantly higher in the SNL+Lv-shPKIA-AS1 group than the SNL+Lv-NC group following infection ($P < 0.05$, $N = 8$ rats per group) (**Figure 2D**). These results suggest that knockdown of PKIA-AS1 attenuates SNL-induced neuropathic pain.

Next, we assessed whether PKIA-AS1 overexpression alone is sufficient to cause neuropathic pain–like symptoms in uninjured control rats. Seven days after infection with Lv-PKIA-AS1, real-time PCR showed that expression of PKIA-AS1 in the spinal cord was fivefold higher than in control rats or rats infected with the control lentivirus ($P < 0.05$, $N = 5$) (**Figure 3A**). The PWT in rats infected with Lv-PKIA-AS1 started to decrease by the second day post-infection and was even lower on days 4, 6, and 9 ($P < 0.01$, $N = 8$ rats per group) compared with rats infected with control lentivirus (**Figure 3B**), indicating progressive development of hyperalgesia. Similarly, PWL was significantly shorter in rats following Lv-PKIA-AS1 infection compared to rats infected with the control lentivirus ($P < 0.05$, $N = 8$ rats for each group) 2, 4, 6, and 9 days after infection (**Figure 3C**). These results suggest that overexpression of PKIA-AS1 alone is sufficient to produce hyperalgesia.

PKIA-AS1-Induced Neuropathic Pain Is Associated With Neuroinflammation

To investigate the effects of PKIA-AS1 on neuroinflammation associated with NP, we evaluated the activation of astrocyte and microglia as well as the expression levels of inflammatory cytokines interleukin (IL)-6, IL-1β, IL-12 and tumor necrosis factor (TNF-)-α expression in spinal cord. As expected, SNL induced astrocytic and microglial activation as evaluated by increased GFAP and Iba-1 expression levels, respectively, while PKIA-AS1 knockdown substantially reduced glial activation (**Figure 4A**). PKIA-AS1 knockdown also inhibited SNL-mediated upregulation of IL-6, IL-1β, and TNF-α at both mRNA and protein levels in spinal cord (**Figures 4B,C**). These findings suggest that knockdown of PKIA-AS1 represses neuropathic pain by inhibiting neuroinflammation.

PKIA-AS1 Interacts With CDK6

The potential mechanisms underlying regulation of neuropathic pain by PKIA-AS1 were then investigated. To identify possible targets of PKIA-AS1, we screened numerous differentially expressed proteins in spinal cord tissues after PKIA-AS1 overexpression (**Figure 5A**). The detail information on the top 10 most upregulated and downregulated proteins is listed in **Table 2**. One of the most upregulated proteins is CDK6, which has been strongly implicated in inflammation (Handschick et al., 2014). We then confirmed the expression of CDK6 in spinal cord tissues from rats infected with PKIA-AS1. Indeed, Lv-PKIA-AS1 infection induced CDK6 overexpression at both mRNA and protein levels (**Figures 5B,C**). We further demonstrated that Lv-PKIA-AS1 infection upregulated CDK6 gene promotor activity (**Figure 5D**). We next tested whether PKIA-AS1 interacts with CDK6 promoter by conducting RNA

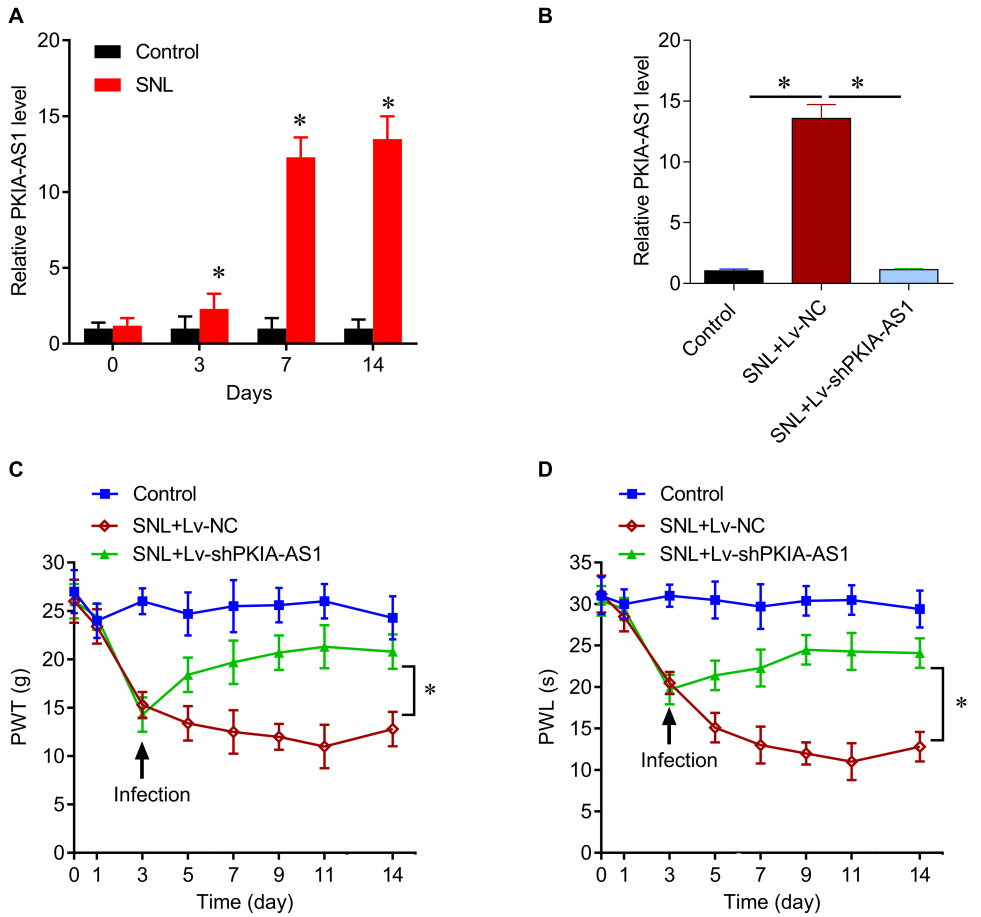


FIGURE 2 | lncRNA PKIA-AS1 expression is increased in the SNL spinal cord and contributes to the SNL-induced neuropathic pain. **(A)** Real-time PCR data show the expressions of PKIA-AS1 in the SNL spinal cord on different time points. **(B)** Real-time PCR data show that the expressions of PKIA-AS1 in the SNL spinal cord treated with shPKIA-AS1 lentivirus were significantly lower than that of the SNL+Lv-NC group. **(C,D)** shRNA silencing of PKIA-AS1 alleviates mechanical hyperalgesia **(C)** and thermal hyperalgesia **(D)** in the SNL rats. $N = 8$ for each group, $^*P < 0.05$ vs. control group. SNL, spinal never ligation; PWT, paw withdrawal threshold; PWL, paw withdrawal latency; lncRNA, long non-coding RNA.

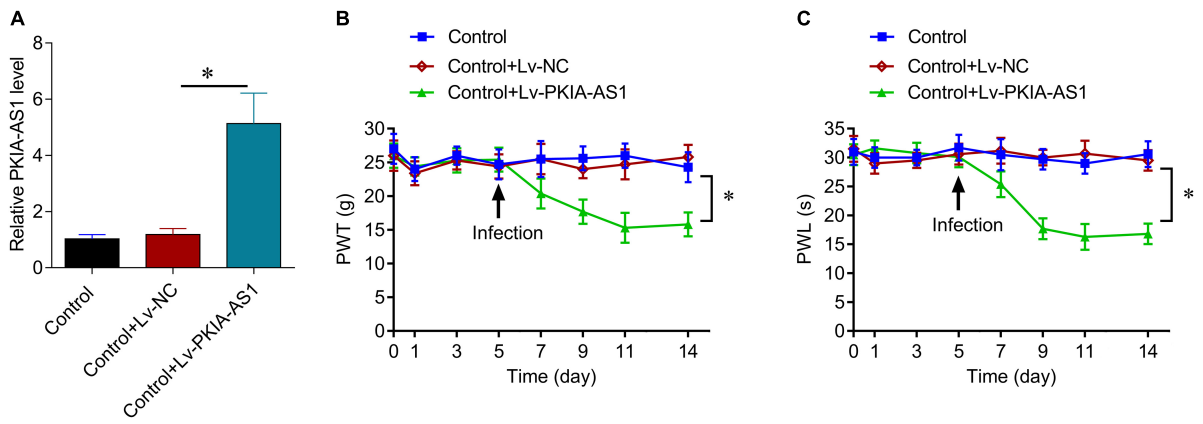


FIGURE 3 | Overexpression of PKIA-AS1 is sufficient to cause pain behavior in rats. **(A)** Real-time PCR show that the expression of PKIA-AS1 in the control rats 6 days after infection of PKIA-AS1 lentivirus was significantly higher than that of the control group. $^*P < 0.05$. **(B,C)** Overexpression of PKIA-AS1 produced mechanical hyperalgesia **(B)** and thermal hyperalgesia **(C)** in the control rats. $N = 8$ for each group, $^*P < 0.05$. PWT, paw withdrawal threshold; PWL, paw withdrawal latency.

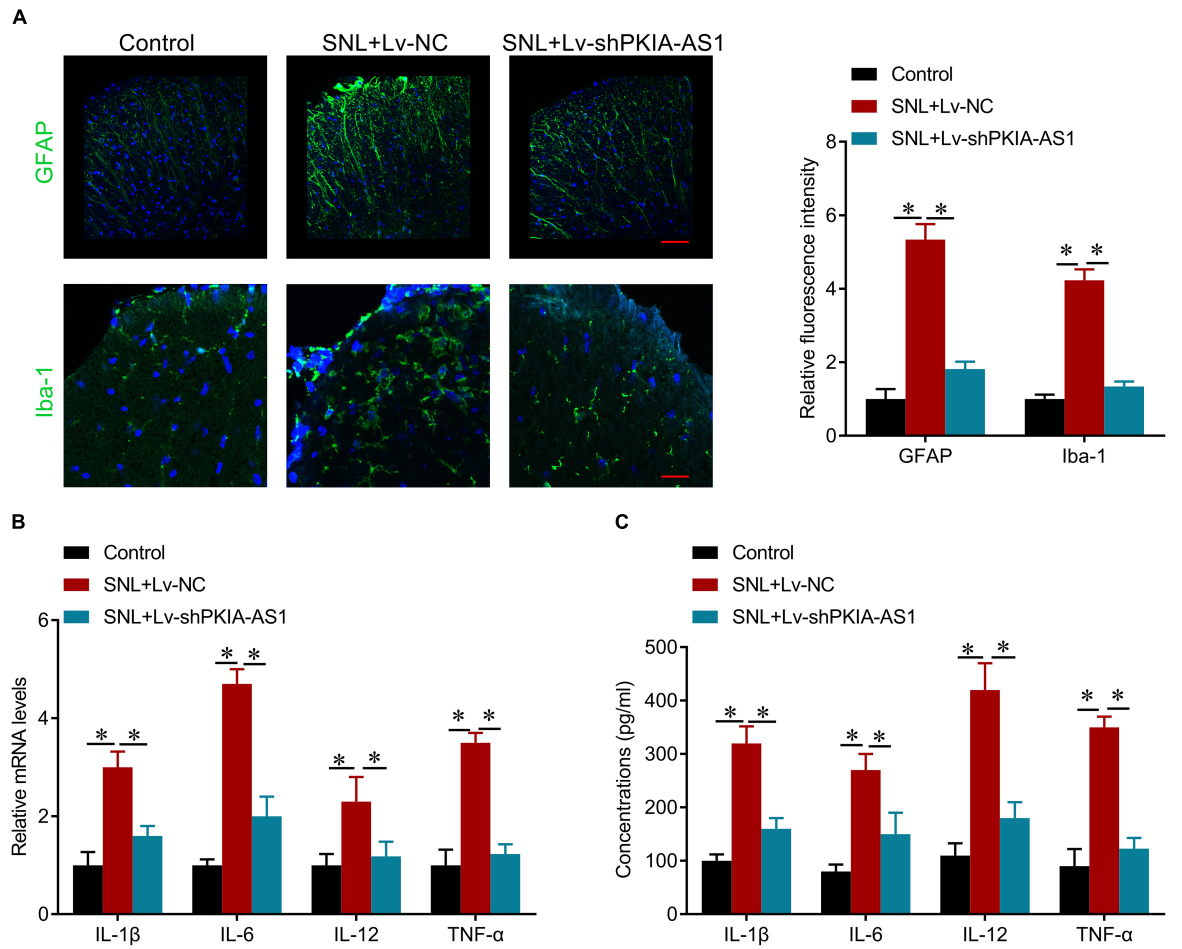


FIGURE 4 | shRNA silencing of PKIA-AS1 repressed neuroinflammation in SNL rats. **(A)** Immunofluorescence assay results show that silencing of PKIA-AS1 repressed SNL-mediated astrocyte and microglia activation evaluated by GFAP and Iba-1, respectively. Scale bar: 100 μm, $N = 8$ for each group. **(B)** mRNA levels of IL-1β, IL-6, IL-12, and TNF-α in L5 spinal cord tissues in the rats 6 days after infection of PKIA-AS1 lentivirus. **(C)** The protein levels of IL-1β, IL-6, IL-12, and TNF-α in the L5 spinal cord of rats were tested by ELISA at postoperative day 6. $N = 8$ for each group; $^*P < 0.05$.

TABLE 2 | The detail information of the top 10 most up-regulated and 10 most down-regulated proteins.

Upregulated proteins	Fold changes (PKIA-AS1/control)	*P*-value	Downregulated proteins	Fold changes (PKIA-AS1/control)	*P*-value
CDK6	19.33	0.000730853	Galectin-7	−14.06	0.005513955
Myosin	14.13	0.002566788	Histidine triad nucleotide-binding protein 2	−12.01	0.004340288
Alpha-crystallin B chain	10.45	0.000169286	Palate lung and nasal epithelium clone protein	−10.46	0.025461992
Myoglobin	9.33	0.017749647	Apolipoprotein A	−9.32	0.006539903
Creatine kinase M-type	9.91	0.007387786	Pyridoxine-5′-phosphate oxidase	−8.33	0.005393046
Creatine kinase M-type	8.90	0.001036429	Peroxiredoxin-2	−7.58	0.000836037
Fibrinogen	7.25	0.001054321	Fructose-bisphosphate aldolase A	−6.64	0.010053958
Pyruvate kinase	6.80	0.001121332	Ribosomal protein SA	−4.41	0.036115645
Model of actin-fimbrin abd2 complex	5.00	0.001233447	Keratin, type II cytoskeletal 1	−3.78	0.016436261
Vimentin	5.23	0.00020316	Keratin 5	−6.48	0.01137424

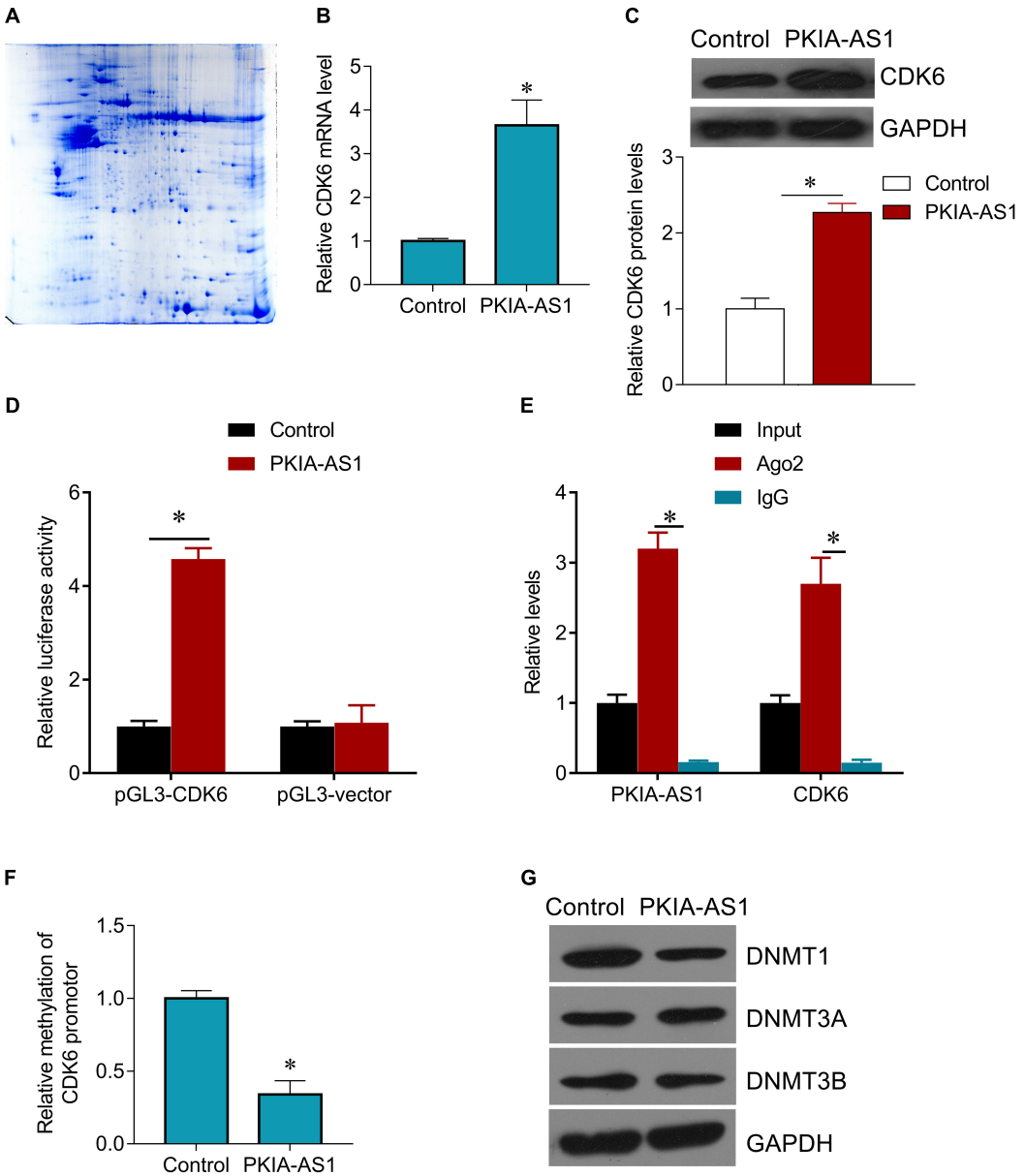


FIGURE 5 | PKIA-AS1 epigenetically regulates CDK6 by hypomethylating its promotor. **(A)** The differential protein spots from 2-DE gels by differential proteomics analysis. The gel was stained with coomassie brilliant blue. 2-DE, two-dimensional polyacrylamide gel electrophoresis. **(B)** CDK6 mRNA expression in PC12 cells infected with Lv-PKIA-AS1. **(C)** CDK6 protein expression in PC12 cells infected with Lv-PKIA-AS1. **(D)** Dual luciferase assay shown that PKIA-AS1 induced CDK6 promotor activity. **(E)** The correlation between PKIA-AS1, CDK6 promotor and Ago2 was detected by RIP assay. Cellular lysates were immunoprecipitated using Ago2 antibody or IgG. PKIA-AS1 and CDK6 promotor expression was tested by qRT-PCR. **(F)** PC12 cells were infected with PKIA-AS1 lentivirus. qMSP was perform to analyze CDK6 promoter methylation. **(G)** DNMT1, DNMT3a, and DNMT3b protein levels were assessed by western blot in PC12 cells infected with Lv-PKIA-AS1; $^*P < 0.05$.

pulldown assays in PC12 cells infected with Lv-PKIA-AS1 or control lentivirus. Both PKIA-AS1 and CDK6 promoter were more abundant in the Ago2 pellet than in the IgG pellet (**Figure 5E**), demonstrating that the CDK6 promoter interacts PKIA-AS1. We further tested how PKIA-AS1 regulates CDK6 promoter activity. The methylation status of CDK6 promoter was evaluated by quantitative methylation-specific PCR (qMSP) of the PC12 cells following Lv-PKIA-AS1 infection. Overexpression of PKIA-AS1 downregulated methylation of CDK6 promoter, suggesting that enhanced CDK6 expression in the SNL spinal cord is mediated by promoter hypomethylation induced by PKIA-AS1 (**Figure 5F**). In addition, PKIA-AS1 overexpression significantly inhibited DNMT1 expression, but not DNMT3A and DNMT3B expression (**Figure 5G**), suggesting that PKIA-AS1 regulates CDK6 expression by decreasing DNMT1-catalyzed methylation of CDK6 promoter.

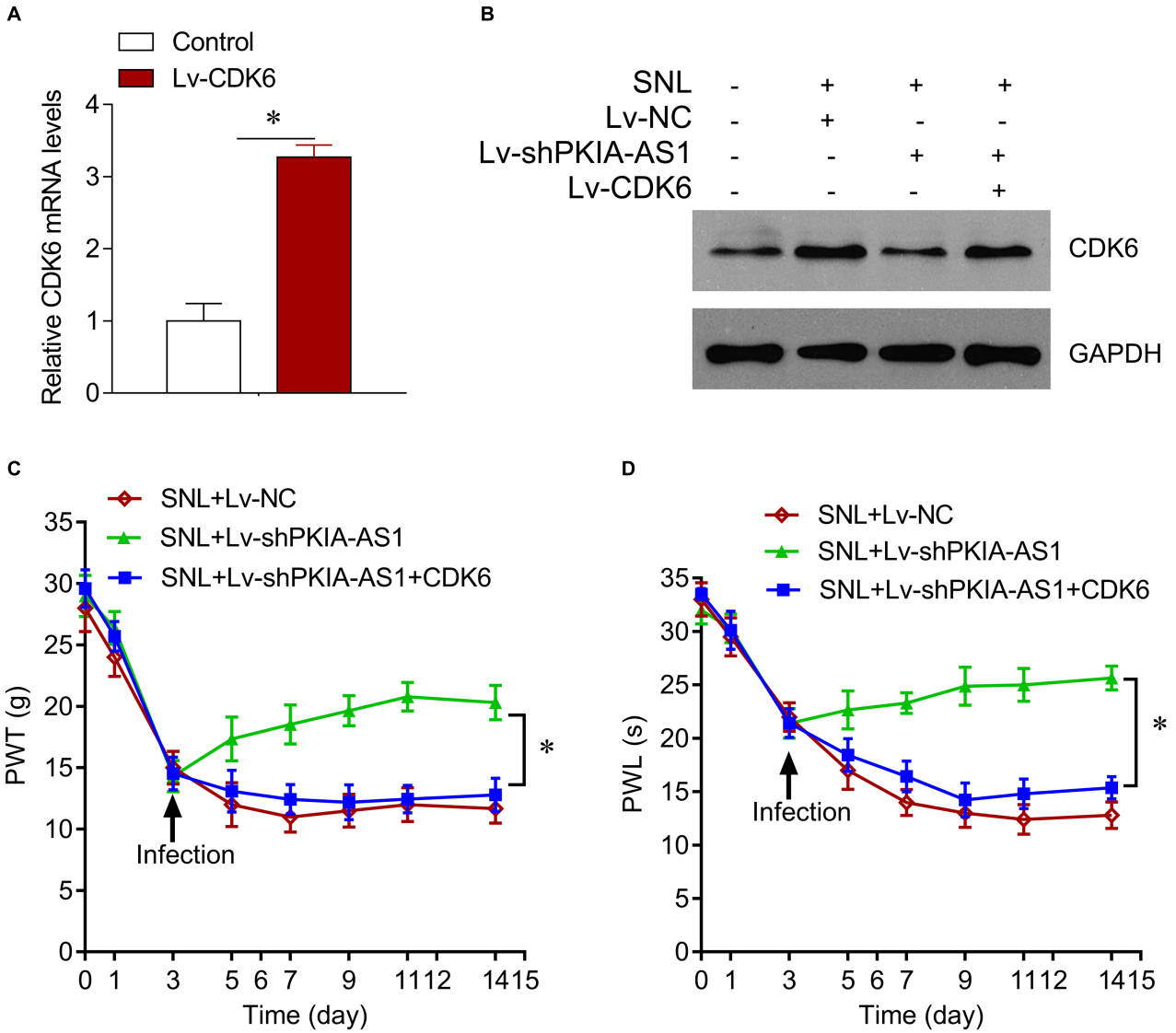


FIGURE 6 | PKIA-AS1 modulated neuropathic pain by regulating CDK6. **(A)** CDK6 mRNA expression in SNL rat models infected with Lv-CDK6 6 days after lentivirus infection. **(B)** CDK6 protein expression in the spinal cord tissues of rats infected with indicated viruses. **(C)** The effect of CDK6 on mechanical allodynia was evaluated by PWT. **(D)** The effect of CDK6 on thermal hyperalgesia was assessed by PWL. $N = 8$ for each group; $^*P < 0.05$. PWT, paw withdrawal threshold; PWL, paw withdrawal latency.

PKIA-AS1 Regulates Neuropathic Pain Progression Through CDK6

We further investigated whether PKIA-AS1 controls neuropathic pain via CDK6. Expression of CDK6 was significantly increased in SNL model rats compared with control rats, whereas CDK6 expression was inhibited by PKIA-AS1 knockdown. In addition, PKIA-AS1 knockdown-mediated inhibition of CDK6 was reversed by Lv-CDK6 infection (**Figures 6A,B**). We found that Lv-CDK6 infection reversed the attenuation of mechanical allodynia and thermal hyperalgesia by Lv-shPKIA-AS1 infection following SNL (**Figures 6C,D**). Moreover, Lv-CDK6 reversed the suppression of IL-1β, IL-6, IL-12, and TNF-α mRNA and protein expression by Lv-shPKIA-AS1 (**Figures 7A,B**). Collectively, these results indicate that an epigenetic regulatory pathway involving PKIA-AS1 and CDK6 mediates SNL-induced neuropathic pain.

DISCUSSION

We have identified the lncRNA PKIA-AS1 as a major regulator of SNL associated with NP. First, PKIA-AS1 was significantly upregulated in the SNL model rat spinal cord. Furthermore, both gain-of-function and loss-of-function studies confirmed that PKIA-AS1 was necessary for generating SNL-induced neuropathic pain. Our results suggest that PKIA-AS1 is a critical regulator of SNL-induced neuropathic

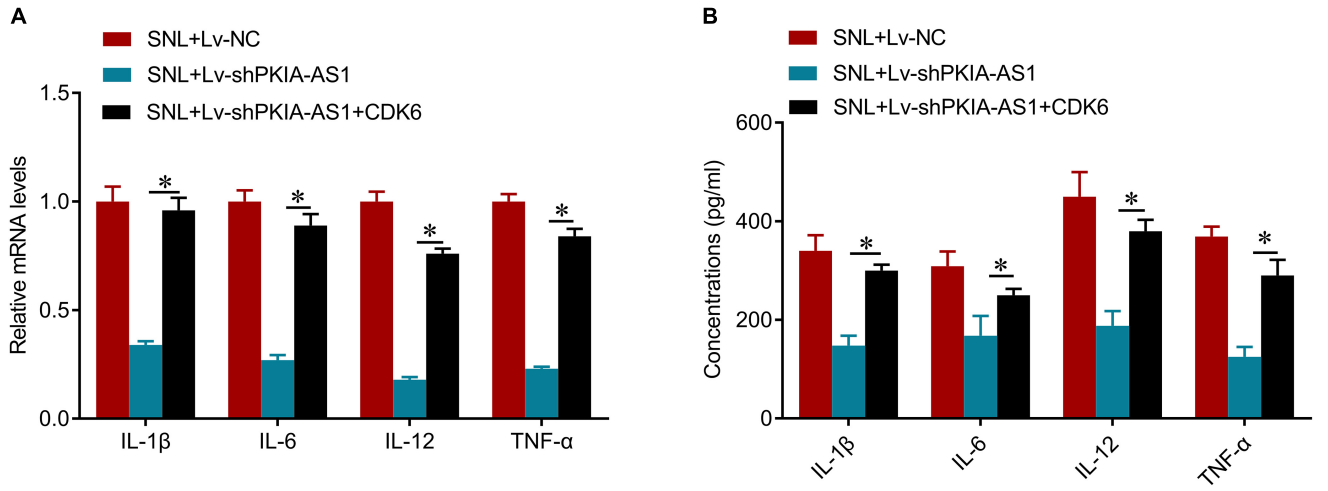


FIGURE 7 | shRNA silencing of PKIA-AS1 inhibits neuroinflammation by regulating CDK6 in SNL rats. **(A)** mRNA levels of IL-1β, IL-6, IL-12, and TNF-α in L5 spinal cord tissues in the rats 6 days after lentivirus infection. **(B)** The protein levels of IL-1β, IL-6, IL-12, and TNF-α in the L5 spinal cord of rats were tested by ELISA 6 days after lentivirus infection. $N = 8$ for each group; $^*P < 0.05$.

pain, and that manipulation of PKIA-AS1 expression could potentially be used to improve spinal nerve ligation-induced neuropathic pain.

Peripheral inflammation and nerve injury can alter the expression of numerous genes, including lncRNAs, in affected pain pathways (Jiang et al., 2015; Wu et al., 2018). Moreover, numerous lncRNAs have been identified in the pain-related regions, such as dorsal root ganglion and spinal cord of mouse, rat, and human (Hu et al., 2016; Dou et al., 2017; Mo et al., 2018). The spinal cord dorsal horn is responsible for relaying and modulating pain-related signals from nociceptors to the supraspinal brain regions. The expression of the lncRNA colon cancer associated transcript-1 (CCAT1) was found to decrease in the spinal cord, dorsal root ganglion, hippocampus, and anterior cingulate cortex from day 1 to day 5 after chronic sciatic nerve injury (CCI). Over-expression of lncRNA CCAT1 alleviated CCI-induced mechanical allodynia (Dou et al., 2017). In the present study, the expression of another lncRNA, PKIA-AS1 was markedly increased in the spinal cord following SNL and was associated with heightened pain sensitivity, whereas shRNA-mediated knockdown of PKIA-AS1 alleviated thermal and mechanical hypersensitivity caused by SNL. These results suggest that upregulation of PKIA-AS1 in the spinal cord may be an important contributor to SNL-induced neuropathic pain. This possibility is further supported by our findings that PKIA-AS1 overexpression in spinal cord of uninjured rats was sufficient to induce pain-related behaviors. In the present study, the expression profiles of lncRNA were obtained from whole, unperfused spinal cord tissues after SNL so the specific cells overexpressing this lncRNA are currently unknown. Additional studies are needed to assess whether PKIA-AS1 and the other lncRNAs differentially expressed in the SNL spinal cord are altered in neurons, microglia. and (or) astrocytes.

We identified many possible targets of PKIA-AS1 regulation by proteomic assay, and confirmed that CDK6 is an interaction partner of PKIA-AS1. We further demonstrated that PKIA-AS1 interacts with CDK6 promoter and enhances promoter activity by modulating its methylation status. Our results strongly support the notion that PKIA-AS1 interacts with CDK6 promoter to enhance its expression and function. Cyclin-dependent kinases (CDKs) control diverse biological processes via the regulation of the cell cycle and gene expression (Peng et al., 2013). CDKs transcriptionally induce proinflammatory genes during the G1 phase of cell cycle. Further, cytokine-induced recruitment of CDK6 to the nuclear chromatin fraction is associated with activation of NF-κB, STAT, and AP-1 transcription factor families. CDK6 can recruit NF-κB subunit p65 to its target sites (Schmitz and Kracht, 2016). The demonstrated involvement of CDKs in proinflammatory gene expression makes these proteins promising target for treatment of chronic inflammatory diseases. CDK6 has been implicated in the proliferation, differentiation, and survival of neurons (Beukelaers et al., 2011; Mi et al., 2013; Caron et al., 2018; Hasenpusch-Theil et al., 2018). For example, preventing CDK6 over-activation can reduce 6-hydroxy-dopamine-induced neuronal death (Alquezar et al., 2015). According to previous studies, CDK6 is localized to the cytoplasm (Kohrt et al., 2009). CDK6 also regulates astrocyte proliferation and microglial activation (Zhao et al., 2013; Gu et al., 2016), suggesting that CDK6 is involved with inflammatory pain. In our study, we demonstrate for the first time that PKIA-AS1 epigenetically controls CDK6 expression by modulating promoter methylation, thereby regulating proinflammatory cytokine release, and ultimately controlling neuropathic pain.

In conclusion, PKIA-AS1 plays an important role in the pathogenesis of neuropathic pain through direct interaction with CDK6. Silencing PKIA-AS1 may be a complementary approach

to reduce neuropathic pain induced by spinal nerve ligation through downregulation of CDK6 expression.

AUTHOR CONTRIBUTIONS

J-ZH and H-BL designed the study. JZH and Z-JR performed cell biological experiments and *in vivo* experiments. ML, PL, L-YJ, Z-XL, C-YD and YC analyzed and interpreted the data. All authors contributed to writing the manuscript. All authors read and approved the final manuscript.

FUNDING

This study was supported by the National Natural Science Foundation of China (Nos. 81672174 and 81874004).

SUPPLEMENTARY MATERIAL

The Supplementary Material for this article can be found online at: https://www.frontiersin.org/articles/10.3389/fncel.2019.00050/full#supplementary-material

REFERENCES

Alquezar, C., Barrio, E., Esteras, N., de la Encarnacion, A., Bartolome, F., Molina, J. A., et al. (2015). Targeting cyclin D3/CDK6 activity for treatment of Parkinson's disease. *J. Neurochem.* 133, 886–897. doi: 10.1111/jnc.13070

Bali, K. K., and Kuner, R. (2014). Noncoding RNAs: key molecules in understanding and treating pain. *Trends Mol. Med.* 20, 437–448. doi: 10.1016/j.molmed.2014.05.006

Beukelaers, P., Vandenbosch, R., Caron, N., Nguyen, L., Belachew, S., Moonen, G., et al. (2011). Cdk6-dependent regulation of G(1) length controls adult neurogenesis. *Stem Cells* 29, 713–724. doi: 10.1002/stem.616

Caron, N., Genin, E. C., Marlier, Q., Verteneuil, S., Beukelaers, P., Morel, L., et al. (2018). Proliferation of hippocampal progenitors relies on p27-dependent regulation of Cdk6 kinase activity. *Cell. Mol. Life Sci.* 75, 3817–3827. doi: 10.1007/s00018-018-2832-x

Coraggio, V., Guida, F., Boccella, S., Scafuro, M., Paino, S., Romano, D., et al. (2018). Neuroimmune-driven neuropathic pain establishment: a focus on gender differences. *Int. J. Mol. Sci.* 19:E281. doi: 10.3390/ijms19010281

Dones, I., and Levi, V. (2018). Spinal cord stimulation for neuropathic pain: current trends and future applications. *Brain Sci.* 8:E138. doi: 10.3390/brainsci8080138

Dou, L., Lin, H., Wang, K., Zhu, G., Zou, X., Chang, E., et al. (2017). Long non-coding RNA CCAT1 modulates neuropathic pain progression through sponging miR-155. *Oncotarget* 8, 89949–89957. doi: 10.18632/oncotarget.21192

Gu, J., Ni, Y., Xu, L., Xu, H., and Cai, Z. (2016). Nanog interact with CDK6 to regulates astrocyte cells proliferation following spinal cord injury. *Biochem. Biophys. Res. Commun.* 469, 1097–1103. doi: 10.1016/j.bbrc.2015.12.053

Gwak, Y. S., and Hulsebosch, C. E. (2011). GABA and central neuropathic pain following spinal cord injury. *Neuropharmacology* 60, 799–808. doi: 10.1016/j.neuropharm.2010.12.030

Gwak, Y. S., Kang, J., Unabia, G. C., and Hulsebosch, C. E. (2012). Spatial and temporal activation of spinal glial cells: role of gliopathy in central neuropathic pain following spinal cord injury in rats. *Exp. Neurol.* 234, 362–372. doi: 10.1016/j.expneurol.2011.10.010

Handschick, K., Beuerlein, K., Jurida, L., Bartkuhn, M., Muller, H., Soelch, J., et al. (2014). Cyclin-dependent kinase 6 is a chromatin-bound cofactor for NF-kappaB-dependent gene expression. *Mol. Cell* 53, 193–208. doi: 10.1016/j.molcel.2013.12.002

Hasenpusch-Theil, K., West, S., Kelman, A., Kozic, Z., Horrocks, S., McMahon, A. P., et al. (2018). Gli3 controls the onset of cortical neurogenesis by regulating the radial glial cell cycle through Cdk6 expression. *Development* 145:dev163147. doi: 10.1242/dev.163147

Hu, J., Ni, S., Cao, Y., Zhang, T., Wu, T., Yin, X., et al. (2016). The angiogenic effect of microRNA-21 targeting TIMP3 through the regulation of MMP2 and MMP9. *PLoS One* 11:e0149537. doi: 10.1371/journal.pone.0149537

Jiang, B. C., Sun, W. X., He, L. N., Cao, D. L., Zhang, Z. J., and Gao, Y. J. (2015). Identification of lncRNA expression profile in the spinal cord of mice following spinal nerve ligation-induced neuropathic pain. *Mol. Pain* 11:43. doi: 10.1186/s12990-015-0047-9

Kohrt, D. M., Crary, J. I., Gocheva, V., Hinds, P. W., and Grossel, M. J. (2009). Distinct subcellular distribution of cyclin dependent kinase 6. *Cell Cycle* 8, 2837–2843. doi: 10.4161/cc.8.17.9521

Li, G., Jiang, H., Zheng, C., Zhu, G., Xu, Y., Sheng, X., et al. (2017). Long noncoding RNA MRAK009713 is a novel regulator of neuropathic pain in rats. *Pain* 158, 2042–2052. doi: 10.1097/j.pain.0000000000001013

Liu, C., Li, C., Deng, Z., Du, E., and Xu, C. (2018). Long non-coding RNA BC168687 is involved in TRPV1-mediated diabetic neuropathic pain in rats. *Neuroscience* 374, 214–222. doi: 10.1016/j.neuroscience.2018.01.049

Liu, Z., Liang, Y., Wang, H., Lu, Z., Chen, J., Huang, Q., et al. (2017). LncRNA expression in the spinal cord modulated by minocycline in a mouse model of spared nerve injury. *J. Pain Res.* 10, 2503–2514. doi: 10.2147/JPR.S147055

McKelvey, R., Berta, T., Old, E., Ji, R. R., and Fitzgerald, M. (2015). Neuropathic pain is constitutively suppressed in early life by anti-inflammatory neuroimmune regulation. *J. Neurosci.* 35, 457–466. doi: 10.1523/JNEUROSCI.2315-14.2015

Mi, D., Carr, C. B., Georgala, P. A., Huang, Y. T., Manuel, M. N., Jeanes, E., et al. (2013). Pax6 exerts regional control of cortical progenitor proliferation via direct repression of Cdk6 and hypophosphorylation of pRb. *Neuron* 78, 269–284. doi: 10.1016/j.neuron.2013.02.012

Mo, C., Xu, M., Wen, C., Chang, R., Huang, C., Zou, W., et al. (2018). Normalizing JMJD6 expression in rat spinal dorsal horn alleviates hyperalgesia following chronic constriction injury. *Front. Neurosci.* 12:542. doi: 10.3389/fnins.2018.00542

Peng, B., Cao, J., Yi, S., Wang, C., Zheng, G., and He, Z. (2013). Inhibition of proliferation and induction of G1-phase cell-cycle arrest by dFMGEN, a novel genistein derivative, in lung carcinoma A549 cells. *Drug Chem. Toxicol.* 36, 196–204. doi: 10.3109/01480545.2012.710620

Plassais, J., Lagoutte, L., Correard, S., Paradis, M., Guaguere, E., Hedan, B., et al. (2016). A point mutation in a lincRNA upstream of GDNF is associated to a canine insensitivity to pain: a spontaneous model for human sensory neuropathies. *PLoS Genet.* 12:e1006482. doi: 10.1371/journal.pgen.1006482

Schmitz, M. L., and Kracht, M. (2016). Cyclin-dependent kinases as coregulators of inflammatory gene expression. *Trends Pharmacol. Sci.* 37, 101–113. doi: 10.1016/j.tips.2015.10.004

Shao, J., Wang, J., Huang, J., Liu, C., Pan, Y., Guo, Q., et al. (2018). Identification of lncRNA expression profiles and ceRNA analysis in the spinal cord of morphine-tolerant rats. *Mol. Brain* 11:21. doi: 10.1186/s13041-018-0365-8

Tan, Y., Yang, J., Xiang, K., Tan, Q., and Guo, Q. (2015). Suppression of microRNA-155 attenuates neuropathic pain by regulating SOCS1 signalling pathway. *Neurochem. Res.* 40, 550–560. doi: 10.1007/s11064-014-1500-2

Vieira, A. S., Dogini, D. B., and Lopes-Cendes, I. (2018). Role of non-coding RNAs in non-aging-related neurological disorders. *Braz. J. Med. Biol. Res.* 51:e7566. doi: 10.1590/1414-431X20187566

Walters, E. T. (2014). Neuroinflammatory contributions to pain after SCI: roles for central glial mechanisms and nociceptor-mediated host defense. *Exp. Neurol.* 258, 48–61. doi: 10.1016/j.expneurol.2014.02.001

Wayne, N. P. (2018). Severe chronic pain following spinal cord damage: a pragmatic perspective for prescribing opioids. *Spinal Cord. Ser. Cases* 4:65. doi: 10.1038/s41394-018-0094-3

Wu, S., Bono, J., and Tao, Y. X. (2018). Long noncoding RNA (lncRNA): a target in neuropathic pain. *Expert Opin. Ther. Targets* 23, 15–20. doi: 10.1080/14728222.2019.1550075

Xia, L. X., Ke, C., and Lu, J. M. (2018). NEAT1 contributes to neuropathic pain development through targeting miR-381/HMGB1 axis in CCI rat models. *J. Cell. Physiol.* 233, 7103–7111. doi: 10.1002/jcp.26526

Yan, X. T., Lu, J. M., Wang, Y., Cheng, X. L., He, X. H., Zheng, W. Z., et al. (2018). XIST accelerates neuropathic pain progression through regulation of miR-150 and ZEB1 in CCI rat models. *J. Cell. Physiol.* 233, 6098–6106. doi: 10.1002/jcp.26453

Yang, J., Zhou, M., Zhao, R., Peng, S., Luo, Z., Li, X., et al. (2014). Identification of candidate biomarkers for the early detection of nasopharyngeal carcinoma by quantitative proteomic analysis. *J. Proteomics* 109, 162–175. doi: 10.1016/j.jprot.2014.06.025

Zhang, Z. J., Cao, D. L., Zhang, X., Ji, R. R., and Gao, Y. J. (2013). Chemokine contribution to neuropathic pain: respective induction of CXCL1 and CXCR2 in spinal cord astrocytes and neurons. *Pain* 154, 2185–2197. doi: 10.1016/j.pain.2013.07.002

Zhao, H., Wang, J., Gao, L., Wang, R., Liu, X., Gao, Z., et al. (2013). MiRNA-424 protects against permanent focal cerebral ischemia injury in mice involving suppressing microglia activation. *Stroke* 44, 1706–1713. doi: 10.1161/STROKEAHA.111.000504

Zhou, J., Xiong, Q., Chen, H., Yang, C., and Fan, Y. (2017). Identification of the spinal expression profile of non-coding RNAs involved in neuropathic pain following spared nerve injury by sequence analysis. *Front. Mol. Neurosci.* 10:91. doi: 10.3389/fnmol.2017.00091

Conflict of Interest Statement: The authors declare that the research was conducted in the absence of any commercial or financial relationships that could be construed as a potential conflict of interest.

Copyright © 2019 Hu, Rong, Li, Li, Jiang, Luo, Duan, Cao and Lu. This is an open-access article distributed under the terms of the Creative Commons Attribution License (CC BY). The use, distribution or reproduction in other forums is permitted, provided the original author(s) and the copyright owner(s) are credited and that the original publication in this journal is cited, in accordance with accepted academic practice. No use, distribution or reproduction is permitted which does not comply with these terms.

frontiers in Cellular Neuroscience

ORIGINAL RESEARCH
published: 22 February 2019
doi: 10.3389/fncel.2019.00058

Long Non-coding RNAs Associated With Neurodegeneration-Linked Genes Are Reduced in Parkinson's Disease Patients

Maximilianos Elkouris[1], Georgia Kouroupi[2], Alexios Vourvoukelis[3], Nikolaos Papagiannakis[3,4], Valeria Kaltezioti[1], Rebecca Matsas[2], Leonidas Stefanis[3,4], Maria Xilouri[3] and Panagiotis K. Politis[1]**

[1] Center for Basic Research, Biomedical Research Foundation of the Academy of Athens, Athens, Greece, [2] Laboratory of Cellular and Molecular Neurobiology, Hellenic Pasteur Institute, Athens, Greece, [3] Center of Clinical Research, Experimental Surgery and Translational Research, Biomedical Research Foundation of the Academy of Athens, Athens, Greece, [4] First Department of Neurology, National and Kapodistrian University of Athens Medical School, Athens, Greece

Transcriptome analysis has identified a plethora of long non-coding RNAs (lncRNAs) expressed in the human brain and associated with neurological diseases. However, whether lncRNAs expression levels correlate with Parkinson's disease (PD) pathogenesis remains unknown. Herein, we show that a number of lncRNA genes encompassing transcriptional units in close proximity to PD-linked protein-coding genes, including *SNCA*, *LRRK2*, *PINK1*, *DJ-1*, *UCH-L1*, *MAPT* and *GBA1*, are expressed in human dopaminergic cells and post-mortem material, such as cortex, *Substantia Nigra* and cerebellum. Interestingly, these lncRNAs are upregulated during neuronal differentiation of SH-SY5Y cells and of dopaminergic neurons generated from human fibroblast-derived induced pluripotent stem cells. Importantly, six lncRNAs are found under-expressed in the nigra and three in the cerebellum of PD patients compared to controls. Simultaneously, *SNCA* mRNA levels are increased in the nigra, while *LRRK2* and *PINK1* mRNA levels are decreased both in the nigra and the cerebellum of PD subjects compared to controls, indicating a possible correlation between the expression profile of the respective lncRNAs with their adjacent coding genes. Interestingly, all dysregulated lncRNAs are also detected in human peripheral blood mononuclear cells and four of them in exosomes derived from human cerebrospinal fluid, providing initial evidence for their potential use as diagnostic tools for PD. Our data raise the intriguing possibility that these lncRNAs may be involved in disease pathogenesis by regulating their neighboring PD-associated genes and may thus represent novel targets for the diagnosis and/or treatment of PD or related diseases.

Keywords: long-non coding RNAs, Parkinson's disease, alpha-synuclein, LRRK2, *Substantia Nigra*, exosomes

OPEN ACCESS

Edited by:
José A. G. Agúndez, University of Extremadura, Spain

Reviewed by:
Silvia Zucchelli, Università degli Studi del Piemonte Orientale, Italy
Dennis Qing Wang, Zhujiang Hospital, Southern Medical University, China

***Correspondence:**
Maria Xilouri
mxilouri@bioacademy.gr
Panagiotis K. Politis
ppolitis@bioacademy.gr

Received: *08 September 2018*
Accepted: *05 February 2019*
Published: *22 February 2019*

Citation:
Elkouris M, Kouroupi G, Vourvoukelis A, Papagiannakis N, Kaltezioti V, Matsas R, Stefanis L, Xilouri M and Politis PK (2019) Long Non-coding RNAs Associated With Neurodegeneration-Linked Genes Are Reduced in Parkinson's Disease Patients. Front. Cell. Neurosci. 13:58. doi: 10.3389/fncel.2019.00058

Abbreviations: CSF, cerebrospinal fluid; iPSCs, induced pluripotent stem cells; lncRNAs, long non-coding RNAs; PBMCs, peripheral blood mononuclear cells; SN, *Substantia Nigra*.

INTRODUCTION

Exploration of non-coding genome has uncovered a growing list of formerly unknown regulatory lncRNAs with critical roles in the pathophysiology of many neurological diseases, including schizophrenia, bipolar disorder, cerebral ischemia, Alzheimer's disease and Huntington's disease (Faghihi et al., 2008; Johnson et al., 2010; Ng et al., 2013; Akula et al., 2014; Barry et al., 2014; Wang J. et al., 2017; Sarkar et al., 2018), and other diseases (Zhang et al., 2019). Interestingly, the expression of lncRNAs is found to be altered during cellular senescence, which represents a major risk factor for the development of many neurodegenerative diseases (Chakrabarti and Mohanakumar, 2016; Ghanam et al., 2017). A common theme emerging from these studies is that lncRNAs control the expression of nearby protein-coding genes *in cis* and that deregulation of this relationship could lead to brain diseases. The majority of these lncRNAs, which are considered to be expressed in the nervous system, have only been identified in genome-wide expression screens; intriguingly, their involvement in Parkinson's disease (PD) is only beginning to be explored (Saracchi et al., 2014; Soreq et al., 2014; Ni et al., 2017; Marki et al., 2018).

In regards to PD, recent studies have identified lncRNAs that may alter the expression of PD-linked genes, such as *PINK1*, *UCH-L1*, *LRRK2,* and *SNCA*. In particular, NaPINK1, a human-specific lncRNA transcribed from the antisense orientation of the *PINK1* locus was found to stabilize PINK1 expression and its silencing resulted in decreased *PINK1* expression in neurons (Scheele et al., 2007; Chiba et al., 2009). Similarly, *UCHL1-AS1*, an antisense transcript of *UCH-L1*, was reported to enhance loading of *UCH-L1* mRNA to heavy polysomes for a more efficient translation, thus increasing protein synthesis (Carrieri et al., 2012). A subsequent study showed that *UCHL1-AS1* is a component of the *NURR1*-dependent dopaminergic gene network and is down-regulated in *in vitro* (MPP+) and *in vivo* (MPTP) toxin-induced models of PD (Carrieri et al., 2015). The activity of *UCHL1-AS1* is reported to be dependent on two functional domains: the overlapping region that defines target specificity and the inverted SINE element of B2 subclass (invSINEB2) that confers protein synthesis activation. These properties classified *UCHL1-AS1* as a representative member of a new functional class of natural and synthetic RNAs that increase protein synthesis named SINEUPs (Zucchelli et al., 2015). Based on the structure of this lncRNA, the authors designed synthetic SINEUPs targeting the endogenous PD-associated protein DJ-1, which proved to be active in different neuronal cell lines, suggesting that SINEUPs may represent valuable tools to increase synthesis of targeted proteins.

In addition, a recent report has shown that overexpression of the highly conserved neuron-specific lncRNA *MALAT1* (metastasis associated lung adenocarcinoma transcript 1), upregulated the expression of α-Synuclein (SNCA), whereas inhibition of MALAT1 downregulated SNCA expression only at the protein level rather than the mRNA level (Zhang et al., 2016). Finally, *HOTAIR* lncRNA (Hox transcript antisense intergenic RNA), transcribed from the HOXC locus, has been reported to be upregulated in the MPTP mouse model of PD. This upregulated HOTAIR was shown to increase the stability of *LRRK2* mRNA and to upregulate its expression, thus inducing dopaminergic neuronal apoptosis (Wang S. et al., 2017).

To investigate further the role of lncRNAs in PD pathogenesis, we have identified seven human lncRNA genes producing transcripts in close genomic proximity to PD-related genes, including *SNCA (PARK4)*, *LRRK2 (PARK8)*, *UCH-L1 (PARK5)*, *PINK1 (PARK6)*, *DJ-1 (PARK7)*, *GBA1*, and *MAPT*. These lncRNA genes have been formerly annotated by human genome consortia (ENCODE and FANTOM) and are thought to be potentially expressed in human cells. By detailed expression studies we showed that these lncRNAs are expressed in human dopaminergic SH-SY5Y cells and iPSC-derived human dopaminergic neurons, as well as in human post-mortem material derived from PD patients and controls. Importantly, our expression studies suggest that most of these lncRNAs are found to be under-expressed in the SN and three of them in the cerebellum of PD patients, compared to control subjects. Intriguingly, the majority of the aforementioned lncRNAs can be detected in human peripheral tissues, such as PBMCs and exosomes derived from CSF, suggesting their potential use as biomarkers. This line of research suggests a possible role of lncRNAs in PD pathogenesis or in neuronal responses associated with PD-related pathogenic effects.

MATERIALS AND METHODS

Human Brain Specimens

A total of 17 cases (n = 8 non-demented controls; n = 9 PD cases) were included for the present study. Autopsy material encompassing the SN and the cerebellum was collected with full ethical permission, following donation by next of kin, and were kindly provided by the Parkinson's Disease UK Brain Bank (PDUKBB). The referring specialist Neurologist in care of the patient locally made the clinical diagnosis, in accordance with internationally recognized criteria. Full clinical information and neuropathological reports are available upon request from the PDUKBB. The demographic details of these cohorts are shown in **Table 1**. Regarding the time from cardiac arrest to RNA isolation, this information is shown in **Table 1**. PMD (post-mortem delay) = 16.3 ± 6.7 for the Controls and 18 ± 6.97 for the PD subjects. The brain tissues arrived in dry ice and stored at −80°C, until further analysis. On the day of RNA isolation, the tissues were transferred on dry ice and Trizol reagent was added to all of them immediately, in order to avoid the thawing of the tissue. Study of these brains was performed following approval by the Ethical Committee of the Biomedical Research Foundation of the Academy of Athens. In preliminary experiments (presented in **Figure 1**) we also used autopsy material from the Netherlands Brain Bank, kindly provided to us by Dr Margarita Chrysanthou-Piterou from the Research Unit of Histochemistry and Electron Microscopy, University of Athens Medical School.

TABLE 1 | Table presenting the demographic details for control (n = 8) and PD (n = 9) cohorts (n.a., non-applicable).

Sample	Sex	Age (years)	Onset (years)	Duration (years)	PMD (hours)
Parkinson's disease (n = 9)	5M:4F	81 ± 3.65	65.9 ± 7.99	15.1 ± 5.63	16.3 ± 6.7
Controls (n = 8)	4M:4F	82.1 ± 6.03	n.a.	n.a.	18 ± 6.97

Isolation of Peripheral Blood Mononuclear Cells (PBMCs)

Patients with PD (n = 20) and age-matched healthy subjects (n = 20) were enrolled in the study from the 2nd Department of Neurology, Attikon University Hospital, Athens, Greece. Collection of samples was performed according to a protocol approved by the Scientific Council of "Attikon" Hospital, and all participating subjects signed informed consents. The diagnosis of idiopathic PD was made according to the criteria of Gelb et al. (1999). Motor function was evaluated with the Unified Parkinson Disease Rating Scale (UPDRS) III. Patients were also assessed for Hoehn & Yahr stage. Enrolled healthy controls were spouses and blood donors with no known family history of PD. The demographic details of these cohorts are shown in **Table 2**. PBMCs were isolated from whole blood by Biocoll Separating Solution (Biochrom AG) density gradient centrifugation. Briefly, blood samples were diluted with the same amount of Phosphate Buffer Saline (PBS, Gibco), layered on Biocoll and centrifuged (500 *g*, 20 min, 4°C). PBMCs were collected from the interface between plasma and Biocoll, washed twice with PBS, aliquoted and stored at −80°C until further analysis.

SH-SY5Y Cell Culture

SH-SY5Y cells were cultured in DMEM (Life Technologies) supplemented with 1% penicillin/streptomycin (Life Technologies) and 10% Fetal Bovine Serum (Life Technologies). Neuronal differentiation was performed with 10 μM all *trans* Retinoic acid (RA) as previously described (Vekrellis et al., 2009). The efficient differentiation of these cells into a neuronal-like phenotype was verified by immunostaining with the neuronal marker βIII-tubulin (**Supplementary Figure 2**). Proliferating and neuronally differentiated SH-SY5Y cells (7 days following initial RA addition) were used for this study.

Human iPSC Culture and Neuronal Differentiation

Skin fibroblasts derived from a control subject (age of skin biopsy 43 years old) were obtained through the MEFOPA study (MEndelianFOrms Of PArkinsonism). All study procedures were approved by the scientific council and ethical committee of Attikon University Hospital, Athens, Greece and the participant provided written informed consent. Fibroblasts were cultured in Dulbecco's modified Eagle's medium (DMEM, Life Technologies) supplemented with 10% fetal bovine serum (FBS, Life Technologies), 2 mM GlutaMax (Life Technologies) and 1% penicillin/streptomycin (Life Technologies). iPSCs were generated using the 'Yamanaka' reprogramming method by transducing human fibroblasts with retroviral vectors expressing the human cDNAs for OCT4, SOX2, KLF4 and C-MYC, as previously described (Takahashi et al., 2007). At least two iPSC lines were used for the current study. iPSCs were cultured on irradiated mouse embryonic fibroblasts (MEFs, Globalstem) in iPSC medium consisting of KnockOut DMEM (KO-DMEM, Life Technologies), 20% Knockout Serum Replacement (KSR, Life Technologies), 2 mM GlutaMax (Life Technologies), MEM Non-Essential Amino Acids (100x MEM NEAA, Life Technologies), 100 mM β-mercaptoethanol (Life Technologies) and 10 ng/ml human basic FGF (bFGF, Miltenyi). Medium was changed daily and cells were passaged as small clumps using collagenase (1 mg/ml, Life Technologies) every 3 to 6 days. iPSCs have been tested for their pluripotency *in vitro* and *in vivo*, as well as for their karyotype integrity (Kouroupi et al., 2017). Neural induction has been achieved by dual suppression of the SMAD signaling pathway using a combination of Noggin and SB431542 (Chambers et al., 2009). Dopaminergic differentiation was favored by culturing cells in B27/N2-medium containing human recombinant sonic hedgehog (SHH, R&D Systems) and murine recombinant fibroblast growth factor 8b (FGF-8b, R&D Systems) in the beginning, followed by brain-derived neurotrophic factor (BDNF, R&D Systems), glial cell-derived neurotrophic factor (GDNF, R&D Systems), ascorbic acid (AA, Sigma) and cyclic AMP (cAMP, Sigma) for terminal differentiation (Soldner et al., 2009). After almost 50 DIV of neuronal differentiation, cells were either harvested for RNA extraction or fixed for immunofluorescence staining (**Figure 2A**).

Immunofluorescence Staining

Cells were fixed with 4% paraformaldehyde (Sigma-Aldrich) for 20 min at room temperature. Samples were blocked with 0.1% Triton X-100 (Sigma-Aldrich) and 5% donkey serum in PBS for 30 min and were subsequently incubated with primary antibodies against NANOG (marker for pluripotency; R&D Systems), βIII-tubulin (neuronal marker; Cell Signaling Technology), MAP2 (neuronal marker; Merck-Millipore) and tyrosine hydroxylase (TH, marker for dopaminergic lineage; Merck-Millipore) at 4°C overnight, followed by incubation with appropriate secondary antibodies (Molecular Probes, Thermo Fisher Scientific) conjugated to AlexaFluor 488 (green) or 546 (red), for at least 1 h at room temperature. Coverslips were mounted with ProLong Gold antifade reagent with DAPI (Cell Signaling Technology) and images were acquired using a Leica TCS-SP5II confocal microscope (LEICA Microsystems).

RNA Extraction, cDNA Synthesis, and Real-Time PCR

Total RNA was extracted from the various cell types (SH-SY5Y, human fibroblasts, iPSCs, iPSC-derived neurons, PBMCs) and

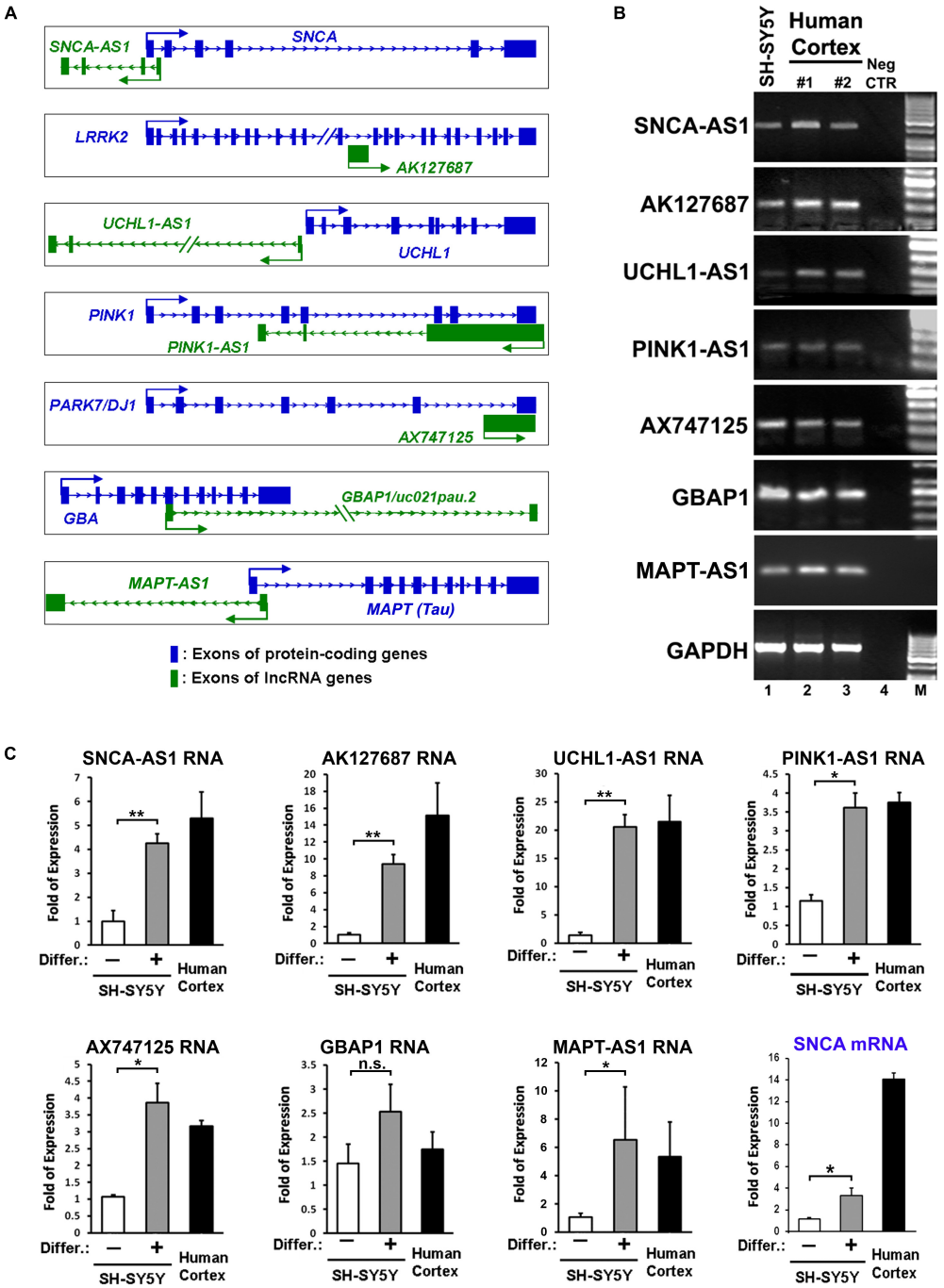


FIGURE 1 | Identification and expression of lncRNAs within loci of protein coding genes related to Parkinson's disease (PD). **(A)** Schematic representation of sense (*AK127687*, *AX747125*, *GBAP1*) and antisense (*SNCA-AS1*, *UCHL1-AS1*, *PINK1-AS1*, *MAPT-AS1*) lncRNA genes and their corresponding PD-linked protein coding genes. **(B)** Expression of the annotated lncRNA genes in human cortex and RA-differentiated or non-differentiated SH-SY5Y cells by conventional PCR analysis. As negative control a no-RT sample (Neg CTR) was used. As negative control **(C)** Relative RNA expression levels of the annotated lncRNA genes normalized to relative *GAPDH* levels, as well as relative SNCA mRNA levels, in SH-SY5Y cells treated with or without retinoic acid and in the human cortex from two independent individuals ($n = 2$), performed by qPCR analysis. All data are presented as the mean ± SEM from three independent experiments performed in triplicates (*$p < 0.05$, **$p < 0.01$, two-tailed Student's *t*-test).

from human post-mortem material using the TRIzol® Reagent (Ambion). Following digestion with DNase I, 1 μg of total RNA was used for first strand cDNA synthesis with the reverse transcription system (Invitrogen), according to manufacturer's instructions. Primers were designed to anneal to sequences in exons on both sides of an intron. Only for AK127687

TABLE 2 | Table presenting the demographic details for control (n = 20) and PD (n = 20) cohorts, in which the analysis of PBMCs was performed (n.a., non-applicable).

Sample	Sex	Age (years)	Onset (years)	Duration (years)	UPDRS III (points)
Parkinson's disease (n = 20)	13M:7F	64.95 ± 11.5	59.47 ± 11.4	5.47 ± 6.5	16.94 ± 9.2
Controls (n = 20)	9M:11F	63.43 ± 7.5	n.a.	n.a.	n.a.

and AX747125, which are intron less, primers were inevitably designed within one exon. Quantitative PCR analyses were carried out in Light Cycler 96 (Roche) Real time PCR detection system by using FastStart Essential DNA Green Master (Roche). The nucleotide sequences of primer sets used are shown in **Supplementary Table 1**.

CSF Sample Collection and Exosome Isolation

Lumbar puncture was performed at the L4-S1 interspace, between 9 and 12 AM after overnight fasting from two adult male non-PD subjects. Approximately 5 ml of CSF were drawn from these subjects and were collected in three polypropylene tubes. The first 2 ml-tube was used for routine diagnostic purposes. The following two tubes were immediately (within 30 min) centrifuged at 500 × g for the removal of cells, aliquoted (0.5 ml) into 1 ml polypropylene tubes and stored at −80°C until analysis. They were thawed only once, just before the assay. The isolation of the exosomes was performed as previously described (Thery et al., 2006). Briefly, the collected CSF was centrifuged at 100,000 × g for 2 h at 4°C. The supernatant (S100) was discarded and the pellet (P100) containing the externalized vesicles was reconstituted in 600 μl TRIzol® Reagent and proceeded for RNA extraction as above.

Statistical Analysis

All data are shown as mean ± standard error of mean (SEM). Statistical analysis was performed using GraphPad Prism 5.0. Non-parametric Mann–Whitney test or two-tailed Student's t-test was used to assess the significance of differences between two groups, and non-parametric Spearman's rho was used to assess the correlation between different variables of each sample. Probability values less than 0.05 ($p < 0.05$) were considered significant. The computed statistical power of the t-tests utilized to compare the data obtained in PD patients and Control subjects is 20.1% for the SN, 25.3% for the cerebellum and 26.3% for the analysis of PBMCs.

RESULTS

Neuronal Expression of Human lncRNAs Associated With PD-Linked Genes

To investigate the involvement of lncRNAs in PD pathogenesis, we bioinformatically screened eight human genes, genetically linked to PD, for close proximity with lncRNA genes (based on publicly available data from UCSC genome browser, ENCODE and GTEX databases). In particular, we screened *SNCA*, *LRRK2*, *UCH-L1, PINK1*, *DJ-1*, *GBA1*, *MAPT,* and *PARK2 (PARKIN) genes*. Our analysis focused on genes linked to hereditary autosomal dominant PD, such as *SNCA (PARK4), LRRK2 (PARK8),* and *UCH-L1 (PARK5)*. According to genome wide association studies (GWASs) polymorphisms within the *SNCA* and *LRRK2* loci represent the most common genetic factors in the sporadic disease (Nalls et al., 2014; Hernandez et al., 2016). We have also chosen to screen *PINK1* (*PARK6*) (Valente et al., 2004; Marongiu et al., 2008), *PARKIN* (*PARK2*) (Kitada et al., 1998) and *DJ-1* (*PARK7*) (Bonifati et al., 2003; van der Merwe et al., 2015) because they are implicated in early-onset autosomal recessive PD. Finally, we have screened the *GBA1* gene, encoding for the lysosomal enzyme β-glucocerebrosidase (GCase) and the *MAPT* gene, encoding for the protein Tau, since both of them are considered susceptibility genes for the development of the disease (Davis et al., 2016). For *GBA1* in particular, genetic evidence has linked heterozygous *GBA1* mutations with PD, which in some populations, represent the strongest risk factor for PD, while an association of tagging SNPs within *SCARB2*, the gene encoding for the lysosomal membrane protein LIMP2 (responsible for the intra-lysosomal transport of GCase) with PD, has been also reported (Michelakakis et al., 2012).

Based on this analysis, we initially identified lncRNAs encompassing transcriptional units in close proximity (less than 0.5 kb genomic distance) to seven out of eight of these genes (with the exception of *PARK2*) designated as *SNCA-AS1*, *AK127687*, *UCHL1-AS1*, *PINK1*-AS1, *AX747125*, *GBAP1/uc021pau.2* and *MAPT-AS1*, respectively (**Figure 1A**). Of these, the *UCHL1-AS1*, the *PINK-AS1* and the *MAPT-AS1* have been previously reported to control the expression of *UCHL1* (Carrieri et al., 2012, 2015), *PINK1* (Scheele et al., 2007; Chiba et al., 2009), and *MAPT* (Coupland et al., 2016), respectively, but with the exception of *MAPT-AS1,* an analysis of their expression levels in correlation to the expression of the respective protein coding genes in human PD-affected areas was lacking. Interestingly, all these lncRNAs were expressed in human SH-SY5Y dopaminergic cells and in the human cortex (**Figure 1B**). The neuronal expression of three of these lncRNAs (*SNCA-AS1*, *UCHL1-AS1,* and *MAPT-AS1*; for the other four lncRNAs there were no available data) was also confirmed by analyzing the publicly available expression data from GTEX database (**Supplementary Figure 1**). To examine their pattern of expression during neuronal differentiation, we differentiated SH-SY5Y cells with the addition of 10 μM of RA, which resulted in increased expression of the mRNA levels of neuronal or dopaminergic markers *MAP2*, *NURR1* and *PITX3* (**Supplementary Figure 2A**) and of the protein levels of bIII-tubulin (**Supplementary Figure 2B**), as compared to proliferating cells (-RA). The expression levels of all these lncRNAs, except *GBAP1*, were significantly upregulated upon

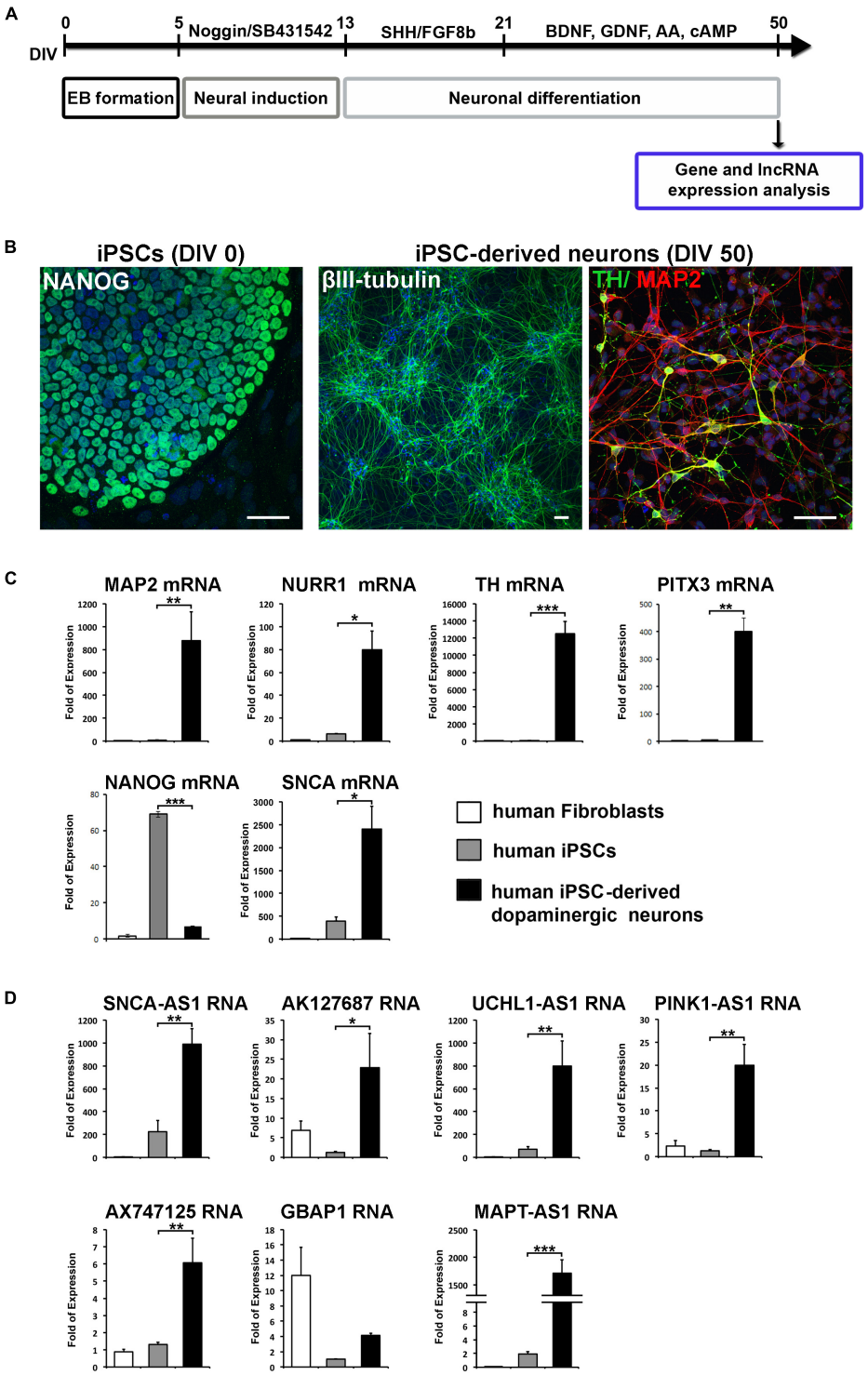


FIGURE 2 | Specific expression of the identified lncRNAs in human iPSCs-derived dopaminergic neurons. **(A)** Schematic drawing of the protocol used for neuronal differentiation of iPSCs and timeline of analysis. At 50 DIV cells were either harvested for gene and lncRNA expression analysis or for phenotypic characterization by immunofluorescence staining. **(B)** Immunostaining of iPSCs for *NANOG* (pluripotency marker; green) and iPSC-derived neurons for *βIII-tubulin* (neuronal marker; green), *MAP2* (neuronal marker; red) and *TH* (dopaminergic neuronal marker; green). Cell nuclei are counterstained with DAPI (blue). Scale bar: 40 μm. **(C)** Real time RT-qPCR analysis showing the relative mRNA expression of *NANOG* (pluripotency), *SNCA*, *MAP2* (neuronal marker) and dopaminergic lineage markers *NURR1, TH,* and *PITX3*, normalized to relative *GAPDH* levels, in human fibroblasts, iPSCs and iPSC-derived neurons. **(D)** Real time RT-qPCR analysis showing the relative RNA expression of the identified lnc genes normalized to relative *GAPDH* levels in human fibroblasts, iPSCs and iPCSs-derived dopaminergic neurons. All data are presented as the mean ± SEM from three independent experiments performed in triplicates (*$p < 0.05$, **$p < 0.01$, ***$p < 0.005$, two-tailed Student's *t*-test).

neuronal differentiation of dopaminergic SH-SY5Y cells ($p < 0.05$ for *PINK1*-AS1, *AX747125,* and *MAPT-AS1*; $p < 0.01$ for *SNCA-AS1*, *AK127687,* and *UCHL1-AS1*) to levels comparable to those detected in the human cortex, following the same trend as the *SNCA* mRNA levels, encoding for the neuronal protein SNCA (**Figure 1C**). The neuronal specificity of these lncRNAs was further evaluated in human iPSC lines and iPSC-derived neurons. In particular, skin fibroblasts of a healthy subject were reprogrammed to iPSCs, which have been extensively characterized for pluripotency and evaluated for their ability to terminally differentiate into dopaminergic neurons, as recently described (Kouroupi et al., 2017). Two iPSC lines were differentiated to dopaminergic neurons following a dual SMAD inhibition protocol (Chambers et al., 2009; Soldner et al., 2009) (**Figure 2A**). βIII-tubulin+ and MAP2+ neurons were efficiently generated from the iPSC lines, while almost 20% of MAP2+ neurons were found to express also tyrosine hydroxylase (TH; dopaminergic neurons) at 50 days *in vitro* (DIV; **Figure 2B**). To further verify the differentiation efficiency of iPSCs into dopaminergic neurons, we compared mRNA expression levels of neuronal (*MAP2*) and dopaminergic (*NURR1*, *TH, PITX3*) genes in fibroblasts, iPSCs and iPSC-derived neurons. All four transcripts were greatly induced in terminally differentiated cells ($p < 0.05$ for *NURR1*; $p < 0.01$ for *MAP2* and *PITX3*; $p < 0.001$ for *TH*), providing further evidence for the dopaminergic identity of the iPSC-derived neurons (**Figure 2C**). In contrast, mRNA levels of the pluripotency marker *NANOG* were significantly up-regulated during the reprogramming of fibroblasts to iPSCs and dramatically decreased in the iPSC-derived neurons ($p < 0.001$), further supporting the terminally differentiated state of the resulting neurons (**Figure 2C**). Furthermore, *SNCA* mRNA expression levels were found significantly augmented in the iPSC-derived dopaminergic neurons ($p < 0.05$) (**Figure 2C**). In agreement with the findings in the SH-SY5Y cells, all lncRNAs, except *GBAP1*, were highly increased in the iPSC-derived dopaminergic neurons ($p < 0.05$ for *AK127687*; $p < 0.01$ for *SNCA-AS1*, *UCHL1-AS1*, *PINK1*-AS1 and *AX747125*; $p < 0.001$ for *MAPT-AS1*) (**Figure 2D**). These data further suggest a correlation between the six (*SNCA-AS1*, *AK127687*, *UCHL-AS1*, *PINK1-AS1*, *AX747125,* and *MAPT-AS1*) out of the seven identified lncRNAs with neuronal differentiation and/or with the dopaminergic phenotype in particular.

LncRNAs Associated With PD-Linked Genes Are Found Under-Expressed in PD Brains

The elevated expression of six out of seven annotated lncRNAs in the iPSC-derived dopaminergic neurons prompted us to assess their relative expression levels in two human brain regions with different vulnerability in PD, the SN and the cerebellum derived from PD patients or age- and sex-matched control subjects (**Table 1**). Interestingly, all transcripts were expressed in the SN of healthy subjects, and all six lncRNAs exhibited remarkable under-expression in the SN of PD patients normalized relative to *GAPDH* levels ($p < 0.01$ for *SNCA-AS1*, *AK127687*; $p < 0.001$ for *UCHL1-AS1*, *PINK1-AS1*, *AX747125,* and *MAPT-AS1*) (**Figure 3A**). Only *GBAP1* transcript levels were not affected in the nigra of PD patients. To exclude that this dramatic decrease in the lncRNA expression merely represents the outcome of massive neuronal cell death in the SN of PD patients, we additionally normalized expression levels of these lncRNAs with the geometric mean of *NURR1-MAPT-GAPDH* levels, used as additional reference genes. Normalization of lncRNA expression levels versus the geometric mean of *NURR1-MAPT-GAPDH* levels gave similar results, since all six lncRNAs -except *GBAP1*- were still dramatically and significantly under-expressed in the SN of PD patients ($p < 0.05$ for *SNCA-AS1* and *UCHL1-AS1*; $p < 0.01$ for *AK127687*, *PINK1-AS1*, *AX747125,* and *MAPT-AS1*) (**Supplementary Figure 3**). To further exclude the possibility that this effect was non-specific, we have analyzed the expression of two PD-irrelevant lncRNAs, *hSNHG1,* and *hSNHG5*. As shown in **Supplementary Figure 4**, expression levels of both lncRNAs were similar between controls and PD nigral samples.

Given that lncRNAs can functionally operate near their site of synthesis by regulating the transcription of their proximal gene(s) (Ponjavic et al., 2009; Wang and Chang, 2011; Qureshi and Mehler, 2012; Briggs et al., 2015), we analyzed the expression levels of the corresponding nearby genes. Interestingly, we found significant expression alterations for three of them in the SN of PD patients, namely for *SNCA* ($p < 0.05$), *LRRK2* ($p < 0.01$), and *PINK1* ($p < 0.001$) (**Figure 3B**). The mRNA levels of *LRRK2* and *PINK1* were found to be under-expressed in PD patients similar to their respective lncRNAs (**Figures 3A,B**). In contrast, *SNCA* mRNA levels were found increased in PD patients, exhibiting a discordant expression pattern with that of its antisense lncRNA (**Figures 3A,B**). To test whether such lncRNA transcript alterations may represent a hallmark of PD affected brain areas, we assessed the relative lncRNA expression in the cerebellum of the same PD patients and controls, an area that receives dopaminergic projection from the ventral tegmental area/SN and that has been shown to exhibit pathological changes following dopaminergic degeneration in PD patients and PD-like animal models (reviewed in Wu and Hallett, 2013). Three out of six lncRNAs [*AK127687* ($p < 0.05$), *UCHL1-AS1* ($p < 0.05$), and *MAPT-AS1* ($p < 0.05$)] were found decreased in the cerebellum of PD subjects (**Figure 4A**). Interestingly, the mRNA levels of *LRRK2* ($p < 0.001$) and *PINK1* ($p < 0.01$) followed a similar pattern to that in the nigra (**Figure 4B**). In contrast to the data obtained from the nigral tissues of the same PD patients, no changes were detected in the *SNCA-AS1* lncRNA or the *SNCA* mRNA levels in the cerebellar tissues derived from the same PD patients.

RT-PCR Based Detection of LncRNAs in PBMCs and in CSF-Derived Exosomes

To further assess whether the aforementioned lncRNAs are also found dysregulated in peripheral tissues of PD patients, we analyzed their expression levels in PBMCs derived from sporadic PD patients and age- and sex-matched controls (**Table 2**). Real time RT-qPCR analysis showed that all six lncRNAs were expressed in human PBMCs (**Figure 5A**). However, the relative RNA expression of these lncRNAs, normalized to relative

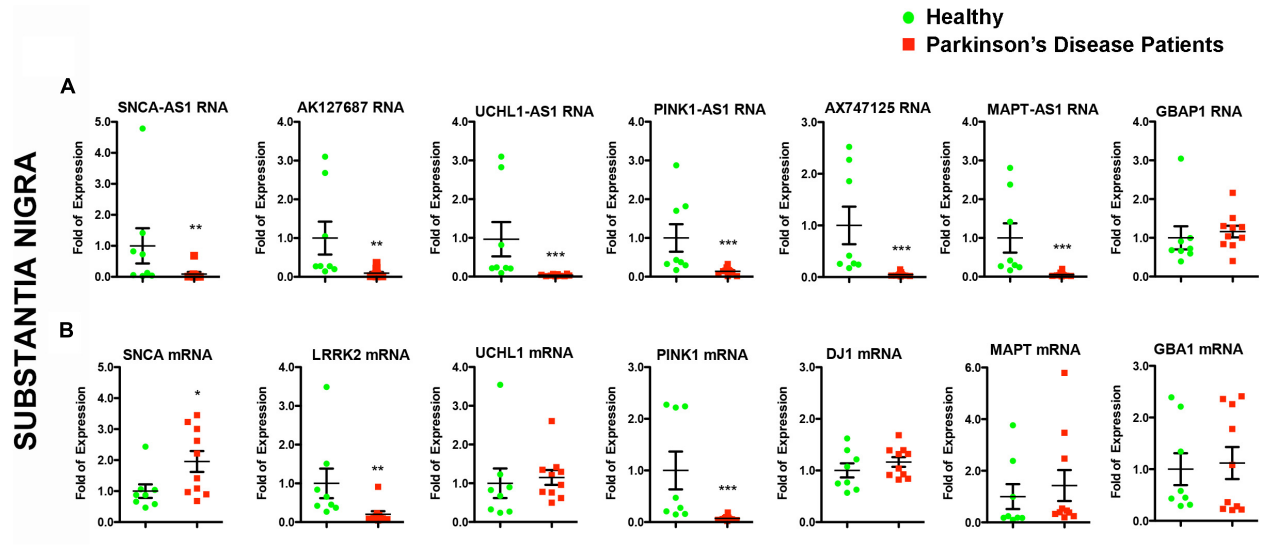


FIGURE 3 | Relative RNA expression of lncRNAs and their corresponding protein coding genes in the SN of PD patients and controls. Real time RT-qPCR analysis of RNA expression of lncRNA genes **(A)** and their corresponding PD-linked genes **(B)** normalized relative to *GAPDH* levels, in the SN of PD patients and controls. All data are presented as the mean ± SEM (*$p < 0.05$, **$p < 0.01$, ***$p < 0.001$, Mann–Whitney *t*-test).

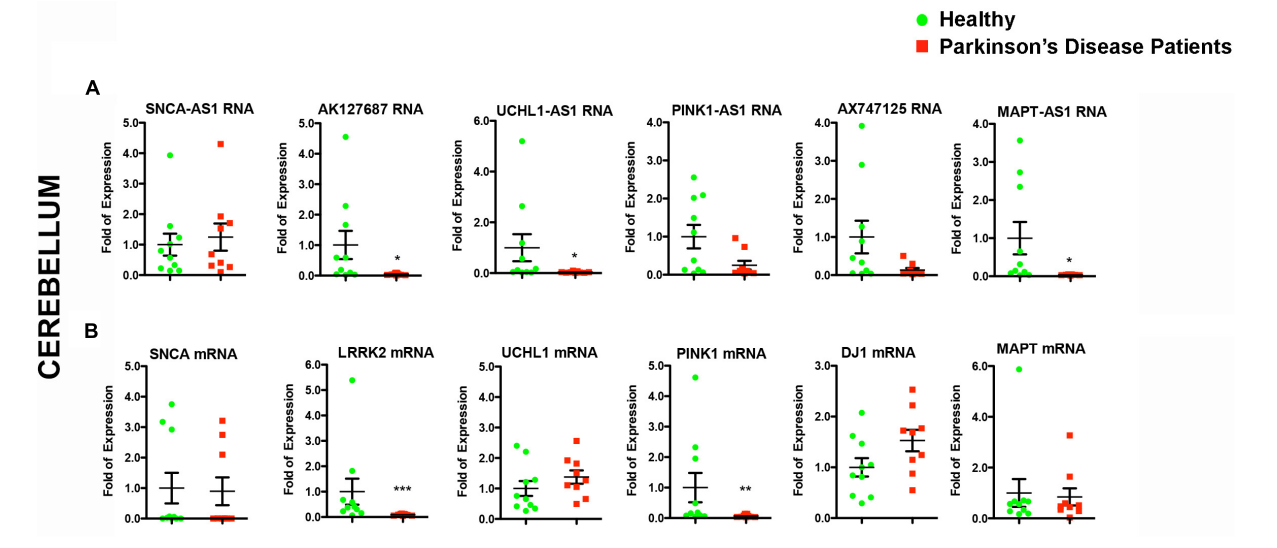


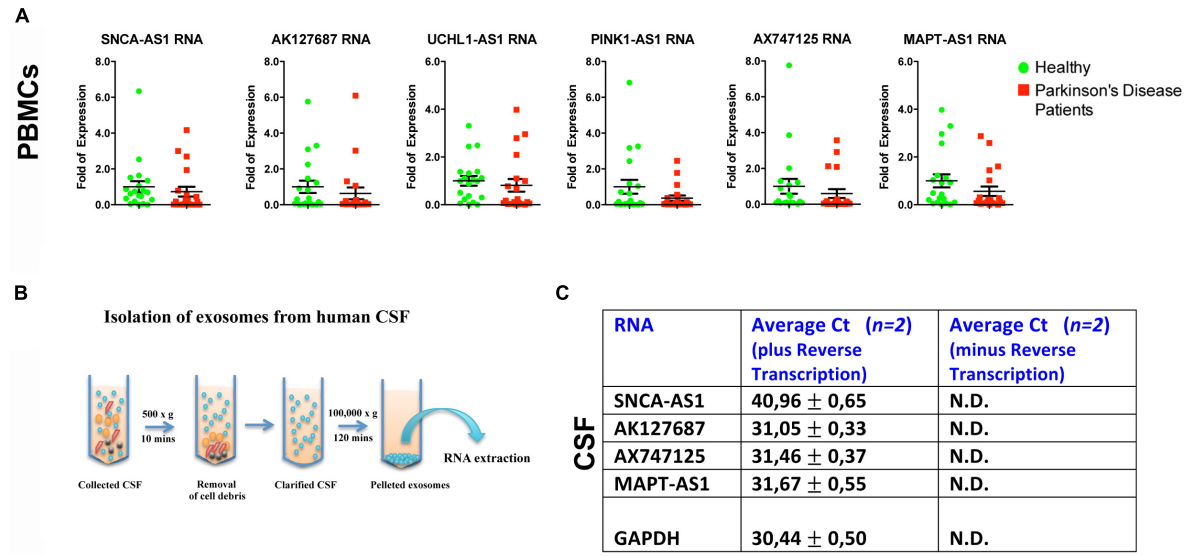
FIGURE 4 | Relative RNA expression of lncRNAs and their corresponding protein coding genes in the cerebellum of PD patients and controls. Real time RT-qPCR analysis of RNA expression of lncRNA genes **(A)** and their corresponding PD-linked genes **(B)** in the cerebellum of the same PD and controls subjects. All data are presented as the mean ± SEM (*$p < 0.05$, **$p < 0.01$, ***$p < 0.001$, Mann–Whitney *t*-test).

GAPDH expression levels, did not reveal statistically significant differences between PBMCs derived from PD patients and controls, although a slight trend for reduced expression in patients was observed for all lncRNAs tested (**Figure 5A**).

Importantly, by isolating exosomes from CSF derived from two non-PD subjects, we observed that that four out of the six lncRNAs *SNCA-AS1*, *MAPT-AS1*, *AK127687* and *AX747125*, could be detected in CSF-derived exosomes, as compared to the control samples (cDNAs prepared without reverse transcriptase) (**Figures 5B,C**). Three out of four were detected in levels similar to that of *GAPDH*, which has been previously reported to be found in exosomes (Xiao et al., 2012; Gezer et al., 2014; Yang et al., 2016; Barbagallo et al., 2018).

DISCUSSION

In recent years, the investigation into the role of lncRNAs in mammalian genome has uncovered an additional layer of gene regulation, suggesting their implication in many



RNA	Average Ct (*n=2*) (plus Reverse Transcription)	Average Ct (*n=2*) (minus Reverse Transcription)
SNCA-AS1	40,96 ± 0,65	N.D.
AK127687	31,05 ± 0,33	N.D.
AX747125	31,46 ± 0,37	N.D.
MAPT-AS1	31,67 ± 0,55	N.D.
GAPDH	30,44 ± 0,50	N.D.

FIGURE 5 | Relative expression of lncRNAs in PBMCs of PD patients and controls and in CSF-derived exosomes of non-PD subjects. **(A)** qPCR analysis of RNA expression of lnc genes normalized to relative *GAPDH* levels, in PBMCs derived from PD patients and controls. All data are presented as the mean ± SEM (Mann–Whitney *t*-test). **(B)** Cartoon depicting CSF exosome isolation and subsequent RNA extraction. **(C)** Detection (Average Ct values) of lncRNAs *SNCA-AS1*, *AK127687*, *AX747125*, and *MAPT-AS1* in CSF-derived exosomes of two non-PD subjects in comparison with the same samples without the reverse transcription step (negative control) or with the *GAPDH* (positive control) by Real time RT-qPCR analysis. N.D., not detected.

biological processes during brain development and progression of neurological diseases (reviewed by Ng et al., 2013; Barry, 2014; Briggs et al., 2015). The majority of lncRNAs previously associated with neurodegenerative diseases have only been identified in genome-wide expression screens and their functions remain largely unknown (Antoniou et al., 2014; Kraus et al., 2017; Pereira Fernandes et al., 2018). Understanding the role of lncRNAs in neurodegenerative diseases and specifically in PD could offer novel insights for elucidating the molecular mechanisms of the disease. To this end, in the current study we have found that, at least, six out of the seven identified lncRNAs exhibit elevated expression during directed differentiation of human iPSCs to dopaminergic neurons, or neuronal differentiation of SH-SY5Y cells, and that these lncRNAs are also expressed in the human cortex, SN and cerebellum in healthy individuals.

We should stress that our study focused mostly on genes linked to familial PD, such as *SNCA, LRRK2, UCH-L1*, *PINK1* and *DJ1*, as well as on the *GBA1* and *MAPT* genes, given that both of them are considered to be strong susceptibility genes. Beyond *SNCA* and *LRRK2*, whose contribution to PD pathogenesis is supported strongly by genetic studies, we have chosen to also study *UCH-L1* gene, although its genetic link to PD has been questioned (Lincoln et al., 1999; Maraganore et al., 1999, 2004; Healy et al., 2006). Our interest on *UCH-L1* was based on prior studies of our lab, showing that the S18Y polymorphic variant exerts antioxidant properties both *in vitro* (Kyratzi et al., 2008) and *in vivo* (Xilouri et al., 2012). Moreover, it should be noted that GWAS studies also suggested the contribution of other genes in the risk of developing PD, such as the human leukocyte antigen (*HLA*) locus, encoding MHCII molecules (Hamza et al., 2010; Alonso-Navarro et al., 2014; Jimenez-Jimenez et al., 2016), thus implicating innate immune function in disease pathogenesis. An analysis of a possible implication of altered levels of lncRNAs in close proximity to the *HLA* gene might be of interest for future studies.

Collectively, our data correlate the expression of the identified lncRNAs with human neuronal identity and indicate a possible role for these lncRNAs in the human brain. Considering that these lncRNAs are transcribed from genomic loci that have been previously genetically linked with PD pathogenesis, our observations raise the critical question of whether part of this genetic linkage or association is due to a potential involvement of these RNA molecules in PD pathogenesis. Accordingly, here we found that six of these lncRNAs are under-expressed in the SN and three out of six (*AK127687*, *UCHL1-AS1,* and *MAPT-AS1*) in the cerebellum of PD patients.

Such data may support a potential correlation between the expression levels of these lncRNAs and PD pathogenesis. The SN is the area mainly involved in PD pathogenesis whereas the cerebellum is an area that may have certain roles in PD pathophysiology (Caligiore et al., 2016). In particular, neuroimaging studies in humans have found that PD patients have altered cerebellar activation during motor execution, motor learning and at rest (Wu and Hallett, 2013) In contrast to the SN, where SNCA-rich Lewy bodies are the main histopathological hallmark of the disease, no Lewy bodies are detected in the cerebellum of PD patients and some studies have reported decreased cerebellar *SNCA* mRNA levels (Fuchs et al., 2008). In our study, we have

not detected alterations in the *SNCA* mRNA levels or the *SNCA-AS1* lncRNA levels in the cerebellum of PD patients, compared to controls. In contrast, in both SN and cerebellum, we detected decreased levels of *LRRK2* mRNA and of its corresponding lncRNA (*AK127687*), suggestive of a possible association between the expression levels of this lncRNA and PD pathogenesis, through influencing of LRRK2 levels. In agreement with our findings, decreased *LRRK2* mRNA levels in the cerebellum of PD patients have been also previously reported (Sharma et al., 2011). Moreover, in accordance with our hypothesis of a functional role of these dysregulated lncRNAs in controlling the expression of nearby protein coding genes, previous studies have reported the ability of *MAPT-AS1*, *PINK1-AS1,* and *UCHL1-AS1* to directly affect expression levels of *MAPT*, *PINK1,* and *UCHL1* genes, respectively (Scheele et al., 2007; Carrieri et al., 2012, 2015; Coupland et al., 2016). Interestingly, *MAPT-AS1* was also recently reported to be under-expressed in many brain regions of PD affected patients, including putamen, anterior cingulate cortex, visual cortex, and cerebellum (Coupland et al., 2016). These observations are in good agreement with our data and further confirm and validate our analyses.

We have carefully addressed the possibility that the under-expression of the six lncRNAs in the nigra of PD patients, observed in our study, might represent a non-specific result. As the expression of these lncRNAs showed a marked association with the establishment of a neuronal phenotype, our results could reflect nigral neuronal loss. However, the difference between PD patients and controls remained highly significant even following normalization with the geometric mean of *NURR1-MAPT-GAPDH*. Furthermore, mRNA levels of genes expressed selectively in neurons (*MAPT, UCH-L1*) showed no difference between the nigral tissues of PD and control brains. Moreover, we have not observed a generalized decrease of such lncRNA's expression in degenerating SH-SY5Y cells exposed to the neurotoxin MPP^+ (data not shown), suggesting again that the findings in PD brains do not reflect non-specific neurodegeneration. Therefore, we believe that our findings truly mirror under-expression of the studied lncRNAs in remaining nigral neurons or in the largely intact cerebellar neurons in the context of PD.

As lncRNAs can act at both directions of transcriptional regulation, either activating or repressing gene expression (Wang and Chang, 2011; Guttman and Rinn, 2012; Flynn and Chang, 2014), such lncRNAs might represent key components for the regulation of PD-linked genes. This may be especially important regarding the regulation of *SNCA* expression, which is strongly linked to both idiopathic and genetic forms of PD. However, based on our experimental evidence, we cannot exclude the possibility that these differences could represent secondary effects of other pathogenetic mechanisms underlying PD progression, i.e., chromatin reorganization of the affected loci. To our knowledge, this is the first time that such a correlation between PD-affected brain regions and specific lncRNAs is established, although further experimentation is needed to understand the precise molecular mechanism of their action.

It is important to note that these lncRNAs were detected in peripheral tissues such as PBMCs and CSF (**Figure 5**), even though no statistically significant differences were observed between the PBMCs of controls and PD patients. Such data do not rule out the possibility that a difference might exist, but that a larger number of samples is required so that the trends observed in the present analyses reach statistical significance. We have only performed proof of principle analysis in human CSF exosomes, establishing that four out of the six lncRNAs are detected in this biological material. Clearly, further studies will be needed to investigate whether the expression levels of these lncRNAs in CSF exosomes, reflecting presumably their total brain levels, are different between PD and controls. Moreover, another approach would be to isolate neuronally-derived exosomes from plasma of PD subjects and controls and compare the expression levels of lncRNAs, as it was previously reported for levels of *SNCA* (Shi et al., 2014). It is expected that this neuronal enrichment may lead to more marked differences in PD vs. controls, probably reflecting specific brain-related changes. A growing body of evidence suggests that exosomal lncRNAs circulating in serum or urine may represent potential diagnosis biomarkers and prognosis indicators in cancer (Dragomir et al., 2018; Gramantieri et al., 2018; Sun et al., 2018); whether such a role could be attributed to neuronally-derived exosomes remains to be explored. The emerging importance of lncRNAs as diagnostic tools is further supported by recent studies that utilized RNA-sequencing data analysis to identify differential expression levels of lncRNAs in leukocytes of PD patients compared to controls, as well as in the human SN of PD patients (Soreq et al., 2014; Ni et al., 2017).

Collectively, our data suggest that lncRNAs are associated with PD pathogenesis and may thus represent novel targets for the diagnosis and/or treatment of PD and related disorders.

AUTHOR CONTRIBUTIONS

ME, MX, and PP performed experiments, analyzed the data and prepared the manuscript. GK and RM generated and characterized human iPSCs and iPSC-derived neurons, AV, NP, and VK performed experiments. LS, MX, and PP designed and supervised the project. PP conceived the original idea of this manuscript and initially identified the selected lncRNAs. All authors critically read and approved the manuscript.

FUNDING

This work was supported by an Aristeia-II grant from the General Secretariat of Research and Technology (GSRT) of the Greek Ministry of Education (4786) to PP and Fondation Sante grant to PP, and by an ARISTEIA I (GSRT) grant (463) to LS. GK and RM acknowledge funding from a Stavros Niarchos Foundation donation to the Hellenic Pasteur Institute, as part of the Foundation's initiative to support the Greek Research Center Ecosystem.

ACKNOWLEDGMENTS

We would like to thank Dr. Margarita Chrysanthou-Piterou (Research Unit of Histochemistry and Electron Microscopy, University of Athens Medical School) for kindly providing the human cortex tissue, obtained from the Netherlands Brain Bank. We would also like to thank Dr. Antigone Dimas for critically reading the manuscript.

SUPPLEMENTARY MATERIAL

The Supplementary Material for this article can be found online at: https://www.frontiersin.org/articles/10.3389/fncel.2019.00058/full#supplementary-material

FIGURE S1 | Expression analysis of lncRNAs *SNCA-AS1*, *UCHL1-AS1,* and *MAPT-AS1* in various human tissues and organs, based on GTEX database. The expression data for the three lncRNAs were analyzed and downloaded from the publicly available GTEX webpage, https://gtexportal.org/home/.

FIGURE S2 | Confirmation of neuronal differentiation of SH-SY5Y cells with the addition of RA. **(A)** Relative mRNA expression levels of *MAP2*, *NURR1,* and *PITX3* in the absence (−) or presence (+) of RA, performed by RT-qPCR analysis. All data are presented as the mean ± SEM from three independent experiments performed in triplicates (*$p < 0.05$, **$p < 0.01$, ***$p < 0.001$, two-tailed Student's *t*-test). **(B)** Immunofluorescence analysis of the same cells under the same conditions with the anti-bIII-tubulin antibody (TuJ1), as indicated.

FIGURE S3 | Relative RNA expression of PD-linked lncRNAs in the *Substantia Nigra* of PD patients and controls normalized to the geometric mean of *GAPDH-NURR1-MAPT l*evels. Real time RT-qPCR analysis of RNA expression of lncRNA genes normalized to the geometric mean of *GAPDH-PPI1A-RPLI3A* levels in the *Substantia Nigra* of controls and PD patients. All data are presented as the mean ± SEM from three independent experiments performed in triplicates.

FIGURE S4 | Relative RNA expression of non PD-linked lncRNAs in the *Substantia Nigra* of PD patients and controls. Real time RT-qPCR analysis of hSNHG1 and hSNHG5 lncRNA RNA expression normalized to GAPDH in the *Substantia Nigra* of controls and PD patients. All data are presented as the mean ± SEM from three independent experiments performed in triplicates.

REFERENCES

Akula, N., Barb, J., Jiang, X., Wendland, J. R., Choi, K. H., Sen, S. K., et al. (2014). RNA-sequencing of the brain transcriptome implicates dysregulation of neuroplasticity, circadian rhythms and GTPase binding in bipolar disorder. *Mol. Psychiatry* 19, 1179–1185. doi: 10.1038/mp.2013.170

Alonso-Navarro, H., Jimenez-Jimenez, F. J., Garcia-Martin, E., and Agundez, J. A. (2014). Genomic and pharmacogenomic biomarkers of Parkinson's disease. *Curr. Drug Metab.* 15, 129–181. doi: 10.2174/1389200215021403271754O4

Antoniou, D., Stergiopoulos, A., and Politis, P. K. (2014). Recent advances in the involvement of long non-coding RNAs in neural stem cell biology and brain pathophysiology. *Front. Physiol.* 5:155. doi: 10.3389/fphys.2014.00155

Barbagallo, C., Brex, D., Caponnetto, A., Cirnigliaro, M., Scalia, M., Magnano, A., et al. (2018). LncRNA UCA1, upregulated in CRC biopsies and downregulated in serum exosomes, controls mRNA expression by RNA-RNA interactions. *Mol. Ther. Nucleic Acids* 12, 229–241. doi: 10.1016/j.omtn.2018.05.009

Barry, G. (2014). Integrating the roles of long and small non-coding RNA in brain function and disease. *Mol. Psychiatry* 19, 410–416. doi: 10.1038/mp.2013.196

Barry, G., Briggs, J. A., Vanichkina, D. P., Poth, E. M., Beveridge, N. J., Ratnu, V. S., et al. (2014). The long non-coding RNA Gomafu is acutely regulated in response to neuronal activation and involved in schizophrenia-associated alternative splicing. *Mol. Psychiatry* 19, 486–494. doi: 10.1038/mp.2013.45

Bonifati, V., Rizzu, P., Van Baren, M. J., Schaap, O., Breedveld, G. J., Krieger, E., et al. (2003). Mutations in the DJ-1 gene associated with autosomal recessive early-onset parkinsonism. *Science* 299, 256–259.

Briggs, J. A., Wolvetang, E. J., Mattick, J. S., Rinn, J. L., and Barry, G. (2015). Mechanisms of long non-coding RNAs in mammalian nervous system development, plasticity, disease, and evolution. *Neuron* 88, 861–877. doi: 10.1016/j.neuron.2015.09.045

Caligiore, D., Helmich, R. C., Hallett, M., Moustafa, A. A., Timmermann, L., Toni, I., et al. (2016). Parkinson's disease as a system-level disorder. *NPJ Parkinsons Dis.* 2:16025. doi: 10.1038/npjparkd.2016.25

Carrieri, C., Cimatti, L., Biagioli, M., Beugnet, A., Zucchelli, S., Fedele, S., et al. (2012). Long non-coding antisense RNA controls Uchl1 translation through an embedded SINEB2 repeat. *Nature* 491, 454–457. doi: 10.1038/nature11508

Carrieri, C., Forrest, A. R., Santoro, C., Persichetti, F., Carninci, P., Zucchelli, S., et al. (2015). Expression analysis of the long non-coding RNA antisense to Uchl1 (AS Uchl1) during dopaminergic cells' differentiation in vitro and in neurochemical models of Parkinson's disease. *Front. Cell Neurosci.* 9:114. doi: 10.3389/fncel.2015.00114

Chakrabarti, S., and Mohanakumar, K. P. (2016). Aging and neurodegeneration: a tangle of models and mechanisms. *Aging Dis.* 7, 111–113. doi: 10.14336/AD.2016.0312

Chambers, S. M., Fasano, C. A., Papapetrou, E. P., Tomishima, M., Sadelain, M., and Studer, L. (2009). Highly efficient neural conversion of human ES and iPS cells by dual inhibition of SMAD signaling. *Nat. Biotechnol.* 27, 275–280. doi: 10.1038/nbt.1529

Chiba, M., Kiyosawa, H., Hiraiwa, N., Ohkohchi, N., and Yasue, H. (2009). Existence of Pink1 antisense RNAs in mouse and their localization. *Cytogenet. Genome Res.* 126, 259–270. doi: 10.1159/000251963

Coupland, K. G., Kim, W. S., Halliday, G. M., Hallupp, M., Dobson-Stone, C., and Kwok, J. B. (2016). Role of the long non-coding RNA MAPT-AS1 in regulation of Microtubule Associated Protein Tau (MAPT) expression in parkinson's disease. *PLoS One* 11:e0157924. doi: 10.1371/journal.pone.0157924

Davis, A. A., Andruska, K. M., Benitez, B. A., Racette, B. A., Perlmutter, J. S., and Cruchaga, C. (2016). Variants in GBA, SNCA, and MAPT influence parkinson disease risk, age at onset, and progression. *Neurobiol. Aging* 37, .e1–.e209. doi: 10.1016/j.neurobiolaging.2015.09.014

Dragomir, M., Chen, B., and Calin, G. A. (2018). Exosomal lncRNAs as new players in cell-to-cell communication. *Transl. Cancer Res.* 7, S243–S252. doi: 10.21037/tcr.2017.10.46

Faghihi, M. A., Modarresi, F., Khalil, A. M., Wood, D. E., Sahagan, B. G., Morgan, T. E., et al. (2008). Expression of a noncoding RNA is elevated in alzheimer's disease and drives rapid feed-forward regulation of beta-secretase. *Nat. Med.* 14, 723–730. doi: 10.1038/nm1784

Flynn, R. A., and Chang, H. Y. (2014). Long noncoding RNAs in cell-fate programming and reprogramming. *Cell Stem Cell* 14, 752–761. doi: 10.1016/j.stem.2014.05.014

Fuchs, J., Tichopad, A., Golub, Y., Munz, M., Schweitzer, K. J., Wolf, B., et al. (2008). Genetic variability in the SNCA gene influences alpha-synuclein levels in the blood and brain. *FASEB J.* 22, 1327–1334.

Gelb, D. J., Oliver, E., and Gilman, S. (1999). Diagnostic criteria for parkinson disease. *Arch. Neurol.* 56, 33–39.

Gezer, U., Ozgur, E., Cetinkaya, M., Isin, M., and Dalay, N. (2014). Long non-coding RNAs with low expression levels in cells are enriched in secreted exosomes. *Cell Biol. Int.* 38, 1076–1079. doi: 10.1002/cbin.10301

Ghanam, A. R., Xu, Q., Ke, S., Azhar, M., Cheng, Q., and Song, X. (2017). Shining the light on senescence associated LncRNAs. *Aging Dis.* 8, 149–161. doi: 10.14336/AD.2016.0810

Gramantieri, L., Baglioni, M., Fornari, F., Laginestra, M. A., Ferracin, M., Indio, V., et al. (2018). LncRNAs as novel players in hepatocellular carcinoma recurrence. *Oncotarget* 9, 35085–35099. doi: 10.18632/oncotarget.26202

Guttman, M., and Rinn, J. L. (2012). Modular regulatory principles of large non-coding RNAs. *Nature* 482, 339–346. doi: 10.1038/nature10887

Hamza, T. H., Zabetian, C. P., Tenesa, A., Laederach, A., Montimurro, J., Yearout, D., et al. (2010). Common genetic variation in the HLA region is

associated with late-onset sporadic Parkinson's disease. *Nat. Genet.* 42, 781–785. doi: 10.1038/ng.642

Healy, D. G., Abou-Sleiman, P. M., Casas, J. P., Ahmadi, K. R., Lynch, T., Gandhi, S., et al. (2006). UCHL-1 is not a parkinson's disease susceptibility gene. *Ann. Neurol.* 59, 627–633.

Hernandez, D. G., Reed, X., and Singleton, A. B. (2016). Genetics in parkinson disease: mendelian versus non-mendelian inheritance. *J. Neurochem.* 139(Suppl. 1), 59–74. doi: 10.1111/jnc.13593

Jiménez-Jiménez, F. J., Alonso-Navarro, H., Garcia-Martin, E., and Agúndez, J. A. (2016). Advances in understanding genomic markers and pharmacogenetics of Parkinson's disease. *Expert Opin. Drug Metab. Toxicol.* 12, 433–448. doi: 10.1517/17425255.2016.1158250

Johnson, R., Richter, N., Jauch, R., Gaughwin, P. M., Zuccato, C., Cattaneo, E., et al. (2010). Human accelerated region 1 noncoding RNA is repressed by rest in huntington's disease. *Physiol. Genomics* 41, 269–274. doi: 10.1152/physiolgenomics.00019.2010

Kitada, T., Asakawa, S., Hattori, N., Matsumine, H., Yamamura, Y., Minoshima, S., et al. (1998). Mutations in the parkin gene cause autosomal recessive juvenile parkinsonism. *Nature* 392, 605–608.

Kouroupi, G., Taoufik, E., Vlachos, I. S., Tsioras, K., Antoniou, N., Papastefanaki, F., et al. (2017). Defective synaptic connectivity and axonal neuropathology in a human iPSC-based model of familial parkinson's disease. *Proc. Natl. Acad. Sci. U.S.A.* 114, E3679–E3688. doi: 10.1073/pnas.1617259114

Kraus, T. F. J., Haider, M., Spanner, J., Steinmaurer, M., Dietinger, V., and Kretzschmar, H. A. (2017). Altered long noncoding RNA expression precedes the course of parkinson's disease-a preliminary report. *Mol. Neurobiol.* 54, 2869–2877. doi: 10.1007/s12035-016-9854-x

Kyratzi, E., Pavlaki, M., and Stefanis, L. (2008). The S18Y polymorphic variant of UCH-L1 confers an antioxidant function to neuronal cells. *Hum. Mol. Genet.* 17, 2160–2171. doi: 10.1093/hmg/ddn115

Lincoln, S., Vaughan, J., Wood, N., Baker, M., Adamson, J., Gwinn-Hardy, K., et al. (1999). Low frequency of pathogenic mutations in the ubiquitin carboxy-terminal hydrolase gene in familial Parkinson's disease. *Neuroreport* 10, 427–429.

Maraganore, D. M., Farrer, M. J., Hardy, J. A., Lincoln, S. J., Mcdonnell, S. K., and Rocca, W. A. (1999). Case-control study of the ubiquitin carboxy-terminal hydrolase L1 gene in Parkinson's disease. *Neurology* 53, 1858–1860.

Maraganore, D. M., Lesnick, T. G., Elbaz, A., Chartier-Harlin, M. C., Gasser, T., Kruger, R., et al. (2004). UCHL1 is a Parkinson's disease susceptibility gene. *Ann. Neurol.* 55, 512–521.

Marki, S., Goblos, A., Szlavicz, E., Torok, N., Balicza, P., Bereznai, B., et al. (2018). The rs13388259 intergenic polymorphism in the genomic context of the BCYRN1 gene is associated with parkinson's disease in the hungarian population. *Parkinsons Dis.* 2018:9351598. doi: 10.1155/2018/9351598

Marongiu, R., Ferraris, A., Ialongo, T., Michiorri, S., Soleti, F., Ferrari, F., et al. (2008). PINK1 heterozygous rare variants: prevalence, significance and phenotypic spectrum. *Hum. Mutat.* 29:565. doi: 10.1002/humu.20719

Michelakakis, H., Xiromerisiou, G., Dardiotis, E., Bozi, M., Vassilatis, D., Kountra, P. M., et al. (2012). Evidence of an association between the scavenger receptor class B member 2 gene and parkinson's disease. *Mov. Disord.* 27, 400–405. doi: 10.1002/mds.24886

Nalls, M. A., Pankratz, N., Lill, C. M., Do, C. B., Hernandez, D. G., Saad, M., et al. (2014). Large-scale meta-analysis of genome-wide association data identifies six new risk loci for parkinson's disease. *Nat. Genet.* 46, 989–993. doi: 10.1038/ng.3043

Ng, S. Y., Lin, L., Soh, B. S., and Stanton, L. W. (2013). Long noncoding RNAs in development and disease of the central nervous system. *Trends Genet.* 29, 461–468. doi: 10.1016/j.tig.2013.03.002

Ni, Y., Huang, H., Chen, Y., Cao, M., Zhou, H., and Zhang, Y. (2017). Investigation of long non-coding RNA Expression profiles in the substantia nigra of parkinson's disease. *Cell Mol. Neurobiol.* 37, 329–338. doi: 10.1007/s10571-016-0373-0

Pereira Fernandes, D., Bitar, M., Jacobs, F. M. J., and Barry, G. (2018). Long non-coding RNAs in neuronal aging. *Noncoding RNA* 4:E12. doi: 10.3390/ncrna4020012

Ponjavic, J., Oliver, P. L., Lunter, G., and Ponting, C. P. (2009). Genomic and transcriptional co-localization of protein-coding and long non-coding RNA pairs in the developing brain. *PLoS Genet.* 5:e1000617. doi: 10.1371/journal.pgen.1000617

Qureshi, I. A., and Mehler, M. F. (2012). Emerging roles of non-coding RNAs in brain evolution, development, plasticity and disease. *Nat. Rev. Neurosci.* 13, 528–541.

Saracchi, E., Fermi, S., and Brighina, L. (2014). Emerging candidate biomarkers for parkinson's disease: a review. *Aging Dis.* 5, 27–34. doi: 10.14366/AD.2014.050027

Sarkar, S., Russell, A. E., Engler-Chiurazzi, E. B., Porter, K. N., and Simpkins, J. W. (2018). MicroRNAs and the genetic nexus of brain aging, neuroinflammation, neurodegeneration, and brain trauma. *Aging Dis.* 9:409.

Scheele, C., Petrovic, N., Faghihi, M. A., Lassmann, T., Fredriksson, K., Rooyackers, O., et al. (2007). The human PINK1 locus is regulated in vivo by a non-coding natural antisense RNA during modulation of mitochondrial function. *BMC Genomics* 8:74. doi: 10.1186/1471-2164-8-74

Sharma, S., Bandopadhyay, R., Lashley, T., Renton, A. E., Kingsbury, A. E., Kumaran, R., et al. (2011). LRRK2 expression in idiopathic and G2019S positive Parkinson's disease subjects: a morphological and quantitative study. *Neuropathol. Appl. Neurobiol.* 37, 777–790. doi: 10.1111/j.1365-2990.2011.01187.x

Shi, M., Liu, C., Cook, T. J., Bullock, K. M., Zhao, Y., Ginghina, C., et al. (2014). Plasma exosomal alpha-synuclein is likely CNS-derived and increased in Parkinson's disease. *Acta Neuropathol.* 128, 639–650. doi: 10.1007/s00401-014-1314-y

Soldner, F., Hockemeyer, D., Beard, C., Gao, Q., Bell, G. W., Cook, E. G., et al. (2009). Parkinson's disease patient-derived induced pluripotent stem cells free of viral reprogramming factors. *Cell* 136, 964–977. doi: 10.1016/j.cell.2009.02.013

Soreq, L., Guffanti, A., Salomonis, N., Simchovitz, A., Israel, Z., Bergman, H., et al. (2014). Long non-coding RNA and alternative splicing modulations in Parkinson's leukocytes identified by RNA sequencing. *PLoS Comput. Biol.* 10:e1003517. doi: 10.1371/journal.pcbi.1003517

Sun, Z., Yang, S., Zhou, Q., Wang, G., Song, J., Li, Z., et al. (2018). Emerging role of exosome-derived long non-coding RNAs in tumor microenvironment. *Mol. Cancer* 17:82. doi: 10.1186/s12943-018-0831-z

Takahashi, K., Tanabe, K., Ohnuki, M., Narita, M., Ichisaka, T., Tomoda, K., et al. (2007). Induction of pluripotent stem cells from adult human fibroblasts by defined factors. *Cell* 131, 861–872.

Thery, C., Amigorena, S., Raposo, G., and Clayton, A. (2006). Isolation and characterization of exosomes from cell culture supernatants and biological fluids. *Curr. Protoc. Cell Biol.* 30, 3.22.1–3.22.29. doi: 10.1002/0471143030.cb0322s30

Valente, E. M., Abou-Sleiman, P. M., Caputo, V., Muqit, M. M., Harvey, K., Gispert, S., et al. (2004). Hereditary early-onset Parkinson's disease caused by mutations in PINK1. *Science* 304, 1158–1160.

van der Merwe, C., Jalali Sefid Dashti, Z., Christoffels, A., Loos, B., and Bardien, S. (2015). Evidence for a common biological pathway linking three parkinson's disease-causing genes: parkin, PINK1 and DJ-1. *Eur. J. Neurosci.* 41, 1113–1125. doi: 10.1111/ejn.12872

Vekrellis, K., Xilouri, M., Emmanouilidou, E., and Stefanis, L. (2009). Inducible over-expression of wild type alpha-synuclein in human neuronal cells leads to caspase-dependent non-apoptotic death. *J. Neurochem.* 109, 1348–1362. doi: 10.1111/j.1471-4159.2009.06054.x

Wang, J., Cao, B., Han, D., Sun, M., and Feng, J. (2017). Long non-coding RNA H19 induces cerebral ischemia reperfusion injury via activation of autophagy. *Aging Dis.* 8, 71–84. doi: 10.14336/AD.2016.0530

Wang, S., Zhang, X., Guo, Y., Rong, H., and Liu, T. (2017). The long noncoding RNA HOTAIR promotes parkinson's disease by upregulating LRRK2 expression. *Oncotarget* 8, 24449–24456. doi: 10.18632/oncotarget.15511

Wang, K. C., and Chang, H. Y. (2011). Molecular mechanisms of long noncoding RNAs. *Mol. Cell* 43, 904–914. doi: 10.1016/j.molcel.2011.08.018

Wu, T., and Hallett, M. (2013). The cerebellum in parkinson's disease. *Brain* 136, 696–709. doi: 10.1093/brain/aws360

Xiao, D., Ohlendorf, J., Chen, Y., Taylor, D. D., Rai, S. N., Waigel, S., et al. (2012). Identifying mRNA, microRNA and protein profiles of melanoma exosomes. *PLoS One* 7:e46874. doi: 10.1371/journal.pone.0046874

Xilouri, M., Kyratzi, E., Pitychoutis, P. M., Papadopoulou-Daifoti, Z., Perier, C., Vila, M., et al. (2012). Selective neuroprotective effects of the S18Y polymorphic variant of UCH-L1 in the dopaminergic system. *Hum. Mol. Genet.* 21, 874–889. doi: 10.1093/hmg/ddr521

Yang, L., Xu, L., Wang, Q., Wang, M., and An, G. (2016). Dysregulation of long non-coding RNA profiles in human colorectal cancer and its association with overall survival. *Oncol. Lett.* 12, 4068–4074.

Zhang, Q. S., Wang, Z. H., Zhang, J. L., Duan, Y. L., Li, G. F., and Zheng, D. L. (2016). Beta-asarone protects against MPTP-induced Parkinson's disease via regulating long non-coding RNA MALAT1 and inhibiting alpha-synuclein protein expression. *Biomed Pharmacother.* 83, 153–159. doi: 10.1016/j.biopha.2016.06.017

Zhang, Y., Zhang, L., Wang, Y., Ding, H., Xue, S., Qi, H., et al. (2019). MicroRNAs or long noncoding RNAs in diagnosis and prognosis of coronary artery disease. *Aging Dis.* 10:617.

Zucchelli, S., Fasolo, F., Russo, R., Cimatti, L., Patrucco, L., Takahashi, H., et al. (2015). SINEUPs are modular antisense long non-coding RNAs that increase synthesis of target proteins in cells. *Front. Cell Neurosci.* 9:174. doi: 10.3389/fncel.2015.00174

Conflict of Interest Statement: The authors declare that the research was conducted in the absence of any commercial or financial relationships that could be construed as a potential conflict of interest.

Copyright © 2019 Elkouris, Kouroupi, Vourvoukelis, Papagiannakis, Kaltezioti, Matsas, Stefanis, Xilouri and Politis. This is an open-access article distributed under the terms of the Creative Commons Attribution License (CC BY). The use, distribution or reproduction in other forums is permitted, provided the original author(s) and the copyright owner(s) are credited and that the original publication in this journal is cited, in accordance with accepted academic practice. No use, distribution or reproduction is permitted which does not comply with these terms.

frontiers in Cellular Neuroscience

METHODS
published: 27 February 2019
doi: 10.3389/fncel.2019.00049

A Novel Optical Tissue Clearing Protocol for Mouse Skeletal Muscle to Visualize Endplates in Their Tissue Context

Marion Patrick Ivey Williams[1], *Matteo Rigon*[1], *Tatjana Straka*[1,2], *Sarah Janice Hörner*[1,2], *Manfred Thiel*[3], *Norbert Gretz*[4,5], *Mathias Hafner*[1,5], *Markus Reischl*[6] and *Rüdiger Rudolf*[1,2,5,7]*

[1] Institute of Molecular and Cell Biology, Mannheim University of Applied Sciences, Mannheim, Germany, [2] Interdisciplinary Center for Neurosciences, Heidelberg University, Heidelberg, Germany, [3] Department of Anesthesiology and Surgical Intensive Care Medicine, Medical Faculty Mannheim, Heidelberg University, Mannheim, Germany, [4] Medical Faculty Mannheim, Medical Research Center, Heidelberg University, Mannheim, Germany, [5] Medical Faculty Mannheim, Institute of Medical Technology, Mannheim University of Applied Sciences, Mannheim, Germany, [6] Institute for Automation and Applied Informatics, Karlsruhe Institute of Technology, Eggenstein-Leopoldshafen, Germany, [7] Institute of Toxicology and Genetics, Karlsruhe Institute of Technology, Eggenstein-Leopoldshafen, Germany

Neuromuscular junctions (NMJs) mediate skeletal muscle contractions and play an important role in several neuromuscular disorders when their morphology and function are compromised. However, due to their small size and sparse distribution throughout the comparatively large, inherently opaque muscle tissue the analysis of NMJ morphology has been limited to teased fiber preparations, longitudinal muscle sections, and flat muscles. Consequently, whole mount analyses of NMJ morphology, numbers, their distribution, and assignment to a given muscle fiber have also been impossible to determine in muscle types that are frequently used in experimental paradigms. This impossibility is exacerbated by the lack of optical tissue clearing techniques that are compatible with clear and persistent NMJ stains. Here, we present MYOCLEAR, a novel and highly reproducible muscle tissue clearing protocol. Based on hydrogel-based tissue clearing methods, this protocol permits the labeling and detection of all NMJs in adult hindleg extensor digitorum longus muscles from wildtype and diseased mice. The method is also applicable to adult mouse diaphragm muscles and can be used for different staining agents, including toxins, lectins, antibodies, and nuclear dyes. It will be useful in understanding the distribution, morphological features, and muscle tissue context of NMJs in hindleg muscle whole mounts for biomedical and basic research.

Keywords: acetylcholine receptor, hydrogel embedding, NMJ, optical tissue clearing, skeletal muscle

OPEN ACCESS

Edited by:
Thomas Fath,
Macquarie University, Australia

Reviewed by:
Frederic A. Meunier,
The University of Queensland, Australia
Leonardo Sacconi,
Università degli Studi di Firenze, Italy

***Correspondence:**
Rüdiger Rudolf
r.rudolf@hs-mannheim.de

Received: *12 October 2018*
Accepted: *01 February 2019*
Published: *27 February 2019*

Citation:
Williams MPI, Rigon M, Straka T, Hörner SJ, Thiel M, Gretz N, Hafner M, Reischl M and Rudolf R (2019) A Novel Optical Tissue Clearing Protocol for Mouse Skeletal Muscle to Visualize Endplates in Their Tissue Context. Front. Cell. Neurosci. 13:49. doi: 10.3389/fncel.2019.00049

INTRODUCTION

Vertebrate NMJs are the synapses between cholinergic motor neurons and skeletal muscle fibers that mediate voluntary muscle contraction. They are embedded in a complex of many different cellular tissue components, with their pre- and postsynaptic apparatuses juxtaposed onto each other. Depending on the species, NMJs are about 10–50 μm in diameter and come in varying forms, such as grape-, plaque-, or pretzel-shaped structures (Lu and Lichtman, 2007). The latter

design is of particular interest as it is prevalent in rodent NMJs and is often used as an indicator for neuromuscular disorders or other disease states when fragmentation, simplification, growth, shrinkage, and other such deviations occur (Lyons and Slater, 1991; Valdez et al., 2010; Carnio et al., 2014; Rudolf et al., 2014). In healthy adult mouse muscle, each syncytial fiber is roughly 50 μm in diameter and up to 4 cm in length; it contains thousands of myonuclei and is precisely innervated by one NMJ (Krause, 1863). This is different during embryonic development and the perinatal stages, where most muscle fibers are contacted by more than one neuron (Lee et al., 2017). This sort of poly-innervation is corrected within the first 2 to 3 postnatal weeks. Nevertheless, it can reappear during denervation—reinnervation cycles and other non-physiological conditions that frequently occur in genetic, acquired, and aging muscle diseases (Gorio et al., 1983). Previous and more recent studies increasingly suggest important feed forward and feedback mechanisms between the different cell types that mutually affect cell behavior (Carnio et al., 2014; Wu et al., 2015; Khan et al., 2016; Lee et al., 2017; Dobrowolny et al., 2018). So far, synoptic consideration of pathophysiological processes on the entire musculoskeletal organ has been severely hampered by two main factors. First, the mentioned mono-innervation of muscle fibers in combination with the extreme discrepancy between small NMJ size and large muscle fiber dimensions leads to an unequal distribution of these components in the organ; therefore, effects seen in one part of the muscle might not occur in others. Second, from a technical point of view, optical tissue clearing methods that would allow for such analysis of NMJs in their whole mount context have been lacking so far.

Introduced by Chung et al., CLARITY (Clear Lipid-exchanged Acrylamide-hybridized Rigid Imaging/Immunostaining/*in situ* hybridization-compatible Tissue-hydrogel) is one of the many new tissue clearing methods available and has gained a great deal of attention due to its robustness and compatibility with many different stainings (Chung and Deisseroth, 2013; Chung et al., 2013). This protocol and its variations (Lee et al., 2014; Tomer et al., 2014; Yang et al., 2014; Kim et al., 2015; Kleffel et al., 2016; Greenbaum et al., 2017; Du et al., 2018; Wang et al., 2018) address Refractive Index (RI) heterogeneity by first embedding the tissue in an acrylamide/bis-acrylamide based hydrogel. In addition to increasing tissue stability and porosity, this stabilizes the RI across the tissue from the estimated $n = 1.50$ of dry tissue to $n = 1.457$. Lipids are then drawn out of the embedded samples via active clearing in an electrophoresis chamber that applies a current and a continual stream of SDS over the tissue. This process increases the homogeneity of the RI throughout the sample even further, since lipids tend to have varying RIs and can increase light scattering when imaging deep into tissue. Even though this is a very promising method, Milgroom et al found it was incompatible with α-bungarotoxin (BGT) (Milgroom and Ralston, 2016), the most widely used postsynaptic NMJ marker, which labels nicotinic acetylcholine receptors (AChRs) with unmatched specificity. Their hypothesis was that the additional cross-linking and fixation prevented access of the toxin to the acetylcholine receptors (AChR). This incompatibility was further validated by Zhang et al., who found that even a modified passive CLARITY method resulted in the absence of BGT signals and appears to be very sensitive to standard optical clearing procedures (Zhang et al., 2018). Another study did report the presence of BGT fluorescence signals with the use of *in vivo* injected BGT in combination with a modified organic-solvent clearing protocol based on 3DISCO (Chen et al., 2016). Nonetheless, the combination of fluorophore compatibility/stability, tissue shrinkage, and the fact that *in vivo* injection of BGT hampers *post-hoc* stainings make this protocol and other organic solvent-based methods less than ideal for most applications.

Here, we address many of these issues by introducing a new optical tissue clearing protocol that is based on aldehyde fixation and hydrogel embedding. This robust protocol enables transparency of samples with a thickness >700 μm and is compatible with mouse diaphragm as well as EDL muscles. Additionally, it presents long-term fluorophore stability of NMJ staining in mouse skeletal muscle whole mounts.

MATERIALS AND METHODS

Animals and Sample Preparation

In the current study, adult C57BL/10J, and BL10/JMDX mice were used. Animals were maintained in a local animal facility and their use and care were approved by German authorities according to EC directive 2010/63. For all experiments, adult mice were euthanized by cervical dislocation. Either whole hind limbs or just EDL muscles as well as diaphragm muscles were freshly dissected. Samples were then immediately immersed in 4% PFA/1x PBS and incubated for a minimum of 24 h on a roller mixer at 4°C.

MYOCLEAR

A detailed protocol including reagent and equipment lists, photos of custom-made devices, and troubleshooting can be found in the **Supplementary Methods** section. Briefly, muscles were either freshly dissected or taken from PFA fixed mouse muscles. However, we recommend dissecting muscles from PFA fixed specimens since this tends to drastically reduce accidental damage to the tissue. Then, 100 mg of VA-044 initiator (final concentration 0.25%) and 40 ml of freshly prepared hydrogel monomer solution (A4P0) were added to 50 ml light resistant Falcon tubes, briefly hand mixed, and kept on ice to prevent premature polymerization. One muscle was then placed in each falcon tube and incubated on a roller mixer for 5 days at 4°C. After, muscles were degassed for 1 h via a custom-built degassing apparatus which allowed nitrogen to bubble over the samples (see **Supplementary Methods** section for photograph). The caps of the Falcon tubes were then loosely placed back on and the tubes transferred to an air tight desiccator where they were vacuumed under a 90 kPa negative pressure for an additional hour in order to purge any remaining oxygen from the sample. The desiccator was then flushed with nitrogen, Falcon tube caps tightened, and placed in a hot water bath at 37°C for 4 h with shaking for polymerization. Samples were then removed from the Falcon tube and excess hydrogel removed by washing samples with 1x PTwH overnight on a roller mixer at room temperature. It is

important to note that in lieu of using a desiccator and hot water bath, we found that using Life Canvas's EasyGel system resulted in comparable results and made sample handling simpler and easier. However, the custom-built nitrogen bubbling apparatus was still needed to ensure uniform hydrogel polymerization.

For NMJ plus nuclei labeling, samples were stained as follows, inspired by the iDISCO staining protocol (Renier et al., 2014): Samples were washed in 1x PTwH with solution changes every hour for 2 h. After washing, samples were incubated in blocking and permeabilization solution (BnP) with shaking at 37°C for 48 h. Then, the BnP solution was replaced with 1 ml of fresh BnP solution, the dyes added [BGT-AF647 (1:200), BGT-AF555 (1:200), and/or DRAQ5 (1:300)], and allowed to incubate for 5 days at 37°C with shaking. After, samples were thoroughly washed in 1x PTwH with solution changes every 10 min, 15 min, 30 min, 1 h, and then every 2 h for a minimum of 2 days. The detergent was then removed by washing samples in distilled water for 4–8 h with frequent solution changes. Lastly, samples were incubated in 88% glycerol at room temperature for a minimum of 24 h for RI matching and long-term storage. Additionally, it was found that samples were stable for many months when stored in this manner. For indirect immunofluorescence staining, samples were processed as described above, with modifications as detailed in the **Supplementary Methods**. A list of primary and secondary antibodies and their dilutions can also be found there.

X-CLARITY

For all samples stained after active clearing, a Biozym X-CLARITY protocol was followed, excluding the perfusion step. This is available for download from their website, https://www.biozym.com/. Briefly, EDL muscles were dissected from PFA fixed hind limbs and washed for 3 h in PBS at 4°C. Samples were then transferred to 50 ml light resistant falcon tubes containing 40 ml of freshly prepared 4% PFA/A4P0 monomer solution and 100 mg of VA-044 initiator, followed by a 5-day incubation on a roller mixer at 4°C. Then, samples were degassed via partial vacuum for 1 h, flushed with nitrogen, and incubated at 37°C for 3 h in a hot water bath to induce polymerization. Afterwards, samples were washed for 1–2 h in 1x PBS on a roller mixer at RT to remove excess hydrogel, transferred to an X-Clarity brain slice tissue holder, and lowered into the X-Clarity ETC chamber, where they were cleared for 3 h with 4% SDS buffer at a flow rate of 30 rpm; temperature: 37°C; current: 1.5 A. After, samples were thoroughly washed in PBST at 37°C for 24 h, then stored at 4°C in 1x PBS. For staining, samples were processed following the immunostaining section described in the Biozym protocol, with a dilution factor of 1:200 and 1:500 for BGT-AF647 and Wheat Germ Agglutinin CF488 conjugate (WGA-488; Biotium), respectively. Lastly, prepared samples were kept in 88% glycerol for storage and imaging.

Active and Passive CLARITY

EDL muscles were processed following the MYOCLEAR protocol described above, followed by either active or passive clearing for 24 h in the X-CLARITY ETC tissue clearing system. Here, a steady flow of 4% SDS at a rate of 30 rpm was applied to the samples and the current either left off for passive clearing or adjusted according to the experiment for active clearing, with the maximum temperature recorded at the end of each run, see **Supplementary Methods** section. For experiments that addressed the effect refixation would have on preserving BGT fluorescence, samples were stained, incubated in 4% PFA for 24 h at 4°C, and then cleared. Lastly, all samples were stored and mounted in 88% Glycerol for imaging and kept at room temperature.

Microscopy

Single stack acquisitions were imaged using a Leica Microsystems TCS SP2 equipped with a Leica Microsystems HC PL AP0 20x/0.75 IMM CORE CS2 objective, Leica confocal software version 2.61, a KrAr laser (488 nm, 514 nm), a diode-pumped laser (561 nm), and a HeNe laser (633 nm). For tile scans, an upright Leica Microsystems TCS SP8 equipped with LAS X software, a 488 nm laser, a 561 nm laser, a 633 nm laser, and Leica Microsystems clarity objective HC FLUOTAR L 25x/1.00 IMM (ne = 1.457) was used. 3D imaging of whole mount muscle samples was performed in 88% glycerol immersion using 6-cm round plastic dishes. Muscles were fixed by surgical thread knotted around the distal and proximal tendons. Visualization worked best after at least 24 h of temperature adjustment of the sample in the microscope room. During this period, the sample was kept in the dark.

Fiber Number and Image Analysis, Figure Preparation, and Statistics

Transversal EDL cryo-sections (15-μm thick) from C57BL/10J mice were stained with WGA-488 (1:1,000 dilution in 2% BSA/PBS) for 15 min at RT to outline muscle fibers. After washing and embedding in Mowiol, sections were imaged with an inverted Leica SP8 microscope. After acquisition, all images were electronically processed using either Leica Microsystems LAS X core or ImageJ software. Signal-to-Noise-Ratio (SNR) measurements were done in ImageJ. Here, NMJs were segmented and mean intensities of the NMJs and standard deviation (SD) of adjacent fiber background regions were measured. The ratio of NMJ intensities vs. background SD was determined as SNR for each synapse. Numbers displayed in the text indicate the average of several SNR values per sample. For quantitative analysis of NMJ and fiber numbers, position of all observed NMJs / fibers was completed using the multi-point tool of ImageJ. This determined the xyz-position of the center of each NMJ / fiber. For analysis of critical morphological parameters of NMJs according to Jones et al. (2016), five square ROIs, each 500 × 500 μm, were selected per muscle. Then, all en face NMJs per ROI were manually thresholded and segmented using the magic wand tool in ImageJ. Then, area, perimeter and bounding rectangle diagonal were measured for every segmented NMJ. The number of AChR clusters per NMJs was counted manually. The diagonal of the bounding rectangle was calculated from the bounding rectangle sides while the fragmentation index was determined using the term: fragmentation index = 1–[1/(number of AChR clusters)]. Spectral un-mixing (Zimmermann et al., 2002) used the ImageJ plugin SpectralUnmixing (https://imagej.nih.gov/ij/plugins/spectral-unmixing.html). All figures were assembled

using Adobe Illustrator. Mean values and standard deviations were calculated in Microsoft Excel. Normal distribution and homo/heteroscedasticity of data were probed using Kolmogorov-Smirnov test and *F*-test, respectively. According to these results and the type of data, statistical significance was evaluated using either one-way Analysis of Variance (ANOVA) with Tukey's *post-hoc* test, unpaired two-tailed *t*-test, or Kruskal-Wallis test. Bar graphs are presented as mean ± SD. *P*-values were indicated as $^{*}(p < 0.05)$, $^{**}(p \leq 0.01)$, $^{***}(p \leq 0.001)$, or $^{****}(p \leq 0.0001)$. $P \geq 0.05$ was considered not significant.

RESULTS

An SDS-Free Hydrogel-Based Clearing Protocol Retains NMJ Staining

Previous attempts of optically clearing whole skeletal muscles using hydrogel-based, CLARITY-derived protocols yielded good tissue transparency but led to a quantitative loss of BGT fluorescence. To address possible reasons for this, we tested several variations of the procedure that was previously described by Milgroom and Ralston (2016). Samples were PFA fixed, embedded in hydrogel, and then stained with BGT-AF647 for NMJ labeling. Once stained, muscles were thoroughly washed for a minimum of 2 days, incubated in 88% glycerol overnight, and imaged to check for BGT-AF647 fluorescence. Notably, BGT-AF647 fluorescence was observed in all hydrogel-embedded samples (**Supplementary Figure 1A**, left panels). After initial imaging, glycerol was removed from the samples by washing for 24 h in PTwH at RT and were then actively cleared using an X-CLARITY tissue clearing system. A variety of settings, including different electrophoresis strengths, the addition of PFA fixation after BGT-AF647 staining, as well as a passive CLARITY protocol using a constant flow of SDS with no current, were tested. These modifications resulted in a reduced SNR of NMJ labeling in the cleared tissue (**Supplementary Figure 1A**, see lower left angles in panels for SNR values); samples that were post-fixed with PFA before clearing were less affected. However, also these re-fixed samples exhibited a large decrease in fluorescence intensity of the BGT-AF647 staining and were still far from acceptable quality. Thus, supporting the findings of previous studies which state the incompatibility of CLARITY-based protocols with BGT-NMJ staining.

The next step was to determine the effects of SDS on BGT staining: whether it washed out the membrane bound AChRs, simply quenched the fluorophore, or denatured the AChRs to the point BGT would not be able to bind. Samples were processed following the X-CLARITY protocol. Briefly, samples were PFA fixed, hydrogel embedded, actively cleared using an X-CLARITY machine, stained with either WGA-488 or BGT-AF647, and incubated in 88% glycerol for imaging. It was found here that staining the samples post-clearing with BGT-AF647 continued to result in an absence of NMJ signals, data not shown. However, NMJs in total were not destroyed by these techniques. Indeed, the lectin WGA could nicely identify the proteoglycan-rich ECM at the NMJs (**Supplementary Figures 1B,C**, see arrowheads in **Supplementary Figure 1C** for some examples of NMJs) besides other structures, such as blood vessels. Therefore, it might be assumed that SDS caused either quenching of the fluorophores or that it denatured the AChRs. The latter would, in turn, release BGT-AF647 from the AChR for samples stained before clearing and impede BGT-AF647 from binding altogether for samples stained post-clearing. With this in mind, SDS was excluded from all other experiments due to its role as a potential risk factor for the maintenance of BGT binding sites on NMJs.

With the recent introduction of a new free-of-acrylamide SDS based tissue clearing protocol (Xu et al., 2017), the necessity of the embedded hydrogel and its effect on tissue needed to be explored. In theory, the embedded hydrogel not only homogenizes the RI throughout the sample but also increases the porosity of it; resulting in better penetration and uniformity of staining (Chung and Deisseroth, 2013; Chung et al., 2013). To test the effects of the hydrogel, samples were PFA fixed and either embedded in hydrogel, then stained with BGT-AF647 or vice versa. Both being compared in **Figure 1**, we found that staining samples after hydrogel embedding led to a better SNR (**Figure 1G**, **Supplementary Figure 2**) and increased the overall imaging depth of the sample (**Figure 1G**, **Supplementary Figure 2**). This confirmed the need of embedding samples with hydrogel and resulted in the final protocol termed MYOCLEAR. This method represents a passive hydrogel-based clearing method for the visualization of NMJs in fixed mouse muscles and is summarized in **Figure 2**.

Muscle Fibers, Nuclei, and NMJs Can Be Visualized by Virtue of Green/Red Autofluorescence and Spectral Unmixing of Near-Infrared Fluorescence Signals

Number and position of myonuclei can serve as relevant parameters in muscle research. Specifically, detection of centro-nucleated fibers in diseased and regenerating muscle or analyzing the presence of fundamental subsynaptic nuclei at NMJs would need determination of these parameters. Thus, we sought to use Draq5, a near-infrared nuclear dye, in combination with a red-fluorescent BGT-AlexaFluor555 conjugate on MYOCLEAR-treated EDL muscles. As shown in red in **Figures 3A,B**, nuclei were well-stained and visible in the Draq5 channel. Conversely, NMJs, indicated by arrowheads in **Figure 3B**, were barely visible due to massive, PFA-induced autofluorescence (both shown in green). Consequently, this made the quality of these results inadequate for analysis. Furthermore, the intense level of autofluorescence was also observed in the 500–550 nm wavelength range when samples were stained with BGT-AlexaFluor488, data not shown.

To mitigate the autofluorescence-induced limitation observed in short-wavelength fluorescence channels, we utilized two slightly spectrally separated near-infrared dyes, BGT-AF647 (maxima of excitation and emission, 650 and 665 nm, respectively) and Draq5 (maxima of excitation and emission, 646 and 681 nm, respectively). Muscles were PFA fixed, hydrogel embedded, co-stained with the dyes mentioned above, incubated in 88% glycerol, and then imaged using a 633 nm wavelength excitation laser for both. Each dye was acquired separately and

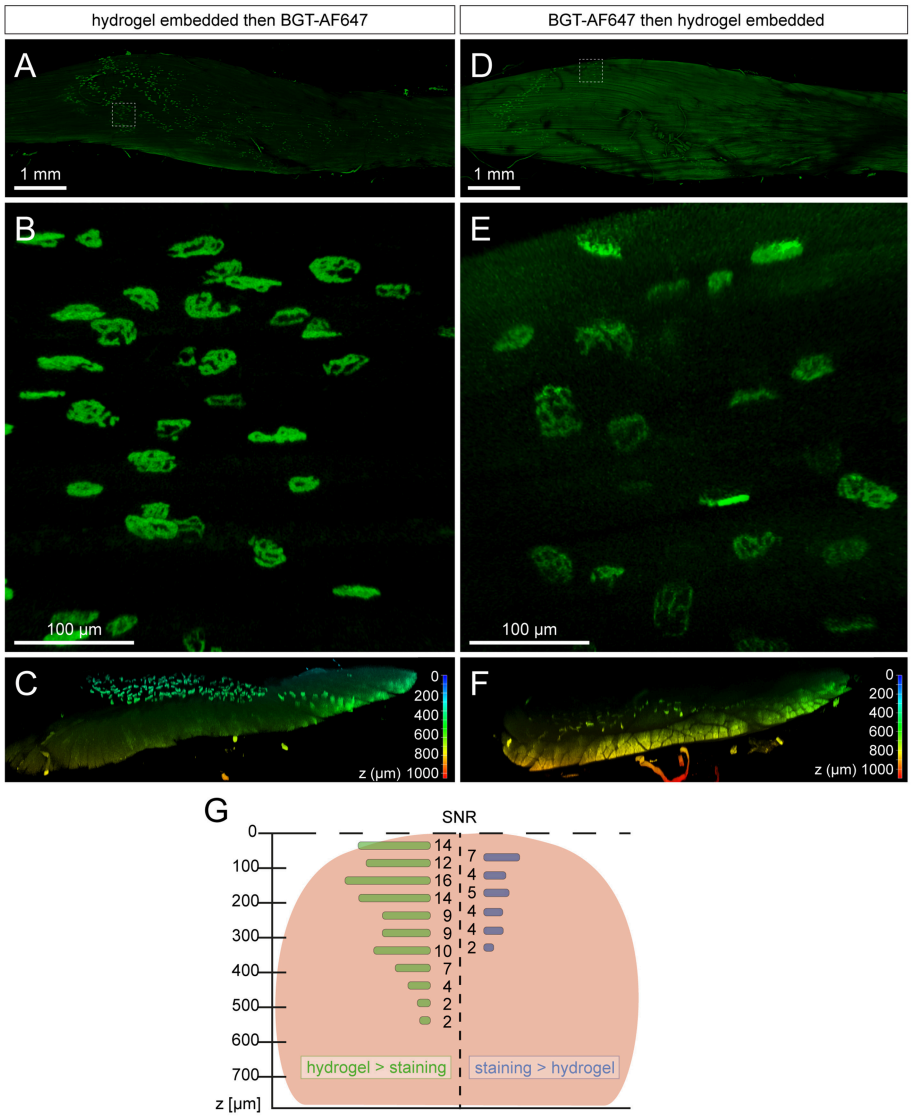


FIGURE 1 | Sequence of staining and hydrogel embedding affects overall imaging depth and quality of muscle samples. All samples were imaged in 3D using a Leica SP8 confocal microscope and images were processed with Leica LAS X software. **(A–C)** Mouse EDL muscle was PFA-fixed, hydrogel embedded, stained with BGT-AF647, and then RI matched in 88% glycerol before imaging. **(D–F)** Mouse EDL was PFA-fixed, stained with BGT-AF647, hydrogel embedded, and then RI matched in 88% glycerol before imaging. **(A,D)** depict overviews of the whole mouse EDL muscles with the boxed region representing zooms shown in **(B,E)**. **(C,F)** portray cross sections cropped from the center of the EDL imaging data and depth-coded on the z-axis in order to visualize imaging depth and quality for both methods. **(G)** Graphical display of NMJ-signal SNRs in correspondence to muscle tissue depth and staining / clearing order. Muscle tissue extension in the central muscle region is depicted in the background as reddish round shape. Mean SNR values are shown as horizontal bars with corresponding numbers next to it. Left and right halves correspond to muscles shown in **(C,F)**, respectively.

their emission detection windows adjusted to 643–679 nm and 685–778 nm for BGT-AF647 and Draq5, respectively. **Figure 3C** depicts a maximum-z projection of an EDL-whole mount scanned over a thickness of 1.2 mm. In addition, **Figure 3D** and **Supplementary Video S1** show a zoom view of the boxed region and a rotation of the data projection, respectively. Nuclei and NMJs could be clearly distinguished. An additional spectral un-mixing step (see chapter Fiber number and image analysis, figure preparation, and statistics) was then added for more accurate segmentation results. **Figures 3E,F** show depth-coded side views of BGT-AF647 and Draq5, respectively, and reveal a good signal penetration for both over a depth range of about 1 mm. **Figure 3F** displays some elongated structures, which likely represent blood vessels traversing the muscle. To assess the compatibility of MYOCLEAR with muscle types other than EDL, we applied the protocol to adult mouse diaphragm. Confocal analysis revealed that the procedure was good to achieve complete penetration of diaphragm muscle in z (**Figures 4A–D**).

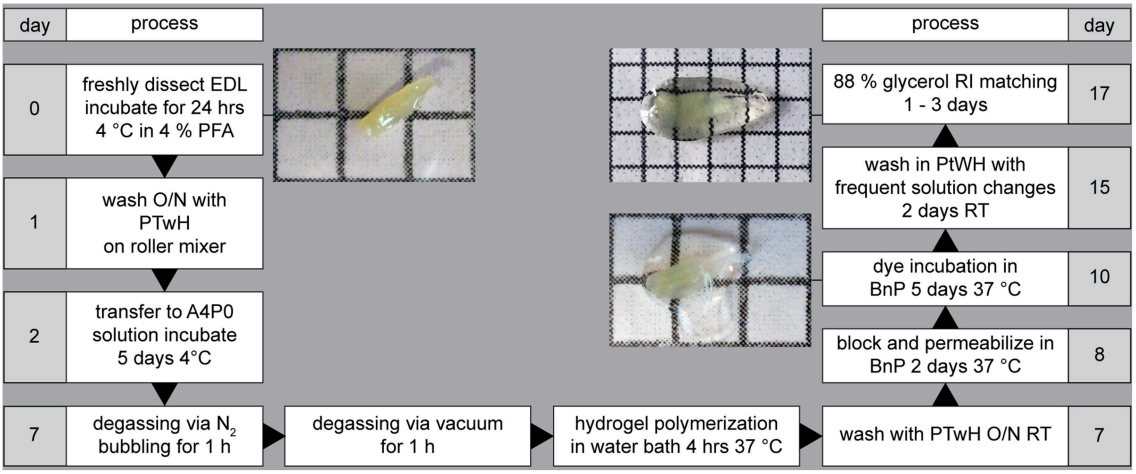


FIGURE 2 | Overview of the MYOCLEAR protocol. MYOCLEAR can be divided into three major stages: hydrogel embedding (days 2–7), staining (days 8–15), and RI matching (days 16–17). The panel gives a graphical overview on the detailed descriptions found in Materials and Methods and **Supplementary Methods** sections. Photographs next to processing days 0, 10, and 17 show the appearance of EDL muscles at the start of the clearing protocol, before staining, and upon RI matching, respectively.

The insert in **Figure 4A** shows that NMJs were well-preserved in these samples. The apparent fragmentation in the large overview in **Figure 4A** is due to nuclei partially covering many synapses.

Whole Mount Analysis Detects Local Heterogeneity of NMJ Fragmentation Index in mdx Muscle

Wildtype skeletal muscle, as tested so far, is characterized by extremely homogeneous tissue composition. Conversely, diseased muscles might exhibit large amounts of fibrosis, fatty tissue, immune cell aggregates, or other changes that can affect the optical characteristics of muscle tissue and their transparency after clearing. Thus, we looked at muscles from wildtype and dystrophic mdx mice. The latter are characterized by extensive fibrosis (Piñol-Jurado et al., 2018) and fragmented NMJs (Lyons and Slater, 1991; Röder et al., 2012). We found that applying MYOCLEAR to wildtype and mdx muscles resulted in data of comparable quality. As expected, NMJ structure was clearly different between the two; with wildtype NMJs displaying coherent pretzel-like structures and mdx NMJs demonstrating fragmented morphology. Next, whole mount imaging data was acquired for some wildtype and mdx mouse EDLs that were processed with MYOCLEAR and stained with BGT-AF647. The numbers of visible NMJs were then quantified by hand using the multi-point tool in ImageJ. Representative muscles are depicted in **Figures 5A,B** which illustrates the ability of this protocol to detect hundreds of NMJs. In quantitative terms, 1082.3 ± 29.5 and 1019.5 ± 14.8 (each mean ± SD) NMJs were counted in wildtype and mdx muscles, respectively. **Figures 5A',B'** show representative high-power images of a few NMJs from each of the corresponding muscles. These panels demonstrate the normal, pretzel-like structure of NMJs in wildtype (**Figure 5A'**) as compared to the fragmented appearance in the mdx muscle (**Figure 5B'**). An important advantage of whole mounts should be that heterogeneity of objects or effects of treatments within the entire organ can be better observed than in individual tissue sections. To assess this point, key morphological parameters of NMJs from different ROIs of both, wildtype and mdx muscles were determined and compared. Therefore, a subset of criteria recently introduced by Jones et al. was applied (Jones et al., 2016). In detail, area, fragmentation index, perimeter, and bounding rectangle diagonal of NMJs from five different ROIs (**Figures 5C–F**) per muscle were determined. NMJ areas, perimeters, and bounding rectangle diagonals were similar between all ROIs of a given muscle and also apparently not different between wildtype and mdx. Conversely, NMJ fragmentation index was higher in mdx than in wildtype and, furthermore, varied considerably within a given mdx muscle.

VAChT Antibody Staining Confirms Integrity of NMJ Presynaptic Apparatus Upon MYOCLEAR

BGT-AF647 and lectin staining data suggested that the NMJ ECM and postsynaptic apparatus remained intact during MYOCLEAR processing. To address presynaptic integrity and the amenability of the clearing protocol for immunofluorescence staining, we first processed EDL muscles with the MYOCLEAR protocol and then stained nuclei and the presynaptic NMJ marker protein vAChT using Draq5 and anti-vAChT antibody, respectively. As depicted in **Figure 6A**, the obtained antibody staining was concentrated in the NMJ regions, although considerable noisy signals were also observed outside the synaptic regions. Yet, NMJ presynapses showed normal coherent appearance, demonstrating that the clearing procedure did not affect this part either. The general integrity of the major muscle compartment was also confirmed by immunostaining with a

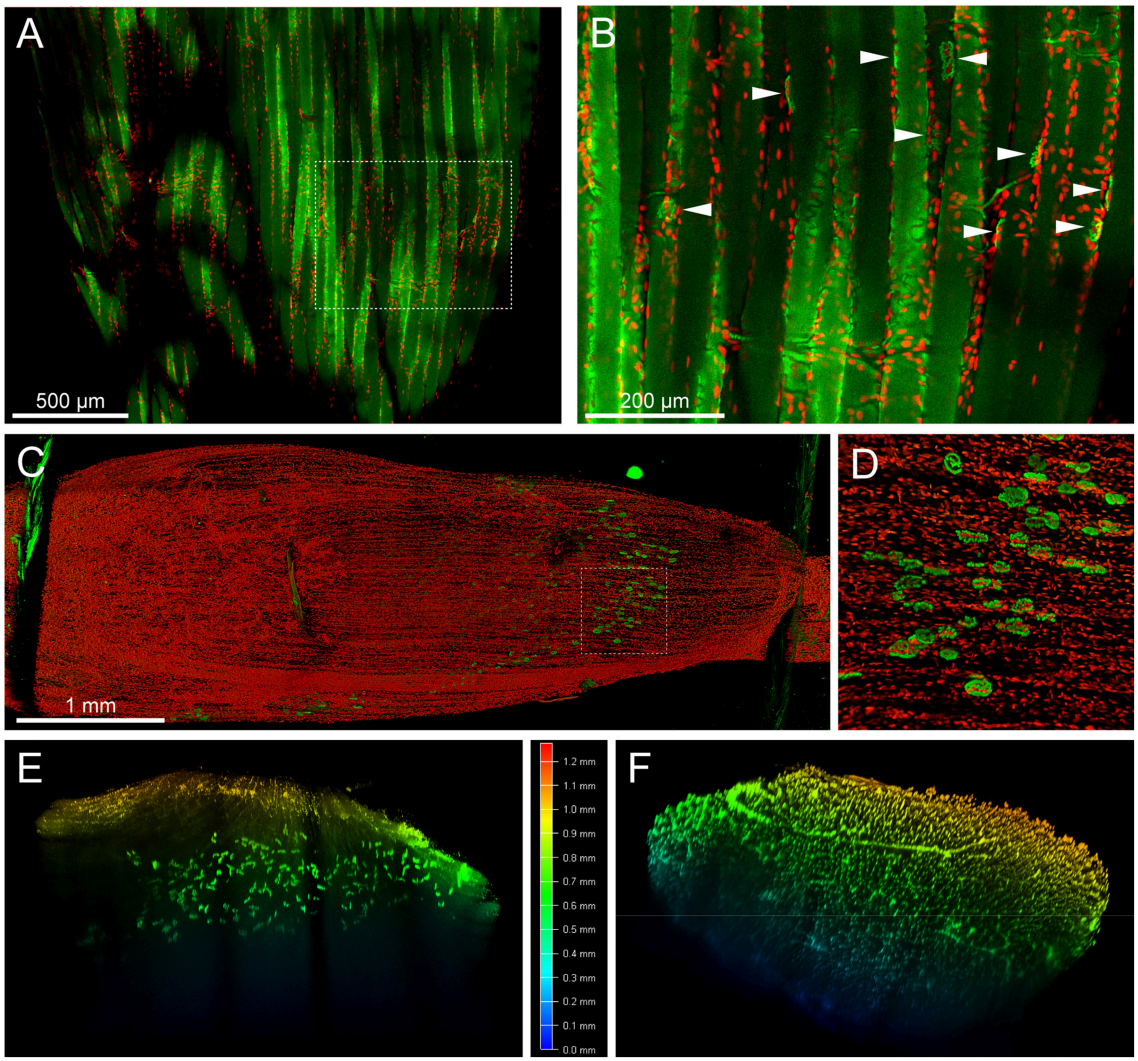


FIGURE 3 | MYOCLEAR enables imaging of muscle fibers, myonuclei, and NMJs by using red autofluorescence and spectral unmixing of far-red wavelengths dyes. **(A,B)** Mouse EDL was processed via the MYOCLEAR protocol and stained with BGT-AF555 and Draq5. **(A)** depicts a confocal section of the EDL, with **(B)** representing a zoom of the boxed region. Strong autofluorescence of the tissue in the AF555 channel (green) resulted in a poor SNR for NMJ detection (some NMJs are highlighted in **B**, arrowheads). In contrast, the near-infrared dye Draq5 displayed crisp and clear nuclei. **(C–F)** Mouse EDL muscle was processed via the MYOCLEAR protocol and stained with BGT-AF647 and Draq5. In order to overcome the auto-fluorescence shown in this figure, the emission windows for each dye were adjusted according to their peak values and acquired separately using the same 633-nm excitation laser on a SP8 confocal microscope. The images were processed using Leica LAS X software and spectrally un-mixed in ImageJ. **(C)** Maximum-z projection of the whole EDL before applying spectral un-mixing. Draq5, red; BGT-AF647, green. Green autofluorescence of the thread keeping the muscle in place for imaging is visible at the proximal and distal ends of the muscle. **(D)** Zoom view of the boxed region in **(A)**. **(E,F)** Z-axis depth coding for signals of BGT-AF647 **(E)** and Draq5 **(F)** shown as cross sections after spectral un-mixing.

few additional antibodies. Nicely, dystrophin outlined muscle fibers and was also enriched in the NMJ regions as expected (**Figure 6B**). Further labeling with collagen I antibody showed the distribution of large blood vessels, capillaries, and fascia cells (**Figure 6C**). Finally, immunostaining of troponin I retrieved the regular pattern of sarcomeric striations (**Figure 6D**).

DISCUSSION

Although previous attempts of optically clearing whole skeletal muscles using hydrogel-based, CLARITY-derived protocols yielded sufficient muscle tissue transparency, they led to a quantitative loss of BGT fluorescence. This was true for both, active (Milgroom and Ralston, 2016) and passive CLARITY protocols (Zhang et al., 2018). The interpretation in these studies was that hydrogel cross-linking coupled with PFA fixation prevented access of the toxin to AChRs. Conversely, we present a hydrogel and PFA based skeletal muscle clearing protocol that nicely retains BGT-based NMJ staining and exhibits a good light penetration of approximately 1,000 µm in mouse EDL muscle. This suggests, that SDS rather than hydrogel or PFA led to the loss of BGT staining. For simplicity, this method was termed MYOCLEAR. It allows for the analysis of whole mount NMJ

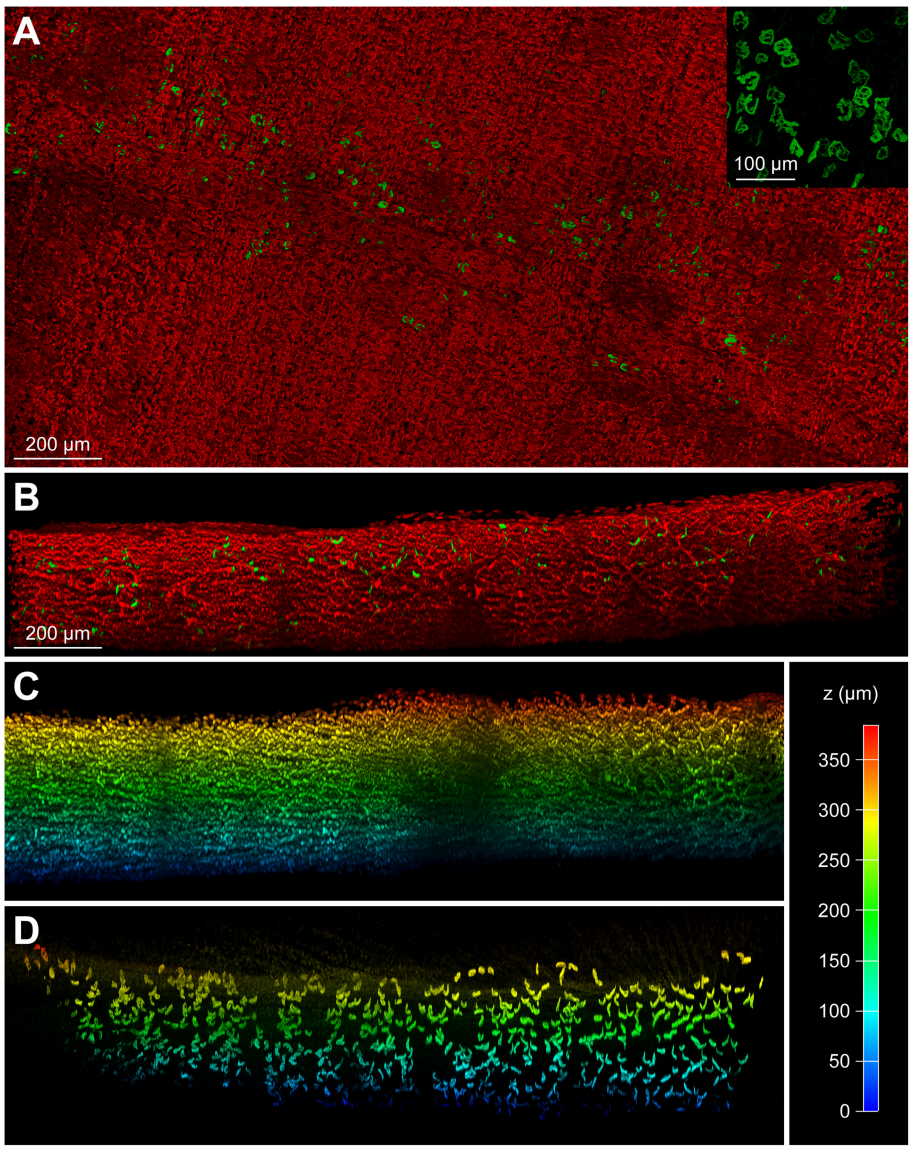


FIGURE 4 | MYOCLEAR is functional with adult mouse diaphragm muscle. Adult mouse diaphragm muscles were processed using the MYOCLEAR protocol and stained with Draq5 and BGT-AF647. **(A)** Maximum-z projection of a representative tile stack showing fluorescence signals of BGT and Draq5 in green and red, respectively. Note, that NMJs are not fragmented but partially covered by myonuclei. This is evident in the insert, which shows only BGT signals of a small region. **(B)** Side view to show depth extension of fluorescence signals. The entire depth of around 500 µm of the diaphragm became transparent. **(C,D)** Depth coded side views of nuclear **(C)** and NMJ signals **(D)**. Pseudocolor code is explained on the right side.

counts in correlation to myonuclei analysis and is also compatible with diaphragm, as well as with other dyes, including lectins and antibodies. Given that the protocol is based on an initial PFA fixation step, it should be compatible with easy handling and material exchange.

Permutation of the protocol settings revealed that staining and image quality were superior if BGT labeling occurred after PFA fixation and hydrogel embedding. Since both methods (i.e., staining before or after hydrogel embedding) received ample washing steps, it is safe to assume the hydrogel either supports BGT-AF647 in a way that it can reach its target more accurately or aids in washing out unspecific BGT-AF647 signals. The present protocol presents strong autofluorescence in the blue to red fluorescence wavelength range, which is most likely due to PFA-fixation induced chromophore formation (Baschong et al., 2001). In the near infrared range, though, the autofluorescence issue was not present and thus AlexaFluo647 and Draq5 dyes worked well. Although the autofluorescence obtained in the green and red fluorescence channels might be considered a limitation of the MYOCLEAR protocol, it can also be rather useful for tracking individual muscle fibers over their whole length. Additionally, it can be used to assess pathophysiologically relevant features,

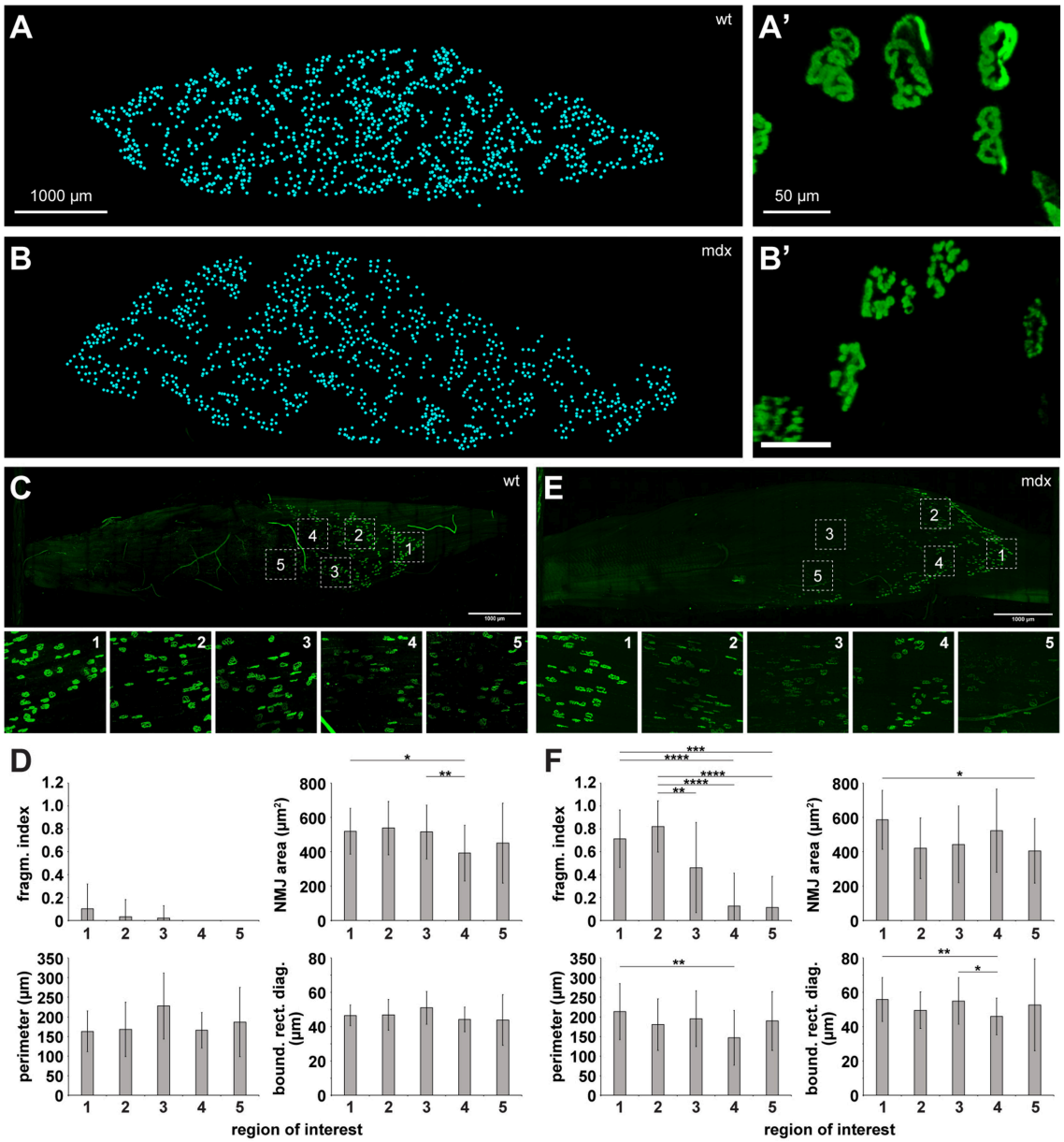


FIGURE 5 | Analysis of whole mount NMJ morphology and quantification of NMJ numbers is enabled in wildtype and mdx muscles upon clearing. EDL muscles from wildtype **(A,A',C,D)** and dystrophic mdx mice **(B,B',E,F)** were processed using the MYOCLEAR protocol and stained with BGT-AF647. **(A,B)** Maximum-z projections of all NMJs detected by hand segmentation. Each cyan spot represents a single NMJ. **(A',B')** High-power images of some representative NMJs from each muscle shown in **(A,B)**. **(C,E)** Upper panels, maximum-z projections of representative muscles showing BGT-staining signals. Lower panels, high power display of ROIs 1–5 in corresponding upper panel. **(D,F)** Quantitative analysis of key morphological parameters: area, fragmentation index, perimeter, and bounding rectangle diagonal of NMJs. Depicted are mean ± SD for all en face NMJs detected as a function of ROI number. $^{*}p < 0.05$, $^{**}p \leq 0.01$, $^{***}p \leq 0.001$, $^{****}p \leq 0.0001$.

including centro-nucleated regions, fiber atrophy, fiber splitting, the occurrence of poly-innervation, and other general structural information.

Given that most standard available fluorescence microscopy systems exhibit excitation lasers typically up to 633 nm wavelength, the use of near infrared dyes compatible with MYOCLEAR is somewhat limited. To permit at least two different structures to be simultaneously marked, we used the slightly wavelength-shifted dyes AlexaFluor647 and Draq5 in combination with spectral unmixing (Zimmermann et al., 2002). Using hand segmentation of BGT-AF647 stained and cleared EDL wholemounts, slightly more than one thousand NMJs were identified in each muscle. According to literature, the amount of muscle fibers in an adult mouse EDL ranges from 758 to 1,147 (White et al., 2010; Bloemberg and Quadrilatero, 2012). To confirm this, we performed fiber counts from our own

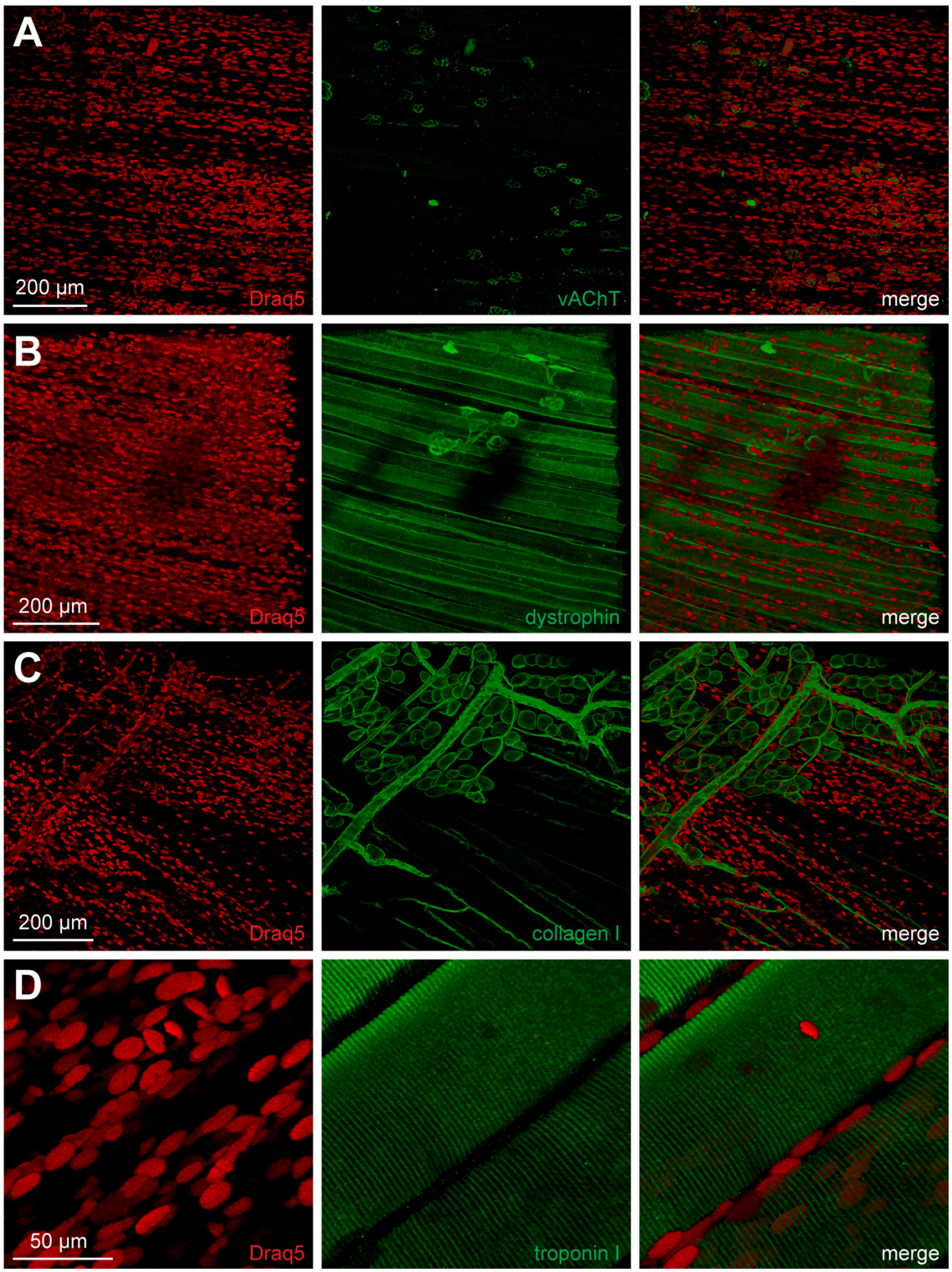


FIGURE 6 | Integrity of NMJ presynapse and other muscle structures is maintained upon clearing. Adult mouse EDL muscles were processed using the MYOCLEAR protocol and co-stained with Draq5 and antibodies against either NMJ presynapse (**A**, vAChT), sarcolemma (**B**, dystrophin), ECM (**C**, collagen I), or sarcomere (**D**, troponin I). Images show maximum-z projections of confocal z-stacks with an interplane interval of 2 µm and depths from muscle surface of 466, 665, 104, and 214 µm for **(A–D)**, respectively.

animals by analyzing cross sections of contralateral muscles. This revealed fiber numbers of 1,052 ± 42 (mean ± SD) per EDL muscle. Thus, taking into account that each muscle fiber in adult muscle is innervated by one single NMJ (Krause, 1863), this finding supports that the total number of NMJs obtained in our cleared muscles represents most, if not all, of the NMJs in the tissue. However, it must be stated that NMJs beyond a depth of about 700 to 800 μm from the surface were hardly above background and would render automated segmentation, volumetric, or in-depth morphological analyses of these synapses impossible. If such information is needed, it would be necessary to image muscles from both sides and eliminate the overlapping NMJs.

MYOCLEAR was found to retain morphological integrity of presynapse, synaptic cleft, and postsynapse. In many experimental paradigms, considerable regional heterogeneity of critical morphological parameters of the neuromuscular apparatus might be expected, such as for NMJ degeneration/regeneration in dystrophic mouse models (Haddix et al., 2018), terminal sprouting upon neurotoxin application (Wright et al., 2007; Duregotti et al., 2015), or in aging muscle (Valdez et al., 2010). Therefore, a more holistic picture of observed changes in the whole mount might yield relevant new insights. For wildtype and mdx EDL muscles, we addressed the principal applicability of our samples to study a subset of morphological criteria as recently proposed by Jones et al. (2016). This revealed differences with respect to the amplitude and regional heterogeneity of NMJ fragmentation index between wildtype and mdx, suggesting that whole mount analysis might serve as a valuable tool for future investigations of neuromuscular disorders. Certainly, immunofluorescence procedures will be a relevant asset to perform more in-depth analyses in this context. Thus, it was evaluated, whether the present clearing protocol is compatible with antibody staining. Indeed, immunostaining with all tested antibodies against presynapse (vAChT), sarcomere (troponin I), sarcolemma (dystrophin), and extracellular matrix (collagen I) yielded the expected staining patterns, although depth penetration still needs to be optimized. Apart from vAChT, which was visible beyond 500 μm deep in the tissue, the other markers were visible only for about 200–300 μm of depth. It will be necessary to examine if additional techniques for dye distribution, such as stochastic electrotransport or similar procedures (Kim et al., 2015; Nehrhoff et al., 2016) might solve the issue of penetration. Also, the limitation of MYOCLEAR to near-infrared dyes requests evaluation of further dye combinations that would be compatible with AF647 and Draq5. We tested secondary antibodies coupled to PE-Cy7, but were not successful due to low secondary antibody specificity.

In summary, future work will have to deal with skeletal muscle clearing protocols that are compatible with a wider spectral range to incorporate more than just two dyes in one sample as well as with reaching a higher depth penetration of antibodies. Furthermore, besides improving the MYOCLEAR protocol, an automated quantitative determination of NMJ numbers and characteristics, such as size and fragmentation, would likely be a major analytical request for cleared muscles. We have started to work on such automated detection algorithms, but they need further improvement before being valid. Though, **Supplementary Video S2** shows a future prospect of advantages of such an approach. It depicts a 3D view of all NMJs detected in the muscle sample shown in **Figure 5C**. Yellow-coded NMJs were detected by auto segmentation, blue NMJs were detected by hand. It is evident that three-dimensional information gives a much more plastic view on the synapse band in this muscle.

ETHICS STATEMENT

This study was carried out in accordance with the recommendations of EC directive 2010/63. The protocol was approved by the Regierungspräsidium Karlsruhe.

AUTHOR CONTRIBUTIONS

MW, MRi, TS, SH, and MRe performed the experiments and analyzed data. MW, MT, NG, MH, and RR planned experiments, contributed material, and wrote the paper.

FUNDING

RR is funded by DFG grant RU923/8-2. This work was funded by the German Federal Ministry of Research (BMBF) as part of the Innovation Partnership M^2Aind, project M^2OGA (03FH8I02IA) within the framework Starke Fachhochschulen—Impuls für die Region (FH-Impuls). MW and MRi are fellows of the graduate training group TASCDT funded by the Ministerium für Wissenschaft, Forschung und Kunst Baden-Württemberg. SH is a fellow of the Albert-und-Anneliese-Konanz Stiftung.

ACKNOWLEDGMENTS

We are grateful to the animal facility for animal care.

SUPPLEMENTARY MATERIAL

The Supplementary Material for this article can be found online at: https://www.frontiersin.org/articles/10.3389/fncel.2019.00049/full#supplementary-material

REFERENCES

Baschong, W., Suetterlin, R., and Laeng, R. H. (2001). Control of Autofluorescence of Archival Formaldehyde-fixed, Paraffin-embedded Tissue in Confocal Laser Scanning Microscopy (CLSM). *J. Histochem. Cytochem.* 49, 1565–1571. doi: 10.1177/002215540104901210

Bloemberg, D., and Quadrilatero, J. (2012). Rapid determination of myosin heavy chain expression in rat, mouse, and human skeletal muscle using multicolor immunofluorescence analysis. *PLoS ONE* 7:e35273. doi: 10.1371/journal.pone.0035273

Carnio, S., LoVerso, F., Baraibar, M. A., Longa, E., Khan, M. M., Maffei, M., et al. (2014). Autophagy impairment in muscle induces neuromuscular

junction degeneration and precocious aging. *Cell Rep.* 8, 1509–1521. doi: 10.1016/j.celrep.2014.07.061

Chen, W., Yu, T., Chen, B., Qi, Y., Zhang, P., Zhu, D., et al. (2016). *In vivo* injection of α-bungarotoxin to improve the efficiency of motor endplate labeling. *Brain Behav.* 6:e00468. doi: 10.1002/brb3.468

Chung, K., and Deisseroth, K. (2013). CLARITY for mapping the nervous system. *Nat. Methods* 10, 508–513. doi: 10.1038/nmeth.2481

Chung, K., Wallace, J., Kim, S.-Y., Kalyanasundaram, S., Andalman, A. S., Davidson, T. J., et al. (2013). Structural and molecular interrogation of intact biological systems. *Nature* 497, 332–337. doi: 10.1038/nature12107

Dobrowolny, G., Martini, M., Scicchitano, B. M., Romanello, V., Boncompagni, S., Nicoletti, C., et al. (2018). Muscle expression of *SOD1 G93A* triggers the dismantlement of neuromuscular junction *via* PKC-theta. *Antioxid. Redox Signal.* 28, 1105–1119. doi: 10.1089/ars.2017.7054

Du, H., Hou, P., Zhang, W., and Li, Q. (2018). Advances in CLARITY-based tissue clearing and imaging. *Exp. Ther. Med.* 16, 1567–1576. doi: 10.3892/etm.2018.6374

Duregotti, E., Zanetti, G., Scorzeto, M., Megighian, A., Montecucco, C., Pirazzini, M., et al. (2015). Snake and spider toxins induce a rapid recovery of function of botulinum neurotoxin paralysed neuromuscular junction. *Toxins* 7, 5322–5336. doi: 10.3390/toxins7124887

Gorio, A., Carmignoto, G., Finesso, M., Polato, P., and Nunzi, M. G. (1983). Muscle reinnervation–II. Sprouting, synapse formation and repression. *Neuroscience* 8, 403–416.

Greenbaum, A., Chan, K. Y., Dobreva, T., Brown, D., Balani, D. H., Boyce, R., et al. (2017). Bone CLARITY: clearing, imaging, and computational analysis of osteoprogenitors within intact bone marrow. *Sci. Transl. Med.* 9:eaah6518. doi: 10.1126/scitranslmed.aah6518

Haddix, S. G., Lee, Y. I., Kornegay, J. N., and Thompson, W. J. (2018). Cycles of myofiber degeneration and regeneration lead to remodeling of the neuromuscular junction in two mammalian models of Duchenne muscular dystrophy. *PLoS ONE* 13:e0205926. doi: 10.1371/journal.pone.0205926

Jones, R. A., Reich, C. D., Dissanayake, K. N., Kristmundsdottir, F., Findlater, G. S., Ribchester, R. R., et al. (2016). NMJ-morph reveals principal components of synaptic morphology influencing structure–function relationships at the neuromuscular junction. *Open Biol.* 6:160240. doi: 10.1098/rsob.160240

Khan, M. M., Lustrino, D., Silveira, W. A., Wild, F., Straka, T., Issop, Y., et al. (2016). Sympathetic innervation controls homeostasis of neuromuscular junctions in health and disease. *Proc. Natl. Acad. Sci. U.S.A.* 113, 746–750. doi: 10.1073/pnas.1524272113

Kim, S.-Y., Cho, J. H., Murray, E., Bakh, N., Choi, H., Ohn, K., et al. (2015). Stochastic electrotransport selectively enhances the transport of highly electromobile molecules. *Proc. Natl. Acad. Sci. U.S.A.* 112, E6274–E6283. doi: 10.1073/pnas.1510133112

Kleffel, S., Lee, N., Lezcano, C., Wilson, B. J., Sobolewski, K., Saab, K. R., et al. (2016). ABCB5-targeted chemoresistance reversal inhibits merkel cell carcinoma growth. *J. Invest. Dermatol.* 136, 838–846. doi: 10.1016/j.jid.2015.12.038

Krause, W. (1863). Über die endigung der muskelnerven. Zweiter artikel. *Zeitschrift. Rat. Med.* 20, 1–18.

Lee, H., Park, J.-H., Seo, I., Park, S.-H., and Kim, S. (2014). Improved application of the electrophoretic tissue clearing technology, CLARITY, to intact solid organs including brain, pancreas, liver, kidney, lung, and intestine. *BMC Dev. Biol.* 14:48. doi: 10.1186/s12861-014-0048-3

Lee, Y. I., Thompson, W. J., and Harlow, M. L. (2017). Schwann cells participate in synapse elimination at the developing neuromuscular junction. *Curr. Opin. Neurobiol.* 47, 176–181. doi: 10.1016/j.conb.2017.10.010

Lu, J., and Lichtman, J. W. (2007). Imaging the neuromuscular junction over the past centuries. *Sheng Li Xue Bao* 59, 683–696.

Lyons, P. R., and Slater, C. R. (1991). Structure and function of the neuromuscular junction in young adult mdx mice. *J. Neurocytol.* 20, 969–981.

Milgroom, A., and Ralston, E. (2016). Clearing skeletal muscle with CLARITY for light microscopy imaging. *Cell Biol. Int.* 40, 478–483. doi: 10.1002/cbin.10578

Nehrhoff, I., Bocancea, D., Vaquero, J., Vaquero, J. J., Ripoll, J., Desco, M., et al. (2016). 3D imaging in CUBIC-cleared mouse heart tissue: going deeper. *Biomed. Opt. Express.* 7, 3716–3720. doi: 10.1364/BOE.7.003716

Piñol-Jurado, P., Suárez-Calvet, X., Fernández-Simón, E., Gallardo, E., de la Oliva, N., Martínez-Muriana, A., et al. (2018). Nintedanib decreases muscle fibrosis and improves muscle function in a murine model of dystrophinopathy. *Cell Death Dis.* 9:776. doi: 10.1038/s41419-018-0792-6

Renier, N., Wu, Z., Simon, D. J., Yang, J., Ariel, P., and Tessier-Lavigne, M. (2014). iDISCO: a simple, rapid method to immunolabel large tissue samples for volume imaging. *Cell* 159, 896–910. doi: 10.1016/j.cell.2014.10.010

Röder, I. V., Strack, S., Reischl, M., Dahley, O., Khan, M. M., Kassel, O., et al. (2012). Participation of myosin Va and Pka type I in the regeneration of neuromuscular junctions. *PLoS ONE* 7:e40860. doi: 10.1371/journal.pone.0040860

Rudolf, R., Khan, M. M., Labeit, S., and Deschenes, M. R. (2014). Degeneration of neuromuscular junction in age and dystrophy. *Front. Aging. Neurosci.* 6:99. doi: 10.3389/fnagi.2014.00099

Tomer, R., Ye, L., Hsueh, B., and Deisseroth, K. (2014). Advanced CLARITY for rapid and high-resolution imaging of intact tissues. *Nat. Protoc.* 9, 1682–1697. doi: 10.1038/nprot.2014.123

Valdez, G., Tapia, J. C., Kang, H., Clemenson, G. D., Gage, F. H., Lichtman, J. W., et al. (2010). Attenuation of age-related changes in mouse neuromuscular synapses by caloric restriction and exercise. *Proc. Natl. Acad. Sci. U.S.A.* 107, 14863–14868. doi: 10.1073/pnas.1002220107

Wang, Z., Zhang, J., Fan, G., Zhao, H., Wang, X., Zhang, J., et al. (2018). Imaging transparent intact cardiac tissue with single-cell resolution. *Biomed. Opt. Express.* 9:423. doi: 10.1364/BOE.9.000423

White, R. B., Biérinx, A.-S., Gnocchi, V. F., and Zammit, P. S. (2010). Dynamics of muscle fibre growth during postnatal mouse development. *BMC Dev. Biol.* 10:21. doi: 10.1186/1471-213X-10-21

Wright, M. C., Cho, W.-J., and Son, Y.-J. (2007). Distinct patterns of motor nerve terminal sprouting induced by ciliary neurotrophic factor vs. *Botulinum toxin. J. Comp. Neurol.* 504, 1–16. doi: 10.1002/cne.21439

Wu, H., Barik, A., Lu, Y., Shen, C., Bowman, A., Li, L., et al. (2015). Slit2 as a β-catenin/Ctnnb1-dependent retrograde signal for presynaptic differentiation. *Elife* 4:e07266. doi: 10.7554/eLife.07266

Xu, N., Tamadon, A., Liu, Y., Ma, T., Leak, R. K., Chen, J., et al. (2017). Fast free-of-acrylamide clearing tissue (FACT)-an optimized new protocol for rapid, high-resolution imaging of three-dimensional brain tissue. *Sci. Rep.* 7:9895. doi: 10.1038/s41598-017-10204-5

Yang, B., Treweek, J. B. B., Kulkarni, R. P. P., Deverman, B. E. E., Chen, C.-K., Lubeck, E., et al. (2014). Single-cell phenotyping within transparent intact tissue through whole-body clearing. *Cell* 158, 945–958. doi: 10.1016/j.cell.2014.07.017

Zhang, W., Liu, S., Zhang, W., Hu, W., Jiang, M., Tamadon, A., et al. (2018). Skeletal muscle CLARITY: a preliminary study of imaging the three-dimensional architecture of blood vessels and neurons. *Cell J.* 20, 132–137. doi: 10.22074/cellj.2018.5266

Zimmermann, T., Rietdorf, J., Girod, A., Georget, V., and Pepperkok, R. (2002). Spectral imaging and linear un-mixing enables improved FRET efficiency with a novel GFP2-YFP FRET pair. *FEBS Lett.* 531, 245–249. doi: 10.1016/s0014-5793(02)03508-1

Conflict of Interest Statement: The authors declare that the research was conducted in the absence of any commercial or financial relationships that could be construed as a potential conflict of interest.

Copyright © 2019 Williams, Rigon, Straka, Hörner, Thiel, Gretz, Hafner, Reischl and Rudolf. This is an open-access article distributed under the terms of the Creative Commons Attribution License (CC BY). The use, distribution or reproduction in other forums is permitted, provided the original author(s) and the copyright owner(s) are credited and that the original publication in this journal is cited, in accordance with accepted academic practice. No use, distribution or reproduction is permitted which does not comply with these terms.

frontiers in Cellular Neuroscience

ORIGINAL RESEARCH
published: 19 March 2019
doi: 10.3389/fncel.2019.00074

Photobiomodulation and Coenzyme Q_{10} Treatments Attenuate Cognitive Impairment Associated With Model of Transient Global Brain Ischemia in Artificially Aged Mice

Farzad Salehpour[1,2,3], Fereshteh Farajdokht[1], Javad Mahmoudi[1], Marjan Erfani[1,4], Mehdi Farhoudi[1], Pouran Karimi[1], Seyed Hossein Rasta[2,5,6], Saeed Sadigh-Eteghad[1], Michael R. Hamblin[7,8,9] and Albert Gjedde[1,10,11,12,13]*

[1] Neurosciences Research Center, Tabriz University of Medical Sciences, Tabriz, Iran, [2] Department of Medical Physics, Tabriz University of Medical Sciences, Tabriz, Iran, [3] ProNeuroLIGHT LLC, Phoenix, AZ, United States, [4] Higher Educational Institute of Rab-Rashid, Tabriz, Iran, [5] Department of Medical Bioengineering, Tabriz University of Medical Sciences, Tabriz, Iran, [6] School of Medical Sciences, University of Aberdeen, Aberdeen, United Kingdom, [7] Wellman Center for Photomedicine, Massachusetts General Hospital, Boston, MA, United States, [8] Department of Dermatology, Harvard Medical School, Boston, MA, United States, [9] Harvard-MIT Health Sciences and Technology, Cambridge, MA, United States, [10] Departments of Clinical Research and Nuclear Medicine, Odense University Hospital, University of Southern Denmark, Odense, Denmark, [11] Department of Neuroscience, University of Copenhagen, Copenhagen, Denmark, [12] Department of Neurology & Neurosurgery, McGill University, Montreal, QC, Canada, [13] Department of Radiology and Radiological Science, Johns Hopkins University, Baltimore, MD, United States

OPEN ACCESS

Edited by:
Dirk M. Hermann,
University of Duisburg-Essen,
Germany

Reviewed by:
James P. Kesby,
The University of Queensland,
Australia
Jorge Matias-Guiu,
Complutense University of Madrid,
Spain

***Correspondence:**
Saeed Sadigh-Eteghad
Saeed.sadigetegad@gmail.com

Received: 25 October 2018
Accepted: 14 February 2019
Published: 19 March 2019

Citation:
Salehpour F, Farajdokht F, Mahmoudi J, Erfani M, Farhoudi M, Karimi P, Rasta SH, Sadigh-Eteghad S, Hamblin MR and Gjedde A (2019) Photobiomodulation and Coenzyme Q_{10} Treatments Attenuate Cognitive Impairment Associated With Model of Transient Global Brain Ischemia in Artificially Aged Mice. Front. Cell. Neurosci. 13:74. doi: 10.3389/fncel.2019.00074

Disturbances in mitochondrial biogenesis and bioenergetics, combined with neuroinflammation, play cardinal roles in the cognitive impairment during aging that is further exacerbated by transient cerebral ischemia. Both near-infrared (NIR) photobiomodulation (PBM) and Coenzyme Q_{10} (CoQ_{10}) administration are known to stimulate mitochondrial electron transport that potentially may reverse the effects of cerebral ischemia in aged animals. We tested the hypothesis that the effects of PBM and CoQ_{10}, separately or in combination, improve cognition in a mouse model of transient cerebral ischemia superimposed on a model of aging. We modeled aging by 6-week administration of D-galactose (500 mg/kg subcutaneous) to mice. We subsequently induced transient cerebral ischemia by bilateral occlusion of the common carotid artery (BCCAO). We treated the mice with PBM (810 nm transcranial laser) or CoQ_{10} (500 mg/kg by gavage), or both, for 2 weeks after surgery. We assessed cognitive function by the Barnes and Lashley III mazes and the What-Where-Which (WWWhich) task. PBM or CoQ_{10}, and both, improved spatial and episodic memory in the mice. Separately and together, the treatments lowered reactive oxygen species and raised ATP and general mitochondrial activity as well as biomarkers of mitochondrial biogenesis, including SIRT1, PGC-1α, NRF1, and TFAM. Neuroinflammatory responsiveness declined, as indicated by decreased iNOS, TNF-α, and IL-1β levels with the PBM

and CoQ_{10} treatments. Collectively, the findings of this preclinical study imply that the procognitive effects of NIR PBM and CoQ_{10} treatments, separately or in combination, are beneficial in a model of transient global brain ischemia superimposed on a model of aging in mice.

Keywords: transcranial photobiomodulation, Coenzyme Q_{10}, aging, global ischemia, mitochondrial biogenesis, neuroinflammation, learning and memory

INTRODUCTION

Aging is a multifactorial process characterized by progressive decline of physiological functions and potential development of a wide array of diseases (López-Otín et al., 2013). Cognitive impairment is one of the most important aspects of aging brains (Harada et al., 2013). Mitochondrial dysfunction negatively affects neuronal metabolism by means of oxidative stress. Neuroinflammation is active in normally aging brains and is implicated in subsequent cognitive decline (Bishop et al., 2010; Khorrami et al., 2014). As a consequence of the limited availability of aged animals, and the costs of obtaining and housing an adequate number of such animals for experimental studies, natural aging models can be prohibitive. As sufficient natural aging is lengthy, rapid access to aged animals is a limiting factor of pre-clinical research. As an alternative approach, we modeled natural aging by chronic administration of D-galactose to rodents. D-galactose is a reducing hexose sugar that enters the brain and reacts with many cellular components at high concentration, producing oxidative damage to lipids and DNA (Ho et al., 2003; Sadigh-Eteghad et al., 2017). The chronic D-galactose treatment induces changes that resemble natural aging and mimics several characteristics of brain aging (Wei et al., 2005; Sadigh-Eteghad et al., 2017). The administration to rodents has been shown to cause neurocognitive impairments, including memory deficits, increased inflammatory responses and mitochondrial dysfunction (Shan et al., 2009; Sadigh-Eteghad et al., 2017; Salehpour et al., 2017).

Cerebral ischemia is a major risk factor during aging with consequences for the occurrence and severity of cognitive impairment (Chen et al., 2010). Cardiovascular events such as heart attacks and strokes are more common in older individuals, and the likelihood and severity of brain damage are correspondingly higher due to mitochondrial dysfunction. Therefore, age-related structural and functional changes potentially increase the vulnerability of the brain to ischemic insults (Ueno et al., 2002). During cerebral ischemia, the reduced blood flow and the subsequent lack of oxygen, glucose, and other nutrients disturb cellular homeostasis (Chen et al., 2011). Excessive production of reactive oxygen species (ROS) in mitochondria activates signaling pathways that ultimately result in further mitochondrial dysfunction and abnormal bioenergetics (Onyango et al., 2010; Olmez and Ozyurt, 2012). Transient bilateral common carotid artery occlusion (BCCAO) is a well-established experimental approach in rodents that exploits the adverse influence of acute cerebral hypoperfusion on cognitive mechanisms (Schiavon et al., 2014).

Due to the inverse relationship between the capacity for endogenous mitochondrial biogenesis and chronological aging, the ability of the brain to recover from an ischemic insult is much reduced in older individuals (López-Lluch et al., 2008). Upstream regulators of mitochondrial biogenesis, e.g., transcription factors such as SIRT1 (silent mating-type information regulation 2 homolog 1) and PGC1-α (peroxisome proliferator-activated receptor gamma coactivator-1 alpha) play key roles in the pathophysiology of brain ischemia (Chen et al., 2011). Down-regulation of markers of mitochondrial biogenesis such as NRF1 (nuclear respiratory factor 1) and TFAM (mitochondrial transcription factor A), as well as lower numbers of mitochondria, are observed in reperfusion injury after ischemia (Liu et al., 2014). In addition, decreased cerebral blood flow (CBF) yields pro-inflammatory responses such as production of tumor necrosis factor-α (TNF-α) and interleukin (IL) IL-1β from the ischemic endothelium which leads to larger infarction volumes and exacerbates brain injury (Anrather and Iadecola, 2016). In addition, NO produced by inducible NO synthase (iNOS) in activated microglia and damaged cerebrovascular endothelium is involved in the detrimental inflammatory response to an ischemic insult (Zoppo et al., 2000). The evidence suggests that mitochondria are the key targets both of ischemic injury and brain aging (Gjedde, 2005; Reddy, 2008). Here, we exploit the knowledge that the mitochondria are targets both of aging and of ischemic insults to the brain, with a potential for development of novel therapeutic approaches based on stimulation of mitochondrial biogenesis and bioenergetics. In this study, the interventions stimulated mitochondrial biogenesis and bioenergetics by regulation of the electron transfer chain (ETC).

The first intervention of interest is an application of a low power of light. Transcranial photobiomodulation (PBM) with low-levels of red to near-infrared (NIR) light (wavelengths 600–1100 nm) has been proposed as a non-invasive method of stimulation in brain disorders (Hamblin, 2016; Salehpour and Rasta, 2017). The procognitive benefits of this light-based intervention have been observed in animal models of Alzheimer's disease (De Taboada et al., 2011) and aging (Salehpour et al., 2017), and in patients with acute stroke (Hamblin, 2017), traumatic brain injury (TBI) (Naeser et al., 2014; Morries et al., 2015), and dementia (Berman et al., 2017; Saltmarche et al., 2017). Absorption of light by mitochondrial complex IV, the cytochrome c oxidase (CCO) and subsequent increase in ATP production have been proposed as a main mechanism of action of PBM therapy (de Freitas and Hamblin, 2016), thought to act by augmentation of cerebral bioenergetics (Dong et al., 2015), inhibition of neuroinflammation (Lee et al., 2016; Salehpour et al., 2018b), and increase of antioxidant activity (Lu et al., 2017).

The second potential intervention of interest is administration of Coenzyme Q_{10} (CoQ_{10}), also known as ubiquinone, that transfers electrons from complexes I and II to complex III (Dallner and Sindelar, 2000). CoQ_{10} supplementation is held to improve mitochondrial function by promotion of ATP production (Hargreaves, 2014) and mitochondrial biogenesis (Noh et al., 2013; Khorrami et al., 2014). In neurons, the action of CoQ_{10} has been shown to protect mitochondria and lipid membranes (Somayajulu et al., 2005), as has the beneficial effect of CoQ_{10} supplementation on the inflammatory response of endothelial cells (Gao et al., 2012), and the neuroprotective properties of CoQ_{10} against learning impairment in aged animals (Mcdonald et al., 2005; Shetty et al., 2013).

Here, we test the hypothesis that the added effects of senescence modeled by D-galactose in mice followed by BCCAO can be reversed by the beneficial effects on mitochondria of NIR light PBM and CoQ_{10} supplementation (alone or in combination), as evidenced by the potential procognitive and neuroprotective actions of the interventions.

MATERIALS AND METHODS

Animals and Experimental Groups

According to the research design, 90 adult male BALB/c mice, 8–10-weeks-old and weighing 20–25 g, were purchased from Laboratory Animal Center of Tabriz University of Medical Sciences (TUOMS) Tabriz, Iran. Mice were socially housed in standard cages (five/cage), kept under controlled conditions at the temperature of 24 ± 2°C on a 12/12 h light and dark cycle, and fed standard pellet food with tap water *ad libitum*. The experiments were performed under an approved protocol of TUOMS Ethics Committee (No: IR.TBZMED.REC.1396.576) and were in accordance with NIH guidelines. After a week of adaptation, mice were randomly divided into two groups: control ($n = 15$) and the artificially aged (AA) ($n = 75$). The control group received normal saline (NS) (0.9% NaCl, 0.2 ml/mice) and the AA group received D-galactose (500 mg/kg/daily) (Sigma, St. Louis, MO, United States) by subcutaneous (s.c.) injection once per day for 6 weeks (Salehpour et al., 2017). At the end of the sixth week, mice in the AA group were divided into two groups: AA either separately ($n = 15$) or followed by transient global brain ischemia (GBI) ($n = 60$). The AA mice received sham surgery. Ischemic AA mice were then subdivided into four groups that received (I) sham PBM + vehicle gavage (AA+GBI), (II) sham PBM + CoQ_{10} gavage (CoQ_{10}), (III) real PBM + vehicle gavage (PBM), and (IV) real PBM + CoQ_{10} gavage (PBM + CoQ_{10}) ($n = 15$ per group).

We compared a vehicle-treated group of AA mice to a vehicle-treated control group (AA vs. control), and we compared a vehicle and sham-laser treated group of AA mice that we further stressed with transient GBI to the vehicle-treated group of AA mice (AA+GBI vs. AA). Three globally ischemic AA groups then received three different therapeutic interventions (CoQ_{10}, PBM, or PBM+CoQ_{10}) that we compared to a globally brain ischemic group of AA mice (AA+GBI) given only sham treatments (CoQ_{10}, PBM, or PBM+CoQ_{10} vs. AA+GBI).

Figure 1 shows the study design including procedures and time periods.

Surgery

We induced transient global cerebral ischemia with the BCCAO method as previously described (Soares et al., 2016). Briefly, animals were anesthetized with inhalation of isoflurane (4%) and intraperitoneal injection of xylazine (4 mg/kg) and maintained with 1.5% isoflurane in 70% nitrous oxide and 30% oxygen through a plastic facemask. Rectal temperature was maintained at 37°C with a heating blanket and monitored during operation. A midline anterior incision was made in the neck to expose the both common carotid arteries. Each artery was encircled with 3-0 silk thread and the vagus nerve separated. Transient global cerebral ischemia was induced by BCCAO for 20 min using microaneurysm clips (Aesculap, Germany) and CBF reduction was confirmed by laser Doppler flowmeter (LDF) (LaserFlo, Vasamedics Inc., St Paul, MN, United States). Then, anesthesia was turned off, the skin incision was sutured, and the mice were placed in a recovery cage. For sham surgery, the AA group was exposed to the same anesthetic and surgical procedures without occlusion of the carotid arteries.

Treatments

We performed the PBM therapy with a NIR laser (Thor Photomedicine, Chesham, United Kingdom) at 810 nm wavelength, 200 mW maximum output power, and 6.66 W/cm^2 irradiance with a spot size of 0.03 cm^2. The laser operated at

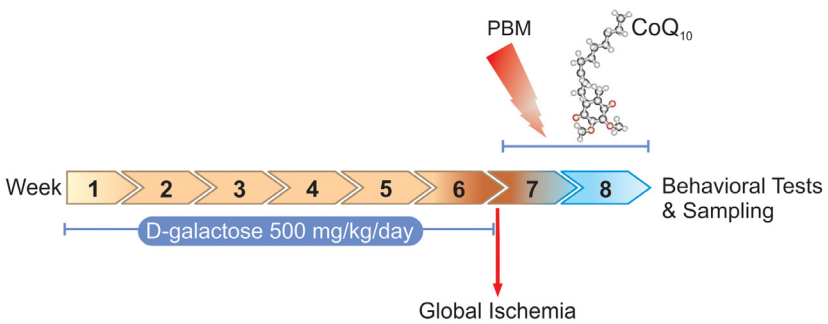


FIGURE 1 | Timescale of D-galactose administration, global ischemia induction, PBM and/or CoQ_{10} treatments, behavioral tasks, and sampling.

10-Hz PW frequency on at 88% duty cycle. For each irradiation session a total energy of 1 J (fluence of 33.3 J/cm^2) was delivered to the head (Salehpour et al., 2017). For transcranial PBM therapy, each mouse was held firmly and the laser probe was positioned over the midline of the dorsal surface of the head in region between eyes and ears. The CoQ_{10} was purchased from Sigma-Aldrich (United States). The CoQ_{10} group received the treatment (500 mg/kg/day) via gavage (Schilling et al., 2001). CoQ10 was dissolved in soybean oil as a vehicle. The combination group received the same daily dose of CoQ_{10} and treated with PBM 2 hr before the gavage.

The AA+GBI group received oral vehicle and underwent identical PBM therapy procedures except that the laser device remained inactive. All oral administrations had a volume of 8 ml/kg body weight. All treatments were applied once a day for 14 consecutive days.

Behavioral Assessments

Neurological Impairment

In order to evaluate neurological performance, mice were subjected to neurological severity score testing (NSS) on the day before starting the learning and memory tasks. The motor ability, balance, reflexes, and alertness of the animals were assessed as different aspects of neurological outcome (Beni-Adani et al., 2001). The scale ranges from 0 to 10. The intact control mice were given the score of zero (0), whereas a score of 10 reveals greatest neurological impairment. All behavioral testing was carried out by one person blinded to the experimental groups.

Barnes Maze Task

The spatial learning and memory abilities were evaluated using a Barnes task as described previously (Salehpour et al., 2017). The maze consisted of a black circular platform 100 cm in diameter with 20 evenly spaced holes located 3.0 cm from the perimeter. A movable rectangular escape box (20 × 15 × 5 cm) was located under the escape hole. The maze was placed in a quiet room where spatial cues (four basic shapes: triangle, square, circle, and horizontal rectangle) were located on the walls. Mice were encouraged to escape by a buzzer (80 dB white noise). The task procedure had three sessions including adaptation, training, and a probe trial, and took 5 days. On first day, each mouse was habituated to the task platform by gently guiding the mouse from the maze center to the target hole. The mouse was allowed to remain undisturbed in the escape box for 1 min after entering it. Each mouse then underwent 4 days of training with four 3-min trials per day, each separated by a 3-min interval. 24 h following the last training trial, a probe trial was performed, that is, the escape box was removed and the mouse was allowed to explore the maze freely for 3 min. Between trials, the maze was cleaned with 70% alcohol to remove odor cues. Trials were recorded using a digital camera mounted above the maze and the performance of mice was analyzed using a video tracking program Etho Vision^{TM} (Noldus, Netherlands). The performance during the training trials was evaluated by the latency time to find the target hole. Additionally, the time spent in the target quadrant, and correct/wrong relative time (time spent around the holes) during the probe session was calculated.

Lashley III Maze

Spatial reference memory and learning were evaluated using the Lashley III maze task, which is based on navigation with visual and food cues (Matzel et al., 2003). Briefly, the lateral walls and ceiling of the maze were constructed from black or transparent Plexiglas, respectively. The maze consisted of three separable parts including start box, maze arms, and goal box. The maze arms had four lanes that were evenly spaced along the maze. The small cup containing sugar reward was located in the goal box as motivation. Before the start of the test, mice were fasted for 12 h. Mice were moved to the testing room for 30 min prior to placement in the maze. At the beginning of testing, each mouse was placed in the start box for 15 s and then the Plexiglas sliding door was opened to allow the animal to explore the four alleys of the maze for 6 min. The trial is completed when the animal has entered the goal box at the end of the maze. Mice were trained once a day for 5 days and all experimental procedures were recorded using a digital camera and analyzed by a video tracking program Etho Vision^{TM} (Noldus, Netherlands). The learning index was measured as mean time in correct arms divided by total escape time during 5 days. The number of errors (i.e., a turn in an incorrect direction) and latency time to reach the goal box were also parameters of interest (Bressler et al., 2010).

What-Where-Which (WWWhich) Task

This task has been described in detail earlier (Salehpour et al., 2017) and is therefore described here briefly. The apparatus consisted of two different contexts, namely contexts 1 and 2, made of Plexiglas. All objects for testing were assembled from LEGO® bricks. At the beginning of the task, each mouse was habituated to each context for 5 min for 1 day. After 24 h, as an exposure session, two different objects (A and B) were first located in the context 1 and the mouse was given 3 min to explore it. Then, the mouse was returned to the cage for 30 s and the locations of the objects were switched (B and A) in the context 2. Next, the mouse was placed in the context 2 and was allowed to explore it for 3 min. The test session was carried out after a 5 min interval, when the mouse encountered two copies of one of the objects (A or B) located in one of the two contexts (1 or 2) for 3 min. Exposure and test sessions were performed in 2 trials for 2 days with new objects for each day. The total observation time (sum of time spent exploring both novel and familiar objects) and locomotor activity were videotaped and data extracted using a video tracking program Etho Vision^{TM} (Noldus, Netherlands). The episodic-like memory was defined by the discrimination index (DI) as follows: DI = (N−F)/(N+F), where N and F represent the exploration time on the novel and familiar objects, respectively.

Biochemical Assessments

Sampling and Mitochondrial Isolation

Mice were sacrificed with an overdose of ketamine (100 mg/kg) and xylazine (10 mg/kg), at 24 h after the last behavioral test. The whole brain (excluding cerebellum) was quickly taken out

from the skull and placed in ice-cold isolation buffer. Then, brain tissues were cut into small pieces and homogenized in ice-cold extraction buffer. The samples were centrifuged at 600 × *g* in 4°C for 5 min. The supernatant liquid was transferred into a new tube and centrifuged at 12,000 × *g* in 4°C for 15 min. The pellet was resuspended in storage buffer. Protein levels were determined by Bradford method (Bradford, 1976).

Mitochondrial ROS Levels

For evaluation of the ROS level in brain mitochondria, the fluorescent dye, dichlorohydro-fluorescein diacetate (DCFDA), was used (Novalija et al., 2003). The mitochondria were incubated with 2-μM DCFDA at 37°C for 20 min. The fluorescence intensity was determined (λ_{ex} = 485 nm, λ_{em} = 530 nm) in a fluorescence microplate reader. The ROS levels were represented as fluorescence intensity and normalized to samples protein.

ATP Colorimetric Assay

All procedures were done according the colorimetric assay kit (MAK190, Sigma, United States). Briefly, the homogenized brain tissue was mixed with ATP assay buffer followed by development buffer and the absorbance was measured at 570 nm. A standard curve was used to obtain the ATP concentration and presented in units of μmol per g tissue.

Mitochondrial Activity

Mitochondrial labeling was performed using MitoTracker Probes (Cell signaling, United States). The MitoTracker Green (MTG) was directly added into mitochondrial suspension (100–400 nM) and incubated for 30 min. The fluorescence intensity was determined (λ_{ex} = 490 nm, λ_{em} = 516 nm) in a fluorescence microplate reader. The mitochondrial activity was represented as fluorescence intensity and normalized to sample protein content.

Western Blotting

Cytosolic and mitochondrial proteins of interest were analyzed by Western blot method as described previously (Sadigh-Eteghad et al., 2015). Briefly, proteins were separated using 12.5% polyacrylamide gel and transferred onto a poly-vinylidene-difluoride (PVDF) membrane (Roche, United Kingdom). Membranes were incubated with anti-SIRT1 (sc-15404), PGC1-α (sc-5815), NRF1 (sc-101102), TFAM (sc-166965), iNOS (sc-8310), TNF-α (ab6671), and IL-1β (sc-7884) primary antibodies in 1:500 concentration. Finally, membranes were placed in ECL prime Western blotting detection reagent (Amersham, United Kingdom). Signals were visualized by exposure to autoradiography film (Kodak, United States). Anti-GAPDH (sc-32233) and cytochrome c (sc-13156) antibodies were used for internal control of cytosolic and mitochondrial proteins, respectively. The signal intensity of each band was quantitated using ImageJ 1.62 software (National Institutes of Health, United States).

Statistics

Descriptive data were expressed as mean ± S.E.M. Comparison of different experimental groups was carried out by a one-way ANOVA followed by the *post hoc* Tukey test. All analyses were performed using Graph Pad Prism 6.01 (Graph Pad Software Inc., La Jolla, CA, United States). A p-value < 0.05 was considered statistically significant.

RESULTS

We designed the experiments to answer two main questions: Did the cerebral ischemia further exacerbate the effects of artificial aging, and did one or more of three hypothetically beneficial interventions reverse the effects of the aging exacerbated by ischemia? The design of the interventions yielded the assessments below, as applied to each group of mice.

Behavioral Assessments

Neurological Severity

No mice in any experimental group exhibited any behavioral change, as determined by NSS test (data not shown).

Barnes Maze

Training session

The values of the animals' velocity indices revealed no statistical differences among experimental groups for all four days of the training session. The one-way ANOVA followed by Tukey test showed that AA mice delayed the finding of the escape box on the 2nd ($p < 0.05$), 3rd ($p < 0.01$), and 4th ($p < 0.05$) day. There were no significant difference between the effects of artificial aging with or without subsequent ischemia in terms of latency ($p > 0.05$). The interventions, CoQ_{10} and PBM, both separately and together, significantly reduced the latency on the 3rd and 4th days of training (separately $p < 0.05$, together 3rd day $p < 0.01$, 4th day $p < 0.001$; **Figure 2A**).

Probe session

As shown in **Figure 2B**, the AA mice spent a significantly shorter time in the target quadrant ($p < 0.01$). No significant difference was observed between the aged mice with or without added ischemia in terms of time spent in the target quadrant ($p > 0.05$), but the subsequent treatment with CoQ_{10} and PBM separately or together caused treated mice to spend more time ($p < 0.05$, $p < 0.01$, and $p < 0.001$, respectively).

The correct-to-wrong relative times significant differed between the AA and control groups ($p < 0.001$). There were no significant differences between the AA and AA+GBI groups ($p > 0.05$), but the CoQ_{10} ($p < 0.01$), PBM ($p < 0.05$), and combination ($p < 0.01$) treatments significantly increased the correct-to-wrong relative times in the probe session (**Figures 2C,D**), although the effects of the three treatments did not differ.

Lashley III Maze

As shown in **Figures 3A,D**, the mean latency to reach the goal box was significantly higher in the AA group compared to the control group on the 1st and 2nd (for both, $p < 0.001$), 3rd, 4th, and 5th (for all, $p < 0.05$) days. There were no significant differences between the AA and AA+GBI groups in terms of mean latency ($p > 0.05$). The latency time on the 2nd, 3rd, 4th, and 5th days of training were significantly decreased after CoQ_{10} ($p < 0.01$, $p < 0.01$, $p < 0.001$, and $p < 0.001$) and PBM treatments

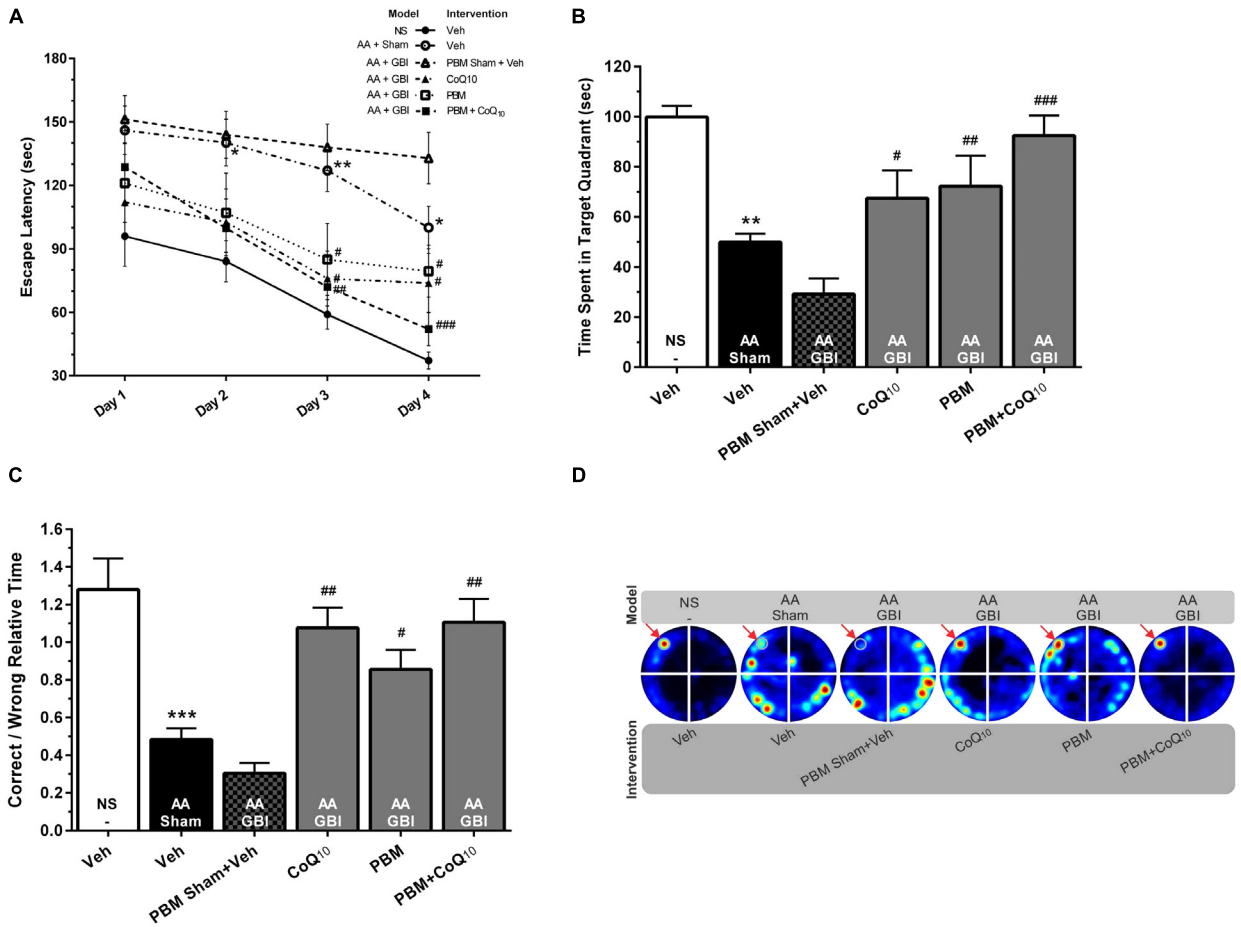


FIGURE 2 | (A) Escape latencies in training sessions in different groups. Differences among groups were analyzed for each day. **(B)** Time spent in the target quadrant and **(C)** relative error time in probe sessions in different groups. **(D)** Corresponding heat maps display the combined traces of the mice from experimental groups during the probe session. Values represent the mean ± SEM, (n = 15). $^{*}p < 0.05$, $^{**}p < 0.01$, and $^{***}p < 0.001$ compared with the NS (control). $^{\#}p < 0.05$, $^{\#\#}p < 0.01$, and $^{\#\#\#}p < 0.001$ compared with the AA + GBI. AA, artificially aged; CoQ_{10}, Coenzyme Q_{10}; GBI, global brain ischemia; NS, normal saline; PBM, photobiomodulation; Veh, Vehicle.

($p < 0.05$, $p < 0.05$, $p < 0.001$, and $p < 0.01$), respectively. In addition, the combination group showed a significant decrease in the latency on the 2nd ($p < 0.05$), 3rd ($p < 0.01$), 4th ($p < 0.001$), and 5th ($p < 0.01$) days.

The mean value of the number of errors was significantly higher in the AA group on days 2–5 days (for all, $p < 0.05$). There were no significant differences between the AA and AA+GBI groups in terms of the number of errors ($p > 0.05$). The number of errors on the 4th and 5th days of training, respectively, were decreased in CoQ_{10} ($p < 0.01$, and $p < 0.05$) and PBM (for both, $p < 0.05$) groups. In addition, the combination group showed a significant decrease in the number of errors on the 2nd and 3rd (for both, $p < 0.05$), 4th ($p < 0.001$), and 5th ($p < 0.01$) days (**Figure 3B**).

As shown in **Figure 3C**, the AA mice exhibited a lower learning index compared to control mice ($p < 0.01$). No significant difference was observed between the AA and AA+GBI groups in terms of learning index ($p > 0.05$). On the other hand, CoQ_{10} ($p < 0.01$), PBM ($p < 0.05$), and combination ($p < 0.001$) treatments significantly increased mean values of the learning index during 5-day trials.

What-Where-Which (WWWhich) Task

There were no significant differences in locomotor activity and total observation time among groups (for both, $p > 0.05$) (data not shown). Artificial aging significantly impaired the DI in comparison to the control group ($p < 0.001$), while no significant difference was observed between the AA and AA+GBI groups ($p > 0.05$). The CoQ_{10}, PBM, and combination groups notably increased the DI value as a recognition performance ($p < 0.05$, $p < 0.01$, and $p < 0.001$, respectively) (**Figure 4**).

Biochemical Assessments

Mitochondrial ROS

The cerebral mitochondrial ROS levels rose markedly in the AA group ($p < 0.001$), and rose even further in the AA+GBI group ($p < 0.01$). Both PBM and CoQ_{10} treatments, alone and

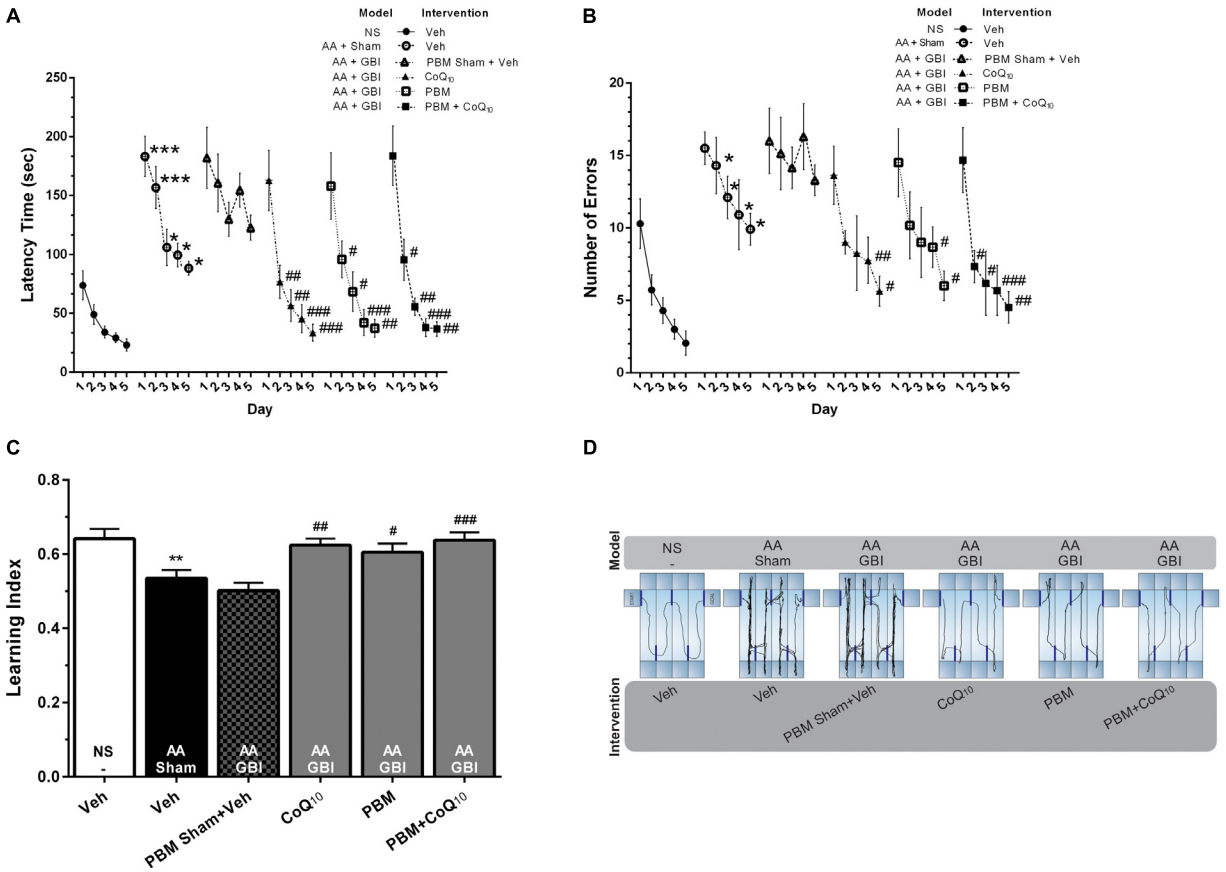


FIGURE 3 | (A) Latency times and **(B)** number of errors in different groups. Differences among groups were analyzed for each day. **(C)** Learning index in different groups. **(D)** Corresponding sample tracks display the exploratory patterns during the last day of test. Values represent the mean ± SEM, (n = 15). $^{*}p < 0.05$, $^{**}p < 0.01$, and $^{***}p < 0.001$ compared with the NS (control). $^{\#}p < 0.05$, $^{\#\#}p < 0.01$, and $^{\#\#\#}p < 0.001$ compared with the AA + GBI. AA, artificially aged; CoQ_{10}, Coenzyme Q_{10}; GBI, global brain ischemia; NS, normal saline; PBM, photobiomodulation; Veh, Vehicle.

in combination, significantly returned the ROS values to the AA group level (for all, $p < 0.001$), as shown in **Figure 5A**.

ATP

The AA group mice had significantly reduced ATP levels ($p < 0.001$), with further significant reduction in the AA+GBI group ($p < 0.05$), and the CoQ_{10} ($p < 0.05$), PBM ($p < 0.05$), and combination ($p < 0.01$), treatments significantly returned the ATP levels to the AA group level (**Figure 5B**).

Active Mitochondria Levels

There was a lower active mitochondria level in the AA group ($p < 0.01$), with no further significant decline in the AA+GBI group ($p > 0.05$). The PBM, CoQ_{10} (for both, $p < 0.05$), and in combination ($p < 0.01$) separately, markedly and equally raised the active mitochondria level (**Figure 5C**).

Western Blotting

SIRT1

SIRT1 levels were decreased in the AA group ($p < 0.001$), whereas no significant difference was observed between the AA and AA+GBI groups ($p > 0.05$). The CoQ_{10} ($p < 0.05$), PBM ($p < 0.05$), and combination ($p < 0.001$) treatments partially restored the SIRT1 levels (**Figures 6A,D**).

PGC1-α

Artificial aging significantly reduced the PGC-1α levels ($p < 0.001$). Also, the AA+GBI group exhibited significantly lower PGC-1α expression compared to the AA group ($p < 0.01$). Both CoQ_{10} and PBM groups had significantly raised PGC1-α levels ($p < 0.001$). In addition, the levels of PGC1-α were markedly upregulated in the combination group ($p < 0.001$; **Figures 6B,D**).

NRF1

Artificial aging significantly lowered NRF1 expression ($p < 0.001$) that further declined in the AA+GBI group ($p < 0.05$). The reductions were reversed by the CoQ_{10}, PBM, and combination treatments ($p < 0.05$, $p < 0.001$, and $p < 0.001$, respectively), as shown in **Figures 6C,D**.

Cytosolic TFAM

Cytosolic TFAM was decreased in the AA group ($p < 0.01$), whereas no significant difference was observed between the AA and AA+GBI groups ($p > 0.05$). Although CoQ_{10} treatment

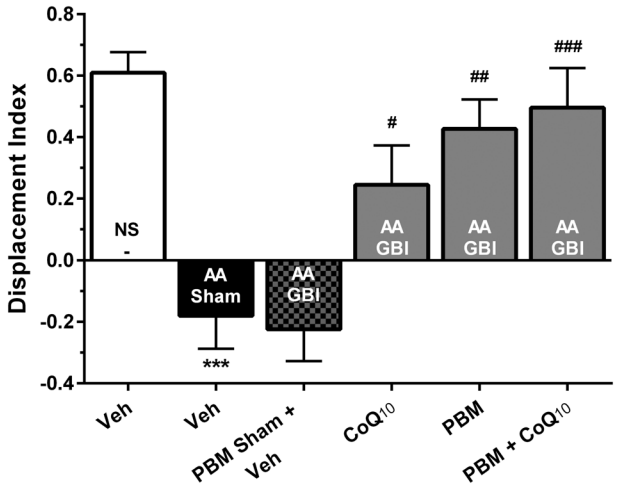


FIGURE 4 | Displacement index (DI) in different groups. Each bar represents the mean ± SEM, (n = 15). $^{***}p < 0.001$ compared with the NS (control). $^{\#}p < 0.05$, $^{\#\#}p < 0.01$, and $^{\#\#\#}p < 0.001$ compared with the AA + GBI. AA, artificially aged; CoQ_{10}, Coenzyme Q_{10}; GBI, global brain ischemia; NS, normal saline; PBM, photobiomodulation; Veh, Vehicle.

partially increased cytosolic TFAM levels ($p < 0.01$), this increase was much more pronounced in both PBM and combination treatment groups (for both, $p < 0.001$) (**Figures 7A,C**).

Mitochondrial TFAM

As shown in **Figures 7B,C**, mitochondrial TFAM was decreased in the AA group ($p < 0.05$), whereas no significant difference was observed between the AA and AA+GBI groups ($p > 0.05$). However, both PBM and CoQ_{10} treatments, alone or in combination, remarkably increased mitochondrial TFAM levels (for all, $p < 0.001$).

iNOS

The artificial aging caused a significant increase in iNOS levels ($p < 0.001$) that was further pronounced in the AA+GBI group compared to the AA group ($p < 0.05$). Both the PBM and CoQ_{10} treatments, alone and in combination, significantly reversed the effect on the iNOS levels (for all, $p < 0.001$) (**Figures 8A,D**).

*IL-1*β

As shown in **Figures 8B,D**, the AA group did not show a significant increase in IL-1β levels ($p > 0.05$). However, the AA+GBI group displayed significantly elevated IL-1β levels compared to the AA group ($p < 0.05$). On the other hand, the CoQ_{10} ($p < 0.001$), PBM ($p < 0.001$), and combination ($p < 0.01$) treatments showed significantly reduced IL-1β expression levels.

TNF-α

As shown in **Figures 8C,D**, a remarkable increase was observed in cerebral TNF-α levels in the AA group ($p < 0.001$). Also, a strong increase in TNF-α levels was observed in the AA+GBI group compared to the AA group ($p < 0.05$). However, both PBM and CoQ_{10} treatments, alone or in combination, significantly decreased TNF-α expression levels (for all, $p < 0.001$).

DISCUSSION

Here, we demonstrated significant and substantial improvements in neurobehavioral and molecular variables, including cerebral bioenergetics and mitochondrial biogenesis, as well as the neuroinflammatory response to artificial aging, in mice subjected to a model of transient global ischemia, by the PBM or CoQ_{10} treatments, or both.

Impaired mitochondrial function and inflammatory responses are considered crucial steps in the mechanisms involved in the model of brain aging induced by D-galactose (Shan et al., 2009; Kumar et al., 2010). In previous studies, aged animals were shown to be more sensitive to cerebral injury induced by an ischemic event (Canese et al., 1998; Xu et al., 2008), and transient BCCAO is known to induce an ischemia-reperfusion injury associated with oxidative damage to cortical neurons (Yabuki and Fukunaga, 2013).

Mitochondria are the principal organelles responsible for ATP generation and neuronal energy homeostasis (Onyango et al., 2010). Injured cerebrovascular endothelium in contrast is considered to be both source and target for ROS (Strasser et al., 1997). Age-related over-production of ROS results in endothelial apoptosis through oxidation of mitochondrial proteins and damage to and mutations in mitochondrial DNA (Dai and Rabinovitch, 2009). Likewise, a large body of evidence demonstrates that increased mitochondrial ROS generation follows chronic administration of D-galactose (Pratchayasakul et al., 2017), simulating the ROS generated in aging brain. Furthermore, transient reductions of CBF can deprive the brain of O_2 and glucose, further exacerbating mitochondrial dysfunction (Sakoh et al., 2000).

Cerebral ischemia is prevalent in the aged population (Chen et al., 2010). In addition, susceptibility to oxidative stress caused by ischemic injury typically is higher in the aging brain compared to the young healthy brain (Lucas and Szweda, 1998). Therefore, oxidative damage induced by ischemic brain insults in the aged population plays a cardinal role in the mitochondrial dysfunction and subsequent cognitive decline in these subjects (Fukui et al., 2002).

Based on the preliminary study using 810 nm laser light in BALB/c mice (Salehpour et al., 2017), the fluence that reaches the cortical surface is only 8 J/cm^2, when 33.3 J/cm^2 of laser fluence is delivered to the scalp. In terms of light penetration through the brain tissues of BALB/c mice, it has been reported that approximately 3% of 810 nm laser photons reach a depth in the brain of 5 mm, the distance from skull surface to substantia nigra compacta (SNc) region (Reinhart et al., 2017). Therefore, it could be presumed that in this study 0.25 J/cm^2 of NIR light reaches the brainstem, which is in the biostimulatory range for PBM therapy (Sharma et al., 2011; Moro et al., 2014).

A main mechanism of the beneficial effect of NIR PBM therapy relies on the improvement of mitochondrial function by direct stimulation of the ETC (Salehpour et al., 2018d). In this context, Lapchak and de Taboada (Lapchak and De Taboada, 2010) reported an increase in ATP content following 808 nm laser therapy and proposed this mechanism as a possible explanation for the reduction of ischemic tissue and the behavioral

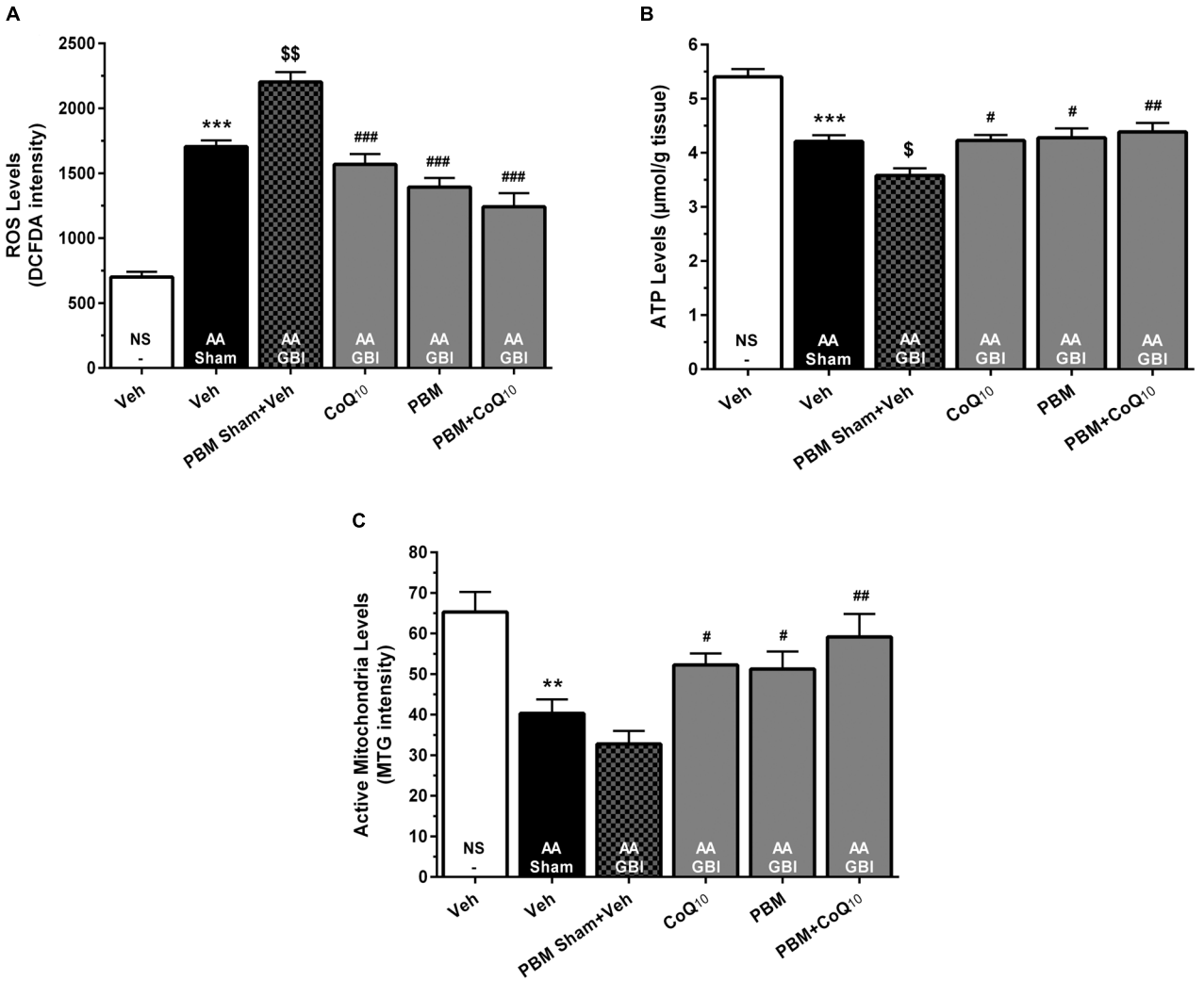


FIGURE 5 | (A) DCFDA intensity as mitochondrial ROS levels, **(B)** ATP content, and **(C)** MitoTracker Green (MTG) intensity as mitochondrial activity in brain tissue of different groups. Each bar represents the mean ± SEM, (n = 8). $^{**}p < 0.01$ and $^{***}p < 0.001$ compared with the NS (control). $^{\$}p < 0.05$ and $^{\$\$}p < 0.01$ compared with the AA.$^{\#}p < 0.05$, $^{\#\#}p < 0.01$, and $^{\#\#\#}p < 0.001$ compared with PBM- AA + GBI. AA, artificially aged; CoQ_{10}, Coenzyme Q_{10}; GBI, global brain ischemia; NS, normal saline; PBM, photobiomodulation; Veh, Vehicle.

improvements following experimentally induced stroke. Previous experiments with specific cognitive impairment models have shown that NIR PBM therapy can improve mitochondrial functions by increasing ATP (Dong et al., 2015; Salehpour et al., 2017) and mitochondrial membrane potential (MMP) (Salehpour et al., 2017), and decreasing the over-production of ROS (Dong et al., 2015; Salehpour et al., 2017, 2018c).

In the current study, NIR PBM therapy significantly affected mitochondrial dysfunction induced by global ischemia and D-galactose administration, as shown by increased ATP synthesis and suppressed ROS production. To enhance the therapeutic efficiency of PBM, we combined PBM with CoQ_{10}, a critical cofactor in the mitochondrial ETC known to improve mitochondrial function. Four weeks of CoQ_{10} supplementation exerted neuroprotection by decreasing the infarct volume of an ischemic hemisphere in aged mice (Li et al., 2007). Oral administration of CoQ_{10} for 30 days improved brain bioenergetics and reduced the effects of transient cerebral ischemia on mitochondrial function as indicated by increased O_2 consumption and ATP production (Horecky et al., 2011). It is known that CoQ_{10} acts as a potent free radical scavenger against cerebral ischemia-induced oxidative damage (Ostrowski, 2000). Thus, our results, along with others, confirm that CoQ_{10} supplementation rescues mitochondrial function and prevents brain damage produced by a model of cerebral ischemia applied to a model of aging in mice.

Altogether, data from the CoQ_{10} and PBM combination regimen demonstrated slightly better results than those of each separate treatment in terms of ATP and ROS levels. In this regard, Dong et al. (Dong et al., 2015) have shown that NIR (810 nm) PBM therapy in combination with lactate or pyruvate synergistically increased hippocampal

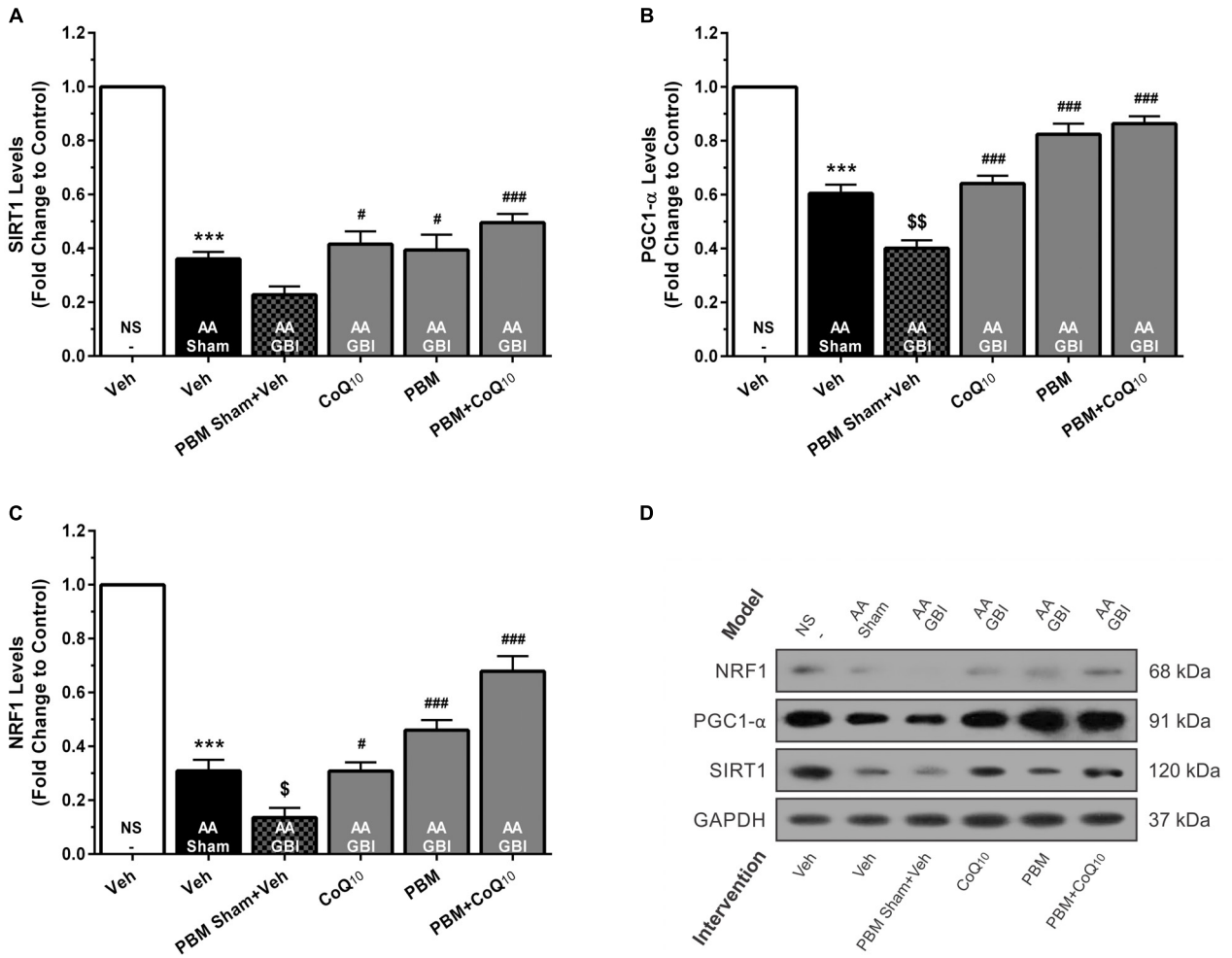


FIGURE 6 | (A) SIRT1, **(B)** PGC1-α, and **(C)** NRF1 levels in brain tissue of different groups. Each bar represents the mean ± SEM, (n = 6). $^{***}p < 0.001$ compared with the NS (control). $^{\$}p < 0.05$ and $^{\$\$}p < 0.01$ compared with the AA. $^{\#}p < 0.05$ and $^{\#\#\#}p < 0.001$ compared with AA + GBI. **(D)** Representative images of SIRT1, PGC1-α and NRF1 protein levels detected by western blot. The GAPDH was used as an internal control. AA, artificially aged; CoQ_{10}, Coenzyme Q_{10}; GBI, global brain ischemia; NRF1, nuclear respiratory factor 1; NS, normal saline; PBM, photobiomodulation; PGC1-α, peroxisome proliferator-activated receptor gamma coactivator-1 alpha; SIRT1, silent mating-type information regulation 2 homolog 1; Veh, Vehicle.

ATP levels in a mouse model of TBI. However, results from ROS levels did not show any significant differences among combination and separate treatment groups (Dong et al., 2015).

Although an exact understanding of the cellular mechanisms underlying the suppression of cerebral overproduction of ROS after PBM therapy is still missing, the upregulation of total antioxidant capacity and some individual antioxidant enzymes [such as superoxide dismutase (SOD) and glutathione peroxidase (GPx)] may contribute to the beneficial effects (Lu et al., 2017; Salehpour et al., 2018c). Besides antioxidants, SIRT1 is linked to the oxidative stress response in cerebral ischemia (Raval et al., 2008). Cellular defenses attenuate mitochondrial oxidative damage, via activation of SIRT1 in cerebral ischemic injury (Yang et al., 2015). In addition, SIRT1 directly affects PGC1-α activity via phosphorylation and deacetylation (Cantó and Auwerx, 2009). PGC1-α is a transcriptional coactivator that upregulates the aforementioned antioxidant enzymes, SOD and GPx (St-Pierre et al., 2003). Studies have shown a key role of PGC1-α-mediated ROS metabolism in cerebral ischemia (Chen et al., 2011). In this regard, a rise in PGC1-α expression level has been proposed as a protective mechanism against ROS-mediated neuronal death (St-Pierre et al., 2006). The antioxidant effect of alpha-lipoic acid through the up-regulation of SIRT1-dependent PGC1-α expression has also been reported in a rat cerebral ischemia model (Fu et al., 2014). In our study, PBM and/or CoQ_{10} significantly increased SIRT1 and PGC1-α expression, and it seems that activation of SIRT1/PGC1-α pathway could be another possible explanation for observed reduction in ROS (**Figure 9**).

Total mitochondrial contents and the integrity of mitochondrial DNA both are adversely affected by cerebral ischemia because of the increase of oxidative stress (Chen et al., 2011). Mitochondrial biogenesis alters the size and number of

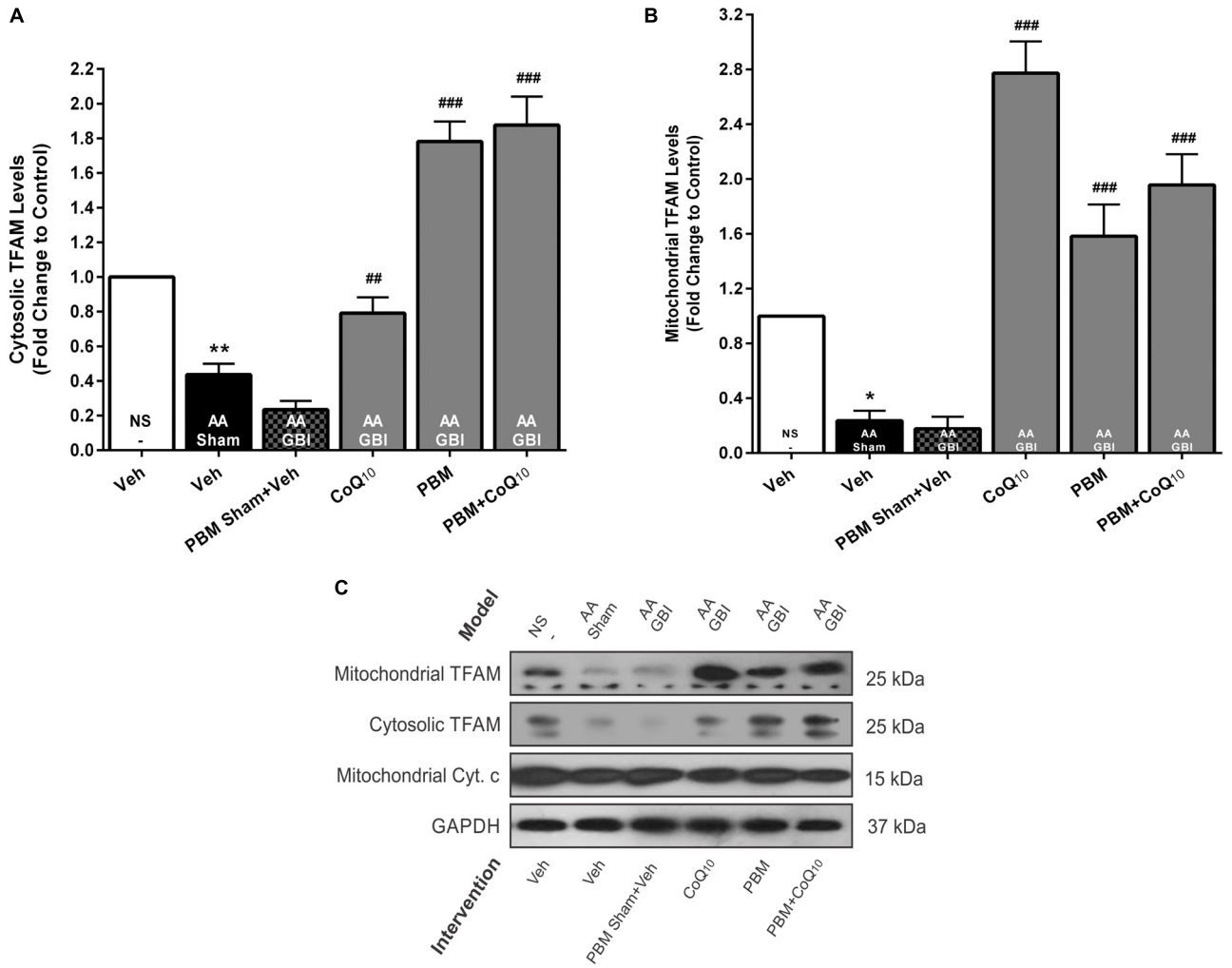


FIGURE 7 | (A) Cytosolic and **(B)** mitochondrial TFAM levels in brain tissue of different groups. Each bar represents the mean ± SEM, ($n = 6$). $^{*}p < 0.05$ and $^{**}p < 0.01$ compared with the NS (control). $^{\#\#}p < 0.01$ and $^{\#\#\#}p < 0.001$ compared with AA + GBI. **(C)** Representative images of cytosolic and mitochondrial TFAM protein levels detected by western blot. The GAPDH and Cyt. c were used as cytosolic and mitochondrial internal controls, respectively. AA, artificially aged; CoQ_{10}, Coenzyme Q_{10}; Cyt. c, cytochrome c; GBI, global brain ischemia; NS, normal saline; PBM, photobiomodulation; TFAM, mitochondrial transcription factor; Veh, Vehicle.

individual mitochondrial units. Another essential function of PGC1-α, as a master activator of mitochondrial biogenesis, is regulation of mitochondrial content via transcription factors such as NRF1 and NRF2, which in turn upregulate mitochondrial gene expression, and TFAM can affect nuclear DNA (Hock and Kralli, 2009). For instance, down-regulation of PGC1-α in aluminum-treated rats along with a decrease of NRF1 and TFAM (which act downstream from PGC1-α) resulted in decrease of mitochondrial DNA copy number and mitochondrial abundance in the hippocampus and corpus striatum regions of the brain (Sharma et al., 2013). Moreover, SIRT1 could directly interact with PGC-1α and increase its activity and expression, leading to upregulation of mitochondrial gene expression (Nemoto et al., 2005). Therefore, activation of mitochondrial biogenesis, and thus the level of mitochondrial activity in neurons, has substantial therapeutic potential since it may improve cerebral bioenergetics in both ischemic brain insults and in general aging.

Although activation of mitochondrial biogenetic regulators after PBM therapy has been reported in muscle (Nguyen et al., 2014) and mesenchymal stem cells (Yin et al., 2017), there is no reported evaluation of stimulatory effects of NIR PBM therapy on neuronal mitochondrial biogenesis in the cerebral ischemic aging model. It has been demonstrated that 4 days of NIR laser irradiation (with dual wavelengths of 808+980 nm) can induce mitochondrial biogenesis by elevation of SIRT1 and PGC-1α in C_2C_{12} muscle cells (Nguyen et al., 2014). Likewise, 660 nm light has been shown to increase the expression of mitochondrial biogenesis-associated genes including PGC-1α, NRF1, and TFAM in mesenchymal stem cells at 24 h post-irradiation (Yin et al., 2017). Increased transcription of NRF1 and TFAM through the upregulation of SIRT1 and PGC-1α expressions has also been

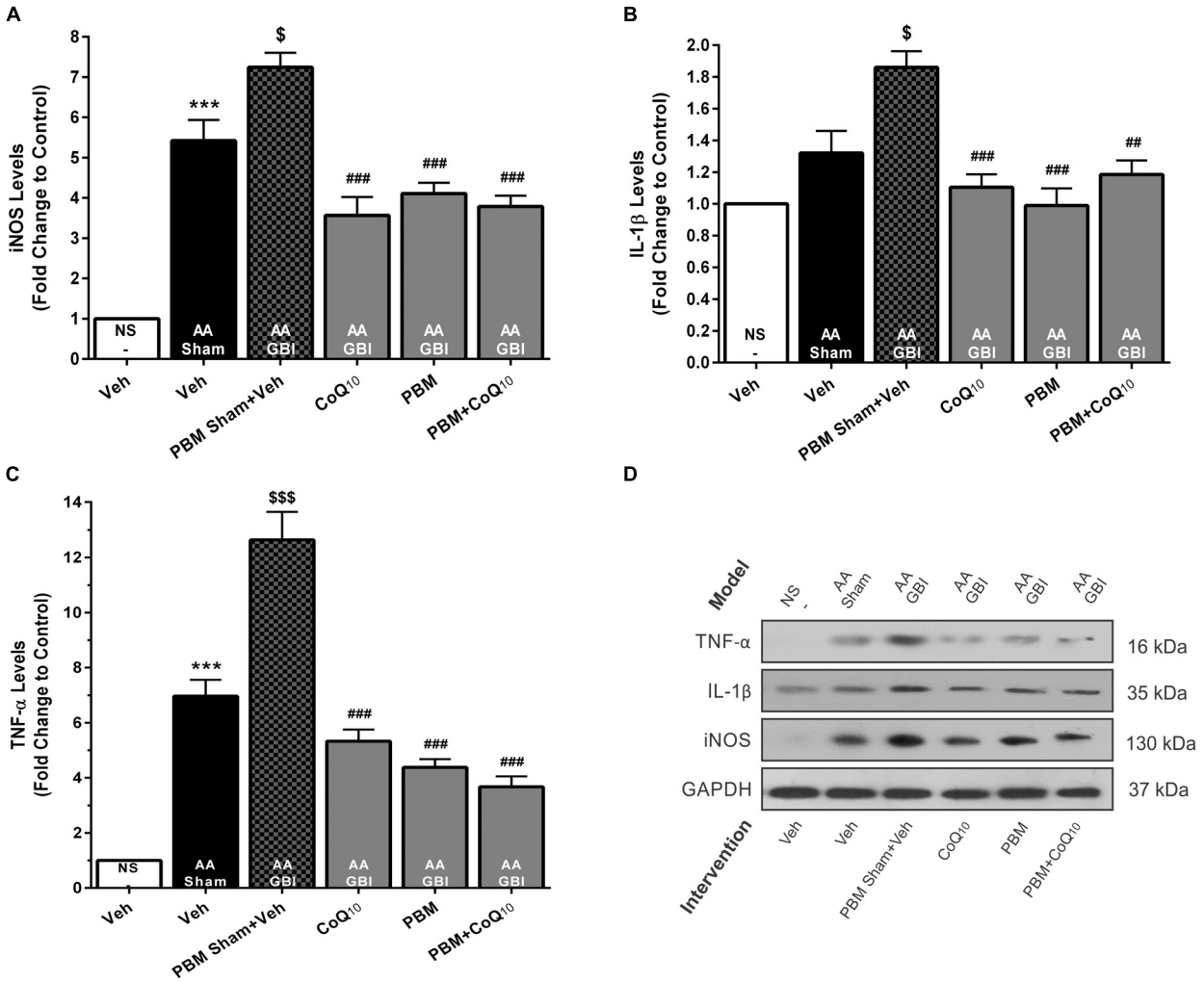


FIGURE 8 | (A) The iNOS, **(B)** IL-1β, and **(C)** TNF-α levels in brain tissue of different groups. Each bar represents the mean ± SEM, ($n = 6$). $^{***}p < 0.001$ compared with the NS (control). $^{\$}p < 0.05$ and $^{\$\$\$}p < 0.001$ compared with the AA. $^{\#\#}p < 0.01$ and $^{\#\#\#}p < 0.001$ compared with AA + GBI. **(D)** Representative images of iNOS, IL-1β, and TNF-α protein levels detected by western blot. The GAPDH was used as an internal control. AA, artificially aged; CoQ_{10}, Coenzyme Q_{10}; GBI, global brain ischemia; IL-1β, interleukin-1β; iNOS, inducible NO synthase; NS, normal saline; PBM, photobiomodulation; TFAM, mitochondrial transcription factor; TNF-α, tumor necrosis factor-α; Veh, Vehicle.

proposed for aging rat skeletal muscle following 810 nm PBM therapy (Shaafi et al., 2014).

The present data showed that both PBM and/or CoQ_{10} could remarkably activate expression of genes, which are involved in mitochondrial biogenesis. Based on the findings from this preclinical research, we suggest that stimulation of the SIRT1/PGC1-α/NRF1/TFAM signaling pathway by NIR PBM and CoQ_{10} could regulate neuronal mitochondrial biogenesis, thereby providing neuroprotection against delayed cell death after cerebral ischemia, especially in aged brains (**Figure 9**). Taken together, mitochondrial function is linked to mitochondrial content that potentially can be improved by PBM therapy. Increased mitochondrial activity in the brain following 810 nm laser irradiation has been reported by this laboratory in animal models of cognitive impairment (Salehpour et al., 2017, 2018c), in line with the present results. Likewise, 2 weeks of CoQ_{10} treatment notably augmented the mitochondrial activity. Hence, the findings provide evidence that stimulation of neuronal mitochondrial biogenesis may be one of the key mechanisms for NIR PBM and CoQ_{10} to increase mitochondrial content and/or function, thus, attenuating cognitive impairment in a model of global cerebral ischemia superimposed on a model of aging.

It is believed that microglial cells activated in response to brain ischemic insults exacerbate cerebral injury by releasing pro-inflammatory TNF-α and IL-1β (Lakhan et al., 2009). The accelerated proliferation of glial and endothelial cells after an ischemic insult results in rapid infarct development in senescent animals that display age-dependent ischemic outcomes (Popa-Wagner et al., 2007). Decreased levels of TNF-α (De Taboada et al., 2011; Lu et al., 2017; Yang et al., 2018) and IL-1β (Moreira et al., 2009; De Taboada et al., 2011; Zhang et al.,

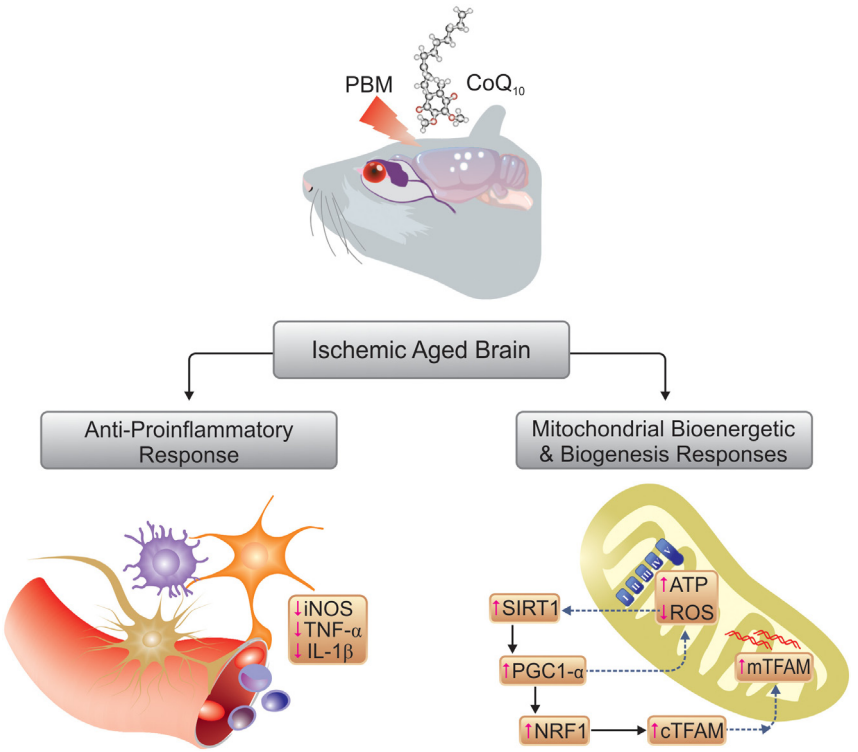


FIGURE 9 | Schematic illustration of mechanisms involved in therapeutic effects of PBM and CoQ_{10}.

2014; Lee et al., 2017; Lu et al., 2017) have been reported in specific animal brain injury models following transcranial PBM therapy. Pre-treatment with NIR PBM also resulted in significant reduction of cerebral TNF-α and IL-1β levels in ischemic mice (Lee et al., 2016). In accordance with the previous reports, our results showed increased inflammatory responses in a model of concurrent global ischemia superimposed on a model of aging in mice, while both PBM and/or CoQ_{10} partially, but significantly, attenuated the expression levels of TNF-α and IL-1β. Besides the proinflammatory cytokines, increased activity of iNOS in glia and infiltrating neutrophils leads to excessive amounts of free radicals following ischemic injury (Lakhan et al., 2009). The NO produced by iNOS within microglia and cerebrovascular endothelium is also involved in the deleterious inflammatory response occurring after ischemia (Zoppo et al., 2000). *In vitro* (Yang et al., 2010) and *in vivo* (Leung et al., 2002; Lee et al., 2016) studies support the idea that the anti-neuroinflammatory effects of transcranial PBM therapy may at least partly be due to its ability to modulate iNOS activity. In addition, CoQ_{10} treatment has been reported to attenuate hippocampal TNF-α levels in a pentylenetetrazole-induced cognitive dysfunction model (Bhardwaj and Kumar, 2016), and this finding is in good agreement with our data (**Figure 9**). Moreover, a study by Tsai et al. (Tsai et al., 2012) showed that CoQ_{10} could protect human endothelial cells from oxidative stress via decreasing iNOS expression.

To test whether PBM and/or CoQ_{10} protected against global ischemia-induced cognitive impairment performance in our aged-mouse model, we evaluated the animals in a test of spatial and episodic-like memories. Since the hippocampus plays a key role in the consolidation of memories related to spatial navigation, we subjected mice to the Barnes and Lashley III mazes as hippocampus-dependent spatial learning and memory tasks. The data showed that administration of D-galactose and global ischemia induction together significantly impaired spatial learning and memory, which is in line with previous reports (Xu et al., 2000; Sadigh-Eteghad et al., 2017; Salehpour et al., 2017). On the other hand, 2 weeks of PBM and/or CoQ_{10} treatments significantly reversed this deficiency. The procognitive benefits of NIR PBM therapy to spatial memory have been shown with the Morris water maze (De Taboada et al., 2011; Dong et al., 2015) and Barnes maze (Lu et al., 2017; Salehpour et al., 2017, 2018c) in different animal models. It is well established that the hippocampal bioenergetic capacity and neuronal survival are linked to spatial memory and learning (Sadowski et al., 2004).

In this study, we tentatively conclude that augmentation of brain bioenergetic capacity and the accompanying neuroprotective effects were reflected in improved learning and memory performances in both NIR PBM and CoQ10 treated mice. We observed that NIR PBM therapy notably improved the episodic memory of the D-galactose-treated mice in the BCCAO model of cerebral ischemia. This result is in line with previous reports of Lu et al. (Lu et al., 2017) and Salehpour et al. (Salehpour et al., 2017, 2018c) who demonstrated enhanced recognition memory after transcranial 810-nm

laser therapy. Moreover, CoQ_{10} supplementation significantly rescued recognition memory as indicated by higher DI which is in line with other work (Llewellyn et al., 2015).

Since both chronic injection of D-galactose and subjection of animals to global cerebral ischemia result in systemic damage to the brain and nervous system, we examined the whole brain for possible neurochemical alterations. Furthermore, to test whether treatments protected against global ischemia-induced cognitive decline in the aged animal model, we subjected mice to the Barnes maze and Lashley III maze (as hippocampus-dependent spatial learning and memory tasks) and the WWWhich task (as a prefrontal cortex-dependent episodic memory task).

We note that the Red/NIR light propagation in the brain raises an important issue for purposes of treatment. Lambert-Beer's law explains attenuation of photon propagation in biological media. Most recently, we showed that approximately 1% of the light incident onto the scalp surface reaches a 1-mm depth from the cortical surface, penetrating the dorsal hippocampus of the mouse, when a laser beam is focused on the bregma, (Salehpour et al., 2018a). Therefore, in the current study, we assumed that the cortical neurons and upper layers of the hippocampus received more photons than deeper structures (i.e., thalamus and hypothalamus). Given this, we also assumed that the neurochemical effects would be stronger if only the hippocampus had been sampled. However, further studies are needed to gain more insight into specific brain regions (i.e., hippocampus, prefrontal cortex, and amygdala) that are affected by PBM therapy of cognitive impairment.

Although the administration of CoQ_{10} affects brain function systemically and globally, the upper cortical layers are mainly affected by transcranial PBM therapy due to the aforementioned biophysical properties. Hence, the restricted light penetration is a potential interpretative limitation of the studies (brain and non-brain tissues) of possible synergistic effects of the combination of PBM therapy and pharmacotherapy strategies.

CONCLUSION

We conclude that NIR PBM combined with CoQ_{10} had multiple mechanisms of action, targeting mitochondrial bioenergetics and biogenesis as well as anti-neuroinflammation in this model of ischemic brain damage in AA animals. The present study suggests that the PBM and CoQ_{10} treatments, alone or in combination, have procognitive effect in ischemic damage to aged brains of mice. It is noteworthy that the translation of the concepts of the current study in terms of models and conditions into humans is challenging. However, considering the number of elderly patients that sustain significant brain damage following a heart attack or ischemic stroke each year, it makes sense to test this relatively inexpensive and completely non-hazardous intervention (or combination of interventions) in humans. Further complementary preclinical and clinical studies are warranted for clarification of other potential applications in this area.

AUTHOR CONTRIBUTIONS

FS, FF, ME, JM, PK, and SR performed the experiments, interpreted the results, and wrote the first draft manuscript. SS-E and MF designed the experiments. SS-E, MH and AG critically interpreted data and critically revised and approved the manuscript.

FUNDING

This research was supported by a grant from Neurosciences Research Center – Tabriz University of Medical Sciences, (Grant No. 58782) to SS-E, and publication grants from Danish Alzheimer Foundation and University of Southern Denmark to AG. MH was supported by United States NIH grant R01AI050875.

REFERENCES

Anrather, J., and Iadecola, C. (2016). Inflammation and stroke: an overview. *Neurotherapeutics* 13, 661–670. doi: 10.1007/s13311-016-0483-x

Beni-Adani, L., Gozes, I., Cohen, Y., Assaf, Y., Steingart, R. A., Brenneman, D. E., et al. (2001). A peptide derived from activity-dependent neuroprotective protein (ADNP) ameliorates injury response in closed head injury in mice. *J. Pharmacol. Exp. Ther.* 296, 57–63.

Berman, M. H., Halper, J. P., Nichols, T. W., Jarrett, H., Lundy, A., and Huang, J. H. (2017). Photobiomodulation with near infrared light helmet in a pilot, placebo controlled clinical trial in dementia patients testing memory and cognition. *J. Neurol. Neurosci.* 8:176. doi: 10.21767/2171-6625.1000176

Bhardwaj, M., and Kumar, A. (2016). Neuroprotective mechanism of Coenzyme Q10 (CoQ10) against PTZ induced kindling and associated cognitive dysfunction: possible role of microglia inhibition. *Pharmacol. Rep.* 68, 1301–1311. doi: 10.1016/j.pharep.2016.07.005

Bishop, N. A., Lu, T., and Yankner, B. A. (2010). Neural mechanisms of ageing and cognitive decline. *Nature* 464, 529–535. doi: 10.1038/nature08983

Bradford, M. M. (1976). A rapid and sensitive method for the quantitation of microgram quantities of protein utilizing the principle of protein-dye binding. *Anal. Biochem.* 72, 248–254.

Bressler, A., Blizard, D., and Andrews, A. (2010). Low-stress route learning using the Lashley III maze in mice. *J. Vis. Exp.* 39:1786. doi: 10.3791/1786

Canese, R., Fortuna, S., Lorenzini, P., Podo, F., and Michalek, H. (1998). Transient global brain ischemia in young and aged rats: differences in severity and progression, but not localisation, of lesions evaluated by magnetic resonance imaging. *MAGMA* 7, 28–34.

Cantó, C., and Auwerx, J. (2009). Caloric restriction, SIRT1 and longevity. *Trends. Endocrinol. Metab.* 20, 325–331. doi: 10.1016/j.tem.2009.03.008

Chen, R. L., Balami, J. S., Esiri, M. M., Chen, L. K., and Buchan, A. M. (2010). Ischemic stroke in the elderly: an overview of evidence. *Nat. Rev. Neurol.* 6, 256–265.

Chen, S. D., Yang, D. I., Lin, T. K., Shaw, F. Z., Liou, C. W., and Chuang, Y. C. (2011). Roles of oxidative stress, apoptosis, PGC-1α and mitochondrial biogenesis in cerebral ischemia. *Int. J. Mol. Sci.* 12, 7199–7215.

Dai, D. F., and Rabinovitch, P. S. (2009). Cardiac aging in mice and humans: the role of mitochondrial oxidative stress. *Trends Cardiovasc. Med.* 19, 213–220. doi: 10.1016/j.tcm.2009.12.004

Dallner, G., and Sindelar, P. J. (2000). Regulation of ubiquinone metabolism. *Free Radic. Biol. Med.* 29, 285–294.

de Freitas, L. F., and Hamblin, M. R. (2016). Proposed mechanisms of photobiomodulation or low-level light therapy. *IEEE J. Sel.*

Top. Quantum Electron. 22, 348–364. doi: 10.1109/JSTQE.2016.2561201

De Taboada, L., Yu, J., El-Amouri, S., Gattoni-Celli, S., Richieri, S., McCarthy, T., et al. (2011). Transcranial laser therapy attenuates amyloid-β peptide neuropathology in amyloid-β protein precursor transgenic mice. *J. Alzheimers Dis.* 23, 521–535. doi: 10.3233/JAD-2010-100894

Dong, T., Zhang, Q., Hamblin, M. R., and Wu, M. X. (2015). Low-level light in combination with metabolic modulators for effective therapy of injured brain. *J. Cereb. Blood Flow Metab.* 35, 1435–1444. doi: 10.1038/jcbfm.2015.87

Fu, B., Zhang, J., Zhang, X., Zhang, C., Li, Y., Zhang, Y., et al. (2014). Alpha-lipoic acid upregulates SIRT1-dependent PGC-1α expression and protects mouse brain against focal ischemia. *Neuroscience* 281, 251–257. doi: 10.1016/j.neuroscience.2014.09.058

Fukui, K., Omoi, N. O., Hayasaka, T., Shinnkai, T., Suzuki, S., Abe, K., et al. (2002). Cognitive impairment of rats caused by oxidative stress and aging, and its prevention by vitamin E. *Ann. N. Y. Acad. Sci.* 959, 275–284.

Gao, L., Mao, Q., Cao, J., Wang, Y., Zhou, X., and Fan, L. (2012). Effects of coenzyme Q10 on vascular endothelial function in humans: a meta-analysis of randomized controlled trials. *Atherosclerosis* 221, 311–316. doi: 10.1016/j.atherosclerosis.2011.10.027

Gjedde, A. (2005). The pathways of oxygen in brain II: competitions for cytochrome c oxidase and nos are keys to flow-metabolism coupling. *Adv. Exp. Med. Biol.* 566, 277–284.

Hamblin, M. R. (2016). Shining light on the head: photobiomodulation for brain disorders. *BBA Clin.* 6, 113–124.

Hamblin, M. R. (2017). Photobiomodulation for traumatic brain injury and stroke. *J. Neurosci. Res.* 96, 731–743. doi: 10.1002/jnr.24190

Harada, C. N., Love, M. C. N., and Triebel, K. (2013). Normal cognitive aging. *Clin. Geriatr. Med.* 29, 737–752. doi: 10.1016/j.cger.2013.07.002

Hargreaves, I. (2014). Coenzyme Q 10 as a therapy for mitochondrial disease. *Int. J. Biochem. Cell Biol.* 49, 105–111. doi: 10.1016/j.biocel.2014.01.020

Ho, S. C., Liu, J. H., and Wu, R. Y. (2003). Establishment of the mimetic aging effect in mice caused by D-galactose. *Biogerontology* 4, 15–18.

Hock, M. B., and Kralli, A. (2009). Transcriptional control of mitochondrial biogenesis and function. *Annu. Rev. Physiol.* 71, 177–203. doi: 10.1146/annurev.physiol.010908.163119

Horecky, J., Gvozdjáková, A., Kucharská, J., Obrenovich, M. E., Palacios, H. H., Li, Y., et al. (2011). Effects of coenzyme Q and creatine supplementation on brain energy metabolism in rats exposed to chronic cerebral hypoperfusion. *Curr. Alzheimer Res.* 8, 868–875.

Khorrami, A., Ghanbarzadeh, S., Mahmoudi, J., Nayebi, A., Maleki-Dizaji, N., and Garjani, A. (2014). Investigation of the memory impairment in rats fed with oxidized-cholesterol-rich diet employing passive avoidance test. *Drug Res.* 65, 231–237. doi: 10.1055/s-0034-1370950

Kumar, A., Prakash, A., and Dogra, S. (2010). Naringin alleviates cognitive impairment, mitochondrial dysfunction and oxidative stress induced by D-galactose in mice. *Food Chem. Toxicol.* 48, 626–632. doi: 10.1016/j.fct.2009.11.043

Lakhan, S. E., Kirchgessner, A., and Hofer, M. (2009). Inflammatory mechanisms in ischemic stroke: therapeutic approaches. *J. Transl. Med.* 7:97. doi: 10.1186/1479-5876-7-97

Lapchak, P. A., and De Taboada, L. (2010). Transcranial near infrared laser treatment (NILT) increases cortical adenosine-5'-triphosphate (ATP) content following embolic strokes in rabbits. *Brain Res.* 1306, 100–105. doi: 10.1016/j.brainres.2009.10.022

Lee, H. I., Lee, S. W., Kim, N. G., Park, K. J., Choi, B. T., Shin, Y. I., et al. (2017). Low-level light emitting diode (LED) therapy suppresses inflammasome-mediated brain damage in experimental ischemic stroke. *J. Biophotonics* 10, 1502–1513. doi: 10.1002/jbio.201600244

Lee, H. I., Park, J. H., Park, M. Y., Kim, N. G., Park, K. J., Choi, B. T., et al. (2016). Pre-conditioning with transcranial low-level light therapy reduces neuroinflammation and protects blood-brain barrier after focal cerebral ischemia in mice. *Restor. Neurol. Neurosci.* 34, 201–214. doi: 10.3233/RNN-150559

Leung, M. C., Lo, S. C., Siu, F. K., and So, K. F. (2002). Treatment of experimentally induced transient cerebral ischemia with low energy laser inhibits nitric oxide synthase activity and up-regulates the expression of transforming growth factor-beta 1. *Lasers Surg. Med.* 31, 283–288.

Li, G., Zou, L., Jack, C. R., Yang, Y., and Yang, E. S. (2007). Neuroprotective effect of Coenzyme Q10 on ischemic hemisphere in aged mice with mutations in the amyloid precursor protein. *Neurobiol. Aging* 28, 877–882.

Liu, L., Zhang, W., Wang, L., Li, Y., Tan, B., Lu, X., et al. (2014). Curcumin prevents cerebral ischemia reperfusion injury via increase of mitochondrial biogenesis. *Neurochem. Res.* 39, 1322–1331. doi: 10.1007/s11064-014-1315-1

Llewellyn, K. J., Nalbandian, A., Gomez, A., Wei, D., Walker, N., and Kimonis, V. E. (2015). Administration of CoQ 10 analogue ameliorates dysfunction of the mitochondrial respiratory chain in a mouse model of Angelman syndrome. *Neurobiol. Dis.* 76, 77–86.

López-Lluch, G., Irusta, P. M., Navas, P., and de Cabo, R. (2008). Mitochondrial biogenesis and healthy aging. *Exp. Gerontol.* 43, 813–819. doi: 10.1016/j.exger.2008.06.014

López-Otín, C., Blasco, M. A., Partridge, L., Serrano, M., and Kroemer, G. (2013). The hallmarks of aging. *Cell* 153, 1194–1217. doi: 10.1016/j.cell.2013.05.039

Lu, Y., Wang, R., Dong, Y., Tucker, D., Zhao, N., Ahmed, M. E., et al. (2017). Low-level laser therapy for beta amyloid toxicity in rat hippocampus. *Neurobiol. Aging* 49, 165–182. doi: 10.1016/j.neurobiolaging.2016.10.003

Lucas, D. T., and Szweda, L. I. (1998). Cardiac reperfusion injury: aging, lipid peroxidation, and mitochondrial dysfunction. *Proc. Natl. Acad. Sci. U.S.A.* 95, 510–514.

Matzel, L. D., Han, Y. R., Grossman, H., Karnik, M. S., Patel, D., Scott, N., et al. (2003). Individual differences in the expression of a "general" learning ability in mice. *Int. J. Neurosci.* 23, 6423–6433.

Mcdonald, S. R., Sohal, R. S., and Forster, M. J. (2005). Concurrent administration of coenzyme Q 10 and α-tocopherol improves learning in aged mice. *Free Radic. Biol. Med.* 38, 729–736.

Moreira, M. S., Velasco, I. T., Ferreira, L. S., Ariga, S. K. K., Barbeiro, D. F., Meneguzzo, D. T., et al. (2009). Effect of phototherapy with low intensity laser on local and systemic immunomodulation following focal brain damage in rat. *J. Photochem. Photobiol. B* 97, 145–151. doi: 10.1016/j.jphotobiol.2009.09.002

Moro, C., Massri, N. E., Torres, N., Ratel, D., De Jaeger, X., Chabrol, C., et al. (2014). Photobiomodulation inside the brain: a novel method of applying near-infrared light intracranially and its impact on dopaminergic cell survival in MPTP-treated mice. *J. Neurosurg.* 120, 670–683. doi: 10.3171/2013.9.JNS13423

Morries, L. D., Cassano, P., and Henderson, T. A. (2015). Treatments for traumatic brain injury with emphasis on transcranial near-infrared laser phototherapy. *Neuropsychiatr. Dis. Treat.* 11, 2159–2175. doi: 10.2147/NDT.S65809

Naeser, M. A., Zafonte, R., Krengel, M. H., Martin, P. I., Frazier, J., Hamblin, M. R., et al. (2014). Significant improvements in cognitive performance post-transcranial, red/near-infrared light-emitting diode treatments in chronic, mild traumatic brain injury: open-protocol study. *Korean J. Neurotrauma* 31, 1008–1017. doi: 10.1089/neu.2013.3244

Nemoto, S., Fergusson, M. M., and Finkel, T. (2005). SIRT1 functionally interacts with the metabolic regulator and transcriptional coactivator PGC-1α. *J. Biol. Chem.* 280, 16456–16460.

Nguyen, L. M., Malamo, A. G., Larkin-Kaiser, K. A., Borsa, P. A., and Adhihetty, P. J. (2014). Effect of near-infrared light exposure on mitochondrial signaling in C 2 C 12 muscle cells. *Mitochondrion* 14, 42–48. doi: 10.1016/j.mito.2013.11.001

Noh, Y., Kim, K., Shim, M., Choi, S., Choi, S., Ellisman, M., et al. (2013). Inhibition of oxidative stress by coenzyme Q10 increases mitochondrial mass and improves bioenergetic function in optic nerve head astrocytes. *Cell Death Dis.* 4:e820. doi: 10.1038/cddis.2013.341

Novalija, E., Kevin, L. G., Eells, J. T., Henry, M. M., and Stowe, D. F. (2003). Anesthetic preconditioning improves adenosine triphosphate synthesis and reduces reactive oxygen species formation in mitochondria after ischemia by a redox dependent mechanism. *J. Am. Soc. Anesthesiol.* 98, 1155–1163.

Olmez, I., and Ozyurt, H. (2012). Reactive oxygen species and ischemic cerebrovascular disease. *Neurochem. Int.* 60, 208–212. doi: 10.1016/j.neuint.2011.11.009

Onyango, I. G., Lu, J., Rodova, M., Lezi, E., Crafter, A. B., and Swerdlow, R. H. (2010). Regulation of neuron mitochondrial biogenesis and relevance to brain health. *Biochim. Biophys. Acta* 1802, 228–234. doi: 10.1016/j.bbadis.2009.07.014

Ostrowski, R. P. (2000). Effect of coenzyme Q 10 on biochemical and morphological changes in experimental ischemia in the rat brain. *Brain Res. Bull.* 53, 399–407.

Popa-Wagner, A., Badan, I., Walker, L., Groppa, S., Patrana, N., and Kessler, C. (2007). Accelerated infarct development, cytogenesis and apoptosis

following transient cerebral ischemia in aged rats. *Acta Neuropathol.* 113, 277–293.

Pratchayasakul, W., Chattipakorn, N., and Chattipakorn, S. C. (2017). Role of D-galactose-induced brain aging and its potential used for therapeutic interventions. *Exp. Gerontol.* 101, 13–36. doi: 10.1016/j.exger.2017.10.029

Raval, A. P., Lin, H. W., Dave, K. R., DeFazio, R. A., Morte, D. D., Kim, E. J., et al. (2008). Resveratrol and ischemic preconditioning in the brain. *Curr. Med. Chem.* 15, 1545–1551.

Reddy, P. H. (2008). Mitochondrial medicine for aging and neurodegenerative diseases. *Neuromolecular Med.* 10, 291–315. doi: 10.1007/s12017-008-8044-z

Reinhart, F., El Massri, N., Torres, N., Chabrol, C., Molet, J., Johnstone, D. M., et al. (2017). The behavioural and neuroprotective outcomes when 670 nm and 810 nm near infrared light are applied together in MPTP-treated mice. *Neurosci. Res.* 117, 42–47. doi: 10.1016/j.neures.2016.11.006

Sadigh-Eteghad, S., Majdi, A., McCann, S. K., Mahmoudi, J., Vafaee, M. S., and Macleod, M. R. (2017). D-galactose-induced brain ageing model: a systematic review and meta-analysis on cognitive outcomes and oxidative stress indices. *PLoS One* 12:e0184122. doi: 10.1371/journal.pone.0184122

Sadigh-Eteghad, S., Talebi, M., Mahmoudi, J., Babri, S., and Shanehbandi, D. (2015). Selective activation of α 7 nicotinic acetylcholine receptor by PHA-543613 improves Aβ 25–35-mediated cognitive deficits in mice. *Neuroscience* 298, 81–93.

Sadowski, M., Pankiewicz, J., Scholtzova, H., Ji, Y., Quartermain, D., Jensen, C. H., et al. (2004). Amyloid-β deposition is associated with decreased hippocampal glucose metabolism and spatial memory impairment in APP/PS1 mice. *J. Neuropathol. Exp. Neurol.* 63, 418–428.

Sakoh, M., Røhl, L., Gyldensted, C., Gjedde, A., and Østergaard, L. (2000). Cerebral blood flow and blood volume measured by magnetic resonance imaging bolus tracking after acute stroke in pigs. *Stroke* 31, 1958–1964.

Salehpour, F., Ahmadian, N., Rasta, S. H., Farhoudi, M., Karimi, P., and Sadigh-Eteghad, S. (2017). Transcranial low-level laser therapy improves brain mitochondrial function and cognitive impairment in D-galactose–induced aging mice. *Neurobiol. Aging* 58, 140–150.

Salehpour, F., De Taboada, L., Cassano, P., Kamari, F., Mahmoudi, J., Ahmadi-Kandjani, S., et al. (2018a). A protocol for transcranial photobiomodulation therapy in mice. *Vis. Exp.* 141:e59076.

Salehpour, F., Farajdokht, F., Cassano, P., Sadigh-Eteghad, S., Erfani, M., Hamblin, M. R., et al. (2018b). Near-infrared photobiomodulation combined with coenzyme Q10 for depression in a mouse model of restraint stress: reduction in oxidative stress, neuroinflammation, and apoptosis. *Brain Res. Bull.* 144, 213–222. doi: 10.1016/j.brainresbull.2018.10.010

Salehpour, F., Farajdokht, F., Erfani, M., Sadigh-Eteghad, S., Shotorbani, S. S., Hamblin, M. R., et al. (2018c). Transcranial near-infrared photobiomodulation attenuates memory impairment and hippocampal oxidative stress in sleep-deprived mice. *Brain Res.* 1682, 36–43. doi: 10.1016/j.brainres.2017.12.040

Salehpour, F., Mahmoudi, J., Kamari, F., Sadigh-Eteghad, S., Rasta, S. H., and Hamblin, M. R. (2018d). Brain photobiomodulation therapy: a narrative review. *Mol. Neurobiol.* 55, 6601–6636. doi: 10.1007/s12035-017-0852-4

Salehpour, F., and Rasta, S. H. (2017). The potential of transcranial photobiomodulation therapy for treatment of major depressive disorder. *Rev. Neurosci.* 28, 441–453. doi: 10.1515/revneuro-2016-0087

Saltmarche, A. E., Naeser, M. A., Ho, K. F., Hamblin, M. R., and Lim, L. (2017). Significant improvement in cognition in mild to moderately severe dementia cases treated with transcranial plus intranasal photobiomodulation: case series report. *Photomed. Laser Surg.* 35, 432–441. doi: 10.1089/pho.2016.4227

Schiavon, A. P., Soares, L. M., Bonato, J. M., Milani, H., Guimaraes, F. S., and de Oliveira, R. M. W. (2014). Protective effects of cannabidiol against hippocampal cell death and cognitive impairment induced by bilateral common carotid artery occlusion in mice. *Neurotox. Res.* 26, 307–316. doi: 10.1007/s12640-014-9457-0

Schilling, G., Coonfield, M. L., Ross, C. A., and Borchelt, D. R. (2001). Coenzyme Q10 and remacemide hydrochloride ameliorate motor deficits in a Huntington's disease transgenic mouse model. *Neurosci. Lett.* 315, 149–153.

Shaafi, S., Mahmoudi, J., Pashapour, A., Farhoudi, M., Sadigh-Eteghad, S., and Akbari, H. (2014). Ketogenic diet provides neuroprotective effects against ischemic stroke neuronal damages. *Adv. Pharm. Bull.* 4, 479–481. doi: 10.5681/apb.2014.071

Shan, Q., Lu, J., Zheng, Y., Li, J., Zhou, Z., Hu, B., et al. (2009). Purple sweet potato color ameliorates cognition deficits and attenuates oxidative damage and inflammation in aging mouse brain induced by D-galactose. *J. Biomed. Biotechnol.* 2009:564737. doi: 10.1155/2009/564737

Sharma, D. R., Sunkaria, A., Wani, W. Y., Sharma, R. K., Kandimalla, R. J., Bal, A., et al. (2013). Aluminium induced oxidative stress results in decreased mitochondrial biogenesis via modulation of PGC-1α expression. *Toxicol. Appl. Pharmacol.* 273, 365–380.

Sharma, S. K., Kharkwal, G. B., Sajo, M., Huang, Y. Y., De Taboada, L., McCarthy, T., et al. (2011). Dose response effects of 810 nm laser light on mouse primary cortical neurons. *Lasers Surg. Med.* 43, 851–859. doi: 10.1002/lsm.21100

Shetty, R. A., Forster, M. J., and Sumien, N. (2013). Coenzyme Q10 supplementation reverses age-related impairments in spatial learning and lowers protein oxidation. *Age* 35, 1821–1834. doi: 10.1007/s11357-012-9484-9

Soares, L. M., De Vry, J., Steinbusch, H. W., Milani, H., Prickaerts, J., and de Oliveira, R. M. W. (2016). Rolipram improves cognition, reduces anxiety-and despair-like behaviors and impacts hippocampal neuroplasticity after transient global cerebral ischemia. *Neuroscience* 326, 69–83. doi: 10.1016/j.neuroscience.2016.03.062

Somayajulu, M., McCarthy, S., Hung, M., Sikorska, M., Borowy-Borowski, H., and Pandey, S. (2005). Role of mitochondria in neuronal cell death induced by oxidative stress; neuroprotection by Coenzyme Q 10. *Neurobiol. Dis.* 18, 618–627.

St-Pierre, J., Drori, S., Uldry, M., Silvaggi, J. M., Rhee, J., Jäger, S., et al. (2006). Suppression of reactive oxygen species and neurodegeneration by the PGC-1 transcriptional coactivators. *Cell* 127, 397–408.

St-Pierre, J., Lin, J., Krauss, S., Tarr, P. T., Yang, R., Newgard, C. B., et al. (2003). Bioenergetic analysis of peroxisome proliferator-activated receptor γ coactivators 1α and 1β (PGC-1α and PGC-1β) in muscle cells. *J. Biol. Chem.* 278, 26597–26603.

Strasser, A., Stanimirovic, D., Kawai, N., McCarron, R., and Spatz, M. (1997). Hypoxia modulates free radical formation in brain microvascular endothelium. *Acta Neurochir. Suppl.* 70, 8–11.

Tsai, K. L., Huang, Y. H., Kao, C. L., Yang, D. M., Lee, H. C., Chou, H. Y., et al. (2012). A novel mechanism of coenzyme Q10 protects against human endothelial cells from oxidative stress-induced injury by modulating NO-related pathways. *J. Nutr. Biochem.* 23, 458–468. doi: 10.1016/j.jnutbio.2011.01.011

Ueno, M., Tomimoto, H., Akiguchi, I., Wakita, H., and Sakamoto, H. (2002). Blood–brain barrier disruption in white matter lesions in a rat model of chronic cerebral hypoperfusion. *J. Cereb. Blood Flow Metab.* 22, 97–104.

Wei, H., Li, L., Song, Q., Ai, H., Chu, J., and Li, W. (2005). Behavioural study of the D-galactose induced aging model in C57BL/6J mice. *Behav. Brain Res.* 157, 245–251.

Xu, J., Murakami, Y., Matsumoto, K., Tohda, M., Watanabe, H., Zhang, S., et al. (2000). Protective effect of Oren-gedoku-to (Huang-Lian-Jie-Du-Tang) against impairment of learning and memory induced by transient cerebral ischemia in mice. *J. Ethnopharmacol.* 73, 405–413.

Xu, K., Sun, X., Puchowicz, M. A., and LaManna, J. C. (2008). Increased sensitivity to transient global ischemia in aging rat brain. *Adv. Exp. Med. Biol.* 599, 199–206.

Yabuki, Y., and Fukunaga, K. (2013). Oral administration of glutathione improves memory deficits following transient brain ischemia by reducing brain oxidative stress. *Neuroscience* 250, 394–407. doi: 10.1016/j.neuroscience.2013.07.017

Yang, L., Tucker, D., Dong, Y., Wu, C., Lu, Y., Li, Y., et al. (2018). Photobiomodulation therapy promotes neurogenesis by improving post-stroke local microenvironment and stimulating neuroprogenitor cells. *Exp. Neurol.* 299, 86–96. doi: 10.1016/j.expneurol.2017.10.013

Yang, X., Askarova, S., Sheng, W., Chen, J., Sun, A. Y., Sun, G. Y., et al. (2010). Low energy laser light (632.8 nm) suppresses amyloid-β peptide-induced oxidative and inflammatory responses in astrocytes. *Neuroscience* 171, 859–868. doi: 10.1016/j.neuroscience.2010.09.025

Yang, Y., Jiang, S., Dong, Y., Fan, C., Zhao, L., Yang, X., et al. (2015). Melatonin prevents cell death and mitochondrial dysfunction via a SIRT1-dependent mechanism during ischemic-stroke in mice. *J. Pineal Res.* 58, 61–70. doi: 10.1111/jpi.12193

Yin, K., Zhu, R., Wang, S., and Zhao, R. C. (2017). Low-level laser effect on proliferation, migration, and antiapoptosis of mesenchymal stem cells. *Stem Cells Dev.* 26, 762–775. doi: 10.1089/scd.2016.0332

Zhang, Q., Zhou, C., Hamblin, M. R., and Wu, M. X. (2014). Low-level laser therapy effectively prevents secondary brain injury induced by immediate early responsive gene X-1 deficiency. *J. Cereb. Blood Flow Metab.* 34, 1391–1401. doi: 10.1038/jcbfm.2014.95

Zoppo, G., Ginis, I., Hallenbeck, J. M., Iadecola, C., Wang, X., and Feuerstein, G. Z. (2000). Inflammation and stroke: putative role for cytokines, adhesion molecules and iNOS in brain response to ischemia. *Brain Pathol.* 10, 95–112.

Conflict of Interest Statement: FS is a consultant for ProNeuroLIGHT LLC, Phoenix, AZ, United States. MH is on the following Scientific Advisory Boards: Transdermal Cap Inc., Cleveland, OH, United States; Photothera Inc., Carlsbad, CA, United States; BeWell Global Inc., Wan Chai, Hong Kong; Hologenix Inc. Santa Monica, CA, United States; LumiThera, Inc., Poulsbo, WA, United States; Vielight, Toronto, ON, Canada; Bright Photomedicine, São Paulo, Brazil; Quantum Dynamics LLC, Cambridge, MA, United States; Global Photon Inc, Bee Cave, TX, United States; Medical Coherence, Boston MA, United States; NeuroThera, Newark, DE, United States; JOOVV Inc., Minneapolis–Saint Paul, MN, United States; AIRx Medical, Inc., Pleasanton, CA, United States; FIR Industries, Inc., Ramsey, NJ, United States; UVLRx Therapeutics, Oldsmar, FL, United States; Ultralux UV Inc, Lansing, MI, United States; Illumiheal & Petthera, Shoreline, WA, United States; MB Laser Therapy, Houston, TX, United States. He has been a Consultant for: Lexington int., Boca Raton, FL, United States; USHIO Corp., Japan; Merck KGaA, Darmstadt, Germany; Philips Electronics Nederland B.V.; Johnson & Johnson Inc., Philadelphia, PA; Sanofi-Aventis Deutschland GmbH, Frankfurt, Germany. He is a Stockholder in Global Photon Inc., Bee Cave, TX, United States and Mitonix, Newark, DE, United States. AG serves on advisory boards of The Dana Foundation, United States, and the Velux Stiftung and Daylight Academy, Switzerland. As the owner of MINDexult CVR, Denmark, he gives regular lectures and teaching sessions to pharmaceutical companies. He is the President of Landsforeningen til Bekæmpelse af Hjernesygdomme, Denmark.

The remaining authors declare that the research was conducted in the absence of any commercial or financial relationships that could be construed as a potential conflict of interest.

Copyright © 2019 Salehpour, Farajdokht, Mahmoudi, Erfani, Farhoudi, Karimi, Rasta, Sadigh-Eteghad, Hamblin and Gjedde. This is an open-access article distributed under the terms of the Creative Commons Attribution License (CC BY). The use, distribution or reproduction in other forums is permitted, provided the original author(s) and the copyright owner(s) are credited and that the original publication in this journal is cited, in accordance with accepted academic practice. No use, distribution or reproduction is permitted which does not comply with these terms.

frontiers in Cellular Neuroscience

ORIGINAL RESEARCH
published: 12 April 2019
doi: 10.3389/fncel.2019.00145

Silencing MicroRNA-134 Alleviates Hippocampal Damage and Occurrence of Spontaneous Seizures After Intraventricular Kainic Acid-Induced Status Epilepticus in Rats

Xiaoying Gao[1†], Mian Guo[2†], Dawei Meng[3†], Feixiang Sun[2†], Lianyue Guan[4], Ying Cui[5], Yan Zhao[2], Xichun Wang[6], Xin Gu[7], Jiahang Sun[2] and Sihua Qi[1*]*

[1] Department of Anesthesiology, The Fourth Affiliated Hospital of Harbin Medical University, Harbin, China, [2] Department of Neurosurgery, The Second Affiliated Hospital of Harbin Medical University, Harbin, China, [3] Department of Neurosurgery, Aviation General Hospital of China Medical University, Beijing, China, [4] Department of Hepatobilary-Pancreatic Surgery, China-Japan Union Hospital of Jilin University, Changchun, China, [5] Department of Radiotherapy, Cancer Hospital of Harbin Medical University, Harbin, China, [6] Department of Neurosurgery, Heilongjiang Provincial Hospital, Harbin, China, [7] Department of Head and Neck Surgery, Cancer Hospital of Harbin Medical University, Harbin, China

OPEN ACCESS

Edited by:
Antonio Gambardella, Università degli Studi "Magna Græcia" di Catanzaro, Italy

Reviewed by:
Muddanna Sakkattu Rao, Kuwait University, Kuwait
Jian-Fu Chen, University of Southern California, United States

***Correspondence:**
Jiahang Sun
sunjiahang978675@sina.com
Sihua Qi
qisihua2007@sina.com

[†] *These authors have contributed equally to this work*

Received: *06 July 2018*
Accepted: *22 March 2019*
Published: *12 April 2019*

Citation:
Gao X, Guo M, Meng D, Sun F, Guan L, Cui Y, Zhao Y, Wang X, Gu X, Sun J and Qi S (2019) Silencing MicroRNA-134 Alleviates Hippocampal Damage and Occurrence of Spontaneous Seizures After Intraventricular Kainic Acid-Induced Status Epilepticus in Rats. Front. Cell. Neurosci. 13:145. doi: 10.3389/fncel.2019.00145

Epilepsy is a disorder of abnormal brain activity typified by spontaneous and recurrent seizures. MicroRNAs (miRNAs) are short non-coding RNAs, critical for the post-transcriptional regulation of gene expression. MiRNA dysregulation has previously been implicated in the induction of epilepsy. In this study, we examined the effect of silencing miR-134 against status epilepticus (SE). Our results showed that level of miR-134 was significantly up-regulated in rat brain after Kainic acid (KA)-induced SE. TUNEL staining showed that silencing miR-134 alleviated seizure-induced neuronal apoptosis in the CA3 subfield of the hippocampus. Western blot showed that a miR-134 antagonist suppressed lesion-induced endoplasmic reticulum (ER) stress and apoptosis related expression of CHOP, Bim and Cytochrome C, while facilitated the expression of CREB at 24 h post KA-induced lesion in the hippocampus. Consistently, silencing miR-134 significantly diminished loss of CA3 pyramidal neurons using Nissl staining as well as reducing aberrant mossy fiber sprouting (MFS) in a rat epileptic model. In addition, the results of EEG and behavior analyses showed seizures were alleviated by miR-134 antagonist in our experimental models. These results suggest that silencing miR-134 modulates the epileptic phenotype by upregulating its target gene, CREB. This in turn attenuates oxidative and ER stress, inhibits apoptosis, and decreases MFS long term. This indicates that silencing miR-134 might be a promising intervention for the treatment of epilepsy.

Keywords: microRNA-134, hippocampal neurons, oxidative stress, epilepsy, CREB

INTRODUCTION

Epilepsy is a common, chronic neurologic disorder characterized by recurrent spontaneous seizure, which affects an estimated 50 million people globally. The already existing anti-epileptogenic therapeutics have exhibited limited clinical efficacy, with a significant fraction of epilepsy patients remaining refractory to treatment (Jimenez-Mateos et al., 2012). Although a large number of studies using clinical neuroimaging in conjunction with experiments in model systems have indicated that seizures may cause neuronal death under certain circumstances (Ben-Ari, 1985; Henshall and Simon, 2005), our current understanding of the mechanistic processes underlying seizure-related cell death remains poorly understood.

The excitotoxicity is always thought to be one of the leading causes of cell death in animal models of epilepsy and humans (Olney et al., 1986). Recent studies have shown that oxidative stress, defined as a disruption of pro-oxidant/anti-oxidant balance, is potentially toxic for neuronal cells and increases the production of reactive oxygen species (ROS) and redox (Uttara et al., 2009). The aberrant ROS levels and redox balance can result in endoplasmic reticulum (ER) dysfunction, ER stress, and the unfolded protein response, which play a fundamental role in the pathogenesis of epilepsy. Thus, antioxidants may be new therapeutic options in seizure related diseases. Previous studies have attempted to develop effective therapeutics by targeting and modulating apoptotic pathways, particularly in neural model systems. CHOP, known as the marker of the ER stress, is responsible for most ER stress-related-apoptosis. cAMP-responsive element-binding protein (CREB), a ubiquitously expressed transcription factor, controls proliferation and differentiation during neural development, and also functions as a key regulator of neuronal plasticity, learning, and memory in the adult brain. CREB exerts profound neuro-protective actions against various insults, including ischemia, traumatic injury, and neuro-degeneration.

MicroRNAs (miRNAs) are an evolutionarily conserved class of short non-coding RNAs that post-transcriptionally regulate gene expression, which play critical roles in normal development, the establishment of cell fate, and myriad cellular processes in all organs, particularly the brain (Ouyang et al., 2013). Loss or aberrant function of miRNAs has been linked to a diverse array of brain disorders, such as epilepsy (Jimenez-Mateos et al., 2015). A study by Guo J. et al. (2014), revealed a possible pathogenetic role of phosphorylation of CREB (p-CREB)/miRNA-132 (miR-132) signal pathway in temporal lobe epilepsy (TLE) by modulating the dendritic plasticity. Huang et al. (2014), pointed out that microRNA-132 silencing decreases the spontaneous recurrent seizures. Aronica et al. (2010), also demonstrated that expression of miR-146a was involved in the modulation of the astroglial inflammatory response occurring in TLE. In addition, Cai et al. (2016), demonstrated that miR-155 antagonist alleviated of epilepsy by induction of the expression of brain-derived neurotrophic factor (BDNF). Previous studies have revealed the neuroprotective effect of a miR-134 antagomir, which can reduce ischemic injury (Huang et al., 2015) and cause prolonged seizure suppression. Moreover, downregulation of miR-134 attenuates hydrogen peroxide (H_2O_2)-induced retinal ganglion cell (RGC) apoptosis.

In this study, we examined whether miR-134 was involved in protecting neurons from oxidative stress-induced damage and thereby improving the long-term symptoms and progression of occurrence of spontaneous seizures.

MATERIALS AND METHODS

Ethics Statement

All animal work was performed in accordance with the Chinese Animal Welfare Act and all experiments involving animals were approved by the Medical Ethics Committee of the Second Clinical College of Harbin Medical University (Approval ID: 201001).

Animals

Animal experiments performed in compliance with the National Institutes of Health guidelines for the use of laboratory animals. Adult male Sprague-Dawley rats weighing 210–250 g, were obtained from the Harbin Medical University 2nd Affiliated Hospital Laboratories, China, and housed with a 12-h light/dark cycle. Rats were given food and water *ad libitum* for at least 1 week before all experiment. All experiments were performed in the morning.

Seizure Models

Rats were anesthetized with isoflurane (5% induction, 1–2% maintenance), then immobilized in a stereotaxic apparatus (WPI Stoelting, United States) with a plane of incision bar set at 3.3 ± 0.33 mm below the interaural line. After making a midline incision, the skull was exposed and one burr hole was drilled according to the coordinates: 3.7 mm posterior to the bregma, 4.1 mm lateral to the midline, and 3.5 mm under the dura. Each rat was injected with 1.0 μL of KA (0.5 μg in 1.0 μL Saline) (Sigma-Aldrich) in the right lateral ventricle at the speed of 0.2 μL/min. The epileptic rats were further used for experiments (Xie et al., 2011). Duration and severity of seizure activity were documented. The behaviors of the seizure models were scored as Racine's Scale Evaluation (Racine et al., 1972). Only rats exhibiting at least 1 h of continuous seizures graded at stage 4/5 were included in this study. After application of KA for 60 min, all rats received lorazepam (Ativan, 10 mg/kg, i.p.) to terminate seizures. All rats were euthanized at 24 h or 2 months following anesthesia with isoflurane, and brain tissue was stored for subsequent analysis.

Intracerebroventricular Injections

Intracerebroventricular injections was performed as previously described (Antagomirs Targeting MicroRNA-134 Increase Limk1 Levels After Experimental Seizures *in Vitro* and *in Vivo*). Briefly, after controlled by diazepam administration, the SE rats were immediately anesthetized with sodium pentobarbital (30 mg/kg) and placed in a stereotaxic frame. The rats were inserted with a 23-gauged stainless-steel guide cannula into the bilateral ventricle through a hole drilled through the skull 4.4 mm below the top of the skull, 1.5 mm lateral and 0.8 mm posterior

to the bregma. Rats received 2 μL infusion of either vehicle (normal saline) or antagomirs targeting miR-134 (Ant-134: 5′-CC CCUCUGGUCAACCAGUCACA-Chol-3′) (full length nucleotide 2′-methoxy modification, GenePharma, Shanghai, China) in artificial cerebrospinal fluid at a speed of 0.2 μL/min. The cannula was remained in the brain for additional 10 min. Rats were sacrificed at the indicated time for further analyses.

Animal Grouping

A total of 144 rats were randomly divided into four groups ($n = 36$ per group). For the SE+ant-134 group (SE+ant-134), antagomir. Rats in the SE+vehicle group (SE+vehicle) were stereotaxically injected with KA plus the equal volume of normal saline. Rats in the control group (control) were stereotaxically injected with the equal volume of normal saline. Six rats were used for PCR and western blot (24 h) in each group, 5 for TUNEL assays (24 h) in each group, 6 for PCR (7 days) in SE and SE+ant-134 groups, 6 for PCR (2 m) in SE and SE+ant-134 groups, 4 for Nissl staining (2 m) in all groups, four for Timm staining (2 m) in four groups, four for EEG and behavioral study (2 m) in SE and SE+ant-134 groups. In the control group, 19 rats were sacrificed (11 at 24 h and 8 in 2 m), and the remaining 17 rats were killed. The SE group, 35 rats were sacrificed (11 at 24 h, 6 on 7 days and 18 in 2 m), and 1 died. In the SE+ant-134 group, 35 rats were sacrificed at the end of the experiment (11 at 24 h, 6 on 7 days and 18 in 2 m) and 1 died. In the SE+vehicle group, 35 rats were sacrificed (11 at 24 h, 6 on 7 days and 18 in 2 m) and 1 died. All rats were euthanized at 24 h or 2 months following treatment with isoflurane, and brain tissue was stored for subsequent analysis.

Rat Brain Tissue Processing

Rats were sacrificed by decapitation after anesthetized with chloral hydrate (350 mg/kg, i.p.). The hippocampus was dissected, and then stored in liquid nitrogen for Western blot assay and Real-time quantitative polymerase chain reaction (RT-qPCR). The remaining rats in each group were anesthetized and perfused with normal saline followed by post-fixation in 4% paraformaldehyde for 24 h at 4°C, embedded in paraffin and sectioned at 5 μm for terminal deoxynucleotidyl transferase dUTP nick-end labeling (TUNEL) staining and Nissl staining.

Real-Time Quantitative Polymerase Chain Reaction

miRNA-134 levels were measured by RT-qPCR with Taqman probes as previously described (Aronica et al., 2010; Guo M. et al., 2014). Total RNA was extracted from the cells by using TRIzol (Invitrogen) according to the manufacturer's instructions, and cDNA was synthesized using a TaqMan miRNA reverse-transcription kit (Applied Biosystems, Foster City, CA, United States) following the manufacturer's instruction. PCR system (10 μL) contained 5 μL of Taq PCR Master Mix, 1 μL of template cDNA, and 0.2 μL of forward and reverse primers of the target gene, miRNA-134 and reference gene U6. RT-qPCR was carried out on ABI 7500 system (Applied Biosystems, Foster City, CA, United States). The cycle threshold (Ct) values were calculated using the SDS 1.4 software (Applied Biosystems, Foster City, CA, United States), and the miR-134 expression was normalized with U6 SnRNA using the $2^{-\Delta\Delta Ct}$ method.

Western Analysis

Protein isolation from hippocampal tissues was performed as previously (Zhou et al., 2010) described for either total cell isolates or cytosolic subcellular fractionated samples. Protein fraction was collected and homogenized on ice in RIPA buffer with protein concentration assessed and normalized with a Bradford protein assay kit (Beyotime, Shanghai, China). The following primary antibodies were used: anti-CHOP (1:200, Abcam), anti-CREB (1:200, Abcam), anti-Bim (1:200, Abcam), and anti-Cytochrome C (1:300, Abcam), anti-cleaved-caspase-3 (1:500, Cell Signaling Technology). Primary antibody detection was performed using secondary antibodies conjugated to horseradish peroxidase (Jackson Immuno Research). GAPDH expression in the same membrane was simultaneously determined as an internal reference. Western blots were imaged with a luminescent analyzer (GE Healthcare Bio-Sciences AB, Uppsala, Sweden) and quantification performed using Image Quant TL (GE Healthcare Bio-Sciences AB, Uppsala, Sweden).

TUNEL Staining

After 24 h of lorazepam administration, TUNEL staining was performed on hippocampal sections to assess neuronal death (n = 5/group). TUNEL staining was performed using an *in situ* Cell Death Detection Kit (Roche), according to the manufacturer's protocol (Wang et al., 2011). The sections were post-fixed in ethanol-acetic acid (2:1 vol/vol) and rinsed. Afterward, the sections were incubated with proteinase K (100 μg/mL), rinsed, incubated in 3% hydrogen peroxide, permeabilized with 0.5% Triton X-100, rinsed again, and incubated in the TUNEL reaction mixture. The sections were rinsed and visualized using Converter-POD with 0.03% DAB. Mayer's hematoxylin (Dako, Glostrup, Denmark) was used as a counterstain, and sections were mounted onto gelatin-coated slides. The slides were air-dried overnight at room temperature, and coverslipped using Permount (Fisher Scientific). The numbers of TUNEL-positive cells in the hippocampal CA3 region were counted under a light microscope with 400 × magnification (Olympus, Tokyo, Japan). The extent of brain damage was evaluated by the average number of TUNEL-positive cells counted in 10 microscopic fields per group with square sampling regions (200 μm × 130 μm) and they were expressed as the number of cells per mm^2 in the hippocampal CA3 region.

Nissl Staining

Hippocampal neurons were visualized by Nissl staining (Zhang et al., 2002). Rats were euthanized with isoflurane 2 months after induction of SE, followed by sectioning and mounting of hippocampal slices. Sections were rehydrated in distilled water and stained with 0.5% crystal violet solution for 10 min. The brain slices in each section were imaged by the bright field microscopy (400×, Leica DM5000B). Normal neurons with visible nuclei in the CA3 subfield of hippocampal area were manually circled and counted within a unbiased counting fields (200 μm × 130 μm) per group. And they were expressed as the number of cells per

mm^2 in the hippocampal CA3 region. Neuronal numbers within the grid were evaluated from five brain sections per rat at different section depths for both the right and left sides of the brain.

TIMM Staining

TIMM staining was performed as previously described (Xie et al., 2011). Serial coronal sections (8 μm) were collected with a cryocut (Leica VT 1000S). Every fifth section was collected on slides and dried at room temperature overnight. For the visualization of MFS, sections were developed using the following solution: 120 mL of 50% gum arabic, 10 mL of 47% sodium citrate buffer, 10 mL of 51% citrate buffer, 60 mL of 5.78% hydroquinone and 212.25 mg silver nitrate. The physical development was performed in the dark at room temperature for 120 min. The sections were rinsed in tap water, then dehydrated, cleared, and coverslipped in Entellan (107961.0100; Merck). Evaluation of these stains were conducted in accordance with the methodology outlined in Shetty and Turner (1997). The molecular layer, especially in naive animals, was divided in three parts of equal size, including the inner, middle and outer molecular layers (IML, MML, and OML, respectively). As the border between different layers is difficult to identify, the density of Timm-positive staining was made in the whole molecular layers by image J analysis software. Density measurements were evaluated from 10 brain sections per rat 400 mm^2 apart for both the right and left sides of the brain.

Electroencephalogram (EEG) and Analysis

For recoding of EEG, experimental mice were anesthetized with pentobarbital sodium (50 mg/kg) and placed in stereotaxic frame. Two skull-mounted recording electrodes were placed bilaterally on the duramater of the fronto-parietal cortex. All the electrodes were assembly fixed in place with dental cement during the surgical process. EEG setting: filter setting is the following. The high cut filter was 50 Hz and the low cut filter was 1.5 Hz. The time-constant was 0.1. Alternating current (a.c.) filters (50 Hz) were on. Continuous (24 h per day) EEG data were collected for 14 consecutive days after SE. EEG data were reviewed and manually scored by an observer unaware of experimental treatment with epileptic seizures defined as high frequency (>5 Hz) high amplitude (>2 × baseline) polyspike discharges of ≥ 5 s duration. The analysis of EEG frequency and amplitude was performed and analyzed by LabChart Pro v7 software (ADInstruments, Oxford, United Kingdom). The EEG results show the number of spikes per epoch (10 s) in SE and SE+ant-134 groups. EEG waveforms had amplitudes of 500 μV and frequencies ranging between 0 and 75 Hz.

Analysis of Spontaneous Seizures by Continuous Video Monitoring

Animals distinguished by ear clips were housed in clear Perspex cages. Webcam-style cameras connected to laptop computers were placed 40 cm from cages in a room equipped with safe lights for night-time recordings. Videos from 5 days continuous (24 h per day) monitoring periods during weeks 3–4 post-SE were reviewed by an observer blind of experimental treatment. Behavioral analysis of spontaneous seizures was conducted by continuous video monitoring (n = 4/group). Only these rats graded 4 and above by Racine Scale, with typical seizure character such as continuous rearing and falling, severe tonic-clonic seizures, were recorded. As suggested, a new graph describing seizure frequency for all animals/groups was added. Graphs showed the average seizure attack times of individual animals on each day during the 5 days continuous video monitoring following SE with vehicle group and Ant-134 mice. Average seizure attack times of individual animals in each group were calculated and compared using the t-test.

Statistical Analyses

Data analyses were performed using GraphPad InStat version 3.00 (GraphPad Software, San Diego, CA, United States). An unpaired, two-tailed Student's t-test was used for comparisons between two groups. Multiple-group comparisons were performed using either one-way analysis of variance (ANOVA) where appropriated, followed by Turkey's HSD *post hoc* multiple comparison test for two-way comparisons. All data are presented as the mean ± standard error of the mean (SEM). A value of $p < 0.05$ was considered statistically significant.

RESULTS

Status Epilepticus Regulates miR-134 Expression

We first demonstrated that miR-134 levels were influenced by epileptic brain activity in rodents. Real-time quantitative PCR (RT-qPCR) revealed that 24 h following induction of SE there was an increase in miR-134 levels in the whole hippocampus, as compared to the control group. Furthermore, miR-134 levels were relatively decreased in the SE+ant-134 group (**Figure 1A**). 24 h after 0.12 nmol of miR-134 antagonist was injected into the rat ventricle, there was a significant decrease of miR-134. Recovery of miR-134 expression levels began after 7 days, consistent with other tissues (Krutzfeldt et al., 2005), and fully recovered after 2 months (**Figure 1B**).

miR-134 Antaogmirs Resultant Neuronal Death

We next assessed neuronal death in hippocampal sections from SE, SE+ant-134, and SE+vehicle group rats. SE and SE+vehicle group rats displayed extensive lesions and TUNEL-positive staining in the CA3 subfield of the hippocampus (**Figure 2A**). However, ant-134 administration dramatically reduced the number of seizure-induced TUNEL-positive neurons (**Figure 2A**). Consistently, cleaved Caspase-3, the hallmark of

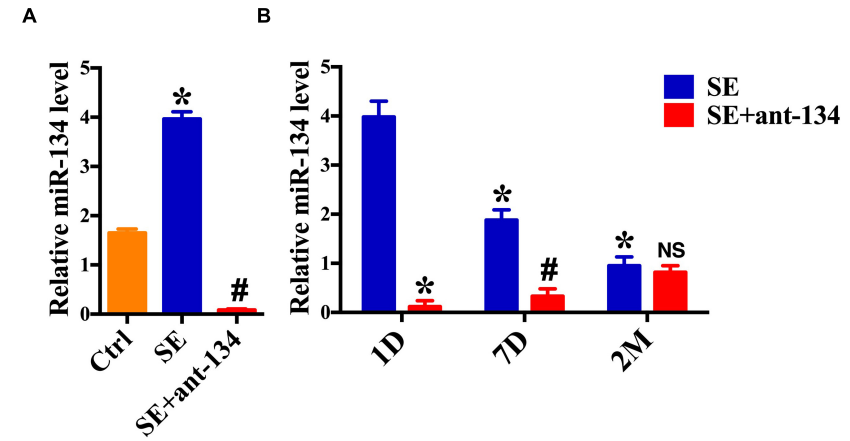


FIGURE 1 | miR-134 is regulated by status epilepticus (SE). **(A)** RT-qPCR measurement of miR-134 levels in hippocampi from control rats (n = 6), SE+ant-134 rats (n = 6) and rats subjected to SE (n = 6) at 24 h after SE. ANOVA; *$p < 0.05$ compared with Ctrl, #$p < 0.05$ compared with SE. **(B)** RT-qPCR measurement of miR-134 levels in hippocampi from SE+ant-134 (n = 6) and SE rats (n = 6) at various time points. ANOVA; *$p < 0.05$ compared with SE after 1 day; #$p < 0.05$ compared with SE at 7 days. NS. No significant.

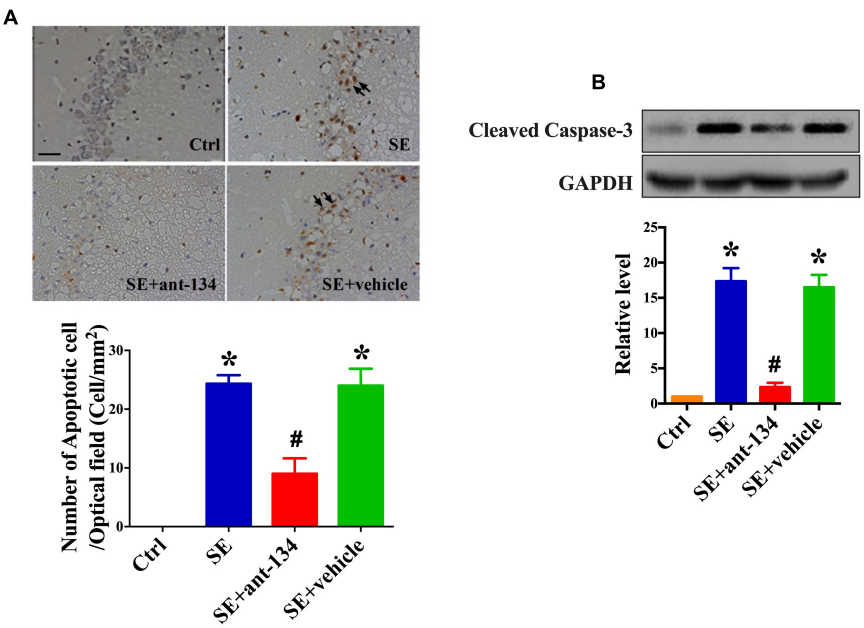


FIGURE 2 | miR-134 antagomirs reduce neuronal death. **(A)** The representative images of TUNEL stained hippocampal CA3 sections and quantification of TUNEL-positive cells in control (n = 5), SE (n = 5), SE+ant-134 (n = 5), and SE+vehicle (n = 5) groups at 24 h post-SE. The arrows indicated the apoptosis cells. Scale bar = 20 μm. **(B)** Western blot analysis of cleaved Caspase-3 and the quantification result. ANOVA; *$p < 0.05$ compared with control group, #$p < 0.05$ compared with SE+vehicle group.

apoptosis was downregulated after silencing miR-134 compared with the SE models (**Figure 2B**).

Silencing miR-134 Restores CREB Expression and Inhibits ER Stress-Mediated Neuronal Death

To determine the function of miR-134 in ER stress-induced neuronal apoptosis, we investigated the effect of miR-134 antagonists on the expression of relevant proteins. It has been shown that miR-134 serves as a regulator of CREB expression. We found that CREB protein levels were downregulated in the hippocampus after KA-induced SE. Analysis of the hippocampus in SE+ant-134 group rats showed upregulation of CREB protein levels compared with SE+vehicle group rats (**Figures 3A,B**).

We next specifically interrogated the role of ant-134 on SE-mediated ER stress. As expected, SE dramatically increased expression of the ER stress marker CHOP. Compared with the

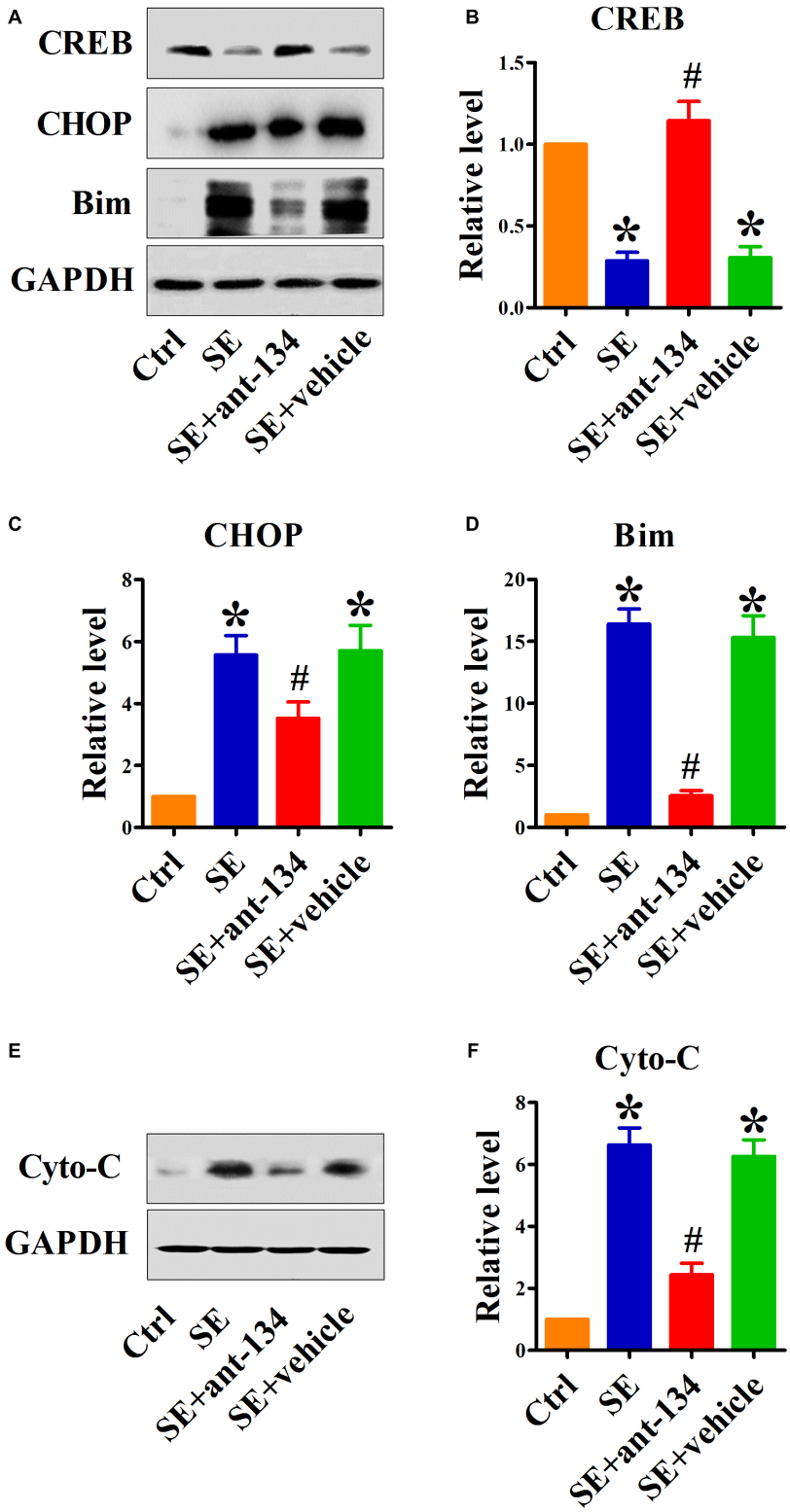


FIGURE 3 | Silencing miR-134 restores CREB expression and inhibits ER stress-mediated neuronal apoptosis. **(A)** Representative Western blot showing CREB, CHOP and Bim protein levels in whole cells of control (n = 6), SE (n = 6), SE+ant-134 (n = 6), and SE+vehicle (n = 6) rats at 24 h after status epilepticus (SE). Quantification of **(B)** CREB, **(C)** CHOP, and **(D)** Bim protein levels. Cytochrome C **(E)** protein levels in cytoplasm and **(F)** quantification analysis. GAPDH was included as a loading control. ANOVA; *p < 0.05 compared with control; #p < 0.05 compared with SE+vehicle.

SE group, the SE+ant-134 group had decreased CHOP protein levels, while CHOP expression in the SE+vehicle group did not change (**Figure 3C**).

Because CHOP is a known transcriptional inducer of Bim, to investigate the influence of silencing miR-134 on ER stress-induced apoptosis, we quantified the pro-apoptotic proteins Bim and cytoplasmic cytochrome C (cyto-C). Ant-134 inhibited the increase of Bim (**Figure 3D**) and cyto-C protein levels (**Figures 3E,F**) induced by SE, while the vehicle injection did not block the increase in Bim and cyto-C protein levels.

miR-134 Antagomir Administration Rescues KA-Induced Hippocampal Injury

We used Nissl staining to evaluate hippocampal architecture in each of our experimental groups at 2 months post KA administration. After counting the number of neurons in CA3 and comparing these values across groups, we found that the KA-induced lesion caused significant CA3 neuronal degeneration (**Figure 4A**). However, this degeneration could be rescued by administration of ant-134, as the total number of neurons present in the SE+ant-134 group was increased relative to that of the SE+vehicle group (**Figure 4B**). These data suggest that concomitant silencing of miR-134 during seizure induction can persistently attenuate neuronal death in CA3.

miR-134 Antagomir Treatment Reduces Seizure-Induced Mossy Fiber Sprouting (MFS)

In both human and animal epilepsy models, DG granule cell mossy fibers undergo significant reorganization of their terminal projections. We used Timm's staining, which specifically labels mossy fiber synaptic boutons by virtue of their high zinc content, to identify aberrant mossy fiber sprouting (MFS) following KA-mediated SE induction. We also assessed the effect of ant-134 infusion on KA-induced MFS at 2 months post-lesion. The SE and SE+vehicle groups exhibited significant MFS that mainly

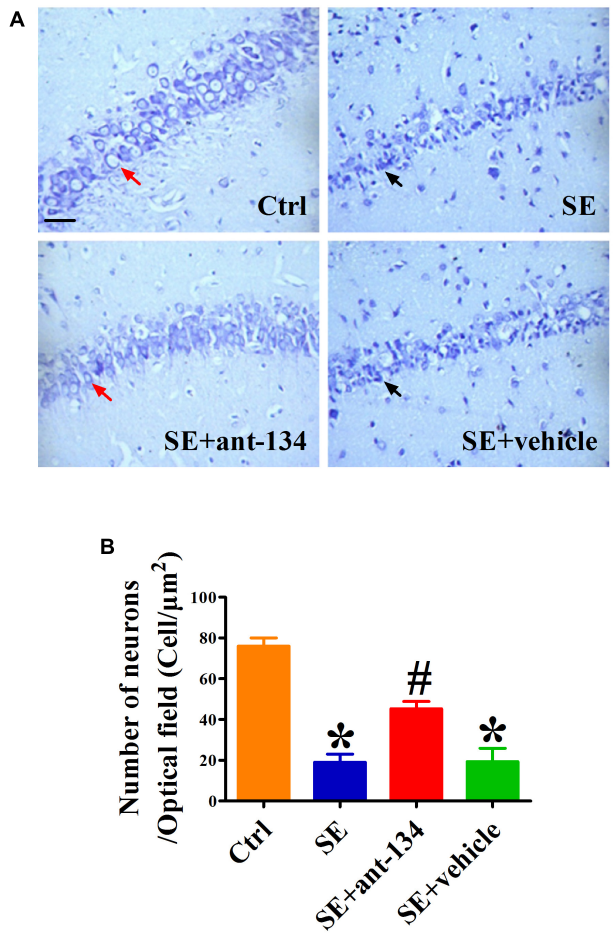


FIGURE 4 | Hippocampal cytoarchitecture visualized with Nissl staining. **(A)** The representative images of Nissl stained CA3 sections of rat brains from control (n = 4), SE (n = 4), SE+vehicle (n = 4), and SE+ant-134 (n = 4) groups at 2 months following SE. **(B)** Quantification of number of neurons in CA3. The red arrows indicated the normal neurons. The apoptosis cells were indicated by the black arrows. Scale bar = 20 μm. ANOVA; *p < 0.05 compared with control group, #p < 0.05 compared with SE+vehicle group.

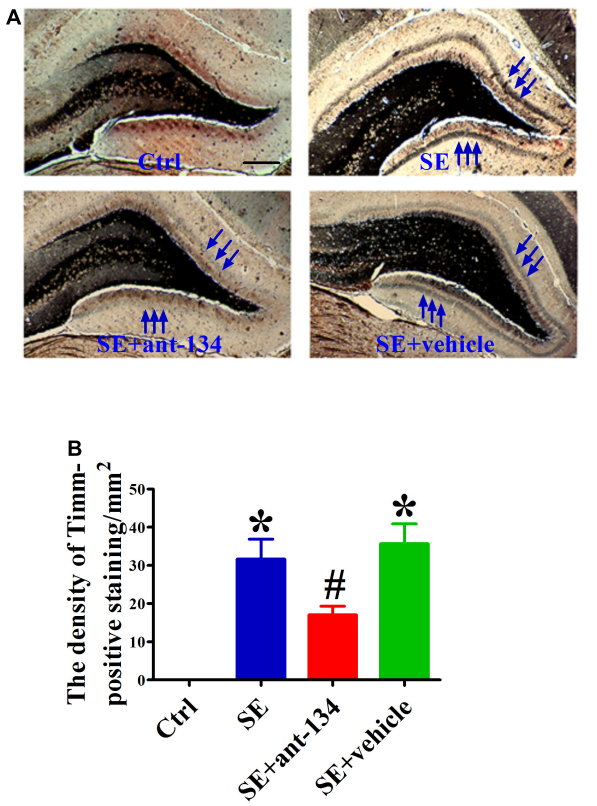


FIGURE 5 | Comparison of KA-lesion induced MFS using Timm's staining in DH. **(A)** The representative photomicrographs of Timm's staining in the hippocampus of rat brain sections from control (n = 4), SE (n = 4), SE+ant-134 (n = 4), and SE+vehicle (n = 4) groups at 24 h after SE. Scale bars = 200 μm. **(B)** Quantitative data for density of sprouting into the molecular layer. Scale bars = 200 μm. ANOVA; *p < 0.05 compared with SE group; #p < 0.05 compared with SE+vehicle.

projected into the inner molecular (**Figure 5A**). As expected, the band of Timm staining was visibly reduced in the SE+ant-134 group (**Figure 5B**).

miR-134 Antagomirs Protect the Later Occurrence of Spontaneous Seizures

Hippocampal activity was monitored with electroencephalography (EEG) at 2 months after KA-lesion. The EEG results showed that the number of spikes per epoch (10 s) in SE+ant-134 groups was dramatically decreased compared with the SE+vehicle group (**Figure 6**). Additionally, the SE+ant-134 group presented with a significantly lower frequency (24.8 ± 7.2/min) of abnormal spikes than that of the SE group (57.8 ± 6.4/min). These results suggest that miR-134 antagomirs may reduce abnormal neuronal discharge in the epileptic hippocampus over the long-term.

The Antagomirs of miR-134 Relieved the Seizure Behavior of Rats

We also scored seizure the activity of rats at 2 months post KA-induced SE. Four rats were selected in each group and uninterrupted video was monitored. The number of seizure attacks (Racine Score 1∼5) of each rat in SE+vehicle group (**Figure 7A**) and SE+ant-134 group (**Figure 7B**) was scored during the 5 days. The total number of seizure attacks of SE+ant-134 group (48 times) was significantly decreased than the SE group (92 times) and SE+vehicle group (86 times). The average seizure level of SE+ant-134 group was downregulated than SE+vehicle group (**Figure 7C**). These results showed that ant-134 attenuated the seizure score, which can serve as a potential treatment for epilepsy.

DISCUSSION

This study demonstrates that inhibition of miR-134 effectively protects hippocampal neurons from status epilepticus-induced neuronal death in an animal model of epilepsy. MiR-134 inhibition also attenuates aberrant MFS from granule cells in the dentate gyrus (DG), which may in the long-term lead to decreased diseased neuronal discharges in the epileptic brain. These findings suggest that silencing miR-134 may be an appropriate intervention to treat status epilepticus (SE), attenuate seizure-related structural damage to the hippocampus, and prevent the induction of later spontaneous seizure events. Additionally, we find that miR-134 inhibition restores CREB expression and decreases CHOP and Bim expression, genes that are relevant to ER stress-mediated apoptosis. Therefore, the likely mechanism whereby inhibition of miR-134 affects the epileptic brain is through reducing CREB expression. This study not only supports the prospect of exploring miR-134 antagomirs clinically, but also provides a basis for discovering a detailed mechanism of action.

Epilepsy is a common neurological disorder that has an estimated prevalence of 50 million people and accounts for around 1% of the global disease burden. While epilepsy is often spontaneous, it is possible that up to 50% of cases are acquired, and this number increases as people age. Like cerebrovascular diseases and neurodegeneration, epileptic brain tissue exhibits both increased ROS production and chronic inflammation, and it is likely that this inflammatory state contributes to, or even initiates, the disorder (Glass et al., 2010). Although the full mechanism remains to be elucidated, there is some evidence that mitochondrial complexes I and II as well as membrane-bound NADPH oxidases play a role in elevating ROS levels (Kumagai and Sumi, 2007). Furthermore, ROS-mediated oxidative stress likely plays an important role in epilepsy symptoms get worse and neuronal death. We have previously shown that that ant-134 treatment reduces hippocampal oxidative stress by assaying SOD activity and quantifying MDA and 4_HNE levels (Sun et al., 2017). MicroRNAs (miRNAs) play important roles in the pathogenesis of neurologic disorders and it is therefore unsurprising they have demonstrated promise as therapeutics. For instance, in a pilocarpine model of SE, miR-134 knockdown was shown to effectively suppress seizures and facilitate neuroprotection (Jimenez-Mateos et al., 2015). Increased miR-134 expression reduces dendritic spine volume of hippocampal neurons, and this anatomical change has been identified as a consistent marker of epilepsy. Apart from the apparent benefits of using a miR-134 antagonist (ant-134) to reduce seizure frequency and intensity, in this study we wanted to determine whether ant-134 could reduce neuronal injury in a SE model in rats. Previous studies reported that when produced via intra-amygdala microinjection of KA, SE develops following the propagation of seizures through the entorhinal cortex and perforant pathway to the hippocampus. In the present study, we observed that the number of apoptotic cells in hippocampal CA3 as assed by TUNEL staining was significantly reduced by ant-134 administration as compared with controls. This difference also appeared in the western blot analyses of proapoptotic proteins Bim and cytochrome C. From these results, we speculate that miR-134 inhibition can play a protective role in epilepsy-induced damage of hippocampal neurons.

To determine the mechanism by which miR-134 inhibition reduces neuronal damage, we decided to investigate the role of the ER, which can engender a stress response that causes apoptosis and contributes to pathologies, including epilepsy. The ER plays critical roles in calcium storage as well as protein folding, assembly, and modification. ER stress can be induced by an array of pathophysiological conditions, including ischemia, oxidative stress, or infection (Ron, 2002). If ER stress is overwhelming, pro-apoptotic signals dominate, and cells undergo apoptosis. In particular, ER stress is partially mediated by an increased expression of the pro-apoptotic transcription factor C/EBP homologous protein (CHOP), which is thought to play a critical role in apoptosis in a variety of cardiac and neurological disorders (Fu et al., 2010; Zou et al., 2012). CHOP, in turn, stimulates the cell-death inducer Bim. Thus, apoptosis following ER stress may result from increased transcriptional efficacy of CHOP, which in turn upregulates expression of the pro-apoptotic Bim protein (Puthalakath et al., 2007). This mechanism is consistent with our results. Overall, we found that downregulating miR-134 does indeed reduce hippocampal CHOP and Bim expression. However, it is

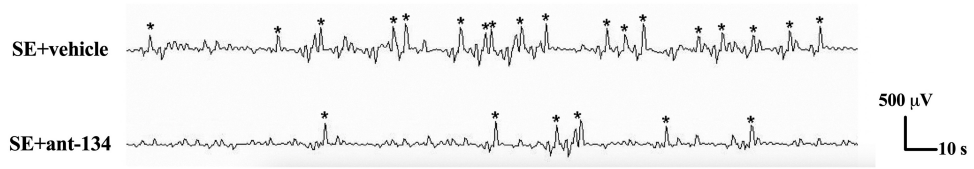


FIGURE 6 | Representative EEG recordings of abnormal spikes from SE (n = 4) and SE+ant-134 (n = 4) groups at 2 months. Asterisk indicates the abnormal spikes of epileptic brain. The duration of the recording time is 10 s and the amplitude scale is 500 μV.

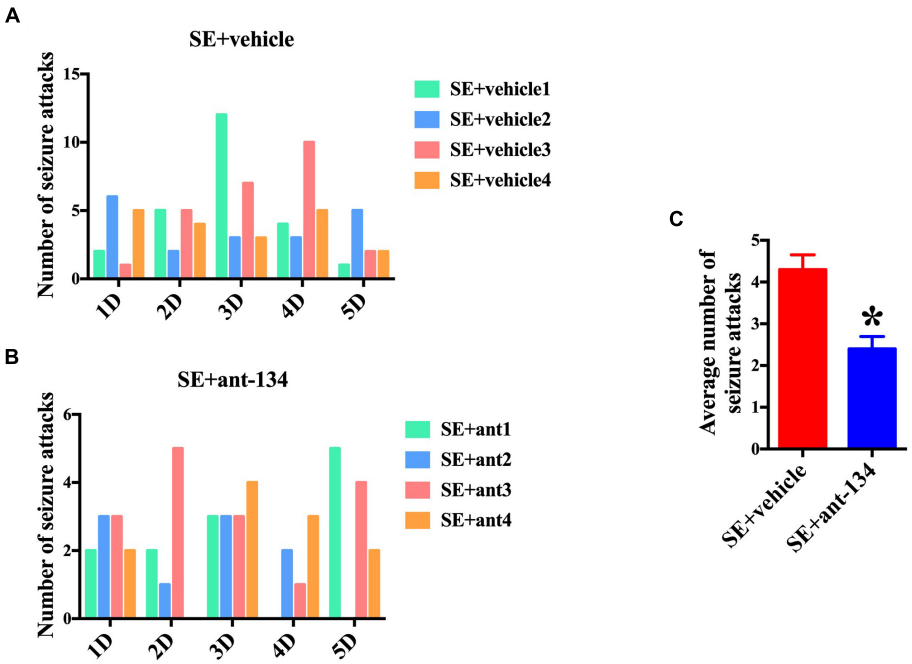


FIGURE 7 | Behavioral analysis of rats between miR-134 antagomirs and vehicle group. Graphs show the number of seizure behaviors each day for individual animals during 5 days continuous video monitoring following SE (n = 4) for **(A)** vehicle (n = 4) and **(B)** Ant-134 (n = 4) group. **(C)** The average number of seizure behaviors per rat during the monitoring periods. t-Test; *$p < 0.05$ compared with SE+vehicle.

unlikely that reducing Bim activity is the only mechanism by which ant-134 reduces neuronal damage, as many other pro-apoptotic proteins and pathways are activated following seizures. Furthermore, a research showed after seizures, hippocampal CA3 neurodegeneration was reduced in Bim-deficient mice, while neocortex damage in Bim-deficient mice was comparable with that in wild-type mice. These results suggested the region-specific differential contributions of Bim to seizure-induced neuronal death (Murphy et al., 2010). To further understand the mechanism of ER stress-induced neuron damage, we turned our attention to CREB, a leucine zipper family transcription factor that is ubiquitously expressed (Yamashima, 2012). CREB controls proliferation and differentiation during neural development, and also functions as a key regulator of neuronal plasticity, learning, and memory in the adult brain. CREB is neuroprotective against various insults, including ischemia, traumatic injury, and neurodegeneration (Shaywitz and Greenberg, 1999; Zanassi et al., 2001; Zhu et al., 2004). In fact, there are several studies that implicate CREB activation in adult neurogenesis, including in the dentate gyrus following ischemic injury. Furthermore, Qiu et al. (2013) have shown that CREB knockdown reduced the protective ability of cocaine- and amphetamine-regulated transcript (CART) protein to inhibit cerebral ischemia/reperfusion-induced ER stress and neuronal apoptosis. Additionally, Li et al. (2015) have shown that nicotinamide protects hepatocytes against ER stress via activation of the cAMP/PKA/CREB pathway. Regarding the relationship between CREB and miR-134, previous studies indicate that downregulation of miR-134 increases CREB expression, which attenuates H_2O_2-induced RGC apoptosis (Shao et al., 2015). Also, resveratrol might function as a neuroprotective agent by reducing miR-134 and increasing CREB expression (Zhao et al., 2013). In this study, we demonstrate that miR-134 inhibition results in CREB Increased expression and a decrease in ER stress-induced apoptosis. Our results substantiate the idea that CREB plays a crucial role in preventing hippocampal neuronal injury induced by epilepsy. Given these findings, as well as CREB's importance throughout the nervous system, CREB may be an ideal target

for future therapeutic intervention in epilepsy, among other neurological disorders.

Studies conducted with human patients and animal models have suggested that mossy fibers that lose their normal synaptic targets following degeneration of CA3 pyramidal neurons and DG hilus interneurons may begin to sprout abnormally (Mathern et al., 1996; Shetty and Turner, 1997; Rao et al., 2006). Given the importance of neuronal degeneration in producing MFS, one of the main characteristic anatomical phenotypes of epilepsy, it was worth investigating whether the decreases in neuronal death in injured hippocampi following miR-134 antagomir treatment can contribute to reducing MFS. Indeed, our results indicate that anti-134 treatment reduced aberrant MFS throughout the dentate gyrus. Previous research has shown that miR-134 antagomirs suppress seizures by modulating dendritic spine density (Jimenez-Mateos et al., 2012) and size (Schratt et al., 2006). However, most studies have focused mainly on the transient effects of anti-miR-134 treatment, with follow-up ranging from 3 to 14 days post SE induction. Our results not only further support the antiepileptogenic effect of miR-134 antagomirs, but also indicate that this protective effect can last up to 2 months after KA-induced SE. This long-term effect suggests that miR-134 antagomirs may have therapeutic potential in the treatment of epilepsy.

Overall, the present study establishes a significant role for miR-134 antagomirs in the alleviation of hippocampal neuron injury following KA-induced SE, which has been shown to contribute to the onset and occurrence of spontaneous seizures and other neurological disorders. However, future work should investigate the impact of miR-134 on characteristic epilepsy phenotypes such as aberrant neuronal circuitry, which gives rise to epilepsy symptoms like impaired spatial navigation and memory. Additionally, it will be crucial to determine the clinical feasibility of incorporating miR-134 into an epilepsy treatment regimen, taking into account limitations such as the blood-brain barrier.

ETHICS STATEMENT

This study was carried out in accordance with the recommendations of 'National Institutes of Health guide for the care and use of laboratory animals.' The protocol was approved by the 'Research Ethics Committee of Harbin Medical University.'

AUTHOR CONTRIBUTIONS

XGa and MG wrote the manuscript and analyzed the data. DM and LG performed the animal experiments. FS made great contribution to the revision of the manuscript. YC and YZ performed the RT-qPCR experiments. XW and XGu conducted Western Blot experiments. JS and SQ designed the study and revised the manuscript.

FUNDING

This study was supported by grants from the National Natural Science Foundation of China (Grant Nos. 81401087, 81773161, and 81572472), the Natural Science Foundation of Heilongjiang Province (Grant No. QC2014C099), and the Post-doctoral Foundation of Heilongjiang Province (Grant No. LBH-Z16106).

REFERENCES

Aronica, E., Fluiter, K., Iyer, A., Zurolo, E., Vreijling, J., van Vliet, E. A., et al. (2010). Expression pattern of miR-146a, an inflammation-associated microRNA, in experimental and human temporal lobe epilepsy. *Eur. J. Neurosci.* 31, 1100–1107. doi: 10.1111/j.1460-9568.2010.07122.x

Ben-Ari, Y. (1985). Limbic seizure and brain damage produced by kainic acid: mechanisms and relevance to human temporal lobe epilepsy. *Neuroscience* 14, 375–403. doi: 10.1016/0306-4522(85)90299-4

Cai, Z., Li, S., Li, S., Song, F., Zhang, Z., Qi, G., et al. (2016). Antagonist targeting microRNA-155 protects against lithium-pilocarpine-induced status epilepticus in c57bl/6 mice by activating brain-derived neurotrophic factor. *Front. Pharmacol.* 7:129. doi: 10.3389/fphar.2016.00129

Fu, H. Y., Okada, K., Liao, Y., Tsukamoto, O., Isomura, T., Asai, M., et al. (2010). Ablation of C/EBP homologous protein attenuates endoplasmic reticulum-mediated apoptosis and cardiac dysfunction induced by pressure overload. *Circulation* 122, 361–369. doi: 10.1161/CIRCULATIONAHA.109.917914

Glass, C. K., Saijo, K., Winner, B., Marchetto, M. C., and Gage, F. H. (2010). Mechanisms underlying inflammation in neurodegeneration. *Cell* 140, 918–934. doi: 10.1016/j.cell.2010.02.016

Guo, J., Wang, H., Wang, Q., Chen, Y., and Chen, S. (2014). Expression of p-CREB and activity-dependent miR-132 in temporal lobe epilepsy. *Int. J. Clin. Exp. Med.* 7, 1297–1306.

Guo, M., Jiang, Z., Zhang, X., Lu, D., Ha, A. D., Sun, J., et al. (2014). miR-656 inhibits glioma tumorigenesis through repression of BMPR1A. *Carcinogenesis* 35, 1698–1706. doi: 10.1093/carcin/bgu030

Henshall, D. C., and Simon, R. P. (2005). Epilepsy and apoptosis pathways. *J. Cereb. Blood Flow Metab.* 25, 1557–1572. doi: 10.1038/sj.jcbfm.9600149

Huang, W., Liu, X., Cao, J., Meng, F., Li, M., Chen, B., et al. (2015). mir-134 regulates ischemia/reperfusion injury-induced neuronal cell death by regulating CREB signaling. *J. Mol. Neurosci.* 55, 821–829. doi: 10.1007/s12031-014-0434-0

Huang, Y., Guo, J., Wang, Q., and Chen, Y. (2014). MicroRNA-132 silencing decreases the spontaneous recurrent seizures. *Int. J. Clin. Exp. Med.* 7, 1639–1649.

Jimenez-Mateos, E. M., Engel, T., Merino-Serrais, P., Fernaud-Espinosa, I., Rodriguez-Alvarez, N., Reynolds, J., et al. (2015). Antagomirs targeting microRNA-134 increase hippocampal pyramidal neuron spine volume in vivo and protect against pilocarpine-induced status epilepticus. *Brain Struct. Funct.* 220, 2387–2399. doi: 10.1007/s00429-014-0798-5

Jimenez-Mateos, E. M., Engel, T., Merino-Serrais, P., McKiernan, R. C., Tanaka, K., Mouri, G., et al. (2012). Silencing microRNA-134 produces neuroprotective and prolonged seizure-suppressive effects. *Nat. Med.* 18, 1087–1094. doi: 10.1038/nm.2834

Krutzfeldt, J., Rajewsky, N., Braich, R., Rajeev, K. G., Tuschl, T., Manoharan, M., et al. (2005). Silencing of microRNAs in vivo with 'antagomirs'. *Nature* 438, 685–689. doi: 10.1038/nature04303

Kumagai, Y., and Sumi, D. (2007). Arsenic: signal transduction, transcription factor, and biotransformation involved in cellular response and toxicity. *Annu. Rev. Pharmacol. Toxicol.* 47, 243–262. doi: 10.1146/annurev.pharmtox.47.120505.105144

Li, J., Dou, X., Li, S., Zhang, X., Zeng, Y., and Song, Z. (2015). Nicotinamide ameliorates palmitate-induced ER stress in hepatocytes via cAMP/PKA/CREB

pathway-dependent sirt1 upregulation. *Biochim. Biophys. Acta* 1853, 2929–2936. doi: 10.1016/j.bbamcr.2015.09.003

Mathern, G. W., Babb, T. L., Leite, J. P., Pretorius, K., Yeoman, K. M., and Kuhlman, P. A. (1996). The pathogenic and progressive features of chronic human hippocampal epilepsy. *Epilepsy Res.* 26, 151–161. doi: 10.1016/S0920-1211(96)00052-6

Murphy, B. M., Engel, T., Paucard, A., Hatazaki, S., Mouri, G., Tanaka, K., et al. (2010). Contrasting patterns of bim induction and neuroprotection in bim-deficient mice between hippocampus and neocortex after status epilepticus. *Cell Death Differ.* 17, 459–468. doi: 10.1038/cdd.2009.134

Olney, J. W., Collins, R. C., and Sloviter, R. S. (1986). Excitotoxic mechanisms of epileptic brain damage. *Adv. Neurol.* 44, 857–877.

Ouyang, Y. B., Xu, L., Lu, Y., Sun, X., Yue, S., Xiong, X. X., et al. (2013). Astrocyte-enriched miR-29a targets PUMA and reduces neuronal vulnerability to forebrain ischemia. *Glia* 61, 1784–1794. doi: 10.1002/glia.22556

Puthalakath, H., O'Reilly, L. A., Gunn, P., Lee, L., Kelly, P. N., Huntington, N. D., et al. (2007). ER stress triggers apoptosis by activating BH3-only protein Bim. *Cell* 129, 1337–1349. doi: 10.1016/j.cell.2007.04.027

Qiu, B., Hu, S., Liu, L., Chen, M., Wang, L., Zeng, X., et al. (2013). CART attenuates endoplasmic reticulum stress response induced by cerebral ischemia and reperfusion through upregulating BDNF synthesis and secretion. *Biochem. Biophys. Res. Commun.* 436, 655–659. doi: 10.1016/j.bbrc.2013.05.142

Racine, R. J., Gartner, J. G., and Burnham, W. M. (1972). Epileptiform activity and neural plasticity in limbic structures. *Brain Res.* 47, 262–268. doi: 10.1016/0006-8993(72)90268-5

Rao, M. S., Hattiangady, B., Reddy, D. S., and Shetty, A. K. (2006). Hippocampal neurodegeneration, spontaneous seizures, and mossy fiber sprouting in the F344 rat model of temporal lobe epilepsy. *J. Neurosci. Res.* 83, 1088–1105. doi: 10.1002/jnr.20802

Ron, D. (2002). Translational control in the endoplasmic reticulum stress response. *J. Clin. Invest.* 110, 1383–1388. doi: 10.1172/JCI16784

Schratt, G. M., Tuebing, F., Nigh, E. A., Kane, C. G., Sabatini, M. E., Kiebler, M., et al. (2006). A brain-specific microRNA regulates dendritic spine development. *Nature* 439, 283–289. doi: 10.1038/nature04367

Shao, Y., Yu, Y., Zhou, Q., Li, C., Yang, L., and Pei, C. G. (2015). Inhibition of miR-134 protects against hydrogen peroxide-induced apoptosis in retinal ganglion cells. *J. Mol. Neurosci.* 56, 461–471. doi: 10.1007/s12031-015-0522-9

Shaywitz, A. J., and Greenberg, M. E. (1999). CREB: a stimulus-induced transcription factor activated by a diverse array of extracellular signals. *Annu. Rev. Biochem.* 68, 821–861. doi: 10.1146/annurev.biochem.68.1.821

Shetty, A. K., and Turner, D. A. (1997). Fetal hippocampal cells grafted to kainate-lesioned CA3 region of adult hippocampus suppress aberrant supragranular sprouting of host mossy fibers. *Exp. Neurol.* 143, 231–245. doi: 10.1006/exnr.1996.6363

Sun, J., Gao, X., Meng, D., Xu, Y., Wang, X., Gu, X., et al. (2017). Antagomirs targeting mirorna-134 attenuates epilepsy in rats through regulation of oxidative stress, mitochondrial functions and autophagy. *Front. Pharmacol.* 8:524. doi: 10.3389/fphar.2017.00524

Uttara, B., Singh, A. V., Zamboni, P., and Mahajan, R. T. (2009). Oxidative stress and neurodegenerative diseases: a review of upstream and downstream antioxidant therapeutic options. *Curr. Neuropharmacol.* 7, 65–74. doi: 10.2174/157015909787602823

Wang, Q., Zhang, X., Ding, Q., Hu, B., Xie, Y., Li, X., et al. (2011). Limb remote postconditioning alleviates cerebral reperfusion injury through reactive oxygen species-mediated inhibition of delta protein kinase C in rats. *Anesth. Analg.* 113, 1180–1187. doi: 10.1213/ANE.0b013e31822b885f

Xie, C., Sun, J., Qiao, W., Lu, D., Wei, L., Na, M., et al. (2011). Administration of simvastatin after kainic acid-induced status epilepticus restrains chronic temporal lobe epilepsy. *PLoS One* 6:e24966. doi: 10.1371/journal.pone.0024966

Yamashima, T. (2012). 'PUFA-GPR40-CREB signaling' hypothesis for the adult primate neurogenesis. *Prog. Lipid Res.* 51, 221–231. doi: 10.1016/j.plipres.2012.02.001

Zanassi, P., Paolillo, M., Feliciello, A., Avvedimento, E. V., Gallo, V., and Schinelli, S. (2001). cAMP-dependent protein kinase induces cAMP-response element-binding protein phosphorylation via an intracellular calcium release/ERK-dependent pathway in striatal neurons. *J. Biol. Chem.* 276, 11487–11495. doi: 10.1074/jbc.M007631200

Zhang, X., Cui, S. S., Wallace, A. E., Hannesson, D. K., Schmued, L. C., Saucier, D. M., et al. (2002). Relations between brain pathology and temporal lobe epilepsy. *J. Neurosci.* 22, 6052–6061. doi: 10.1523/JNEUROSCI.22-14-06052.2002

Zhao, Y. N., Li, W. F., Li, F., Zhang, Z., Dai, Y. D., Xu, A. L., et al. (2013). Resveratrol improves learning and memory in normally aged mice through microRNA-CREB pathway. *Biochem. Biophys. Res. Commun.* 435, 597–602. doi: 10.1016/j.bbrc.2013.05.025

Zhou, Y., Lekic, T., Fathali, N., Ostrowski, R. P., Martin, R. D., Tang, J., et al. (2010). Isoflurane posttreatment reduces neonatal hypoxic-ischemic brain injury in rats by the sphingosine-1-phosphate/phosphatidylinositol-3-kinase/Akt pathway. *Stroke* 41, 1521–1527. doi: 10.1161/STROKEAHA.110.583757

Zhu, D. Y., Lau, L., Liu, S. H., Wei, J. S., and Lu, Y. M. (2004). Activation of cAMP-response-element-binding protein (CREB) after focal cerebral ischemia stimulates neurogenesis in the adult dentate gyrus. *Proc. Natl. Acad. Sci. U.S.A.* 101, 9453–9457. doi: 10.1073/pnas.0401063101

Zou, X. J., Yang, L., and Yao, S. L. (2012). Endoplasmic reticulum stress and C/EBP homologous protein-induced bax translocation are involved in angiotensin II-induced apoptosis in cultured neonatal rat cardiomyocytes. *Exp. Biol. Med.* 237, 1341–1349. doi: 10.1258/ebm.2012.012041

Conflict of Interest Statement: The authors declare that the research was conducted in the absence of any commercial or financial relationships that could be construed as a potential conflict of interest.

Copyright © 2019 Gao, Guo, Meng, Sun, Guan, Cui, Zhao, Wang, Gu, Sun and Qi. This is an open-access article distributed under the terms of the Creative Commons Attribution License (CC BY). The use, distribution or reproduction in other forums is permitted, provided the original author(s) and the copyright owner(s) are credited and that the original publication in this journal is cited, in accordance with accepted academic practice. No use, distribution or reproduction is permitted which does not comply with these terms.

frontiers in Cellular Neuroscience

ORIGINAL RESEARCH
published: 12 April 2019
doi: 10.3389/fncel.2019.00144

Acute and Post-acute Neuromodulation Induces Stroke Recovery by Promoting Survival Signaling, Neurogenesis, and Pyramidal Tract Plasticity

*Ahmet B. Caglayan[1,2], Mustafa C. Beker[1,2], Berrak Caglayan[2,3], Esra Yalcin[1,2], Aysun Caglayan[1,2], Burak Yulug[4], Lutfu Hanoglu[5], Selim Kutlu[6], Thorsten R. Doeppner[2,7], Dirk M. Hermann[8] and Ertugrul Kilic[1,2]**

[1] Department of Physiology, Faculty of Medicine, Istanbul Medipol University, Istanbul, Turkey, [2] Regenerative and Restorative Medical Research Center, Istanbul, Turkey, [3] Department of Medical Biology, Faculty of Medicine, Istanbul Medipol University, Istanbul, Turkey, [4] Department of Neurology, Faculty of Medicine, Alanya Alaaddin Keykubat University, Antalya, Turkey, [5] Department of Neurology, Faculty of Medicine, Istanbul Medipol University, Istanbul, Turkey, [6] Department of Physiology, Faculty of Medicine, Necmettin Erbakan University, Konya, Turkey, [7] Department of Neurology, Faculty of Medicine, University of Goettingen, Göttingen, Germany, [8] Department of Neurology, Faculty of Medicine, University of Duisburg-Essen, Essen, Germany

OPEN ACCESS

Edited by:
Rena Li,
Roskamp Institute, United States

Reviewed by:
Ayman ElAli,
Research Center of the CHU de Québec, Canada
Anna Maria Pugliese,
University of Florence, Italy
Mathias Hoehn,
Max-Planck-Gesellschaft (MPG), Germany

***Correspondence:**
Ertugrul Kilic
ekilic@medipol.edu.tr;
kilic44@yahoo.com

Received: 13 December 2018
Accepted: 22 March 2019
Published: 12 April 2019

Citation:
Caglayan AB, Beker MC, Caglayan B, Yalcin E, Caglayan A, Yulug B, Hanoglu L, Kutlu S, Doeppner TR, Hermann DM and Kilic E (2019) Acute and Post-acute Neuromodulation Induces Stroke Recovery by Promoting Survival Signaling, Neurogenesis, and Pyramidal Tract Plasticity. Front. Cell. Neurosci. 13:144. doi: 10.3389/fncel.2019.00144

Repetitive transcranial magnetic stimulation (rTMS) has gained interest as a non-invasive treatment for stroke based on the data promoting its effects on functional recovery. However, the exact action mechanisms by which the rTMS exert beneficial effects in cellular and molecular aspect are largely unknown. To elucidate the effects of high- and low-frequency rTMS in the acute-ischemic brain, we examined how rTMS influences injury development, cerebral blood flow (CBF), DNA fragmentation, neuronal survival, pro- and anti-apoptotic protein activations after 30 and 90 min of focal cerebral ischemia. In addition, inflammation, angiogenesis, growth factors and axonal outgrowth related gene expressions, were analyzed. Furthermore, we have investigated the effects of rTMS on post-acute ischemic brain, particularly on spontaneous locomotor activity, perilesional tissue remodeling, axonal sprouting of corticobulbar tracts, glial scar formation and cell proliferation, in which rTMS was applied starting 3 days after the stroke onset for 28 days. In the high-frequency rTMS received animals reduced DNA fragmentation, infarct volume and improved CBF were observed, which were associated with increased Bcl-xL activity and reduced Bax, caspase-1, and caspase-3 activations. Moreover, increased angiogenesis, growth factors; and reduced inflammation and axonal sprouting related gene expressions were observed. These results correlated with reduced microglial activation, neuronal degeneration, glial scar formation and

improved functional recovery, tissue remodeling, contralesional pyramidal tract plasticity and neurogenesis in the subacute rTMS treated animals. Overall, we propose that high-frequency rTMS in stroke patients can be used to promote functional recovery by inducing the endogenous repair and recovery mechanisms of the brain.

Keywords: neurodegeneration, apoptosis, tissue remodeling, rTMS, cerebral ischemia

INTRODUCTION

Ischemic- stroke is a global health-care condition which mainly results in motor impairment and causes long-term disability (Langhorne et al., 2009). Brain injury following ischemic-stroke develops from free radical generations, excitotoxicity, peri-infarct depolarizations, inflammation, and apoptosis (Dirnagl et al., 1999). While brain has endogenous capacity to protect neurons and restore the lost neuronal function, this capacity is often limited and insufficient to promote survival and recovery. Therefore, both protection of neurons in the acute-stroke and promotion of post-stroke motor recovery are believed to be critical in stroke treatment. Motor performance is also affected from the imbalanced interhemispheric inhibition which results in the increased inhibition of the ipsilateral primary motor cortex and hence, decreased motor outcome (Liepert et al., 2000; Murase et al., 2004).

Transcranial magnetic stimulation (TMS), a non-invasive neuromodulation technique of alternating magnetic fields, has been proposed to enhance cortical excitability in the affected hemisphere (Khedr et al., 2005; Lefaucheur, 2006). Recently, repetitive TMS (rTMS) which uses short and repeated magnetic bursts has been demonstrated to exert longer lasting effects than non-repetitive TMS (Hsu et al., 2012; Chervyakov et al., 2015) and is currently being investigated for the treatment of several neurological and psychiatric conditions including depression (Dell'osso et al., 2011), Parkinson's disease (Wagle Shukla et al., 2016), Alzheimer's disease (Koch et al., 2017), and stroke (Lefaucheur, 2006).

Recent experimental studies revealed that 60 Hz TMS treatment attenuates tail and limp paralysis, oxidative stress and cell death via activation of antioxidant system after experimental autoimmune encephalomyelitis in rats (Medina-Fernandez et al., 2017). It was revealed that high frequency rTMS increases cell proliferation and synaptic plasticity and inhibits apoptotic cell death through activation of BDNF, CREB, ERK, and AKT signaling pathways in neuronal cells after oxygen glucose deprivation *in vitro* (Baek et al., 2018). Furthermore, it was shown that rTMS ameliorates cognitive deficits, lesion size via activation of Bcl-2 and inhibition of Bax after ischemic stroke (Guo et al., 2017) and cytochrome-c release and inflammation after hemicerebellectomy in rats (Sasso et al., 2016). Although rTMS has gained great interest in treatment of patients with neurodegenerative disorders, there are inconsistent data on the efficacy of high and low-frequency rTMS in cellular and molecular aspects.

Although there are several studies conducted in humans, the action mechanism responsible for the positive effects of rTMS treatment has not been fully elucidated, partially due to the lack of detailed experimental studies. In this context, we conducted these studies to investigate the molecular and physiological changes induced by inhibitory low (1 Hz) and excitatory high-frequency rTMS (20 Hz) on the acute pathophysiological events and sub-acute recovery processes after occlusion of the middle cerebral artery (MCA) in mice. Here, we provide evidence that high-frequency rTMS induces neuronal survival and regional cerebral blood flow (CBF), while reducing infarct volume and apoptotic cell death. Furthermore, high-frequency rTMS also induced neurogenesis, neuronal plasticity, perilesional tissue remodeling, promoted axonal sprouting and subsequent functional recovery as well as changes in the levels of inflammation-, growth-, angiogenesis-, or neuronal plasticity- related genes in mice.

MATERIALS AND METHODS

Animals and Experimental Procedures

All experimental procedures were carried out with government approval according to NIH guidelines for the care and use of laboratory animals. Ethical committee approval was obtained from Istanbul Medipol University. In this study, three sets of experiments were performed to examine the effects of rTMS stimulation (**Figure 1A**) on the short term and long term outcomes of ischemic stroke; (i) for the analysis of infarct volume- (n = 8–9), laser speckle imaging- (LSI) and gene expression- analyses (n = 5) (**Figure 1B**); (ii) for the analysis of disseminate ischemic injury, protein expression, DNA fragmentation, and neuronal survival (**Figure 1C**; n = 6–7 mice/group), and (iii) for the analysis of long-term behavioral analyzes, tract tracing studies, neuronal degeneration, glial scar formation, microglial activation and cell proliferation (**Figure 1D**; n = 12 mice/group). Experimental protocols were summarized in **Figure 1**. In brief, each experimental set contained 10–12 week-old male Balb/c mice (22–25 g). In the first set, animals were subjected to 90 min of focal cerebral ischemia (FCI), followed by 24 h reperfusion, in this model necrotic cell death following infarct formation is observed (**Figure 1B**). In the second, animals were subjected to 30 min ischemia, followed by 72 h reperfusion induces disseminated or apoptotic cell death (**Figure 1C**). In the third set, animals were subjected to 30 min ischemia, followed by 42 days reperfusion, it is a short term ischemia and allows animal survival for a long term experiment in the context of ethical concerns (**Figure 1D**). Animals were maintained under a constant 12:12-h light–dark regimen with ad libitum access to food and water. In the each set, animals were divided into three groups based on the application regimen of repetitive transcranial magnetic stimulation

(rTMS); control group (did not receive rTMS), 1 Hz group (received 1 Hz rTMS) and 20 Hz group (received 20 Hz rTMS) under 1% isofluorane anesthesia.

Induction of Focal Cerebral Ischemia

Focal cerebral ischemia was induced by middle cerebral artery occlusion (MCAo). Animals were anesthetized with 1% isofluorane (30% O_2, reminder N_2O), and rectal temperature was maintained between 36.5 and 37.0°C using a feedback-controlled heating system. During the experiments, CBF was measured using a laser Doppler flowmetry (LDF) with a flexible 0.5 mm fiber optic probe (Perimed), which was attached to the intact skull overlying the MCA territory (2 mm posterior/6 mm lateral from bregma). LDF changes were monitored up to 1 min after the onset of reperfusion or just before rTMS treatment. For the induction of FCI, a midline neck incision was made, and the left common and external carotid arteries were isolated and ligated. A microvascular clip (FE691; Aesculap) was temporarily placed on the internal carotid artery. A 8-0 nylon monofilament (Ethilon; Ethicon) coated with silicon resin (Xantopren; diameter of the coated thread: 180–190 μm) was introduced through a small incision into the common carotid artery and advanced 9 mm distal to the carotid bifurcation for MCAo. In the first set in which mice were exposed to 90 min of MCAo, animals were sacrificed under deep anesthesia (4% isofluorane) 24 h after the onset of MCAo. Brains were removed, frozen on dry ice, and cut on a cryostat into coronal 18-μm sections for studying infarct volume. In the second set, animals were sacrificed 72 h after the onset of MCAo and in the third set, animals were sacrificed 42 days after MCAo. In the third set, to label proliferating cells, 50 mg/kg 5-Bromo-2′-deoxyuridine (BrdU, #B5002 Sigma) was intraperitoneally injected to all animals starting from day 3 to the end of the experiment after MCAo (Doeppner et al., 2017) and animals were transcardially perfused with 0.9% NaCl at 42 days after the MCAo. Brain tissue was frozen on dry ice and cut on a cryostat into 18-μm coronal sections (Kilic et al., 2010).

Repetitive Transcranial Magnetic (rTMS) Stimulation

To examine the effects of rTMS stimulation on the short term and long term outcomes of ischemic stroke, three sets of experiments were carried out. In the each set, animals were divided into three groups based on the application regimen of rTMS; control group (did not receive rTMS), 1 Hz group and 20 Hz group. In the first set, mice were exposed to 90 min of MCAo, received one session of stimulation for 10 min under anesthesia immediately after the induction of reperfusion. In the second set, mice were exposed to 30 min of MCAo and received three sessions of stimulation for 10 min per day under anesthesia starting from the induction of reperfusion. In the third set, animals were subjected to 30 min MCAo. A regimen of 10 min rTMS per day for 28 days was initiated 3 days after the ischemia/reperfusion. Each 10 min treatment session consists of 5 s stimulation followed by 55 s rest period repeated for 10 times and performed under anesthesia. Control animals were placed under the rTMS coil under anesthesia but did not receive stimulation.

In all sets, a magnetic stimulator (Neurosoft, Avm Saglik) with a figure-of-eight coil (38 mm inner diameter, 94 mm outer diameter) was used to stimulate rTMS. Although both hemispheres were affected by rTMS stimulation to some extend, the stimulation site was set as the primary motor cortex (left M1) by placing the rTMS device over. Motor evoked potentials (MEPs) were measured at the biceps femoris (BF) muscle of the right hind limb using an electromyography as previously described (Ogiue-Ikeda et al., 2003; Yoon et al., 2011). The resting motor threshold (RMT) was defined as the lowest stimulator output where the peak-to-peak amplitude of MEP was greater than 5% of its maximal amplitude in at least half of 10 trials. The rTMS stimulation was applied as follows; 5 s stimulation followed by 55 s rest for a total duration of 10 min at either 1 Hz or 20 Hz. Stimulation intensity was set at 100% of the RMT (i.e., 26% of the maximum output of the stimulator).

Infarct Volume Analysis

For the evaluation of infarct volume, coronal brain sections were collected at four equidistant brain levels, 2 mm apart, from mice exposed to 90 min MCAo, which were stained with cresyl violet according to a standard protocol (Caglayan et al., 2017). For each section, the border between infarcted and non-infarcted areas was outlined using ImageJ (National Institute of Health, Bethesda, MD, United States). Infarct area was calculated by subtracting the area of the non-infarcted ipsilateral hemisphere from that of the contralateral side. Infarct volume was calculated by integration of infarct areas.

Laser Speckle Imaging (LSI)

To evaluate the effect of rTMS on microcirculation, LSI was carried out as described previously (Beker et al., 2015) with minor modifications. Briefly, mice were exposed to 90 min MCAo as described above. Starting 1 min after reperfusion, real-time CBF changes were recorded by Pericam PSI System (Perimed). To evaluate the CBF changes in the ischemic core and ischemic penumbra regions of interest (ROI) covering 1.0 mm × 5.5 mm (in lateral and rostrocaudal direction, respectively) were defined 0.5 and 1.5 lateral and 0.5 mm posterior to the bregma, in which mean CBF was calculated using a blood perfusion imaging software (PIMSoft; Perimed). Regional CBF was recorded throughout the 60 min observation period after rTMS treatment. From the measurements obtained, relative CBF changes (in %) at the end of the observation period which is compared with the values of before rTMS treatment after MCAo.

Analysis of DNA Fragmentation/Apoptosis

For the evaluation of neuronal injury, coronal brain sections at the level of the bregma of mice exposed to 30 min MCAo were fixed with 4% paraformaldehyde (PFA)/0.1 M phosphate buffered saline (PBS) and were labeled using a TUNEL kit (In Situ Cell Death Detection Kit; Roche). Sections were counterstained with 4′, 6-diamidino- 2-phenylindole (DAPI). Stainings were analyzed by quantifying DNA fragmented cells (which in 30 min MCAo are equivalent to neurons) in 12 adjacent ROI in the striatum,

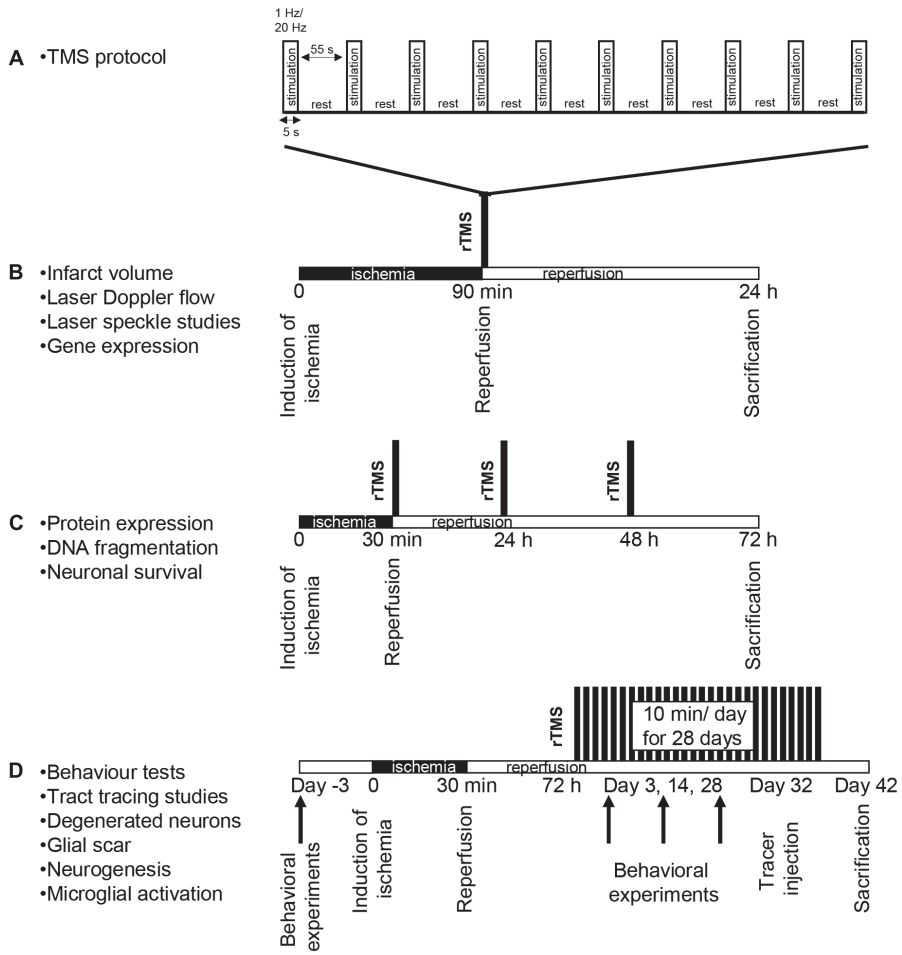


FIGURE 1 | Experimental design. Stimulation method of repetitive transcranial magnetic stimulation (rTMS) **(A)** and experimental protocol for 90 min ischemia 24 h reperfusion set **(B)**, for 30 min ischemia 72 h reperfusion set **(C)** and for long term set following 30 min ischemia **(D)**. In the first experimental setup, animals received either low-frequency (1 Hz) or high-frequency (20 Hz) rTMS for a total of 10 min with repeated 5 s stimulation and 55 s resting periods with the onset of reperfusion **(A)**. Control animals were placed under the rTMS coil but not subjected to stimulation. All rTMS stimulations were carried out under anesthesia and control animals received sham stimulation under anesthesia.

each measuring 62,500 μm^2, under a laser scanning confocal microscope (LSM 780, Carl Zeiss) (Caglayan et al., 2017).

Analysis of Neuronal Survival

For the analyzes of neuronal survival, adjacent brain sections of the same animals were fixed in 4% paraformaldehyde (PFA)/0.1 M PBS, washed and immersed for 1 h in 0.1 M PBS containing 0.3% Triton X-100 (PBS-T)/10% normal goat serum. Sections were incubated overnight at 4°C with Cy3-conjugated monoclonal mouse anti-NeuN (MAB377C3; Chemicon). Next day, sections were incubated with 4′, 6-diamidino-2-phenylindole (DAPI). Sections were analyzed using a laser scanning confocal Zeiss LSM780 microscope (Carl Zeiss). Nine different ROI in the striatum, each measuring 62,500 μm^2, were evaluated. Mean numbers of NeuN+ cells were analyzed in the ischemic and contralesional striatum. By dividing results obtained in both hemispheres, the percentage of surviving neurons in the ischemic striatum was determined.

Analysis of Capillary Density

For the analysis of capillary density, brain sections of the same animals were fixed in 4% PFA/0.1 M PBS, washed and immersed for 1 h in 0.1 M PBS containing 0.3% Triton X-100 (PBS-T)/10% normal goat serum. Sections were incubated overnight at 4°C with anti-CD31 (ab28364; Abcam) that were detected with Alexa Fluor 488-conjugated secondary antibody. Next day, sections were washed with 0.1 M PBS and incubated with DAPI. Sections were evaluated by counting the number of CD31 positive vessel profiles in rectangular fields, measuring 500,000 μm^2.

Western Blot Analysis

Tissue samples from ischemic striatum of control (no treatment), 1 Hz rTMS or 20 Hz rTMS applied animals were obtained 72 h after 30 min of MCAo. To analyze the apoptotic protein expressions, Western blot of these samples were performed as previously described (Kelestemur et al., 2016; Beker et al., 2017).

Membranes were blocked with 5% non-fat milk (Blotto, #sc-2324, ChemCruz) in Tris-buffered saline (TBS) containing 0.1% Tween (TBS-T; blocking solution) for 1 h at room temperature, washed in TBS-T, and incubated overnight with a primary antibody against Bcl-xL (#2764, Cell Signaling), Bax (#2772, Cell Signaling), cleaved caspase-1 (#22165, Santa Cruz), total caspase-3 (ab13847, Abcam), or cleaved caspase-3 (#9664, Cell Signaling). Individual blots were performed at least three times. Protein loading was controlled by stripping and reprobing with anti-β-actin antibody (#4970, Cell Signaling). Protein levels were analyzed densitometrically using an image analysis software (ImageJ; National Institute of Health, Bethesda, MD, United States), corrected with values determined on β-actin blots and expressed as relative values compared with the control group.

Gene Expression Analysis by RT-PCR

Tissue samples from striatum of control (no treatment), 1 Hz rTMS or 20 Hz rTMS applied animals were obtained 24 h after 90 min of MCAo. Total RNA was extracted using AllPrep DNA/RNA/Protein Mini Kit (#80004, Qiagen). Quality and quantity of RNA samples were determined by spectrophotometric analysis. cDNA was synthesized from 1 μL total RNA using Transcriptor First Strand cDNA Synthesis Kit (#04896866001, Roche). qPCR was performed in triplicates for each sample and repeated three times using SsoAdvanced Universal SYBR Green Supermix (#172-5272, Bio-Rad) in CFX Connect™ Real-Time PCR Detection System (#185-5201, Bio-Rad). GAPDH and β-actin were used as internal controls. Relative expression of each gene was calculated as fold-change of the control using the comparative Ct method ($2^{-\Delta\Delta Ct}$) and normalized to GAPDH and β-actin. Primer pairs used are given in **Supplementary Table S1**.

Functional Neurological Tests

Grip Strength Test

The grip strength test consists of a spring balance coupled with a Newtonmeter (Medio-Line Spring Scale, metric, 300 g) that is attached to a triangular steel wire, which the animal instinctively grasps. When pulled by the tail, the animal exerts force on the steel wire (Kilic et al., 2010). Grip strength was evaluated at the right paretic forepaw, the left non-paretic forepaw being wrapped with adhesive tape. Grip strength was evaluated five times on occasion of each test, for which mean values were calculated. From these data, percentage values (post-ischemic vs. pre-ischemic) were computed. Pre-ischemic results did not differ between groups.

RotaRod Test

RotaRod test was used for the analyses of the effect of rTMS on motor coordination. The RotaRod is a rotating drum with a speed accelerating from 6 to 40 rpm (model 47600;Ugo Basile, Comerío, Italy),which allows to assess motor coordination skills (Kilic et al., 2014). Maximum speed is reached after 245 s, and the time at which the animal drops off the drum is evaluated (maximum testing time: 300 s). Measurements were performed five times each on the same occasion when grip strength was evaluated. For all five measurements, mean values were computed, from which percentage values (post-ischemic vs. pre-ischemic) were calculated. Pre-ischemic data did not differ between groups.

Open Field Test

Open field test was used for the evaluation of locomotor activity of animals. The open field is a round arena (diameter: 150 cm) covered by a white plastic floor, surrounded by a 35 cm high sidewall made of white polypropylene, which allows to measure spontaneous locomotor activity and exploration behavior (Kilic et al., 2008). The arena is divided into three sections, including an outer wall zone (17.7% of diameter, close to the wall), an intermediate transition zone (32.3% of diameter), and an inner zone (50% of diameter, the center of the arena). Each mouse was released near the wall and observed for 10 min. Animal paths were tracked with an electronic imaging system (Anymaze, Stoelting Europe). To determine measures of exploratory behavior and anxiety, the time resting and progressing were assessed.

Tail Suspension Test

For the analysis of depressive-like state of animals, tail suspension test was performed in mice that were suspended 50 cm above the floor using an adhesive tape placed 1 cm from the tip of the tail. Total immobility time was recorded for 5 min, indicating depressive-like state of animals.

Assessment of Brain Atrophy, Degeneration, and Glial Scar

For the evaluation of striatum atrophy, coronal brain sections were taken from the animals of the third set, stained with cresyl violet according to a previously described protocol (Kilic et al., 2014). Striatal area was outlined using an image analysis system (Image J; National Institutes of Health). For the evaluation of degenerating cells, sections were stained with Fluorojade C (#AG325 Millipore) according to manufacturer's protocol. In case of GFAP stainings, the area of scar tissue was outlined using the Zen Blue software (version 2012; Carl Zeiss).

Immunohistochemistry for Cell Proliferation Studies and Microglial Activation

To analyze the proliferating cells, 18-μm thick brain sections were prepared using a cryostat (CM1950, Leica) from the animals of the second set. Sections were then blocked in 10% goat serum (#G9023, Sigma) in PBS solution and incubated with monoclonal rat anti-BrdU antibody (#ab6326, Abcam). To identify the BrdU(+) proliferating cells, double staining was performed using anti-NeuN (#MAB377C3, Millipore), anti-GFAP (#3656, Cell Signaling) or anti-Iba1 (#019-1974, Wako) antibodies overnight at 4°C. On the next day, sections were washed with PBS and incubated with the appropriate secondary antibodies for 1 h at room temperature. Sections were then imaged with a laser scanning confocal microscopy (LSM 780,

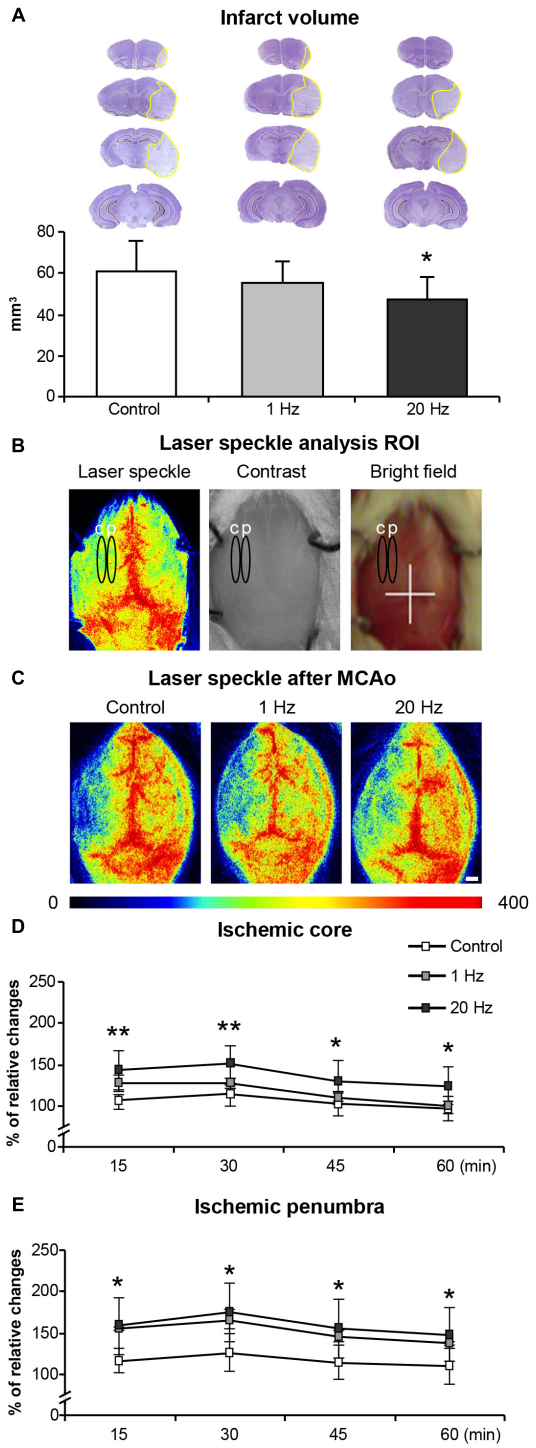


FIGURE 2 | Effects of rTMS on infarct volume and post-ischemic regional cerebral blood flow (CBF). Infarct volume **(A)**, laser speckle analysis ROI **(B)**, laser speckle images (LSI) after rTMS treatment **(C)** microcirculation on ischemic core **(D)**, and penumbra **(E)**. Letter c on **(B)** represents ischemic core area, letter p represents penumbra area. Data were evaluated by one-way ANOVA followed by LSD tests. Data are presented as mean ± SD values (n = 8–9 mice/group for infarct volume/n = 5/group for microcirculation analysis). *$p < 0.05$ compared with control for **(A)**, **$p < 0.01$/*$p < 0.05$ comparison between control and 20 Hz rTMS groups for **(D,E)**.

Carl Zeiss). Nine different ROI in the ischemic striatum, each measuring 62,500 μm^2, were evaluated. Numbers of double immunopositive cells were counted blindly.

Delivery of Biotinylated Dextran Amine (BDA) and Axonal Projection Analysis

To evaluate the axonal projections induced by rTMS treatment, animals were subjected to 30 min of MCAo and received no treatment, 1 Hz rTMS or 20 Hz rTMS for 28 days. At the end of the completion of behavior tests, 10% Biotinylated Dextran Amine (BDA, 10,000 MW, #D1956, Invitrogen) diluted in 0.01 M PBS was injected into contralateral motor cortex (0.5 mm rostral and 2.5 mm lateral to the bregma) of animals as described previously (Kilic et al., 2014). Sections were washed in PBS, blocked with 10% normal goat serum in PBS for 1 h at room temperature and incubated with AlexaFluor 555 conjugated streptavidin (#S21381, Invitrogen) for 90 min at room temperature. Sections were then imaged with confocal microscopy (LSM 780, Carl Zeiss). A 1000 μm-thick virtual straight line was drawn on images at the midline to separate the hemispheres. Numbers of axons crossing the line were counted blindly and averages for each of the three groups were calculated.

Statistical Analysis

Statistical analyses were performed using SPSS (version 15, SPSS, Inc.) software. Data were evaluated by one-way ANOVA followed by LSD tests. Data are presented as mean ± SD values. Throughout the study, p-values < 0.05 were considered significant.

RESULTS

High-Frequency rTMS Decreases Infarct Volume and Enhances Microcirculation

The LDF values reproducibly decreased to −15–20% of pre-ischemic control during MCAo. Reproducibility of reperfusion onset was also recorded by LDF after 90 min of MCAo. LDF measurements during ischemia did not reveal differences in CBF differences among the experimental groups (data not shown). Infarct volume as evaluated by cresyl violet staining was significantly reduced in the high-frequency rTMS applied animals when compared with control or low-frequency groups (**Figure 2A**). Interestingly, low-frequency rTMS also resulted in a slight, but not significant, decrease in the infarct volume. Moreover, to investigate the hemodynamic effects of rTMS, instantaneous CBF of the ischemic core was evaluated at different time points using LSI (**Figure 2C**).

Although we used LDF for the evaluation of CBF changes, it does not provide accurate absolute regional CBF values because of the small size of flexible optic probe used. Therefore, we have evaluated regional CBF by using more accurate LSI just after rTMS treatments represented in **Figures 2B,C**. In contrast to control and low-frequency TMS, high-frequency rTMS significantly increased regional CBF above the ischemic

core and penumbra at 15, 30, 45, and 60 min after reperfusion (**Figures 2D,E**). More pronounced increase in CBF was observed in the ischemic core region in high-frequency rTMS treated animals but not in low-frequency group (**Figure 2C**). Low-frequency rTMS increased CBF particularly in the ischemic penumbra region but it was not statistically significant (**Figure 2E**).

High-Frequency rTMS Reduces Apoptotic Cell Death and Capillary Injury, While Promoting Neuronal Survival

To determine the effects of rTMS on apoptotic cell death mechanisms, the second experimental setup which consisted of 30 min of MCAo followed by 72 h reperfusion was used, as it induces a less severe injury which is accompanied by selective neuronal cell death (Beker et al., 2015). DNA fragmentation as assessed at the end of 72 h using TUNEL assay was significantly decreased in the high-frequency rTMS group (**Figure 3A**). Neuronal survival, as evaluated by NeuN immunopositive cell count in the ipsilateral and contralateral striata and given as the per cent of total NeuN+ cells of the contralateral hemisphere, was also significantly increased in the 20 Hz rTMS group (**Figure 3B**). On the other hand, low-frequency rTMS demonstrated a slight (and non-significant) decrease in DNA fragmentation and a slight increase in the neuronal survival when compared with control. We have also studied capillary injury after 30 min of MCAo by evaluating CD31 positive cells. Vascular density was significantly increased in 20 Hz rTMS treated animals compared with controls and 1 Hz rTMS groups. As compared with control, 20 Hz rTMS protected capillary integrity significantly ($p = 0.007$). Capillary density were 85 $\pm$ 8 in 20 Hz rTMS, 67 $\pm$ 6 in 1 Hz rTMS ($p = 0.008$ compared with 20 Hz rTMS) and 65 $\pm$ 7 vessel/square in control animals ($p = 0.007$ compared with 20 Hz rTMS). Next, we investigated the expressions of apoptosis-related proteins; Bcl-xL, Bax, cleaved caspase-1, and cleaved caspase-3 in the ipsilateral hemisphere using Western blot analysis. High-frequency rTMS significantly increased protein levels of anti-apoptotic Bcl-xL (**Figure 3C**), while decreasing protein levels of neuronal death-associated Bax (**Figure 3D**), cleaved caspase-1 (**Figure 3E**) and cleaved caspase-3/caspase-3 (**Figure 3F**).

rTMS Reduces Inflammatory Responses, Increases Angiogenesis, Growth Factors, and Reduces Axonal Outgrowth Inhibitors Related Gene Expressions

The sustained effect of rTMS on the neurons was ascribed to its ability to modulate gene expression and hence, cause long-term alterations in the intracellular signaling. To study whether low-frequency and high-frequency rTMS exerted such effects, we determined the expressions of a number of genes related to inflammation, angiogenesis, plasticity and trophic factors in animals subjected to no stimulation, 1 Hz rTMS or 20 Hz rTMS after 90 min MCAo using qPCR analyses. High-frequency rTMS significantly decreased the expressions of inflammation-related genes; IL1β, TNFα, and TGFβ (**Figures 4A–C**) and MMP9 (**Figure 4D**), while significantly upregulating angiogenesis-related VEGF-A and VEGF-B (**Figures 4E,F**). Evaluation of neuroplasticity related gene expression demonstrated that high-frequency rTMS significantly increased growth-promoting gene GAP43 (**Figure 4G**), whereas significantly decreased growth inhibiting genes Ncam1 (**Figure 4H**), Neurocan, Versican, Ephrin A5, and Ephrin B1 (**Figures 4L–O**) when compared with low frequency rTMS. Of the trophic factors analyzed, high-frequency rTMS significantly increased the expression of CNTF, CDNF, and MANF (**Figures 4I–K**) when compared with low frequency rTMS. It is interesting that the expression of axonal growth related gene Netrin1 was downregulated by 20 Hz rTMS (**Figure 4P**).

Functional Recovery Is Enhanced by High-Frequency rTMS

Functional recovery was assessed at days 3, 14, and 28 in the third experimental setup in which mice were subjected to 30 min MCAo. Grip strength and motor coordination assessments indicated a significant increase in the motor force in the paretic right forelimb in the high-frequency rTMS group when compared with control animals at 28 days after MCAo (**Figures 5A,B**). Time spent mobile in tail suspension test was evaluated to investigate the effect of rTMS on depression. Even though there was no significant difference among the groups at day 3 or day 14, high-frequency rTMS significantly increased time spent mobile at day 28 when compared with control and low-frequency rTMS (**Figure 5C**). High-frequency rTMS also significantly increased the spontaneous exploration behavior, as evaluated by open-field test, at day 28 when compared with low-frequency rTMS (**Figure 5D**). As expected, high-frequency rTMS significantly improved all the functional parameters evaluated, supporting the human studies indicating its promising effects on motor functions (Takeuchi et al., 2009; Khedr et al., 2010).

High-Frequency rTMS Decreases Striatal Atrophy and Glial Scar Formation, While Promoting Neurogenesis, and Axonal Projections

Striatal area was evaluated to examine the effect of rTMS treatments on long term tissue damage. Striatal area (**Figure 6A**), number of degenerating cells (**Figure 6B**) and glial scar area (**Figure 6C**) were significantly decreased in the 20 Hz rTMS group. To examine the proliferating cells in the ischemic striatum, BrdU+ cells were analyzed and results indicated a significant increase in the number of BrdU+ cells in animals of the third experimental setup. When stained with specific cellular markers, BrdU+ cells indicate the differentiation of the specific cell type. Thus, double staining with mature neuronal nuclei, NeuN, and BrdU antibodies revealed significantly increased neurogenesis in the high-frequency rTMS group when compared with low-frequency rTMS (**Figure 7A**). Number of proliferating astrocytes, as demonstrated by double immunostaining with glial marker, GFAP, and BrdU was slightly, but not significantly, increased with 20 Hz rTMS (**Figure 7B**). We further analyzed the microglial activation

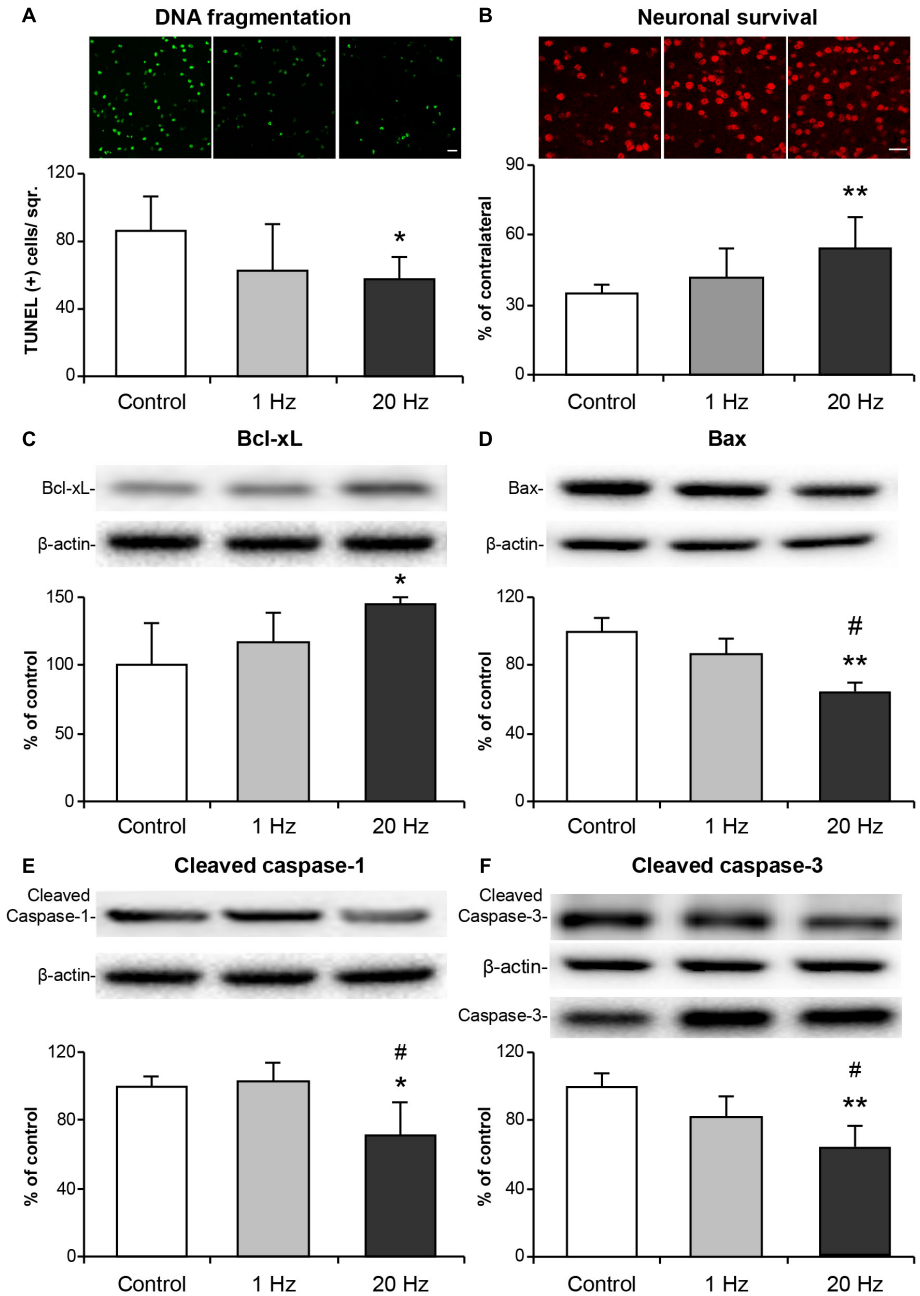


FIGURE 3 | 20 Hz rTMS reduces DNA fragmentation, pro-apoptotic protein expressions and promotes neuronal survival. Disseminate neuronal injury in the striatum was assessed by terminal transferase dUTP nick end labeling (TUNEL) **(A)**, neuronal survival was assessed using NeuN stained brain sections **(B)**, expressions of anti-apoptotic Bcl-xL **(C)**, pro-apoptotic Bax **(D)**, inflammation related cleaved caspase-1 **(E)**, pro-apoptotic cleaved caspase-3 **(F)** were demonstrated with Western blot. Data are mean ± SD values (n = 6–7 mice/group). Data were evaluated by one-way ANOVA followed by LSD tests. Data are presented as mean ± SD values. $^{**}p < 0.01$/$^{*}p < 0.05$ compared with control/$^{\#}p < 0.05$ compared with 1 Hz rTMS. Scale bars are 100 μm.

in the ischemic striatum by counting Iba1+ cells and found that the number of Iba1+ cells in ischemic striatum was significantly reduced by high-frequency rTMS (**Figure 7C**). On the other hand, high-frequency rTMS slightly decreased the number of Iba1/BrdU double immunopositive cells in the ischemic striatum; while low-frequency rTMS resulted in a slight increase (**Figure 7D**).

In addition, in the third experimental setup, corticobulbar projections following ischemia were determined using BDA injections after 28 days of daily rTMS treatment to allow the completion of the formation of new axonal connections (**Figure 8A**). Axonal projections were evaluated at the facial nucleus level (bregma −5.8 to −6.3 mm) by drawing a virtual straight line (yellow line, **Figure 8B**) at

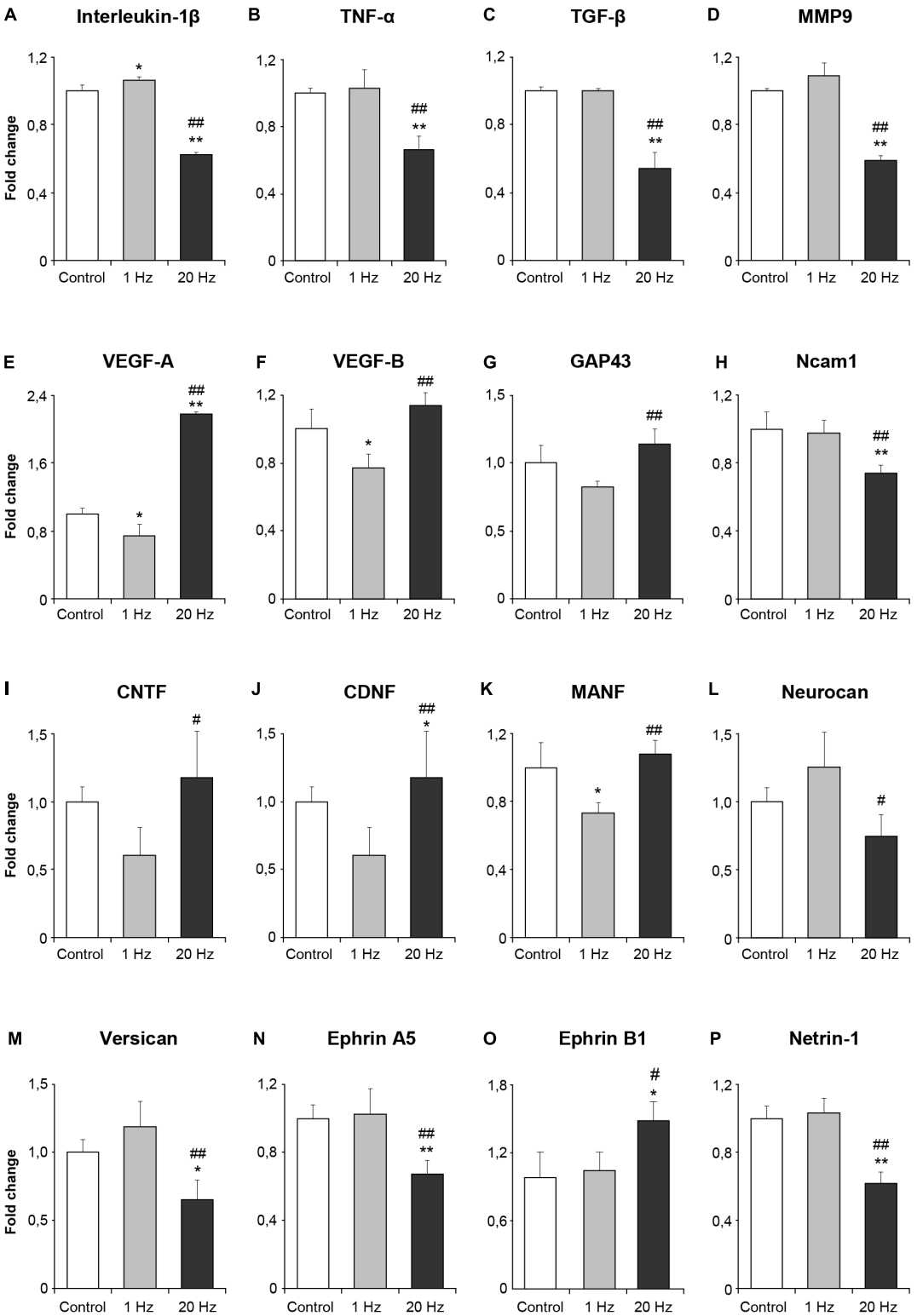


FIGURE 4 | Effect of rTMS on gene expression after cerebral ischemia. Inflammation-related genes after ischemia IL1β **(A)**, TNFα **(B)** and TGFβ **(C)** and MMP9 **(D)**, angiogenesis-related VEGF-A **(E)** and VEGF-B **(F)**, neuroplasticity related GAP43 **(G)** and Ncam1 **(H)**, the trophic factors CNTF **(I)**, CDNF **(J)**, MANF **(K)** and Neurocan **(L)**, growth inhibiting genes Versican **(M)**, Ephrin A5 **(N)** and Ephrin B1 **(O)**, axonal growth related gene Netrin1 **(P)**. Data were evaluated by one-way ANOVA followed by LSD tests. Data are presented as mean ± SD values (n = 8–9 mice/group). $^{**}p < 0.01/^{*}p < 0.05$ compared with control, $^{\#\#}p < 0.01/^{\#}p < 0.05$ compared with 1 Hz rTMS.

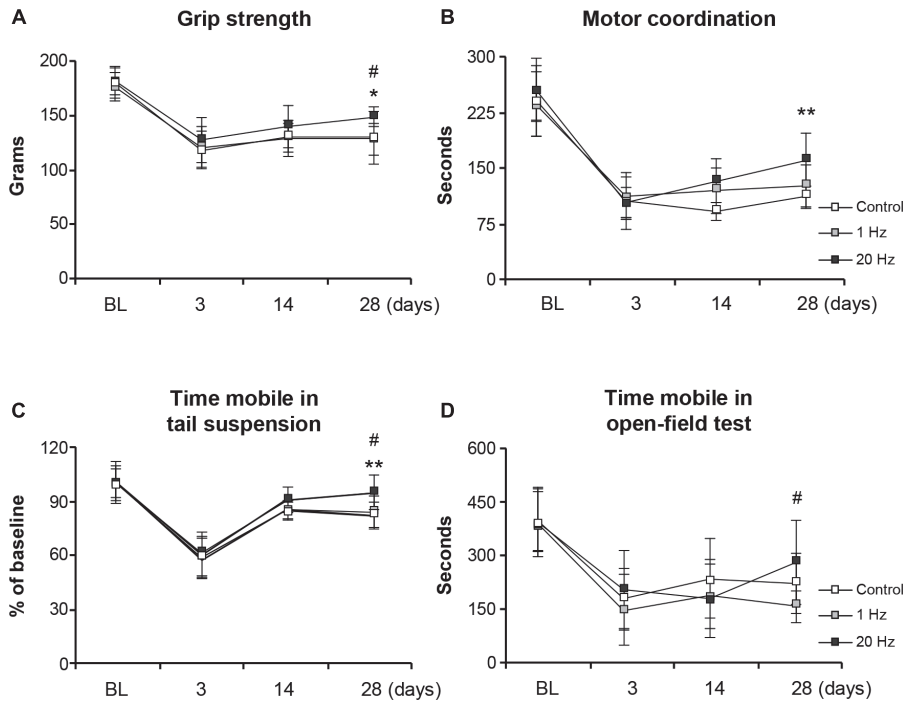


FIGURE 5 | 20 Hz rTMS promotes post-ischemic grip strength and motor coordination, thus reducing depression. Evaluation of post-ischemic recovery of grip strength **(A)**, motor coordination **(B)**, depression **(C)**, and spontaneous activity **(D)**. Data were evaluated by one-way ANOVA followed by LSD tests. Data are presented as mean ± SD values ($n = 12$ mice/group). $^{**}p < 0.01$/$^{*}p < 0.05$ compared with control, $^{\#}p < 0.05$ compared with 1 Hz rTMS.

the midline to separate the two hemispheres and to count the number of axons crossing the virtual line. Significantly increased number of axonal projections was observed in the 20 Hz rTMS group, whereas 1 Hz rTMS only slightly increased the number of fibers crossing to the other hemisphere (**Figure 8C**).

DISCUSSION

According to the World Health Organization, stroke is the third leading cause of disability worldwide (Johnson et al., 2016). Although it is estimated that each year 15 million people suffer from a stroke episode, due to the limited usable time frame of tissue plasminogen activator, only a small per cent of patients can actually benefit from the only treatment available (Thrift et al., 2014). To this end, rTMS was promoted as a non-invasive approach that can help restoring the unbalanced interhemispheric inhibition which results in increased inhibition in the ischemic hemisphere and subsequent worsening in motor function. The physiological effect of rTMS on neuronal activity has not been well-studied. However, the electric currents necessary to stimulate the brain can be produced by rapidly changing magnetic fields. It is assumed that the mechanisms underlying rTMS after-effects appear as observed for long-term potentiation (LTP) and long-term depression (LTD) (Klomjai et al., 2015).

The effects of rTMS on motor recovery following stroke have been reported in meta-analyses of human studies with 362 patients (Hsu et al., 2012; Le et al., 2014). However, the cellular mechanisms mediating rTMS's neuroprotective and restorative activities need to be elucidated. For these aims we made use of mice to examine the roles of low- and high-frequencies of rTMS in the development of (i) brain injury; (ii) brain perfusion; (iii) apoptosis and related signaling pathways; (iv) inflammation, angiogenesis, growth factors and axonal outgrowth related gene expressions after 30 and 90 min of FCI. Thirty min of FCI is a short term ischemic injury model based on MCAo, causing only disseminate neuronal injury in the ischemia-vulnerable striatum, but not the overlying cortex. In this model, acute pathophysiological changes are completed 72 h after MCAo (Kilic et al., 2013). However, 90 min of MCAo causes necrotic cell death or infarct development in the striatum and overlying cortex (Kilic et al., 2013). Therefore two different durations of MCAo model were recruited for the evaluation of acute role of rTMS in the development of injury and related events. For the post-acute role of rTMS, 30 min of MCAo and 42 days reperfusion model was used. For the evaluation of restorative effects of rTMS, treatment was started 3 days after MCAo, just after the completion of acute pathophysiological changes, in order to investigate spontaneous locomotor activity, perilesional tissue remodeling, axonal sprouting of corticobulbar tracts, glial scar formation, and neurogenesis. Here, we have shown that high-frequency rTMS reduced infarct volume, apoptosis and inflammation-related

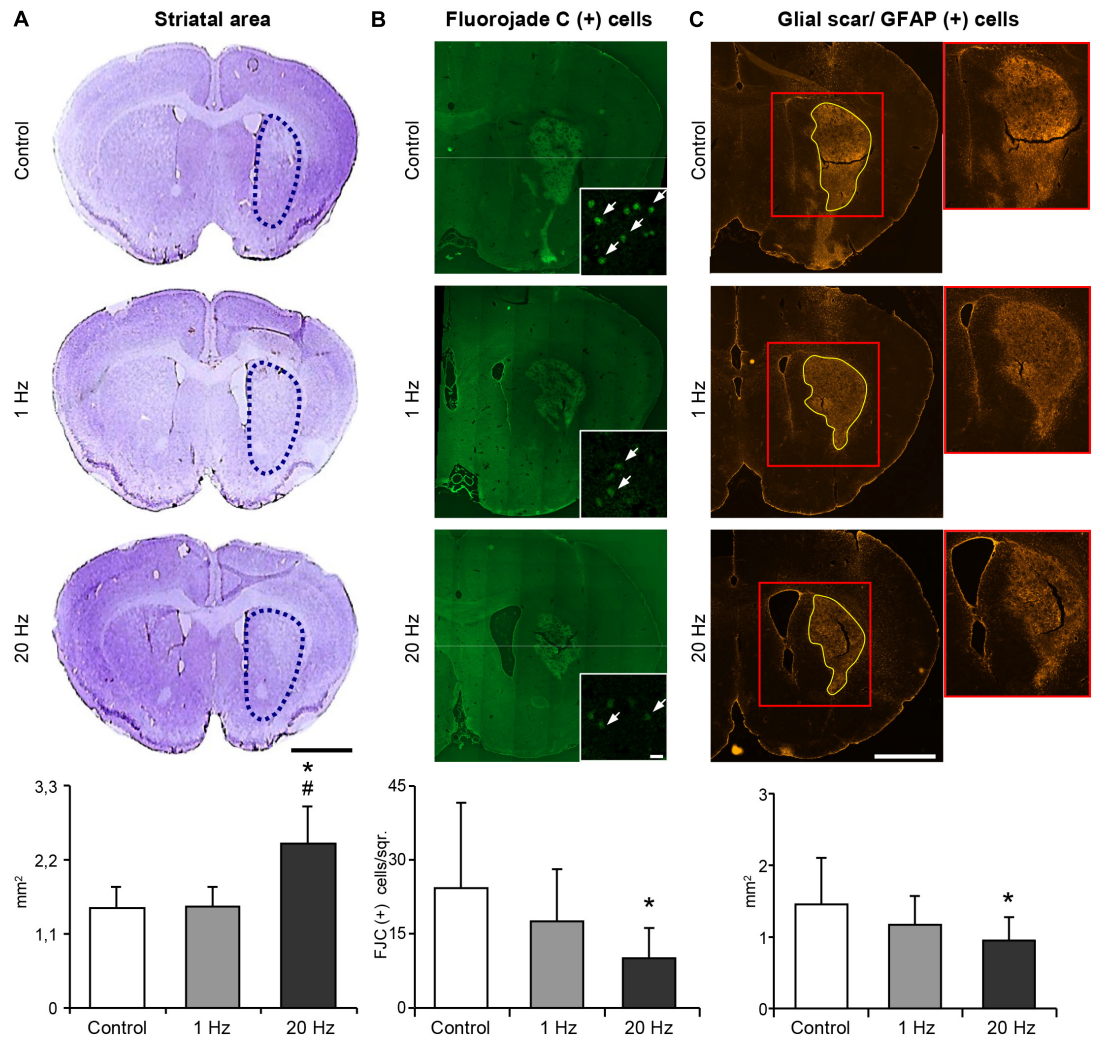


FIGURE 6 | 20 Hz rTMS inhibits delayed neuronal loss and reduces glial scar formation. Striatal atrophy was assessed by cresyl violet staining in the ischemic striatum of animals subjected to 30 min ischemia followed by 42 days reperfusion **(A)**. Dotted black lines indicate the area of ischemic striatum in cresyl violet stained sections. Quantification of striatal area is given in the graphs below. Significantly increased striatal area indicates that 20 Hz rTMS significantly decreased striatal atrophy. Degenerating cells were counted using Fluorojade C stained brain sections **(B)**. 20 Hz rTMS-applied animals displayed significantly decreased number of Fluorojade C (+) cells. White arrows indicate Fluorojade C (+) cells. Glial scar area was measured in GFAP-stained sections in animals subjected to 30 min ischemia followed by 42 days reperfusion **(C)** and high-frequency rTMS resulted in the significantly decreased glial scar area when compared with control. Data were evaluated by one-way ANOVA followed by LSD tests. Data are presented as mean ± SD values (n = 7–8 mice/group). $^{*}p < 0.05$ compared with control group and $^{\#}p < 0.05$ compared with 1 Hz rTMS. Scale bar is 2 mm **(A,C)** 50 μm **(B)**.

gene expression and increased neuronal survival, neurogenesis, contralesional axonal projections and regional CBF, which resulted in improved functional recovery.

For the stimulation of brain, we chose figure-of-eight coiled rTMS due to its producing maximum current at the midline of the figure-eight (Hallett, 2007). Although we assumed that both hemispheres might have been affected by rTMS stimulation to some extent, the main stimulation site was set as the primary motor cortex (left M1). Maximum current or MEPs were measured at the biceps femoris (BF) muscle of the right hind limb using an electromyography as previously described (Ogiue-Ikeda et al., 2003; Yoon et al., 2011). Brain perfusion was monitored by LDF. Although LDF has been in use for the analyses of CBF changes after ischemic stroke in animal experiments, it does not provide accurate absolute regional CBF values because of the small size of flexible optic probe used. Therefore, we have evaluated real time regional CBF also by using more accurate LSI method just after rTMS treatments (Beker et al., 2015). Our data suggest that particularly high- frequency rTMS increased regional CBF in the ischemic core and penumbra. Low-frequency rTMS had almost no effect on brain perfusion in the ischemic-core, while moderate increase in CBF in penumbra was observed. To the best of our knowledge, there is no study measuring CBF in mice reported. However, an overall increase in CBF was observed after 15 Hz rTMS (Loo et al., 2003) and also partially increased CBF on the ipsilateral side of the stimulation

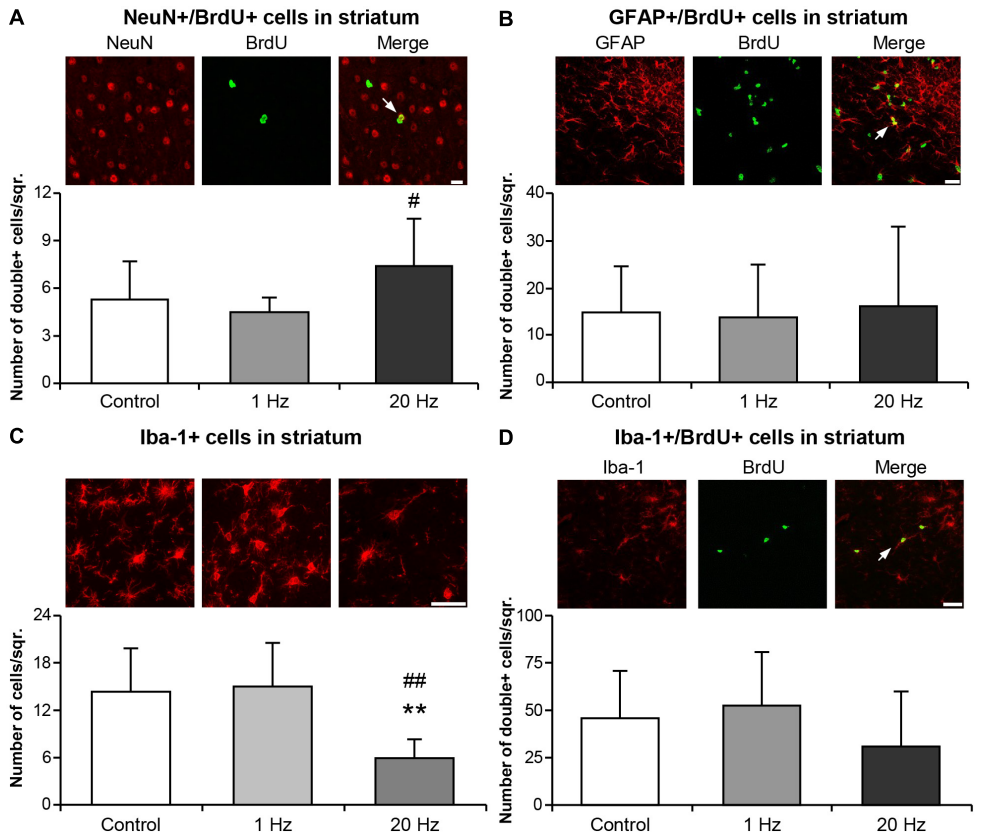


FIGURE 7 | Neurogenesis was induced and Iba-1+ microglial activation was inhibited by 20 Hz rTMS. Post-ischemic cell proliferation was assessed by 5-Bromo-2′-deoxyuridine (BrdU) immunostaining in the ischemic striatum. Co-expressions of BrdU and NeuN **(A)**, GFAP **(B)**, and Iba-1 **(D)**, and microglial activation **(C)** were evaluated from animals subjected to 30 min ischemia followed by 42 days reperfusion. Data were evaluated by one-way ANOVA followed by LSD tests. Data are presented as mean ± SD values (n = 7–8 mice/group). $^{**}p < 0.01$ compared with control group and $^{\#\#}p < 0.01/^{\#}p < 0.05$ compared with 1 Hz rTMS. White arrows indicate double immunopositive stainings. Scale bar is 100 μm **(A,D)** 50 μm **(B,C)**.

after 1 Hz low-frequency of rTMS treatment was revealed in humans (Mesquita et al., 2013).

In the present study, we found that 20 Hz rTMS reduced infarct volume and apoptotic cell death while enhancing neuronal survival, possibly through the enhancement of excitability of neurons in the ipsilateral hemisphere and regulation of apoptosis-related proteins Bax, Bcl-xL, caspase 1, and caspase 3. Moreover, in the subacute phase high-frequency rTMS inhibited delayed neuronal loss and glial scar formation after cerebral ischemia. Increased number of surviving neurons and decreased DNA fragmentation as well as striatal atrophy significantly correlated with functional recovery on the behavioral tests performed. In accordance with our results, high-frequency rTMS was reported to reduce ischemic injury, analyzed by microPET 7 days after MCAo in rats (Gao et al., 2010), and improves functional recovery and cell proliferation 14 days after MCAo (Luo et al., 2017). Furthermore, it was also revealed that high frequency rTMS increased cell proliferation and synaptic plasticity and inhibited apoptotic cell death through activation of BDNF, CREB, ERK, and AKT signaling pathways in neuronal cell culture after oxygen glucose deprivation (Baek et al., 2018). Beneficial effects of rTMS on motor recovery were reported in stroke patients (Hsu et al., 2012). Indeed, we showed that muscular strength and motor coordination were enhanced by high-frequency rTMS. Depression analysis of post-ischemic animals revealed that high-frequency rTMS reduced the depression levels of animals. The ameliorating effect of rTMS on depression has long been known and to date, there are at least four FDA approved rTMS systems for clinical use in depression (Zhang et al., 2014).

Focal cerebral ischemia has been reported to induce neurogenesis in the injured hemisphere in humans (Huttner et al., 2014). In addition to the subventricular zone and subgranular zone of the dentate gyrus in which new neurons are produced in the adult brain, neurogenesis also occurs in the ischemic striatum or cortex, although these areas are not normally accepted as neuron-generating areas in the adult brain (Lindvall and Kokaia, 2015). It is believed that enhancing the endogenous neurogenesis after stroke may support the tissue repair and functional recovery (Lu et al., 2017). Here, we demonstrated that 20 Hz rTMS induced neurogenesis in the ischemic striatum 42 days after MCAo, suggesting that high-frequency rTMS can be implemented to promote functional

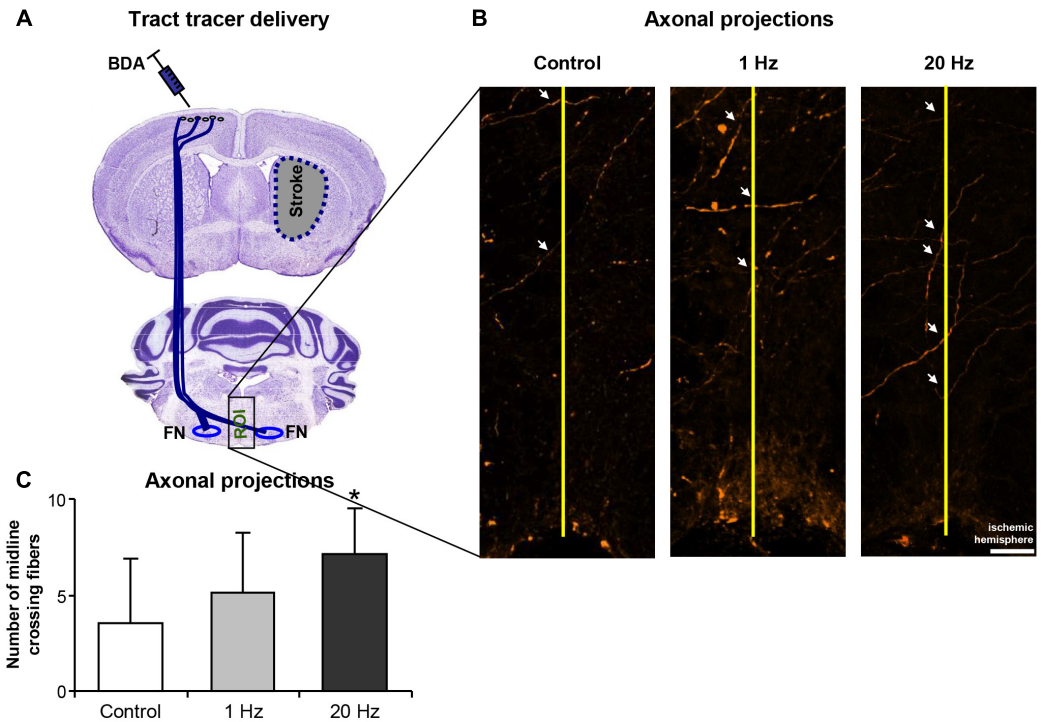


FIGURE 8 | 20 Hz rTMS stimulates plasticity following cerebral ischemia. Midline crossing axon fibers in facial nuclei was traced by BDA administration after cerebral ischemia (for placement of tracer injections see **A**). Axonal projections were evaluated by drawing a virtual straight line (yellow line, **B**) at the midline to separate the two hemispheres and to count the number of axons crossing the virtual line **(C)**. Data were evaluated by one-way ANOVA followed by LSD tests. Data are presented as mean ± SD values. $^*p < 0.05$ compared with control group. Arrows show axonal projections. Scale bar is 100 μm.

recovery. In line with our findings, rTMS-induced neurogenesis was observed in the hippocampi of healthy (Ueyama et al., 2011) and ischemic rats (Guo et al., 2014, 2017; Luo et al., 2017). In addition to neurogenesis, astrocyte and microglial activation also play a role in the repair and plasticity processes in response to ischemic stroke. Consistent with our results, proliferating astrocytes were evaluated in rat hippocampus after high intensity TMS application and a significant alteration was not found (Zhang et al., 2014; Luo et al., 2017). Therefore, we surmised that the increase in neurogenesis may result from the rTMS-induced neural stem cell proliferation and subsequent preferential differentiation into neuronal lineage rather than glial cells. The number of Iba1+ cells was significantly reduced with 20 Hz rTMS in the ischemic striatum and we observed a non-significant trend toward reduction in new-born microglia (BrdU/Iba1 double immunopositive cells). Similarly, decreased number of GFAP and Iba1+ cells was shown in a rat model of spinal cord injury in response to high-frequency (25 Hz) rTMS treatment (Kim et al., 2013) as well as in rats treated with rTMS after focal brain injury (Sasso et al., 2016).

Prolonged aftereffects imply that high-frequency rTMS may result in changes in the overall gene expression profile. Indeed, we observed significant changes in a number of genes related with inflammation, synaptic plasticity, trophic factors, and angiogenesis in the high-frequency rTMS group. Our results indicate that rTMS reduces inflammation-related gene expression (IL1β, TNFα, MMP9, and TGFβ), as suggested using a pulsed electromagnetic field following ischemia (Pena-Philippides et al., 2014). Therefore, we hypothesize that high-frequency rTMS alleviates inflammatory response to ischemic injury not only by downregulating the inflammation-related genes but also by inhibiting the accumulation of Iba1+ cells in the ischemic striatum.

In addition, angiogenesis-related gene expression (VEGF-A, VEGF-B) was induced with high-frequency rTMS. It is of importance that VEGF-A and VEGF-B were also implicated with neurogenesis (Jin et al., 2002; Sun et al., 2006), further supporting the use of rTMS to stimulate neurogenesis following ischemic injury. Moreover, expressions of neurotrophic factors were significantly upregulated by high-frequency rTMS, suggesting that these factors may be important in the therapeutical activity of rTMS.

In parallel with gene expression data demonstrating the downregulation of axon growth inhibitor genes by high-frequency rTMS, we observed that contralesional axonal projections were at least doubled by high-frequency rTMS. Consistent with previous reports suggesting rTMS-induced plasticity (Ogiue-Ikeda et al., 2003; Ahmed and Wieraszko, 2006), we demonstrated neural plasticity in both molecular and structural levels and connected the increased plasticity related molecules reported in rodent studies to the motor functional recovery observed in human patients.

Notably, there are also discrepancies in the clinical data on the outcomes of low-frequency and high-frequency rTMS; however, high-frequency rTMS is generally more likely to produce favorable results. Overall, our results demonstrated that high-frequency (20 Hz) rTMS resulted in better outcomes than low-frequency (1 Hz) rTMS in both acute and subacute ischemic injury models in mice.

CONCLUSION

Our results demonstrate that high-frequency rTMS decreases infarct volume and apoptosis, activates neuronal survival, neurogenesis, neuronal plasticity, and regional CBF. In addition, rTMS induces changes in gene expression, axonal projections and eventually functional recovery, altogether suggesting the complex nature of rTMS-induced mechanisms. Although rTMS was believed to exert its effects mainly by blocking apoptosis, we propose a wider range of mechanisms involved in its favorable effects, mainly consisting of neural-related processes. Overall, our data strongly support the rationale for the use of non-invasive high-frequency rTMS therapy in stroke patients in order to promote functional recovery through the induction of endogenous repair and recovery mechanisms of the brain.

ETHICS STATEMENT

All experimental procedures were carried out with government approval according to NIH guidelines for the care and use of laboratory animals. Ethical committee approval was obtained from Istanbul Medipol University.

AUTHOR CONTRIBUTIONS

ABC, MB, and EK: study concept and design. ABC, MB, BC, EY, and AC: data acquisition and analysis. BY, LH, SK, DH, TD, and EK: manuscript and figure drafting.

FUNDING

This work was funded by Turkish Academy of Sciences (TUBA) and Necmettin Erbakan University (Scientific Research Project No. 161318006).

ACKNOWLEDGMENTS

We would like to thank Dr. Mehmet Yagmur for his unique technical support.

SUPPLEMENTARY MATERIAL

The Supplementary Material for this article can be found online at: https://www.frontiersin.org/articles/10.3389/fncel.2019.00144/full#supplementary-material

TABLE S1 | List of qPCR primers used. Primer sequences were obtained from Harvard Primerbank.

REFERENCES

Ahmed, Z., and Wieraszko, A. (2006). Modulation of learning and hippocampal, neuronal plasticity by repetitive transcranial magnetic stimulation (rTMS). *Bioelectromagnetics* 27, 288–294. doi: 10.1002/bem.20211

Baek, A., Kim, J. H., Pyo, S., Jung, J. H., Park, E. J., Kim, S. H., et al. (2018). The differential effects of repetitive magnetic stimulation in an in vitro neuronal model of ischemia/reperfusion injury. *Front. Neurol.* 9:50. doi: 10.3389/fneur.2018.00050

Beker, M. C., Caglayan, A. B., Kelestemur, T., Caglayan, B., Yalcin, E., Yulug, B., et al. (2015). Effects of normobaric oxygen and melatonin on reperfusion injury: role of cerebral microcirculation. *Oncotarget* 6, 30604–30614. doi: 10.18632/oncotarget.5773

Beker, M. C., Caglayan, B., Yalcin, E., Caglayan, A. B., Turkseven, S., Gurel, B., et al. (2017). Time-of-day dependent neuronal injury after ischemic stroke: implication of circadian clock transcriptional factor bmal1 and survival kinase AKT. *Mol. Neurobiol.* 55, 2565–2576. doi: 10.1007/s12035-017-0524-524

Caglayan, B., Caglayan, A. B., Beker, M. C., Yalcin, E., Beker, M., Kelestemur, T., et al. (2017). Evidence that activation of P2X7R does not exacerbate neuronal death after optic nerve transection and focal cerebral ischemia in mice. *Exp. Neurol.* 296, 23–31. doi: 10.1016/j.expneurol.2017.06.024

Chervyakov, A. V., Chernyavsky, A. Y., Sinitsyn, D. O., and Piradov, M. A. (2015). Possible mechanisms underlying the therapeutic effects of transcranial magnetic stimulation. *Front. Hum. Neurosci.* 9:303. doi: 10.3389/fnhum.2015.00303

Dell'osso, B., Camuri, G., Castellano, F., Vecchi, V., Benedetti, M., Bortolussi, S., et al. (2011). Meta-review of metanalytic studies with repetitive transcranial magnetic stimulation (rTMS) for the treatment of major depression. *Clin. Pract. Epidemiol. Ment. Health* 7, 167–177. doi: 10.2174/1745017901107010167

Dirnagl, U., Iadecola, C., and Moskowitz, M. A. (1999). Pathobiology of ischaemic stroke: an integrated view. *Trends Neurosci.* 22, 391–397. doi: 10.1016/S0166-2236(99)01401-0

Doeppner, T. R., Kaltwasser, B., Sanchez-Mendoza, E. H., Caglayan, A. B., Bahr, M., and Hermann, D. M. (2017). Lithium-induced neuroprotection in stroke involves increased miR-124 expression, reduced RE1-silencing transcription factor abundance and decreased protein deubiquitination by GSK3beta inhibition-independent pathways. *J. Cereb. Blood Flow Metab.* 37, 914–926. doi: 10.1177/0271678X16647738

Gao, F., Wang, S., Guo, Y., Wang, J., Lou, M., Wu, J., et al. (2010). Protective effects of repetitive transcranial magnetic stimulation in a rat model of transient cerebral ischaemia: a microPET study. *Eur. J. Nucl. Med. Mol. Imaging* 37, 954–961. doi: 10.1007/s00259-009-1342-3

Guo, F., Han, X., Zhang, J., Zhao, X., Lou, J., Chen, H., et al. (2014). Repetitive transcranial magnetic stimulation promotes neural stem cell proliferation via the regulation of MiR-25 in a rat model of focal cerebral ischemia. *PLoS One* 9:e109267. doi: 10.1371/journal.pone.0109267

Guo, F., Lou, J., Han, X., Deng, Y., and Huang, X. (2017). Repetitive transcranial magnetic stimulation ameliorates cognitive impairment by enhancing neurogenesis and suppressing apoptosis in the hippocampus in rats with ischemic stroke. *Front. Physiol.* 8:559. doi: 10.3389/fphys.2017.00559

Hallett, M. (2007). Transcranial magnetic stimulation: a primer. *Neuron* 55, 187–199. doi: 10.1016/j.neuron.2007.06.026

Hsu, W. Y., Cheng, C. H., Liao, K. K., Lee, I. H., and Lin, Y. Y. (2012). Effects of repetitive transcranial magnetic stimulation on motor functions in patients with stroke: a meta-analysis. *Stroke* 43, 1849–1857. doi: 10.1161/STROKEAHA.111.649756

Huttner, H. B., Bergmann, O., Salehpour, M., Racz, A., Tatarishvili, J., Lindgren, E., et al. (2014). The age and genomic integrity of neurons after cortical stroke in humans. *Nat. Neurosci.* 17, 801–803. doi: 10.1038/nn.3706

Jin, K., Zhu, Y., Sun, Y., Mao, X. O., Xie, L., and Greenberg, D. A. (2002). Vascular endothelial growth factor (VEGF) stimulates neurogenesis in vitro and in vivo. *Proc. Natl. Acad. Sci. U.S.A.* 99, 11946–11950. doi: 10.1073/pnas.182296499

Johnson, W., Onuma, O., Owolabi, M., and Sachdev, S. (2016). Stroke: a global response is needed. *Bull. World Health Organ.* 94, 634–634A. doi: 10.2471/BLT.16.181636

Kelestemur, T., Yulug, B., Caglayan, A. B., Beker, M. C., Kilic, U., Caglayan, B., et al. (2016). Targeting different pathophysiological events after traumatic brain injury in mice: role of melatonin and memantine. *Neurosci. Lett.* 612, 92–97. doi: 10.1016/j.neulet.2015.11.043

Khedr, E. M., Ahmed, M. A., Fathy, N., and Rothwell, J. C. (2005). Therapeutic trial of repetitive transcranial magnetic stimulation after acute ischemic stroke. *Neurology* 65, 466–468. doi: 10.1212/01.wnl.0000173067.84247.36

Khedr, E. M., Etraby, A. E., Hemeda, M., Nasef, A. M., and Razek, A. A. (2010). Long-term effect of repetitive transcranial magnetic stimulation on motor function recovery after acute ischemic stroke. *Acta Neurol. Scand.* 121, 30–37. doi: 10.1111/j.1600-0404.2009.01195.x

Kilic, E., ElAli, A., Kilic, U., Guo, Z., Ugur, M., Uslu, U., et al. (2010). Role of Nogo-A in neuronal survival in the reperfused ischemic brain. *J. Cereb. Blood Flow Metab.* 30, 969–984. doi: 10.1038/jcbfm.2009.268

Kilic, E., Kilic, U., Bacigaluppi, M., Guo, Z., Abdallah, N. B., Wolfer, D. P., et al. (2008). Delayed melatonin administration promotes neuronal survival, neurogenesis and motor recovery, and attenuates hyperactivity and anxiety after mild focal cerebral ischemia in mice. *J. Pineal Res.* 45, 142–148. doi: 10.1111/j.1600-079X.2008.00568.x

Kilic, E., Reitmeir, R., Kilic, U., Caglayan, A. B., Beker, M. C., Kelestemur, T., et al. (2014). HMG-CoA reductase inhibition promotes neurological recovery, peri-lesional tissue remodeling, and contralesional pyramidal tract plasticity after focal cerebral ischemia. *Front. Cell Neurosci.* 8:422. doi: 10.3389/fncel.2014.00422

Kilic, U., Yilmaz, B., Reiter, R. J., Yuksel, A., and Kilic, E. (2013). Effects of memantine and melatonin on signal transduction pathways vascular leakage and brain injury after focal cerebral ischemia in mice. *Neuroscience* 237, 268–276. doi: 10.1016/j.neuroscience.2013.01.059

Kim, J. Y., Choi, G. S., Cho, Y. W., Cho, H., Hwang, S. J., and Ahn, S. H. (2013). Attenuation of spinal cord injury-induced astroglial and microglial activation by repetitive transcranial magnetic stimulation in rats. *J. Korean Med. Sci.* 28, 295–299. doi: 10.3346/jkms.2013.28.2.295

Klomjai, W., Katz, R., and Lackmy-Vallee, A. (2015). Basic principles of transcranial magnetic stimulation (TMS) and repetitive TMS (rTMS). *Ann. Phys. Rehabil. Med.* 58, 208–213. doi: 10.1016/j.rehab.2015.05.005

Koch, G., Bonni, S., Pellicciari, M. C., Casula, E. P., Mancini, M., Esposito, R., et al. (2017). Transcranial magnetic stimulation of the precuneus enhances memory and neural activity in prodromal Alzheimer's disease. *Neuroimage* 169, 302–311. doi: 10.1016/j.neuroimage.2017.12.048

Langhorne, P., Coupar, F., and Pollock, A. (2009). Motor recovery after stroke: a systematic review. *Lancet Neurol.* 8, 741–754. doi: 10.1016/S1474-4422(09)70150-4

Le, Q., Qu, Y., Tao, Y., and Zhu, S. (2014). Effects of repetitive transcranial magnetic stimulation on hand function recovery and excitability of the motor cortex after stroke: a meta-analysis. *Am. J. Phys. Med. Rehabil.* 93, 422–430. doi: 10.1097/PHM.0000000000000027

Lefaucheur, J. P. (2006). Stroke recovery can be enhanced by using repetitive transcranial magnetic stimulation (rTMS). *Neurophysiol. Clin.* 36, 105–115. doi: 10.1016/j.neucli.2006.08.011

Liepert, J., Hamzei, F., and Weiller, C. (2000). Motor cortex disinhibition of the unaffected hemisphere after acute stroke. *Muscle Nerve* 23, 1761–1763. doi: 10.1002/1097-4598(200011)23:11<1761::AID-MUS14>3.0.CO;2-M

Lindvall, O., and Kokaia, Z. (2015). Neurogenesis following stroke affecting the adult brain. *Cold Spring Harb. Perspect. Biol.* 7:a019034. doi: 10.1101/cshperspect.a019034

Loo, C. K., Sachdev, P. S., Haindl, W., Wen, W., Mitchell, P. B., Croker, V. M., et al. (2003). High (15 Hz) and low (1 Hz) frequency transcranial magnetic stimulation have different acute effects on regional cerebral blood flow in depressed patients. *Psychol. Med.* 33, 997–1006. doi: 10.1017/S0033291703007955

Lu, J., Manaenko, A., and Hu, Q. (2017). Targeting adult neurogenesis for poststroke therapy. *Stem Cells Int.* 2017:5868632. doi: 10.1155/2017/5868632

Luo, J., Zheng, H., Zhang, L., Zhang, Q., Li, L., Pei, Z., et al. (2017). High-frequency repetitive transcranial magnetic stimulation (rTMS) improves functional recovery by enhancing neurogenesis and activating bdnf/trkb signaling in ischemic rats. *Int. J. Mol. Sci.* 18:E455. doi: 10.3390/ijms18020455

Medina-Fernandez, F. J., Escribano, B. M., Aguera, E., Aguilar-Luque, M., Feijoo, M., Luque, E., et al. (2017). Effects of transcranial magnetic stimulation on oxidative stress in experimental autoimmune encephalomyelitis. *Free Radic. Res.* 51, 460–469. doi: 10.1080/10715762.2017.1324955

Mesquita, R. C., Faseyitan, O. K., Turkeltaub, P. E., Buckley, E. M., Thomas, A., Kim, M. N., et al. (2013). Blood flow and oxygenation changes due to low-frequency repetitive transcranial magnetic stimulation of the cerebral cortex. *J. Biomed. Opt.* 18:067006. doi: 10.1117/1.JBO.18.6.067006

Murase, N., Duque, J., Mazzocchio, R., and Cohen, L. G. (2004). Influence of interhemispheric interactions on motor function in chronic stroke. *Ann. Neurol.* 55, 400–409. doi: 10.1002/ana.10848

Ogiue-Ikeda, M., Kawato, S., and Ueno, S. (2003). The effect of repetitive transcranial magnetic stimulation on long-term potentiation in rat hippocampus depends on stimulus intensity. *Brain Res.* 993, 222–226. doi: 10.1016/j.brainres.2003.09.009

Pena-Philippides, J. C., Yang, Y., Bragina, O., Hagberg, S., Nemoto, E., and Roitbak, T. (2014). Effect of pulsed electromagnetic field (PEMF) on infarct size and inflammation after cerebral ischemia in mice. *Transl Stroke Res.* 5, 491–500. doi: 10.1007/s12975-014-0334-1

Sasso, V., Bisicchia, E., Latini, L., Ghiglieri, V., Cacace, F., Carola, V., et al. (2016). Repetitive transcranial magnetic stimulation reduces remote apoptotic cell death and inflammation after focal brain injury. *J. Neuroinflammation* 13:150. doi: 10.1186/s12974-016-0616-5

Sun, Y., Jin, K., Childs, J. T., Xie, L., Mao, X. O., and Greenberg, D. A. (2006). Vascular endothelial growth factor-B (VEGFB) stimulates neurogenesis: evidence from knockout mice and growth factor administration. *Dev. Biol.* 289, 329–335. doi: 10.1016/j.ydbio.2005.10.016

Takeuchi, N., Tada, T., Toshima, M., Matsuo, Y., and Ikoma, K. (2009). Repetitive transcranial magnetic stimulation over bilateral hemispheres enhances motor function and training effect of paretic hand in patients after stroke. *J. Rehabil. Med.* 41, 1049–1054. doi: 10.2340/16501977-0454

Thrift, A. G., Cadilhac, D. A., Thayabaranathan, T., Howard, G., Howard, V. J., Rothwell, P. M., et al. (2014). Global stroke statistics. *Int. J. Stroke* 9, 6–18. doi: 10.1111/ijs.12245

Ueyama, E., Ukai, S., Ogawa, A., Yamamoto, M., Kawaguchi, S., Ishii, R., et al. (2011). Chronic repetitive transcranial magnetic stimulation increases hippocampal neurogenesis in rats. *Psychiatry Clin. Neurosci.* 65, 77–81. doi: 10.1111/j.1440-1819.2010.02170.x

Wagle Shukla, A., Shuster, J. J., Chung, J. W., Vaillancourt, D. E., Patten, C., Ostrem, J., et al. (2016). Repetitive transcranial magnetic stimulation (rTMS) therapy in parkinson disease: a meta-analysis. *PM R* 8, 356–366. doi: 10.1016/j.pmrj.2015.08.009

Yoon, K. J., Lee, Y. T., and Han, T. R. (2011). Mechanism of functional recovery after repetitive transcranial magnetic stimulation (rTMS) in the subacute cerebral ischemic rat model: neural plasticity or anti-apoptosis? *Exp. Brain Res.* 214, 549–556. doi: 10.1007/s00221-011-2853-2

Zhang, Y., Mao, R. R., Chen, Z. F., Tian, M., Tong, D. L., Gao, Z. R., et al. (2014). Deep-brain magnetic stimulation promotes adult hippocampal neurogenesis and alleviates stress-related behaviors in mouse models for neuropsychiatric disorders. *Mol. Brain* 7:11. doi: 10.1186/1756-6606-7-11

Conflict of Interest Statement: The authors declare that the research was conducted in the absence of any commercial or financial relationships that could be construed as a potential conflict of interest.

Copyright © 2019 Caglayan, Beker, Caglayan, Yalcin, Caglayan, Yulug, Hanoglu, Kutlu, Doeppner, Hermann and Kilic. This is an open-access article distributed under the terms of the Creative Commons Attribution License (CC BY). The use, distribution or reproduction in other forums is permitted, provided the original author(s) and the copyright owner(s) are credited and that the original publication in this journal is cited, in accordance with accepted academic practice. No use, distribution or reproduction is permitted which does not comply with these terms.

frontiers in Cellular Neuroscience

ORIGINAL RESEARCH
published: 10 May 2019
doi: 10.3389/fncel.2019.00174

From Ganglion Cell to Photoreceptor Layer: Timeline of Deterioration in a Rat Ischemia/Reperfusion Model

*Marina Palmhof, Viktoria Frank, Pascal Rappard, Emely Kortenhorn, Julia Demuth, Nora Biert, Gesa Stute, H. Burkhard Dick and Stephanie C. Joachim**

Experimental Eye Research, University Eye Hospital, Ruhr-University Bochum, Bochum, Germany

OPEN ACCESS

Edited by:
Xin Qi,
Case Western Reserve University, United States

Reviewed by:
Karl Farrow,
Neuroelectronics Research Flanders, Belgium
David Hicks,
UPR3212 Institut des Neurosciences Cellulaires et Intégratives (INCI), France

***Correspondence:**
Stephanie C. Joachim
stephanie.joachim@rub.de

Specialty section:
This article was submitted to Cellular Neuropathology, a section of the journal Frontiers in Cellular Neuroscience

Received: *14 December 2018*
Accepted: *11 April 2019*
Published: *10 May 2019*

Citation:
Palmhof M, Frank V, Rappard P, Kortenhorn E, Demuth J, Biert N, Stute G, Dick HB and Joachim SC (2019) From Ganglion Cell to Photoreceptor Layer: Timeline of Deterioration in a Rat Ischemia/Reperfusion Model. Front. Cell. Neurosci. 13:174. doi: 10.3389/fncel.2019.00174

Neuronal damage and impaired vision in different retinal disorders are induced, among other factors, by ischemia/reperfusion (I/R). Since the mechanisms and the progression of ischemic injury are still not completely clarified, a timeline of this retinal degeneration is needed. In this study, we investigated protein and mRNA alterations at 2, 6, 12, and 24 h as well as 3 and 7 days after ischemia to determine the course of an ischemic insult through the whole retina. Moreover, functional analyses were performed at later stages. We detected a significant functional loss of cells in the inner nuclear layer and photoreceptors at 3 and 7 days. Additionally, the thickness of the whole retina was decreased at these points in time, indicating a severe degradation of all retinal layers. Immunohistological and qRT-PCR analyses of retinal ganglion cells (RGCs), glial cells, AII amacrine, cone and rod bipolar as well as cone and rod photoreceptor cells confirmed this first assumption. Our results show that all investigated cell types were damaged by ischemia induction. Especially RGCs, cone bipolar cells, and photoreceptor cones are very sensitive to I/R. These cells were lost shortly after ischemia induction with a progressive course up to 7 days. In addition, Müller cell gliosis was observed over the entire period of time. These results provide evidence, that I/R induces damage of the whole retina at early stages and increases over time. In conclusion, our study could demonstrate the intense impact of an ischemic injury. The ischemic defect spreads across the whole retina right up to the outer layers in the long-term and thus seems to impair the visual perception already during the stimulus processing. In addition, our findings indicate that the cone pathway seems to be particularly affected by this damage.

Keywords: ischemia/reperfusion, ERG, retinal thickness, retinal ganglion cell, timeline, photoreceptor, amacrine cell, bipolar cell

Abbreviations: AMD, age-related macular degeneration; ERG, electroretinogram; GCL, ganglion cell layer; H&E, hematoxylin & eosin; I/R, ischemia/reperfusion; INL, inner nuclear layer; IOP, intraocular pressure; IPL, inner plexiform layer; ONL, outer nuclear layer; OPL, outer plexiform layer; PRL, photoreceptor layer; qRT-PCR, quantitative real-time PCR; RGCs, retinal ganglion cells; SEM, standard error mean.

INTRODUCTION

Retinal neurodegenerative diseases, including AMD, diabetic retinopathy, glaucoma, and retinal vein occlusion, are multi factorial and so far insufficiently investigated. One common pathomechanism of these disorders, which can lead to the visual disturbance through to loss of vision, is ischemia (Kim et al., 2013; Nakahara et al., 2015).

Retinal ischemia is defined as a lack of retinal blood flow. In order to investigate this process experimentally a transient ischemia is induced in animals for a defined period of time with a subsequent natural reperfusion. Different animal models exist to induce transient ischemia and to investigate its impact on the retina. One of the most used models is the so-called pressure-induced I/R model. This model imitates the ischemic events associated with high IOP, as it occurs in glaucoma (Buchi et al., 1991; Weinreb and Khaw, 2004; Vidal-Sanz et al., 2012). The circulatory disorder of the retina is induced in this model by a temporary raise of the IOP, which results in a compression of the blood vessels and thus in a reduced blood supply. The consequence for the several retinal cell types is a lower oxygenation capacity and supply of nutrients followed by the formation of oxidative stress during the recurring blood flow (Kaur et al., 2008; Minhas et al., 2012; Kim et al., 2013). These conditions result in a loss of retinal functionality, inflammation, and retinal tissue damage, including neuronal cell death (Szabo et al., 1991; Dijk et al., 2004a; Kaur et al., 2008; Belforte et al., 2011; Joachim et al., 2012; Minhas et al., 2012; Andreeva et al., 2014; Schmid et al., 2014; Nakahara et al., 2015). Cell death is triggered by different cell death mechanisms such as apoptosis and autophagy (Buchi, 1992; Singh et al., 2001; Rosenbaum et al., 2010; Piras et al., 2011). Several research groups were able to show a functional disorder of the inner retinal cell layers via ERG measurements (Schmid et al., 2014). Furthermore, it is known that RGCs and other inner retinal cells, like amacrine cells, are mainly affected by I/R (Lam et al., 1999; Goldblum and Mittag, 2002; Zheng et al., 2004; Bek, 2009; Nakano et al., 2011; Schmid et al., 2014).

However, most studies only analyzed single points in time after I/R with a focus on the inner retinal layers. There are only a few studies on photoreceptors with distinct results concerning the ischemic impact. For example, Zhao et al. (2013) could not detect any effect on photoreceptors after a 17 min transient global ischemia. They examined the tissue 6, 12, and 48 h after ischemia, but neither immunoreactivity nor fluorescent density of rod and cone markers were altered due to ischemia. Apart from the fact that the degree and duration of an ischemia induction also affect the severity of the damage, it is assumed that photoreceptors are more tolerant against ischemia. However, it is necessary to draw up a temporal progress of degeneration including the investigation of the outer retinal layers for a better understanding, as the mechanism of ischemic neuronal damage is not yet fully researched and understood. Therefore, we analyzed six different points in time after 60 min of ischemia (at 140 mmHg): 2 h, 6 h, 12 h, 24 h, 3 days, and 7 days. We demonstrated an impaired functionality of the INL and photoreceptors, via ERG measurements, as well as a progressive loss of amacrine, cone bipolar and cone photoreceptor cells, via immunohistology and qRT-PCR. Also, RGCs are very sensitive to ischemia. The number of this cell type decreased progressively over time. Moreover, an increased expression of macroglia was detected, starting as early as 2 h post I/R.

MATERIALS AND METHODS

Animals

Male Brown-Norway rats (7–8 weeks old; Charles River Laboratories, Sulzfeld, Germany) were used for the analyses. The study was approved by the animal care committee of North Rhine-Westphalia (Germany), all experiments were carried out in accordance with the ARVO statement for the use of animals in ophthalmic and vision research. Rats were housed under environmentally controlled conditions (12-h light-dark cycle) with free access to chow and water.

Induction of Ischemia/Reperfusion

Retinal I/R was induced as previously described (Schmid et al., 2014; Joachim et al., 2017; Palmhof et al., 2018). Animals were anesthetized with a ketamine/xylazine/vetranquil cocktail (0.65/0.65/0.2 ml; 1.5 ml/kg body weight). One eye per animal was dilated using 5% tropicamide (Pharma Stulln, Stulln, Germany) and anesthetized topically with conjuncain (Bausch & Lomb, Berlin, Germany). In addition, metamizol (100 mg/kg; Zentiva, Frankfurt am Main, Germany), a non-opioid analgesic drug, was administered subcutaneously. By elevating a saline reservoir containing 0.9% NaCl (Fresenius SE & Co. KGaA, Bad Homburg, Germany), the IOP was raised to 140 mmHg for 60 min. The saline reservoir was connected to a 27-gauge needle (Terumo Europe, Leuven, Belgium), which was placed into the anterior chamber of one eye. Retinal ischemia was confirmed by observing whitening of the retina and reperfusion was reassured by observing the returning blood flow with an ophthalmoscope (Mini 300; Heine Optotechnik, Herrsching, Germany). The contralateral eye remained untreated and served as control.

Electroretinogram Measurements

Retinal function was monitored using full-field flash electroretinography (HMsERG system; OcuScience LLC, Rolla, MO, United States). The measurements were performed 3 (n = 9/group) and 7 days (n = 10/group) after induction of I/R. Therefore, rats were first dark adapted under dim red light as previously described (Palmhof et al., 2018). After anesthesia of the animals with a ketamine/xylazine cocktail (100/4 mg/kg), the eyes were dilated with 5% tropicamide and topically anesthetized with conjuncain. Reference electrodes were placed subcutaneously below the right and left ear and a ground electrode was placed in the base of the tail. After application of methocel (Omni Vision, Puchheim, Germany), contact lenses including silver thread recording electrodes were attached central on the cornea. Scotopic flash ERGs were recorded at 0.1, 0.3, 1, 3, 10, and 25 cd.s/m^2. At the light intensities of 0.1–3 candela (cd) four measurements were taken per light intensity, respectively. At 10 and 25 cd one measurement was performed. The light intensity was increased

60 s after the previous light stimulus, respectively. Regarding the light intensities of 0.1–3 cd, the waiting period (inter-stimulus interval) between the individual light stimuli within one light intensity lasted 10 s. Signals obtained from the corneal surface were amplified, digitized, averaged, and stored using commercial software (ERGView 4.380R; OcuScience LLC) for later analysis. A 150 Hz filtering of the data was applied before evaluating the a- and b-wave amplitudes. After a transfer of the data to a spreadsheet program (Excel; Microsoft Corp., Redmond, WA, United States), statistical analysis followed (Statistica V12; Statsoft, Tulsa, OK, United States).

Tissue Collection and Processing

At all points in time (2 h, 6 h, 12 h, 24 h, 3 days, and 7 days after I/R) the eyes were removed and processed for (immuno-) histology (n = 7–8/group) and qRT-PCR (n = 5/group). For (immuno-) histology, the eye balls were fixed in 4% paraformaldehyde, incubated in 30% sucrose, embedded in optical cutting temperature medium (Tissue-Tek; Thermo Fisher Scientific, Cheshire, United Kingdom), and stored at −80°C. With a cryostat (Thermo Fisher Scientific, Walldorf, Germany), 10 μm thick retinal cross-sections were prepared for further stainings. For qRT-PCR analyses, the retina was dissected out, snap frozen in a lysis buffer with β-mercaptoethanol (Sigma-Aldrich, Steinheim, Germany) in liquid nitrogen, and stored at −80°C until RNA extraction.

Retinal Histology

Three sections per eye were stained with H&E to obtain a structural overview of the retinal layers (n = 7–8/group/point in time). After the H&E staining, all slides were dehydrated in ethanol following incubation in xylene before being mounted with Eukitt (O. Kindler GmbH & Co, Freiburg, Germany). Two pictures per H&E stained retinal cross-section were taken at a distance of 1,500 μm dorsal and ventral to the optic nerve with a microscope equipped with a CCD camera (Axio Imager M1, Carl Zeiss Microscopy). The thickness of the whole retina (excluding the outer segment) and retinal layers (GCL, IPL, INL, OPL, ONL) was analyzed via a measuring tool in the Zen 2012 software (Zeiss) (Horstmann et al., 2013). For each analysis, three measurements per picture were prepared and then averaged.

Immunohistology of Retinal Sections

Retinal cross-sections (n = 7–8/group/point in time) were also used for immunohistochemistry, as described previously (Reinehr et al., 2016; Palmhof et al., 2018). Therefore, the sections were first dried and rehydrated in PBS, followed by blocking in 10–20% appropriate serum with or without 1% BSA in 0.1% Triton X-100 in PBS. Six retinal sections per eye were used for each staining. RGCs, AII amacrine cells, cone as well as rod bipolar cells, macroglia, and cone as well as rod photoreceptor cells were investigated using specific antibodies (**Table 1**). Additionally, DAPI (4′,6-Diamidin-2-phenylindol; Serva Electrophoresis, Heidelberg, Germany) was applied as a nuclear stain. For each staining, negative controls were performed by utilizing only the secondary antibody. Four pictures per retinal cross-section, two from each periphery and two from the central part, were taken with a fluorescence microscope as described previously (Axio Imager M1 and M2; Carl Zeiss Microscopy) (Schmid et al., 2014; Joachim et al., 2017). The pictures were taken at a distance of approximately 300 and 3,100 μm dorsal and ventral to the optic nerve. All digitalized images were transferred to Corel Paint Shop Photo Pro (V 13; Corel Corp., Fremont, CA, United States), masked, and equal excerpts were cut out of each picture, which were used for the evaluation. The cut outs were prepared of a defined area of the retina with a total size of 800 pixel × 600 pixel (125.14 μm × 93.86 μm).

Evaluation was carried out under masked conditions with ImageJ software (V 1.44p; NIH, Bethesda, MD, United States). The Brn-3a$^+$, cone arrestin$^+$, parvalbumin$^+$, PKCα$^+$, recoverin$^+$, and opsin$^+$ cells were counted and averaged for each eye (Schmid et al., 2014). For analysis of the GFAP and rhodopsin staining, the images were transferred to ImageJ, where they first were transformed into gray scale. After subtraction of the background (GFAP: 50 pixel; rhodopsin: 78.5 pixel), the lower (GFAP: 5.2; rhodopsin: 4.75) and upper thresholds (GFAP: 255; rhodopsin: 258.46) were set. Background subtraction and lower and upper threshold represent mean values of both groups. For each picture, the percentage of the GFAP$^+$ and rhodopsin$^+$ labeled area was measured using an ImageJ macro.

Quantitative Real-Time PCR Analysis of Retinal Tissue

Total RNA from retinal tissue (n = 5/group/point in time) was extracted and purified according to the manufacturer's instructions using the Gen Elute Mammalian Total RNA Miniprep Kit (Sigma-Aldrich). RNA concentration and purity were determined via spectrophotometry (BioSpectrometer; Eppendorf, Hamburg, Germany). To receive cDNA, 1 μg of total RNA was reverse-transcribed with a cDNA-synthesis kit (First Strand cDNA Synthesis Kit; Thermo Fisher Scientific, Waltham, MA, United States) and random hexamer primers (Sigma-Aldrich). A PikoReal 96 Real-Time PCR System (Thermo Fisher Scientific) with SYBR Green (DyNAmo Flash SYBR Green qPCR Kit; Thermo Fisher Scientific) was used to perform qRT-PCR experiments. Primer efficiencies of each primer set were calculated based on a dilution series of 5–125 ng cDNA (Joachim et al., 2017). The relative *Gfap*, *Opn1mw*, *Opn1sw*, *Pou4f1*, *Recoverin*, and *Rhodopsin* mRNA expression was evaluated. For normalization and relative quantification, *C*t values of the housekeeping genes *Actin* and *Cyclophilin* were consulted (**Table 2**).

Statistics

ERG and (immuno-) histological data are presented as mean ± SEM and qRT-PCR data as median ± quartile + minimum + maximum. At the (immuno-) histological analyses the controls were always set to 100%. Regarding statistic of electroretinography and histology, both groups, at each point in time, were compared using Student's t-test (Statistica V13; Dell, Tulsa, OK, United States). For statistical evaluation of relative expression variations in qRT-PCR analyses, data were analyzed by REST© software (QIAGEN GmbH, Hilden,

TABLE 1 | List of used primary and secondary antibodies, including cell type, dilution, and company.

Primary antibody	Cell type	Species clonality, type	Dilution	Company and order number	Secondary antibody	Dilution	Company
Brn-3a	Retinal ganglion cells (RGCs)	Goat, polyclonal, IgG	1:100	Santa Cruz Biotechnology, Heidelberg, Germany (sc-31984)	Donkey anti-goat Alexa Fluor 488	1:500	Dianova, Hamburg, Germany
Cone arrestin	Photoreceptor cones	Rabbit, polyclonal, IgG	1:500	Millipore, Darmstadt, Germany (AB15282)	Donkey anti-rabbit Alexa Fluor 555	1:500	Invitrogen, Darmstadt, Germany
GFAP	Macroglia	Chicken, polyclonal, IgG	1:1000	Millipore (AB5541)	Donkey anti-chicken Cy3	1:700	Millipore
Opsin (red/green)	Photoreceptor cones	Rabbit, polyclonal, IgG	1:2000	Millipore (AB5405)	Donkey anti-rabbit Alexa Fluor 555	1:600	Invitrogen
Parvalbumin	All amacrine cells	Goat, polyclonal, IgG	1:100	Swant, Marly, Switzerland (PVG-213)	Donkey anti-goat Alexa Fluor 488	1:500	Invitrogen
PKCα	Rod bipolar cells	Mouse, monoclonal, IgG	1:500	Santa Cruz Biotechnology (sc-8393)	Goat anti-mouse Alexa Fluor 488	1:500	Invitrogen
Recoverin	Cone bipolar cells	Rabbit, polyclonal, IgG	1:1000	Millipore (AB5585)	Donkey anti-rabbit Alexa Fluor 555	1:400	Invitrogen
Rhodopsin	Photoreceptor rods	Mouse, monoclonal, IgG	1:400	Abcam, Cambridge, United Kingdom (ab3267)	Goat anti-mouse Alexa Fluor 488	1:500	Invitrogen

Germany) using a pairwise fixed reallocation and randomization test. *P*-values below 0.05 were considered statistically significant.

RESULTS

The ERG measurements 3 days after I/R showed a significant decrease of the a-wave amplitude in ischemic eyes in comparison to the control group ($p < 0.05$; **Figure 1B** and **Table 3A**). The analyses of this amplitude display the photoreceptor activity. Also, the amplitude of the b-wave ($p < 0.001$), which reflects the cell activity of the INL, was significantly reduced after ischemia (**Figure 1C** and **Table 3A**). At this point in time, the reduction of the b-wave amplitude was more intensive than the one of the a-wave (**Figure 1A**). This effect of ischemia induction was still prominent after 7 days (**Figure 1D**). Also, at this later point in time, a significant diminution of the a-wave amplitude was revealed after ischemic injury ($p < 0.001$; **Figure 1E** and **Table 3B**). Compared to day 3, a stronger ischemic-induced decrease was noticed at all light intensities. The same observations were made for the b-wave amplitude. A significant decline of the b-wave amplitude was measured in ischemic eyes at all light intensities after 7 days ($p < 0.001$; **Figure 1F** and **Table 3B**).

TABLE 2 | List of primer pairs used for analyses of RGCs, cells of the INL, and photoreceptor mRNA expression in control and ischemic retinae by qRT-PCR.

Gene	Primer sequence	Amplicon size	Primer efficiency
β-*Actin-F* β-*Actin-R*	cccgcgagtacaaccttct cgtcatccatggcgaact	72 bp	1.000
Cyclophilin-F *Cyclophilin-R*	tgctggaccaaacacaaatg cttcccaaagaccacatgct	88 bp	1.000
Brn-3a (Pou4f1)-F *Brn-3a (Pou4f1)-R*	ctggccaacctcaagatcc cgtgagcgactcgaacct	72 bp	0.732
Gfap-F *Gfap-R*	tttctccaacctccagatcc gaggtggccttctgacacag	64 bp	0.875
Opn1mw-F *Opn1mw-R*	tcatcgtgctctgctacctc tctttctgttgctttgccact	64 bp	1.000
Opn1sw-F *Opn1sw-R*	ccccatcatctactgcttcat agccagacatgtcagattcgt	98 bp	1.000
Recoverin-F *Recoverin-R*	aagatctgggcgtcctttg agggtcccctcgatgaat	71 bp	1.000
Rhodopsin-F *Rhodopsin-R*	accttgagggcttctttgc tcaatggccaggactacca	70 bp	1.000

For relative quantification of mRNA levels, the house-keeping genes Actin and Cyclophilin were used. The primer sequence, the predicted amplicon size and the primer efficiency are indicated. bp, base pairs; F, forward; R, reverse.

The H&E stained retinal cross-sections were utilized to measure the thickness of the different retinal layers. A distinct degradation of the whole retina started on day 3 after I/R (**Figure 2A**). This observation was confirmed by the measurements. A significant reduced thickness of the whole retina was detected at day 3 ($p < 0.001$) and 7 ($p < 0.001$) in ischemic eyes when compared to the control group (**Figure 2B** and **Table 4**). Regarding the GCL alone, an ischemic-induced damage was established at an earlier point in time. A significantly thinner GCL in ischemic eyes was already noticeable after 6 h ($p = 0.036$; **Figure 2C** and **Table 4**). This difference was still evident at 12 h ($p = 0.0009$), 24 h ($p < 0.001$), 3 days ($p < 0.001$), and 7 days ($p < 0.001$) in comparison to control retinae. Also, changes in the layer thickness in the other retinal layers (IPL, INL, OPL, and ONL) were measured after ischemia induction. Here, the layer thicknesses were reduced mainly at 3 and 7 days ($p < 0.001$; **Table 4**). However, the OPL also seems to be sensitive to an ischemic injury. A decrease of this layer was already present 6 h after ischemia ($p = 0.001$; **Table 4**).

Since the GCL showed such an early and strong degeneration via H&E staining, we then focused on RGCs at the different points in time. Therefore, the specific ganglion cell marker

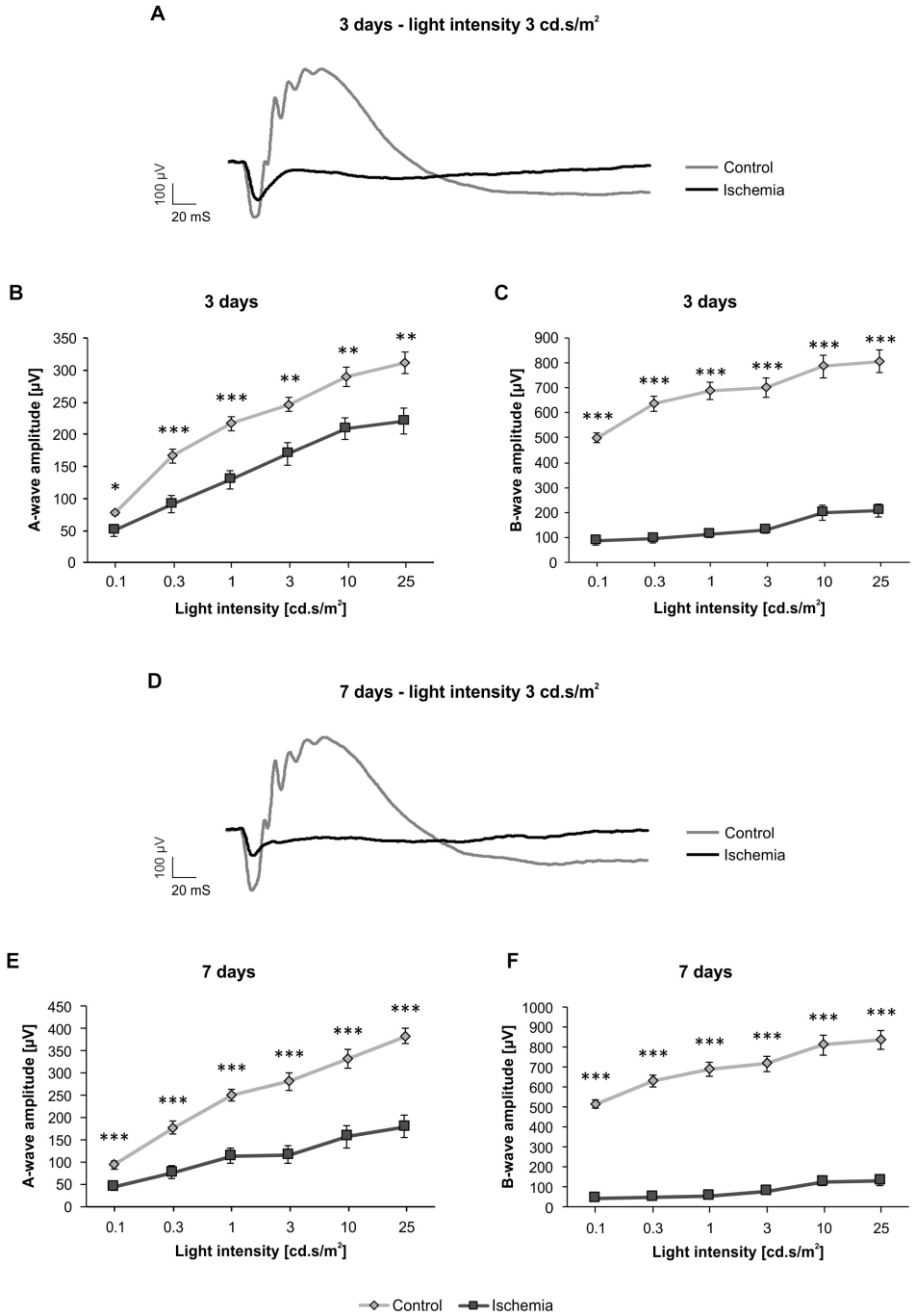


FIGURE 1 | Electroretinogram (ERG) measurements were performed 3 (n = 9/group) and 7 (n = 10/group) days after ischemia induction. **(A)** Representative ERG recording 3 days after ischemia induction. The average graph of the obtained waveforms of control eyes and the contralateral ischemic eyes at 3 cd.s/m^2 is shown. **(B)** A significant decrease of the a-wave amplitude ($p < 0.05$) was noted in ischemic eyes compared to control ones 3 days after I/R at all measured light intensities. **(C)** Additionally, a significantly lower b-wave amplitude ($p < 0.001$) was revealed in the ischemic group at this point in time. **(D)** Representative ERG recording 7 days after I/R. The average graph of the obtained waveforms of control eyes and the contralateral ischemic eyes at 3 cd.s/m^2 is represented. **(E)** 7 days after ischemia induction, the significant reduction of the a-wave amplitude ($p < 0.001$) was still prominent and more pronounced. **(F)** A similar effect could be observed regarding the b-wave amplitude ($p < 0.001$) at this point in time. *$p < 0.05$, **$p < 0.01$, ***$p < 0.001$.

anti-Brn-3a was applied on the sections. A progressive regression of RGCs was observed over time (**Figure 3A**). Statistical analyses of the immunohistological staining validated this impression. Significantly fewer Brn-3a$^+$ ganglion cells were detected in the ischemic retinae starting after 2 h (p = 0.032). This RGC loss was prominent until day 7 (6 h: p = 0.026; 12 h: p = 0.002;

TABLE 3A | Analyses of the a- and b-wave amplitude of the ERG measurements (mean ± SEM) at 3 days.

	3 days					
Light intensity [cd.s/m^2]	**0.1**	**0.3**	**1**	**3**	**10**	**25**
A-wave amplitude [µm]						
Control	77.7 ± 3.5	166.3 ± 10.5	216.7 ± 10.9	246.7 ± 11.1	289.9 ± 15.1	311.4 ± 16.7
Ischemia	50.3 ± 9.0	91.4 ± 13.7	129.9 ± 14.3	169.9 ± 17.2	208.9 ± 17.3	221.1 ± 19.7
P-value	0.012	0.0005	0.0002	0.002	0.003	0.003
B-wave amplitude [µm]						
Control	499.2 ± 18.8	635.6 ± 29.1	687.0 ± 35.0	700.5 ± 37.7	785.1 ± 45.0	806.3 ± 43.6
Ischemia	87.7 ± 17.1	96.5 ± 17.9	113.4 ± 14.7	130.9 ± 14.3	200.6 ± 30.3	208.3 ± 25.4
P-value	<0.001	<0.001	<0.001	<0.001	<0.001	<0.001

Significant values are marked in red.

TABLE 3B | Analyses of the a-and b-wave amplitude of the ERG measurements (mean ± SEM) at 7 days.

	7 days					
Light intensity [cd.s/m^2]	**0.1**	**0.3**	**1**	**3**	**10**	**25**
A-wave amplitude [µm]						
Control	93.7 ± 8.7	177.0 ± 14.3	249.7 ± 12.9	280.8 ± 18.9	333.2 ± 21.0	383.7 ± 17.4
Ischemia	45.4 ± 8.0	76.5 ± 14.9	113.9 ± 17.0	116.1 ± 20.4	156.5 ± 25.6	179.6 ± 25.0
P-value	0.0007	0.0001	<0.001	<0.001	<0.001	<0.001
B-wave amplitude [µm]						
Control	515.8 ± 19.3	630.0 ± 29.9	689.6 ± 37.3	718.4 ± 38.7	811.4 ± 48.8	837.4 ± 48.4
Ischemia	43.6 ± 10.1	49.1 ± 9.9	55.9 ± 7.9	79.0 ± 11.0	127.4 ± 18.8	130.8 ± 21.1
P-value	<0.001	<0.001	<0.001	<0.001	<0.001	<0.001

Significant values are marked in red.

24 h, 3 days, 7 days: $p < 0.001$; **Figure 3B** and **Table 5**). Over time, a progressive course was established with an obvious decrease at day 3 (**Figure 3B** and **Table 5**). In addition, qRT-PCR analyses were performed to evaluate the *Brn-3a* (*Pou4f1*) expression on mRNA level. Compared to control retinae, a significant down-regulation of the relative *Brn-3a* expression was detected from 12 h ($p = 0.003$) on (**Figure 3C** and **Table 5**). The expression of *Brn-3a* mRNA remained diminished until day 7 (24 h: $p = 0.007$; 3 days: $p = 0.006$; 7 days: $p = 0.001$; **Figure 3C** and **Table 5**).

The ERG measurements showed a functional disorder of the cells in the INL 3 and 7 days after ischemia induction. Thus, we examined those cells in the next step. AII amacrine cells were labeled using anti-parvalbumin. While a similar number of parvalbumin$^+$ cells was present in both groups at the early points in time (2–24 h), fewer parvalbumin$^+$ amacrine cells were noted in the ischemic group at later points in time (3 and 7 days; **Figure 4A**). This observation was underpinned by statistical analyses. At 3 ($p < 0.001$) and 7 days ($p < 0.001$), ischemic retinae displayed a significant loss of parvalbumin$^+$ cells (**Figure 4B** and **Table 6A**).

Bipolar cells, especially cone bipolar cells, were detected using the marker anti-recoverin. Anti-PKCα was used to visualize rod bipolar cells. The immunolabeling showed a progressive diminution of recoverin$^+$ cells over time, while the number of rod bipolar cells remained unchanged between both groups and all points in time (**Figures 5A,B**). Evaluating the staining of bipolar cones revealed a significant lower number of recoverin$^+$ cells in ischemic eyes at 12 h ($p = 0.015$), 24 h ($p < 0.001$), 3 days ($p = 0.001$), and 7 days ($p < 0.001$) when compared to the control group (**Figure 5C** and **Table 6B**). In contrast, cell counts of rod bipolar cells indicated no differences in the cell number of PKCα$^+$ cells between control and ischemic retinae at all points in time (2 h, 6 h, 12 h, 24 h, 3 days, 7 days: $p > 0.05$; **Figure 5E** and **Table 6C**). The relative expression level of *Recoverin* mRNA was investigated via qRT-PCR. Comparison of all points in time showed a significant down-regulation of *Recoverin* mRNA expression at 6 h ($p = 0.024$), 12 h ($p = 0.006$), and 24 h ($p < 0.001$) after ischemia. However, at 3 ($p = 0.515$) and 7 days ($p = 0.406$) ischemic retinae displayed a similar level as control eyes (**Figure 5D** and **Table 6B**).

In order to evaluate macroglia, the expression of GFAP was investigated on protein as well as on mRNA level. GFAP is mainly expressed by astrocytes and Müller glia. Regarding immunoreactivity, GFAP was present in controls of all six points in time in close proximity to the GCL. After I/R induction, an increase in positive signal area was observed with formation of processes (**Figure 6A**). Analyses of the immunohistological staining revealed a significantly larger GFAP$^+$ signal area at all points in time after ischemia in comparison to control retinae (2 h: $p = 0.044$; 6 h: $p = 0.048$; 12 h: $p = 0.013$; 24 h: $p = 0.047$; 3 days: $p = 0.047$; 7 days: $p = 0.004$; **Figure 6B** and **Table 7**). In addition, a significant up-regulation of *Gfap* mRNA was noted in ischemic retinae at 12 and 24 h as well as 3 and 7 days

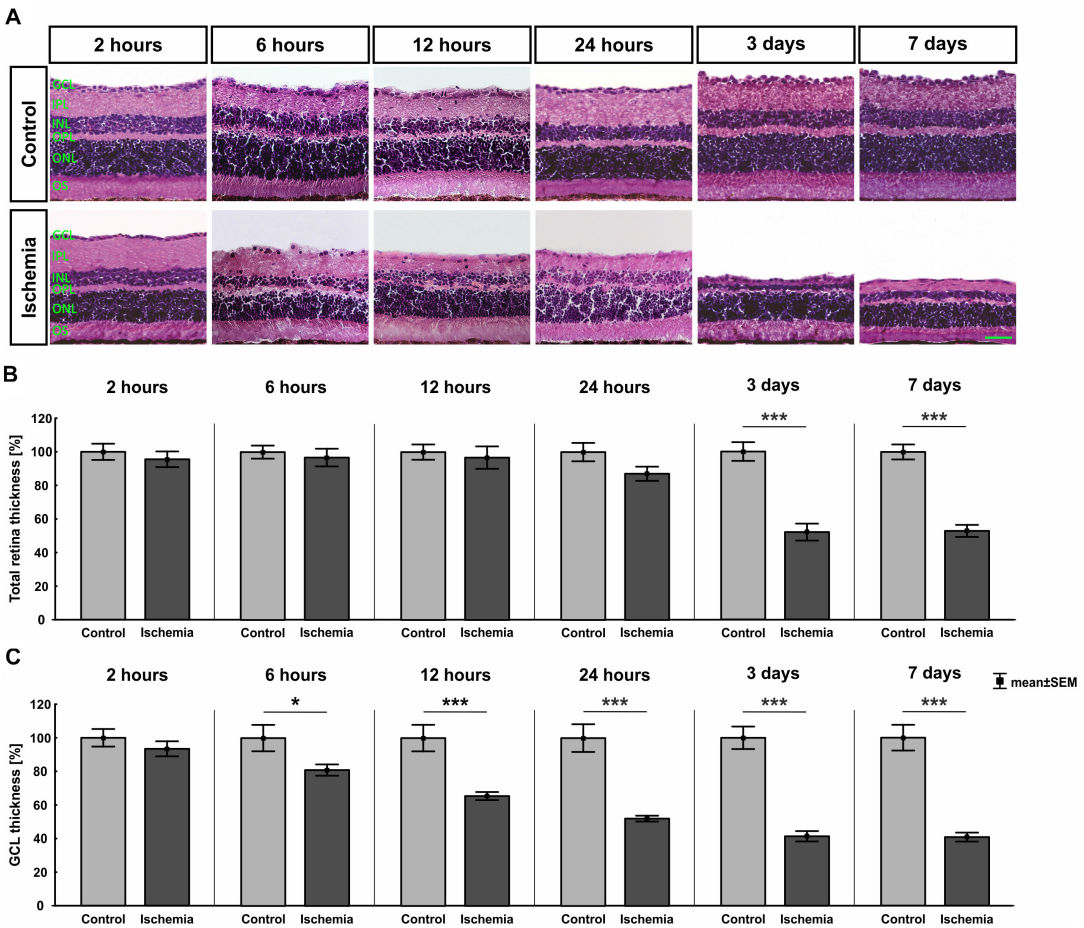


FIGURE 2 | (A) Retinal cross-sections of all points in time were stained with H&E (n = 7–8/group). A decline of the total retinal thickness was observed in the ischemia group over time. **(B)** A significant decrease of the whole retinal thickness was measured in ischemic eyes starting at day 3 after I/R (3 days, 7 days: $p < 0.001$). **(C)** The GCL seems to be most sensitive against an ischemic insult. The thickness of this layer was significantly reduced already at 6 h ($p = 0.036$). This degeneration progressed over time (12 h: $p = 0.0009$; 24 h, 3 days, 7 days: $p < 0.001$). *$p < 0.05$, ***$p < 0.001$. GCL, ganglion cell layer; IPL, inner plexiform layer; INL, inner nuclear layer; OPL, outer plexiform layer; ONL, outer nuclear layer; OS, outer segment. Scale bar: 20 μm.

(12 h: $p = 0.037$; 24 h: $p = 0.007$; 3 days: $p = 0.004$; 7 days: $p = 0.003$; **Figure 6C** and **Table 7**).

Also, the activity of photoreceptors was impaired by I/R. Therefore, we investigated the outer retinal layer further. Antibodies specific to opsin as well as cone arrestin were used to visualize photoreceptor cones. While opsin$^+$ cells were seen in the PRL, cone arrestin$^+$ cell bodies were localized in the ONL. Fewer opsin$^+$ and cone arrestin$^+$ cells were detected in ischemic eyes at 12 h, 24 h, 3 days, and 7 days (**Figures 7A,B**). This observation was confirmed by statistical analyses. Two hours after ischemia, control (100.0 ± 4.2% $\triangleq$ 40.9 ± 1.7 cells/mm) and ischemic retinae (96.8 ± 5.4% $\triangleq$ 39.6 ± 2.2 cells/mm) had very similar numbers of opsin$^+$ cells ($p = 0.6$). Opsin cell counts revealed a significant reduced cell number at 12 h ($p = 0.0002$), 24 h ($p = 0.0007$), and 3 days ($p = 0.0009$) after ischemia. At 7 days, only 74.4 ± 5.4% of opsin$^+$ cells ($\triangleq$ 38.9 ± 2.8 cells/mm) were still present in the ischemia group in comparison to 100.0 ± 3.9% ($\triangleq$ 52.2 ± 2.0 cells/mm) in the control group ($p = 0.002$; **Figure 7C** and **Table 8A**). In regard to cone arrestin, the control group (100.0 ± 4.3% $\triangleq$ 53.4 ± 2.3 cells/mm) and the ischemia group (94.1 ± 2.6% $\triangleq$ 50.2 ± 1.4 cells/mm) displayed comparable cell numbers ($p = 0.3$). But absolute numbers for this cell type were a little bit higher than for opsin. Significantly fewer arrestin$^+$ cones were counted from 6 h post I/R on in comparison to controls (6 h: $p = 0.004$; 12 h: $p = 0.023$; 24 h, 3 days: $p < 0.001$). At 7 days, 51.9 ± 5.8% arrestin$^+$ cells ($\triangleq$ 28.3 ± 3.2 cells/mm) were observed in the ischemia group in contrast to 100.0 ± 2.2% ($\triangleq$ 54.6 ± 1.2 cells/mm) in the control group ($p < 0.001$; **Figure 7F** and **Table 8B**). In order to differentiate between short-wavelength and medium-wavelength sensitive cone opsin we also evaluated the expression levels of *Opn1sw* (short-wavelength sensitive cone opsin) and *Opn1mw* (medium-wavelength sensitive cone opsin) mRNA. Regarding *Opn1sw* mRNA, a significantly reduced expression was noted 6 h after ischemia ($p = 0.003$). This down-regulation was also present after 12 h ($p = 0.002$), 24 h ($p = 0.005$),

TABLE 4 | Analyses of the layer thicknesses (%) of the H&E stained cross-sections at all points in time.

	H&E [%]					
Points in time	**2 h**	**6 h**	**12 h**	**24 h**	**3 days**	**7 days**
Total retina						
Control	100.0 ± 4.8	100.0 ± 3.9	100.0 ± 4.5	100.0 ± 5.5	100.0 ± 5.6	100.0 ± 4.5
Ischemia	95.6 ± 4.7	96.8 ± 5.3	96.7 ± 6.7	87.1 ± 4.2	52.0 ± 5.0	53.0 ± 3.6
P-value	0.518	0.636	0.691	0.084	<0.001	<0.001
GCL						
Control	100.0 ± 5.2	100.0 ± 7.9	100.0 ± 7.9	100.0 ± 8.3	100.0 ± 6.7	100.0 ± 7.7
Ischemia	93.4 ± 4.5	81.0 ± 3.4	65.5 ± 2.4	52.1 ± 1.7	41.4 ± 3.1	40.8 ± 2.7
P-value	0.357	0.036	0.0009	<0.001	<0.001	<0.001
IPL						
Control	100.0 ± 7.4	100.0 ± 4.6	100.0 ± 9.0	100.0 ± 7.5	100.0 ± 8.2	100.0 ± 6.3
Ischemia	97.1 ± 6.6	101.9 ± 9.7	97.9 ± 9.3	79.5 ± 6.5	22.8 ± 2.8	21.6 ± 2.1
P-value	0.772	0.873	0.876	0.058	<0.001	<0.001
INL						
Control	100.0 ± 4.4	100.0 ± 6.1	100.0 ± 5.3	100.0 ± 5.2	100.0 ± 4.6	100.0 ± 3.8
Ischemia	95.3 ± 4.1	88.7 ± 6.0	78.6 ± 4.4	88.9 ± 6.0	48.4 ± 6.4	45.4 ± 3.5
P-value	0.453	0.210	0.008	0.183	<0.001	<0.001
OPL						
Control	100.0 ± 3.4	100.0 ± 2.7	100.0 ± 5.0	100.0 ± 6.4	100.0 ± 10.6	100.0 ± 4.7
Ischemia	91.7 ± 3.4	84.6 ± 2.6	77.4 ± 4.1	78.2 ± 3.7	43.7 ± 5.8	58.5 ± 3.7
P-value	0.104	0.001	0.003	0.010	0.0004	<0.001
ONL						
Control	100.0 ± 3.1	100.0 ± 4.0	100.0 ± 4.7	100.0 ± 4.5	100.0 ± 3.4	100.0 ± 4.0
Ischemia	95.4 ± 3.6	89.4 ± 3.8	90.8 ± 4.2	92.1 ± 3.1	66.2 ± 4.0	74.4 ± 4.0
P-value	0.351	0.077	0.165	0.168	<0.001	0.0004

Control groups were set at 100%. Significant values are marked in red. GCL, ganglion cell layer; IPL, inner plexiform layer; INL, inner nuclear layer; OPL, outer plexiform layer; ONL, outer nuclear layer.

and 3 days (p = 0.009; **Figure 7D** and **Table 8A**). Although there was a trend, there were no significant differences in *Opn1sw* mRNA level detected anymore between ischemic and control retinae at day 7 (p = 0.058; **Figure 7D** and **Table 8A**). A significant decrease of *Opn1mw* mRNA level was measured in ischemic retinae from 6 h on (p = 0.002). This down-regulation was present throughout the study (12 h: p = 0.002; 24 h: p = 0.003; 3 days: p = 0.008; 7 days: p = 0.003; **Figure 7E** and **Table 8A**).

Photoreceptor rods were labeled with anti-rhodopsin. From 12 h on, distinct changes concerning the rhodopsin structure were noted. A resolution and disorganization of the photoreceptor rod structure was observed on all ischemic retinae (**Figure 8A**). However, statistical analyses displayed no significant differences in rhodopsin^{+} staining area at any point in time between both groups (2 h: p = 0.317; 6 h: p = 0.703; 12 h: p = 0.584; 24 h: p = 0.181; 3 days: p = 0.407; 7 days: p = 0.579; **Figure 8B** and **Table 8C**). While the staining area was comparable over time, a significantly reduced expression of relative *Rhodopsin* mRNA was noted at 6 h (p = 0.026), 12 h (p = 0.007), 24 h (p < 0.001), and 3 days (p = 0.008) after ischemia via qRT-PCR (**Figure 8C** and **Table 8C**). However, no difference in *Rhodopsin* mRNA level was measured between ischemic and control retinae at day 7 (p = 0.26; **Figure 8C** and **Table 8C**).

DISCUSSION

Neurodegenerative diseases that affect the retina, like AMD, diabetic retinopathy, glaucoma, and retinal vascular occlusion, are still not properly treatable or even curable. This is due to the complexity of the underlying mechanisms of the progress of the diseases. It is known that ischemia is mainly involved in the degeneration of the retina (Cai et al., 2015). However, the impact of an ischemic injury on the retina and its cell types, especially over time, has not been fully explored and understood. Particularly, for the development of new therapy options and drug testing it is important to know how the ischemic damage spreads and evolves over time. Some research groups have investigated different points in time after ischemia induction and tried to create a timeline of retinal degeneration. However, in these studies, the researchers were focused only on the early or late points in time or solely inner retinal layers, like the GCL and INL (Unoki and LaVail, 1994; Weber et al., 1996; Dijk et al., 2004a,b; Slater et al., 2008; Kim et al., 2013; Zhao et al., 2013). For example, the group around Zhao et al. prepared analyses regarding retinal morphology at early points in time, from 6 until 48 h (Zhao et al., 2013). Sellés-Navarro et al. (1996) and Kim et al. (2013) examined morphological changes at later points in time (3–28 days and 5–30 days) with a focus on retinal thickness and/or RGC loss. There are also publications which demonstrated

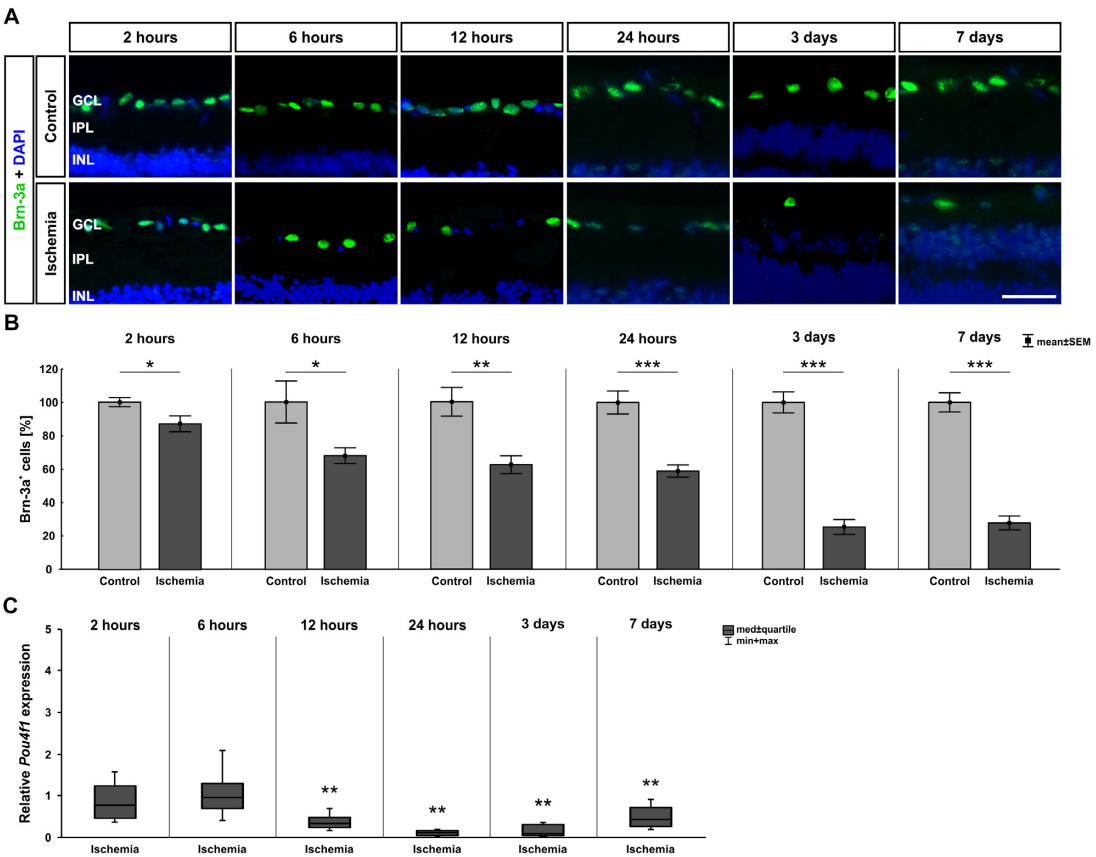


FIGURE 3 | (A) Brn-3a (green) was used to stain RGCs on retinae of all points in time (n = 7–8/group). Cell nuclei were labeled with DAPI (blue). Fewer Brn-3a$^+$ cells were observed in the ischemia group over time. **(B)** A significant RGC loss was noted 2 h after I/R (p = 0.032), which remained until day 7 and became increasingly stronger over the time (6 h: p = 0.026; 12 h: p = 0.002; 24 h, 3 days, 7 days: $p < 0.001$). **(C)** Via qRT-PCR, a significant down-regulation of *Pou4f1* mRNA levels was verified starting 12 h after ischemia (12 h: p = 0.003; 24 h: p = 0.007; 3 days: p = 0.006; 7 days: p = 0.001). *$p < 0.05$, **$p < 0.01$, ***$p < 0.001$. GCL, ganglion cell layer; IPL, inner plexiform layer; INL, inner nuclear layer. Scale bar: 20 μm.

TABLE 5 | Analyses of the Brn-3a staining (%), control groups were all set at 100%.

	Brn-3a					
Points in time	**2 h**	**6 h**	**12 h**	**24 h**	**3 days**	**7 days**
Immunohistology [cells in %]						
Control	100.0 ± 2.7	100.0 ± 12.5	100.0 ± 8.6	100.0 ± 6.9	100.0 ± 6.3	100.0 ± 5.7
Ischemia	87.1 ± 4.7	68.0 ± 4.7	62.4 ± 5.3	58.9 ± 3.7	25.4 ± 4.5	27.7 ± 4.2
P-value	0.032	0.026	0.002	<0.001	<0.001	<0.001
qRT-PCR [fold expression]						
Relative expression	0.751	0.948	0.318	0.107	0.097	0.42
P-value	0.281	0.693	0.003	0.007	0.006	0.001

Relative Pou4f1 mRNA expression (med) at all points in time are also shown. Significant values are marked in red.

long-term analyses (e.g., 12 h–15 days, 1–31 days, or 2 h–7 days), but these studies focused only on specific factors, like the profile of the retinal transcriptome, the apoptosis of RGCs, or the behavior of the INL and its cell types, respectively (Dijk et al., 2004a,b; Agudo et al., 2008; Slater et al., 2008). Furthermore, different animal models were used in the mentioned studies to induce retinal damage, including transient global ischemia, (pressure-induced) retinal I/R, optic nerve transection, optic nerve crush, or anterior ischemic optic neuropathy (Dijk et al., 2004a; Agudo et al., 2008; Slater et al., 2008; Kim et al., 2013; Zhao et al., 2013). Accordingly, this has different ischemic effects on the degeneration of the retina and its cell types.

We used the pressure-induced I/R model to imitate the ischemic events associated with high IOP, as it occurs in glaucoma (Weinreb and Khaw, 2004; Vidal-Sanz et al., 2012). Our goal was to induce ischemic damage directly and locally to the retina and

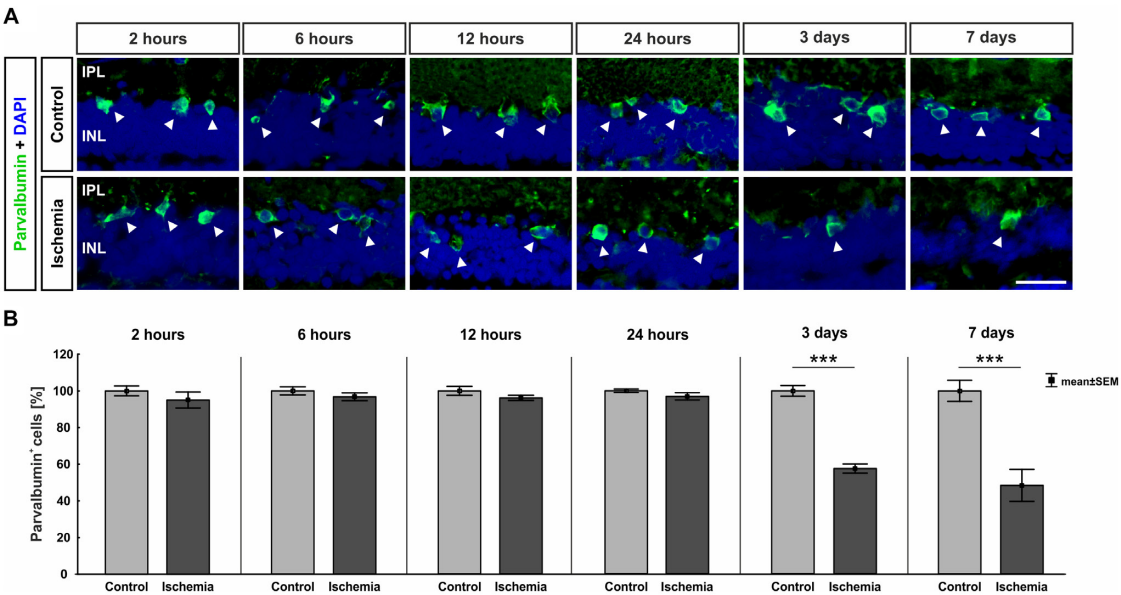


FIGURE 4 | (A) All amacrine cells were marked with an anti-parvalbumin antibody (green, arrows), while DAPI was used to label cell nuclei (blue; n = 7–8/group). A lower number of parvalbumin$^+$ amacrine cells was noted at the later points in time. **(B)** A significant regression of parvalbumin$^+$ cells was detected 3 ($p < 0.001$) and 7 days ($p < 0.001$) after ischemia. ***$p < 0.001$. IPL, inner plexiform layer; INL, inner nuclear layer. Scale bar: 20 μm.

TABLE 6A | Analyses of the parvalbumin staining (%) at all points in time.

	Parvalbumin					
Points in time	**2 h**	**6 h**	**12 h**	**24 h**	**3 days**	**7 days**
Immunohistology [cells in %]						
Control	100.0 ± 2.7	100.0 ± 2.2	100.0 ± 2.4	100.0 ± 1.0	100.0 ± 2.9	100.0 ± 5.8
Ischemia	95.0 ± 4.4	96.7 ± 2.1	96.2 ± 1.4	96.9 ± 2.0	57.5 ± 2.5	48.4 ± 8.7
P-value	0.349	0.306	0.195	0.186	<0.001	<0.001

Control groups were set at 100%. Significant values are marked in red.

thus to create a progress of inner and outer retinal degeneration from an early stage, right after induction, to a late stage after retinal I/R injury. We wanted to determine the impact of ischemic injury on the entire retina and find out how the damage is developing over the course of time for a better understanding of this degeneration. Therefore, we analyzed six points in time after I/R: 2 h, 6 h, 12 h, 24 h, 3 days, and 7 days. Firstly, we focused on the functionality and structure of the inner and outer retina. We verified a progressive damage regarding both, the function and the appearance. The later the retinae were investigated, the stronger was the degree of ischemic impact on the tissue.

Impairing of Neuronal Function

Whether impulse transmission is maintained in retinal neurons can be measured by electroretinography. Activity of the photoreceptors (a-wave) and the cells in the INL (b-wave) can be determined with a scotopic ERG. In this context, it should be noted that some studies discuss the relationship between anesthesia and its impact on the ERG outcome (Brown and Green, 1984; Tanskanen et al., 1996; Chaudhary et al., 2003; Nair et al., 2011). The group around Nair et al. (2011), for example, examined ketamine/xylazine, which was used for anesthesia in the current study. They evaluated the effects of this anesthetics on the eye movement and the recorded retinal function. Eye movement could potentially provoke amplitude variations in ERG and thus affect the recordings of functional response. According to Nair et al. (2011) the use of ketamine/xylazine does not completely suppress eye movement. Therefore, in our studies conjuncain is used in addition to anesthetize the eyes topically. This numbs the cornea and counteracts possible eye movements. However, Nair et al. (2011) were also able to show that the greatest a- and b-wave amplitudes in scotopic ERG were detected using ketamine/xylazine. This finding justifies the use of ketamine/xylazine anesthesia as the preferred anesthetic for ERG studies in rats (Nair et al., 2011).

In our study, ERG measurements were performed 3 and 7 days after the ischemic insult and demonstrated a distinct reduction in function at both points in time. During the course of this we noted that the functional restriction increased over time since the decline in amplitudes was stronger after 7 days. In previous studies of our research group where ERG analyses were performed 14 and 21 days after I/R, the size of the a- and

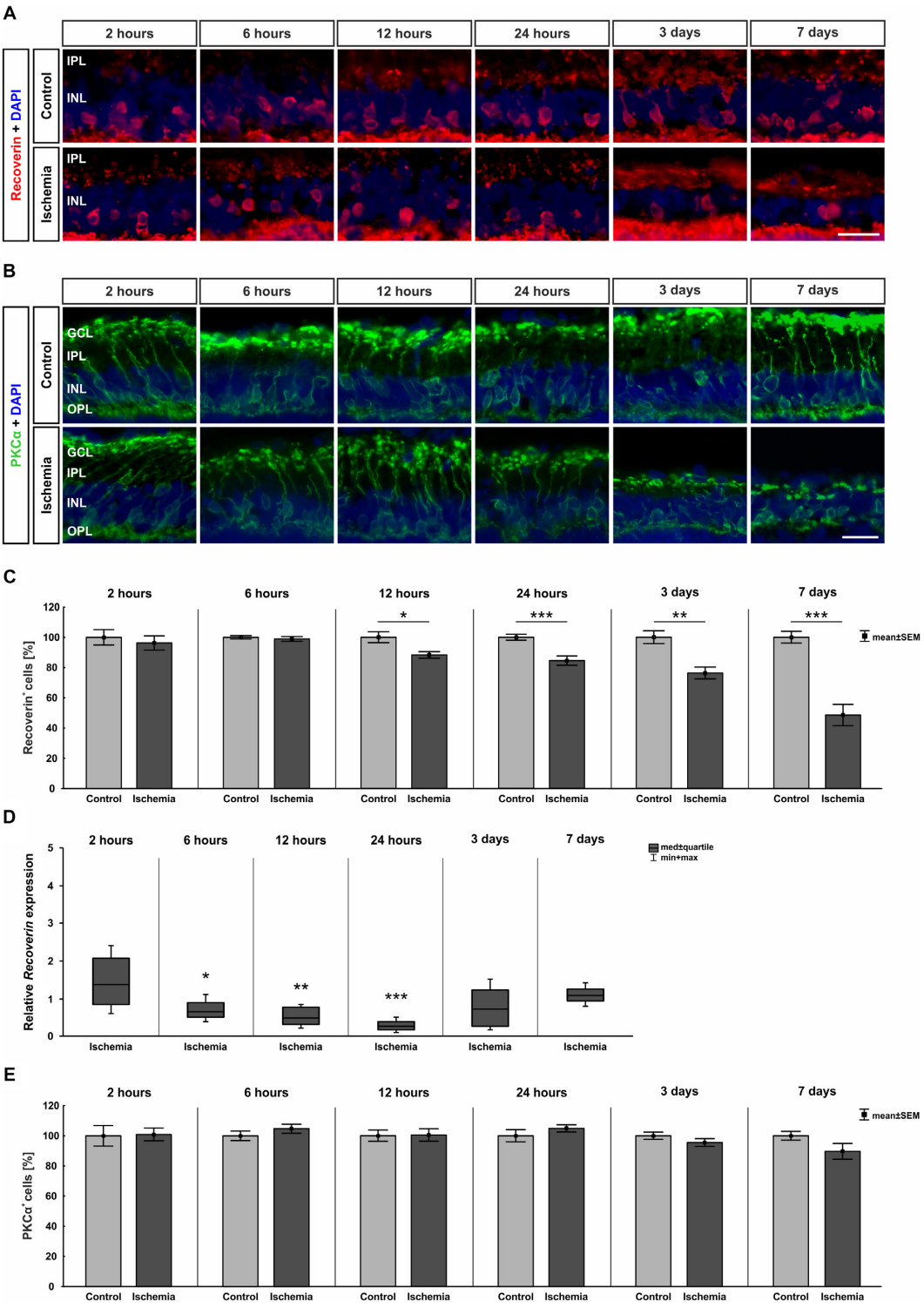


FIGURE 5 | (A) Cone bipolar cells were stained with anti-recoverin (red) and cell nuclei with DAPI (blue; n = 7–8/group). After ischemia induction, fewer cells were observed over time. **(B)** Anti-PKCα was used to detect rod bipolar cells (green) and DAPI for cell nuclei (blue; n = 7–8/group). The cells were equally stained in both groups. **(C)** Counting of cone bipolar cells displayed a significant reduction of recoverin$^+$ cells at 12 h (p = 0.015), 24 h (p < 0.001), 3 days (p = 0.001), and 7 days (p < 0.001) after ischemia induction. **(D)** On mRNA level, a significant down-regulation of *Recoverin* mRNA expression was shown in the ischemia group at 6 h (p = 0.024), 12 h (p = 0.006), and 24 h (p < 0.001). **(E)** Evaluation of rod bipolar cells revealed no differences in cell number between both groups and all points in time. *p < 0.05, **p < 0.01, ***p < 0.001. GCL, ganglion cell layer; IPL, inner plexiform layer; INL, inner nuclear layer; OPL, outer plexiform layer. Scale bars: 20 μm.

TABLE 6B | Evaluation of recoverin staining (%) as well as of expression levels of *Recoverin* mRNA (med) at all points in time.

	Recoverin					
Points in time	**2 h**	**6 h**	**12 h**	**24 h**	**3 days**	**7 days**
Immunohistology [cells in %]						
Control	100.0 ± 5.1	100.0 ± 1.1	100.0 ± 3.6	100.0 ± 2.0	100.0 ± 4.2	100.0 ± 3.9
Ischemia	96.3 ± 4.7	98.9 ± 1.6	88.3 ± 2.2	84.5 ± 3.1	76.3 ± 3.9	48.6 ± 7.0
P-value	0.597	0.594	0.015	<0.001	0.001	<0.001
qRT-PCR [fold expression]						
Relative expression	1.377	0.656	0.474	0.273	0.727	1.076
P-value	0.169	0.024	0.006	<0.001	0.515	0.406

Regarding staining, control groups were set at 100%. Significant values are marked in red.

TABLE 6C | Evaluation of the PKCα staining (%) at all points in time.

	PKCα					
Points in time	**2 h**	**6 h**	**12 h**	**24 h**	**3 days**	**7 days**
Immunohistology [cells in %]						
Control	100.0 ± 6.8	100.0 ± 3.1	100.0 ± 3.8	100.0 ± 4.0	100.0 ± 2.4	100.0 ± 2.9
Ischemia	100.9 ± 4.2	104.7 ± 3.0	100.5 ± 4.2	104.9 ± 2.4	95.5 ± 2.6	89.6 ± 5.2
P-value	0.912	0.296	0.938	0.314	0.218	0.106

Control groups were set at 100%.

b-wave amplitudes was comparable to or even lower than the ones after 7 days (Schmid et al., 2014; Palmhof et al., 2018). This leads to the assumption, that the impairment of function worsens over time. Hence, our data demonstrate that the effect of an ischemic injury spreads out through the retina. Kim et al. (2013) also described a functional disturbance of the retina after ischemic injury. They measured a significant decrease of the a-wave amplitudes first at 21 and 28 days after I/R with a recovery at day 35, which they explain with an early retinal detachment and later reattachment. Nevertheless, the b-wave amplitudes were significantly diminished at day 7 with an ongoing reduction over time until day 35 (Kim et al., 2013). These findings correlate with our data and suggestions. Interestingly, another study from Zhao et al. (2013) revealed a complete loss of the a- and b-wave amplitudes during ischemia, still a decrease at 1 h, and almost recovery of both amplitudes at 48 h after reperfusion (Zhao et al., 2013). However, it should be noted that in comparison to our study the duration of ischemia there was only 17 min. In addition, another model, the so called 4-vessel occlusion model, was used to induce the transient global ischemia and the dark adaption of the animals prior the ERG measurements lasted 70 min instead of 8 h, as in our study. All these factors can influence the outcome. Obviously, the strength and the progress of degeneration vary depending on the type of I/R induction, in particular with regard to the temporal aspect. Considering the period from 2 h to 7 days post I/R, we were able to show for the first time that inducting ischemia by transiently elevating the IOP seems to generate an early and much stronger impairment of function of both, the photoreceptors and the INL cells. In addition, we demonstrated that this damage increases over time until day 7 without any recovery. This leads to the assumption that visual impairment will worsen over time in neurodegenerative retinal diseases associated with ischemic processes. Especially, the longer it remains untreated.

Progressive Degeneration of RGCs, Retinal Thickness, and the Inner Retinal Layer Including Müller Cell Gliosis

It is well investigated that I/R leads to a significant ganglion cell death (Unoki and LaVail, 1994; Adachi et al., 1996; Weber et al., 1996; Zheng et al., 2007; Wang et al., 2011; Schmid et al., 2014). Also, this cell type reacts particularly sensitive. But the timeline of this degeneration had not been studied in detail yet. Our results show that ischemic processes have such a strong impact, that first signs of an RGC decrease could be detected immunohistologically already 2 h and on mRNA level 12 h after induction. A significant thinning of the GCL was measured as early as 6 h after ischemia. Furthermore, we demonstrated that with advancing examination times, the damage intensified. After 3 days, approximately 75% of the Brn-3a$^+$ RGCs were lost and a significant reduction of the whole retinal thickness was observed. These results are consistent with the data from existing publications, which examined a few different points in time post ischemia. 17 min of transient global ischemia led to a reduced number of ßIII-tubulin$^+$ RGCs at 6 until 48 h (Zhao et al., 2013). Although the impact of this short ischemia seems to be not strong enough to trigger changes in layer thickness. The authors identified no significant differences in this regard. A study by Sellés-Navarro et al. (1996), where the RGC survival was analyzed at later points in time (5–30 days) after pressure-induced ischemia, indicated RGC loss during the whole study period, starting at day 5. Kim et al. (2013) also performed a pressure-induced retinal ischemia, but in a mouse model. Cell counts in the GCL at five different points in time

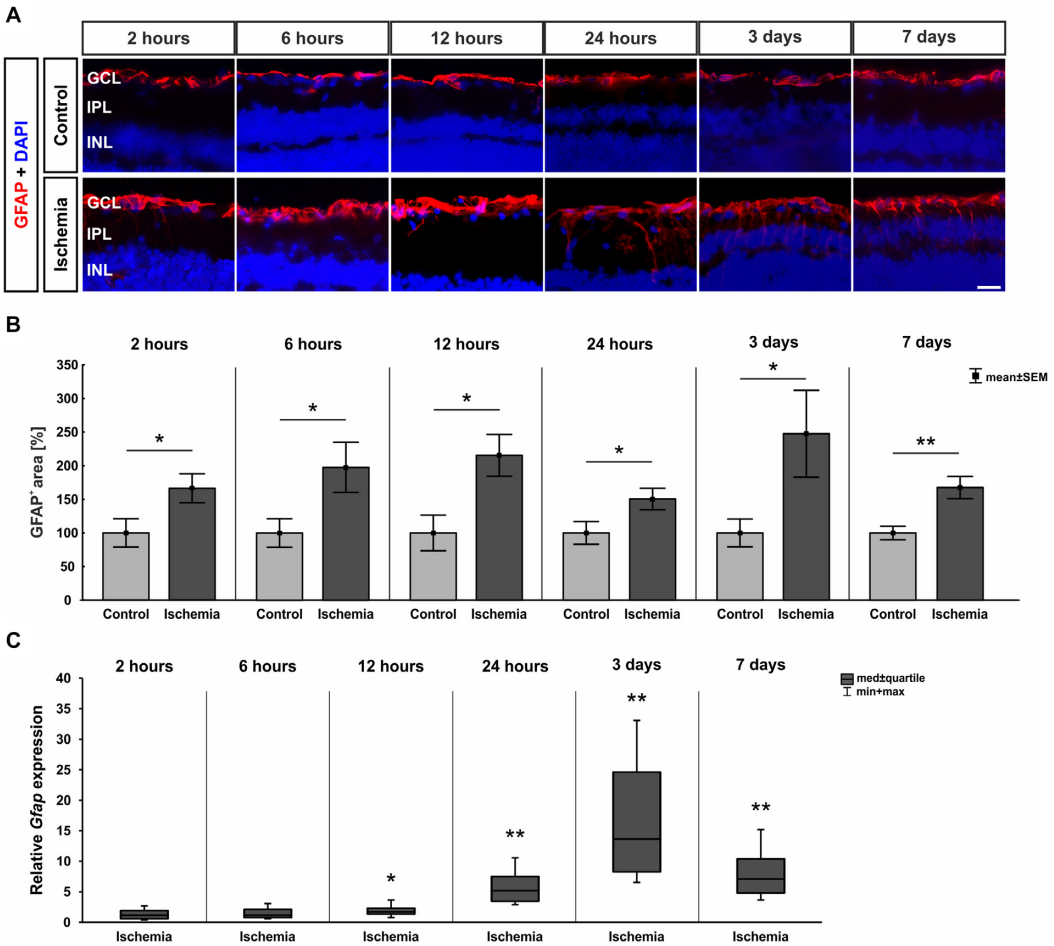


FIGURE 6 | (A) Macroglia were detected with anti-GFAP (red), while DAPI was used for cell nuclei (blue; n = 7–8/group). Control retinae displayed GFAP in the GCL and NFL, while the signal spread to inner layers after ischemia. **(B)** An increase of GFAP$^+$ area was measured after I/R for all points in time (2 h: p = 0.044; 6 h: p = 0.048; 12 h: p = 0.013; 24 h: 0.047; 3 days: 0.047; 7 days: 0.004). **(C)** Compared to controls, *Gfap* mRNA level was significantly higher at 12 h (p = 0.037), 24 h (0.007), 3 days (p = 0.004), and 7 days (p = 0.003) after ischemia. *$p < 0.05$, **$p < 0.01$. GCL, ganglion cell layer; IPL, inner plexiform layer; INL, inner nuclear layer. Scale bar: 20 μm.

TABLE 7 | Analyses of the GFAP area (%), where control groups were set at 100%.

	GFAP					
Points in time	**2 h**	**6 h**	**12 h**	**24 h**	**3 days**	**7 days**
Immunohistology [area fraction in %]						
Control	100.0 ± 21.0	100.0 ± 21.1	100.0 ± 26.4	100.0 ± 16.8	100.0 ± 20.7	100.0 ± 10.1
Ischemia	166.4 ± 21.5	197.7 ± 37.4	215.6 ± 31.1	150.5 ± 16.0	247.6 ± 64.6	167.6 ± 16.5
P-value	0.044	0.048	0.013	0.047	0.047	0.004
qRT-PCR [fold expression]						
Relative expression	1.198	1.246	1.774	5.239	13.771	7.147
P-value	0.511	0.374	0.037	0.007	0.004	0.003

Relative Gfap mRNA expression (med) at all points in time was also evaluated. Significant values are marked in red.

(3–28 days) revealed a significant decline, with a progressive course, which did not start until day 14. Concerning retinal thickness, a significant thinning of the whole retinal thickness in ischemic eyes was measured beginning at day 21 after injury (Kim et al., 2013). After optic nerve transection and optic nerve crush, RGC death was first observed at day 7 post-lesion and went on until day 15, respectively whereby transection of the optic nerve caused greater damage than the crush (Agudo et al., 2008). Although in these studies the RGC loss was detected at a later point in time post I/R than ours, all this data supports the

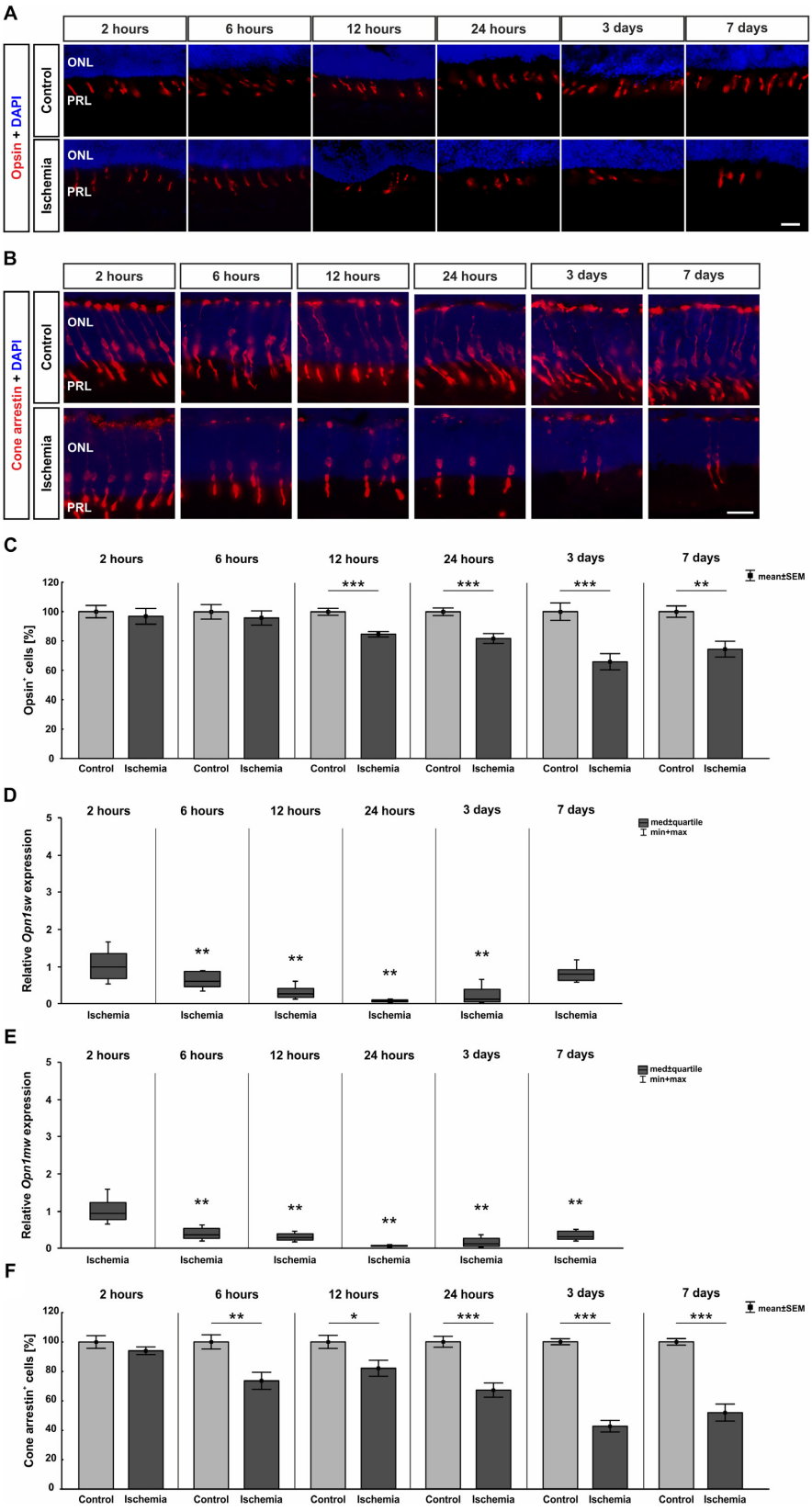


FIGURE 7 | Continued

FIGURE 7 | (A) Cone photoreceptor cells were visualized using anti-opsin (red) and cell nuclei (blue) using DAPI (n = 7–8/group). At 24 h, 3 days, and 7 days fewer opsin$^+$ cells could be seen in retinae underlying I/R. **(B)** A second marker, anti-cone arrestin (red), was used to mark cones more specifically, while DAPI was again used for the cell nuclei (blue; n = 7–8/group). Fewer arrestin$^+$ cell bodies were observed in the ONL of ischemic eyes from 6 h on **(C)**. Statistical analyses demonstrated a significant decreased number of opsin$^+$ cells starting at 12 h (12 h, 24 h, 3 days: $p < 0.001$; 7 days: $p = 0.002$). **(D)** A down-regulation of *Opn1sw* mRNA expression was noted after ischemia at 6, 12, and 24 h and 3 days (all: $p < 0.01$), which was no longer significant on day 7. **(E)** Regarding *Opn1mw*, its mRNA expression was significantly decreased 6 h after I/R and stayed constantly low until day 7 (all: $p < 0.01$). **(F)** A reduction in number of cone arrestin$^+$ cells was detected as early as 6 h after ischemia induction (6 h: $p = 0.004$; 12 h: $p = 0.023$; 24 h, 3 days, 7 days: $p < 0.001$). $^*p < 0.05$, $^{**}p < 0.01$, $^{***}p < 0.001$. ONL, outer nuclear layer; PRL, photoreceptor layer. Scale bars: 20 μm.

TABLE 8A | Analyses of the opsin staining (%) at all points in time.

	Opsin					
Points in time	**2 h**	**6 h**	**12 h**	**24 h**	**3 days**	**7 days**
Immunohistology [cells in %]						
Control	100.0 ± 4.2	100.0 ± 4.9	100.0 ± 2.4	100.0 ± 2.6	100.0 ± 5.9	100.0 ± 3.9
Ischemia	96.8 ± 5.4	95.8 ± 4.8	84.7 ± 1.9	81.8 ± 3.3	65.9 ± 5.5	74.4 ± 5.4
P-value	0.646	0.552	0.0002	0.0007	0.0009	0.002
qRT-PCR: *Opn1sw* [fold expression]						
Relative expression	0.997	0.614	0.260	0.075	0.134	0.791
P-value	0.992	0.003	0.002	0.005	0.009	0.058
qRT-PCR: *Opn1mw* [fold expression]						
Relative expression	0.945	0.372	0.279	0.058	0.119	0.326
P-value	0.621	0.002	0.002	0.003	0.008	0.003

Control groups were set at 100%. In addition, levels of Opn1sw and Opn1mw mRNA expression were evaluated. Significant values are marked in red.

TABLE 8B | Analyses of the cone arrestin staining (%) at all points in time.

	Cone arrestin					
Points in time	**2 h**	**6 h**	**12 h**	**24 h**	**3 days**	**7 days**
Immunohistology [cells in %]						
Control	100.0 ± 4.3	100.0 ± 4.9	100.0 ± 4.5	100.0 ± 3.7	100.0 ± 2.0	100.0 ± 2.2
Ischemia	94.1 ± 2.6	73.6 ± 5.8	82.1 ± 5.4	67.2 ± 4.9	42.6 ± 3.9	51.9 ± 5.8
P-value	0.258	0.004	0.023	<0.001	<0.001	<0.001

Control groups were set at 100%. Significant values are marked in red.

progressive ischemic-induced damage we were able to prove with our model. Nevertheless, it should be pointed out that in contrast to other studies, we were able to verify the progressive damage of the RGCs and the GCL starting immediately after pressure-induced I/R, indicating the significant extent of this process.

In addition to the GCL, the INL reacts sensitively to ischemic processes. Kim et al. (2013) also described a damage of the INL 3 days after ischemia. Our ERG data indicated that the INL was affected at this point in time, as well. Several studies exhibit, that amacrine as well as bipolar cells are extremely sensitive to ischemic stress (Dijk et al., 2004a,b; Lee et al., 2011; Li et al., 2011). Our group also demonstrated this in previous studies. An ischemic-induced loss of cholinergic amacrine cells was detected after 14 and 21 days (Schmid et al., 2014; Joachim et al., 2017; Palmhof et al., 2018). In addition, significantly fewer glycinergic AII amacrine cells as well as cone bipolar cells were observed 14 days after induction of ischemia (Palmhof et al., 2018). Moreover, Kim et al. (2010) detected a decreased parvalbumin-expressing AII amacrine cell number at later points in time, 4 and 8 weeks after I/R injury. For this reason, it was particularly interesting to examine the course of damage of these cells in the INL at early and late stages post I/R. In this study we could demonstrate that glycinergic AII amacrine cells seem to be more resistant to this damage than cone bipolar cells. While we detected a significant loss of recoverin$^+$ cone bipolar cells already at 12 h, the number of parvalbumin$^+$ AII amacrine cells decreased significantly later, after 3 days, with a progressive loss over time. Zhao et al. (2013) investigated amacrine and cone bipolar cells in their timeline. They displayed a significantly reduced cell number of calretinin$^+$ amacrine cells during the whole study period (6–48 h), but the number of cells between the investigated points in time stayed similar. Concerning recoverin$^+$ cone bipolar cells, significantly fewer cells were only noted at 6 and 12 h after ischemic injury (Zhao et al., 2013). The researchers around Dijk et al. (2004b) performed long-term analyses of different sub-types of amacrine and bipolar cells as well. Regarding AII amacrine cells they investigated the expression levels of *Parvalbumin* mRNA via qRT-PCR between 2 h and 4 weeks after I/R induction. Interestingly, they detected a gradual decrease of *Parvalbumin* transcript levels with

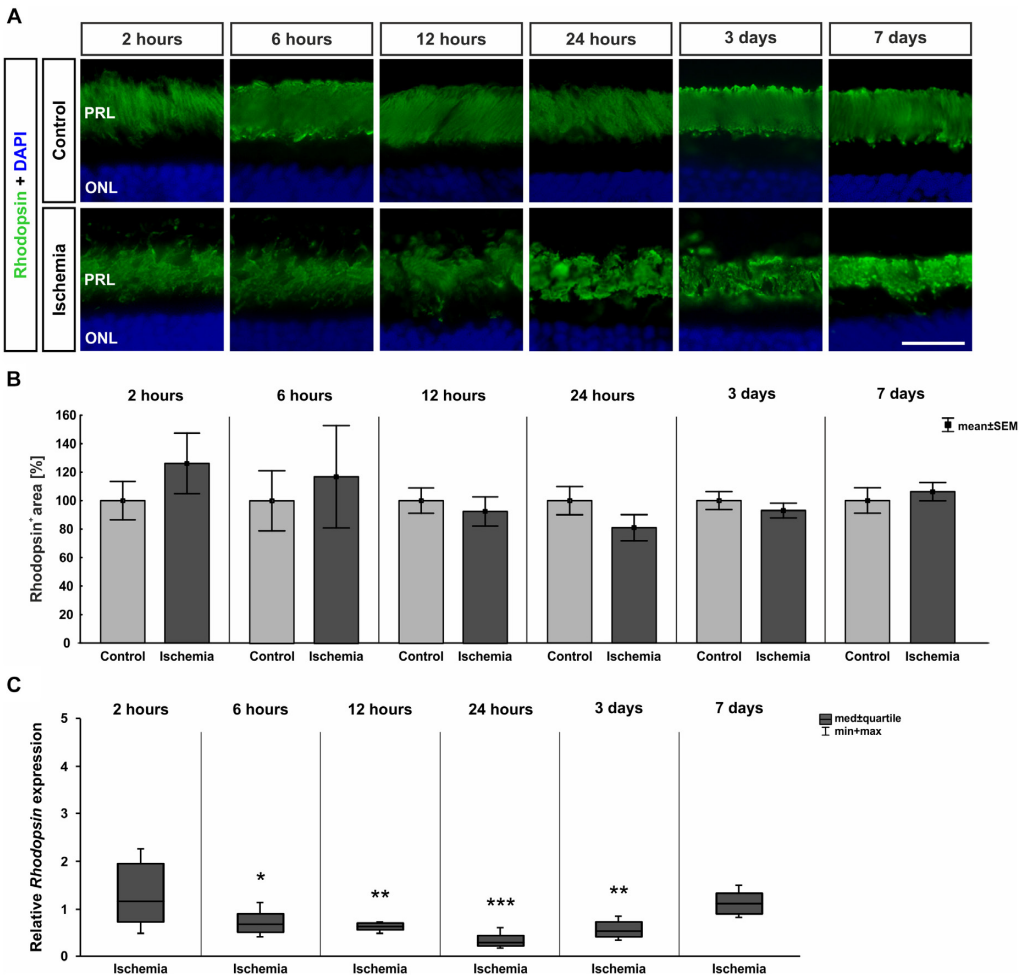


FIGURE 8 | (A) Rod photoreceptor cells were stained with anti-rhodopsin (green; n = 7–8/group). DAPI marked cell nuclei (blue). While in control retinae the structure was well defined, a disorganization was noted after ischemia at later points in time. **(B)** Regarding the analyses of rhodopsin$^+$ staining area, no differences were seen at all points in time. **(C)** Certainly, on mRNA level, a significant down-regulation of *Rhodopsin* mRNA expression could be shown in the ischemia group after 6 h (p = 0.026), 12 h (p = 0.007), 24 h ($p < 0.001$), and 3 days (p = 0.008). *$p < 0.05$, **$p < 0.01$, ***$p < 0.001$. PRL, photoreceptor layer; ONL, outer nuclear layer. Scale bar: 20 μm.

TABLE 8C | Analyses of the rhodopsin area (%) and relative *Rhodopsin* mRNA expression (med) at all points in time.

	Rhodopsin					
Points in time	**2 h**	**6 h**	**12 h**	**24 h**	**3 days**	**7 days**
Immunohistology [area fraction in %]						
Control	100.0 ± 13.4	100.0 ± 21.1	100.0 ± 8.9	100.0 ± 9.9	100.0 ± 6.3	100.0 ± 8.9
Ischemia	126.1 ± 21.3	116.9 ± 35.9	92.4 ± 10.2	81.0 ± 9.2	93.0 ± 5.2	106.3 ± 6.5
P-value	0.317	0.703	0.584	0.181	0.407	0.579
qRT-PCR [fold expression]						
Relative expression	1.164	0.686	0.621	0.301	0.526	1.108
P-value	0.521	0.026	0.007	<0.001	0.008	0.26

Significant values are marked in red.

progressing reperfusion time starting already at 6 h (Dijk et al., 2004b). In case of bipolar cells they focused on rod bipolar cells, which they labeled with PKCα. This sub-type stayed unaffected at all analyzed points in time (2 h–7 days) (Dijk et al., 2004a). A previous study by our group equally revealed no signs of rod bipolar cell degeneration at a late point in time, 21 days after I/R (Schmid et al., 2014). This corresponds to our current results, as the number of PKCα$^+$ bipolar cells remained unaltered in

the timeframe of our evaluation. These comparisons reveal that the different sub-types of the INL cells, namely of amacrine and bipolar cells, react differently to an ischemic injury. Regarding all underlying findings it can be concluded that bipolar cells are generally more resistant to I/R than amacrine cells. However, relating to the various sub-types we were able to show for the first time, as far as we are aware, that cone bipolar cells are more susceptible against ischemic injury than glycinergic AII amacrine cells. Moreover, we were also able to detect a progressive degeneration of cone bipolar cells over time, for the first time.

Besides retinal neurons, glial cells, like macroglia, are resident in the retina. These include two basic cell types, astrocytes and Müller glia (de Hoz et al., 2016). Pathological conditions such as ischemic damage, neurodegeneration/-inflammation, or trauma lead to an activation of these cells. This process which is associated with an up-regulation of the intermediate filament GFAP, is known as gliosis (Ramirez et al., 2001; Peng et al., 2014). It is reported that transient retinal ischemia leads to Müller cell gliosis (Hirrlinger et al., 2010; Kim et al., 2013). Kim et al. (2013) analyzed 5 points in time (3, 7, 14, 21, and 28 days) via immunohistochemistry and displayed progressive gliosis in retinae that underwent pressure-induced ischemia. Another study by Mages et al. (2019) determined an GFAP up-regulation in Müller cells at 3 days post I/R, with a constantly high level of protein as well as mRNA up to 14 days. We also noted Müller cell gliosis throughout the study. We detected an increased GFAP expression on protein level starting already at 2 h and on mRNA level at 12 h after ischemia induction. Thus, our evaluations correspond with previous published findings. Moreover, we demonstrated that Müller glia are activated at a very early stage of ischemic injury.

Long-Term Photoreceptor Changes

As mentioned before, most of the analyses regarding the ischemic impact on the retina were performed on the inner retinal layers, due to the assumption that photoreceptors are more tolerant against an ischemia insult. However, previously mentioned data indicate that ischemic damage spreads in the long-term across the whole retina. In addition, analyses of eyes from patients with diabetic retinopathy or of retinae from a rhesus monkey with type 2 diabetes suggest a susceptibility of the photoreceptors. Using adaptive optics scanning laser ophthalmoscopy, photoreceptor abnormalities were found in eyes of diabetic retinopathy patients (Nesper et al., 2017). Regarding the diabetic hypertensive monkey retina, histopathological analyses revealed a severe decline in number of photoreceptor inner and outer segments (Johnson et al., 2005). Therefore, we analyzed both, rod and cone photoreceptors. With regards to the morphology, photoreceptor cones appear to be more sensitive against the ischemic insult than rods. We verified a progressive reduction of opsin$^+$ and cone arrestin$^+$ cone photoreceptor cells starting at 12 and 6 h post ischemia, respectively. In contrast, no changes in rhodopsin$^+$ staining area were noted at all investigated points in time. Indeed, a disorganized structure of rod photoreceptors was observed with progressing examination point in time indicating a structural ischemic damage of rods. Unoki and LaVail (1994) observed shorter and more disorganized photoreceptor outer segments 7 and 14 days after pressure-induced ischemia, indicating a sublethal impairment of photoreceptor cells. The impact of ischemic injury on photoreceptor cones and rods, specifically regarding a temporal degeneration, have hardly been studied so far. A study by Zhao et al. described no alterations in rhodopsin immunoreactivity at 6–48 h after ischemia (Zhao et al., 2013). Our immunohistological results of photoreceptor rods analyses correspond with these findings. However, we measured a significant down-regulation of *Rhodopsin* mRNA expression after 6, 12, and 24 h, and 3 days, which returned to control levels at day 7 after ischemia. Regarding photoreceptor cones, there are so far no investigations in terms of the temporal ischemic influence, to our knowledge. For the first time, we analyzed both photoreceptor cell types, rods and cones, at these early points in time, namely from 2 h on and were able to describe the sensitivity of photoreceptor cones against I/R over time with a progressive course. However, further examinations of this retinal cell type need to be performed, especially as the stimulus processing begins here. In this regard, photopic ERG recordings should be performed in further studies, to investigate cone photoreceptors in more detail.

Since we were able to show a strong ischemia induced damage overall, the association of ischemic extent with anesthesia, especially ketamine, should be referred to, at this point. This subject is part of discussion in some studies, which reported a potential tissue protection by ketamine due to its anti-inflammatory properties (Tsukahara et al., 1992; Frassdorf et al., 2009; Eroglu, 2014). In this regard, myocardial and intestinal injury as well as ischemic injury in the rabbit retina was investigated. Several studies showed that ketamine itself could mitigate ischemic injury and diminish ischemic-induced tissue damage of the different organs (Tsukahara et al., 1992; Frassdorf et al., 2009; Eroglu, 2014). However, the protective effect of ketamine was investigated as a pretreatment therapy. The group of Tsukahara et al. (1992) applied ketamine in the rabbit retina intravitreally 1 h before ischemia induction. In contrast to this, we used ketamine for anesthesia in a cocktail with xylazine and vetranquil via intraperitoneal injection. As we demonstrated such massive retinal injury, it can be assumed that the used dose and application type had no protective effects on the ischemic-induced damage in our study. Moreover, ketamine/xylazine is a common anesthesia for the induction of I/R in rodents (Unoki and LaVail, 1994; Produit-Zengaffinen et al., 2009; Abcouwer et al., 2010; David et al., 2011; Kara et al., 2014; Varga et al., 2017; Lin et al., 2019).

CONCLUSION

According to our knowledge, this is the first study to characterize temporal I/R-induced damage throughout the entire retina from the GCL to PRL. Therefore, several cell types of the GCL, INL, and PRL were investigated at six points in time after retinal ischemia. The results demonstrate that ischemic injury, especially pressure-induced I/R, is so intense that it leads to a total retinal deterioration including functional impairment. This retinal ischemic damage appears at a very early point in

time, practically right after I/R induction, increases, and spreads with time. In addition to the RGCs, we demonstrated Müller cell gliosis and, for the first time, that cone bipolar and cone photoreceptor cells also seem to be particularly sensitive to I/R, as a progressive cell loss was observed, starting at very early stages. Thus, we suppose that the cone pathway is affected more strongly by ischemic injury. These novel findings should contribute to better understanding of the temporal course of ischemic processes and to the development of new therapeutic approaches. Therefore, the treatment should start as early as possible and include photoreceptors.

ETHICS STATEMENT

This study was approved by the animal care committee of North Rhine-Westphalia (Germany), all experiments were carried out in accordance with the Association for Research in Vision and Ophthalmology (ARVO) statement for the use of animals in ophthalmic and vision research.

AUTHOR CONTRIBUTIONS

MP performed experiments, analyzed data, and wrote the manuscript. VF, PR, EK, and JD performed experiments and analyzed the data. NB and GS performed the experiments. HBD revised the manuscript. SCJ designed the study and revised the manuscript. All authors read and approved the final manuscript.

FUNDING

This study was in part supported by Bayer Vital GmbH.

ACKNOWLEDGMENTS

We acknowledge support by the DFG Open Access Publication Funds of the Ruhr-Universität Bochum.

REFERENCES

Abcouwer, S. F., Lin, C. M., Wolpert, E. B., Shanmugam, S., Schaefer, E. W., Freeman, W. M., et al. (2010). Effects of ischemic preconditioning and bevacizumab on apoptosis and vascular permeability following retinal ischemia-reperfusion injury. *Invest. Ophthalmol. Vis. Sci.* 51, 5920–5933. doi: 10.1167/iovs.10-5264

Adachi, M., Takahashi, K., Nishikawa, M., Miki, H., and Uyama, M. (1996). High intraocular pressure-induced ischemia and reperfusion injury in the optic nerve and retina in rats. *Graefes Arch. Clin. Exp. Ophthalmol.* 234, 445–451. doi: 10.1007/bf02539411

Agudo, M., Perez-Marin, M. C., Lonngren, U., Sobrado, P., Conesa, A., Canovas, I., et al. (2008). Time course profiling of the retinal transcriptome after optic nerve transection and optic nerve crush. *Mol. Vis.* 14, 1050–1063.

Andreeva, K., Zhang, M., Fan, W., Li, X., Chen, Y., Rebolledo-Mendez, J. D., et al. (2014). Time-dependent gene profiling indicates the presence of different phases for ischemia/reperfusion injury in retina. *Ophthalmol. Eye Dis.* 6, 43–54. doi: 10.4137/OED.S17671

Bek, T. (2009). Inner retinal ischaemia: current understanding and needs for further investigations. *Acta Ophthalmol.* 87, 362–367. doi: 10.1111/j.1755-3768.2008.01429.x

Belforte, N., Sande, P. H., de Zavalia, N., Fernandez, D. C., Silberman, D. M., Chianelli, M. S., et al. (2011). Ischemic tolerance protects the rat retina from glaucomatous damage. *PLoS One* 6:e23763. doi: 10.1371/journal.pone.0023763

Brown, C. H., and Green, D. G. (1984). Rod saturation in b-wave of the rat electroretinogram under two different anesthetics. *Vision Res.* 24, 87–90. doi: 10.1016/0042-6989(84)90147-0

Buchi, E. R. (1992). Cell death in the rat retina after a pressure-induced ischaemia-reperfusion insult: an electron microscopic study. I. Ganglion cell layer and inner nuclear layer. *Exp. Eye Res.* 55, 605–613. doi: 10.1016/s0014-4835(05)80173-3

Buchi, E. R., Suivaizdis, I., and Fu, J. (1991). Pressure-induced retinal ischemia in rats: an experimental model for quantitative study. *Ophthalmologica* 203, 138–147. doi: 10.1159/000310240

Cai, M., Zhang, X., Li, Y., and Xu, H. (2015). Toll-like receptor 3 activation drives the inflammatory response in oxygen-induced retinopathy in rats. *Br. J. Ophthalmol.* 99, 125–132. doi: 10.1136/bjophthalmol-2014-305690

Chaudhary, V., Hansen, R., Lindgren, H., and Fulton, A. (2003). Effects of telazol and nembutal on retinal responses. *Doc. Ophthalmol.* 107, 45–51.

David, J., Melamud, A., Kesner, L., Roth, S., Rosenbaum, P. S., Barone, F. C., et al. (2011). A novel calpain inhibitor for treatment of transient retinal ischemia in the rat. *Neuroreport* 22, 633–636. doi: 10.1097/WNR.0b013e32834959c5

de Hoz, R., Rojas, B., Ramirez, A. I., Salazar, J. J., Gallego, B. I., Trivino, A., et al. (2016). Retinal macroglial responses in health and disease. *Biomed Res. Int.* 2016:2954721. doi: 10.1155/2016/2954721

Dijk, F., Kraal-Muller, E., and Kamphuis, W. (2004a). Ischemia-induced changes of AMPA-type glutamate receptor subunit expression pattern in the rat retina: a real-time quantitative PCR study. *Invest. Ophthalmol. Vis. Sci.* 45, 330–341.

Dijk, F., van Leeuwen, S., and Kamphuis, W. (2004b). Differential effects of ischemia/reperfusion on amacrine cell subtype-specific transcript levels in the rat retina. *Brain Res.* 1026, 194–204. doi: 10.1016/j.brainres.2004.08.034

Eroglu, A. (2014). The effect of intravenous anesthetics on ischemia-reperfusion injury. *Biomed Res. Int.* 2014:821513. doi: 10.1155/2014/821513

Frassdorf, J., De Hert, S., and Schlack, W. (2009). Anaesthesia and myocardial ischaemia/reperfusion injury. *Br. J. Anaesth.* 103, 89–98. doi: 10.1093/bja/aep141

Goldblum, D., and Mittag, T. (2002). Prospects for relevant glaucoma models with retinal ganglion cell damage in the rodent eye. *Vision Res.* 42, 471–478. doi: 10.1016/s0042-6989(01)00194-8

Hirrlinger, P. G., Ulbricht, E., Iandiev, I., Reichenbach, A., and Pannicke, T. (2010). Alterations in protein expression and membrane properties during Muller cell gliosis in a murine model of transient retinal ischemia. *Neurosci. Lett.* 472, 73–78. doi: 10.1016/j.neulet.2010.01.062

Horstmann, L., Schmid, H., Heinen, A. P., Kurschus, F. C., Dick, H. B., and Joachim, S. C. (2013). Inflammatory demyelination induces glia alterations and ganglion cell loss in the retina of an experimental autoimmune encephalomyelitis model. *J. Neuroinflamm.* 10:120. doi: 10.1186/1742-2094-10-120

Joachim, S. C., Jehle, T., Boehm, N., Gramlich, O. W., Lagreze, W. A., Pfeiffer, N., et al. (2012). Effect of ischemia duration on autoantibody response in rats undergoing retinal ischemia-reperfusion. *Ophthalmic Res.* 48, 67–74. doi: 10.1159/000335965

Joachim, S. C., Renner, M., Reinhard, J., Theiss, C., May, C., Lohmann, S., et al. (2017). Protective effects on the retina after ranibizumab treatment in an ischemia model. *PLoS One* 12:e0182407. doi: 10.1371/journal.pone.0182407

Johnson, M. A., Lutty, G. A., McLeod, D. S., Otsuji, T., Flower, R. W., Sandagar, G., et al. (2005). Ocular structure and function in an aged monkey with spontaneous diabetes mellitus. *Exp. Eye Res.* 80, 37–42. doi: 10.1016/j.exer.2004.08.006

Kara, S., Gencer, B., Karaca, T., Tufan, H. A., Arikan, S., Ersan, I., et al. (2014). Protective effect of hesperetin and naringenin against apoptosis in

ischemia/reperfusion-induced retinal injury in rats. *Sci. World J.* 2014:797824. doi: 10.1155/2014/797824

Kaur, C., Foulds, W. S., and Ling, E. A. (2008). Hypoxia-ischemia and retinal ganglion cell damage. *Clin. Ophthalmol.* 2, 879–889.

Kim, B. J., Braun, T. A., Wordinger, R. J., and Clark, A. F. (2013). Progressive morphological changes and impaired retinal function associated with temporal regulation of gene expression after retinal ischemia/reperfusion injury in mice. *Mol. Neurodegener.* 8:21. doi: 10.1186/1750-1326-8-21

Kim, S. A., Jeon, J. H., Son, M. J., Cha, J., Chun, M. H., and Kim, I. B. (2010). Changes in transcript and protein levels of calbindin D28k, calretinin and parvalbumin, and numbers of neuronal populations expressing these proteins in an ischemia model of rat retina. *Anat. Cell Biol.* 43, 218–229. doi: 10.5115/acb.2010.43.3.218

Lam, T. T., Abler, A. S., and Tso, M. O. (1999). Apoptosis and caspases after ischemia-reperfusion injury in rat retina. *Invest. Ophthalmol. Vis. Sci.* 40, 967–975.

Lee, J. H., Shin, J. M., Shin, Y. J., Chun, M. H., and Oh, S. J. (2011). Immunochemical changes of calbindin, calretinin and SMI32 in ischemic retinas induced by increase of intraocular pressure and by middle cerebral artery occlusion. *Anat. Cell Biol.* 44, 25–34. doi: 10.5115/acb.2011.44.1.25

Li, S. Y., Yang, D., Yeung, C. M., Yu, W. Y., Chang, R. C., So, K. F., et al. (2011). Lycium barbarum polysaccharides reduce neuronal damage, blood-retinal barrier disruption and oxidative stress in retinal ischemia/reperfusion injury. *PLoS One* 6:e16380. doi: 10.1371/journal.pone.0016380

Lin, L. T., Chen, J. T., Tai, M. C., Chen, Y. H., Chen, C. L., Pao, S. I., et al. (2019). Protective effects of hypercapnic acidosis on Ischemia-reperfusion-induced retinal injury. *PLoS One* 14:e0211185. doi: 10.1371/journal.pone.0211185

Mages, K., Grassmann, F., Jagle, H., Rupprecht, R., Weber, B. H. F., Hauck, S. M., et al. (2019). The agonistic TSPO ligand XBD173 attenuates the glial response thereby protecting inner retinal neurons in a murine model of retinal ischemia. *J Neuroinflamm.* 16:43. doi: 10.1186/s12974-019-1424-5

Minhas, G., Morishita, R., and Anand, A. (2012). Preclinical models to investigate retinal ischemia: advances and drawbacks. *Front. Neurol.* 3:75. doi: 10.3389/fneur.2012.00075

Nair, G., Kim, M., Nagaoka, T., Olson, D. E., Thule, P. M., Pardue, M. T., et al. (2011). Effects of common anesthetics on eye movement and electroretinogram. *Doc. Ophthalmol.* 122, 163–176. doi: 10.1007/s10633-011-9271-4

Nakahara, T., Hoshino, M., Hoshino, S., Mori, A., Sakamoto, K., and Ishii, K. (2015). Structural and functional changes in retinal vasculature induced by retinal ischemia-reperfusion in rats. *Exp. Eye Res.* 135, 134–145. doi: 10.1016/j.exer.2015.02.020

Nakano, N., Ikeda, H. O., Hangai, M., Muraoka, Y., Toda, Y., Kakizuka, A., et al. (2011). Longitudinal and simultaneous imaging of retinal ganglion cells and inner retinal layers in a mouse model of glaucoma induced by N-methyl-D-aspartate. *Invest. Ophthalmol. Vis. Sci.* 52, 8754–8762. doi: 10.1167/iovs.10-6654

Nesper, P. L., Scarinci, F., and Fawzi, A. A. (2017). Adaptive optics reveals photoreceptor abnormalities in diabetic macular ischemia. *PLoS One* 12:e0169926. doi: 10.1371/journal.pone.0169926

Palmhof, M., Lohmann, S., Schulte, D., Stute, G., Wagner, N., Dick, H. B., et al. (2018). Fewer functional deficits and reduced cell death after ranibizumab treatment in a retinal ischemia model. *Int. J. Mol. Sci.* 19:E1636.

Peng, L., Parpura, V., and Verkhratsky, A. (2014). EDITORIAL neuroglia as a central element of neurological diseases: an underappreciated target for therapeutic intervention. *Curr. Neuropharmacol.* 12, 303–307. doi: 10.2174/1570159X12999140829152550

Piras, A., Gianetto, D., Conte, D., Bosone, A., and Vercelli, A. (2011). Activation of autophagy in a rat model of retinal ischemia following high intraocular pressure. *PLoS One* 6:e22514. doi: 10.1371/journal.pone.0022514

Produit-Zengaffinen, N., Pournaras, C. J., and Schorderet, D. F. (2009). Retinal ischemia-induced apoptosis is associated with alteration in Bax and Bcl-x(L) expression rather than modifications in Bak and Bcl-2. *Mol. Vis.* 15, 2101–2110.

Ramirez, J. M., Ramirez, A. I., Salazar, J. J., de Hoz, R., and Trivino, A. (2001). Changes of astrocytes in retinal ageing and age-related macular degeneration. *Exp. Eye Res.* 73, 601–615. doi: 10.1006/exer.2001.1061

Reinehr, S., Reinhard, J., Gandej, M., Kuehn, S., Noristani, R., Faissner, A., et al. (2016). Simultaneous complement response via lectin pathway in retina and optic nerve in an experimental autoimmune glaucoma model. *Front. Cell. Neurosci.* 10:140. doi: 10.3389/fncel.2016.00140

Rosenbaum, D. M., Degterev, A., David, J., Rosenbaum, P. S., Roth, S., Grotta, J. C., et al. (2010). Necroptosis, a novel form of caspase-independent cell death, contributes to neuronal damage in a retinal ischemia-reperfusion injury model. *J. Neurosci. Res.* 88, 1569–1576. doi: 10.1002/jnr.22314

Schmid, H., Renner, M., Dick, H. B., and Joachim, S. C. (2014). Loss of inner retinal neurons after retinal ischemia in rats. *Invest. Ophthalmol. Vis. Sci.* 55, 2777–2787. doi: 10.1167/iovs.13-13372

Sellés-Navarro, I., Villegas-Perez, M. P., Salvador-Silva, M., Ruiz-Gomez, J. M., and Vidal-Sanz, M. (1996). Retinal ganglion cell death after different transient periods of pressure-induced ischemia and survival intervals. A quantitative in vivo study. *Invest. Ophthalmol. Vis. Sci.* 37, 2002–2014.

Singh, M., Savitz, S. I., Hoque, R., Gupta, G., Roth, S., Rosenbaum, P. S., et al. (2001). Cell-specific caspase expression by different neuronal phenotypes in transient retinal ischemia. *J. Neurochem.* 77, 466–475. doi: 10.1046/j.1471-4159.2001.00258.x

Slater, B. J., Mehrabian, Z., Guo, Y., Hunter, A., and Bernstein, S. L. (2008). Rodent anterior ischemic optic neuropathy (rAION) induces regional retinal ganglion cell apoptosis with a unique temporal pattern. *Invest. Ophthalmol. Vis. Sci.* 49, 3671–3676. doi: 10.1167/iovs.07-0504

Szabo, M. E., Droy-Lefaix, M. T., Doly, M., and Braquet, P. (1991). Free radical-mediated effects in reperfusion injury: a histologic study with superoxide dismutase and EGB 761 in rat retina. *Ophthalmic Res.* 23, 225–234. doi: 10.1159/000267107

Tanskanen, P., Kylma, T., Kommonen, B., and Karhunen, U. (1996). Propofol influences the electroretinogram to a lesser degree than thiopentone. *Acta Anaesthesiol. Scand.* 40, 480–485. doi: 10.1111/j.1399-6576.1996.tb04472.x

Tsukahara, Y., Blair, N. P., Eappen, D. C., Moy, J. J., Takahashi, A., Shah, G. K., et al. (1992). Ketamine suppresses ischemic injury in the rabbit retina. *Invest. Ophthalmol. Vis. Sci.* 33, 1822–1825.

Unoki, K., and LaVail, M. M. (1994). Protection of the rat retina from ischemic injury by brain-derived neurotrophic factor, ciliary neurotrophic factor, and basic fibroblast growth factor. *Invest. Ophthalmol. Vis. Sci.* 35, 907–915.

Varga, B., Priksz, D., Lampe, N., Bombicz, M., Kurucz, A., Szabo, A. M., et al. (2017). Protective Effect of *Prunus cerasus* (Sour Cherry) seed extract on the recovery of ischemia/reperfusion-induced retinal damage in zucker diabetic fatty rat. *Molecules* 22:E1782. doi: 10.3390/molecules22101782

Vidal-Sanz, M., Salinas-Navarro, M., Nadal-Nicolas, F. M., Alarcon-Martinez, L., Valiente-Soriano, F. J., de Imperial, J. M., et al. (2012). Understanding glaucomatous damage: anatomical and functional data from ocular hypertensive rodent retinas. *Prog. Retin. Eye Res.* 31, 1–27. doi: 10.1016/j.preteyeres.2011.08.001

Wang, L., Li, C., Guo, H., Kern, T. S., Huang, K., and Zheng, L. (2011). Curcumin inhibits neuronal and vascular degeneration in retina after ischemia and reperfusion injury. *PLoS One* 6:e23194. doi: 10.1371/journal.pone.0023194

Weber, M., Mohand-Said, S., Hicks, D., Dreyfus, H., and Sahel, J. A. (1996). Monosialoganglioside GM1 reduces ischemia–reperfusion-induced injury in the rat retina. *Invest. Ophthalmol. Vis. Sci.* 37, 267–273.

Weinreb, R. N., and Khaw, P. T. (2004). Primary open-angle glaucoma. *Lancet* 363, 1711–1720.

Zhao, Y., Yu, B., Xiang, Y. H., Han, X. J., Xu, Y., So, K. F., et al. (2013). Changes in retinal morphology, electroretinogram and visual behavior after transient global ischemia in adult rats. *PLoS One* 8:e65555. doi: 10.1371/journal.pone.0065555

Zheng, G. Y., Zhang, C., and Li, Z. G. (2004). Early activation of caspase-1 after retinal ischemia and reperfusion injury in mice. *Chin. Med. J.* 117, 717–721.

Zheng, L., Gong, B., Hatala, D. A., and Kern, T. S. (2007). Retinal ischemia and reperfusion causes capillary degeneration: similarities to diabetes. *Invest. Ophthalmol. Vis. Sci.* 48, 361–367.

Conflict of Interest Statement: The authors declare that the research was conducted in the absence of any commercial or financial relationships that could be construed as a potential conflict of interest.

Copyright © 2019 Palmhof, Frank, Rappard, Kortenhorn, Demuth, Biert, Stute, Dick and Joachim. This is an open-access article distributed under the terms of the Creative Commons Attribution License (CC BY). The use, distribution or reproduction in other forums is permitted, provided the original author(s) and the copyright owner(s) are credited and that the original publication in this journal is cited, in accordance with accepted academic practice. No use, distribution or reproduction is permitted which does not comply with these terms.

frontiers in Cellular Neuroscience

MINI REVIEW
published: 22 May 2019
doi: 10.3389/fncel.2019.00227

Wnt Signaling Deregulation in the Aging and Alzheimer's Brain

Ernest Palomer†, Johanna Buechler† and Patricia C. Salinas**

Department of Cell and Developmental Biology, University College London, London, United Kingdom

Growing evidence suggests that synaptic signaling is compromised in the aging brain and in Alzheimer's disease (AD), contributing to synaptic decline. Wnt signaling is a prominent pathway at the synapse and is required for synaptic plasticity and maintenance in the adult brain. In this review, we summarize the current knowledge on deregulation of Wnt signaling in the context of aging and AD. Emerging studies suggest that enhancing Wnt signaling could boost synaptic function during aging, and ameliorate synaptic pathology in AD. Although further research is needed to determine the precise contribution of deficient Wnt signaling to AD pathogenesis, targeting Wnt signaling components may provide novel therapeutic avenues for synapse protection or restoration in the brain.

Keywords: Wnt, aging brain, synapse degeneration, synaptic maintenance, Alzheimer's disease

OPEN ACCESS

Edited by:
Lavinia Alberi,
SICHH, Switzerland

Reviewed by:
Claire S. Durrant,
University of Cambridge,
United Kingdom
Paola Bovolenta,
Spanish National Research Council
(CSIC), Spain

****Correspondence:***
Ernest Palomer
e.palomer@ucl.ac.uk
Patricia C. Salinas
p.salinas@ucl.ac.uk

†Co-first authors

Specialty section:
This article was submitted to Cellular Neuropathology, a section of the journal Frontiers in Cellular Neuroscience

Received: *16 November 2018*
Accepted: *06 May 2019*
Published: *22 May 2019*

Citation:
Palomer E, Buechler J and Salinas PC (2019) Wnt Signaling Deregulation in the Aging and Alzheimer's Brain. Front. Cell. Neurosci. 13:227. doi: 10.3389/fncel.2019.00227

INTRODUCTION

Wnt signaling was originally discovered as a tumorigenic pathway in the early 1980s. Almost four decades later, this prominent pathway has been implicated in numerous cellular processes from early embryonic development to tissue homeostasis. This signaling cascade is also linked to a variety of diseases, from cancer to bone and cardiovascular diseases. In the nervous system, Wnt signaling plays a vital role from early patterning of the nervous system to higher functions including synaptic plasticity and memory in the adult brain. In this review, we will focus on new studies indicating a deregulation of the Wnt signaling pathway in the aging brain and Alzheimer's disease (AD).

Alzheimer's Disease

Alzheimer's disease is a devastating neurodegenerative disorder that accounts for two thirds of all dementia cases, and is characterized by progressive cognitive impairment and memory loss leading to difficulties in the performance of daily tasks (Apostolova, 2016). The AD brain displays extracellular Amyloid beta (Aß) deposition, intracellular Tau aggregates (neurofibrillary tangles), and widespread neuronal death at late AD stages. However, synapse loss is the prominent event in early stages of AD and represents the best pathological correlate of cognitive decline in patients (Terry et al., 1991). Current models propose that synaptic dysfunction and degeneration in AD are initiated by oligomers of Aß, a key pathogenic molecule, which negatively regulates signaling pathways that are crucial for synaptic function and stability (Forner et al., 2017). Consistent with this view, increasing evidence suggests that Aß triggers deregulation of Wnt signaling, resulting in the dampening of this important cascade at the synapse. These changes in the Wnt pathway could contribute to synapse dysfunction and degeneration, thereby promoting the progression of AD.

Wnt Signaling Pathway

Wnt proteins are a family of secreted lipoproteins that activate different intracellular signaling pathways by binding to several receptors and co-receptors at the cell surface. Three major Wnt signaling pathways have been described: canonical Wnt/ß-catenin, planar cell polarity (PCP), and Wnt/Ca^{2+} pathways, which lead to changes in gene expression and/or cytoskeleton reorganization. The most extensively studied cascade is the canonical Wnt pathway that controls the expression of Wnt target genes by stabilizing cytoplasmic ß-catenin and by inducing the reorganization of the cellular cytoskeleton (Nusse and Clevers, 2017). In absence of Wnt ligands, ß-catenin is phosphorylated by Gsk3ß and CK1 in the cytoplasm, leading to its degradation (**Figure 1A**; Nusse and Clevers, 2017). Upon binding of Wnt ligands to their receptors Frizzled and co-receptors LRP5/6, the scaffold proteins Disheveled (Dvl) and Axin are recruited to form a signalosome at the cell membrane. This in turn allows ß-catenin accumulation in the cytoplasm and its translocation to the nucleus, where it associates with TCF/LEF and other co-factors to regulate Wnt target gene transcription (**Figure 1B**; Nusse and Clevers, 2017). The Wnt PCP pathway leads to transcriptional changes and cytoskeleton reorganization upon Wnt ligand binding to Frizzled receptors, without the requirement of Wnt co-receptors LRP5/6 (Seifert and Mlodzik, 2007). This signaling cascade activates the small GTPases RhoA and Rac1, which in turn activate the kinases ROCK and JNK, respectively (**Figure 1C**; Seifert and Mlodzik, 2007). The third pathway is the Wnt/Ca^{2+} cascade, in which binding of Wnts to Frizzled receptors leads to phospholipase C (PLC) activation, release of Ca^{2+} from intracellular stores and activation of CaMKII and PKC, resulting in transcriptional changes and actin remodeling (De, 2011).

Wnt Signaling at the Mature Synapse

Wnt signaling has been implicated in axonal pathfinding, dendritogenesis, synapse formation, synaptic plasticity, and maintenance (Budnik and Salinas, 2011; Dickins and Salinas, 2013; McLeod and Salinas, 2018). A fine balance of canonical and non-canonical PCP Wnt signaling is required for maintaining mature synapses. Decreased levels of canonical Wnt signaling with the concomitant activation of the PCP pathway leads to synapse disassembly (Marzo et al., 2016; Sellers et al., 2018). In addition, canonical and non-canonical Wnt pathways play a role in synaptic plasticity at the mature synapse. For example, different Wnt proteins are involved in early or late phases of long-term potentiation (LTP). *In vivo* studies show that canonical Wnt signaling is required for the early phase of LTP and also sufficient to enhance it (Ivanova et al., 2017). Non-canonical Wnt signaling pathways have been implicated in both early and late phases of LTP. Wnt7a/b through its receptor frizzled 7, participates in early LTP phases by promoting AMPAR recruitment at the synapses *in vitro* (McLeod et al., 2018). As this process is CaMKII dependent, it is likely to be due to the activation of Wnt/Ca^{2+} pathway. In addition, Wnt5a regulates basal NMDAR currents and influences late phase of LTP by activating the Wnt PCP pathway in hippocampal slices (Cerpa et al., 2011). Altogether, these studies demonstrate that canonical and non-canonical Wnt signaling are relevant pathways at the mature synapse.

WNT SIGNALING AND AGING

Reduced synaptic strength and function occur during normal aging (Morrison and Baxter, 2012; Petralia et al., 2014). Age is the biggest risk factor for late-onset AD, as growing synaptic vulnerability may increase the susceptibility of synapses to toxic molecules such as Aß. Consistent with this view, various signaling pathways, which are crucial for synapse integrity, undergo changes in the aging brain (Bishop et al., 2010). Of particular interest is the Wnt signaling pathway, which is required for synaptic plasticity (McLeod et al., 2018), synaptic maintenance (Marzo et al., 2016) and is altered during aging (Matarin et al., 2015; García-Velázquez and Arias, 2017).

Wnt Signaling Deregulation in the Human Aging Brain

A recent study showed that Wnt components expression is affected in the aging human brain. Indeed expression of Wnt ligands *WNT2B*, *WNT6*, and *WNT7a* and frizzled receptors *FZD2* and *FZD3* is downregulated in the aged human brain (Folke et al., 2018). Additionally, the same study showed that the secreted frizzled-related protein 1 (*SFRP1*) is upregulated in the aged human brain (Folke et al., 2018). Interestingly, SFRPs sequester Wnt ligands in the extracellular space, thus increased *SFRP1* could interfere with many Wnt pathways. Together, these findings suggest that Wnt signaling is dampened in the aged human brain.

Dampening Wnt Signaling in the Aged Rodent Brain

In the aged rodent brain, several Wnt pathway elements are also downregulated. For example, the expression of the Wnt ligands *Wnt2*, *Wnt4,* and *Wnt9a*, and transcription factors *Lef1* and *Tcf3* is downregulated (**Figure 2A**; Hofmann et al., 2014). In the dentate gyrus region of the hippocampus, *Wnt3* and *Wnt3a* expression progressively declines between 1 and 22 months of age (Okamoto et al., 2011). Moreover, a specific reduction in canonical Wnt signaling is evident in the hippocampus of aged rats, where Dvl2, Axin2 and nuclear ß-catenin are downregulated (**Figure 2A**; Orellana et al., 2015). A similar deficiency in Wnt signaling is observed in a mouse model of accelerated aging (Bayod et al., 2015). Reduced Wnt signaling in the aging brain also arises from increased levels of endogenous secreted Wnt antagonist such as Dickkopf-1 (Dkk1) in the aging mouse brain (**Figure 2A**; Scott et al., 2013; Seib et al., 2013). Altogether these data demonstrate a dampening of Wnt signaling in the aging brain of rodents as not only Wnt ligands and intracellular components of the pathway are

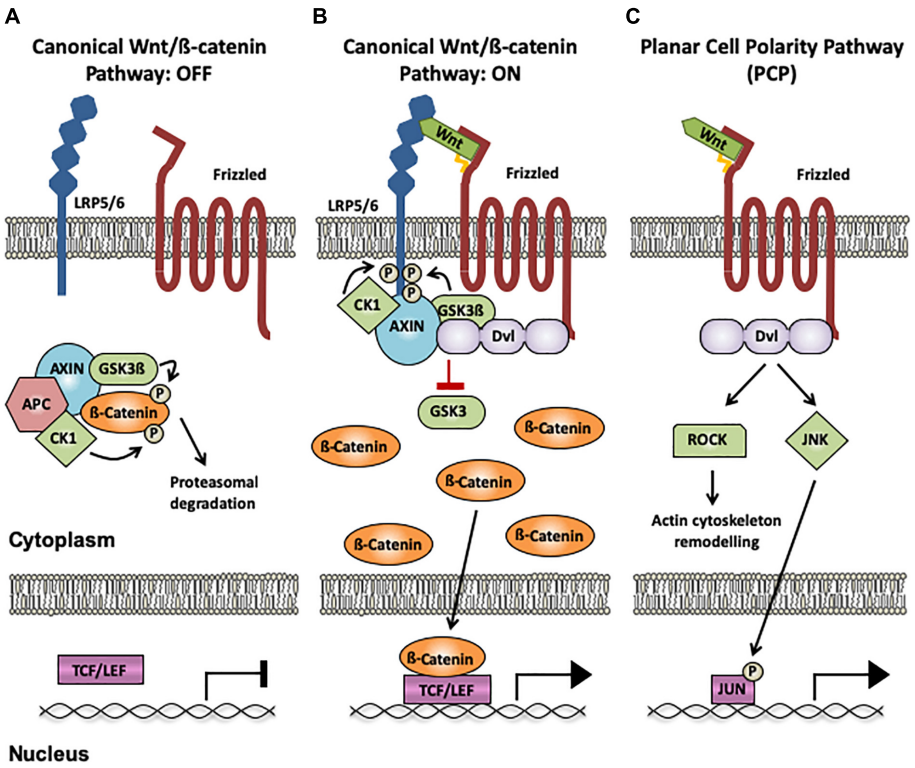


FIGURE 1 | Wnt signaling pathways. **(A)** Canonical Wnt/ß-catenin pathway OFF: In the absence of Wnt binding to Frizzled (Fz) receptors and LRP5/6 co-receptors, ß-catenin interacts with the destruction complex (CK1, GSK3β, Axin1 and APC), resulting in its phosphorylation by Gsk3β and CK1 and its subsequent degradation by the proteasome. **(B)** Canonical Wnt/ß-catenin pathway ON: When a Wnt ligand binds to LRP5/6 and Fz receptors, the scaffold protein Disheveled (Dvl) recruits Axin1 and the kinases CK1 and GSK3ß to the membrane, disrupting the destruction complex and impairing ß-catenin phosphorylation and degradation. ß-catenin accumulates in the cytoplasm and subsequently translocates to the nucleus, where it acts as an activator of TCF/LEF-mediated transcription of Wnt target genes. **(C)** The Planar Cell Polarity (PCP) pathway: The PCP does not require LRP5/6 and is ß-catenin-independent. When Wnts bind to Fz receptors, Dvl is activated, resulting in increased activation of ROCK and JNK through the small GTPases RhoA and Rac1, respectively. Changes in ROCK activity induce actin remodeling, and JNK activation can promote gene transcription via Jun phosphorylation. The palmitate group in Wnt ligands is indicated as a yellow tail. CK1, casein kinase 1; GSK3β, glycogen synthase kinase 3β; Axin1, axis inhibition protein 1; APC, adenomatous polyposis coli; TCF, T-cell factor; LEF, lymphocyte-enhancer-binding factor; Rock, Rho associated coiled-coil-containing protein kinase 1; RhoA, RAS homolog gene-family member A; JNK, Jun N-terminal kinase.

downregulated, but also the potent canonical Wnt antagonist Dkk1 is upregulated.

Discrepancies Between the Human and Rodent Aging Brain

Although Wnt signaling is reduced in both the human and rodent aging brain, the specific deregulated Wnt signaling components are not exactly the same (see above). A possible explanation is that the studies have been conducted in different areas of the brain, where Wnt components are differentially expressed under basal conditions. For example, most of rodent studies analyzed the hippocampus, whereas human studies have been performed in the prefrontal cortex. Nonetheless, the data presented showed that Wnt signaling is reduced in the aging brain, possibly contributing to the observed age-related synaptic decline (Morrison and Baxter, 2012; Petralia et al., 2014). Thus, boosting Wnt signaling in the aging brain may strengthen synaptic resilience, slow down cognitive decline and decrease the risk of pathological transitions toward dementia in elderly individuals.

WNT SIGNALING AND ALZHEIMER'S DISEASE

Deregulation of Wnt signaling may also contribute to synapse vulnerability in the context of AD. Indeed, reduced Wnt signaling has a direct impact on synapses (Marzo et al., 2016). In addition, deficient Wnt signaling could also induce indirect effects on synapses by activating the amyloidogenic pathway (Liu et al., 2014) or by interfering with microglial survival (Zheng et al., 2017).

Antagonizing Canonical Wnt Signaling in AD

Several studies have shown that the canonical Wnt antagonist Dkk1 is up-regulated in brains of AD patients and AD mouse models (Caricasole et al., 2004; Rosi et al., 2010). Dkk1 inhibits

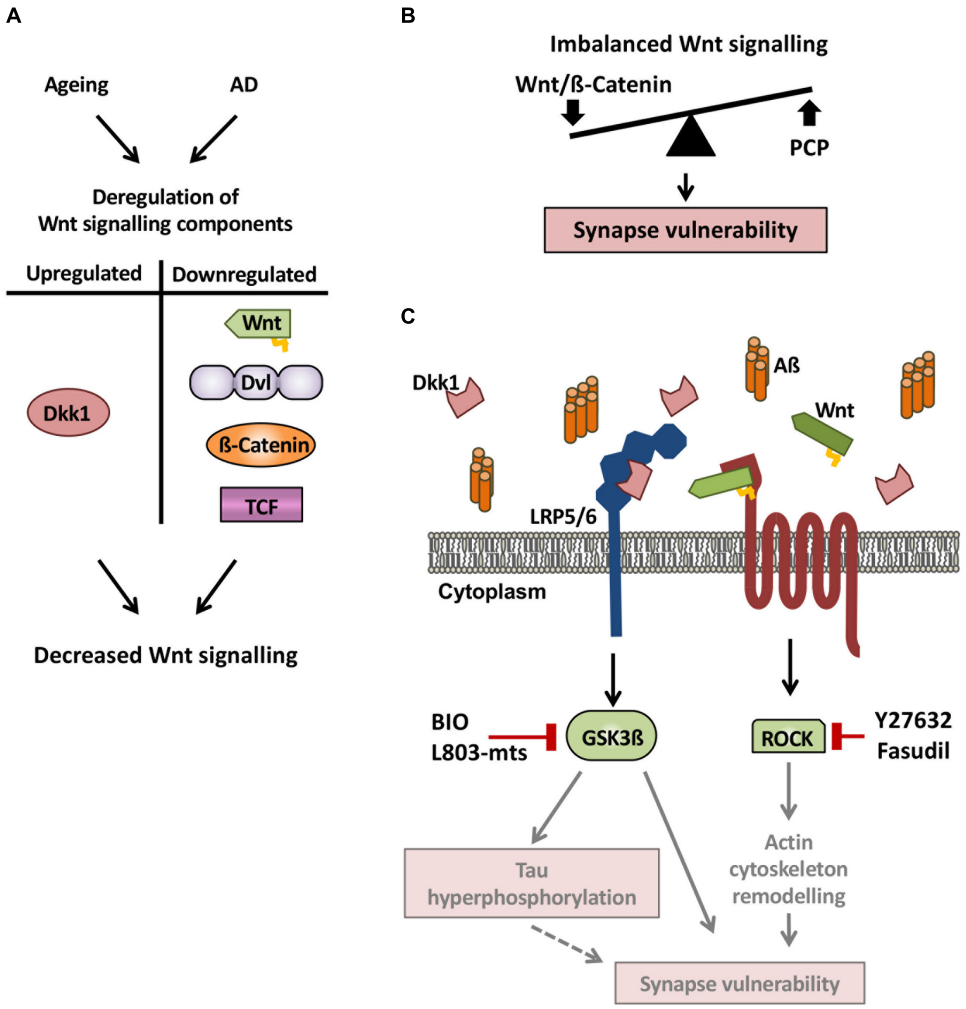


FIGURE 2 | Wnt signaling deregulation in the aging brain and in AD. **(A)** Wnt signaling components are deregulated in both the aging and AD brain. Notably, the Wnt antagonist Dkk1 is upregulated, whereas Wnt ligands, Dvl, ß-catenin, and TCF are downregulated, leading to decreased canonical Wnt signaling. **(B)** As Dkk1 mainly affects the canonical Wnt signaling pathway, we propose a model by which elevation of Dkk1 results in an imbalance between the Wnt/ß-catenin and PCP pathways, resulting in synaptic defects and synapse loss. **(C)** In the brain of AD subjects and AD mouse models, the Wnt antagonist Dkk1 is elevated, leading to increased activity of both Gsk3ß and ROCK, thus resulting in reduced Wnt/ß-catenin signaling and increased PCP signaling. The activation of these two kinases leads to synapse vulnerability but the precise mechanisms downstream remain to be defined. A possible mechanism is that tau phosphorylation and actin remodeling contribute to synaptic changes (gray arrows and diffuse red boxes in the scheme) and subsequent cognitive deficits. These results suggest that pharmacologically targeting Wnt signaling could be a promising therapeutic strategy for synapse protection in AD.

canonical Wnt signaling by interacting with LRP5/6 Wnt co-receptors, thus impairing the binding of Wnt proteins to both Frizzled and LRP5/6. This inhibition of Wnt signaling by Dkk1 leads to increased Gsk3ß activity and reduced cytoplasmic ß-catenin levels – both features which are observed in the brains of AD patients (Zhang et al., 1998; Pei et al., 1999; Kawamura et al., 2001). In addition, *Dkk1* expression is rapidly elevated by Aß in hippocampal neurons, resulting in reduced canonical Wnt signaling and concomitant synapse loss (**Figure 2**; Purro et al., 2012; Sellers et al., 2018). Interestingly, synapses are protected from Aß insult when Dkk1 is blocked, suggesting that Dkk1 is required for Aß-mediated synapse loss (Purro et al., 2012). To mimic the effect of Aß on synapses through Dkk1, a transgenic mouse model was generated that inducibly expresses Dkk1 in the brain (iDkk1 mice). Induced Dkk1 expression results in synapse loss in the striatum (Galli et al., 2014) and hippocampus (Marzo et al., 2016) without affecting cell viability. Moreover, iDkk1 mice exhibit reduced synaptic transmission, impaired LTP and enhanced LTD in the adult hippocampus, accompanied by long-term memory deficits (Marzo et al., 2016). Thus, increased expression of Dkk1 in the adult brain reproduces several of the phenotypic aspects observed in AD models (Marchetti and Marie, 2011; Esquerda-Canals et al., 2017). Interestingly, a variant of the Wnt/Dkk1 receptor LRP6, which displays reduced Wnt signaling in cell lines, is associated with an increased risk for late-onset AD (De Ferrari et al., 2007). This finding further strengthens the link

between deficient Wnt signaling and AD. In addition, neuronal deletion of LRP6 in the postnatal forebrain leads to synaptic loss and exacerbates AD pathology in an AD mouse model (Liu et al., 2014). Collectively, these results support the view that Aß-induced inhibition of Wnt signaling through Dkk1 contributes to synaptic impairment and cognitive deficits in AD.

Wnt Signaling Involvement in Aß Production and Tau Tangles

Several additional lines of evidence further suggest that deficiency in Wnt signaling contributes to AD pathogenesis. First, the canonical co-receptor LRP6 modulates the processing of the Aß precursor protein (APP) and knock-out of LRP6 leads to increased Aß production in an AD mouse model (Liu et al., 2014). This is further supported by *in vitro* studies showing that suppression of canonical Wnt signaling or activation of the Wnt-PCP pathway promotes the amyloidogenic processing of APP, leading to increased production of Aß through a feedback loop mechanism (Tapia-Rojas et al., 2016; Elliott et al., 2018). In addition, several other Wnt pathway components, including ß-catenin, Tcf4, Gsk3ß, and Dvl1, have been implicated in modulating APP processing (Mudher et al., 2001; Liu et al., 2014; Parr et al., 2015; Tapia-Rojas et al., 2016). Second, reduced Wnt signaling leads to increased Gsk3ß activity, which contributes to tau hyperphosphorylation (Scali et al., 2006; Salcedo-Tello et al., 2014), a key pathological hallmark of AD. Conditional overexpression of Gsk3ß in the brain causes neurodegeneration and learning deficits (Hernández et al., 2002). Collectively, this data suggests that reduced Wnt signaling is involved in a negative feedback loop promoting the exacerbation of AD pathology, which in turn would dampen Wnt signaling further by Aß-mediated increase in Dkk1 expression.

AD Associated Genes Are Linked to Reduced Wnt Signaling

Several AD susceptibility genes (including *APOE*, *TREM2,* and *Clusterin*) are linked to aberrant Wnt signaling. For example, ApoE4, a major genetic risk factor for late-onset AD, inhibits canonical Wnt signaling in cell lines (Caruso et al., 2006). More recently, a study showed that TREM2, which is linked to late-onset AD, promotes microglia proliferation through Wnt signaling (Zheng et al., 2017). Finally, the AD-associated protein Clusterin (Harold et al., 2009; Lambert et al., 2009) is involved in Aß-driven *Dkk1* expression, as soluble Aß promotes the intracellular accumulation of Clusterin and subsequent Dkk1 upregulation, whereas knock-down of Clusterin prevents induction of *Dkk1* expression and protects against Aß neurotoxicity (Killick et al., 2014). Not only AD risk factors are linked to reduced Wnt signaling. For example, Wnt signaling promotes the expression of RE1-Silencing Transcription factor (REST) during normal aging (Willert et al., 2002; Lu et al., 2014). In turn, REST represses pro-apoptotic genes and exerts a protective function against oxidative stress and Aß neurotoxicity (Lu et al., 2014). Thus, diminished Wnt signaling could contribute to reduced REST levels observed in AD (Lu et al., 2014), resulting in increased susceptibility to Aß toxicity.

In summary, a growing body of evidence suggests that Wnt signaling is deregulated in AD, which could contribute to synapse degeneration and cognitive decline. This deficiency in Wnt signaling may further exacerbate key pathological processes including Aß production and Tau hyperphosphorylation.

PROTECTIVE EFFECTS OF WNT SIGNALING AGAINST Aß

Activation or restoration of Wnt signaling has protective effects in the context of Aβ-induced synaptic degeneration. Dkk1-induced synapse loss, impaired synaptic plasticity and cognitive defects can be fully reversed *in vivo* upon restoration of Wnt signaling through the cessation of Dkk1 expression (Marzo et al., 2016). *In vitro,* synapses can be protected against Dkk1 by inhibiting two kinases regulated by Wnt signaling: Gsk3ß and ROCK (**Figure 2C**; Marzo et al., 2016). Consistently, *in vivo* inhibition of Gsk3ß by the specific substrate-competitive inhibitor L803-mts peptide improves cognition in AD mouse models (Avrahami et al., 2013; Licht-Murava et al., 2016). In addition, *in vivo* inhibition of ROCK by fasudil improves cognition (Sellers et al., 2018) and reduces Aß load in AD rodent models (Elliott et al., 2018; **Figure 2C**). These studies suggest that Dkk1-induced synapse loss is reversible and mediated through the inhibition of canonical Wnt signaling and the concomitant activation of the Wnt/PCP pathway (**Figure 2B**).

Increased levels of Wnt ligands are particularly protective against Aß-mediated cell toxicity. For example, exogenous Wnt3a prevents Aß neurotoxicity in cell lines and cultured hippocampal neurons (De Ferrari et al., 2003; Alvarez et al., 2004; Chacón et al., 2008). Aß-induced synaptic damage is also alleviated by Wnt5a in acute hippocampal slices, which prevents the dispersal of postsynaptic clusters and protects against defects in excitatory postsynaptic currents elicited by Aß (Cerpa et al., 2010). In summary, a number of studies strongly suggests that restoring or boosting Wnt signaling could protect cells and synapses from Aß toxicity and ameliorate AD pathology.

POTENTIAL SIDE EFFECTS OF BOOSTING WNT SIGNALING

Given the role of Wnts in cancer, the challenge is how to develop treatments to boost Wnt signaling in neurodegenerative diseases without promoting cancer. Mutations in several Wnt signaling pathway components have been linked to colorectal cancer, in particular loss of function mutations in APC leading to high levels of active ß-catenin (Zhan et al., 2017). Also, transgenic models overexpressing Wnt1, and inducing high levels of ß-catenin activation, lead to mammary gland adenocarcinomas in mice (Tsukamoto et al., 1988). In addition, in several other cancers in which Wnt signaling plays a role, mutations in other oncogenic genes are required (White et al., 2012). For example, active ß-catenin levels are increased in a *Pten* knock-out hematopoietic

stem cells induced T-lymphoblastic leukemia (T-ALL) mouse model (Guo et al., 2008). In this T-ALL model, the primary mutation is in the *Pten* gene, however, the ablation of one ß-catenin allele decreases the incidence and delays the appearance of the T-ALL (Guo et al., 2008). These studies suggest that high levels of the canonical Wnt signaling are required for cancer and that in many cases Wnt signaling activation is a secondary effect of other oncogenic mutations. In addition, different preclinical and clinical studies have tested GSK inhibitors as possible therapies for Alzheimer's disease and for different types of cancer (Walz et al., 2017). Therefore, boosting Wnt signaling in a regulated manner could provide a viable approach for the treatment of neurodegenerative diseases without increasing the incidence of cancer.

CONCLUSION

Compelling evidence supports the notion that Wnt signaling is deregulated in the aging brain and in AD (**Figure 2B**). Notably, the Wnt antagonist Dkk1 induces AD-related synaptic loss and cognitive impairment. Further mechanistic insights are required to elucidate how GSK3ß and ROCK activation lead to synapse loss in a synergic way. One could postulate that ROCK induces actin remodeling, which could lead to spine loss. However, the role of GSK3ß is less clear. Interestingly, the closely related protein Dkk3 is elevated in plasma and cerebrospinal fluid of AD patients, however, its role in the adult brain is still largely unexplored. In addition to Dkks, SFRPs represent another class of endogenous Wnt antagonists, which inhibit Wnt signaling by sequestering Wnt ligands. It is currently unknown whether these antagonists are similarly deregulated in the aging brain and in AD. Although two Wnt ligands are protective against Aß-induced synaptotoxicity in cultured neurons, their *in vivo* role has not been demonstrated. Moreover, we still lack a comprehensive view of the expression and activity of other Wnt ligands in the context of brain aging and AD. Further studies on key Wnt components such as Wnt secreted factors and Wnt receptors could provide more mechanistic insight into how deregulation of Wnt signaling contributes to cognitive decline during normal aging and in AD. Targeting components of the Wnt signaling pathway could open therapeutic avenues for boosting synaptic resilience and enhancing cognition in elderly people and people living with AD.

AUTHOR CONTRIBUTIONS

All authors contributed the same in the process of reading the literature and writing the manuscript. Figures were prepared by EP.

FUNDING

This work was supported by the MRC (MR/M024083/1), Alzheimer's Research United Kingdom (ARUK-PG2012-12 and ARUK-PG2018A-002), Wellcome Trust 4-year Ph.D. scholarship (102267/Z/13/Z), and European Commission Horizon 2020 (H2020 MSCA-IF 749209).

REFERENCES

Alvarez, A. R., Godoy, J. A., Mullendorff, K., Olivares, G. H., Bronfman, M., and Inestrosa, N. C. (2004). Wnt-3a overcomes beta-amyloid toxicity in rat hippocampal neurons. *Exp. Cell Res.* 297, 186–196. doi: 10.1016/j.yexcr.2004.02.028

Apostolova, L. G. (2016). Alzheimer disease. *Continuum* 22, 419–434. doi: 10.1212/CON.0000000000000307

Avrahami, L., Farfara, D., Shaham-Kol, M., Vassar, R., Frenkel, D., and Eldar-Finkelman, H. (2013). Inhibition of glycogen synthase kinase-3 ameliorates β-amyloid pathology and restores lysosomal acidification and mammalian target of rapamycin activity in the Alzheimer disease mouse model: in vivo and in vitro studies. *J. Biol. Chem.* 288, 1295–1306. doi: 10.1074/jbc.M112.409250

Bayod, S., Felice, P., Andrés, P., Rosa, P., Camins, A., Pallàs, M., et al. (2015). Downregulation of canonical Wnt signaling in hippocampus of SAMP8 mice. *Neurobiol. Aging* 36, 720–729. doi: 10.1016/j.neurobiolaging.2014.09.017

Bishop, N. A., Lu, T., and Yankner, B. A. (2010). Neural mechanisms of ageing and cognitive decline. *Nature* 464, 529–535. doi: 10.1038/nature08983

Budnik, V., and Salinas, P. C. (2011). Wnt signaling during synaptic development and plasticity. *Curr. Opin. Neurobiol.* 21, 151–159. doi: 10.1016/j.conb.2010.12.002

Caricasole, A., Copani, A., Caraci, F., Aronica, E., Rozemuller, A. J., Caruso, A., et al. (2004). Induction of dickkopf-1, a negative modulator of the Wnt pathway, is associated with neuronal degeneration in Alzheimer's brain. *J. Neurosci.* 24, 6021–6027. doi: 10.1523/JNEUROSCI.1381-04.2004

Caruso, A., Motolese, M., Iacovelli, L., Caraci, F., Copani, A., Nicoletti, F., et al. (2006). Inhibition of the canonical Wnt signaling pathway by apolipoprotein E4 in PC12 cells. *J. Neurochem.* 98, 364–371. doi: 10.1111/j.1471-4159.2006.03867.x

Cerpa, W., Farías, G. G., Godoy, J. A., Fuenzalida, M., Bonansco, C., and Inestrosa, N. C. (2010). Wnt-5a occludes Abeta oligomer-induced depression of glutamatergic transmission in hippocampal neurons. *Mol. Neurodegener.* 5:3. doi: 10.1186/1750-1326-5-3

Cerpa, W., Gambrill, A., Inestrosa, N. C., and Barria, A. (2011). Regulation of NMDA-receptor synaptic transmission by wnt signaling. *J. Neurosci.* 31, 9466–9471. doi: 10.1523/JNEUROSCI.6311-10.2011

Chacón, M. A., Varela-Nallar, L., and Inestrosa, N. C. (2008). Frizzled-1 is involved in the neuroprotective effect of Wnt3a against abeta oligomers. *J. Cell. Physiol.* 217, 215–227. doi: 10.1002/jcp.21497

De, A. (2011). Wnt/Ca2+ signaling pathway: a brief overview. *Acta Biochim. Biophys. Sin.* 43, 745–756. doi: 10.1093/abbs/gmr079

De Ferrari, G. V., Chacón, M. A., Barría, M. I., Garrido, J. L., Godoy, J. A., Olivares, G., et al. (2003). Activation of Wnt signaling rescues neurodegeneration and behavioral impairments induced by beta-amyloid fibrils. *Mol. Psychiatry* 8, 195–208. doi: 10.1038/sj.mp.4001208

De Ferrari, G. V., Papassotiropoulos, A., Biechele, T., Wavrant De-Vrieze, F., Avila, M. E., Major, M. B., et al. (2007). Common genetic variation within the low-density lipoprotein receptor-related protein 6 and late-onset Alzheimer's disease. *Proc. Natl. Acad. Sci. U.S.A.* 104, 9434–9439. doi: 10.1073/pnas.0603523104

Dickins, E. M., and Salinas, P. C. (2013). Wnts in action: from synapse formation to synaptic maintenance. *Front. Cell. Neurosci* 7:162. doi: 10.3389/fncel.2013.00162

Elliott, C., Rojo, A. I., Ribe, E., Broadstock, M., Xia, W., Morin, P., et al. (2018). A role for APP in Wnt signalling links synapse loss with β-amyloid production. *Transl. Psychiatry* 8:179. doi: 10.1038/s41398-018-0231-6

Esquerda-Canals, G., Montoliu-Gaya, L., Güell-Bosch, J., and Villegas, S. (2017). Mouse models of Alzheimer's Disease. *J. Alzheimers Dis.* 57, 1171–1183. doi: 10.3233/JAD-170045

Folke, J., Pakkenberg, B., and Brudek, T. (2018). Impaired Wnt signaling in the prefrontal cortex of Alzheimer's disease. *Mol. Neurobiol.* 56, 873–891. doi: 10.1007/s12035-018-1103-z

Forner, S., Baglietto-Vargas, D., Martini, A. C., Trujillo-Estrada, L., and LaFerla, F. M. (2017). Synaptic impairment in Alzheimer's Disease: a dysregulated symphony. *Trends Neurosci.* 40, 347–357. doi: 10.1016/j.tins.2017.04.002

Galli, S., Lopes, D. M., Ammari, R., Kopra, J., Millar, S. E., Gibb, A., et al. (2014). Deficient Wnt signalling triggers striatal synaptic degeneration and impaired motor behaviour in adult mice. *Nat. Commun.* 5:4992. doi: 10.1038/ncomms5992

García-Velázquez, L., and Arias, C. (2017). The emerging role of Wnt signaling dysregulation in the understanding and modification of age-associated diseases. *Ageing Res. Rev.* 37, 135–145. doi: 10.1016/j.arr.2017.06.001

Guo, W., Lasky, J. L., Chang, C.-J., Mosessian, S., Lewis, X., Xiao, Y., et al. (2008). Multi-genetic events collaboratively contribute to Pten-null leukaemia stem-cell formation. *Nature* 453, 529–533. doi: 10.1038/nature06933

Harold, D., Abraham, R., Hollingworth, P., Sims, R., Gerrish, A., Hamshere, M. L., et al. (2009). Genome-wide association study identifies variants at CLU and PICALM associated with Alzheimer's disease. *Nat. Genet.* 41, 1088–1093. doi: 10.1038/ng.440

Hernández, F., Borrell, J., Guaza, C., Avila, J., and Lucas, J. J. (2002). Spatial learning deficit in transgenic mice that conditionally over-express GSK-3beta in the brain but do not form tau filaments. *J. Neurochem.* 83, 1529–1533. doi: 10.1046/j.1471-4159.2002.01269.x

Hofmann, J. W., McBryan, T., Adams, P. D., and Sedivy, J. M. (2014). The effects of aging on the expression of Wnt pathway genes in mouse tissues. *Age* 36:9618. doi: 10.1007/s11357-014-9618-3

Ivanova, O. Y., Dobryakova, Y. V., Salozhin, S. V., Aniol, V. A., Onufriev, M. V., Gulyaeva, N. V., et al. (2017). Lentiviral modulation of Wnt/β-catenin signaling affects *In Vivo* LTP. *Cell. Mol. Neurobiol.* 37, 1227–1241. doi: 10.1007/s10571-016-0455-z

Kawamura, Y., Kikuchi, A., Takada, R., Takada, S., Sudoh, S., Shibamoto, S., et al. (2001). Inhibitory effect of a presenilin 1 mutation on the Wnt signalling pathway by enhancement of beta-catenin phosphorylation. *Eur. J. Biochem.* 268, 3036–3041. doi: 10.1046/j.1432-1327.2001.02197.x

Killick, R., Ribe, E. M., Al-Shawi, R., Malik, B., Hooper, C., Fernandes, C., et al. (2014). Clusterin regulates β-amyloid toxicity via dickkopf-1-driven induction of the wnt-PCP-JNK pathway. *Mol. Psychiatry* 19, 88–98. doi: 10.1038/mp.2012.163

Lambert, J.-C., Heath, S., Even, G., Campion, D., Sleegers, K., Hiltunen, M., et al. (2009). Genome-wide association study identifies variants at CLU and CR1 associated with Alzheimer's disease. *Nat. Genet.* 41, 1094–1099. doi: 10.1038/ng.439

Licht-Murava, A., Paz, R., Vaks, L., Avrahami, L., Plotkin, B., Eisenstein, M., et al. (2016). A unique type of GSK-3 inhibitor brings new opportunities to the clinic. *Sci. Signal.* 9:ra110. doi: 10.1126/scisignal.aah7102

Liu, C.-C., Tsai, C.-W., Deak, F., Rogers, J., Penuliar, M., Sung, Y. M., et al. (2014). Deficiency in LRP6-mediated wnt signaling contributes to synaptic abnormalities and amyloid pathology in Alzheimer's Disease. *Neuron* 84, 63–77. doi: 10.1016/j.neuron.2014.08.048

Lu, T., Aron, L., Zullo, J., Pan, Y., Kim, H., Chen, Y., et al. (2014). REST and stress resistance in ageing and Alzheimer's disease. *Nature* 507, 448–454. doi: 10.1038/nature13163

Marchetti, C., and Marie, H. (2011). Hippocampal synaptic plasticity in Alzheimer's disease: what have we learned so far from transgenic models? *Rev. Neurosci.* 22, 373–402. doi: 10.1515/RNS.2011.035

Marzo, A., Galli, S., Lopes, D., McLeod, F., Podpolny, M., Segovia-Roldan, M., et al. (2016). Reversal of synapse degeneration by restoring Wnt signalling in the adult hippocampus. *Curr. Biol.* 26, 2551–2561. doi: 10.1016/j.cub.2016.07.024

Matarin, M., Salih, D. A., Yasvoina, M., Cummings, D. M., Guelfi, S., Liu, W., et al. (2015). A genome-wide gene-expression analysis and database in transgenic mice during development of amyloid or tau pathology. *Cell Rep.* 10, 633–644. doi: 10.1016/j.celrep.2014.12.041

McLeod, F., Bossio, A., Marzo, A., Ciani, L., Sibilla, S., Hannan, S., et al. (2018). Wnt signaling mediates LTP-dependent spine plasticity and AMPAR localization through frizzled-7 receptors. *Cell Rep.* 23, 1060–1071. doi: 10.1016/j.celrep.2018.03.119

McLeod, F., and Salinas, P. C. (2018). Wnt proteins as modulators of synaptic plasticity. *Curr. Opin. Neurobiol.* 53, 90–95. doi: 10.1016/j.conb.2018.06.003

Morrison, J. H., and Baxter, M. G. (2012). The ageing cortical synapse: hallmarks and implications for cognitive decline. *Nat. Rev. Neurosci.* 13, 240–250. doi: 10.1038/nrn3200

Mudher, A., Chapman, S., Richardson, J., Asuni, A., Gibb, G., Pollard, C., et al. (2001). Dishevelled regulates the metabolism of amyloid precursor protein via protein kinase C/mitogen-activated protein kinase and c-Jun terminal kinase. *J. Neurosci.* 21, 4987–4995. doi: 10.1523/jneurosci.21-14-04987.2001

Nusse, R., and Clevers, H. (2017). Wnt/β-catenin signaling, disease, and emerging therapeutic modalities. *Cell* 169, 985–999. doi: 10.1016/j.cell.2017.05.016

Okamoto, M., Inoue, K., Iwamura, H., Terashima, K., Soya, H., Asashima, M., et al. (2011). Reduction in paracrine Wnt3 factors during aging causes impaired adult neurogenesis. *FASEB J.* 25, 3570–3582. doi: 10.1096/fj.11-184697

Orellana, A. M. M., Vasconcelos, A. R., Leite, J. A., de Sá Lima, L., Andreotti, D. Z., Munhoz, C. D., et al. (2015). Age-related neuroinflammation and changes in AKT-GSK-3β and WNT/ β-CATENIN signaling in rat hippocampus. *Aging* 7, 1094–1111. doi: 10.18632/aging.100853

Parr, C., Mirzaei, N., Christian, M., and Sastre, M. (2015). Activation of the Wnt/ β -catenin pathway represses the transcription of the β -amyloid precursor protein cleaving enzyme (BACE1) via binding of T-cell factor-4 to BACE1 promoter. *FASEB J.* 29, 623–635. doi: 10.1096/fj.14-253211

Pei, J. J., Braak, E., Braak, H., Grundke-Iqbal, I., Iqbal, K., Winblad, B., et al. (1999). Distribution of active glycogen synthase kinase 3beta (GSK-3beta) in brains staged for Alzheimer disease neurofibrillary changes. *J. Neuropathol. Exp. Neurol.* 58, 1010–1019. doi: 10.1097/00005072-199909000-00011

Petralia, R. S., Mattson, M. P., and Yao, P. J. (2014). Communication breakdown: the impact of ageing on synapse structure. *Ageing Res. Rev.* 14, 31–42. doi: 10.1016/j.arr.2014.01.003

Purro, S. A., Dickins, E. M., and Salinas, P. C. (2012). The secreted wnt antagonist dickkopf-1 is required for amyloid -mediated synaptic loss. *J. Neurosci.* 32, 3492–3498. doi: 10.1523/JNEUROSCI.4562-11.2012

Rosi, M. C., Luccarini, I., Grossi, C., Fiorentini, A., Spillantini, M. G., Prisco, A., et al. (2010). Increased dickkopf-1 expression in transgenic mouse models of neurodegenerative disease. *J. Neurochem.* 112, 1539–1551. doi: 10.1111/j.1471-4159.2009.06566.x

Salcedo-Tello, P., Hernández-Ortega, K., and Arias, C. (2014). Susceptibility to GSK3β-induced tau phosphorylation differs between the young and aged hippocampus after Wnt signaling inhibition. *J. Alzheimers Dis.* 39, 775–785. doi: 10.3233/JAD-130749

Scali, C., Caraci, F., Gianfriddo, M., Diodato, E., Roncarati, R., Pollio, G., et al. (2006). Inhibition of Wnt signaling, modulation of Tau phosphorylation and induction of neuronal cell death by DKK1. *Neurobiol. Dis.* 24, 254–265. doi: 10.1016/j.nbd.2006.06.016

Scott, E. L., Zhang, Q.-G., Han, D., Desai, B. N., and Brann, D. W. (2013). Long-term estrogen deprivation leads to elevation of Dickkopf-1 and dysregulation of Wnt/β-Catenin signaling in hippocampal CA1 neurons. *Steroids* 78, 624–632. doi: 10.1016/j.steroids.2012.11.004

Seib, D. R. M., Corsini, N. S., Ellwanger, K., Plaas, C., Mateos, A., Pitzer, C., et al. (2013). Loss of Dickkopf-1 restores neurogenesis in old age and counteracts cognitive decline. *Cell Stem Cell* 12, 204–214. doi: 10.1016/j.stem.2012.11.010

Seifert, J. R. K., and Mlodzik, M. (2007). Frizzled/PCP signalling: a conserved mechanism regulating cell polarity and directed motility. *Nat. Rev. Genet.* 8, 126–138. doi: 10.1038/nrg2042

Sellers, K. J., Elliott, C., Jackson, J., Ghosh, A., Ribe, E., Rojo, A. I., et al. (2018). Amyloid β synaptotoxicity is Wnt-PCP dependent and blocked by fasudil. *Alzheimers Dement.* 14, 306–317. doi: 10.1016/j.jalz.2017.09.008

Tapia-Rojas, C., Burgos, P. V., and Inestrosa, N. C. (2016). Inhibition of Wnt signaling induces amyloidogenic processing of amyloid precursor protein and the production and aggregation of Amyloid-β (Aβ)42peptides. *J. Neurochem.* 139, 1175–1191. doi: 10.1111/jnc.13873

Terry, R. D., Masliah, E., Salmon, D. P., Butters, N., DeTeresa, R., Hill, R., et al. (1991). Physical basis of cognitive alterations in alzheimer's disease: synapse loss is the major correlate of cognitive impairment. *Ann. Neurol.* 30, 572–580. doi: 10.1002/ana.410300410

Tsukamoto, A. S., Grosschedl, R., Guzman, R. C., Parslow, T., and Varmus, H. E. (1988). Expression of the int-1 gene in transgenic mice is associated with

mammary gland hyperplasia and adenocarcinomas in male and female mice. *Cell* 55, 619–625. doi: 10.1016/0092-8674(88)90220-6

Walz, A., Ugolkov, A., Chandra, S., Kozikowski, A., Carneiro, B. A., O'halloran, T. V., et al. (2017). Molecular pathways molecular pathways: revisiting glycogen synthase kinase-3b as a target for the treatment of cancer. *Clin. Cancer Res.* 23, 1891–1897. doi: 10.1158/1078-0432.CCR-15-2240

White, B. D., Chien, A. J., and Dawson, D. W. (2012). Dysregulation of Wnt/β-catenin signaling in gastrointestinal cancers. *Gastroenterology* 142, 219–232. doi: 10.1053/J.GASTRO.2011.12.001

Willert, J., Epping, M., Pollack, J. R., Brown, P. O., and Nusse, R. (2002). A transcriptional response to Wnt protein in human embryonic carcinoma cells. *BMC Dev. Biol.* 2:8.

Zhan, T., Rindtorff, N., and Boutros, M. (2017). Wnt signaling in cancer. *Oncogene* 36, 1461–1473. doi: 10.1038/onc.2016.304

Zhang, Z., Hartmann, H., Do, V. M., Abramowski, D., Sturchler-Pierrat, C., Staufenbiel, M., et al. (1998). Destabilization of beta-catenin by mutations in presenilin-1 potentiates neuronal apoptosis. *Nature* 395, 698–702. doi: 10.1038/27208

Zheng, H., Jia, L., Liu, C.-C., Rong, Z., Zhong, L., Yang, L., et al. (2017). TREM2 promotes microglial survival by activating Wnt/β-catenin pathway. *J. Neurosci.* 37, 1772–1784. doi: 10.1523/JNEUROSCI.2459-16.2017

Conflict of Interest Statement: The authors declare that the research was conducted in the absence of any commercial or financial relationships that could be construed as a potential conflict of interest.

Copyright © 2019 Palomer, Buechler and Salinas. This is an open-access article distributed under the terms of the Creative Commons Attribution License (CC BY). The use, distribution or reproduction in other forums is permitted, provided the original author(s) and the copyright owner(s) are credited and that the original publication in this journal is cited, in accordance with accepted academic practice. No use, distribution or reproduction is permitted which does not comply with these terms.

frontiers in Cellular Neuroscience

ORIGINAL RESEARCH
published: 17 July 2019
doi: 10.3389/fncel.2019.00310

Comprehensive Evaluation of White Matter Damage and Neuron Death and Whole-Transcriptome Analysis of Rats With Chronic Cerebral Hypoperfusion

Wenxian Li[1,2†], Di Wei[3†], Jianye Liang[4], Xiaomei Xie[1], Kangping Song[1] and Li'an Huang[1]*

[1] Department of Neurology, The First Affiliated Hospital, Jinan University, Guangzhou, China, [2] Department of Neurology, The Second Affiliated Hospital, Xi'an Jiaotong University, Xi'an, China, [3] Department of Urology, Xijing Hospital, The Fourth Military Medical University, Xi'an, China, [4] Medical Imaging Center, The First Affiliated Hospital, Jinan University, Guangzhou, China

OPEN ACCESS

Edited by:
Dirk M. Hermann,
University of Duisburg-Essen, Germany

Reviewed by:
Nikolaus Plesnila,
Institute for Stroke and Dementia Research (ISD), Germany
Mohammad Taghi Mansouri,
Department of Anesthesiology, Columbia University Irving Medical Center, United States

***Correspondence:**
Li'an Huang
huanglian1306@126.com

[†]These authors have contributed equally to this work

Specialty section:
This article was submitted to Cellular Neuropathology, a section of the journal Frontiers in Cellular Neuroscience

Received: 25 January 2019
Accepted: 25 June 2019
Published: 17 July 2019

Citation:
Li W, Wei D, Liang J, Xie X, Song K and Huang L (2019) Comprehensive Evaluation of White Matter Damage and Neuron Death and Whole-Transcriptome Analysis of Rats With Chronic Cerebral Hypoperfusion. Front. Cell. Neurosci. 13:310. doi: 10.3389/fncel.2019.00310

Background/Aims: Chronic cerebral hypoperfusion (CCH) is induced by chronic deficit of brain perfusion, contributes to a persistent or progressive cognitive dysfunction, which is characterized by diverse neuropathological manifestations. There are currently no effective medications available. White matter damage (WMD) and cortical neuron death may be caused by CCH, which are related to cognitive impairment, while the underlying molecular mechanisms remain unclear. In the study, a database of the transcriptome level was built to determine potential biomarkers in cortex of CCH.

Methods: CCH was induced in male Sprague-Dawley rats by permanent occlusion of the bilateral common carotid arteries. Rats were randomly divided into three groups: Sham-operated group (n = 24), the 4th and 8th week of CCH groups (total = 56, n = 28 for each group). Cognitive function was evaluated using the Morris water maze task. WMD and neuron damage were detected using diffusion tensor imaging and histological analysis, respectively. Western blotting analysis of various markers was used to examine neuronal death. Whole-transcriptome microarray was performed to assess mRNA, circRNA, and lncRNA expression profiles at 4th and 8th weeks after CCH. Diversified bioinformatic tools were performed to analyze and predict the key biological processes and signaling pathways of differentially expressed RNAs and co-expressed potential target genes. Co-expression networks of mRNA–circRNA–miRNA and lncRNA–mRNA were constructed.

Results: Compared to the sham group, cognitive impairment, disintegration of white matter, blood-brain barrier damage and neuron death were induced by CCH. Neuron death including apoptosis and necroptosis might occur in the cortex of CCH. We constructed the regulatory networks of whole-transcriptomic including differentially expressed mRNAs, circRNAs, and lncRNAs, and related biological functions and pathways involved in neurological disease, cell death and survival, energy and metabolism, et al. Our results also indicated that Cyr61 mRNA may play a role in the CCH-related cortical neuronal death.

Conclusion: WMD and cortical neuronal death are worthy of attention in the pathogenesis of CCH. Additionally, the present results provide potential evidence at the whole-transcription level for CCH, offering candidate biomarkers and therapeutic targets.

Keywords: chronic cerebral hypoperfusion, white matter damage, neuron death, whole-transcriptome, vascular dementia

INTRODUCTION

Chronic cerebral hypoperfusion (CCH) is induced by moderate and persistent decrease of cerebral blood flow (CBF). Such pattern of hypoperfusion results in the development and progression of cognitive impairment, such as vascular dementia (VD) (Du et al., 2017). Clinical researches suggested that cerebral hypoperfusion precedes and possibly contributes to onset of dementia (Ruitenberg et al., 2005). And in the general population, cerebral hypoperfusion is associated with accelerated cognitive decline and an increased risk of dementia (Wolters et al., 2017). The subtypes of clinical VD also explicitly includes hypoperfusion dementia (O'Brien and Thomas, 2015). Vascular cognitive deficits are secondary to any type of cerebrovascular disease, the deficit brain perfusions have been identified and raised (Sun et al., 2016). Different from the narrow time window of acute cerebral ischemia, CCH/chronic cerebral ischemia is an available state that can be regulated. CCH experimental model is an effective tool to study the pathological condition, process of degeneration, and mechanisms underlying ischemic cognitive impairment (Du et al., 2017). A minimally invasive bilateral common carotid arterial occlusion (BCCAO) surgery has been used to develop a model of CCH (Zhang T. et al., 2017; Zou et al., 2018; Mao et al., 2019).

Most known mechanisms of CCH include neuroinflammation, oxidative stress injury, dysfunction of neurotransmitter system and mitochondria, disturbance of lipid metabolism, and alterations of growth factors (Du et al., 2017). Neuronal cell death is hallmark of VD induced by CCH (Chen et al., 2017; Mao et al., 2019). Except for the loss of hippocampal neurons, neuron death/neurodegeneration in cortex is another characteristic in CCH brain due to long-term hypoperfusion attack. In addition, white matter damage (WMD) has been frequently detected by imaging scans in clinical subcortical ischemic VD patients induced by CCH. Cerebral WMD contains the loss of oligodendrocyte and demyelination, which takes place after CCH and leads to axonal degeneration (Ma et al., 2018). Therefore, neuron death in cortex may be related to WMD and cognitive impairment directly. However, we know little about the complex pathogenesis of CCH, particularly at the molecular level.

Human genome-wide association studies have demonstrated that a large number of disease-associated genomic variations exist outside the protein-coding genes (Gopalakrishnan et al., 2015). Transcriptomic analyses such as mRNAs, circRNAs, and lncRNAs can provide comprehensive, complete, and specific information relating to a given tissue at a specific time, which bring many advantages including the discovery of novel genomic sequences and the accurate quantification of expression levels. These advantages allow us to create an in-depth understanding of molecular mechanisms and therefore make it possible to identify innovative therapeutic targets (Sun et al., 2019). However, comprehensive analyses of differentially expressed profiles of the whole transcriptome for diseases of the nervous system have not yet been investigated.

In this study, we examined expression profiles and related networks of mRNAs, circRNAs and lncRNAs, in the cortical tissue of a CCH rat model. Gene Ontology (GO), Kyoto Encyclopedia of Genes and Genomes (KEGG), and Reactome enrichment analyses and Ingenuity Pathway Analysis (IPA) were performed in this study. Co-expression and networks of potential targeting relationship were constructed. In addition, diffusion tensor imaging (DTI) was used to specifically investigate the disintegration of white matter, and various methods to examine cell death. The present study has provided new insights into the molecular mechanisms of CCH using whole transcriptome sequencing and bioinformatic approaches.

MATERIALS AND METHODS

Ethics Statement

All animal work was performed in accordance with the Chinese Animal Welfare Act and all experiments involving animals were approved by the Laboratory Animal Ethics Committee of Jinan University (Approval No. IACUC-20180130-03).

Animals and Surgery

Sprague-Dawley rats were purchased from Laboratory Animal Center, Southern Medical University [Quality certificate No. SYXK(guangdong) 2017-0174, Guangzhou, China]. Eight-week-old male Sprague Dawley rats (weighed between 350 and 400 g) were specific pathogen free. We kept individually in a vivarium of constant temperature (25 ± 1°C) and 40–70% humidity and exposed them to unlimited food and water. We also exposed them to alternating 12:12-h light and dark cycle (light cycle: from 8:00 am to 8:00 pm; dark cycle: from 8:00 pm to 8:00 am) for 4 weeks of

Abbreviations: Apold1, apolipoprotein L domain containing 1; Atf3, activating transcription factor 3; Cyr61, cysteine-rich angiogenic inducer 61 or CCN family member 1 (CCN1); HIF1α, hypoxia-inducible factor 1α; Iift1, interferon-induced protein with tetratricopeptide repeats 1; Iift3, interferon-induced protein with tetratricopeptide repeats 3; MLKL, mixed lineage kinase domain-like protein; NR4A2, NR4A orphan nuclear receptor family member 2; PDE4C, phosphodiesterase 4C; pRIPK3, phosphorylated receptor-interactive protein kinase 1 protein; RIPK1, receptor-interactive protein kinase 1; RIPK3, receptor-interactive protein kinase 3 protein; TNFα, tumor necrosis factor α; ZO-1, Zonula occludens-1.

adaptive feeding, before all the animal experiments. Precautions were taken to keep the number of animals used to a low and to mitigate pain.

A total of 80 rats were used and randomized in this study. BCCAO operation was used to induce CCH in rats. Each rat was anesthetized with an intraperitoneal injection of 3% pentobarbital sodium salt (0.2 mL/kg body weight). A median incision was made in the rat's neck, and the bilateral common carotid arteries and the vagus nerves were then separated and isolated. In the BCCAO rats, the bilateral carotid arteries were double-ligated with 2-0 sutures. The BCCAO groups, or the CCH groups, included two subgroups: the 4th week of CCH group (CCH 4W; $n = 28$) and the 8th week of CCH group (CCH 8W; $n = 28$). In the sham-operated group ($n = 24$), the bilateral carotid arteries were separated as did in the BCCAO rats but were not ligated. The wounds were then closed. The body temperature of the rats was maintained at $37 \pm 2°C$ using a heating lamp during surgery as well as during recovery from anesthesia.

Morris Water Maze Task

The cognitive function was evaluated using the Morris water maze task (MWT) (Ethovison XT, Noldus Information Technology Co., Hague, Netherlands). A total of 18 rats (Sham, $n = 6$; CCH 4W, $n = 6$; CCH 8W, $n = 6$) were assessed. The test was performed according to our previously described protocol (Jing et al., 2015; Xiong et al., 2017).

Magnetic Resonance Imaging

To evaluate white matter integrity, magnetic resonance imaging (MRI) with DTI detection was conducted using a Discovery 750 3.0T scanner (an 8-channel wrist coil, GE Healthcare, Milwaukee, WI, United States). The corpus callosum (CC) and both external capsules (ECs), where white matter tracts are the most abundant in the rat brain, were selected for T2-weighted imaging (T2WI; **Figure 4A**). Scanning methods according to a previous protocol, and data acquisition was performed using parameters as described previously (Jing et al., 2015; Choi et al., 2016; Xiong et al., 2017). The DTI parameter maps of fractional anisotropy (FA) were calculated.

Rats in the vehicle group ($n = 6$) were scanned using MRI at three time points: pre-occlusion and 4th and 8th weeks after BCCAO (vehicle).

Evaluation of Neuronal Damage Using Hematoxylin and Eosin and Nissl Staining

The rats were euthanized, and the rat-brain samples were collected and fixed in 4% paraformaldehyde for 48 h; subsequently, these brain samples were embedded in paraffin and sectioned at 5-μm intervals. To evaluate neuron damage, hematoxylin and eosin (HE) and Nissl staining were carried out according to the manufacturer's instructions. The mounted slides were then examined and photographed using a Nikon® DS-U3 imaging system (Japan).

Fluoro-Jade B Histofluorescence

To investigate neurodegeneration, sham- and BCCAO-operated animals (three rats in each group were assessed for statistical analysis) were used for Fluoro-Jade B (FJB) (Millipore) histofluorescence analysis. FJB and DAPI (Sigma) staining were performed according to a previous protocol (Caccamo et al., 2017). All images were acquired using a Nikon® C2 confocal microscope (Japan) under 200 magnification.

Immunohistochemical Staining

Immunohistochemical staining was performed as described previously (Kiyota et al., 2018). For $A\beta_{1-42}$ immunostaining ($A\beta_{1-42}$ antibody, 1:100; Abcam), Image J was used to measure intracellular $A\beta_{1-42}$-positive cells and the total areas of plaques after adjusting for the threshold. Intracellular $A\beta_{1-42}$-positive cells and extracellular $A\beta_{1-42}$ plaques and were measured, respectively. Three rats in each group were assessed for statistical analysis.

To confirm WMD, diaminobenzidine staining for myelin basic protein (MBP; 1:100, Abcam) and luxol fast blue (LFB; Sigma) stainings were performed as previously described (Choi et al., 2016; Ghaiad et al., 2017) to examine WMD. The WMD was evaluated in the CC and both ECs. In the MBP staining, normal myelination was scored 3 (Choi et al., 2016), and in the LFB staining, demyelination was scored from 0 to 3. A score of 0 refers to a normal myelin status; a score of 1 indicates demyelination of one-third of the myelin tract fibers; a score of 2 indicates demyelination of two-thirds of the myelin tract fibers; a score of 3 refers to complete demyelination(Ghaiad et al., 2017). Scores from different sections were summed up to obtain an average score for each group. Data were pooled from 3 sections at 200 magnifications for each rat, and 3 rats in each group were assessed for statistical analysis.

RNA Isolation

Total RNA was isolated from cerebral cortex tissues using HiPure Total RNA Mini Kit (Magen) according to the manufacturer's protocol. The concentration and integrity of the extracted total RNA were estimated by Qubit 3.0 Fluorometer (Invitrogen) and Agilent 2100 Bioanalyzer (Applied Biosystems), respectively. RNA samples with an RIN value of at least 7.0 or higher were used for further processing.

Library Preparation for RNA Sequencing

An RNA-seq library was prepared with approximately 1 μg of total RNA using a KAPA RNA HyperPrep Kit with RiboErase (HMR) for Illumina® (Kapa Biosystems). Briefly, ribosomal RNA was removed from the total RNA. Next, the ribominus RNA was fragmented, and the first strand and directional second strand synthesis was performed. A tailing and adapter ligation were subsequently performed using the purified cDNA. Finally, the purified, adapter-ligated DNA was amplified. The DNA library quality and concentration were assessed using a DNA 1000 chip on an Agilent 2100 Bioanalyzer. Accurate quantification for sequencing applications was determined using a qPCR-based KAPA Biosystems Library Quantification kit (Kapa

Biosystems). Each library was diluted to a final concentration of 10 nM and pooled equimolar prior to clustering. In all samples, 150 bp paired-end (PE150) sequencing was performed. The experimental technical process is shown in the **Figure 1A**. The technical process of analysis is shown in the **Figure 1B**.

Differential mRNA, circRNA, and lncRNA Screen and Clustering Analysis

For analyzing of whole-transcriptome (mRNA, circRNA, and lncRNA) expression, the reads were first mapped to the latest UCSC transcript set using Bowtie2 (version 2.1.0) (Langmead and Salzberg, 2012), and the gene expression level was estimated using RSEM (version 1.2.15) (Li and Dewey, 2011). We used the transcripts set form Lncipedia[1] for lncRNA expression analysis. Trimmed mean of *M*-values was used to normalize gene expression. Differentially expressed RNAs were identified using the edgeR program (Robinson et al., 2010). RNAs showing altered expression with $P < 0.05$ and fold change (FC) > 1.5 were considered differentially expressed. For circRNA expression analysis, the reads were genome mapped using STAR software (Dobin et al., 2013), and DCC software (Cheng et al., 2016) was used to identify the circRNA and to estimate the circRNA expression. Trimmed mean of *M*-values was used to normalize the expression. Differentially expressed RNAs were identified using the edgeR program, and miRanda (Enright et al., 2003) was used to predict the miRNA target of the circRNA. R was used to generate the figure.

GO, KEGG and Reactome Enrichment Analysis

GO and KEGG analysis were used to determine key biological processes and signaling pathways during CCH process. Gene functions were classified into three subgroups: biological process (BP), cellular component (CC), and molecular function (MF). GO analysis[2] was conducted to construct meaningful annotation of genes and gene products in a wide variety of organisms. GO terms with a $p < 0.05$ were selected and integrated using Venn analysis. The top 15 enriched GO terms among the groups were ranked by fold enrichment, and the enrichment scores were presented.

KEGG pathway/Reactome enrichment analysis was performed to generate pathway clusters on the molecular interaction and reaction networks in differentially regulated gene profiling that covered present knowledge. The −log10 (*P*-value) denotes the significance among differentially expressed RNAs.

Ingenuity Pathway Analysis

Ingenuity pathway analysis was used to decipher mRNA expression patterns related functions, diseases and networks about VD induced by CCH. The mRNA expression data obtained from three samples of CCH 4W and CCH 8W tissues and four normal controls were imported into the IPA Tool (Ingenuity H Systems, Redwood City, CA, United States)[3]. The IPA tool computes a score for each network according to the fit of the set of supplied focus genes. These scores indicate the likelihood of focus genes belonging to a network versus those obtained by chance. The canonical pathways generated by IPA are the most significant for the uploaded dataset. Fischer's exact test with FDR option was used to calculate the significance of the canonical pathway. Based on the Ingenuity Knowledge Base of different networks, BP and/or diseases were then algorithmically generated based on the connectivity of genes within the datasets. Comparisons were performed between the CCH groups and the sham group. The mRNAs showing significant differences in expression levels between groups will be submitted to IPA for human diseases and disorders under the molecular and cellular functions categories and pathway analysis.

Co-expression Networks of mRNA–circRNA–miRNA and mRNA–lncRNA

The co-expression networks were constructed based on the correlation analysis between the differentially expressed mRNAs, circRNAs, and lncRNAs, and the expression of these RNAs was analyzed by Pearson's correlation coefficient. The absolute coefficient value of 0.8 between RNAs was considered relevant for network construction. *P*-value < 0.05 was considered statistically significant.

Quantitative Real-Time Polymerase Chain Reaction

Real-time polymerase chain reaction (qPCR) was performed to validate the results of the transcriptome analyses. cDNA (2 μl) was quantified in duplicate for each sample using a Light Cycler 480 SYBR Green I master kit (Roche) on a Light Cycler 480 II according to the manufacturer's instruction. Cycling conditions were: 95°C for 10 min, 40 cycles of 95°C for 15 s and 60°C for 60 s. Melt curve cycles immediately followed, and the conditions were: 95°C for 5 s, 60°C for 1 min, and then a gradual temperature rise to 95°C at a rate of 0.3°C/s followed by 60°C for 15 s. Melt curve analysis was performed to verify primer specificity, and all primers were tested in a dilution series before use. For Cyr61 mRNA, $n = 9$ in each group, for other mRNAs, $n = 6$ in each group. Data are displayed as FC above proliferative condition mRNA levels using $2^{\wedge(\Delta\Delta Ct)}$ values. Primer sequences were described as follows:

Cyr61-S: CATCTCCACACGAGTTACCAA
Cyr61-A: CGGACTGGTTCTGGGGATTTC
NR4A2-S: CTGTCAGCATTACGGTGTTCG
NR4A2-A: CTTCGGTTTTGAGGGTAGACG
PDE4C-S: CTTGAAGACACCAACAAATGG
PDE4C-A: CCTGGAGAACGCTGAAGATAA
Apold1-S: TCTACTTCATCGTCTTCTTCGG
Apold1-A: CTCCAGGCTCTCAGACAGTTT
Atf3-S: ATTCGCCATCCAGAACAAGC
Atf3-A: AGCAGCAATTTTGTTTCTTTCC
Iift1-S: GCTACCACCTTCACAGCAACC

[1]http://www.lncipedia.org
[2]http://www.geneontology.org
[3]http://www.ingenuity.com

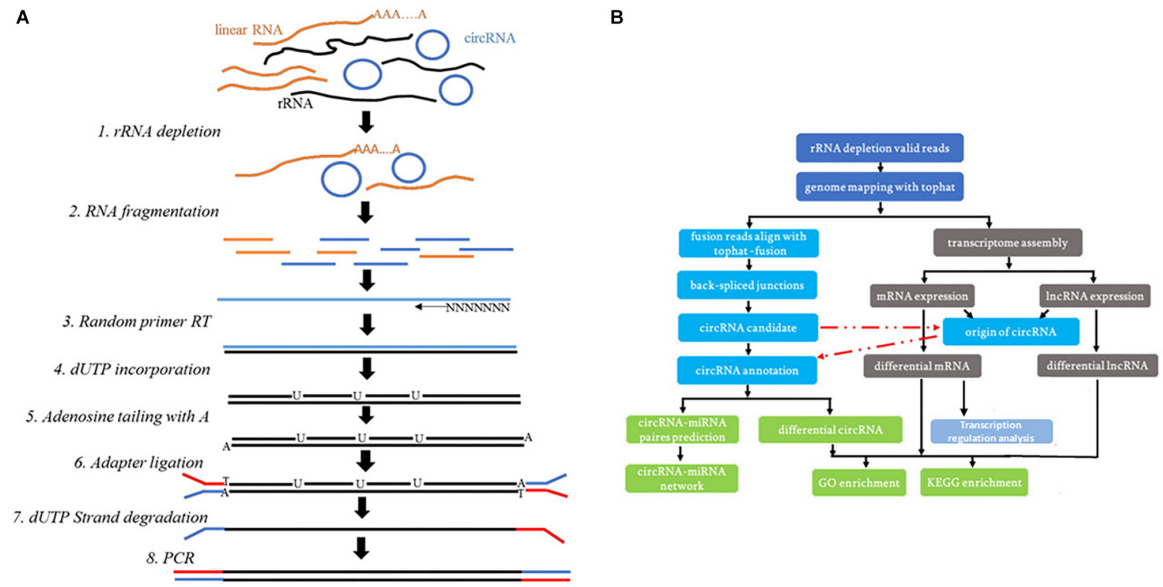


FIGURE 1 | (A) The experimental technical process. **(B)** The technical process of the whole-transcriptome analysis.

Iift1-A: ATCCTCACTTCCAAATCAGGTAT
Iift3-S: GAAGGATGGACACGCCTAAAG
Iift3-A: CCAAGGCATCTTCAACCAAC
R-actin-S: TGCTATGTTGCCCTAGACTTCG
R-actin-A: GTTGGCATAGAGGTCTTTACGG

Western Blot Analysis

Proteins expression of fresh cortical tissue samples were analyzed by western blotting. All tissues were lysed in radioimmunoprecipitation assay buffer, and total protein concentrations were determined with a BCA Protein Assay Kit (Thermo Scientific). Total protein (10–20 μg) was loaded for each sample into pre-cast 4–12% bis-tris gels and run with 3-(*N*-morpholino) propanesulfonic acid buffer (Invitrogen). Gels were transferred onto polyvinylidene fluoride or polyvinylidene difluoride membranes (Millipore). Antigen-specific primary antibodies were incubated overnight at 4°C and detected with species-specific horseradish-peroxidase-conjugated secondary antibodies. An ECL Western Blotting Detection kit (GE Healthcare) was used to obtain a chemiluminescence signal, which was detected using Amersham Hyperfilm ECL (GE Healthcare). Bands of interest were normalized to β-actin (1:3000, Abcam) for a loading control. The following antibodies were used in this study: Caspase 1+P10+P12 (1:3000, Abcam); HIF1α (1:1000, Abcam); TNF α (1:1000, Abcam); RIPK1 (1:1000, Abcam); RIPK 3 (1:1000, Abcam); pRIPK3 (1:1000, Signalway Antibody); MLKL (1:1000, Signalway Antibody); Bcl-2 (1:1000, Abcam); Bax (1:2000, Abcam); Cleaved Caspase 3 (1:1000, Abcam); ZO-1 (1:1000, Merck-Millipore); Occludin (1:1000, Abcam); Cyr61 (1:500, Abcam). The protein bands were quantitatively analyzed with AlphaEase FC software.

Statistical Analysis

Identical results for imaging/histopathology were obtained by the two readers (one, a major in medical imaging/pathology and the other, a major in neurology) (agreement); The final result was obtained after discussion between the two readers in disagreement (disagreement).

For brain tissue staining analysis/Morris water maze task/whole-transcriptome sequencing analysis, the cortical tissues of the three groups were numbered randomly. The experimenters and the analyzers did not know which groups the rats belonged to.

All non-bioinformatic data were analyzed using SPSS (Windows version 19.0, Abacus Concepts Inc., Chicago, IL, United States). The data were expressed as mean ± standard deviation (SD). All data are representative of at least three experiments performed in triplicate unless otherwise indicated. After assessing the normal distribution with the Shapiro–Wilk test, within-group data were analyzed with either one or two-way analysis of variance (ANOVA), Fisher's least significant difference (LSD) test was used to compare the groups if the homogeneity of variance was determined, whereas Tamhane's T2 test was used to compare the groups if the homogeneity of variance was not determined. Non-parametric Kruskal–Wallis *H* test was used for non-normal distributed variables followed by Nemenyi test was used for comparison between two groups. $P < 0.05$ was considered statistically significant.

RESULTS

Cognitive Impairment

The sham-operated rats quickly learned to find the hidden platform in the MWT (day 1 vs. day 3, $t = 4.12$, $^{\wedge\wedge}P < 0.01$;

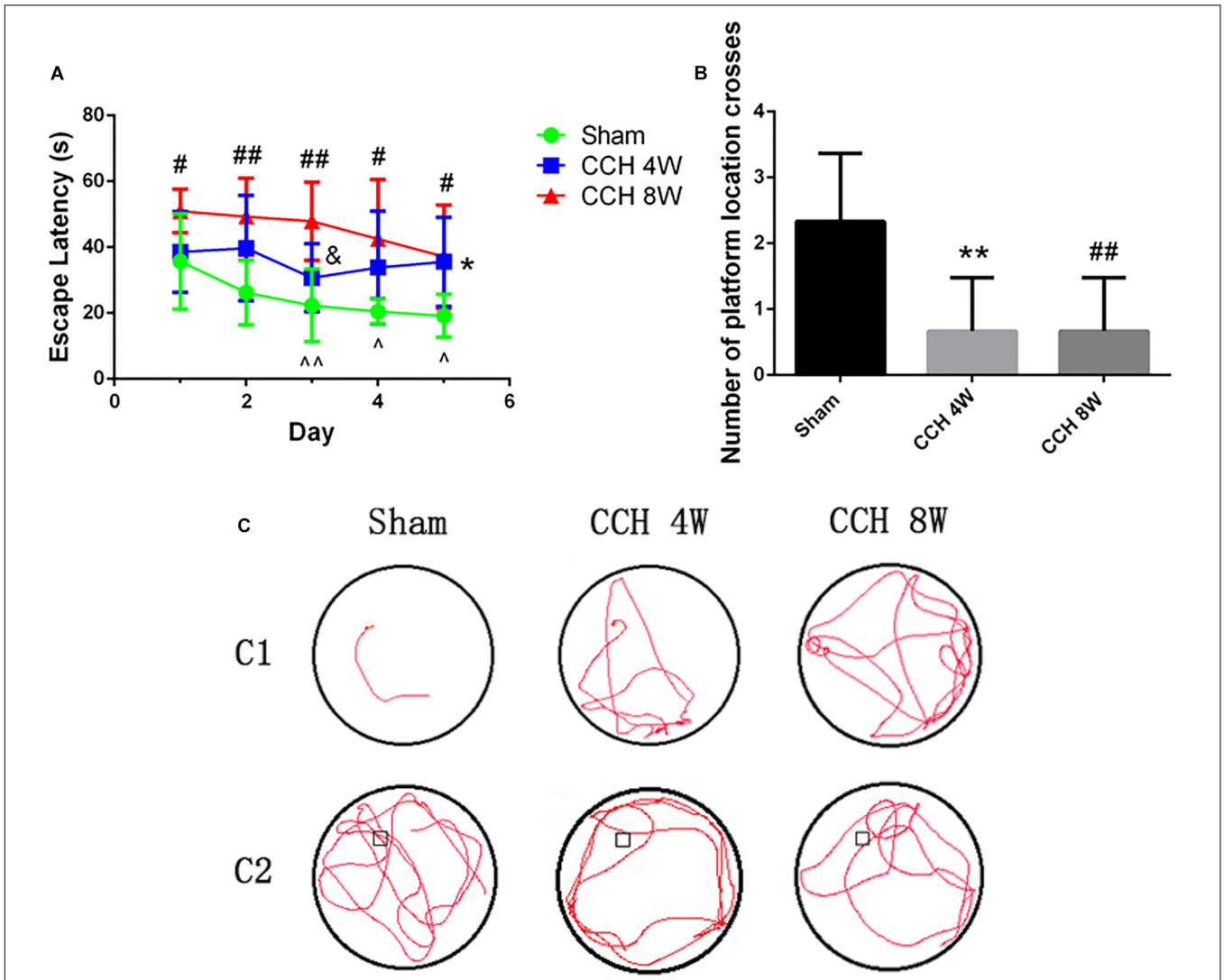


FIGURE 2 | CCH exacerbates cognitive deficits. **(A)** The EL significantly differed between the CCH 4W or CCH 8W group and the sham-operated group. **(B)** The number of platform location crossings during a single 60 s probe trial. **(C)** Representative trajectories of EL **(C1)**, number of platform location crosses **(C2)**. $n = 6$ in each groups. Values are expressed as the mean ± SD. $^{*}P < 0.05$, $^{**}P < 0.01$, CCH 4W compared with sham rats; $^{\#}P < 0.05$, $^{\#\#}P < 0.01$, CCH 8W compared with sham rats; $^{\&}P < 0.05$, CCH 8W compared with CCH 4W rats; $^{\wedge}P < 0.05$, $^{\wedge\wedge}P < 0.01$, intergroup comparison of sham group.

day 1 vs. day 4, $t = 2.78$, $^{\wedge}P < 0.05$; day 1 vs. day 5, $t = 3.48$, $^{\wedge}P < 0.05$) (**Figure 2**). The CCH 4W and CCH 8W groups took a longer time (escape latency [EL]) to find the hidden platform than did those in the sham ($^{*}P < 0.05$, CCH 4W vs. the sham; $^{\#}P < 0.05$, $^{\#\#}P < 0.01$, CCH 8W vs. the sham; $^{\&}P < 0.05$, CCH 4W vs. CCH 8W; **Figure 2A**). In the probe trial, the number of platform location crossings was lower in the CCH 4W and CCH 8W groups than in the sham group ($^{**}P < 0.01$, CCH 4W vs. the sham; $^{\#\#}P < 0.01$, CCH 8W vs. the sham), indicating poor memory in the CCH rats (**Figure 2B**). Representative trajectories are shown in **Figure 2C** (**Figure 2C1**, the trajectory of EL; **Figure 2C2**, number of platform location crosses).

Neuronal Morphology in the Cortex

HE and Nissl staining revealed significant morphological changes of neurons in the CCH groups (**Figure 3A**). We found more neuron damage happened in CCH groups, especially in CCH 8W (HE staining $F = 266.46$, $P < 0.001$; Sham vs. CCH 4W, $^{***}P < 0.001$; Sham vs. CCH 8W, $^{\#\#\#}P < 0.001$; CCH 4W vs. CCH 8W, $^{\&\&\&}P < 0.001$). The same as Nissl staining ($H = 7.26$, $P < 0.05$; Sham vs. CCH 8W, $^{\#}P < 0.05$). Quantitative analysis of morphological damage of neurons is shown in **Figures 3A1,A2**.

In sham-operated rats, almost no neurons were stained with FJB. However, FJB positive cells were easily identified in the CCH 4W and CCH 8W groups. Additionally, the CCH 8W group showed a greater number of denatured neurons than the CCH 4W group ($F = 87.05$, $P < 0.001$; Sham vs. CCH 4W,

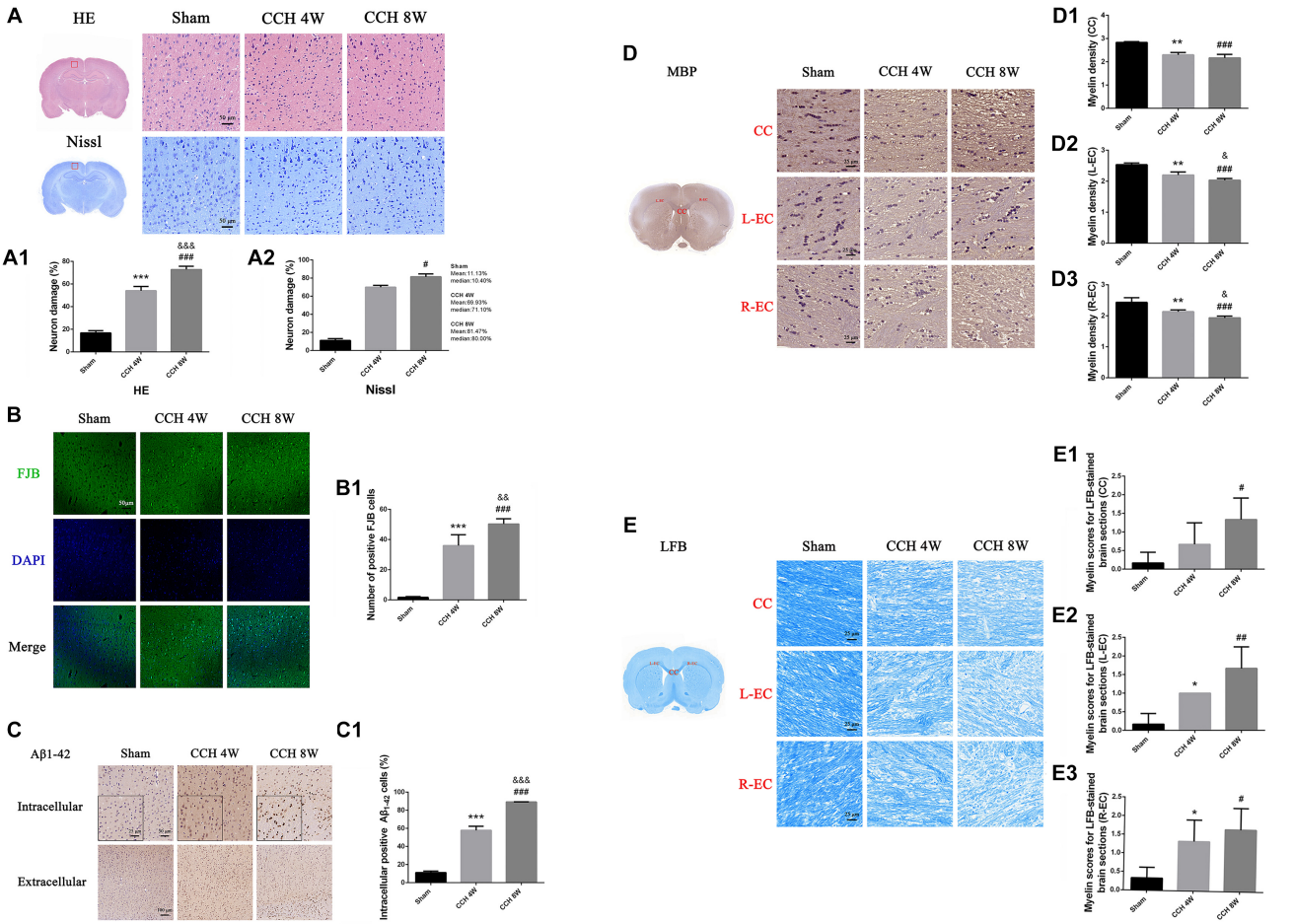


FIGURE 3 | (A) HE and Nissl staining showed representative images of neuronal damage. Scale bar = 50 μm; magnification, 200×. **(A1)** Quantitative analysis results of HE staining. **(A2)** Quantitative analysis results of Nissl staining. **(B)** FJB staining showed representative images of neuronal degeneration. Scale bar = 50 μm; magnification, 200×. **(B1)** Quantitative analysis results of FJB staining. **(C)** Representative immunohistochemistry images of intracellular positive $A\beta_{1\text{-}42}$ cells (magnification: 200×) and extracellular Aβ plaque burdens (magnification: 100×) in the cortex in the sham-operated, CCH 4W, and CCH 8W groups. **(C1)** Quantification of intracellular positive $A\beta_{1\text{-}42}$ cells. **(D)** Diaminobenzidine staining of MBP in the CC, L-EC (left-EC), and R-EC (right-EC) areas. Scale bar = 25 μm. Magnification, 400×. **(D1–D3)** Myelin density of the CC, L-EC, R-EC. **(E)** Representative images of LFB-stained coronal sections (scale bar = 25 μm; magnification, 400×) and histological scoring. **(E1–E3)** Myelin scores of the CC, L-EC, R-EC. $n = 3$ in each groups. Values are expressed as the mean ± SD. $^{*}P < 0.05$, $^{**}P < 0.01$, $^{***}P < 0.001$, CCH 4W compared with sham rats; $^{\#}P < 0.05$, $^{\#\#}P < 0.01$, $^{\#\#\#}P < 0.001$, CCH 8W compared with sham rats; $^{\&}P < 0.05$, $^{\&\&}P < 0.01$, $^{\&\&\&}P < 0.001$, CCH 8W compared with CCH 4W rats.

$^{***}P < 0.001$; Sham vs. CCH 8W, $^{\#\#\#}P < 0.001$; CCH 4W vs. CCH 8W, $\&\&P < 0.01$) (**Figures 3B,B1**).

Intracellular Aβ-Positive Cells and Extracellular Aβ Plaques

Figure 3C shows representative images of intracellular Aβ-positive cells (200 magnification) and the extracellular Aβ plaque burden (100 magnification) in the sham, CCH 4W and CCH 8W groups. The number of intracellular Aβ1-42 positive cells was significantly higher in the CCH 4W and CCH 8W groups than in the sham ($F = 608.86$, $P < 0.001$; Sham vs. CCH 4w, $^{***}P < 0.001$; Sham vs. CCH 8W, $^{\#\#\#}P < 0.001$; CCH 4W vs. CCH 8W, $\&\&\&P < 0.001$) (**Figure 3C1**). No significant differences in the extracellular Aβ1-42 plaque deposition were found among the three groups.

Effects of CCH on Brain Myelin Status

After CCH, the loss of MBP was prominent in the CC ($F = 32.94$, $P < 0.01$; Sham vs. CCH 4W, $^{**}P < 0.01$; Sham vs. CCH 8W, $^{\#\#\#}P < 0.001$) and both ECs (L-EC: $F = 35.00$, $P < 0.001$; Sham vs. CCH 4W, $^{**}P < 0.01$; Sham vs. CCH 8W, $^{\#\#\#}P < 0.001$; CCH 4W vs. CCH 8W, $\&P < 0.05$; R-EC: $F = 19.00$, $P < 0.01$; Sham vs. CCH 4W, $^{**}P < 0.01$; Sham vs. CCH 8W, $^{\#\#\#}P < 0.001$; CCH 4W vs. CCH 8W, $\&P < 0.05$.) (**Figures 3D,D1–D3**).

CCH promoted changes in brain myelin status, including the increase in the demyelination score and the significant decline in LFB stain intensity (CC: Sham vs. CCH 8W, $\#P < 0.05$; L-EC: $F = 12.20$, $P < 0.01$; Sham vs. CCH 4W, $^{*}P < 0.05$; Sham vs. CCH

8W, ##$P < 0.01$; R-EC: $F = 5.78$, $P < 0.05$; Sham vs. CCH 4W, *$P < 0.05$; Sham vs. CCH 8W, #$P < 0.05$)(**Figures 3E,E1–E3**).

White Matter Integrity in DTI

The areas with white matter tracts (CC and both ECs), were selected for T2WI (**Figure 4A**). Compared with the state of baseline, FA was significantly reduced in the CC ($F = 15.01$, $P < 0.001$; CCH 4W vs. baseline, *$P < 0.05$; CCH 8W vs. baseline, ###$P < 0.001$; CCH 4W vs. CCH 8W, &&$P < 0.01$) and L-EC ($F = 6.895$, $P < 0.01$; CCH 4W vs. baseline, *$P < 0.05$; CCH 8W vs. baseline, ##$P < 0.01$) in rats with BCCAO. Representative tractography (**Figure 4A**) and quantitative analyses (**Figures 4A1–A3**) revealed more abundant white matter tracts in the sham rats.

Altered Protein Expression Associated With Neuron Death and BBB Damage After BCCAO

HIF-1α protein expression was significantly higher in the CCH groups, especially in CCH 8W group than in the sham group ($F = 17.53$, $P < 0.01$; Sham vs. CCH 4W, *$P < 0.05$; Sham vs. CCH 8W, ##$P < 0.01$; CCH 4W vs. CCH 8W, &$P < 0.05$) (**Figure 5B**), indicating the presence of CCH in the BCCAO rats.

Three types of cell death models, including pyroptosis, necroptosis, and apoptosis, were evaluated. Pyroptosis, identified by active caspase 1 P10 and P12 subunits, was not activated in CCH, even though the expression of pro-caspase 1 (Sham vs. CCH 4W, *$P < 0.05$; Sham vs. CCH 8W, #$P < 0.05$) was significantly higher in the CCH groups relative to the sham group (**Figure 5A**). However, necroptosis, identified by active TNFα ($F = 15.03$, $P < 0.01$; CCH 8W vs. Sham, ##$P < 0.01$; CCH 8W vs. CCH 4W, &$P < 0.05$), RIPK1 (CCH 4W vs. Sham, *$P < 0.05$; CCH 8W vs. Sham, #$P < 0.05$), RIPK3 ($F = 11.64$, $P < 0.05$; CCH 4W vs. Sham, **$P < 0.01$; CCH 8W vs. Sham, ##$P < 0.01$), pRIPK3 ($F = 16.65$, $P < 0.01$; CCH 4W vs. Sham, *$P < 0.05$; CCH 8W vs. Sham, ##$P < 0.01$; CCH 8W vs. CCH 4W, &$P < 0.05$), and MLKL ($F = 16.91$, $P < 0.01$; CCH 4W vs. Sham, *$P < 0.05$; CCH 8W vs. Sham, ##$P < 0.01$; CCH 8W vs. CCH 4W, &$P < 0.05$) (**Figure 5B**), and apoptosis, identified by apoptosis markers including Bax ($F = 10.56$, $P < 0.05$; CCH 4W vs. Sham, *$P < 0.05$; CCH 8W vs. Sham, ##$P < 0.01$), Bax/Bcl-2 ratio ($F = 5.53$, $P < 0.05$; CCH 4W vs. Sham, *$P < 0.05$; CCH 8W vs. Sham, #$P < 0.05$) and cleaved caspase 3 ($F = 10.63$, $P < 0.05$; CCH 4W vs. Sham, *$P < 0.05$; CCH 8W vs. Sham, ##$P < 0.01$) (**Figure 5B**), increased 4th and 8th weeks after BCCAO. In addition, the expression of occludin ($F = 18.75$, $P < 0.01$; CCH 4W vs. Sham, *$P < 0.05$; CCH 8W vs. Sham, ##$P < 0.01$; CCH 8W vs. CCH 4W, &$P < 0.05$) and ZO-1 ($F = 28.39$, $P < 0.01$; CCH 4W vs. Sham, **$P < 0.01$; CCH 8W vs. Sham, ##$P < 0.01$; CCH 8W vs. CCH 4W, &$P < 0.05$) decreased in the CCH 4W and CCH 8W groups (**Figure 5C**). Quantification of the band intensities is presented in the adjacent graphs (**Figures 5A1,B1–B9,C1,C2**).

Differentially Expressed lncRNA, mRNA, and circRNA Profiles

A total of 11806 mRNAs were detected, and 300 mRNAs were differentially expressed in three CCH 4W tissues compared with four controls (FC ≥ 1.5, $P < 0.05$, and FDR < 0.05). Among the 300 mRNAs, 107 were upregulated, and 193 were downregulated

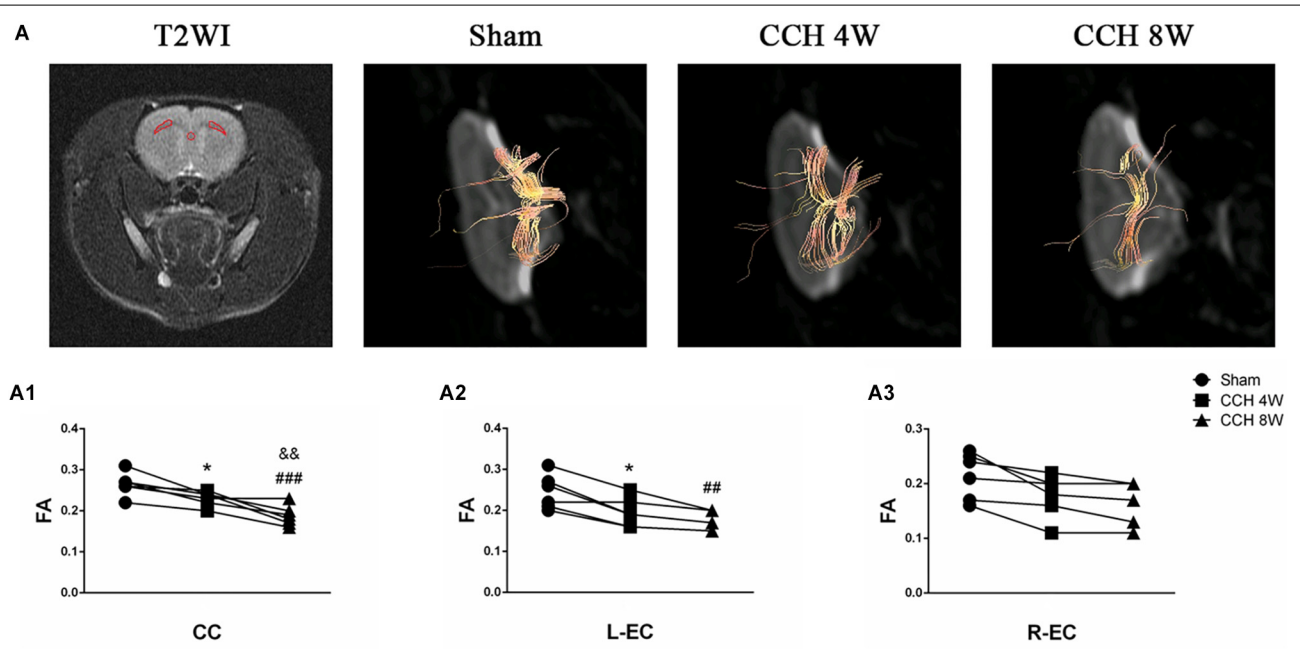


FIGURE 4 | Evaluation of the white matter fibers by DTI. **(A)** Selected regions of interest in the CC and both ECs in T2WI. Representative tractography in three groups. **(A1–A3)** Quantitative analysis of FA value of DTI parameters. $n = 6$ in each groups. *$P < 0.05$, CCH 4W compared with sham rats; ##$P < 0.01$, ###$P < 0.001$, CCH 8W compared with sham rats; &&$P < 0.01$, CCH 8W compared with CCH 4W rats.

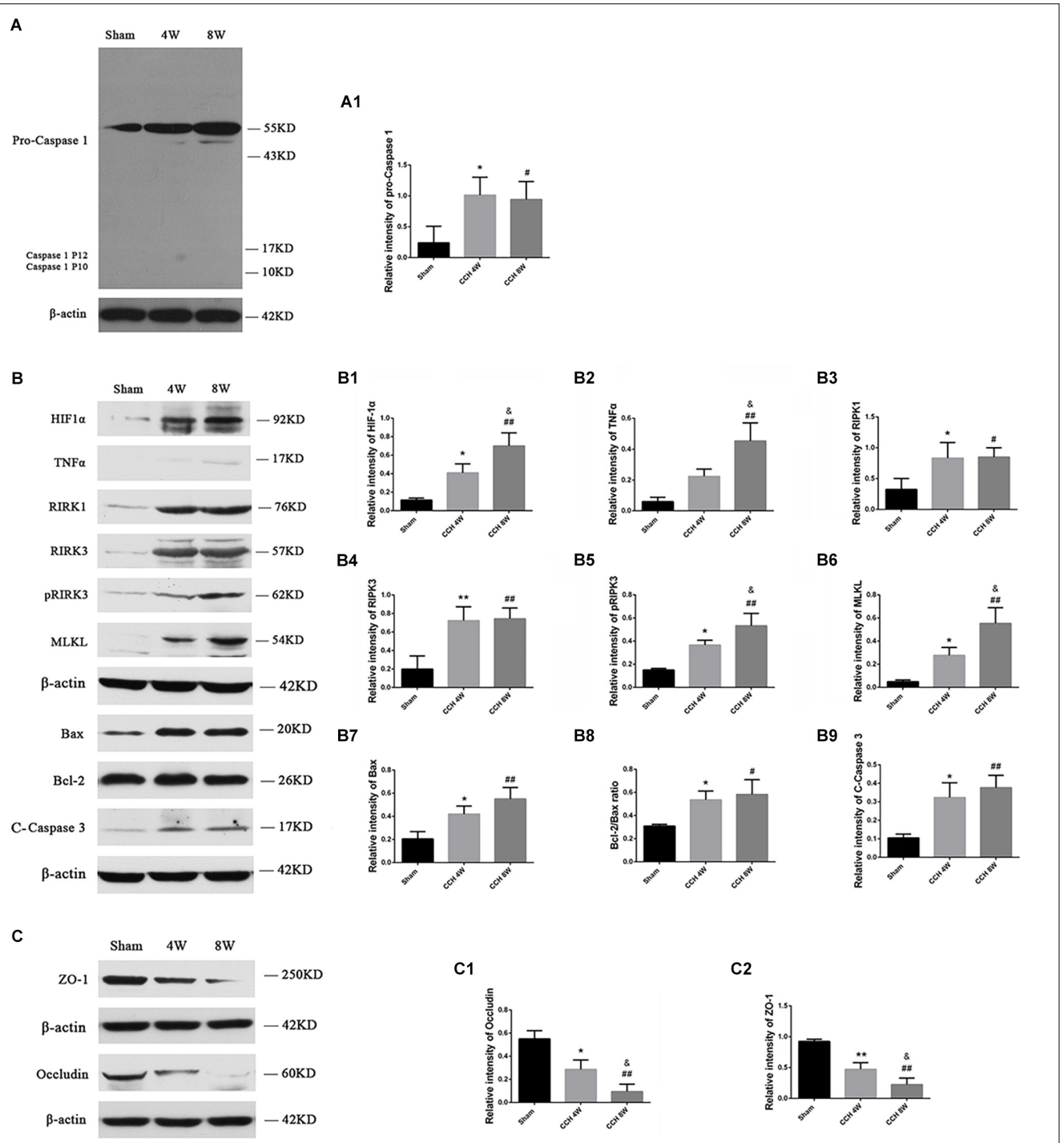


FIGURE 5 | (A) Western blot analysis of pro-caspase 1, caspase 1 P12, and caspase 1 P10 protein in the cortex. **(B)** Western blot analysis of HIF-1α, TNFα, RIPK1, RIPK3, pRIPK3, MLKL, Bax, Bcl-2 and cleaved caspase 3 protein, and ratio of Bax/Bcl-2 in the cortex. **(C)** The expression of ZO-1 and occludin was lower in the CCH 4W and CCH 8W rats, especially in CCH 8W groups. Quantification of the band intensities is presented in the adjacent graphs **(A1,B1–B9,C1,C2)**. $n = 3$ in CCH 4W and CCH 8W rats, $n = 2$ in sham rats. Values are expressed as the mean ± SD. $^{*}P < 0.05$, $^{**}P < 0.01$, CCH 4W compared with sham rats; $^{\#}P < 0.05$, $^{\#\#}P < 0.01$, CCH 8W compared with sham rats; $^{\&}P < 0.05$, CCH 8W compared with CCH 4W rats.

(**Figure 6A1**). The microarray analysis identified a total of 4109 circRNAs and 14472 lncRNAs, which were dysregulated in CCH. Filtering analysis identified 205 differentially expressed circRNAs between CCH 4W and control tissues; among these circRNAs, 114 were upregulated, and 91 were downregulated (**Figure 6A3**). In addition, 491 lncRNAs were shown to be differentially

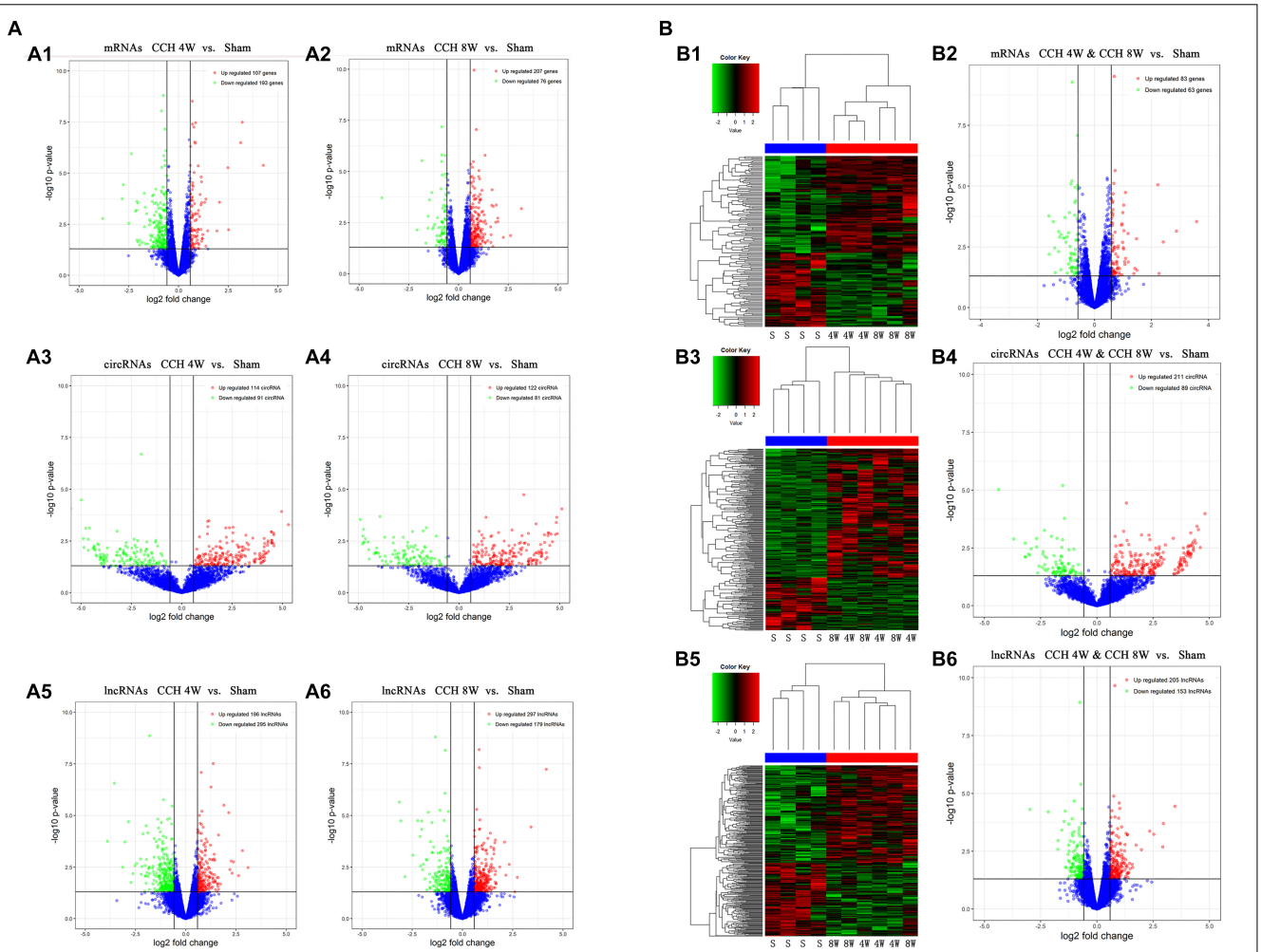


FIGURE 6 | Assessment of circRNA, lncRNA, and mRNA expression profiles in the screening phase. **(A) (A1**,**A2)** Expression profiles (volcano plots) of mRNAs in the CCH 4W and CCH 8W rats, compared with the sham rats (**A1**, CCH 4W; **A2**, CCH 8W). **(A3**,**A4)** Expression profiles (volcano plots) of circRNAs in the CCH 4W and CCH 8W rats, compared with the sham rats (**A3**, CCH 4W; **A4**, CCH 8W). **(A5**,**A6)** Expression profiles (volcano plots) of lncRNAs in the CCH 4W and CCH 8W rats, compared with the sham rats (**A5**, CCH 4W; **A6**, CCH 8W). **(B) (B1**,**B2)** Expression profiles of mRNAs in CCH 4W&CCH 8W rats compared with the sham rats (**B1** for clustering analysis and **B2** for volcano plots). **(B3**,**B4)** Expression profiles of circRNAs in CCH 4W&CCH 8W rats compared with the sham rats (**B3** for clustering analysis and **B4** for volcano plots). **(B5**,**B6)** Expression profiles of lncRNAs in CCH 4W&CCH 8W rats compared with the sham rats (**B5** for clustering analysis and **B6** for volcano plots). S, sham; 4W, CCH 4W; 8W, CCH 8W; genes, mRNAs.

expressed: 196 lncRNAs were upregulated, and 295 lncRNAs were downregulated (FC $\geq$ 1.5, P < 0.05, and FDR < 0.05; **Figure 6A5**). Coding gene profiles revealed that 3 mRNAs had FC $\geq$ 10, Amy1a and LOC100134871 were the most upregulated (FC = 19) and downregulated mRNA (FC = −452), respectively. In total, 19 circRNAs, including 1 upregulated circRNA and 18 downregulated circRNAs, had FC $\geq$ 10. CircKdm4c (FC = 31) and CircMyo19 (FC = −59) were the most upregulated and downregulated circRNAs, respectively. In addition, five lncRNAs displayed FC $\geq$ 10. LncOlr1718 (FC = 660) was the most upregulated lncRNA, and lncStyxl1 (FC = −122) was the most downregulated lncRNA.

In total, 283 differentially expressed mRNAs were identified in three CCH 8W tissues compared with four controls (FC $\geq$ 1.5, P < 0.05, and FDR < 0.05). Among the 283 mRNAs, 207 were upregulated, and 76 were downregulated (**Figure 6A2**). In addition, 203 differentially expressed circRNAs were identified between CCH 8W and control tissues; among the 203 circRNAs, 122 were upregulated, and 81 were downregulated (**Figure 6A4**). Moreover, 476 differentially expressed lncRNAs were found; among them, 297 and 179 lncRNAs were upregulated and downregulated, respectively (FC $\geq$ 1.5, P < 0.05, and FDR < 0.05; **Figure 6A6**). The coding gene profile revealed that only 1 mRNA, RT1-CE11, had FC $\geq$ 10, and RT1-CE11 was the most downregulated mRNA (FC = −14). Furthermore, 11 circRNAs, including 5 upregulated circRNA and 6 downregulated circRNAs, displayed FC $\geq$ 10. circRbl2 (FC = 29) and CircMyo19 (FC = −59) were the most upregulated and downregulated circRNAs, respectively. Two lncRNAs, including 1 upregulated and 1 downregulated lncRNAs, displayed FC $\geq$ 10. LncOlr1735

(FC = 17) was the most upregulated lncRNA, and lncCkmt2 (FC = −97) was the most downregulated lncRNA.

In total, 146 differentially expressed mRNAs were identified in six CCH samples compared with four controls (FC ≥ 1.5, $P < 0.05$, and FDR < 0.05). Among the 146 mRNAs, 83 and 63 mRNAs were upregulated and downregulated, respectively (**Figures 6B1,B2**). Filtering analysis identified 300 differentially expressed circRNAs in the CCH samples compared with controls; among them, 211 were upregulated, and 89 were downregulated (**Figures 6B3,B4**). In addition, 358 differentially expressed lncRNAs were identified; among these lncRNAs, 205 and 153 lncRNAs were upregulated and downregulated, respectively (FC ≥ 1.5, $P < 0.05$, and FDR < 0.05; **Figures 6B5,B6**). The coding gene profile revealed that 1 mRNA, identified as Amy1a, had FC ≥ 10, and Amy1a was the most upregulated mRNA (FC = 11). Moreover, 49 circRNAs, including 46 upregulated lncRNA and 3 downregulated circRNAs, displayed FC ≥ 10. CircNpepps (FC = 27) and CircMyo19 (FC = −59) were the most upregulated and downregulated circRNAs, respectively. Three upregulated lncRNAs displayed FC ≥ 10, and LncOlr1718 (FC = 332) was the most upregulated lncRNA.

GO, KEGG, and Reactome Enrichment Analysis in the CCH Groups

GO Enrichment Analysis

The changes in mRNA levels were associated with BP in response to peptides in six CCH samples (CCH 4W and CCH 8W) compared with four controls: CC was associated with extracellular matrix and the apical part of the cell, and MF was associated with carboxylic acid binding (**Figure 7A1**). The apparent changes in circRNA associated with BP were single-organism behavior. CC was associated with postsynaptic elements, and MF was associated with protein serine/threonine kinase activity (**Figure 7A2**). The apparent changes in lncRNA were associated with the positive regulation of neurogenesis. CC was associated with postsynaptic elements, and MF was associated with transcription factor activity, transcription factor binding, and protein binding (**Figure 7A3**).

KEGG Enrichment Analysis

Differentially expressed mRNAs

Our data showed that the top three pathways were HTLV-1 infection, Epstein-Barr virus infection, and neuroactive ligand-receptor interaction in the six CCH samples compared with four controls (**Figure 7B1**).

Differentially expressed circRNAs

The MAPK signaling pathway, glucagon signaling pathway, and dopaminergic synapse were the top three pathways (**Figure 7B3**).

Differentially expressed lncRNAs

The cGMP-PKG signaling pathway, Rap1 signaling pathway, and the insulin secretion pathway were the top three pathways (**Figure 7B5**).

Reactome Enrichment Analysis

Differentially expressed mRNAs

The top 5 pathways identified were extracellular matrix organization, stimuli-sensing channels, transport of vitamins, nucleosides, and related molecules, including cytosolic sensors of pathogen-associated DNA, in the six CCH samples compared

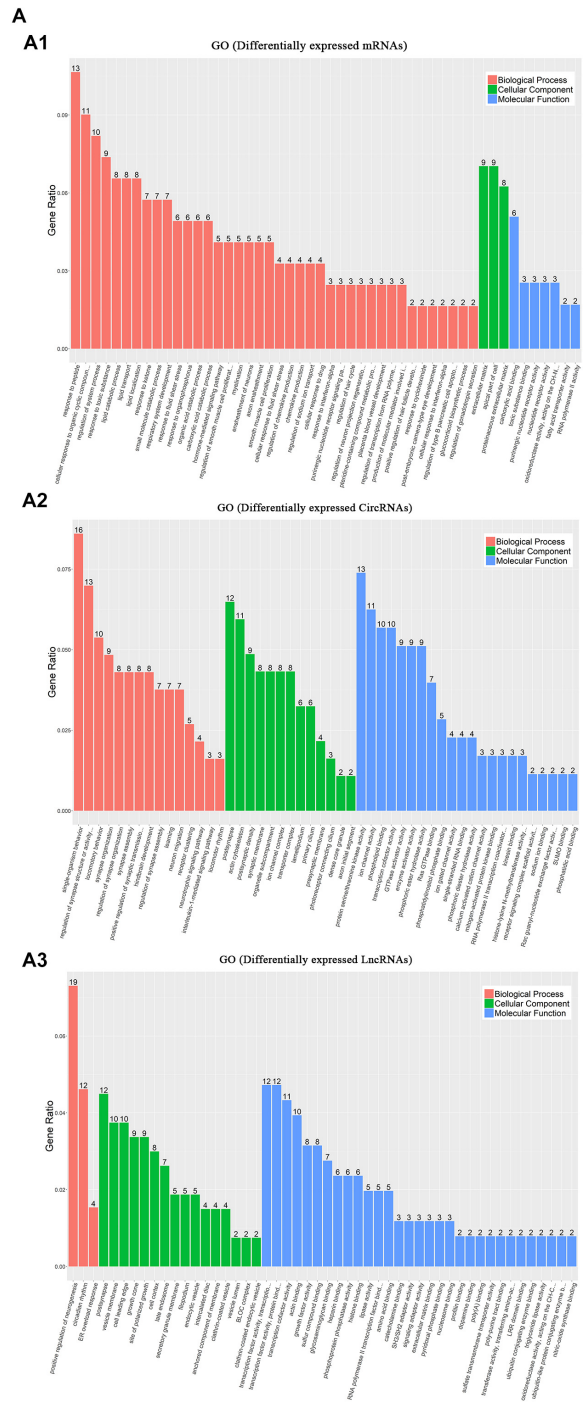


FIGURE 7 | Continued

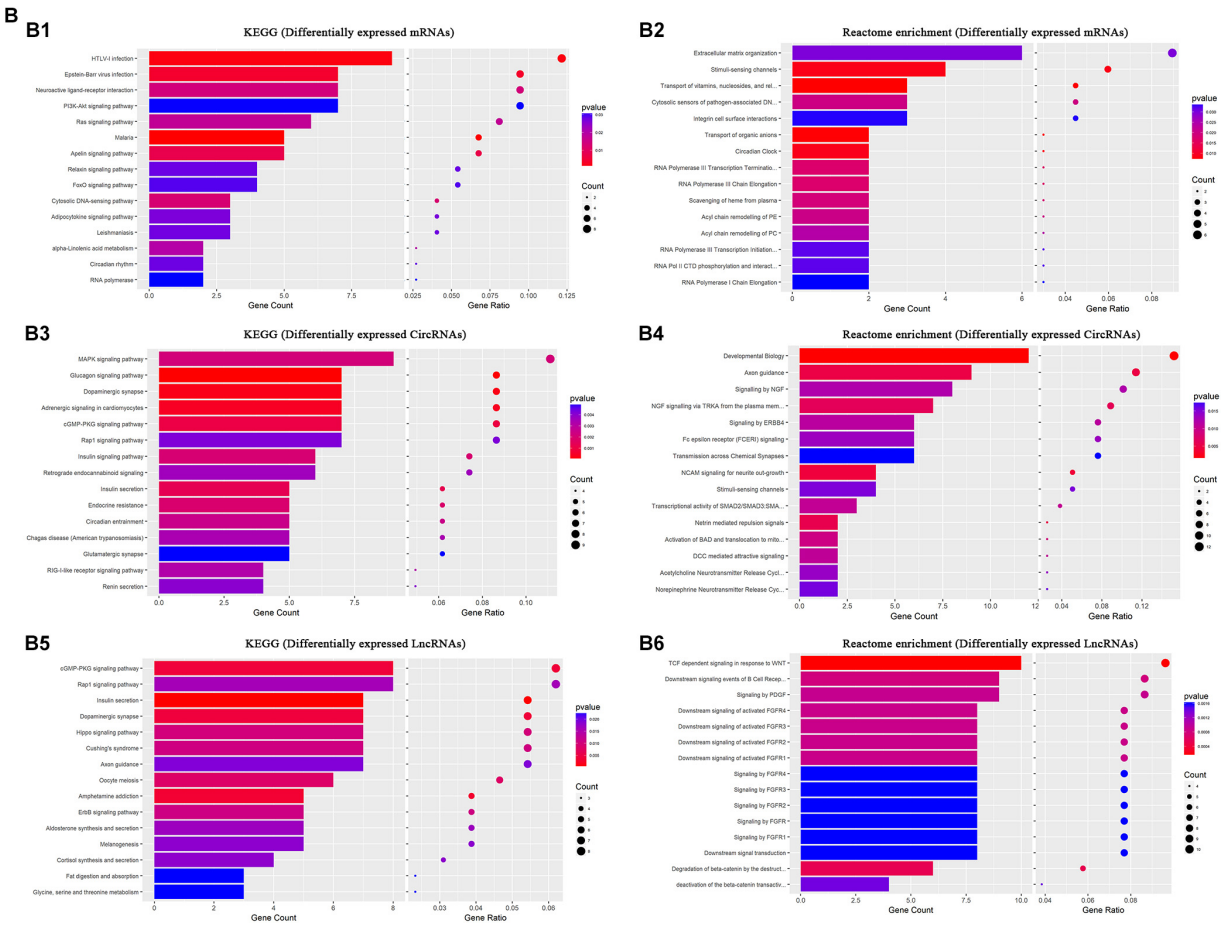


FIGURE 7 | GO, KEGG, and Reactome enrichment analysis. In six CCH samples (CCH 4W and CCH 8W) compared with four sham controls: **(A)** GO annotation of upregulated and downregulated mRNAs **(A1)**, circRNAs **(A2)**, and lncRNAs **(A3)** of BPs, CCs, MFs. **(B)** KEGG analysis of upregulated and downregulated mRNAs **(B1)**, circRNAs **(B3)**, and lncRNAs **(B5)** with top 15 enrichment scores. **(B)** Reactome enrichment analysis of upregulated and downregulated mRNAs **(B2)**, circRNAs **(B4)**, and lncRNAs **(B6)** with top 15 enrichment scores.

with four controls, and integrin cell surface interactions also played a crucial role in the pathogenesis of CCH (**Figure 7B2**).

Differentially expressed circRNAs

Developmental biology, axon guidance, signaling by NGF, NGF signaling via TRKA from the plasma membrane, and signaling by ERBB4 were the top 5 pathways in circRNAs (**Figure 7B4**).

Differentially expressed lncRNAs

TCF dependent signaling in response to WNT, downstream signaling events of B cell receptor, signaling by PDGF, downstream signaling of activated FGFR3 and FGFR4 were the top 5 pathways in lncRNAs (**Figure 7B6**).

Construction of the circRNA–miRNA and mRNA–circRNA–miRNA Co-expression Network in the CCH Groups

A circRNA–miRNA co-expression network was constructed based on the microarray analysis in the six CCH samples compared with four controls. A network map containing 283 circRNAs, 749 miRNAs, and 7223 relationships was constructed (**Figure 8A**). A mRNA–circRNA–miRNA co-expression network map containing 32 mRNAs, 55 circRNAs, and 42 miRNAs was constructed, and 34 relationships between circRNA and mRNA and 50 relationships between circRNA and miRNA were observed (**Figure 8B**).

Co-expression of lncRNAs–mRNAs and Function Prediction

The co-expression network suggests that one lncRNA may correlate with multiple mRNAs in CCH samples compared with the sham. We chose some significantly expressed coding genes and lncRNAs in the CCH groups to build a network, according to the degree of correlation (**Figure 8C**).

As we known, mRNAs are implicated in a number of BPs. For example, the network revealed that downregulated lncRNAs, identified as NONRATT016029.2 and NONRATT016027.2, were positively correlated with the Ckmt2. The network may suggest

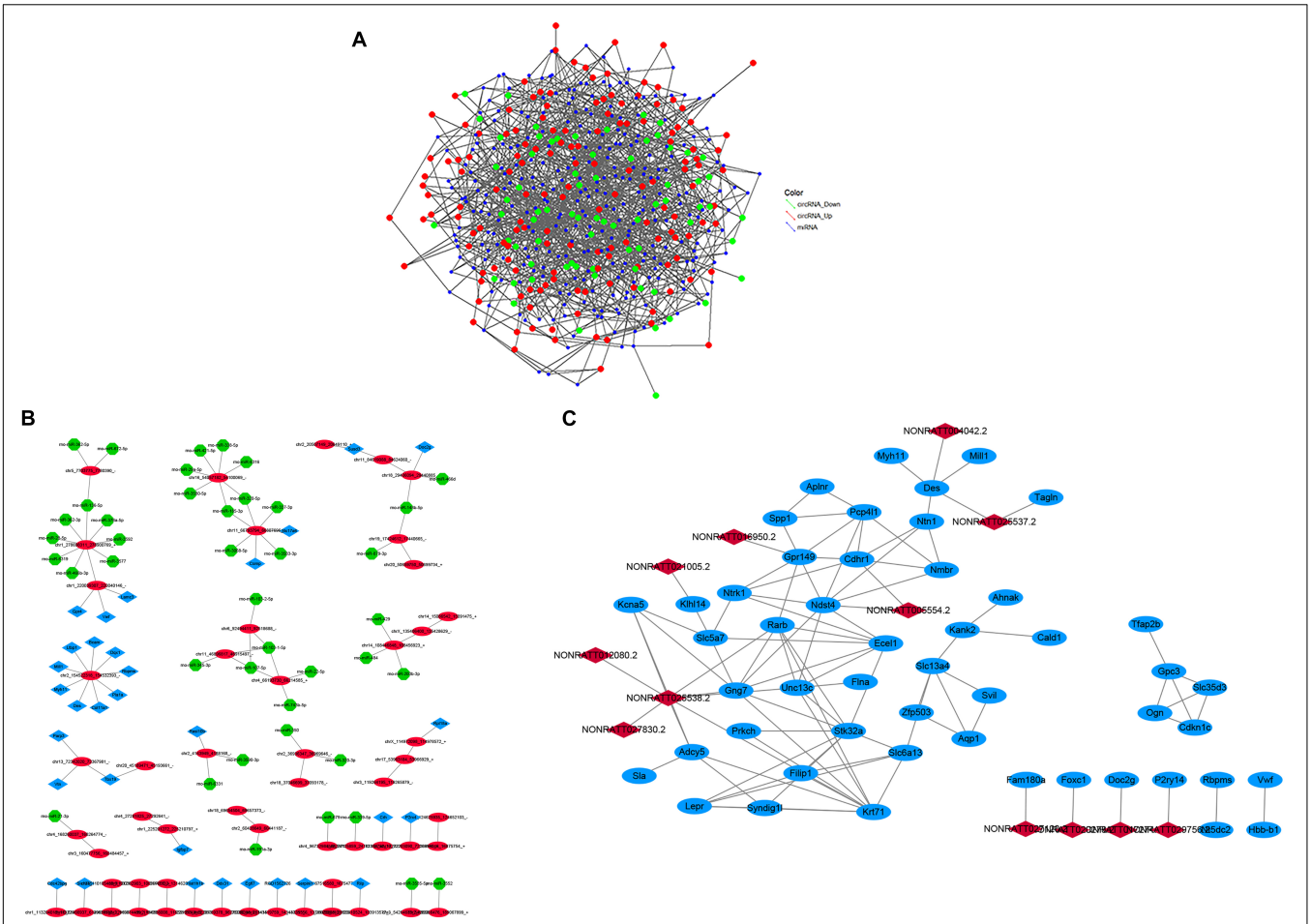


FIGURE 8 | (A) The circRNA-miRNA co-expression network. circRNA and miRNA were indicated with three colored deformed diamonds. The red color represents the high expression, green color represents the low expression of circRNA, blue color represents miRNA. The size of diamonds represents FC of circRNAs, and a larger size represents a higher FC. **(B)** The mRNA–circRNA–miRNA co-expression network. Blue square nodes represent mRNAs, red circle nodes represent circRNAs, green shape nodes represent miRNAs. Solid lines represent relationships. **(C)** The lncRNA-mRNA co-expression network. Blue circle nodes represent mRNAs, red square nodes represent lncRNAs. Solid lines represent relationships.

TABLE 1 | Biological functions associated with chronic cerebral hypoperfusion.

Network	Top functions	*p*-value	Focus mRNAs
Diseases and disorders			
1	Cancer, organismal injury, and abnormalities	<0.001	129
2	Infectious diseases	<0.001	27
3	Hematological disease, immunological disease	<0.01	27
4	Metabolic disease	<0.01	17
5	Neurological disease	<0.001	15
Molecular and cellular functions			
1	Cell death and survival	<0.001	38
2	Cellular movement	<0.001	28
3	Gene expression	<0.01	24
4	Cellular growth and proliferation	<0.001	16
5	Cell-to-cell signaling and interaction	<0.01	16

The most significant disease and disordered biological functions associated with CCH-correlated mRNAs were related to cancer (upper panel). Cell death and survival were the top significant molecular and cellular functional categories (bottom panel).

that the regulation between lncRNAs and mRNAs, which is implicated in CCH.

IPA in the CCH Groups

Biological Functions Associated With CCH

The most significant disorders associated with CCH-correlated mRNAs were related to cancer, organismal injury and abnormalities, infectious disease, hematological disease, immunological disease, metabolic disease, and neurological disease (**Table 1**, upper panel), and 15 focus genes were related to neurological disease. Cell death and survival were among the most significant molecular and cellular function categories (**Table 1**, bottom panel).

Canonical Pathways Analysis

To gain further insights into the pathogenesis of CCH, we analyzed CCH-correlated genes to elucidate dominant canonical pathways. The top 10 canonical signaling pathways were categorized (**Table 2**).

Network Analysis

Figure 9 shows the molecular networks of differentially expressed genes analyzed by the IPA. These genes were involved in the ERK1/2, AKT, PI3K, NF-κBIA, ras, and SGK1 signaling pathways in the CCH 4W group (**Figure 9A**) and the NF-κB (complex), NF-κBIA, interferon-α, and interferon-β signaling pathways in the CCH 8W group (**Figure 9B**).

Function of Cysteine Rich Angiogenic Inducer 61 (Cyr61)

Nine mRNAs were involved in neurological disease and cell death and survival (**Figure 10A**). Four mRNAs had the same trend in the CCH 4W and CCH 8W groups: Cyr61, ALB, NR4A2, and PDE4C. After comparing the 4 mRNAs in rats with those in humans by Blast®[4], Cyr61 may be associated with the neuronal death caused by CCH in the cerebral cortex (FDR > 2; Identified score, 87%; **Figure 10B**). The expression of mRNAs (Cyr61, NR4A2, PDE4C) were verified by qPCR, only the Cyr61 mRNA expression trend was consistent with the sequencing results (H = 22.37, $P < 0.001$; CCH 4W vs. Sham, $^{*}P < 0.05$; CCH 8W vs. Sham, $^{\#\#}P < 0.01$; CCH 8W vs. CCH 4W, $\&P < 0.05$) (**Figures 10C–E**). Western blotting analysis demonstrated that

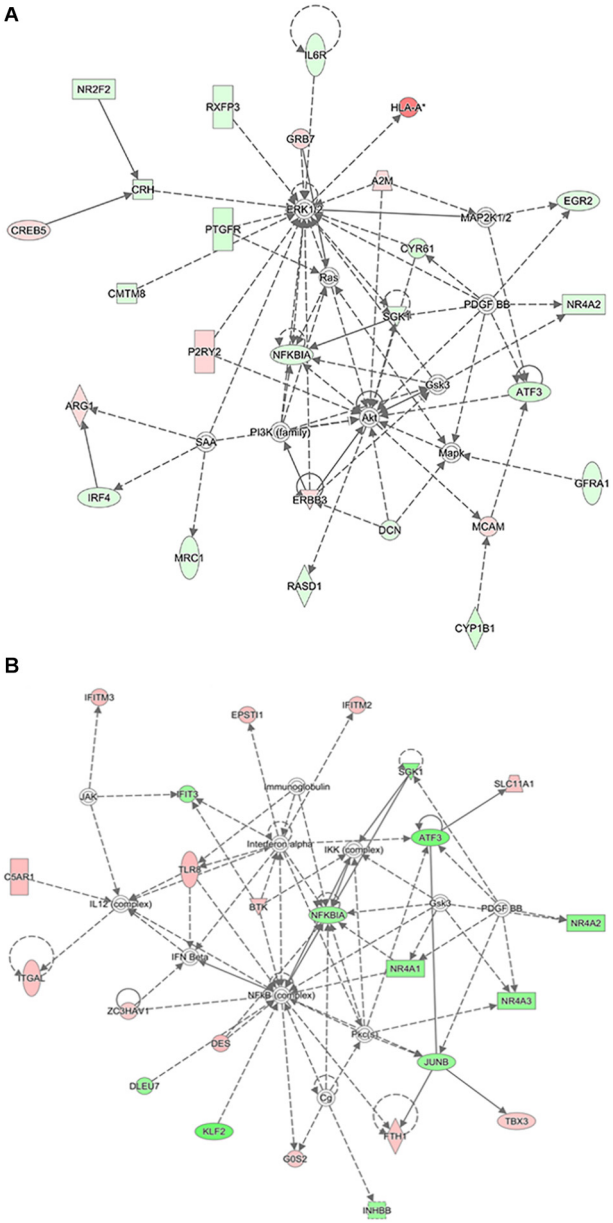


FIGURE 9 | Ingenuity pathway analysis. IPA showed top interaction networks for differentially regulated mRNAs in CCH 4W **(A)** and CCH 8W **(B)** rats. Those highlighted with red color are upregulated mRNAs and those with green are downregulated mRNAs.

TABLE 2 | Top 10 significantly changed canonical signaling pathways in CCH rats compared with sham controls.

Ingenuity canonical pathways		−log (*p*-value)
1	Glycine betaine degradation	2.71
2	Role of macrophages, fibroblasts and endothelial cells in rheumatoid arthritis	2.35
3	Mitochondrial L-carnitine shuttle pathway	2.24
4	Acute phase response signaling	2.24
5	p38 MAPK signaling	2.06
6	Atherosclerosis signaling	2.01
7	Iron homeostasis signaling pathway	1.97
8	Adipogenesis pathway	1.92
9	Caveolar-mediated endocytosis signaling	1.92
10	EIF2 signaling	1.84

The top 10 canonical signaling pathways were categorized in order based on the level of statistical significance.

[4]https://blast.ncbi.nlm.nih.gov/Blast.cgi

the expression of Cyr61 showed an opposite trend with increased time of CCH ($F = 53.96$, $P < 0.001$; CCH 4W vs. Sham, $^{**}P < 0.01$; CCH 8W vs. Sham, $^{###}P < 0.001$; CCH 8W vs. CCH 4W, $\&P < 0.05$) (**Figures 10F,F1**). Cyr61 was associated with 15 mRNAs, 10 circRNAs, and 10 lncRNAs (**Figures 10G,H**). Four mRNAs (Apold1, Atf3, Iift1, Iift3) of 15 mRNAs were verified by qPCR, and there were synergy effect between Apold1 ($H = 9.59$, $P < 0.01$; CCH 8W vs. Sham, $\#\#P < 0.01$), Atf3 ($H = 6.38$, $P < 0.05$; CCH 8W vs. Sham, $\#P < 0.05$), Iift1 ($H = 11.70$, $P < 0.01$; CCH 4W vs. Sham, $^{*}P < 0.05$; CCH 8W vs. Sham, $\#\#P < 0.01$) and Cyr61 in CCH (**Figures 10I1–I4**).

DISCUSSION

Vascular dementia is one of the most common causes of dementia after Alzheimer's disease (AD), which occurs in about 15∼20% of all the dementia. VD may occur post-stroke, due to idiopathic or genetic small vessel disease or because of chronic hypoperfusion due to carotid artery stenosis/occlusion. However, no licensed diagnosis and treatments are available (Chmayssani et al., 2007; Iadecola, 2013; O'Brien and Thomas, 2015; Choi et al., 2016). This is mainly because clinically VD has diversity and complexity in cerebrovascular pathologic conditions, risk factors, progression, and severity of disease (Du et al., 2017). CCH is a common consequence of diversiform cerebral vascular disorders and hemodynamic changes. Increasing evidence has suggested that CCH state/chronic cerebral ischemia is a premonitory symptom, which is associated with occurrence of VD (Du et al., 2017; Duncombe et al., 2017). A clinical population-based study indicated that a lower baseline cerebral hypoperfusion was associated with accelerated cognitive decline and an increased risk of dementia (Wolters et al., 2017). Accordingly, it is essential to get a better understanding of CCH induced VD (Du et al., 2017). The limitations associated with current clinical diagnosis and treatment are related to limitations in knowledge of the molecular mechanisms of CCH involved. Considering the difficulty and ethical nature of the human brain tissue's provenance, laboratory rats have been used for decades to model diseases of the human central nervous system (CNS). BCCAO operation is currently recognized as a appropriate model of CCH to investigate the pathogenesis and therapeutics, especially to examine cognitive decline associated with cerebrovascular diseases (Du et al., 2017; Zhang T. et al., 2017; Zou et al., 2018; Kato et al., 2019; Mao et al., 2019). The chronic hypoperfusive conditions related to vascular cognitive impairment show a ∼20–30% decrease in blood flow, the level of hypoperfusion induced by BCCAO rat model was consistent with this trend (Duncombe et al., 2017). And previous studies considered that 4–8 weeks after BCCAO operation was the later stage (chronic phase) of the CCH process (Ma et al., 2015; Zhang X. et al., 2017; Kato et al., 2019). Therefore, the CCH model was available in this study.

In this research, from a brand-new perspective, WMD, different ways of cortical neuron death and whole-transcriptome analysis of rats with CCH were evaluated comprehensively.

Disintegration of the White Matter

Cerebral white matter is comprised of nerve fibers interconnecting neurons in the cerebral cortex or the deep structures (Tomimoto, 2015). Emerging evidence indicates that reduced cerebral perfusion may contribute to several diseases characterized by WMD. WMD is another reflection of CCH and cerebral hypoxia, and a relationship is found between cognitive impairment and WMD (Iadecola, 2013; Choi et al., 2016). In addition, the imaging changes of hypoperfusion dementia including white matter lesions (O'Brien and Thomas, 2015).

DTI is highly sensitive to the directional diffusivities of water where tissues are oriented according to particular directions of white matter tracts (Choi et al., 2016). In our study, considering that white matter tracts are the most abundant in the CC and both ECs in the rat brain, reduced FA in the CC and both ECs may suggest the presence of concomitant axonal damage in the brain after CCH. Additionally, MBP is located in the dense myelin sheath and nucleus pulposus, LFB specifically binds to myelin; therefore, MBP and LFB staining can be used to assess the shape and monitor the change of the myelin sheath. The results indicate that WMD induced by CCH is characterized by disintegration of diverse white matter components. Considering the integrity of white matter, other mechanisms might be also involved in the disintegration of the white matter, such as neuron death. Different degrees of WMD may lead to morphological changes in cerebral cortex and its associated regions, the networks between neurons are impaired and their viability would be impaired.

Cognitive Impairments, Aβ Deposition, BBB Injury and Neuron Death in CCH

Previous studies indicate that CCH is generally associated with a chain of disruption of homeostatic interactions, led to neuronal damage; experimental studies suggest that the damaging effects of such imbalances contribute to and exacerbate the course of VD (Jing et al., 2015; Du et al., 2017). The Morris water maze task examines the animals' abilities to spatial learning and reference memory, making it ideal for many experimental models (Vorhees and Williams, 2006). Our study revealed cognitive impairments are induced by CCH, especially in CCH 8W. Spatial reference memory is thought to be related to not only the integrity of the hippocampus, but also cortex (Block and Schwarz, 1997). It had been reported that reference memory dysfunction will not occur until more than 60% of the neurons in the hippocampal CA1 sector are lost, and previous study showed that hippocampal neurons displayed significant damage since 8 weeks after BCCAO (Zou et al., 2018). CCH 4W might be in the transition progression of cognitive impairment. Therefore, change of biochemical indicators can also occur before severe cognitive impairment (Jing et al., 2015; Zou et al., 2018).

The number of intracellular Aβ-positive cells was greater in the CCH than the sham-operated, but Aβ plaque deposition was similar in these groups. $A\beta_{1-42}$ was reported to enhance BBB permeability through reduction of tight junction proteins expression (Chan et al., 2018). In this study, the BBB was significantly damaged after CCH with decreased tight junction proteins including ZO-1 and Occludin. Aβ toxicity increases

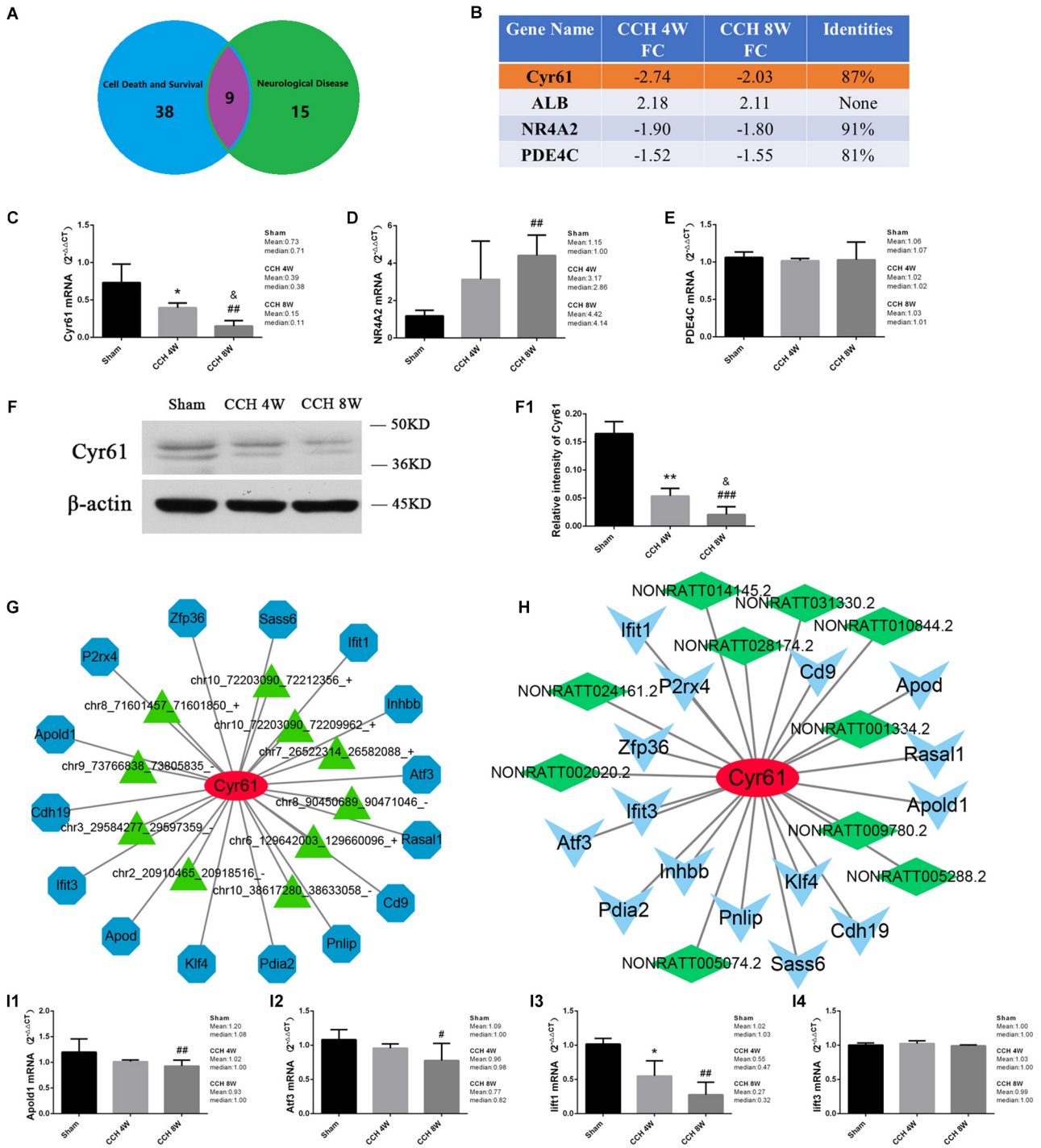


FIGURE 10 | (A) The common mRNAs in BF in neurological diseases and cell survival and death, CCH. 4W&CCH 8W compared with sham rats. **(B)** Conservative analysis. **(C–E)** qPCR analysis of expression of Cyr61, NR4A2, PDE4C mRNA. **(F)** Western blot analysis of Cyr61 protein. **(F1)** Quantitative analysis of western blot. **(G)** Co-expression network of Cyr61 mRNA with the associated mRNAs and circRNAs. Blue nodes represent mRNAs, and green triangle nodes represent circRNAs. Solid lines represent relationships. **(H)** Co-expression network of Cyr61 mRNA with the associated mRNAs and lncRNAs. Blue triangles represent mRNAs, and green squares represent lncRNAs. Solid lines represent relationships. **(I1–I4)** qPCR analysis of Apold1, Atf3, lift1, lift3 mRNA. Values are expressed as the mean ± SD. $^{*}P < 0.05$, $^{**}P < 0.01$, CCH 4W compared with sham rats; $^{\#}P < 0.05$, $^{\#\#}P < 0.01$, $^{\#\#\#}P < 0.001$, CCH 8W compared with sham rats; $^{\&}P < 0.05$, CCH 8W compared with CCH 4W rats; ns, not significant.

the formation of reactive oxygen species (ROS) and intracellular calcium levels, resulting in neuron death (Song et al., 2018). Considering Aβ plaque deposition is the remarkable pathological feature of AD, the pathogenesis and neuropathological changes caused by VD and AD are still different. In our study, we found intracellular Aβ deposition in CCH groups, which may be related to neuron death. A previous study indicated that extracellular Aβ plaque deposition occurred later than intracellular Aβ accumulation in the cortex of CCH rats (Zou et al., 2018). Therefore, extracellular Aβ deposition may occur after neurons' death in later stage of CCH.

Additionally, significant neurodegeneration and neuron death were observed in the cortex. Apoptosis and necroptosis were both expressed in the CCH groups. Classically, cell death has been classified into apoptosis and necrosis. Apoptosis is a programmed form of cell death, but in the process of programmed cell death, the process of cell death can also be driven by other molecular pathways, which include programmed cell necrosis, such as necroptosis triggered by treatment with TNF (Linkermann and Green, 2014), inflammation related pyroptosis, or caspase 1-dependent cell death (Bergsbaken et al., 2009). The process of active pyroptosis was not detected in the CCH rats in the study. Apoptosis and necroptosis are not mutually exclusive, and both may occur in the same organ (Linkermann and Green, 2014). Salvatore et al. found that activated necroptosis induced hippocampus neuronal loss in AD (Caccamo et al., 2017). Even though hippocampus was demonstrated to have important role in cognitive function, from another perspective, CCH is induced by a moderate and continuous decrease in the CBF of cortex (Du et al., 2017), which leads to hypoxia of brain tissue followed by a series of neuropathological changes, which eventually lead to the impairment of cognitive function (Raz et al., 2016; Duncombe et al., 2017). Due to the cross-linking of the cortex and the hippocampus (Tomimoto, 2015), thus, CCH affects the hippocampus to a certain extent after the damage to the cortical-hippocampal communication network. Therefore, relationship between neuron death and transcriptional changes in cortical tissue have certain research value in the cognitive impairment induced by CCH. Additionally, WMD and neuron death may be the cause and effect of each other. Therefore, understanding the basic molecular mechanisms underlying the process of cortical neuron death in VD induced by CCH will be invaluable to the development of potential therapeutic approaches.

Different Expression Profiles and Networks of the Whole Transcriptome in Chronic Cerebral Hypoperfusion

In this study, comparing CCH 4W group with CCH 8W group, some of the factors showed a statistically significant difference, but there were also a few factors showing non-significant changes, measured in brain tissues. The differences observed between macroscopic pathological phenomena and microscopic biochemical changes, highlight the importance of exploring the mechanism at a microscopic level.

Recently, progress has been made in understanding the formation and biogenesis of circRNAs, adding more evidence and possibilities to their biological applications. Studies have investigated the potential role of circRNAs as biomarkers of AD and tumors (Dou et al., 2016). In our study, the 2 most downregulated circRNAs were chr10_72203090_72212356_+ and chr10_72203090_72209962_+. Their target gene, Myo19, is involved in mitochondrial motility.

MicroRNAs (miRNA) are small (∼22 nt) single-stranded RNAs that are important regulators of several BPs, circRNAs regulate gene expression via specific miRNA binding sites (Vijayan et al., 2017; Wu et al., 2018). The circRNA–miRNA network may serve as a powerful regulation pathway in CCH. In our study, miRNAs were highly expressed in the CCH rats. In addition, miR-26b-targeted circRNAs were chr6_122804706_122817427_- and chr7_53979119_54012529_+; miR-195-targeted circRNAs were chr14_28418125_28536253_−, chr15_70769051_70832121_+, and chr20_14319169_14340940_−; miR-501-3p-targeted circRNAs were chr11_46896817_46915497_−, chr7_33866231_33886951_−, chr15_104270169_104283452_−, chr17_75579711_75616081_+, chr17_75588945_75604406_+ and chr4_8223839_8242710_−. The results suggest that CCH-related processes, such as mitochondrial motility, microglial activation and neurotoxicity, neuron degeneration and death, memory deficits, and white matter lesions, may be related to the circRNA–miRNA networks. It has already been proven that some miRNAs are functional in vascular cognitive impairment. For example, miRNA-195 prevents dendritic degeneration and neuron death in CCH rats (Chen et al., 2017); the TNFα–miR-501-3p–ZO-1 axis plays an important role in the pathogenesis of CCH induced memory deficits and WMD (Toyama et al., 2018).

lncRNA has been shown to regulate gene expression at various levels and has emerged as a major source of bio-targets for cancer therapeutics (Wu et al., 2018). The biological function of lncRNAs is multifaceted. The regulatory role of lncRNAs is not solitary but through a large complex network that involves mRNAs, miRNAs, and proteins. Several lncRNAs have been shown to be critical in regulating cellular processes and diseases, but many other functions of lncRNAs have not been elucidated (Dou et al., 2016). Therefore, the functional forecast of lncRNAs is based on the annotations of the co-expressed mRNAs' function. The lncRNA–mRNA network showed that the downregulated lncRNAs, NONRATT016029.2 and NONRATT016027.2, were positively correlated with the Ckmt2 gene. The creatine kinase phosphagen system, including Ckmt2, is fundamental to cellular energy homeostasis, and decreased creatine kinase activity is a characteristic of ischemia-reperfusion injury and cell death (Zervou et al., 2017).

Biological Function Analysis

Advanced bioinformatic tools including GO analysis and KEGG pathway analysis, have been applied to determine key biological processes and signaling pathways during diseases (Yu et al., 2016).

The KEGG pathway analysis of differentially expressed mRNAs revealed neuroactive ligand-receptor interaction, PI3K-Akt signaling and ras signaling pathways could play pivotal roles in the pathogenesis of CCH. The most significant GO items

were response to peptide, extracellular matrix and carboxylic acid binding. Reactome enrichment analysis found that the top pathways were extracellular matrix organization, cytosolic sensors of pathogen-associated DNA, integrin cell surface interactions, et al.

The KEGG pathway analysis of differentially expressed circRNAs and lncRNAs revealed that MAPK signaling, glucagon signaling, dopaminergic synapse cGMP-PKG signaling could play pivotal roles in CCH. The most significant GO items were regulation of synapse structure or activity, protein serine/threonine kinase activity, transcription factor activity and binding. Reactome enrichment analysis showed that axon guidance and signaling by NGF and PDGF might also play a crucial role.

The aforementioned results suggest that energy metabolism, signal transmission, dopaminergic synapse signaling, cell death and survival, and neurotrophic factors regulate the associated pathways in CCH-related VD.

IPA of Neuron Death Induced by CCH

IPA software program can analyze the gene expression patterns using a build-in scientific literature based database (Yu et al., 2016). The application of IPA analysis helps to decipher related functions, diseases, networks and even upstream regulator, thus may provide some new knowledge about VD induced by CCH.

In particular, IPA revealed nine mRNAs in CCH tissues, which are involved in cell death and survival, apoptosis, necrosis, and neurological diseases. Additionally, the conservative score of Cyr61 was the highest, it is similar to humans. The present results revealed downregulation of Cyr61 mRNA and protein in CCH. Cyr61 is associated with cell proliferation, chemotaxis, angiogenesis, and cell adhesion. Cyr61 appears to play a role in wound healing, where it is upregulated in skin fibroblasts, the expression of a number of genes involved in angiogenesis and matrix remodeling. Cyr61 has been reported to participate in multiple functions, such as migration, proliferation, apoptosis in non-CNS organs (Jun and Lau, 2011). Moreover, Cyr61 is suggested to play an important role in the modulation of inflammatory cytokines and chemokines production (Kular et al., 2011). The expression and function of Cyr61 in the CNS remains poorly understood (Jones and Bouvier, 2014). And Atf3 is one of the most critical genes for ROS-induced stress responses, upregulates p53 expression and induces apoptosis in cells (Zhao et al., 2016). Ifit1 is a negative regulator of the inflammatory gene program (John et al., 2018). But little is known about the role of them in neurological diseases, further investigation is needed.

Perspectives of Transcriptome Study in CCH and Significance of Clinical Transformation

The study of the genetics and epigenetics of neurological diseases both in mammalian model organisms and in humans is beginning to focus on genetic variants, which exist outside protein-coding genes, as potential drivers of pathogenesis. The conventional view of gene-regulation has focused on protein-coding genes until the discovery of numerous non-coding RNAs, including lncRNAs and circRNAs. Mapping studies, combined with whole-genome sequencing data using CCH rat models, have begun to provide evidence for the genetic basis of inheritance of traits (such as VD), which are exerted by non-protein-coding elements. A database of the transcriptome levels of differentially expressed RNAs and the co-expression networks and biological functions were built at the experimental animal level. The results in the present study should set a stage for inquiry of mRNAs, circRNAs, lncRNAs as candidates regulating the etiology of CCH. Validation of potential transcriptome biomarkers will provide experimental basis for further potential clinical targets of CCH related VD.

However, there are several limitations to this research which need to be considered. First, more time points of experimental groups are required in further investigation. Second, it is important to use as many animal models of CCH-induced VD and methods for evaluating cognitive function as possible to avoid problems associated with bias. Moreover, further experimental verification must be acquired with regards to analysis and compare to specimens such as cerebrospinal fluid/blood in patients in the next phase of our study.

CONCLUSION

The present study elucidated WMD and different ways of cortical neuronal death were implicated in CCH, and thus resulted in cognitive impairment. The expression profiles and networks of mRNA–circRNA–miRNA and lncRNA–mRNA were profiled, and potential bioinformatic analysis were annotated. The study indicates that Cyr61 may be a key factor for cortical neuronal death in CCH. We plan to set up a database for further research, and the present results would inspire neuroscientific researchers to study the role of transcriptomic events in CCH, provide a fundamental basis including candidate biomarkers and therapeutic targets for the further clinical application.

ETHICS STATEMENT

All experiments were conducted in accordance with National Institutes of Health guide for the care and use of laboratory animals. The protocol was approved by Laboratory Animal Ethics Committee of Jinan University.

AUTHOR CONTRIBUTIONS

WL and DW wrote the manuscript. WL, DW, JL, XX, and KS carried out the experiments. WL, XX, and JL contributed to imaging experiments. XX and KS contributed to Morris water

maze task. WL and DW contributed to sample collection. XX and KS contributed to neuropathological experiments. WL, DW, JL, XX, and KS contributed to data analyses. LH designed the study and revised the manuscript.

FUNDING

This work was supported by the specific fund for science and technology innovation strategy of Guangdong Province, China (No. 32218145), the specific science-technology project of the prophylaxis and treatment of major diseases, China (No. ZX-01-C2016083), the project of public benefit research and capacity building, China (No. 32417016), and the cerebrovascular disease construction platform project of Guangdong Province, China (No. 89017014).

ACKNOWLEDGMENTS

We would like to thank Geneseed Biotech Co., Ltd. for their technical support in our whole-transcriptome sequencing analysis. The data were also uploaded as **Supplementary Materials**. We would also like to thank Editage® for editing and polishing of the manuscript.

SUPPLEMENTARY MATERIAL

The Supplementary Material for this article can be found online at: https://www.frontiersin.org/articles/10.3389/fncel.2019.00310/full#supplementary-material

FIGURE S1 | Full western blots from *in vivo* experiments.

REFERENCES

Bergsbaken, T., Fink, S. L., and Cookson, B. T. (2009). Pyroptosis: host cell death and inflammation. *Nat. Rev. Microbiol.* 7, 99–109. doi: 10.1038/nrmicro2070

Block, F., and Schwarz, M. (1997). Correlation between hippocampal neuronal damage and spatial learning deficit due to global ischemia. *Pharmacol. Biochem. Behav.* 56, 755–761.

Caccamo, A., Branca, C., Piras, I. S., Ferreira, E., Huentelman, M. J., Liang, W. S., et al. (2017). Necroptosis activation in Alzheimer's disease. *Nat. Neurosci.* 20, 1236–1246. doi: 10.1038/nn.4608

Chan, Y., Chen, W., Wan, W., Chen, Y., Li, Y., and Zhang, C. (2018). Abeta1-42 oligomer induces alteration of tight junction scaffold proteins via RAGE-mediated autophagy in bEnd.3 cells. *Exp. Cell Res.* 369, 266–274. doi: 10.1016/j.yexcr.2018.05.025

Chen, X., Jiang, X. M., Zhao, L. J., Sun, L. L., Yan, M. L., Tian, Y., et al. (2017). MicroRNA-195 prevents dendritic degeneration and neuron death in rats following chronic brain hypoperfusion. *Cell Death Dis.* 8:e2850. doi: 10.1038/cddis.2017.243

Cheng, J., Metge, F., and Dieterich, C. (2016). Specific identification and quantification of circular RNAs from sequencing data. *Bioinformatics* 32, 1094–1096. doi: 10.1093/bioinformatics/btv656

Chmayssani, M., Festa, J. R., and Marshall, R. S. (2007). Chronic ischemia and neurocognition. *Neuroimaging Clin. N. Am.* 17, 313–324.

Choi, B. R., Kim, D. H., Back, D. B., Kang, C. H., Moon, W. J., Han, J. S., et al. (2016). Characterization of white matter injury in a rat model of chronic cerebral hypoperfusion. *Stroke* 47, 542–547. doi: 10.1161/STROKEAHA.115.011679

Dobin, A., Davis, C. A., Schlesinger, F., Drenkow, J., Zaleski, C., Jha, S., et al. (2013). STAR: ultrafast universal RNA-seq aligner. *Bioinformatics* 29, 15–21. doi: 10.1093/bioinformatics/bts635

Dou, C., Cao, Z., Yang, B., Ding, N., Hou, T., Luo, F., et al. (2016). Changing expression profiles of lncRNAs, mRNAs, circRNAs and miRNAs during osteoclastogenesis. *Sci. Rep.* 6:21499. doi: 10.1038/srep21499

Du, S. Q., Wang, X. R., Xiao, L. Y., Tu, J. F., Zhu, W., He, T., et al. (2017). Molecular mechanisms of vascular dementia: what can be learned from animal models of chronic cerebral hypoperfusion? *Mol. Neurobiol.* 54, 3670–3682. doi: 10.1007/s12035-016-9915-1

Duncombe, J., Kitamura, A., Hase, Y., Ihara, M., Kalaria, R. N., and Horsburgh, K. (2017). Chronic cerebral hypoperfusion: a key mechanism leading to vascular cognitive impairment and dementia. Closing the translational gap between rodent models and human vascular cognitive impairment and dementia. *Clin. Sci.* 131, 2451–2468. doi: 10.1042/CS20160727

Enright, A. J., John, B., Gaul, U., Tuschl, T., Sander, C., and Marks, D. S. (2003). MicroRNA targets in *Drosophila*. *Genome Biol.* 5:R1.

Ghaiad, H. R., Nooh, M. M., El-Sawalhi, M. M., and Shaheen, A. A. (2017). Resveratrol promotes remyelination in cuprizone model of multiple sclerosis: biochemical and histological study. *Mol. Neurobiol.* 54, 3219–3229. doi: 10.1007/s12035-016-9891-5

Gopalakrishnan, K., Kumarasamy, S., Mell, B., and Joe, B. (2015). Genome-wide identification of long noncoding RNAs in rat models of cardiovascular and renal disease. *Hypertension* 65, 200–210. doi: 10.1161/HYPERTENSIONAHA.114.04498

Iadecola, C. (2013). The pathobiology of vascular dementia. *Neuron* 80, 844–866. doi: 10.1016/j.neuron.2013.10.008

Jing, Z., Shi, C., Zhu, L., Xiang, Y., Chen, P., Xiong, Z., et al. (2015). Chronic cerebral hypoperfusion induces vascular plasticity and hemodynamics but also neuronal degeneration and cognitive impairment. *J. Cereb. Blood Flow Metab.* 35, 1249–1259. doi: 10.1038/jcbfm.2015.55

John, S. P., Sun, J., Carlson, R. J., Cao, B., Bradfield, C. J., Song, J., et al. (2018). IFIT1 exerts opposing regulatory effects on the inflammatory and interferon gene programs in LPS-activated human macrophages. *Cell Rep.* 25:e106. doi: 10.1016/j.celrep.2018.09.002

Jones, E. V., and Bouvier, D. S. (2014). Astrocyte-secreted matricellular proteins in CNS remodelling during development and disease. *Neural Plast.* 2014:321209. doi: 10.1155/2014/321209

Jun, J. I., and Lau, L. F. (2011). Taking aim at the extracellular matrix: CCN proteins as emerging therapeutic targets. *Nat. Rev. Drug Discov.* 10, 945–963. doi: 10.1038/nrd3599

Kato, H., Kanai, Y., Watabe, T., Ikeda, H., Horitsugi, G., and Hatazawa, J. (2019). Quantitative measurement of regional cerebral blood flow and oxygen metabolism in a rat model of cerebral hypoperfusion. *Brain Res.* 1719, 208–216. doi: 10.1016/j.brainres.2019.05.032

Kiyota, T., Machhi, J., Lu, Y., Dyavarshetty, B., Nemati, M., Zhang, G., et al. (2018). URMC-099 facilitates amyloid-beta clearance in a murine model of Alzheimer's disease. *J. Neuroinflamm.* 15:137. doi: 10.1186/s12974-018-1172-y

Kular, L., Pakradouni, J., Kitabgi, P., Laurent, M., and Martinerie, C. (2011). The CCN family: a new class of inflammation modulators? *Biochimie* 93, 377–388. doi: 10.1016/j.biochi.2010.11.010

Langmead, B., and Salzberg, S. L. (2012). Fast gapped-read alignment with Bowtie 2. *Nat. Methods* 9, 357–359. doi: 10.1038/nmeth.1923

Li, B., and Dewey, C. N. (2011). RSEM: accurate transcript quantification from RNA-Seq data with or without a reference genome. *BMC Bioinform.* 12:323. doi: 10.1186/1471-2105-12-323

Linkermann, A., and Green, D. R. (2014). Necroptosis. *N. Engl. J. Med.* 370, 455–465.

Ma, J., Yan, H., Wang, R., Bo, S., Lu, X., Zhang, J., et al. (2018). Protective effect of carnosine on white matter damage in corpus striatum induced by chronic cerebral hypoperfusion. *Neurosci. Lett.* 683, 54–60. doi: 10.1016/j.neulet.2018.06.032

Ma, J., Zhang, J., Hou, W. W., Wu, X. H., Liao, R. J., Chen, Y., et al. (2015). Early treatment of minocycline alleviates white matter and cognitive impairments after chronic cerebral hypoperfusion. *Sci. Rep.* 5:12079. doi: 10.1038/srep12079

Mao, L., Yang, T., Li, X., Lei, X., Sun, Y., Zhao, Y., et al. (2019). Protective effects of sulforaphane in experimental vascular cognitive impairment: contribution of the Nrf2 pathway. *J. Cereb. Blood Flow Metab.* 39, 352–366. doi: 10.1177/0271678X18764083

O'Brien, J. T., and Thomas, A. (2015). Vascular dementia. *Lancet* 386, 1698–1706. doi: 10.1016/S0140-6736(15)00463-8

Raz, L., Knoefel, J., and Bhaskar, K. (2016). The neuropathology and cerebrovascular mechanisms of dementia. *J. Cereb Blood Flow Metab.* 36, 172–186.

Robinson, M. D., Mccarthy, D. J., and Smyth, G. K. (2010). edgeR: a Bioconductor package for differential expression analysis of digital gene expression data. *Bioinformatics* 26, 139–140. doi: 10.1093/bioinformatics/btp616

Ruitenberg, A., Den Heijer, T., Bakker, S. L., Van Swieten, J. C., Koudstaal, P. J., Hofman, A., et al. (2005). Cerebral hypoperfusion and clinical onset of dementia: the rotterdam study. *Ann. Neurol.* 57, 789–794.

Song, H., Huang, L. P., Li, Y., Liu, C., Wang, S., Meng, W., et al. (2018). Neuroprotective effects of cordycepin inhibit Abeta-induced apoptosis in hippocampal neurons. *Neurotoxicology* 68, 73–80. doi: 10.1016/j.neuro.2018.07.008

Sun, J., Wang, J., Zhang, N., Yang, R., Chen, K., and Kong, D. (2019). Identification of global mRNA expression profiles and comprehensive bioinformatic analyses of abnormally expressed genes in cholestatic liver disease. *Gene* 707, 9–21. doi: 10.1016/j.gene.2019.04.078

Sun, Y., Cao, W., Ding, W., Wang, Y., Han, X., Zhou, Y., et al. (2016). Cerebral blood flow alterations as assessed by 3D ASL in cognitive impairment in patients with subcortical vascular cognitive impairment: a marker for disease severity. *Front. Aging Neurosci.* 8:211. doi: 10.3389/fnagi.2016.00211

Tomimoto, H. (2015). White matter integrity and cognitive dysfunction: radiological and neuropsychological correlations. *Geriatr. Gerontol. Int.* 15(Suppl. 1), 3–9. doi: 10.1111/ggi.12661

Toyama, K., Spin, J. M., Deng, A. C., Huang, T. T., Wei, K., Wagenhauser, M. U., et al. (2018). MicroRNA-mediated therapy modulating blood-brain barrier disruption improves vascular cognitive impairment. *Arterioscler. Thromb. Vasc. Biol.* 38, 1392–1406. doi: 10.1161/ATVBAHA.118.310822

Vijayan, M., Kumar, S., Bhatti, J. S., and Reddy, P. H. (2017). Molecular links and biomarkers of stroke, vascular dementia, and alzheimer's disease. *Prog. Mol. Biol. Transl. Sci.* 146, 95–126. doi: 10.1016/bs.pmbts.2016.12.014

Vorhees, C. V., and Williams, M. T. (2006). Morris water maze: procedures for assessing spatial and related forms of learning and memory. *Nat. Protoc.* 1, 848–858.

Wolters, F. J., Zonneveld, H. I., Hofman, A., Van Der Lugt, A., Koudstaal, P. J., Vernooij, M. W., et al. (2017). Cerebral perfusion and the risk of dementia: a population-based study. *Circulation* 136, 719–728. doi: 10.1161/CIRCULATIONAHA.117.027448

Wu, Y., Zhang, Y., Niu, M., Shi, Y., Liu, H., Yang, D., et al. (2018). Whole-transcriptome analysis of CD133+CD144+ cancer stem cells derived from human laryngeal squamous cell carcinoma cells. *Cell Physiol. Biochem.* 47, 1696–1710. doi: 10.1159/000490992

Xiong, Z., Lu, W., Zhu, L., Zeng, L., Shi, C., Jing, Z., et al. (2017). Dl-3-n-butylphthalide treatment enhances hemodynamics and ameliorates memory deficits in rats with chronic cerebral hypoperfusion. *Front. Aging Neurosci.* 9:238. doi: 10.3389/fnagi.2017.00238

Yu, J., Gu, X., and Yi, S. (2016). Ingenuity pathway analysis of gene expression profiles in distal nerve stump following nerve injury: insights into wallerian degeneration. *Front. Cell Neurosci.* 10:274. doi: 10.3389/fncel.2016.00274

Zervou, S., Whittington, H. J., Ostrowski, P. J., Cao, F., Tyler, J., Lake, H. A., et al. (2017). Increasing creatine kinase activity protects against hypoxia / reoxygenation injury but not against anthracycline toxicity in vitro. *PLoS One* 12:e0182994. doi: 10.1371/journal.pone.0182994

Zhang, T., Gu, J., Wu, L., Li, N., Sun, Y., Yu, P., et al. (2017). Neuroprotective and axonal outgrowth-promoting effects of tetramethylpyrazine nitrone in chronic cerebral hypoperfusion rats and primary hippocampal neurons exposed to hypoxia. *Neuropharmacology* 118, 137–147. doi: 10.1016/j.neuropharm.2017.03.022

Zhang, X., Huang, X., Fang, C., Li, Q., Cui, J., Sun, J., et al. (2017). miR-124 regulates the expression of BACE1 in the hippocampus under chronic cerebral hypoperfusion. *Mol. Neurobiol.* 54, 2498–2506. doi: 10.1007/s12035-016-9845-y

Zhao, Q., Yang, X., Cai, D., Ye, L., Hou, Y., Zhang, L., et al. (2016). Echinacoside protects against MPP(+)-induced neuronal apoptosis via ROS/ATF3/CHOP pathway regulation. *Neurosci. Bull.* 32, 349–362. doi: 10.1007/s12264-016-0047-4

Zou, W., Song, Y., Li, Y., Du, Y., Zhang, X., and Fu, J. (2018). The Role of autophagy in the correlation between neuron damage and cognitive impairment in rat chronic cerebral hypoperfusion. *Mol. Neurobiol.* 55, 776–791. doi: 10.1007/s12035-016-0351-z

Conflict of Interest Statement: The authors declare that the research was conducted in the absence of any commercial or financial relationships that could be construed as a potential conflict of interest.

Copyright © 2019 Li, Wei, Liang, Xie, Song and Huang. This is an open-access article distributed under the terms of the Creative Commons Attribution License (CC BY). The use, distribution or reproduction in other forums is permitted, provided the original author(s) and the copyright owner(s) are credited and that the original publication in this journal is cited, in accordance with accepted academic practice. No use, distribution or reproduction is permitted which does not comply with these terms.

frontiers in Cellular Neuroscience

REVIEW
published: 19 July 2019
doi: 10.3389/fncel.2019.00327

Epigenetics in Neurodevelopment: Emerging Role of Circular RNA

*Shujuan Meng[1,2,3], Hecheng Zhou[1,2,3], Ziyang Feng[1,2,3], Zihao Xu[1,2,3], Ying Tang[1,2,3] and Minghua Wu[1,2,3]**

[1] Hunan Provincial Tumor Hospital, The Affiliated Tumor Hospital of Xiangya Medical School, Central South University, Changsha, China, [2] Key Laboratory of Carcinogenesis and Cancer Invasion, Ministry of Education, Cancer Research Institute, School of Basic Medical Science, Central South University, Changsha, China, [3] Key Laboratory of Carcinogenesis, Ministry of Health, Cancer Research Institute, School of Basic Medical Science, Central South University, Changsha, China

Canonical epigenetic modifications, including DNA methylation, histone modification and chromatin remodeling, play a role in numerous life processes, particularly neurodevelopment. Epigenetics explains the development of cells in an organism with the same DNA sequence into different cell types with various functions. However, previous studies on epigenetics have only focused on the chromatin level. Recently, epigenetic modifications of RNA, which mainly include 6-methyladenosine (m^6A), pseudouridine, 5-methylcytidine (m^5C), inosine (I), 2′-*O*-ribosemethylation, and 1-methyladenosine (m^1A), have gained increasing attention. Circular RNAs (circRNAs), which are a type of non-coding RNA without a 5′ cap or 3′ poly (A) tail, are abundantly found in the brain and might respond to and regulate synaptic function. Also, circRNAs have various functions, such as microRNA sponge, regulation of gene transcription and interaction with RNA binding protein. In addition, circRNAs are methylated by N^6-methyladenosine (m^6A). In this review, we discuss the crucial roles of epigenetic modifications of circRNAs, such as m^6A, in the genesis and development of neurons and in synaptic function and plasticity. Thus, this type of changes in circRNAs might be a therapeutic target in central nervous system (CNS) disorders and could aid the diagnosis and treatment of these disorders.

Keywords: circular RNA, epigenomics, neurodevelopment, m^6A, non-coding RNA

OPEN ACCESS

Edited by:
Antonio Gambardella, Università degli Studi "Magna Græcia" di Catanzaro, Italy

Reviewed by:
Gloria Bertoli, Institute of Bioimaging and Molecular Physiology, National Research Council, Italy
In-Hyun Park, Yale University, United States

***Correspondence:**
Minghua Wu
wuminghua554@aliyun.com

Specialty section:
This article was submitted to Cellular Neuropathology, a section of the journal Frontiers in Cellular Neuroscience

Received: *13 February 2019*
Accepted: *03 July 2019*
Published: *19 July 2019*

Citation:
Meng S, Zhou H, Feng Z, Xu Z, Tang Y and Wu M (2019) Epigenetics in Neurodevelopment: Emerging Role of Circular RNA. Front. Cell. Neurosci. 13:327. doi: 10.3389/fncel.2019.00327

Abbreviations: ADAR, adenosine deaminases acting on RNA; ADAT, adenosine deaminases acting on tRNA; ALKBH5, AlkB homolog 5; ARID1B, AT-rich interactive domain-containing protein 1B; Bdnf, brain-derived neurotrophic factor; CHD, chromodomain helicase DNA-binding protein; circRNA, circular RNA; ciRS-7, circular RNA sponge for miR-7; CNS, central nervous system; CoREST, corepressor for element-1-silencing transcription factor; DSCAM, Down Syndrome cell adhesion molecule; FTO, fat mass-and-obesity-associated protein; GBM, glioblastoma multiforme; HATs, histone acetyltransferases; HDACs, histone deacetylases; IRESs, internal ribosome entry sites; ISWI, Imitation SWItch; LTP, long-term potentiation; m^1A, 1-methyladenosine; m^5C, 5-methylcytidine; m^5C, carbon 5 of cytosine; m^6A, N^6-methyladenosine; m^7G, N^7-methylguanosine; MeRIP-Seq, methylated RNA immunoprecipitation with next-generation sequencing; METTL14, methyltransferase-like 14; METTL3, methyltransferase-like 3; miRNA, microRNA; N-CoR, nuclear receptor corepressor; Nm, 2′-*O*-methylation; NuRD, nucleosome remodeling and deacetylase complex of histone acetylation; PTC, peptidyltransferase center; PTMs, post-translational modifications; SAM, S-adenosyl methionine; SWI/SNF, SWItch/Sucrose Non-Fermentable; TRBP, transactivation response RNA-binding protein; UTRs, untranslated regions; WTAP, Wilms' tumor 1-associating protein; YTHDC, YTH domain-containing protein; YTHDF, YTH domain-containing family.

INTRODUCTION

Epigenomics, which refers to all the molecular pathways that modulate the expression of a genotype into a particular phenotype without any changes to the genome, plays an important role in the growth and development of mammals (Dupont et al., 2009). Research on canonical epigenetics has concentrated on DNA modifications and chromatin variations, and RNA epigenetic modifications, particularly those in non-coding RNAs, have recently garnered increasing attention. With the development of RNA deep sequencing technology and bioinformatics approaches, circRNAs have become increasing important among non-coding RNAs. Unlike linear RNAs, circRNAs have covalently closed loop structures without 5′ caps or 3′ poly-A tails due to back-splicing (Bolisetty and Graveley, 2013). Because of their stability (Suzuki and Tsukahara, 2014), evolutionary conservatism (Jeck et al., 2013) and high abundance (Gruner et al., 2016), circRNAs act as miRNA sponges (Hansen et al., 2013; Memczak et al., 2013), factors of RNA splicing (Ashwal-Fluss et al., 2014), and modulators of the expression of parental genes (Li Z. et al., 2015). circRNAs can also serve as biomarkers for numerous diseases (Meng et al., 2017). The latest studies have demonstrated that circRNAs can be methylated by m^6A (Yang et al., 2017; Zhou et al., 2017), and its translation is enhanced by METTL3 and METTL14, and inhibited by FTO (Yang et al., 2017). Both circRNAs and m^6A are involved in RNA processing and are related to neurodevelopment (Dominissini et al., 2012; Meyer et al., 2012; Rybak-Wolf et al., 2015). So, this review describes the effect of canonical epigenetics in neurodevelopment, summarizes the progress on RNA epigenetics and circRNAs, and suggests the relationship between neurodevelopment and circRNA epigenetics.

CANONICAL EPIGENETICS AND NEURODEVELOPMENT

Epigenetics is involved in many vital biological processes and plays an important role in the growth and development of organisms. Epigenetics explains how cells that carry the same genetic information differentiate into different cell types with various functions (Gapp et al., 2014). It is difficult to succeed in the treatment of neurological diseases, such as Parkinson's disease, Alzheimer's disease (AD), gliomas, and epilepsy. Thus, a study of the relationship between epigenetics and neurodevelopment contributes to our understanding of the occurrence and development of these diseases. The traditional epigenetics processes include DNA methylation, histone modification and chromatin remodeling. In this section, we demonstrate that DNA methylation, histone modification and chromatin remodeling play a role in neurodevelopment.

DNA Methylation and Neurodevelopment

DNA methylation, as a covalent modification of genomic DNA, modifies gene expression and provides a mechanism for transmitting and perpetuating epigenetic information through DNA replication and cell division (Harman and Martin, 2019). Early development includes two stages of epigenetic programming: the first stage involves DNA demethylation or remethylation and the reprograming of histone PTMs in somatic cells, and the second stage guarantees and rebuilds parental imprints during germ cell development through DNA methylation (van Montfoort et al., 2012; Gapp et al., 2014). In addition, the neurodevelopment process also highly depends on DNA methylation (Gapp et al., 2014). Specifically, DNA methylation is observed at CpG islands in the mammalian genome, where it can modulate gene expression (Jones, 2012), through the addition of a methyl group to m^5C molecules (Pulido Fontes et al., 2015). Brain DNA has one of the highest levels of m^5Cs in human organs (Kriaucionis and Heintz, 2009; LaSalle et al., 2013), and DNA methylation is required for neuronal differentiation in mammals (Takizawa et al., 2001; Mohn et al., 2008). In addition, researchers have found that DNA methylation changes with LTP and m^5C methyltransferase regulate synaptic plasticity in the hippocampus (Levenson et al., 2006). Some recent studies confirmed that in the presence of LTP, the methylation status of LTP genes undergoes widespread changes in the adult brain (Maag et al., 2017). These studies also showed that the methylation of Bdnf CpG islands is related to isoform switching from transcripts (Maag et al., 2017). Coincidentally, some researchers have identified that CpG island enriched for genes related to development and neurodifferentiation in schizophrenia patients, and widespread DNA methylation changes in schizophrenia-associated CpGs, were related to the transition from fetal brain cortex to postnatal development (Jaffe et al., 2016) (**Figure 1A**). Sleep deprivation can alter the cortical genome-wide distribution of DNA methylation, and these differences are enriched in gene pathways involving in the synapse formation and synaptic plasticity (Massart et al., 2014). In addition, some studies have found that gene-specific DNA methylation occurs in response to folic acid supplementation during pregnancy and is related to brain development and function (Caffrey et al., 2018).

Histone Modification and Neurodevelopment

The basic structural unit of chromatin is the nucleosome, which is composed of one H3/H4 tetramer, two H2A and H2B dimers, and one H1 molecule. Histone modification refers to the set of covalent PTMs of histone proteins, and these modifications, which mainly include methylation, acetylation, phosphorylation, ubiquitination, sumoylation, and ADP-ribosylation (Berger, 2007), have been proven to be important in stem cell differentiation and neurodevelopment (Podobinska et al., 2017). For instance, class I and II HDACs, which contain two catalytic domains, act as the regulators of histone acetylation in mammals (Zhang et al., 2006; Podobinska et al., 2017). Many protein complexes that contain HDACs, such as SIN3/HDAC (Silverstein and Ekwall, 2005), the NuRD (Xue et al., 1998), co-repressor for element-1-silencing transcription factor (CoREST) (Shi et al., 2004) and the nuclear receptor co-repressor (N-CoR) (Jepsen et al., 2007), play important roles in neurodevelopment. These complexes not only catalyze the deacetylation of histones but are also associated with the activation of gene expression

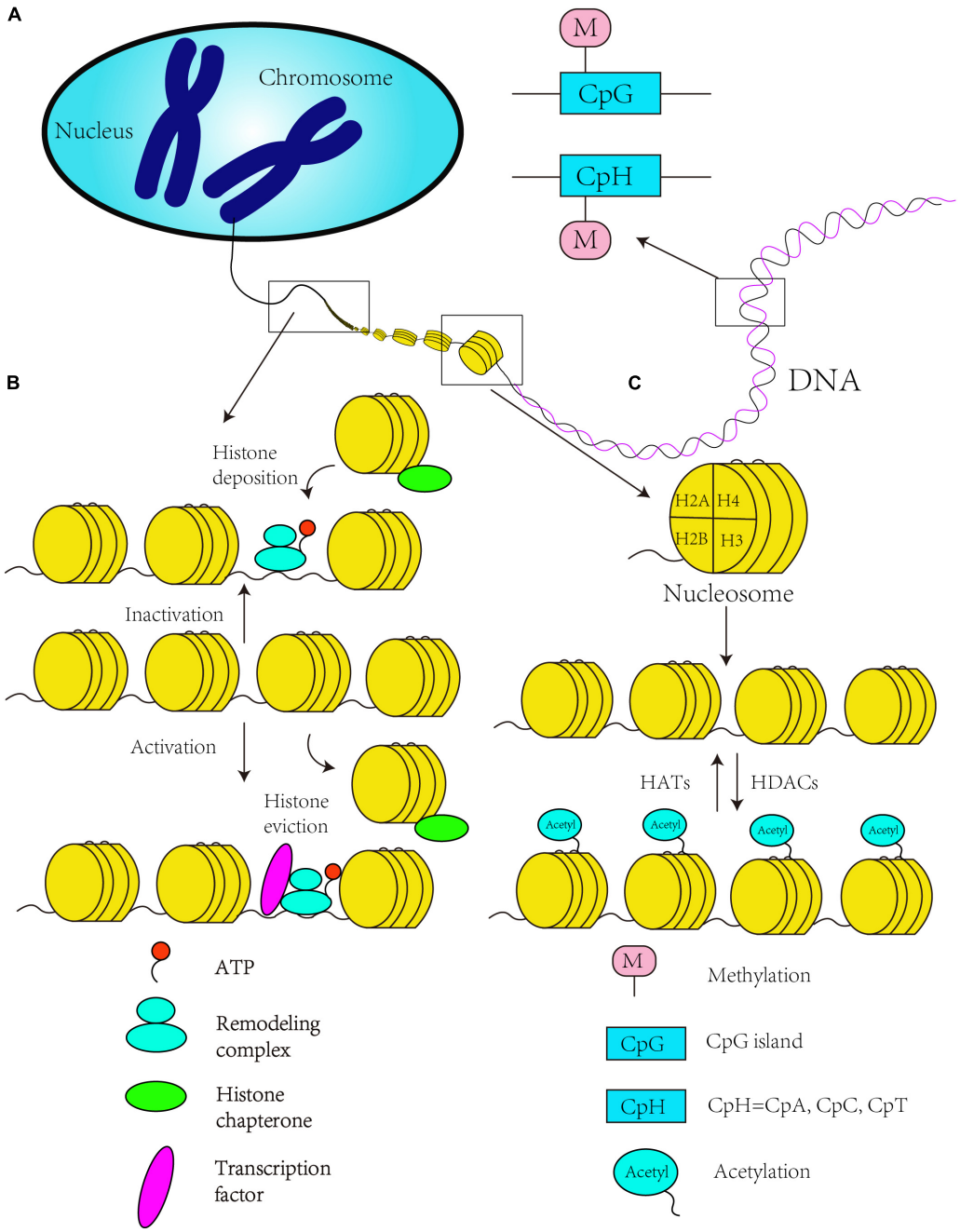


FIGURE 1 | Canonical epigenetics mechanism. **(A)** DNA methylation in the CpG and CpH context. **(B)** Chromatin remodeling is ATP dependent. ATP-dependent remodeling complexes regulate DNA accessibility, and histone chaperones move and transfer histones on and off a locus. An open chromatin structure enables RNA polymerase II to catalyze the transcription when the histone is evicted, while chromatin state change to inactivity to inhibit gene transcription with the histone deposition of chromosome. **(C)** The acetylation of histone tails by histone acetyltransferases (HATs) establishes a more relaxed state in the chromatin that results in transcriptional activation (activated state). Histone deacetylation by HDACs reverses the activating chromatin state to a "inactive" chromatin state to inhibit gene transcription.

(Shimbo et al., 2013) or involved in the neural commitment and differentiation of stem cells (Podobinska et al., 2017). Learning and memory are vitally important processes in the growth and development of individual, and are necessary in brain development. Some animal experiments have shown that lacking HDAC2 or HDAC3 could improve learning (Guan et al., 2009; McQuown et al., 2011; Narayan and Dragunow, 2017), while loss of HDAC4 and HDAC5 has been shown to damage memory function (Kim et al., 2012; Sando, et al., 2012; Agis-Balboa et al., 2013), especially, HDAC4, which also participates

in experience-dependent plasticity of synaptic (Agis-Balboa et al., 2013). Conversely, in the aged brain, HDACs and HATs, as transcription repressors to catalyze histone deacetylation, have been reported to be altered, and could be linked to age-related altered gene transcription (Barter and Foster, 2018). Some scientists have proven that the same isoforms of HDAC3 and HDAC4 were undetectable in the human AD prefrontal cortex compared to mouse models of AD, which had relatively high concentrations (Anderson et al., 2015). And comparison to the control cases, HDAC1 and HDAC2 were decreased but HDAC5 and HDAC6 were significantly increased in AD patient (Anderson et al., 2015), which implied that isoform selectivity of HDACs could be a target of therapy (Narayan and Dragunow, 2017). Although HDAC4 is undetectable in normal human brain, the expression of brain tumor tissue was increased (de Ruijter et al., 2003). Interestingly, deletion or mutation of HDAC4 results in reduced expression of *RAI1* can cause mental retardation, such as Smith–Magenis syndrome (Williams et al., 2010) (**Figure 1C**).

Chromatin Remodeling and Neurodevelopment

Chromatin remodeling refers to dynamic modifications of the chromatin architecture that regulate transcription through displacement and rearrangement of the nucleosome. The process of chromatin remodeling is driven by ATP (Zaghlool et al., 2016), and chromatin remodeling complexes can be classified into four main classes: SWI/SNF, ISWI, INO80, and Mi2/CHD (Olave et al., 2002; Choi et al., 2015) (**Figure 1B**). A few recent studies have focused on chromatin remodeling and neurodevelopment. The Wnt signaling pathway is one of the most important pathways in embryonic development and axis patterning (Salinas, 2012), and some researchers have found that this signaling pathway can be repressed by one of the BRG1-associated factors in the ARID1B chromatin remodeling complex (also known as the SWI/SNF-A complex) (Vasileiou et al., 2015). This signaling pathway can be affected by a mutation in bromodomain adjacent to zinc finger domain protein 1A (BAZ1A), which encodes ATP-utilizing chromatin assembly and remodeling factor 1 (ACF1) (Zaghlool et al., 2016), and the mutation in BAZ1A also affects the development of proper synaptic functions (Zaghlool et al., 2016). Furthermore, chromatin remodeling might be influenced by persistent exposure to 6OH-BDE-47 (brominated diphenyl ether, BDE) and thereby affects downstream processes, such as synapse development and the overall functional maturity of neurons (Poston et al., 2018). Also, chromatin remodeling can be regulated by non-coding RNAs. For example, microRNA-9 and microRNA-124a could inhibit the expression of gene *BAF53a* (also known as ACTL6a), which is a component of SWI/SNF chromatin remodeling complexes, by corresponding to the recognition sites of 3′ untranslated region. Ultimately, neural progenitor proliferation was repressed (Yoo et al., 2009). As for the aging brain, chromatin remodeling driven by histone modifications is tightly related to the enzymes which can regulate the process of modifications added or removed (Harman and Martin, 2019). However, regulation and function of these enzymes is altered during brain aging leading to changes in the epigenome (Pal and Tyler, 2016). To some extent, these studies have demonstrated that chromatin remodeling plays a role in neurodevelopment and can affect embryonic development.

RNA MODIFICATION

Epigenomics refers to stable and heritable changes in gene expression that do not alter the DNA sequence (Berger et al., 2009). However, epigenetic modifications occur not only in DNA but also in RNA, called the epitranscriptome, but the heritability of RNA modifications needs further study. Epitranscriptome includes more than 100 types of RNA modifications (Sun et al., 2016), and researchers have found that RNA modifications are abundant in tRNAs, rRNAs, and snRNAs but relatively rare in mRNAs (Lee et al., 2014; Sun et al., 2016). But in the last several years, technological advances improving our ability to identify mRNA modifications and recent studies of the cellular transcriptome have focused attention on epitranscription (Flamand and Meyer, 2019). Many of these modified transcripts in the brain are associated with autism and other neurodevelopmental disorders, and have implied that the epitranscriptome may impact the development and maturation of synapses (Washbourne, 2015; Flamand and Meyer, 2019). To a great extent, these modifications enrich the functions of RNA and genetic diversity (Maden, 1990; Wang X. et al., 2014; Zhang and Jia, 2016), and the common RNA modifications include pseudouridine (Ψ), m^6A, 5-methylcytosine (m^5C), m^7G, N^1-methyladenosine, and N_m (Sun et al., 2016; Zhang and Jia, 2016). This section summarizes the most common types of epigenetic modifications of RNA.

N^6-Methyladenosine (m^6A)

N^6-Methyladenosine, which refers to the methylation of position N^6 of adenosine, is one of the most abundant modifications of mRNAs found in all eukaryotes. Early studies used mass spectrometry to detect this modification and revealed that the relative m^6A content ranged from 0.1 to 0.4% (Wei et al., 1975), which corresponds to the modification of approximately three to five sites in each mRNA (Wei et al., 1975; Lee et al., 2014). The m^6A modification, which is post-transcriptionally decoded by m^6A methyltransferase, is a prevalent internal modification in eukaryotic mRNA (Wang X. et al., 2014), and always occurs in the consensus sequence RRACH (R = G or A; H = A, C or U) (Niu et al., 2013). To detect and analyze the location of m^6A, researchers have developed a m^6A-specific MeRIP-Seq approach and found that m^6A is mainly concentrated in the 3′ UTRs of mRNAs, long internal exons and the stop codons (Meyer et al., 2012). The distribution of m^6A in tissue-specific sites has also been investigated, and the results revealed that this modification is most abundantly found in the heart, brain and kidney (Meyer et al., 2012). Furthermore, the distribution of m^6A is richer in the adult brain than in the fetal brain (Meyer et al., 2012). Coincidentally, Dominissini D et al. used an m^6A-seq approach and found that the sites modified by m^6A are highly conserved in humans and mice (Dominissini et al., 2012). Antibody-based crosslinking strategies have been developed in recent years to

increase the resolution of m^6A (Chen K. et al., 2015; Linder et al., 2015; Roundtree and He, 2016).

To more accurately describe the process of m^6A, researchers have used the terms "writer," "eraser," and "readers," and these terms are extensively used for many types of modifications, not just m^6A methyltransferase. This modification is considered a "writer," which uses the SAM cofactor as the methyl donor, and this cofactor is post-transcriptionally methylated at the N^6 position of adenosine. m^6A methyltransferase consists of METTL3, METTL14 and the regulatory subunit WTAP (Bokar et al., 1994; Liu et al., 2014; Ping et al., 2014). METTL14 has enzymatic activity (Liu et al., 2014), interacts with METTL3 and preferentially methylates the conserved GGACU and GGAUU sequences (Liu et al., 2014). Even though it does not have the activity of methyltransferase due to the lack of a catalytic center, WTAP can locate the methyltransferase complex to nuclear speckles by interacting with METTL3 and METTL14 (Ping et al., 2014). The knockdown of METTL3 causes changes in the splicing patterns and alternative polyadenylation, and influences RNA stability, transcriptional silencing, and translation (Dominissini et al., 2012; Schwartz et al., 2014; Ke et al., 2015; Meyer et al., 2015; Zhou et al., 2015; Lin et al., 2016; Patil et al., 2016; Wang X. et al., 2016; Pendleton et al., 2017). A recent study revealed a new mechanism of m^6A: METTL16, a long unknown U6 snRNA methyltransferase able to control the SAM levels, which influence the level of m^6A in most cells by regulating the expression of human MAT2A (Pendleton et al., 2017).

The discovery of m^6A demethylating enzymes, named "erasers," focused on FTO (Dina et al., 2007) and ALKBH5, which are proteins that belong to the Fe (II) and 2-oxoglutarate-dependent oxygenase superfamily (Jia et al., 2011; Zheng et al., 2013) and oxidize m^6A through N^6-hydroxymethyladenosine (hm^6A) and N^6-formyladenosine (f^6A) intermediates (Fu et al., 2013). Recent studies have shown that FTO participates in many vital life processes, such as the regulation of dopaminergic signaling in the brain (Hess et al., 2013), the mRNA splicing of adipogenetic regulatory factors (Ben-Haim et al., 2015), adipogenesis (Zhao et al., 2014), and the enhancement of leukemic oncogene-mediated cell transformation and leukemogenesis (Li Z. et al., 2017). Both FTO and ALKBH5 are important in cells, and in HeLa cells, these demethylating enzymes also affect the processing, nuclear export and metabolism of mRNA (Zheng et al., 2013).

The effector proteins of m^6A, which are called "readers," include the YT521-B homology (YTH) family, which encodes five proteins, namely the YTH domain family (YTHDF) proteins 1, 2 and 3 and the YTH domain-containing (YTHDC) proteins 1 and 2 in mammals (Zhang et al., 2010; Li Z. et al., 2017). To date, four of these proteins have been shown to exhibit m^6A selectivity *in vitro* and *in vivo* (Wang X. et al., 2014; Xu et al., 2014; Roundtree and He, 2016). YTHDF2 and YTHDC1 have a conserved hydrophobic binding pocket specific for m^6A and participate in the process regulating the methylation and transcript fate of mRNA (Luo and Tong, 2014; Wang X. et al., 2014; Xu et al., 2014). In addition, the high-resolution mapping of transcription-binding sites has revealed that YTHDF1 and YTHDF2 prefer to bind to the GGACU conserved sequence motif in mRNA, which shows substantial overlap with sites of m^6A methylation (Zhu et al., 2014; Wang et al., 2015; Roundtree and He, 2016).

N^6-Methyladenosine plays a critical role in the development of an organism, and changes in the levels of m^6A have an impact on many life processes, including tissue development, stem cell self-renewal (Wang Y. et al., 2014; Zhao et al., 2014) and differentiation (Geula et al., 2015). m^6A can also control the heat shock response (Zhou et al., 2015), circadian clocks (Fustin et al., 2013), and processes associated with the fate and function of RNAs, such as the stability, splicing, transport, localization and translation of RNAs (Zheng et al., 2013; Wang X. et al., 2014; Wang Y. et al., 2014; Wang et al., 2015; Zhao et al., 2014; Meyer et al., 2015; Zhou et al., 2015), primary microRNA processing (Alarcon et al., 2015; Chen T. et al., 2015), and RNA-protein interactions (Dominissini et al., 2012; Meyer et al., 2012; Liu et al., 2015). Similarly, in neurodevelopment, m^6A still has a critical role in reducing brain volume (Ho et al., 2010). In the developing cortex, m^6A is abundant and controls the ample transcripts involved in neurogenesis and neuronal differentiation (Yoon et al., 2017; Flamand and Meyer, 2019). With the age growing, the m^6A levels is increasing, especially in adulthood via controlling synaptic plasticity in the mature brain (Meyer et al., 2012). However, a considerable body of evidence indicates a relationship between m^6A and diseases. In fact, it has been demonstrated that m^6A is related to obesity, diabetes and cancer (Klungland and Dahl, 2014; Zelinski et al., 2014). Meanwhile, FTO also participate in regulation of learning and memory. For instance, decreasing the expression of *Fto* in the hippocampus causes the enhanced contextual fear memory and impaired LTP (Walters et al., 2017; Engel et al., 2018). Recent studies have shown that ALKBH5 and the depletion of m^6A drive the formation of cancer stem cells (Jaffrey and Kharas, 2017). Coincidentally, a study conducted in 2017 revealed that m^6A is relevant to the self-renewal and tumorigenesis of glioblastoma stem cells (Cui et al., 2017).

Other RNA Modifications

Most studies on m^5C have focused on DNA, and m^5C is rare in RNA (Roundtree and He, 2016). However, researchers have discovered that m^5C is enriched in the 3′-UTRs (Chhabra, 2015). 3-Methylcytidine (m^3C) was first discovered in total RNA from *Saccharomyces cerevisiae* (Hall, 1963). The studies discovered that METTL2 and METTL6 have m^3C modifications in specific tRNAs and that METTL8 only induces m^3C modifications in mRNA in humans and mice (Xu et al., 2017). Some researchers successfully characterized RNA methylation in mixtures of either isomers of RNA or non-isomeric RNA forms and identified the RNA methylation modifications, including m^6A, m^5C, m^3U, and m^5U, by top-down mass spectrometry (Glasner et al., 2017).

Pseudouridine is also a relatively abundant type of RNA modification, and the relative amount of pseudouridine in RNA is in the range of 0.2–0.6% (Li X. et al., 2015). Pseudouridine formation involves two mechanisms: one is dependent on tRNA-pseudouridine synthase I and the other relies on a type of H/ACA box snoRNA (Charette and Gray, 2000; Ofengand, 2002). In rRNA, pseudouridine mainly appears in PTCs, decoding

centers and the A-site finger region (ASF) (Jack et al., 2011). Thus, this modification might participate in the processing of rRNA, the assembly of ribosomes and the maintenance of advanced structures (Kiss et al., 2010). Studies have shown that in snRNA (U1, U2, U3, U4, U5, and U6), pseudouridine is highly conserved in different types of species (Yu et al., 2011). In 2011, some researchers showed that stop codons could be transformed into sense codons by pseudouridylation (Karijolich and Yu, 2011).

Inosine is a normal and essential post-transcriptional RNA modification introduced by specific deaminases (Alseth et al., 2014). In tRNA, this process is catalyzed by ADAT, whereas in mRNA and non-coding RNA, ADAR catalyze the process (Bass et al., 1997). In fact, A-to-I RNA editing plays a significant physiological role in neuronal function (Behm and Ohman, 2016). RNA encoding glioma-associated oncogene 1 (GLI1) is edited such that an arginine is changed to a glycine (R/G) in the protein. The GLI1 mRNA is highly edited, which induces an increase in the capacity of GLI1 to activate transcription by adenosine deamination in the normal cerebellum, but the process is obviously decreased in cell lines originating from cerebellar tumors (Shimokawa et al., 2013). Researchers have found that ADAR2 auto-editing is increased during mouse brain development and in rat primary cortical neuronal cultures, which suggests that ADAR2 activity is globally elevated (Hang et al., 2008; Behm and Ohman, 2016). In addition, modulated GluA2-4 R/G editing and alternative splicing generates AMPA receptors, which can adapt to differential rapid fast-synaptic transmission during development (Grosskreutz et al., 2003).

EPIGENETIC MODIFICATIONS OF CIRCULAR RNAs

In recent years, circRNAs have been one of the most frequently studied types of non-coding RNA. Due to their unique features, which are described above, circRNAs are known as miRNA sponges (Hansen et al., 2013; Memczak et al., 2013) and might also serve as potential biomarkers for a number of diseases, particularly cancers (Meng et al., 2017). Although numerous biological functions of circRNAs remain unknown, this field of research is being continuously explored. Some of the endogenous circRNAs identified to date have the capability of being translated into proteins through a process driven by the IRESs (Legnini et al., 2017). In early 2017, a group of researchers found that circRNAs can be widely methylated by m^6A, as determined through the m^6A immunoprecipitation of RNA samples treated with the RNase R exoribonuclease, and are efficiently translated through short sequences consisting of the m^6A site as IRESs in human cells (Yang et al., 2017). The initiation of this m^6A-mediated translation requires the eIF4G2 initiation factor and the YTHDF3 m^6A reader, and the translation process is enhanced by METTL3/14 and inhibited by FTO (Yang et al., 2017). These researchers also inferred that proteins translated by circRNAs can be correlated with environmental stress (Yang et al., 2017). Coincidentally, other researchers designed a computational pipeline named AutoCirc to analyze the results from RNA and m^6A immunoprecipitation and further demonstrated that m^6A modifications are extensively observed in circRNAs. These researchers also showed that m^6A circRNAs have highly cell-specific expression (Zhou et al., 2017), and revealed that circRNAs with m^6A modifications also have long single exons. In addition, the researchers compared m^6A circRNAs and m^6A mRNAs and validated that the methylated exons in mRNAs are different from the exons that form m^6A circRNAs (Zhou et al., 2017). Additionally, m^6A circRNAs are related to mRNA stability through interaction with YTHDF1/YTHDF2 (**Figure 2**; Zhou et al., 2017). These studies expand the yield of RNA modifications and circRNAs, and more questions regarding circRNA modifications need to be expounded.

CircRNAs AND NEURODEVELOPMENT

In 2015, researchers used high-resolution *in situ* hybridization to verify that circRNAs are most abundantly found in the human brain (You et al., 2015), and some researchers have attempted to determine the reason for the enrichment of circRNAs in the brain (Chen and Schuman, 2016). It is well known that there are long introns (Jeck et al., 2013; Liang and Wilusz, 2014; Zhang et al., 2014) that flank circularized exons; thus, researchers have inferred that brain-specific genes might carry additional sequence features that can promote circRNA formation (Chen and Schuman, 2016). Although many functions of the circRNAs in brain remain unclear, it is undisputed that the circRNA levels in neurons are dynamically modulated. These studies illustrate that circRNAs play a vital role in neurodevelopment through these mechanism.

MicroRNA Sponge and Interaction With RNA Binding Proteins

Serving as a microRNA sponge was the first discovered function of circRNAs in 2013. The ciRS-7 contains more than 70

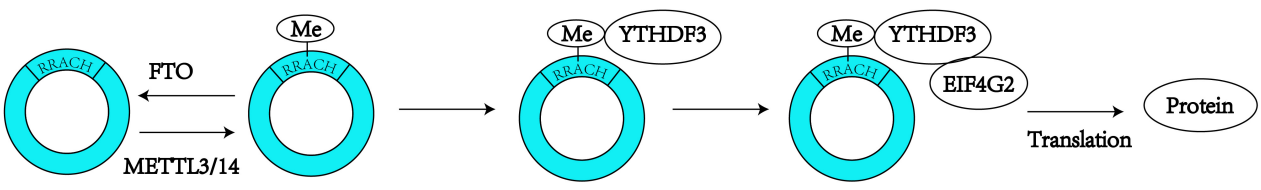


FIGURE 2 | N^6-Methyladenosine modification is always found to occur in the consensus sequence identified as: RRACH (R = G or A; H = A, C or U). M^6A modification can promote the translation of the circRNAs.

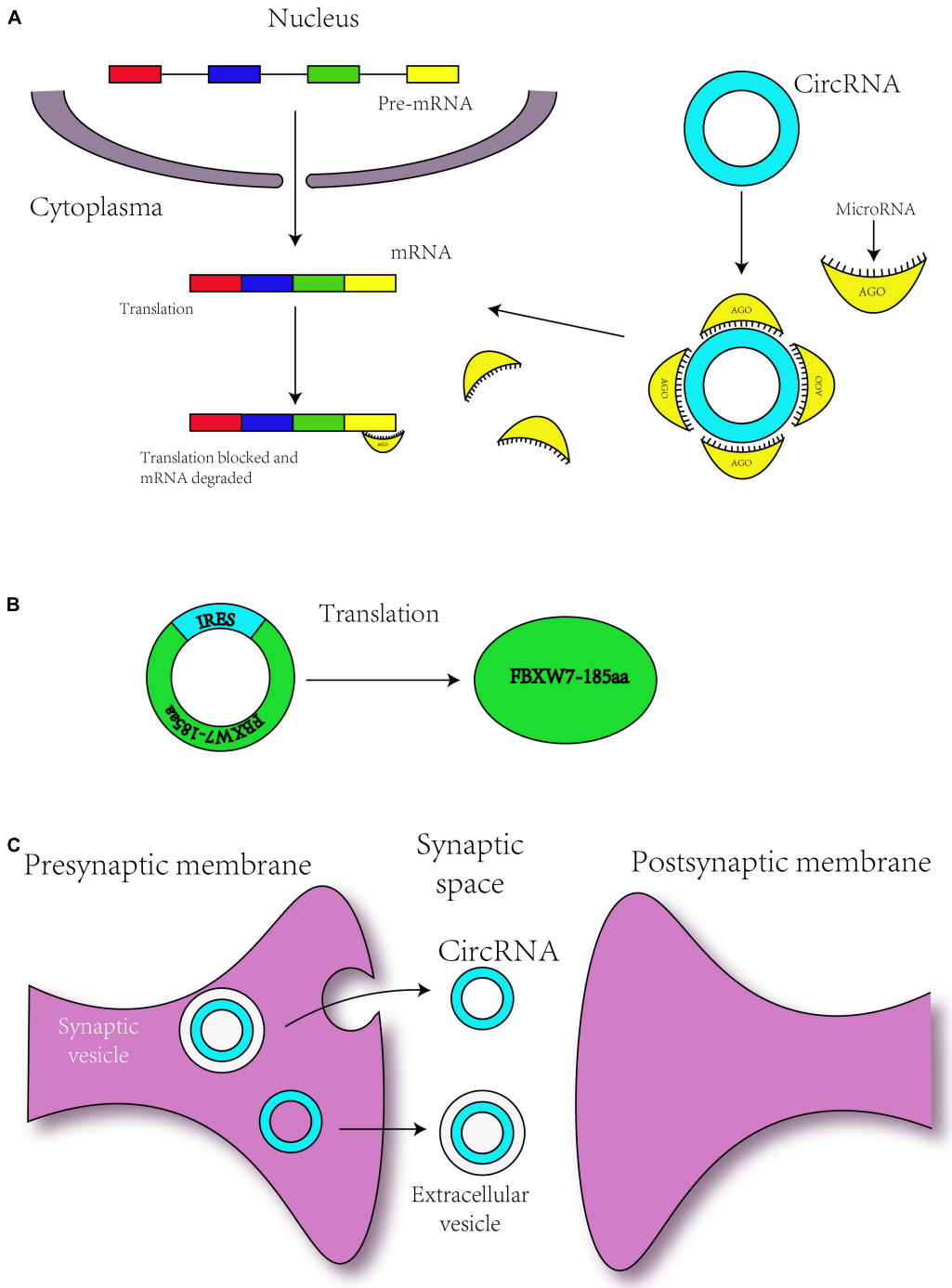


FIGURE 3 | Circular RNAs are related to neurodevelopment through different mechanisms. **(A)** circRNAs regulate the translation of mRNAs by serving as miRNA sponges. **(B)** Some circRNAs with an IRES sequence can translate proteins, and this translation is driven by IRES. **(C)** circRNAs may transmit the information to environment by synaptosomes or extracellular vesicle such as exosomes.

conserved binding sites for miRNA-7, and ciRS-7 can bind with Argonaute (AGO) protein (**Figure 3A**; Hansen et al., 2013). Additionally, the co-expression of ciRS-7 and miR-7 is distinctly high in neocortical and hippocampal neurons, which implies a high degree of endogenous interaction (Hansen et al., 2013). In 2017, researchers established the Cdr1as-loss mouse model by CRISPR/Cas9 (Piwecka and Glazar, 2017). Circ-Cdr1as reportedly binds to miR-7 and miR-671 (Hansen et al., 2011, 2013), and researchers have found that miR-7 and miR-671 are deregulated post-transcriptionally in the Cdr1as-knock-off brain.

Furthermore, the expression of immediate early genes, such as Fos, which is the direct target of miR-7, is increased in the Cdr1as-loss mouse brain (Piwecka and Glazar, 2017). Cdr1as-knockout mice show defects in neuropsychiatric behaviors, which suggests that Cdr1as might be crucial for neuron-controlled behavior (Piwecka and Glazar, 2017). To ensure its interaction with RNA-binding proteins, Circ-Foxo3 is able to bind with many types of proteins, such as cell cycle-related proteins (Du et al., 2016), and thus, might participate in neuronal cell division in neurodevelopment.

Regulation of Gene Transcription

Circular RNAs can also regulate gene transcription, but these effects are achieved via varied mechanisms. These circRNAs always exist in the nucleus. For example, in HeLa and HEK293 cells, circ-EIF3J and circ-PAIP2 are exon-intron circRNAs or EIciRNAs and interact with U1 snRNP to promote transcription of their parental genes (Li Z. et al., 2015). In 2013, researchers found a circular intronic RNA denoted ci-ankrd52 and found that this circRNA might affect the rate or efficiency of transcription as a positive regulator of Pol II transcription (Zhang et al., 2013). Therefore, these circRNAs might be related to transcription in neurons (Li Z. et al., 2015; van Rossum et al., 2016).

Translation

As mentioned above, m^6A can mediate the translation of circRNAs, but circRNAs can also be translated via other mechanisms. Some circRNAs contain the IRES responsible for driving translation, for instance, circ-ZNF609 and circMbl3 were found to translate proteins (Legnini et al., 2017; Pamudurti et al., 2017). In addition, in 2017, some researchers have found that circ-FBXW7 is abundantly expressed in the normal human brain and can encode a novel 21-kDa protein, the translation of which is driven by IRES (**Figure 3B**; Yang et al., 2018). The upregulation of this new protein can inhibit the proliferation and cell cycle acceleration of glioma cells (Yang et al., 2018). As a consequence, circRNAs might translate the proteins to regulate the process of neurodevelopment.

Neurodevelopment and Synaptic Function

In 2015, some researchers have confirmed that circRNAs with biological functions are correlated with synaptic function and are significantly enriched in synapses, parts of the synapse, presynaptic active zones, presynaptic membranes and postsynaptic density (**Figure 3C**; You et al., 2015). circDscam, circKlhl2, circElavl3, circNlgn1, circGigyf2, circNbea, and circRmst are derived from synapse-related genes (You et al., 2015), indicating a relationship between circRNAs and synaptic function. In addition, highly expressed circRNAs are derived from synaptic genes, such as Dscam and Homer1, and might participate in Wnt signaling, axon guidance and TGF-β signaling (Veno et al., 2015; You et al., 2015). During hippocampal and Drosophila brain development, the expression of circRNAs is developmentally upregulated (Westholm et al., 2014; You et al., 2015) and can be regulated by neural plasticity (You et al., 2015). These findings revealed the role of circRNAs in brain development. Other researchers have found that the expression level of circRNAs shows differences among various brain areas (Rybak-Wolf et al., 2015).

THE POTENTIAL ROLES OF circRNA EPIGENETIC MODIFICATIONS IN NEURODEVELOPMENT

As mentioned above, m^6A is one of the most abundant methylation patterns in mRNA and is also present in circRNAs (Yang et al., 2017; Zhou et al., 2017). In addition, FTO, as m^6A demethylating enzymes, were found to display dynamic expression in postnatal neurodevelopment (Li L. et al., 2017). FTO deficiency not only results in a decreased brain size and a reduced body weight but also leads to impairments in learning and memory (Li L. et al., 2017). Further studies have illustrated that m^6A is indispensable for the regulation of RNA fate and function, which are central to differentiation and growth (Geula et al., 2015). In addition, the majority of circRNAs are upregulated during the development of the Drosophila brain, but some circRNAs are downregulated (You et al., 2015; Zhou et al., 2017). By serving as miRNA sponges, circRNAs are involved in the regulation of RNA processing, such as alternative splicing, pre-RNA splicing and RNA editing (Hansen et al., 2013; Starke et al., 2015; van Rossum et al., 2016). Their expression level is regulated by synaptic plasticity during neurodevelopment. As a result, we hypothesized various mechanisms through which epigenetic circRNAs affect neurodevelopment. First, the epigenetic modification of circRNAs might occupy miRNA sites, which can prevent miRNA-mRNA binding. Second, during neurodevelopment, epigenetic circRNAs might transmit information to the microenvironment by exosomes. Exosomes were first found in 1983 as a type of 50-nm vesicles (Harding et al., 2013), and play a significant role in intracellular and extracellular communication. Some studies have demonstrated that pre-miRNAs with Dicer, AGO2, and *trans*-activation response RNA binding protein (TRBP) are present in exosomes of breast cancer cells (Melo et al., 2014). Therefore, circRNAs with epigenomic changes might regulate the biogenesis and contents of exosomes to participate in the early formation and plasticity of synapses. Third, some circRNAs can translate the protein, and these proteins might play a role in RNA processing. Thus, we can infer that epigenetic modifications of circRNAs, such as m^6A, might play a vital role in genesis and neurodevelopment by impacting the alternative splicing of RNAs and in synaptic function and plasticity by influencing RNA processing. In addition, circRNAs participate in many CNS diseases, such as GBM (Zhu et al., 2017), CNS lymphoma (Baraniskin et al., 2016), cerebral ischemia (Ouyang et al., 2013), stroke (Ouyang et al., 2013), Alzheimer's disease (Wu et al., 2013), Huntington's disease (Wu et al., 2013), and Parkinson's disease (Wu et al., 2013). This finding indicates that circRNAs might serve as biomarkers of CNS disorders (Qu et al., 2015; Lu and Xu, 2016). Therefore, in view of these data, changes in the epigenetic modifications of circRNAs might influence RNA stability and lead to neuronal disorders.

circRNAs might be a therapeutic target of CNS disorders and can potentially aid the diagnosis of various diseases.

CONCLUSION

In conclusion, although changes in the epigenetic modifications of circRNAs could exert an effect on neurodevelopment and CNS diseases, considerable studies are needed to confirm this finding. It is thus important to identify the changes in circRNA epigenetic modifications in neurodevelopment and to find the mechanisms of these modifications, which could reveal the roles of circRNAs in CNS diseases. These studies might aid the diagnosis and treatment of CNS diseases.

AUTHOR CONTRIBUTIONS

ZF, ZX, and YT collected the related manuscript. SM drafted and revised the manuscript. HZ drew the figures. MW participated in the design of the review and helped to draft and revised the manuscript. All authors read and approved the final manuscript.

FUNDING

This work was supported by the National Key Technology Research and Development Program of the Ministry of Science and Technology of China (2014BAI04B02) to MW.

REFERENCES

Agis-Balboa, R. C., Pavelka, Z., Kerimoglu, C., and Fischer, A. (2013). Loss of HDAC5 impairs memory function: implications for Alzheimer's disease. *J. Alzheimers. Dis.* 33, 35–44. doi: 10.3233/jad-2012-121009

Alarcon, C. R., Lee, H., Goodarzi, H., Halberg, N., and Tavazoie, S. F. (2015). N6-methyladenosine marks primary microRNAs for processing. *Nature* 519, 482–485. doi: 10.1038/nature14281

Alseth, I., Dalhus, B., and Bjoras, M. (2014). Inosine in DNA and RNA. *Curr. Opin. Genet. Dev.* 26, 116–123. doi: 10.1016/j.gde.2014.07.008

Anderson, K. W., Chen, J., Wang, M., Mast, N., Pikuleva, I. A., and Turko, I. V. (2015). Quantification of histone deacetylase isoforms in human frontal cortex, human retina, and mouse brain. *PLoS One* 10:e0126592. doi: 10.1371/journal.pone.0126592

Ashwal-Fluss, R., Meyer, M., Pamudurti, N. R., Ivanov, A., Bartok, O., Hanan, M., et al. (2014). circRNA biogenesis competes with pre-mRNA splicing. *Mol. Cell* 56, 55–66. doi: 10.1016/j.molcel.2014.08.019

Baraniskin, A., Zaslavska, E., Nopel-Dunnebacke, S., Ahle, G., Seidel, S., Schlegel, U., et al. (2016). Circulating U2 small nuclear RNA fragments as a novel diagnostic biomarker for primary central nervous system lymphoma. *Neuro. Oncol.* 18, 361–367. doi: 10.1093/neuonc/nov144

Barter, J. D., and Foster, T. C. (2018). Aging in the brain: new roles of epigenetics in cognitive decline. *Neuroscientist* 24, 516–525. doi: 10.1177/1073858418780971

Bass, B. L., Nishikura, K., Keller, W., Seeburg, P. H., Emeson, R. B., O'Connell, M. A., et al. (1997). A standardized nomenclature for adenosine deaminases that act on RNA. *RNA* 3, 947–949.

Behm, M., and Ohman, M. (2016). RNA editing: a contributor to neuronal dynamics in the mammalian brain. *Trends Genet.* 32, 165–175. doi: 10.1016/j.tig.2015.12.005

Ben-Haim, M. S., Moshitch-Moshkovitz, S., and Rechavi, G. (2015). FTO: linking m^6A demethylation to adipogenesis. *Cell Res.* 25 3–4. doi: 10.1038/cr.2014.162

Berger, S. L. (2007). The complex language of chromatin regulation during transcription. *Nature* 447, 407–412. doi: 10.1038/nature05915

Berger, S. L., Kouzarides, T., Shiekhattar, R., and Shilatifard, A. (2009). An operational definition of epigenetics. *Genes Dev.* 23, 781–783. doi: 10.1101/gad.1787609

Bokar, J. A., Rath-Shambaugh, M. E., Ludwiczak, R., Narayan, P., and Rottman, F. (1994). Characterization and partial purification of mRNA N6-adenosine methyltransferase from HeLa cell nuclei. Internal mRNA methylation requires a multisubunit complex. *J. Biol. Chem.* 269, 17697–17704.

Bolisetty, M. T., and Graveley, B. R. (2013). Circuitous route to transcription regulation. *Mol. Cell* 51, 705–706. doi: 10.1016/j.molcel.2013.09.012

Caffrey, A., Irwin, R. E., McNulty, H., Strain, J. J., Lees-Murdock, D. J., McNulty, B. A., et al. (2018). Gene-specific DNA methylation in newborns in response to folic acid supplementation during the second and third trimesters of pregnancy: epigenetic analysis from a randomized controlled trial. *Am. J. Clin. Nutr.* 107, 566–575. doi: 10.1093/ajcn/nqx069

Charette, M., and Gray, M. W. (2000). Pseudouridine in RNA: what, where, how, and why. *IUBMB Life* 49, 341–351. doi: 10.1080/152165400410182

Chen, K., Lu, Z., Wang, X., Fu, Y., Luo, G. Z., Liu, N., et al. (2015). High-resolution N(6) -methyladenosine (m(6) A) map using photo-crosslinking-assisted m(6) A sequencing. *Angew. Chem.* 54, 1587–1590. doi: 10.1002/anie.201410647

Chen, T., Hao, Y. J., Zhang, Y., Li, M. M., Wang, M., Han, W., et al. (2015). m(6)A RNA methylation is regulated by microRNAs and promotes reprogramming to pluripotency. *Cell Stem. Cell* 1, 289–301. doi: 10.1016/j.stem.2015.01.016

Chen, W., and Schuman, E. (2016). Circular RNAs in brain and other tissues: a functional enigma. *Trends Neurosci.* 39, 597–604. doi: 10.1016/j.tins.2016.06.006

Chhabra, R. (2015). miRNA and methylation: a multifaceted liaison. *Chembiochem* 16, 195–203. doi: 10.1002/cbic.201402449

Choi, K. Y., Yoo, M., and Han, J. H. (2015). Toward understanding the role of the neuron-specific BAF chromatin remodeling complex in memory formation. *Exp. Mol. Med.* 47:e155. doi: 10.1038/emm.2014.129

Cui, Q., Shi, H., Ye, P., Li, L., Qu, Q., Sun, G., et al. (2017). m^6A RNA Methylation regulates the self-renewal and tumorigenesis of glioblastoma stem cells. *Cell Rep.* 18, 2622–2634. doi: 10.1016/j.celrep.2017.02.059

de Ruijter, A. J., van Gennip, A. H., Caron, H. N., Kemp, S., and van Kuilenburg, A. B. (2003). Histone deacetylases (HDACs): characterization of the classical HDAC family. *Biochem. J.* 370(Pt 3), 737–749. doi: 10.1042/bj20021321

Dina, C., Meyre, D., Gallina, S., Durand, E., Korner, A., Jacobson, P., et al. (2007). Variation in FTO contributes to childhood obesity and severe adult obesity. *Nat. Genet.* 39, 724–726. doi: 10.1038/ng2048

Dominissini, D., Moshitch-Moshkovitz, S., Schwartz, S., Salmon-Divon, M., Ungar, L., Osenberg, S., et al. (2012). Topology of the human and mouse m^6A RNA methylomes revealed by m^6A-seq. *Nature* 485, 201–206. doi: 10.1038/nature11112

Du, W. W., Yang, W., Liu, E., Yang, Z., Dhaliwal, P., and Yang, B. B. (2016). Foxo3 circular RNA retards cell cycle progression via forming ternary complexes with p21 and CDK2. *Nucleic. Acids Res.* 44, 2846–2858. doi: 10.1093/nar/gkw027

Dupont, C., Armant, D. R., and Brenner, C. A. (2009). Epigenetics: definition, mechanisms and clinical perspective. *Semin. Reprod. Med.* 27, 351–357. doi: 10.1055/s-0029-1237423

Engel, M., Eggert, C., Kaplick, P. M., Eder, M., Roh, S., Tietze, L., et al. (2018). The role of m(6)A/m-RNA methylation in stress response regulation. *Neuron* 99, 389.e9–403.e9. doi: 10.1016/j.neuron.2018.07.009

Flamand, M. N., and Meyer, K. D. (2019). The epitranscriptome and synaptic plasticity. *Curr. Opin. Neurobiol.* 59, 41–48. doi: 10.1016/j.conb.2019.04.007

Fu, Y., Jia, G., Pang, X., Wang, R. N., Wang, X., Li, C. J., et al. (2013). FTO-mediated formation of N6-hydroxymethyladenosine and N6-formyladenosine in mammalian RNA. *Nat. Commun.* 4:1798. doi: 10.1038/ncomms2822

Fustin, J. M., Doi, M., Yamaguchi, Y., Hida, H., Nishimura, S., Yoshida, M., et al. (2013). RNA-methylation-dependent RNA processing controls the speed of the circadian clock. *Cell* 155, 793–806. doi: 10.1016/j.cell.2013.10.026

Gapp, K., Woldemichael, B. T., Bohacek, J., and Mansuy, I. M. (2014). Epigenetic regulation in neurodevelopment and neurodegenerative diseases. *Neuroscience* 264, 99–111. doi: 10.1016/j.neuroscience.2012.11.040

Geula, S., Moshitch-Moshkovitz, S., Dominissini, D., Mansour, A. A., Kol, N., Salmon-Divon, M., et al. (2015). Stem cells. m^6A mRNA methylation facilitates

resolution of naive pluripotency toward differentiation. *Science* 347, 1002–1006. doi: 10.1126/science.1261417

Glasner, H., Riml, C., Micura, R., and Breuker, K. (2017). Label-free, direct localization and relative quantitation of the RNA nucleobase methylations m^6A, m^5C, m^3U, and m^5U by top-down mass spectrometry. *Nucleic Acids Res.* 45, 8014–8025. doi: 10.1093/nar/gkx470

Grosskreutz, J., Zoerner, A., Schlesinger, F., Krampfl, K., Dengler, R., and Bufler, J. (2003). Kinetic properties of human AMPA-type glutamate receptors expressed in HEK293 cells. *Eur. J. Neurosci.* 17, 1173–1178. doi: 10.1046/j.1460-9568.2003.02531.x

Gruner, H., Cortes-Lopez, M., Cooper, D. A., Bauer, M., and Miura, P. (2016). CircRNA accumulation in the aging mouse brain. *Sci. Rep.* 6:38907. doi: 10.1038/srep38907

Guan, J. S., Haggarty, S. J., Giacometti, E., Dannenberg, J. H., Joseph, N., Gao, J., et al. (2009). HDAC2 negatively regulates memory formation and synaptic plasticity. *Nature* 459, 55–60. doi: 10.1038/nature07925

Hall, R. H. (1963). Isolation Of 3-Methyluridine And 3-Methylcytidine from solubleribonucleic acid. *Biochem. Biophys. Res. Commun.* 12, 361–364. doi: 10.1016/0006-291x(63)90105-0

Hang, P. N., Tohda, M., and Matsumoto, K. (2008). Developmental changes in expression and self-editing of adenosine deaminase type 2 pre-mRNA and mRNA in rat brain and cultured cortical neurons. *Neurosci. Res.* 61, 398–403. doi: 10.1016/j.neures.2008.04.007

Hansen, T. B., Jensen, T. I., Clausen, B. H., Bramsen, J. B., Finsen, B., Damgaard, C. K., et al. (2013). Natural RNA circles function as efficient microRNA sponges. *Nature* 495, 384–388. doi: 10.1038/nature11993

Hansen, T. B., Wiklund, E. D., Bramsen, J. B., Villadsen, S. B., Statham, A. L., Clark, S. J., et al. (2011). miRNA-dependent gene silencing involving Ago2-mediated cleavage of a circular antisense RNA. *EMBO J.* 30, 4414–4422. doi: 10.1038/emboj.2011.359

Harding, C. V., Heuser, J. E., and Stahl, P. D. (2013). Exosomes: looking back three decades and into the future. *J. Cell Biol.* 200, 367–371. doi: 10.1083/jcb.201212113

Harman, M. F., and Martin, M. G. (2019). Epigenetic mechanisms related to cognitive decline during aging. *J. Neurosci. Res.* doi: 10.1002/jnr.24436 [Epub ahead of print].

Hess, M. E., Hess, S., Meyer, K. D., Verhagen, L. A., Koch, L., Bronneke, H. S., et al. (2013). The fat mass and obesity associated gene (Fto) regulates activity of the dopaminergic midbrain circuitry. *Nat. Neurosci.* 16, 1042–1048. doi: 10.1038/nn.3449

Ho, A. J., Stein, J. L., Hua, X., Lee, S., Hibar, D. P., Leow, A. D., et al. (2010). A commonly carried allele of the obesity-related FTO gene is associated with reduced brain volume in the healthy elderly. *Proc. Natl. Acad. Sci. U.S.A.* 107, 8404–8409. doi: 10.1073/pnas.0910878107

Jack, K., Bellodi, C., Landry, D. M., Niederer, R. O., Meskauskas, A., Musalgaonkar, S., et al. (2011). rRNA pseudouridylation defects affect ribosomal ligand binding and translational fidelity from yeast to human cells. *Mol. Cell* 44, 660–666. doi: 10.1016/j.molcel.2011.09.017

Jaffe, A. E., Gao, Y., Deep-Soboslay, A., Tao, R., Hyde, T. M., Weinberger, D. R., et al. (2016). Mapping DNA methylation across development, genotype and schizophrenia in the human frontal cortex. *Nat. Neurosci.* 19, 40–47. doi: 10.1038/nn.4181

Jaffrey, S. R., and Kharas, M. G. (2017). Emerging links between m^6A and misregulated mRNA methylation in cancer. *Genome Med.* 9:2. doi: 10.1186/s13073-016-0395-398

Jeck, W. R., Sorrentino, J. A., Wang, K., Slevin, M. K., Burd, C. E., Liu, J., et al. (2013). Circular NAs are abundant, conserved, and associated with ALU repeats. *RNA* 19, 141–157. doi: 10.1261/rna.035667.112

Jepsen, K., Solum, D., Zhou, T., McEvilly, R. J., Kim, H. J., Glass, C. K., et al. (2007). SMRT-mediated repression of an H3K27 demethylase in progression from neural stem cell to neuron. *Nature* 450, 415–419. doi: 10.1038/nature06270

Jia, G., Fu, Y., Zhao, X., Dai, Q., Zheng, G., Yang, Y., et al. (2011). N6-methyladenosine in nuclear RNA is a major substrate of the obesity-associated FTO. *Nat. Chem. Biol.* 7, 885–887. doi: 10.1038/nchembio.687

Jones, P. A. (2012). Functions of DNA methylation: islands, start sites, gene bodies and beyond. *Nat. Rev. Genet.* 13, 484–492. doi: 10.1038/nrg3230

Karijolich, J., and Yu, Y. T. (2011). Converting nonsense codons into sense codons by targeted pseudouridylation. *Nature* 474, 395–398. doi: 10.1038/nature10165

Ke, S., Alemu, E. A., Mertens, C., Gantman, E. C., Fak, J. J., Mele, A., et al. (2015). A majority of m^6A residues are in the last exons, allowing the potential for 3' UTR regulation. *Genes Dev.* 29, 2037–2053. doi: 10.1101/gad.269415.115

Kim, M. S., Akhtar, M. W., Adachi, M., Mahgoub, M., Bassel-Duby, R., Kavalali, E. T., et al. (2012). An essential role for histone deacetylase 4 in synaptic plasticity and memory formation. *J. Neurosci.* 32, 10879–10886. doi: 10.1523/jneurosci.2089-12.2012

Kiss, T., Fayet-Lebaron, E., and Jady, B. E. (2010). Box H/ACA small ribonucleoproteins. *Mol. Cell* 37, 597–606. doi: 10.1016/j.molcel.2010.01.032

Klungland, A., and Dahl, J. A. (2014). Dynamic RNA modifications in disease. *Curr. Opin. Genet. Dev.* 26, 47–52. doi: 10.1016/j.gde.2014.05.006

Kriaucionis, S., and Heintz, N. (2009). The nuclear DNA base 5-hydroxymethylcytosine is present in purkinje neurons and the brain. *Science* 324, 929–930. doi: 10.1126/science.1169786

LaSalle, J. M., Powell, W. T., and Yasui, D. H. (2013). Epigenetic layers and players underlying neurodevelopment. *Trends Neurosci.* 36, 460–470. doi: 10.1016/j.tins.2013.05.001

Lee, M., Kim, B., and Kim, V. N. (2014). Emerging roles of RNA modification: m(6)A and U-tail. *Cell* 158, 980–987. doi: 10.1016/j.cell.2014.08.005

Legnini, I., Di Timoteo, G., Rossi, F., Morlando, M., Briganti, F., Sthandier, O., et al. (2017). Circ-ZNF609 Is a circular RNA that can be translated and functions in myogenesis. *Mol. Cell* 66, 22.e9–37.e9. doi: 10.1016/j.molcel.2017.02.017

Levenson, J. M., Roth, T. L., Lubin, F. D., Miller, C. A., Huang, I. C., Desai, P., et al. (2006). Evidence that DNA (cytosine-5) methyltransferase regulates synaptic plasticity in the hippocampus. *J. Biol. Chem.* 281, 15763–15773. doi: 10.1074/jbc.M511767200

Li, L., Zang, L., Zhang, F., Chen, J., Shen, H., Shu, L., et al. (2017). Fat mass and obesity-associated (FTO) protein regulates adult neurogenesis. *Hum. Mol. Genet.* 26, 2398–2411. doi: 10.1093/hmg/ddx128

Li, X., Zhu, P., Ma, S., Song, J., Bai, J., Sun, F., et al. (2015). Chemical pulldown reveals dynamic pseudouridylation of the mammalian transcriptome. *Nat. Chem. Biol.* 11, 592–597. doi: 10.1038/nchembio.1836

Li, Z., Huang, C., Bao, C., Chen, L., Lin, M., Wang, X., et al. (2015). Exon-intron circular RNAs regulate transcription in the nucleus. *Nat. Struct. Mol. Biol.* 22, 256–264. doi: 10.1038/nsmb.2959

Li, Z., Weng, H., Su, R., Weng, X., Zuo, Z., Li, C., et al. (2017). FTO plays an oncogenic role in acute myeloid leukemia as a n6-methyladenosine rna demethylase. *Cancer Cell* 31, 127–141. doi: 10.1016/j.ccell.2016.11.017

Liang, D., and Wilusz, J. E. (2014). Short intronic repeat sequences facilitate circular RNA production. *Genes Dev.* 28, 2233–2247. doi: 10.1101/gad.251926.114

Lin, S., Choe, J., Du, P., Triboulet, R., and Gregory, R. I. (2016). The m(6)A methyltransferase METTL3 promotes translation in human cancer cells. *Mol. Cell* 62, 335–345. doi: 10.1016/j.molcel.2016.03.021

Linder, B., Grozhik, A. V., Olarerin-George, A. O., Meydan, C., Mason, C. E., and Jaffrey, S. R. (2015). Single-nucleotide-resolution mapping of m^6A and m^6Am throughout the transcriptome. *Nat. Methods* 12, 767–772. doi: 10.1038/nmeth.3453

Liu, J., Yue, Y., Han, D., Wang, X., Fu, Y., Zhang, L., et al. (2014). A METTL3-METTL14 complex mediates mammalian nuclear RNA N6-adenosine methylation. *Nat. Chem. Biol.* 10, 93–95. doi: 10.1038/nchembio.1432

Liu, N., Dai, Q., Zheng, G., He, C., Parisien, M., and Pan, T. (2015). N(6)-methyladenosine-dependent RNA structural switches regulate RNA-protein interactions. *Nature* 518, 560–564. doi: 10.1038/nature14234

Lu, D., and Xu, A. D. (2016). Mini review: circular rnas as potential clinical biomarkers for disorders in the central nervous system. *Front. Genet.* 7:53. doi: 10.3389/fgene.2016.00053

Luo, S., and Tong, L. (2014). Molecular basis for the recognition of methylated adenines in RNA by the eukaryotic YTH domain. *Proc. Natl. Acad. Sci. U.S.A.* 111, 13834–13839. doi: 10.1073/pnas.1412742111

Maag, J. L., Kaczorowski, D. C., Panja, D., Peters, T. J., Bramham, C. R., Wibrand, K., et al. (2017). Widespread promoter methylation of synaptic plasticity genes in long-term potentiation in the adult brain in vivo. *BMC Genomics* 18:250. doi: 10.1186/s12864-017-3621-x

Maden, B. E. (1990). The numerous modified nucleotides in eukaryotic ribosomal RNA. *Prog. Nucleic Acid Res. Mol. Biol.* 39, 241–303. doi: 10.1016/s0079-6603(08)60629-7

Massart, R., Freyburger, M., Suderman, M., Paquet, J., El Helou, J., Belanger-Nelson, E., et al. (2014). The genome-wide landscape of DNA methylation and hydroxymethylation in response to sleep deprivation impacts on synaptic plasticity genes. *Transl. Psychiatry* 4:e347. doi: 10.1038/tp.2013.120

McQuown, S. C., Barrett, R. M., Matheos, D. P., Post, R. J., Rogge, G. A., Alenghat, T., et al. (2011). HDAC3 is a critical negative regulator of long-term memory formation. *J. Neurosci.* 31, 764–774. doi: 10.1523/jneurosci.5052-10.2011

Melo, S. A., Sugimoto, H., O'Connell, J. T., Kato, N., Villanueva, A., Vidal, A., et al. (2014). Cancer exosomes perform cell-independent microRNA biogenesis and promote tumorigenesis. *Cancer Cell* 26, 707–721. doi: 10.1016/j.ccell.2014.09.005

Memczak, S., Jens, M., Elefsinioti, A., Torti, F., Krueger, J., Rybak, A., et al. (2013). Circular RNAs are a large class of animal RNAs with regulatory potency. *Nature* 495, 333–338. doi: 10.1038/nature11928

Meng, S., Zhou, H., Feng, Z., Xu, Z., Tang, Y., Li, P., et al. (2017). CircRNA: functions and properties f a novel potential biomarker for cancer. *Mol. Cancer* 16:94. doi: 10.1186/s12943-017-0663-662

Meyer, K. D., Patil, D. P., Zhou, J., Zinoviev, A., Skabkin, M. A., Elemento, O., et al. (2015). 5' UTR m(6)A Promotes Cap-Independent Translation. *Cell* 163, 999–1010. doi: 10.1016/j.cell.2015.10.012

Meyer, K. D., Saletore, Y., Zumbo, P., Elemento, O., Mason, C. E., and Jaffrey, S. R. (2012). Comprehensive analysis of mRNA methylation reveals enrichment in 3' UTRs and near stop codons. *Cell* 149, 1635–1646. doi: 10.1016/j.cell.2012.05.003

Mohn, F., Weber, M., Rebhan, M., Roloff, T. C., Richter, J., Stadler, M. B., et al. (2008). Lineage-specific polycomb targets and de novo DNA methylation define restriction and potential of neuronal progenitors. *Mol. Cell* 30, 755–766. doi: 10.1016/j.molcel.2008.05.007

Narayan, P., and Dragunow, M. (2017). Alzheimer's disease and histone code alterations. *Adv. Exp. Med. Biol.* 978, 321–336. doi: 10.1007/978-3-319-53889-1_17

Niu, Y., Zhao, X., Wu, Y. S., Li, M. M., Wang, X. J., and Yang, Y. G. (2013). N6-methyl-adenosine (m^6A) in RNA: an old modification with a novel epigenetic function. *Genomics Proteom. Bioinform.*11, 8–17. doi: 10.1016/j.gpb.2012.12.002

Ofengand, J. (2002). Ribosomal RNA pseudouridines and pseudouridine synthases. *FEBS Lett.* 514, 17–25. doi: 10.1016/s0014-5793(02)02305-0

Olave, I. A., Reck-Peterson, S. L., and Crabtree, G. R. (2002). Nuclear actin and actin-related proteins in chromatin remodeling. *Annu. Rev. Biochem.* 71, 755–781. doi: 10.1146/annurev.biochem.71.110601.135507

Ouyang, Y. B., Stary, C. M., Yang, G. Y., and Giffard, R. (2013). MicroRNAs: innovative targets for cerebral ischemia and stroke. *Curr. Drug Targets* 14, 90–101.

Pal, S., and Tyler, J. K. (2016). Epigenetics and aging. *Sci. Adv.* 2:e1600584. doi: 10.1126/sciadv.1600584

Pamudurti, N. R., Bartok, O., Jens, M., Ashwal-Fluss, R., Stottmeister, C., Ruhe, L., et al. (2017). Translation of CircRNAs. *Mol. Cell* 66, 9.e7–21.e7. doi: 10.1016/j.molcel.2017.02.021

Patil, D. P., Chen, C. K., Pickering, B. F., Chow, A., Jackson, C., Guttman, M., et al. (2016). m(6)A RNA methylation promotes XIST-mediated transcriptional repression. *Nature* 537, 369–373. doi: 10.1038/nature19342

Pendleton, K. E., Chen, B., Liu, K., Hunter, O. V., Xie, Y., Tu, B. P., et al. (2017). The U6 snRNA m^6A methyltransferase METTL16 regulates SAM synthetase intron retention. *Cell* 169, 824.e14–835.e14. doi: 10.1016/j.cell.2017.05.003

Ping, X. L., Sun, B. F., Wang, L., Xiao, W., Yang, X., Wang, W. J., et al. (2014). Mammalian WTAP is a regulatory subunit of the RNA N6-methyladenosine methyltransferase. *Cell Res.* 24, 177–189. doi: 10.1038/cr.2014.3

Piwecka, M., and Glazar, P. (2017). Loss of a mammalian circular RNA locus causes miRNA deregulation and affects brain function. *Science* 357:eaam8526. doi: 10.1126/science.aam8526

Podobinska, M., Szablowska-Gadomska, I., Augustyniak, J., Sandvig, I., Sandvig, A., and Buzanska, L. (2017). Epigenetic modulation of stem cells in neurodevelopment: the role of methylation and acetylation. *Front. Cell Neurosci.* 11:23. doi: 10.3389/fncel.2017.00023

Poston, R. G., Dunn, C. J., Sarkar, P., and Saha, R. N. (2018). Persistent 6-OH-BDE-47 exposure impairs functional neuronal maturation and alters expression of neurodevelopmentally-relevant chromatin remodelers. *Environ. Epigenet. 4:dvx020*. doi: 10.1093/eep/dvx020

Pulido Fontes, L., Quesada Jimenez, P., and Mendioroz Iriarte, M. (2015). Epigenetics and epilepsy. *Neurologia* 30, 111–118. doi: 10.1016/j.nrl.2014.03.012

Qu, S., Yang, X., Li, X., Wang, J., Gao, Y., Shang, R., et al. (2015). Circular RNA: a new star of noncoding RNAs. *Cancer Lett.* 365, 141–148. doi: 10.1016/j.canlet.2015.06.003

Roundtree, I. A., and He, C. (2016). RNA epigenetics–chemical messages for posttranscriptional gene regulation. *Curr. Opin. Chem. Biol.* 30, 46–51. doi: 10.1016/j.cbpa.2015.10.024

Rybak-Wolf, A., Stottmeister, C., Glazar, P., Jens, M., Pino, N., Giusti, S., et al. (2015). Circular RNAs in the mammalian brain are highly abundant, conserved, and dynamically expressed. *Mol. Cell* 58, 870–885. doi: 10.1016/j.molcel.2015.03.027

Salinas, P. C. (2012). Wnt signaling in the vertebrate central nervous system: from axon guidance to synaptic function. *Cold Spring Harb. Perspect. Biol.* 4 :a008003. doi: 10.1101/cshperspect.a008003

Sando, R., Gounko, N., Pieraut, S., Liao, L., Yates, J., and Maximov, A. (2012). HDAC4 governs a transcriptional program essential for synaptic plasticity and memory. *Cell* 151, 821–834. doi: 10.1016/j.cell.2012.09.037

Schwartz, S., Mumbach, M. R., Jovanovic, M., Wang, T., Maciag, K., Bushkin, G. G., et al. (2014). Perturbation of m^6A writers reveals two distinct classes of mRNA methylation at internal and 5' sites. *Cell Rep.* 8, 284–296. doi: 10.1016/j.celrep.2014.05.048

Shi, Y., Lan, F., Matson, C., Mulligan, P., Whetstine, J. R., Cole, P. A., et al. (2004). Histone demethylation mediated by the nuclear amine oxidase homolog LSD1. *Cell* 119, 941–953. doi: 10.1016/j.cell.2004.12.012

Shimbo, T., Du, Y., Grimm, S. A., Dhasarathy, A., Mav, D., Shah, R. R., et al. (2013). MBD3 localizes at promoters, gene bodies and enhancers of active genes. *PLoS Genet.* 9:e1004028. doi: 10.1371/journal.pgen.1004028

Shimokawa, T., Rahman, M. F., Tostar, U., Sonkoly, E., Stahle, M., Pivarcsi, A., et al. (2013). RNA editing of the GLI1 transcription factor modulates the output of Hedgehog signaling. *RNA Biol.* 10, 321–333. doi: 10.4161/rna.23343

Silverstein, R. A., and Ekwall, K. (2005). Sin3: a flexible regulator of global gene expression and genome stability. *Curr. Genet.* 47, 1–17. doi: 10.1007/s00294-004-0541-545

Starke, S., Jost, I., Rossbach, O., Schneider, T., Schreiner, S., Hung, L. H., et al. (2015). Exon circularization requires canonical splice signals. *Cell Rep.* 10, 103–111. doi: 10.1016/j.celrep.2014.12.002

Sun, W. J., Li, J. H., Liu, S., Wu, J., Zhou, H., Qu, L. H., et al. (2016). RMBase: a resource for decoding the landscape of RNA modifications from high-throughput sequencing data. *Nucleic Acids Res.* 44, D259–D265. doi: 10.1093/nar/gkv1036

Suzuki, H., and Tsukahara, T. (2014). A view of pre-mRNA splicing from RNase R resistant RNAs. *Int. J. Mol. Sci.* 15, 9331–9342. doi: 10.3390/ijms15069331

Takizawa, T., Nakashima, K., Namihira, M., Ochiai, W., Uemura, A., Yanagisawa, M., et al. (2001). DNA methylation is a critical cell-intrinsic determinant of astrocyte differentiation in the fetal brain. *Dev. Cell* 1, 749–758. doi: 10.1016/s1534-5807(01)00101-0

van Montfoort, A. P., Hanssen, L. L., de Sutter, P., Viville, S., Geraedts, J. P., and de Boer, P. (2012). Assisted reproduction treatment and epigenetic inheritance. *Hum. Reprod. Update* 18, 171–197. doi: 10.1093/humupd/dmr047

van Rossum, D., Verheijen, B. M., and Pasterkamp, R. J. (2016). Circular RNAs: novel regulators of neuronal development. *Front. Mol. Neurosci.* 9:74. doi: 10.3389/fnmol.2016.00074

Vasileiou, G., Ekici, A. B., Uebe, S., Zweier, C., Hoyer, J., Engels, H., et al. (2015). Chromatin-remodeling-factor arid1b represses wnt/beta-catenin signaling. *Am. J. Hum. Genet.* 97, 445–456. doi: 10.1016/j.ajhg.2015.08.002

Veno, M. T., Hansen, T. B., Veno, S. T., Clausen, B. H., Grebing, M., Finsen, B., et al. (2015). Spatio-temporal regulation of circular RNA expression during porcine embryonic brain development. *Genome Biol.* 16:245. doi: 10.1186/s13059-015-0801-803

Walters, B. J., Mercaldo, V., Gillon, C. J., Yip, M., Neve, R. L., Boyce, F. M., et al. (2017). The role of the RNA demethylase FTO (Fat Mass and Obesity-Associated) and mRNA Methylation in hippocampal memory formation. Neuropsychopharmacology42, 1502–1510. doi: 10.1038/npp.2017.31

Wang, X., Feng, J., Xue, Y., Guan, Z., Zhang, D., Liu, Z., et al. (2016). Structural basis of N(6)-adenosine methylation by the METTL3-METTL14 complex. *Nature* 534, 575–578. doi: 10.1038/nature18298

Wang, X., Lu, Z., Gomez, A., Hon, G. C., Yue, Y., Han, D., et al. (2014). N6-methyladenosine-dependent regulation of messenger RNA stability. *Nature* 505, 117–120. doi: 10.1038/nature12730

Wang, X., Zhao, B. S., Roundtree, I. A., Lu, Z., Han, D., Ma, H., et al. (2015). N(6)-methyladenosine modulates messenger rna translation efficiency. *Cell* 161, 1388–1399. doi: 10.1016/j.cell.2015.05.014

Wang, Y., Li, Y., Toth, J. I., Petroski, M. D., Zhang, Z., and Zhao, J. C. (2014). N6-methyladenosine modification destabilizes developmental regulators in embryonic stem cells. *Nat. Cell Biol.* 16, 191–198. doi: 10.1038/ncb2902

Washbourne, P. (2015). Synapse assembly and neurodevelopmental disorders. *Neuropsychopharmacology* 40, 4–15. doi: 10.1038/npp.2014.163

Wei, C. M., Gershowitz, A., and Moss, B. (1975). Methylated nucleotides block 5' terminus of HeLa cell messenger RNA. *Cell* 4, 379–386. doi: 10.1016/0092-8674(75)90158-0

Westholm, J. O., Miura, P., Olson, S., Shenker, S., Joseph, B., Sanfilippo, P., et al. (2014). Genome-wide analysis of drosophila circular RNAs reveals their structural and sequence properties and age-dependent neural accumulation. *Cell Rep.* 9, 1966–1980. doi: 10.1016/j.celrep.2014.10.062

Williams, S. R., Aldred, M. A., Der Kaloustian, V. M., Halal, F., Gowans, G., McLeod, D. R., et al. (2010). Haploinsufficiency of HDAC4 causes brachydactyly mental retardation syndrome, with brachydactyly type E, developmental delays, and behavioral problems. *Am. J. Hum. Genet.* 87, 219–228. doi: 10.1016/j.ajhg.2010.07.011

Wu, P., Zuo, X., Deng, H., Liu, X., Liu, L., and Ji, A. (2013). Roles of long noncoding RNAs in brain development, functional diversification and neurodegenerative diseases. *Brain. Res. Bull.* 97, 69–80. doi: 10.1016/j.brainresbull.2013.06.001

Xu, C., Wang, X., Liu, K., Roundtree, I. A., Tempel, W., Li, Y., et al. (2014). Structural basis for selective binding of m^6A RNA by the YTHDC1 YTH domain. *Nat. Chem. Biol.* 10, 927–929. doi: 10.1038/nchembio.1654

Xu, L., Liu, X., Sheng, N., Oo, K. S., Liang, J., Chionh, Y. H., et al. (2017). Three distinct 3-methylcytidine (m^3C) methyltransferases modify tRNA and mRNA in mice and humans. *J. Biol. Chem.* 292, 14695–14703. doi: 10.1074/jbc.M117.798298

Xue, Y., Wong, J., Moreno, G. T., Young, M. K., Cote, J., and Wang, W. (1998). NURD, a novel complex with both ATP-dependent chromatin-remodeling and histone deacetylase activities. *Mol. Cell* 2, 851–861. doi: 10.1016/s1097-2765(00)80299-3

Yang, Y., Fan, X., Mao, M., Song, X., Wu, P., Zhang, Y., et al. (2017). Extensive translation of circular RNAs driven by N6-methyladenosine. *Cell Res.* 27, 626–641. doi: 10.1038/cr.2017.31

Yang, Y., Gao, X., Zhang, M., Yan, S., Sun, C., Xiao, F., et al. (2018). Novel role of FBXW7 Circular RNA in repressing glioma tumorigenesis. *J. Natl. Cancer Inst.* 110. 304–315. doi: 10.1093/jnci/djx166

Yoo, A. S., Staahl, B. T., Chen, L., and Crabtree, G. R. (2009). MicroRNA-mediated switching of chromatin-remodelling complexes in neural development. *Nature* 460, 642–646. doi: 10.1038/nature08139

Yoon, K. J., Ringeling, F. R., Vissers, C., Jacob, F., Pokrass, M., Jimenez-Cyrus, D., et al. (2017). Temporal control of mammalian cortical neurogenesis by m(6)A methylation. *Cell* 171, 877.e17–889.e17. doi: 10.1016/j.cell.2017.09.003

You, X., Vlatkovic, I., Babic, A., Will, T., Epstein, I., Tushev, G., et al. (2015). Neural circular RNAs are derived from synaptic genes and regulated by development and plasticity. *Nat. Neurosci.* 18, 603–610. doi: 10.1038/nn.3975

Yu, A. T., Ge, J., and Yu, Y. T. (2011). Pseudouridines in spliceosomal snRNAs. *Protein Cell* 2, 712–725. doi: 10.1007/s13238-011-1087-1081

Zaghlool, A., Halvardson, J., Zhao, J. J., Etemadikhah, M., Kalushkova, A., Konska, K., et al. (2016). A Role for the chromatin-remodeling factor BAZ1A in neurodevelopment. *Hum. Mutat.* 37, 964–975. doi: 10.1002/humu.23034

Zelinski, E. L., Deibel, S. H., and McDonald, R. J. (2014). The trouble with circadian clock dysfunction: multiple deleterious effects on the brain and body. *Neurosci. Biobehav. Rev.* 40, 80–101. doi: 10.1016/j.neubiorev.2014.01.007

Zhang, X. O., Wang, H. B., Zhang, Y., Lu, X., Chen, L. L., and Yang, L. (2014). Complementary sequence-mediated exon circularization. *Cell* 159, 134–147. doi: 10.1016/j.cell.2014.09.001

Zhang, X., and Jia, G. F. (2016). RNA epigenetic modification: N6-methyladenosine. *Yi Chuan* 38. 275–288. doi: 10.16288/j.yczz.16-049

Zhang, Y., Gilquin, B., Khochbin, S., and Matthias, P. (2006). Two catalytic domains are required for protein deacetylation. *J. Biol. Chem.* 281, 2401–2404. doi: 10.1074/jbc.C500241200

Zhang, Y., Zhang, X. O., Chen, T., Xiang, J. F., Yin, Q. F., Xing, Y. H., et al. (2013). Circular intronic long noncoding RNAs. *Mol. Cell* 51, 792–806. doi: 10.1016/j.molcel.2013.08.017

Zhang, Z., Theler, D., Kaminska, K. H., Hiller, M., de la Grange, P., Pudimat, R., et al. (2010). The YTH domain is a novel RNA binding domain. *J. Biol. Chem.* 285, 14701–14710. doi: 10.1074/jbc.M110.104711

Zhao, X., Yang, Y., Sun, B. F., Shi, Y., Yang, X., Xiao, W., et al. (2014). FTO-dependent demethylation of N6-methyladenosine regulates mRNA splicing and is required for adipogenesis. *Cell Res.* 24, 1403–1419. doi: 10.1038/cr.2014.151

Zheng, G., Dahl, J. A., Niu, Y., Fedorcsak, P., Huang, C. M., Li, C. J., et al. (2013). ALKBH5 is a mammalian RNA demethylase that impacts RNA metabolism and mouse fertility. *Mol. Cell* 49, 18–29. doi: 10.1016/j.molcel.2012.10.015

Zhou, C., Molinie, B., Daneshvar, K., Pondick, J. V., Wang, J., Van Wittenberghe, N., et al. (2017). Genome-wide maps of m^6A circRNAs identify widespread and cell-type-specific methylation patterns that are distinct from mRNAs. *Cell Rep.* 20, 2262–2276. doi: 10.1016/j.celrep.2017.08.027

Zhou, J., Wan, J., Gao, X., Zhang, X., Jaffrey, S. R., and Qian, S. B. (2015). Dynamic m(6)A mRNA methylation directs translational control of heat shock response. *Nature* 526, 591–594. doi: 10.1038/nature15377

Zhu, J., Ye, J., Zhang, L., Xia, L., Hu, H., Jiang, H., et al. (2017). Differential expression of circular RNAs in glioblastoma multiforme and its correlation with prognosis. *Transl. Oncol.* 10, 271–279. doi: 10.1016/j.tranon.2016.12.006

Zhu, T., Roundtree, I. A., Wang, P., Wang, X., Wang, L., Sun, C., et al. (2014). Crystal structure of the YTH domain of YTHDF2 reveals mechanism for recognition of N6-methyladenosine. *Cell Res.* 24, 1493–1496. doi: 10.1038/cr.2014.152

Conflict of Interest Statement: The authors declare that the research was conducted in the absence of any commercial or financial relationships that could be construed as a potential conflict of interest.

Copyright © 2019 Meng, Zhou, Feng, Xu, Tang and Wu. This is an open-access article distributed under the terms of the Creative Commons Attribution License (CC BY). The use, distribution or reproduction in other forums is permitted, provided the original author(s) and the copyright owner(s) are credited and that the original publication in this journal is cited, in accordance with accepted academic practice. No use, distribution or reproduction is permitted which does not comply with these terms.

frontiers in Cellular Neuroscience

REVIEW
published: 30 July 2019
doi: 10.3389/fncel.2019.00339

Cellular Prion Protein as a Receptor of Toxic Amyloid-β42 Oligomers Is Important for Alzheimer's Disease

Yuan Zhang[1], Yanfang Zhao[2], Lei Zhang[1], Wanpeng Yu[1], Yu Wang[1] and Wenguang Chang[1]*

[1] *Institute for Translational Medicine, Qingdao University, Qingdao, China,* [2] *School for Life Science, Institute of Biomedical Research, Shandong University of Technology, Zibo, China*

The pathological features of Alzheimer's disease (AD) include senile plaques induced by amyloid-β (Aβ) protein deposits, neurofibrillary tangles formed by aggregates of hyperphosphorylated tau proteins and neuronal cell loss in specific position within the brain. Recent observations have suggested the possibility of an association between AD and cellular prion protein (PrP^C) levels. PrP^C is a high affinity receptor for oligomeric Aβ and is important for Aβ-induced neurotoxicity and thus plays a critical role in AD pathogenesis. The determination of the relationship between PrP^C and AD and the characterization of PrP^C binding to Aβ will facilitate the development of novel therapies for AD.

Keywords: cellular prion protein, amyloid-β, oligomers, receptor, Alzheimer's disease

OPEN ACCESS

Edited by:
Antonio Gambardella, Università degli Studi Magna Græcia di Catanzaro, Italy

Reviewed by:
Diana Laura Castillo-Carranza, Hampton University, United States
Helmut Kessels, Netherlands Institute for Neuroscience (KNAW), Netherlands

****Correspondence:***
Yuan Zhang
yuan_zhang84@126.com

Specialty section:
This article was submitted to Cellular Neuropathology, a section of the journal Frontiers in Cellular Neuroscience

Received: *21 April 2019*
Accepted: *10 July 2019*
Published: *30 July 2019*

Citation:
Zhang Y, Zhao Y, Zhang L, Yu W, Wang Y and Chang W (2019) Cellular Prion Protein as a Receptor of Toxic Amyloid-β42 Oligomers Is Important for Alzheimer's Disease. Front. Cell. Neurosci. 13:339. doi: 10.3389/fncel.2019.00339

BACKGROUND

Alzheimer's disease (AD) is a progressive neurodegenerative disorder representing the most common cause of dementia in the elderly. The hallmarks of AD include senile plaques induced by amyloid-β (Aβ) protein deposits, neurofibrillary tangles formed by aggregates of hyperphosphorylated tau proteins and neuronal cell loss in specific position within the brain (Di Lazzaro, 2018). Soluble Aβ and prefibrillar oligomers have been recognized as early and key factors in AD-related synaptic dysfunction. It had initially been suspected that Aβ plaques are directly toxic to neurons, however, studies have revealed that the level of Aβ plaque deposits is not closely associated with the severity of AD (Selkoe, 2011). However, recent studies have shown a strong correlation between the oligomeric forms of Aβ and neurotoxicity and the severity of cognitive impairment in AD (Benilova et al., 2012; Kayed and Lasagna-Reeves, 2013).

The physiological prion protein (PrP^C) is an evolutionarily highly conserved protein that is present in all investigated mammals. PrP^C is attached to the outer surface of the cell membrane by a glycosylphosphatidylinositol (GPI)-anchor. PrP^C is a glycoprotein that expressed in the brain and was first reported to be associated with prion diseases (Singh and Udgaonkar, 2015). Recent observations have indicated the possibility of a connection between prion diseases and AD (Onodera, 2017). PrP^C mediates at a certain extent of the toxic effects of Aβ oligomers and thus plays an important role in AD pathogenesis (Salazar and Strittmatter, 2017; Brody and Strittmatter, 2018; Purro et al., 2018). PrP^C is a high affinity receptor for oligomeric Aβ, and the expression of PrP^C is important for Aβ-induced neurotoxicity, as demonstrated by the loss of long-term potentiation (LTP) and memory impairment in AD mouse models (Gimbel et al., 2010; Kostylev et al., 2015). PrP^C deficiency confers resistance to the synaptic toxicity of oligomeric Aβ in mice and *in vitro* in hippocampal slice cultures (Barry et al., 2011). These findings support the hypothesis that the interaction between PrP^C and Aβ is necessary for neurotoxicity and neuronal cell loss in AD.

CHANGES IN PrP^C INVOLVED IN AD PATHOLOGY

Characteristics of Distinct PrP^C Isoforms in AD Brains

PrP^C is an N-glycosylated GPI-anchored protein usually present in lipid rafts, which is variably glycosylated at two highly conserved sites, namely, the asparagine resides at positions 181 and 197 of the human PrP^C (**Figure 1**). Distinct phenotypes and binding domains are characterized by specific mechanisms during AD progression. N-glycan attachment to these sites in PrP^C results in diglycosylated, monoglycosylated and unglycosylated isoforms (Wiseman et al., 2015). The ratios of diglycosylated, monoglycosylated and unglycosylated PrP^C have been shown to be variable in AD brains.

Velayos et al. (2009) found that the unglycosylated isoform predominates in AD patients, unlike in controls, indicating a shift in the profile of PrP^C glycosylation in AD pathological progression. Saijo et al. (2011) also observed significantly higher levels of unglycosylated PrP^C in the temporal cortex of amnestic mild cognitive impairment (aMCI) patients, but not of mild AD (mAD) patients, compared to that of NCI and AD patients. The higher levels of the unglycosylated isoform compared to the other isoforms in AD patients supports the hypothesis that the presence of certain glycosylation forms has a critical role in AD.

Additionally, Zafar et al. (2017) demonstrated a significant 1.2-fold decrease in the levels of diglycosylated PrP^C isoforms in rapidly progressive AD (rpAD) patients compared to controls but significantly increased total PrP^C levels in slow progressive AD (spAD) and rpAD patients. This study indicates that posttranslationally modified PrP^C isoforms are changed in the different pathological processes of AD, revealing that the different phenotypes of PrP^C may be risk factors for the slow or rapid progression of AD pathology.

Extensive structural analysis has shown that the unglycosylated fragment of residues 90–231 PrP^C lacks the flexible N-terminal part of the protein (Wuthrich and Riek, 2001). Studies have indicated the energetic stabilization of the structural region of PrP^C in residues 127–227 due to the consequence of the presence of an N-glycan at Asn^{197}. In contrast, an N-glycan at Asn^{181}, which is located in a stable secondary structure, does not influence PrP^C conformation but may play a functional role (Zuegg and Gready, 2000; Ermonval et al., 2003). Thus, this evidence indicates that distinct PrP^C isoforms are involved in the association of altered PrP^C interacting proteins with AD pathology. The glycosylation pattern of PrP^C, which may become a potential diagnostic biomarker for pathology, is related to the severity of AD.

Altered Levels of PrP^C Involved in AD Pathology

PrP^C play an important role in the pathogenesis of AD. Some pathological evidence indicates that PrP^C deposits often accompany Aβ plaques in AD (Schwarze-Eicker et al., 2005; Takahashi et al., 2011). The importance of the association between PrP^C and Aβ is greatly strengthened when it was demonstrated that PrP^C was the receptor for the high affinity to Aβ42 oligomers on cells (Purro et al., 2018).

Reported data suggest a regulatory influence of PrP^C expression in the pathological process of AD. The altered expression of PrP^C in aging and the development of AD are associated with disease progression, and it has been observed that PrP^C is decreased in the hippocampus and temporal cortex in aging and sporadic AD but not in familial AD, suggesting that PrP^C expression reduced reflects a main mechanism of disease and is not merely a minor consequence of other AD-associated changes (Whitehouse et al., 2010). In a study by Velayos et al. (2009), there was a tendency for a lower expression of PrP^C in AD patients than in healthy patients, which indicated that existing PrP^C expression may play a protective role in AD.

In addition, other studies have focused on PrP^C expression level alterations in advanced stages of AD, mainly stage Braak III to VI, most likely due to neuronal loss. Vergara et al. (2015) demonstrated that, in AD patients with Braak stages I–VI, PrP^C protein expression in the brain increases in the early stages of AD and peaks at approximately stage III. Thereafter, PrP^C expression decreases until the manifestation of clinical symptoms in both cases (Vergara et al., 2015).

However, there are some conflicting results regarding the elevation of membrane-binding PrP^C levels in brain tissue of AD patients compared with that of patients with mild cognitive impairment (MCI) or no cognitive impairment (NCI) (Larson et al., 2012; Beland et al., 2014). There have also been some studies showing that there is no significant diversity in the expression level of PrP^C between AD patients and healthy people (Saijo et al., 2011; Dohler et al., 2014; Abu Rumeileh et al., 2017). The discrepancy may due to the lack of specificity of the assay for the prion protein. Diglycosylated fragments overlap with mono- and nonglycosylated forms of full-length PrP^C, which may potentially affect the quantification of PrP^C levels and explain the discrepancy. As Saijo et al. (2011) further demonstrated, there were no differences in total PrP^C levels, however, the glycosylated forms were observed to be significantly changed in AD.

These studies reinforce the hypothesis that changes in PrP^C levels are critical for AD pathological development. Clarifying the possible relationship between cognitive decline, PrP^C expression and differentially glycosylated PrP^C is extremely important for the identification of AD.

PrP^C MEDIATES NEUROTOXICITY BY Aβ OLIGOMERS

Regions of PrP^C Involved in Binding to Aβ

The crucial role of PrP^C in neurodegeneration, especially in AD, is complex. The distinct functions of the various domains of PrP^C have been associated with determining the early trigger of AD pathophysiology. The amino-terminal octapeptide repeat domain of PrP^C (resides 60–95) participates in extracellular copper ion binding (Viles et al., 1999; Jackson et al., 2001). The unstructured central domain of PrP^C (residues 95–134)

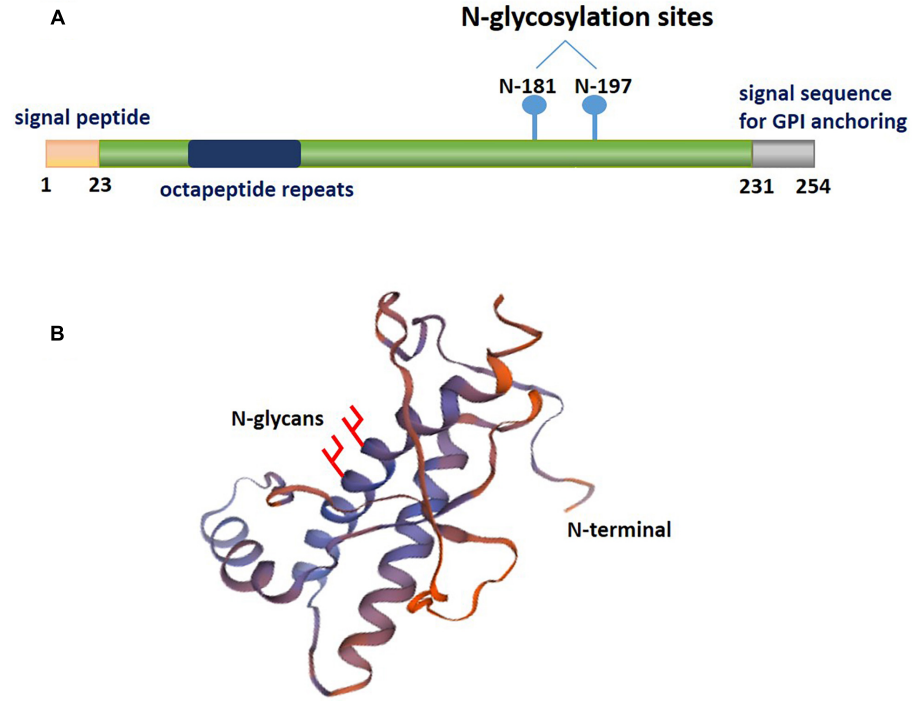


FIGURE 1 | A schematic illustrating the posttranslational modifications of PrP^C. The relative size and localization of N-glycans in a schematic representation of the structural domains of PrP^C. **(A)** The structure of PrP^C can be divided into two distinct domains: a disordered N-terminal domain and an α-helical C-terminal domain. The N-terminal domain include a positively charged region at the N-terminus that is important for the endocytosis of PrP^C, octapeptide repeats that allow PrP^C to bind ions, and a hydrophobic tract. The C-terminal domain consists of three α-helices and two short β-strands. This domain is also the site of posttranslational modifications in PrP^C; up to two N-glycans are added to the α-helical domain, and a GPI anchor at the C-terminus attaches PrP^C to the outer surface of the plasma membrane. **(B)** The three-dimensional structure of residues 90-31 of recombinant human PrP^C (PDB #2lsb.1.A), as determined by NMR spectroscopy.

contains a charge cluster (residues 95–110) and a segment with hydrophobic character (residues 112–134), which has been implicated in playing a critical role in neurodegenerative activity (Baumann et al., 2007; Li et al., 2007; Lauren et al., 2009).

Several independent studies have shown that the interaction of Aβ oligomers with the N-terminal residues of the PrP^C protein region appears critical for neuronal toxicity (Lauren et al., 2009). The PrP^C-Aβ42 interaction provides important mechanistic insights into the pathophysiology of AD-related neurodegeneration. Dohler et al. showed that PrP^C-Aβ binding always occurs in AD brains and is never detected in nondemented controls and that the binding of Aβ aggregates to PrP^C is restricted to the N-terminus of PrP^C (Dohler et al., 2014). Antibodies targeting PrP^C N-terminal residues can prevent synaptic plasticity deficits induced by Aβ oligomers (Didonna et al., 2015). For instance, Lauren et al. (2009) found that the deletion of residues 32–121 of PrP^C abrogates binding to Aβ42 oligomers, indicating that the globular domain alone cannot mediate the role of binding to Aβ. The hydrophobic region of PrP^C (residues 105–125) is not an essential determinant for binding activity due to this region binds Aβ42 oligomers in a way that is indistinguishable from its binding to full-length PrP^C and further the Δ32–106 variant was similar to the Δ32–121 variant, having no Aβ42-oligomer affinity (Lauren et al., 2009). Pretreatment with an antibody against residues 93–109 of PrP^C, 6D11, can prevent neuronal cell death by oligomeric Aβ42 and rescues cognitive deficits in APP/PS1 transgenic mice, while another antibody against residues 144–152 of PrP^C, 6H4, fails to block oligomeric Aβ-induced neuronal toxicity (Chung et al., 2010; Kudo et al., 2012). Recently, another antibody against resides 23–111 of PrP^C was reported to rescue synapses and cognitive deficits in APP/PS1 mice (Cox et al., 2019).

The addition of a synthetic peptide of PrP^C residues 98–107 can reduce the neurotoxicity of Aβ oligomers in primary hippocampal cells, whereas the addition of a peptide of PrP^C residues 213–230 has no effect on Aβ-induced neurotoxicity (Kudo et al., 2012). Blocking residues 95–105 of PrP^C, but not its C-terminal residues, can effectively prevent the inhibition of LTP (Barry et al., 2011; Larson et al., 2012). In addition, Chen et al. indicated that both N-terminal residues 23–27 region and the 92–110 region, which are critically important for PrP^C interactions with Aβ42 oligomers because the deletion of either of these regions results in a major loss of binding, are highly flexible and natively unstructured (Chen et al., 2010). Zou et al. demonstrated three Aβ42-specific PrP^C peptide regions, including N-terminal residues 47–59, 53–65, and 87–99, as well as three Aβ42-nonspecific peptides, including residues 25–37, 37–49, and 99–111 from the N-terminal domain of PrP^C. These Aβ42-specific binding sites are localized in the octapeptide repeat region of the unstructured N-terminal domain. The regions

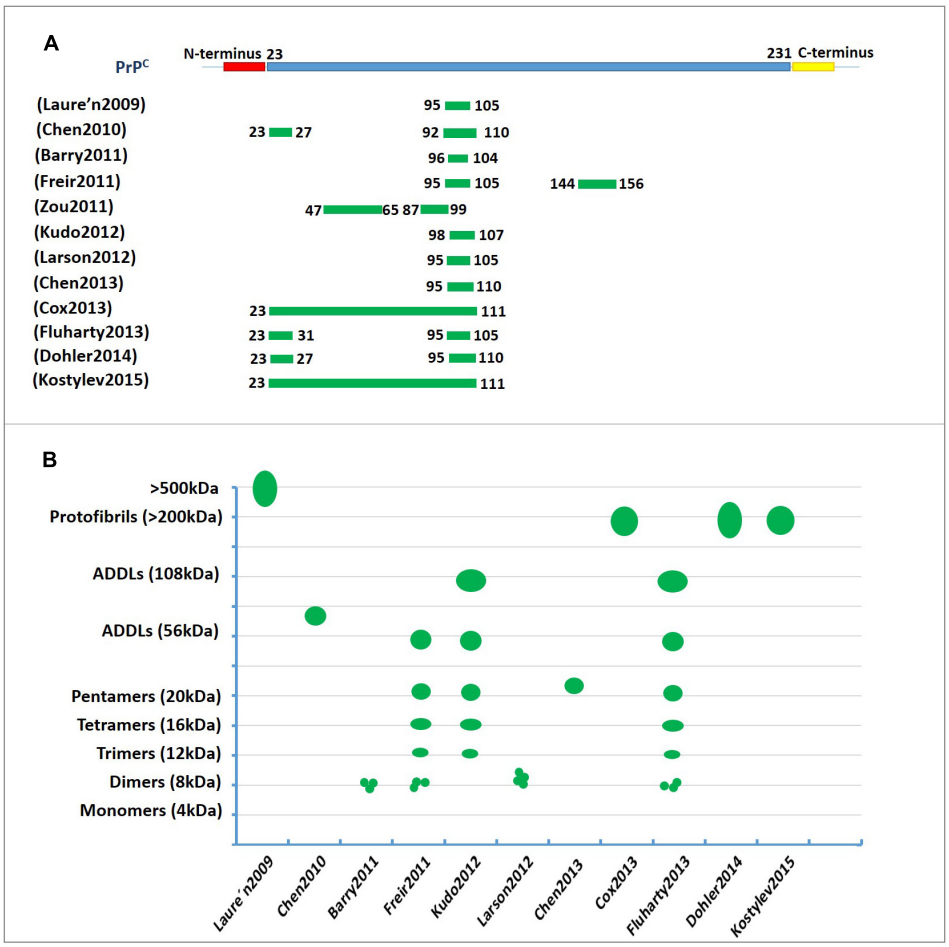


FIGURE 2 | The characterization of PrP^C binding to Aβ42. **(A)** The regions involved in PrP^C binding to amyloid-β (Aβ). The green lines represent the amino acid sequence of PrP^C involved in binding to Aβ. The residue 95–110 region of PrP^C contains the critical amino acid sequence for binding oligomeric Aβ. **(B)** A diagram depicting the binding of amyloid-β (Aβ) in various aggregation states to PrP^C. The green represents the molecular weights of Aβ assemblies bound to PrP^C published in previous studies. The Y-axis represents the molecular weight of the various Aβ42 oligomers. ADDL, Aβ-derived diffusible ligand.

have important implications regarding the pathophysiological consequences of Aβ-PrP^C interactions (Zou et al., 2011).

Collectively, these studies strongly suggest that N-terminal residues 23–27 and the 95–110 region of PrP^C contain the critical amino acid binding sequence for oligomer Aβ-induced synaptic impairment and neuronal cell death (**Figure 2A** and **Table 1**). These soluble recombinant PrP proteins and their fragments are strong inhibitors of the cytotoxic and synaptotoxic effects of Aβ42. The identification of specific huPrP regions that are crucial for the interaction with Aβ may also contribute to the development of therapeutic strategies for targeting this interaction.

PrP^C-Aβ- Binding Assemblies

For decades, research on the molecular mechanism of AD has focused on the compositions of the plaques that are one of the characteristics of the disease (Gouras et al., 2010, 2015). In recent years, it has been found that low molecular weight Aβ aggregates form as Aβ oligomers, and highly structured protofibrils have now emerged as the key neurotoxins in AD (Sakono and Zako, 2010; Brouillette, 2014).

Membrane-binding PrP^C, as a receptor for Aβ oligomers, has been demonstrated to be involved in regulating LTP in the hippocampus, which is induced by oligomeric Aβ42. Recently, it was found that PrP^C can interact not only with the oligomeric form of Aβ, but also with other forms. For example, synthetic Aβ oligomers, Aβ-derived diffusible ligands (ADDLs) and soluble extracts from AD brains have been reported to interact with PrP^C, yet all of these forms of Aβ are unsuccessful at abolishing LTP in PrP-null mice (Freir et al., 2011). Zou et al. (2011) demonstrated that recombinant human PrP (huPrP) also exhibits high affinity and specificity for Aβ42 oligomers from brain extracts of AD patients, and recombinant huPrP may represent an intrinsic molecular spectrum of PrP^C *in vivo*. The inhibition of LTP by human brain extracts containing dimeric amyloid-β is prevented by an antibody fragment (Fab) directed to PrP^C *in vivo* in rats (Barry et al., 2011). Further findings indicate that fragments of the PrP^C protein can prevent

deficits in synaptic plasticity and neuronal death induced by toxic dimers and trimers of Aβ oligomers species (Scott-McKean et al., 2016). The above studies have revealed that the interaction of certain amyloid species with PrP^C leads to neuronal degeneration, and these Aβ species are oligomeric forms with low molecular weights.

Recently, studies have indicated that neurotoxins comprise high molecular weight Aβ assemblies, referred to as ADDLs, which are found to impair synaptic plasticity and memory dysfunction in AD. PrP^C has also been shown to bind to ADDLs, which are tightly related with cognitive impairment in multiple mouse models of Alzheimer's disease (Fluharty et al., 2013; Kostylev et al., 2015). Freir et al. demonstrated that PrP^C is a major component for the inhibition of LTP by ADDLs from AD brains, which is consistent with research showing that oligomeric Aβ assemblies bind with strong specificity to PrP^C to trigger the disruption of synaptic plasticity *in vitro* and *in vivo* (Freir et al., 2011; Kostylev et al., 2015).

However, a separate study indicated that PrP^C shows strong binding to high molecular mass assemblies of Aβ (158–300 kDa) derived from the brains of Alzheimer's disease patients, but not to small synthetic oligomeric Aβ42 (Dohler et al., 2014). It is possible Aβ protofibrils or high molecular mass assemblies correlate better than either globular oligomers or amyloid fibrils with PrP^C binding. High molecular mass assemblies are not simply chains of globular oligomers, but instead contain a defined triple helical nanotube structure that may relate to their specific PrP^C-dependent toxicity (Nicoll et al., 2013; Purro et al., 2018). It is possible that the connections of Aβ42 and PrP^C are not exclusive, and other sterically similar β-sheet rich assemblies might interact with and signal through PrP^C (Resenberger et al., 2011).

Thus, PrP^C appears to be important to mediate the plasticity impairments induced by certain Aβ species or conformations that must be clarified in the future. **Figure 2B** and **Table 1** show the molecular weights and aggregation states of Aβ42 binding to PrP^C currently. Dimers, ∼108 kDa oligomers and ADDLs display a much higher ability to interact with PrP^C.

Characterization of Soluble and Insoluble Aβ in AD

The major components of Aβ aggregates that form in AD brain are neuritic plaques, diffuse amyloid, and vascular amyloid. A variety of other assemblies including Aβ protofibrils and soluble oligomers of various sizes have also been identified (Caughey and Lansbury, 2003; Haass and Selkoe, 2007). Evidence suggests that Aβ oligomers are soluble and may spread throughout the brain, yet amyloid fibrils are larger and insoluble and may assemble into amyloid plaques (Ferreira et al., 2015). However, the present findings strongly support that soluble Aβ oligomers are more detrimental to synaptic plasticity.

Aβ oligomers are categorized by molecular weight as low-molecular-weight (LMW) oligomers ranging from dimers-tetramers and high-molecular-weight (HMW) oligomers ranging from ∼50 to 150 kDa (Figueiredo et al., 2013). A recent study indicated that LMW and HMW oligomers have differential binding affinities for neurons and neurotoxicity. LMW oligomers acutely impair synaptic plasticity, whereas HMW oligomers induce neuronal oxidative stress via activation of NMDA receptors (Wisniewski et al., 2011).

However, other studies have shown that both soluble and insoluble fractions of brain homogenates bind to PrP^C in transgenic mouse models of AD (Zou et al., 2011; Larson et al., 2012). Dohler et al. (2014) demonstrated that optimal binding to PrP^C occurs in the insoluble fraction of Aβ. Their data show that Aβ is present as insoluble oligomers in all tested high molecular weight fractions. Another study using AD and healthy brains also showed the preferential binding of high molecular weight Aβ42 assemblies to PrP^C, which occurs mainly in the insoluble fraction of Aβ, in AD (Zou et al., 2011).

In fact, the composition, concentration and purity of Aβ samples from AD brains are always different. For synthetic

TABLE 1 | The characterization of PrP^C binding to Aβ42.

Studies	The positions of PrP^C binding to Aβ	The forms and sources of Aβ42		Detection methods
Lauren et al., 2009	PrP^C 95–105	Oligomers (∼500 kDa)	Synthesized	SEC
Chen et al., 2010	PrP^C 23–27, PrP^C 92–110	Oligomers (>75 kDs)	Synthesized	AFM
Barry et al., 2011	PrP^C 96–104	Dimers (8 kDs)	Brain-derived	WB
Freir et al., 2011	PrP^C 95–105, helix-1 (PrP^C 144–156)	ADDLs (8∼56 kDs)	Synthesized/brain-derived	SEC
Zou et al., 2011	PrP^C 47–59, PrP^C 53–65, PrP^C 87–99	Oligomers	Brain-derived	SEC
Kudo et al., 2012	PrP^C 98–107	ADDLs (trimer∼24 mer, 108 kDa)	Synthesized	AFM/WB
Larson et al., 2012	PrP^C 95–105	Dimers (8∼9 kDa)	Brain-derived	SEC
Chen et al., 2010	PrP^C 95–110	Oligomers (>25 kDs)	Synthesized	TEM/ WB
Cox et al., 2019	PrP^C 23–111	Globulomer AβO (∼200 kDa)	Brain-derived	SEC
Fluharty et al., 2013	PrP^C 23–31, PrP^C 95–105	ADDLs (Dimers 8–108 kDs)	Synthesized	SEC
Dohler et al., 2014	PrP^C 23–27, PrP^C 95–110	Dimers to pentamers (8∼21 kDa)	Synthesized	SEC
		150∼300 kDa	Brain-derived	
Kostylev et al., 2015	PrP^C 23–111	Globulomer AβO (∼200 kDa)	Brain-derived	SEC

Summary of publications identified the regions of PrP^C binding to Aβ42, and the sources and aggregation states of Aβ42 used. AFM, Atomic Force Microscope; SEC, Size exclusion chromatography; TEM, Transmission Electron Microscopy; WB, Western Blot; ADDLs, Aβ-derived diffusible ligand.

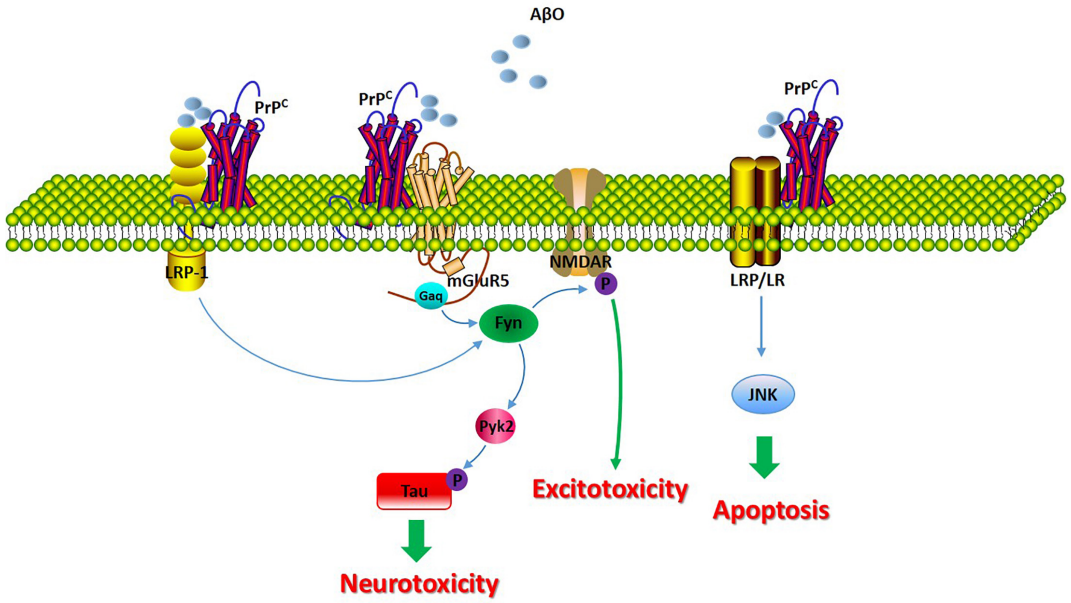


FIGURE 3 | The molecular consequences of the PrP^C/Aβ interaction in AD. The signaling pathway involved in the PrP^C/Aβ interaction in AD. The PrP^C/Aβ complex can interact with mGluR5, LRP1, and LRP/LR. The PrP^C/Aβ complex induces Fyn activation, leading to the further phosphorylation of the NR2B subunit of the NMDA receptor and to the destabilization of dendritic spines. Additionally, Fyn activation of Pyk2 leads to the further phosphorylation of tau. LRP1 functions as a transmembrane coreceptor that is involved in PrP^C/AβO-mediated Fyn activation. LRP/LR is a transmembrane receptor involved in the apoptotic signaling pathway through interactions with PrP^C-Aβ.

Aβ42, small oligomeric species show prominent binding to PrP^C, whereas in AD brains larger protein assemblies containing Aβ42 bind efficiently to PrP^C (Dohler et al., 2014). Furthermore, the natural separation of different Aβ aggregates present in AD brain samples is complex because preparation methods can disrupt and alter the conformation of Aβ assemblies (Stine et al., 2011). Synthetic Aβ is generally soluble, while the Aβ extracted from AD brains may contain both soluble and insoluble fractions (**Table 1**). Some soluble oligomers may bind to other macromolecules or to cell membranes and can therefore become insoluble (Dohler et al., 2014).

In addition, Wildburger et al. (2017) recently found 26 unique proteoforms in soluble and more insoluble Aβ aggregates of AD brain samples, including 73% N-terminal truncations and 30% C-terminal truncations of the total Aβ proteoforms. The Aβ proteoforms segregated between the soluble and more insoluble aggregates, with N-terminal truncations predominating in the insoluble material and C-terminal truncations segregating into the soluble aggregates. This result suggests that the Aβ aggregates in AD are heterogeneous and offers much new evidence for investigation into the pathological mechanisms of AD.

MOLECULAR CONSEQUENCES OF THE PrP^C/AβO INTERACTION IN AD

The molecular and cellular consequences of the PrP^C-Aβ oligomer interaction are dependent on raft-based complexes. The integrity of cholesterol-rich lipid rafts is critical for the interaction between Aβ42 with PrP^C. It has been demonstrated that the PrP^C-mediated toxicity of Aβ oligomers and the activation of downstream pathways require lipid rafts (Rushworth et al., 2013). GPI-anchored PrP^C is localized to the cholesterol-rich lipid raft microdomains of the plasma membrane (Taylor and Hooper, 2006). Cholesterol depletion disrupts these rafts with PrP^C being redistributed into nonraft regions of the membrane (Taylor et al., 2005). A study revealed that the disruption of the rafts causes a significant reduction in Aβ oligomer binding to cells and prevents the activation of Fyn kinase (Rushworth et al., 2013).

A growing body of evidence suggests that PrP^C mediates downstream intracellular processes through many different receptors, including the metabotropic glutamate receptors mGluR1 and mGluR5, the α7 nicotinic acetylcholine receptor, the kainite receptor GluR6/7, and AMPA receptor subunits GluA1 and GluA2 (Zhao et al., 2010; Carulla et al., 2011; Jeong and Park, 2015; Haas and Strittmatter, 2016). These studies indicate that PrP^C functions as an extracellular scaffolding protein that is able to organize multiprotein complexes that mediate intracellular signal transduction at the cell surface.

A separate study implicated group I mGluR signaling in the regulation of Aβ42 toxicity in neurons and in AD mouse models, and Aβ42 oligomers interact with PrP^C to increase metabotropic glutamate receptor 5 (mGluR5)-dependent long-term depression (LTD) and LTP (Hu et al., 2014). Another study showed that the role of the Aβ/PrP^C complex in AD pathophysiology; the complex has been demonstrated to induce intracellular Fyn activation, leading to the further phosphorylation of the NR2B subunit of the N-methyl-D-aspartate (NMDA) receptor and to

the destabilization of dendritic spines (Um et al., 2012; Brody and Strittmatter, 2018). In addition, Pyk2 has been reported to be a downstream effector of PrP^C-Aβ signaling. This study revealed Pyk2 as a direct tyrosine kinase of tau that is active downstream of Fyn (Li and Gotz, 2018).

Recently, the Aβ-PrP^C complex was reported to be internalized into endosomes via low-density lipoprotein 1 (LRP1) in AD. Rushworth et al. (2013) revealed that PrP^C-mediated binding and toxicity and the subsequent PrP^C-mediated internalization of Aβ oligomers are dependent upon LRP1. Research has indicated that LRP1 functions as a transmembrane coreceptor that is involved in the PrP^C-mediated binding of Aβ oligomers (Rushworth et al., 2013).

The laminin receptor (LRP/LR) has been demonstrated to play a significant role in the interaction between Aβ and PrP^C, given that the laminin receptor binds and internalizes PrP^C. The blockade of LRP/LR ameliorates the detrimental effect of PrP^C overexpression on cell viability upon exposure to exogenous Aβ (Pinnock et al., 2016). The binding of Aβ to PrP^C leads to the induction of apoptosis by interacting with LRP/LR, which, as a transmembrane receptor, may influence the activity of the JNK signaling pathway. However, the proapoptotic signals pathways may not be directly transduced by PrP^C, as PrP^C is not a transmembrane protein and therefore must be transduced through other receptors binding to PrP^C, such as LRP/LR (Da Costa Dias et al., 2014).

Thus, further investigations have been made to expound these complex and their downstream pathways to prevent neurotoxic consequences (**Figure 3**).

CONCLUSION

Currently most researches show that PrP^C may play an important role in the pathogenesis of AD. There is a connection between AD and PrP^C levels. PrP^C, as a high affinity receptor for oligomeric Aβ and ADDLs (8∼108 kDa), is essential for Aβ-induced synaptic toxicity. N-terminal residues 23–27 and the 95–110 region of PrP^C contain the critical amino acid sequence for oligomer Aβ-induced synaptic impairment and neuronal cell death.

However, there is some controversy about the neurotoxicity of PrP^C. Some literature reports that PrP^C deletion does not inhibit the toxic effects of Aβ oligomers. For example, Balducci et al. (2010) demonstrated that Aβ oligomers induced *in vivo* memory impairment and bound PrP^C with high affinity but found that PrP^C is not responsible for the recognition impairment in AD induced by Aβ. However, others have reported that PrP^C is a key receptor mediating toxic effects, but these assumption have not been confirmed (Larson et al., 2012). Perhaps PrP^C is not the unique receptor that mediates synaptic damage induced by Aβ oligomers. PrP^C has been involved in neurotoxic signaling with high-affinity binding to Aβ oligomers, suggesting that the interaction of PrP^C with Aβ is part of a common molecular pathway. The most recent investigations indicated the existence of a strong interaction between Aβ oligomers and PrP^C and suggest that this interaction may impact synaptic plasticity functions. Further investigations will be necessary to clarify the involvement of PrP^C in the neuropathology of AD. The identification of specific huPrP regions that are crucial for the interaction with Aβ may also contribute to the development of therapeutic strategies that target this interaction.

AUTHOR CONTRIBUTIONS

YuZ conceived and designed the manuscript. YuZ, YaZ, and LZ analyzed and collected the literature. WY, YW, and WC collected the literature. YuZ wrote the review. All authors revised the manuscript.

FUNDING

This work was supported by funding from the Qingdao Applied Basic Research Project (No.18-2-2-48-jch), Shandong Provincial Natural Science Foundation of China (No. ZR2016CQ23), and National Natural Science Foundation of China (No. 81603357).

REFERENCES

Abu Rumeileh, S., Lattanzio, F., Stanzani Maserati, M., Rizzi, R., Capellari, S., and Parchi, P. (2017). Diagnostic Accuracy of a Combined Analysis of Cerebrospinal Fluid t-PrP, t-tau, p-tau, and Abeta42 in the Differential Diagnosis of Creutzfeldt-Jakob Disease from Alzheimer's Disease with Emphasis on Atypical Disease Variants. *J. Alzheimer's Dis.* 55, 1471–1480. doi: 10.3233/JAD-160740

Balducci, C., Beeg, M., Stravalaci, M., Bastone, A., Sclip, A., Biasini, E., et al. (2010). Synthetic amyloid-beta oligomers impair long-term memory independently of cellular prion protein. *Proc. Natl. Acad. Sci.U.S.A.* 107, 2295–2300. doi: 10.1073/pnas.0911829107

Barry, A. E., Klyubin, I., Mc Donald, J. M., Mably, A. J., Farrell, M. A., Scott, M., et al. (2011). Alzheimer's disease brain-derived amyloid-beta-mediated inhibition of LTP in vivo is prevented by immunotargeting cellular prion protein. *J. Neurosci.* 31, 7259–7263. doi: 10.1523/JNEUROSCI.6500-10.2011

Baumann, F., Tolnay, M., Brabeck, C., Pahnke, J., Kloz, U., Niemann, H. H., et al. (2007). Lethal recessive myelin toxicity of prion protein lacking its central domain. *EMBO J.* 26, 538–547. doi: 10.1038/sj.emboj.7601510

Beland, M., Bedard, M., Tremblay, G., Lavigne, P., and Roucou, X. (2014). Abeta induces its own prion protein N-terminal fragment (PrPN1)-mediated neutralization in amorphous aggregates. *Neurobiol. Aging.* 35, 1537–1548. doi: 10.1016/j.neurobiolaging.2014.02.001

Benilova, I., Karran, E., and De Strooper, B. (2012). The toxic Abeta oligomer and Alzheimer's disease: an emperor in need of clothes. *Nat. Neurosci.* 15, 349–357. doi: 10.1038/nn.3028

Brody, A. H., and Strittmatter, S. M. (2018). Synaptotoxic signaling by amyloid beta oligomers in Alzheimer's disease through prion protein and mGluR5. *Adv. Pharmacol.* 82, 293–323. doi: 10.1016/bs.apha.2017.09.007

Brouillette, J. (2014). The effects of soluble Abeta oligomers on neurodegeneration in Alzheimer's disease. *Curr. Pharm. Design.* 20, 2506–2519. doi: 10.2174/13816128113199990498

Carulla, P., Bribian, A., Rangel, A., Gavin, R., Ferrer, I., Caelles, C., et al. (2011). Neuroprotective role of PrPC against kainate-induced epileptic seizures and cell death depends on the modulation of JNK3 activation by GluR6/7-PSD-95 binding. *Mol. Biol. Cell.* 22, 3041–3054. doi: 10.1091/mbc.E11-04-0321

Caughey, B., and Lansbury, P. T. (2003). Protofibrils, pores, fibrils, and neurodegeneration: separating the responsible protein aggregates from the

innocent bystanders. *Annu. Rev. Neurosci.* 26, 267–298. doi: 10.1146/annurev.neuro.26.010302.081142

Chen, S., Yadav, S. P., and Surewicz, W. K. (2010). Interaction between human prion protein and amyloid-beta (Abeta) oligomers: role OF N-terminal residues. *J. Biol. Chem.* 285, 26377–26383. doi: 10.1074/jbc.M110.145516

Chung, E., Ji, Y., Sun, Y., Kascsak, R. J., Kascsak, R. B., Mehta, P. D., et al. (2010). Anti-PrPC monoclonal antibody infusion as a novel treatment for cognitive deficits in an Alzheimer's disease model mouse. *BMC Neurosci.* 11:130. doi: 10.1186/1471-2202-11-130

Cox, T. O., Gunther, E. C., Brody, A. H., Chiasseu, M. T., Stoner, A., Smith, L. M., et al. (2019). Anti-PrP(C) antibody rescues cognition and synapses in transgenic alzheimer mice. *Ann. Clin. Transl. Neurol.* 6, 554–574. doi: 10.1002/acn3.730

Da Costa Dias, B., Jovanovic, K., Gonsalves, D., Moodley, K., Reusch, U., Knackmuss, S., et al. (2014). The 37kDa/67kDa laminin receptor acts as a receptor for Abeta42 internalization. *Sci. Rep.* 4:5556. doi: 10.1038/srep05556

Di Lazzaro, V. (2018). Emergence of neurophysiological biomarkers of Alzheimer disease. *J. Neurol.Neurosurg.Psychiatry*. 89:1235. doi: 10.1136/jnnp-2018-318867

Didonna, A., Venturini, A. C., Hartman, K., Vranac, T., Curin Serbec, V., and Legname, G. (2015). Characterization of four new monoclonal antibodies against the distal N-terminal region of PrP(c). *PeerJ.* 3:e811. doi: 10.7717/peerj.811

Dohler, F., Sepulveda-Falla, D., Krasemann, S., Altmeppen, H., Schluter, H., Hildebrand, D., et al. (2014). High molecular mass assemblies of amyloid-beta oligomers bind prion protein in patients with Alzheimer's disease. *Brain J. Neurol.* 137, 873–886. doi: 10.1093/brain/awt375

Ermonval, M., Mouillet-Richard, S., Codogno, P., Kellermann, O., and Botti, J. (2003). Evolving views in prion glycosylation: functional and pathological implications. *Biochimie.* 85, 33–45. doi: 10.1016/s0300-9084(03)00040-3

Ferreira, S. T., Lourenco, M. V., Oliveira, M. M., and De Felice, F. G. (2015). Soluble amyloid-beta oligomers as synaptotoxins leading to cognitive impairment in Alzheimer's disease. *Front. Cell. Neurosci.* 9:191. doi: 10.3389/fncel.2015.00191

Figueiredo, C. P., Clarke, J. R., Ledo, J. H., Ribeiro, F. C., Costa, C. V., Melo, H. M., et al. (2013). Memantine rescues transient cognitive impairment caused by high-molecular-weight abeta oligomers but not the persistent impairment induced by low-molecular-weight oligomers. *J. Neurosci.* 33, 9626–9634. doi: 10.1523/JNEUROSCI.0482-13.2013

Fluharty, B. R., Biasini, E., Stravalaci, M., Sclip, A., Diomede, L., Balducci, C., et al. (2013). An N-terminal fragment of the prion protein binds to amyloid-beta oligomers and inhibits their neurotoxicity in vivo. *J. Biol. Chem.* 288, 7857–7866. doi: 10.1074/jbc.M112.423954

Freir, D. B., Nicoll, A. J., Klyubin, I., Panico, S., Mc Donald, J. M., Risse, E., et al. (2011). Interaction between prion protein and toxic amyloid beta assemblies can be therapeutically targeted at multiple sites. *Nat. Commun.* 2:336. doi: 10.1038/ncomms1341

Gimbel, D. A., Nygaard, H. B., Coffey, E. E., Gunther, E. C., Lauren, J., Gimbel, Z. A., et al. (2010). Memory impairment in transgenic Alzheimer mice requires cellular prion protein. *J. Neurosci.* 30, 6367–6374. doi: 10.1523/JNEUROSCI.0395-10.2010

Gouras, G. K., Olsson, T. T., and Hansson, O. (2015). beta-Amyloid peptides and amyloid plaques in Alzheimer's disease. *Neurotherapeutics* 12, 3–11.

Gouras, G. K., Tampellini, D., Takahashi, R. H., and Capetillo-Zarate, E. (2010). Intraneuronal beta-amyloid accumulation and synapse pathology in Alzheimer's disease. *Acta Neuropathol.* 119, 523–541. doi: 10.1007/s00401-010-0679-9

Haas, L. T., and Strittmatter, S. M. (2016). Oligomers of Amyloid beta Prevent Physiological Activation of the Cellular Prion Protein-Metabotropic Glutamate Receptor 5 Complex by Glutamate in Alzheimer Disease. *J. Biol. Chem.* 291, 17112–17121. doi: 10.1074/jbc.M116.720664

Haass, C., and Selkoe, D. J. (2007). Soluble protein oligomers in neurodegeneration: lessons from the Alzheimer's amyloid beta-peptide. *Nat. Rev. Mol. Cell Biol.* 8, 101–112. doi: 10.1038/nrm2101

Hu, N. W., Nicoll, A. J., Zhang, D., Mably, A. J., O'Malley, T., Purro, S. A., et al. (2014). mGlu5 receptors and cellular prion protein mediate amyloid-beta-facilitated synaptic long-term depression in vivo. *Nat. Commun.* 5:3374. doi: 10.1038/ncomms4374

Jackson, G. S., Murray, I., Hosszu, L. L., Gibbs, N., Waltho, J. P., Clarke, A. R., et al. (2001). Location and properties of metal-binding sites on the human prion protein. *Proc. Natl. Acad. Sci. U.S.A.* 98, 8531–8535. doi: 10.1073/pnas.151038498

Jeong, J. K., and Park, S. Y. (2015). Neuroprotective effect of cellular prion protein (PrPC) is related with activation of alpha7 nicotinic acetylcholine receptor (alpha7nAchR)-mediated autophagy flux. *Oncotarget* 6, 24660–24674. doi: 10.18632/oncotarget.4953

Kayed, R., and Lasagna-Reeves, C. A. (2013). Molecular mechanisms of amyloid oligomers toxicity. *J. Alzheimer's Dis.* 33(Suppl. 1), S67–S78.

Kostylev, M. A., Kaufman, A. C., Nygaard, H. B., Patel, P., Haas, L. T., Gunther, E. C., et al. (2015). Prion-Protein-interacting Amyloid-beta Oligomers of High Molecular Weight Are Tightly Correlated with Memory Impairment in Multiple Alzheimer Mouse Models. *J. Biol. Chem.* 290, 17415–17438. doi: 10.1074/jbc.M115.643577

Kudo, W., Lee, H. P., Zou, W. Q., Wang, X., Perry, G., Zhu, X., et al. (2012). Cellular prion protein is essential for oligomeric amyloid-beta-induced neuronal cell death. *Hum. Mol. Genetics.* 21, 1138–1144. doi: 10.1093/hmg/ddr542

Larson, M., Sherman, M. A., Amar, F., Nuvolone, M., Schneider, J. A., Bennett, D. A., et al. (2012). The complex PrP(c)-Fyn couples human oligomeric Abeta with pathological tau changes in Alzheimer's disease. *J. Neurosci.* 32, 16857a–16871a. doi: 10.1523/JNEUROSCI.1858-12.2012

Lauren, J., Gimbel, D. A., Nygaard, H. B., Gilbert, J. W., and Strittmatter, S. M. (2009). Cellular prion protein mediates impairment of synaptic plasticity by amyloid-beta oligomers. *Nature.* 457, 1128–1132. doi: 10.1038/nature07761

Li, A., Christensen, H. M., Stewart, L. R., Roth, K. A., Chiesa, R., and Harris, D. A. (2007). Neonatal lethality in transgenic mice expressing prion protein with a deletion of residues 105-125. *EMBO J.* 26, 548–558. doi: 10.1038/sj.emboj.7601507

Li, C., and Gotz, J. (2018). Pyk2 is a novel tau tyrosine kinase that is regulated by the tyrosine kinase fyn. *J. Alzheimer's Dis.* 64, 205–221. doi: 10.3233/JAD-180054

Nicoll, A. J., Panico, S., Freir, D. B., Wright, D., Terry, C., Risse, E., et al. (2013). Amyloid-beta nanotubes are associated with prion protein-dependent synaptotoxicity. *Nat. Commun.* 4:2416. doi: 10.1038/ncomms3416

Onodera, T. (2017). Dual role of cellular prion protein in normal host and Alzheimer's disease. *Proc. Japan Acad. Ser. BPhys. Biol. Sci.* 93, 155–173. doi: 10.2183/pjab.93.010

Pinnock, E. C., Jovanovic, K., Pinto, M. G., Ferreira, E., Dias Bda, C., Penny, C., et al. (2016). LRP/LR antibody mediated rescuing of amyloid-beta-induced cytotoxicity is dependent on PrPc in Alzheimer's disease. *J. Alzheimer's Dis.* 49, 645–657. doi: 10.3233/JAD-150482

Purro, S. A., Nicoll, A. J., and Collinge, J. (2018). Prion protein as a toxic acceptor of amyloid-beta oligomers. *Biol. psychiatry.* 83, 358–368. doi: 10.1016/j.biopsych.2017.11.020

Resenberger, U. K., Harmeier, A., Woerner, A. C., Goodman, J. L., Muller, V., Krishnan, R., et al. (2011). The cellular prion protein mediates neurotoxic signalling of beta-sheet-rich conformers independent of prion replication. *EMBO J.* 30, 2057–2070. doi: 10.1038/emboj.2011.86

Rushworth, J. V., Griffiths, H. H., Watt, N. T., and Hooper, N. M. (2013). Prion protein-mediated toxicity of amyloid-beta oligomers requires lipid rafts and the transmembrane LRP1. *J. Biol. Chem.* 288, 8935–8951. doi: 10.1074/jbc.M112.400358

Saijo, E., Scheff, S. W., and Telling, G. C. (2011). Unaltered prion protein expression in Alzheimer disease patients. *Prion.* 5, 109–116. doi: 10.4161/pri.5.2.16355

Sakono, M., and Zako, T. (2010). Amyloid oligomers: formation and toxicity of Abeta oligomers. *FEBS J.* 277, 1348–1358. doi: 10.1111/j.1742-4658.2010.07568.x

Salazar, S. V., and Strittmatter, S. M. (2017). Cellular prion protein as a receptor for amyloid-beta oligomers in Alzheimer's disease. *Biochem. Biophys. Res. Commun.* 483, 1143–1147. doi: 10.1016/j.bbrc.2016.09.062

Schwarze-Eicker, K., Keyvani, K., Gortz, N., Westaway, D., Sachser, N., and Paulus, W. (2005). Prion protein (PrPc) promotes beta-amyloid plaque formation. *Neurobiol. Aging.* 26, 1177–1182. doi: 10.1016/j.neurobiolaging.2004.10.004

Scott-McKean, J. J., Surewicz, K., Choi, J. K., Ruffin, V. A., Salameh, A. I., Nieznanski, K., et al. (2016). Soluble prion protein and its N-terminal fragment prevent impairment of synaptic plasticity by Abeta oligomers: implications for

novel therapeutic strategy in Alzheimer's disease. *Neurobiol. Dis.* 91, 124–131. doi: 10.1016/j.nbd.2016.03.001

Selkoe, D. J. (2011). Alzheimer's disease. *Cold Spring Harb. Perspect. Biol.* 3:a004457. doi: 10.1101/cshperspect.a004457

Singh, J., and Udgaonkar, J. B. (2015). Molecular mechanism of the misfolding and oligomerization of the prion protein: current understanding and its implications. *Biochemistry* 54, 4431–4442. doi: 10.1021/acs.biochem.5b00605

Stine, W. B., Jungbauer, L., Yu, C., and LaDu, M. J. (2011). Preparing synthetic Abeta in different aggregation states. *Methods Mol. Biol.* 670, 13–32. doi: 10.1007/978-1-60761-744-0_2

Takahashi, R. H., Tobiume, M., Sato, Y., Sata, T., Gouras, G. K., and Takahashi, H. (2011). Accumulation of cellular prion protein within dystrophic neurites of amyloid plaques in the Alzheimer's disease brain. *Neuropathology* 31, 208–214. doi: 10.1111/j.1440-1789.2010.01158.x

Taylor, D. R., and Hooper, N. M. (2006). The prion protein and lipid rafts. *Mol. Membr. Biol.* 23, 89–99. doi: 10.1080/09687860500449994

Taylor, D. R., Watt, N. T., Perera, W. S., and Hooper, N. M. (2005). Assigning functions to distinct regions of the N-terminus of the prion protein that are involved in its copper-stimulated, clathrin-dependent endocytosis. *J. Cell Sci.* 118, 5141–5153. doi: 10.1242/jcs.02627

Um, J. W., Nygaard, H. B., Heiss, J. K., Kostylev, M. A., Stagi, M., Vortmeyer, A., et al. (2012). Alzheimer amyloid-beta oligomer bound to postsynaptic prion protein activates Fyn to impair neurons. *Nat. Neurosci.* 15, 1227–1235. doi: 10.1038/nn.3178

Velayos, J. L., Irujo, A., Cuadrado-Tejedor, M., Paternain, B., Moleres, F. J., and Ferrer, V. (2009). The cellular prion protein and its role in Alzheimer disease. *Prion* 3, 110–117. doi: 10.4161/pri.3.2.9135

Vergara, C., Ordonez-Gutierrez, L., Wandosell, F., Ferrer, I., del Rio, J. A., and Gavin, R. (2015). Role of PrP(C) expression in tau protein levels and phosphorylation in Alzheimer's disease evolution. *Mol. Neurobiol.* 51, 1206–1220. doi: 10.1007/s12035-014-8793-7

Viles, J. H., Cohen, F. E., Prusiner, S. B., Goodin, D. B., Wright, P. E., and Dyson, H. J. (1999). Copper binding to the prion protein: structural implications of four identical cooperative binding sites. *Proc Natl. Acad. Sci.U.S.A.* 96, 2042–2047. doi: 10.1073/pnas.96.5.2042

Whitehouse, I. J., Jackson, C., Turner, A. J., and Hooper, N. M. (2010). Prion protein is reduced in aging and in sporadic but not in familial Alzheimer's disease. *J. Alzheimer's Dis.* 22, 1023–1031. doi: 10.3233/JAD-2010-101071

Wildburger, N. C., Esparza, T. J., LeDuc, R. D., Fellers, R. T., Thomas, P. M., Cairns, N. J., et al. (2017). Diversity of amyloid-beta proteoforms in the Alzheimer's disease brain. *Sci. Rep.* 7:9520. doi: 10.1038/s41598-017-10422-x

Wiseman, F. K., Cancellotti, E., Piccardo, P., Iremonger, K., Boyle, A., Brown, D., et al. (2015). The glycosylation status of PrPC is a key factor in determining transmissible spongiform encephalopathy transmission between species. *J. Virol.* 89, 4738–4747. doi: 10.1128/JVI.02296-14

Wisniewski, M. L., Hwang, J., and Bahr, B. A. (2011). Submicromolar Abeta42 reduces hippocampal glutamate receptors and presynaptic markers in an aggregation-dependent manner. *Biochim. Biophys. Acta.* 1812, 1664–1674. doi: 10.1016/j.bbadis.2011.09.011

Wuthrich, K., and Riek, R. (2001). Three-dimensional structures of prion proteins. *Adv. Protein Chem.* 57, 55–82. doi: 10.1016/s0065-3233(01)57018-7

Zafar, S., Shafiq, M., Younas, N., Schmitz, M., Ferrer, I., and Zerr, I. (2017). Prion protein interactome: identifying novel targets in slowly and rapidly progressive forms of Alzheimer's disease. *J. Alzheimer's Dis.* 59, 265–275. doi: 10.3233/JAD-170237

Zhao, W. Q., Santini, F., Breese, R., Ross, D., Zhang, X. D., Stone, D. J., et al. (2010). Inhibition of calcineurin-mediated endocytosis and alpha-amino-3-hydroxy-5-methyl-4-isoxazolepropionic acid (AMPA) receptors prevents amyloid beta oligomer-induced synaptic disruption. *J. Biol. Chem.* 285, 7619–7632. doi: 10.1074/jbc.M109.057182

Zou, W. Q., Xiao, X., Yuan, J., Puoti, G., Fujioka, H., Wang, X., et al. (2011). Amyloid-beta42 interacts mainly with insoluble prion protein in the Alzheimer brain. *J. Biol. Chem.* 286, 15095–15105. doi: 10.1074/jbc.M110.199356

Zuegg, J., and Gready, J. E. (2000). Molecular dynamics simulation of human prion protein including both N-linked oligosaccharides and the GPI anchor. *Glycobiology* 10, 959–974. doi: 10.1093/glycob/10.10.959

Conflict of Interest Statement: The authors declare that the research was conducted in the absence of any commercial or financial relationships that could be construed as a potential conflict of interest.

Copyright © 2019 Zhang, Zhao, Zhang, Yu, Wang and Chang. This is an open-access article distributed under the terms of the Creative Commons Attribution License (CC BY). The use, distribution or reproduction in other forums is permitted, provided the original author(s) and the copyright owner(s) are credited and that the original publication in this journal is cited, in accordance with accepted academic practice. No use, distribution or reproduction is permitted which does not comply with these terms.

frontiers in Cellular Neuroscience

ORIGINAL RESEARCH
published: 06 August 2019
doi: 10.3389/fncel.2019.00360

TMEM16A Inhibition Preserves Blood–Brain Barrier Integrity After Ischemic Stroke

Pin-yi Liu[1†], Zhi Zhang[1†], Yi Liu[2], Xue-lian Tang[2], Shu Shu[2], Xin-yu Bao[2], Yan Zhang[2], Yue Gu[2], Yun Xu[1,2,3,4,5] and Xiang Cao[1,2,3,4,5*]*

[1] Department of Neurology, Nanjing Drum Tower Hospital Clinical College of Nanjing Medical University, Nanjing, China, [2] Department of Neurology, Nanjing Drum Tower Hospital, Medical School and The State Key Laboratory of Pharmaceutical Biotechnology, Institute of Brain Science, Nanjing University, Nanjing, China, [3] Jiangsu Key Laboratory for Molecular Medicine, Nanjing University Medical School, Nanjing, China, [4] Jiangsu Province Stroke Center for Diagnosis and Therapy, Nanjing, China, [5] Nanjing Neuropsychiatry Clinic Medical Center, Nanjing, China

The inflammatory response plays a pivotal role in Blood–Brain Barrier (BBB) destruction following ischemic brain injury. Enhanced leukocyte adhesion to vascular endothelial cells is an essential event in the inflammatory process. TMEM16A, a newly discovered protein regulating calcium-activated chloride channels, is widely expressed in eukaryotes. Recent studies have suggested that upregulated expression of TMEM16A is associated with the occurrence and development of many diseases. However, the role of TMEM16A in regulating BBB integrity after ischemic stroke has not been fully investigated. In this study, we found that TMEM16A is mainly expressed in brain endothelial cells and upregulated after ischemic stroke in the mouse brain. Caccinh-A01, an TMEM16A inhibitor that reduced its upregulation, attenuated brain infarct size and neurological deficits after ischemic stroke. ICAM-1 and MPO expression and BBB permeability were decreased after TMEM16A inhibitor administration. In addition, TMEM16A silencing rescued oxygen-glucose deprivation/reoxygenation (OGD/R)-induced transendothelial permeability *in vitro* accompanied by decreased ICAM-1 expression and leukocyte adhesion. Furthermore, our mechanistic study showed that TMEM16A knockdown alleviated NF-κB activation and nuclear translocation, indicating that TMEM16A knockdown downregulated OGD/R-induced ICAM-1 expression in an NF-κB-dependent manner. Finally, NF-κB inhibitor treatment also alleviated OGD/R-induced BBB permeability, confirming that activated NF-κB and increased ICAM-1 are essential factors involved in ischemia-induced BBB damage. Thus, our research provides a promising treatment strategy against BBB destruction after ischemic stroke, and TMEM16A may become a potential target for the treatment of ischemic stroke.

Keywords: blood–brain barrier, transmembrane protein 16A, intercellular adhesion molecule-1, ischemic stroke, NF-κB

OPEN ACCESS

Edited by:
Thomas Fath,
Macquarie University, Australia

Reviewed by:
Zhanyang Yu,
Massachusetts General Hospital, Harvard Medical School, United States
Hermona Soreq,
The Hebrew University of Jerusalem, Israel

***Correspondence:**
Yun Xu
xuyun20042001@aliyun.com
Xiang Cao
xiangcao1988@163.com

[†]These authors have contributed equally to this work as co-first authors

Specialty section:
This article was submitted to Cellular Neuropathology, a section of the journal Frontiers in Cellular Neuroscience

Received: *08 May 2019*
Accepted: *23 July 2019*
Published: *06 August 2019*

Citation:
Liu P-y, Zhang Z, Liu Y, Tang X-l, Shu S, Bao X-y, Zhang Y, Gu Y, Xu Y and Cao X (2019) TMEM16A Inhibition Preserves Blood–Brain Barrier Integrity After Ischemic Stroke. Front. Cell. Neurosci. 13:360. doi: 10.3389/fncel.2019.00360

INTRODUCTION

The blood–brain barrier (BBB) is a barrier with highly selective permeability that protects the brain from many chemicals and bacterial threats. It is mainly composed of cerebral endothelial cells that are connected by Tight Junction (TJ) proteins (Obermeier et al., 2013). Clinically, BBB breakdown is a major contributing factor to neurological disorders including stroke and traumatic injury.

Moreover, BBB breakdown is often associated with poor prognosis in ischemic stroke (Warach and Latour, 2004; Ji et al., 2017). Following ischemic stroke, BBB is disrupted, which allows leukocytes to infiltrate into the brain. Once leukocytes enter the brain tissue, they induce a secondary injury after reperfusion (Jiang et al., 2018). Intercellular adhesion molecule-1 (ICAM-1) plays an important role in leukocyte infiltration and it is mainly expressed on endothelial cells (Liu Y. et al., 2014; Cheng et al., 2018). Thus, inhibition of ICAM-1 after ischemic stroke prevents leukocyte adhesion and benefits BBB function recovery.

Transmembrane protein 16A (TMEM16A), also known as anoctamin-1, is a molecular identity of calcium-activated chloride channels expressed in a number of cell types and tissues including epithelial cells, sensory neurons, airway smooth muscle cells, cardiac muscle cells, and endothelial cells (Liu et al., 2010; Kunzelmann et al., 2012; Wu et al., 2014; Wang et al., 2018). TMEM16A has been demonstrated to play a critical role in mucus secretion, neural excitation, water-electrolyte balance and cell proliferation (Huang et al., 2012; Lin et al., 2015; Deng et al., 2016). Recently, it was found that TMEM16A participates in the pathophysiological processes during cardiac ischemia in cardiac vascular endothelial cells (Wu et al., 2014). Regarding stroke, TMEM16A is involved in hypertension-induced cerebrovascular remodeling through regulating smooth muscle cell proliferation (Wang et al., 2012). In human umbilical vein endothelial cells, TMEM16A was reported to bind Nox2 directly and then affect reactive oxygen species (ROS) generation (Ma et al., 2017). Before this study, it was unclear whether TMEM16A plays a role in brain endothelial cells and regulates BBB integrity after ischemic stroke.

In the present study, we found that TMEM16A is expressed in mouse brain endothelial cells and Human Brain Microvascular Endothelial Cells (HBMECs). Ischemia-induced BBB damage is accompanied by an increase in TMEM16A expression. Inhibition or knockdown of TMEM16A significantly protected against BBB disruption by downregulating ICAM-1 in a nuclear factor-kappa B (NF-κB)-dependent manner. Based on the above findings, our study identified a novel functional property of TMEM16A in brain endothelial cells, which may provide a new therapeutic target for the treatment of ischemia-induced BBB damage.

MATERIALS AND METHODS

Reagents and Antibodies

T16ainh-A01, Caccinh-A01, 2,3,5-triphenyltetrazolium chloride (TTC), Evans Blue (EB) and FITC-dextran were purchased from Sigma-Aldrich (St. Louis, MO, United States). The antibodies against TMEM16A, CD31, Na/K ATPase, and mouse IgG were obtained from Abcam (Cambridge, MA, United States). Primary antibodies against NF-κB p65, phosphor-p65, and Myeloperoxidase (MPO) were from Cell Signaling Biotechnology (Hertfordshire, United Kingdom). Anti-GAPDH, anti-Lamin b, anti-HSP90, Dapi, and horseradish peroxidase (HRP)-linked secondary antibodies were obtained from Bioworld Biotechnology (Minneapolis, MN, United States). The antibodies targeting ZO-1, Occludin, Claudin-5, and ICAM-1 were provided by Invitrogen (Carlsbad, CA, United States). The DiI dye was purchased from Beyotime Biotech (Nantong, China). PDTC (a selective NF-κB inhibitor) was from Selleck Chemicals (LLC, Houston, TX, United States).

Cell Culture

Primary microglia, astrocytes and neurons were cultured as we previously described (Cao et al., 2018; Jin et al., 2018). Briefly, primary microglia and astrocytes were prepared from 1–2 days old new born C57/BL6J mice. 10–12 days later, the microglia were separated from astrocytes by shaking the culture flasks at 180 rpm for 2 h. Primary cortical neurons were isolated from E15-17 C57/BL6J mice embryos. They were cultured and maintained in B27/neurobasal medium (Invitrogen) supplemented with glutamine for 10 days. Primary cultures of brain microvascular endothelial cells were prepared from cortices of adult mice. The cortices tissue was carved and digested with 0.2% collagenase/dispase containing 20 U/ml DNase I. Endothelial cells were grown in endothelial cell medium (ECM, ScienCell, Carlsbad, CA, United States) plus 5% fetal bovine serum (Biological Industries, Israel), antibiotics (100 units/ml penicillin and 100 μg/ml streptomycin) in a humidified atmosphere with 5% CO_2 at 37°C. The purity of the microglia, astrocytes, neurons, and endothelial cells was greater than 90% as determined by Iba-1, GFAP, MAP-2, and CD31 staining.

HBMECs and THP-1 (human monocytic cell line) cells were purchased from ScienCell Research Laboratories. They were cultured in ECM and RPMI 1640 (HyClone, Logan, UT, United States). All experiments with HBMECs and THP-1 cells were used below 10 passages.

Middle Cerebral Artery Occlusion Model in Mice

Two-month-old male C57/BL6J mice weighing about 25 g were purchased from the Animal Model Center of Nanjing University (Nanjing, Jiangsu, China). All procedures were approved by the Animal care and Use Committee at Nanjing University. In Middle Cerebral Artery Occlusion (MCAO) model, mice were anesthetized with pentobarbital sodium (45 mg/kg i.p.). A 6/0 sutures (Doccol Corporation, MA, United States) was inserted through internal carotid artery into the beginning of the middle cerebral artery (MCA) until the ipsilateral blood flow of MCA supply territory decreased to below 30% of baseline monitored by a laser Doppler flowmetry (Perimed Corporation, Stockholm, Sweden). After 60 min, the filament was withdrawn to allow blood reperfusion. Sham-operated groups underwent the same procedures expect for the insertion of the filament into the MCA. The mice were subjected to the dose of 5 mg/kg T16ainh-A01 and Caccinh-A01 or the same amount of saline by caudal vein injection within 15 min after the onset of reperfusion.

Behavioral Test

For neurological function assessment, a Neurological severity scores (NSS) was used on day 1 and day 3 after MCAO. NSS is a composite test of motor, sensory, balance and reflex, which was

graded on a scale of 0 to 18. Higher score means more serious symptoms. All tests were assessed in a blinded manner.

The rotarod test was used to assess motor deficit and sensorimotor coordination (Tatulli et al., 2018). The mice were trained for 3 days before MCAO using a rotarod device (RWD Life Science, Shenzhen, China). The rotating rod was accelerated from 4 to 40 rpm over 5 min. All the mice were trained three times a day, and each training lasts for 5 min with a 15 min interval for rest. On days 1 and 3 after MCAO, the time that each mouse fell from the rotating rod was recorded.

The grip strength test was used to measure the maximal muscular strength by mouse forelimbs (Akhtar et al., 2013). The mouse was suspended by the tail and approached to the T-bar of the apparatus (GS3, Bioseb, France). Once the mouse grasped the T-bar with two forelimbs, the animal was pulled backward until its grip is broken. The maximal force was recorded and six such tests were acquired per mouse. The mean force was calculated for analysis.

Infarct Volume Calculation

Infarct volume was calculated as previously described (Meng et al., 2019). Mice were anesthetized and sacrificed 24 and 72 h after MCAO by 2% TTC (Sigma-Aldrich) staining. Mouse brains were sliced into five coronal sections (1-mm thick), and then stained with TTC at 37°C for 15 min. After 4% paraformaldehyde fixation, the slices are photographed and analyzed by ImageJ software. The value of infarct volume is calculated as a percentage of the whole brain after correcting for edema.

Quantitation of BBB Permeability

Evans Blue extravasation is a classical method to examine the change of BBB permeability. Mice were injected with 2% EB (Sigma-Aldrich) after MCAO. Two hours later, animals were perfused with saline, and then the brains were cut into slices for analysis. Each hemisphere was weighed and homogenized in *N,N*-dimethyl formamide (Sigma-Aldrich). The samples were centrifuged, collected and quantified as previously described (Tang et al., 2018). Briefly, the supernatants were analyzed at 620 nm by a microplate reader (Tecan Trading AG, Switzerland). Results are expressed as micrograms of EB per gram of wet brain weight in comparison with a standard solution.

Immunofluorescence Analysis

The mice were anesthetized and scarified via cardiac perfusion with pre-cold 0.9% saline followed by 4% paraformaldehyde. The brains were cut into 20 μm coronal sections by a cryostat microtome (Leica, Wetzlar, Germany). After blocking with 2% BSA, brain sections were immunostained with antibodies against CD31 (1:500), TMEM16A (1:200), ZO-1 (1:200), Occludin (1:200), Claudin-5 (1:500), and Mouse IgG (1:500) overnight at 4°C. The sections were washed with phosphate buffered saline (PBS) for three times and then incubated with the indicated secondary antibodies for 2 h in the dark at room temperature (RT). Thereafter, the cell nuclei were stained with DAPI (1:500). Images were photographed using a fluorescence microscope (Olympus BX51, Japan).

Protein Preparation, Co-immunoprecipitation, and Western Blotting Analysis

Whole proteins were lysed with the lysis buffer (Thermo Fisher Scientific, Rockford, IL) for 30 min on ice. After centrifuging (12500 rpm) at 4°C for 15 min, the supernatants were immunoprecipitated with indicated antibodies overnight. The precleared Protein A/G Plus-agarose beads (Millipore, Billerica, MA, United States) were incubated with immunocomplexes for 4 h. The total protein concentrations were quantified by a BCA protein assay kit (Pierce Biotechnology, Rockford, IL, United States). Equal quantities of proteins were separated with 10–12% SDS-PAGE and then transferred onto PVDF membranes (Millipore). The membranes were blocked with 5% slim milk for 1 h at RT, followed by an overnight incubation with primary antibodies against TMEM16A (1:500), ZO-1 (1:500), Occludin (1:1000), Claudin-5 (1:500), MPO (1:1000), NF-κB p65 (1:1000), phosphor-NF-κB p65 (1:1000), Na/K ATPase (1:1000), HSP90 (1:1000), GAPDH (1:5000), and Lamin b (1:2000). Subsequently, the proteins were incubated with secondary antibody for another 2 h at RT and scanned with a Gel-Pro system (Tanon Technologies, Shanghai, China). The intensity of the blots was quantified with ImageJ software.

Cytoplasmic-and-nuclear or membrane-and-cytoplasmic protein fractions from HBMECs were extracted using NE-PER nuclear and cytoplasmic extraction assays or a Mem-PER Plus Membrane protein Extraction Kit (Thermo Fisher Scientific) as previously described (Weng et al., 2017). The following steps are the same as Western blotting.

Real-Time PCR

Total RNA was extracted at 1, 3 and 7 days after MCAO with Trizol reagent (Invitrogen) and reversed transcribed to cDNA using a PrimeScript RT Reagent Kit (Takara, Dalian, China) according to the manufacturer's instruction. Real-time PCR was performed on a StepOne Plus PCR System (Applied Biosystems, Foster City, CA, United States) with SYBER Green assay (Applied Biosystems). Corresponding primers were shown as follows: TMEM16A: F: GAAGCGGAAGCAGCGCTATG and R: AGTGGAGCCAGAGGGAAGGA; GAPDH: F: GCCAAGG CTGTGGGCAAGGT and R: TCTCCAGGCGGCACGTCAGA.

Oxygen-Glucose Deprivation/ Reoxygenation (OGD/R) Treatment

Human Brain Microvascular Endothelial Cells were treated with OGD to mimic acute ischemia *in vitro*. Briefly, HBMECs were seeded onto the inner surface of collagen-coated Transwell inserts (6.5 mm diameter, 0.4 μm pore size; Corning Costar, NY), which were placed in wells of a 24 well plate with complete growth media ECM. When the monolayer of HBMECs became confluent, culture mediums of the cells were replaced with glucose-free DMEM, and the cells were placed in a hypoxia chamber (Billups-Rothenberg, Del Mar, CA, United States) which was previously flushed with 95% N_2/5% CO_2. After 4 h incubation, the cells were returned to regular medium and incubated under normal conditions (95% O_2/5% CO_2, and

37°C) for another 20 h. Control cells were cultured in normal medium and environment all the time. For stimulation, HBMECs were preincubated with PDTC (100 μM) for 1 h prior to the OGD/R treatment.

Measurement of Transendothelial Electrical Resistance (TEER)

The TEER of HBMEC monolayer was performed after 4 h OGD following by 20 h reoxygenation by using a portable epithelial voltohmmeter (EVOM, World Precision Instruments, Sarasota, FL, United States) according to the manufacturer's instruction. All independent experiments were measured in triplicate. A Transwell without any cells was served as a blank control.

FITC-Dextran Transendothelial Permeability Assay

The FITC-dextran transendothelial permeability assay was also applied to test the permeability of HBMEC monolayer. In brief, 0.1 mg/ml of FITC-labeled dextran (MW, 70000, Sigma-Aldrich) was added to the upper chamber after 4 h OGD following by 20 h reoxygenation. After incubation for another 20 min, 100 μl of supernatants from the lower compartment were analyzed by a microplate reader (excitation 490 nm, emission 520 nm). At least three independent experiments were performed.

Transfection Experiments

The lentivirus mediated inhibition (Lv-shTMEM16A) or overexpression of TMEM16A (Lv-TMEM16A) and control lentivirus were obtained from GenePharma (Shanghai, China). HBMECs were cultured and incubated for 1 day with Lv-shTMEM16A or Lv-TMEM16A (MOI = 10), which were then replaced by fresh medium for another 3 days. The expression of TMEM16A was detected by Western blotting and immunofluorescence analysis.

Assessment for THP-1 Cell Adhesion to HBMECs

To mimic leukocyte adhesion in the brain, THP-1 cells were used to adhere HBMECs *in vitro*. In brief, THP-1 cells were maintained in RPMI 1640 medium containing 10 μM DiI dye at 37°C for 20 min. After washing three times by PBS, the fluorescence-labeled THP-1 cells were added to the HBMEC monolayer (the ratio of HBMECs to THP-1 is 10:1) and allowed to adhere for another 30 min at 37°C. The mixed cells were then gently washed three times with PBS. Images were also photographed using Olympus BX51 fluorescence microscope and the fluorescence intensity was analyzed by Tecan microplate reader (excitation 549 nm, emission 565 nm). HBMEC monolayer was used as a blank control.

Cell Viability Assays

Human Brain Microvascular Endothelial Cells were plated at 1×10^4 cells/well in 96-well plates and treated with or without Lv-shTMEM16A. After OGD/R treatment for 24 h, the culture media were removed. HBMECs viability was detected by the Cell Counting Kit-8 (CCK-8; Dojindo Laboratories, Tokyo, Japan) according to the manufacturer's instruction. The optical density was measured at 450 nm by a microplate reader.

Statistical Analysis

Results are expressed as mean ± SEM or median and 25th and 75th percentiles for skewed variables. In addition, we performed Student's *t*-test among 2 groups or one-way analysis of variance (ANOVA) followed by Bonferroni's *post hoc* test among three or more groups for continuous variables with normal distribution, and Kruskal–Wallis test tests followed by Dunn–Bonferroni *post hoc* method for skewed variables. Statistical calculations were performed with SPSS 18.0. *P*-values < 0.05 were considered statistically significant.

RESULTS

TMEM16A Is Mainly Expressed in the Brain Endothelial Cells and Upregulated After Ischemic Stroke

Several studies reported that TMEM16A is expressed in many endothelial cell types, including cardiac vascular endothelial cells, human umbilical vein endothelial cells, and mouse aortic endothelial cells (Suh et al., 1999; Zhong et al., 2000; Wu et al., 2014). However, little is known about the function and expression of TMEM16A in brain endothelial cells and the ischemia-induced inflammatory response. We measured TMEM16A expression after MCAO using Western blotting and real-time PCR assays. As shown in **Figures 1A–C**, TMEM16A protein and mRNA levels were markedly increased in the ipsilateral brain cortex on days 1 and 3 after MCAO. However, increased TMEM16A expression returned to basal levels on day 7 after MCAO. Furthermore, the expression profiles of TMEM16A were analyzed in four cell types in mouse brains. TMEM16A protein expression was more abundant in brain endothelial cells, than in neurons, microglia and astrocytes (**Figures 1D,E**). These findings suggest that TMEM16A may play an essential role in brain endothelial cells after ischemic stroke.

Targeted Inhibition of TMEM16A Attenuated Brain Infarct Size and Neurological Deficits After Ischemic Stroke

T16ainh-A01 and Caccinh-A01 are two selective inhibitors of TMEM16A. Both compounds have been demonstrated to inhibit TMEM16A activity, but Caccinh-A01 can also reduce TMEM16A protein levels by facilitating endoplasmic reticulum-associated, proteasomal turnover of TMEM16A (Bill et al., 2014). To determine the effect of TMEM16A inhibitors after ischemic stroke, the infarct size of mouse brains was measured by TTC at different time points. The results showed that Caccinh-A01, not T16ainh-A01, significantly reduced infarction: 29.50 (22.63–31.88) with MCAO-saline treatment vs. 17.25 (15.38–22.63) with MCAO-Caccinh-A01 treatment at 24 h ($p < 0.05$); 27.75 (23.63–32.25) with MCAO-saline treatment vs. 15.75

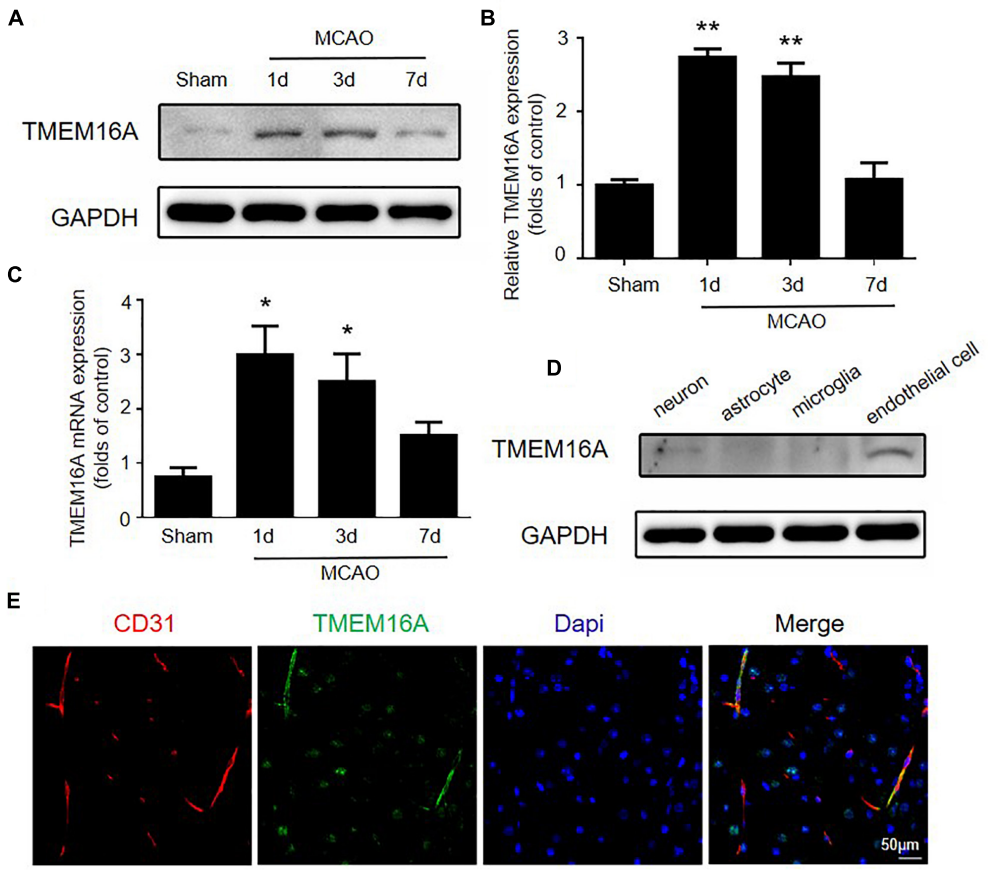


FIGURE 1 | The expression of TMEM16A was upregulated after ischemic stroke. **(A,B)** TMEM16A protein and **(C)** mRNA expression 60 min following MCAO at different time points after the onset of reperfusion. **(D)** TEME16A protein expression in neurons, microglia, astrocytes, and brain endothelial cells. **(E)** Representative double-immunofluorescence staining of CD31 and TMEM16A in the mouse brain (bar = 50 μm). Values are the mean ± SEM for three mice in each group. One asterisk indicates $P < 0.05$ and two asterisks indicate $P < 0.01$ vs. sham-operated groups.

(12.13–21.23) with MCAO-Caccinh-A01 treatment at 72 h ($p < 0.05$; $n = 6$/group) (**Figures 2A,B**).

Neurological severity scores, the grip strength test and rotarod test were applied to test motor function, sensorimotor coordination,and muscular strength on each mouse after ischemic injury. As shown in **Figures 2C–E**, mice treated with Caccinh-A01 manifested better behavioral performance at 24 and 72 h than mice in the saline group (NSS: 10.50 (9.25–11.00) with MCAO-saline treatment vs. 6.50 (5.75–10.00) with MCAO-Caccinh-A01 treatment at 24 h, $p < 0.01$; 9.50 (7.75–10.00) with MCAO-saline treatment vs. 5.00 (3.75–6.00) with MCAO-Caccinh-A01 treatment at 72 h, $p < 0.01$. Grip strength test: 55.50 (24.00–79.25) with MCAO-saline treatment vs. 81.50 (69.25–90.00) with MCAO-Caccinh-A01 treatment at 24 h, $p < 0.05$; 61.50 (53.00–86.75) with MCAO-saline treatment vs. 94.00 (81.00–106.25) with MCAO-Caccinh-A01 treatment at 72 h, $p < 0.05$. Rotarod test: 47.50 (20.75–80.25) with MCAO-saline treatment vs. 115.00 (74.75–196.25) with MCAO-Caccinh-A01 treatment at 24 h, $p < 0.01$; 64.00 (46.50–104.00) with MCAO-saline treatment vs. 137.00 (96.75–232.50) with MCAO-Caccinh-A01 treatment at 72 h, $p < 0.01$. $n = 10$/group). Taken together, these data indicated that TMEM16A inhibition alleviated ischemic brain injury in MCAO mice.

Targeted Inhibition of TMEM16A Attenuated-BBB Disruption After Ischemic Stroke

The effects of TMEM16A inhibition on BBB permeability were evaluated by Evans blue extravasation and IgG immunostaining. The results showed that increased Evans blue and IgG leakage were observed in the ischemic hemisphere on day 3 after MCAO, while there were significantly reduced Evans blue and IgG signals in Caccinh-A01 treated mice (**Figures 3A,B**). Since BBB is mainly composed of endothelial cells that are connected by TJ proteins, we further evaluated the protein expression of ZO-1, occludin, and claudin-5 by immunofluorescence and Western blotting. As shown in **Figure 3C**, ZO-1, occludin, and claudin-5 were dominantly and continuously distributed along the cerebral microvessels in a normal brain. However, the alignment of these three TJ proteins was seriously damaged in the ischemic hemisphere on days 1 and 3 after MCAO,

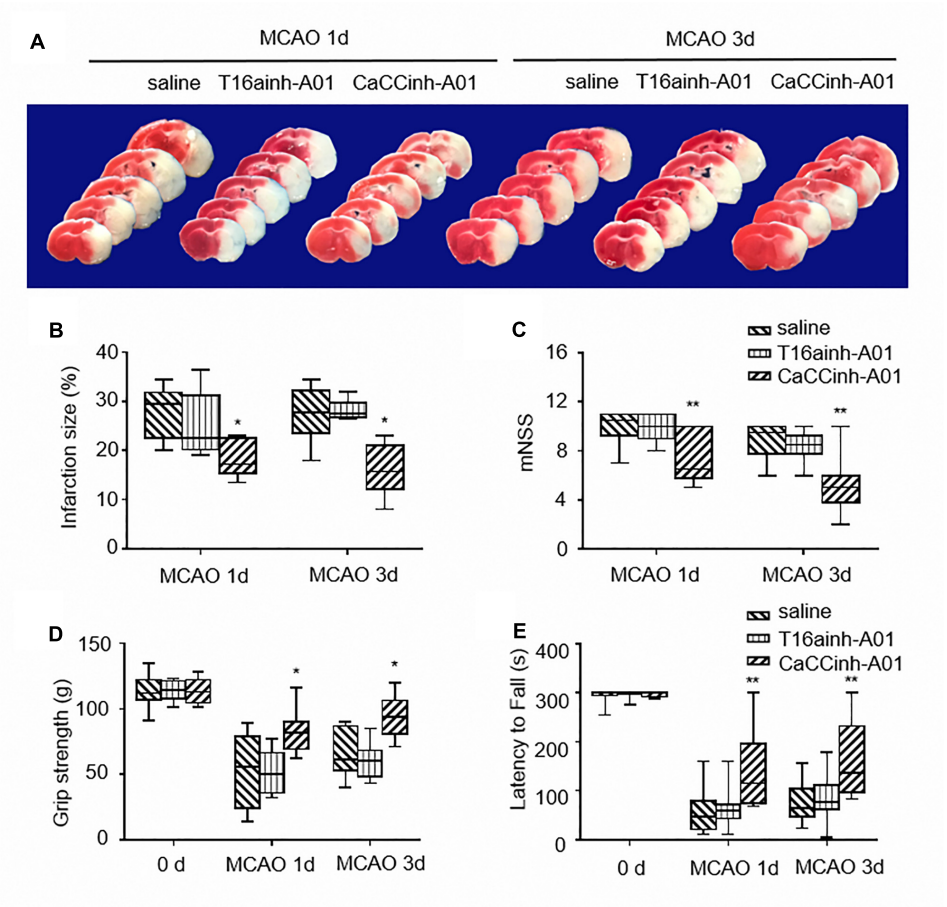


FIGURE 2 | TMEM16A inhibitors reduced infarct volume and improved neurological outcomes after ischemic stroke. **(A)** Representative brain sections stained with TTC at different time points after MCAO. **(B)** Infarct volume (n = 6). **(C)** The results of NSS scores, **(D)** the grip strength and **(E)** the rotarod tests (n = 10). Values are the median (25th and 75th percentiles). One asterisk indicates $P < 0.05$ and two asterisks indicate $P < 0.01$ vs. MCAO-saline groups.

indicating a disruption of BBB after ischemic stroke. The loss of ZO-1, occludin, and claudin-5 was attenuated in Caccinh-A01 treated mice compared with the MCAO-saline group. Consistent with this finding, Western blotting analysis confirmed that the reduction of these three TJ proteins was significantly reduced after Caccinh-A01 treatment (**Figure 3D**). At the same time, Caccinh-A01 markedly inhibited TMEM16A expression in the ischemic hemisphere after MCAO, while T16ainh-A01could not (**Supplementary Figure S1**).

Endothelial cells expressed a relatively low level of ICAM-1 in the homeostatic state. In hypoxic conditions, however, its expression was significantly increased. ICAM-1 upregulation facilitates neutrophil adhesion and infiltration, which are deleterious to BBB integrity. MPO was used to evaluate neutrophil accumulation. Thus, we also investigated the expression of ICAM-1 and MPO after MCAO with or without TMEM16A inhibition. We found that the protein levels of ICAM-1 and MPO were greatly downregulated in the MCAO-Caccinh-A01 group compared with the MCAO-saline groups (**Figure 3D**). These blots were quantified by densitometry (**Figure 3E**). Therefore, we concluded that TMEM16A inhibition could alleviate the disruption of BBB permeability after ischemic stroke by reducing ICAM-1 expression and neutrophil accumulation.

TMEM16A Silencing Rescued OGD/R-Induced Transendothelial Permeability *in vitro*

To further validate the effect of TMEM16A on the BBB, OGD/R models were used to mimic *in vivo* ischemia/reperfusion injury in an *in vitro* BBB model. OGD/R elevated TMEM16A expression in HBMECs, and we silenced TMEM16A expression with lentivirus before OGD/R. The transduction efficiency of Lv-shTMEM16A was tested by Western blotting and immunofluorescence (**Figures 4A,B**, $P < 0.01$). Both Lv-shTMEM16A-1 and Lv-shTMEM16A-3 were effective in silencing TMEM16A expression in HBMECs. Lv-shTMEM16A-3 was selected for the further experiments. After 4 h of OGD followed by 20 h of reoxygenation, the expression levels of TJ proteins (ZO-1, occludin and claudin-5) were significantly downregulated, accompanied by elevated TMEM16A. However, TMEM16A knockdown restored

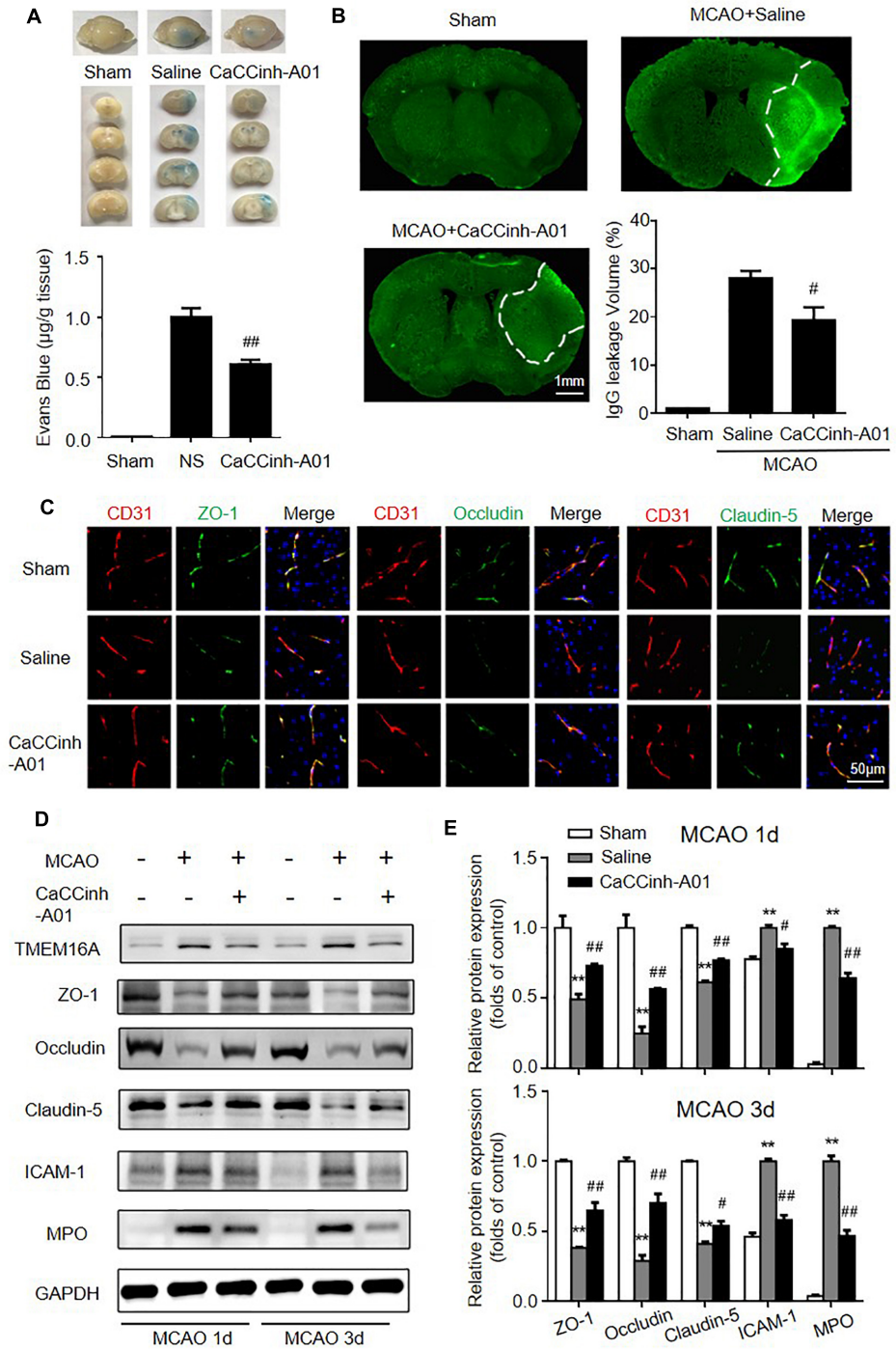


FIGURE 3 | TMEM16A inhibition attenuated BBB disruption after ischemic stroke. **(A)** Evans blue staining and **(B)** IgG extravasation in sham-operated groups, MCAO-Saline groups and MCAO-Caccinh-A01 groups on day 3 after MCAO (bar = 1 mm). **(C)** Representative immunofluorescence staining of ZO-1, occludin and claudin-5 on day 3 after MCAO (bar = 50 μm). **(D,E)** Representative Western blotting results of TMEM16A, ZO-1, occludin, claudin-5, ICAM-1 and MPO on days 1 and 3 after MCAO. Values are the mean ± SEM. Two asterisks indicate $P < 0.01$ vs. sham-operated groups. One number sign indicates $P < 0.05$ and two number signs indicate $P < 0.01$ vs. MCAO-saline groups.

the protein levels of these three TJ proteins (**Figures 4C,D**). To further confirm this phenomenon, we isolated membrane protein to observe TJ proteins expression after OGD/R with or without Lv-shTMEM16A-3. The results also showed that TMEM16A knockdown upregulated the protein levels of ZO-1, occludin and claudin-5 after OGD/R in membrane fraction

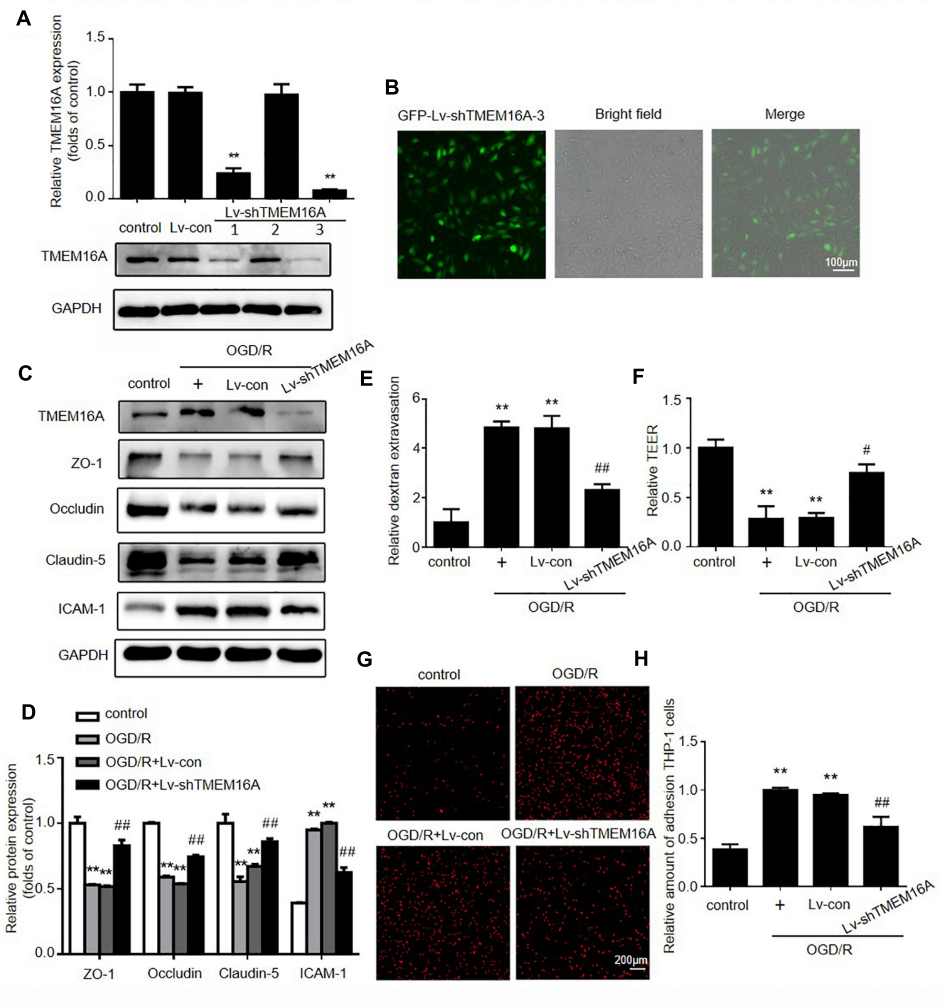


FIGURE 4 | Silencing TMEM16A rescued OGD/R-induced transendothelial permeability *in vitro*. **(A)** TMEM16A expression was tested by Western blotting and **(B)** immunofluorescence after Lv-shTMEM16A infection for 3 days. **(C,D)** Representative Western blotting results of TMEM16A, ZO-1, occludin, claudin-5, and ICAM-1 after OGD/R treatments. **(E)** Quantification of transendothelial permeability detected by dextran leakage and **(F)** TEER assay. **(G,H)** Representative images of OGD/R-induced adhesion of THP-1 cells to HBMEC monolayers (bar = 200 μm). Values are the mean ± SEM. Two asterisks indicate $P < 0.01$ vs. control groups. One number sign indicates $P < 0.05$ and two number signs indicate $P < 0.01$ vs. OGD/R alone groups.

(**Supplementary Figure S2A**). In addition, ICAM-1 expression was upregulated in ODG/R, while TMEM16A silencing inhibited this upregulation (**Figures 4C,D**).

Furthermore, FITC-dextran permeability and TEER assays were applied to explore the role of TMEM16A in OGD/R-induced transendothelial permeability. As expected, we found that TMEM16A knockdown significantly increased TEER values and decreased the OGD/R-induced FITC-dextran permeability (**Figures 4E,F**). To mimic leukocyte adhesion in the brain, human monocytic THP-1 cells were co-cultured with HBMECs. The results showed that THP-1 cells barely adhered to HBMECs in the untreated group. TMEM16A knockdown significantly reduced OGD/R-stimulated adhesion of THP-1 cells to HBMEC monolayers (**Figures 4G,H**). Therefore, these results demonstrated that TMEM16A knockdown also protected brain endothelial cells against OGD/R-induced transendothelial hyperpermeability, as well as THP-1 cell adhesion at the cellular level. Due to OGD/R may induce cell death, we also tested the cell viability after OGD/R with or without Lv-shTMEM16A. As shown in **Supplementary Figure S2B**, both OGD/R and TMEM16A knockdown did not significantly alter cell viability, which was consistent with our previously published article (Zhao et al., 2019). Taken together, these results indicated that the protective effect of TMEM16A knockdown on BBB integrity is independent of alterations in cell viability.

TMEM16A Silencing Exerted a Protective Effect by Decreasing ICAM-1 via the NF-κB Signaling Pathway

The expression of ICAM-1 can be regulated by the nuclear transcriptional factor NF-κB. To expand our understanding of

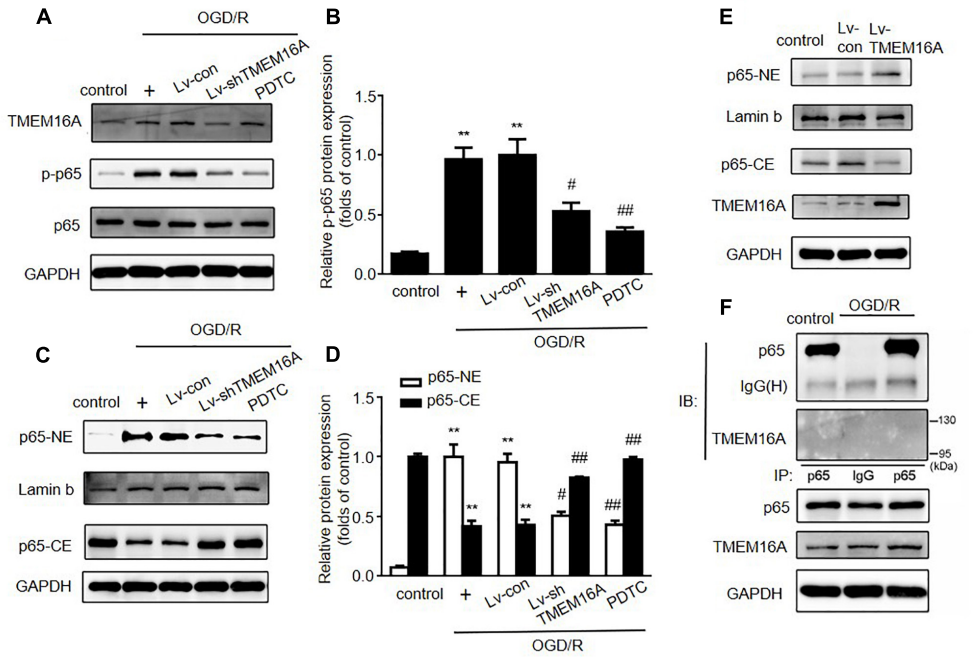


FIGURE 5 | Silencing TMEM16A suppressed the activation of the NF-κB signaling pathway. **(A,B)** TMEM16A, NF-κB p-p65 and NF-κB p65 protein expression following OGD/R treatments. **(C–E)** NF-κB p65 protein expression in the cytoplasm and nucleus following OGD/R treatments in TMEM16A knockdown and overexpressing Human Brain Microvascular Endothelial Cells. **(F)** The interaction between TMEM16A and NF-κB p65 by co-immunoprecipitation. Values are the mean ± SEM. Two asterisks indicate $P < 0.01$ vs. control groups. One number sign indicates $P < 0.05$ and two number signs indicate $P < 0.01$ vs. OGD/R alone groups.

the mechanisms underlying the protective effect of TMEM16A knockdown against BBB disruption, we next detected whether NF-κB signaling was involved in this process. As shown in **Figures 5A,B**, after 4 h of OGD followed by 20 h of reoxygenation, the expression of phosphor-NF-κB (p-p65) was significantly increased. After TMEM16A knockdown, the increase in p-p65 was prevented. Because activated NF-κB p65 translocates into the nucleus and then initiates the transcription of many inflammatory genes, such as ICAM-1. Western blotting was used to confirm whether TMEM16A silencing could also affect NF-κB p65 nuclear translocation. The results showed that a sharp increase in the nuclear translocation of NF-κB p65 was found after OGD/R treatments. However, TMEM16A knockdown prevented NF-κB p65 from entering the nucleus (**Figures 5C,D**). Furthermore, NF-κB p65 translocation was strongly enhanced after TMEM16A-overexpression in HBMECs (**Figure 5E**). To further determine the effect of TMEM16A on NF-κB p65, we analyzed the interaction between these two proteins. However, TMEM16A did not physically bind NF-κB p65 (**Figure 5F**). These data indicated that TMEM16A could regulate NF-κB p65 activity without direct physical interaction.

PDTC, a selective inhibitor of NF-κB p65, was used to further determine the role of NF-κB signaling in ischemia-induced BBB disruption. Our present study showed that PDTC not only blocked NF-κB p65 translocation to the nucleus (**Figure 5C**) and reduced the expression of ICAM-1 (**Figures 6A,B**), but also increased TEER values and decreased the OGD/R-induced FITC-dextran permeability (**Figures 6C,D**). The protective effect of PDTC was equivalent to that of TMEM16A knockdown. Overall, TMEM16A silencing attenuates BBB disruption under hypoxic conditions by downregulating ICAM-1 levels via the NF-κB signaling pathway.

DISCUSSION

In the present study, we discovered that TMEM16A is upregulated in ischemia-induced brain injury *in vivo* and the OGD/R model *in vitro*, which is accompanied by ischemia-induced BBB damage. The TMEM16A inhibitor Caccinh-A01 attenuated brain infarct size, improved neurological outcomes and lowered BBB permeability after ischemic stroke. In addition, both the TMEM16A inhibitor and TMEM16A knockdown could also decrease neutrophil infiltration. We further revealed that the protective effects of TMEM16A inhibition or silencing were mediated by the downregulation of ICAM-1 in an NF-κB-dependent manner. A selective inhibitor of NF-κB (PDTC) was used to compare the effect of TMEM16A silencing. We found that similarly to TMEM16A knockdown, PDTC also reduced ICAM-1 expression and alleviated endothelial injury in the OGD/R model. Taken together, the results confirmed that TMEM16A silencing protected the BBB against ischemia or hypoxia partly through downregulating ICAM-1.

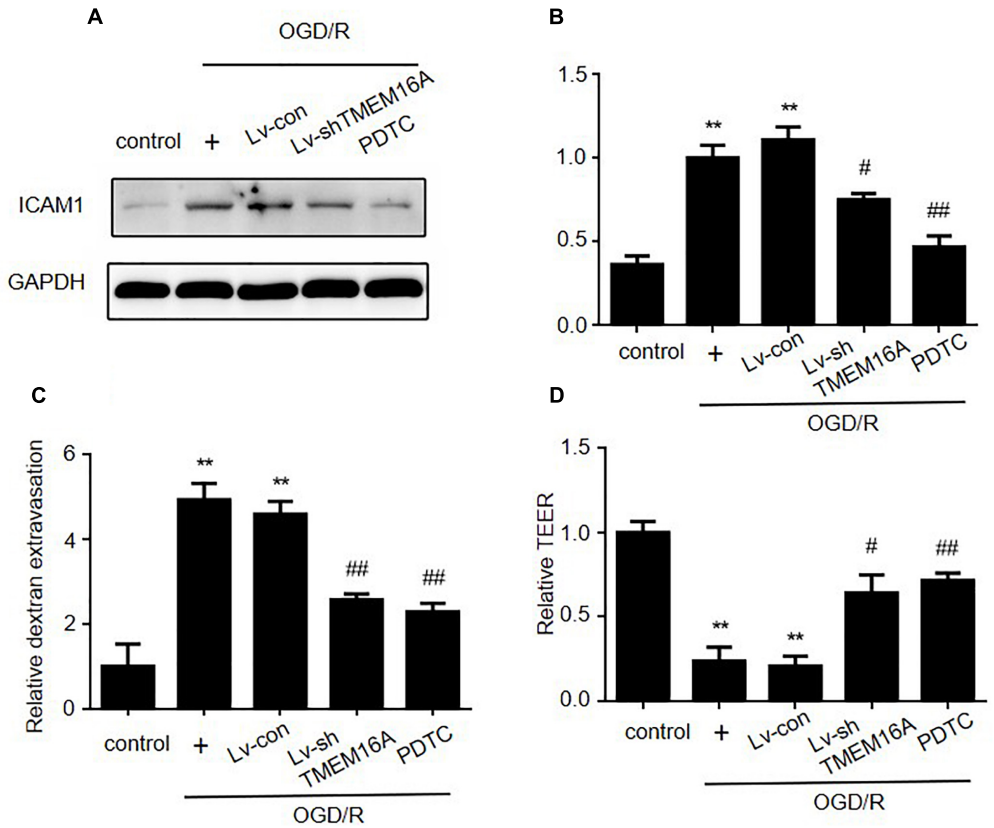


FIGURE 6 | Silencing TMEM16A exerts its BBB protective effect by decreasing ICAM-1 expression via the NF-κB signaling pathway. **(A,B)** ICAM-1 protein expression following OGD/R treatments with TMEM16A knockdown, with or without PDTC treatment. **(C)** Quantification of transendothelial permeability detected by dextran leakage and **(D)** a TEER assay. Values are the mean ± SEM. Two asterisks indicate $P < 0.01$ vs. control groups. One number sign indicates $P < 0.05$ and two number signs indicate $P < 0.01$ vs. OGD/R alone groups.

TMEM16A is a newly discovered molecular basis of calcium-activated chloride channels. It has 8 transmembrane segments and a highly conserved domain of unknown function (Ji et al., 2019). Zhang et al. (2013) found that TMEM16A is upregulated in an ovalbumin-stimulated chronic asthma mouse model, and functional blockage of TMEM16A prevents airway hyperresponsiveness. Following treatment with interleukin-13 (IL-13), Qin et al. (2016) demonstrated that both mRNA and protein levels of TMEM16A were increased in a human bronchial epithelial cell line. Treatment with TMEM16A inhibitor could suppress IL-13-induced TMEM16A-mediated mucus production. In addition, the mRNA and protein levels of TMEM16A were also significantly increased by exposure of cardiac vascular endothelial cells to hypoxia, indicating that TMEM16A participates in ischemia-induced damage in the heart (Wu et al., 2014). These studies revealed that TMEM16A plays a critical role in many diseases, while the effect of TMEM16A in ischemic stroke remains elusive. We first found that TMEM16A levels were markedly increased in the ipsilateral brain cortex on days 1 and 3 after MCAO and that TMEM16A is mainly expressed in brain endothelial cells. These results suggested that TMEM16A functioned mainly in endothelial cells during ischemia in the brain.

In the following experiments, we administered two selective inhibitors of TMEM16A (Caccinh-A01 and T16ainh-A01) to mice within 15 min after the onset of reperfusion. We did not find any articles that mentioned these two inhibitors in stroke research. However, several published articles related to other diseases have used T16ainh-A01 and Caccinh-A01. Pineda-Farias et al. (2015) intrathecally administered 10 μg/rat CaCCinh-A01 and T16ainh-A01 in a neuropathic pain model. Qi et al. (2018) prepared 0.12 mg/mouse T16ainh-A01 and injected it subcutaneously into sexually mature mice weighing 25–30 g. In our study, we used the same dose of T16ainh-A01 and CaCCinh-A01. The mice we used weighed approximately 25 g, and 5 mg/kg equals to 0.125 mg/mouse. As previously described, T16ainh-A01 and Caccinh-A01 have different inhibitory effects on TMEM16A. Caccinh-A01 was used to facilitate the degradation of TMEM16A in many types of tissues and T16ainh-A01 could only inhibit the channel activity of TMEM16A (Bill et al., 2014; Tian et al., 2018). In our present study, Caccinh-A01 obviously attenuated brain infarct size and neurological deficits by reducing the expression of TMEM16A. However, T16ainh-A01 could not reverse the upregulation of TMEM16A and did not affect the infarct size or the impaired sensorimotor functions, suggesting

that ischemic-induced increase in TMEM16A exacerbated brain damage independent of TMEM16A biochemical activity.

The Blood–Brain Barrier is a highly selective semipermeable border that separates the central nervous system from the circulating blood. As a multicellular vascular structure, the BBB is composed of cerebral endothelial cells, pericytes, astrocyte end-feet, and basal membrane. Among them, endothelial cells, which have continuous intercellular TJ proteins, are the core component of the BBB. The disruption of the BBB exacerbates brain injury after ischemic stroke. Jiao et al. (2011) found that the expression levels of the TJ- associated proteins ZO-1, occludin and claudin-5 were significantly decreased after MCAO, which was consistent with our results. Our previous studies showed that reducing BBB leakage and damage could improve neurological outcomes, not only for MCAO-treated mice but also for acute ischemic stroke patients (Ji et al., 2017; Tang et al., 2018). In our study, we demonstrated that TMEM16A inhibition could reduce Evans blue staining and IgG extravasation and increase TJ proteins expression in brain tissues, leading to improved outcomes in an ischemic stroke mouse model. However, it is unclear how the TMEM16A inhibitor exerts its neuroprotective effects. ICAM-1 is a critical endothelia-associated transmembrane protein that stabilizes cell-cell interactions and facilitates leukocyte endothelial transmigration. Treatment with anti-ICAM-1 antibody reduced apoptosis in MCAO rats (Chopp et al., 1996). A number of studies have reported that MCAO significantly upregulated ICAM-1 expression and neutrophil infiltration at 24 h after the onset of reperfusion. Low-moderate ethanol consumption or metformin could alleviate ICAM-1 expression and neutrophil infiltration and improve BBB functions (Liu Y. et al., 2014; Xu et al., 2019). Therefore, inhibiting ICAM-1 upregulation in endothelial cells and accompanying neutrophil infiltration might be a promising strategy in treating ischemic stroke. In this study, the results showed that TMEM16A inhibition or knockdown could reduce ICAM-1 expression and neutrophil accumulation *in vivo* and *in vitro*.

Ischemic stroke and BBB disruption are age-related diseases/phenomena. A large contemporary cohort study by Fonarow et al. (2010) found that older stroke patients differ in clinical characteristics and experience higher in-hospital mortality than younger patients. Ritzel et al. (2018) also demonstrated that age alters the immunological response to stroke, as they found that neutrophil invasion into the brain was increased in aged animals and infiltrating monocytes produced higher levels of ROS and extracellular matrix-degrading enzymes (matrix metallopeptidase 9, MMP9), which, however, can be reversed by receiving bone marrow from young animals. Regarding age-related BBB change, a study using advanced MRI that measures BBB integrity showed that BBB dysfunction is an early event in aging brain (Montagne et al., 2015). Also, aged mice showed lower levels of occludin and ZO-1 than young mice (Elahy et al., 2015). In the present study, we used adult mice (about 2-month old) to perform MCAO, and aged mice could be used to confirm our results in the future.

It has been widely reported that NF-κB is a pivotal transcription factor with a role in the development of the inflammatory response (Yang et al., 2018; Zhang et al., 2018). In resting cells, NF-κB is located in the cytosol. In an activated state, however, NF-κB could be phosphorylated and translocated into the nucleus, promoting the expression of inflammation-associated genes, such as ICAM-1. The present study revealed that knockdown of TMEM16A suppressed NF-κB activation and nuclear translocation. However, overexpression of TMEM16A reversed this effect. These findings were consistent with the results of other studies in human bronchial epithelial cells and glioma cell lines (Liu J. et al., 2014; Lin et al., 2015). To further explore the association of TMEM16A and NF-κB, we also used immunoprecipitation assays to study their physical interaction. However, we failed to observe the direct binding of these two proteins, implying that the effect of TMEM16A on NF-κB might be related to another signaling protein. Tracey (2002) first discovered the neural mechanisms and functional anatomy of the cholinergic anti-inflammatory reflex. The α7 subunit of the nicotinic acetylcholine receptor (α7nAChR) is an important component in the vagus nerve-based cholinergic anti-inflammatory pathway, which inhibits NF-κB nuclear translocation. Using an α7nAChR agonist could inhibit proinflammatory cytokines. However, these effects were blocked by α7nAChR knockdown or α7nAChR antagonist (Wang et al., 2004; Parrish et al., 2008). Whether TMEM16A could affect α7nAChR expression needs to be investigated in the future. The selective inhibitor of NF-κB also alleviated the disruption of BBB permeability, confirming that NF-κB and ICAM-1 upregulation are essential factors involved in ischemia-induced BBB damage.

CONCLUSION

In summary, our research demonstrated that inhibiting the aberrant upregulation of TMEM16A could reverse ischemia-induced BBB injury by downregulating ICAM-1 levels in an NF-κB signaling dependent manner. These findings suggested that TMEM16A may become a potential target for the treatment of ischemic stroke.

DATA AVAILABILITY

The datasets generated for this study are available on request to the corresponding author.

ETHICS STATEMENT

All procedures were approved by the Animal care and Use Committee at Nanjing University.

AUTHOR CONTRIBUTIONS

YX and XC conceived, designed, and coordinated the study. XC, ZZ, P-yL, YL, and X-lT performed the experiments and analyzed the data. X-yB, YZ, and YG helped with primary cells, culture,

and induction of MCAO model. XC and P-yL wrote, revised, and checked the data analysis. All authors revised and approved the final version of the manuscript.

FUNDING

This study was supported by the National Natural Science Foundation of China (Nos. 81701170 and 81630028), the Natural Science Foundation of Jiangsu Province of China (No. BK20170122), the Key Research and Development Program of Jiangsu Province of China (No. BE2016610), and Jiangsu Province Key Medical Discipline (No. ZDXKA2016020).

SUPPLEMENTARY MATERIAL

The Supplementary Material for this article can be found online at: https://www.frontiersin.org/articles/10.3389/fncel.2019.00360/full#supplementary-material

REFERENCES

Akhtar, M., Maikiyo, A. M., Najmi, A. K., Khanam, R., Mujeeb, M., and Aqil, M. (2013). Neuroprotective effects of chloroform and petroleum ether extracts of Nigella sativa seeds in stroke model of rat. *J. Pharm. Bioallied Sci.* 5, 119–125. doi: 10.4103/0975-7406.111825

Bill, A., Hall, M. L., Borawski, J., Hodgson, C., Jenkins, J., Piechon, P., et al. (2014). Small molecule-facilitated degradation of ANO1 protein: a new targeting approach for anticancer therapeutics. *J. Biol. Chem.* 289, 11029–11041. doi: 10.1074/jbc.M114.549188

Cao, X., Jin, Y., Zhang, H., Yu, L., Bao, X., Li, F., et al. (2018). The anti-inflammatory Effects of 4-((5-Bromo-3-chloro-2-hydroxybenzyl) amino)-2-hydroxybenzoic acid in lipopolysaccharide-activated primary microglial cells. *Inflammation* 41, 530–540. doi: 10.1007/s10753-017-0709-z

Cheng, Z., Wang, L., Qu, M., Liang, H., Li, W., Li, Y., et al. (2018). Mesenchymal stem cells attenuate blood-brain barrier leakage after cerebral ischemia in mice. *J. Neuroinflamm.* 15:135. doi: 10.1186/s12974-018-1153-1

Chopp, M., Li, Y., Jiang, N., Zhang, R. L., and Prostak, J. (1996). Antibodies against adhesion molecules reduce apoptosis after transient middle cerebral artery occlusion in rat brain. *J. Cereb. Blood Flow Metab.* 16, 578–584. doi: 10.1097/00004647-199607000-00007

Deng, L., Yang, J., Chen, H., Ma, B., Pan, K., Su, C., et al. (2016). Knockdown of TMEM16A suppressed MAPK and inhibited cell proliferation and migration in hepatocellular carcinoma. *Onco Targets Ther.* 9, 325–333. doi: 10.2147/OTT.S95985

Elahy, M., Jackaman, C., Mamo, J. C., Lam, V., Dhaliwal, S. S., Giles, C., et al. (2015). Blood-brain barrier dysfunction developed during normal aging is associated with inflammation and loss of tight junctions but not with leukocyte recruitment. *Immun. Ageing* 12:2. doi: 10.1186/s12979-015-0029-9

Fonarow, G. C., Reeves, M. J., Zhao, X., Olson, D. M., Smith, E. E., Saver, J. L., et al. (2010). Age-related differences in characteristics, performance measures, treatment trends, and outcomes in patients with ischemic stroke. *Circulation* 121, 879–891. doi: 10.1161/CIRCULATIONAHA.109.892497

Huang, W. C., Xiao, S., Huang, F., Harfe, B. D., Jan, Y. N., and Jan, L. Y. (2012). Calcium-activated chloride channels (CaCCs) regulate action potential and synaptic response in hippocampal neurons. *Neuron* 74, 179–192. doi: 10.1016/j.neuron.2012.01.033

Ji, B., Zhou, F., Han, L., Yang, J., Fan, H., Li, S., et al. (2017). Sodium tanshinone IIA sulfonate enhances effectiveness Rt-PA treatment in acute ischemic stroke patients associated with ameliorating blood-brain barrier damage. *Transl. Stroke Res.* 8, 334–340. doi: 10.1007/s12975-017-0526-6

Ji, Q., Guo, S., Wang, X., Pang, C., Zhan, Y., Chen, Y., et al. (2019). Recent advances in TMEM16A: structure, function, and disease. *J. Cell. Physiol.* 234, 7856–7873. doi: 10.1002/jcp.27865

Jiang, X., Andjelkovic, A. V., Zhu, L., Yang, T., Bennett, M. V. L., Chen, J., et al. (2018). Blood-brain barrier dysfunction and recovery after ischemic stroke. *Prog. Neurobiol.* 163-164, 144–171. doi: 10.1016/j.pneurobio.2017.10.001

Jiao, H., Wang, Z., Liu, Y., Wang, P., and Xue, Y. (2011). Specific role of tight junction proteins claudin-5, occludin, and ZO-1 of the blood-brain barrier in a focal cerebral ischemic insult. *J. Mol. Neurosci.* 44, 130–139. doi: 10.1007/s12031-011-9496-4

Jin, Y., Tang, X., Cao, X., Yu, L., Chen, J., Zhao, H., et al. (2018). 4-((5-(Tert-butyl)-3-chloro-2-hydroxybenzyl) amino)-2-hydroxybenzoic acid protects against oxygen-glucose deprivation/reperfusion injury. *Life Sci.* 204, 46–54. doi: 10.1016/j.lfs.2018.04.056

Kunzelmann, K., Schreiber, R., Kmit, A., Jantarajit, W., Martins, J. R., Faria, D., et al. (2012). Expression and function of epithelial anoctamins. *Exp. Physiol.* 97, 184–192. doi: 10.1113/expphysiol.2011.058206

Lin, J., Jiang, Y., Li, L., Liu, Y., Tang, H., and Jiang, D. (2015). TMEM16A mediates the hypersecretion of mucus induced by interleukin-13. *Exp. Cell Res.* 334, 260–269. doi: 10.1016/j.yexcr.2015.02.026

Liu, B., Linley, J. E., Du, X., Zhang, X., Ooi, L., Zhang, H., et al. (2010). The acute nociceptive signals induced by bradykinin in rat sensory neurons are mediated by inhibition of M-type K+ channels and activation of Ca2+-activated Cl- channels. *J. Clin. Invest.* 120, 1240–1252. doi: 10.1172/JCI41084

Liu, J., Liu, Y., Ren, Y., Kang, L., and Zhang, L. (2014). Transmembrane protein with unknown function 16A overexpression promotes glioma formation through the nuclear factor-kappaB signaling pathway. *Mol. Med. Rep.* 9, 1068–1074. doi: 10.3892/mmr.2014.1888

Liu, Y., Tang, G., Li, Y., Wang, Y., Chen, X., Gu, X., et al. (2014). Metformin attenuates blood-brain barrier disruption in mice following middle cerebral artery occlusion. *J. Neuroinflamm.* 11:177. doi: 10.1186/s12974-014-0177-4

Ma, M. M., Gao, M., Guo, K. M., Wang, M., Li, X. Y., Zeng, X. L., et al. (2017). TMEM16A contributes to endothelial dysfunction by facilitating Nox2 NADPH oxidase-derived reactive oxygen species generation in hypertension. *Hypertension* 69, 892–901. doi: 10.1161/HYPERTENSIONAHA.116.08874

Meng, H., Zhao, H., Cao, X., Hao, J., Zhang, H., Liu, Y., et al. (2019). Double-negative T cells remarkably promote neuroinflammation after ischemic stroke. *Proc. Natl. Acad. Sci. U.S.A.* 116, 5558–5563. doi: 10.1073/pnas.1814394116

Montagne, A., Barnes, S. R., Sweeney, M. D., Halliday, M. R., Sagare, A. P., Zhao, Z., et al. (2015). Blood-brain barrier breakdown in the aging human hippocampus. *Neuron* 85, 296–302. doi: 10.1016/j.neuron.2014.12.032

Obermeier, B., Daneman, R., and Ransohoff, R. M. (2013). Development, maintenance and disruption of the blood-brain barrier. *Nat. Med.* 19, 1584–1596. doi: 10.1038/nm.3407

Parrish, W. R., Rosas-Ballina, M., Gallowitsch-Puerta, M., Ochani, M., Ochani, K., Yang, L. H., et al. (2008). Modulation of TNF release by choline requires alpha7 subunit nicotinic acetylcholine receptor-mediated signaling. *Mol. Med.* 14, 567–574. doi: 10.2119/2008-00079.Parrish

Pineda-Farias, J. B., Barragan-Iglesias, P., Loeza-Alcocer, E., Torres-Lopez, J. E., Rocha-Gonzalez, H. I, Perez-Severiano, F., et al. (2015). Role of anoctamin-1 and bestrophin-1 in spinal nerve ligation-induced neuropathic pain in rats. *Mol Pain* 11:41. doi: 10.1186/s12990-015-0042-1

Qi, Q., Yang, Y., Wu, K., and Xie, Q. (2018). Inhibition of TMEM16A impedes embryo implantation and decidualization in mice. *Reproduction* [Epub ahead of print].

Qin, Y., Jiang, Y., Sheikh, A. S., Shen, S., Liu, J., and Jiang, D. (2016). Interleukin-13 stimulates MUC5AC expression via a STAT6-TMEM16A-ERK1/2 pathway in human airway epithelial cells. *Int. Immunopharmacol.* 40, 106–114. doi: 10.1016/j.intimp.2016.08.033

Ritzel, R. M., Lai, Y. J., Crapser, J. D., Patel, A. R., Schrecengost, A., Grenier, J. M., et al. (2018). Aging alters the immunological response to ischemic stroke. *Acta Neuropathol.* 136, 89–110. doi: 10.1007/s00401-018-1859-2

Suh, S. H., Vennekens, R., Manolopoulos, V. G., Freichel, M., Schweig, U., Prenen, J., et al. (1999). Characterisation of explanted endothelial cells from mouse aorta: electrophysiology and Ca2+ signalling. *Pflugers Arch.* 438, 612–620. doi: 10.1007/s004249900085

Tang, X., Liu, K., Hamblin, M. H., Xu, Y., and Yin, K. J. (2018). Genetic deletion of kruppel-like factor 11 aggravates ischemic brain injury. *Mol. Neurobiol.* 55, 2911–2921. doi: 10.1007/s12035-017-0556-9

Tatulli, G., Mitro, N., Cannata, S. M., Audano, M., Caruso, D., D'Arcangelo, G., et al. (2018). Intermittent fasting applied in combination with rotenone treatment exacerbates dopamine neurons degeneration in mice. *Front. Cell. Neurosci.* 12:4. doi: 10.3389/fncel.2018.00004

Tian, X. Q., Ma, K. T., Wang, X. W., Wang, Y., Guo, Z. K., and Si, J. Q. (2018). Effects of the calcium-activated chloride channel inhibitors T16Ainh-A01 and CaCCinh-A01 on cardiac fibroblast function. *Cell Physiol. Biochem.* 49, 706–716. doi: 10.1159/000493036

Tracey, K. J. (2002). The inflammatory reflex. *Nature* 420, 853–859. doi: 10.1038/nature01321

Wang, H., Liao, H., Ochani, M., Justiniani, M., Lin, X., Yang, L., et al. (2004). Cholinergic agonists inhibit HMGB1 release and improve survival in experimental sepsis. *Nat. Med.* 10, 1216–1221. doi: 10.1038/nm1124

Wang, M., Yang, H., Zheng, L. Y., Zhang, Z., Tang, Y. B., Wang, G. L., et al. (2012). Downregulation of TMEM16A calcium-activated chloride channel contributes to cerebrovascular remodeling during hypertension by promoting basilar smooth muscle cell proliferation. *Circulation* 125, 697–707. doi: 10.1161/CIRCULATIONAHA.111.041806

Wang, P., Zhao, W., Sun, J., Tao, T., Chen, X., Zheng, Y. Y., et al. (2018). Inflammatory mediators mediate airway smooth muscle contraction through a G protein-coupled receptor-transmembrane protein 16A-voltage-dependent Ca(2+) channel axis and contribute to bronchial hyperresponsiveness in asthma. *J. Allergy Clin. Immunol.* 141, 1259.e11–1268.e11. doi: 10.1016/j.jaci.2017.05.053

Warach, S., and Latour, L. L. (2004). Evidence of reperfusion injury, exacerbated by thrombolytic therapy, in human focal brain ischemia using a novel imaging marker of early blood-brain barrier disruption. *Stroke* 35(11 Suppl. 1), 2659–2661. doi: 10.1161/01.STR.0000144051.32131.09

Weng, L., Zhang, H., Li, X., Zhan, H., Chen, F., Han, L., et al. (2017). Ampelopsin attenuates lipopolysaccharide-induced inflammatory response through the inhibition of the NF-kappaB and JAK2/STAT3 signaling pathways in microglia. *Int. Immunopharmacol.* 44, 1–8. doi: 10.1016/j.intimp.2016.12.018

Wu, M. M., Lou, J., Song, B. L., Gong, Y. F., Li, Y. C., Yu, C. J., et al. (2014). Hypoxia augments the calcium-activated chloride current carried by anoctamin-1 in cardiac vascular endothelial cells of neonatal mice. *Br. J. Pharmacol.* 171, 3680–3692. doi: 10.1111/bph.12730

Xu, G., Li, C., Parsiola, A. L., Li, J., McCarter, K. D., Shi, R., et al. (2019). Dose-dependent influences of ethanol on ischemic stroke: role of Inflammation. *Front. Cell. Neurosci.* 13:6. doi: 10.3389/fncel.2019.00006

Yang, X., Chen, S., Shao, Z., Li, Y., Wu, H., Li, X., et al. (2018). Apolipoprotein E deficiency exacerbates spinal cord injury in mice: inflammatory response and oxidative stress mediated by NF-kappaB signaling pathway. *Front. Cell. Neurosci.* 12:142. doi: 10.3389/fncel.2018.00142

Zhang, C. H., Li, Y., Zhao, W., Lifshitz, L. M., Li, H., Harfe, B. D., et al. (2013). The transmembrane protein 16A Ca(2+)-activated Cl- channel in airway smooth muscle contributes to airway hyperresponsiveness. *Am. J. Respir. Crit. Care Med.* 187, 374–381. doi: 10.1164/rccm.201207-1303OC

Zhang, F., Yan, C., Wei, C., Yao, Y., Ma, X., Gong, Z., et al. (2018). Vinpocetine inhibits NF-kappaB-Dependent inflammation in acute ischemic stroke patients. *Transl. Stroke Res.* 9, 174–184. doi: 10.1007/s12975-017-0549-z

Zhao, Q., Yu, Z., Zhang, F., Huang, L., Xing, C., Liu, N., et al. (2019). HDAC3 inhibition prevents oxygen glucose deprivation/reoxygenation-induced transendothelial permeability by elevating PPARgamma activity *in vitro*. *J. Neurochem.* 149, 298–310. doi: 10.1111/jnc.14619

Zhong, N., Fang, Q. Z., Zhang, Y., and Zhou, Z. N. (2000). Volume- and calcium-activated chloride channels in human umbilical vein endothelial cells. *Acta Pharmacol. Sin.* 21, 215–220.

Conflict of Interest Statement: The authors declare that the research was conducted in the absence of any commercial or financial relationships that could be construed as a potential conflict of interest.

Copyright © 2019 Liu, Zhang, Liu, Tang, Shu, Bao, Zhang, Gu, Xu and Cao. This is an open-access article distributed under the terms of the Creative Commons Attribution License (CC BY). The use, distribution or reproduction in other forums is permitted, provided the original author(s) and the copyright owner(s) are credited and that the original publication in this journal is cited, in accordance with accepted academic practice. No use, distribution or reproduction is permitted which does not comply with these terms.

frontiers in Cellular Neuroscience

ORIGINAL RESEARCH
published: 20 September 2019
doi: 10.3389/fncel.2019.00402

In vitro Characterization of Gut Microbiota-Derived Bacterial Strains With Neuroprotective Properties

Suaad Ahmed[1], Alessandro Busetti[1], Parthena Fotiadou[1], Nisha Vincy Jose[1], Sarah Reid[1], Marieta Georgieva[1], Samantha Brown[1], Hayley Dunbar[1], Gloria Beurket-Ascencio[1], Margaret I. Delday[1,2], Anna Ettorre[1] and Imke E. Mulder[1]*

[1] 4D Pharma Research Ltd., Aberdeen, United Kingdom, [2] School of Medicine and Dentistry, Institute of Medical Sciences, Foresterhill, University of Aberdeen, Aberdeen, United Kingdom

Neurodegenerative diseases are disabling, incurable, and progressive conditions characterized by neuronal loss and decreased cognitive function. Changes in gut microbiome composition have been linked to a number of neurodegenerative diseases, indicating a role for the gut-brain axis. Here, we show how specific gut-derived bacterial strains can modulate neuroinflammatory and neurodegenerative processes *in vitro* through the production of specific metabolites and discuss the potential therapeutic implications for neurodegenerative disorders. A panel of fifty gut bacterial strains was screened for their ability to reduce pro-inflammatory IL-6 secretion in U373 glioblastoma astrocytoma cells. *Parabacteroides distasonis* MRx0005 and *Megasphaera massiliensis* MRx0029 had the strongest capacity to reduce IL-6 secretion *in vitro*. Oxidative stress plays a crucial role in neuroinflammation and neurodegeneration, and both bacterial strains displayed intrinsic antioxidant capacity. While MRx0005 showed a general antioxidant activity on different brain cell lines, MRx0029 only protected differentiated SH-SY5Y neuroblastoma cells from chemically induced oxidative stress. MRx0029 also induced a mature phenotype in undifferentiated neuroblastoma cells through upregulation of microtubule-associated protein 2. Interestingly, short-chain fatty acid analysis revealed that MRx0005 mainly produced C1-C3 fatty acids, while MRx0029 produced C4-C6 fatty acids, specifically butyric, valeric and hexanoic acid. None of the short-chain fatty acids tested protected neuroblastoma cells from chemically induced oxidative stress. However, butyrate was able to reduce neuroinflammation *in vitro*, and the combination of butyrate and valerate induced neuronal maturation, albeit not to the same degree as the complex cell-free supernatant of MRx0029. This observation was confirmed by solvent extraction of cell-free supernatants, where only MRx0029 methanolic fractions containing butyrate and valerate showed an anti-inflammatory activity in U373 cells and retained the ability to differentiate neuroblastoma cells. In summary, our results suggest that the pleiotropic nature of live biotherapeutics, as opposed to isolated metabolites, could be a promising novel drug class in drug discovery for neurodegenerative disorders.

Keywords: gut microbiota-derived bacterial strains, microbiome, neurodegenerative diseases, neuroinflammation, neuroprotection, oxidative stress, gut-brain axis, short-chain fatty acids

OPEN ACCESS

Edited by:
Shawn Hayley,
Carleton University, Canada

Reviewed by:
Hari Prasad Osuru,
University of Virginia, United States
Danuta Jantas,
Institute of Pharmacology (PAS), Poland

***Correspondence:**
Anna Ettorre
anna.ettorre@4dpharmaplc.com;
ettorreanna@gmail.com

Specialty section:
This article was submitted to Cellular Neuropathology, a section of the journal Frontiers in Cellular Neuroscience

Received: *01 April 2019*
Accepted: *19 August 2019*
Published: *20 September 2019*

Citation:
Ahmed S, Busetti A, Fotiadou P, Vincy Jose N, Reid S, Georgieva M, Brown S, Dunbar H, Beurket-Ascencio G, Delday MI, Ettorre A and Mulder IE (2019) In vitro Characterization of Gut Microbiota-Derived Bacterial Strains With Neuroprotective Properties. Front. Cell. Neurosci. 13:402. doi: 10.3389/fncel.2019.00402

INTRODUCTION

Neurodegenerative diseases (NDDs) such as Parkinson's disease (PD) and Alzheimer's disease (AD) are disabling, incurable disorders, often associated with aging. Progressive and irreversible loss of neurons, neuroinflammation and degeneration of cellular functions and structures often associated with oxidative stress, are common features of NDDs (Habib et al., 2018). NDDs have a profound impact on the life expectancy of individuals and the socio-economy of the world population (Group, 2017). In recent years, there has been mounting interest in the gut microbiota and its interaction with the immune and central nervous system (CNS) (Fung et al., 2017). Alterations of the microbiota composition in neurodegenerative diseases including PD and AD have been well documented (Gerhardt and Mohajeri, 2018; Sun and Shen, 2018). Shifts in gut bacterial populations, possibly due to environmental and internal stress factors, can contribute to inflammation by altering the production of key signaling molecules in the host. Conversely, changes in host physiology can also affect the composition and diversity of the gut microbiota (Hollister et al., 2014; Fung et al., 2017).

The gut microbiota exerts important effects on brain functions and can affect physiological processes such as host stress responses (Cryan and Dinan, 2012; Foster and McVey Neufeld, 2013), behavior related to depression and anxiety (Foster and McVey Neufeld, 2013) and even susceptibility to autism (Hsiao et al., 2013; Foster et al., 2017). Gut bacteria can also exert neuroprotective effects, for instance by producing metabolites used by the host as neurotransmitters. About 95% of the serotonin in the human body is produced in the digestive tract and plays an important part in gut motor function and digestion, as well as in various cognitive and mood disorders (Yano et al., 2015). In mice, it has been shown that a particular subset of gut bacteria directly stimulates synthesis and release of intestinal serotonin (Yano et al., 2015). Germ-free mice produce lower than normal levels of dopamine and adrenaline, two important molecules involved in the response of the CNS to stress (Asano et al., 2012). Many gut bacteria can produce short-chain fatty acids (SCFAs) from dietary fiber. A reduction in SCFA concentration in fecal samples of PD patients has been described recently, highlighting a potential link between these metabolites and neurological disease (Unger et al., 2016).

The vagus nerve serves as a direct communication path between gut bacteria and the central nervous system (CNS). Recent publications indicate that the effects of a *Lactobacillus rhamnosus* strain on the CNS seem to depend on signals relayed by the vagus nerve (Bravo et al., 2011) and that gut commensal bacteria can influence anxiety-like symptoms in a mouse model of colitis only if the vagus nerve remains functionally intact (Bercik et al., 2011). The CNS and gastrointestinal (GI) tract also communicate through humoral and cellular mediators via the hypothalamic-pituitary-adrenal axis and the immune system by means of cytokines, chemokines and small peptides (De Palma et al., 2014).

Notwithstanding the different cell types and etiology associated with NDDs, inflammation is a major contributing factor to disease (Stephenson et al., 2018). Peripheral immune cells can contribute to neuroinflammation through the production of pro-inflammatory cytokines that are able to cross the blood-brain barrier (BBB) and activate microglia cells. Moreover, when the BBB is disrupted, the brain parenchyma can be exposed to pathogens and immune cells (Hirsch and Hunot, 2009; Zhan et al., 2018).

Stress stimuli can increase gut permeability, which in turn facilitates translocation of gut bacteria and immune responses in the gut mucosa (Keita and Soderholm, 2010). Gram-negative bacteria in the gut can release cell membrane components such as lipopolysaccharide (LPS), which can engage Toll-like receptor 4 (TLR4) on host cells and trigger a pro-inflammatory response (Rakoff-Nahoum et al., 2004). Low levels of circulating LPS can compromise both passive and active BBB mechanisms, rendering the CNS vulnerable to neurotoxic substances and activated immune cells from the periphery (Varatharaj and Galea, 2017). TLR activation by pathogen-associated molecular patterns (such as LPS) and damage-associated molecular patterns (e.g., α-synuclein in PD) is a dynamic process. TLR activation triggers a series of downstream molecular pathways leading to the translocation of NF-κB to the nucleus and culminating in upregulation of pro-inflammatory cytokine expression. Therefore, therapeutic interventions aimed at interfering with TLR signaling could decrease pro-inflammatory cytokine responses leading to an overall reduction of neuroinflammation, oxidative stress and neuronal death (Fellner et al., 2013; Rietdijk et al., 2016).

We have identified gut microbiota strains that possess modulatory activity on human cell biology and physiology readouts relevant to neurodegeneration and neuroinflammation which may then be developed as Live Biotherapeutics. Here, we describe the *in vitro* characterization of two gut bacterial strains with potential neuroprotective properties, namely *Parabacteroides distasonis* MRx0005 and *Megasphaera massiliensis* MRx0029, and report their ability to modulate both neuroinflammation and barrier function *in vitro*.

MATERIALS AND METHODS

Cells and Reagents

Trypsin/EDTA, sterile phosphate buffered saline (PBS), Dulbecco's modified Eagle's medium (DMEM with 4.5 g/L D-glucose), Minimum Essential Medium Eagle (MEME), Nutrient Mixture F-12 Ham, heat inactivated Foetal Bovine Serum (FBS), L-Glutamine, penicillin, streptomycin, retinoic acid, 4′,6-diamidino-2-phenylindole (DAPI), HPLC-grade diethyl ether, formic acid, acetic acid, propionic acid, butyric acid, hexanoic acid and phosphoric acid were purchased from Sigma-Aldrich (Millipore, United Kingdom).

hIL-6 and hIL-8 ELISA kits were purchased from Peprotech (London, United Kingdom).

HPLC-grade hexane, ethyl acetate, acetonitrile, water and methanol, Dichloro-fluorescein diacetate (DCFDA), BCA protein assay kit and general tissue culture plasticware (Corning) were purchased from Fisher Scientific (Loughborough, United Kingdom).

HEK293 reporter cells stably expressing human TLR4 were purchased from InvivoGen, U373 cells from Sigma-Aldrich, SH-SY5Y cells and HT29-MTX-E12 (HT29-mtx) from the European Collection of Authenticated Cell Cultures (ECACC, Public Health England, Salisbury, United Kingdom).

Valeric acid, monoclonal anti-MAP2 (sc-74421) and anti-β3-tubulin (clone 2G10, sc-80005) antibodies were purchased from Santa Cruz Biotechnology.

Anti-β-actin antibody (ab1801) and Alexa Flour 594 conjugated Phalloidin (ab176757) were purchased from Abcam (United Kingdom).

Bacterial Culture – Collection of Bacterial Cell-Free Supernatants

A total of 50 proprietary bacterial strains from the 4D Pharma Ltd., culture collection, a strain library consisting of isolates derived from fecal samples of healthy human donors, were grown anaerobically in Yeast Casitone Fatty Acids$^+$ broth media (YCFA$^+$, E&O Labs, Scotland, United Kingdom) (Yuille et al., 2018). Viable cell counts (VCC) were determined using an Automated Spiral Plater (Don Whitley Scientific, Bingley, United Kingdom) and a Protocol 3 Completed Automated Colony Counting and Chromogenic Identification System (Synbiosis, Cambridge, United Kingdom). Bacterial cell-free supernatants (BCFS) were obtained from stationary phase cultures (inoculated from an overnight culture of a subbed colony from a streaked freezer stock) by centrifuging 10 ml of cultures at 5000 × *g* for 5 min and filtering using a 0.2 μM filter (Millipore, United Kingdom). 1 ml aliquots of the bacterial cell-free supernatants were stored at −80°C until use.

Preparation of MRx0005 and MRx0029 Cultures

Strains MRx0005 and MRx0029 were cultured to stationary phase as described above in a total of 100 ml of YCFA$^+$ media. BCFS were prepared as described above. 20 ml aliquots of each BCFS (untreated control) were stored at −80°C until needed for sequential extraction.

Sequential Solvent Extractions – Preparation of Crude Extracts of MRx0005 and MRx0029

Three biological replicates of MRx0005 and MRx0029 BCFSs and YCFA$^+$ (media control) were extracted sequentially with HPLC-grade hexane (HEX), diethyl ether (DE), ethyl acetate (EtOAc), acetonitrile (ACN) and methanol (MeOH). Briefly, 20 ml of BCFS were placed in glass vials and extracted at room temperature (RT) in 20 ml of HEX on a rotary shaker (70 rpm) for 30 min. A total of three extractions were performed on each BCFS and YCFA$^+$ media control. The remaining aqueous layers were then extracted at RT in 20 ml of DE, EtOAc on a MX-RD-Pro rotary shaker (70 rpm) for 30 min a total of three times. The combined extracts of each sample were dried under reduced pressure in an R-300 rotary evaporator equipped with a V-300 vacuum pump (Büchi, Flawil, Switzerland) at a temperature not exceeding 30°C. The resulting extracts were re-solubilized in 2 ml of corresponding solvent and aliquoted in four 1.5 ml Eppendorf tubes (500 μl each corresponding to 5 ml of original sample). The remaining aqueous layers were then extracted at RT in 20 ml of DE, EtOAc on a MX-RD-Pro rotary shaker (70 rpm) for 30 min a total of three times. The combined extracts of each sample were dried under reduced pressure in a R-300 rotary evaporator equipped with a V-300 vacuum pump (Büchi, Flawil, Switzerland) at a temperature not exceeding 30°C. The resulting extracts were re-solubilized in 2 ml of corresponding solvent and aliquoted in four 1.5 ml Eppendorf tubes (500 μl each corresponding to 5 ml of original sample).

The remaining aqueous layers were evaporated to dryness using an R-300 rotary evaporator. The resulting dry extracts were extracted for 30 min in 20 ml of ACN a total of three times. The ACN extracts were combined, evaporated to dryness using a rotary evaporator, resolubilised in 2 ml of ACN and aliquoted in four 1.5 ml Eppendorf tubes (500 μl each). The remaining dry extracts (ACN insoluble portion of the extracts) were then extracted for 30 min in 20 ml of MeOH a total of three times. The MeOH extracts were combined, evaporated to dryness using an R-300 Rotary Evaporator, resolubilised in 2 ml of MeOH and aliquoted in four 1.5 ml Eppendorf tubes (500 μl each).

Aliquots of the crude extracts were kept overnight at −20°C inducing the precipitation of proteinaceous components. Following overnight precipitation, each aliquot was centrifuged at 10,000 × *g* for 6 min and transferred to a new 2 ml tube. Overnight precipitation was repeated three times after which extracts were dried in a RVC 2-18 CDPlus speedvac (Christ, Osterode am Harz, Germany) and weighed. All dried aliquots of each extract were stored at −80°C until further use.

SCFA Extraction From Bacterial Cell-Free Supernatants

Short-chain fatty acid extraction from YCFA$^+$, YCFA$^+$ spiked with a standard mix of SCFAs (40 mM acetic acid and 20 mM formic acid, propionic acid, butyric acid, valeric acid and hexanoic acid) as well as the methanol extracts of MRx0005 and MRx0029 and YCFA$^+$ (media control) was conducted according to the method of De Baere et al. (2013).

HPLC Analysis of SCFAs

HPLC detection and quantification of SCFAs was conducted according to the method of De Baere et al. (2013) with slight modifications. Briefly, HPLC analysis was performed using a Waters e2695 HPLC system equipped with a Waters Photodiode Array (PDA) detector 2998 (Waters Limited, Elstree, United Kingdom). HPLC analysis of SCFAs standards, SCFAs extracted from MRx0005 and MRx0029 BCFS and MRx0005 and MRx0029 hexane, diethyl ether, ethyl acetate, acetonitrile and methanol extracts were performed using an Xselect® HSS T3 3.5 μm × 4.6 mm × 150 mm LC column (Waters Limited, Elstree, United Kingdom). The LC analysis was performed using the photodiode array detector (PDA) set to analyse wavelengths of 200–800 nm. SCFA detection and quantification was performed at 210 nm. The mobile phase consisted in 25 mM sodium phosphate buffer in HPLC water (pH adjusted to 3.0

using phosphoric acid (A) and acetonitrile (B). The LC method for SCFA detection and quantification was run using the solvent system with the following gradient: t0′ A = 95%, B = 5%; t10′ A = 95%, B = 5%; t30′ A = 30%, B = 70%; t31′ A = 0%, B = 100%; t36′ A = 0%, B = 100%; t38′ A = 5%, B = 95%; t60′ A = 5%, B = 95%; flow = 1 ml/min.

A seven-point calibration curve was prepared for each SCFA by injecting 20 µl of a two-fold serial dilution of a SCFA (40 mM acetic acid and 20 mM formic acid, propionic acid, butyric acid, valeric acid and hexanoic acid). Qutification- extraction efficiency was calculated using the formula below:

[SCFA in $YCFA^+$ spiked and extracted]/[SCFA in $YCFA^+$ spiked not extracted]

Extraction efficiency was used to determine the concentrations of individual SCFAs in each sample. The production of specific SCFAs was calculated by subtracting the amount of corresponding SCFA present in the unspiked media control.

Targeted Metabolomics: Bacterial Metabolites and Fatty Acid Analysis

Sample analysis was carried out by MS-Omics (Copenhagen, Denmark). A mixed pooled sample (QC sample) was created by taking an aliquot from each sample. This sample was analyzed with regular intervals throughout the sequence. Matrix effects were tested for quantified compounds by spiking the QC sample in a minimum of two levels.

For GC-metabolite analysis, samples were derivatized with methyl chloroformate using a slightly modified version of the protocol described by Smart et al. (2010). All samples were analyzed in a randomized order. Analysis was performed using GC (7890B, Agilent) coupled with a quadrupole detector (59977B, Agilent). Raw data was converted to netCDF format using Chemstation (Agilent), before the data was imported and processed in Matlab R2014b (Mathworks, Inc.) using the PARADISe software described by Johnsen et al. (2017).

For SCFA analysis, samples were acidified using hydrochloric acid, and deuterium-labeled internal standards were added. Analysis was performed using a high-polarity column (Zebron™ ZB-FFAP, GC Cap. Column 30 m × 0.25 mm × 0.25 µm) installed in a GC (7890B, Agilent) coupled with a quadrupole detector (59977B, Agilent). Raw data was converted to netCDF format using Chemstation (Agilent), before the data was imported and processed in Matlab R2014b (Mathworks, Inc.) using the PARADISe software described by Johnsen et al. (2017).

Quantification of Bacterial Indole Production From L-Tryptophan

Bacterial Indole production was quantified using an assay described previously (Sasaki-Imamura et al., 2010). Bacteria were cultured to stationary phase of growth. 0.5 mM indole in $YCFA^+$ media was used as a positive chemical control in this assay. The Indole assay was performed using 24-well (non-treated) assay plates. 100 mM tryptophan solution in HCl was dispensed into each well to give a final concentration of 6 mM. 1 ml stationary phase bacterial culture was added to each well and incubated for a further 48 h. Assay plates were centrifuged at 3,500 × *g* at RT for 10 min. The supernatant was retained, and the pellet discarded. In a 96-well plate 140 µl supernatant was dispensed in triplicate. 140 µl Kovac's reagent was added and the absorbance read at 540 nm using a BioRad iMark microplate absorbance reader. The standard curve was prepared by plotting absorbance as a function of final Indole concentration (mM). Indole concentration of the test sample was calculated using the equation extrapolated from linear regression of the standard curve.

2,2-Diphenyl-1-Picrylhydrazyl (DPPH) Free-Radical Assay

BCFS were thawed at 4°C for approximately 2 h prior to use. All samples were diluted 1:2 in 1.5 ml microfuge tubes using sterile 5 mM PBS pH 7 yielding a final volume of 1 ml. A stock solution of 500 µM Trolox in 5 mM PBS, pH 7 was prepared to make the standard curve. Lazaroid antioxidant U83836E was included (200 µM in 100% methanol) as a positive control. The DPPH assay was performed in a 96-well plate as described previously (Chai et al., 2012) with minor modifications made. In brief, 10 µl sample/standard/control was added, in triplicate, to corresponding wells of a 96-well plate. 200 µl of a 200 µmol/L DPPH solution was added to three empty wells as a control. 190 µl of 200 µmol/L DPPH was added to sample/standard/control wells and plates incubated in the dark for 30 min at RT. Absorbance was read at 515 nm using a BioRad iMark microplate absorbance reader. DPPH radical scavenging activity was calculated as follows:

$$\textit{DPPH radical scavenging activity}\ (\%) = [1 - (A_{\text{sample}} - A_{\text{blank}})/A_{\text{control}})] \times \textit{Dilutionfactor} \times 100$$

where A_{sample} was the average absorbance of sample + 200 µmol/L DPPH, $A_{control}$ was the average absorbance of methanol DPPH without sample, and A_{blank} is the average absorbance of $YCFA^{\pm}$ media blank.

2,2′-Azino-Bis-3-Ethylbenzthiazoline-6-Sulfonic Acid (ABTS) Assay

The total antioxidant capacity assay was performed using the Antioxidant Assay Kit according to the manufacturer's instructions. Briefly, all samples were diluted 1:4 in 1X assay buffer. In a 96-well plate, 10 µl standard/control/sample was added in triplicate. 20 µl myoglobin working solution was added to all standard/control/sample wells. 150 µl ABTS substrate solution was added to each well and the absorbance measured at 405 nm using a BioRad iMark microplate absorbance reader.

Bacterial Cell-Free Supernatants Used in Cell-Based Assays

10% v/v of BCFS was used throughout all the cell-based assays presented in this study. During the assay development stage,

a range of $YCFA^+$ volumes across all assay platform was tested for interference. At 10% v/v, $YCFA^+$ media did not affect *per se* the different biochemical and cellular read-outs. $YCFA^+$, the bacterial growth media considered our blank, is a rich media containing amino-acids, vitamins and SCFAs, so it is expected to interfere at some level with biochemical and cellular assays. Moreover, the results from metabolomics analysis further support the use of 10% v/v as the right compromise to allow a clear appreciation of the effects attributable to the different bacterial metabolites. A concentration of BCFS higher than 10% v/v would have altered the pH of the culture media with dramatic effects on cell viability or would have overly activated the cells in our *in vitro* assays.

Reporter Assay for HEK-Blue hTLR4

HEK293-Blue reporter cells stably expressing human TLR4 (HEK-TLR4), were cultured according to the manufacturer's instructions. Briefly, HEK-TLR4 cells were maintained in DMEM 4.5 g/L D-glucose supplemented with 10% (v/v) heat-inactivated FBS, 4 mM L-Glutamine, 100 U/ml penicillin, 100 μg/ml streptomycin, 100 μg/ml normocin, 1X HEK-Blue selection media.

Briefly, cells were washed with PBS, dissociated in PBS and collected in growth media. Cells were plated in 96-well plates at a density of 25,000 cells/well. To evaluate the effect of bacteria strains on LPS inducing NF-κB promoter activation, cells were treated with 10 ng/ml LPS in presence or absence of 10% supernatants and incubated in a CO_2 incubator. Treatments proceeded for 22 h at 37°C and 5% CO_2, after which the detection of Secreted Embryonic Alkaline Phosphatase (SEAP) activity from cell culture supernatant was performed using QUANTI-blue solution according to manufacturer's instructions. Briefly, 20 μl of cell-free supernatant was collected and analyzed for the presence of SEAP by mixing with 200 μl of sterile-filtered QUANTI-Blue detection media. After 2 h incubation at 37°C, optical density was measured at 655 nm on a microplate reader (iMark microplate, Bio-Rad).

U373 Cell Treatment

U373 is a human glioblastoma astrocytoma cell line. Cells (passage 20th–37th) were maintained in 25 ml MEME supplemented with 10% heat-inactivated FBS, 4 mM L-Glutamine, 100 U/ml penicillin, 100 μg/ml streptomycin and 5 μg/ml plasmocin, 1% Non-Essential Amino Acids, 1% Sodium Pyruvate (referred to throughout as full growth media).

Cells were plated in 24-well plates at a density of 100,000 cells/well in 1 ml of full growth media and left to rest at 37°C and 5% CO_2 for 72 h.

BCFS Treatment

On the day of the treatment, the media was removed from each well, cells were rinsed with 0.5 ml wash media (serum free MEME), 0.9 ml stimulation media (MEME media containing 2% FBS) containing 1 μg/ml LPS was added to the appropriate wells and incubated at 37°C and 5% CO_2. After 1 h pre-incubation, cells were removed from CO_2 incubator and treated with 100 μl bacteria supernatant. Media control was used as control.

SCFA Treatment

Cells were pre-treated for 1 h with 1 μg/ml LPS indicated above and incubated at 37°C and 5% CO_2. After 1 h pre-incubation, cells were removed from CO_2 incubator and treated with increasing concentration of fresh prepared Sodium Butyrate (SB), Sodium Valerate (SV) and Hexanoic Acid (HA).

MRx0005 and MRx0029 Fraction Treatment

Cells were pre-treated for 1 h with 1 μg/ml LPS as indicated above. Afterward, cells were removed from CO_2 incubator and treated with 100 μl of the different fractions. Fractions from media were used as controls.

Following each treatment, cells were incubated for 24 h incubation at 37°C and 5% CO_2. Afterward cell-free supernatants were collected and centrifugated at 10,000 × *g* at 4°C for 3 min. Samples were aliquoted in 1.5 ml microtubes and stored in −80°C for hIL-6 and hIL-8 ELISA.

HMC3 Cell Treatment

Human microglia HMC3 cells were grown in glutamine-supplemented EMEM media containing 15% heat inactivated FBS and 100 U/ml penicillin and 100 μg/ml streptomycin. HMC3 cells were plated in 24 well plates at a density of 50,000 cells/well. Cells were left in CO_2 incubator to rest for 48 h. The cells were then washed in blank EMEM and pre-treated in 2% FBS growth media with 10 ng/ml TNF-α for 1 h. Thereafter 10% cell-free bacterial supernatants for MRx0005 and MRx0029 stationary growth cultures were added to TNF-α-treated and untreated wells and incubated in CO_2 incubator at 37°C for 24 h. Cell-free supernatants were collected and centrifugated at 10,000 × *g* for 3 min and 4°C. Samples were aliquoted in 1.5 ml microtubes and stored in −80°C for hIL-6 and hIL-8 ELISA.

Measurement of IL-6 and IL-8 From U373 and HMC3 Cells

Secretion of IL-6 and IL-8 was analyzed using hIL-6 and hIL-8 Standard ELISA Kits, according to the manufacturer's protocol in the cell-free supernatants from U373 and HMC3 cells treated as described above. Samples were measured at 405 nm with correction wavelength set at 655 nm on a microplate reader (iMark, Bio-Rad). Raw data were plotted and analyzed using GraphPad Prism 7 software. The hIL-6 ELISA development kit allows the quantitative measurement of human IL-6 within the range of 24-1500 pg/ml, while hIL-8 ELISA kit the range is 15.6-1000 pg/ml.

ROS Measurement in U373, HMC3, and SH-SY5Y Cells

To evaluate ROS production, U373 cells and HMC3 were plated in black 96 well plates at a density of 10,000 cells/well. U373 cells were rested for 72 h while HMC3 were left to rest for 48 h. Cells were washed with pre-warmed PBS and stained with 10 μM DCFDA molecular probe for 20 min in growth medium

containing 2% FBS. Afterward, the cells were washed with pre-warmed PBS again and treated with 100 μM TBHP in the presence or absence of 10% BCFS for 2 h.

Neuroblastoma SH-SY5Y cells were grown in 50% MEM and 50% Nutrient Mixture F-12 Ham media supplemented with 2 mM L-Glutamine, 10% heat-inactivated FBS, 100 U/ml penicillin and 100 μg/ml streptomycin. Cells were plated in growth medium on a black 96-well plates at 5,000 cells/well and placed in CO_2 incubator. After 24 h, media was replaced with differentiation medium (growth medium containing 1% FBS) and 10 μM retinoic acid (RA). Differentiation medium was replaced every other day and cells were used after 10 days of differentiation. On Day 10, cells were washed with pre-warmed PBS and stained with 10 μM DCFDA molecular probe for 20 min in growth medium containing 1% FBS. Then, cells were washed with pre-warmed PBS again and treated with 100 μM TBHP in the presence or absence of 10% BCFS for 2 h. After the different treatments, plates were examined under light microscope for obvious changes in cell morphology (e.g., round cells, irregular shape, cell detachment). No dramatic changes in the morphology were observed in any of the cell lines used.

Fluorescence intensity was measured using a TECAN plate reader at Excitation 485 nm/Emission 530 nm. Raw data were plotted and analyzed using GraphPad Prism 7 software.

Gene Expression in SH-SY5Y Cells

SH-SY5Y were plated in 6-well plates at a density of 0.5×10^6 cells. After 24 h, cells were treated in differentiation medium (growth medium containing 1% FBS without RA) with 10% BCFS or $YCFA^+$ or 10 μM RA for 24 h. Thereafter, representative images were taken using a phase contrast EVOS XL core microscope at 40×/0.65 magnification. Cells were collected, and total RNA was isolated according to the RNeasy mini kit protocol (Qiagen). cDNA was made using the High Capacity cDNA reverse transcription kit (Applied Biosystems). Gene expression was measured by qPCR. GAPDH was used as internal control. Fold change was calculated according to the $2^{-\Delta\Delta Ct}$ method. Primer sets are listed in **Supplementary Table S1**.

Immunolabelling and Cell Imaging in SH-SY5Y Cells

Cells were seeded onto 8-well chamber slides (Marienfeld Laboratory Glassware) at 5×10^4 cells/well overnight and treated with 10% BCFS for 24 h. Afterward, cells were fixed with 4% paraformaldehyde in PBS (pH 7.3) for 20 min at RT. Fixed cells were washed with PBS, and permeabilized with 1% Triton X-100 in PBS for 10 min. After washing with PBS, the slides were incubated with blocking buffer (4% BSA/PBS) for 1 h at RT before adding anti-MAP2 antibody or β3-tubulin antibodies diluted in 1% BSA/PBS for 1 h at 4°C. They were then washed twice with PBS, followed by incubation with Alexa Fluor-488 conjugated anti-mouse antibody and Alexa Fluor-594 conjugated Phalloidin for 1 h at RT. After washing 3X with PBS, slides were labeled with DAPI and mounted with Vectashield® (Vector Laboratories). Slides were viewed using an Axioskop 50 microscope (Zeiss) equipped with a 63×/1.2 W Korr objective and filter sets suitable for detection of the fluorochromes used. Manual exposure times for the digital acquisition of images immuno-labeled with MAP-2 were kept constant allowing comparison between different wells and treatments. Phalloidin (F-actin) and DAPI (nuclei) exposure times varied to suit the field of view. Randomized fields of view were acquired using a QImaging camera controlled by Image Pro Plus software. Images were saved as TIFF files and opened in Adobe Photoshop CC 2015.1.2. Images of MAP2, DAPI and Phalloidin were then overlaid and merged. Representative images were selected to illustrate the differences in abundance and location of the proteins examined.

Immunoblotting in SH-SY5Y Cells

SH-SY5Y cells were cultured under the indicated conditions described above, treated with MRx0005 and MRx0029 for 24 h and lysed in RIPA buffer containing a cocktail of protease inhibitors (Roche Diagnostics, United Kingdom). Protein concentration was estimated using the BCA protein assay kit, separated by SDS-PAGE and transferred to a PVDF membrane. Membranes were then blocked with 5% non-fat dry milk or 5% BSA and incubated overnight at 4°C with the primary antibodies (MAP2 and β3-tubulin, respectively). The blots were then incubated with the appropriate horseradish peroxidase (HRP)-conjugated secondary antibody, and proteins were detected by chemiluminescence detection kit (Pierce Biotechnology, Rockford, IL, United States). For both MAP2 and β3-tubulin, β-actin served as a control to monitor protein loading variability amongst samples.

Statistical Analysis

Normally distributed data are presented as mean ± SEM; One-way Anova (Sidak's multiple comparison test) was used to analyse the data presented in this paper. A p value < 0.05 was deemed significant in all cases.

RESULTS

In vitro Cytokine Modulation After Exposure of a Glioblastoma Astrocytoma Cell Line to Different Bacterial Strains

As neuroinflammation plays a pivotal role in neurodegenerative diseases (NDDs), the stationary phase bacterial cell-free supernatants (BCFS) of 50 bacterial strains from our proprietary MicroRx (MRx) culture collection were screened for their capacity to induce an anti-inflammatory response in the U373 glioblastoma astrocytoma cell line after treatment with lipopolysaccharide (LPS). After 24 h of treatment, secretion of the pro-inflammatory cytokine IL-6 was measured by ELISA. U373 cells secreted a significant amount of IL-6 in response to LPS in the presence of 2% serum, which provides the soluble form of CD14, the co-receptor for TLR4 (Flo et al., 2002) (**Figure 1**). Out of the fifty strains tested, MRx0005 (a *P. distasonis* strain) and MRx0029 (a *M. massiliensis* strain) displayed the strongest reduction of IL-6 in U373 cells after treatment with LPS

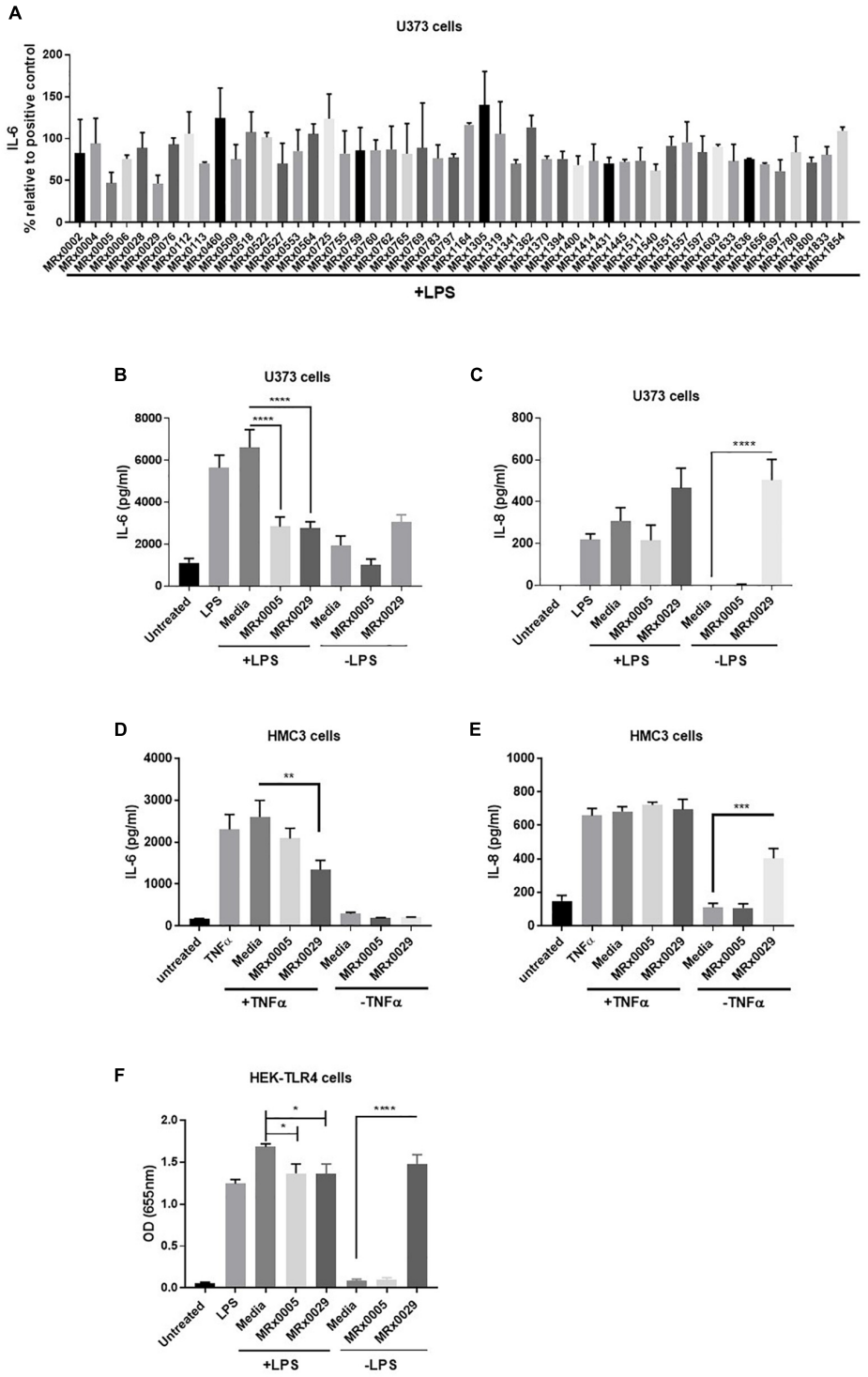


FIGURE 1 | Differential mode of action between MRx0005 and MRx0029: implication for neuroinflammation. U373 cells were pre-treated with 1 μg/ml LPS followed by 10% bacterial cell-free supernatants (BCFS) or media alone. Cell-free supernatants were collected 24 h after treatment from U373 cells and secretion of IL-6 was measured by ELISA. Data are mean ± SEM (n = 2) **(A)**. U373 cells were treated with 1 μg/ml LPS followed by 10% BCFS from MRx0005 and MRx0029 and secretion of IL-6 **(B)** and IL-8 **(C)** measured by ELISA. Controls included also cells treated with BCFS alone. Data are mean ± SEM (n = 5 for IL-6, n = 4 for IL-8). HMC3 cells were pre-treated with TNF-α and then with 10% BCFS from MRx0005 and MRx0029 or media alone for 24 h and IL-6 **(D)** and IL-8 **(E)** measured by ELISA. Controls included also cells treated with BCFS alone. Data are mean ± SEM (n = 3). **(F)** HEK-Blue hTLR4 cells were treated with 10 ng/ml LPS in the presence of 10% BCFS from MRx0005 and MRx0029 or media as control. Controls included also cells treated with BCFS alone. After 22 h, NF-κB-induced SEAP activity was measured using QUANTI-Blue at 655 nm. Data are mean ± SEM (n = 5).

(**Figure 1A**) and were therefore selected for further investigation of their potential neuroprotective profile.

In vitro Cytokine Modulation of Multiple Brain-Derived Cell Lines After Exposure to MRx0005 and MRx0029

U373 cells were again treated with LPS, and secretion of IL-6 and IL-8 was measured. BCFS from stationary phase cultures of both MRx0005 and MRx0029 significantly down-regulated the production of IL-6 in U373 cells pre-treated with LPS (**Figure 1B**). Although not significant, MRx0029 alone slightly increased the basal level of IL-6 compared to the media alone. Interestingly, a different signature for the two strains was observed for IL-8 secretion by U373 cells. MRx0005 decreased the amount of LPS-induced IL-8, while only negligible levels of IL-8 were produced in the absence of LPS (**Figure 1C**). On the contrary, MRx0029 induced higher IL-8 secretion than the respective controls, both alone and after LPS challenge (**Figure 1C**). As activation of microglia represents a prominent feature in neuroinflammation associated with several NDDs, human immortalized microglial clone 3 (HMC3) cells were exposed to LPS or TNF-α to induce secretion of proinflammatory cytokines such as IL-6 and IL-8 (Dello Russo et al., 2018), however, TNF-α was used in subsequent experiments as it gave a higher response than LPS (**Figures 1D,E**). Neither MRx0005 nor MRx0029 reduced the production of IL-8 (**Figure 1E**). Of note, MRx0005 had only a marginal effect in this *in vitro* model of neuroinflammation, while MRx0029 significantly reduced IL-6 secretion in TNF-α-treated HMC3 cells. Interestingly, neither strain induced IL-6 secretion *per se* (**Figure 1D**) and again MRx0029 alone induced IL-8 secretion, as shown in U373 cells (**Figure 1E**).

Inhibition of NF-κB Promoter Activation by MRx0005 and MRx0029

TLR4 is expressed by glial cells and binds LPS, to promote a cascade of events that culminates in activation of transcription factors including NF-κB and pro-inflammatory gene induction. To verify whether treatment with either strain would be able to interfere with NF-κB-Ap1 promoter activity induced by engagement of TLR4, HEK-TLR4 cells were treated with MRx0005 and MRx0029 alone or in combination with LPS. Both MRx0005 and MRx0029 significantly inhibited NF-κB-Ap1 promoter activation induced by LPS (**Figure 1F**). Interestingly, MRx0029 induced NF-κB-Ap1 promoter activation on its own, but MRx0005 did not (**Figure 1F**), thus suggesting that, although both strains are gram-negative bacteria, either MRx0005 interferes with the LPS signaling pathway, or a low amount/chemically different LPS is produced/shed by this strain.

Antioxidant Capacity of MRx0005 and MRx0029

Bacteria can produce several antioxidant compounds as primary and secondary metabolites. To capture the synergistic and redox interactions among the different molecules present in the bacterial supernatants, we used three biochemical assays aimed at characterizing their antioxidant potential: the indole production assay, the total radical-trapping antioxidant parameter (TRAP) using the 2,2-diphenyl-1-picrylhydrazyl (DPPH) assay and the Trolox equivalent antioxidant capacity (TEAC) assay.

Indole derivatives are known for their antioxidant and cytoprotective activity (Estevao et al., 2010). The indole test is used to determine the ability of an organism to convert the amino acid tryptophan to form indole. The free-radical scavenging ability of antioxidants can be predicted from standard one-electron potentials by evaluating the capacity of an antioxidant to reduce an oxidant through color change. The TEAC assay measures the antioxidant capacity of a compound or a mixture of compounds.

Although both strains displayed clear indole-forming capacity, MRx0029 production was significantly higher than MRx0005 (0.3 and 0.2 mM, respectively, **Figure 2A**). The same trend was observed in relation to the ability to act as a radical scavenger in the DPPH assay and the total antioxidant capacity when compared to the lazaroid antioxidant molecule U83836E, a potent inhibitor of lipid peroxidation, or to a standard solution of Trolox, a water-soluble antioxidant derivative of Vitamin E (**Figures 2B,C**). Indeed, both strains showed anti-scavenging and antioxidant capacity, although MRx0029 performed better than MRx0005.

Neuroprotection From Oxidative Stress by MRx0005 and MRx0029 Is Cell-Type Dependent

In parallel to the evaluation of the antioxidant activity of MRx0005 and MRx0029, we evaluated the ability of these strains to protect U373, HMC3 and retinoic acid (RA)-differentiated SH-SY5Y cells from reactive oxygen species (ROS) generated by treatment with Tert-Butyl Hydrogen Peroxide (TBHP). MRx0005 protected HMC3 and, albeit only partially, U373 cells from TBHP-induced ROS, while MRx0029 not only showed no protection, but appeared to slightly increase ROS production (both results were not statistically significant, **Figures 2D,E**). However, in differentiated SH-SY5Y cells, which recapitulate most of the features of neurons *in vitro*, both MRx0005 and MRx0029 treatment resulted in significant protection from ROS induced by TBHP (**Figure 2F**). These results suggested a cell preference of MRx0029 in protecting cells from hydrogen peroxide-induced ROS cytotoxicity involved in neuroinflammation and neurodegeneration.

MRx0029 Induces a Neuron-Like Phenotype in Undifferentiated SH-SY5Y Cells

Interestingly, treatment of undifferentiated SH-SY5Y cells with MRx0029 BCFS induced a differentiated phenotype after 24 h, as depicted in **Figure 3A**. MRx0029 treatment induced morphological features similar to those of cells treated with RA, a chemical commonly used for terminal differentiation of neuroblastoma cells. Qualitative cellular evaluation using bright-field phase-contrast microscopy showed that treatment with MRx0029 indeed altered the morphology of the cells.

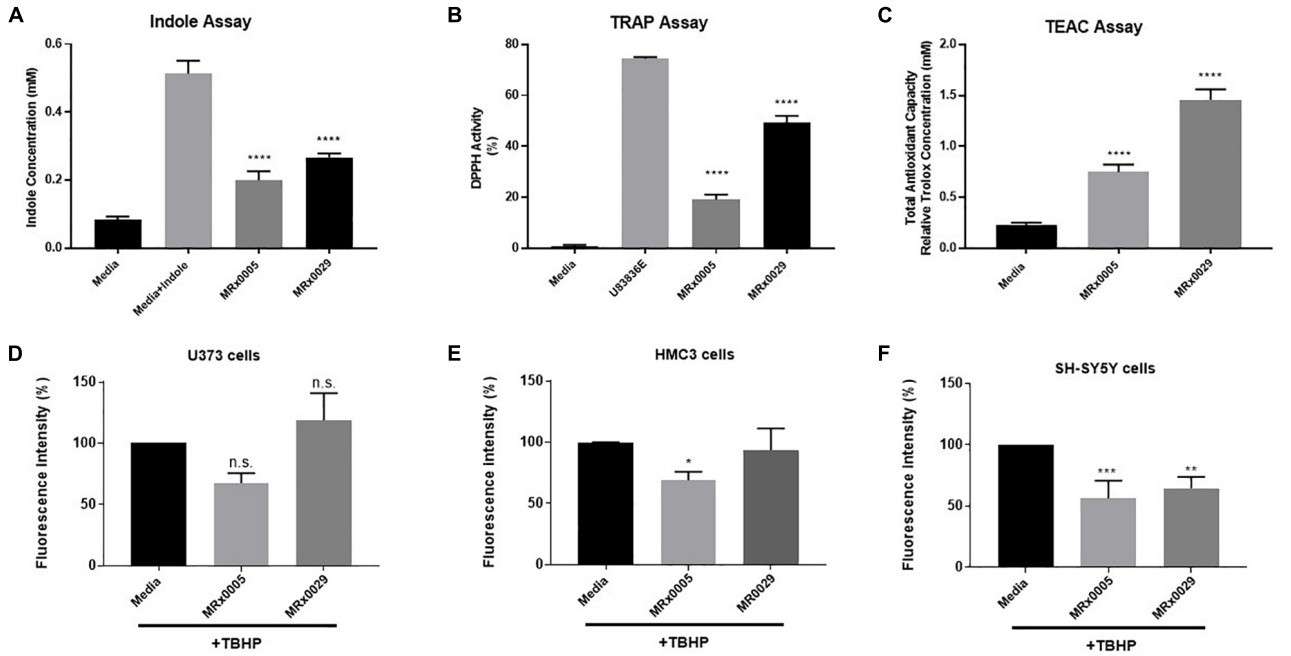


FIGURE 2 | Antioxidant capacity of MRx0005 and MRx0029: Implication for neuro-protection. MRx0005 and MRx0029 bacteria were grown to stationary phase. Biochemical assays were performed as described in section "Material and Methods." **(A)** Indole concentration (mM); **(B)** DPPH scavenging activity assay reported as percentage related to positive control compound U83836E; **(C)** Total antioxidant capacity relative to Trolox concentration (mM). Each value in the graph represents the mean of three experiments corresponding to three cultures of MRx0005 and MRx0029. Data are mean ± SEM (n = 3). **(D)** U373 cells, **(E)** HMC3 cells, and **(F)** differentiated SH-SY5Y cells were stained with DCFDA probe, then treated with 10% BCFS from MRx0005 and MRx0029 or media in the presence of TBHP for 2 h, followed by measurement of fluorescence intensity at Ex/Em = 485/530 nm. Data are mean ± SEM (respectively n = 4, n = 3, and n = 4).

Cell bodies appeared larger and were more elongated than untreated cells, with neurite processes branching out to network with neighboring cells (**Figure 3A**). To further characterize the observed phenotype of MRx0029-treated cells, we investigated the expression of genes associated with neuronal differentiation, such as microtubule-associated protein 2 (MAP2) and synaptophysin (SYP). qPCR analysis revealed that MAP2 transcript was upregulated only by MRx0029. Both MRx0005 and MRx0029 slightly upregulated SYP when compared to untreated control, but not when compared to media alone. Media *per se* significantly upregulated expression of SYP in undifferentiated SH-SY5Y.

As MAP2 gene expression was upregulated solely by MRx0029 treatment (**Figure 3B**), we investigated whether this was reflected at protein level and how its cellular distribution in SH-SY5Y cells was affected (**Figures 3C,D**). To this end, we first performed immunofluorescent labeling of undifferentiated SH-SY5Y cells treated with MRx0005, MRx0029 and media and semi-quantified these results by Western blot analysis. As shown in **Figure 3C**, MAP2 staining was increased in MRx0029-treated cells compared to MRx0005 or media-treated cells. The staining was localized both in the cytoplasm and along the length of the extended neurites (**Figure 3C** panel c, yellow arrows). This pattern was also revealed with the use of another MAP2 antibody (data not shown). Western blot analysis further confirmed and semi-quantified the MAP2 upregulation induced by MRx0029 (**Figure 3D**). Since MAP2 is considered a marker of terminal neuronal differentiation, the results implied that MRx0029 induces neuronal differentiation in SH-SY5Y cells. Two more lines of evidence supported this notion. The staining pattern of Phalloidin in MRx0029-treated cells revealed rearrangement of the cytoskeleton with loss of flattening morphology, large cell bodies and small actin fibers and appearance of long extended neurites, enlarged growth cones and sprouting of minor neurites. Secondly, the appearance of nuclear condensation in some of the cells treated with MRx0029 (**Figure 3C**, panels C and F) were indicative of the pro-apoptotic phase associated with the terminal differentiation process which the cells were undergoing. We also examined the expression of the pre-terminal neuronal differentiation marker β-tubulin. Immunofluorescent labeling of SH-SY5Y cells treated with MRx0005 and MRx0029 showed an increase in staining over media-treated cells (**Figure 3C**, Panel G-L). However, at the protein level there was no statistical difference between the two strains (**Figure 3E**), even though MRx0029 appeared to have a higher expression level than media-treated cells.

Distinct Metabolic Signatures of MRx0005 and MRx0029 Associated With Neuroprotective Phenotypes

Non-digestible carbohydrates are fermented by some members of the gut microbiota to metabolites, such as short-chain fatty acids (SCFAs), medium-chain fatty acids (MCFAs), succinate

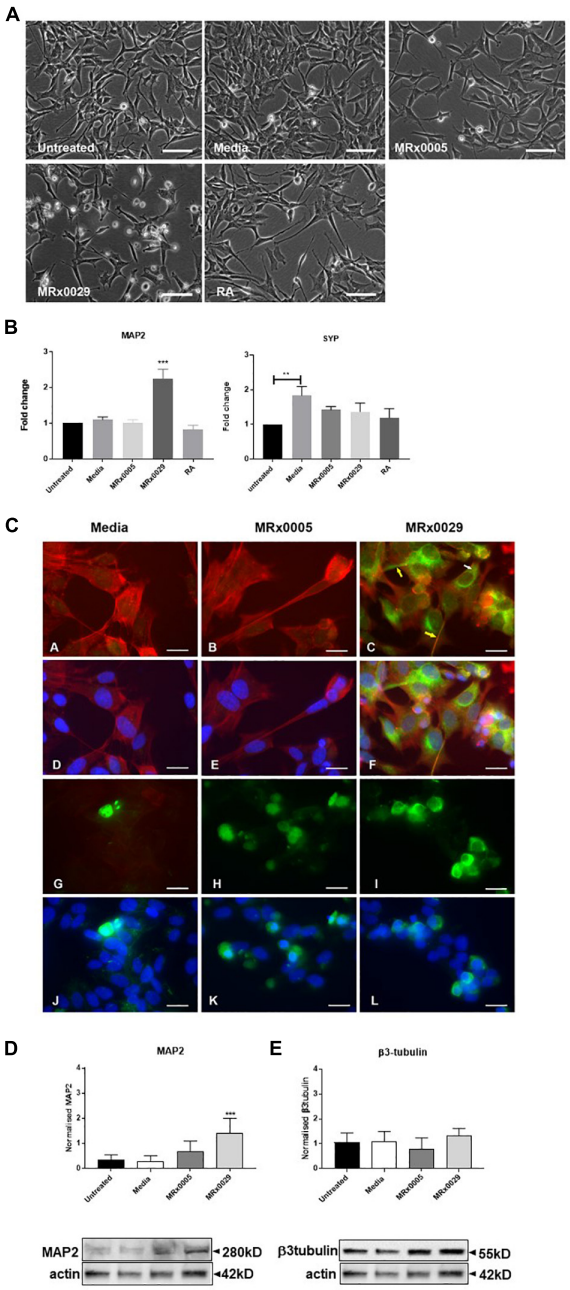


FIGURE 3 | MRx0029 induced SH-SY5Y cells differentiation. Undifferentiated SH-SY5Y cells were treated with 10% MRx0005, MRx0029, media, 10 μM RA for 24 h. **(A)** Representative images using phase contrast microscope to show differences in morphology. Magnification 400×. Scale bar = 10 μm **(B)** Treated cells as described above were collected, total RNA isolated for qPCR to quantify MAP2 and SYP gene expression. Data are mean ± SEM (n = 3). **(C) (a–c)** Representative images of immunolabelled cells with Phalloidin (red) and MAP2 (green), **(d–f)** and merged with DAPI (blue) images; **(g–i)** β3-tubulin immunolabelled cells (green) and **(j–l)** merged with DAPI (blue) images. Magnification 630×. Scale bar = 5 μm. **(D,E)** Western blot analysis of effects of MRx0005 and MRx0029 treatment on SH-SY5Y cells. Western blot membranes were probed with antibodies to **(D)** MAP2 and **(E)** β3-tubulin. Actin was used as a loading control. Lower panels: representative blots from one of five separate experiments; upper panels: relative densitometric intensity. Data are mean ± SEM (n = 5).

and lactate (Morrison and Preston, 2016), that can directly influence the host response to neuroinflammation, oxidative stress and cell-to-cell communication (Marcobal et al., 2013). As both MRx0005 and MRx0029 are fermentative anaerobes, we investigated whether we could identify specific metabolites from the BCFS of these strains that could be related to neuroprotection or neuroinflammation.

Fatty acid analysis, using targeted metabolomics, revealed an interesting dichotomy in the two strains: MRx0005 mainly produced acetic and propanoic acid (C2-C3), while MRx0029 produced butanoic (butyric), pentanoic (valeric) and hexanoic (caproic) acid, both in the linear and branched forms (C4-C6) (**Figure 4A**). Moreover, MRx0005 was found to produce high levels of succinic acid, a dicarboxylic acid with multiple metabolic activities, while the ratio of 4-hydroxy-phenylacetic acid:media was higher in MRx0029 BCFS than in MRx0005 (**Figure 4B**). Representative HPLC chromatograms for SCFA standards, media alone, MRx0005 and MRx0029 are reported in **Figure 4C**. HPLC analysis of BCFS was used to monitor the production of formic, acetic, propionic, butyric, valeric, and hexanoic acid (based on retention time and absorbance spectrum of relevant SCFAs) by MRx0005 and MRx0029. Representative chromatograms for SCFA standards overlaid to MRx0005 and MRx0029 BCFS extracted for SCFAs are reported in **Figure 4C**. HPLC analysis confirmed the production of acetic and propionic acid by MRx0005 and the production of butyric, valeric and hexanoic acid by MRx0029.

Effect of SCFAs on Neuroinflammation and Neurodifferentiation

To investigate the role of SCFAs in reducing secretion of IL-6, U373 cells were treated with increasing concentrations of sodium butyrate (SB), sodium valerate (SV) and hexanoic acid (HA). The concentrations tested covered the range of concentrations measured in the BCFS for the different fatty acids and took into account the fact that only 10% of the above-mentioned supernatants was used in the cell-based assays. Interestingly, only SB inhibited LPS-induced secretion of IL-6 in U373 cells in a concentration-dependent manner (**Figure 5A**). Moreover, both SB and SV increased LPS-induced secretion of IL-8 in the same cells (**Figure 5B**), suggesting that the presence of both these SCFAs likely contributed to IL-8 induction when MRx0029 was added to the culture (**Figures 5A,B**). HA did not inhibit IL-6 or IL-8 secretion after challenge with LPS. None of the SFCAs tested induced *per se* secretion of IL-6 and IL-8 above the basal level (untreated cell control). In fact, only SB (at the highest concentration tested) decreased the basal level of IL-6 but not IL-8 (**Figures 5A,B**). The reconstituted mixture of the three SCFAs reproduced the biological activity of MRx0029 cell-free supernatant, both in the presence and absence of LPS.

To understand whether SCFAs were also involved in neuroprotection, differentiated SH-SY5Y cells were treated with TBHP in the presence or absence of SB, SV and HA. Interestingly, none of the SCFAs tested was able to protect differentiated SH-SY5Y cells from ROS (**Figure 5C**), suggesting that other classes of metabolites produced by our strains are responsible for their

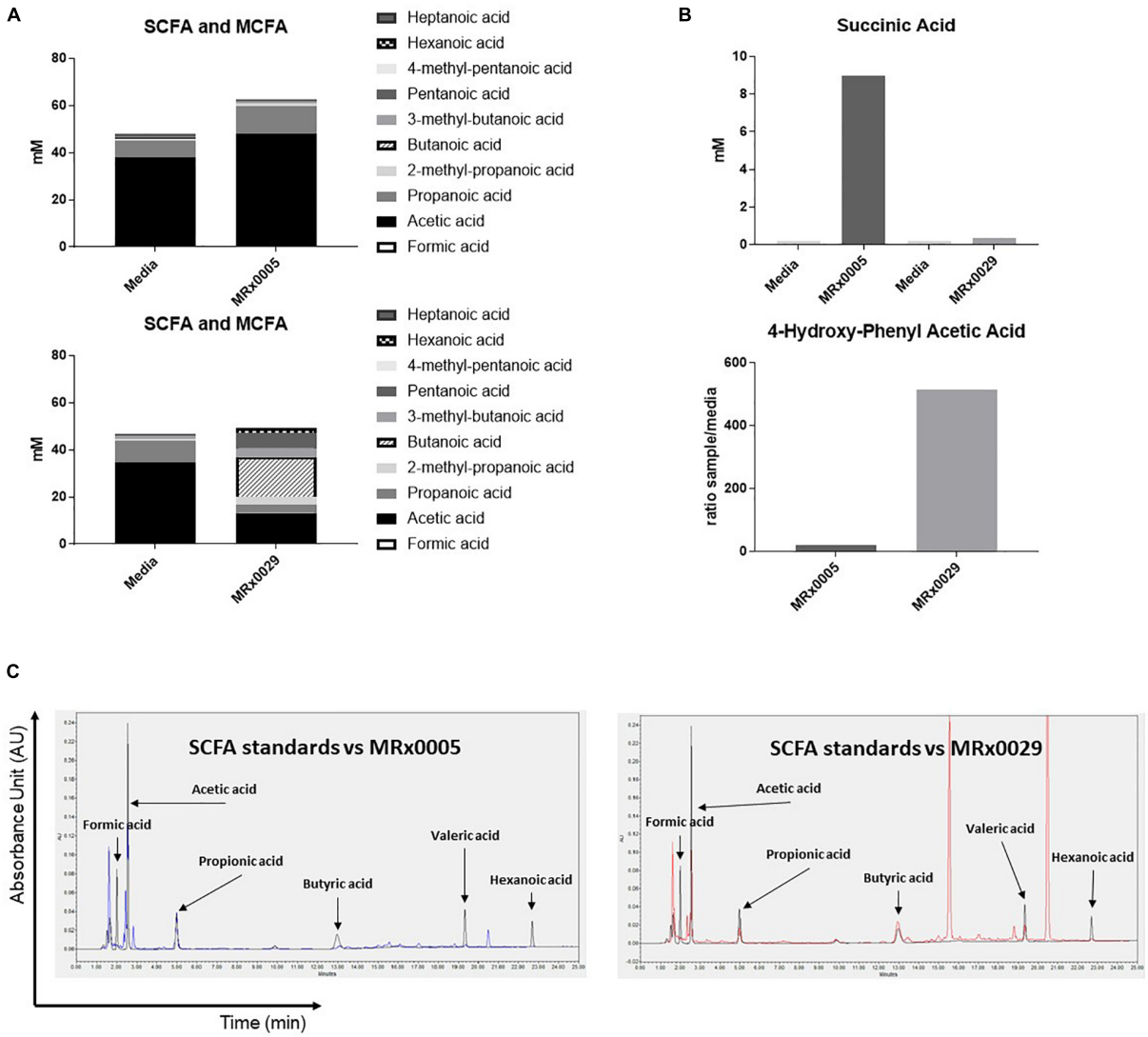


FIGURE 4 | Difference in metabolites produced by MRx0005 and MRx0029. Bacteria were grown to stationary phase and processed as described in section "Materials and Methods." YCFA^{+} was processed alongside MRx0005 and MRx0029. Authentic chemical standards were compared to retention time and mass spectra for the identified metabolites and/or based on library matching of the acquired MS spectra with the NIST library. Only metabolites that differed between the two strains are reported in this figure. **(A)** SCFA and MCFA profile (mM). **(B)** Succinic acid (mM) and 4-hydroxy-phenyl acetic acid (ratio sample/media). The data presented in **(A,B)** are from one experiment (n = 1). **(C)** Representative chromatograms for MRx0005 (left panel in blue) and MRx0029 (right panel in red) overlaid to a standard mix of SCFAs and MCFAs (Formic acid 10 mM, Acetic acid 20 mM, Propionic acid 10 mM, Butyric acid 10 mM, Valeric acid 10 mM, and Hexanoic acid 10 mM in black).

antioxidant activity on neuron-like cells. We also investigated whether SB, SV and HA were able to induce a mature phenotype in undifferentiated neuroblastoma cells. Indeed, butyrate and partially valerate exerted an activity in upregulating MAP2 gene expression in SH-SY5Y cells (**Figure 5D**), albeit not reaching the same fold-change shown for MRx0029 cell-free supernatant (**Figures 3B**, **5G**). As butyrate seems to be the short-chain fatty acid with more prominent activity in both reducing IL-6 secretion from LPS-treated U373 cells and upregulation of MAP2 gene in neuroblastoma cells, two other strains, MRx0071 and MRx1342, known to be butyrate producers (Yuille et al., 2018), were tested in the same assays conducted above. As expected, MRx0071 and MRx1342 reduced LPS-induced IL-6 secretion by U373 cells (**Figure 5E**) without affecting the redox buffering capacity toward reactive oxygen of differentiated SH-SY5Y cells (**Figure 5F**). Interestingly, even though both MRx0071 and MRx1342 induced an increase in the fold change of MAP2 gene expression above the media control samples, they did not reach the significant increase seen following treatment with MRx0029, thus further supporting the hypothesis that other metabolites might contribute to the *in vitro* activity of MRx0029 (**Figure 5G**).

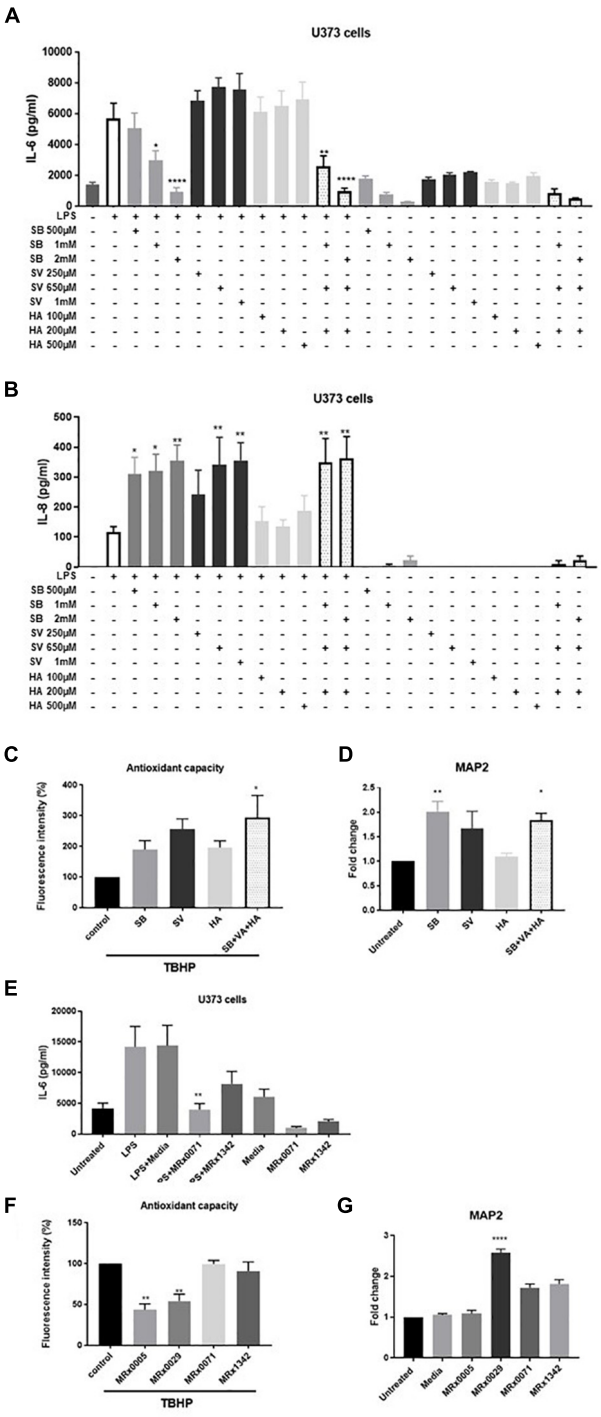


FIGURE 5 | Short-chain fatty acids effect on neuroinflammation and neuroprotection. U373 cells were treated with increasing concentrations of Sodium Butyrate (SB, 500 μM–2 mM), Sodium Valerate (SV, 250 μM–1 mM), or Hexanoic acid (HA, 100–500 μM) in the presence or absence of 1 μg/ml LPS as reported in section "Materials and Methods." Cell-free supernatants were collected 24 h after treatment and secretion of IL-6 **(A)** and IL-8 **(B)** were measured by ELISA. Differentiated SH-SY5Y were treated with 2 mM SB, 0.65 mM SV, and 0.2 mM HA or a combination of the three SCFA at the same concentration found in 10% BCFS from MRx0029. For ROS evaluation, *(Continued)*

FIGURE 5 | Continued
cell treatment in the presence of 100 μM of TBHP for 2 h. Fluorescence intensity was measured at Ex/Em = 485/530 nm. **(D)** Undifferentiated cells were treated with 10% BCFS from MRx0005, MRx0029, MRx0071, and MRx1342. After 24 h, cells were collected, total RNA isolated for qPCR to quantify MAP2 gene expression. Data are mean ± SEMSH-SY5Y cells were treated with 2 mM SB, 0.65 mM SV, 0.2 mM HA or a combination of the three SCFA as described above. After 24 h, cells were collected, total RNA isolated for qPCR to quantify MAP2 gene expression. Data are mean ± SEM (n = 3). **(E)** U373 cells were treated with 10% BCFS from MRx0071 and MRx1342, two butyrate-producing strains from 4D pharma culture collection. Cell-free supernatants were collected 24 h after treatment and secretion of IL-6 was measured. **(F)** Differentiated SH-SY5Y cells and were stained with DCFDA and then treated with 10% BCFS from MRx0005, MRx0029, MRx0071, and MRx1342 in the presence of TBHP for 2 h, followed by measurement of fluorescence intensity at Ex/Em = 485/530 nm. **(G)** Undifferentiated SH-SY5Y (n = 3).

Evaluation of the Biochemical Complexity and *in vitro* Activity of De-Proteinased MRx0005 and MRx0029 Culture Supernatants

BCFS are complex mixtures of secondary metabolites, including peptides and proteins. With the aim of further confirming whether the anti-neuroinflammatory activity of MRx0029 and MRx0005 activity was mainly due to SCFAs, BCFS were sequentially extracted with different solvents of increasing polarity. HPLC analysis of the de-proteinased crude extracts (hexane, F5; diethyl ether, F4; ethyl acetate, F3; acetonitrile, F4; methanol, F1) of MRx0005 and MRx0029 supernatants was conducted to analyse the biochemical complexity of the stationary phase BCFS of the two strains as well as to sub-fractionate compounds based on polarity and solubility. HPLC analysis confirmed the selective extraction and crude fractionation of compounds present in the de-proteinased supernatants (data not shown). U373 cells were treated with the unfractionated BCFS or the different fractions from MRx0005 and MRx0029 both in the presence and absence of LPS. BCFS were collected 24 h after treatment and analyzed by ELISA for IL-6 and IL-8 secretion. The methanolic fraction F1 of MRx0029 decreased IL-6 production and appeared to recapitulate the activity of the unfractionated supernatant, further indicating that the presence of butyrate is associated with the anti-inflammatory activity of this strain. The unfractionated MRx0005 supernatant had a superior effect on IL-6 inhibition compared to the methanolic fraction F1 of this strain (**Figure 6A**). The partial loss of activity might be ascribable both to the removal of a proteinaceous bioactive component of the supernatant or be related to the decrease in availability of a compound like succinic acid due to the chemical processes in place to separate the different fractions. In the absence of LPS, only the unfractionated MRx0029 retained its ability to induce IL-6 (**Figure 6B**). As expected, unfractionated MRx0029 induced IL-8 secretion in U373 cells both in the presence and absence of LPS, and the same activity was produced by the methanolic fraction F1, thus reiterating the important role of butyric and valeric acid in IL-8 production by these neuronal cells (**Figures 6C,D**).

Moreover, HPLC analysis confirmed the selective extraction and fractionation of compounds present in the de-proteinased extracts, as well as corroborated the presence of acetate and propionate in the methanolic fraction of MRx0005 and butyrate, valerate and hexanoate in the methanolic fraction of MRx0029 (**Figures 6E,F**).

DISCUSSION

Neuroinflammation is a common factor in neurodegenerative diseases such as Parkinson's disease (PD) and Alzheimer's disease (AD) (Stephenson et al., 2018). Both genetic (e.g., in rare Mendelian forms of PD and AD) and environmental triggers (e.g., pollutants, neurotoxic metals) play a pivotal role in inducing sustained inflammation in different regions of the brain and in the periphery. Changes in the composition of the human gut microbiome may contribute to neuroinflammation and have indicated the importance of the so-called gut-brain axis in disease setting and progression (Rea et al., 2016). Alterations in gut barrier permeability are associated with host immune responses to molecules of gut bacterial origin, such as lipopolysaccharides (LPS), which are able to reach the systemic circulation and induce a proinflammatory response (Hayes et al., 2018). Cytokines and chemokines are involved in the repair of damaged tissues as well as in the amplification of the proinflammatory response (Charo and Ransohoff, 2006). Proinflammatory cytokines such as IL-6 and IL-8 have been detected in the serum of PD and AD patients and correlate with disease progression and decline of cognitive functions (Reale et al., 2009).

We first investigated the ability of individual members of the gut microbiome to influence neuroinflammatory processes. For this purpose, human glioblastoma astrocytoma U373 cells were treated with LPS, and IL-6 and IL-8 secretion was measured in the cell supernatants. As we hypothesized that bacterial metabolites might confer protection in neuroinflammatory processes, we treated the U373 cells with bacterial supernatants from a panel of bacterial strains. Out of 50 bacterial supernatants tested, MRx0005 and MRx0029 showed a remarkable activity in reducing IL-6 secretion by U373 cells after treatment with LPS.

MRx0005 (*P. distasonis*) and MRx0029 (*M. massiliensis*) are strains from the 4D Pharma culture collection originally isolated from the fecal samples of healthy human donors which we have identified as having protective potential. *P. distasonis* is an obligately anaerobic Gram-negative, rod-shaped, non-spore forming and non-motile bacterial species from the Bacteroidetes phylum (Sakamoto and Benno, 2006). *P. distasonis* is a common member of the commensal microbiota in the human intestine and strains of this species have been studied for their beneficial effects on Multiple Sclerosis (Cekanaviciute et al., 2017). *M. massiliensis* is an obligately anaerobic Gram-negative coccobacillus, which is non-spore forming, non-motile and is a member of the Firmicutes phylum (Padmanabhan et al., 2013). Together with the phylum Bacteroidetes, Firmicutes are a dominant part of the human gut microbiota (Turnbaugh and Gordon, 2009).

The strong reduction in IL-6 secretion by U373 cells treated with MRx0005 and MRx0029 cell-free supernatants together with the intrinsic biotherapeutic potential of these two species prompted us to further characterize these two strains. U373 cells produced IL-8 in response to LPS. Like IL-6, IL-8 is a pro-inflammatory cytokine whose presence in the serum is associated with cognitive dysfunction in the elderly (Baune et al., 2008). Interestingly, IL-8 can also work as a neurotrophic factor by promoting survival of hippocampal neuronal cultures (Araujo and Cotman, 1993). We showed that MRx0005, but not MRx0029, was able to reduce IL-8 production. This could be of relevance in relation to the ability of MRx0029 to induce *per se* significant levels of IL-8.

As LPS is a ligand for TLR4, a similar experimental setting was used with the HEK-TLR4 reporter cell line. While both strains reduced NF-kB activation after treatment with LPS, only MRx0029 induced NF-kB activation *per se*, thus further confirming the observations made in U373 cells. Further work is needed to understand whether the potency of the response might be related to different isoforms of LPS or the quantity secreted by the two strains.

Oxidative stress is associated with cellular neurodegenerative processes in different regions of the brain (Chen et al., 2012). As bacteria can produce different antioxidant metabolites and detoxifying enzymes (Li et al., 2003; Lin et al., 2014), we evaluated the intrinsic scavenging and total antioxidant capacity of both strains by measuring the production of indole, the total radical-trapping antioxidant parameter (TRAP) and the antioxidant capacity of cell-free supernatants in relation to Trolox. Overall, MRx0029 showed a superior antioxidant capacity than MRx0005. However, only MRx0005 conferred protection from reactive oxygen species (ROS) in glioblastoma U373 cells and microglia HMC3 cells. Interestingly, differentiated neuroblastoma SH-SY5Y cells treated with cell-free supernatants showed that MRx0029 was as good as MRx0005 in protecting these cells from TBHP toxicity, suggesting a surprisingly specific tropism of MRx0029 for neuron-like cells.

Differentiated SH-SY5Y cells recapitulate many of the biochemical and functional properties of neurons (Agholme et al., 2010; Forster et al., 2016) and are a commonly used model for NDDs. When undifferentiated SH-SY5Y cells were treated with cell-free supernatants from MRx0005 and MRx0029, microscopic examination revealed that SH-SY5Y cells treated with MRx0029 resembled a neuron-like phenotype, with multiple elongated processes on an oblong body. Gene expression of markers distinctive for differentiated neurons, such as microtubule-associated protein 2 (MAP2) and synaptophysin (SYP), indeed confirmed that MRx0029 induced a differentiated phenotype in neuroblastoma cells. MAP2 upregulation was observed both at gene and protein levels. Further, immunofluorescent labeling revealed that MAP2 localized in the neurites and dendrites as well as in perikarya of mature neurons (Tanapat, 2013). Phalloidin staining indicated a mature neuron-like rearrangement of the cytoskeleton, so we investigated the expression and staining pattern of β3-tubulin, another neurogenesis-associated differentiation marker which plays a role in neuron-specific intracellular structural and transport processes (Pellegrini et al., 2017). Once again, MRx0029

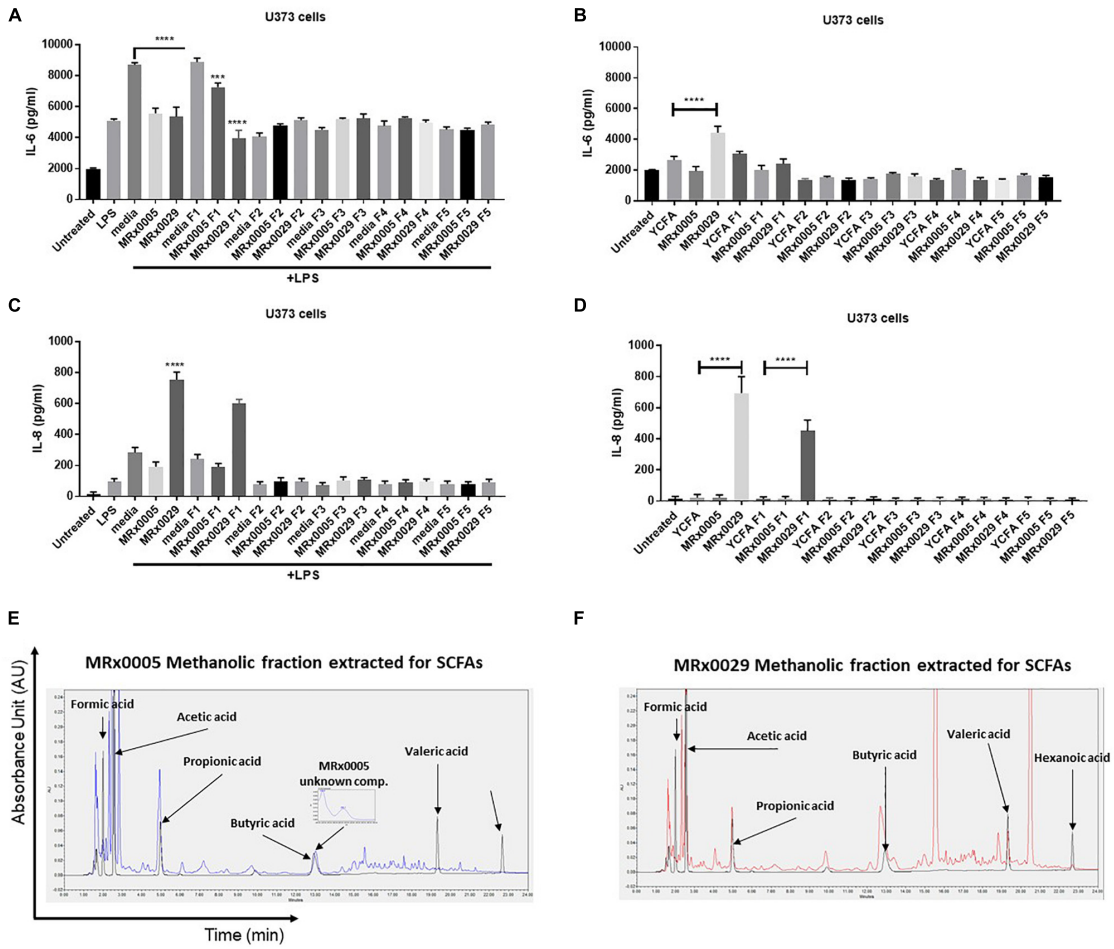


FIGURE 6 | Biochemical characterization and *in vitro* evaluation of the biological activity of MRx0005 and MRx0029 culture supernatant fractions. BCFS from three biological replicates from MRx0005 and MRx0029 were mixed with different solvents of increasing polarity and extracts used in cell-based assays. 10% BCFS, media alone, five different fractions and blank media treated with the same solvents used to prepare the fractions were added to U373 cells in the presence or absence of LPS as described in section "Materials and Methods." Cell-free supernatants were collected 24 h after treatment and secretion of IL-6 and IL-8 was measured by ELISA. IL-6 secretion measured in U373 cells **(A)** pre-treated with 1 μg/ml LPS or in the absence of LPS **(B)**; IL-8 secretion measured in U373 cells **(C)** pre-treated with 1 μg/ml LPS or in the absence of LPS **(D). (E,F)** The MeOH fractions from MRx0005 and MRx0029 were analyzed by HPLC for SCFAs band MCFAs. Representative examples of HPLC chromatograms are shown for MRx0005 and MRx0029. The methanolic fractions for MRx0005 **(E)** and MRx0029 **(F)** were extracted for SCFAs and MCFAs and then overlaid to a standard mix of SCFAs and MCFAs (Formic acid 10 mM, Acetic acid 20 mM, Propionic acid 10 mM, Butyric acid 10 mM, Valeric acid 10 mM, and Hexanoic acid 10 mM in black). The chromatograms highlight the lack of butyric, valeric and hexanoic acid in the MRx0005 methanolic fraction and their presence in the MRx0029 methanolic fraction.

but not MRx0005 induced an upregulation at protein level of β3-tubulin, albeit not to a significant level.

The tandem increase of protein expression of β3-tubulin and more importantly of MAP2 by MRx0029 further strengthens our hypothesis of a tropism of MRx0029 toward a mature phenotype, suggesting that MRx0029 metabolites might alter microtubule dynamics in neuron-like cells. Moreover, as MAP2 promotes neurite outgrowth, which play a major role in re-networking of damaged neurons and synaptogenesis, MAP2 expression might go beyond being a marker of neuronal differentiation and indicate "neuronal re-wiring" associated with the therapeutic outcome of neuropathological disease (Abdanipour et al., 2015).

Overall, we have demonstrated that MRx0005 and MRx0029 affect host function differently in different types of brain cells, with distinct effects on inflammation and neuronal cells. The caveat here is that the cells we have used in this study are either immortalized or derived from tumors. This choice was made to assure a reproducibility of the data at this stage of the project. More investigation using primary microglia cells and neurons are undoubtedly necessary and planned to further understand the biological meaning behind our findings.

We postulate that the effects observed on neuroinflammation and oxidative stress are mediated by bacterial production of different classes of metabolites. SCFAs produced by gut bacteria are typically recognized as positive modulators of host functions. SCFAs mediate water and sodium intake by epithelial cells and play an important role in the proliferation, differentiation and regulation of epithelial cells (Wang et al., 2019). For

example, propionate and butyrate participate in the preservation of mucosal integrity, thwart the proliferation of pathogens in the gut and have been shown to modulate energy metabolism through the gut-brain axis (den Besten et al., 2013; van der Beek et al., 2017; Li et al., 2018). Valeric acid interferes with β-amyloid peptides 1-40 and 1-42 fibril formation *in vitro* and prevents α-synuclein monomers from pairing up and aggregating into fibrils (Ho et al., 2018). Hexanoic acid has been shown to reduce the colonization and dysbiotic expansion of potentially pathogenic bacteria in the gut (Van Immerseel et al., 2004). Succinic acid plays a neuroprotective role in oxidative phosphorylation, a key step for synaptic trafficking of proteins to proximal and distal regions (Budd and Nicholls, 1998). It also augments mitochondrial activity and together with BDNF supports vulnerable neurons in neurodegenerative disorders (Ferro et al., 2017).

MRx0029 is a strong producer of butyric, valeric and hexanoic acid and we investigated the ability of these SCFAs to decrease neuroinflammation in glioblastoma cells and oxidative stress in neuron-like cells. They were tested as single SCFAs and in combination at the same concentrations present in the cell-free supernatant. Interestingly, only butyric acid was able to reduce IL-6 secretion in the presence of LPS in a concentration-dependent manner. Neither valeric nor hexanoic acid inhibited IL-6 or IL-8 secretion in the presence of LPS. The combination of the three SCFAs reconstituted at the same concentration measured in MRx0029 supernatant recapitulated the activity of the supernatant, suggesting that butyrate drove the anti-inflammatory activity of MRx0029. However, butyrate and valeric acid were only partially involved in the ability of MRx0029 to induce a mature phenotype in neuroblastoma cells. It has been reported that medium-chain fatty acids can promote neurite outgrowth (Kamata et al., 2007).

To simplify the complexity of the supernatant and assess the activity of the SCFAs, the cell-free supernatants from MRx0005 and MRx0029 were extracted with solvents of increasing polarity. Only the methanolic fraction of MRx0029 containing butyric, valeric and hexanoic acid produced the same effects on U373 cells as described above. Of note, the methanolic fraction of MRx0005 containing acetate and propionate only partially recapitulated the anti-inflammatory activity of MRx0005, which might be due to the removal of proteinaceous bioactive molecules or to the chemical treatment resulting in the potential generation of esters of fatty acids such as succinate. Our theory is that is the synergistic activity of SCFAs and other metabolites produced by MRx0029 creates the neurotrophic activity of this strain and supports its potential therapeutic use as an LPB in the treatment of NDDs.

MRx0029 is a histone deacetylase (HDAC) inhibitor through its production of butyrate, as shown in a research paper recently published by our group (Yuille et al., 2018). Wakade and Chong investigated the neuroprotective mechanisms of butyric acid in the context of Parkinson's disease by analyzing the relationship between the niacin receptor and dopamine levels (Wakade and Chong, 2014). Butyric acid has the potential to beneficially impact Parkinson's symptoms by reducing inflammation, increasing dopamine synthesis (by improving the amount of free niacin that is available for dopamine synthesis) and boosting mitochondrial function to provide cells with more energy (Donohoe et al., 2011; Bourassa et al., 2016). Our findings highlight how the activity of a specific combination of SCFAs can affect neuropathological aspects of NDDs and how the use of LBPs rather than the single purified metabolite could be therapeutically successful.

In summary, this study provides compelling evidence of how using our *in vitro* screening platform we have identified two gut-derived bacteria that can modulate relevant cell types targeted by neuroinflammation and oxidative stress in NDDs. The strains *P. distasonis* MRx0005 and *M. massiliensis* MRx0029 both have an anti-inflammatory signature, however, MRx0029 seems to preferentially protect neurons from cytotoxicity induced by oxidative stress. More investigations using relevant *in vitro* and *in vivo* models are underway to fully dissect the molecular pathways behind the therapeutic use of these bacteria strains in neurodegenerative diseases.

DATA AVAILABILITY

16S gene sequences for MRx0005 and MRx0029 are disclosed in International Patent Publication Nos. WO2018/229189 and WO2018/229216, respectively, filed by 4D Pharma Research Ltd. The data supporting the findings in this paper are available within the article and its **Supplementary Information Files**.

ETHICS STATEMENT

Ethical approval for collection of faecal samples from healthy human donors was granted from the West of Scotland Research Ethics Committee (Ref. 15/WS/0277). The biological samples have been obtained with any necessary informed written consent from the volunteering participants.

AUTHOR CONTRIBUTIONS

In vitro experiments: AE, SA, and AB designed the experiments; SA, PF, NV, MG, SB, GB-A, and MD performed the majority of the *in vitro* experiments; SR, HD, and AB validated, performed, and analyzed the microbiological-related data output; AE coordinated and managed the research project; AE, SA, PF, and AB analyzed the data. IM oversaw the overall research plan. AE wrote the manuscript with the assistance of SA and AB. All authors have read and commented on the manuscript and have approved the final version of the manuscript.

FUNDING

This work was privately funded by 4D Pharma PLC. The authors of the study, who are employees of (or in the case of MID, are funded by) 4D Pharma Research Ltd., a wholly owned subsidiary of the funder, were responsible for the design and execution of the study, as well as the analysis of the results obtained.

ACKNOWLEDGMENTS

The authors are grateful to Dr. Nicole Reichardt and the 4D Pharma Isolation Team for their technical assistance with bacterial culture.

SUPPLEMENTARY MATERIAL

The Supplementary Material for this article can be found online at: https://www.frontiersin.org/articles/10.3389/fncel.2019.00402/full#supplementary-material

REFERENCES

Abdanipour, A., Schluesener, H. J., Tiraihi, T., and Noori-Zadeh, A. (2015). Systemic administration of valproic acid stimulates overexpression of microtubule-associated protein 2 in the spinal cord injury model to promote neurite outgrowth. *Neurol. Res.* 37, 223–228. doi: 10.1179/1743132814Y.0000000438

Agholme, L., Lindstrom, T., Kagedal, K., Marcusson, J., and Hallbeck, M. (2010). An in vitro model for neuroscience: differentiation of SH-SY5Y cells into cells with morphological and biochemical characteristics of mature neurons. *J. Alzheimers Dis.* 20, 1069–1082. doi: 10.3233/JAD-2010-091363

Araujo, D. M., and Cotman, C. W. (1993). Trophic effects of interleukin-4, -7 and -8 on hippocampal neuronal cultures: potential involvement of glial-derived factors. *Brain Res.* 600, 49–55. doi: 10.1016/0006-8993(93)90400-h

Asano, Y., Hiramoto, T., Nishino, R., Aiba, Y., Kimura, T., Yoshihara, K., et al. (2012). Critical role of gut microbiota in the production of biologically active, free catecholamines in the gut lumen of mice. *Am. J. Physiol. Gastrointest. Liver Physiol.* 303, G1288–G1295. doi: 10.1152/ajpgi.00341.2012

Baune, B. T., Ponath, G., Golledge, J., Varga, G., Arolt, V., Rothermundt, M., et al. (2008). Association between IL-8 cytokine and cognitive performance in an elderly general population–the MEMO-Study. *Neurobiol. Aging* 29, 937–944. doi: 10.1016/j.neurobiolaging.2006.12.003

Bercik, P., Denou, E., Collins, J., Jackson, W., Lu, J., Jury, J., et al. (2011). The intestinal microbiota affect central levels of brain-derived neurotropic factor and behavior in mice. *Gastroenterology* 141, 599.e3–609.e3. doi: 10.1053/j.gastro.2011.04.052

Bourassa, M. W., Alim, I., Bultman, S. J., and Ratan, R. R. (2016). Butyrate, neuroepigenetics and the gut microbiome: can a high fiber diet improve brain health? *Neurosci. Lett.* 625, 56–63. doi: 10.1016/j.neulet.2016.02.009

Bravo, J. A., Forsythe, P., Chew, M. V., Escaravage, E., Savignac, H. M., Dinan, T. G., et al. (2011). Ingestion of *Lactobacillus* strain regulates emotional behavior and central GABA receptor expression in a mouse via the vagus nerve. *Proc. Natl. Acad. Sci. U.S.A.* 108, 16050–16055. doi: 10.1073/pnas.1102999108

Budd, S. L., and Nicholls, D. G. (1998). Mitochondria in the life and death of neurons. *Essays Biochem.* 33, 43–52. doi: 10.1042/bse0330043

Cekanaviciute, E., Yoo, B. B., Runia, T. F., Debelius, J. W., Singh, S., Nelson, C. A., et al. (2017). Gut bacteria from multiple sclerosis patients modulate human T cells and exacerbate symptoms in mouse models. *Proc. Natl. Acad. Sci. U.S.A.* 114, 10713–10718. doi: 10.1073/pnas.1711235114

Chai, Y. Y., Wang, F., Li, Y. L., Liu, K., and Xu, H. (2012). Antioxidant activities of stilbenoids from rheum emodi wall. *Evid. Based Complement. Alternat. Med.* 2012:603678. doi: 10.1155/2012/603678

Charo, I. F., and Ransohoff, R. M. (2006). The many roles of chemokines and chemokine receptors in inflammation. *N Engl. J. Med.* 354, 610–621. doi: 10.1056/NEJMra052723

Chen, X., Guo, C., and Kong, J. (2012). Oxidative stress in neurodegenerative diseases. *Neural Regen. Res.* 7, 376–385. doi: 10.3969/j.issn.1673-5374.2012.05.009

Cryan, J. F., and Dinan, T. G. (2012). Mind-altering microorganisms: the impact of the gut microbiota on brain and behaviour. *Nat. Rev. Neurosci.* 13, 701–712. doi: 10.1038/nrn3346

De Baere, S., Eeckhaut, V., Steppe, M., De Maesschalck, C., De Backer, P., Van Immerseel, F., et al. (2013). Development of a HPLC-UV method for the quantitative determination of four short-chain fatty acids and lactic acid produced by intestinal bacteria during in vitro fermentation. *J. Pharm. Biomed. Anal.* 80, 107–115. doi: 10.1016/j.jpba.2013.02.032

De Palma, G., Collins, S. M., Bercik, P., and Verdu, E. F. (2014). The microbiota-gut-brain axis in gastrointestinal disorders: stressed bugs, stressed brain or both? *J. Physiol.* 592, 2989–2997. doi: 10.1113/jphysiol.2014.273995

Dello Russo, C., Cappoli, N., Coletta, I., Mezzogori, D., Paciello, F., Pozzoli, G., et al. (2018). The human microglial HMC3 cell line: where do we stand? A systematic literature review. *J. Neuroinflammation* 15:259. doi: 10.1186/s12974-018-1288-0

den Besten, G., van Eunen, K., Groen, A. K., Venema, K., Reijngoud, D. J., and Bakker, B. M. (2013). The role of short-chain fatty acids in the interplay between diet, gut microbiota, and host energy metabolism. *J. Lipid Res.* 54, 2325–2340. doi: 10.1194/jlr.R036012

Donohoe, D. R., Garge, N., Zhang, X., Sun, W., O'Connell, T. M., Bunger, M. K., et al. (2011). The microbiome and butyrate regulate energy metabolism and autophagy in the mammalian colon. *Cell Metab.* 13, 517–526. doi: 10.1016/j.cmet.2011.02.018

Estevao, M. S., Carvalho, L. C., Ribeiro, D., Couto, D., Freitas, M., Gomes, A., et al. (2010). Antioxidant activity of unexplored indole derivatives: synthesis and screening. *Eur. J. Med. Chem.* 45, 4869–4878. doi: 10.1016/j.ejmech.2010.07.059

Fellner, L., Irschick, R., Schanda, K., Reindl, M., Klimaschewski, L., Poewe, W., et al. (2013). Toll-like receptor 4 is required for alpha-synuclein dependent activation of microglia and astroglia. *Glia* 61, 349–360. doi: 10.1002/glia.22437

Ferro, A., Carbone, E., Zhang, J., Marzouk, E., Villegas, M., Siegel, A., et al. (2017). Short-term succinic acid treatment mitigates cerebellar mitochondrial OXPHOS dysfunction, neurodegeneration and ataxia in a Purkinje-specific spinocerebellar ataxia type 1 (SCA1) mouse model. *PLoS One* 12:e0188425. doi: 10.1371/journal.pone.0188425

Flo, T. H., Ryan, L., Latz, E., Takeuchi, O., Monks, B. G., Lien, E., et al. (2002). Involvement of toll-like receptor (TLR) 2 and TLR4 in cell activation by mannuronic acid polymers. *J. Biol. Chem.* 277, 35489–35495. doi: 10.1074/jbc.M201366200

Forster, J. I, Koglsberger, S., Trefois, C., Boyd, O., Baumuratov, A. S., Buck, L., et al. (2016). Characterization of differentiated SH-SY5Y as neuronal screening model reveals increased oxidative vulnerability. *J. Biomol. Screen* 21, 496–509. doi: 10.1177/1087057115625190

Foster, J. A., and McVey Neufeld, K. A. (2013). Gut-brain axis: how the microbiome influences anxiety and depression. *Trends Neurosci.* 36, 305–312. doi: 10.1016/j.tins.2013.01.005

Foster, J. A., Rinaman, L., and Cryan, J. F. (2017). Stress & the gut-brain axis: regulation by the microbiome. *Neurobiol. Stress* 7, 124–136. doi: 10.1016/j.ynstr.2017.03.001

Fung, T. C., Olson, C. A., and Hsiao, E. Y. (2017). Interactions between the microbiota, immune and nervous systems in health and disease. *Nat. Neurosci.* 20, 145–155. doi: 10.1038/nn.4476

Gerhardt, S., and Mohajeri, M. H. (2018). Changes of colonic bacterial composition in parkinson's disease and other neurodegenerative diseases. *Nutrients* 10:E708. doi: 10.3390/nu10060708

Group, G. B. D. N. D. C. (2017). Global, regional, and national burden of neurological disorders during 1990-2015: a systematic analysis for the global burden of disease study 2015. *Lancet Neurol.* 16, 877–897. doi: 10.1016/S1474-4422(17)30299-5

Habib, R., Noureen, N., and Nadeem, N. (2018). Decoding common features of neurodegenerative disorders: from differentially expressed genes to pathways. *Curr. Genomics* 19, 300–312. doi: 10.2174/1389202918666171005100549

Hayes, C. L., Dong, J., Galipeau, H. J., Jury, J., McCarville, J., Huang, X., et al. (2018). Commensal microbiota induces colonic barrier structure and functions that contribute to homeostasis. *Sci. Rep.* 8:14184. doi: 10.1038/s41598-018-32366-6

Hirsch, E. C., and Hunot, S. (2009). Neuroinflammation in Parkinson's disease: a target for neuroprotection? *Lancet Neurol.* 8, 382–397. doi: 10.1016/S1474-4422(09)70062-6

Ho, L., Ono, K., Tsuji, M., Mazzola, P., Singh, R., and Pasinetti, G. M. (2018). Protective roles of intestinal microbiota derived short chain fatty acids in

Alzheimer's disease-type beta-amyloid neuropathological mechanisms. *Expert Rev. Neurother.* 18, 83–90. doi: 10.1080/14737175.2018.1400909

Hollister, E. B., Gao, C., and Versalovic, J. (2014). Compositional and functional features of the gastrointestinal microbiome and their effects on human health. *Gastroenterology* 146, 1449–1458. doi: 10.1053/j.gastro.2014.01.052

Hsiao, E. Y., McBride, S. W., Hsien, S., Sharon, G., Hyde, E. R., McCue, T., et al. (2013). Microbiota modulate behavioral and physiological abnormalities associated with neurodevelopmental disorders. *Cell* 155, 1451–1463. doi: 10.1016/j.cell.2013.11.024

Johnsen, L. G., Skou, P. B., Khakimov, B., and Bro, R. (2017). Gas chromatography - mass spectrometry data processing made easy. *J. Chromatogr. A* 1503, 57–64. doi: 10.1016/j.chroma.2017.04.052

Kamata, Y., Shiraga, H., Tai, A., Kawamoto, Y., and Gohda, E. (2007). Induction of neurite outgrowth in PC12 cells by the medium-chain fatty acid octanoic acid. *Neuroscience* 146, 1073–1081. doi: 10.1016/j.neuroscience.2007.03.001

Keita, A. V., and Soderholm, J. D. (2010). The intestinal barrier and its regulation by neuroimmune factors. *Neurogastroenterol. Motil.* 22, 718–733. doi: 10.1111/j.1365-2982.2010.01498.x

Li, Y., Hugenholtz, J., Abee, T., and Molenaar, D. (2003). Glutathione protects *Lactococcus lactis* against oxidative stress. *Appl. Environ. Microbiol.* 69, 5739–5745. doi: 10.1128/aem.69.10.5739-5745.2003

Li, Z., Yi, C. X., Katiraei, S., Kooijman, S., Zhou, E., Chung, C. K., et al. (2018). Butyrate reduces appetite and activates brown adipose tissue via the gut-brain neural circuit. *Gut* 67, 1269–1279. doi: 10.1136/gutjnl-2017-314050

Lin, Y., Jain, R., and Yan, Y. (2014). Microbial production of antioxidant food ingredients via metabolic engineering. *Curr. Opin. Biotechnol.* 26, 71–78. doi: 10.1016/j.copbio.2013.10.004

Marcobal, A., Kashyap, P. C., Nelson, T. A., Aronov, P. A., Donia, M. S., Spormann, A., et al. (2013). A metabolomic view of how the human gut microbiota impacts the host metabolome using humanized and gnotobiotic mice. *ISME J.* 7, 1933–1943. doi: 10.1038/ismej.2013.89

Morrison, D. J., and Preston, T. (2016). Formation of short chain fatty acids by the gut microbiota and their impact on human metabolism. *Gut Microbes* 7, 189–200. doi: 10.1080/19490976.2015.1134082

Padmanabhan, R., Lagier, J. C., Dangui, N. P., Michelle, C., Couderc, C., Raoult, D., et al. (2013). Non-contiguous finished genome sequence and description of *Megasphaera* massiliensis sp. nov. *Stand. Genomic Sci.* 8, 525–538. doi: 10.4056/sigs.4077819

Pellegrini, L., Wetzel, A., Granno, S., Heaton, G., and Harvey, K. (2017). Back to the tubule: microtubule dynamics in Parkinson's disease. *Cell Mol. Life Sci.* 74, 409–434. doi: 10.1007/s00018-016-2351-6

Rakoff-Nahoum, S., Paglino, J., Eslami-Varzaneh, F., Edberg, S., and Medzhitov, R. (2004). Recognition of commensal microflora by toll-like receptors is required for intestinal homeostasis. *Cell* 118, 229–241. doi: 10.1016/j.cell.2004.07.002

Rea, K., Dinan, T. G., and Cryan, J. F. (2016). The microbiome: a key regulator of stress and neuroinflammation. *Neurobiol. Stress* 4, 23–33. doi: 10.1016/j.ynstr.2016.03.001

Reale, M., Greig, N. H., and Kamal, M. A. (2009). Peripheral chemo-cytokine profiles in Alzheimer's and Parkinson's diseases. *Mini Rev. Med. Chem.* 9, 1229–1241. doi: 10.2174/138955709789055199

Rietdijk, C. D., Van Wezel, R. J. A., Garssen, J., and Kraneveld, A. D. (2016). Neuronal Toll-like receptors and neuro-immunity in Parkinson's disease, Alzheimer's disease and stroke. *Neuroimmunol. Neuroinflamm.* 3, 27–37.

Sakamoto, M., and Benno, Y. (2006). Reclassification of *Bacteroides* distasonis, *Bacteroides* goldsteinii and *Bacteroides* merdae as *Parabacteroides* distasonis gen. nov., comb. nov., *Parabacteroides* goldsteinii comb. nov. and *Parabacteroides* merdae comb. nov. *Int. J. Syst. Evol. Microbiol.* 56(Pt 7), 1599–1605. doi: 10.1099/ijs.0.64192-0

Sasaki-Imamura, T., Yano, A., and Yoshida, Y. (2010). Production of indole from L-tryptophan and effects of these compounds on biofilm formation by *Fusobacterium nucleatum* ATCC 25586. *Appl. Environ. Microbiol.* 76, 4260–4268. doi: 10.1128/AEM.00166-10

Smart, K. F., Aggio, R. B., Van Houtte, J. R., and Villas-Boas, S. G. (2010). Analytical platform for metabolome analysis of microbial cells using methyl chloroformate derivatization followed by gas chromatography-mass spectrometry. *Nat. Protoc.* 5, 1709–1729. doi: 10.1038/nprot.2010.108

Stephenson, J., Nutma, E., van der Valk, P., and Amor, S. (2018). Inflammation in CNS neurodegenerative diseases. *Immunology* 154, 204–219. doi: 10.1111/imm.12922

Sun, M. F., and Shen, Y. Q. (2018). Dysbiosis of gut microbiota and microbial metabolites in Parkinson's Disease. *Ageing Res. Rev.* 45, 53–61. doi: 10.1016/j.arr.2018.04.004

Tanapat, P. (2013). Neuronal Cell Markers. *Mater Methods* 3:196. doi: 10.13070/mm.en.3.196

Turnbaugh, P. J., and Gordon, J. I. (2009). The core gut microbiome, energy balance and obesity. *J. Physiol.* 587(Pt 17), 4153–4158. doi: 10.1113/jphysiol.2009.174136

Unger, M. M., Spiegel, J., Dillmann, K. U., Grundmann, D., Philippeit, H., Burmann, J., et al. (2016). Short chain fatty acids and gut microbiota differ between patients with Parkinson's disease and age-matched controls. *Parkinsonism Relat. Disord.* 32, 66–72. doi: 10.1016/j.parkreldis.2016.08.019

van der Beek, C. M., Dejong, C. H. C., Troost, F. J., Masclee, A. A. M., and Lenaerts, K. (2017). Role of short-chain fatty acids in colonic inflammation, carcinogenesis, and mucosal protection and healing. *Nutr. Rev.* 75, 286–305. doi: 10.1093/nutrit/nuw067

Van Immerseel, F., De Buck, J., Boyen, F., Bohez, L., Pasmans, F., Volf, J., et al. (2004). Medium-chain fatty acids decrease colonization and invasion through hilA suppression shortly after infection of chickens with *Salmonella enterica* serovar Enteritidis. *Appl. Environ. Microbiol.* 70, 3582–3587. doi: 10.1128/AEM.70.6.3582-3587.2004

Varatharaj, A., and Galea, I. (2017). The blood-brain barrier in systemic inflammation. *Brain Behav. Immun.* 60, 1–12. doi: 10.1016/j.bbi.2016.03.010

Wakade, C., and Chong, R. (2014). A novel treatment target for Parkinson's disease. *J. Neurol. Sci.* 347, 34–38. doi: 10.1016/j.jns.2014.10.024

Wang, K., Liao, M., Zhou, N., Bao, L., Ma, K., Zheng, Z., et al. (2019). *Parabacteroides* distasonis alleviates obesity and metabolic dysfunctions via production of succinate and secondary bile acids. *Cell Rep.* 26, 222.e5–235.e5. doi: 10.1016/j.celrep.2018.12.028

Yano, J. M., Yu, K., Donaldson, G. P., Shastri, G. G., Ann, P., Ma, L., et al. (2015). Indigenous bacteria from the gut microbiota regulate host serotonin biosynthesis. *Cell* 161, 264–276. doi: 10.1016/j.cell.2015.02.047

Yuille, S., Reichardt, N., Panda, S., Dunbar, H., and Mulder, I. E. (2018). Human gut bacteria as potent class I histone deacetylase inhibitors in vitro through production of butyric acid and valeric acid. *PLoS One* 13:e0201073. doi: 10.1371/journal.pone.0201073

Zhan, X., Stamova, B., and Sharp, F. R. (2018). Lipopolysaccharide associates with amyloid plaques, neurons and oligodendrocytes in Alzheimer's disease brain: a review. *Front. Aging Neurosci.* 10:42. doi: 10.3389/fnagi.2018.00042

Conflict of Interest Statement: All authors were employees of (or in the case of MID, seconded full-time to 4D Pharma Ltd.) 4D Pharma Research Ltd., while engaged in the research project. AE, SA, PF, and IM were named as inventors in all or some the patents listed above.

Copyright © 2019 Ahmed, Busetti, Fotiadou, Vincy Jose, Reid, Georgieva, Brown, Dunbar, Beurket-Ascencio, Delday, Ettorre and Mulder. This is an open-access article distributed under the terms of the Creative Commons Attribution License (CC BY). The use, distribution or reproduction in other forums is permitted, provided the original author(s) and the copyright owner(s) are credited and that the original publication in this journal is cited, in accordance with accepted academic practice. No use, distribution or reproduction is permitted which does not comply with these terms.

frontiers in Cellular Neuroscience

ORIGINAL RESEARCH
published: 15 January 2020
doi: 10.3389/fncel.2019.00591

TREM2 Regulates Heat Acclimation-Induced Microglial M2 Polarization Involving the PI3K-Akt Pathway Following EMF Exposure

*Gen-Lin He[1,2], Zhen Luo[1], Ting-Ting Shen[1], Ze-Ze Wang[1], Ping Li[1], Xue Luo[1], Ju Yang[1], Yu-Long Tan[1], Yuan Wang[3], Peng Gao[4] and Xue-Sen Yang[1,2]**

[1]Department of Tropical Medicine, Army Medical University, Chongqing, China, [2]Key Laboratory of Extreme Environmental Medicine, Ministry of Education of China, Army Medical University, Chongqing, China, [3]Department of Nuclear Medicine, Xi'nan Hospital, Army Medical University, Chongqing, China, [4]Key Laboratory of Medical Protection for Electromagnetic Radiation, Ministry of Education, Army Medical University, Chongqing, China

The function of triggering receptor expressed on myeloid cells-2 (TREM2) has been described within microglia with a beneficial activated phenotype. However, the role of TREM2 underlying microglial phenotypic alterations in the cross-tolerance protection of heat acclimation (HA) against the inflammatory stimuli electromagnetic field (EMF) exposure is less well known. Here, we investigated the TREM2-related signaling mechanism induced by HA in EMF-stimulated N9 microglial cells (N9 cells). We found that EMF exposure significantly increased the production of pro-inflammatory cytokines tumor necrosis factor-α (TNF-α, IL-1β, and IL-6), and the expression of M1 markers (CD11b and CD86); meanwhile, decreased the levels of anti-inflammatory cytokines (IL-4 and IL-10) and the expression of M2 markers (CD206 and Arg1) in N9 cells. Clearly, HA treatment decreased the secretion of TNF-α, IL-1β and IL-6 and the expression of CD11b and CD86, and enhanced the production of IL-4 and IL-10 and the expression of CD206 and Arg1. Moreover, TREM2 esiRNA and selective inhibitor of PI3K clearly decreased anti-inflammatory cytokines production, M2 markers expression, and phosphorylation of PI3K and Akt following HA plus EMF stimulation. These results indicate that TREM2 and PI3K-Akt pathway are involved in the cross-tolerance protective effect of HA in microglial polarization towards the EMF exposure. This finding inspires future studies that aim to explore the non-drug approaches underlying EMF stimulation and other central nervous system (CNS) inflammatory diseases.

Keywords: EMF, heat acclimation, microglial polarization, TREM2, PI3K-Akt pathway

OPEN ACCESS

Edited by:
Chao Deng,
University of Wollongong, Australia

Reviewed by:
Maria Antonietta Panaro,
University of Bari Aldo Moro, Italy
Sun Young Park,
Pusan National University,
South Korea

****Correspondence:***
Xue-Sen Yang
xuesenyyy@hotmail.com

Received: *01 October 2019*
Accepted: *30 December 2019*
Published: *15 January 2020*

Citation:
He G-L, Luo Z, Shen T-T, Wang Z-Z, Li P, Luo X, Yang J, Tan Y-L, Wang Y, Gao P and Yang X-S (2020) TREM2 Regulates Heat Acclimation-Induced Microglial M2 Polarization Involving the PI3K-Akt Pathway Following EMF Exposure. Front. Cell. Neurosci. 13:591. doi: 10.3389/fncel.2019.00591

INTRODUCTION

Over the past few decades, scientific experiments have reported contradictory results regarding the potential effects of electromagnetic fields (EMFs) on the nervous system (D'Andrea et al., 2003). Several studies have suggested that glial reactivity exhibits a specific sensitivity to EMF exposure (Mausset-Bonnefont et al., 2004; Brillaud et al., 2007; Ammari et al., 2008). As the first line of defense in the central nervous system (CNS), macrophage-like microglia acquire different activation

states to modulate immune reactions and the clearance and pro-/anti- inflammatory responses under both physiological and pathological conditions. Although our previous studies revealed the pharmacological outcomes against M1 inflammatory activation in EMF-stimulated N9 microglial cells (N9 cells), approaches for modulating microglial activation states to the M2 phenotype remain poorly understood.

Heat acclimation (HA) is thought to be able to enhance innate cytoprotective pathways against novel stressors *via* cross-tolerance mechanisms (Horowitz, 2017). HA provides neuroprotection against a variety of stressors, including heatstroke (Yi et al., 2017), hyperoxia (Arieli et al., 2003), and traumatic brain injury (Shein et al., 2008). To date, these effects have not yet been studied in response to EMF exposure; however, similar beneficial roles are hypothesized. Additional evidence has revealed that high-energy EMFs have thermal effects (Yang et al., 2010), implying particular roles for heat resistance of acclimation following EMF exposure. It has been reported that HA enhances the presence of microglia with properties of the M2 phenotype, which express the neurotrophin brain-derived neurotrophic factor (BDNF; Shein et al., 2008); this linking the beneficial effects of HA on synaptic properties to an enhancement of neuronal survival (Bessis et al., 2007). Importantly, post-experimental traumatic brain injury and, microglial immunoreactivity are also enhanced upon the alleviation of injury in HA-treated mice (Shein et al., 2008). These results suggest that microglia may be involved in HA-induced neuroprotection.

During activation, microglia polarize towards classically activated (type I)/alternatively activated (type II; M1/M2) phenotypes (Mills, 2012), depending on the stimulus and the receptor signals that are triggered. Clearly, the M2 polarization of microglial populations is believed to be neuroprotective to cells and can be observed in HA mice (Shein et al., 2008). M2 microglia produce anti-inflammatory cytokines including IL-4 and IL-10 and express high levels of CD206 and Arg1. In contrast, persistent M1 polarization of microglia is a prominent cause of an excessive production of pro-inflammatory factors, such as tumor necrosis factor-α (TNF-α), IL-1β and IL-6, and M1 markers CD11b and CD86. The phenotype shift may be associated with the regulation of cellular responses by several sensome receptors, including triggering receptor expressed on myeloid cells-2 (TREM2; Hickman et al., 2013). TREM2 signaling increases phagocytosis and the expression of an anti-inflammatory phenotype in microglia (Neumann and Takahashi, 2007; Kleinberger et al., 2014). However, the molecular mechanisms underlying the triggering microglial phenotypic alterations in HA are less well known.

Given the cross-tolerance mechanism of HA and the potential for microglial reaction upon HA, we tested whether HA attenuates M1 polarization (pro-inflammatory cytokines TNF-α, IL-1β and IL-6, and M1 markers CD11b and CD86) and mediates M2 polarization (anti-inflammatory cytokines IL-4 and IL-10, and M2 markers CD206 and Arg1) in EMF-stimulated N9 cells. Moreover, we utilized pharmacological and enzymatically prepared siRNA (esiRNA) to investigate the molecular mechanisms that regulate the microglial phenotype by HA in EMF-stimulated N9 cells. We demonstrated that HA ameliorates the microglial inflammatory response and shifts the microglial phenotype from M1 to M2 *via* the TREM2 pathway following EMF exposure. These results may provide critical information for the importance of HA in neurologic disorders associated with the regulation of microglial phenotypes.

MATERIALS AND METHODS

Cell Culture and Treatment

Immortalized murine microglial N9 cells were grown in Iscove's modified Dulbecco's medium (IMDM; HyClone, Logan, UT, USA) supplemented with 10% heat-inactivated fetal bovine serum (FBS; HyClone), 2 mM glutamine, 100 U/ml penicillin, 100 μg/ml streptomycin, and 50 μM 2-mercaptoethanol (Sigma–Aldrich, St. Louis, MO, USA). Resuscitated N9 cells were used within 3–10 passages, and they were passaged every 3 days. One-half of the cell culture medium was replaced with fresh medium every 2 days. The cell culture medium was replaced with serum-free IMDM supplemented with or without LY294002 (a selective inhibitor of phosphatidylinositol 3 kinase (PI3K), 10 μM) or esiRNA (20 nM; Sigma–Aldrich, St. Louis, MO, USA), and the cells were incubated for 30 min or 12 h during the HA process but prior to the end of last cycle. The solvent controls were performed using dimethyl sulfoxide (DMSO; Sigma–Aldrich, St. Louis, MO, USA) and a transient transfection reagent DharmaFECT (GE Healthcare Dharmacon, Lafayette, CO, USA).

Cellular Heat Acclimation

To culture the cells for a suitable duration for cellular HA, the cells were seeded in 25 cm^2 T-flasks (3×10^6 cells/flask) and 24-well plates (1×10^5 cells/well) at 37°C in a humidified 5% CO_2 atmosphere. For HA, we exposed the cells to intermittent temperatures between 37°C and 39.5°C, mimicking the repeated thermal exposure to acquiring HA that has been previously reported (Patton et al., 2018). The cells were maintained in two incubators under a 20/4-h cycle of 37°C/39.5°C for 72 h. The culture medium was replaced with fresh preheated medium every 2 days.

Exposure System

Cells were exposed to a pulsed EMF with 2.45 GHz microwaves in an anechoic chamber, as previously described (Yang et al., 2010). Briefly, cells were exposed to a pulsed EMF in an anechoic chamber. The ambient air temperature inside the anechoic chamber was 25°C to 26°C. A 90 mW EMF pulse was delivered through a rectangular horn antenna connected horizontally to a handset (Philips PM 7320X, Sivers IMA, Kista, Sweden). The pulse width was 2 μs, and the pulse repetition rate was 500 pulses per second. Cells were exposed to 2.45 GHz-pulsed microwaves for 20 min at an average specific absorption rate of 6 W/kg. The medium temperature was maintained at 37°C by circulating heated water through the upper and lower chamber. During sham exposure, cultures were placed in the same conditions but without EMF exposure.

Enzyme-Linked Immunosorbent Assay (ELISA)

After the designated treatment, cell culture supernatants were collected and stored at −80°C until use for detecting TNF-α, interleukin (IL)-1β, IL-6, IL-4, and IL-10, using the Enzyme-Linked Immunosorbent Assay (ELISA) kits (eBioscience, San Diego, CA, USA) according to the manufacturers' instructions. Cells were washed three times with ice-cold PBS and resuspended in 100 μl ice-cold PBS. Ten-microliter aliquots of the cell collections were quantified using a cell counter (TC20, Bio-Rad, Hercules, CA, USA).

Immunoblot Analysis

Cells were washed with ice-cold PBS and scraped in RIPA lysis buffer containing protease and phosphatase inhibitors (Roche, Penzberg, Germany) for 30 min on ice. Lysates were centrifuged at 12,000 rpm for 10 min at 4°C. Whole-cell extracts (80 μg/lane) were separated using 6 or 10% SDS-polyacrylamide gel and then transferred onto PVDF membranes (Bio-Rad, Hercules, CA, USA). The membranes were blocked in PBS with 5% non-fat milk for 1 h and then incubated with their respective primary antibodies against rat anti-mouse CD11b (1:800, AbD Serotec, Oxford, UK), mouse anti-mouse CD86 (1:800, Abcam, Cambridge, MA, USA), and rat anti-mouse TREM2 (1:500, Merck Millipore, Temecula, CA, USA), and with antibodies purchased from Santa-Cruz Biotechnology (Santa Cruz, USA) that recognize mouse anti-mouse CD206 (1:100) and mouse anti-mouse Arg1 (1:100), and from Cell Signaling Technology (Danvers, MA, USA) that recognize rabbit anti-mouse phosphor-PI3K p85 Tyr458 (p-PI3K, 1:800), rabbit anti-mouse phospho-Akt Ser473 (p-Akt, 1:1,000). The membranes were washed four times for 5 min each in Tris-buffered saline Tween-20 (TBST) and then incubated with horseradish peroxidase (HRP)-conjugated secondary antibodies (ZsBio) for 1 h at room temperature. After incubation, the membranes were reacted with enhanced chemiluminescence reagent (Bio-Rad, Hercules, CA, USA), and the signal was detected using a ChemiDoc MP gel imaging system (Bio-Rad, Hercules, CA, USA). β-actin (1:1,000; Sigma–Aldrich, St. Louis, MO, USA) was used as an internal control. Relative band densities were determined by densitometric analysis using Image Lab software (Bio-Rad, Hercules, CA, USA).

siRNA Transfection

Cells were seeded in 25 cm^2 T-flasks or 24-well plates. Following 60 h of HA, the cells were transfected with an esiRNA (Sigma–Aldrich, St. Louis, MO, USA) targeting TREM2 (20 nM) or a control esiRNA using DharmaFECT (GE Healthcare Dharmacon, Lafayette, CO, USA) in Opti-MEM (Invitrogen Life Technologies, CA, USA) following the manufacturer's protocol. After culturing, the effects of esiRNA on protein expression were analyzed using Western blotting.

Immunofluorescence

Cells were grown on coverslips in 24-well plates. After being fixed and permeabilized, the cells were blocked with goat serum (ZsBio) for 20 min at room temperature and washed three times in PBS. The cells were incubated with rat anti-mouse TREM2 (Merck Millipore), rabbit anti-mouse phosphor-Ser473-Akt (Cell Signaling Technology, Danvers, MA, USA), and/or mouse anti-mouse CD206 (Santa Cruz) antibodies at 37°C for 1 h. After being washed, the slides were incubated for 1 h at 37 °C with rabbit anti-mouse AlexaFluor 488 (Life Technologies, Carlsbad, CA, USA), goat anti-rat CF568 (Sigma–Aldrich, St. Louis, MO, USA), and chicken anti-rabbit CF633 antibodies (Sigma–Aldrich, St. Louis, MO, USA) in the dark. The slides were then washed and mounted with an aqueous-based anti-fade mounting medium. Images of stained cells were captured using an LSM 780 confocal laser-scanning microscope (Carl Zeiss GmbH, Jena, Germany).

Statistical Analysis

Statistical analyses were performed using SPSS PASW Statistics 18.0 software (SPSS, Inc., Somers, NY, USA). Each experiment was repeated a minimum of three times, and the data are expressed as the means ± SEM. Significant differences between the groups were assessed by one- or two-way ANOVA followed by Tukey's test. Statistical significance was established at $P < 0.05$, unless otherwise indicated.

RESULTS

Heat Acclimation Regulates Microglial Polarization in EMF-Stimulated N9 Cells

The production of pro-/anti-inflammatory mediators and M1/M2 cell surface marker expression were determined to test whether HA regulates microglial polarization in EMF-stimulated N9 cells. Consistent with previous studies of neuroprotective functions after HA (Shein et al., 2007a), we found that HA was shown to not alter cell state, and suppressed the production of pro-inflammatory cytokines and increased the production of anti-inflammatory cytokines in N9 cells 12 h after a 20-min EMF exposure (**Figure 1**). The 20-min EMF treatment was identified as a threshold condition representing the time of duration beyond which cytotoxicity significantly increases as explained in a previous study (He et al., 2016). In addition, based on the previous time effect experiments of EMF-induced pro-inflammatory responses (Yang et al., 2010; He et al., 2014), the threshold 12-h recovery time after EMF exposure with prominent pro-inflammatory activity was employed in the present study. Clearly, ELISA detection indicated that EMF exposure resulted in increased levels of TNF-α (**Figure 1A**), IL-1β (**Figure 1B**), but not IL-6 (**Figure 1C**), and decreased levels of IL-4 (**Figure 1D**) and IL-10 (**Figure 1E**). In contrast, compared to the EMF-exposed group, the production of TNF-α, IL-1β, and IL-6 dramatically decreased, and the production of IL-4 and IL-10 significantly increased in EMF-stimulated N9 cells pretreated with HA (HA-plus-EMF-stimulated N9 cells). Compared to the non-HA and sham exposed-control cells, HA-treated N9 cells exhibited slightly increased levels of TNF-α and IL-1β and a significant increase in IL-4 and IL-10. Moreover, Western blotting analysis showed that the expression of M2 markers CD206 and arginase 1 (Arg1) was significantly increased in HA-treated N9 cells (**Figure 2B**). Consistent

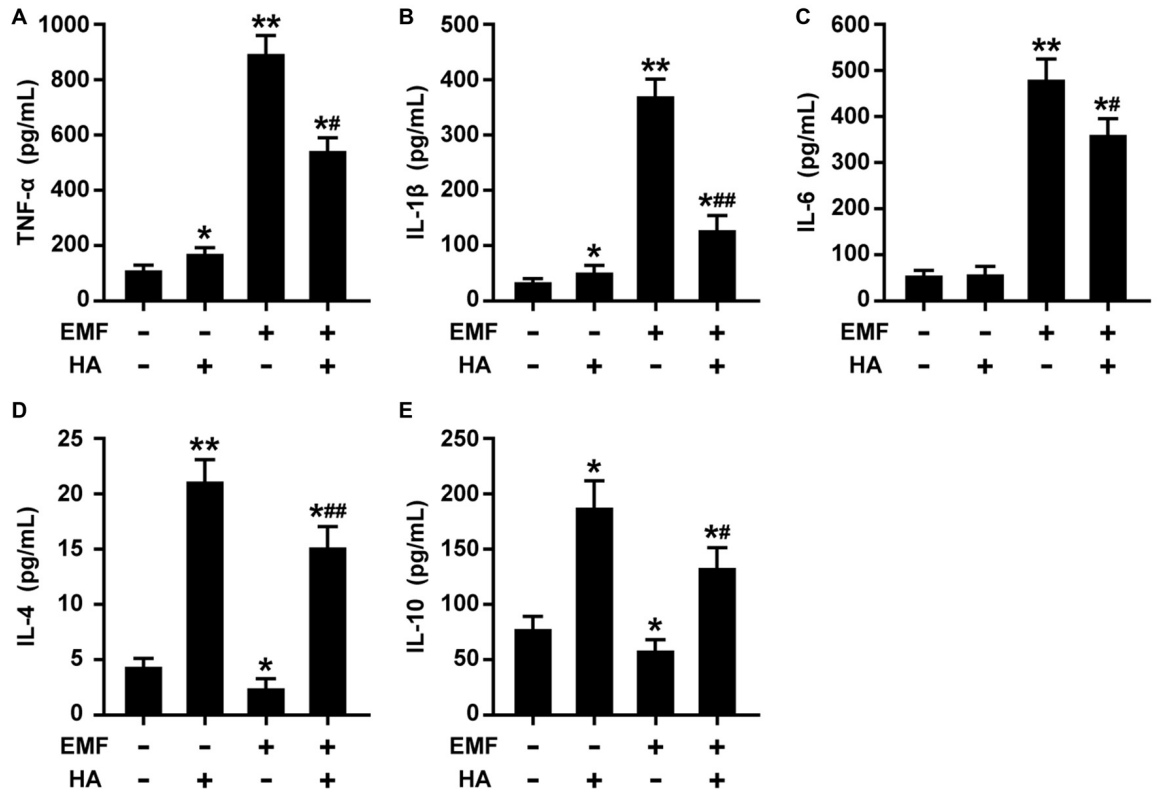


FIGURE 1 | Heat acclimation (HA) regulates the production of pro-/anti-inflammatory mediators in electromagnetic field (EMF)-stimulated N9 cells. N9 cells were pretreated with or without a 72-h HA process (20/4-h cycle of 37°C/39.5°C) and then exposed to 2.45-GHz EMF or sham-exposed for 20 min. Enzyme-Linked Immunosorbent Assay (ELISA) of tumor necrosis factor-α (TNF-α) **(A)**, IL-1β **(B)**, IL-6 **(C)**, IL-4 **(D)**, and IL-10 **(E)** production in the cell culture supernatants of N9 cells with or without HA pretreatment 12 h after EMF exposure. Data are presented as means ± SEM of three independent experiments. $^{*}P < 0.05$, $^{**}P < 0.01$ vs. the sham-exposed control group; $^{\#}P < 0.05$, $^{\#\#}P < 0.01$ vs. the EMF-exposed group.

with the weak induction of pro-inflammatory mediators by HA treatment, the expression of M1 marker CD86 was also slightly increased in HA-treated N9 cells, compared to the non-HA and sham exposed-control cells (**Figure 2A**). It was also found that EMF exposure significantly increased the expression of cell surface marker CD11b and M1 marker CD86 (**Figure 2A**) and decreased the expression of CD206 and Arg1 (**Figure 2B**), and these effects were reversed by HA pre-conditioning. These results indicate the ability of HA treatment to regulate microglial phenotypes in response to EMF stimulation.

Alterations in TREM2 and Akt Are Associated With the Modulatory Effects of HA

Given the essential role of Akt phosphorylation in HA-induced neuroprotection (Shein et al., 2007b) and the important protective functions of cell phenotype activation by microglial TREM2 (Piccio et al., 2007), we examined the levels of TREM2 expression and PI3K and Akt phosphorylation in EMF-stimulated N9 cells pretreated with HA. Western blotting analysis showed that the expression of TREM2 was significantly decreased in the EMF-stimulated N9 cells (**Figure 3A**). HA treatment dramatically augmented TREM2 expression 12 h after EMF exposure (**Figure 3A**). Subsequently, phosphorylation of PI3K and Akt were quite low both in the sham-exposed control cells and in the EMF-stimulated N9 cells (**Figure 3B**). Similar to TREM2 expression, HA treatment clearly enhanced the phosphorylation of PI3K and Akt, compared to the control cells (**Figure 3B**). Moreover, HA treatment significantly reversed the low level of PI3K and Akt phosphorylation 12 h after EMF exposure (**Figure 3B**). These findings suggest that TREM2 expression and Akt phosphorylation play important roles in the regulatory effects of HA in EMF-stimulated N9 cells.

esiRNA TREM2 Abolishes the Amelioration of Microglial M2 Polarization by HA

To further confirm the involvement of TREM2 in M2 microglial phenotype regulation, esiRNA was used to evaluate the effect of silencing TREM2 on microglial M2 polarization in EMF-stimulated N9 cells with HA preconditioning. The knockdown of TREM2 by a specific esiRNA was confirmed 24 h post-transfection, and the effectiveness of TREM2 inhibition was confirmed by Western blotting. TREM2 esiRNA suppressed

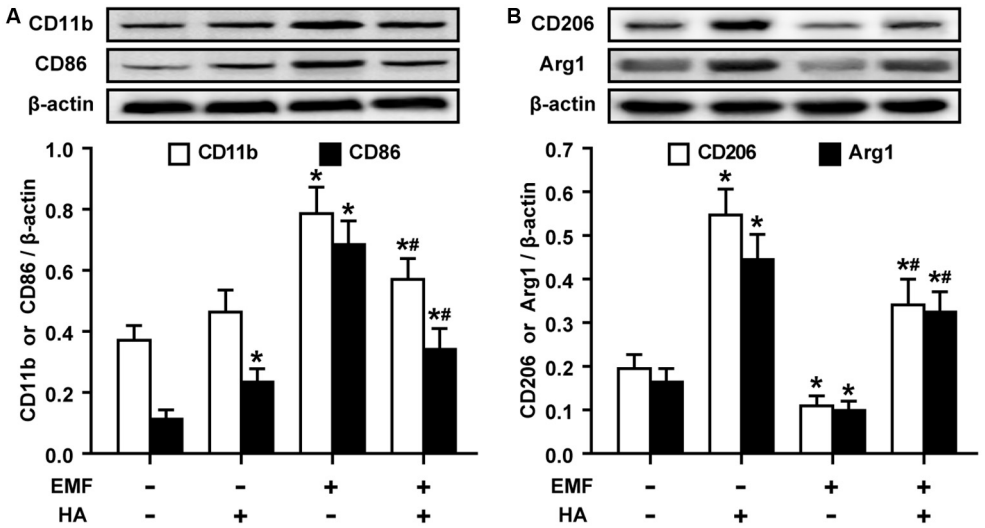


FIGURE 2 | HA regulates the expression of cell surface markers in EMF-stimulated N9 cells. N9 cells were pretreated with or without a 72-h HA process (20/4-h cycle of 37°C/39.5°C) and then exposed to 2.45-GHz EMF or sham-exposed for 20 min. Levels of cell surface marker CD11b and M1 marker CD86 **(A)**, and M2 markers CD206 and Arg1 **(B)** in total cell lysates were analyzed using Western blotting, and the corresponding densitometric analyses were represented. Data are presented as means ± SEM of three independent experiments. $^{*}P < 0.05$ vs. the sham-exposed control group; $^{\#}P < 0.05$ vs. the EMF-exposed group.

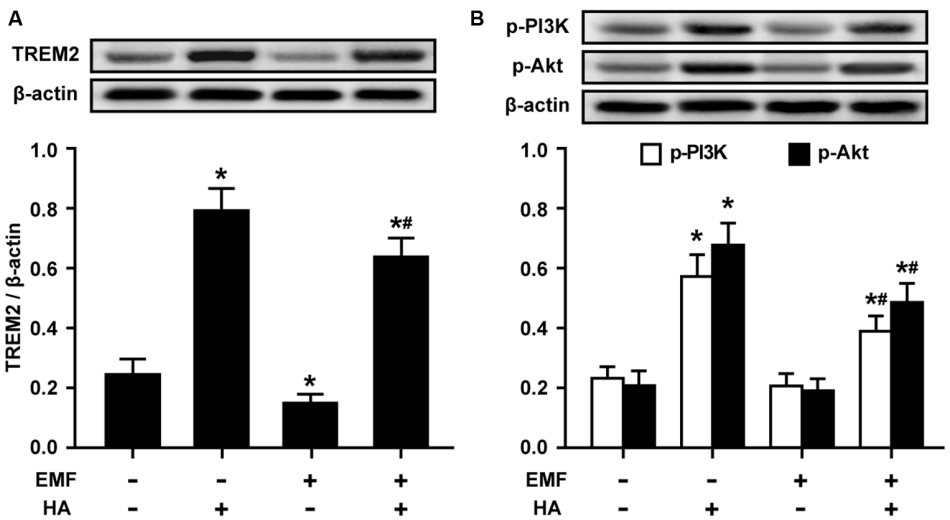


FIGURE 3 | Effects of HA on the expression of triggering receptor expressed on myeloid cells-2 (TREM2) and the phosphorylation of PI3K and Akt in EMF-stimulated N9 cells. N9 cells were pretreated with or without a 72-h HA process (20/4-h cycle of 37°C/39.5°C) and then exposed to 2.45-GHz EMF or sham-exposed for 20 min. Levels of TREM2 **(A)**, and phosphorylation of PI3K and Akt **(B)** in total cell lysates were analyzed using Western blotting, and the corresponding densitometric analyses were represented. Data are presented as means ± SEM of three independent experiments. $^{*}P < 0.05$ vs. the sham-exposed control group; $^{\#}P < 0.05$ vs. the EMF-exposed group.

the expression of TREM2 in both control and HA-plus-EMF-treated N9 cells (**Figure 4A**), which were incubated with esi-TREM2 12 h during the HA process but prior to the end of HA and 12 h after a 20-min consequent EMF exposure. The secretion of IL-4 and IL-10 was dramatically decreased in both control and HA-plus-EMF-treated N9 cells treated with esi-TREM2 (**Figure 4B**). Consistent with the inhibition of anti-inflammatory mediators by esi-TREM2, it was found that the levels of the M2 markers CD206 and Arg1 were significantly attenuated by esi-TREM2 treatment in both control and HA-plus-EMF-treated N9 cells (**Figure 4C**). Similarly, confocal microscopy provided further evidence of the expression of TREM2 and CD206 and showed a strong increase in fluorescence intensity in HA-plus-EMF-treated N9 cells (**Figure 4D**). In contrast, esi-TREM2 abrogated the increased expression of TREM2 and CD206 evoked by HA plus EMF treatment

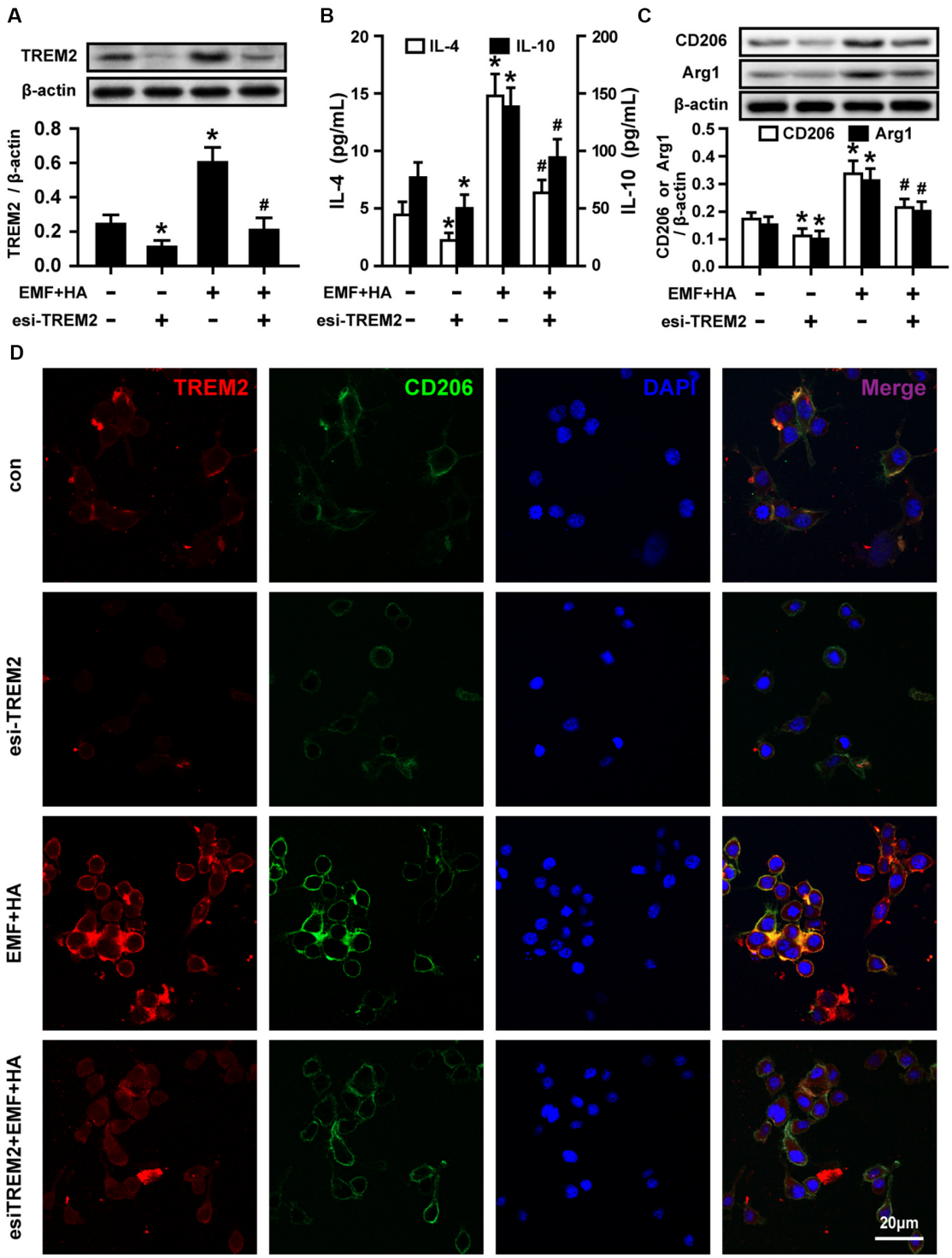


FIGURE 4 | Effects of TREM2 esiRNA on M2 microglial phenotype regulation in EMF-stimulated N9 cells with HA preconditioning. N9 cells were transfected with or without TREM2 esiRNA (20 nM) at 60 h during the uncompleted 72-h HA and then continuously cultured 12 h to complete the HA process and the 24 h transfection of TREM2 esiRNA. Western blotting quantification of TREM2 **(A)**, and M2 markers CD206 and Arg1 **(C)**, and ELISA of anti-inflammatory cytokines IL-4 and IL-10 **(B)** production of in either control or HA-plus-EMF-treated N9 cells with or without TREM2 esiRNA. Data are presented as means ± SEM of three independent experiments. $^{*}P < 0.05$ vs. the non-HA and sham-exposed control group; $^{\#}P < 0.05$ vs. the HA-plus-EMF-exposed group. **(D)** Confocal immunofluorescence microscopy was performed on cultures that were immunoreacted with antibodies against TREM2 and CD206 with esi-TREM2 treatment in HA-plus-EMF-treated N9 cells. Scale bar: 20 μm.

(**Figures 4C,D**). These results indicate that TREM2 esiRNA abolishes the M2 microglial phenotype induced by HA in EMF-treated N9 cells and that TREM2 may be the intracellular signal molecule that mediates M2 polarization of microglia during HA.

Inhibition of Akt Blocks the TREM2-Mediated Amelioration of Microglial M2 Polarization

To reveal the regulatory signaling effector underlying the TREM2-mediated amelioration of microglial M2 polarization by HA, PI3K and Akt phosphorylation were measured upon treatment with TREM2 esiRNA. TREM2 esiRNA treatment was found to attenuate the phosphorylation of PI3K and Akt in HA-plus-EMF-treated N9 cells (**Figure 5**). To further investigate whether the mechanism by which HA regulates microglial phenotypes is related to the activation of the PI3K-Akt pathway, the PI3K inhibitor LY294002 was used to assess the inhibitory effects of PI3K-Akt on M2 polarization in HA-plus-EMF-treated N9 cells. As expected, LY294002 treatment was found to attenuate the phosphorylation of PI3K and Akt in both control and HA-plus-EMF-treated N9 cells (**Figure 5**). Moreover, the secretion of IL-4 (**Figure 6A**) and IL-10 (**Figure 6B**), and the expression of CD206 and Arg1 (**Figure 6C**) were significantly decreased by LY294002 treatment in HA-plus-EMF-treated N9 cells. Interestingly, the cells treated with LY294002 alone showed a significant change in IL-4 and IL-10 production but not CD206 and Arg1 expression, compared to that in the control cells. In addition, a similar inhibition of CD206 and p-Akt immunoreactivity was observed upon pre-treatment with LY294002 by microscopy (**Figure 6D**). These results indicate that microglial TREM2-mediated M2 polarization induced by HA in EMF-stimulated N9 cells is attributable in part to the PI3K-Akt pathway.

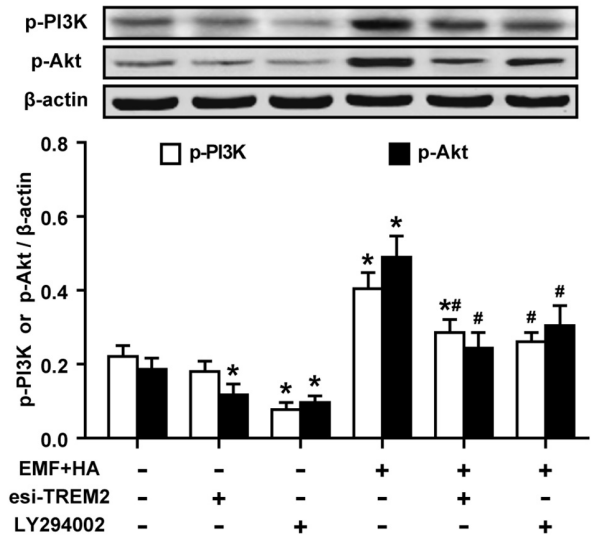


FIGURE 5 | Effects of TREM2 esiRNA and the PI3K inhibitor LY294002 on the phosphorylation of PI3K and Akt in EMF-stimulated N9 cells with HA preconditioning. N9 cells were transfected with or without TREM2 esiRNA (20 nM) at 60 h during the uncompleted 72-h HA and then continuously cultured 12 h to complete the HA process and the 24 h transfection of TREM2 esiRNA. Alternatively, N9 cells were treated with or without LY294002 (10 μM) for 30 min prior to the end of the 72-h HA process. Levels of PI3K and Akt phosphorylation in total cell lysates were analyzed using Western blotting, and the corresponding densitometric analyses were represented. Data are presented as means ± SEM of three independent experiments. $^{*}P < 0.05$ vs. the non-HA and sham-exposed control group; $^{\#}P < 0.05$ vs. the HA-plus-EMF-exposed group.

DISCUSSION

Changes in morphology, cell number, surface receptor expression, and the production of cytokines were evaluated to characterize the immunomodulatory effects of microglia against neuronal stress or stimuli (Ransohoff and Perry, 2009; Zhang et al., 2018). In the present study, we observed pro-inflammatory M1 activation and a significant decrease in the microglial M2 phenotype in N9 cells after EMF exposure. These findings are consistent with our previous data, which indicated a pro-inflammatory response and a decrease in phagocytosis in EMF-treated N9 cells (He et al., 2014). Notably, as a beneficial intervention, HA treatment significantly suppressed the secretion of pro-inflammatory cytokines and the expression of M1 markers and increases the secretion of anti-inflammatory cytokines and the expression of M2 markers in N9 cells 12 h after EMF exposure. Studies involving TREM2 esiRNA and the pharmacological inhibition of PI3K-Akt signaling provided evidence that HA improved microglial M2 polarization in EMF-stimulated N9 cells. These results are in agreement with those of other studies that reported altered cytokine expression and Akt phosphorylation in the brains of heat acclimated mice (Shein et al., 2007a,b). Taken together, the results of these studies showed that the PI3K-Akt signaling pathway may ultimately contribute to the TREM2-dependent immunoregulation of microglial M2 polarization by HA treatment in EMF-treated N9 cells.

It is well known that microglia play a crucial role in various neurological and neurodegenerative disorders through their diverse phenotypes and their ability to shift functions (Orihuela et al., 2016). Over the past few decades, a strong glial reaction in different brain regions has been observed in several studies of EMF effects (Mausset-Bonnefont et al., 2004; Brillaud et al., 2007). In previous work, we demonstrated that EMF may act primarily as a stress inducer and mediate pro-inflammatory activation and a decrease in the phagocytic activity of microglia (He et al., 2014). Consistently, in the present study, we observed an increased production of pro-inflammatory cytokines (TNF-α, IL-1β, and IL-6), cell surface marker CD11b, and M1 marker CD86 and detected decreased anti-inflammatory cytokines (IL-4 and IL-10) and M2 markers (CD206 and Arg1) in EMF-stimulated N9 cells. Notably, the present data and our previous results indicate that EMF exposure is related to an increased risk of neuroinflammatory processes and impaired microglial clearance and is thus associated with an over-activated phenotype of microglia. In support of this, a recent study reported the amelioration of neural injuries *via* shifting

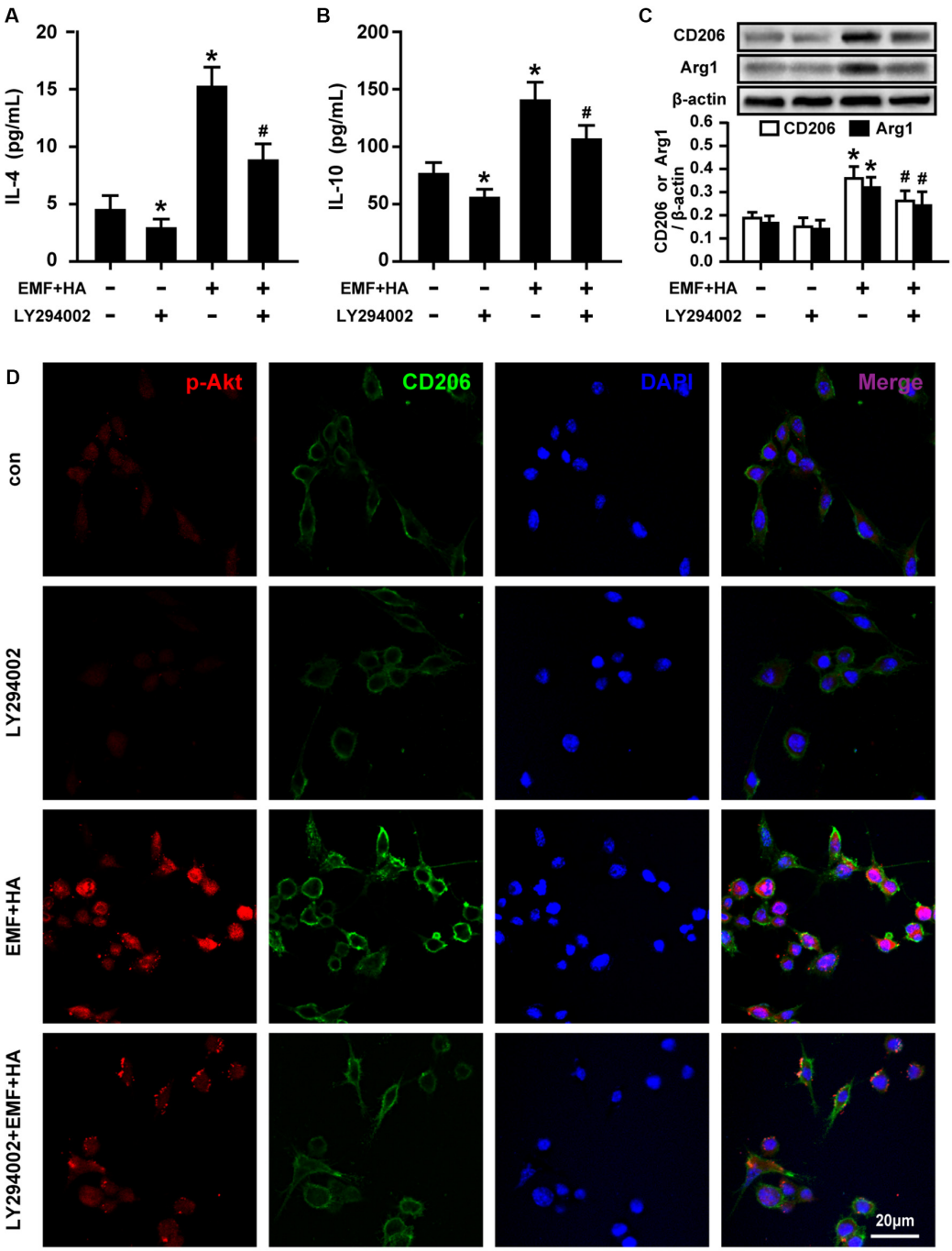


FIGURE 6 | Effects of LY294002 on M2 microglial phenotype regulation in EMF-stimulated N9 cells with HA preconditioning. N9 cells were treated with or without LY294002 (10 μM) for 30 min prior to the end of the 72-h HA process. ELISA of anti-inflammatory cytokines IL-4 **(A)** and IL-10 **(B)** production of in either control or HA plus EMF-treated N9 cells with or without LY294002 pretreatment. **(C)** The expression of CD206 and Arg1 were determined, and the corresponding densitometric analyses were represented. Data are presented as means ± SEM of three independent experiments. $^{*}P < 0.05$ vs. the non-HA and sham-exposed control group; $^{\#}P < 0.05$ vs. the HA-plus-EMF-exposed group. **(D)** Confocal immunofluorescence microscopy was performed on cultures that were immunoreacted with antibodies against p-Akt and CD206 with LY294002 treatment in HA-plus-EMF-treated N9 cells. Scale bar: 20 μm.

microglia from a pro-inflammatory to an anti-inflammatory phenotype as a result of EMF exposure (Zhang et al., 2019). However, extending the methodological and pharmaceutical focus regarding the control of M1/M2 marker expression as well as pro-/anti-inflammatory cytokine production in EMF-stimulated microglia remains a central challenge. Thus,

an effective therapeutic option might reveal the detailed mechanisms of the neuroprotective effect of the microglial M2 phenotype upon EMF exposure.

The associated cellular and molecular protective mechanisms of heat-induced tolerance/adaptations attained during HA may be responsible for the attenuation of adverse injury and enhancement of cytoprotective signals (Horowitz, 2017). Remarkably, we delineated the strong immunoregulatory capabilities of HA against the pro-inflammatory M1 phenotype evoked by EMF exposure in N9 cells. In support of this, HA rats and mice display improved functional recovery and reduced cerebral edema formation after closed head injury (Shohami et al., 1994; Shein et al., 2005). Moreover, the neuroprotective role of HA has been reported to be associated with altered levels of cytokines and BDNF of microglia (Shein et al., 2008). Apart from this, in this study, a similar protective M2 phenotype of microglia characterized by increases in IL-4 and IL-10 production and the expression of the M2 markers CD206 and Arg1 is also found in EMF-stimulated N9 cells pre-treated with HA. Taken together, our results combined with those of previous studies suggest, in part, the involvement of microglial reactions in the regulatory role of HA in EMF-stimulated N9 cells. Notably, the regulation of microglial polarization has been clearly reported to possess potential immunoregulatory capabilities using numerous natural compounds. Recently, Schisantherin A exhibits anti-inflammatory effects *via* the activation of the ERK-Nrf2 pathway in lipopolysaccharide (LPS)-activated BV-2 microglial cells (Li et al., 2018). Yang et al. (2017) demonstrated that resveratrol reduces inflammatory damage and promotes microglial polarization to the M2 phenotype *via* PGC-1α in LPS-activated BV-2 cells. In addition, fingolimod, an agonist of the S1P (sphingosine-1-phosphate) receptor, primes microglial M2 polarization *via* the STAT3 pathway in mice with white matter ischemia (Qin et al., 2017). Additionally, malibatol A has been found to regulate microglial M1/M2 polarization through the activation of PPARγ in experimental middle cerebral artery occlusion mice (Pan et al., 2015). However, external HA as a non-drug physical intervention to trigger microglial phenotypic alterations challenges various signaling proteins and receptors. The microglial sensome includes some highly enriched gene transcripts, even including unknown transcripts of sensomes that have not been previously described in microglia (Hickman et al., 2013). Thus, the underlying mechanism of microglial polarization due to HA pre-treatment following EMF exposure remains to be fully clarified.

Triggering receptor expressed on myeloid cells 2 (TREM2) is an innate regulatory receptor of microglia that is linked to the inhibition of inflammatory responses and the potentiation of phagocytic effects in the CNS (Takahashi et al., 2005; Zhong et al., 2015; Xiang et al., 2016; Mazaheri et al., 2017). In this study, the understanding of microglial immunomodulatory phenotypes was expanded, and HA pre-treatment was also found to induce a robust increase in TREM2 expression, which is in line with the elevation of Akt phosphorylation. Additionally, a few genes associated with the direct regulation of microglial TREM2 were detected. A recent study by Boza-Serrano et al. (2019) demonstrated the role of the direct interaction between TREM2 and gal3 in driving microglial activation in Alzheimer's disease (AD). Zhong et al. (2015) reported that TREM2-DAP12 interactions are required for signal transduction that triggers microglial polarization and consequent cytokine release (Zhao et al., 2018). Additionally, increasing evidence has demonstrated that APOE isoforms interact with TREM2 in association with AD pathogenesis (Wolfe et al., 2018). Although the immunomodulatory mechanisms of TREM2 action and the associated effects of intervening in this mechanism have been widely described, the exact mechanism by which TREM2 regulates microglial polarization during EMF exposure remains to be solved.

In the present study, we demonstrated that microglial TREM2-mediated M2 polarization induced by HA is attributable in part to the phosphorylation of PI3K and Akt in EMF-stimulated N9 cells. In support of these findings, PI3K-Akt signaling has been reported to be required for TREM2-mediated immune modulation (Sun et al., 2013; Zhu et al., 2014; Wolfe et al., 2018). Moreover, increasing evidence has indicated a potential direct link between M2 polarization and the activation of mTOR *via* the PI3K-Akt pathway (Weichhart and Saemann, 2008; Byles et al., 2013; Mercalli et al., 2013). In addition, the PI3K-Akt pathway has been shown to elicit the anti-inflammatory M2-like effects of insulin on macrophage phenotype switching in a diabetic rat model and human monocytic THP-1 cells (Yu et al., 2019). Other investigators, however, have argued that PI3K-Akt is essential in LPS-activated M1 inflammatory microglia (Cianciulli et al., 2016). Thus, the role of PI3K-Akt pathway in stress responses is controversial. This discrepancy may be partly attributable to the intensity, frequency, and duration of the different experimental stimuli. Therefore, it is clear that the mechanism of microglial polarization to stress is complex and multifaceted. Despite the immunomodulatory effect on microglial phenotypes by HA in our study, the TREM2-mediated PI3K-Akt signaling pathway represents a potential therapeutic target for enhancing M2 microglial polarization following EMF exposure.

CONCLUSION

Our data provided detailed information regarding the pro-/anti-inflammatory cytokines and M1/M2 markers involved in the regulation of microglial phenotypes in EMF-activated N9 microglial cells. Additionally, we also provide evidence to suggest that TREM2 and Akt signaling, at least in part, trigger microglial M2 polarization through HA in EMF-stimulated N9 cells. Regardless of the detailed mechanism by which Akt is involved in TREM2-mediated M2 polarization, HA as a non-drug treatment permits an extended effort to allow for more cytoprotective signals related to microglial immune responses in neurodegenerative diseases.

DATA AVAILABILITY STATEMENT

All datasets generated for this study are included in the article.

AUTHOR CONTRIBUTIONS

X-SY and G-LH contributed to the conception, design of the study, designed and performed the experiments, analyzed the data, and wrote the article. YW and PG provided the EMF exposure system. PL and Y-LT performed the esiRNA and pharmacological intervention approach. G-LH, Z-ZW, and JY carried out the confocal double-label immunofluorescence assays. ZL, T-TS, and XL contributed to ELISA and western blotting assays. All authors read and approved the final manuscript.

FUNDING

This work was supported by grants from the National Natural Science Foundation of China (Nos. 81472952 and 81773396).

ACKNOWLEDGMENTS

We thank Hai-Ying Ran for her expertise in confocal microscopy, data acquisition and analysis. We also thank Dr. Yun Bai (Army Medical University, China) for her kind gift of N9 microglial cells.

REFERENCES

Ammari, M., Brillaud, E., Gamez, C., Lecomte, A., Sakly, M., Abdelmelek, H., et al. (2008). Effect of a chronic GSM 900 MHz exposure on glia in the rat brain. *Biomed. Pharmacother.* 62, 273–281. doi: 10.1016/j.biopha.2008.03.002

Arieli, Y., Eynan, M., Gancz, H., Arieli, R., and Kashi, Y. (2003). Heat acclimation prolongs the time to central nervous system oxygen toxicity in the rat. Possible involvement of HSP72. *Brain Res.* 962, 15–20. doi: 10.1016/s0006-8993(02)03681-8

Bessis, A., Béchade, C., Bernard, D., and Roumier, A. (2007). Microglial control of neuronal death and synaptic properties. *Glia* 55, 233–238. doi: 10.1002/glia.20459

Boza-Serrano, A., Ruiz, R., Sanchez-Varo, R., García-Revilla, J., Yang, Y., Jimenez-Ferrer, I., et al. (2019). Galectin-3, a novel endogenous TREM2 ligand, detrimentally regulates inflammatory response in Alzheimer's disease. *Acta Neuropathol.* 138, 251–273. doi: 10.1007/s00401-019-02013-z

Brillaud, E., Piotrowski, A., and de Seze, R. (2007). Effect of an acute 900 MHz GSM exposure on glia in the rat brain: a time-dependent study. *Toxicology* 238, 23–33. doi: 10.1016/j.tox.2007.05.019

Byles, V., Covarrubias, A. J., Ben-Sahra, I., Lamming, D. W., Sabatini, D. M., Manning, B. D., et al. (2013). The TSC-mTOR pathway regulates macrophage polarization. *Nat. Commun.* 4:2834. doi: 10.1038/ncomms3834

Cianciulli, A., Calvello, R., Porro, C., Trotta, T., Salvatore, R., and Panaro, M. A. (2016). PI3k/Akt signalling pathway plays a crucial role in the anti-inflammatory effects of curcumin in LPS-activated microglia. *Int. Immunopharmacol.* 36, 282–290. doi: 10.1016/j.intimp.2016.05.007

D'Andrea, J. A., Chou, C. K., Johnston, S. A., and Adair, E. R. (2003). Microwave effects on the nervous system. *Bioelectromagnetics* 24, S107–S147. doi: 10.1002/bem.10179

He, G. L., Liu, Y., Li, M., Chen, C. H., Gao, P., Yu, Z. P., et al. (2014). The amelioration of phagocytic ability in microglial cells by curcumin through the inhibition of EMF-induced pro-inflammatory responses. *J. Neuroinflammation* 11:49. doi: 10.1186/1742-2094-11-49

He, G., Luo, Z., Shen, T., Li, P., Yang, J., Luo, X., et al. (2016). Inhibition of STAT3- and MAPK-dependent PGE2 synthesis ameliorates phagocytosis of fibrillar β-amyloid peptide (1–42) *via* EP2 receptor in EMF-stimulated N9 microglial cells. *J. Neuroinflammation* 13:296. doi: 10.1186/s12974-016-0762-9

Hickman, S. E., Kingery, N. D., Ohsumi, T. K., Borowsky, M. L., Wang, L. C., Means, T. K., et al. (2013). The microglial sensome revealed by direct RNA sequencing. *Nat. Neurosci.* 16, 1896–1905. doi: 10.1038/nn.3554

Horowitz, M. (2017). Heat acclimation-mediated cross-tolerance: origins in within-life epigenetics? *Front. Physiol.* 8:548. doi: 10.3389/fphys.2017.00548

Kleinberger, G., Yamanishi, Y., Suárez-Calvet, M., Czirr, E., Lohmann, E., Cuyvers, E., et al. (2014). TREM2 mutations implicated in neurodegeneration impair cell surface transport and phagocytosis. *Sci. Transl. Med.* 6:243ra286. doi: 10.1126/scitranslmed.3009093

Li, C., Chen, T., Zhou, H., Zhang, C., Feng, Y., Tang, F., et al. (2018). Schisantherin A attenuates neuroinflammation in activated microglia: role of Nrf2 activation through ERK phosphorylation. *Cell. Physiol. Biochem.* 47, 1769–1784. doi: 10.1159/000491059

Mausset-Bonnefont, A. L., Hirbec, H., Bonnefont, X., Privat, A., Vignon, J., and de Seze, R. (2004). Acute exposure to GSM 900-MHz electromagnetic fields induces glial reactivity and biochemical modifications in the rat brain. *Neurobiol. Dis.* 17, 445–454. doi: 10.1016/j.nbd.2004.07.004

Mazaheri, F., Snaidero, N., Kleinberger, G., Madore, C., Daria, A., Werner, G., et al. (2017). TREM2 deficiency impairs chemotaxis and microglial responses to neuronal injury. *EMBO Rep.* 18, 1186–1198. doi: 10.15252/embr.201743922

Mercalli, A., Calavita, I., Dugnani, E., Citro, A., Cantarelli, E., Nano, R., et al. (2013). Rapamycin unbalances the polarization of human macrophages to M1. *Immunology* 140, 179–190. doi: 10.1111/imm.12126

Mills, C. D. (2012). M1 and M2 macrophages: oracles of health and disease. *Crit. Rev. Immunol.* 32, 463–488. doi: 10.1615/critrevimmunol.v32.i6.10

Neumann, H., and Takahashi, K. (2007). Essential role of the microglial triggering receptor expressed on myeloid cells-2 (TREM2) for central nervous tissue immune homeostasis. *J. Neuroimmunol.* 184, 92–99. doi: 10.1016/j.jneuroim.2006.11.032

Orihuela, R., McPherson, C. A., and Harry, G. J. (2016). Microglial M1/M2 polarization and metabolic states. *Br. J. Pharmacol.* 173, 649–665. doi: 10.1111/bph.13139

Pan, J., Jin, J. L., Ge, H. M., Yin, K. L., Chen, X., Han, L. J., et al. (2015). Malibatol A regulates microglia M1/M2 polarization in experimental stroke in a PPARγ-dependent manner. *J. Neuroinflammation* 12:51. doi: 10.1186/s12974-015-0270-3

Patton, M. G., Gillum, T. L., Szymanski, M. C., Gould, L. M., Lauterbach, C. J., Vaughan, R. A., et al. (2018). Heat acclimation increases inflammatory and apoptotic responses to subsequent LPS challenge in C2C12 myotubes. *Cell Stress Chaperones* 23, 1117–1128. doi: 10.1007/s12192-018-0923-0

Piccio, L., Buonsanti, C., Mariani, M., Cella, M., Gilfillan, S., Cross, A. H., et al. (2007). Blockade of TREM-2 exacerbates experimental autoimmune encephalomyelitis. *Eur. J. Immunol.* 37, 1290–1301. doi: 10.1002/eji.200636837

Qin, C., Fan, W. H., Liu, Q., Shang, K., Murugan, M., Wu, L. J., et al. (2017). Fingolimod protects against ischemic white matter damage by modulating microglia toward M2 polarization *via* STAT3 pathway. *Stroke* 48, 3336–3346. doi: 10.1161/strokeaha.117.018505

Ransohoff, R. M., and Perry, V. H. (2009). Microglial physiology: unique stimuli, specialized responses. *Annu. Rev. Immunol.* 27, 119–145. doi: 10.1146/annurev.immunol.021908.132528

Shein, N. A., Doron, H., Horowitz, M., Trembovler, V., Alexandrovich, A. G., and Shohami, E. (2007a). Altered cytokine expression and sustained hypothermia following traumatic brain injury in heat acclimated mice. *Brain Res.* 1185, 313–320. doi: 10.1016/j.brainres.2007.09.024

Shein, N. A., Tsenter, J., Alexandrovich, A. G., Horowitz, M., and Shohami, E. (2007b). Akt phosphorylation is required for heat acclimation-induced neuroprotection. *J. Neurochem.* 103, 1523–1529. doi: 10.1111/j.1471-4159.2007.04862.x

Shein, N. A., Grigoriadis, N., Horowitz, M., Umschwief, G., Alexandrovich, A. G., Simeonidou, C., et al. (2008). Microglial involvement in neuroprotection following experimental traumatic brain injury in heat-acclimated mice. *Brain Res.* 1244, 132–141. doi: 10.1016/j.brainres.2008.09.032

Shein, N. A., Horowitz, M., Alexandrovich, A. G., Tsenter, J., and Shohami, E. (2005). Heat acclimation increases hypoxia-inducible factor 1α and erythropoietin receptor expression: implication for neuroprotection after closed head injury in mice. *J. Cereb. Blood Flow Metab.* 25, 1456–1465. doi: 10.1038/sj.jcbfm.9600142

Shohami, E., Novikov, M., and Horowitz, M. (1994). Long term exposure to heat reduces edema formation after closed head injury in the rat. *Acta Neurochir. Suppl.* 60, 443–445. doi: 10.1007/978-3-7091-9334-1_121

Sun, M., Zhu, M., Chen, K., Nie, X., Deng, Q., Hazlett, L. D., et al. (2013). TREM-2 promotes host resistance against *Pseudomonas aeruginosa* infection by suppressing corneal inflammation *via* a PI3K/Akt signaling pathway. *Invest. Ophthalmol. Vis. Sci.* 54, 3451–3462. doi: 10.1167/iovs.12-10938

Takahashi, K., Rochford, C. D., and Neumann, H. (2005). Clearance of apoptotic neurons without inflammation by microglial triggering receptor expressed on myeloid cells-2. *J. Exp. Med.* 201, 647–657. doi: 10.1084/jem.20041611

Weichhart, T., and Saemann, M. D. (2008). The PI3K/Akt/mTOR pathway in innate immune cells: emerging therapeutic applications. *Ann. Rheum. Dis.* 67, iii70–iii74. doi: 10.1136/ard.2008.098459

Wolfe, C. M., Fitz, N. F., Nam, K. N., Lefterov, I., and Koldamova, R. (2018). The role of APOE and TREM2 in Alzheimer's disease-current understanding and perspectives. *Int. J. Mol. Sci.* 20:E81. doi: 10.3390/ijms20010081

Xiang, X., Werner, G., Bohrmann, B., Liesz, A., Mazaheri, F., Capell, A., et al. (2016). TREM2 deficiency reduces the efficacy of immunotherapeutic amyloid clearance. *EMBO Mol. Med.* 8, 992–1004. doi: 10.15252/emmm.201606370

Yang, X., He, G., Hao, Y., Chen, C., Li, M., Wang, Y., et al. (2010). The role of the JAK2-STAT3 pathway in pro-inflammatory responses of EMF-stimulated N9 microglial cells. *J. Neuroinflammation* 7:54. doi: 10.1186/1742-2094-7-54

Yang, X., Xu, S., Qian, Y., and Xiao, Q. (2017). Resveratrol regulates microglia M1/M2 polarization *via* PGC-1α in conditions of neuroinflammatory injury. *Brain Behav. Immun.* 64, 162–172. doi: 10.1016/j.bbi.2017.03.003

Yi, J., He, G., Yang, J., Luo, Z., Yang, X., and Luo, X. (2017). Heat acclimation regulates the autophagy-lysosome function to protect against heat stroke-induced brain injury in mice. *Cell. Physiol. Biochem.* 41, 101–114. doi: 10.1159/000455979

Yu, T., Gao, M., Yang, P., Liu, D., Wang, D., Song, F., et al. (2019). Insulin promotes macrophage phenotype transition through PI3K/Akt and PPAR-γ signaling during diabetic wound healing. *J. Cell. Physiol.* 234, 4217–4231. doi: 10.1002/jcp.27185

Zhang, X., Lv, M., Zhu, X., Tian, L., Li, J., Shao, Y., et al. (2019). Isoflurane preconditioning ameliorates electromagnetic pulse-induced neural damage by shifting microglia polarization toward anti-inflammatory phenotype *via* upregulation of SOCS1. *Int. Immunopharmacol.* 68, 48–57. doi: 10.1016/j.intimp.2018.12.064

Zhang, L., Zhang, J., and You, Z. (2018). Switching of the microglial activation phenotype is a possible treatment for depression disorder. *Front. Cell. Neurosci.* 12:306. doi: 10.3389/fncel.2018.00306

Zhao, Y., Wu, X., Li, X., Jiang, L. L., Gui, X., Liu, Y., et al. (2018). TREM2 is a receptor for β-amyloid that mediates microglial function. *Neuron* 97, 1023.e7–1031.e7. doi: 10.1016/j.neuron.2018.01.031

Zhong, L., Chen, X. F., Zhang, Z. L., Wang, Z., Shi, X. Z., Xu, K., et al. (2015). DAP12 stabilizes the C-terminal fragment of the triggering receptor expressed on myeloid cells-2 (TREM2) and protects against LPS-induced pro-inflammatory response. *J. Biol. Chem.* 290, 15866–15877. doi: 10.1074/jbc.m115.645986

Zhu, M., Li, D., Wu, Y., Huang, X., and Wu, M. (2014). TREM-2 promotes macrophage-mediated eradication of *Pseudomonas aeruginosa via* a PI3K/Akt pathway. *Scand. J. Immunol.* 79, 187–196. doi: 10.1111/sji.12148

Conflict of Interest: The authors declare that the research was conducted in the absence of any commercial or financial relationships that could be construed as a potential conflict of interest.

Copyright © 2020 He, Luo, Shen, Wang, Li, Luo, Yang, Tan, Wang, Gao and Yang. This is an open-access article distributed under the terms of the Creative Commons Attribution License (CC BY). The use, distribution or reproduction in other forums is permitted, provided the original author(s) and the copyright owner(s) are credited and that the original publication in this journal is cited, in accordance with accepted academic practice. No use, distribution or reproduction is permitted which does not comply with these terms.

frontiers in Cellular Neuroscience

ORIGINAL RESEARCH
published: 28 January 2020
doi: 10.3389/fncel.2020.00003

The Pomace Extract Taurisolo Protects Rat Brain From Ischemia-Reperfusion Injury

Dominga Lapi[1], Mariano Stornaiuolo[2], Lina Sabatino[3], Eduardo Sommella[2], Giancarlo Tenore[2], Maria Daglia[2], Rossana Scuri[4], Martina Di Maro[1], Antonio Colantuoni[1] and Ettore Novellino[2]*

[1]*Department of Clinical Medicine and Surgery, University of Naples "Federico II", Naples, Italy,* [2]*Department of Pharmacy, University of Naples "Federico II", Naples, Italy,* [3]*Department of Science and Technology, University of Sannio, Benevento, Italy,* [4]*Department of Translational Research and New Technologies in Medicine and Surgery, University of Pisa, Pisa, Italy*

Taurisolo® is a pomace extract from Aglianico Grapes, a wine cultivar native to Campania (Southern Italy). It exhibits a very high polyphenolic content and, consumed as a nutraceutical, is effective in reducing the level of Trimethylamine N-oxide (TMAO), a cardiovascular disease risk factor marker. We here show the effects of Taurisolo® on rat brain microvascular alterations induced by a diminution in cerebral blood flow (CBFD) for 30 min, due to bilateral common carotid artery occlusion, and subsequent blood flow restoration (CBFR) for 60 min. The rat pial microcirculation was investigated by intravital fluorescence microscopy through a parietal closed window implanted into the skull bone. The rat pial arterioles were classified according to Strahler's ordering scheme, from smaller penetrating arterioles up to the larger ones. Western blotting analysis and mass spectrometry (MS)-based metabolomics were used to investigate the expression of endothelial nitric oxide synthase (eNOS) or the presence of peroxidized cardiolipin and several inflammatory mediators, respectively. Radical Oxygen Species (ROS) formation and neuronal loss were assessed. In rats CBFD and CBFR caused a decrease in arteriolar diameter, increase in fluorescent leakage and in adhesion of leukocytes to venular walls, reduction in the length of perfused capillaries and increment of ROS formation with large infarct size. Taurisolo®, intravenously or orally administered, induced pial arteriolar dilation (up to >30% of baseline), prevented fluorescent leakage, adhesion of leukocytes, ROS formation, while facilitated capillary perfusion and significantly reduced infarct size. These effects were accompanied by an increase in eNOS expression. Mass-spectrometry metabolomics analysis detected a marked decrease in the amount

OPEN ACCESS

Edited by:
Dirk M. Hermann, University of Duisburg-Essen, Germany

Reviewed by:
Gunnar P. H. Dietz, University of Göttingen, Germany
Tommaso Angelone, University of Calabria, Italy

****Correspondence:***
Dominga Lapi
dominga.lapi@unina.it

Received: *07 August 2019*
Accepted: *07 January 2020*
Published: *28 January 2020*

Citation:
Lapi D, Stornaiuolo M, Sabatino L, Sommella E, Tenore G, Daglia M, Scuri R, Di Maro M, Colantuoni A and Novellino E (2020) The Pomace Extract Taurisolo Protects Rat Brain From Ischemia-Reperfusion Injury. Front. Cell. Neurosci. 14:3. doi: 10.3389/fncel.2020.00003

Abbreviations: TMAO, Trimethylamine N-oxide; CBFDD, iminution of cerebral blood flow; CBFR, Restoration of cerebral blood flow; eNOS, Endothelial nitric oxide synthase; ROS, Reactive oxygen species; TxB2, Thromboxane B2; ECCG, Epigallocatechin; PGI, Protected Geographical Indication; NO, Nitric oxide; i.v., Intravenous; b.w., Bodyweight; L-NIO, N5-(l-Iminoethyl)-L-ornithine dihydrochloride; i.p., Intraperitoneal; aCSF, Artificial cerebrospinal fluid; FITC, Fluorescein isothiocyanate; NGL, Normalized gray levels; BFCL, Capillary showing blood flow length; DCFH-DA, Dichlorofluorescein-diacetate; DCF, Dichlorofluorescein; TTC, 2,3,5-triphenyltetrazolium chloride; PMSF, phenylmethylsulfonyl fluoride; SDS-PAGE, Sodium Dodecyl Sulfate—PolyAcrylamide Gel Electrophoresis; TBST, Tris-Buffered Saline, 0.1% Tween® 20 Detergent; HPLC-DAD, High-performance liquid chromatography-diode-array detector; SEM, Standard error of the mean; MS, Mass spectrometry; AA, Arachidonic acid; COX, Cyclooxygenase; PGF2 α, Prostaglandin F2 α; PGD2, Prostaglandin D2; PGI2, Prostacyclin 2; PGF1 α, Prostaglandin F1 α.

of peroxidized cardiolipin and pronounced reduction in pro-inflammatory prostaglandins and thromboxane Txb2. Altogether, these results extend the nutraceutical potential of Taurisolo® and suggest their eligibility for preventing brain damage due to ischemia-reperfusion injury.

Keywords: ischemia-reperfusion, brain injury, ROS, polyphenols, antioxidants

INTRODUCTION

Endogenous antioxidants, like melatonin and glutathione, have been shown to exert preventive effects on an ischemia-reperfusion injury, a complication resulting from the rapid restoration of the blood flow supply after an ischemic insult (Lapi et al., 2011; Zhou et al., 2018). Recently, plant extracts enriched in polyphenols (Brosková et al., 2013), epigallocatechin, epigallocatechin-3-gallate (ECCG; Aneja et al., 2004), oleuropein and malvidin (Lapi et al., 2015, 2016) have been included among the nutraceuticals endowed with a protective effect against ischemia-reperfusion injury. Their mechanisms of action have been mainly linked to their antioxidant potential and their ability to counterbalance oxidative stress (Zhou et al., 2018). Upon an IR event, indeed, a burst of reactive oxygen species (ROS) is produced by several cell types (Zorov et al., 2014). This massive ROS production induces oxidative damage, reduces ATP production and leads to necrotic or apoptotic cell death. ROS-mediated damage will also trigger the inflammatory response (Eltzschig and Eckle, 2011), i.e., a production of prostaglandins, contributing to the formation of interstitial edema, reduction of arteriolar diameter and venular wall alterations. Much evidence indicates that nutraceutical inhibits mitochondrial oxidative stress and ROS production resulting in a partial reduction of brain damage (Brosková et al., 2013).

The mitochondria are the primary intracellular source of ROS. Among phospholipid species, cardiolipin has interesting chemical and structural properties and has also a highly specialized physiological distribution, being almost exclusively located in the inner mitochondrial membrane where it is biosynthesized (Paradies et al., 2014). Several studies indicate that cardiolipin is involved in the regulation of main mitochondrial bioenergetic processes, optimizing the activity of key mitochondrial inner membrane proteins involved in oxidative phosphorylation (Houtkooper and Vaz, 2008). Furthermore, alterations to cardiolipin structure, content, and acyl chain composition are responsible for mitochondrial dysfunction in multiple tissues in a variety of physiopathological settings (Petrosillo et al., 2003; Paradies et al., 2009, 2013).

Our research group has recently identified the antioxidant property of the Pomace (called Taurisolo®), obtained from Aglianico Grapes, a wine cultivar native to Campania region (Southern Italy), listed as a Protected Geographical Indication (PGI) product [Commission Regulation (EC) No. 417/2006]. Taurisolo® exhibits a very high polyphenolic content, specifically represented by resveratrol, catechins and their derivatives. On the basis of its anti-oxidant activity, we here challenged Taurisolo® in preventing IR injury damage, by evaluating the effects of its acute (intravenous) or chronic (oral) treatment in rats subjected to cerebral hypoperfusion and reperfusion. We here show that Taurisolo® reduced the main IR-dependent pial microvascular changes, such as microvascular permeability increase, leukocyte adhesion, reduction in perfused capillary length, ROS formation and neuronal loss.

Furthermore, employing high-resolution mass spectrometry (MS) techniques and measuring cardiolipin peroxidation and arginine catabolites, we further show that Taurisolo® reduces cell membrane alterations and increases NO production.

MATERIALS AND METHODS

Experimental Groups

Male Wistar rats weighing 250–300 g (Charles River, Italy) were randomly assigned to four groups (**Table 1**):

1. Sham-operated group (SO group), rats (n = 60) fed with a control diet and subjected to the surgical procedure, in turn they were divided into four subgroups:
   (a) SO-S subgroup (n = 12) was injected with intravenous (i.v.) saline solution (0.9% NaCl);
   (b) SO-T subgroup (n = 24), successively divided in SO-Tiv (n = 12) and SO-Tor (n = 12) subgroups, receiving i.v. Taurisolo®, 10 mg/kg body weight (b.w.) or oral Taurisolo®, 20 mg/kg b.w./die, intragastrically administered under light ether anesthesia for 1 month, respectively;
   (c) SO-L subgroup (n = 12), administered with intravenous L-NIO [N5-(1-Iminoethyl)-L-ornithine dihydrochloride, a potent, irreversible inhibitor of eNOS, endothelial nitric oxide synthase], 10 mg/kg b.w.
   (d) SO-LTiv subgroup (n = 12) administered with intravenous L-NIO (10 mg/kg b.w.) plus intravenous Taurisolo® (10 mg/kg b.w.).
2. Hypo-reperfused group (H group), rats (n = 15) fed with a control diet, subjected to a diminution in cerebral blood flow (CBFD) for 30 min and restoration of cerebral blood flow (CBFR) for 60 min.
3. Taurisolo® -treated group, divided in:
   (a) subgroup Tiv: rats (n = 15), subjected to intravenous administration of Taurisolo®, 10 mg/kg b.w. 10 min prior to CBFD and at the beginning of CBFR;
   (b) subgroup Tor: rats (n = 15) fed with Taurisolo® (20 mg/kg b.w./die) supplemented diet; Taurisolo® was dissolved in 1 ml of distilled water and intragastrically administered under light ether anesthesia for 1 month; at

TABLE 1 | Experimental groups with relative treatment.

Groups	Subgroups	Treatments
Sham operated (SO)	SO-S	i.v. administration of saline solution (0.9% NaCl).
	SO-Tiv	i.v. administration of Taurisolo® (10 mg/kg b. w.).
	SO-Tor	oral administration of Taurisolo® (20 mg/kg b.w./die for 1 month).
	SO-L	i.v administration of L-NIO (10 mg/kg b.w.).
	SO-LTiv	i.v. administration of L-NIO (10 mg/kg b.w.) plus Taurisolo® (10 mg/kg b. w.).
Hypo-reperfused group (H-group)		induction of CBFD for 30 min and of CBFR for 60 min.
Taurisolo®- treated group (T group)	Tiv	i.v. administration of Taurisolo®, 10 mg/kg b.w. 10 min prior to CBFD and at the beginning of CBFR.
	Tor	oral administration of Taurisolo® (20 mg/kg b.w./dye) for 1 month and induction of CBFD and of CBFR.
L-NIO + Taurisolo®- treated group (LT group)	L-Tiv	i.v. administration of L-NIO (10 mg/kg b.w). prior to i.v. Taurisolo®, 10 mg/kg b.w and induction of CBFD and CBFR.
	L-Tor	oral administration of Taurisolo® (20 mg/kg b.w./die) for 1 month and i.v administration of L-NIO 10 min prior to CBFD and at the beginning of CBFR.

the end of treatment animals were subjected to CBFD and CBFR.

4. L-NIO plus Taurisolo® -treated rats ($n = 20$), divided into two subgroups:
   (a) rats subjected to intravenous administration of L-NIO, 10 mg/kg b.w. prior to i.v. Taurisolo®, 10 mg/kg b.w., 10 min prior to CBFD and at the beginning of CBFR (L-Tiv subgroup, $n = 10$);
   (b) rats subjected to orally administration of Taurisolo®, 20 mg/kg b.w./die for 1 month and to L-NIO injection 10 min prior to CBFD and at the beginning of CBFR (L-Tor subgroup, $n = 10$).

Taurisolo® dosages were determined by pilot experiments. We tried several dosages by intravenous administration: 3, 5, 8, 10, 12, 15, 18, 20, 22, 25 mg/kg b.w. dosages and we observed that a dosage lower of 5 mg was ineffective. In the range between 8 and 20 mg/kg b.w. Taurisolo® exerted a protective effect on pial microcirculation. We observed as well that doses above 20 mg/kg b.w did not further improve the protective effects exerted by the lower dosages. Therefore, to avoid a high concentration of the substance, we chose to use 10 mg/kg b.w. a concentration similar to those of previously studied anti-oxidant molecules. Oral administration of Taurisolo® at the dosages of 10, 15, 20, 25 mg/die shorter than 15 days did not have significant effects; therefore, we report the data obtained after 30 days of treatment at the dosage of 20 mg/kg b.w./die, effective in the protection.

Surgery Procedure

The experiments were performed following the Guide for the Care and Use of Laboratory Animals published by the US National Institutes of Health (NIH Publication No. 85-23, revised 1996) and to institutional rules for the care and handling of experimental animals, as previously reported (Lapi et al., 2012a). The protocol was approved by the "Federico II" University Medical School of Naples, Ethical Committee (n° 2011/0059997, 24/05/2011).

Animals were anesthetized with intraperitoneal (i.p.) injection of α-chloralose (60 mg/kg b.w. for induction; afterward 30 mg/kg b.w.) and mechanically ventilated after tracheotomy, according to the experimental protocol previously reported (Lapi et al., 2012b). Two catheters were placed, one in the right femoral artery and the other in the left femoral vein, respectively, for the measurement of arterial blood pressure and to inject the fluorescent tracers [fluorescein isothiocyanate, FITC bound to dextran, molecular weight 70 kDa (FD 70), 50 mg/100 g b.w., as 5% wt/vol solution in 3 min just once at the start of experiment after 30 min of the preparation stabilization; rhodamine 6 G, 1 mg/100 g b.w. in 0.3 ml, as a bolus with supplemental injection throughout CBFD and CBFR (final volume 0.3 ml·100 g^{-1}·h^{-1}) to label leukocytes for adhesion evaluation]. Both carotid arteries were prepared for clamping.

Blood gases were measured on arterial blood samples at 30 min intervals (ABL5; Radiometer, Copenhagen, Denmark). The parameters monitored in all animals were: heart rate, mean arterial blood pressure, respiratory CO_2 and blood gases values. They were stable within physiological ranges. Rectal temperature was recorded and maintained at 37.0 ± 0.5°C, as previously reported (Lapi et al., 2016). The visualization of pial microvasculature was carried out as previously reported (Lapi et al., 2012a). Briefly, a closed cranial window was positioned at the level of the left frontoparietal cortex through an incision in the skin to operate a craniotomy. The cerebral cortex was preserved from overheating caused by drilling with saline solution superfusion of the skull. The dura mater was gently cut and displayed on the corner; a quartz microscope coverglass was bound to the skull bone. Artificial cerebrospinal fluid (aCSF) was superfused on the cerebral surface with a rate of 0.5 ml/min. The composition of the aCSF was 119.0 mM NaCl, 2.5 mM KCl, 1.3 mM $MgSO_4 \bullet 7H_2O$, 1.0 mM NaH_2PO_4, 26.2 mM $NaHCO_3$, 2.5 mM $CaCl_2$ and 11.0 mM glucose (equilibrated with 10.0% O_2, 6.0% CO_2 and 84.0% N_2; pH 7.38 ± 0.02).

Hypoperfusion was induced by clamping both common carotid arteries, previously prepared (CBFD) for 30 min, and after removing the clamping the pial microcirculation was observed for 60 min (CBFR).

Fluorescence Microscopy

Pial microvascular networks were *in vivo* observed by fluorescence microscopy (Lapi et al., 2012b). The microscope (Leitz Orthoplan, Wetzlar, Germany) set up was armed with long-distance objectives [2.5 ×, numerical aperture (NA) 0.08; 10 ×, NA 0.20; 20×, NA 0.25; 32×, NA 0.40], a 10× eyepiece and a filter block (Ploemopak, Leitz) used for FITC and rhodamine 6 G. The epi-illumination was provided by a 100-Watt mercury lamp. Moreover, a heat filter prevented overheating of the preparations (Leitz KG1). A DAGE MTI 300 low-light-level camera was utilized to televise the pial microvascular networks; the recordings were stored through a computer-based frame grabber (Pinnacle DC 10 plus, Avid Technology, Burlington, MA, USA).

Determination of Microvascular Parameters

Microvascular parameters, index of microvascular damage, were measured off-line utilizing a computerized imaging technique (Lapi et al., 2012b, 2016). First, the arterioles were measured and classified in orders by Strahler's method (Lapi et al., 2008), utilizing a frame by frame computerized method (Microvascular Imaging Program, MIP).

The arteriolar diameter changes were evaluated in all orders of pial arterioles; however, we have shown the data collected in 30 arterioles of order 3 for each rat group or subgroup studied.

The increase in microvascular permeability was measured by evaluating fluorescent dextran extravasation from venules and expressed as normalized gray levels (NGLs): NGL = (I − Ir)/Ir, where, Ir was the baseline gray level at the microvasculature filling with fluorescence, and I was the value at the end of CBFD or CBFR. Gray levels were obtained using the MIP image program by averaging data derived from 5 windows, measuring 50 × 50 mM (10× objective) and located outside the venules. To localize the same regions of interest a computer-assisted device for XY movement of the microscope table was used.

Adhesion of leukocytes to the vessel walls (45 venules for every group or subgroup) over a 30-s time-period was reported as number of adherent cells/100 μm of venular length (v.l.)/30 s, utilizing appropriate magnification (20× and 32× objectives; Lapi et al., 2012a). Perfused capillaries were evaluated as the length of the capillaries showing blood flow (BFCL), assessed by MIP image in an area of 150 × 150 μm (Lapi et al., 2016).

During the whole experimental period, we monitored arterial blood pressure (mean) by a Gould Windograf recorder (model 13-6615-10S, Gould, OH, USA) and heart rate by Viggo-Spectramed P10E2 transducer; Oxnard, CA, USA, linked to the catheterized femoral artery (Lapi et al., 2012b). The arterial blood gases (ABL5; Radiometer, Copenhagen, Denmark) were measured at 30 min intervals, as previously reported (Lapi et al., 2012b), as well as the hematocrit in basal conditions, at the end of CBFD and CBFR.

ROS Production Assessment

The pial layer was superfused with aCSF, containing 250 mM 2′-7′-dichlorofluorescein-diacetate (DCFH-DA) at 37.0 ± 0.5°. The consequent test was carried out after 30 min CBFD (n = 3) and 60 min CBFR (n = 3), as previously reported (Lapi et al., 2013). DCFH-DA is widely used *in vivo* as a marker for oxidative stress of the cells and tissues (Wang and Joseph, 1999). DCF fluorescence intensity, related to the intracellular ROS level, was assessed using an appropriate filter (522 nm) and measured by NGL (Watanabe, 1998). For this analysis, three rats from each experimental group were used.

Tissue Damage Evaluation

At the end of the CBFR, rats were sacrificed to evaluate tissue damage. The isolated brains were rostrocaudal cut into coronal sections (1 mm) by a vibratome (Campden Instrument, 752 M; Lafayette, IN, USA). The slices obtained were incubated in 2% 2, 3,5-triphenyl tetrazolium chloride (TTC; 20 min) at 37°C and in 10% formalin overnight (Lapi et al., 2013). TTC, a white salt, is reduced to red 1,3,5-triphenyl formazan by dehydrogenases in living cells.

A computerized image analysis (Image-Pro Plus; Rockville, MD, USA) was utilized to identify the location and extent of necrotic areas. The infarct size was quantified by manual measurements, according to the following formula: [(area of non-hypoperfused, or area not subjected to cerebral blood flow decrease, cortex or striatum − area of remaining hypoperfused, or area subjected to cerebral blood flow decrease, cortex or striatum)/area of non-hypoperfused cortex or striatum] × 100 (Bederson et al., 1986).

Western Blotting Protocol

Tissue specimens from cortex and striatum were treated as previously reported (Lapi et al., 2016). They were homogenized by Polytron (Brinkman Instruments, Westbury, NY, USA) in buffer with the following components: 50 mM HEPES, 150 mM NaCl, 5 mM EGTA, 150 mM $MgCl_2$, 1% glycerol, 1% Triton X-100, 1 mM phenylmethylsulfonyl fluoride (PMSF), 1 mM trypsin inhibitor. Bradford assay (BioRad, Berkeley, CA, USA) was used to quantify protein concentration. The stirred (1 h, 4°C) homogenate was centrifuged at 14,000 rpm for 20 min. The Bradford procedure (BioRad, Berkeley, CA, USA) was utilized to determine the protein concentration in the supernatant. The same amounts of proteins were run on 7.5% Sodium Dodecyl Sulfate-PolyAcrylamide Gel Electrophoresis (SDS-PAGE) under reducing conditions, then transferred to polyvinylidene difluoride membranes (PVDF; Invitrogen, Carlsbad, CA, USA). 5% w/v BSA in Tris-buffered saline and 0.1% Tween 20 (TBST) were used to block the membrane for 1 h at room temperature. Filters were incubated with specific antibodies at 4°C overnight, washed in TBST and then incubated with horseradish peroxidase-conjugated secondary antibodies (1:1,000, GE-HealthCare, Little Chalfont, UK) for 1 h at room temperature. Peroxidase activity was detected by the ECL system (GE-HealthCare, Little Chalfont, UK) after washing. Normalized protein loading was obtained incubating the same filters with anti-tubulin antibody (Sigma-Aldrich, Milan, Italy) and the intensity of each band was quantified by densitometry (ChemiDoc, XRS, Bio-Rad). We assessed the protein concentration of endothelial NO synthase (eNOS) compared with tubulin concentration. To reveal the

proteins of interest, specific antibodies were utilized: rabbit polyclonal anti-eNOS (1:1,000). We purchased anti-eNOS and anti-tubulin antibodies from Cell Signaling Technology Inc. (Danvers, MA, USA).

Grape Pomace Extract Supplement Preparation

Taurisolo® was obtained from Aglianico cultivar grape, collected during the harvest in autumn 2016. The product was formulated by the Department of Pharmacy, University of Naples "Federico II" (Naples, Italy). Large scale production of Taurisolo® has been accomplished by MBMed Company (Turin, Italy). The grape has been extracted with water at 50°C. After centrifugation, the extract underwent a spray-drying process with maltodextrins as support, obtaining a fine powder, containing a pomace: maltodextrins ratio 1:1 (w/w). Taurisolo® has been used to formulate the nutraceuticals.

The High Performance Liquid Chromatography-diode-array detector (HPLC-DAD) analysis indicates that the main polyphenols contained in Taurisolo® are (values are expressed in μg/g Taurisolo® ± standard deviation of three repetitions): Gallic acid 1463.4 ± 65.5; Syringic acid 539.2 ± 6.02, Caffeic acid 20.7 ± 0.76, p-coumaric acid 27.9 ± 0.66, Ferulic acid 10.5 ± 0.70, Resveratrol 13.6 ± 0.64, Catechin 4087.0 ± 64.5, Epicatechin 886.0 ± 7.82, Quercetin 40.22 ± 7.11, Rutin 28.4 ± 0.70, Procyanidin B1 dimer 62.8 ± 0.59, Procyanidin B2 dimer 426.5 ± 5.92, Procyanidin B3 dimer 22.05 ± 6.61, Procyanidin B4 dimer 56.6 ± 0.88, Procyanidin C2 trimer 44.6 ± 0.66. Taurisolo® was standardized and we had uniformity in the dosage administration.

Mass Spectrometry-Based Metabolomics, Statistics and Analysis

Rat brains were homogenized using a potter in 1 ml of pre-chilled methanol/water 1:1 solution, containing 10 nmol of internal standard, and centrifuged at 10,000 *g* for 10 min at 4°C (Ser et al., 2015). The resulting supernatants were collected and transferred into Eppendorf tubes and stored at −80°C. Analyses were performed according to a previous protocol (Sommella et al., 2019). Data were acquired on a SolariX XR 7T (Bruker Daltonics, Bremen, Germany). The instrument was tuned with a standard solution of sodium trifluoracetate. Mass spectra were recorded in a broadband mode in the range 100–1,500 m/z, with an ion accumulation of 20 ms, with 32 scans using 2 million data points (2M). Nebulizing (N2) and drying gases (air) were set at 1 and 4 ml/min, respectively, with a drying temperature of 200°C. Both positive and negative ESI ionization were employed. Five replicates of each injection were carried out. The instrument was controlled by Bruker FTMS Control, MS spectra were elaborated with Compass Data Analysis version 4.2 (Bruker); identification of compounds based on accurate MS measurements was performed by Compound Crawler ver. 3.0 and Metaboscape 3.0 (Bruker). Metabolites signals were normalized using internal standards.

We utilized three animals for microvascular studies, three for ROS quantification, three for TTC staining, three for Western blot analysis and three for mass-spectrometry metabolomics analysis for each experimental group or subgroup.

Statistical Analysis

Comparisons and differences were analyzed for statistical significance by two-way ANOVA and Bonferroni *post hoc* test. For comparison of diameter and length of vessels, due to distribution of data computed by the Kolmogorov–Smirnov test, nonparametric tests were used: Mann–Whitney and Kruskal–Wallis tests. All data (graphs, bars or lines) are reported as the mean and standard error of the mean (SEM). Statistical analysis was performed using Statistica software (StatSoft, Tulsa, OK, USA) and Minitab (Minitab Inc., State College, PA, USA).

RESULTS

Microvascular Changes

To examine whether Taurisolo® alleviated brain hypoperfusion-reperfusion damage we assessed the microvascular changes of rat pial microcirculation in sham-operated rats, in ischemic animals and in Taurisolo®-treated rats by fluorescence microscopy. As reported in **Figures 1A–C**, in sham-operated rats there were no changes in arteriolar diameter at the end of observation time, while in ischemic animals we detected reduction in diameter of arterioles, increase in fluorescent dextran leakage on the venous side of microcirculation and in DCF fluorescence due to marked formation of ROS (**Figures 1D–F**). In Taurisolo®-treated animals by i.v. or oral administration we detected an increase in arteriolar diameter accompanied by a significant decrease in fluorescent leakage on the venous side of microcirculation and reduction of DCF fluorescence, indicating a reduction in ROS formation (**Figures 1G–I,J–L**).

Moreover, TTC assays showed a significant decrease in infarct size induced by Taurisolo®, as reported in **Figure 2**. In particular, the hypoperfusion and the subsequent reperfusion caused significant damage in cortex and striatum cerebral tissue of both hemispheres in H rats (**Figure 2B**), compared to the SO-S subgroup (**Figure 2A**). Cortex infarct size was 9.2 ± 1.8% ($p < 0.01$ vs. non-hypoperfused cortex), while in the striatum the damage was more marked (striatum infarct size 32.5 ± 3.7%, $p < 0.01$ vs. non-hypoperfused cortex). Animals treated with Taurisolo®, intravenously or orally administered, and subjected to CBFD and CBFR showed neuronal damage significantly diminished when compared to the H group (**Figures 2C,D**, respectively). The damage appears to be localized to the striatum (infarct sizes were 7.0 ± 1.5% and 10.6 ± 1.0% in rats treated with i.v. Taurisolo® or with oral Taurisolo®, respectively, $p < 0.01$ vs. hypoperfused striatum).

These results prompted us to quantify the effects of Taurisolo® on ROS formation, as indicated by DCF assays, and on the diameter changes of pial arterioles, classified as reported in **Table 2**. **Figure 3** reports the DCF fluorescence intensity in sham-operated animals, in hypoperfused and in Taurisolo®-treated rats. The ROS formation was really marked in hypoperfused animals, while Taurisolo® was effective in reducing fluorescence intensity and consequently ROS formation.

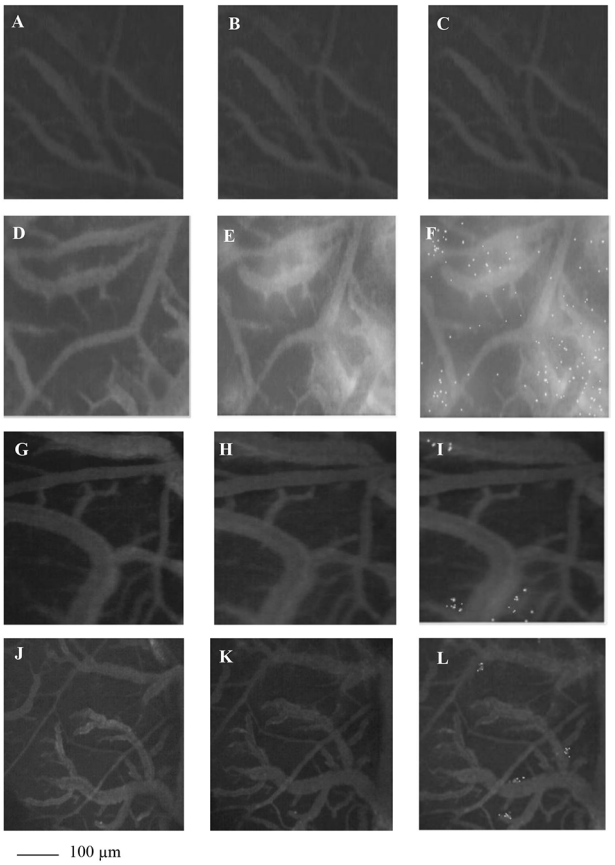


FIGURE 1 | The images of the pial microvascular networks obtained by computer-assisted method under baseline conditions **(A)**, after restoration of cerebral blood flow (CBFR; **B)** and after Dichlorofluorescein (DCF) local administration **(C)** in a rat of SO-S group: there were no changes in the diameter of the microvessels, in microvascular leakage and in radical oxygen species (ROS) formation; in **(D)** the computer-assisted images of a rat of H group under baseline conditions, after CBFR **(E)** and after DCF local administration **(F)**: the arterioles present reduction in diameter; the marked changes in the color of interstitium (from black to white) due to fluorescence dextran leakage; while the ROS formation were highlighted by numerous fluorescent spots. In **(G)**, the computer-assisted images of the pial microvascular networks under baseline conditions, after CBFR **(H)** and after DCF **(I)** local administration in a rat treated with intravenous Taurisolo®: no leakage of fluorescent-dextran and no ROS formation were detected. The computer-assisted images of the pial microvascular networks under baseline conditions **(J)**, after CBFR **(K)** and after DCF local administration **(L)** in a rat treated with oral Taurisolo®: neither permeability nor ROS formation were evident.

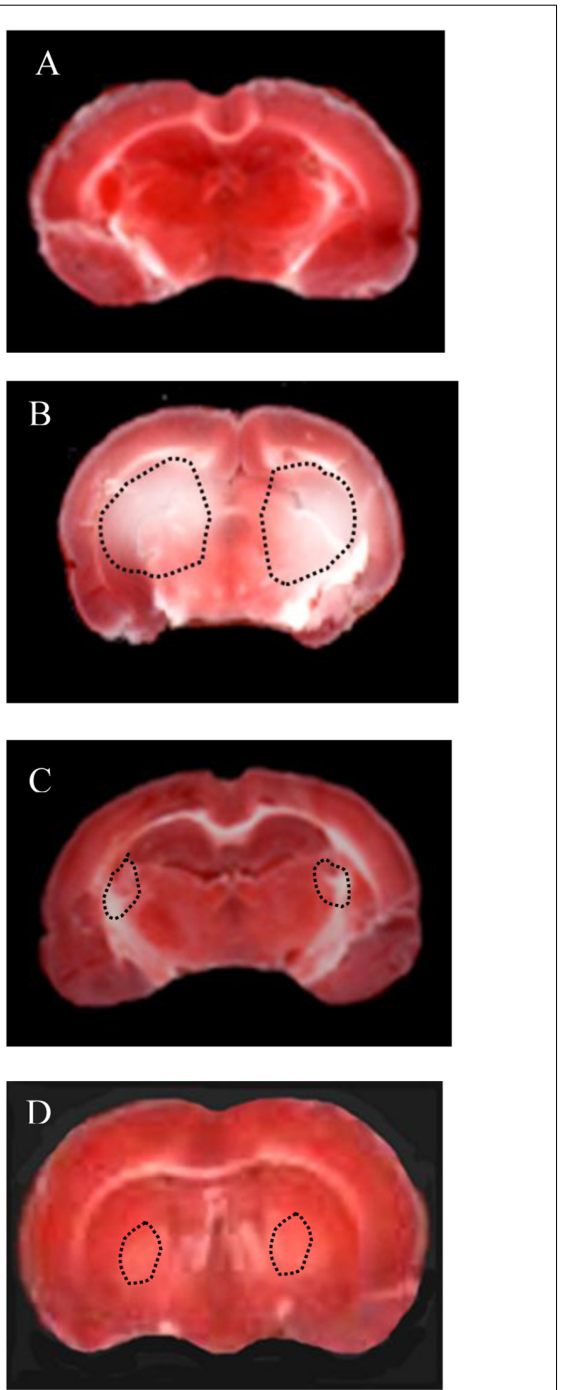


FIGURE 2 | Triphenyl tetrazolium chloride (TTC) staining of coronal brain slices from a rat of Sham-operated group (**A**: sham-operated animal), from a rat of H group (**B**: hypoperfused after 60 min of CBFR), from a rat of Tiv subgroup (**C**: after 60 min of CBFR) and from a rat of Tor subgroup **(D**: after 60 min of CBFR). The lesion in the striatum is shown by the dashed black line.

Moreover, we evaluated the diameter variations in all experimental groups (**Figure 4**). In the SO-S subgroup during the entire observation period, we did not detect any change in arteriolar diameter; furthermore, the rats treated with intravenous or oral administration of Taurisolo® (SO-Tiv and SO-Tor subgroup) did not show any alteration in diameter. In addition, the intravenous administration of L-NIO, specific inhibitor of eNOS (SO-L subgroup), or of L-NIO plus Taurisolo® (SO-LTiv subgroup) did not cause significant changes in arteriolar diameter. On the other hand, the animals subjected to hypoperfusion and reperfusion (H group) showed marked changes in diameter: CBFD caused a reduction in diameter (by 10.8 ± 1.5% of baseline in order 3 arterioles; $p < 0.01$ vs. baseline and SO-S subgroup; **Table 2** and **Figure 4**).

TABLE 2 | Diameter and length of each pial arteriolar order under baseline conditions, classified by Strahler's scheme.

Order	Arterioles (*n*)	Diameter (μm)	Length (μm)	Rats (*n*)
5	32	63.2 ± 4.5*	1,205 ± 310	60
4	64	45.5 ± 2.7*	943 ± 225	60
3	175	32.8 ± 2.2*	540 ± 115	60
2	263	25.0 ± 2.0*	355 ± 87	60
1	228	16.5 ± 1.8*	157 ± 75	60

*Arterioles (n): number of arterioles observed for each vessel order. Rats (n): number of rats where the classification by Strahler's method was performed, corresponding to the animals belonging to the Sham Operated group. *p < 0.01 vs. different order.*

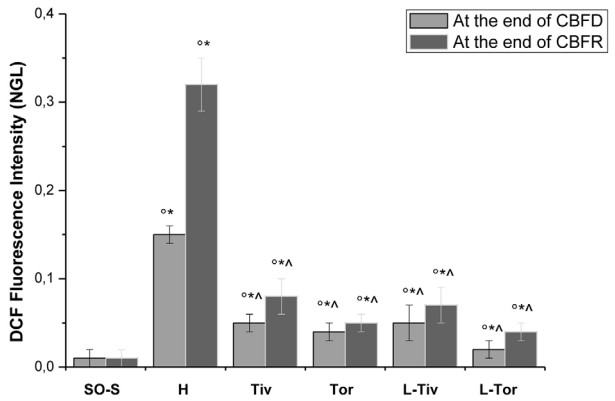


FIGURE 3 | DCF fluorescence intensity measured *in vivo* by Normalized Gray Levels (NGLs) after 30 min of diminution in cerebral blood flow (CBFD) and after 60 min of CBFR in the different experimental groups: SO-S, H, Tiv (10 mg/kg b.w. of Taurisolo® administered i.v. prior to CBFD and at the beginning of CBFR), Tor (20 mg/kg b.w. of Taurisolo® orally administered for 1 month and subjected to CBFD and CBFR), L-Tiv (L-NIO 10 mg/kg i.v. prior to i.v. Taurisolo® i.v.) and L-Tor (L-NIO 10 mg/kg i.v. prior to oral Taurisolo®) subgroups, treated before CBFD and at the beginning of CBFR. °$p < 0.01$ vs. baseline, *$p < 0.01$ vs. SO-S subgroup and ^$p < 0.01$ vs. H group.

After 60 min CBFR, pial arteriolar diameters significantly decreased (by 16.5 ± 1.8% of baseline, $p < 0.01$ vs. baseline and SO-S subgroup; **Table 3** and **Figure 4**). Taurisolo®, intravenously administered (Tiv subgroup), protected the pial microvasculature from damage induced by hypoperfusion and reperfusion. At the end of CBFD, pial arterioles slightly dilated by 5.0 ± 1.2% of baseline ($p < 0.01$ vs. baseline, SO-S subgroup and H group; **Figure 4**). At the end of CBFR, pial arteriolar diameters markedly increased (by 35.0 ± 1.8% of baseline, $p < 0.01$), indicating significant dilation of arterioles compared with H group and SO-S subgroup (**Table 3** and **Figure 4**).

The animals fed with Taurisolo® supplemented diet, 20 mg/kg b.w./die for 1 month (Tor subgroup), were highly protected from microvascular damage induced by CBFD and CBFR. After CBFD, pial arteriolar diameters did not significantly change compared to baseline conditions and the SO-S subgroup (diameter decreased by 2.0 ± 1.0% of baseline, $p < 0.01$ vs. H group; **Figure 4**). At the end of CBFR, the arteriolar diameters significantly increased by 12 ± 2% of baseline ($p < 0.01$ vs. baseline, SO-S subgroup and H group; **Table 3** and **Figure 4**).

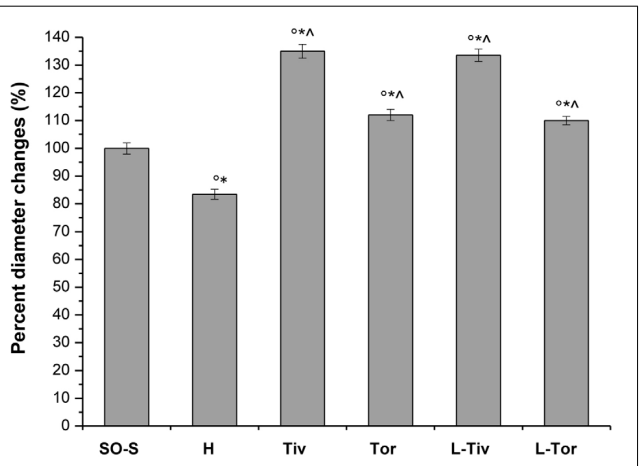


FIGURE 4 | Diameter changes in order 3 arterioles expressed as a percentage change of baseline after 60 min of CBFR in the different experimental groups: SO-S, H, Tiv (10 mg/kg b.w. of Taurisolo® administered i.v. prior to CBFD and at the beginning of CBFR), Tor (20 mg/kg b.w. of Taurisolo® orally administered for 1 month and subjected to CBFD and CBFR), L-Tiv (L-NIO 10 mg/kg i.v. prior to i.v. Taurisolo®) and L-Tor (L-NIO 10 mg/kg i.v. prior to oral Taurisolo®) subgroups, treated before CBFD and at the beginning of CBFR. °$p < 0.01$ vs. baseline, *$p < 0.01$ vs. SO-S subgroup and ^$p < 0.01$ vs. H group.

To clarify the mechanism of pial arteriolar dilation induced by Taurisolo®, we administered L-NIO, a specific inhibitor of eNOS, prior to Taurisolo®. The animals treated with intravenous administration of L-NIO plus Taurisolo® (L-Tiv subgroup) and subjected to CBFD and CBFR did not show any significant changes in arteriolar diameter compared with baseline conditions. Therefore, vasodilation induced by intravenous administration of Taurisolo® was abolished by L-NIO administration. The same pattern was observed in rats belonging to the L-Tor subgroup; in these animals, the intravenous administration of L-NIO 10 min prior to CBFD and at the beginning of CBFR was able to abolish the vasodilation induced by the oral treatment of Taurisolo® both at the end of CBFD and at the end of CBFR.

Then, we quantified the effects of Taurisolo® on the changes in microvascular permeability, known to be markedly induced by CBFD and CBFR; therefore, we assessed FITC leakage on the venous side of microcirculation. In sham-operated animals (SO-S subgroup) we did not observe microvascular leakage (0.01 ± 0.01 NGL; **Table 3**, **Figure 5**) nor in the rats treated with intravenous or oral administration of Taurisolo® (SO-Tiv and SO-Tor subgroup): microvascular permeability did not increase (0.02 ± 0.01 NGL and 0.01 ± 0.01 NGL, respectively). Finally, the intravenous administration of L-NIO (SO-L subgroup) or of L-NIO plus Taurisolo® (SO-LTiv subgroup) did not cause significant changes in microvascular leakage. On the contrary, in H group rats CBFD caused an increase in microvascular permeability (0.18 ± 0.02 NGL; $p < 0.01$ vs. baseline and SO-S subgroup; **Figure 5**). The increase was further incremented at the end of 60 min CBFR when microvascular permeability was really marked

TABLE 3 | Changes of the microvascular parameters evaluated at the end of the restoration of cerebral blood flow (CBFR) in SO-S, H, Tiv [10 mg/kg b.w. of Taurisolo® administered i.v. prior to diminution of cerebral blood flow (CBFD) and at the beginning of CBFR], Tor (20 mg/kg b.w. of Taurisolo® orally administered for 1 month and subjected to CBFD and CBFR), L-Tiv (L-NIO 10 mg/kg i.v. prior to i.v. Taurisolo® i.v.) and L-Tor (L-NIO 10 mg/kg i.v. administered prior to CBFD and at the beginning of CBFR) subgroups.

Subgroups	Number of rats (*n*)	Percent diameter changes	Microvascular leakage (NGL)	Number of adhering leukocytes/100 μm of venular length/30 s	Reduction of the length of perfused capillaries (BFCL, %)	DCF fluorescence intensity (NGL)
SO-S	12	100 ± 2	0.01 ± 0.01	1 ± 1	2.0 ± 1.5	0.01 ± 0.01
H	15	83.5 ± 1.8°*	0.45 ± 0.02°*	7 ± 2°*	45.0 ± 2.2°*	0.32 ± 0.03°*
Tiv	15	135.0 ± 2.5°*^	0.04 ± 0.01°*^	2 ± 1°^	15.0 ± 1.2°*^	0.08 ± 0.02°*^
Tor	15	112 ± 2°*^	0.05 ± 0.01°*^	3 ± 1°*^	6.0 ± 1.5°*^	0.05 ± 0.01°*^
LTiv	10	93.0 ± 2.2°*^	0.06 ± 0.02°*^	4 ± 2°^	13.0 ± 1.6°*^	0.07 ± 0.02°*^
LTor	10	90.6 ± 1.5°*^	0.04 ± 0.01°*^	2 ± 1°^	8.5 ± 2.0°*^	0.04 ± 0.01°*^

°$p < 0.01$ vs. baseline, *$p < 0.01$ vs. SO-S subgroup and ^$p < 0.01$ vs. H group.

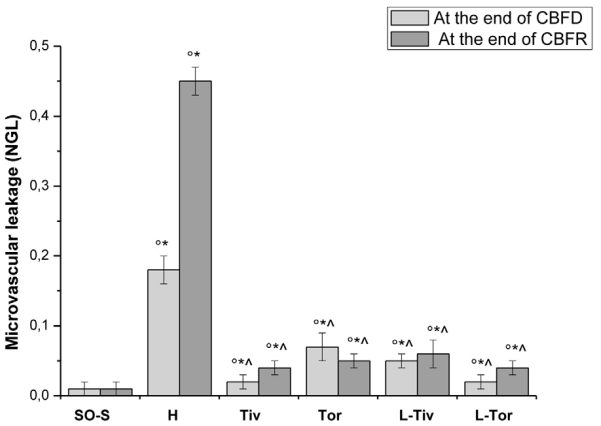


FIGURE 5 | Microvascular permeability increase quantified by NGLs after 30 min of CBFD and after 60 min of CBFR in the different experimental groups: SO-S, H, Tiv (10 mg/kg b.w. of Taurisolo® administered i.v. prior to CBFD and at the beginning of CBFR), Tor (20 mg/kg b.w. of Taurisolo® orally administered for 1 month and subjected to CBFD and CBFR), L-Tiv (L-NIO 10 mg/kg i.v. prior to i.v. Taurisolo®) and L-Tor (L-NIO 10 mg/kg i.v. prior to oral Taurisolo®) subgroups, treated before CBFD and at the beginning of CBFR. °$p < 0.01$ vs. baseline, *$p < 0.01$ vs. SO-S subgroup and ^$p < 0.01$ vs. H group.

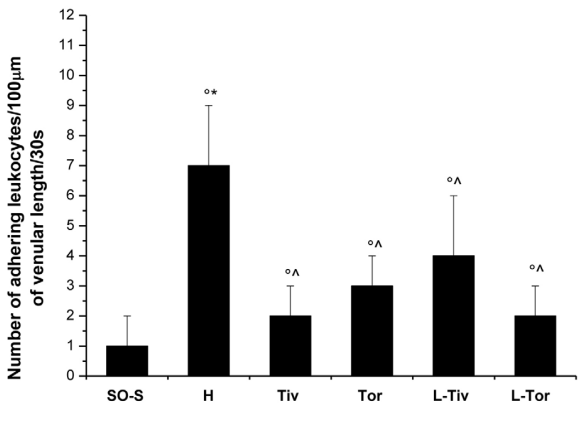


FIGURE 6 | Number of leukocytes adhered to venular walls after 60 min of CBFR in the different experimental groups: SO-S, H, Tiv (10 mg/kg b.w. of Taurisolo® administered i.v. prior to CBFD and at the beginning of CBFR), Tor (20 mg/kg b.w. of Taurisolo® orally administered for 1 month and subjected to CBFD and CBFR), L-Tiv (L-NIO 10 mg/kg i.v. prior to i.v. Taurisolo® i.v.) and L-Tor (L-NIO 10 mg/kg i.v. prior to oral Taurisolo®) subgroups, treated before CBFD and at the beginning of CBFR. °$p < 0.01$ vs. baseline, *$p < 0.01$ vs. SO-S subgroup and ^$p < 0.01$ vs. H group. Each entry = 45 venules.

(0.45 ± 0.02 NGL, $p < 0.01$ vs. baseline and vs. SO-S subgroup; **Figure 5**).

Taurisolo®, intravenously administered (Tiv subgroup), protected the pial microvasculature from damage induced by CBFD and CBFR. At the end of CBFD, fluorescent dextran leakage decreased when compared with H group (0.02 ± 0.01 NGL; $p < 0.01$ vs. H group; **Figure 5**). At the end of the CBFR, fluorescent dextran leakage was markedly reduced compared with the H group (0.04 ± 0.01 NGL, $p < 0.01$ vs. H group and SO-S subgroup; **Figure 5**).

The animals fed with Taurisolo® supplemented diet, 20 mg/kg b.w./die for 1 month (Tor subgroup), were markedly protected from microvascular damage induced by CBFD and CBFR. After CBFD, microvascular leakage was prevented compared to the H group (0.07 ± 0.02 NGL, $p < 0.01$ vs. baseline, SO-S subgroup and H group; **Figure 5**).

The animals treated with intravenous administration of L-NIO plus Taurisolo® (L-Tiv subgroup) and subjected to CBFD and CBFR did not show significant changes in fluorescent leakage compared with baseline conditions. L-NIO administration did not affect its protective effects on microvascular leakage that were observed also in the Tiv subgroup (**Table 3** and **Figure 5**).

The same pattern was observed in rats belonging to the L-Tor subgroup; in these animals, the intravenous administration of L-NIO 10 min prior to CBFR and at the beginning of CBFD was unable to abolish the prevention of fluorescent leakage due to the oral treatment of Taurisolo® both at the end of CBFD and at the end of CBFR.

An increase in leakage and arteriolar dilation have been indicated as key mechanisms related to leukocyte adhesion to vessel walls and to capillary perfusion. Therefore, we evaluated the number of leukocytes adhered to venular walls and the BFCL in the different experimental groups and subgroups. As reported in **Figure 6**, in SO-S animals there was no significant sticking of leukocytes to venular wall (1 ± 1/100 μm of v.l./30 s), while in H group there was a significant increase in the number of adhered leukocytes (7 ± 2/100 μm v.l./30 s; $p < 0.01$ vs. baseline and

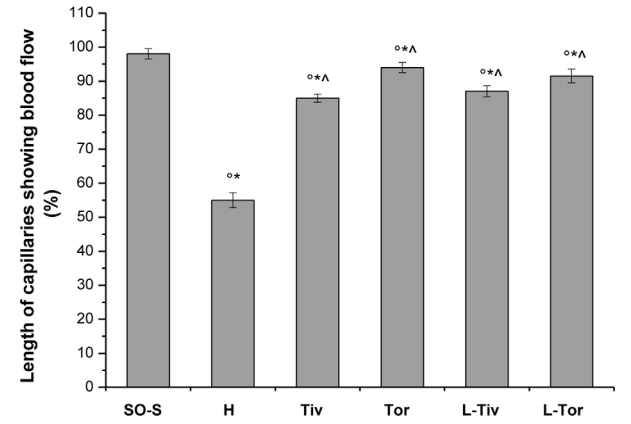


FIGURE 7 | Percent decrease in the length of perfused capillaries after 60 min of CBFR in the different experimental groups: SO-S, H, Tiv (10 mg/kg b.w. of Taurisolo® administered i.v. prior to CBFD and at the beginning of CBFR), Tor (20 mg/kg b.w. of Taurisolo® orally administered for 1 month and subjected to CBFD and CBFR), L-Tiv (L-NIO 10 mg/kg i.v. prior to i.v. Taurisolo® i.v.) and L-Tor (L-NIO 10 mg/kg i.v. prior to oral Taurisolo®) subgroups, treated before CBFD and at the beginning of CBFR. $^{\circ}p < 0.01$ vs. baseline, $^{*}p < 0.01$ vs. SO-S subgroup and $^{\wedge}p < 0.01$ vs. H group.

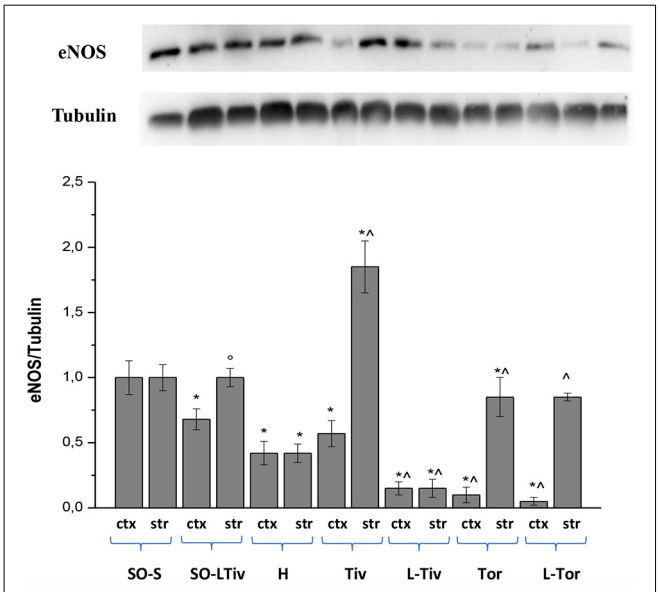


FIGURE 8 | Western blotting of endothelial nitric oxide synthase (eNOS) expression in two regions: cortex (ctx) and striatum (str), at the end of CBFR in SO-S, SO-LTiv, H, Tiv (10 mg/kg b.w. of Taurisolo® administered i.v. prior to CBFD and at the beginning of CBFR), Tor (20 mg/kg b.w. of Taurisolo® orally administered for 1 month and subjected to CBFD and CBFR), L-Tiv (L-NIO 10 mg/kg i.v. prior to i.v. Taurisolo®) and L-Tor (L-NIO 10 mg/kg i.v. prior to oral Taurisolo®) subgroups, treated before CBFD and at the beginning of CBFR. We compared all data, normalizing the results on SO-S values. $^{\circ}p < 0.05$ vs. H group; $^{*}p < 0.01$ vs. SO-S subgroup and $^{\wedge}p < 0.01$ vs. H group (same region). Each entry: nine evaluations.

SO-S subgroup). In Taurisolo®-treated animals by i.v. or oral administration, there were significant reductions in the number of adhered leukocytes ($2 \pm 1/100$ μm v.l./30 s, $p < 0.01$ vs. H group; $3 \pm 1/100$ μm v.l./30 s, $p < 0.01$ vs. H group, respectively). Administration of L-NIO prior to Taurisolo® was effective in partially reducing the protective effects of I.v. Taurisolo®, while the oral route was less affected by L-NIO. The perfusion of capillaries was quantified by computer-assisted methods. We evaluated the overall BFCL: in SO-S animals all capillaries were perfused, while BFCL was markedly reduced in H animals (by $45.0 \pm 2.2\%$, $p < 0.01$ vs. baseline and SO-S subgroup; **Figure 7**). In all Taurisolo®-treated animals the capillaries were perfused, with percent reduction from $15.0 \pm 1.2\%$ of baseline in Tiv animals ($p < 0.01$ vs. baseline, SO-S subgroup and H group) to $6.0 \pm 1.5\%$ of baseline in Tor rats ($p < 0.05$ vs. baseline, SO-S subgroup; $p < 0.01$ vs. H group). The administration of L-NIO did not decrease the perfusion of capillaries preserved by Taurisolo®.

Western Blotting

We tried to clarify the mechanism of arteriolar dilation induced by Taurisolo® and we utilized a specific inhibitor of eNOS, known to play a crucial role in arteriolar dilation. The responses we obtained with L-NIO encouraged us to assess eNOS expression in the cortex and striatum of our experimental animals by Western Blotting. Diminution and subsequent restoration of cerebral blood flow did significantly decrease eNOS expression both in cortex and striatum of H group animals, compared to that detected in SO-S animals, as reported in **Figure 8**, where we normalized all data on SO-S rat results (assigned 1 value). There was a marked increase in the striatum eNOS expression of Tiv subgroup animals compared to the striatum values in H animals ($p < 0.01$); this trend was observed also in the cortex where the increase was slight compared to cortex values in H group ($p < 0.05$). In Tor subgroups rats, there was a significant increase in eNOS expression in the striatum compared to that observed in H animals, while in the cortex there was a decrease in expression. However, in L-Tiv rat subgroup there was no increase in eNOS expression compared to H animals, during inhibition by L-NIO; in L-Tor subgroup animals there was an increase in eNOS expression in the striatum when compared to H animals, notwithstanding eNOS inhibition, while a decrease was observed in eNOS expression in the cortex. Administration of L-NIO plus Taurisolo® in sham-operated animals did not induce significant changes in the striatum eNOS expression, but a reduction in the cortex expression was observed when compared to SO-S data.

Metabolomic Profiles

To identify the mechanisms operative in the protection exerted by Taurisolo® on hypoperfusion and reperfusion-induced microvascular damage, metabolites were extracted from brains of rats belonging to H group, Tiv or Tor subgroups, SO-S and SO-Tiv or Tor subgroups, respectively. Upon extraction, the sample was profiled by MS analysis and compared (**Table 4**). Brains from the H group presented a significant increase in peroxidized cardiolipins, indicating an increase in peroxidation of mitochondrial lipids (Horvath and Daum, 2013).

The hypoperfusion and the subsequent reperfusion triggered, as well, the activity of cellular lipases. These, in turn, induced

TABLE 4 | Fold change[1] (over SO-S group) measured for the indicated metabolites in H, Tiv, Tor, SO-Tiv and SO-Tor group.

Metabolite	H	Tiv	Tor	SO-Tiv	SO-Tor
Cardiolipin CL (62:2)	$3.4 \pm 0.4^{***}$	$1.7 \pm 0.3^{*}$	$2.0 \pm 0.4^{*}$	$1.2 \pm 0.2^{n.s}$	$1.4 \pm 0.1^{*}$
PGD2	$12.1 \pm 0.4^{***}$	$2.2 \pm 0.3^{**}$	$3.2 \pm 0.2^{**}$	$0.7 \pm 0.3^{n.s}$	$0.5 \pm 0.2^{*}$
PGF2 α	$5.9 \pm 0.4^{***}$	$1.3 \pm 0.1^{n.s.}$	$2.3 \pm 0.2^{n.s.}$	$1.2 \pm 0.1^{n.s.}$	$1.0 \pm 0.1^{n.s.}$
6-keto-PGF1 α	$3.2 \pm 0.5^{***}$	$1.4 \pm 0.2^{n.s.}$	$1.6 \pm 0.3^{*}$	$1.2 \pm 0.1^{n.s.}$	$1.3 \pm 0.2^{n.s.}$
TxB2	$16.1 \pm 0.6^{***}$	$3.1 \pm 0.3^{***}$	$2.6 \pm 0.1^{***}$	$1.1 \pm 0.1^{n.s.}$	$1.2 \pm 0.2^{n.s.}$

*Metabolites were extracted from rat brains and analyzed by Mass Spectrometry (see "Materials and Methods" section). [1](n = 3. Shown is mean ± SEM) ***p < 0.001; **p < 0.01; *p < 0.05; n.s.: non statistically different from SO-S group.*

TABLE 5 | Fold change[1] (over SO-S group) measured for the indicated metabolites in H, Tiv, Tor, SO-Tiv and SO-Tor group.

Metabolite	H	Tiv	Tor	SO-Tiv	SO-Tor
L-Arginine	$1.1 \pm 0.1^{n.s}$	$0.8 \pm 0.1^{*}$	$0.7 \pm 0.1^{**}$	$1.9 \pm 0.2^{***}$	$1.8 \pm 0.1^{***}$
L-Citrulline	$1.3 \pm 0.1^{*}$	$2.8 \pm 0.1^{***}$	$3.2 \pm 0.3^{***}$	$0.9 \pm 0.2^{n.s}$	$0.7 \pm 0.2^{*}$
L-Ornithine	$1.1 \pm 0.3^{n.s.}$	$1.0 \pm 0.1^{n.s.}$	$1.0 \pm 0.2^{n.s.}$	$1.1 \pm 0.2^{n.s.}$	$1.0 \pm 0.1^{n.s.}$

*Metabolites were extracted from rat brains and analyzed by Mass Spectrometry (see "Materials and Methods" section). [1](n = 3. Shown is mean ± SEM) ***p < 0.001; **p < 0.01; *p < 0.05; n.s.: non statistically different from SO-S group.*

the release of free fatty acids, particularly arachidonic acid (AA), whose metabolites, in particular, COX products were investigated. Compared to SO-S animals, the H group showed significant increases in the pro-inflammatory prostaglandin PGF2 α, as well as in PGD2 and in 6-keto-PGFl α (a derivative of the prostacyclin PGI2; Tegtmeier et al., 1990; Bultel-Poncé et al., 2015). It is worth noting that thromboxane Txb2 levels were more than 10 times higher compared to the levels detected in SO-S animals.

Tiv and Tor subgroups presented lower levels of peroxidized cardiolipins, almost half levels compared to H group values. All prostaglandins were significantly reduced by Taurisolo® treatment, even though the response was different according to the properties of each prostaglandin. PGD2 values were more than 10 times higher in H animals compared to SO-S rats; the treatment with Taurisolo® decreased the PGD2 levels to 2–3 times higher than those observed in SO-S animals. PGF2 α values increased more than five times in H group rats, while in Taurisolo® treated animals the levels of this prostaglandin were not significantly different compared to those detected in SO-S animals. 6-keto-PGF1 α values increased more than three times in H rats compared to SO-S animals. Taurisolo®, i.v. administered, was effective in decreasing the levels of this prostaglandin to the values observed in SO-S animals, while the oral administration of Taurisolo® was able to halve the levels detected in H rats. The diminution in thromboxane Txb2 was marked: from 16 folds (on the average) to 3–2 folds after treatment compared to SO-S group. A decreased amount of prostaglandin PGD2 was detected also in SO-Tor subgroup, prior to hypoperfusion-induced damage, with the same trend observed in the SO-Tiv subgroup.

MS analysis of arginine and citrulline, two amino acids playing a fundamental role in the biosynthesis of nitric oxide, indicates that in H group animals, submitted to hypoperfusion and recovery of blood flow, the level of arginine did not change compared to SO-S group, while there was a modest increment in the levels of citrulline, indicating a slight increase in NO production. On the other hand, in animals treated with Taurisolo®, the levels of citrulline, highly increased, while decreasing the levels of arginine, demonstrated that there was a significant increase in NO release (**Table 5**). The levels of arginine in SO-S animals increased after Taurisolo® treatment, pointing toward Taurisolo® increasing intracellular arginine availability, useful for its conversion to citrulline and consequent NO release. Ornithine's levels, the third investigated amino acid, did not change among the different experimental groups, indicating substantial metabolic steady-state conditions in all animals.

DISCUSSION

The present data indicate that Taurisolo®, a nutraceutical endowed with antioxidant activity, was effective in decreasing the damage to the brain microcirculation, induced by reduction and successive recovery of cerebral blood flow. Taurisolo® administered to rats by intravenous infusion or by oral supplementation was effective in preventing the decrease in pial arteriolar diameter, the increase in microvascular permeability and adhesion of leukocytes, the reduction in capillary perfusion, when compared with the changes observed in ischemic animals (H group, submitted to bilateral occlusion of common carotid arteries). As detected by TTC staining of brain slice and survival of cerebral tissue, Taurisolo® limited the infarct size.

The venous administration caused a fast response with higher increase in vessel diameter, at the end of cerebral blood flow decrease, and marked rise by 35.0 ± 1.8% of baseline at reperfusion, compared with the results by oral supplementation: no change at the end of CBFD and arteriolar dilation by 12.0 ± 2.0% of baseline at the end of reperfusion. Moreover, with the administration of i.v., there was a slight reduction in capillary perfusion (by 15.0 ± 1.2% of baseline compared to that observed in H group: by 45.0 ± 2.2% of baseline). It is important to note that the oral supplementation better preserved capillary perfusion with a reduction by 6.0 ± 1.5% of baseline, significantly different compared with i.v. Taurisolo®-treated rats and H group animals. Both routes of administration did not

differ on the ROS overall formation, because the amounts of fluorescence were quite in the same range, with a prevalence in prevention for the oral administration (0.05 ± 0.01 vs. 0.08 ± 0.02, respectively).

All these effects could be related to the antioxidant properties of Taurisolo® able to decrease ROS formation, known to be a key factor in the mechanisms causing brain ischemia-reperfusion injury.

Usually, antioxidant molecules can have both protective as well as dangerous effects according to their dosages. However, we did not observe damage with higher dosages, because no one antioxidant was able to revert the prevention of increased leakage of macromolecules or decreased capillary perfusion. At least we did not observe any leakage with the highest dosages.

Moreover, it is worth noting that the dilation of arteriolar networks induced by Taurisolo® appears to be crucial in preventing the decrease in capillary perfusion. Western blotting data, indeed, demonstrate the increase in expression of eNOS in both cortex and striatum in i.v.-Taurisolo®-treated rats. Moreover, inhibition of eNOS by L-NIO blunted arteriolar dilation at the end of perfusion recovery in animals treated with Taurisolo®, but L-NIO did not reduce the levels of eNOS expression induced by Taurisolo® at least in the striatum of orally-treated animals.

Moreover, the present data confirm the microvascular changes in ischemic animals reported in previous studies, where the increase in ROS formation was one of the main factors in ischemia-reperfusion injury (Lapi et al., 2016).

The protective effects triggered by Taurisolo® were confirmed by the Mass-Spectrometry analysis of metabolomic data. As reported in **Tables 4**, **5**, cardiolipin oxidation, very high in H group animals, was reduced by Taurisolo® administered by the intravenous or oral route, with the former more active. In previous studies, cardiolipin has been shown to play a pivotal role in the mitochondrial damage due to ischemia, with the increase in ROS production. Our data support the previous observations (Haines and Dencher, 2002; Petrosillo et al., 2003; Chicco and Sparagna, 2007; Claypool, 2009; Camara et al., 2011; Hausenloy and Yellon, 2013; Zhou et al., 2018).

Furthermore, Taurisolo® effectively hampered the production of inflammation mediators such as all evaluated prostaglandins, especially PGD2. It is interesting to point out the dramatic reduction in thromboxane TxB2 values induced by Taurisolo®, able to decrease the release of this vasoconstrictor factor produced by endothelial cells, effective in inducing intraluminal blood coagulation. Moreover, the MS analysis of arginine and citrulline levels demonstrates that the increase in NO release during hypoperfusion and recovery of blood flow in H group animals was modest, as indicated by the corresponding values of arginine and citrulline (1.1 vs. 1.3 on the average, respectively). On the other hand, in Taurisolo®-treated animals the release of NO, taking into account the increase in citrulline levels and the decrease in arginine contents, was significantly higher compared to the values detected in H group animals. Consequently, these data indicate a very high release of NO-induced by Taurisolo® treatment. Moreover, it is worth noting that Taurisolo® in SO-S animals was able to increase the baseline levels of arginine, indicating that this could induce an increment in NO bioavailability and release. These effects on arginine and citrulline levels were accompanied by substantial metabolic steady-state conditions, represented by stable ornithine concentrations in all experimental group animals. Moreover, altogether these data suggest that Taurisolo® may explicate a general anti-inflammatory effect. It is interesting to observe that metabolomic data corresponded to Western Blotting results, indicating an increase in eNOS expression in Taurisolo® treated animals, observed mainly in i.v. injected animals compared with those orally administered. However, metabolomics data demonstrate that orally administered Taurisolo® was effective in inducing a very high formation of citrulline and consequently a very high release of NO. The discrepancy between metabolomic and Western Blotting results may be due to the different protocols for the two assays because more tissue was used for metabolomic data compared to Western Blotting technique, focused on cortical and striatal regions, where different vascular structures and amounts could be investigated.

The effects of Taurisolo® are likely the result of the synergistic activity of its components. Resveratrol and catechins have been extensively studied in the last decade revealing protective effects against ischemia-reperfusion injury in several organs in experimental models or in humans (Khurana et al., 2013; Menditto et al., 2015; Chen et al., 2016; Putignano et al., 2017; Koushki et al., 2018; Li et al., 2019). In our previous studies, we tried to assess the effects of quercetin, malvidin, cyanidin, catechin and other phenolic compounds in the same model of rat brain ischemia-reperfusion injury as in the present study. We observed that quercetin protects pial microvasculature against damage induce by hypoperfusion and reperfusion at the dosage of 5 and 10 mg/kg b.w. We used dosages of catechin and cyanidin in the same range as for quercetin and we found significant protection with all polyphenolic substances (Lapi et al., 2012a; Mastantuono et al., 2015, 2018). The amounts of polyphenols present in the pomace extract are smaller than those previously used (Lapi et al., 2012a, 2015; Mastantuono et al., 2015, 2018); however, the protection exerted by Taurisolo® was significant. Therefore, it is reasonable to suggest that the natural mixture of polyphenols, a component of the pomace extract, could potentiate the effects of each substance, facilitating protection of cerebral microcirculation during ischemia-reperfusion injury. In future experiments we will plan to assess the effects of gallic acid and syringic acid, two of the main components of Taurisolo®, on hypoperfusion and reperfusion injury in rat pial microcirculation.

In conclusion, Taurisolo® was effective in the preservation of vascular integrity and cellular functions, finally preventing brain damage due to cerebral hypoperfusion, one of the most important human pathological conditions in the World, the third cause of disability and death. Furthermore, the effects of Taurisolo®, orally-administered, suggest that Taurisolo® could be useful to prevent widespread oxidation in brain structure during aging-related changes in brain perfusion.

DATA AVAILABILITY STATEMENT

The datasets generated for this study are available on request to the corresponding author.

ETHICS STATEMENT

The animal study was reviewed and approved by the "Federico II" University Medical School of Naples, Ethical Committee (n° 2011/0059997, 24/05/2011).

AUTHOR CONTRIBUTIONS

DL, LS and MM performed the animal experiments and wrote the manuscript. MS, GT, MD and ES performed the mass spectrometry analysis. RS elaborated data. EN and AC revised and assisted on manuscript writing. DL, EN and AC wrote the manuscript. All authors contributed to the final version of the manuscript.

FUNDING

This study is part of the project "Nutraceutica come supporto nutrizionale nel paziente oncologico" (CUP: B83D18000140007).

ACKNOWLEDGMENTS

We acknowledge the assistance received from the staff of the Laboratory of Molecular Biology of Department of Pharmacy of the University Federico II of Naples.

REFERENCES

Aneja, R., Hake, P. W., Burroughs, T. J., Denenberg, A. G., Wong, H. R., and Zingarelli, B. (2004). Epigallocatechin, a green tea polyphenol, attenuates myocardial ischemia reperfusion injury in rats. *Mol. Med.* 10, 55–62. doi: 10.2119/2004-00032.aneja

Bederson, J. B., Pitts, L. H., Germano, S. M., Nishimura, M. C., Davis, R. L., and Bartkowski, H. M. (1986). Evaluation of 2,3,5-triphenyltetrazolium chloride as a stain for detection and quantification of experimental cerebral infarction in rats. *Stroke* 17, 1304–1308. doi: 10.1161/01.str.17.6.1304

Brosková, Z., Drábiková, K., Sotníková, R., Fialová, S., and Knezl, V. (2013). Effect of plant polyphenols on ischemia-reperfusion injury of the isolated rat heart and vessels. *Phyther. Res.* 27, 1018–1022. doi: 10.1002/ptr.4825

Bultel-Poncé, V., Durand, T., Guy, A., Oger, C., and Galano, J.-M. (2015). Non enzymatic metabolites of polyunsaturated fatty acids: friend or foe. *Pak. J. Pharm. Sci.* 23:D118. doi: 10.1051/ocl/2015055

Camara, A. K. S., Bienengraeber, M., and Stowe, D. F. (2011). Mitochondrial approaches to protect against cardiac ischemia and reperfusion injury. *Front. Physiol.* 2:13. doi: 10.3389/fphys.2011.00013

Chen, X. Q., Hu, T., Han, Y., Huang, W., Yuan, H. B., Zhang, Y. T., et al. (2016). Preventive effects of catechins on cardiovascular disease. *Molecules* 21:E1759. doi: 10.3390/molecules21121759

Chicco, A. J., and Sparagna, G. C. (2007). Role of cardiolipin alterations in mitochondrial dysfunction and disease. *Am. J. Phisiol. Cell Physiol.* 292, C33–C44. doi: 10.1152/ajpcell.00243.2006

Claypool, S. M. (2009). Cardiolipin, a critical determinant of mitochondrial carrier protein assembly and function. *Biochim. Biophys. Acta* 1788, 2059–2068. doi: 10.1016/j.bbamem.2009.04.020

Eltzschig, H. K., and Eckle, T. (2011). Ischemia and reperfusion—from mechanism to translation. *Nat. Med.* 17, 1391–1401. doi: 10.1038/nm.2507

Haines, T. H., and Dencher, N. A. (2002). Cardiolipin: a proton trap for oxidative phosphorylation. *FEBS Lett.* 528, 35–39. doi: 10.1016/s0014-5793(02)03292-1

Hausenloy, D. J., and Yellon, D. M. (2013). Myocardial ischemia-reperfusion injury: a neglected therapeutic target. *J. Clin. Invest.* 123, 92–100. doi: 10.1172/JCI62874

Horvath, S. E., and Daum, G. (2013). Progress in lipid research lipids of mitochondria. *Prog. Lipid Res.* 52, 590–614. doi: 10.1016/j.plipres.2013.07.002

Houtkooper, R. H., and Vaz, F. M. (2008). Cardiolipin, the heartof mitochondrial metabolism. *Cell. Mol. Life Sci.* 65, 2493–2506. doi: 10.1007/s00018-008-8030-5

Khurana, S., Venkataraman, K., Hollingsworth, A., Piche, M., and Tai, T. C. (2013). Polyphenols: benefits to the cardiovascular system in health and in aging. *Nutrients* 5, 3779–37827. doi: 10.3390/nu5103779

Koushki, M., Amiri-Dashatan, N., Ahmadi, N., Abbaszadeh, H. A., and Rezaei-Tavirani, M. (2018). Resveratrol: a miraculous natural compound for diseases treatment. *Food Sci. Nutr.* 26, 2473–2490. doi: 10.1002/fsn3.855

Lapi, D., Chiurazzi, M., Di Maro, M., Mastantuono, T., Battiloro, L., Sabatino, L., et al. (2016). Malvidin's effects on rat pial microvascular permeability changes due to hypoperfusion and reperfusion injury. *Front. Cell. Neurosci.* 10:153. doi: 10.3389/fncel.2016.00153

Lapi, D., Di Maro, M., Mastantuono, T., Battiloro, L., Sabatino, L., Muscariello, E., et al. (2015). Effects of oleuropein and pinoresinol on microvascular damage induced by hypoperfusion and reperfusion in rat pial circulation. *Microcirculation* 22, 79–90. doi: 10.1111/micc.12175

Lapi, D., Marchiafava, P. L., and Colantuoni, A. (2008). Geometric characteristics of arterial network of rat pial microcirculation. *J. Vasc. Res.* 45, 69–77. doi: 10.1159/000109078

Lapi, D., Mastantuono, T., Sapio, D., Paterni, M., and Colantuoni, A. (2013). Pial microvascular responses induced by transient bilateral common carotid artery occlusion in Zucker rats. *Clin. Hemorheol. Microcirc.* 54, 415–429. doi: 10.3233/ch-131763

Lapi, D., Vagnani, S., Cardaci, E., Paterni, M., and Colantuoni, A. (2011). Rat pial microvascular responses to melatonin during bilateral common carotid artery occlusion and reperfusion. *J. Pineal Res.* 51, 136–144. doi: 10.1111/j.1600-079x.2011.00870.x

Lapi, D., Vagnani, S., Pignataro, G., Esposito, E., Paterni, M., and Colantuoni, A. (2012a). Protective effects of quercetin on rat pial microvascular changes during transient bilateral common carotid artery occlusion and reperfusion. *Front. Physiol.* 3:32. doi: 10.3389/fphys.2012.00032

Lapi, D., Vagnani, S., Pignataro, G., Esposito, E., Paterni, M., and Colantuoni, A. (2012b). Rat pial microvascular responses to transient bilateral common carotid artery occlusion and reperfusion: quercetin's mechanism of action. *Front. Physiol.* 3:99. doi: 10.3389/fphys.2012.00099

Li, H., Xia, N., Hasselwander, S., and Daiber, A. (2019). Resveratrol and vascular function. *Int. J. Mol. Sci.* 20:E2155. doi: 10.3390/ijms20092155

Mastantuono, T., Battiloro, L., Sabatino, L., Chiurazzi, M., Di Maro, M., Muscariello, E., et al. (2015). Effects of citrus flavonoids against microvascular damage induced by hypoperfusion and reperfusion in rat pial circulation. *Microcirculation* 22, 378–390. doi: 10.1111/micc.12207

Mastantuono, T., Di Maro, M., Chiurazzi, M., Battiloro, L., Muscariello, E., Nasti, G., et al. (2018). Rat pial microvascular changes during cerebral blood flow decrease and recovery: effects of cyanidin administration. *Front. Physiol.* 9:540. doi: 10.3389/fphys.2018.00540

Menditto, E., Guerriero, F., Orlando, V., Crola, C., Di Somma, C., Illario, M., et al. (2015). Self-assessment of adherence to medication: a case study in campania region community-dwelling population. *J. Aging Res.* 2015:682503. doi: 10.1155/2015/682503

Paradies, G., Paradies, V., De Benedictis, V., Ruggiero, F. M., and Petrosillo, G. (2014). Functional role of cardiolipin in mitochondrial bioenergetics. *Biochim. Biophys. Acta* 1837, 408–417. doi: 10.1016/j.bbabio.2013.10.006

Paradies, G., Paradies, V., Ruggiero, F. M., and Petrosillo, G. (2013). Changes in the mitochondrial permeability transition pore in aging and age-associated diseases. *Mech. Ageing Dev.* 134, 1–9. doi: 10.1016/j.mad.2012.12.006

Paradies, G., Petrosillo, G., Paradies, V., and Ruggiero, F. M. (2009). Role of cardiolipin peroxidation and Ca^{++} in mitochondrial disfunction and disease. *Cell Calcium* 45, 643–650. doi: 10.1016/j.ceca.2009.03.012

Petrosillo, G., Ruggiero, F. M., and Paradies, G. (2003). Role of reactive oxygen species and cardiolipin in the release of cytochrome c from mitochondria. *FASEB J.* 17, 2202–2208. doi: 10.1096/fj.03-0012com

Putignano, D., Bruzzese, D., Orlando, V., Fiorentino, D., Tettamanti, A., and Menditto, E. (2017). Differences in drug use between men and women: an Italian cross sectional study. *BMC Womens Health* 17:73. doi: 10.1186/s12905-017-0424-9

Ser, Z., Liu, X., Tang, N. N., and Locasale, J. W. (2015). Extraction parameters for metabolomics from cultured cells. *Anal. Biochem.* 475, 22–28. doi: 10.1016/j.ab.2015.01.003

Sommella, E., Badolati, N., Riccio, G., Salviati, E., Bottone, S., Dentice, M., et al. (2019). A boost in mitochondrial activity underpins the cholesterol-lowering effect of annurca apple polyphenols on hepatic cells. *Nutrients* 11:E163. doi: 10.3390/nu11010163

Tegtmeier, F., Weber, C., Heister, U., Haker, I., Scheller, D., Nikolov, R., et al. (1990). Eicosanoids in rat brain during ischemia and reperfusion—correlation to DC depolarization. *J. Cereb. Blood Flow Metab.* 10, 358–364. doi: 10.1038/jcbfm.1990.65

Wang, H., and Joseph, J. A. (1999). Quantifying cellular oxidative stress by dichlorofluorescein assay using microplate reader. *Free Radic. Biol. Med.* 27, 612–616. doi: 10.1016/s0891-5849(99)00107-0

Watanabe, S. (1998). *In vivo* fluorometric measurement of cerebral oxidative stress using 2′-7′-dichlorofluorescein (DCF). *Keio J. Med.* 47, 92–98. doi: 10.2302/kjm.47.92

Zhou, T., Prather, E. R., Garrison, D. E., and Zuo, L. (2018). Interplay between ROS and antioxidants during ischemia-reperfusion injuries in cardiac and skeletal muscle. *Int. J. Mol. Sci.* 19:E417. doi: 10.3390/ijms19020417

Zorov, D. B., Juhaszova, M., and Sollott, S. J. (2014). Mitochondrial reactive oxygen species (ROS) and ROS-induced ROS release. *Physiol. Rev.* 94, 909–950. doi: 10.1152/physrev.00026.2013

Conflict of Interest: The authors declare that the research was conducted in the absence of any commercial or financial relationships that could be construed as a potential conflict of interest.

Copyright © 2020 Lapi, Stornaiuolo, Sabatino, Sommella, Tenore, Daglia, Scuri, Di Maro, Colantuoni and Novellino. This is an open-access article distributed under the terms of the Creative Commons Attribution License (CC BY). The use, distribution or reproduction in other forums is permitted, provided the original author(s) and the copyright owner(s) are credited and that the original publication in this journal is cited, in accordance with accepted academic practice. No use, distribution or reproduction is permitted which does not comply with these terms.

frontiers in Cellular Neuroscience

ORIGINAL RESEARCH
published: 30 January 2020
doi: 10.3389/fncel.2019.00585

Treatment With Liraglutide Exerts Neuroprotection After Hypoxic–Ischemic Brain Injury in Neonatal Rats *via* the PI3K/AKT/GSK3β Pathway

*Shan-shan Zeng†, Jun-jie Bai†, Huai Jiang, Jin-jin Zhu, Chang-chang Fu, Min-zhi He, Jiang-hu Zhu, Shang-qin Chen, Pei-jun Li, Xiao-qin Fu and Zhen-lang Lin**

Department of Neonatology, The Second Affiliated Hospital and Yuying Children's Hospital, Wenzhou Medical University, Wenzhou, China

OPEN ACCESS

Edited by:
Chao Deng,
University of Wollongong, Australia

Reviewed by:
Thorsten Roland Doeppner,
University Medical Center Göttingen, Germany
Mengliang Zhou,
Jinling Hospital, China

***Correspondence:**
Zhen-lang Lin
linzhenlang@hotmail.com

†These authors have contributed equally to this work and share first authorship

Received: *03 September 2019*
Accepted: *23 December 2019*
Published: *30 January 2020*

Citation:
Zeng S-s, Bai J-j, Jiang H, Zhu J-j, Fu C-c, He M-z, Zhu J-h, Chen S-q, Li P-j, Fu X-q and Lin Z-l (2020) Treatment With Liraglutide Exerts Neuroprotection After Hypoxic–Ischemic Brain Injury in Neonatal Rats via the PI3K/AKT/GSK3β Pathway. Front. Cell. Neurosci. 13:585. doi: 10.3389/fncel.2019.00585

Neonatal hypoxic–ischemic (HI) brain injury is a detrimental disease, which results in high mortality and long-term neurological deficits. Nevertheless, the treatment options for this disease are limited. Thus, the aim of the present study was to assess the role of liraglutide in neonatal HI brain injury in rats and investigate the associated mechanisms. The results showed that treatment with liraglutide significantly reduced infarct volume and ameliorated cerebral edema, decreased inflammatory response, promoted the recovery of tissue structure, and improved prognosis following HI brain injury. Moreover, treatment with liraglutide inhibited apoptosis and promoted neuronal survival both in the rat model and following oxygen-glucose deprivation (OGD) insult. LY294002, an inhibitor of phosphoinositide 3-kinase (PI3K), partially reversed these therapeutic effects, suggesting that the PI3K/protein kinase B (Akt) pathway was involved. In conclusion, our data revealed that treatment with liraglutide exerts neuroprotection after neonatal HI brain injury *via* the PI3K/Akt/glycogen synthase kinase-3β (GSK3β) pathway and may be a promising therapy for this disease.

Keywords: neonatal hypoxic–ischemic brain injury, liraglutide, neuroprotection, apoptosis, PI3K/AKT/GSK3β

INTRODUCTION

Despite the advancements in medical technology and nursing, hypoxic–ischemic (HI) brain injury in newborns is associated with a high disability rate and mortality. Its incidence is approximately 1–8 and 26 cases per 1,000 live births in developed and developing countries, respectively (Douglas-Escobar and Weiss, 2015). Furthermore, surviving infants suffer from various degrees of neurological deficits (e.g., epilepsy, learning difficulties, cerebral palsy, and mental retardation), which require long-term or even lifelong recovery (Al-Macki et al., 2009). The physical and mental pain, as well as the high cost of HI encephalopathy, has been

a constant source of stress for the families of patients with HI brain injury. Hypothermia, as a standard treatment, plays an important role in reducing the rates of mortality and disability, to some extent; however, it has a narrow therapeutic window of 6 h (Chiang et al., 2017). Therefore, the development of more effective and safer treatment strategies is warranted.

Previous studies have indicated that inflammation plays a crucial role in the deterioration and process of brain damage induced by HI injury in newborns. Once hypoxia–ischemia occurs in the neonatal brains, the development of inflammation will be promptly triggered (Hagberg et al., 2015; Solevåg et al., 2019). Immune cells, cytokines, oxidative stress, and chemokines are the main components of inflammatory processes. In addition, apoptosis, especially in neonatal brain damage after hypoxia–ischemia, is essential in various diseases of the central nervous system (Northington et al., 2011). Substantial studies confirmed that apoptosis causes delayed death of developing brain cells, leading to massive cell loss and neurodegeneration (Northington et al., 2005; Rocha-Ferreira and Hristova, 2016). Thus, lessening apoptosis serves as a useful therapeutic target following hypoxia–ischemia.

Liraglutide, a long-acting glucagon-like peptide-1 (GLP-1) analogue, has been widely used in the clinical treatment of type 2 diabetes owing to its efficacy and safety (Scott, 2014). GLP-1 is a visceral-derived insulin-stimulating hormone, which is secreted into the bloodstream and bound to the GLP-1 receptor (GLP-1R; Vilsboll, 2009). Additionally, GLP-1R plays a role in blood glucose homeostasis and is extensively expressed in the central nervous system, including neurons, cell bodies, and dendrites in the brain (Hamilton and Hölscher, 2009; Cork et al., 2015). Compared with other GLP-1 analogues, liraglutide has a 13-h half-life, binding to serum albumin to avoid the proteolytic degradation of dipeptide peptide-4. Moreover, liraglutide has been shown to cross the blood–brain barrier (Hunter and Hölscher, 2012). Numerous studies have suggested that liraglutide exerts neuroprotective effects against injury and diseases of the nervous system, such as Alzheimer's disease (McClean et al., 2011; McClean and Hölscher, 2014), Parkinson's disease (Aviles-Olmos et al., 2014; Badawi et al., 2017), acute ischemic stroke (Yang et al., 2016; Dong et al., 2017), and traumatic brain injury (DellaValle et al., 2014; Hakon et al., 2015). A recently published study indicated that liraglutide could alleviate chronic inflammation and mitochondrial stress induced by status epilepticus (Wang et al., 2018). Thus, far, the specific mechanism through which liraglutide exerts its effects on neonatal HI brain injury remains uncertain.

The phosphoinositide 3-kinase (PI3K)/protein kinase B (Akt) signaling pathway participates in a diversity of physiological and pathogenetic processes, such as cell apoptosis, proliferation, and differentiation. Some research studies have demonstrated that this signaling pathway protects neurons from apoptosis in different brain diseases (Ye et al., 2019). Glycogen synthase kinase-3β (GSK3β), one of the downstream targets of activated Akt, has been closely associated with energy metabolism, body shape development, and nerve cell development. Activation of GSK3β further exacerbates cell damage by increasing the activity of caspase 3 cleavage, which is an early step in apoptosis (King et al., 2001). Moreover, a recent study showed that the PI3K/Akt/GSK3β signaling pathway plays a vital role in neuroprotection after intracerebral hemorrhage (Chen et al., 2019b).

In this study, we examined the neuroprotective role of liraglutide in neonatal brain damage induced by HI injury, and we determined whether the PI3K/Akt/GSK3β signaling pathway is involved in this process.

MATERIALS AND METHODS

Animals and Ethical Permission

All animal experimental procedures and care were performed according to the National Institutes of Health Guide for the Care and Use of Laboratory Animals and approved by the Animal Care and Use Committee of Wenzhou Medical University (ethic number: wydw2014-0058). Sprague–Dawley rats (weight: 200–250 g) were provided by the Animal Center of the Chinese Academy of Science (Shanghai, China). Adult rats were freely crossbred to deliver offspring for the follow-up studies. They were housed in an individual environment under specific pathogen-free conditions and a 12-h light/dark cycle at 23 ± 2°C and 60 ± 10% humidity, with *ad libitum* access to standard food and fresh water.

Neonatal Hypoxic–Ischemic Brain Injury Model and Administration of Drug

The neonatal HI brain injury model was generated on postnatal day 7 (P 7) using male rat pups, as described by Vannucci and Vannucci (2005). In brief, the 7-days-old pups were fully anesthetized with 3% isoflurane and sustained with 1% isoflurane. Subsequently, they underwent left common carotid artery ligation in 5 min and recovered for 2 h in their dam after surgery. Following sufficient rest, the pups were placed in a chamber for 2.5 h, in an environment of a humidified gas mixture (8% oxygen and 92% nitrogen) at a flow rate of 3 L/min. A water bath of 37.5°C was placed underneath the chamber to maintain a constant temperature. Pups in the sham group were not subjected to ligation of the common carotid arteries or hypoxic conditions.

Clinical-grade liraglutide was purchased from Novo Nordisk (Princeton, NJ, USA) and dissolved in sterile 0.9% normal saline. The liraglutide-treated HI group received different doses of liraglutide (i.e., 100, 200, or 400 μg/kg) immediately after hypoxia through intraperitoneal injection at 24-h intervals until the animals were euthanized, to determine the most effective dose. Meanwhile, the pups in the vehicle-treated HI group received an equal volume of sterile 0.9% normal saline. The PI3K inhibitor LY294002 (Selleck, Shanghai, China) was dissolved in 1% dimethyl sulfoxide to further evaluate whether liraglutide activated the PI3K/Akt/GSK3β pathway. Five microliters of LY294002 (50 nmol/kg; Ye et al., 2019) was administered *via* intracerebroventricular injection 30 min prior to HI using a stereotaxic apparatus (RWD, Shenzhen, China). LY294002 was injected into the lateral ventricle (2 mm rostral, 1.5 mm outside the bregma, and 2.5 mm below the skull; Zhou et al., 2017) at a speed of 1 μl/min. After injection, the needle remained in place

for another 10 min and was subsequently extracted at a rate of 1 mm/min.

Infarct Volume Measurement

Staining with 2,3,5-triphenyltetrazolium chloride (TTC) was used as previously described (Tian et al., 2013) to measure the infarct volume relieved by the administration of drug. After HI injury (24 h), pups from each group were anesthetized and perfused with 0.9% cold normal saline. The brains were immediately stored at −80°C for 6 min and sectioned into coronal slices (thickness: 2 mm). Subsequently, the brain slices were immersed in a 1% TTC (Sigma–Aldrich, St. Louis, MO USA) solution in the dark for 20 min at 37°C and fixed in 4% paraformaldehyde (PFA) overnight. Brain infarct volumes were calculated using the ImageJ software (National Institutes of Health, Bethesda, MD, USA).

Water Content in the Brain

The 7-days-old rats under deep anesthesia were sacrificed 24 h after HI injury for brain analyses. The brains from each group were rapidly removed, and the hemispheres were separated into the ipsilateral and contralateral. The injured hemispheres were weighted to measure wet weight (accuracy to 0.1 mg). Subsequently, each hemisphere was placed in an oven (100°C) for 72 h to calculate the dry weight (accuracy to 0.1 mg) as previously described (Zhang et al., 2016). The degree of brain edema was calculated according to the wet/dry method: percent brain water = [(wet weight − dry weight)/wet weight] × 100%.

Quantitative Real-Time Reverse Transcription–Polymerase Chain Reaction

Total RNA was extracted from the samples using the TriPure Isolation Reagent (Roche, South San Francisco, CA, USA) according to the instructions provided by the manufacturer. NanoDrop spectrometry (Thermo Fisher Scientific, Waltham, MA, USA) was used to quantify the concentration of total RNA; only samples with an optical density 260/280 ratio >1.8 were selected. RNA (0.5 μg) was used to synthesize the cDNA utilizing the PrimeScript™ RT Reagent Kit (TaKaRa, Kusatsu, Japan) and Bio-Rad MyCycler™ thermal cycler for the reverse transcription–polymerase chain reaction. With the use of the SYBR Green PCR Master Mix (Bio-Rad, Hercules, CA, USA), samples were amplified by the real-time polymerase chain reaction system. β-Actin was used for standardization. The forward and reverse primer sequences are shown in **Table 1**. Subsequently, we calculated the fluorescence threshold value (cycle threshold value) *via* the SDS Enterprise Database software. The cycle threshold values of the correlative genes were normalized to those of β-actin in the same sample. Next, the levels of gene expression (fold change) in the vehicle- and liraglutide-treated groups were measured and compared with those reported in the sham group.

Histological Staining

After HI injury (24 h or 7 days), the rats were anesthetized and subjected to cardiac perfusion with 20 ml of normal saline. Subsequently, they were perfused with 4% PFA for better fixation. The brains of the rats were fixed in 4% PFA for 12 h at 4°C. Next, brains were embedded in paraffin and sectioned into 5-μm slices along the coronal plane for subsequent staining after dehydration with graded ethanol and xylene. Hematoxylin and eosin (H&E) staining and Nissl staining were used based on the protocol provided by the manufacturer to assess histopathological changes. Meanwhile, different organs (e.g., the heart, liver, lungs, pancreas, and kidneys) were stained with H&E for the histopathological assessment of side effects following the previous steps. The bright-field images were captured with a light microscope (Olympus IX73, Tokyo, Japan). Nissl-stained brain sections were analyzed through the ImageJ software to quantify the damage caused to neurons.

TABLE 1 | Primers used in the studies.

Gene	Forward primers	Reverse primers
TNF-α	TACTCCCAGGTTCTCTTCAAGG	GGAGGCTGACTTTCTCCTGGTA
IL-18	AAACCCGCCTGTGTTCGA	TCAGTCTGGTCTGGGATTCGT
IL-1β	CACCTCTCAAGCAGAGCACAG	GGGTTCCATGGTGAAGTCAAC
IL-6	GAGTTGTGCAATGGCAATTC	ACTCCAGAAGACCAGAGCAG
Inos	AGGCCACCTCGGATATCTCT	GCTTGTCTCTGGGTCCTCTG
β-Actin	AAGTCCCTCACCCTCCCAAAAG	AAGCAATGCTGTCACCTTCCC

Note: TNF-α, tumor necrosis factor-alpha; IL, interleukin; iNOS, inducible nitric oxide synthase.

Immunofluorescence and Immunohistochemistry

Coronal 5-μm sections were selected for immunofluorescence (7 days after HI injury) and immunohistochemical (24 h after HI injury) analyses. After deparaffinization and rehydration, sections were boiled in citrate buffer for 20 min for antigen retrieval. The slices were incubated in 3% hydrogen peroxide for 15 min to block the endogenous peroxidase activity. Subsequently, they were blocked with 5% bovine serum albumin in 10 mM of phosphate-buffered saline (PBS) for 30 min at 37°C. For the immunofluorescence analysis, the sections were incubated with primary antibodies targeting the following protein: tumor necrosis factor-alpha (TNF-α; 1:200, AF7014; Affinity Biosciences, Cincinnati, OH, USA). The sections were washed thrice with PBS and treated with the Alexa Fluor 488 goat anti-rabbit secondary antibody (1:1,000, Abcam, Cambridge, UK) for 1 h at 37°C in a dark humidified chamber. The primary antibodies were diluted in 10 mM of PBS containing 1% bovine serum albumin and 0.2% Triton X-100. After being washed thrice with PBS, the sections were treated with the goat anti-rabbit IgG (H + L) DyLight 405 sary antibody (1:200, BS10012; Bioworld) for 1 h at 37°C in a dark humidified chamber. The sections were washed thrice with PBS Tween 20, and the nuclei were labeled with 4′,6-diamidino-2-phenylindole for 7 min. All images were captured using a fluorescence microscope (Olympus, Tokyo, Japan). For the immunohistochemical analysis, the sections were incubated with antibodies against microtubule-associated protein 2 (MAP-2; 1:200, sc-20172; Santa Cruz Biotechnology, Dallas, TX, USA), myelin basic protein (MBP; 1:200, sc-13914; Santa Cruz Biotechnology, Dallas, TX, USA), and phospho-GSK3 beta (Ser9; p-GSK3β; 1:200, AF2016; Affinity Biosciences, Cincinnati, OH, USA) at 4°C overnight. After being washed thrice with PBS, the sections were treated with donkey anti-goat

secondary antibody (1:1,000, sc-2020; Santa Cruz Biotechnology, Dallas, TX, USA) for 2 h at 37°C. Subsequently, the reaction was colored with 3,3′-diaminobenzidine. The images were captured using a light microscope (Olympus, Tokyo, Japan).

Cell Culture and Drug Treatment

PC12 cells were purchased from the Type Culture Collection of the Chinese Academy of Sciences (Shanghai, China). They were cultured in Dulbecco's modified Eagle's medium (DMEM; Gibco, Grand Island, NY, USA) supplemented with 10% fetal bovine serum (Gibco, Grand Island, NY, USA), 100 U/ml of streptomycin, and 100 U/ml of penicillin in an environment of 5% carbon dioxide at 37°C. After attachment, the cells were treated with 50 ng/ml of nerve growth factor (NGF; Promega, Madison, WI, USA) and cultured in serum-free DMEM for 6 days to induce neurite formation. Subsequently, cells were subjected to an *in vitro* oxygen-glucose deprivation (OGD) insult for 8 h with a mixed gas consisting of 95% nitrogen and 5% carbon dioxide. Meanwhile, the culture medium was replaced with glucose-free DMEM. LY294002 (10 μM) was used for 30 min before other treatment. After the OGD, the culture medium was replaced with original medium, and liraglutide was added. The plates were continually cultured in a normoxic incubator for reoxygenation in an atmosphere of 5% carbon dioxide at 37°C for 24 h. The cells of the control group were cultured under normal conditions without oxygen or glucose deprivation.

Cell Counting Kit-8 Assay

Cell Counting Kit-8 (CCK8; C0038; Beyotime, Shanghai, China) assays were used to evaluate cell viability, assess whether liraglutide could alleviate OGD-induced cell death, and determine the optimal concentration. PC12 cells were plated in 96-well plates at a density of 2×10^4 cells/well. Different doses of liraglutide (0, 10, 100, and 1,000 nM) were added after OGD. Next, 10 μl of CCK-8 solution per well was added after reoxygenation, and the optical density was measured using a microplate reader (Tecan Group Limited, Männedorf, Switzerland) at 490 nm.

Terminal Deoxynucleotidyl Transferase dUTP Nick End Labeling Staining

The *in situ* Cell Death Detection Kit (Roche, South San Francisco, CA, USA) was used to detect apoptotic DNA fragmentation. *In vivo*, terminal deoxynucleotidyl transferase dUTP nick end labeling (TUNEL) staining was performed 24 h after HI injury. The brain sections (thickness: 5 μm) obtained 24 h after HI injury were deparaffinized and rehydrated. Subsequently, they were incubated with 20 μg/ml of proteinase K working solution (ST533; Beyotime, Shanghai, China) for 20 min at 37°C. After OGD injury for 24 h, PC12 cells were cultured in six-well plates with 4% PFA *in vitro* for 1 h, and 0.1% Triton X-100 was incubated in 0.1% sodium citrate for 2 min on ice. After being washed thrice with PBS, the sections and cells were incubated with a TUNEL reaction mixture in a dark humidified chamber for 1 h at 37°C. The negative group was treated by omitting the terminal deoxynucleotidyl transferase enzyme. The sections were washed thrice with PBS, followed by incubation with 4′,6-diamidino-2-phenylindole for 7 min at room temperature. All apoptotic changes were detected using a fluorescence microscope (Olympus, Tokyo, Japan). The apoptotic cells were characterized by green fluorescence, and 4′,6-diamidino-2-phenylindole labeled the nuclei with blue color, according to the instructions provided by the manufacturer. The ratio of the number of apoptotic cells to the total number of cells represented the apoptosis index, which was analyzed using the ImageJ software.

Western Blotting

Rats were decapitated under deep anesthesia 24 h and 7 days after HI injury, and brain tissue was immediately stored at −80°C until analysis. The brain tissue was homogenized with radioimmunoprecipitation assay buffer (P0013B; Beyotime) and further centrifuged at 12,000 rpm for 30 min at 4°C. The extraction was initially quantified with bicinchoninic acid reagents (P0012S; Beyotime). Subsequently, the protein concentrations were quantified using bicinchoninic acid reagents. Equivalent amounts of protein (50 μg) were loaded and separated through 6% or 10% sodium dodecyl sulfate–polyacrylamide gel electrophoresis and transferred onto polyvinylidene difluoride membranes (Bio-Rad, Hercules, CA, USA). After being blocked for 2 h at room temperature, the membranes were incubated with the primary antibodies overnight at 4°C. The primary antibodies used included B-cell lymphoma-2 (Bcl-2; 1:1,000, #2876; Cell Signaling Technology), cleaved caspase 3 (1:1,000, 9664S; Cell Signalling Technology, Danvers, MA, USA), TNF-α (1:1,000, AF7014; Affinity Biosciences, Cincinnati, OH, USA), MAP-2 (1:1,000, #4542S; Cell Signalling Technology, Danvers, MA, USA), MBP (1:1,000, ab40390; Abcam, Cambridge, UK), Akt (1:1,000, #9272; Cell Signalling Technology, Danvers, MA, USA), phospho-Akt (Ser473; 1:1,000, #9271; Cell Signalling Technology, Danvers, MA, USA), GSK3β (1:1,000, #9315; Cell Signalling Technology, Danvers, MA, USA), phospho-GSK3β (ser9; 1:1,000, #5558; Cell Signalling Technology, Danvers, MA, USA), and β-actin (1:5,000, 66009–1-Ig; Proteintech). After being washed thrice in tris-buffered saline and Tween 20, the membranes were incubated with the appropriate secondary antibodies, namely, goat anti-rabbit IgG (1:2,000, #7074, Cell Signalling Technology, Danvers, MA, USA) or goat anti-mouse IgG (1:2,000, #7076; Cell Signalling Technology, Danvers, MA, USA) for 1 h at room temperature. The signals were detected using a ChemiDoc XRS + Imaging System (Bio-Rad, Hercules, CA, USA). All experiments were repeated at least in triplicate, and the gray values of the bands were analyzed using the Image Lab 5.0 software (Bio-Rad, Hercules, CA, USA).

Longa Assessment

Three weeks post HI injury, neurobehavioral tests were performed to evaluate the injury or improvement of nerve function after the administration of drug in rats. There are five levels of neurological examination: 0, normal function, no neurological deficit; 1, the right forepaw could not be fully extended, mild neurological deficit; 2, keep turning to

the right while walking, moderate neurological deficit; 3, body leaning to the right while walking, severe neurological deficit; and 4, unable to walk spontaneously, unconsciousness. All neurobehavioral tests, using a double-blind procedure, were performed in triplicate.

Berderson Behavioral Test

At 28 days of age, the Berderson behavioral test was performed to evaluate the degree of contralateral paralysis in rats. Briefly, the rats were lifted 1 m in the air to observe the flexion of the forelimbs, and the score was as follows: 0, rats extended the forelimbs to the ground without neurological deficits; 1, rats sustained flexion injury to the hemisphere of the affected limb in different postures including mild wrist flexion, shoulder adduction elbow extension to severe postures, complete wrist and elbow flexion, shoulder rotation, and adduction; and 2, rats were placed on a large paperboard where they could grip tightly. Gentle pressure was used behind the shoulder until the forelimbs slid several inches in each direction. Rats with normal or mild functional impairment exhibited similar lateral resistance to slippage; and 3, rats consistently circled toward the paretic side. All neurobehavioral tests, using a double-blind procedure, were performed in triplicate.

Statistical Analysis

The quantitative results were presented as the mean ± standard error of the mean from three independent experiments. Student's *t*-test was used to assess the statistical significance between two experimental groups. For the comparison of more than two groups, one-way analysis of variance was used followed by Tukey's test. All statistical analyses were performed using GraphPad Prism 6.0 (GraphPad Software Inc., San Diego, CA, USA). $P < 0.05$ denoted statistical significance.

RESULTS

Treatment With Liraglutide Reduced Infarct Volume and Ameliorated Cerebral Edema

Liraglutide (100, 200, and 400 nmol/kg) was administered through intraperitoneal injection immediately after HI brain injury to examine its role in this process and determine the most effective dose. According to the quantitative analysis of the TTC-stained sections, all three doses effectively reduced infarct volume, and the 200 nmol/kg resulted in the most pronounced effect. Therefore, 200 nmol/kg of liraglutide was used in all following experiments as the standard treatment (**Figures 1A,B**).

Regarding cerebral edema, the shape of brains and water content in the brains were examined 24 h after HI. Evidently, owing to edema, the ipsilateral brains obtained from the HI group were larger compared with those obtained from the sham group and HI + Liraglutide group (**Figure 1C**). The results of the water content analysis indicated that the content in the ipsilateral brain of the HI group was significantly increased in contrast to that measured in the sham group. Of note, the HI + Liraglutide group, compared with the HI group, exhibited a marked reduction (**Figures 1C,D**).

Treatment With Liraglutide Decreased the Expression of Inflammatory Factors at Both the mRNA and Protein Levels

Several inflammatory markers were assessed 24 h after HI injury using real-time reverse transcription–polymerase chain reaction to verify whether treatment with liraglutide can reduce the release of inflammatory cytokines. The mRNA expression levels of TNF-α, IL-18, IL-1β, IL-6, and cyclooxygenase-2 in the HI group were markedly increased compared with those detected in the sham group. Nevertheless, the mRNA levels of these inflammatory factors were significantly decreased in the HI + Liraglutide group (**Figure 2A**). Additionally, the levels of TNF-α in the sham group were the lowest and increased after the HI insult (**Figure 2B**). Furthermore, the protein expression of TNF-α in the HI + Liraglutide group was markedly inhibited (**Figures 2B,C**). In the sham group, immunofluorescence staining of TNF-α showed low expression in both the cortex (**Figure 2D**) and hippocampus (**Figure 2E**). Positive immunoreactivity for TNF-α was strongly found in the HI group, indicating a prominent release of inflammatory cytokines in the cortex and hippocampus. In contrast to the HI group, we observed a lower fluorescence signal for TNF-α.

Long-Term Neuroprotective Effects of Treatment With Liraglutide

Meanwhile, H&E staining was conducted to investigate whether liraglutide exerts any effect on the important organs (in terms of pathology) after 7 days of continuous administration (**Figure 3A**). There was no apparent difference between the sham group and liraglutide-treated group. To further investigate the neuroprotection of treatment with liraglutide against HI-induced brain injury, rats from each group were sacrificed to observe the brain atrophy and tissue loss at day 14.

Seven days post HI insult, Nissl staining was used to evaluate the histopathological and neuronal transformation in the ipsilateral cortex and hippocampus. We counted the numbers of Nissl bodies in the injured hemisphere to investigate the protective effect of liraglutide. The Nissl bodies were large and abundant and remained well arranged around the nuclei. In contrast, after HI injury, we observed decreased and disorganized neurons and even the absence of neurons (**Figures 3B–F**).

Moreover, after treatment with liraglutide, the brain atrophy was ameliorated (**Figure 4A**). And there was an increase in the number of neurons and Nissl bodies. Immunohistochemical analysis of MAP-2 (a biomarker for neurons) and MBP (a biomarker for oligodendrocytes) and western blotting were applied to determine whether liraglutide was able to accelerate remyelination and axonal repair in neonatal pups. As shown in **Figures 4B–E**, we found the lowest protein expression of MAP-2 and MBP in the vehicle-treated HI group. In contrast, there was a significant increase in the level of both proteins after treatment with liraglutide. Correspondingly, the results of the immunohistochemical analysis showed the same trend. Both MAP-2 and MBP were weakly expressed in the HI group, whereas treatment with liraglutide upregulated the expression of the positive area.

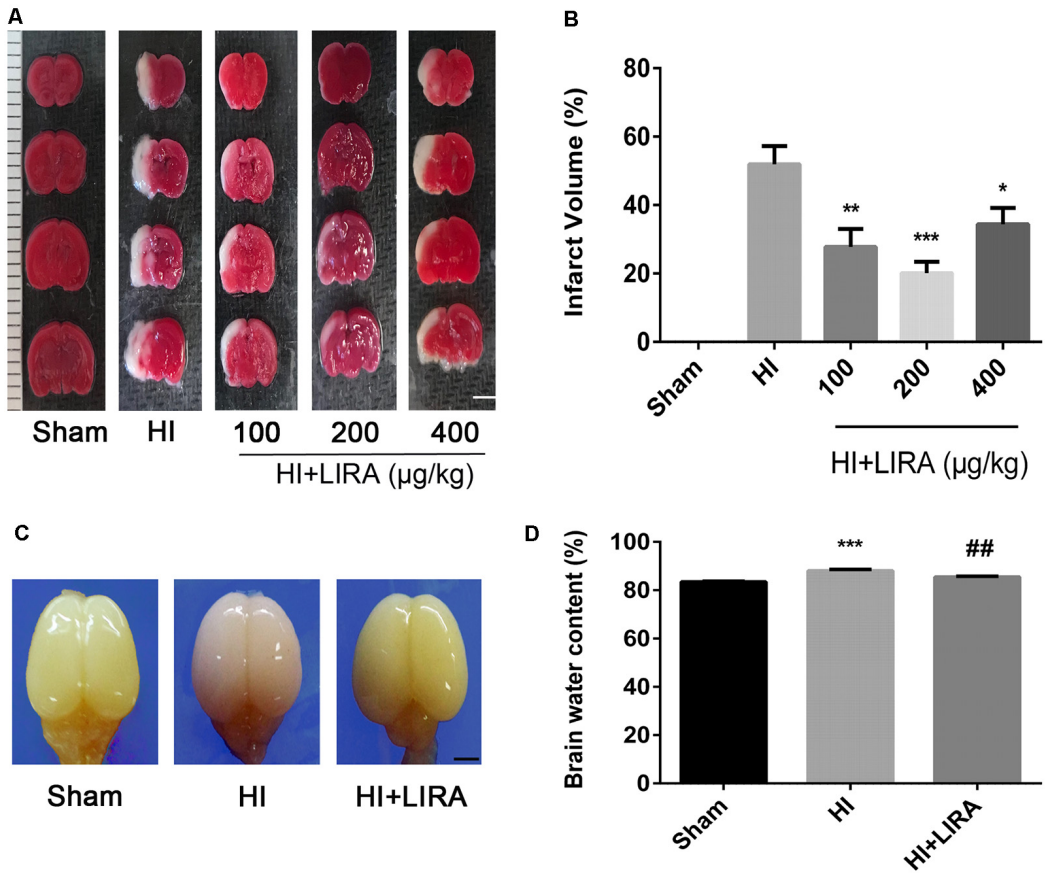


FIGURE 1 | Treatment with liraglutide attenuated the infarct volume and cerebral edema after hypoxic–ischemic (HI) brain injury. **(A)** Representative 2,3,5-triphenyltetrazolium chloride (TTC)-stained coronal brain sections 24 h after HI brain injury. Scale bar = 1 mm. **(B)** Quantitative analysis of infarct volume. $^{*}P < 0.05$, $^{**}P < 0.01$, and $^{***}P < 0.001$ vs. the HI group. Values represent the mean ± SEM. $n = 4$. **(C)** The general shape of the brain 24 h after HI. $n = 5$. Scale bar = 1 mm. **(D)** Quantification of the water content in the ipsilateral brain hemisphere 24 h after HI. $^{***}P < 0.001$ vs. the sham group. $^{\#\#}P < 0.01$ vs. the HI group. Values are presented as mean ± SEM. $n = 5$.

Treatment With Liraglutide Exerted Neuroprotection by Activating the PI3K/Akt/GSK3β Pathway

The PI3K inhibitor LY294002 was used to evaluate whether liraglutide activated the PI3K/Akt/GSK3β pathway. According to the quantitative analysis, the HI + Liraglutide + LY294002 group, compared with the HI + Liraglutide group, showed a markedly increased volume of cerebral infarction (**Figures 6A,B**) and water content in the brain (**Figures 6C,D**). In addition, western blotting was performed to measure the levels of proteins involved in the PI3K/Akt/GSK3β pathway. The levels of p-Akt and p-GSK3β in the HI group were lower than those reported in the sham group, and they increased after the HI insult. However, the levels of both proteins were increased compared with those recorded in the HI group, whereas protein expression in the HI + Liraglutide + LY294002 group was dramatically inhibited (**Figure 6E**). The levels of Akt and GSK3β among the four groups were not statistically significant (**Figure 6F**). Moreover, the number of dying cells (i.e., shrunken nucleus and decreased neuronal density) was significantly increased in the HI + Liraglutide + LY294002 group (**Figure 6G**). Correspondingly, the results of the immunohistochemical analysis showed the same trend. P-GSK3β was weakly expressed in the HI group, whereas treatment with liraglutide upregulated the number of positive cells of p-GSK3β. Moreover, the number of positive cells of p-GSK3β was obviously decreased in the HI + Liraglutide + LY294002 group (**Figure 6H**). To eliminate effects caused by LY294002 only, we did experiments to compare HI + LY294002 group with the HI group. There were no statistically significant differences between the two groups in infarct volume, degree of brain edema, tissue structure, prognosis *in vivo* and cell viability *in vitro* (**Supplementary Figure S1**). These data revealed that the neuroprotection of liraglutide involved the activation of the PI3K/Akt/GSK3β pathway.

The Anti-Apoptotic Effect of Liraglutide Could be Inhibited by LY294002 Both *in vivo* and *in vitro*

The CCK8 assay was performed to confirm whether treatment with liraglutide protects against injury induced by OGD and

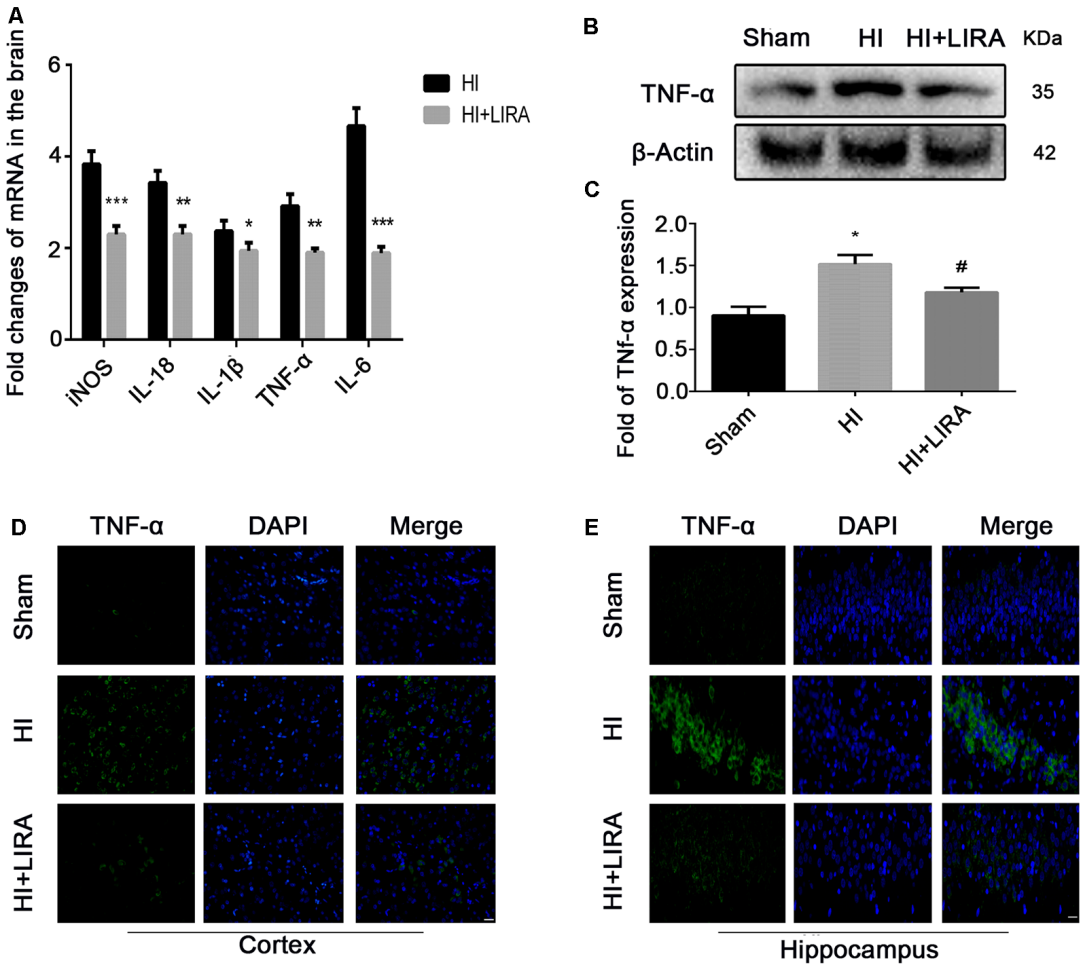


FIGURE 2 | Treatment with liraglutide decreased the inflammatory response at both the mRNA and protein levels. **(A)** The levels of mRNA expression in brain tissue 24 h after hypoxic–ischemic (HI) injury normalized to those of β-actin for each sample. $^{*}P < 0.05$, $^{**}P < 0.01$, and $^{***}P < 0.001$ vs. the HI group. $n = 5$. Values are presented as mean ± SEM. $n = 5$. Protein expression level **(B)** and quantification data **(C)** of tumor necrosis factor-alpha (TNF-α) 24 h after HI injury. $^{*}P < 0.05$ vs. the sham group. $^{\#}P < 0.05$ vs. the HI group. Values are presented as mean ± SEM. $n = 3$. Representative images of immunofluorescence staining of TNF-α (green) in the cortex **(D)**, hippocampus **(E)**, and nucleus (blue) labeled with DAPI. Scale bar = 25 μm.

to determine the most effective dose. As shown in **Figure 5A**, 10^{-6} mM of liraglutide exerted the best protection. TUNEL staining was performed to explore whether liraglutide could inhibit neuronal apoptosis both *in vivo* and *in vitro*. *In vitro*, the control group showed low expression. The number of TUNEL-positive apoptotic cells was markedly decreased in the OGD + LIRA group compared with the OGD group. The OGD + Liraglutide + LY294002 group showed an increase in the number of TUNEL-positive apoptotic cells (**Figures 7A,B**). *in vivo*, the results showed the same trend as those obtained *in vitro*. However, the anti-apoptotic effect of liraglutide was inhibited by LY294002. The number of TUNEL-positive cells was significantly increased in the HI group 24 h after HI injury. In contrast, a significant reduction in the number of TUNEL-positive cells was detected in the HI + Liraglutide group. However, the number of TUNEL-positive cells was significantly increased in the HI + Liraglutide + LY294002 group compared with that observed in the HI + Liraglutide group, indicating that this protective effect was partially reversed by LY294002 (**Figures 7C,D**). Furthermore, the protein expression levels of Bcl-2 and cleaved caspase 3 were determined through western blotting. Quantitative data demonstrated that liraglutide reversed the HI-induced increase in the expression level of cleaved caspase 3 (**Figure 7E**). Meanwhile, the expression level of the anti-apoptotic protein Bcl-2 was significantly increased after treatment with liraglutide compared with that reported in the HI group (**Figures 7E,F**). In the HI + Liraglutide + LY294002 group, the level of Bcl-2 was decreased, whereas that of cleaved caspase 3 increased. These differences were statistically significant vs. those of the HI + Liraglutide group (**Figures 7E–G**). Collectively, these results indicate that liraglutide exerted an anti-apoptotic effect against HI injury, and the protective effect was partially reversed by LY294002 both *in vivo* and *in vitro*.

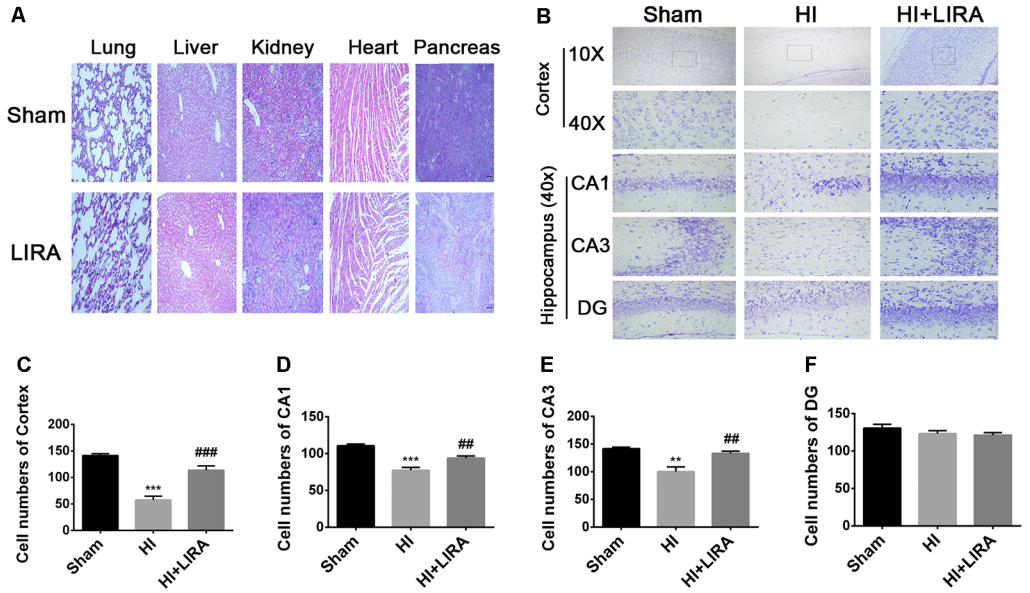


FIGURE 3 | Treatment with liraglutide reduced the damage in tissue structure and neuron loss after HI injury. **(A)** Representative images of H&E staining of the heart, liver, lung, pancreas, and kidney at day 7 post-treatment with liraglutide. Scale bar = 50 μm. **(B)** Representative images and quantification data **(C–F)** of Nissl staining in the cortex and hippocampus of CA1, CA3, and dentate gyrus at day 7 post HI injury. Scale bar = 25 μm, 100 μm. Values are presented as mean ± SEM. $n = 5$. $^{**}P < 0.01$ and $^{***}P < 0.001$ vs. the sham group. $^{\#\#}P < 0.01$ and $^{\#\#\#}P < 0.001$ vs. the HI group. Values are presented as mean ± SEM. $n = 5$.

Liraglutide Improved the Prognosis of Rats After Hypoxic–Ischemic Injury

The bodyweight of the rats was measured at 7, 14, and 28 days of age. Prior to HI injury (at day 7), the bodyweights did not show significant differences between the groups. However, the HI + Liraglutide group showed improvements in bodyweight at day 14 than in the HI group. However, there was no significant difference between the HI + Liraglutide group and HI + Liraglutide + LY294002 group at day 14. At day 28, the rats in the HI + Liraglutide group continued to exhibit improvements in bodyweight in contrast to the HI group, whereas the HI + Liraglutide + LY294002 group showed little improvements in contrast to the HI + Liraglutide group. Following long-term treatment with liraglutide, the HI + Liraglutide group exhibited greater weight gains than the HI group and the HI + Liraglutide + LY294002 group (**Figure 8A**).

Furthermore, at day 28, the Longa assessment and the Berderson behavioral test were performed to evaluate the injury and improvement of nerve function, respectively. At 28 days of age, these assessments indicated that the HI + Liraglutide group showed better mobility and flexion than did the HI group. In addition, the HI + Liraglutide + LY294002 group got higher scores, which revealed that the rats in this group did not perform well in these two tests (**Figures 8B,C**).

DISCUSSION

Neonatal HI brain injury, caused mainly by perinatal asphyxia, is associated with death and long-term neurological impairments in newborns. According to numerous animal studies and randomized clinical trials, therapeutic hypothermia is currently the standard treatment for this condition. However, approximately 50% the infants treated with hypothermia expire or suffer neurodevelopmental disability (Azzopardi et al., 2009; Liu and McCullough, 2013). Thus, it is important to develop new effective therapeutic approaches targeting the pathogenesis of HI brain injury through the processes of apoptosis, inflammation, oxidative stress, and excitotoxicity (Fernández-López et al., 2014).

Liraglutide has shown its unique neuroprotective effect in reducing the level of oxidative stress, apoptosis, and inflammation as well as in promoting the proliferation of neurons and the recovery of cognitive function in the central nervous system in experimental models and clinical patients (Zhu et al., 2016; Gejl et al., 2017; Guthrie, 2018). Moreover, liraglutide exerts positive effects on weight loss, blood pressure, hyperlipidemia, and glycemic control in the clinic. Thus, many studies have investigated its effects on the cardiovascular, endocrine, and nervous systems (Ishii et al., 2017; Babic et al., 2018; Bahtiyar et al., 2018). In animal models and clinical patients, there were no adverse events or reproductive toxicity found posttreatment with liraglutide. In this study, we did not observe obvious histopathological changes in other important organs after seven consecutive days of administration of liraglutide. Therefore, we suggest that liraglutide may be a safe therapeutic option for neonatal HI brain injury.

In our study, we found that liraglutide protected both short-term and long-term functions. Specifically, we found that

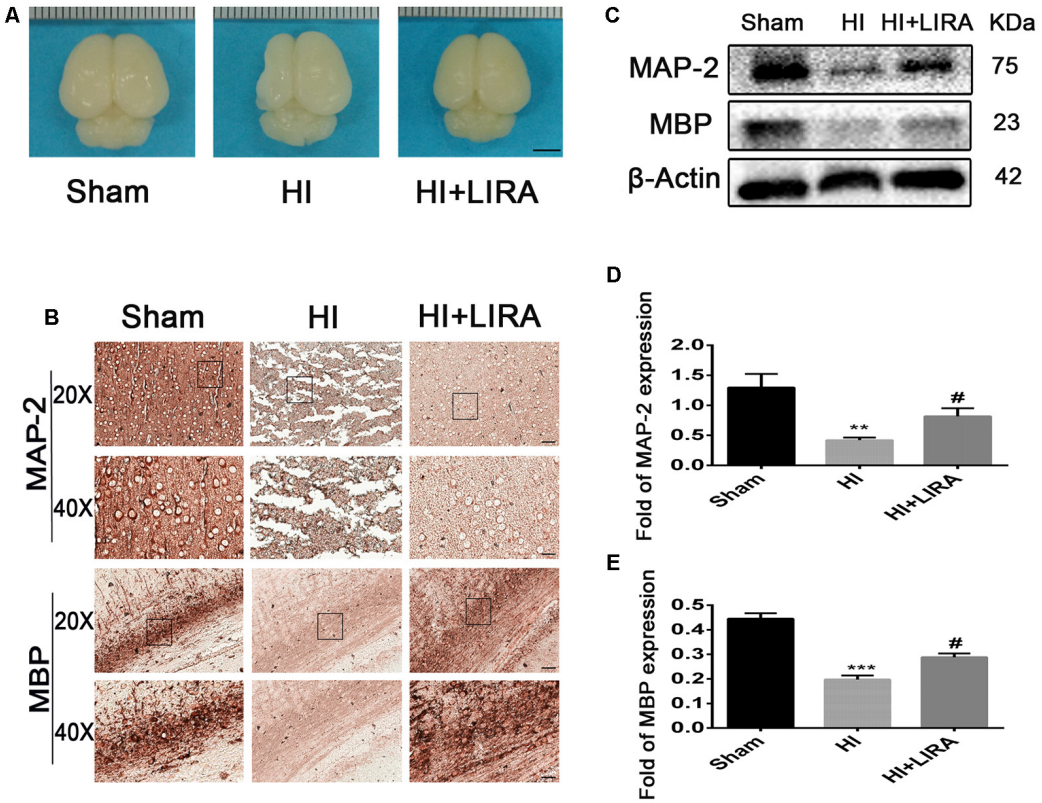


FIGURE 4 | Treatment with liraglutide decreased brain atrophy, enhanced axonal repair, and accelerated remyelination after HI injury. **(A)** General observation of rat brains from each group at day 7 post HI injury. Scale bar = 1 mm. **(B)** Representative images of immunohistochemical staining for microtubule-associated protein 2 (MAP-2) and myelin basic protein (MBP). Scale bar = 25 μm, 50 μm. Protein expression level **(C)** and quantification data of MAP-2 **(D)** and MBP **(E)** at day 7 post HI injury. $^{**}P < 0.01$ and $^{***}P < 0.001$ vs. the sham group. $^{\#}P < 0.05$ vs. the HI group. Values are presented as mean ± SEM. $n = 3$.

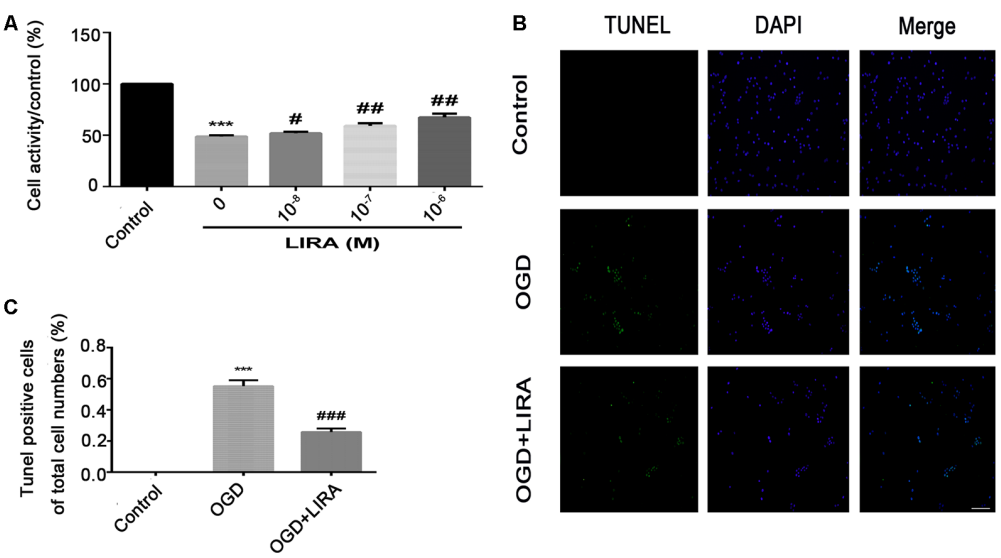


FIGURE 5 | Treatment with liraglutide alleviated cell death and apoptosis induced by oxygen-glucose deprivation (OGD). **(A)** Cell viability after reoxygenation for 24 h following OGD for 8 h with different doses of liraglutide. $^{***}P < 0.001$ versus the control group. $^{\#}P < 0.05$ and $^{\#\#}P < 0.01$ versus the OGD group. Values are presented as mean ± SEM. $n = 3$. **(B)** Representative images of terminal deoxynucleotidyl transferase dUTP nick end labeling (TUNEL) staining (green); the nucleus (blue) was labeled with DAPI 24 h HI injury. Scale bar = 50 μm. **(C)** Quantification data of TUNEL staining. $^{***}P < 0.001$ vs. the control group. $^{\#\#\#}P < 0.001$ vs. the OGD group. Values presented as mean ± SEM. $n = 4$.

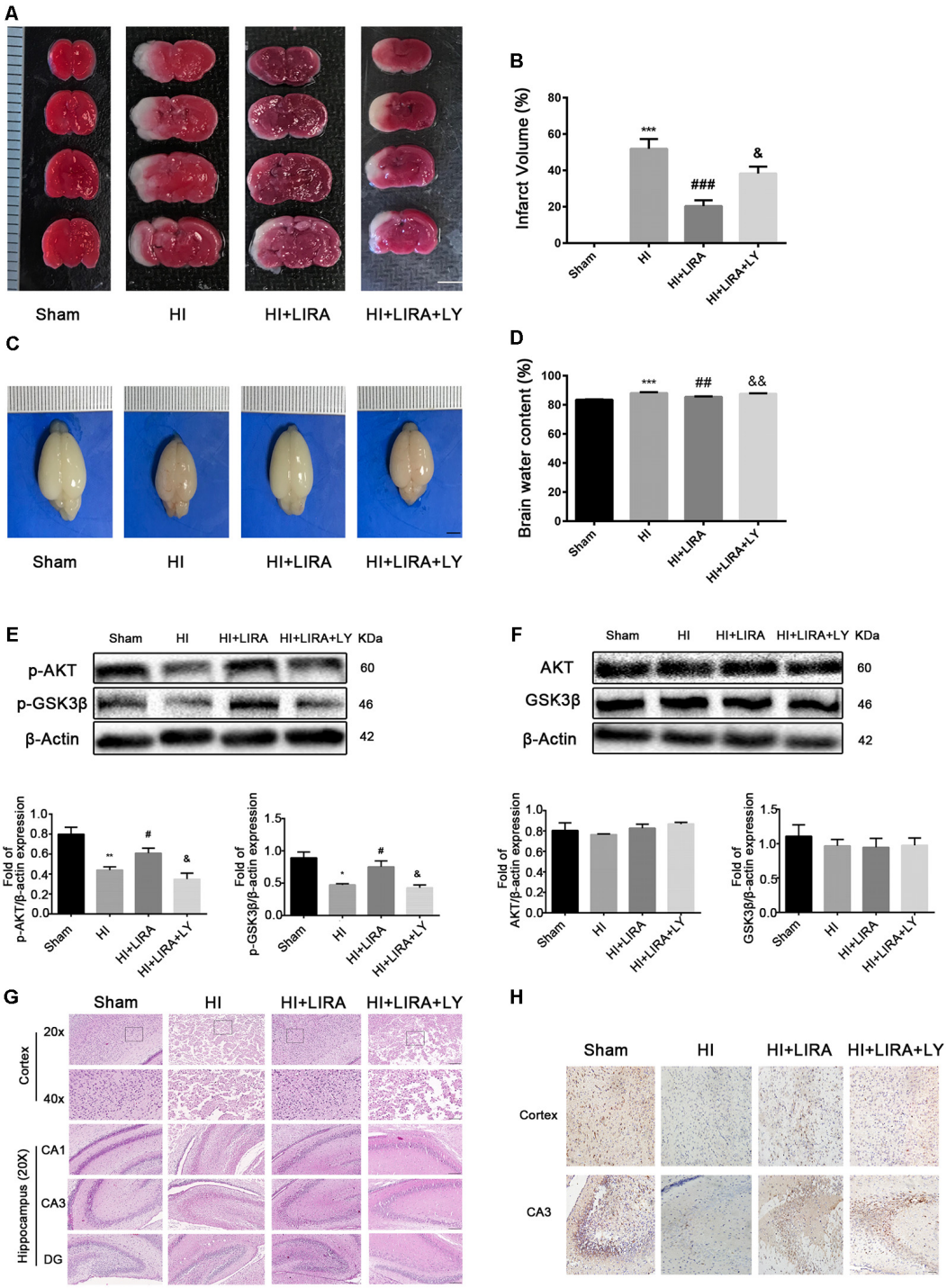


FIGURE 6 | Treatment with liraglutide (LIRA) exerted neuroprotection by activating the phosphoinositide 3-kinase (PI3K)/protein kinase B (Akt)/glycogen synthase kinase-3β (GSK3β) pathway. **(A)** Representative TTC-stained coronal brain sections 24 h after HI. $n = 4$. Scale bar = 1 mm. **(B)** Quantitative analysis of infarct volume. $^{***}P < 0.001$ vs. the sham group. $^{\#\#\#}P < 0.001$ vs. the HI group. $^{\&}P < 0.05$ vs. the HI + LIRA group. Values are presented as mean ± SEM. $n = 4$. **(C)** The general shape of the brain 24 h after HI. $n = 5$. Scale bar = 1 mm. **(D)** Quantification of water content in the ipsilateral brain hemisphere 24 h after HI. $^{***}P < 0.001$ vs. the sham group. $^{\#\#}P < 0.01$ vs. the HI group. $^{\&\&}P < 0.01$ vs. the HI + LIRA group. Values are presented as mean ± SEM. $n = 5$. **(E)** Protein expression level and quantification data of p-AKT and p-GSK3β 24 h after HI injury. $^{*}P < 0.05$ and $^{**}P < 0.01$ vs. the sham group. $^{\#}P < 0.05$ vs. the HI group. $^{\&}P < 0.05$ vs. the HI + LIRA group. Values are presented as mean ± SEM. $n = 3$. **(F)** Protein expression level and quantification data of AKT and GSK3β 24 h after HI injury. Values are presented as mean ± SEM. $n = 3$. **(G)** Representative images of H&E staining in the cortex and hippocampus of CA1, CA3, and dentate gyrus at day 7 post HI injury. Scale bar = 25 μm, 50 μm. **(H)** Representative images of immunohistochemical staining for p-GSK3β. Scale bar = 50 μm.

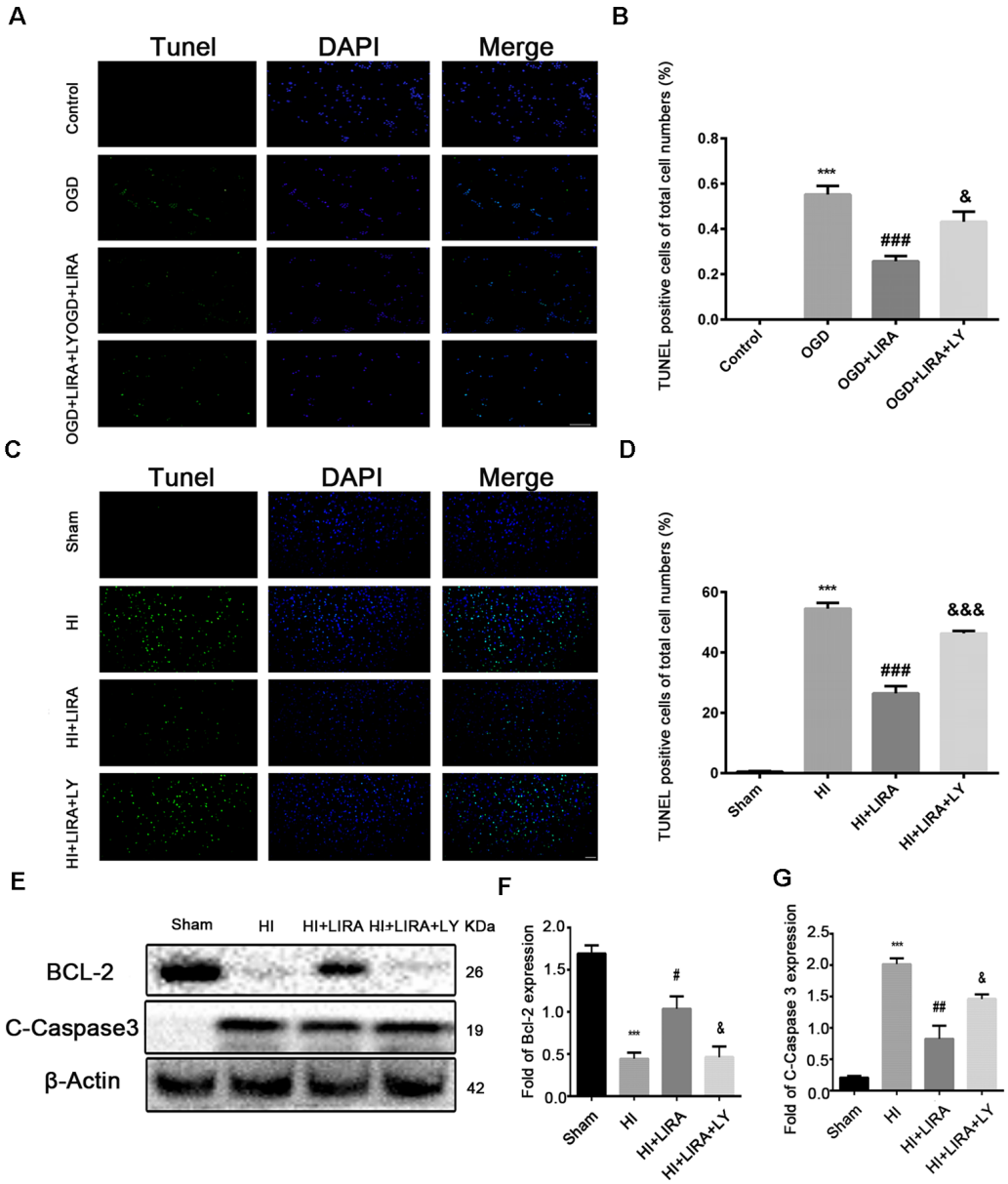


FIGURE 7 | The anti-apoptotic effect of liraglutide (LIRA) could be inhibited by LY294002 both *in vivo* and *in vitro*. **(A)** Representative images of terminal deoxynucleotidyl transferase dUTP nick end labeling (TUNEL) staining (green) and nucleus (blue) were labeled with DAPI after OGD injury in PC12 cells. Scale bar = 50 μm. **(B)** Quantification data of TUNEL staining *in vitro*. $^{***}P < 0.001$ vs. control group.$^{###}P < 0.001$ vs. the OGD group. $^{\&\&}P < 0.01$ vs. the OGD + LIRA group. Values are presented as mean ± SEM. $n = 4$. **(C)** Representative images of TUNEL staining (green); the nucleus (blue) was labeled with DAPI 24 h post hypoxic–ischemic (HI) injury in the animal model. Scale bar = 50 μm. **(D)** Quantification data of TUNEL staining *in vivo*. $^{***}P < 0.001$ vs. the sham group. $^{###}P < 0.001$ vs. the HI group. $^{\&\&\&}P < 0.001$ vs. the HI + LIRA group. Values are presented as mean ± SEM. $n = 5$. Protein expression level **(E)** and quantification data of Bcl-2 **(F)** and C-Caspase 3 **(G)** 24 h after HI injury. $^{***}P < 0.001$ vs. the sham group. $^{\#}P < 0.05$ and $^{\#\#}P < 0.01$ vs. the HI group. $^{\&}P < 0.05$ vs. the HI + LIRA group. Values are presented as mean ± SEM. $n = 3$.

treatment with liraglutide decreased the brain infarct volume and the degree of cerebral edema, inhibited inflammatory response and neuronal apoptosis, promoted the recovery of histomorphology, and improved the bodyweight and behavior disorders. Thus, the present data suggest a promising therapeutic strategy against neonatal HI brain injury.

Our results clearly showed that treatment with liraglutide improved neonatal brain injury in pups after HI. First, through TTC staining, we determined that the optimal concentration of liraglutide for a single intraperitoneal injection was 200 nmol/kg. Treatment with liraglutide reduced brain infarct volume 24 h after HI injury, showing evidence of a direct neuroprotective role.

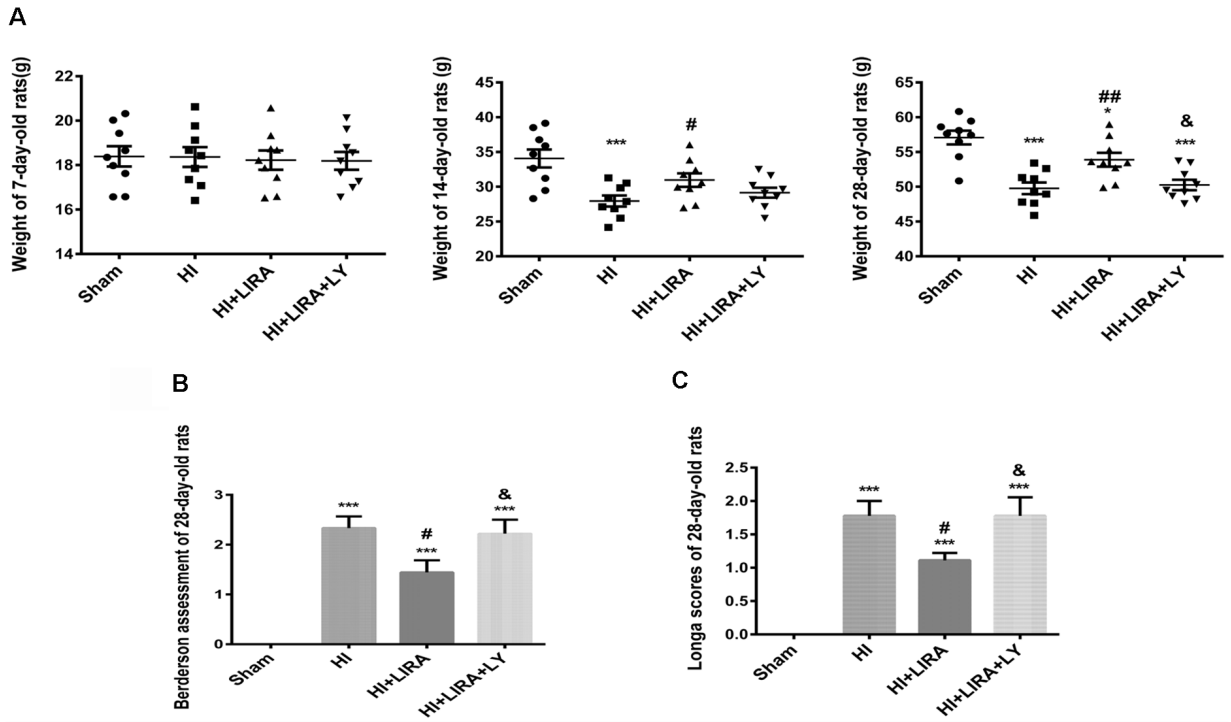


FIGURE 8 | Liraglutide (LIRA) improved the prognosis of rats post HI injury. **(A)** Weights of rats on days 7, 14, and 28. $^{*}P < 0.05$ and $^{***}P < 0.001$ vs. the sham group. $^{\#}P < 0.05$ and $^{\#\#}P < 0.01$ vs. the HI group. $^{\&}P < 0.05$ vs. the HI + LIRA group. Values are presented as mean ± SEM. $n = 9$. Quantification data of the Berderson behavioral test **(B)** and Longa assessment **(C)** at day 28. $^{***}P < 0.001$ vs. the sham group. $^{\#}P < 0.05$ and $^{\#\#}P < 0.01$ vs. the HI group. $^{\&}P < 0.05$ vs. the HI + LIRA group. Values are presented as mean ± SEM. $n = 9$.

For the cerebral edema, significant enlargement of the ipsilateral brain in gross morphology could be observed as a result of HI injury. *in vitro*, we revealed that liraglutide promoted cell survival and suppressed cell apoptosis in the OGD model. After seven consecutive days of administration, liraglutide reduced brain tissue loss and attenuated brain atrophy. In addition, the results of the H&E, Nissl, and MAP-2 staining suggest that liraglutide maintained neuronal structure and function. MBP staining indicated the protective effect of liraglutide on the white matter. These results confirmed that liraglutide exerts short-term protective effects.

Previous studies have indicated that the consequences of neonatal HI brain injury are not temporary, leading to neuropathies associated with the activation of neuroinflammatory processes. To our knowledge, liraglutide exerts a favorable anti-inflammatory effect in many animal models (McClean and Hölscher, 2014; Wang et al., 2018). The level of inflammatory cytokines at both the mRNA and protein levels can be used to evaluate the inflammatory response. Our experiments detected the increased expression of these inflammatory factors in brain tissue following HI and clearly demonstrated that liraglutide plays an effective role in anti-neuroinflammation against neonatal brain injury by inhibiting the mRNA and protein expression in rats.

Current evidence suggests that activation of the PI3K/Akt and its downstream pathways suppresses neuronal apoptosis in models of HI brain injury (Tu et al., 2018) and under OGD conditions (Ye et al., 2019). GSK3β is a serine/threonine protein kinase with broad expression and one of the downstream targets of Akt. It is essential in energy metabolism (Martin et al., 2018) and nerve cell development (Chen et al., 2019a). The levels of GSK3β can be decreased by phosphorylation at the ser9 site (Xu et al., 2017; Chen et al., 2019b). Additionally, GSK3β (Ser9) can be phosphorylated by Akt, inhibiting its enzymatic activity. An increasing body of evidence indicates that activation of PI3K/Akt and inhibition of GSK3β play a neuroprotective role in many brain injury models, including experimental ischemic stroke (Valerio et al., 2011), subarachnoid hemorrhage-induced early brain injury (Ma et al., 2016), traumatic brain injury (Zhang et al., 2018), and intracerebral hemorrhage (Chen et al., 2019b). A recent study showed that liraglutide inhibits the apoptosis of osteoblastic MC3T3-E1 cells induced by serum deprivation partly through the PI3K/Akt/GSK3β signaling pathway (Wu et al., 2018). Hence, we investigated whether the mechanism of liraglutide involved in protecting against neonatal HI brain injury is related to the activation of the PI3K/Akt/GSK3β signaling pathway. Using the PI3K inhibitor of LY294002, we found that Akt phosphorylation was decreased in both the HI group and HI + Liraglutide + LY294002 group. In addition, treatment with liraglutide markedly increased the protein expression of activated Akt. Subsequently, liraglutide inhibited

the activity of GSK3β by increasing the phosphorylation at the ser9 site. We observed that LY294002 could fully or partly reverse the protection offered by liraglutide in various manners, such as increasing the infarct volume and cerebral edema and reducing the prognostic effect, compared with those reported in the HI + Liraglutide group. Overall, we demonstrated that liraglutide exerted its neuroprotective effect by activating the PI3K/Akt/GSK3β signaling pathway.

Apoptosis plays an important role in HI brain injury (Zhu et al., 2005; Northington et al., 2011). Apoptosis is more pronounced in immature animal brains compared with juvenile and adult brains (Semple et al., 2013). Thus, the decrease of apoptosis has been considered a therapeutic target against HI injury in newborns. Numerous research studies reported that liraglutide suppresses apoptosis and promotes neurological functional recovery in some central nervous system diseases, such as traumatic brain injury (Li et al., 2015) and spinal cord injury (Chen et al., 2017). To the best of our knowledge, caspase 3 is one of the most representative indicators of apoptosis, and cleaved caspase 3 is released at high levels specifically following HI (Feng et al., 2014; Tu et al., 2019). The Bcl-2 family, especially Bcl-2, also protects neurons from apoptosis. It restricts the activity of caspase 3 and enhances cell survival. Our results, compared with those reported in the HI group, showed that liraglutide could downregulate the expression of cleaved caspase 3 and upregulate that of Bcl-2. Moreover, a decreasing number of TUNEL-positive cells was observed in rats with neonatal HI brain treated with liraglutide. Therefore, we confirmed that liraglutide plays a protective role through its anti-apoptotic activity after HI injury in newborn rats. However, LY294002 reversed the anti-apoptotic function of liraglutide both *in vitro* and *in vivo*. We illustrated that liraglutide inhibits neuronal apoptosis following HI and OGD by activating the PI3K/Akt/GSK3β signaling pathway.

This study was characterized by limitations. Several reports have demonstrated the neuroprotective effects of GLP-1R in terms of reducing oxidative stress and inhibiting apoptosis (Hamilton and Hölscher, 2009). Activation of GLP-1R stimulates adenylyl cyclase signaling, leading to an increase in the levels of cAMP that activate protein kinase A (PKA) and subsequently phosphorylate cAMP response element-binding protein (CREB). Activation of CREB regulates the transcription of the Bcl-2 proteins (Chen et al., 2017). In our study, the role of GLP-1R was not explored. Thus, as one of the downstream targets of Akt, mammalian target of rapamycin (mTOR) may also exert its influence on HI injury in newborns. Therefore, it is necessary to thoroughly investigate the possible underlying mechanism involved in this process. Additionally, a recent study showed that the protective effects of liraglutide may be associated with increased mTOR expression *via* activation of the AMPK and PI3K/Akt signaling pathways in rats with type 2 diabetes (Yang et al., 2018). Additional cell experiments are warranted to confirm the role of liraglutide. Considering the limitations of therapeutic hypothermia in the treatment of neonatal encephalopathy, it is vital to explore whether liraglutide augments hypothermic neuroprotection. Therefore, in our future study, a combination of liraglutide and hypothermia will be investigated.

CONCLUSION

The present study demonstrated that treatment with liraglutide reduced infarct volume and ameliorated cerebral edema, decreased inflammatory response, promoted the recovery of tissue structure, and improved prognosis post HI insult *via* the PI3K/Akt/GSK3β signaling pathway. Furthermore, treatment with liraglutide inhibited apoptosis and promoted neuronal survival in both rat model and OGD insult experiments. The pathogenesis of neonatal HI brain injury is complicated, and effective treatment methods are currently limited. Therefore, liraglutide may be a promising and inexpensive therapeutic option in this setting. Further studies are warranted to confirm the mechanism.

DATA AVAILABILITY STATEMENT

The datasets of our study are available from the corresponding author upon reasonable request.

ETHICS STATEMENT

The animal study was reviewed and approved by the Animal Care and Use Committee of Wenzhou Medical University (ethic number: wydw2014-0058).

AUTHOR CONTRIBUTIONS

SZ and JB drafted the article and designed the study mainly. HJ helped to design experiments. JZ and CF wrote part of the article. MH and JZ designed figures and contributed to analysis of part of the data. PL, XF and SC helped to analyze related data. ZL contributed to critical revision of the manuscript. All the authors approved the final version and agreed to be accountable for the study.

FUNDING

This study was funded by the National Natural Science Foundation of China (No. 81771624), the Beijing Medical and Health Foundation (No. B17137) and Wenzhou Science and Technology Bureau (No. Y20190001).

SUPPLEMENTARY MATERIAL

The Supplementary Material for this article can be found online at: https://www.frontiersin.org/articles/10.3389/fncel.2019.00585/full#supplementary-material.

REFERENCES

Al-Macki, N., Miller, S. P., Hall, N., and Shevell, M. (2009). The spectrum of abnormal neurologic outcomes subsequent to term intrapartum asphyxia. *Pediatr. Neurol.* 41, 399–405. doi: 10.1016/j.pediatrneurol.2009.06.001

Aviles-Olmos, I., Dickson, J., Kefalopoulou, Z., Djamshidian, A., Kahan, J., Ell, P., et al. (2014). Motor and cognitive advantages persist 12 months after exenatide exposure in Parkinson's disease. *J. Parkinsons Dis.* 4, 337–344. doi: 10.3233/jpd-140364

Azzopardi, D. V., Strohm, B., Edwards, A. D., Dyet, L., Halliday, H. L., Juszczak, E., et al. (2009). Moderate hypothermia to treat perinatal asphyxial encephalopathy. *N. Engl. J. Med.* 361, 1349–1358. doi: 10.1056/NEJMoa0900854

Babic, I., Gorak, A., Engel, M., Sellers, D., Else, P., Osborne, A. L., et al. (2018). Liraglutide prevents metabolic side-effects and improves recognition and working memory during antipsychotic treatment in rats. *J. Psychopharmacol.* 32, 578–590. doi: 10.1177/0269881118756061

Badawi, G. A., Abd El Fattah, M. A., Zaki, H. F., and El Sayed, M. I. (2017). Sitagliptin and liraglutide reversed nigrostriatal degeneration of rodent brain in rotenone-induced Parkinson's disease. *Inflammopharmacology* 25, 369–382. doi: 10.1007/s10787-017-0331-6

Bahtiyar, G., Pujals-Kury, J., and Sacerdote, A. (2018). Cardiovascular effects of different GLP-1 receptor agonists in patients with type 2 diabetes. *Curr. Diab. Rep.* 18:92. doi: 10.1007/s11892-018-1043-z

Chen, C., Jiang, X., Li, Y., Yu, H., Li, S., Zhang, Z., et al. (2019a). Low-dose oral copper treatment changes the hippocampal phosphoproteomic profile and perturbs mitochondrial function in a mouse model of Alzheimer's disease. *Free Radic. Biol. Med.* 135, 144–156. doi: 10.1016/j.freeradbiomed.2019.03.002

Chen, C., Zhou, F., Zeng, L., Jiang, Z., and Hu, Z. (2019b). Methylene blue offers neuroprotection after intracerebral hemorrhage in rats through the PI3K/Akt/GSK3β signaling pathway. *J. Cell. Physiol.* 234, 5304–5318. doi: 10.1002/jcp.27339

Chen, J., Wang, Z., Mao, Y., Zheng, Z., Chen, Y., Khor, S., et al. (2017). Liraglutide activates autophagy *via* GLP-1R to improve functional recovery after spinal cord injury. *Oncotarget* 8, 85949–85968. doi: 10.18632/oncotarget.20791

Chiang, M. C., Jong, Y. J., and Lin, C. H. (2017). Therapeutic hypothermia for neonates with hypoxic ischemic encephalopathy. *Pediatr. Neonatol.* 58, 475–483. doi: 10.1016/j.pedneo.2016.11.001

Cork, S. C., Richards, J. E., Holt, M. K., Gribble, F. M., Reimann, F., and Trapp, S. (2015). Distribution and characterisation of glucagon-like peptide-1 receptor expressing cells in the mouse brain. *Mol. Metab.* 4, 718–731. doi: 10.1016/j.molmet.2015.07.008

DellaValle, B., Hempel, C., Johansen, F. F., and Kurtzhals, J. A. (2014). GLP-1 improves neuropathology after murine cold lesion brain trauma. *Ann. Clin. Transl. Neurol.* 1, 721–732. doi: 10.1002/acn3.99

Dong, W., Miao, Y., Chen, A., Cheng, M., Ye, X., Song, F., et al. (2017). Delayed administration of the GLP-1 receptor agonist liraglutide improves metabolic and functional recovery after cerebral ischemia in rats. *Neurosci. Lett.* 641, 1–7. doi: 10.1016/j.neulet.2017.01.045

Douglas-Escobar, M., and Weiss, M. D. (2015). Hypoxic-ischemic encephalopathy: a review for the clinician. *JAMA Pediatr.* 169, 397–403. doi: 10.1001/jamapediatrics.2014.3269

Feng, Y., Lu, S., Wang, J., Kumar, P., Zhang, L., and Bhatt, A. J. (2014). Dexamethasone-induced neuroprotection in hypoxic-ischemic brain injury in newborn rats is partly mediated via Akt activation. *Brain Res.* 1589, 68–77. doi: 10.1016/j.brainres.2014.09.073

Fernández-López, D., Natarajan, N., Ashwal, S., and Vexler, Z. S. (2014). Mechanisms of perinatal arterial ischemic stroke. *J. Cereb. Blood Flow Metab.* 34, 921–932. doi: 10.1038/jcbfm.2014.41

Gejl, M., Brock, B., Egefjord, L., Vang, K., Rungby, J., and Gjedde, A. (2017). Blood-brain glucose transfer in Alzheimer's disease: effect of GLP-1 analog treatment. *Sci. Rep.* 7:17490. doi: 10.1038/s41598-017-17718-y

Guthrie, R. (2018). Practice pearl: liraglutide and cardiovascular and renal events in type 2 diabetes. *Postgrad. Med.* 130, 154–158. doi: 10.1080/00325481.2018.1430446

Hagberg, H., Mallard, C., Ferriero, D. M., Vannucci, S. J., Levison, S. W., Vexler, Z. S., et al. (2015). The role of inflammation in perinatal brain injury. *Nat. Rev. Neurol.* 11, 192–208. doi: 10.1038/nrneurol.2015.13

Hakon, J., Ruscher, K., Romner, B., and Tomasevic, G. (2015). Preservation of the blood brain barrier and cortical neuronal tissue by liraglutide, a long acting glucagon-like-1 analogue, after experimental traumatic brain injury. *PLoS One* 10:e0120074. doi: 10.1371/journal.pone.0120074

Hamilton, A., and Hölscher, C. (2009). Receptors for the incretin glucagon-like peptide-1 are expressed on neurons in the central nervous system. *Neuroreport* 20, 1161–1166. doi: 10.1097/wnr.0b013e32832fbf14

Hunter, K., and Hölscher, C. (2012). Drugs developed to treat diabetes, liraglutide and lixisenatide, cross the blood brain barrier and enhance neurogenesis. *BMC Neurosci.* 13:33. doi: 10.1186/1471-2202-13-33

Ishii, H., Niiya, T., Ono, Y., Inaba, N., Jinnouchi, H., and Watada, H. (2017). Improvement of quality of life through glycemic control by liraglutide, a GLP-1 analog, in insulin-naive patients with type 2 diabetes mellitus: the PAGE1 study. *Diabetol. Metab. Syndr.* 9:3. doi: 10.1186/s13098-016-0202-0

King, T. D., Bijur, G. N., and Jope, R. S. (2001). Caspase-3 activation induced by inhibition of mitochondrial complex I is facilitated by glycogen synthase kinase-3β and attenuated by lithium. *Brain Res.* 919, 106–114. doi: 10.1016/s0006-8993(01)03005-0

Li, Y., Bader, M., Tamargo, I., Rubovitch, V., Tweedie, D., Pick, C. G., et al. (2015). Liraglutide is neurotrophic and neuroprotective in neuronal cultures and mitigates mild traumatic brain injury in mice. *J. Neurochem.* 135, 1203–1217. doi: 10.1111/jnc.13169

Liu, F., and McCullough, L. D. (2013). Inflammatory responses in hypoxic ischemic encephalopathy. *Acta Pharmacol. Sin.* 34, 1121–1130. doi: 10.1038/aps.2013.89

Ma, J., Wang, Z., Liu, C., Shen, H., Chen, Z., Yin, J., et al. (2016). Pramipexole-induced hypothermia reduces early brain injury *via* PI3K/AKT/GSK3β pathway in subarachnoid hemorrhage rats. *Sci. Rep.* 6:23817. doi: 10.1038/srep23817

Martin, S. A., Souder, D. C., Miller, K. N., Clark, J. P., Sagar, A. K., Eliceiri, K. W., et al. (2018). GSK3β regulates brain energy metabolism. *Cell Rep.* 23, 1922.e4–1931.e4. doi: 10.1016/j.celrep.2018.04.045

McClean, P. L., and Hölscher, C. (2014). Lixisenatide, a drug developed to treat type 2 diabetes, shows neuroprotective effects in a mouse model of Alzheimer's disease. *Neuropharmacology* 86, 241–258. doi: 10.1016/j.neuropharm.2014.07.015

McClean, P. L., Parthsarathy, V., Faivre, E., and Hölscher, C. (2011). The diabetes drug liraglutide prevents degenerative processes in a mouse model of Alzheimer's disease. *J. Neurosci.* 31, 6587–6594. doi: 10.1523/jneurosci.0529-11.2011

Northington, F. J., Chavez-Valdez, R., and Martin, L. J. (2011). Neuronal cell death in neonatal hypoxia-ischemia. *Ann. Neurol.* 69, 743–758. doi: 10.1002/ana.22419

Northington, F. J., Graham, E. M., and Martin, L. J. (2005). Apoptosis in perinatal hypoxic-ischemic brain injury: how important is it and should it be inhibited? *Brain Res. Rev.* 50, 244–257. doi: 10.1016/j.brainresrev.2005.07.003

Rocha-Ferreira, E., and Hristova, M. (2016). Plasticity in the neonatal brain following hypoxic-ischaemic injury. *Neural Plast.* 2016:4901014. doi: 10.1155/2016/4901014

Scott, L. J. (2014). Liraglutide: a review of its use in adult patients with type 2 diabetes mellitus. *Drugs* 74, 2161–2174. doi: 10.1007/s40265-014-0321-6

Semple, B. D., Blomgren, K., Gimlin, K., Ferriero, D. M., and Noble-Haeusslein, L. J. (2013). Brain development in rodents and humans: identifying benchmarks of maturation and vulnerability to injury across species. *Prog. Neurobiol.* 106–107, 1–16. doi: 10.1016/j.pneurobio.2013.04.001

Solevåg, A. L., Schmölzer, G. M., and Cheung, P. Y. (2019). Novel interventions to reduce oxidative-stress related brain injury in neonatal asphyxia. *Free Radic. Biol. Med.* 142, 113–122. doi: 10.1016/j.freeradbiomed.2019.04.028

Tian, S. F., Yang, H. H., Xiao, D. P., Huang, Y. J., He, G. Y., Ma, H. R., et al. (2013). Mechanisms of neuroprotection from hypoxia-ischemia (HI) brain injury by up-regulation of cytoglobin (CYGB) in a neonatal rat model. *J. Biol. Chem.* 288, 15988–16003. doi: 10.1074/jbc.m112.428789

Tu, L., Wang, Y., Chen, D., Xiang, P., Shen, J., Li, Y., et al. (2018). Protective effects of notoginsenoside R1 *via* regulation of the PI3K-Akt-mTOR/JNK pathway in neonatal cerebral hypoxic-ischemic brain injury. *Neurochem. Res.* 43, 1210–1226. doi: 10.1007/s11064-018-2538-3

Tu, X., Wang, M., Liu, Y., Zhao, W., Ren, X., Li, Y., et al. (2019). Pretreatment of grape seed proanthocyanidin extract exerts neuroprotective effect in murine

model of neonatal hypoxic-ischemic brain injury by its antiapoptotic property. *Cell. Mol. Neurobiol.* 39, 953–961. doi: 10.1007/s10571-019-00691-7

Valerio, A., Bertolotti, P., Delbarba, A., Perego, C., Dossena, M., Ragni, M., et al. (2011). Glycogen synthase kinase-3 inhibition reduces ischemic cerebral damage, restores impaired mitochondrial biogenesis and prevents ROS production. *J. Neurochem.* 116, 1148–1159. doi: 10.1111/j.1471-4159.2011.07171.x

Vannucci, R. C., and Vannucci, S. J. (2005). Perinatal hypoxic-ischemic brain damage: evolution of an animal model. *Dev. Neurosci.* 27, 81–86. doi: 10.1159/000085978

Vilsboll, T. (2009). Liraglutide: a new treatment for type 2 diabetes. *Drugs Today* 45, 101–113. doi: 10.1358/dot.2009.45.2.1336104

Wang, R. F., Xue, G. F., Holscher, C., Tian, M. J., Feng, P., Zheng, J. Y., et al. (2018). Post-treatment with the GLP-1 analogue liraglutide alleviate chronic inflammation and mitochondrial stress induced by *Status epilepticus*. *Epilepsy Res.* 142, 45–52. doi: 10.1016/j.eplepsyres.2018.03.009

Wu, X., Li, S., Xue, P., and Li, Y. (2018). Liraglutide inhibits the apoptosis of MC3T3#x02013;E1 cells induced by serum deprivation through cAMP/PKA/β-catenin and PI3K/AKT/GSK3β signaling pathways. *Mol. Cells* 41, 234–243. doi: 10.14348/molcells.2018.2340

Xu, H., Li, J., Wang, Z., Feng, M., Shen, Y., Cao, S., et al. (2017). Methylene blue attenuates neuroinflammation after subarachnoid hemorrhage in rats through the Akt/GSK-3β/MEF2D signaling pathway. *Brain Behav. Immun.* 65, 125–139. doi: 10.1016/j.bbi.2017.04.020

Yang, J. L., Chen, W. Y., Chen, Y. P., Kuo, C. Y., and Chen, S. D. (2016). Activation of GLP-1 receptor enhances neuronal base excision repair via PI3K-AKT-induced expression of apurinic/apyrimidinic endonuclease 1. *Theranostics* 6, 2015–2027. doi: 10.7150/thno.15993

Yang, Y., Fang, H., Xu, G., Zhen, Y., Zhang, Y., Tian, J., et al. (2018). Liraglutide improves cognitive impairment via the AMPK and PI3K/Akt signaling pathways in type 2 diabetic rats. *Mol. Med. Rep.* 18, 2449–2457. doi: 10.3892/mmr.2018.9180

Ye, L., Wang, X., Cai, C., Zeng, S., Bai, J., Guo, K., et al. (2019). FGF21 promotes functional recovery after hypoxic-ischemic brain injury in neonatal rats by activating the PI3K/Akt signaling pathway via FGFR1/β-klotho. *Exp. Neurol.* 317, 34–50. doi: 10.1016/j.expneurol.2019.02.013

Zhang, M., Wu, Y., Xie, L., Teng, C. H., Wu, F. F., Xu, K. B., et al. (2018). Isoliquiritigenin protects against bloodbrain barrier damage and inhibits the secretion of pro-inflammatory cytokines in mice after traumatic brain injury. *Int. Immunopharmacol.* 65, 64–75. doi: 10.1016/j.intimp.2018.09.046

Zhang, W., Zhang, H., Mu, H., Zhu, W., Jiang, X., Hu, X., et al. (2016). Omega-3 polyunsaturated fatty acids mitigate blood-brain barrier disruption after hypoxic-ischemic brain injury. *Neurobiol. Dis.* 91, 37–46. doi: 10.1016/j.nbd.2016.02.020

Zhou, Z. Q., Li, Y. L., Ao, Z. B., Wen, Z. L., Chen, Q. W., Huang, Z. G., et al. (2017). Baicalin protects neonatal rat brains against hypoxic-ischemic injury by upregulating glutamate transporter 1 via the phosphoinositide 3-kinase/protein kinase B signaling pathway. *Neural Regen. Res.* 12, 1625–1631. doi: 10.4103/1673-5374.217335

Zhu, C., Wang, X., Xu, F., Bahr, B. A., Shibata, M., Uchiyama, Y., et al. (2005). The influence of age on apoptotic and other mechanisms of cell death after cerebral hypoxia-ischemia. *Cell Death Differ.* 12, 162–176. doi: 10.1038/sj.cdd.4401545

Zhu, H., Zhang, Y., Shi, Z., Lu, D., Li, T., Ding, Y., et al. (2016). The neuroprotection of liraglutide against ischaemia-induced apoptosis through the activation of the PI3K/AKT and MAPK pathways. *Sci. Rep.* 6:26859. doi: 10.1038/srep26859

Conflict of Interest: The authors declare that the research was conducted in the absence of any commercial or financial relationships that could be construed as a potential conflict of interest.

Copyright © 2020 Zeng, Bai, Jiang, Zhu, Fu, He, Zhu, Chen, Li, Fu and Lin. This is an open-access article distributed under the terms of the Creative Commons Attribution License (CC BY). The use, distribution or reproduction in other forums is permitted, provided the original author(s) and the copyright owner(s) are credited and that the original publication in this journal is cited, in accordance with accepted academic practice. No use, distribution or reproduction is permitted which does not comply with these terms.

frontiers in Cellular Neuroscience

ORIGINAL RESEARCH
published: 19 February 2020
doi: 10.3389/fncel.2020.00028

Depletion of LncRNA NEAT1 Rescues Mitochondrial Dysfunction Through NEDD4L-Dependent PINK1 Degradation in Animal Models of Alzheimer's Disease

*Zhonghua Huang[1], Jing Zhao[1], Wei Wang[1], Jun Zhou[2] and Jie Zhang[1]**

[1] Department of Neurology, The Second Xiangya Hospital, Central South University, Changsha, China, [2] Medical Science Research Center, Xiangya Hospital, Central South University, Changsha, China

OPEN ACCESS

Edited by:
Antonio Gambardella, University of Catanzaro, Italy

Reviewed by:
Jorge Matias-Guiu, Complutense University of Madrid, Spain
Hong Peng, Sun Yat-sen University, China

***Correspondence:**
Jie Zhang
zhangjiedoctor@csu.edu.cn;
zhangjie2019@163.com

Specialty section:
This article was submitted to Cellular Neuropathology, a section of the journal Frontiers in Cellular Neuroscience

Received: 24 September 2019
Accepted: 30 January 2020
Published: 19 February 2020

Citation:
Huang Z, Zhao J, Wang W, Zhou J and Zhang J (2020) Depletion of LncRNA NEAT1 Rescues Mitochondrial Dysfunction Through NEDD4L-Dependent PINK1 Degradation in Animal Models of Alzheimer's Disease. Front. Cell. Neurosci. 14:28. doi: 10.3389/fncel.2020.00028

Alzheimer's disease (AD) is the most common neurodegenerative disorder and the main cause of dementia among the elderly worldwide. Unfortunately, the mechanism of AD remains unclear, and no effective therapies are available yet. An increasing amount of studies have demonstrated that long non-coding RNAs (LncRNAs) play a notable role in the pathogenesis of plenty of human diseases, and they have served as biomarkers and potential therapeutic targets. However, the function of LncRNAs in AD remains unclear. This study aimed to explore the potential role of LncRNA nuclear enriched abundant transcript 1 (NEAT1) in AD. We found that LncRNA NEAT1 was upregulated in the AD animal models. Furthermore, we demonstrated that NEAT1 could interact with NEDD4L and promote PTEN-induced putative kinase 1 (PINK1)'s ubiquitination and degradation and then impaired PINK1-dependent autophagy. Collectively, the lncRNA NEAT1 promotes the pathogenesis of AD and serves as a promising novel target for pharmacological intervention.

Keywords: NEAT1, Alzheimer's disease, PINK1, autophagy, NEDD4L

INTRODUCTION

Alzheimer's disease (AD) is a progressive neurodegenerative disease that slowly destroys memory and thinking skills and eventually leads to the loss of cognitive abilities. AD is characterized by several hallmarks, such as abnormal deposition of Aβ in amyloid plaques, neurofibrillary tangles (NFTs) in the brain, deficits in synaptic function and neuron loss, and abnormal accumulation of Tau and phosphorylated Tau (Yang et al., 2018; Chen and Mobley, 2019). Eventually, the brain tissue of AD patient shrinks significantly as the plaques and tangles spread throughout the brain (Yamazaki et al., 2019). AD has been a major burden to society and the main cause of death in older people. The specific pathogenesis of AD is still unclear, and it is urgent that we carry out in-depth research to block the progression of this disease, improve the survival rates of patients, and provide new countermeasures for clinical treatment.

Accumulated evidence has suggested that mitochondrial dysfunction contributes to the pathogenesis of AD and aging-related senile dementia (Moreira et al., 2007; Fukui and Moraes, 2008; Cai and Tammineni, 2016).

The non-coding RNAs account for major proportion of all transcripts according to the project Encyclopedia of DNA Elements (ENCODE) (Consortium, 2012). Long non-coding RNAs (lncRNAs) are greater than 200 nucleotides in length without the protein-coding function (Prinz et al., 2019). Emerging evidence has demonstrated that lncRNAs represent a novel class of pivotal regulators of gene functions and multiple physiological events (Wang et al., 2018, 2019; Yamazaki et al., 2018). They have been found to maintain sub-cellular architecture, stabilize protein complex, and participate in multiple biological processes (Del Vecchio et al., 2018; Gutschner et al., 2018; Liu et al., 2018; Wang et al., 2019; Yan et al., 2019; Yu et al., 2019). First discovered in 2007, nuclear enriched abundant transcript 1 (NEAT1) plays crucial roles both in carcinogenesis (Klec et al., 2019) and non-cancerous diseases, such as neurodegeneration and inflammation (Prinz et al., 2019). NEAT1_1 and NEAT1_2 are two isoforms of NEAT1, which are related lncRNAs that accumulate to high levels in the nucleus (Sasaki et al., 2009). NEAT1 exerts different consequences depending on different downstream mechanisms.

The earliest features of AD have been linked to mitochondrial dysfunction and synaptic damage, including reduced energy production, reactive oxygen species generation, and hypo-metabolisms (Swerdlow, 2012; Fang et al., 2015; Yu et al., 2016). Mitochondrial dysfunctions are critical for the onset and development of AD pathology. Mitophagy is a type of cargo-specific autophagy that is in charge of the clearance of aged or damaged mitochondria. Parkin-mediated mitophagy is a key pathway of mitochondrial quality control. PTEN-induced putative kinase 1 (PINK1) functions as an important regulator in the pathogenesis of AD (Du et al., 2017). PINK1 plays several important roles in the maintenance of mitochondrial integrity and function via mitophagy. A previous study has shown that the expression level of PINK1 is associated with the pathology of AD. Restoring PINK1 can attenuate the Aβ production and amyloid-associated pathology in an AD model via mitophagy (Du et al., 2017).

Mitophagy regulation has emerged as a central problem in the pathogenesis of AD and is a clear therapeutic target for early interference. In this work, we found that the expression level of NEAT1 was upregulated during aging in an APP/PS1 transgenic mouse model. The function and mechanism of NEAT1 in AD were studied. We established a causative link between mitophagy deficits and lncRNA expression in a physiological AD model.

MATERIALS AND METHODS

Reagents

An Aβ ELISA kit was obtained from BIKW Co., Ltd. (Beijing, China). Antibodies against Ubiquitin (Cat.3936), Aβ (Cat.8243), NEDD4L (Cat.5344), PINK1 (Cat.6946), LC3 (Cat.4108), OPTN (Cat.58981), p62 (Cat.885885), and Actin (Cat.3700) were obtained from Cell Signaling Technology (United States). FITC labeled Goat anti Rabbit IgG (Cat.65-6111) and Cyanine5-labeled Goat anti mouse IgG (Cat.M32018) were purchased from ThermoFisher (United States). Antibodies for HA and FLAG were purchased from Sigma (United States). Anti-FLAG M2 magnetic beads (Cat.M8823) and anti-HA magnetic beads (Cat.L-1009) were purchased from Lingyin, Co., Ltd. (Shanghai, China). The magnetic RNA-Protein Pull-Down Kit (Cat.20164) was purchased from ThermoFisher (United States). Real-time PCR kits (Cat.DRR019A) were from Takara (Japan). PINK1, sh-PINK1, NEAT1, and sh-NEAT1 recombinant AAV2 were purchased from Genechem (China). Oligos of siRNAs for PINK1, OPTN, and LC3 were purchased from GemePharma (China).

Animals

APP/PS1 transgenic mice were purchased from the Laboratory Animal Centre of Xiangya Medical School (Xiangya, China). These animals were bred and housed in standard cages in a climate-controlled room (22 ± 1°C and 50 ± 5% humidity) with 12-h light–dark cycles. The study protocol was approved by the Institutional Animal Care and Use Committee (IACUC) of Central South University (Hunan, China), and all experiments were performed according to the Guidelines of the Association for Assessment and Accreditation of Laboratory Animal Care. The mice were grouped into an untreated control group, an intrahippocampal injection of AAV2-PINK1 (5×10^9 pfu/mouse) group, an intrahippocampal injection of AAV2-shNEAT1 group (5×10^9 pfu/mouse), and an intrahippocampal injection of AAV2-shNEAT1/shPINK1 group (5×10^9 pfu/mouse). Each group contained eight mice. At 60 days post-injection, the mice were subjected to Morris water maze (MWM) testing as previously described (Morris, 1984).

Cell Culture

HEK293T, SH-SY5Y, and N2A-APPsw cells were cultured in DMEM supplemented with 10% FBS in a 5% CO_2 atmosphere at 37°C. SH-SY5Y cells were plated in 24-well plates (5×10^5 cells per well) 2 h before the transfection. The cells were transfected with indicated plasmids and cultured for another 24 h, and the cells were then harvested for analysis.

RNA Isolation and RT-PCR Analysis

The mRNA expression was detected by real-time PCR. Total RNA was extracted from brains using an RNA isolation plus kit according to the manufacturer's instructions. PCR product formation was monitored continuously using an ABI 7500. Primer sequences for real-time PCR were NEAT1 (mouse), 5′ TGGCTAGCTCAGGGCTTCAG 3′ (sense), 5′-TCTCCTTGCCAAGCTTCCTTC 3′ (anti-sense); GAPDH (Mouse), 5′ GTATTGGGCGCCTGGTCACC 3′ (sense), and 5′ CGCTCCTGGAAGATGGTGATGGT 3′ (anti-sense). Relative gene expression was normalized to GAPDH, and fold change was calculated using the ΔΔCt method.

RNA Pull-Down Assay

In vitro transcription of NEAT1 and biotin labeling were performed to obtain the biotin-labeled NEAT1 RNAs following

the manufacturer's instructions. The biotinylated sense or antisense NEAT1 was incubated with SH-SY5Y cell lysis (with RNAse inhibitor) overnight at 4°C. Streptavidin beads were used to purify the interacting complexes for 1 h at room temperature, followed by mass spectrometry analysis or immunoblotting using a specific antibody to PINK1 or NEDD4L.

RNA Immunoprecipitation

0.3% Formaldehyde was used to treat SH-SY5Y cells for 10 min at 37°C. After that, the sample was treated with 0.125 M glycine for 5 min at RT. Cells were then washed with PBS buffer three times and centrifuged at 1500 r/min for 2 min. The pellet was then re-suspended in RIPA buffer (1 mM cocktail, 0.1% SDS, 0.5 mM DTT, 50 mM Tris, pH 7.4, 0.5% sodium deoxycholate, 150 mM NaCl, and 1 mM EDTA). The cell lysate was incubated on ice for 30 min with an interval vortex. Antibodies against PINK1, NEDD4L, or IgG control were incubated overnight with the cell lysate at 4°C. Protein G dynabeads were used to recover the RNA/protein complex, and this was followed by washing with RIPA buffer. Finally, the RNA was isolated with Trizol and quantified by real-time PCR.

Western Blot

Cell lysates and pull-down samples were denatured and loaded to 10% SDS-PAGE. After that, the proteins were transferred onto PVDF membranes, followed by milk blocking and incubation with primary (anti-P62, anti-OPTN, anti-NEDD4L, anti-HA, anti-FLAG, and anti-Ubiquitin) and respective second antibodies.

Aβ Measurement

Brain homogenates or N2A-APPsw cultured cells were incubated in 5 M guanidine HCl and 50 mM Tris HCl (pH 8.0) overnight. The concentrations of Aβ were analyzed using the commercially ELISA kits following the manufacturer's instructions. For Aβ immunohistochemistry staining, sections were prepared from 4% paraformaldehyde-fixed brain and stained with Aβ antibody. The positive staining area was determined by image analysis. The investigator was blinded to the mouse genotype.

ATP Level and Cytochorme C Oxidase Activity

ATP levels were measured using the Bioluminescence Assay Kit (Roche) according to the manufacturer's instruction as previously described (Yu et al., 2016). Briefly, the mice were anesthetized, and the brains were quickly removed. The hippocampi were homogenized using a lysis buffer followed by centrifuging at 12,000 r/min for 10 min. The ATP levels in subsequent supernatants were measured. The Cytochrome C Oxidase (CcO) activity of mitochondrial fractions was measured as previously described (Fang et al., 2015).

Statistical Analysis

Each experiment was carried out with triplicate samples. Generally, the experiments were repeated three times. Data are presented as mean ± SE. Difference between two groups was analyzed by respective tests using GraphPad. $p < 0.05$ means statistically significant, * means $p < 0.05$, and ** means $p < 0.01$.

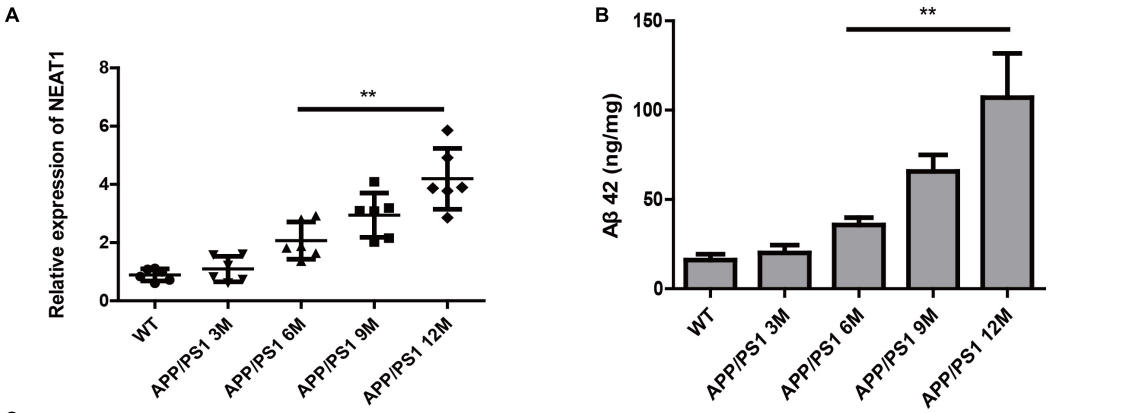
RESULTS

LncRNA NEAT1 Was Elevated in the AD Mouse Model and Interacted With PINK1 and NEDD4L

It has been shown that several lncRNAs were dysregulated in the human brain during aging. By investigating differentially expressed lncRNAs in normal and AD brains, we and others have found that the expression of NEAT1 was significantly increased in both aged and AD brains (Cao et al., 2019). To further demonstrate the function of NEAT1 in the AD process, we assayed the expression level of NEAT1 in brains of APP/PS1 mice. NEAT1 was significantly increased in old APP/PS1 mice (over 6 months old) in a time-dependent manner but not in younger littermates (**Figure 1A**). The expression level of NEAT1 was completely normal in 3-month-old APP/PS1 mice. Similarly, amyloid-β levels showed a similar pattern in brains of APP/PS1 mice (**Figure 1B**). To better understand the molecular mechanisms of NAET1 in pathology of AD, we labeled the lncRNA NEAT1 with biotin and performed an RNA pull-down assay, followed by mass spectrometry. The top nine NEAT1 interaction proteins were listed (**Figure 1C**). PINK1 was identified as a potential NEAT1 interaction protein. As PINK1 signaling participated in AD pathogenesis, we performed an independent RNA pull-down assay and western blotting to validate the interaction between NEAT1 and PINK1. Biotin-labeled NEAT1 could interact with PINK1. Interestingly, NEAT1 could interact with the E3 ubiquitin ligase NEDD4L (**Figure 1D**). Furthermore, the RNA immunoprecipitation experiment using the NEDD4L or PINK1 antibody was carried out to verify the specific interaction (**Figure 1E**).

NEDD4L Interacts With PINK1 and Targets PINK1 for Degradation

PINK1 played important roles in orchestrating the parkin-dependent mitophagy. Ubiquitination plays a conserved role in regulating protein turnover. The endogenous co-immunoprecipitation experiment using a NEDD4L antibody demonstrated that NEDD4L could interact with PINK1 in SH-SY5Y cells (**Figure 2A**). Ectopically expressed FLAG-tagged PINK1 could also be co-immunoprecipitated with NEDD4L (**Figure 2B**). GST pull-down assays showed that PINK1 directly interacted with NEDD4L *in vitro* (**Figure 2C**). PINK1 and NEDD4L did colocalize mostly in the extranuclear region of the SH-SY5Y cells (**Figure 2D**). A Cycloheximide Chase Assay was used to measure the half-life of PINK1. NEDD4L overexpression could exacerbate the degradation of PINK1 in SY-SH5Y cells (**Figure 2E**). NEDD4L overexpression decreased PINK1 protein levels, and NEDD4L knockdown increased the protein level of PINK1 (**Figure 2F**). These results indicated that NEDD4L could interact with PINK1 and target PINK1 for degradation.



C

Gene names	Peptides control	Peptides Pull Down	Score	Intensity Pull Down
PINK1	0	21	323.31	23070000000
USP9X	0	3	133.31	341560000
RIMBP2	1	1	6.8286	299680000
TUBB4B;TUBB4A	4	6	26.567	85776000
GAR1	0	2	11.952	55243000
MPC2	0	2	27.897	51366000
CTSD	0	4	22.663	47995000
HACD3	0	4	43.651	47521000
NEDD4L	0	6	45.551	47145000

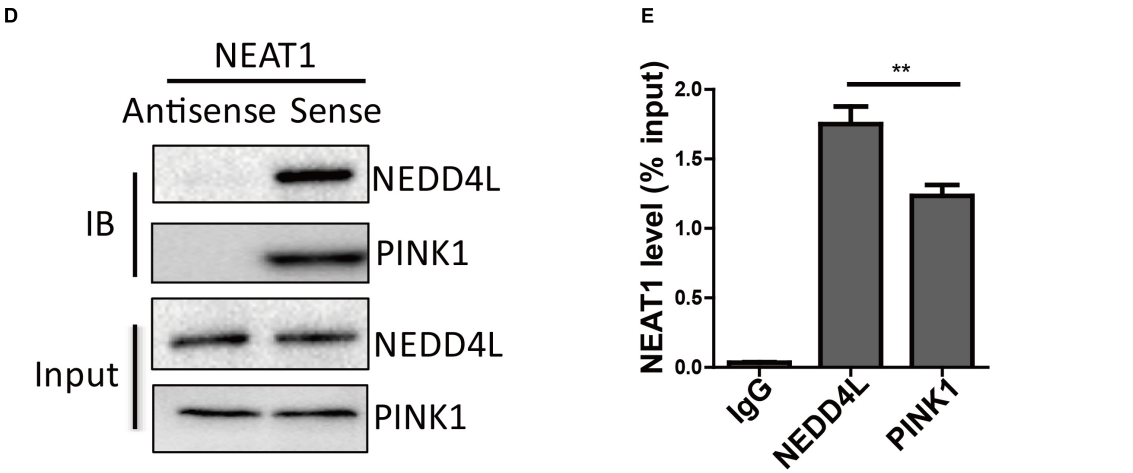


FIGURE 1 | NEAT1 is upregulated in AD mouse models and interacts with PINK1 and NEDD4L. **(A)** Expression of NEAT1 in the hippocampus from APP/PS1 mice of indicated ages was determined by real time PCR. $n = 5$ mice per group. Two-tailed unpaired *t*-test is performed, $^{**}p < 0.01$. **(B)** Amyloid-β levels in the hippocampus from APP/PS1 mice of indicated ages were measured by ELISA. $n = 5$ mice per group. Bars indicate mean ± SEM, $^{**}p < 0.01$. **(C)** Proteins bound to biotinylated NEAT1 in SH-SY5Y cells were identified using mass spectrometry and the top candidates were listed. **(D)** Proteins bound to biotinylated NEAT1 were analyzed by western blot using NEDD4L and PINK1 antibodies in SH-SY5Y cells. **(E)** The recovery of NEAT1 is determined by immunoprecipitation with PINK1 or NEDD4L antibody in SH-SY5Y cells. IgG served as negative control. Data are represented as mean ± SEM of three experiments. A two-tailed unpaired *t*-test was performed, and ** means $p < 0.01$ vs. IgG group.

NEAT1 Promoted NEDD4L-Mediated PINK1 Degradation and Impaired PINK1-Dependent Autophagy

NEAT1 may be a regulator of mitophagy through interacting with NEDD4L and PINK1. NEAT1 overexpression could promote the interaction of PINK1 with NEDD4L (**Figure 3A**). NEAT1 overexpression significantly increased the ubiquitination level of PINK1, while NEAT1 knockdown decreased the ubiquitination level of PINK1 (**Figure 3B**). Moreover, the protein level of PINK1 was increased via NEAT1 knockdown at the same time the autophagy markers were evaluated. Protein levels of P62, OPTN, and LC3 were elevated upon NEAT1 knockdown, whereas these markers were decreased when NEAT1 was overexpressed

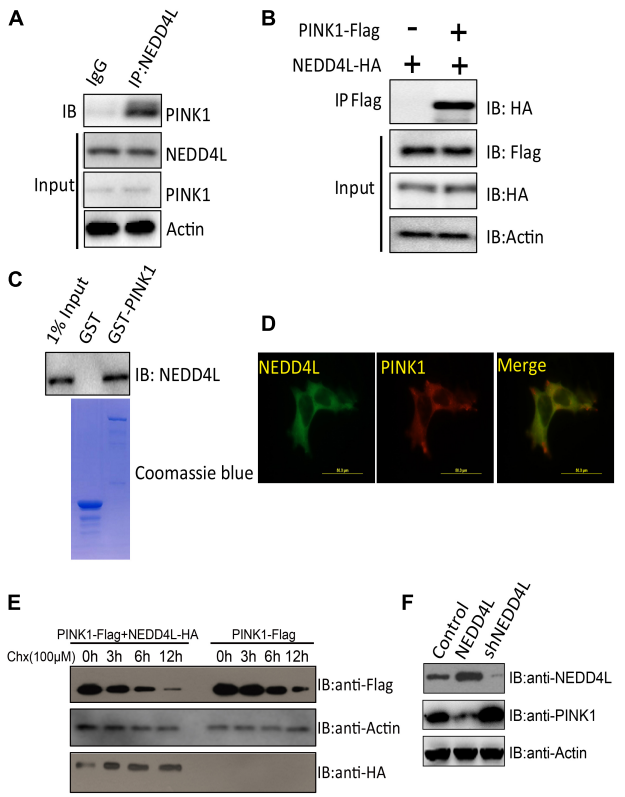


FIGURE 2 | PINK1 was ubiquitinated and degraded by E3 ligase NEDD4L. **(A)** Endogenous NEDD4L interacted with PINK1 in SH-SY5Y cells. SH-SY5Y lysates were immunoprecipitated by an anti-NEDD4L antibody and subjected to western blotting using an anti-PINK1 antibody. **(B)** Flag-tagged PINK1 interacted with NEDD4L-HA. PINK1-Flag and NEDD4L-HA were transfected into SH-SY5Y and co-immunoprecipitation assay was performed. **(C)** GST pull-down assays indicate that recombinant GST-tagged PINK1, but not GST, interacts only with His6-tagged NEDD4L. **(D)** NEDD4L co-localized with PINK1 in SH-SY5Y cells. Immunofluorescence experiments were performed using indicated primary antibodies and respective FITC labeled or Cy5 labeled secondary antibodies. Scale bar: 50 μm. **(E)** NEDD4L-HA and PINK1-Flag expressing SH-SY5Y cells were treated with Cycloheximide (100 μM) for indicated hours. The cell lysates were subjected to western blotting using FLAG or HA antibodies. **(F)** NEDD4L-HA or knockdown plasmids were introduced into SH-SY5Y cells. The cell lysates, 36 h later, were subjected to western blotting.

(**Figure 3C**). The Aβ level in N2A-APPsw cells was significantly decreased when NEAT1 was knocked down. The Aβ reduction mediated by NEAT1 knockdown depends on PINK1, OPTN, and LC3, as depletion of these autophagy adaptor can reverse the Aβ reduction (**Figures 3D,E**).

NEAT1 Regulates Amyloid-β Accumulation in AD Mouse Model

The protein level of PINK1 decreased in 6-month-old and 9-month-old mice as well as 12-month-old APP/PS1 mice compared with the normal mice (**Figure 4A**). AAV-mediated NEAT1 overexpression exacerbated the Aβ production in 9-month-old APP/PS1 mice, whereas the AAV-mediated NEAT1 knockdown inhibited Aβ production (**Figure 4B**). The enzyme activity of CcO was significantly declined in APP/PS1 hippocampus compared to the normal controls. The activity of CcO in the hippocampus of APP/PS1 mice was further reduced with administration of AAV-NEAT1, whereas CcO activity in the NEAT1 knockdown group was restored to the levels similar to non-transgenic mice (**Figure 4C**). In parallel, the decrease of ATP level in APP/PS1 hippocampus was reversed via knocking down NEAT1 (**Figure 4D**). In the brain sections of 9-month-old APP/PS1 mice, the amyloid beta staining shows the similar pattern (**Figure 4E**).

NEAT1 Knockdown Ameliorates Cognitive Impairments in AD Mice

To evaluate the effects of NEAT1 on the pathophysiology of AD, spatial memory was assessed using the MWM. A two-way ANOVA was performed to analyze the latency to platform. Compared with their wild-type littermates, the 12-month-old APP/PS1 mice exhibited a significantly slower learning rate, indicating cognitive deficits in these mice [day 3, $P < 0.001$]. Notably, PINK1 overexpression or NEAT1 depletion significantly ameliorated learning and memory impairment in these APP/PS1 mice (**Figure 5A**). Compared with the normal mice, the PINK1 overexpression or NEAT1 depletion APP/PS1 mice crossed the platform area more often (**Figure 5B**) and took less time to reach the position of platform (**Figure 5C**). PINK1 depletion resulted in the spatial memory defect in the NEAT1-injected APP/PS1 mice, suggesting that the function of NEAT1 was PINK1 dependent (**Figures 5A,C**). There was no detectable difference in swimming distance or velocity between different groups, indicating that NEAT1 or PINK1 had little influence on the motor ability or motivation of these mice (**Figures 5D,E**). Together, our data indicate that the depletion of NEAT1 ameliorates cognitive deficits in AD model mice.

DISCUSSION

Alzheimer's disease has been known to science for more than 100 years, but the pathological mechanism is still unclear. Up to now, there are more than 30 hypotheses trying to explain the pathogenesis of AD, including—but not limited to—the well-known Aβ deposition, NFTs, neuroinflammation, and craniocerebral trauma. With the rapid development of life science in recent years, the industry's in-depth understanding of the complex mechanism of AD has continuously expanded. In the present study, we found that lncRNA NEAT1 was upregulated in APP/PS1 mice that were over 6 months old in a time-dependent manner but not in younger littermates with the same trends of Aβ levels in the hippocampus. In the meantime, using an RNA pull-down assay, PINK1 and E3 ubiquitin ligase NEDD4L were identified as potential NEAT1 interaction proteins. NEAT1 could regulate the interaction between PINK1 and NEDD4L. Our data suggested a working model of NEAT1, illustrated in **Figure 6**, in which the upregulated NEAT1 promoted the ubiquitination and degradation of PINK1, which finally inhibited the autophagy signaling and gave rise to the amyloid accumulation and cognitive decline.

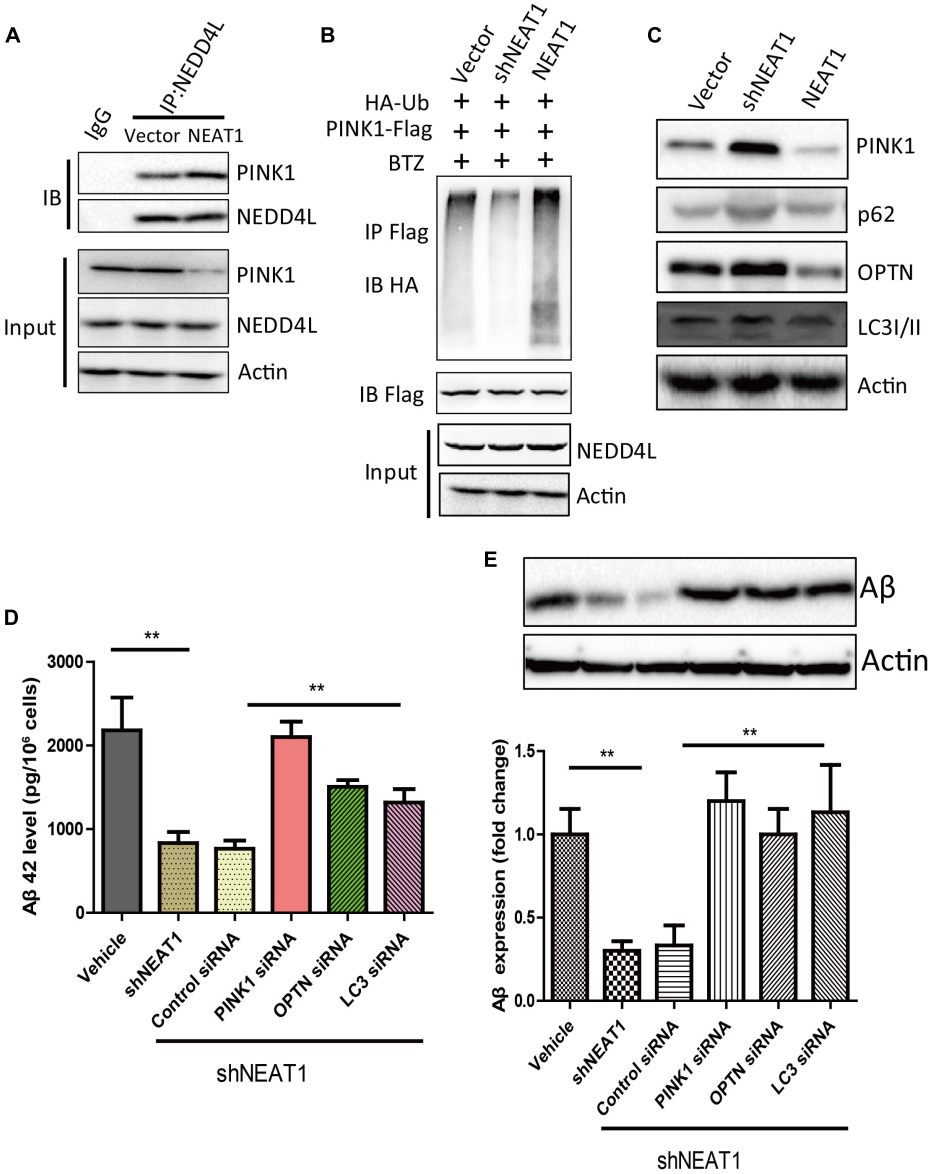


FIGURE 3 | NEAT1 promoted NEDD4L mediated PINK1 degradation and impaired PINK1-dependent autophagy. **(A)** NEAT1 promoted interaction of NEDD4L and PINK1 in SH-SY5Y cells. SH-SY5Y cells were transfected with NEAT1 and cell lysates were immunoprecipitated by anti-NEDD4L antibody and subjected to western blotting using anti-PINK1 antibody. **(B)** NEAT1 regulated ubiquitination of PINK1 in SH-SY5Y cells. NEAT1 or knockdown plasmids accompanied by HA-ubiquitin and PINK1-Flag were delivered into SH-SY5Y cells. The cell lysates were subjected to immunoprecipitation assay followed by western blotting with an anti-Ubiquitin antibody. **(C)** NEAT1 regulated PINK1-dependent autophagy. SH-SY5Y cells transfected with NEAT1 and shNEAT1 were subjected to western blot using PINK1, P62, OPTN, and LC3I/II. **(D)** NEAT1 regulated amyloid-β accumulation via autophagy signaling in N2A-APPsw cells. The levels of amyloid-β42 (Aβ42) in N2A-APPsw cells transduced with lentivirus encoding shNEAT1 and co-transfected with siRNA against PINK1, OPTN, LC3, or control siRNA were measured by amyloid-β ELISA ($n = 4$). $^{**}p < 0.01$ **(E)** Representative immunoblot bands for amyloid-β proteins in N2A-APPsw cell lysates with above treatment, and β-actin served as a loading control. The bar graph presents the quantification of bands for amyloid-β relative to β-actin. $n = 4$ independent experiments of each group. $^{**}p < 0.01$.

The majority of human transcripts are non-coding RNAs, which are composed of microRNAs (miRNAs), piRNAs, siRNAs, cirRNAs, and the lncRNAs (Klec et al., 2019). Despite the non-coding property, lncRNAs are key functional regulators in cellular processes. NEAT1 was part of paraspeckles and was discovered in 2007. Dysregulation of lncRNA NEAT1 was found in an increasing number of diseases. In many cases, NEAT1 functions as a competing endogenous RNA (ceRNA) that sponges miRNA. The transcription or translation of the miRNA downstream targets were hampered and ultimately contribute to diseases. This oncogenic role of NEAT1 in cancers suggests that it may be a promising biomarker and also a candidate therapeutic target pending the completion of further studies into the underlying mechanisms (Carpenter et al., 2013; Ii et al., 2014;

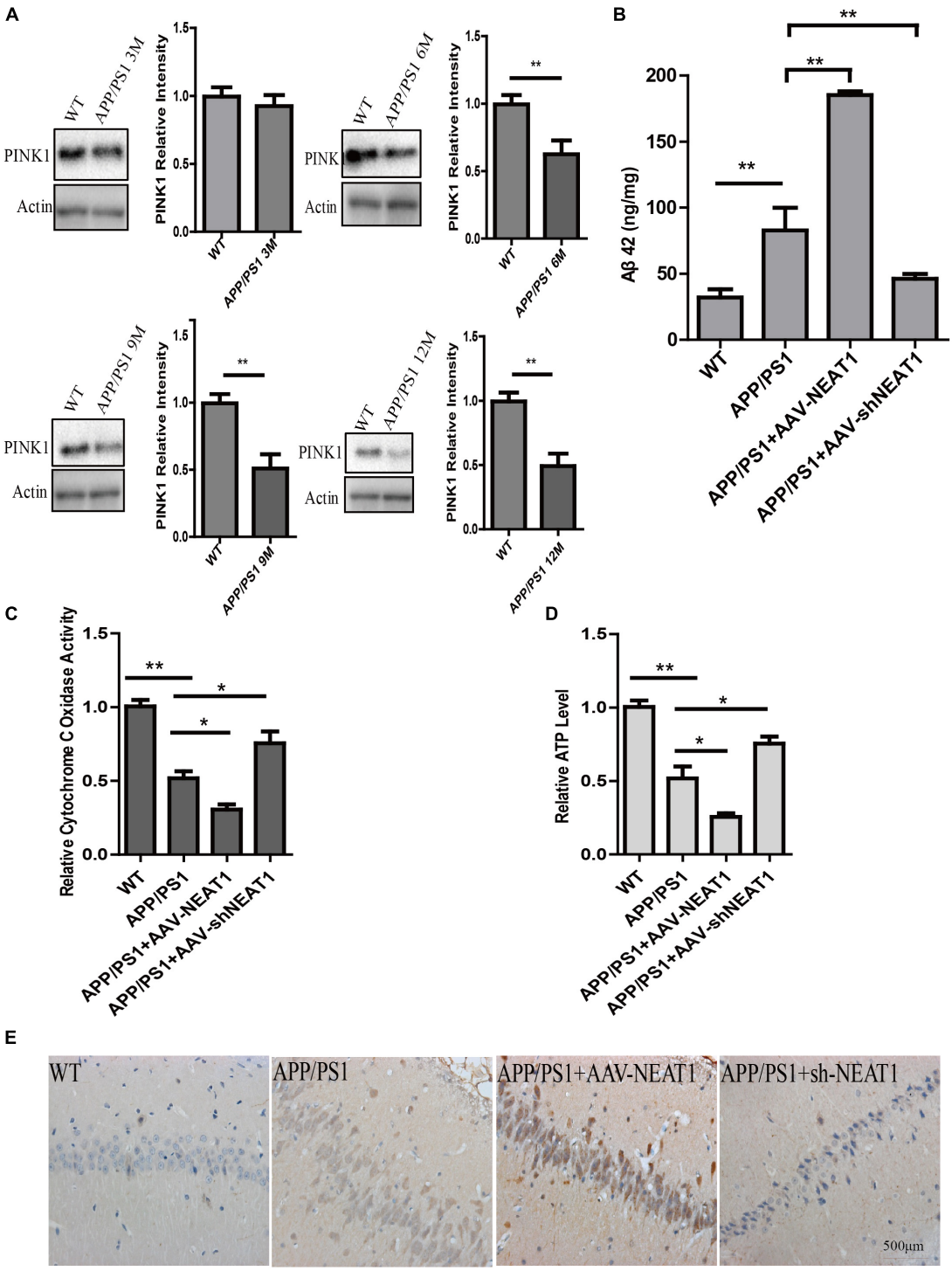


FIGURE 4 | NEAT1 regulates amyloid-β accumulation in AD mouse model. **(A)** Protein level of PINK1 was decreased in the hippocampus of APP/PS1 mice at 6, 9, and 12 months. Hippocampal tissues from APP/PS1 mice of indicated ages were subjected to western blotting using a PINK1 antibody. Representative western blot is shown in the upper panel. $^{**}p < 0.01$, $n = 6$. **(B)** NEAT1 regulated Aβ levels in AD mouse model. Amyloid-β (Aβ) levels in the hippocampus of the 9-month-old APP/PS1 mice, 2 months post-intrahippocampal injection of AAV2-NEAT1 and AAV2-shNEAT1, were measured by ELISA. $^{**}p < 0.01$, $n = 7$ mice per group. **(C,D)** Cytochrome C Oxidase activity **(C)** and ATP levels **(D)** in brain tissues of the indicated mice. $n = 7$ mice per group. $^{*}p < 0.05$, $^{**}p < 0.01$. **(E)** Representative images of Aβ staining in brain sections of the indicated mice.

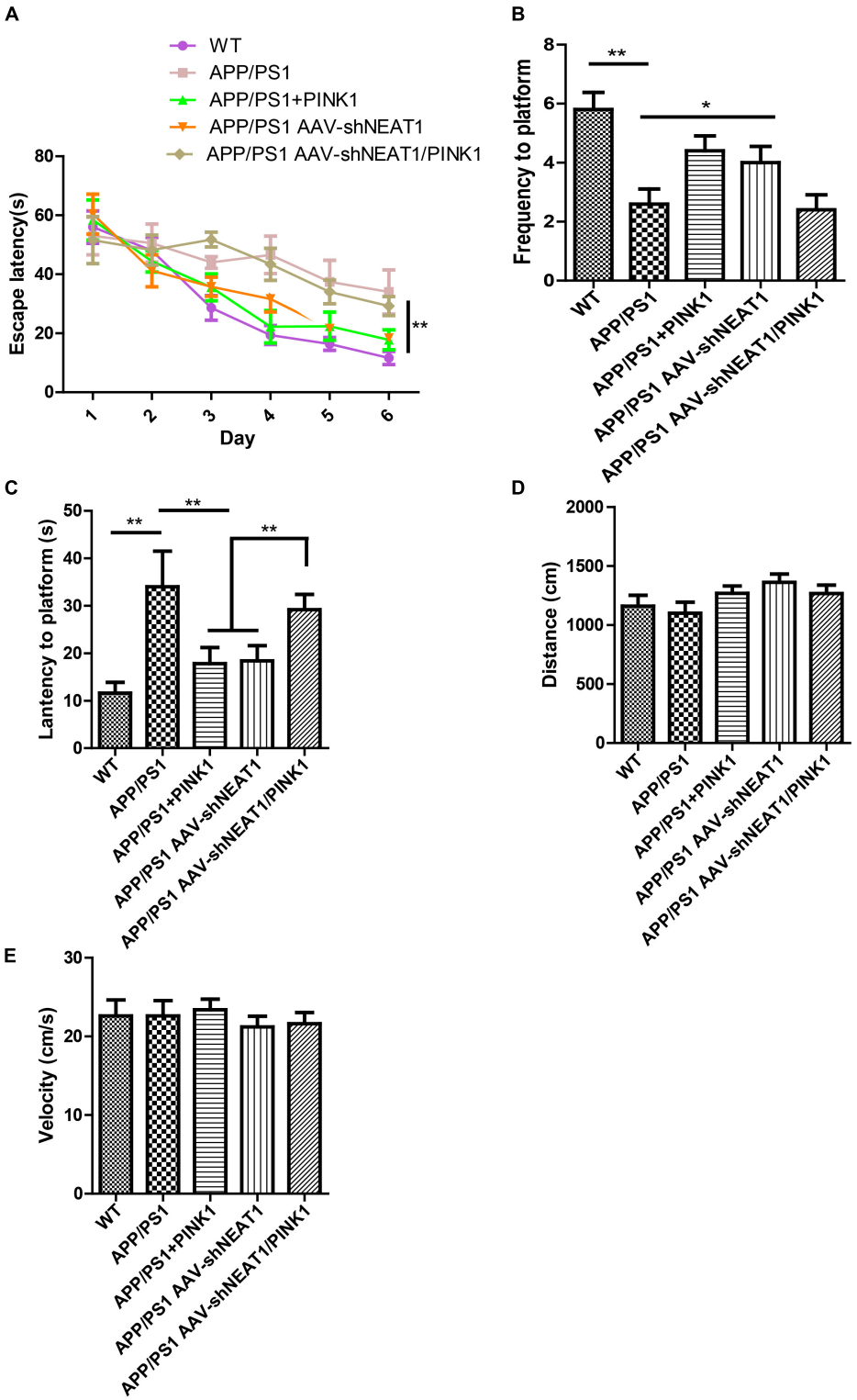


FIGURE 5 | NEAT1 knockdown ameliorates cognitive impairments in AD mice. **(A)** The learning curves of the mice from the different treatment groups (n = 8 per group). 9-month-old mice were intrahippocampally injected with AAV2-PINK1, AAV2-shNEAT1, and AAV2-shNEAT1/shPINK1; 2 months later, these mice were subjected to Morris water maze testing. The data are presented as the mean ± SEM, analyzed by two-way ANOVA test followed by Bonferroni, $^{*}p < 0.05$, $^{**}p < 0.01$. **(B)** The frequency the target position was passed on day 7 (n = 8 per group). The data are presented as the mean ± SEM, analyzed by Kruskal–Wallis test, $^{**}p < 0.01$. **(C)** The latency to find the platform on day 7 (n = 8 per group). The data are presented as the mean ± SEM, analyzed by one-way ANOVA followed by Bonferroni test, $^{**}p < 0.01$. **(D)** The swimming distance on day 7 (n = 8 per group). The data are presented as the mean ± SEM, analyzed by Kruskal–Wallis test. **(E)** The velocity of these mice on day 7 (n = 8 per group). The data are presented as the mean ± SEM, analyzed by a Kruskal–Wallis test.

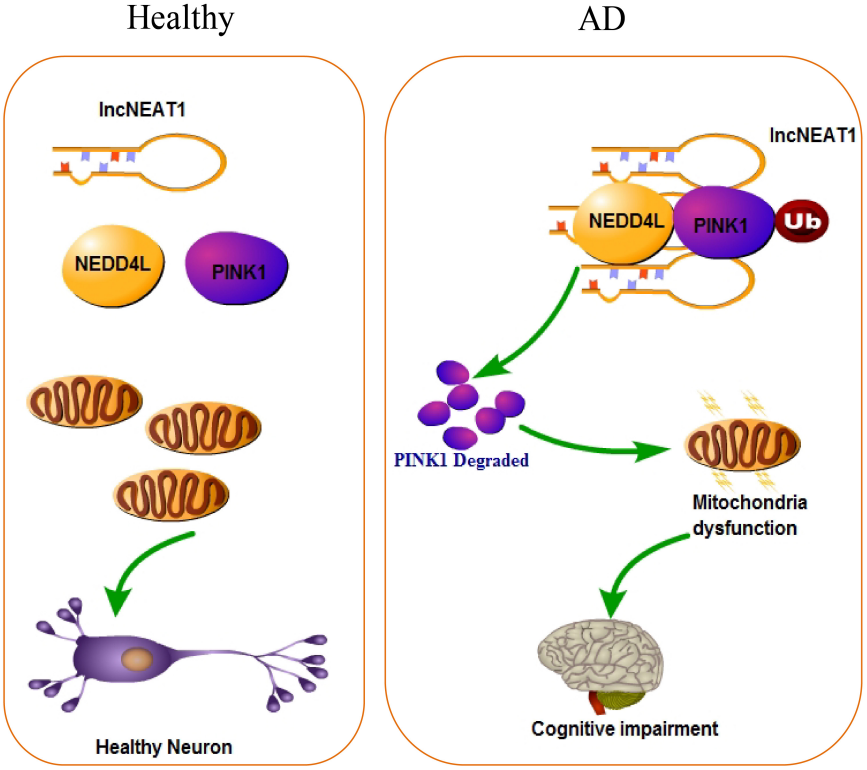


FIGURE 6 | Working model of NEAT1 in healthy neurons and AD.

Liu et al., 2015). Recent studies have indicated that lncRNAs contribute to the development and progression of several brain disorders, including AD (Faghihi et al., 2008; Cao et al., 2019; Yi et al., 2019). Several differentially expressed lncRNAs were identified in human AD brains, including but not limited to n341006, LINC01094, AD-linc1, and NEAT1 (Magistri et al., 2015; Zhou and Xu, 2015; Cao et al., 2019; Zhou et al., 2019). We found that lncRNA NEAT1 was elevated during aging in the APP/PS1 mouse model. A recent study indicated that NEAT1 was significantly elevated in the temporal cortex and hippocampus of AD patients (Spreafico et al., 2018), implying that NEAT1 was a biomarker for AD diagnosis. They further demonstrated that NEAT1 could negatively regulate the expression of cyclin-dependent kinase 5 regulatory subunit 1, an AD related gene, and possibly played a protective role against neuronal death.

NEDD4L is short for neuronal precursor cell-expressed developmentally downregulated 4-like. NEDD4L is a highly conserved eukaryotic E3 ubiquitin ligase, which belongs to the HECT family and is widely expressed in adult mouse brains (Yanpallewar et al., 2016; Zhang et al., 2017). Previous studies showed that NEDD4L regulated plenty of ion channels, including chloride channels, voltage-gated Na^+ channels, voltage-gated K^+ channels, and glutamate transporters (Abriel and Staub, 2005; Bongiorno et al., 2011; Goel et al., 2015). In Parkinson's disease (PD) model, NEDD4L promoted the ubiquitination of glutamate transporters *in vitro* and *in vivo*. NEDD4L knockdown could increase the protein level of glutamate transporters and rescue the motor deficits and tyrosine hydroxylase expression in PD mice, suggesting that NEDD4L could be a potential therapeutic target for the treatment of PD (Zhang et al., 2017). In our study, we demonstrated that NEDD4L was an E3 ubiquitin ligase for PINK1. NEAT1 could increase the interaction of NEDD4L and PINK1, thus promoting the ubiquitination and ubiquitin-dependent proteolysis of PINK1. Our results demonstrated that lncRNA NEAT1 provided a higher degree of complexity to the control of pathogenesis of AD.

Mitochondria provide an essential source of energy and play an important role during development and in AD progression. Cumulative evidence illustrates the importance of mitochondrial quality control in brain function during aging and cognitive deficit (Flannery and Trushina, 2019). Mitophagy was an important regulator of mitochondrial quality control, both in physiological and pathophysiological conditions. It is increasingly recognized that mitophagy is critical for mitochondrial turnover, especially the damaged mitochondrial clearance. PINK1-mediated autophagy signaling promoted the damaged mitochondrial clearance and contributed to amyloid-β degradation and clearance. Depletion of NEAT1 upregulated expression levels of autophagy receptors, such as OPTN, P62, and LC3, in amyloid-β enriched cells. Depletion of NEAT1 showed a reduction in amyloid-β accumulation, while knockdown of PINK1, OPTN, or LC3 abolishes this protective effect, indicating that NEAT1 regulated amyloid pathology via PINK1 activated mitophagy.

Alzheimer's disease represents the leading cause of death in old people across the world. It is invaluable to understand the function of lncRNA NEAT1 in regulating mitophagy which protects brain from cognitive decline. Constitutive mitophagy is a homeostatic mechanism for maintaining mitochondrial quality and global mitochondrial function not only in the brain but also in other tissues. Cumulative data have demonstrated the important role of mitophagy in neuronal degeneration. This study has produced critical insight into the role of lncRNA NEAT1 in AD pathological conditions, and will fundamentally advance our understanding of the interaction between lncRNA and mitophagy in AD. Furthermore, NEAT1 may be a useful diagnosis biomarker for AD. Our study may provide the basis for novel therapeutic approaches in AD and a wide variety of aging and dementia.

DATA AVAILABILITY STATEMENT

All datasets generated for this study are included in the article/supplementary material.

ETHICS STATEMENT

This study was approved by the Institutional Animal Care and Use Committee (IACUC) of Central South University (Hunan, China), and the experiments were conducted according to the Guidelines of the American Physiological Society.

AUTHOR CONTRIBUTIONS

JieZ conceived and designed the study. ZH, JinZ, and WW carried out the experiments and collected all data. ZH, JieZ, and JunZ drafted the manuscript. All authors read and approved the final manuscript.

FUNDING

The study was supported by grants from the National Natural Science Foundation of China (81571382), Hunan Province Science International Cooperation Projects, Grant (2015WK3010 and 2019JJ50879).

REFERENCES

Abriel, H., and Staub, O. (2005). Ubiquitylation of ion channels. *Physiology* 20, 398–407. doi: 10.1152/physiol.00033.2005

Bongiorno, D., Schuetz, F., Poronnik, P., and Adams, D. J. (2011). Regulation of voltage-gated ion channels in excitable cells by the ubiquitin ligases Nedd4 and Nedd4-2. *Channels* 5, 79–88. doi: 10.4161/chan.5.1.13967

Cai, Q., and Tammineni, P. (2016). Alterations in mitochondrial quality control in Alzheimer's disease. *Front. Cell Neurosci.* 10:24. doi: 10.3389/fncel.2016.00024

Cao, M., Li, H., Zhao, J., Cui, J., and Hu, G. (2019). Identification of age- and gender-associated long noncoding RNAs in the human brain with Alzheimer's disease. *Neurobiol. Aging* 81, 116–126. doi: 10.1016/j.neurobiolaging.2019.05.023

Carpenter, S., Aiello, D., Atianand, M. K., Ricci, E. P., Gandhi, P., Hall, L. L., et al. (2013). A long noncoding RNA mediates both activation and repression of immune response genes. *Science* 341, 789–792. doi: 10.1126/science.1240925

Chen, X. Q., and Mobley, W. C. (2019). Alzheimer disease pathogenesis: insights from molecular and cellular biology studies of Oligomeric Abeta and Tau Species. *Front. Neurosci.* 13:659. doi: 10.3389/fnins.2019.00659

Consortium, E. P. (2012). An integrated encyclopedia of DNA elements in the human genome. *Nature* 489, 57–74. doi: 10.1038/nature11247

Del Vecchio, F., Lee, G. H., Hawezi, J., Bhome, R., Pugh, S., Sayan, E., et al. (2018). Long non-coding RNAs within the tumour microenvironment and their role in tumour-stroma cross-talk. *Cancer Lett.* 421, 94–102. doi: 10.1016/j.canlet.2018.02.022

Du, F., Yu, Q., Yan, S., Hu, G., Lue, L. F., Walker, D. G., et al. (2017). PINK1 signalling rescues amyloid pathology and mitochondrial dysfunction in Alzheimer's disease. *Brain* 140, 3233–3251. doi: 10.1093/brain/awx258

Faghihi, M. A., Modarresi, F., Khalil, A. M., Wood, D. E., Sahagan, B. G., Morgan, T. E., et al. (2008). Expression of a noncoding RNA is elevated in Alzheimer's disease and drives rapid feed-forward regulation of beta-secretase. *Nat. Med.* 14, 723–730. doi: 10.1038/nm1784

Fang, D., Wang, Y., Zhang, Z., Du, H., Yan, S., Sun, Q., et al. (2015). Increased neuronal PreP activity reduces Abeta accumulation, attenuates neuroinflammation and improves mitochondrial and synaptic function in Alzheimer disease's mouse model. *Hum. Mol. Genet.* 24, 5198–5210. doi: 10.1093/hmg/ddv241

Flannery, P. J., and Trushina, E. (2019). Mitochondrial dynamics and transport in Alzheimer's disease. *Mol. Cell. Neurosci.* 98, 109–120. doi: 10.1016/j.mcn.2019.06.009

Fukui, H., and Moraes, C. T. (2008). The mitochondrial impairment, oxidative stress and neurodegeneration connection: reality or just an attractive hypothesis? *Trends Neurosci.* 31, 251–256. doi: 10.1016/j.tins.2008.02.008

Goel, P., Manning, J. A., and Kumar, S. (2015). NEDD4-2 (NEDD4L): the ubiquitin ligase for multiple membrane proteins. *Gene* 557, 1–10. doi: 10.1016/j.gene.2014.11.051

Gutschner, T., Richtig, G., Haemmerle, M., and Pichler, M. (2018). From biomarkers to therapeutic targets-the promises and perils of long non-coding RNAs in cancer. *Cancer Metastasis Rev.* 37, 83–105. doi: 10.1007/s10555-017-9718-5

Ii, N. E., Heward, J. A., Roux, B., Tsitsiou, E., Fenwick, P. S., Lenzi, L., et al. (2014). Long non-coding RNAs and enhancer RNAs regulate the lipopolysaccharide-induced inflammatory response in human monocytes. *Nat. Commun.* 5:3979. doi: 10.1038/ncomms4979

Klec, C., Prinz, F., and Pichler, M. (2019). Involvement of the long noncoding RNA NEAT1 in carcinogenesis. *Mol. Oncol.* 13, 46–60. doi: 10.1002/1878-0261.12404

Liu, B., Sun, L., Liu, Q., Gong, C., Yao, Y., Lv, X., et al. (2015). A cytoplasmic NF-kappaB interacting long noncoding RNA blocks IkappaB phosphorylation and suppresses breast cancer metastasis. *Cancer Cell* 27, 370–381. doi: 10.1016/j.ccell.2015.02.004

Liu, X., Liang, Y., Song, R., Yang, G., Han, J., Lan, Y., et al. (2018). Long non-coding RNA NEAT1-modulated abnormal lipolysis via ATGL drives hepatocellular carcinoma proliferation. *Mol. Cancer* 17:90. doi: 10.1186/s12943-018-0838-5

Magistri, M., Velmeshev, D., Makhmutova, M., and Faghihi, M. A. (2015). Transcriptomics profiling of Alzheimer's disease reveal neurovascular defects, altered amyloid-beta homeostasis, and deregulated expression of long noncoding RNAs. *J. Alzheimers Dis.* 48, 647–665. doi: 10.3233/JAD-150398

Moreira, P. I., Siedlak, S. L., Wang, X., Santos, M. S., Oliveira, C. R., Tabaton, M., et al. (2007). Increased autophagic degradation of mitochondria in Alzheimer disease. *Autophagy* 3, 614–615. doi: 10.4161/auto.4872

Morris, R. (1984). Developments of a water-maze procedure for studying spatial learning in the rat. *J. Neurosci. Methods* 11, 47–60. doi: 10.1016/0165-0270(84)90007-4

Prinz, F., Kapeller, A., Pichler, M., and Klec, C. (2019). The implications of the long non-coding RNA NEAT1 in non-cancerous diseases. *Int. J. Mol. Sci.* 20:627. doi: 10.3390/ijms20030627

Sasaki, Y. T., Ideue, T., Sano, M., Mituyama, T., and Hirose, T. (2009). MENepsilon/beta noncoding RNAs are essential for structural integrity of nuclear paraspeckles. *Proc. Natl. Acad. Sci. U.S.A.* 106, 2525–2530. doi: 10.1073/pnas.0807899106

Spreafico, M., Grillo, B., Rusconi, F., Battaglioli, E., and Venturin, M. (2018). Multiple layers of CDK5R1 regulation in Alzheimer's disease implicate long non-coding RNAs. *Int. J. Mol. Sci.* 19:2022. doi: 10.3390/ijms19072022

Swerdlow, R. H. (2012). Mitochondria and cell bioenergetics: increasingly recognized components and a possible etiologic cause of Alzheimer's disease. *Antioxid. Redox. Signal.* 16, 1434–1455. doi: 10.1089/ars.2011.4149

Wang, L., Xia, J. W., Ke, Z. P., and Zhang, B. H. (2019). Blockade of NEAT1 represses inflammation response and lipid uptake via modulating miR-342-3p in human macrophages THP-1 cells. *J. Cell. Physiol.* 234, 5319–5326. doi: 10.1002/jcp.27340

Wang, Y., Hu, S. B., Wang, M. R., Yao, R. W., Wu, D., Yang, L., et al. (2018). Genome-wide screening of NEAT1 regulators reveals cross-regulation between paraspeckles and mitochondria. *Nat. Cell Biol.* 20, 1145–1158. doi: 10.1038/s41556-018-0204-2

Yamazaki, T., Souquere, S., Chujo, T., Kobelke, S., Chong, Y. S., Fox, A. H., et al. (2018). Functional domains of NEAT1 architectural lncRNA induce paraspeckle assembly through phase separation. *Mol. Cell.* 70, 1038–1053. doi: 10.1016/j.molcel.2018.05.019

Yamazaki, Y., Zhao, N., Caulfield, T. R., Liu, C. C., and Bu, G. (2019). Apolipoprotein E and Alzheimer disease: pathobiology and targeting strategies. *Nat. Rev. Neurol.* 15, 501–518. doi: 10.1038/s41582-019-0228-7

Yan, K., Fu, Y., Zhu, N., Wang, Z., Hong, J. L., Li, Y., et al. (2019). Repression of lncRNA NEAT1 enhances the antitumor activity of CD8(+)T cells against hepatocellular carcinoma via regulating miR-155/Tim-3. *Int. J. Biochem. Cell Biol.* 110, 1–8. doi: 10.1016/j.biocel.2019.01.019

Yang, W., Zhou, K., Zhou, Y., An, Y., Hu, T., Lu, J., et al. (2018). Naringin dihydrochalcone ameliorates cognitive deficits and neuropathology in APP/PS1 transgenic mice. *Front. Aging Neurosci.* 10:169. doi: 10.3389/fnagi.2018.00169

Yanpallewar, S., Wang, T., Koh, D. C., Quarta, E., Fulgenzi, G., and Tessarollo, L. (2016). Nedd4-2 haploinsufficiency causes hyperactivity and increased sensitivity to inflammatory stimuli. *Sci. Rep.* 6:32957. doi: 10.1038/srep32957

Yi, J., Chen, B., Yao, X., Lei, Y., Ou, F., and Huang, F. (2019). Upregulation of the lncRNA MEG3 improves cognitive impairment, alleviates neuronal damage, and inhibits activation of astrocytes in hippocampus tissues in Alzheimer's disease through inactivating the PI3K/Akt signaling pathway. *J. Cell. Biochem.* 120, 18053–18065. doi: 10.1002/jcb.29108

Yu, H. M., Wang, C., Yuan, Z., Chen, G. L., Ye, T., and Yang, B. W. (2019). LncRNA NEAT1 promotes the tumorigenesis of colorectal cancer by sponging miR-193a-3p. *Cell Prolif.* 52:e12526. doi: 10.1111/cpr.12526

Yu, Q., Fang, D., Swerdlow, R. H., Yu, H., Chen, J. X., and Yan, S. S. (2016). Antioxidants rescue mitochondrial transport in differentiated Alzheimer's disease trans-mitochondrial cybrid cells. *J. Alzheimer's Dis.* 54, 679–690. doi: 10.3233/JAD-160532

Zhang, Y., He, X., Meng, X., Wu, X., Tong, H., Zhang, X., et al. (2017). Regulation of glutamate transporter trafficking by Nedd4-2 in a Parkinson's disease model. *Cell Death Dis.* 8:e2574. doi: 10.1038/cddis.2016.454

Zhou, M., Zhao, H., Wang, X., Sun, J., and Su, J. (2019). Analysis of long noncoding RNAs highlights region-specific altered expression patterns and diagnostic roles in Alzheimer's disease. *Brief. Bioinform.* 20, 598–608. doi: 10.1093/bib/bby021

Zhou, X., and Xu, J. (2015). Identification of Alzheimer's disease-associated long noncoding RNAs. *Neurobiol. Aging* 36, 2925–2931. doi: 10.1016/j.neurobiolaging.2015.07.015

Conflict of Interest: The authors declare that the research was conducted in the absence of any commercial or financial relationships that could be construed as a potential conflict of interest.

Copyright © 2020 Huang, Zhao, Wang, Zhou and Zhang. This is an open-access article distributed under the terms of the Creative Commons Attribution License (CC BY). The use, distribution or reproduction in other forums is permitted, provided the original author(s) and the copyright owner(s) are credited and that the original publication in this journal is cited, in accordance with accepted academic practice. No use, distribution or reproduction is permitted which does not comply with these terms.

frontiers in Cellular Neuroscience

REVIEW
published: 10 March 2020
doi: 10.3389/fncel.2020.00044

Peroxisomal Dysfunction in Neurological Diseases and Brain Aging

Ndidi-Ese Uzor[1,2], *Louise D. McCullough*[2,3,4] *and Andrey S. Tsvetkov*[1,2,4]*

[1]Department of Neurobiology and Anatomy, University of Texas McGovern Medical School, Houston, TX, United States, [2]The University of Texas Graduate School of Biomedical Sciences, Houston, TX, United States, [3]Department of Neurology, University of Texas McGovern Medical School, Houston, TX, United States, [4]UTHealth Consortium on Aging, University of Texas McGovern Medical School, Houston, TX, United States

Peroxisomes exist in most cells, where they participate in lipid metabolism, as well as scavenging the reactive oxygen species (ROS) that are produced as by-products of their metabolic functions. In certain tissues such as the liver and kidneys, peroxisomes have more specific roles, such as bile acid synthesis in the liver and steroidogenesis in the adrenal glands. In the brain, peroxisomes are critically involved in creating and maintaining the lipid content of cell membranes and the myelin sheath, highlighting their importance in the central nervous system (CNS). This review summarizes the peroxisomal lifecycle, then examines the literature that establishes a link between peroxisomal dysfunction, cellular aging, and age-related disorders that affect the CNS. This review also discusses the gap of knowledge in research on peroxisomes in the CNS.

Keywords: neuronal peroxisomes, peroxisome biogenesis disorders, aging peroxisomes, neurodegenerative disease, peroxisomal dysfunction

OPEN ACCESS

Edited by:
Chao Deng,
University of Wollongong, Australia

Reviewed by:
Björn Spittau,
University Hospital Rostock, Germany
Lorenzo Di Cesare Mannelli,
University of Florence, Italy

***Correspondence:**
Andrey S. Tsvetkov
andrey.s.tsvetkov@uth.tmc.edu

Received: *05 December 2019*
Accepted: *18 February 2020*
Published: *10 March 2020*

Citation:
Uzor N-E, McCullough LD and Tsvetkov AS (2020) Peroxisomal Dysfunction in Neurological Diseases and Brain Aging. Front. Cell. Neurosci. 14:44. doi: 10.3389/fncel.2020.00044

INTRODUCTION

Peroxisomes are small, nearly ubiquitous organelles found in almost all cell types, except mature red blood cells (Gronowicz et al., 1984). Their major functions include the beta-oxidation of very-long-chain fatty acids and lipid peroxidation; as a result of this metabolism, they secrete reactive oxygen species (ROS) as by-products (Reddy and Hashimoto, 2001; Poirier et al., 2006; Lodhi et al., 2015; Park et al., 2019). Peroxisomes also possess enzymes that break down ROS, such as catalase and glutathione peroxidase, which breaks down hydrogen peroxide, and superoxide dismutase, which breaks down superoxide (Nordgren and Fransen, 2014). They degrade prostaglandins, amino acids, polyamines, and purines, and are commonly enriched in the kidneys, liver, pancreas and adrenal glands, which are involved in fat metabolism and detoxification (Magalhães and Magalhães, 1997; Bradford, 2007; Ferdinandusse et al., 2009; Hasegawa et al., 2010; Smith and Aitchison, 2013; Vasko, 2016; Baboota et al., 2019). Furthermore, they are implicated in lipogenic and ROS signaling roles in the heart and intestines (Colasante et al., 2015; Morvay et al., 2017). In the central nervous system (CNS) in particular, peroxisomes synthesize lipids that make up the myelin sheath and cellular membranes, as well as ether phospholipids in neurons and glia; peroxisome dysfunction is also known to impair neuronal migration and membranes (Farooqui and Horrocks, 2001; Powers, 2001; Bottelbergs et al., 2010; Kassmann, 2014). They also play a critical role in breaking down D-serine *via* D-amino acid oxidase (DAO), important in glutamatergic signaling (Sasabe et al., 2014; **Figure 1**). Certain diseases, such as peroxisomal biogenesis disorders, underscore the importance of functional peroxisomes in the CNS. Peroxisomal biogenesis disorders are a subset of diseases where: (1) peroxisomes are either not present, leading to severe neurological phenotypes

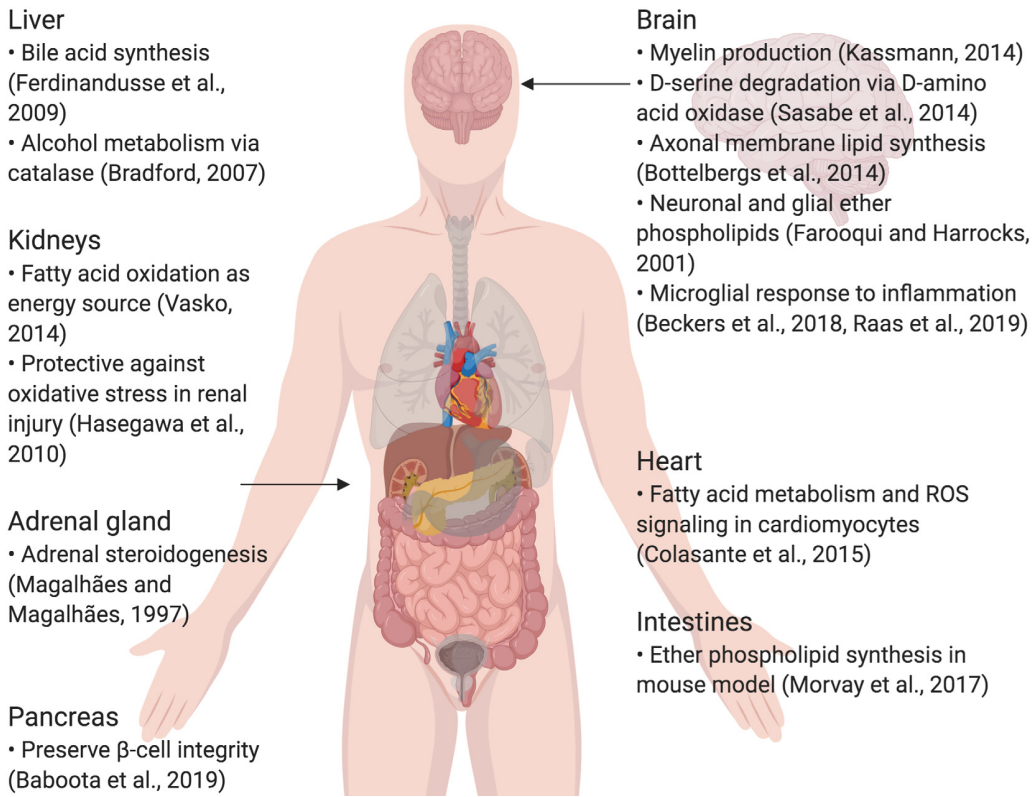


FIGURE 1 | Summary of specialized roles of peroxisomes in some organs, including the brain. Created using BioRender.

(as seen in neonatal adrenoleukodystrophy, where seizures, hypotonia, and loss of vision and hearing occur) and a short lifespan; or (2) genes coding for a single peroxisomal protein are defective, where the symptoms are not as severe (Fujiki et al., 2012; Aubourg et al., 2013). To conclude, peroxisomes are small, but important organelles that play supportive, yet critical roles in maintaining cellular health, especially in the CNS.

This review summarizes peroxisomal biogenesis, and yeast and mammalian pexophagy, with an extended focus on peroxisomes in cellular senescence models, and the peroxisomal dysfunction shared by both age-related neurodegenerative diseases and peroxisomal biogenesis disorders. In all of these conditions, functional peroxisomes move from understudied, secondary organelles to critical sustainers of cellular homeostasis that are disrupted by disease. Future studies will elucidate the role of peroxisomes in aging and CNS function in other diseases and models.

PEROXISOMAL BIOGENESIS

Peroxisomes begin their lifecycle by budding off the endoplasmic reticulum in response to peroxisome proliferator-activated receptor (PPAR) activation due to signaling of the PPAR gamma coactivator-1α (PGC-1α) protein (Bagattin et al., 2010). Unlike mitochondrial proteins, peroxisomal proteins are synthesized on free ribosomes in the cytosol (Koehler, 2000; Jan et al., 2014). After this, peroxisomal proteins are inserted into peroxisomal membranes and matrices by the peroxisomal protein Pex5 (Smith and Aitchison, 2013). Pex5 recognizes the peroxisomal targeting sequence (PTS1) serine-lysine-leucine (SKL), which is found on the C-terminal of many peroxisomal proteins (Brocard and Hartig, 2006). After proteins are inserted, peroxisomes are considered mature and functional. For peroxisomal maintenance, division and maturation, peroxisomes are known to make contact with the endoplasmic reticulum (Hua et al., 2017). To conclude, peroxisomal division and maintenance are modulated by the endoplasmic reticulum, and peroxisomes mature due to peroxisomal protein import into their matrices and membranes.

AUTOPHAGY AND PEXOPHAGY

The peroxisomal lifespan in mammalian cells lasts about 2 to 3 days (Poole et al., 1969; Huybrechts et al., 2009; Moruno-Manchon et al., 2018b). Peroxisomes are then degraded by a selective form of macroautophagy: macropexophagy, which specifically targets peroxisomes (Yang and Klionsky, 2010; Bartoszewska et al., 2012; Cho et al., 2018). A lesser-known form of pexophagy micropexophagy exists, but has only been, so far, observed in yeast models (Strømhaug et al., 2001; Mukaiyama et al., 2004). In macroautophagy, targets for degradation are recognized by a phagophore,

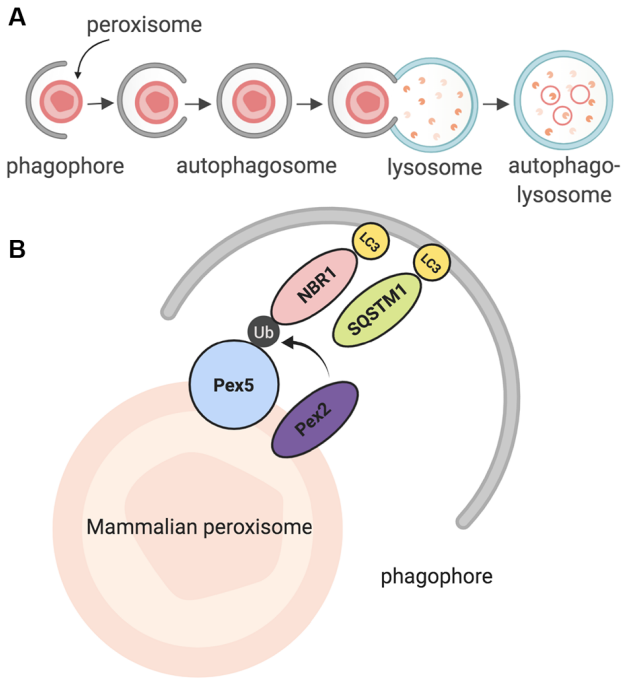
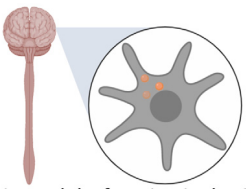


FIGURE 2 | Summary of pexophagy. **(A)** In macropexophagy, a form of macroautophagy selective for peroxisomes, a single membrane known as a phagophore engulfs a peroxisome for degradation. The phagophore matures into an autophagosome, which then fuses with a lysosome. Their fusion creates an autophagolysosome that degrades the target. **(B)** In mammalian systems, pexophagy occurs when Pex2 ubiquitinates Pex5. As a result, autophagy adaptor proteins NBR1 or SQSTM1 (p62) bind to ubiquitinated Pex5, and then eventually bind to LC3 on the phagophore. Due to this process, pexophagy occurs. Created using BioRender.



Peroxisomal dysfunction in the CNS

Age-related CNS diseases and models	Other CNS diseases and models
• Lower level of plasmalogens in Alzheimer's patients' brains (Santos et al., 2005; Kou et al., 2011)	• Various peroxisomal genes negatively affected in peroxisomal biogenesis disorders (Braverman et al., 2016)
• D-amino acid oxidase mutation in amyotrophic lateral sclerosis (Kondori et al., 2017; Kondori et al., 2018)	• Catalase gene expression and protein amount impaired in oxaliplatin neurotoxicity models (Zanardelli et al., 2014)
• Increased number of peroxisomes and catalase expression in ischemic stroke models (Young et al., 2015)	• Increased peroxisomal oxidative stress in doxorubicin chemotherapy neuronal models (Moruno-Manchon et al., 2018b)
• Higher amounts of D-amino acid oxidase in post-stroke dementia patients (Chen et al., 2019)	

FIGURE 3 | Summary of peroxisomal dysfunction in age-related diseases in the CNS, and other diseases that affect the CNS. Created using BioRender.

which matures to form an autophagosome (Reggiori and Tooze, 2009; Mizushima et al., 2011; Feng et al., 2014; Biazik et al., 2015; Moruno Manchon et al., 2015, 2016). The autophagosome envelops the targets and then fuses with an acidic structure known as the lysosome. Together, they form the autophagolysosome, which degrades the target (**Figure 2A**; Nakamura and Yoshimori, 2017; Sasaki et al., 2017). Pexophagy itself uses the same process; however, peroxisomes are targeted *via* particular proteins on their membrane (Jin et al., 2013; Cho et al., 2018). Once recognized, peroxisomes are enveloped by the phagophore, and eventually degraded by the autophagolysosome. Recently, a study in HeLa SH-SY5Ycells and mutant *Drosophila* flies unearthed a novel pexophagy inducer: HSPA9, a heat shock protein which responds to cellular changes such as glucose deprivation (Jo et al., 2020). In summary, peroxisomes that have reached the end of their life cycle are degraded through a selective autophagic process known as pexophagy, due to the enzymatic action of the autophagolysosome.

PEXOPHAGY IN MAMMALS

The foundation of the pexophagy mechanism (and peroxisome biology) began in studies using yeast and plants as models (Lefevre et al., 2013; Williams and van der Klei, 2013; Kao and Bartel, 2015; Young and Bartel, 2016). The *Saccharomyces cerevisiae* yeast homolog of PEX5, Pex5, recognizes cytosolic peroxisomal matrix proteins and delivers them to the peroxisomal membrane (Carvalho et al., 2007). In this model, pexophagy involves Pex3, which is recognized and bound by phosphorylated Atg36, which is itself recognized by Atg8 or Atg11, which are bound to the phagophore (Motley et al., 2012a,b; Farré et al., 2013; Yamashita et al., 2014). In some cases, such as when mitochondria and peroxisomes interact, peroxisomal fission occurs before pexophagy, modulated by Dnm1 and Vps1 (Mao et al., 2014).

Further studies in mammalian models revealed that in order for mammalian pexophagy to begin, PEX5 has to be monoubiquitinated by PEX2, an E3 ubiquitin ligase (Nordgren et al., 2015; Sargent et al., 2016; Germain and Kim, 2020). Previously, it was not clear what directly induces pexophagy; however, recent evidence has shown that increased ROS in the cytosol can stimulate this monoubiquitination, allowing PEX5 to act as a ROS sensor, leading to an increase in peroxisome degradation (Kim et al., 2008; Zhang et al., 2015; Walton et al., 2017). After PEX5 is monoubiquitinated, it is recognized by one of two LC3 adaptor proteins: NBR1, or p62 (SQSTM1); these proteins are then bound to LC3, which is bound to the autophagosome (**Figure 2B**; Kabeya et al., 2000; Kirkin et al., 2009; Deosaran et al., 2013). Together, the interaction of these proteins induces pexophagy in the mammalian cell.

TABLE 1 | Summary of neurological symptoms in neurological and peroxisomal disorders that arise as a result of peroxisomal dysfunction.

Neurological disorder	Peroxisomal protein/function affected	Neurological result
Alzheimer disease	Plasmalogen production	Lowered plasmalogens in the brain, increase in peroxisomal density and VLCAS in gyrus frontalis; peroxisome loss correlated with tau (Santos et al., 2005; Kou et al., 2011)
Amyotrophic lateral sclerosis (ALS)	D-amino acid oxidase (DAO) enzyme	DAO inactivity; increase in D-serine (Kondori et al., 2017, 2018)
Oxaliplatin neuropathy models	Catalase expression and amount	Lipid peroxidation; neuropathic phenotype in an animal model (Zanardelli et al., 2014)
Post-stroke dementia	D-amino acid oxidase (DAO) enzyme	Increase in DAO in patient plasma levels (Chen et al., 2019)
Peroxisomal disorder	**Peroxisomal gene affected**	**Neurological result**
Adult Refsum disease	*PHYH*	Phytanic acid buildup, anosmia, polyneuropathy, hearing and vision loss (Wanders et al., 2011; Wanders and Poll-The, 2017; Gettelfinger and Dahl, 2018)
Infantile Refsum disease	*PEX1*, *PEX3*, *PEX6*, *PEX12*, *PEX26*	Phytanic acid buildup, hypomyelination, hearing and vision loss, polyneuropathy (Warren et al., 2018)
Neonatal adrenoleukodystrophy	*PEX1, PEX2, PEX3, PEX5, PEX6, PEX10, PEX11β, PEX12, PEX13, PEX14, PEX16, PEX19, PEX26*	Buildup of VLCFAs, seizures, hearing loss, neuropathy (Aubourg et al., 1986)
Rhizomelic chondrodysplasia punctata	*PEX7; PEX5* (short isoform)	Epilepsy, seizures, cataracts, neuroregression (Purdue et al., 1999; Malheiro et al., 2015; Landino et al., 2017)
Zellweger syndrome	*PEX1, PEX2, PEX3, PEX5, PEX6, PEX10, PEX11β, PEX12, PEX13, PEX14, PEX16, PEX19, PEX26*	Limited neuronal migration, issues with myelination and brain development (Waterham and Ebberink, 2012; Klouwer et al., 2015)

THE KNOWN: DYSFUNCTIONAL PEROXISOMES AND PEXOPHAGY IN NEURODEGENERATIVE DISEASE, PEROXISOMAL DISORDERS, AND NEUROPATHIES

In the CNS, neurons rely on different forms of autophagy (general and selective) to clear organelles and proteins that are no longer of use; this use of autophagy is due to neurons being post-mitotic and unable to divide, making them more vulnerable than cells that can divide and dilute toxic protein build-up (Moore and Holzbaur, 2016; Evans and Holzbaur, 2019; Stavoe and Holzbaur, 2019a,b). Neuronal autophagy is compartment-specific: it begins at the distal axon, after which axonal autophagosomes then move into the cell soma; the soma also contains its own autophagosomes (Maday and Holzbaur, 2016; Kulkarni et al., 2018; Moruno-Manchon et al., 2018a). Neurons also respond to autophagy inducers differently than other neural cells, underscoring the uniqueness of neuronal autophagy among other forms of autophagy (Ferguson et al., 2009; Pamenter et al., 2012; Bordi et al., 2016; Moruno Manchon et al., 2016; Kulkarni et al., 2019; Sung and Jimenez-Sanchez, 2020).

Interestingly, a common trait of neurodegenerative diseases is the impairment of protein and organelle turnover. Alzheimer disease (AD) is the most common form of dementia in elderly people, with patients exhibiting symptoms such as memory loss and mood changes; the disease eventually destroys neurons in the hippocampus and the cortex (Liang et al., 2008; GBD 2013 Mortality and Causes of Death Collaborators, 2015). In AD, beta-amyloid and tau accumulate, and senescent mitochondria are also present (Zilka et al., 2006; Mitchell, 2009; Nilsson et al., 2013; Shi et al., 2016; Harada et al., 2018). While Parkinson's disease (PD) has a lower prevalence than AD, the number of people with PD has increased over time, as the number of aged people has increased (Dorsey et al., 2018). In PD, neurodegeneration occurs in the substantia nigra, leading to tremors, bradykinesia, postural instability, and rigidity (Jagadeesan et al., 2017). Huntington disease (HD) occurs due to the mutated huntingtin gene and affects the medium spiny neurons in the striatum as well as neurons in the cortex, leading to symptoms such as chorea (jerky movements), rigidity and progressive motor failure (Ehrlich, 2012; Wyant et al., 2017). In Parkinson disease and HD, damaged mitochondria and causative proteins (alpha-synuclein and to a much smaller extent, tau in PD, and mutant huntingtin in HD) accumulate in affected neurons, indicating a problem with autophagy or the ubiquitin/proteasome system (Bloom, 2014; Atik et al., 2016; Zhao et al., 2016; Chiasseu et al., 2017; Zhang et al., 2018; Finkbeiner, 2019; Harrison et al., 2019). Amyotrophic lateral sclerosis (ALS) can be familial or sporadic, leading to neurodegeneration of motor neurons in the CNS; a wide range of genetic mutations can induce this neurodegeneration, including the *SOD1* gene, which codes for superoxide dismutase (Peters et al., 2015). Inducing autophagy improves survival in neuronal ALS models (Barmada et al., 2014). In aging neurons, mitochondrial senescence is observed (Gilmer et al., 2010; Menzies et al., 2017). However, not much is known about how pexophagy, or how peroxisomal proteins are affected by these diseases. First, we will summarize the present data on peroxisomes and pexophagy in neurodegenerative disease studies, then review cases where global peroxisomal disturbances lead to neurodegenerative phenotypes.

In some neurodegenerative diseases, the amount and/or function of peroxisomes may be compromised. In Alzheimer's disease, in which beta-amyloid and tau accumulate in neurons, peroxisomes may be affected. In one study, rat hippocampal cultures with beta-amyloid overexpression were treated with Wy-14.463, a peroxisomal proliferator. This treatment increased peroxisomal number and catalase activity reduced ROS

production, and overall, reduced the degenerative effects of beta-amyloid such as the instability of beta-catenin and the increase of calcium (Santos et al., 2005). In a clinical study, plasmalogens (which peroxisomes synthesize) were negatively affected in post-mortem samples of Alzheimer patients' brains, suggesting a reduction in peroxisomal activity, or a shorter half-life of plamalogens (Goodenowe and Senanayake, 2019). ALS, a disease in which motor neurons degenerate, is linked to peroxisome dysfunction through a genetic mutation that codes for DAO, a peroxisomal enzyme that specifically breaks down D-serine (Kondori et al., 2017, 2018).

In other cases, peroxisome dysfunction, as seen in peroxisome biogenesis disorders, may lead to degenerative neurological symptoms. Peroxisome biogenesis disorders occur due to peroxisome genetic defects, either resulting in single peroxisomal enzyme dysfunction, or in rare cases, the absence of peroxisomes themselves (Braverman et al., 2016). Two groupings of peroxisome biogenesis disorders exist under the Zellweger spectrum (neonatal adrenoleukodystrophy, Zellweger syndrome and infantile Refsum disease), and those outside of it. In Zellweger syndrome, which is inherited in an autosomal recessive manner, one of 13 peroxin (*PEX*) genes is mutated (*PEX1*, *PEX2*, *PEX3*, *PEX5*, *PEX6*, *PEX10*, *PEX11β*, *PEX12*, *PEX13*, *PEX14*, *PEX16*, *PEX19*, *PEX26*), leading to issues with neuronal migration, myelination and brain development (Waterham and Ebberink, 2012; Klouwer et al., 2015; Wang et al., 2015). A cellular model of Zellweger syndrome, particularly of a *Pex5* mutation, has shown an increase in alpha-synuclein Lewy bodies; alpha-synuclein is thought to be a causative agent in Parkinson disease, particularly in familial cases (Yakunin et al., 2010; Riederer et al., 2019). *In vivo*, $Pex5^{-/-}$ mouse brain samples exhibited an increase in alpha-synuclein oligomers in comparison to control, suggesting a correlation between peroxisome dysfunction and PD (Yakunin et al., 2010). Neonatal adrenoleukodystrophy is also an autosomal recessive PBD, but with multiple peroxisomal enzymes affected; infant patients exhibit neurological symptoms such as hearing loss, neuropathy, and demyelination (Aubourg et al., 1986). The last PBD under the Zellweger spectrum is infantile Refsum disease, where a build-up of phytanic acid and other very-long-chain fatty acids in the body (a result of mutated *PEX* genes) leads to neurological symptoms such as mixed neuropathy and hearing loss (Warren et al., 2018). Outside the Zellweger spectrum, adult Refsum disease has similar symptoms to infantile Refsum disease, but the adult-onset disease is due to a mutation in the *PHYH* gene that codes for the peroxisomal enzyme phytanoyl-CoA dioxygenase, which peroxisomes use to break down phytanic acid into pristanic acid (Wanders et al., 2011; Wanders and Poll-The, 2017; Gettelfinger and Dahl, 2018).

Rhizomelic chondrodysplasia punctata (RCDP) is a set of peroxisome biogenesis disorders where peroxisomal genes coding for proteins involved in plasmalogen synthesis are mutated (Barøy et al., 2015). Of note is RCDP type 1, which is due to the mutation of *PEX7*, which codes for PEX7, a peroxisomal receptor that inserts proteins into the peroxisomal membrane that carries peroxisome targeting signal 2 (PTS2; Purdue et al., 1999). This mutation results in severe neurological symptoms such as epilepsy and age-related conditions such as cataracts (Purdue et al., 1999; Malheiro et al., 2015; Landino et al., 2017). In conclusion, peroxisomal dysfunction in the CNS is shared by both neurodegenerative and peroxisomal disorders, leading to disrupted cellular homeostasis that contributes to the pathogenesis of those diseases (**Figure 3** and **Table 1**).

Peroxisomal dysfunction also contributes to neuropathies. For instance, oxaliplatin, a chemotherapy drug for colorectal cancer, is known to cause peripheral neuropathies in patients (Grothey, 2003; Banach et al., 2018). A study uncovered the role of peroxisomes in this mechanism using primary rat astrocyte cultures, a human colon cancer cell line and *ex vivo* analysis of an oxaliplatin neuropathy rat model: peroxisomal catalase expression and levels were impaired with oxaliplatin treatment of cell cultures, and in the dorsal root ganglia and spinal cords of treated animals; this change was also linked with lipid peroxidation in the spinal cord of treated animals (Zanardelli et al., 2014). More recent research has strengthened the role of peroxisome function in neuropathies: the peripheral nerves in peroxisomal mutation mouse models exhibited various abnormalities, such as impaired lysosomal function, accumulation of ganglioside, and a changed redistribution of Kv1 channels and their anchoring proteins that may lead to impaired signaling (Kleinecke et al., 2017). These studies, in conclusion, highlight the important, but previously hidden role that peroxisomal function plays, not only in the CNS but in peripheral nerves as well.

THE SOMEWHAT KNOWN: CELLULAR BIOLOGY OF PEROXISOMES IN NEURAL CELL TYPES

As previously mentioned, peroxisomes are negatively affected by disorders that affect the CNS, leading to undesirable consequences. Some characterization of basal peroxisomal pathways has been made in oligodendrocytes and astrocytes in the CNS (Chistyakov et al., 2014; Di Cesare Mannelli et al., 2014; Aguirre-Rueda et al., 2015; Nury et al., 2018). In the case of neurons, there has also been a focus on peroxisomes (Ballister et al., 2015; Olenick et al., 2016). In hippocampal neurons, it was discovered that preventing tuberous sclerosis complex 2 (TSC2; a regulator of mTORC1 activity) from localizing to peroxisomes led to several axons extending from the neuronal body, indicating a change in morphology (Zhang et al., 2013). In studies of noise-induced hair loss, neurons in mice deficient in pevjakin (a protein associated with neuronal peroxisomes in the auditory pathway), exhibited less peroxisomal proliferation in response to loud sounds in comparison to their wild-type counterparts; peroxisomal proliferation is protective against oxidative stress produced by loud sounds (Defourny et al., 2019). We recently discovered that in neuronal models of doxorubicin treatment (a chemotherapy drug that leads to chemobrain), peroxisomes exhibited increased oxidative stress, which eventually damaged neurons (Kesler, 2014; Wefel et al., 2015; Kesler and Blayney, 2016; Manchon et al., 2016; Moruno-Manchon et al., 2016, 2018b). A more positive link has been found between peroxisomes and ischemic stroke; peroxisomal

volume in *in vitro* and *in vivo* models of ischemia increased after injury, leading to an increased number of peroxisomes, as well as increased expression of peroxisomal catalase (Young et al., 2015). Inhibiting catalase or dynamin-related protein 1 (Drp1), a protein needed for peroxisomal fission, led to increased neuronal susceptibility to death from oxygen-glucose deprivation (OGD), a cellular model of ischemic stroke (Young et al., 2015). These findings inspired a clinical study, which investigated the link between post-stroke dementia (PSD) and peroxisomal DAO, an enzyme that oxidizes D-serine; plasma levels of PSD patients had higher levels of DAO, indicating its role in stroke and stroke-related dementia (Chen et al., 2019). In conclusion, these neuronal studies show that peroxisomal dysfunction can contribute to changes in neuronal morphology, increased oxidative stress, and even death in the CNS. Therefore, it is crucial to keep the negative side effects of treatments on various metabolic pathways, including those that involve peroxisomes, in mind.

THE SOMEWHAT KNOWN: CELLULAR BIOLOGY OF PEROXISOMES IN MICROGLIA

The link between peroxisomal function and inflammation has been established in non-CNS models; however, a few microglial studies have shed light on potential peroxisomal dysfunction mechanisms in the brain (Di Cara et al., 2019). For one, deleting the MFP2 peroxisomal enzyme (which is responsible for β-oxidation) in mouse microglia, switched their state to a pro-inflammatory one, but this change did not affect neuronal health or the microglial response to injury (Beckers et al., 2019). Another study looked at a neuron-specific form of MFP2 deletion and discovered that unlike constitutive *Mfp2*$^{-/-}$ knockouts, *Nestin-Mfp2*$^{-/-}$ knockout brains possessed microglia that were not primed for an inflammatory response (Beckers et al., 2018). Microglial peroxisomal dysfunction, as seen in a microglial model deficient in acyl-CoA oxidase 1 (ACOX1), has also been shown to affect catalase activity, the peroxisome, lipid droplet and mitochondrial number in microglia, as well as the induction of interleukin-1β (IL-1β), the repression of interleukin-6 (IL-6) and the increased expression of *Trem2*, which codes for a cell surface protein that plays a role in microglial phagocytosis (Raas et al., 2019). Taking these studies together, it can be assumed that microglial peroxisomal dysfunction affects the inflammatory response of microglia in the brain, directly and indirectly. The results of these microglial studies stress the importance of the peroxisomal role in inflammation of the CNS: peroxisomal dysfunction in microglia may lead to a pro-inflammatory response that negatively affects the whole system.

THE UNKNOWN: PEROXISOMES IN THE NORMAL AGING CNS

Nonetheless, one gap in the literature exists regarding peroxisomes in the aging CNS, that is unaffected by neurodegenerative disease. Non-neuronal senescence studies have shed some light on peroxisomes in aging cells, such as in senescent human fibroblasts, where there is a reported reduction in the import of PTS1-tagged proteins, an increase in hydrogen peroxide and peroxisomal number, and changes in peroxisomal appearance (Legakis et al., 2002). Proteomic analysis of *C. elegans* also shows a reduction of peroxisomal protein import, as well as a reduction in about 30 peroxisomal proteins, including PRX-5, the nematode homolog of PEX5; PRX-5 was also found to be mislocalized in the aged animals, suggesting that peroxisomal proteins were not properly localized (Narayan et al., 2016). Knocking it out reduced brood size, implicating a potential role of PRX-5 in both development and aging (Narayan et al., 2016). Cell type-specific ribosome profiling of *Drosophila melanogaster* oenocytes (cells involved in liver-like processes) revealed that peroxisomal pathways were downregulated with aging (Huang et al., 2019). Some related evidence exists in post-mortem Alzheimer's studies, where there is an increase in peroxisomal density and very-long-chain fatty acids (but a reduction in plasmalogen levels) in neurons in the gyrus frontalis of AD patients, and a loss of peroxisomes in neuronal processes where phosphorylated tau is present (Kou et al., 2011). However, a search of the literature does not currently reveal evidence of peroxisomal perturbations in the normal aging brain. Another gap in the literature is present when investigating how sex, particularly in age-related neurological disease, affects peroxisomes. For instance, there is evidence that a sex difference exists in response to cerebral ischemia, or ischemic stroke, but it is unknown how these sex-associated differences may affect peroxisomes specifically (Siegel and McCullough, 2013; Mirza et al., 2015; Ritzel et al., 2017). Future studies on age-related neurological changes should investigate how peroxisomal pathways are affected, given the important roles that peroxisomes play in the brain, and how they are affected in other related diseases.

CONCLUSION

As small and understudied as they are, there is ample evidence that peroxisomes play a supportive, yet critical role in the maintenance of the CNS; future studies should investigate the treatment of neurological diseases while keeping the peroxisomal role in maintaining cellular homeostasis in mind.

AUTHOR CONTRIBUTIONS

N-EU wrote the manuscript. All authors contributed to manuscript revision and references, read and approved the submitted version.

FUNDING

This work was supported by the 2017–2018 Russell and Diana Hawkins Family Foundation Discovery Fellowship and the National Institutes of Health, Grant No. R01NS094543-02.

ACKNOWLEDGMENTS

Figures were created in BioRender.

REFERENCES

Aguirre-Rueda, D., Guerra-Ojeda, S., Aldasoro, M., Iradi, A., Obrador, E., Ortega, A., et al. (2015). Astrocytes protect neurons from Aβ1–42 peptide-induced neurotoxicity increasing TFAM and PGC-1 and decreasing PPAR-γ and SIRT-1. *Int. J. Med. Sci.* 12, 48–56. doi: 10.7150/ijms.10035

Atik, A., Stewart, T., and Zhang, J. (2016). α-synuclein as a biomarker for Parkinson's disease. *Brain Pathol.* 26, 410–418. doi: 10.1111/bpa.12370

Aubourg, P., Scotto, J., Rocchiccioli, F., Feldmann-Pautrat, D., and Robain, O. (1986). Neonatal adrenoleukodystrophy. *J. Neurol. Neurosurg. Psychiatry* 49, 77–86. doi: 10.1136/jnnp.49.1.77

Aubourg, P., Wanders, R., Dulac, O., Lassonde, M., and Sarnat, H. B. (2013). "Chapter 163 - Peroxisomal disorders," in *Handbook of Clinical Neurology*, eds O. Dulac, M. Lassonde and Harvey B. Sarnat (Amsterdam, Netherlands: Elsevier), 1593–1609.

Baboota, R. K., Shinde, A. B., Lemaire, K., Fransen, M., Vinckier, S., Van Veldhoven, P. P., et al. (2019). Functional peroxisomes are required for β-cell integrity in mice. *Mol. Metab.* 22, 71–83. doi: 10.1016/j.molmet.2019.02.001

Bagattin, A., Hugendubler, L., and Mueller, E. (2010). Transcriptional coactivator PGC-1α promotes peroxisomal remodeling and biogenesis. *Proc. Natl. Acad. Sci. U S A* 107, 20376–20381. doi: 10.1073/pnas.1009176107

Ballister, E. R., Ayloo, S., Chenoweth, D. M., Lampson, M. A., and Holzbaur, E. L. F. (2015). Optogenetic control of organelle transport using a photocaged chemical inducer of dimerization. *Curr. Biol.* 25, R407–R408. doi: 10.1016/j.cub.2015.03.056

Banach, M., Zygulska, A. L., and Krzemieniecki, K. (2018). Oxaliplatin treatment and peripheral nerve damage in cancer patients: a Polish cohort study. *J. Cancer Res. Ther.* 14, 1010–1013. doi: 10.4103/jcrt.jcrt_971_16

Barmada, S. J., Serio, A., Arjun, A., Bilican, B., Daub, A., Ando, D. M., et al. (2014). Autophagy induction enhances TDP43 turnover and survival in neuronal ALS models. *Nat. Chem. Biol.* 10, 677–685. doi: 10.1038/nchembio.1563

Barøy, T., Koster, J., Strømme, P., Ebberink, M. S., Misceo, D., Ferdinandusse, S., et al. (2015). A novel type of rhizomelic chondrodysplasia punctata, RCDP5, is caused by loss of the PEX5 long isoform. *Hum. Mol. Genet.* 24, 5845–5854. doi: 10.1093/hmg/ddv305

Bartoszewska, M., Williams, C., Kikhney, A., Opaliński, €., van Roermund, C. W. T., de Boer, R., et al. (2012). Peroxisomal proteostasis involves a lon family protein that functions as protease and chaperone. *J. Biol. Chem.* 287, 27380–27395. doi: 10.1074/jbc.m112.381566

Beckers, L., Geric, I., Stroobants, S., Beel, S., Van Damme, P., D'Hooge, R., et al. (2019). Microglia lacking a peroxisomal β-oxidation enzyme chronically alter their inflammatory profile without evoking neuronal and behavioral deficits. *J. Neuroinflammation* 16:61. doi: 10.1186/s12974-019-1442-3

Beckers, L., Stroobants, S., D'Hooge, R., and Baes, M. (2018). Neuronal dysfunction and behavioral abnormalities are evoked by neural cells and aggravated by inflammatory microglia in peroxisomal β-oxidation deficiency. *Front. Cell. Neurosci.* 12:136. doi: 10.3389/fncel.2018.00136

Biazik, J., Ylä-Anttila, P., Vihinen, H., Jokitalo, E., and Eskelinen, E.-L. (2015). Ultrastructural relationship of the phagophore with surrounding organelles. *Autophagy* 11, 439–451. doi: 10.1080/15548627.2015.1017178

Bloom, G. S. (2014). Amyloid-β and tau: the trigger and bullet in Alzheimer disease pathogenesis. *JAMA Neurol.* 71, 505–508. doi: 10.1001/jamaneurol.2013.5847

Bordi, M., Berg, M. J., Mohan, P. S., Peterhoff, C. M., Alldred, M. J., Che, S., et al. (2016). Autophagy flux in CA1 neurons of Alzheimer hippocampus: increased induction overburdens failing lysosomes to propel neuritic dystrophy. *Autophagy* 12, 2467–2483. doi: 10.1080/15548627.2016.1239003

Bottelbergs, A., Verheijden, S., Hulshagen, L., Gutmann, D. H., Goebbels, S., Nave, K.-A., et al. (2010). Axonal integrity in the absence of functional peroxisomes from projection neurons and astrocytes. *Glia* 58, 1532–1543. doi: 10.1002/glia.21027

Bradford, B. U. (2007). Role of peroxisomes in the swift increase in alcohol metabolism. *J. Gastroenterol. Hepatol.* 22, S28–S30. doi: 10.1111/j.1440-1746.2006.04641.x

Braverman, N. E., Raymond, G. V., Rizzo, W. B., Moser, A. B., Wilkinson, M. E., Stone, E. M., et al. (2016). Peroxisome biogenesis disorders in the Zellweger spectrum: an overview of current diagnosis, clinical manifestations, and treatment guidelines. *Mol. Genet. Metab.* 117, 313–321. doi: 10.1016/j.ymgme.2015.12.009

Brocard, C., and Hartig, A. (2006). Peroxisome targeting signal 1: is it really a simple tripeptide? *Biochim. Biophys. Acta* 1763, 1565–1573. doi: 10.1016/j.bbamcr.2006.08.022

Carvalho, A. F., Pinto, M. P., Grou, C. P., Alencastre, I. S., Fransen, M., Sá-Miranda, C., et al. (2007). Ubiquitination of mammalian Pex5p, the peroxisomal import receptor. *J. Biol. Chem.* 282, 31267–31272. doi: 10.1074/jbc.M706325200

Chen, Y.-C., Chou, W.-H., Tsou, H.-H., Fang, C.-P., Liu, T.-H., Tsao, H.-H., et al. (2019). A *post hoc* study of d-amino acid oxidase in blood as an indicator of post-stroke dementia. *Front. Neurol.* 10:402. doi: 10.3389/fneur.2019.00402

Chiasseu, M., Alarcon-Martinez, L., Belforte, N., Quintero, H., Dotigny, F., Destroismaisons, L., et al. (2017). Tau accumulation in the retina promotes early neuronal dysfunction and precedes brain pathology in a mouse model of Alzheimer's disease. *Mol. Neurodegener.* 12:58. doi: 10.1186/s13024-017-0199-3

Chistyakov, D. V., Aleshin, S., Sergeeva, M. G., and Reiser, G. (2014). Regulation of peroxisome proliferator-activated receptor β/δ expression and activity levels by toll-like receptor agonists and MAP kinase inhibitors in rat astrocytes. *J. Neurochem.* 130, 563–574. doi: 10.1111/jnc.12757

Cho, D.-H., Kim, Y. S., Jo, D. S., Choe, S.-K., and Jo, E.-K. (2018). Pexophagy: molecular mechanisms and implications for health and diseases. *Mol. Cells* 41, 55–64. doi: 10.14348/molcells.2018.2245

Colasante, C., Chen, J., Ahlemeyer, B., and Baumgart-Vogt, E. (2015). Peroxisomes in cardiomyocytes and the peroxisome/peroxisome proliferator-activated receptor-loop. *Thromb. Haemost.* 113, 452–463. doi: 10.1160/th14-06-0497

Defourny, J., Aghaie, A., Perfettini, I., Avan, P., Delmaghani, S., and Petit, C. (2019). Pejvakin-mediated pexophagy protects auditory hair cells against noise-induced damage. *Proc. Natl. Acad. Sci. U S A* 116, 8010–8017. doi: 10.1073/pnas.1821844116

Deosaran, E., Larsen, K. B., Hua, R., Sargent, G., Wang, Y., Kim, S., et al. (2013). NBR1 acts as an autophagy receptor for peroxisomes. *J. Cell Sci.* 126, 939–952. doi: 10.1242/jcs.114819

Di Cara, F., Andreoletti, P., Trompier, D., Vejux, A., Bülow, M. H., Sellin, J., et al. (2019). Peroxisomes in immune response and inflammation. *Int. J. Mol. Sci.* 20:E3877. doi: 10.3390/ijms20163877

Di Cesare Mannelli, L., Zanardelli, M., Micheli, L., and Ghelardini, C. (2014). PPAR-γ impairment alters peroxisome functionality in primary astrocyte cell cultures. *Biomed Res. Int.* 2014, 546453–546453. doi: 10.1155/2014/546453

Dorsey, E. R., Elbaz, A., Nichols, E., Abd-Allah, F., Abdelalim, A., Adsuar, J. C., et al. (2018). Global, regional, and national burden of Parkinson's disease, 1990–2016: a systematic analysis for the global burden of disease study 2016. *Lancet Neurol.* 17, 939–953. doi: 10.1016/S1474-4422(18)30295-3

Ehrlich, M. E. (2012). Huntington's disease and the striatal medium spiny neuron: cell-autonomous and non-cell-autonomous mechanisms of disease. *Neurotherapeutics* 9, 270–284. doi: 10.1007/s13311-012-0112-2

Evans, C. S., and Holzbaur, E. L. F. (2019). Quality control in neurons: mitophagy and other selective autophagy mechanisms. *J. Mol. Biol.* 432, 240–260. doi: 10.1016/j.jmb.2019.06.031

Farooqui, A. A., and Horrocks, L. A. (2001). Book review: plasmalogens: workhorse lipids of membranes in normal and injured neurons and glia. *Neuroscientist* 7, 232–245. doi: 10.1177/107385840100700308

Farré, J.-C., Burkenroad, A., Burnett, S. F., and Subramani, S. (2013). Phosphorylation of mitophagy and pexophagy receptors coordinates their interaction with Atg8 and Atg11. *EMBO Rep.* 14, 441–449. doi: 10.1038/embor.2013.40

Feng, Y., He, D., Yao, Z., and Klionsky, D. J. (2014). The machinery of macroautophagy. *Cell Res.* 24, 24–41. doi: 10.1038/cr.2013.168

Ferdinandusse, S., Denis, S., Faust, P. L., and Wanders, R. J. A. (2009). Bile acids: the role of peroxisomes. *J. Lipid Res.* 50, 2139–2147. doi: 10.1194/jlr.R900009-JLR200

Ferguson, C. J., Lenk, G. M., and Meisler, M. H. (2009). Defective autophagy in neurons and astrocytes from mice deficient in PI(3,5)P2. *Hum. Mol. Genet.* 18, 4868–4878. doi: 10.1093/hmg/ddp460

Finkbeiner, S. (2019). The autophagy lysosomal pathway and neurodegeneration. *Cold. Spring Harbor. Perspect. Biol.* doi: 10.1101/cshperspect.a033993 [Epub ahead of print].

Fujiki, Y., Yagita, Y., and Matsuzaki, T. (2012). Peroxisome biogenesis disorders: molecular basis for impaired peroxisomal membrane assembly: in metabolic functions and biogenesis of peroxisomes in health and disease. *Biochim. Biophys. Acta* 1822, 1337–1342. doi: 10.1016/j.bbadis.2012.06.004

GBD 2013 Mortality and Causes of Death Collaborators. (2015). Global, regional and national age-sex specific all-cause and cause-specific mortality for 240 causes of death, 1990–2013: a systematic analysis for the Global Burden of Disease Study 2013. *Lancet* 385, 117–171. doi: 10.1016/S0140-6736(14)61682-2

Germain, K., and Kim, K. P. (2020). Pexophagy: a model for selective autophagy. *Int. J. Mol. Sci.* 21:E578. doi: 10.3390/ijms21020578

Gettelfinger, J. D., and Dahl, J. P. (2018). Syndromic hearing loss: a brief review of common presentations and genetics. *J. Pediatr. Genet.* 7, 1–8. doi: 10.1055/s-0037-1617454

Gilmer, L. K., Ansari, M. A., Roberts, K. N., and Scheff, S. W. (2010). Age-related changes in mitochondrial respiration and oxidative damage in the cerebral cortex of the Fischer 344 rat. *Mech. Ageing Dev.* 131, 133–143. doi: 10.1016/j.mad.2009.12.011

Goodenowe, D. B., and Senanayake, V. (2019). Relation of serum plasmalogens and APOE genotype to cognition and dementia in older persons in a cross-sectional study. *Brain Sci.* 9:E92. doi: 10.3390/brainsci9040092

Gronowicz, G., Swift, H., and Steck, T. L. (1984). Maturation of the reticulocyte *in vitro*. *J. Cell Sci.* 71, 177–197.

Grothey, A. (2003). Oxaliplatin-safety profile: neurotoxicity. *Semin. Oncol.* 30, 5–13. doi: 10.1016/s0093-7754(03)00399-3

Harada, R., Ishiki, A., Kai, H., Sato, N., Furukawa, K., Furumoto, S., et al. (2018). Correlations of ^{18}F-THK5351 PET with postmortem burden of tau and astrogliosis in Alzheimer disease. *J. Nucl. Med.* 59, 671–674. doi: 10.2967/jnumed.117.197426

Harrison, T. M., La Joie, R., Maass, A., Baker, S. L., Swinnerton, K., Fenton, L., et al. (2019). Longitudinal tau accumulation and atrophy in aging and Alzheimer disease. *Ann. Neurol.* 85, 229–240. doi: 10.1002/ana.25406

Hasegawa, K., Wakino, S., Yoshioka, K., Tatematsu, S., Hara, Y., Minakuchi, H., et al. (2010). Kidney-specific overexpression of Sirt1 protects against acute kidney injury by retaining peroxisome function. *J. Biol. Chem.* 285, 13045–13056. doi: 10.1074/jbc.m109.067728

Hua, R., Cheng, D., Coyaud, É., Freeman, S., Di Pietro, E., Wang, Y., et al. (2017). VAPs and ACBD5 tether peroxisomes to the ER for peroxisome maintenance and lipid homeostasis. *J. Cell Biol.* 216, 367–377. doi: 10.1083/jcb.201608128

Huang, K., Chen, W., Zhu, F., Li, P. W.-L., Kapahi, P., and Bai, H. (2019). RiboTag translatomic profiling of *Drosophila* oenocytes under aging and induced oxidative stress. *BMC Genomics* 20:50. doi: 10.1186/s12864-018-5404-4

Huybrechts, S. J., Van Veldhoven, P. P., Brees, C., Mannaerts, G. P., Los, G. V., and Fransen, M. (2009). Peroxisome dynamics in cultured mammalian cells. *Traffic* 10, 1722–1733. doi: 10.1111/j.1600-0854.2009.00970.x

Jagadeesan, A. J., Murugesan, R., Vimala Devi, S., Meera, M., Madhumala, G., Vishwanathan Padmaja, M., et al. (2017). Current trends in etiology, prognosis and therapeutic aspects of Parkinson's disease: a review. *Acta Biomed.* 88, 249–262. doi: 10.23750/abm.v88i3.6063

Jan, C. H., Williams, C. C., and Weissman, J. S. (2014). Principles of ER cotranslational translocation revealed by proximity-specific ribosome profiling. *Science* 346:1257521. doi: 10.1126/science.1257521

Jin, M., Liu, X., and Klionsky, D. J. (2013). SnapShot: selective autophagy. *Cell* 152, 368.e2–368.e2. doi: 10.1016/j.cell.2013.01.004

Jo, D. S., Park, S. J., Kim, A.-K., Park, N. Y., Kim, J. B., Bae, J.-E., et al. (2020). Loss of HSPA9 induces peroxisomal degradation by increasing pexophagy. *Autophagy* doi: 10.1080/15548627.2020.1712812 [Epub ahead of print].

Kabeya, Y., Mizushima, N., Ueno, T., Yamamoto, A., Kirisako, T., Noda, T., et al. (2000). LC3, a mammalian homologue of yeast Apg8p, is localized in autophagosome membranes after processing. *EMBO J.* 19, 5720–5728. doi: 10.1093/emboj/19.21.5720

Kao, Y.-T., and Bartel, B. (2015). Elevated growth temperature decreases levels of the PEX5 peroxisome-targeting signal receptor and ameliorates defects of Arabidopsis mutants with an impaired PEX4 ubiquitin-conjugating enzyme. *BMC Plant Biol.* 15:224. doi: 10.1186/s12870-015-0605-3

Kassmann, C. M. (2014). Myelin peroxisomes - essential organelles for the maintenance of white matter in the nervous system. *Biochimie* 98, 111–118. doi: 10.1016/j.biochi.2013.09.020

Kesler, S. R. (2014). Default mode network as a potential biomarker of chemotherapy-related brain injury. *Neurobiol. Aging* 35, S11–S19. doi: 10.1016/j.neurobiolaging.2014.03.036

Kesler, S. R., and Blayney, D. W. (2016). Neurotoxic effects of anthracycline- vs. nonanthracycline-based chemotherapy on cognition in breast cancer survivors. *JAMA Oncol.* 2, 185–192. doi: 10.1001/jamaoncol.2015.4333

Kim, P. K., Hailey, D. W., Mullen, R. T., and Lippincott-Schwartz, J. (2008). Ubiquitin signals autophagic degradation of cytosolic proteins and peroxisomes. *Proc. Natl. Acad. Sci. U S A* 105, 20567–20574. doi: 10.1073/pnas.0810611105

Kirkin, V., Lamark, T., Sou, Y.-S., Bjørkøy, G., Nunn, J. L., Bruun, J.-A., et al. (2009). A role for NBR1 in autophagosomal degradation of ubiquitinated substrates. *Mol. Cell* 33, 505–516. doi: 10.1016/j.molcel.2009.01.020

Kleinecke, S., Richert, S., de Hoz, L., Brügger, B., Kungl, T., Asadollahi, E., et al. (2017). Peroxisomal dysfunctions cause lysosomal storage and axonal Kv1 channel redistribution in peripheral neuropathy. *Elife* 6:e23332. doi: 10.7554/elife.23332

Klouwer, F. C. C., Berendse, K., Ferdinandusse, S., Wanders, R. J. A., Engelen, M., and Poll-The, B. T. (2015). Zellweger spectrum disorders: clinical overview and management approach. *Orphanet J. Rare Dis.* 10:151. doi: 10.1186/s13023-015-0368-9

Koehler, C. M. (2000). Protein translocation pathways of the mitochondrion. *FEBS Lett.* 476, 27–31. doi: 10.1016/s0014-5793(00)01664-1

Kondori, N. R., Paul, P., Robbins, J. P., Liu, K., Hildyard, J. C. W., Wells, D. J., et al. (2017). Characterisation of the pathogenic effects of the *in vivo* expression of an ALS-linked mutation in D-amino acid oxidase: phenotype and loss of spinal cord motor neurons. *PLoS One* 12:e0188912. doi: 10.1371/journal.pone.0188912

Kondori, N. R., Paul, P., Robbins, J. P., Liu, K., Hildyard, J. C. W., Wells, D. J., et al. (2018). Focus on the role of D-serine and D-amino acid oxidase in amyotrophic lateral sclerosis/motor neuron disease (ALS). *Front. Mol. Biosci.* 5:8. doi: 10.3389/fmolb.2018.00008

Kou, J., Kovacs, G. G., Höftberger, R., Kulik, W., Brodde, A., Forss-Petter, S., et al. (2011). Peroxisomal alterations in Alzheimer's disease. *Acta Neuropathol.* 122, 271–283. doi: 10.1007/s00401-011-0836-9

Kulkarni, A., Chen, J., and Maday, S. (2018). Neuronal autophagy and intercellular regulation of homeostasis in the brain. *Curr. Opin. Neurobiol.* 51, 29–36. doi: 10.1016/j.conb.2018.02.008

Kulkarni, A., Dong, A., Kulkarni, V. V., Chen, J., Laxton, O., Anand, A., et al. (2019). Differential regulation of autophagy during metabolic stress in astrocytes and neurons. *Autophagy* doi: 10.1080/15548627.2019.1703354 [Epub ahead of print].

Landino, J., Jnah, A. J., Newberry, D. M., and Iben, S. C. (2017). Neonatal rhizomelic chondrodysplasia punctata type 1: weaving evidence into clinical practice. *J. Perinat. Neonatal Nurs.* 31, 350–357. doi: 10.1097/JPN.0000000000000282

Lefevre, S. D., van Roermund, C. W., Wanders, R. J. A., Veenhuis, M., and van der Klei, I. J. (2013). The significance of peroxisome function in chronological aging of Saccharomyces cerevisiae. *Aging Cell* 12, 784–793. doi: 10.1111/acel.12113

Legakis, J. E., Koepke, J. I., Jedeszko, C., Barlaskar, F., Terlecky, L. J., Edwards, H. J., et al. (2002). Peroxisome senescence in human fibroblasts. *Mol. Biol. Cell* 13, 4243–4255. doi: 10.1091/mbc.e02-06-0322

Liang, W. S., Dunckley, T., Beach, T. G., Grover, A., Mastroeni, D., Ramsey, K., et al. (2008). Altered neuronal gene expression in brain regions differentially affected by Alzheimer's disease: a reference data set. *Physiol. Genomics* 33, 240–256. doi: 10.1152/physiolgenomics.00242.2007

Lodhi, I. J., Wei, X., Yin, L., Feng, C., Adak, S., Abou-Ezzi, G., et al. (2015). Peroxisomal lipid synthesis regulates inflammation by sustaining neutrophil membrane phospholipid composition and viability. *Cell Metab.* 21, 51–64. doi: 10.1016/j.cmet.2014.12.002

Maday, S., and Holzbaur, E. L. F. (2016). Compartment-specific regulation of autophagy in primary neurons. *J. Neurosci.* 36, 5933–5945. doi: 10.1523/jneurosci.4401-15.2016

Magalhães, M. M., and Magalhães, M. C. (1997). Peroxisomes in adrenal steroidogenesis. *Microsc. Res. Tech.* 36, 493–502. doi: 10.1002/(sici)1097-0029(19970315)36:6<493::aid-jemt6>3.0.co;2-j

Malheiro, A. R., da Silva, T. F., and Brites, P. (2015). Plasmalogens and fatty alcohols in rhizomelic chondrodysplasia punctata and Sjögren-Larsson syndrome. *J. Inherit. Metab. Dis.* 38, 111–121. doi: 10.1007/s10545-014-9795-3

Manchon, J. F. M., Dabaghian, Y., Uzor, N.-E., Kesler, S. R., Wefel, J. S., and Tsvetkov, A. S. (2016). Levetiracetam mitigates doxorubicin-induced DNA and synaptic damage in neurons. *Sci. Rep.* 6:25705. doi: 10.1038/srep25705

Mao, K., Liu, X., Feng, Y., and Klionsky, D. J. (2014). The progression of peroxisomal degradation through autophagy requires peroxisomal division. *Autophagy* 10, 652–661. doi: 10.4161/auto.27852

Menzies, F. M., Fleming, A., Caricasole, A., Bento, C. F., Andrews, S. P., Ashkenazi, A., et al. (2017). Autophagy and neurodegeneration: pathogenic mechanisms and therapeutic opportunities. *Neuron* 93, 1015–1034. doi: 10.1016/j.neuron.2017.01.022

Mirza, M. A., Ritzel, R., Xu, Y., McCullough, L. D., and Liu, F. (2015). Sexually dimorphic outcomes and inflammatory responses in hypoxic-ischemic encephalopathy. *J. Neuroinflammation* 12, 32–32. doi: 10.1186/s12974-015-0251-6

Mitchell, A. J. (2009). CSF phosphorylated tau in the diagnosis and prognosis of mild cognitive impairment and Alzheimer's disease: a meta-analysis of 51 studies. *J. Neurol. Neurosurg. Psychiatry* 80, 966–975. doi: 10.1136/jnnp.2008.167791

Mizushima, N., Yoshimori, T., and Ohsumi, Y. (2011). The role of atg proteins in autophagosome formation. *Annu. Rev. Cell Dev. Biol.* 27, 107–132. doi: 10.1146/annurev-cellbio-092910-154005

Moore, A. S., and Holzbaur, E. L. F. (2016). Spatiotemporal dynamics of autophagy receptors in selective mitophagy. *Autophagy* 12, 1956–1957. doi: 10.1080/15548627.2016.1212788

Moruno Manchon, J. F., Uzor, N.-E., Dabaghian, Y., Furr-stimming, E. E., Finkbeiner, S., and Tsvetkov, A. S. (2015). Cytoplasmic sphingosine-1-phosphate pathway modulates neuronal autophagy. *Sci. Rep.* 5:15213. doi: 10.1038/srep15213

Moruno Manchon, J. F., Uzor, N.-E., Finkbeiner, S., and Tsvetkov, A. S. (2016). SPHK1/sphingosine kinase 1-mediated autophagy differs between neurons and SH-SY5Y neuroblastoma cells. *Autophagy* 12, 1418–1424. doi: 10.1080/15548627.2016.1183082

Moruno-Manchon, J. F., Uzor, N.-E., Ambati, C. R., Shetty, V., Putluri, N., Jagannath, C., et al. (2018a). Sphingosine kinase 1-associated autophagy differs between neurons and astrocytes. *Cell Death Dis.* 9, 521–521. doi: 10.1038/s41419-018-0599-5

Moruno-Manchon, J. F., Uzor, N.-E., Kesler, S. R., Wefel, J. S., Townley, D. M., Nagaraja, A. S., et al. (2018b). Peroxisomes contribute to oxidative stress in neurons during doxorubicin-based chemotherapy. *Mol. Cell. Neurosci.* 86, 65–71. doi: 10.1016/j.mcn.2017.11.014

Moruno-Manchon, J. F., Uzor, N.-E., Kesler, S. R., Wefel, J. S., Townley, D. M., Nagaraja, A. S., et al. (2016). TFEB ameliorates the impairment of the autophagy-lysosome pathway in neurons induced by doxorubicin. *Aging* 8, 3507–3519. doi: 10.18632/aging.101144

Morvay, P. L., Baes, M., and Van Veldhoven, P. P. (2017). Differential activities of peroxisomes along the mouse intestinal epithelium. *Cell Biochem. Funct.* 35, 144–155. doi: 10.1002/cbf.3255

Motley, A. M., Nuttall, J. M., and Hettema, E. H. (2012a). Atg36: the Saccharomyces cerevisiae receptor for pexophagy. *Autophagy* 8, 1680–1681. doi: 10.4161/auto.21485

Motley, A. M., Nuttall, J. M., and Hettema, E. H. (2012b). Pex3-anchored Atg36 tags peroxisomes for degradation in Saccharomyces cerevisiae. *EMBO J.* 31, 2852–2868. doi: 10.1038/emboj.2012.151

Mukaiyama, H., Baba, M., Osumi, M., Aoyagi, S., Kato, N., Ohsumi, Y., et al. (2004). Modification of a ubiquitin-like protein Paz2 conducted micropexophagy through formation of a novel membrane structure. *Mol. Biol. Cell* 15, 58–70. doi: 10.1091/mbc.e03-05-0340

Nakamura, S., and Yoshimori, T. (2017). New insights into autophagosome-lysosome fusion. *J. Cell Sci.* 130, 1209–1216. doi: 10.1242/jcs.196352

Narayan, V., Ly, T., Pourkarimi, E., Murillo, A. B., Gartner, A., Lamond, A. I., et al. (2016). Deep proteome analysis identifies age-related processes in *C. elegans*. *Cell Syst.* 3, 144–159. doi: 10.1016/j.cels.2016.06.011

Nilsson, P., Loganathan, K., Sekiguchi, M., Matsuba, Y., Hui, K., Tsubuki, S., et al. (2013). Aβ secretion and plaque formation depend on autophagy. *Cell Rep.* 5, 61–69.doi: 10.1016/j.celrep.2013.08.042

Nordgren, M., Francisco, T., Lismont, C., Hennebel, L., Brees, C., Wang, B., et al. (2015). Export-deficient monoubiquitinated PEX5 triggers peroxisome removal in SV40 large T antigen-transformed mouse embryonic fibroblasts. *Autophagy* 11, 1326–1340. doi: 10.1080/15548627.2015.1061846

Nordgren, M., and Fransen, M. (2014). Peroxisomal metabolism and oxidative stress. *Biochimie* 98, 56–62. doi: 10.1016/j.biochi.2013.07.026

Nury, T., Sghaier, R., Zarrouk, A., Ménétrier, F., Uzun, T., Leoni, V., et al. (2018). Induction of peroxisomal changes in oligodendrocytes treated with 7-ketocholesterol: attenuation by α-tocopherol. *Biochimie* 153, 181–202. doi: 10.1016/j.biochi.2018.07.009

Olenick, M. A., Tokito, M., Boczkowska, M., Dominguez, R., and Holzbaur, E. L. F. (2016). Hook adaptors induce unidirectional processive motility by enhancing the dynein-dynactin interaction. *J. Biol. Chem.* 291, 18239–18251. doi: 10.1074/jbc.m116.738211

Pamenter, M. E., Perkins, G. A., McGinness, A. K., Gu, X. Q., Ellisman, M. H., and Haddad, G. G. (2012). Autophagy and apoptosis are differentially induced in neurons and astrocytes treated with an *in vitro* mimic of the ischemic penumbra. *PloS One* 7:e51469. doi: 10.1371/journal.pone.0051469

Park, H., He, A., Tan, M., Johnson, J. M., Dean, J. M., Pietka, T. A., et al. (2019). Peroxisome-derived lipids regulate adipose thermogenesis by mediating cold-induced mitochondrial fission. *J. Clin. Invest.* 129, 694–711. doi: 10.1172/jci120606

Peters, O. M., Ghasemi, M., and Brown, R. H. Jr. (2015). Emerging mechanisms of molecular pathology in ALS. *J. Clin. Invest.* 125, 1767–1779. doi: 10.1172/JCI71601

Poirier, Y., Antonenkov, V. D., Glumoff, T., and Hiltunen, J. K. (2006). Peroxisomal β-oxidation—A metabolic pathway with multiple functions. *Biochim. Biophys. Acta* 1763, 1413–1426. doi: 10.1016/j.bbamcr.2006.08.034

Poole, B., Leighton, F., and De Duve, C. (1969). The synthesis and turnover of rat liver peroxisomes. II. Turnover of peroxisome proteins. *J. Cell Biol.* 41, 536–546. doi: 10.1083/jcb.41.2.536

Powers, J. M. (2001). Normal and defective neuronal membranes: structure and function. *J. Mol. Neurosci.* 16, 285–287. doi: 10.1385/jmn:16:2-3:285

Purdue, P. E., Skoneczny, M., Yang, X., Zhang, J.-W., and Lazarow, P. B. (1999). Rhizomelic chondrodysplasia punctata, a peroxisomal biogenesis disorder caused by defects in Pex7p, a peroxisomal protein import receptor: a minireview. *Neurochem. Res.* 24, 581–586. doi: 10.1023/a:1023957110171

Raas, Q., Saih, F. E., Gondcaille, C., Trompier, D., Hamon, Y., Leoni, V., et al. (2019). A microglial cell model for acyl-CoA oxidase 1 deficiency. *Biochim. Biophys. Acta* 1864, 567–576. doi: 10.1016/j.bbalip.2018.10.005

Reddy, J. K., and Hashimoto, T. (2001). Peroxisomal β-oxidation and peroxisome proliferator-activated receptor α: an adaptive metabolic system. *Annu. Rev. Nutr.* 21, 193–230. doi: 10.1146/annurev.nutr.21.1.193

Reggiori, F., and Tooze, S. A. (2009). The EmERgence of autophagosomes. *Dev. Cell* 17, 747–748. doi: 10.1016/j.devcel.2009.12.004

Riederer, P., Berg, D., Casadei, N., Cheng, F., Classen, J., Dresel, C., et al. (2019). α-synuclein in Parkinson's disease: causal or bystander? *J. Neural. Transm* 126, 815–840. doi: 10.1007/s00702-019-02025-9

Ritzel, R. M., Patel, A. R., Spychala, M., Verma, R., Crapser, J., Koellhoffer, E. C., et al. (2017). Multiparity improves outcomes after cerebral ischemia in female mice despite features of increased metabovascular risk. *Pro. Natl. Acad. Sci. U S A* 114, E5673–E5682. doi: 10.1073/pnas.1607002114

Santos, M. J., Quintanilla, R. A., Toro, A., Grandy, R., Dinamarca, M. C., Godoy, J. A., et al. (2005). Peroxisomal proliferation protects from β-amyloid neurodegeneration. *J. Biol. Chem.* 280, 41057–41068. doi: 10.1074/jbc.m505160200

Sargent, G., van Zutphen, T., Shatseva, T., Zhang, L., Di Giovanni, V., Bandsma, R., et al. (2016). PEX2 is the E3 ubiquitin ligase required for pexophagy during starvation. *J. Cell Biol.* 214, 677–690. doi: 10.1083/jcb.201511034

Sasabe, J., Suzuki, M., Imanishi, N., and Aiso, S. (2014). Activity of D-amino acid oxidase is widespread in the human central nervous system. *Front. Synaptic Neurosci.* 6:14. doi: 10.3389/fnsyn.2014.00014

Sasaki, T., Lian, S., Khan, A., Llop, J. R., Samuelson, A. V., Chen, W., et al. (2017). Autolysosome biogenesis and developmental senescence are regulated by both

Spns1 and v-ATPase. *Autophagy* 13, 386–403. doi: 10.1080/15548627.2016.1256934

Shi, C., Zhu, J., Leng, S., Long, D., and Luo, X. (2016). Mitochondrial FOXO3a is involved in amyloid β peptide-induced mitochondrial dysfunction. *J. Bioenerg. Biomembr.* 48, 189–196. doi: 10.1007/s10863-016-9645-0

Siegel, C. S., and McCullough, L. D. (2013). NAD+ and nicotinamide: sex differences in cerebral ischemia. *Neuroscience* 237, 223–231. doi: 10.1016/j.neuroscience.2013.01.068

Smith, J. J., and Aitchison, J. D. (2013). Peroxisomes take shape. *Nat. Rev. Mol. Cell Biol.* 14, 803–817. doi: 10.1038/nrm3700

Stavoe, A. K. H., and Holzbaur, E. L. F. (2019a). Autophagy in neurons. *Ann. Rev. Cell Dev. Biol.* 35, 477–500. doi: 10.1146/annurev-cellbio-100818-125242

Stavoe, A. K. H., and Holzbaur, E. L. F. (2019b). Axonal autophagy: mini-review for autophagy in the CNS. *Neurosci. Lett.* 697, 17–23. doi: 10.1016/j.neulet.2018.03.025

Strømhaug, P. E., Bevan, A., and Dunn, W. A. (2001). GSA11 encodes a unique 208-kDa protein required for pexophagy and autophagy in pichia pastoris. *J. Biol. Chem.* 276, 42422–42435. doi: 10.1074/jbc.m104087200

Sung, K., and Jimenez-Sanchez, M. (2020). Autophagy in astrocytes and its implications in neurodegeneration. *J. Mol. Biol.* doi: 10.1016/j.jmb.2019.12.041 [Epub ahead of print].

Vasko, R. (2016). Peroxisomes and kidney injury. *Antioxid. Redox Signal.* 25, 217–231. doi: 10.1089/ars.2016.6666

Walton, P. A., Brees, C., Lismont, C., Apanasets, O., and Fransen, M. (2017). The peroxisomal import receptor PEX5 functions as a stress sensor, retaining catalase in the cytosol in times of oxidative stress. *Biochim. Biophys. Acta* 1864, 1833–1843. doi: 10.1016/j.bbamcr.2017.07.013

Wanders, R. J. A., Komen, J., and Ferdinandusse, S. (2011). Phytanic acid metabolism in health and disease. *Biochim. Biophys. Acta* 1811, 498–507. doi: 10.1016/j.bbalip.2011.06.006

Wanders, R. J. A., and Poll-The, B. T. (2017). "Role of peroxisomes in human lipid metabolism and its importance for neurological development". *Neurosci. Lett.* 637, 11–17. doi: 10.1016/j.neulet.2015.06.018

Wang, X.-M., Yik, W. Y., Zhang, P., Lu, W., Huang, N., Kim, B. R., et al. (2015). Induced pluripotent stem cell models of Zellweger spectrum disorder show impaired peroxisome assembly and cell type-specific lipid abnormalities. *Stem Cell Res. Ther.* 6, 158–158. doi: 10.1186/s13287-015-0149-3

Warren, M., Mierau, G., Wartchow, E. P., Shimada, H., and Yano, S. (2018). Histologic and ultrastructural features in early and advanced phases of Zellweger spectrum disorder (infantile Refsum disease). *Ultrastruct. Pathol.* 42, 220–227. doi: 10.1080/01913123.2018.1440272

Waterham, H. R., and Ebberink, M. S. (2012). Genetics and molecular basis of human peroxisome biogenesis disorders. *Biochim. Biophys. Acta* 1822, 1430–1441. doi: 10.1016/j.bbadis.2012.04.006

Wefel, J. S., Kesler, S. R., Noll, K. R., and Schagen, S. B. (2015). Clinical characteristics, pathophysiology and management of noncentral nervous system cancer-related cognitive impairment in adults. *CA Cancer J. Clin.* 65, 123–138. doi: 10.3322/caac.21258

Williams, C., and van der Klei, I. J. (2013). Pexophagy-linked degradation of the peroxisomal membrane protein Pex3p involves the ubiquitin-proteasome system. *Biochem. Biophys. Res. Commun.* 438, 395–401. doi: 10.1016/j.bbrc.2013.07.086

Wyant, K. J., Ridder, A. J., and Dayalu, P. (2017). Huntington's disease—update on treatments. *Curr. Neurol. Neurosci. Rep.* 17:33. doi: 10.1007/s11910-017-0739-9

Yakunin, E., Moser, A., Loeb, V., Saada, A., Faust, P., Crane, D. I., et al. (2010). α-synuclein abnormalities in mouse models of peroxisome biogenesis disorders. *J. Neurosci. Res.* 88, 866–876. doi: 10.1002/jnr.22246

Yamashita, S.-I., Abe, K., Tatemichi, Y., and Fujiki, Y. (2014). The membrane peroxin PEX3 induces peroxisome-ubiquitination-linked pexophagy. *Autophagy* 10, 1549–1564. doi: 10.4161/auto.29329

Yang, Z., and Klionsky, D. J. (2010). Eaten alive: a history of macroautophagy. *Nat. Cell Biol.* 12, 814–822. doi: 10.1038/ncb0910-814

Young, P. G., and Bartel, B. (2016). Pexophagy and peroxisomal protein turnover in plants. *Biochim. Biophys. Acta* 1863, 999–1005. doi: 10.1016/j.bbamcr.2015.09.005

Young, J. M., Nelson, J. W., Cheng, J., Zhang, W., Mader, S., Davis, C. M., et al. (2015). Peroxisomal biogenesis in ischemic brain. *Antioxid. Redox Signal.* 22, 109–120. doi: 10.1089/ars.2014.5833

Zanardelli, M., Micheli, L., Cinci, L., Failli, P., Ghelardini, C., and Di Cesare Mannelli, L. (2014). Oxaliplatin neurotoxicity involves peroxisome alterations. PPARγ agonism as preventive pharmacological approach. *PLoS One* 9, e102758–e102758. doi: 10.1371/journal.pone.0102758

Zhang, X., Gao, F., Wang, D., Li, C., Fu, Y., He, W., et al. (2018). Tau pathology in Parkinson's disease. *Front. Neurol.* 9, 809–809. doi: 10.3389/fneur.2018.00809

Zhang, J., Kim, J., Alexander, A., Cai, S., Tripathi, D. N., Dere, R., et al. (2013). A tuberous sclerosis complex signalling node at the peroxisome regulates mTORC1 and autophagy in response to ROS. *Nat. Cell Biol.* 15, 1186–1196. doi: 10.1038/ncb2822

Zhang, J., Tripathi, D. N., Jing, J., Alexander, A., Kim, J., Powell, R. T., et al. (2015). ATM functions at the peroxisome to induce pexophagy in response to ROS. *Nat. Cell Biol.* 17, 1259–1269. doi: 10.1038/ncb3230

Zhao, T., Hong, Y., Li, S., and Li, X.-J. (2016). Compartment-dependent degradation of mutant huntingtin accounts for its preferential accumulation in neuronal processes. *J. Neurosci.* 36, 8317–8328. doi: 10.1523/jneurosci.0806-16.2016

Zilka, N., Filipcik, P., Koson, P., Fialova, L., Skrabana, R., Zilkova, M., et al. (2006). Truncated tau from sporadic Alzheimer's disease suffices to drive neurofibrillary degeneration *in vivo*. *FEBS Lett.* 580, 3582–3588. doi: 10.1016/j.febslet.2006.05.029

Conflict of Interest: The authors declare that the research was conducted in the absence of any commercial or financial relationships that could be construed as a potential conflict of interest.

Copyright © 2020 Uzor, McCullough and Tsvetkov. This is an open-access article distributed under the terms of the Creative Commons Attribution License (CC BY). The use, distribution or reproduction in other forums is permitted, provided the original author(s) and the copyright owner(s) are credited and that the original publication in this journal is cited, in accordance with accepted academic practice. No use, distribution or reproduction is permitted which does not comply with these terms.

frontiers in Cellular Neuroscience

REVIEW
published: 19 June 2020
doi: 10.3389/fncel.2020.00184

Immortalized Dorsal Root Ganglion Neuron Cell Lines

Rainer Viktor Haberberger, Christine Barry and Dusan Matusica*

Anatomy & Histology, College of Medicine and Public Health, Flinders Health & Medical Research Institute, Flinders University, Adelaide, SA, Australia

Pain is one of the most significant causes of suffering and disability world-wide, and arguably the most burdensome global health challenge. The growing number of patients suffering from chronic pain conditions such as fibromyalgia, complex regional pain syndrome, migraine and irritable bowel syndrome, not only reflect the complexity and heterogeneity of pain types, but also our lack of understanding of the underlying mechanisms. Sensory neurons within the dorsal root ganglia (DRG) have emerged as viable targets for effective chronic pain therapy. However, DRG's contain different classes of primary sensory neurons including pain-associated nociceptive neurons, non-nociceptive temperature sensing, mechanosensory and chemoreceptive neurons, as well as multiple types of immune and endothelial cells. This cell-population heterogeneity makes investigations of individual subgroups of DRG neurons, such as nociceptors, difficult. In attempts to overcome some of these difficulties, a limited number of immortalized DRG-derived cell lines have been generated over the past few decades. *In vitro* experiments using DRG-derived cell lines have been useful in understanding sensory neuron function. In addition to retaining phenotypic similarities to primary cultured DRG neurons, these cells offer greater suitability for high throughput assays due to ease of culture, maintenance, growth efficiency and cost-effectiveness. For accurate interpretation and translation of results it is critical, however, that phenotypic similarities and differences of DRG-derived cells lines are methodically compared to native neurons. Published reports to date show notable variability in how these DRG-derived cells are maintained and differentiated. Understanding the cellular and molecular differences stemming from different culture methods, is essential to validate past and future experiments, and enable these cells to be used to their full potential. This review describes currently available DRG-derived cell lines, their known sensory and nociceptor specific molecular profiles, and summarize their morphological features related to differentiation and neurite outgrowth.

Keywords: DRG, immortalized cell lines, 50B11, F-11, ND7/23, ND-C, Med17.11, HD10.6

OPEN ACCESS

Edited by:
Egor Dzyubenko, Essen University Hospital, Germany

Reviewed by:
Tomokazu Tomo Fukuda, Iwate University, Japan
Michael Fleischer, Essen University Hospital, Germany

****Correspondence:***
Rainer Viktor Haberberger
rainer.haberberger@flinders.edu.au

Specialty section:
This article was submitted to Cellular Neuropathology, a section of the journal Frontiers in Cellular Neuroscience

Received: *23 April 2020*
Accepted: *28 May 2020*
Published: *19 June 2020*

Citation:
Haberberger RV, Barry C and Matusica D (2020) Immortalized Dorsal Root Ganglion Neuron Cell Lines. Front. Cell. Neurosci. 14:184. doi: 10.3389/fncel.2020.00184

INTRODUCTION

Cell bodies of sensory neurons are situated in dorsal root ganglia (DRG) or trigeminal ganglia (TG) and possess pseudounipolar processes that divide into two axons, one to innervate targets in the periphery, and the other projecting centrally in the spinal cord dorsal horn (DRG), or in the case of the trigeminal sensory nuclear complex, in the brain stem (TG). These sensory neurons, expressing an abundance of channels and receptors, monitor the environment and convey information

including nociception, temperature and mechanosensation to the central nervous system (CNS) (Platika et al., 1985b; Wood et al., 1990). A substantial proportion of pain research focusses nociceptors, the subgroup of neurons involved in nociception and pain signaling, increasing the understanding of their basic functional properties and their critical roles in the development and maintenance of chronic pain (Wood et al., 1990; Rugiero and Wood, 2009), as well as identifying potential targets for therapeutic intervention. In addition to nociceptors, DRG also contain cell bodies of non-nociceptive temperature sensing, mechanosensory and chemoreceptive neurons, as well as multiple non-neuronal cell types such as immune cells and endothelial cells. The heterogeneous population of sensory neurons within the DRG can be subdivided in multiple subpopulations based on morphological, neurochemical, electrophysiological and transcriptional characteristics (Platika et al., 1985b; Wood et al., 1990; Rugiero and Wood, 2009). This cell-type heterogeneity creates a complex cellular and molecular environment making the investigation of signaling pathways related to specific classes of neuron extremely challenging. For example, analysis of total RNA or proteins obtained from DRG explants (Raymon et al., 1999) reflects average RNA expression levels across multiple groups of neuronal and non-neuronal cells rather than expression levels in a subpopulation of cells such as nociceptive neurons, or a specific type of nociceptor.

Dissociation of DRG neurons either by methods such as fluorescence assisted cell sorting (FACS) (Vetter and Lewis, 2010), or magnetic beads can isolate certain cell types but these methods produce low neuronal yields, require a high number of laboratory animals for isolation of samples suitable for proteomic or biochemical analysis, and are difficult to further it remains challenging to adequately separate subpopulations of cells. The characteristics of small numbers of specific neurons can be assessed only by a limited number of methods such as single cell RT-PCR. Investigations of signaling pathways are compromised by the isolation process and factors such as enzymatic digestion and mechanical stress. In summary, the existence of multiple types of nociceptors coupled with technical limitations in isolating individual nociceptor subtypes from native tissues have limited the advance of knowledge regarding the precise function of specific nociceptors.

Complementing *in vitro* models of isolated and dissociated DRG neurons, immortalized cell lines despite their limitations, have enabled important advances in understanding sensory neuron function. They retain significant phenotypic similarities to primary cultures in addition to greater suitability for high throughput assays due to high consistency, reducing the number of experimental animals required as well as reducing other costs normally associated with isolation and dissociation of primary cells. In the last 3 decades only a handful of DRG-derived immortalized sensory neuronal cell lines have been generated. These include the hybrid cell lines F-11, ND-C, and ND7/23 (Platika et al., 1985b; Wood et al., 1990; Rugiero and Wood, 2009), the mouse cell line MED17.11, the rat cell line 50B11 and human HD10.6 cells (Raymon et al., 1999). All of these cellular models of sensory DRG neurons that were inherently valuable for initial investigations of signaling pathways and responses to drugs and toxins. As expected, each of the aforementioned cell lines has its own unique nociceptor-like characteristics. Hence, a comprehensive evaluation of their advantages and disadvantages when compared directly to naïve sensory DRG neuron subtypes would be helpful to the broader research community. In this review we aim to provide an objective comparison of different elements encompassing DRG derived cell line experiments. This review will provide a platform to compare culture conditions for each cell line, highlighting how have these changed over the years, the methods that were used to investigate the cells and importantly what receptors, signaling pathways and functions have been identified in each cell line. In addition, each cell line will be described regarding its characteristics and usefulness for specific techniques. Particular attention will also be given to describing the use of DRG cell lines to investigate nociceptive signaling.

Immortalized sensory neuron cell lines present valuable tools for the investigation of many aspect of neurobiology, including nociception. All of the cell lines created thus far share a multitude of characteristics with both embryonic and adult mammalian DRG neurones. However, as is the case with most cell lines, these are also contrasted with major characteristic differences that need to be carefully considered prior to their experimental selection. Often these cells do not recapitulate specific DRG neuron subtypes, such as peptidergic and non-peptidergic nociceptors and analysis of calcium responses to nociceptor-related agonists and RNAseq studies have demonstrated marked differences between available DRG-derived cell lines and naïve, primary cultured DRG neurons (Yin et al., 2016; Vetter and Lewis, 2010).

A major factor that explains differences in expression profiles and function is the fact that DRG sensory neurons used in the generation of cell lines are usually of embryonal or neonatal origin. Immortalized neuronal cells generally require exposure to growth factors such as nerve growth factor (NGF) and glial-derived growth factor (GDNF), or high intracellular levels of cAMP induced via dibutyryl cAMP (db-cAMP), activated by agents such as forskolin or retinoic acid (Ghyselinck and Duester, 2019) to differentiate into a postmitotic neuronal phenotype. This phenotype is evident by reduced or absent cell division and the formation of neurites, often accompanied by changes in cell body morphology, and expression levels of molecules characteristic of adult sensory neurons (Boland and Dingledine, 1990a,b).

Recognizing the distinct functional, morphological and neurochemical characteristics of each immortalized sensory cell line compared to native neurons enables judicious interpretation of experimental results, so that these tools can continue to enable important advances in sensory neurobiology. Here we describe each individual cell line including its origin, neurochemical characteristics including sensory and nociceptor-related molecules and endogenous ion channels, and features related to differentiation and neurite outgrowth presented in tables that summarize different methodologies in relation to culturing and differentiating these cells.

F-11 Cells

The immortalized DRG cell line F-11 was generated and first described by Platika et al. (1985a; 1985b). Sensory neurons,

isolated from rat DRG at embryonic days 13–14 were fused with the mouse neuroblastoma cell line N18TG2 via exposure to 55% polyethylenglycol for 2 min. The somatic hybrids were initially grown in Ham's F-12 medium with the addition of hypoxanthine, aminopterin and thymidine (HAT) (**Tables 1**, **3**) to eliminate the parent neuroblastoma N18TG2 which does not express hypoxanthine phosphoribosyltransferase (HPRT).

Karyological analysis of F-11 cells Platika et al. (1985b) showed that these cells contain concomitant mouse and rat chromosomes and isozymes, and subsequent microarray analysis confirmed the functional presence of DNA from rat and mouse with the demonstration of rat and mouse mRNAs (Zeng et al., 2002; Yin et al., 2016). Out of the initial four clones that possessed neuronal properties including neurite outgrowth, action potentials and labeling with neuron-specific gangliosides, only the differentiated F-11 cell line produced action potentials similar to sensory nociceptive DRG neurons, contained substance P-like immunoreactivity and responded to capsaicin (Platika et al., 1985a,b; Chiesa et al., 1997).

Francel et al. (1987a) further characterized F-11 cells and demonstrated their ability to differentiate in the presence of a medium that contained cAMP increasing molecules (**Table 1**). Differentiation was accompanied by a reduction in proliferation and the induction of neurite growth. But not all cells differentiated with initially only 25% of cells showing the appropriate morphological characteristics (Boland and Dingledine, 1990a). Increased levels of cAMP induced by application of the cAMP analog db-cAMP or the adenylate cyclase stimulator forskolin cause greater differentiation and the F-11 cells develop long neurites and change expression levels of receptors and channels (Francel et al., 1987a; Boland and Dingledine, 1990a,b; Ghil et al., 2000; Jahnel et al., 2003; Ambrosino et al., 2013; Hashemian et al., 2017). The concentrations of db-cAMP and forskolin necessary to induce complete differentiation of F-11 cells are 0.5 and 10 mM, respectively (Ghil et al., 2000; Gall-Ianotto et al., 2012). Nevertheless, other factors have been shown to successfully differentiate the cells including nerve growth factor, NGF (Martin et al., 2002) and retinoic acid (Naruse et al., 1992). In addition to growth factors, low serum medium containing 1% FBS for about 2 weeks also promoted differentiation (Pastori et al., 2019) (**Table 1**). In the process of differentiation into a DRG neuron-like phenotype, these cells also change the glycosphingolipid profile that remains different to DRG neurons (Ariga et al., 1995). F-11 cells grow on plastic but for experiments such as Ca^{2+} imaging, cells were grown on poly-L-lysine coated glass coverslips (Hwang et al., 2014).

Undifferentiated F-11 cells are not difficult to culture and passage. However, they start to die after 48–72 h of serum deprivation (0% serum) commonly used in differentiation protocols, and degradation of DNA starts at 24 h, reduction in protein synthesis after 8 h. In the absence of serum, cells still develop neurites which retract after 48 h (Linnik et al., 1993). Interestingly, undifferentiated F-11 cells loose rat and mouse chromosomes during cell division/passages (Cruciani et al., 1994).

RNASeq analysis of undifferentiated F-11 cells confirmed that the cells contained rat and mouse transcript (**Table 2**). In addition, the analysis described that undifferentiated cells do not represent mature sensory neurons. For example the cells only expressed 9 out of 43 neuronal marker mRNAs (Yin et al., 2016). Another unique characteristic is the high expression of the ganglioside GD3 which seems to be important for the ability of F-11 cells to generate tumors when grafted into nude mice (Zeng et al., 2000a,b, 2002).

Differentiated F-11 Cells Represent a Heterogenous Population of Cells

One question of critical importance is, whether F-11 cells represent a single population of sensory-like neurons. Their morphology certainly suggests more than one subtype of cells in culture, where F-11 cells can be small, flat, round, spindle-shaped or large (Boland and Dingledine, 1990a). Sorting of undifferentiated F-11 cells by flow cytometry showed two main populations of cells, larger, less granular, and smaller cells (Linnik et al., 1993). But what is the effect of differentiation on those subpopulations and the overall function of F-11 cells? The use of various formulations of differentiation media can have profound effects on physiological properties of immortalized cells. Voltage-clamp recordings showed that 25% of cells that were differentiated for 1–3 days showed an increased voltage-activated Ba^{2+} current (Boland and Dingledine, 1990b) and antisera directed against stage-specific embryonic oligosaccharides, SSEA-3 and -4 and B23D8, identified different populations of cells which could be separated by subcloning (Boland and Dingledine, 1990a). Interestingly the staining was independent of the different morphologies of F-11 cells (Boland and Dingledine, 1990a) (**Table 2**).

Expression of Neuronal and Nociceptor-Related Receptors and Molecules

The function of DRG neurons and, in particular, nociceptive neurons is associated with specific subsets of molecules such as receptors, channels and enzymes. Whereas stage-specific embryonic markers suggest heterogeneity, neurofilament 200 (NF200), a marker used to identify large DRG neurones in mice and rats, was present in all differentiated F-11 cells, and no immunoreactivity for markers of satellite and glia cells, GFAP and S-100, could be found in F-11 cultures (Boland and Dingledine, 1990a). Transient receptor potential (Trp) channels are present in nociceptors and Trp channel subtypes are key components of pain signaling (Basbaum and Braz, 2010; Naziroglu and Braidy, 2017). Trp family members are expressed in both naïve nociceptive DRG neurons and F-11 cells. Channel proteins such as TrpV1 or TrpA1 are closely associated with nociceptive signaling. Undifferentiated F-11 cells do not express the Trp channel family members TrpA1 (Yin et al., 2016) and TrpV4 (Goswami et al., 2010) but do express rat and mouse Trpv2 (Jahnel et al., 2003). They also express no or very low levels of TrpV1 mRNA and no transcripts for the nociceptor-associated neuropeptide calcitonin gene-related peptide, CGRP (Yin et al., 2016). The absence of nociceptor-related mRNAs and proteins in F-11 cells changes upon differentiation where mouse but not rat

TABLE 1 | Maintenance and differentiation media for dorsal root ganglion cell lines.

Name and original description	Maintenance media		Differentiation media	
F11 Platika et al., 1985a,b	Platika et al. (1985b) Ham's F-12, 15% FCS, HAT1, No Pen/Strep. Francel et al. (1987a) Ham's F-12, 20% FCS, HAT2, 50 IU Penicillin, ? Streptomycin. Boland and Dingledine (1990a) Ham's F-12, 15–20% FCS. HAT2, 10 mM glucose, 12 mM sodium-bicarbonate, no Pen/Strep. Linnik et al. (1993) Ham's F-12, 20% FCS, HAT2, 50 m/ml Penicillin, 50 mg/ml Streptomycin, 50 mg/ml Neomycin.	Kim et al. (2003) DMEM, 10% FBS, 100 IU Penicillin, 100 mg/ml Streptomycin. Rimmerman et al. (2008) Ham's F-12, 17% FCS, ? HAT, ? L-glutamine. Vetter and Lewis (2010) Ham's F-12, 10% FCS, HAT2. Ambrosino et al. (2013) DMEM, 10% FBS, 2 mM L-glutamine, 100 IU Penicillin,? Streptomycin.	Francel et al. (1987a) Ham's F-12, 1% FCS, 0.5 mM db-cAMP, 50 ng/ml NGF (mouse saliva), 2 mM retinoic acid, 5 mg/ml insulin, 100 mg/ml transferrin, 10 mM IBMX, 50 IU Penicillin, ? Streptomycin. Boland and Dingledine (1990a) Ham's F-12, 1% FCS, HAT2, 0.5 mM db-cAMP, 50 ng/ml NGF (2.5S), 10 mM IBMX, no Pen/Strep. Boland and Dingledine (1990b), Ham's F-12, 1% FCS, HAT2, 0.5 mM db-cAMP, 50 ng/ml NGF (2.5S), 10 mM IBMX; second experiment. 2 mM retinoic acid, 5 mg/ml insulin (bovine), 10 mg/ml transferrin, no Pen/Strep. Martinez et al. (2019) DMEM (no sodium pyruvate). *Three media – first* 0.5% FCS, 1 mM db-cAMP, 30 μM forskolin. *Second*: 0.5% FCS, 0.5 mM db-cAMP, 2 ng/ml NGF. *Third*: 0.5% FCS, 10 mM retinoic acid.	Martin et al. (2002) Ham's F-12, 2 mM glutamine. 15% HAT, 100 U/ml Penicillin, 100 μg/ml Streptomycin, 0.5 mM db-cAMP, 10 ng/ml NGF. Kim et al. (2003) DMEM, 0.5% FBS, 0.5 mM db-cAMP OR 30 μM forskolin. Hwang et al. (2008) DMEM, 0.5% FBS, 0.5 mM db-cAMP. Vetter and Lewis (2010) DMEM, 0.5% FBS, 1 mM db-cAMP, 2 nM NGF. Xu et al. (2010) DMEM, 0.5% FBS, 10 mM forskolin, 1% Pen/Strep. Gall-Ianotto et al. (2012), Keratinocyte-serum-free-media (K-SFM), 10 ng/ml NGF, 0.5 mM db-cAMP. Ambrosino et al. (2013), DMEM, 2% FBS, 10 mM retinoic acid. Hashemian et al. (2017) Ham's F-12, 0.5% FCS, 1 mM db-cAMP, 200 mg/ml NGF, 100 IU Penicillin, 100 mg/ml Streptomycin. Naruse et al. (1992) Ham's F-12, 1% FCS, 0.5 mM db-cAMP, crude NGF, 2 mM retinoic acid, 5 mg/ml insulin (bovine), 100 mg/ml transferrin, 10 mM IBMX, 50 IU Penicillin, ? Streptomycin. Pastori et al. (2019) DMEM, 1% FBS, 2 mM glutamine, Penicillin?, Streptomycin?.
ND7/23 Wood et al., 1990	Wood et al. (1990) Leibowitz L-15, 10% FCS, 3.3 g/l NaHCO3, 3 g/l glucose, 100 U/ml Penicillin, 100 mg/m, Streptomycin. Dunn et al. (1991) Leibowitz L-15, 10% FCS. Roobol et al. (1995) DMEM, 10% FBS, 2 mM glutamine, 100 U/ml Penicillin, 100 mg/ml Streptomycin. Wu et al. (2008) DMEM, 10% FBS, 2 mM glutamine, 50 U/ml Penicillin, 50 mg/ml Streptomycin.	Leffler et al. (2012) DMEM, 10% FBS, 25 mM HEPES, 3 mM taurine, 100 U/ml Penicillin, ? mg/ml Streptomycin. Milton (2012) DMEM/Ham's F-12 mix, 10% FCS, 1% non-essential amino acids, 100 U/ml Penicillin, 100 mg/ml Streptomycin. Takaku and Sango (2020) DMEM/Ham's F-12 mix, 5% FCS, ? U/ml Penicillin, ? mg/ml Streptomycin. Ma et al. (2020) DMEM, 10% FBS, 1% Penicillin, 1% Streptomycin, 0.11 g/L sodium-pyruvate.	Wood et al. (1990) L-15, 0.5% FCS, 1 mM db-cAMP, 2 mg/ml NGF. Dunn et al. (1991) L-15, 0.5% FCS, 1 mM db-cAMP, 2 ng/ml NGF. Roobol et al. (1995) DMEM, 0.5% FBS, 2 mM glutamine, 1 mM db-cAMP, 200 ng/ml NGF, 100 U/ml Penicillin, 100 mg/ml Streptomycin. Sivasubramaniam et al. (1997) DMEM, 10% FCS, 0.03% glutamine, 1 mM retinoic acid. Wu et al. (2008) DMEM, 0.5% FBS, 2 mM glutamine, 1 mM db-cAMP. OR 100 ng/ml NGF. Ma et al. (2020) DMEM, 10% FBS, 1 mM db-cAMP, 10 ng/ml NGF, 1% Penicillin, 1% Streptomycin, 0.11 g/L sodium-pyruvate.	Milton (2012) DMEM/Ham's F-12 mix, 10 μM forskolin, 100 mM IBMX. Zhang et al. (2017, 2019) DMEM/Ham's F-12 mix, 0.5% FBS, 1 mM db-cAMP, 50 ng/ml NGF, 20 mM uridine, 20 mM fluorodeoxyuridine. Martinez et al. (2019) DMEM (no sodium pyruvate). *Three media – first:* 0.5% FCS, 1 mM db-cAMP, 60 μM forskolin, 2 ng/ml NGF. *Second:* 0.5% FCS, 1 mM db-cAMP, 1.3 ng/ml NGF. *Third:* 2% FCS, 20 mM retinoic acid, 100 mM IBMX, 2 ng/ml NGF.

(Continued)

TABLE 1 | Continued

Name and original description	Maintenance media		Differentiation media	
50B11 Chen et al., 2007	Chen et al. (2007) Neurobasal medium, 10% FBS, 0.5 mM glutamine, 0.2% glucose, 1 × B-27 supplement. Van Opdenbosch et al. (2012) Neurobasal medium, 10% FCS, 0.27% glutamine, ? glucose (20%), 2% B-27 supplement, 0.1% blasticidin. Pundavela et al. (2014) Neurobasal medium, 10% FCS. Gnavi et al. (2015) Neurobasal medium, 10% FCS, 2% B-27 supplement, 0.22% glucose, 0.2 mM glutamine.	Bestall et al. (2018) Neurobasal medium, 10% FCS, ? B-27 supplement, 0.55 mM glutamine, 11 mM (0.2%) glucose. Mohiuddin et al. (2019) Neurobasal medium, 5% FCS, ? B-27 supplement, ? glutamine.	Chen et al. (2007) Neurobasal medium, 10% FBS, 0.5 mM glutamine, 0.2% glucose, 1 × B-27 supplement, 50 μM forskolin. *In some experiments.* 10 ng/ml NGF, 10 ng/ml GDNF. Vetter and Lewis (2010) Neurobasal medium, 75 μM forskolin. Bhattacherjee et al. (2014) Neurobasal medium, 75 μM forskolin *After 17 h* 50 ng/ml NGF, 50 ng/ml GDNF, 20 nM estrogen, 100 nM angiotensin II. Pundavela et al. (2014) Neurobasal medium, 10% FCS, 5 mM forskolin.	Hulse et al. (2015) Neurobasal medium, 10% FCS, ? B-27 supplement, 0.55 mM glutamine, 11 mM (0.2%) glucose. *After 48 h* 75 μM forskolin. Bestall et al. (2018) Neurobasal medium, 10% FCS, ? B-27 supplement, 0.55 mM glutamine, 11 mM (0.2%) glucose, 1 nM NGF, 75 μM forskolin. Mohiuddin et al. (2019) Neurobasal medium, 5% FCS, ? B-27 supplement, ? mM glutamine, 10 mM forskolin. Gnavi et al. (2015) Neurobasal medium, 10% FCS, 2% B-27 supplement, 0.22% glucose, 0.2 mM glutamine. *After 24 h* 75 μM forskolin.
MED17.11 Doran et al., 2015	Doran et al. (2015) DMEM/Ham's F-12 mix, 10% FBS, ? glutamate, 50 U/ml IFNγ, 0.5% chick embryonic extract, ? Penicillin, ? Streptomycin.		Doran et al. (2015) DMEM/Ham's F-12, 0.5 mM db-cAMP, 25 mM forskolin, 100 ng/ml NGF, 20 ng/ml GDNF, 10 ng/ml bFGF, 5 mg/ml Y-27623.	
HD10.6 Raymon et al., 1999	Raymon et al. (1999) L-15C, 40 ng/ml FGF-2.	Thellman et al. (2017) and Zhang et al. (2020) DMEM/Ham's F-12 mix, 1 × GlutaMax, 1 × B-27, 10 ng/ml PGE1, 0.5 ng/ml bFGF, 50 mg/ml G418 solution.	Raymon et al. (1999) L-15C, 10% FBS, 1 mg/ml tetracycline, 2.5% human serum, 5–10 mM forskolin, 25 ng/ml NGF, 25 ng/ml GDNF, 25 ng/ml CNTF, 80 ng/ml heregulin.	Thellman et al. (2017) NeuralQ basal medium, 1 × GlutaMax, GS21 neuronal supplement, 50 ng/ml NGF, 25 ng/ml GDNF, 25 ng/ml CNTF, 25 ng/ml NT-3, 1 mg/ml doxycycline. Zhang et al. (2020) NeuralQ basal medium, 1 × GlutaMax, 1 × B-27, GS21 neuronal supplement, 50 ng/ml NGF, 25 ng/ml GDNF, 25 ng/ml CNTF, 25 ng/ml NT-3, 1 mg/ml doxycycline, 1 μg/ml tetracycline, 25 μM forskolin.
ND-C Wood et al., 1990	Wood et al. (1990) Leibowitz L-15, 10% FCS, 3.3 g/l NaHCO3, ? g/l glucose, 100 U/ml Penicillin. 100 mg/ml Streptomycin. Wu et al. (2008) DMEM, 10% FBS, 50 U/ml Penicillin, 50 mg/ml Streptomycin, 2 mM glutamine.	Rugiero and Wood (2009) DMEM, 10% FBS, 4.5 g/L glucose, ? mM glutamine, 110 mg/L sodium pyruvate, 10,0000 U/ml penicillin-streptomycin.	Wu et al. (2008) DMEM, 0.5% FBS, 100 ng/ml NGF *or* 1 mM db-cAMP. Hackett et al. (2010) Keratinocyte serum-free medium (KSFM) plus bovine pituitary extract and EGF.	

The table provides an overview over the different components used in maintenance and differentiation media. Question marks are used to indicate absence of information in relation to amounts or concentrations of components. Abbreviations used in the table: Dibutyryl cAMP = db-cAMP; 100 mM hypoxanthine, 1 mM aminopterin, 12 mM thymidine = HAT1 was used to eliminate the parent neuroblastoma cells as the cell line has no HPRT (Platika et al., 1985a); 100 mM hypoxanthine, 0.4 mM aminopterin, 16 mM thymidine = HAT2; Fetal calf serum = FCS; Fetal bovine serum = FBS; 3-Isobutyl-1-methylxanthine = IBMX (phosphodiesterase inhibitor); Dulbecco's Modified Eagle's medium = DMEM; 4-(2-hydroxyethyl)-1-piperazineethanesulfonic acid = HEPES; Nerve growth factor = NGF; Glial-derived-neurotrophic-factor = GDNF; Basic fibroblast growth factor = bFGF; Y-27623 = inhibitor of Rho-associated, coiled-coil containing protein kinase (ROCK), Prostaglandin E1 = PGE1.

TABLE 2 | Methods utilizing dorsal root ganglion cell lines.

	Transcriptomics	Proteomics and immunohistochemistry	Imaging	Transfection	Electrophysiology and Currents	Others
F-11	Single cell RT-PCR (Jahnel et al., 2003). RT-PCR (Jow et al., 2006). Microarray (Zeng et al., 2002). RNA-Seq (Yin et al., 2016; Martinez et al., 2019; Guo et al., 2020). Cloning of mouse TRPV2 (Bender et al., 2005). Promotor/Luciferase reporter assay (Mahapatra et al., 2006). miRNA detection using graphene-PNA complexes (Oh et al., 2019).	Western Blot (Pollard and volume-sensitive, 1993; Ariga et al., 1995; Wood et al., 1988; Zeng et al., 2000a, 2002; Ross et al., 2001; Gall-Ianotto et al., 2012). Gas chromato-graphic/mass spectrometric analysis (Dasgupta and Banerjee, 1996). Affinity precipitation (Ruan et al., 2008). Immunohistochemistry (Pastori et al., 2019).	$^{45}Ca^{2+}$ uptake (Francel et al., 1987a). Fura-2 (Martin et al., 2002). Fluo-4, Poly-D-coated plates (Vetter and Lewis, 2010). Fura-2, glass coverslips (Ambrosino et al., 2013). Fura-2 (Hashemian et al., 2017). FLIPR Calcium-6 (Martinez et al., 2019). Bioluminescence imaging (Hwang et al., 2008). High throughput imaging (Martinez et al., 2019). Live cell imaging and pull down assay (Goswami et al., 2010). NO measurement, DAF-2 imaging (Rimmerman et al., 2008).	Stable transfection (Kim et al., 2003). Transient transfection (Rutter et al., 2005; Goswami et al., 2010; Ambrosino et al., 2013). Adenoviral transfection (Hester et al., 2007). Electroporation (Zhang et al., 2011). Transfection lipofectamine RNAiMAX (Guo et al., 2020).	Whole-cell patch clamp (Boland and Dingledine, 1990b; Ross et al., 2001). Patch clamp workstation (Mollereau et al., 2011). Perforated patch clamp (Ambrosino et al., 2019). Membrane potential measurement (Martinez et al., 2019).	Radioimmunoassay (Platika et al., 1985b). MTT assay (Linnik et al., 1993). HPTLC for glycosphingolipids (Ariga et al., 1995). Rb+ efflux assay (Jow et al., 2006). TrpV1 activation assay (Goswami et al., 2007). cAMP assay and MAPK assay (Fan et al., 2011). Co-culture keratinocytes/F-11 (Gall-Ianotto et al., 2012). EIA assay (Gall-Ianotto et al., 2012). Microfluidic chamber assay (Oh et al., 2019). Dynamic mass redistribution assay (Martinez et al., 2019).
ND7/23	RT-PCR (Tomita et al., 2019). qRT-PCR, miRNAs (Lee et al., 2019; Mukhopadhyay et al., 2019). RNA-Seq (Yin et al., 2016). DNA-affinity pull down assay (Monteiro et al., 2014).	Western Blot. Immunohistochemistry (Ulmann et al., 2007; Wu et al., 2008; Inoue et al., 2012; Binder et al., 2013). Mass spectroscopy (Devaux et al., 2017).	Fura-2 (Ulmann et al., 2007). Fluo-4, Poly-D-coated plates (Vetter and Lewis, 2010; Holmes et al., 2017; Ma et al., 2020).		Whole-cell patch clamp (Zhou et al., 2003, 2019; Morton et al., 2015; Stoetzer et al., 2016). Automated patch clamp platform (Rogers et al., 2016).	Co-culture keratino-cytes/ND7/23 (Ulmann et al., 2007). Time-lapse microscopy (Binder et al., 2013). Luciferase assay (Monteiro et al., 2014). Flow cytometry (Stoetzer et al., 2015). Neurite outgrowth (Mitani et al., 2016; Devaux et al., 2017). Reactive oxygen species (Zhou F. M. et al., 2017; Guo et al., 2018). Biotinylation surface proteins (Zhang et al., 2019). Cell viability (Ulmann et al., 2007; Pires et al., 2017; Akamine et al., 2019; Mukhopadhyay et al., 2019). Cytotoxicity (Nango et al., 2017). TUNEL assay and ROS measurement and Caspase-3 assay (Mukhopadhyay et al., 2019).

(Continued)

TABLE 2 | Continued

	Transcriptomics	Proteomics and immunohistochemistry	Imaging	Transfection	Electrophysiology and Currents	Others
ND-C	qRT-PCR (Wu et al., 2008).	Immunocyto-chemistry (Hackett et al., 2010).		Transfection PromoFectin (Solinski et al., 2010). Transfection lipofectamine (Rugiero and Wood, 2009).	Whole-cell patch clamp (Rugiero and Wood, 2009).	
50B11	RT-PCR (Chen et al., 2007; Geng et al., 2009).	Western Blot (Geng et al., 2009; Van Opdenbosch et al., 2012; Zhu et al., 2016; Bestall et al., 2018). Immunohistochemistry (Chen et al., 2007; Pundavela et al., 2014; Hulse et al., 2015; Mohiuddin et al., 2019).	Fura-2, glass coverslips, rat tail collagen (Chen et al., 2007). Fluo-4, Poly-D-coated plates (Vetter and Lewis, 2010). Fluo-4 (Hulse et al., 2015).	Transfection with inactivated virus (Van Opdenbosch et al., 2012). Plasmid transfection using jetPrime reagent (Van Opdenbosch et al., 2012). Knockdown using shRNA (Geng et al., 2009; Bhattacherjee et al., 2017). siRNA (Zhu et al., 2016).	Whole-cell patch clamp (Chen et al., 2007).	^{86}Rb uptake (Geng et al., 2009). Thallium uptake in single cells (Geng et al., 2009). Co-culture, transwell chambers (Pundavela et al., 2014). Cell cytotoxicity (Mohiuddin et al., 2019). Superoxide dismutase activity (Mohiuddin et al., 2019). Apoptosis assay (Mohiuddin et al., 2019). Click-iT EdU proli-feration assay (Mohiuddin et al., 2019).
HD 10.6	RT-PCR (Raymon et al., 1999). qRT-PCR (Thellman et al., 2017; Zhang et al., 2020).	Western Blot (Raymon et al., 1999; Thellman et al., 2017). Immunohistochemistry (Thellman et al., 2017; Zhang et al., 2020).			Whole-cell patch clamp (Zhang et al., 2020).	HSV-1 infection (Zhang et al., 2020). Cell viability (Zhang et al., 2020).
MED17.11	RT-PCR (Doran et al., 2015).	Immunohistochemistry (Doran et al., 2015).	Fura-2 Poly-*O*-coated plates (Doran et al., 2015).	Transfection pmax GreenFP (Doran et al., 2015).		

TABLE 3 | Summary of characteristics of immortalized DRG neuron cell lines.

	F-11	ND7/23	ND-C	50B11	MED17.11	HD10.6
Species of origin	Rat DRG E13-14 × mouse neuroblastoma cell line N18TG2.	Rat DRG neonatal × mouse neuroblastoma cell line N18TG2.	Rat DRG neonatal × mouse neuroblastoma cell line N18TG2.	Rat DRG E14.5.	Mouse (H2kbtsA58 Immortomouse) DRG E12.5.	Human DRG embryonic - 1st trimester .
First description (see **Table 1**)	Platika et al., 1985a	Wood et al., 1990	Wood et al., 1990	Chen et al., 2007	Doran et al., 2015	Raymon et al., 1999
Culture surface and matrix composition	Glass/plastic. Poly-D-lysine. Gelatin	Glass/plastic. Poly-D-lysine.	Glass/plastic, collagen type I. Laminin.	Glass/plastic. No matrix.	Glas/plastic. Poly-L-ornithine.	Glass – Matrigel coated. poly-D-lysine. Plastic - fibronectin-coated.
Differentiation agents used (see **Table 1**)	db-cAMP, retinoic acid, NGF, BDNF, NT	db-cAMP, retinoic acid, NGF	db-cAMP	Forskolin, NGF, GDNF, estrogen, angiotensin II	Forskolin, NGF, GDNF, bFGF, Y-27623	Forskolin, NGF, GDNF, CNTF, heregulin
RNAseq (see **Table 2**)	Data available for undifferentiated treated and untreated cells.	Data available for undifferentiated cells.	No data available.	No data available.	No data available.	No data available.
Nociceptor-related molecules and responses (see **Table 2**)	Present, predominantly in differentiated cells.	Present, predominantly in differentiated cells.	Some molecules and channels present but no functional TrpV1, TrpA1 channels.	Present, predominantly in differentiated cells.	Present, predominantly in differentiated cells.	Present, predominantly in differentiated cells.
Endogenous Ion channel expression	Voltage-gated Ca^{2+} and Na^{+} channels present, differently expressed in undifferentiated and differentiated cells.	Voltage-gated Ca^{2+} and Na^{+} channels present, differently expressed in undifferentiated and differentiated cells.	Voltage-gated Na^{+} channels and mechanosensitive currents.	Indirect evidence for voltage-gated Ca^{2+} channels, no electrophysiology studies conducted.	Indirect evidence for voltage-gated Na^{+} channels, no electrophysiology studies conducted.	Voltage-gated Ca^{2+} and Na^{+} channels present in differentiated cells.
Primary reported use (see **Table 2**)	Investigation of differentiation and neurite outgrowth.	Transfection and investigation of Voltage-gated Na^{+} channels.	Investigation of mechanosensitivity.	Investigations of toxicity.	Only one descriptive publication.	Investigation of virus transfection.
Experimental considerations	After 5 passages no response to gabapentin, loss of opioid receptors after 10 passages.	Mouse and rat mRNAs and proteins present and expressed.	Has only some characteristics of nociceptors.	Electrophysiological characteristics unknown.	Not available.	Limited description due to low number of publications.

mRNA for TrpV1 is present (Jahnel et al., 2001, 2003; Ambrosino et al., 2013; Yin et al., 2016; Hashemian et al., 2017). In addition to TrpV1, differentiation with retinoic acid and NGF increased also the relative mRNA expression levels for TLR4, cannabinoid and bradykinin receptors (Hashemian et al., 2017) (**Tables 1**, **3**).

Functional TrpV1 channels have been demonstrated with the inward currents, depolarisation and increase in intracellular Ca^{2+} levels in response to the TrpV1 agonist capsaicin (Platika et al., 1985a; Ambrosino et al., 2019; Pastori et al., 2019) and via blockade of the capsaicin-dependent intracellular Ca^{2+}-increase by the antagonist capsazepine (Ambrosino et al., 2013). Early experiments demonstrated the presence of the neuropeptide substance P (SP) but not CGRP via radioimmunoassay in differentiated F-11 cells (Wood et al., 1990). Later it was shown, that F-11 cells that were differentiated in keratinocyte serum-free-medium supplemented with NGF and db-cAMP expressed substance P (SP) and CGRP and released those neuropeptides in response to capsaicin (Gall-Ianotto et al., 2012). Netrin-1 upregulated CGRP mRNA in F-11 cells (Guo et al., 2020). Recent studies also demonstrated that differentiated cells respond to SP with a small inward current (Pastori et al., 2019). Acidic solutions and acetylcholine, but neither capsaicin nor an agonists of the nociceptor-related mas-related gene (Mrg) receptors produced no effects in undifferentiated F-11 cells (Solinski et al., 2010; Yin et al., 2016; Pastori et al., 2019). A high proportion of low-serum differentiated cells responded to glutamate, acetylcholine and acidic solutions (Pastori et al., 2019). In addition to the investigation of endogenous channel proteins, Trp channels and Mrg proteins were also transfected into undifferentiated F-11 cells and investigated (Rutter et al., 2005; Goswami et al., 2007; Solinski et al., 2010).

The presence of molecules in F-11 cells that are characteristic of nociceptors is not restricted to ion channels and peptides. F-11 cells express the endothelial and neuronal isoforms of the nitric oxide synthase (NOS) (Rimmerman et al., 2008) which both have been demonstrated in nociceptive DRG neurons (Henrich et al., 2004; Papadopolou et al., 2004). Activation of NOS with subsequent generation of nitric oxide contributes to distinct pain signaling pathways that lead to central sensitization and also mediate the effects of opioids (Cury et al., 2011).

Opioids and consequently opioid receptors are also innately linked to pain signaling (Francois and Scherrer, 2018). Undifferentiated and differentiated F-11 cells express the opioid receptor subtypes δ and μ but not κ (Fan et al., 1992; Cruciani et al., 1993). Undifferentiated cells showed a ratio for δ and μ surface receptors of 6:1 (Cruciani et al., 1993). Activation of the receptors inhibited adenylate cyclase via $G_{i/o}$ and reduced intracellular cAMP levels (Francel et al., 1987a; Fan et al., 1992) but the experiments suggested that δ receptor activation might also be coupled to G_s-protein signaling (Cruciani et al., 1993). Interestingly, loss of rat and mouse chromosomes in undifferentiated F-11 cells during cell division/passages has been shown to impact on opiate receptor expression. The passage-dependent chromosomal loss caused total absence of δ and μ receptors in F-11 cells after 10 passages (Cruciani et al., 1994).

In addition to opioids, the cannabinoid system is another potential therapeutic target in treatment of pain. Cannabinoid receptors, CB1 and CB2 are expressed in rat DRG neurons (Svizenska et al., 2013; Oliveira-Fusaro et al., 2017) as well as in differentiated and undifferentiated F-11 cells (Ross et al., 2001; Yin et al., 2016; Hashemian et al., 2017). F-11 cells express mouse but not rat CB1 and CB2 mRNA (Hashemian et al., 2017) with the CB1 receptor showing a stronger immunoreactivity in undifferentiated F-11 cells compared to CB2 (Ross et al., 2001).

Bradykinin is a pro-inflammatory mediator that has been shown to modulate pain via activation of two receptor subtypes (BKB1R and BKB2R) present on DRG neurons (Chen et al., 2010; Takemura et al., 2011). Binding sites for bradykinin are present on undifferentiated and differentiated F-11 cells and incubation of undifferentiated cells with bradykinin caused a transient increase in intracellular Ca^{2+} and the $G_{i/o}$-dependent production of IP_3 and DAG (Francel et al., 1987a,b; Francel and Dawson, 1988; Solinski et al., 2010; Vetter and Lewis, 2010; Ambrosino et al., 2019). Even though undifferentiated and differentiated cells possess binding sites for bradykinin, the Ca^{2+} response to bradykinin increased in differentiated F-11 cells (Ambrosino et al., 2019).

The toll-like receptor 4 (TLR4) is a pattern recognition receptor that is expressed by DRG neurons and contributes to inflammatory and chemotherapy-induced pain (Li et al., 2015). F-11 cells express mouse but not rat TLR4 mRNA and protein with increased levels of both in response to differentiation. Isolated and cultured DRG neurons respond to LPS-mediated TLR4 activation with massive increases in interferon β, TNF-α or Il-6 expression but LPS had no effect in differentiated and undifferentiated F-11 cells (Hashemian et al., 2017).

Lipids were also investigated in F-11 cells. Depolarisation of F-11 cells also increased production of the lipid *N*-palmitoyl glycine (PalGly) in undifferentiated cells where the lipid also caused Ca^{2+} influx (Rimmerman et al., 2008).

Ion Channels

F-11 cells express a large variety of ion channels. RNA analysis demonstrated the presence of 223 mouse and 201 rat ion channel genes in undifferentiated F-11 cells (Yin et al., 2016) (**Table 2**). Voltage-gated calcium channels (VGCCs) are key components in pain signaling. Activation of nociceptors includes opening of Ca^{2+}-channels, and drugs that reduce pain such as opioids often block Ca^{2+}-channels. VGCCs can be divided into high-voltage-activated (HVA) and low-voltage-activated (LVA) channels. HVA channels are composed of different subunits, α, β, and γ, whose composition determines types of Ca^{2+} currents (L-type, N-type, P/Q-type, and R-type). The α-subunits are often related to a specific current type, e.g., the α1-subunit $Ca_V2.1$ is related to the P/Q-type current. LVA channels represent the T-type current (Altier and Zamponi, 2008). Neither undifferentiated nor cells differentiated under low-serum conditions expressed LVA channels (Pastori et al., 2019). Undifferentiated F-11 cells express mRNAs for all calcium channel a-subunit (Ca_V) isoforms with $Ca_V3.2$ expressed at the highest level (Yin et al., 2016). Functionally, early and recent studies showed that F-11 cells possess endogenous L-type Ca^{2+}-channels but these were 5-10 times less dense compared to cultured rat DRG neurons (Boland and Dingledine, 1990b; Pastori et al., 2019). Early

studies also suggested that Ca^{2+}-channels expression was higher in differentiated compared to undifferentiated cells (Francel et al., 1987a). In addition to L-type channels, the cells also possess N-type like Ca^{2+}-channels. Functional consequences of depolarisation and subsequent Ca^{2+}-channel activation have been demonstrated by the release of SP-like immunoreactivity from differentiated and undifferentiated F-11 cells (Boland and Dingledine, 1990b). Depolarisation of F-11 cells with KCl caused subsequent activation of VGCCs and increase in intracellular Ca^{2+}-levels (Martin et al., 2002). This response was stronger in differentiated compared to undifferentiated cells and the robust Ca^{2+}-response of differentiated F-11 cells to depolarisation was used for screening of analgesics and investigations into the function of the anticonvulsant and inhibitor of α2δ-subunits containing VGCC, gabapentin (Martin et al., 2002; Martinez et al., 2019). Gabapentin (applied 1–2 min before depolarisation) caused a small dose-dependent reduction of the depolarisation-induced Ca^{2+} influx into F-11 cells (Martin et al., 2002). Interestingly, the response was dependent on passage number as passage numbers > 5 did not respond to gabapentin. Non-responding cells showed marked differences in the relative mRNA expression levels of β_2 and α2δ2- VGCC subunits with a higher expression of β_2 and a lower expression of mRNA for α2δ2 in gabapentin-responsive cells.

With the exception of VGCCs, very few studies investigated changes in ion channel expression levels in F-11 cells. Early studies from Boland and Dingledine that were confirmed by Pastori et al. (2019) demonstrated that all Na+ currents in differentiated and undifferentiated F-11 cells could be blocked by tetrodotoxin (TTX), indicating that the majority of voltage-gated sodium channels (VGSCs) belongs to the class of TTX-sensitive channels (Boland and Dingledine, 1990b; Clement et al., 2007; Wang et al., 2017; Pastori et al., 2019). In addition to TTX, a toxin of the spider *Grammostola rosea* was also able to block Na^+ currents in F-11 cells (Clement et al., 2007). Recently, F-11 cells were used to investigate voltage-gated potassium channels of the Kv7 subgroup. The channels are contributing to the I_{KM} current in nociceptive DRG neurons and are part of TrpV1 signaling. All known Kv7 subunits of the channels were expressed in F-11 cells and a current with similarities to I_{KM} was identified (Ambrosino et al., 2019). Additionally, both undifferentiated and differentiated cells also express the ERG potassium current with increased current density observed in differentiated cells (Faravelli et al., 1996; Pastori et al., 2019).

Differentiation and Neurite Outgrowth

F-11 cells represent undifferentiated sensory neurons but respond to stimuli such as growth factors with changes in cell morphology and neurite outgrowth. Therefore, the cell line was utilized for research into the process of sensory neuron differentiation. Neurite outgrowth and neuronal marker expression in undifferentiated F-11 cells in response to different agents were used as read-outs. When exposed to differentiation medium, neurite formation started after 3 h. Initial studies indicated that after 72 h no new neurite formation could be observed (Francel et al., 1987a) but later it was demonstrated that neurite extension and differentiation could be still demonstrated at day 6 (Gall-Ianotto et al., 2012). Differentiation of F-11 cells in keratinocyte serum-free-medium supplemented with NGF and db-cAMP induced neurite outgrowth that could not be increased by addition of B27 or N2 supplement or addition of BDNF and/or NT-3 (Gall-Ianotto et al., 2012). Recently, long term exposure (12–14 days) to low-serum (1% FCS) without addition of growth factors achieved differentiation in 50% of cells. Compared to undifferentiated cells a significantly higher proportion of low-serum differentiated cells generated action potentials in response to stimulation (Pastori et al., 2019) (**Table 1**).

Novel approaches such as the use of optical imaging reporters to monitor neuronal differentiation processes were utilized to investigate the roles of the transcription factor neurogenin 1 (Ngn1) (Oh et al., 2013). Ngn1 induced neurite outgrowth in undifferentiated F-11 cells and increased the relative mRNA expression levels of neuronal markers Tuj-1, NeuroD, MAP2 and neurofilament-M but not of NeuN (Oh et al., 2013). Further investigations showed a role for the microRNAs miR-124 and miR193a in this process. Increase in miR-124 levels increased neurite outgrowth as well as immunoreactivities for Tuj1 and neurofilament (Jang et al., 2016) whereas miR193a was able to increase the efficiency of Ngn1-mediated differentiation by down-regulating proliferation associated mRNAs. Interestingly, studies investigating Ngn1 and miRNAs also demonstrated the intercellular transport and uptake of miR-193a via exosomes (Oh et al., 2017; Oh et al., 2019).

In addition to the investigation of basic mechanisms underlying neuronal differentiation, drugs and peptides were also investigated to their potential to induce neurite outgrowth. The antidepressant fluoxetine hydrochloride and activation of transfected TrpV4 channels reduced neurite outgrowth and induced growth cone retraction in forskolin-differentiated F-11 cells (Goswami et al., 2010; Xu et al., 2010) whereas the peptide analog PACAP38 caused an 170-fold increase in neurite outgrowth compared to forskolin or db-cAMP (McIlvain et al., 2006) (**Table 2**). A factor produced by macrophages, netrin-1, also increased length and number of neurites in F-11 cells (Guo et al., 2020).

In summary, F-11 cells are widely used in neuroscience and research has utilized a magnitude of different methods to describe the presence and function of neuron-associated mRNAs, miRNAs and proteins in undifferentiated as well as the differentiated F-11cells. F-11 cells express many molecules that are characteristic for sensory neurons and specific for nociceptors, with expression profiles that are highly dependent on differentiation state. A comprehensive analysis of transcripts has only been done for undifferentiated cells. Similarly, at the protein level a lack of comprehensive proteomics in undifferentiated and differentiated cells does not allow conclusions to be drawn with respect to the translational profile of F-11 cells. The cells are widely used for analysis of signaling and neurite outgrowth but the documented presence of mouse and rat mRNAs and proteins in the cell line and the loss of chromosomes when passaged over a longer period are potential limitations should be considered.

ND7/23 Cells

ND7/23 cells were generated by fusion of cultured neonatal rat DRG neurons with N18TG2 mouse neuroblastoma cells in serum-free L-15 medium containing 50% PEG_{1500} (Wood et al., 1990). Undifferentiated cells are round and have no neurites (Wood et al., 1990; Zhang et al., 2017) but maintain neuronal identity and can be stained with neuronal markers such as PGP9.5, MAP1 and Smi 312 (Ulmann et al., 2007). Differentiation was initially induced by db-cAMP and NGF in L15 medium supplied with 0.5% FCS (**Tables 1**, **3**) and treatment induced neurite outgrowth within 24 h (Wood et al., 1990). The differentiation response to the increase in cAMP was recently confirmed but was different depending on the differentiation medium (Martinez et al., 2019) (**Table 1**). Differentiated cells were usually used for between 3 and 14 days (Dunn et al., 1991; Zhang et al., 2017; Amaye et al., 2018; Zhang et al., 2019). Differentiated and undifferentiated ND7/23 cells grow on glass and plastic and on uncoated and poly-D-lysine coated surfaces. High glucose concentrations (≥60 mM) lead to DNA-damage and apoptosis of ND7/23 cells. This could be prevented by use of the caspase inhibitor Ac-LETD-CHO and the a-ketoglutarate analog DMOG (Mukhopadhyay et al., 2019). Another hyperglycemia-related molecule, the hydroxyaldehyde glycolaldehyde exhibited toxicity and also induced c-jun terminal kinase and p-38 MAPK-associated cell death in undifferentiated ND7/23 cells (Akamine et al., 2019).

Expression of Neuronal and Nociceptor-Related Receptors and Molecules

Differentiated ND7/23 cells, similar to F-11 cells, seem to represent a heterogenous population of cells as subpopulations of cells respond differently to the pro-inflammatory mediator and activator of sensory neurons, bradykinin (Wood et al., 1990; Dunn et al., 1991; Ulmann et al., 2007; Ma et al., 2020). Bradykinin exposure depolarised these cells and induced an inward current as well as $^{45}Ca^{2+}$ and Rb^{2+} efflux in differentiated cells (Wood et al., 1990; Dunn et al., 1991; Ulmann et al., 2007) (**Table 2**). Interestingly, this response was the opposite to F-11 cells, which responded with an outward current to bradykinin (Wood et al., 1990). Recently it has been shown that differentiated ND7/23 cells showed a stronger increase in intracellular calcium in response to bradykinin when exposed to conditioned medium collected from hypoxia-stressed intervertebral disks (Ma et al., 2020).

ND7/23 cells were utilized as a model to test and to explore adenovirus vector-mediated and chitosan-based gene delivery in nerve cell. The cells showed robust expression of β-galactosidase in response to adenovirus vector transfection (Sivasubramaniam et al., 1997) as well as internalization of nanoparticles (Oliveira et al., 2010a,b) (**Table 2**). RNAs and proteins were investigated by next generation sequencing (RNA-Seq) and mass spectrometry (MS) and tandem MS, but those studies only investigated undifferentiated ND7/23 cells (Yin et al., 2016; Devaux et al., 2017).

Neuropeptides such as calcitonin-gene related peptide (CGRP) or substance P (SP) are characteristic molecules in subpopulations of nociceptors (Basbaum and Braz, 2010; Haberberger et al., 2019). Radioimmunoassays and immunohistochemistry showed that undifferentiated and differentiated ND7/23 cells contain SP but not CGRP (Wood et al., 1990; Ulmann et al., 2007) (**Table 2**). Another molecule that is used to label nociceptive neuron subpopulations is the isolectin B4 (IB4) which in mice labels NGF-independent, non-peptidergic nociceptors. Incubation with IB4 labeled undifferentiated ND7/23 cells (Ulmann et al., 2007; Inoue et al., 2012). ND7/23 cells did not respond to GABA, another peptide that has been shown to interact with nociceptors (Suburo et al., 1992).

Regarding nociceptive Trp channel expression, undifferentiated ND7/23 cells showed no Ca^{2+} response to agonists of TrpV1 and TrpA1 channels, a finding that was supported by very low or absent mRNA expression levels for the Trp proteins (Ulmann et al., 2007; Yin et al., 2016). Nevertheless the cells were able to take up the TrpV1 activator anandamide (Thors and Fowler, 2006). Studies using RT-PCR showed that undifferentiated and differentiated cells express TrpC mRNAs 3–7 with increased Trpc4 levels in differentiated cells (Wu et al., 2008), whereas RNA-Seq analysis could not detect TrpC4 and 6 in undifferentiated cells (Yin et al., 2016). In addition to TrpV1, the P_2X_3 receptor for ATP is characteristic for subtypes of nociceptors. Undifferentiated ND7/23 cells showed no functional response to the P_2X receptor agonist αβ-meATP, whereas activation of P_2Y receptors caused release of Ca^{2+} from intracellular stores (Ulmann et al., 2007) (**Table 2**). The responses of differentiated cells have not been investigated so far.

Formaldehyde directly activates nociceptors and is used in animal models of acute pain. Undifferentiated ND7/23 cells were used as a model of nociceptors and responded to formaldehyde with an dose-dependent increase in intracellular Ca^{2+} (Fischer et al., 2015).

Acid-sensing ion channels (ASICs) are present on nociceptive DRG neurons and are involved in nociceptive signaling in for example cancer related pain (Lozano-Ondoua et al., 2013). Indirect evidence for the presence of ASICs in differentiated ND7/23 cells was provided by the activation of currents using solutions with a low pH (Moore et al., 2005; Ma et al., 2020).

Serotonin, 5-hydroxytryptamine (5-HT), activates nociceptive DRG neurons and induces pain or itch via interaction with 5-HT receptors (Hachisuka et al., 2010; Lin et al., 2011). 5-HT_3A receptors are involved in pain signaling (Costall and Naylor, 2004) and belong to the class of ligand-gated ion channels that consist of 5-HT_3A homopentamers. Undifferentiated ND7/23 cells express endogenous 5-HT_3A receptors (Morton et al., 2015). Stimulation of the receptors increased the 5-HT_3A-mediated current density in ND7/23 cells (Morton et al., 2015).

Sensory DRG neurons are important components of itch signaling (Akiyama and Carstens, 2013). Undifferentiated ND7/23 cells respond, similar to sensory DRG neuron subpopulations, to the itch-inducing molecules chloroquine and compound 48/80 (Zhou F. M. et al., 2017) and this chloroquine- and compound 48/80-dependent increase in intracellular

Ca^{2+} was decreased by the major green tea polyphenol EGCG (Guo et al., 2018).

Ion Channels

RNA analysis demonstrated the presence of 214 mouse and 189 rat ion channel genes in undifferentiated ND7/23 cells (Yin et al., 2016) including calcium and sodium channels. Based on the activation threshold, VGCCs can be divided into HVA and LVA channels. Undifferentiated ND7/23 cells only expressed a transient LVA current whereas 40–50% of differentiated cells showed LVA and HVA currents (Kobrinsky et al., 1994; Zhang et al., 2017). Differentiation also reduced the activation voltage necessary to induce maximal VGCC opening (Zhang et al., 2017).

ND7/23 cells showed a prominent T-type Ca^{2+}-current and expressed the related $Ca_V3.2$ channel proteins (**Table 3**). The T-type current increased upon differentiation (Mitani et al., 2016; Zhang et al., 2017; Amaye et al., 2018) but interestingly independent of the presence of NGF in the differentiation medium (Zhang et al., 2017). The anticancer drug Bortezomib increased $Ca_V3.2$ channel proteins and T-type currents in ND7/23 cells (Tomita et al., 2019).

Voltage-gated sodium channels (VGSCs) are an additional key component of neuronal excitability. They consist of nine different pore forming α-subunits in combination with four auxiliary β-subunits. Based on the nine α-subunits nine VGSCs, $Na_V1.1$-$Na_V1.9$, have been described (Altier and Zamponi, 2008; Wang et al., 2017). Many studies used ND7/23 cells for transfection and expression of sodium channels. However, RT-PCR and functional studies showed that undifferentiated ND7/23 cells already express endogenous VGSCs with the majority of channels being TTX-sensitive. $Na_V1.7$ and Na_V 1.6 are major subtypes with $Na_V1.2$, Na_V 1.3 and Na_V 1.9 channels contributing only little to activity. $Na_V1.7$, Na_V 1.6 and Na_V 1.9 represent the mouse channel proteins. The accessory subunits β1 and β3 are expressed together with pore-forming α-subunits (John et al., 2004; Leffler et al., 2010; Kennedy et al., 2013; Rogers et al., 2016; Lee et al., 2019). Interestingly, VGSC were not investigated in differentiated cells. Endogenously expressed $Na_V1.7$ and other VGSC were targeted in undifferentiated ND7/23 cells to investigate the mechanisms underlying actions of pain modulating molecules such as local anesthetics, μ-opioid receptor agonists or the toxin bufalin (Leffler et al., 2012; Stoetzer et al., 2017; Tao et al., 2018) but also the antidepressant duloxetine and methadone which blocked endogenous sodium currents (Stoetzer et al., 2015, 2016). The impact of toxins isolated from the venom of the Asian scorpion *Buthus martensi* Karsch on endogenously expressed VGSC in undifferentiated ND7/23 cells was investigated to explain the pain-related effects of the venoms (Zhu et al., 2009, 2015; Feng et al., 2015).

A large number of studies have used ND7/23 cells for the stable and transient transfection of proteins, in particular for investigations of different isoforms and mutations of sodium channels (for example Zhou et al., 2003, 2018, 2019; Dong et al., 2007; Leffler et al., 2010; O'Brien et al., 2012; Vanoye et al., 2013; de Kovel et al., 2014; Savio-Galimberti et al., 2014; Morton et al., 2015; Stoetzer et al., 2015; Wagnon et al., 2017; Wu et al., 2017; Zhou F. M. et al., 2017; Zhou X. et al., 2017; Dash et al., 2018; Li et al., 2018). Most studies transfected cells and electrophysiology was performed after 24–48 h. The reason for the popularity of ND7/23 cells in VGSC research is the endogenous expression of channel-associated proteins in undifferentiated cells which enables and facilitates the incorporation of functional channel proteins into membranes and establishes electrophysiological characteristics that mimic those of naïve channels (Rogers et al., 2016). This review only describes the endogenous expression of ion channels.

Differentiation and Neurite Outgrowth

Compared to F-11 cells few publications have utilized the ND7/23 cell line for investigating differentiation and neurite outgrowth. However, it has been shown that undifferentiated cells give rise to short neurites after 48 h whereas differentiation induces outgrowth of long unbranched neurites (Wu et al., 2008). Extracellular Ca^{2+} is necessary for axon growth but co-culture experiments with keratinocytes rescued axonal growth in the presence of low extracellular Ca^{2+} levels (Ulmann et al., 2007). Notably, Mitani et al. (2016) showed that the prostaglandin PGE_2 and the second messenger cAMP cause neurite outgrowth via the PGE_2/EP_4/cAMP signaling under participation of protein kinase A and $Ca_V3.1$ channels. Inhibition of T-type Ca^{2+}-channels caused a reduction in the number and length of dendritic processes induced by differentiation (Zhang et al., 2017). Expression of the TrpC4 protein was shown to be associated to growth of processes in differentiated ND7/23 cells as shRNA against TrpC4 blocked db-cAMP-induced neurite outgrowth (Wu et al., 2008). The impact of extracellular matrix proteins such as electrospun fibers on neurite outgrowth from differentiated ND7/23 cells was shown with the positive effect of polylactic-glycolic acid fibers (Binder et al., 2013). The involvement of the NGF receptor TrkA in neurite outgrowth was demonstrated in co-culture experiments with keratinocytes. Co-culturing induced neurite outgrowth which was blocked by the TrkA antagonist K252a (Ulmann et al., 2009). Recently it was demonstrated that the neuronal guidance molecule netrin-1 significantly increased neurite outgrowth in undifferentiated F-11 cells (Guo et al., 2020).

The role RhoA signaling and RhoA inhibitors in axon growth were investigated in differentiated (Pires et al., 2017) and undifferentiated NF7/23 cells (Devaux et al., 2017). RhoA inhibitors improved neurite outgrowth in ND7/23 cells that were conditioned with medium from injured spinal cord (Devaux et al., 2017). The neurite outgrowth promoting drug zonisamide induced the phosphorylation of AKT and Erk1/2 (Takaku and Sango, 2020).

In summary, the endogenous presence of accessory subunits that are necessary to express functional ion channels makes ND7/23 cells the working horse of VGSC research. Despite their presence, most papers do not refer to endogenous VGSCs and changes in expression profiles and function of ion channels that occur after differentiation and maturation of ND7/23 cells have not been investigated so far. There are obvious differences in cell function between undifferentiated and differentiated cells. It is not clear if the heterogenous population of undifferentiated ND7/23 cells differentiates into multiple

phenotypes or acquires a more homogenous type of sensory neuron-like cell. Interestingly, even though ND7/23 express a variety of nociceptor-related molecules and are used as models of nociceptors, characteristic channel proteins such as TrpV1 or TrpA1 are absent in undifferentiated cells and have not been investigated in differentiated cells.

ND-C Cells

In addition to ND7/23 cells, ND-C cells were also generated by fusion of cultured neonatal rat DRG neurons with N18TG2 mouse neuroblastoma cells in serum-free L-15 medium containing 50% PEG_{1500} (Wood et al., 1990). Cells were differentiated using db-cAMP and NGF (Wu et al., 2008), and also differentiated using keratinocyte serum free medium (KSFM) (Hackett et al., 2010) (**Tables 1**, **3**). Co-culture experiments demonstrated the ability of ND-C cells to form contacts with other cells such as C2C12 myocytes and to induce epithelial cell proliferation (Hackett et al., 2010).

Expression of Neuronal and Nociceptor-Related Receptors and Molecules

Early studies showed that opioids or d-receptor agonists increased intracellular Ca^{2+} levels in ND-C cells via activation of dihydroperidine-sensitive channels (Tang et al., 1994). In later studies, the cells were analyzed for the presence of TrpC mRNAs and used for transfection of TrpC4. Cells were differentiated in the presence of db-cAMP or NGF and showed increased relative mRNA expression for TrpC4, 5, 6, and 7. TrpC1 was present in undifferentiated cells and did not change and TrpC3 could not be detected (Wu et al., 2008). Differentiated ND-C cells responded to acid but not to the TrpV1 agonist capsaicin which indicates the presence of ASIC-like channels but not TrpV1 (Rugiero and Wood, 2009). In addition to capsaicin and 2-ABP, the cells were also insensitive to the TrpM8 agonist menthol, the TrpA1 activators cinnamaldehyde and mustard oil, and the TrpV4 agonist 4a-PPD. This suggests that the cells have no nociceptive phenotype. Interestingly, ND-C cells were shown to be mechano-sensitive (Rugiero and Wood, 2009).

Ion Channels

Electrophysiology using ND-C cells showed that the cells possess VGSCs which were TTX-sensitive (Rugiero and Wood, 2009) and identified chloride and potassium channels responsible for the hyperpolarisation-gated inward current (Hackett et al., 2010).

Differentiation and Neurite Outgrowth

Cells were differentiated using db-cAMP and NGF (Wu et al., 2008) and a differentiation using KSFM medium supplemented with bovine pituitary extract and EGF differentiated 10% of cells (Hackett et al., 2010) (**Table 1**). When KSFM medium was used, db-cAMP, NGF and dexamethasone had no significant additional effect on differentiation (30–50% of cells) but increased neurite length (**Table 1**). Differentiation on collagen-based matrices induced the growth of processes longer than 200 mM in 1/5th of all cells (Hackett et al., 2010).

In summary, ND-C is a sensory DRG neuron cell line that shares functional similarities with mechanosensitive rather than nociceptive neurons (**Table 3**). This represents a unique opportunity to utilize these cells for investigations of mechanosensitivity.

50B11 Cells

The 50B11 cell line was generated by electroporation and transfection of the SV40 large antigen and subsequent transfection with the human telomerase reverse transcriptase, hTERT, into primary cultured rat embryonal (E14.5) DRG neurons (Chen et al., 2007). Cells were grown in Neurobasal medium containing 10% FBS, 0.5 mM glutamine, 0.2% glucose and B-27 supplement (**Tables 1**, **3**). 50B11 cells grow on uncoated plastic dishes and have a replication rate of about 36 h (Chen et al., 2007). The initial description used a combination of forskolin, NGF and GDNF to start differentiation (Chen et al., 2007). Differentiation induced neurite outgrowth and changed cell morphology. The changes could be induced by forskolin alone and was most stable 20–36 h post forskolin (Bhattacherjee et al., 2014).

Expression of Neuronal and Nociceptor-Related Receptors and Molecules

Differentiated 50B11 cells could be labelled with pan-neuronal markers such as III-tubulin (Chen et al., 2007; Bhattacherjee et al., 2014) and PGP9.5 (Bhattacherjee et al., 2014; Pundavela et al., 2014). In addition, different receptors that are characteristic for nociceptors have been shown to be expressed in 50B11 cells. TrpV1 and TrpA1 receptors are functional in differentiated 50B11 cells as TrpV1 agonist capsaicin and the TrpA1 receptor agonist allyl isothiocyanate, AITC, increased levels of intracellular Ca^{2+} (Chen et al., 2007; Vetter and Lewis, 2010) (**Table 2**). Undifferentiated cells could be activated by ATP but failed to respond to other agents such as acetylcholine and bradykinin (Vetter and Lewis, 2010).

Differentiated 50B11 cells express in addition to TrpV1 other molecules typical for nociceptors such as peripherin, a molecule characteristic for small C-fiber type sensory neurons. Receptor proteins for the nociceptor-related growth factors NGF and GDNF such as trkA, p75NTR, c-Ret, GFRa1, and GFRa2 were detected in differentiated cells using RT-PCR and immunohistochemistry (Chen et al., 2007; Bhattacherjee et al., 2014). Consistent with this, the cells respond to NGF and GDNF (Chen et al., 2007; Bhattacherjee et al., 2014) (see below).

A key transporter in sensory nociceptive neurons is the Na^+-K^+-$2Cl^-$ cotransporter (NKCC1). This transporter together with other cation-chloride cotransporters and potentially regulatory kinases was detected in undifferentiated 50B11 cells via RT-PCR (Geng et al., 2009). Proteins for the kinases SPAK and OSR1 were also present in 50B11 cells and modulated NKCC1 activity (Geng et al., 2009).

Ion Channels

Ion channels are certainly present in 50B11 cells. This is supported by the use of calcium imaging to show activity of cells, but individual channels have so far not been investigated and described using patch-clamp or immunohistochemistry (**Table 2**). Interestingly, action potentials (AP) could be initiated

only in differentiated cells. The only publication that described the ability to generate APs was the initial description of 50B11 cells (Chen et al., 2007).

Differentiation and Neurite Outgrowth

50B11 cells are easy to grow. They grow on uncoated plastic or glass as well as on poly-L-lysin coated surfaces (Chen et al., 2007; Bhattacherjee et al., 2017). 50B11 cells were tested for their ability to grow neurites along artificial extracellular matrices. It was demonstrated that these cells grow and differentiate on 300 nm gelatin and chitosan fibers (Gnavi et al., 2015).

Neurite outgrowth and inhibition of proliferation (as markers of differentiation) could be induced by addition of forskolin usually in a concentration of 75 mM (Van Opdenbosch et al., 2012; Bhattacherjee et al., 2014; Gnavi et al., 2015; Hulse et al., 2015; Bestall et al., 2018) although concentrations of 5, 10, and 50 mM forskolin have been used as well (Chen et al., 2007; Pundavela et al., 2014; Mohiuddin et al., 2019). Forskolin is sufficient to induce neurite outgrowth and establishes and maintains a neuronal phenotype between 20 and 36 h after treatment (Chen et al., 2007; Geng et al., 2009; Bhattacherjee et al., 2014; Hulse et al., 2015).

However, compounding changes to the morphology of 50B11 cells can also be induced by the addition of a variety of growth-inducing factors such as NGF, GDNF, as well as pro-NGF, estrogen and angiotensin II 17 h after forskolin treatment additionally stimulated neurite outgrowth (Bhattacherjee et al., 2014; Pundavela et al., 2014). In addition to differentiating agents, neurite outgrowth in 50B11 cells could also be regulated by knockdown of proteins. Knockdown of the epigenetic controller methyl-CpG binding protein MeCP2 increased neurite outgrowth in differentiated 50B11 cells (Bhattacherjee et al., 2017).

Neurite outgrowth seemed also to be affected by the concentration of glucose in the differentiation medium. The working concentration for glucose in the maintenance and differentiation medium is already high. However, lower as well as higher glucose concentrations inhibited neurite outgrowth (Hulse et al., 2015; Bestall et al., 2018). Differentiation and neurite outgrowth was accompanied by changed mRNA expression levels of receptors for estrogen and angiotensin II (Bhattacherjee et al., 2014).

50B11 cells were also used to investigate the effect of cancer drugs. Studies that investigated the effects of the platinum-based anti-cancer chemotherapeutic cisplatin on 50B11 cells used differentiated (Vencappa et al., 2015) and undifferentiated (Zhu et al., 2016) cells. Cisplatin reduced the protein levels of ATF-3 and the growth factor VEGF-A_{165} and reduced neurite length. Cisplatin also increased levels of caspase 3, ataxin-2 and the spliceosome protein SF3B2.

In summary, 50B11 cells, particularly in the differentiated state, express a variety of sensory neuron and nociceptor-related molecules and seem to represent a suitable model for studies on neurite outgrowth (**Table 3**). Genomic sequencing and proteomic characterizing have not been conducted using the cells so far and in addition, the presence and function of ion channels in differentiated and undifferentiated cells has not been described.

MED17.11 Cells

The mouse embryonic DRG cell line, MED17.11, is a conditionally immortalized mouse cell line. It was generated by using DRG neurons from the H2kbtsA58 Immortomouse, that were isolated from E12.5 DRG (Doran et al., 2015). The cells started to change morphology to bipolar cells after few hours in differentiation medium which contained a cocktail of growth factors (bFGF, NGF, and GDNF), forskolin, db-cAMP, and the ROCK inhibitor Y-27632 (**Tables 1**, **3**). Differentiation was dependent on cell density with 5,000–15,000 cells/cm^2 produced the best differentiation.

Expression of Neuronal and Nociceptor-Related Receptors and Molecules

Undifferentiated cells could be stained for the pan-neuronal markers Tuj1 and FOX3 as well as for the marker of sensory nociceptive neurons, Isl1. The cells were also immunoreactive for the sensory neuron marker advillin. Differentiation induced the mRNA expression of sensory neurons and nociceptor-specific transcription factors FOXS1 and RUNX1. mRNAs for the GDNF receptor cRET, the neuropeptide CGRP and the NGF receptors TrkA and TrkC could be detected (**Table 2**). The Trp channel mRNAs for TrpV1 and TrpV2 were present in differentiated cells whereas TrpA1 mRNA could not be amplified and the TrpA1 agonist cinnamaldehyde had no effect. There was no evidence for functional Trpm8 receptors. Characteristic mRNAs for mechanosensitive receptors, Piezo 1 and 2, were also detected. MED17.11 cells could be labeled with IB4 and contained not only mRNA but also showed immunoreactivity for TrkA and TrkC. More than half of differentiated cells responded to bradykinin, but only about 1/3 to histamine and noradrenaline indicating a functionally heterogenous population of cells (Doran et al., 2015).

Ion Channels

The mRNAs for VGSCs $Na_V1.7$ and $Na_V1.9$ but not $Na_V1.8$ were detected only in differentiated cells. In addition, immunoreactivity for $Na_V1.3$ was present. The presence of TTX-sensitive VGSCs was supported by activation of the channels with veratridine which caused an increase in Ca^{2+}. The presence of VGCCs is likely, as indicated by the increase in intracellular Ca^{2+} in response to depolarisation with KCl.

The single publication using MED17.11 cells did not conduct experiments related to neurite outgrowth.

HD10.6 Cells

In contrast to other sensory neuron-derived cell lines, HD10.6 cells are immortalized human DRG cells. The cell line was first described by Raymon et al. (1999). Cultures of embryonic human DRG were immortalized using LINX *v*-myc as a retroviral vector. Undifferentiated cells divided about every 24 h but were not able to generate action potentials. Using tetracycline (doxycycline) to stop ongoing *v*-myc transcription and using L15-C or Ultraculture medium containing a cocktail of growth factors (**Tables 1**, **3**), cells were differentiated and differentiation was complete after 3–4 days (Raymon et al., 1999). Cells

grow on fibronectin or on poly-D-lysine and Matrigel coated coverslips (Zhang et al., 2020). Twenty years after the initial description, a second study used the cell line to investigate herpes simplex virus infection (Thellman et al., 2017). Short tandem repeat profiling defined the cell line as human, male. Modifications of the differentiation medium (**Table 1**) had no negative effect on nociceptive neuron marker expression (Thellman et al., 2017).

Expression of Neuronal and Nociceptor-Related Receptors and Molecules

The HD10.6 clone showed characteristics of sensory neurons such as b-III tubulin immunoreactivity and immunoreactivities for neurofilament 160 (NF160) as well as peripherin in large populations of differentiated cells. Subpopulation of differentiated cells also contained nociceptor-related molecules such as the neuropeptide substance P, the NGF receptor proteins TrkA and p75. HD10.6 cells expressed the transcription factors DRG11, a factor characteristic for post-migratory sensory neurons. Half of the differentiated cells expressed another DRG-specific transcription factor, Islet-1 (Raymon et al., 1999). In contrast to the initial description, where TrkB, TrkC, and RET could not be detected, strong expression of TrkA, TrkB, TrkC, and RET receptors was described in HD10.6 cells 7 and 14 days post-differentiation (Thellman et al., 2017).

Ion Channels

Differentiated HD10.6 cells expressed TTX-sensitive voltage-gated sodium channels, HVA Ca^{2+}-channels, αβ-methylene-ATP sensitive purinergic P_2X receptors and are sensitive to capsaicin. Recent studies confirmed the presence of TTX-sensitive channels with elimination of about 90% of sodium currents using 250 nM TTX and the detection of Nav1.7 mRNA and protein in differentiated HD10.6 cells (Zhang et al., 2020). Capsaicin responses could be blocked by capsazepine indicating the presence of TrpV1 channels (Raymon et al., 1999; Thellman et al., 2017) (**Table 2**).

Differentiation and Neurite Outgrowth

HD10.6 cells were able to differentiate in the presence of different growth factors (**Table 1**). Differentiation was induced in the presence of human serum, FBS, retinoic acid, forskolin, GDNF, CNTF, NGF, and heregulin b1. Replacement of forskolin with retinoic acid had the same effect (Raymon et al., 1999). The recent study used the growth factors NGF, GDNF, CNTF, and neurotrophin-3 for differentiation (Thellman et al., 2017). Differentiation included neurite outgrowth which was not further investigated.

In summary, the initial description clearly demonstrated an immortalized DRG neuron cell line that has a variety of nociceptor characteristics (**Table 3**). Almost 20 years later a second study used RT-PCR, immunohistochemistry and Ca^{2+}-imaging to further describe HD10.6 cells and use the cells as a model of sensory neurons in the context of herpes simplex virus infection (Thellman et al., 2017).

DISCUSSION

The development of immortalized DRG-derived cell lines has added numerous useful *in vitro* tools targeted at studies ranging from analysis of ion channel function to the description of intercellular RNA transfer via exosomes (**Table 2**). While individual cell lines have in each instance been developed by individual investigators seeking desirable characteristics that lead to their use for a specific set of methodologies, there is significant scope for increasing the utilization of DRG-derived cell lines in high-throughput screening tests investigating nociceptor targeted drug screens as well as basic nociceptor biology (**Table 2**). In most instances this would require additional characterisation of each cell line to better understand their suitability for different experimental approaches. ND7/23 cells for example have been mostly used for investigations of voltage gated sodium channel function, whereas F-11 cells are frequently used for investigations that involve neurite outgrowth and Ca^{2+}-imaging (**Table 2**). The cell lines usually express molecules characteristic for sensory neurons and nociceptors such as neuropeptides CGRP or SP, TTX-resistant sodium channels, the TRPV1 channel and receptors such as bradykinin or opioid receptors. The recent emergence of transcriptomic studies identifying a far-more diverse variety of nociceptive subtypes within dorsal root ganglia, has not only challenged the traditional classification of sensory neurons within the DRG, but the open-source nature of the generated databases provide a focal point of comparison to better classify and understand the phenotypic differences of existing DRG-derived cell lines. An important consideration regulating the phenotype of cell lines not often discussed is that a variety of different media for maintenance and differentiation of the cell lines have been used which can make it difficult to compare experiments between different groups using the same cell line but different media formulations (**Table 1**). Evidence from other sensory cell lines indicates that the use of different media for the culture of the same cell line can produce significant variability in the expression of a number of enzymes and transporters including the catecholaminergic biosynthetic enzymes tyrosine hydroxylase (TH) (Dixon et al., 2005). Studies analyzing the effect of media on the expression of critical neuronal or nociceptive properties are yet to be carried out on existing DRG- cell lines. Another significant aspect that has emerged from the studies reviewed here, is that a large proportion of publications do not directly refer to the overall cell population heterogeneity, which makes it challenging to draw conclusions from selected single cell measurements such as patch clamping or Ca^{2+}-imaging.

A rather underappreciated and unexplored aspect of these studies is the characterization and use of differentiated cells. These immortalized cell lines are often reported with results stemming from the use of undifferentiated or spontaneously differentiated cells, which begs the question of whether many of the published studies fully utilize the potential of these cell lines to represent sensory neurons. It is evident that all of the available cell lines have the capacity to alter their characteristic features such as peptide content or excitability upon exposure to chemical

differentiating agents or growth factors. Hence, the absence of RNA expression profile studies or comprehensive proteomic analyses does not allow a detailed comparison of the impact of differentiation on the neuronal or nociceptive properties of these cell lines. Although none of the cell lines reviewed here is identical to, for example, a certain nociceptor subtype, all of them show mixed expression profiles specific for nociceptors. Therefore, better characterisation and prudent differentiation with appropriate growth factor and mitotic agents could add valuable tools complementing primary cell cultures and aid in reducing the number of animals used in future studies. Besides, these refinements would further help to establish these cell lines as more valuable tools for approaches such as high throughput drug screening where primary cultures are not a viable option. Finally, immortalized cell lines from rat and mice are valuable tools in many ways but the best model for human sensory neurons would be human immortalized cells. Unfortunately, the only human DRG-derived cell line HD10.6 is no longer available to the general research community indicating an unmet need for the creation of human DRG cell lines.

Future Prospects

All of the reviewed cell lines have characteristics that make them highly suitable for future studies. F-11 and ND23/7 cells are suitable for functional studies as the cells share strong characteristics with nociceptors upon differentiation. The presence and expression of different nociceptor-related Trp channel proteins including TRPV1 in addition to activation of ion-channels-induced release of neuropeptides suggest that differentiated F-11 cells possess a high suitability for investigations into nociceptor signaling. Testing of molecules to determine their potential to directly activate or sensitize nociceptors is crucial in developing drugs and treatments. The cells lines can be grown on different surfaces which supports the inclusion into high-throughput systems and the presence of VGCCs allows direct investigations of responses via imaging.

Recent advances in the development of calcium indicators such as GCaMP6s (Qian et al., 2019) allow the creation of stably transfected F-11 or ND7/23 cells to investigate cellular responses in characterized single populations of nociceptor-like neurons via in high throughput assays. Of importance would be human DRG cell lines such as HD10.6 for example for the prediction of nociceptive responses to anti-cancer drugs (Niu and Wang, 2015).

But the potential applications of nociceptor-like cell lines is not restricted to drug testing. There are essential questions in the area of basic science that could be addressed using the cell lines. Sensory nociceptive neurons interact with surrounding cells in the peripheral tissues and in the spinal cord by many mechanisms including via communication via exosomes. Studies investigating the generation of exosomes and sorting mechanisms of exosomes in nociceptive neurons require a homogenous population of cells. F-11 cells have already been used to investigate exosomes (Oh et al., 2017) but the mixed genetic background might restrict experimental options. 50B11 cells or MED17.11 could be used to investigate transcriptional and intercellular basic mechanisms of exosome genesis. More importantly, exosomes may serve as novel potential diagnostic biomarkers for disease conditions and provide potential therapeutic compound leads.

Pain and the development of chronic pain involves an epigenetic component. Epigenetic mechanisms are reversible which makes them attractive targets for treatment of chronic pain. But epigenetic mechanisms in nociceptors are difficult to investigate and far from clearly understood (Penas and Navarro, 2018). Both 50B11 and MED17.11 cell lines have characteristics suitable to investigate the basic mechanisms underlying epigenetic control of nociceptors and to test treatment strategies.

Of course the future advances in nociceptor neuroscience gained by using the immortalized cell lines must be closely coupled to translational experiments involving naïve neurons and whole organisms.

The Limitations of Immortalized Cell Lines

This review describes stable immortalized cell lines that mirror nociceptive sensory neurons. These sensory neuronal-like cell lines were primarily established by fusion of post-mitotic embryonic [F-11 cell line (Platika et al., 1985a)] or neonatal [ND cell lines (Wood et al., 1990)]), rat DRG neurons with mouse N18Tg2 neuroblastoma cells, with the 50B11 (Chen et al., 2007) cells generated without inclusion of mouse genome, the MED17.11 cell line being generated from the immortomouse and the no longer available HD10.6 cell from human embryonic tissues using retroviral infection. All of these hybrid cell lines exhibit multiple DRG-selective properties, including cytoskeletal proteins, synaptic proteins, ion channels, neurotransmitters, and neurotransmitter receptors. However, the expression of markers such as tyrosine hydroxylase and neuropeptide Y in rat DRG-derived ND sub-clones (Suburo et al., 1992), but not 50B11 cells (Chen et al., 2007) confirms that cell lines are derived from different types of nociceptive neurons or that certain properties exhibited by these clones were derived from the neuroblastoma parent cell. More importantly, some of these hybrid cell lines do not contain neuropeptides such as CGRP and Substance P (Suburo et al., 1992) normally present within DRG sensory nociceptor and mechanoceptor populations. Previous reports also show that low-threshold calcium currents are the predominant component of calcium current in differentiated hybrid cells (Boland and Dingledine, 1990b; Kobrinsky et al., 1994) when compared to DRG neurons. Even though capsaicin- and bradykinin-activated currents were expressed by a subset of F-11 cells at early passages, the ability of these cells to express these properties after multiple passages appears to diminish (Kusano and Gainer, 1993). Examining the properties of retrovirally generated HD10.6 neurons, when differentiated, these cells in addition to other sensory neuronal-like cell lines did not express TTX-resistant sodium currents (Raymon et al., 1999), suggesting that some of the nociceptive properties and characteristics are independently controlled by extrinsic cues.

However, these neurons are functional and exhibit many properties specific to subsets of sensory neurons, including characteristics unique to nociceptive sensory neurons. All of these

immortalized DRG-derived cell lines have the potential value for future studies of developmental neurobiology, the identification and validation of novel drug targets, and the development and implementation of drug assays targeting specific nociceptive characteristics.

In summary, immortalized DRG cell lines have the potential to develop into tools more valuable than their current utilization would indicate, and in many ways remain underutilized and incompletely characterized. However, with advanced approaches to cell differentiation and more detailed analysis of nociceptive characteristics they possess considerable potential to support research in areas such preclinical research in basic neurobiology as well as drug development and screening targeted and nociceptors.

AUTHOR CONTRIBUTIONS

All authors listed have made a substantial, direct and intellectual contribution to the work, and approved it for publication. RH and DM researched and summarized the publications. RH created tables. RH, DM, and CB wrote the manuscript.

REFERENCES

Akamine, T., Takaku, S., Suzuki, M., Niimi, N., Yako, H., Matoba, K., et al. (2019). Glycolaldehyde induces sensory neuron death through activation of the c-Jun N-terminal kinase and p-38 MAP kinase pathways. *Histochem. Cell Biol.* 153, 111–119.

Akiyama, T., and Carstens, E. (2013). Neural processing of itch. *Neuroscience* 250, 697–714. doi: 10.1016/j.neuroscience.2013.07.035

Altier, C., and Zamponi, G. W. (2008). Signaling complexes of voltage-gated calcium channels and G protein-coupled receptors. *J. Recept. Signal. Transduct. Res.* 28, 71–81. doi: 10.1080/10799890801941947

Amaye, I. J., Heinbockel, T., Woods, J., Wang, Z., Martin-Caraballo, M., and Jackson-Ayotunde, P. (2018). 6 Hz active anticonvulsant fluorinated N-Benzamide enaminones and their inhibitory neuronal activity. *Int. J. Environ. Res. Public Health* 15:1784. doi: 10.3390/ijerph15081784

Ambrosino, P., Soldovieri, M. V., Di Zazzo, E., Paventi, G., Iannotti, F. A., Mosca, I., et al. (2019). Activation of Kv7 potassium channels inhibits intracellular Ca(2+) increases triggered by TRPV1-mediated pain-inducing stimuli in F11 immortalized sensory neurons. *Int. J. Mol. Sci.* 20:4322. doi: 10.3390/ijms20184322

Ambrosino, P., Soldovieri, M. V., Russo, C., and Taglialatela, M. (2013). Activation and desensitization of TRPV1 channels in sensory neurons by the PPARalpha agonist palmitoylethanolamide. *Br. J. Pharmacol.* 168, 1430–1444. doi: 10.1111/bph.12029

Ariga, T., Blaine, G. M., Yoshino, H., Dawson, G., Kanda, T., Zeng, G. C., et al. (1995). Glycosphingolipid composition of murine neuroblastoma cells: O-acetylesterase gene downregulates the expression of O-acetylated GD3. *Biochemistry* 34, 11500–11507. doi: 10.1021/bi00036a024

Basbaum, A. I., and Braz, J. M. (2010). "Transgenic mouse models for the tracing of "Pain" pathways," in *Translational Pain Research: From Mouse to Man*, eds L. Kruger, and A. R. Light (Boca Raton, FL): CRC Press).

Bender, F. L., Mederos, Y. S. M., Li, Y., Ji, A., Weihe, E., Gudermann, T., et al. (2005). The temperature-sensitive ion channel TRPV2 is endogenously expressed and functional in the primary sensory cell line F-11. *Cell Physiol. Biochem.* 15, 183–194. doi: 10.1159/000083651

Bestall, S. M., Hulse, R. P., Blackley, Z., Swift, M., Ved, N., Paton, K., et al. (2018). Sensory neuronal sensitisation occurs through HMGB-1-RAGE and TRPV1 in high-glucose conditions. *J. Cell Sci.* 131:jcs215939. doi: 10.1242/jcs.215939

Bhattacherjee, A., Liao, Z., and Smith, P. G. (2014). Trophic factor and hormonal regulation of neurite outgrowth in sensory neuron-like 50B11 cells. *Neurosci. Lett.* 558, 120–125. doi: 10.1016/j.neulet.2013.11.018

Bhattacherjee, A., Mu, Y., Winter, M. K., Knapp, J. R., Eggimann, L. S., Gunewardena, S. S., et al. (2017). Neuronal cytoskeletal gene dysregulation and mechanical hypersensitivity in a rat model of Rett syndrome. *Proc. Natl. Acad. Sci. U.S.A.* 114, E6952–E6961.

Binder, C., Milleret, V., Hall, H., Eberli, D., and Luhmann, T. (2013). Influence of micro and submicro poly(lactic-glycolic acid) fibers on sensory neural cell locomotion and neurite growth. *J. Biomed. Mater. Res. B Appl. Biomater.* 101, 1200–1208. doi: 10.1002/jbm.b.32931

Boland, L. M., and Dingledine, R. (1990a). Expression of sensory neuron antigens by a dorsal root ganglion cell line, F-11. *Brain Res. Dev. Brain Res.* 51, 259–266. doi: 10.1016/0165-3806(90)90284-6

Boland, L. M., and Dingledine, R. (1990b). Multiple components of both transient and sustained barium currents in a rat dorsal root ganglion cell line. *J. Physiol.* 420, 223–245. doi: 10.1113/jphysiol.1990.sp017909

Chen, Q., Vera-Portocarrero, L. P., Ossipov, M. H., Vardanyan, M., Lai, J., and Porreca, F. (2010). Attenuation of persistent experimental pancreatitis pain by a bradykinin b2 receptor antagonist. *Pancreas* 39, 1220–1225. doi: 10.1097/mpa.0b013e3181df1c90

Chen, W., Mi, R., Haughey, N., Oz, M., and Hoke, A. (2007). Immortalization and characterization of a nociceptive dorsal root ganglion sensory neuronal line. *J. Peripher. Nerv. Syst.* 12, 121–130. doi: 10.1111/j.1529-8027.2007.00131.x

Chiesa, N., Rosati, B., Arcangeli, A., Olivotto, M., and Wanke, E. (1997). A novel role for HERG K+ channels: spike-frequency adaptation. *J. Physiol.* 501(Pt 2), 313–318. doi: 10.1111/j.1469-7793.1997.313bn.x

Clement, H., Odell, G., Zamudio, F. Z., Redaelli, E., Wanke, E., Alagon, A., et al. (2007). Isolation and characterization of a novel toxin from the venom of the spider *Grammostola rosea* that blocks sodium channels. *Toxicon* 50, 65–74. doi: 10.1016/j.toxicon.2007.02.015

Costall, B., and Naylor, R. J. (2004). 5-HT3 receptors. *Curr. Drug Targets CNS Neurol. Disord.* 3, 27–37.

Cruciani, R. A., Dvorkin, B., Klinger, H. P., and Makman, M. H. (1994). Presence in neuroblastoma cells of a mu 3 receptor with selectivity for opiate alkaloids but without affinity for opioid peptides. *Brain Res.* 667, 229–237. doi: 10.1016/0006-8993(94)91500-8

Cruciani, R. A., Dvorkin, B., Morris, S. A., Crain, S. M., and Makman, M. H. (1993). Direct coupling of opioid receptors to both stimulatory and inhibitory guanine nucleotide-binding proteins in F-11 neuroblastoma-sensory neuron hybrid cells. *Proc. Natl. Acad. Sci. U.S.A.* 90, 3019–3023. doi: 10.1073/pnas.90.7.3019

Cury, Y., Picolo, G., Gutierrez, V. P., and Ferreira, S. H. (2011). Pain and analgesia: the dual effect of nitric oxide in the nociceptive system. *Nitric Oxide* 25, 243–254. doi: 10.1016/j.niox.2011.06.004

Dasgupta, A., and Banerjee, P. (1996). Significantly different fatty acid profiles in various phospholipid head groups of neuroblastoma cell lines. *Life Sci.* 58, 1285–1290. doi: 10.1016/0024-3205(96)00090-2

Dash, B., Han, C., Waxman, S. G., and Dib-Hajj, S. D. (2018). Nonmuscle myosin II isoforms interact with sodium channel alpha subunits. *Mol. Pain* 14:1744806918788638.

de Kovel, C. G., Meisler, M. H., Brilstra, E. H., van Berkestijn, F. M., van 't Slot, R., van Lieshout, S., et al. (2014). Characterization of a de novo SCN8A mutation in a patient with epileptic encephalopathy. *Epilepsy Res.* 108, 1511–1518. doi: 10.1016/j.eplepsyres.2014.08.020

Devaux, S., Cizkova, D., Mallah, K., Karnoub, M. A., Laouby, Z., Kobeissy, F., et al. (2017). RhoA inhibitor treatment at acute phase of spinal cord injury may induce neurite outgrowth and synaptogenesis. *Mol. Cell. Proteomics* 16, 1394–1415. doi: 10.1074/mcp.m116.064881

Dixon, D. N., Loxley, R. A., Barron, A., Cleary, S., and Phillips, J. K. (2005). Comparative studies of PC12 and mouse pheochromocytoma-derived rodent cell lines as models for the study of neuroendocrine systems. *In Vitro Cell Dev. Biol. Anim.* 41, 197–206.

Dong, X. W., Goregoaker, S., Engler, H., Zhou, X., Mark, L., Crona, J., et al. (2007). Small interfering RNA-mediated selective knockdown of Na(V)1.8 tetrodotoxin-resistant sodium channel reverses mechanical allodynia in neuropathic rats. *Neuroscience* 146, 812–821. doi: 10.1016/j.neuroscience.2007.01.054

Doran, C., Chetrit, J., Holley, M. C., Grundy, D., and Nassar, M. A. (2015). Mouse DRG cell line with properties of nociceptors. *PLoS One* 10:e0128670. doi: 10.1371/journal.pone.0128670

Dunn, P. M., Coote, P. R., Wood, J. N., Burgess, G. M., and Rang, H. P. (1991). Bradykinin evoked depolarization of a novel neuroblastoma x DRG neurone hybrid cell line (ND7/23). *Brain Res.* 545, 80–86. doi: 10.1016/0006-8993(91)91272-3

Fan, S. F., Shen, K. F., Scheideler, M. A., and Crain, S. M. (1992). F11 neuroblastoma x DRG neuron hybrid cells express inhibitory mu- and delta-opioid receptors which increase voltage-dependent K+ currents upon activation. *Brain Res.* 590, 329–333. doi: 10.1016/0006-8993(92)91116-v

Fan, Y., Hooker, B. A., Garrison, T. R., El-Kouhen, O. F., Idler, K. B., Holley-Shanks, R. R., et al. (2011). Pharmacological and molecular characterization of a dorsal root ganglion cell line expressing cannabinoid CB(1) and CB(2) receptors. *Eur. J. Pharmacol.* 659, 161–168. doi: 10.1016/j.ejphar.2011.03.020

Faravelli, L., Arcangeli, A., Olivotto, M., and Wanke, E. (1996). A HERG-like K+ channel in rat F-11 DRG cell line: pharmacological identification and biophysical characterization. *J. Physiol.* 496(Pt 1), 13–23. doi: 10.1113/jphysiol.1996.sp021661

Feng, Y. J., Feng, Q., Tao, J., Zhao, R., and Ji, Y. H. (2015). Allosteric interactions between receptor site 3 and 4 of voltage-gated sodium channels: a novel perspective for the underlying mechanism of scorpion sting-induced pain. *J. Venom. Anim. Toxins Incl. Trop. Dis.* 21:42.

Fischer, M. J., Soller, K. J., Sauer, S. K., Kalucka, J., Veglia, G., and Reeh, P. W. (2015). Formalin evokes calcium transients from the endoplasmatic reticulum. *PLoS One* 10:e0123762. doi: 10.1371/journal.pone.0123762

Francel, P., and Dawson, G. (1988). Bradykinin induces the bi-phasic production of lysophosphatidyl inositol and diacylglycerol in a dorsal root ganglion X neurotumor hybrid cell line, F-11. *Biochem. Biophys. Res. Commun.* 152, 724–731. doi: 10.1016/s0006-291x(88)80098-6

Francel, P. C., Harris, K., Smith, M., Fishman, M. C., Dawson, G., and Miller, R. J. (1987a). Neurochemical characteristics of a novel dorsal root ganglion X neuroblastoma hybrid cell line F-11. *J. Neurochem.* 48, 1624–1631. doi: 10.1111/j.1471-4159.1987.tb05711.x

Francel, P. C., Miller, R. J., and Dawson, G. (1987b). Modulation of bradykinin-induced inositol trisphosphate release in a novel neuroblastoma x dorsal root ganglion sensory neuron cell line (F-11). *J. Neurochem.* 48, 1632–1639. doi: 10.1111/j.1471-4159.1987.tb05712.x

Francois, A., and Scherrer, G. (2018). Delta opioid receptor expression and function in primary afferent somatosensory neurons. *Handb. Exp. Pharmacol.* 247, 87–114. doi: 10.1007/164_2017_58

Gall-Ianotto, C. Le, Andres, E., Hurtado, S. P., Pereira, U., and Misery, L. (2012). Characterization of the first coculture between human primary keratinocytes and the dorsal root ganglion-derived neuronal cell line F-11. *Neuroscience* 210, 47–57. doi: 10.1016/j.neuroscience.2012.02.043

Geng, Y., Hoke, A., and Delpire, E. (2009). The Ste20 kinases Ste20-related proline-alanine-rich kinase and oxidative-stress response 1 regulate NKCC1 function in sensory neurons. *J. Biol. Chem.* 284, 14020–14028. doi: 10.1074/jbc.m900142200

Ghil, S. H., Kim, B. J., Lee, Y. D., and Suh-Kim, H. (2000). Neurite outgrowth induced by cyclic AMP can be modulated by the alpha subunit of Go. *J. Neurochem.* 74, 151–158. doi: 10.1046/j.1471-4159.2000.0740151.x

Ghyselinck, N. B., and Duester, G. (2019). Retinoic acid signaling pathways. *Development* 146:dev167502. doi: 10.1242/dev.167502

Gnavi, S., Fornasari, B. E., Tonda-Turo, C., Laurano, R., Zanetti, M., Ciardelli, G., et al. (2015). The effect of electrospun gelatin fibers alignment on schwann cell and axon behavior and organization in the perspective of artificial nerve design. *Int. J. Mol. Sci.* 16, 12925–12942. doi: 10.3390/ijms160612925

Goswami, C., Kuhn, J., Heppenstall, P. A., and Hucho, T. (2010). Importance of non-selective cation channel TRPV4 interaction with cytoskeleton and their reciprocal regulations in cultured cells. *PLoS One* 5:e11654. doi: 10.1371/journal.pone.0011654

Goswami, C., Schmidt, H., and Hucho, F. (2007). TRPV1 at nerve endings regulates growth cone morphology and movement through cytoskeleton reorganization. *FEBS J.* 274, 760–772. doi: 10.1111/j.1742-4658.2006.05621.x

Guo, R., Zhou, F. M., Su, C. J., Liu, T. T., Zhou, Y., Fan, L., et al. (2018). Epigallocatechin-3-gallate attenuates acute and chronic psoriatic itch in mice: involvement of antioxidant, anti-inflammatory effects and suppression of ERK and Akt signaling pathways. *Biochem. Biophys. Res. Commun.* 496, 1062–1068. doi: 10.1016/j.bbrc.2018.01.122

Guo, X., Ding, S., Li, T., Wang, J., Yu, Q., Zhu, L., et al. (2020). Macrophage-derived netrin-1 is critical for neuroangiogenesis in endometriosis. *Int. J. Biol. Macromol.* 148, 226–237. doi: 10.1016/j.ijbiomac.2020.01.130

Haberberger, R. V., Barry, C., Dominguez, N., and Matusica, D. (2019). Human dorsal root ganglia. *Front. Cell. Neurosci.* 13:271. doi: 10.3389/fncel.2019.00271

Hachisuka, J., Furue, H., Furue, M., and Yoshimura, M. (2010). Responsiveness of C neurons in rat dorsal root ganglion to 5-hydroxytryptamine-induced pruritic stimuli in vivo. *J. Neurophysiol.* 104, 271–279. doi: 10.1152/jn.00938.2009

Hackett, J. M., Ferguson, C., Dare, E., McLaughlin, C. R., and Griffith, M. (2010). Optimal neural differentiation and extension of hybrid neuroblastoma cells (NDC) for nerve-target evaluations using a multifactorial approach. *Toxicol. In Vitro* 24, 567–577. doi: 10.1016/j.tiv.2009.10.016

Hashemian, S., Alhouayek, M., and Fowler, C. J. (2017). TLR4 receptor expression and function in F11 dorsal root ganglion x neuroblastoma hybrid cells. *Innate Immun.* 23, 687–696. doi: 10.1177/1753425917732824

Henrich, M., Paddenberg, R., Haberberger, R. V., Scholz, A., Gruss, M., Hempelmann, G., et al. (2004). Hypoxic increase in nitric oxide generation of rat sensory neurons requires activation of mitochondrial complex II and voltage-gated calcium channels. *Neuroscience* 128, 337–345. doi: 10.1016/j.neuroscience.2004.06.057

Hester, I., McKee, S., Pelletier, P., Thompson, C., Storbeck, C., Mears, A., et al. (2007). Transient expression of Nxf, a bHLH-PAS transactivator induced by neuronal preconditioning, confers neuroprotection in cultured cells. *Brain Res.* 1135, 1–11. doi: 10.1016/j.brainres.2006.11.083

Holmes, F. E., Kerr, N., Chen, Y. J., Vanderplank, P., McArdle, C. A., and Wynick, D. (2017). Targeted disruption of the orphan receptor Gpr151 does not alter pain-related behaviour despite a strong induction in dorsal root ganglion expression in a model of neuropathic pain. *Mol. Cell. Neurosci.* 78, 35–40. doi: 10.1016/j.mcn.2016.11.010

Hulse, R. P., Beazley-Long, N., Ved, N., Bestall, S. M., Riaz, H., Singhal, P., et al. (2015). Vascular endothelial growth factor-A165b prevents diabetic neuropathic pain and sensory neuronal degeneration. *Clin. Sci. (Lond)* 129, 741–756. doi: 10.1042/cs20150124

Hwang, D. W., Kang, J. H., Jeong, J. M., Chung, J. K., Lee, M. C., Kim, S., et al. (2008). Noninvasive in vivo monitoring of neuronal differentiation using reporter driven by a neuronal promoter. *Eur. J. Nucl. Med. Mol. Imaging* 35, 135–145. doi: 10.1007/s00259-007-0561-8

Hwang, H., Min, H., Kim, D., Yu, S. W., Jung, S. J., Choi, S. Y., et al. (2014). Imiquimod induces a Toll-like receptor 7-independent increase in intracellular calcium via IP(3) receptor activation. *Biochem. Biophys. Res. Commun.* 450, 875–879. doi: 10.1016/j.bbrc.2014.06.084

Inoue, A., Ohnishi, M., Fukutomi, C., Kanoh, M., Miyauchi, M., Takata, T., et al. (2012). Protein kinase A-dependent substance P expression by pituitary adenylate cyclase-activating polypeptide in rat sensory neuronal cell line ND7/23 cells. *J. Mol. Neurosci.* 48, 541–549. doi: 10.1007/s12031-012-9747-z

Jahnel, R., Bender, O., Munter, L. M., Dreger, M., Gillen, C., and Hucho, F. (2003). Dual expression of mouse and rat VRL-1 in the dorsal root ganglion derived cell line F-11 and biochemical analysis of VRL-1 after heterologous expression. *Eur. J. Biochem.* 270, 4264–4271. doi: 10.1046/j.1432-1033.2003.03811.x

Jahnel, R., Dreger, M., Gillen, C., Bender, O., Kurreck, J., and Hucho, F. (2001). Biochemical characterization of the vanilloid receptor 1 expressed in a dorsal root ganglia derived cell line. *Eur. J. Biochem.* 268, 5489–5496. doi: 10.1046/j.1432-1033.2001.02500.x

Jang, J., Lee, S., Oh, H. J., Choi, Y., Choi, J. H., Hwang, D. W., et al. (2016). Fluorescence imaging of in vivo miR-124a-induced neurogenesis of neuronal progenitor cells using neuron-specific reporters. *EJNMMI Res.* 6:38.

John, V. H., Main, M. J., Powell, A. J., Gladwell, Z. M., Hick, C., Sidhu, H. S., et al. (2004). Heterologous expression and functional analysis of rat Nav1.8 (SNS) voltage-gated sodium channels in the dorsal root ganglion neuroblastoma cell line ND7-23. *Neuropharmacology* 46, 425–438. doi: 10.1016/j.neuropharm.2003.09.018

Jow, F., He, L., Kramer, A., Hinson, J., Bowlby, M. R., Dunlop, J., et al. (2006). Validation of DRG-like F11 cells for evaluation of KCNQ/M-channel modulators. *Assay Drug Dev. Technol.* 4, 49–56. doi: 10.1089/adt.2006.4.49

Kennedy, P. G., Montague, P., Scott, F., Grinfeld, E., Ashrafi, G. H., Breuer, J., et al. (2013). Varicella-zoster viruses associated with post-herpetic neuralgia induce

sodium current density increases in the ND7-23 Nav-1.8 neuroblastoma cell line. *PLoS One* 8:e51570. doi: 10.1371/journal.pone.0051570

Kim, B. J., Ghil, S. H., Kim, M. J., Yun Park, S., Kim, D. S., Hwan Kim, S., et al. (2003). Modulation of the N-type calcium channel gene expression by the alpha subunit of Go. *Brain Res. Mol. Brain Res.* 112, 95–102. doi: 10.1016/s0169-328x(03)00053-6

Kobrinsky, E. M., Pearson, H. A., and Dolphin, A. C. (1994). Low- and high-voltage-activated calcium channel currents and their modulation in the dorsal root ganglion cell line ND7-23. *Neuroscience* 58, 539–552. doi: 10.1016/0306-4522(94)90079-5

Kusano, K., and Gainer, H. (1993). Modulation of voltage-activated Ca currents by pain-inducing agents in a dorsal root ganglion neuronal line, F-11. *J. Neurosci. Res.* 34, 158–169. doi: 10.1002/jnr.490340203

Lee, J., Kim, S., Kim, H. M., Kim, H. J., and Yu, F. H. (2019). NaV1.6 and NaV1.7 channels are major endogenous voltage-gated sodium channels in ND7/23 cells. *PLoS One* 14:e0221156. doi: 10.1371/journal.pone.0221156

Leffler, A., Frank, G., Kistner, K., Niedermirtl, F., Koppert, W., Reeh, P. W., et al. (2012). Local anesthetic-like inhibition of voltage-gated Na(+) channels by the partial mu-opioid receptor agonist buprenorphine. *Anesthesiology* 116, 1335–1346. doi: 10.1097/aln.0b013e3182557917

Leffler, A., Reckzeh, J., and Nau, C. (2010). Block of sensory neuronal Na+ channels by the secreolytic ambroxol is associated with an interaction with local anesthetic binding sites. *Eur. J. Pharmacol.* 630, 19–28. doi: 10.1016/j.ejphar.2009.12.027

Li, Y., Adamek, P., Zhang, H., Tatsui, C. E., Rhines, L. D., Mrozkova, P., et al. (2015). The cancer chemotherapeutic paclitaxel increases human and rodent sensory neuron responses to TRPV1 by activation of TLR4. *J. Neurosci.* 35, 13487–13500. doi: 10.1523/jneurosci.1956-15.2015

Li, Y., Zhu, T., Yang, H., Dib-Hajj, S. D., Waxman, S. G., Yu, Y., et al. (2018). Nav1.7 is phosphorylated by Fyn tyrosine kinase which modulates channel expression and gating in a cell type-dependent manner. *Mol. Pain* 14:1744806918782229.

Lin, S. Y., Chang, W. J., Lin, C. S., Huang, C. Y., Wang, H. F., and Sun, W. H. (2011). Serotonin receptor 5-HT2B mediates serotonin-induced mechanical hyperalgesia. *J. Neurosci.* 31, 1410–1418. doi: 10.1523/jneurosci.4682-10.2011

Linnik, M. D., Hatfield, M. D., Swope, M. D., and Ahmed, N. K. (1993). Induction of programmed cell death in a dorsal root ganglia X neuroblastoma cell line. *J. Neurobiol.* 24, 433–446. doi: 10.1002/neu.480240403

Lozano-Ondoua, A. N., Symons-Liguori, A. M., and Vanderah, T. W. (2013). Cancer-induced bone pain: mechanisms and models. *Neurosci. Lett.* 557(Pt A), 52–59. doi: 10.1016/j.neulet.2013.08.003

Ma, J., Stefanoska, D., Grad, S., Alini, M., and Peroglio, M. (2020). Direct and intervertebral disc-mediated sensitization of dorsal root ganglion neurons by hypoxia and low pH. *Neurospine* 17, 42–59. doi: 10.14245/ns.2040052.026

Mahapatra, N. R., Mahata, M., Ghosh, S., Gayen, J. R., O'Connor, D. T., and Mahata, S. K. (2006). Molecular basis of neuroendocrine cell type-specific expression of the chromogranin B gene: crucial role of the transcription factors CREB, AP-2, Egr-1 and Sp1. *J. Neurochem.* 99, 119–133. doi: 10.1111/j.1471-4159.2006.04128.x

Martin, D. J., McClelland, D., Herd, M. B., Sutton, K. G., Hall, M. D., Lee, K., et al. (2002). Gabapentin-mediated inhibition of voltage-activated Ca2+ channel currents in cultured sensory neurones is dependent on culture conditions and channel subunit expression. *Neuropharmacology* 42, 353–366. doi: 10.1016/s0028-3908(01)00181-2

Martinez, A. L., Brea, J., Monroy, X., Merlos, M., Burgueno, J., and Loza, M. I. (2019). A new model of sensorial neuron-like cells for HTS of novel analgesics for neuropathic pain. *SLAS Discov.* 24, 158–168. doi: 10.1177/2472555218810323

McIlvain, H. B., Baudy, A., Sullivan, K., Liu, D., Pong, K., Fennell, M., et al. (2006). Pituitary adenylate cyclase-activating peptide (PACAP) induces differentiation in the neuronal F11 cell line through a PKA-dependent pathway. *Brain Res.* 1077, 16–23. doi: 10.1016/j.brainres.2005.12.130

Milton, N. G. (2012). In vitro activities of kissorphin, a novel hexapeptide KiSS-1 derivative, in neuronal cells. *J. Amino Acids* 2012:691463.

Mitani, K., Sekiguchi, F., Maeda, T., Tanaka, Y., Yoshida, S., and Kawabata, A. (2016). The prostaglandin E2/EP4 receptor/cyclic AMP/T-type Ca(2+) channel pathway mediates neuritogenesis in sensory neuron-like ND7/23 cells. *J. Pharmacol. Sci.* 130, 177–180. doi: 10.1016/j.jphs.2016.02.008

Mohiuddin, M. S., Himeno, T., Inoue, R., Miura-Yura, E., Yamada, Y., Nakai-Shimoda, H., et al. (2019). Glucagon-like Peptide-1 receptor agonist protects dorsal root ganglion neurons against oxidative insult. *J Diabetes Res.* 2019:9426014.

Mollereau, C., Roumy, M., and Zajac, J. M. (2011). Neuropeptide FF receptor modulates potassium currents in a dorsal root ganglion cell line. *Pharmacol. Rep.* 63, 1061–1065. doi: 10.1016/s1734-1140(11)70623-5

Monteiro, C. B., Costa, M. F., Reguenga, C., Lima, D., Castro, D. S., and Monteiro, F. A. (2014). Paired related homeobox protein-like 1 (Prrxl1) controls its own expression by a transcriptional autorepression mechanism. *FEBS Lett.* 588, 3475–3482. doi: 10.1016/j.febslet.2014.08.006

Moore, P., Ogilvie, J., Horridge, E., Mellor, I. R., and Clothier, R. H. (2005). The development of an innervated epithelial barrier model using a human corneal cell line and ND7/23 sensory neurons. *Eur. J. Cell. Biol.* 84, 581–592. doi: 10.1016/j.ejcb.2004.10.005

Morton, R. A., Baptista-Hon, D. T., Hales, T. G., and Lovinger, D. M. (2015). Agonist- and antagonist-induced up-regulation of surface 5-HT3 A receptors. *Br. J. Pharmacol.* 172, 4066–4077. doi: 10.1111/bph.13197

Mukhopadhyay, D., Hammami, M., Khalouf, A., Shaikh, Y. A., Mohammed, A. K., Hamad, M., et al. (2019). Dimethyloxalylglycine (DMOG) and the Caspase Inhibitor "Ac-LETD-CHO" Protect Neuronal ND7/23 Cells of Gluocotoxicity. *Exp. Clin. Endocrinol. Diabetes*. doi: 10.1055/a-0919-4489

Nango, H., Kosuge, Y., Miyagishi, H., Sugawa, K., Ito, Y., and Ishige, K. (2017). Prostaglandin E2 facilitates neurite outgrowth in a motor neuron-like cell line, NSC-34. *J. Pharmacol. Sci.* 135, 64–71. doi: 10.1016/j.jphs.2017.09.001

Naruse, K., McGehee, D. S., and Oxford, G. S. (1992). Differential responses of Ca-activated K channels to bradykinin in sensory neurons and F-11 cells. *Am. J. Physiol.* 262, C453–C460.

Naziroglu, M., and Braidy, N. (2017). Thermo-sensitive TRP channels: novel targets for treating chemotherapy-induced peripheral pain. *Front. Physiol.* 8:1040. doi: 10.3389/fphys.2017.01040

Niu, N., and Wang, L. (2015). In vitro human cell line models to predict clinical response to anticancer drugs. *Pharmacogenomics* 16, 273–285. doi: 10.2217/pgs.14.170

O'Brien, J. E., Sharkey, L. M., Vallianatos, C. N., Han, C., Blossom, J. C., Yu, T., et al. (2012). Interaction of voltage-gated sodium channel Nav1.6 (SCN8A) with microtubule-associated protein Map1b. *J. Biol. Chem.* 287, 18459–18466. doi: 10.1074/jbc.m111.336024

Oh, H. J., Hwang, D. W., Youn, H., and Lee, D. S. (2013). In vivo bioluminescence reporter gene imaging for the activation of neuronal differentiation induced by the neuronal activator neurogenin 1 (Ngn1) in neuronal precursor cells. *Eur. J. Nucl. Med. Mol. Imaging* 40, 1607–1617. doi: 10.1007/s00259-013-2457-0

Oh, H. J., Kim, J., Park, H., Chung, S., Hwang, D. W., and Lee, D. S. (2019). Graphene-oxide quenching-based molecular beacon imaging of exosome-mediated transfer of neurogenic miR-193a on microfluidic platform. *Biosens. Bioelectron.* 126, 647–656. doi: 10.1016/j.bios.2018.11.027

Oh, H. J., Shin, Y., Chung, S., Hwang, D. W., and Lee, D. S. (2017). Convective exosome-tracing microfluidics for analysis of cell-non-autonomous neurogenesis. *Biomaterials* 112, 82–94. doi: 10.1016/j.biomaterials.2016.10.006

Oliveira, H., Fernandez, R., Pires, L. R., Martins, M. C., Simoes, S., Barbosa, M. A., et al. (2010a). Targeted gene delivery into peripheral sensorial neurons mediated by self-assembled vectors composed of poly(ethylene imine) and tetanus toxin fragment c. *J. Control Release* 143, 350–358. doi: 10.1016/j.jconrel.2010.01.018

Oliveira, H., Pires, L. R., Fernandez, R., Martins, M. C., Simoes, S., and Pego, A. P. (2010b). Chitosan-based gene delivery vectors targeted to the peripheral nervous system. *J. Biomed. Mater. Res. A* 95, 801–810. doi: 10.1002/jbm.a.32874

Oliveira-Fusaro, M. C. G., Zanoni, C. I. S., Dos Santos, G. G., Manzo, L. P., Araldi, D., Bonet, I. J. M., et al. (2017). Antihyperalgesic effect of CB1 receptor activation involves the modulation of P2X3 receptor in the primary afferent neuron. *Eur. J. Pharmacol.* 798, 113–121. doi: 10.1016/j.ejphar.2017.01.030

Papadopolou, S., Hartmann, P., Lips, K. S., Kummer, W., and Haberberger, R. V. (2004). Nicotinic receptor mediated stimulation of NO-generation in neurons of rat thoracic dorsal root ganglia. *Neurosci. Lett.* 361, 32–35. doi: 10.1016/j.neulet.2003.08.064

Pastori, V., D'Aloia, A., Blasa, S., and Lecchi, M. (2019). Serum-deprived differentiated neuroblastoma F-11 cells express functional dorsal root ganglion neuron properties. *PeerJ* 7:e7951. doi: 10.7717/peerj.7951

Penas, C., and Navarro, X. (2018). Epigenetic modifications associated to neuroinflammation and neuropathic pain after neural trauma. *Front. Cell. Neurosci.* 12:158. doi: 10.3389/fncel.2018.00158

Pires, L. R., Lopes, C. D. F., Salvador, D., Rocha, D. N., and Pego, A. P. (2017). Ibuprofen-loaded fibrous patches-taming inhibition at the spinal cord injury site. *J. Mater. Sci. Mater. Med.* 28:157.

Platika, D., Baizer, L., and Fishman, M. C. (1985a). Sensory neurons "immortalized" by fusion with neuroblastoma cells. *Trans. Assoc. Am. Physicians* 98, 301–304.

Platika, D., Boulos, M. H., Baizer, L., and Fishman, M. C. (1985b). Neuronal traits of clonal cell lines derived by fusion of dorsal root ganglia neurons with neuroblastoma cells. *Proc. Natl. Acad. Sci. U.S.A.* 82, 3499–3503. doi: 10.1073/pnas.82.10.3499

Pollard, C. E., and volume-sensitive, A. (1993). Cl- conductance in a mouse neuroblastoma x rat dorsal root ganglion cell line (F11). *Brain Res.* 614, 178–184. doi: 10.1016/0006-8993(93)91032-n

Pundavela, J., Demont, Y., Jobling, P., Lincz, L. F., Roselli, S., Thorne, R. F., et al. (2014). ProNGF correlates with Gleason score and is a potential driver of nerve infiltration in prostate cancer. *Am. J. Pathol.* 184, 3156–3162. doi: 10.1016/j.ajpath.2014.08.009

Qian, Y., Rancic, V., Wu, J., Ballanyi, K., and Campbell, R. E. (2019). A bioluminescent Ca(2+) indicator based on a topological variant of GCaMP6s. *Chembiochem* 20, 516–520. doi: 10.1002/cbic.201800255

Raymon, H. K., Thode, S., Zhou, J., Friedman, G. C., Pardinas, J. R., Barrere, C., et al. (1999). Immortalized human dorsal root ganglion cells differentiate into neurons with nociceptive properties. *J. Neurosci.* 19, 5420–5428. doi: 10.1523/jneurosci.19-13-05420.1999

Rimmerman, N., Bradshaw, H. B., Hughes, H. V., Chen, J. S., Hu, S. S., McHugh, D., et al. (2008). N-palmitoyl glycine, a novel endogenous lipid that acts as a modulator of calcium influx and nitric oxide production in sensory neurons. *Mol. Pharmacol.* 74, 213–224. doi: 10.1124/mol.108.045997

Rogers, M., Zidar, N., Kikelj, D., and Kirby, R. W. (2016). Characterization of endogenous sodium channels in the ND7-23 neuroblastoma cell line: implications for use as a heterologous ion channel expression system suitable for automated patch clamp screening. *Assay Drug Dev. Technol.* 14, 109–130. doi: 10.1089/adt.2016.704

Roobol, A., Holmes, F. E., Hayes, N. V., Baines, A. J., and Carden, M. J. (1995). Cytoplasmic chaperonin complexes enter neurites developing in vitro and differ in subunit composition within single cells. *J. Cell. Sci.* 108(Pt 4), 1477–1488.

Ross, R. A., Coutts, A. A., McFarlane, S. M., Anavi-Goffer, S., Irving, A. J., Pertwee, R. G., et al. (2001). Actions of cannabinoid receptor ligands on rat cultured sensory neurones: implications for antinociception. *Neuropharmacology* 40, 221–232. doi: 10.1016/s0028-3908(00)00135-0

Ruan, B., Pong, K., Jow, F., Bowlby, M., Crozier, R. A., Liu, D., et al. (2008). Binding of rapamycin analogs to calcium channels and FKBP52 contributes to their neuroprotective activities. *Proc. Natl. Acad. Sci. U.S.A.* 105, 33–38. doi: 10.1073/pnas.0710424105

Rugiero, F., and Wood, J. N. (2009). The mechanosensitive cell line ND-C does not express functional thermoTRP channels. *Neuropharmacology* 56, 1138–1146. doi: 10.1016/j.neuropharm.2009.03.012

Rutter, A. R., Ma, Q. P., Leveridge, M., and Bonnert, T. P. (2005). Heteromerization and colocalization of TrpV1 and TrpV2 in mammalian cell lines and rat dorsal root ganglia. *Neuroreport* 16, 1735–1739. doi: 10.1097/01.wnr.0000185958.03841.0f

Savio-Galimberti, E., Weeke, P., Muhammad, R., Blair, M., Ansari, S., Short, L., et al. (2014). SCN10A/Nav1.8 modulation of peak and late sodium currents in patients with early onset atrial fibrillation. *Cardiovasc. Res.* 104, 355–363. doi: 10.1093/cvr/cvu170

Sivasubramaniam, S., Fooks, A., Lee, J., Stacey, G., and Jennings, A. (1997). Gene delivery into neuronal and glial cells by using a replication-deficient adenovirus vector: prospects for neurological gene therapy. *Cytotechnology* 24, 253–259.

Solinski, H. J., Boekhoff, I., Bouvier, M., Gudermann, T., and Breit, A. (2010). Sensory neuron-specific MAS-related gene-X1 receptors resist agonist-promoted endocytosis. . *Mol. Pharmacol.* 78, 249–259. doi: 10.1124/mol.110.063867

Stoetzer, C., Kistner, K., Stuber, T., Wirths, M., Schulze, V., Doll, T., et al. (2015). Methadone is a local anaesthetic-like inhibitor of neuronal Na+ channels and blocks excitability of mouse peripheral nerves. *Br. J. Anaesth.* 114, 110–120. doi: 10.1093/bja/aeu206

Stoetzer, C., Martell, C., de la Roche, J., and Leffler, A. (2017). Inhibition of voltage-gated Na+ channels by bupivacaine is enhanced by the adjuvants buprenorphine, ketamine, and clonidine. *Reg. Anesth. Pain Med.* 42, 462–468. doi: 10.1097/aap.0000000000000596

Stoetzer, C., Papenberg, B., Doll, T., Volker, M., Heineke, J., Stoetzer, M., et al. (2016). Differential inhibition of cardiac and neuronal Na(+) channels by the selective serotonin-norepinephrine reuptake inhibitors duloxetine and venlafaxine. *Eur. J. Pharmacol.* 783, 1–10. doi: 10.1016/j.ejphar.2016.04.051

Suburo, A. M., Wheatley, S. C., Horn, D. A., Gibson, S. J., Jahn, R., Fischer-Colbrie, R., et al. (1992). Intracellular redistribution of neuropeptides and secretory proteins during differentiation of neuronal cell lines. *Neuroscience* 46, 881–889. doi: 10.1016/0306-4522(92)90191-4

Svizenska, I. H., Brazda, V., Klusakova, I., and Dubovy, P. (2013). Bilateral changes of cannabinoid receptor type 2 protein and mRNA in the dorsal root ganglia of a rat neuropathic pain model. *J. Histochem. Cytochem.* 61, 529–547. doi: 10.1369/0022155413491269

Takaku, S., and Sango, K. (2020). Zonisamide enhances neurite outgrowth from adult rat dorsal root ganglion neurons, but not proliferation or migration of Schwann cells. *Histochem. Cell Biol.* 153, 177–184.

Takemura, Y., Furuta, S., Hirayama, S., Miyashita, K., Imai, S., Narita, M., et al. (2011). Upregulation of bradykinin receptors is implicated in the pain associated with caerulein-induced acute pancreatitis. *Synapse* 65, 608–616. doi: 10.1002/syn.20880

Tang, T., Kiang, J. G., and Cox, B. M. (1994). Opioids acting through delta receptors elicit a transient increase in the intracellular free calcium concentration in dorsal root ganglion-neuroblastoma hybrid ND8-47 cells. *J. Pharmacol. Exp. Ther.* 270, 40–46.

Tao, J., Jiang, F., Liu, C., Liu, Z., Zhu, Y., Xu, J., et al. (2018). Modulatory effects of bufalin, an active ingredient from toad venom on voltage-gated sodium channels. *Mol. Biol. Rep.* 45, 721–740. doi: 10.1007/s11033-018-4213-9

Thellman, N. M., Botting, C., Madaj, Z., and Triezenberg, S. J. (2017). An immortalized human dorsal root ganglion cell line provides a novel context to study herpes simplex Virus 1 latency and reactivation. *J. Virol.* 91:e00080-17.

Thors, L., and Fowler, C. J. (2006). Is there a temperature-dependent uptake of anandamide into cells? *Br. J. Pharmacol.* 149, 73–81. doi: 10.1038/sj.bjp.0706831

Tomita, S., Sekiguchi, F., Deguchi, T., Miyazaki, T., Ikeda, Y., Tsubota, M., et al. (2019). Critical role of Cav3.2 T-type calcium channels in the peripheral neuropathy induced by bortezomib, a proteasome-inhibiting chemotherapeutic agent, in mice. *Toxicology* 413, 33–39. doi: 10.1016/j.tox.2018.12.003

Ulmann, L., Rodeau, J. L., Danoux, L., Contet-Audonneau, J. L., Pauly, G., and Schlichter, R. (2007). Trophic effects of keratinocytes on the axonal development of sensory neurons in a coculture model. *Eur. J. Neurosci.* 26, 113–125. doi: 10.1111/j.1460-9568.2007.05649.x

Ulmann, L., Rodeau, J. L., Danoux, L., Contet-Audonneau, J. L., Pauly, G., and Schlichter, R. (2009). Dehydroepiandrosterone and neurotrophins favor axonal growth in a sensory neuron-keratinocyte coculture model. *Neuroscience* 159, 514–525. doi: 10.1016/j.neuroscience.2009.01.018

Van Opdenbosch, N., Van den Broeke, C., De Regge, N., Tabares, E., and Favoreel, H. W. (2012). The IE180 protein of pseudorabies virus suppresses phosphorylation of translation initiation factor eIF2alpha. *J. Virol.* 86, 7235–7240. doi: 10.1128/jvi.06929-11

Vanoye, C. G., Kunic, J. D., Ehring, G. R., and George, A. L. Jr. (2013). Mechanism of sodium channel NaV1.9 potentiation by G-protein signaling. *J. Gen. Physiol.* 141, 193–202. doi: 10.1085/jgp.201210919

Vencappa, S., Donaldson, L. F., and Hulse, R. P. (2015). Cisplatin induced sensory neuropathy is prevented by vascular endothelial growth factor-A. *Am. J. Transl. Res.* 7, 1032–1044.

Vetter, I., and Lewis, R. J. (2010). Characterization of endogenous calcium responses in neuronal cell lines. *Biochem. Pharmacol.* 79, 908–920. doi: 10.1016/j.bcp.2009.10.020

Wagnon, J. L., Barker, B. S., Ottolini, M., Park, Y., Volkheimer, A., Valdez, P., et al. (2017). Loss-of-function variants of SCN8A in intellectual disability without seizures. *Neurol. Genet.* 3:e170.

Wang, J., Ou, S. W., and Wang, Y. J. (2017). Distribution and function of voltage-gated sodium channels in the nervous system. *Channels (Austin)* 11, 534–554. doi: 10.1080/19336950.2017.1380758

Wood, J. N., Bevan, S. J., Coote, P. R., Dunn, P. M., Harmar, A., Hogan, P., et al. (1990). Novel cell lines display properties of nociceptive sensory neurons. *Proc. Biol. Sci.* 241, 187–194. doi: 10.1098/rspb.1990.0084

Wood, J. N., Winter, J., James, I. F., Rang, H. P., Yeats, J., and Bevan, S. (1988). Capsaicin-induced ion fluxes in dorsal root ganglion cells in culture. *J. Neurosci.* 8, 3208–3220. doi: 10.1523/jneurosci.08-09-03208.1988

Wu, D., Huang, W., Richardson, P. M., Priestley, J. V., and Liu, M. (2008). TRPC4 in rat dorsal root ganglion neurons is increased after nerve injury and is necessary for neurite outgrowth. *J. Biol. Chem.* 283, 416–426. doi: 10.1074/jbc.m703177200

Wu, Y., Zou, B., Liang, L., Li, M., Tao, Y. X., Yu, H., et al. (2017). Loperamide inhibits sodium channels to alleviate inflammatory hyperalgesia. *Neuropharmacology* 117, 282–291. doi: 10.1016/j.neuropharm.2017.02.010

Xu, F., Luk, C., Richard, M. P., Zaidi, W., Farkas, S., Getz, A., et al. (2010). Antidepressant fluoxetine suppresses neuronal growth from both vertebrate and invertebrate neurons and perturbs synapse formation between Lymnaea neurons. *Eur. J. Neurosci.* 31, 994–1005. doi: 10.1111/j.1460-9568.2010.07129.x

Yin, K., Baillie, G. J., and Vetter, I. (2016). Neuronal cell lines as model dorsal root ganglion neurons: a transcriptomic comparison. *Mol. Pain* 12:1744806916646111.

Zeng, G., Gao, L., Birkle, S., and Yu, R. K. (2000a). Suppression of ganglioside GD3 expression in a rat F-11 tumor cell line reduces tumor growth, angiogenesis, and vascular endothelial growth factor production. *Cancer Res.* 60, 6670–6676.

Zeng, G., Gao, L., Suetake, K., Joshi, R. M., and Yu, R. K. (2002). Variations in gene expression patterns correlated with phenotype of F-11 tumor cells whose expression of GD3-synthase is suppressed. *Cancer Lett.* 178, 91–98. doi: 10.1016/s0304-3835(01)00817-5

Zeng, G., Gao, L., and Yu, R. K. (2000b). Reduced cell migration, tumor growth and experimental metastasis of rat F-11 cells whose expression of GD3-synthase is suppressed. *Int. J. Cancer* 88, 53–57. doi: 10.1002/1097-0215(20001001)88:1<53::aid-ijc8>3.0.co;2-7

Zhang, H., Wickley, P. J., Sinha, S., Bratz, I. N., and Damron, D. S. (2011). Propofol restores transient receptor potential vanilloid receptor subtype-1 sensitivity via activation of transient receptor potential ankyrin receptor subtype-1 in sensory neurons. *Anesthesiology* 114, 1169–1179. doi: 10.1097/aln.0b013e31820dee67

Zhang, Q., Hsia, S. C., and Martin-Caraballo, M. (2017). Regulation of T-type Ca(2+) channel expression by herpes simplex virus-1 infection in sensory-like ND7 cells. *J. Neurovirol.* 23, 657–670. doi: 10.1007/s13365-017-0545-9

Zhang, Q., Hsia, S. C., and Martin-Caraballo, M. (2019). Regulation of T-type Ca(2+) channel expression by interleukin-6 in sensory-like ND7/23 cells post herpes simplex virus (HSV-1) infection. *J. Neurochem.* 151, 238–254. doi: 10.1111/jnc.14697

Zhang, Q., Martin-Caraballo, M., and Hsia, S. V. (2020). Modulation of voltage-gated sodium channel activity in human dorsal root ganglion neurons by herpesvirus quiescent infection. *J. Virol.* 94:e01823-19.

Zhou, C., Johnson, K. W., Herold, K. F., and Hemmings, H. C. Jr. (2019). Differential inhibition of neuronal sodium channel subtypes by the general anesthetic isoflurane. *J. Pharmacol. Exp. Ther.* 369, 200–211. doi: 10.1124/jpet.118.254938

Zhou, F. M., Cheng, R. X., Wang, S., Huang, Y., Gao, Y. J., Zhou, Y., et al. (2017). Antioxidants attenuate acute and chronic itch: peripheral and central mechanisms of oxidative stress in pruritus. *Neurosci. Bull.* 33, 423–435. doi: 10.1007/s12264-016-0076-z

Zhou, X., Dong, X. W., Crona, J., Maguire, M., and Priestley, T. (2003). Vinpocetine is a potent blocker of rat NaV1.8 tetrodotoxin-resistant sodium channels. *J. Pharmacol. Exp. Ther.* 306, 498–504. doi: 10.1124/jpet.103.051086

Zhou, X., Xiao, Z., Xu, Y., Zhang, Y., Tang, D., Wu, X., et al. (2017). Electrophysiological and pharmacological analyses of Nav1.9 voltage-gated sodium channel by establishing a heterologous expression system. *Front. Pharmacol.* 8:852. doi: 10.3389/fphar.2017.00852

Zhou, X., Zhang, Y., Tang, D., Liang, S., Chen, P., Tang, C., et al. (2018). A chimeric NaV1.8 channel expression system based on HEK293T cell line. *Front. Pharmacol.* 9:337. doi: 10.3389/fphar.2018.00337

Zhu, J., Carozzi, V. A., Reed, N., Mi, R., Marmiroli, P., Cavaletti, G., et al. (2016). Ethoxyquin provides neuroprotection against cisplatin-induced neurotoxicity. *Sci. Rep.* 6:28861.

Zhu, M. M., Tao, J., Tan, M., Yang, H. T., and Ji, Y. H. (2009). U-shaped dose-dependent effects of BmK AS, a unique scorpion polypeptide toxin, on voltage-gated sodium channels. *Br. J. Pharmacol.* 158, 1895–1903. doi: 10.1111/j.1476-5381.2009.00471.x

Zhu, Y., Wu, B., Feng, Y. J., Tao, J., and Ji, Y. H. (2015). Lipid bilayer modification alters the gating properties and pharmacological sensitivity of voltage-gated sodium channel. *Sheng Li Xue Bao* 67, 271–282.

Conflict of Interest: The authors declare that the research was conducted in the absence of any commercial or financial relationships that could be construed as a potential conflict of interest.

Copyright © 2020 Haberberger, Barry and Matusica. This is an open-access article distributed under the terms of the Creative Commons Attribution License (CC BY). The use, distribution or reproduction in other forums is permitted, provided the original author(s) and the copyright owner(s) are credited and that the original publication in this journal is cited, in accordance with accepted academic practice. No use, distribution or reproduction is permitted which does not comply with these terms.

frontiers in Cellular Neuroscience

HYPOTHESIS AND THEORY
published: 05 August 2020
doi: 10.3389/fncel.2020.00229

SARS-CoV-2 Dissemination Through Peripheral Nerves Explains Multiple Organ Injury

Matija Fenrich[1], Stefan Mrdenovic[2,3], Marta Balog[1], Svetlana Tomic[4,5], Milorad Zjalic[1], Alen Roncevic[1], Dario Mandic[6,7], Zeljko Debeljak[7,8] and Marija Heffer[1]**

[1] Laboratory of Neurobiology, Department of Medical Biology and Genetics, Faculty of Medicine Osijek, Josip Juraj Strossmayer University of Osijek, Osijek, Croatia, [2] Department of Hematology, Clinic of Internal Medicine, University Hospital Osijek, Osijek, Croatia, [3] Department of Internal Medicine, Family Medicine and History of Medicine, Faculty of Medicine Osijek, Josip Juraj Strossmayer University of Osijek, Osijek, Croatia, [4] Clinic of Neurology, University Hospital Osijek, Osijek, Croatia, [5] Department of Neurology and Neurosurgery, Faculty of Medicine Osijek, Josip Juraj Strossmayer University of Osijek, Osijek, Croatia, [6] Department of Medical Chemistry, Biochemistry and Clinical Chemistry, Faculty of Medicine Osijek, Josip Juraj Strossmayer University of Osijek, Osijek, Croatia, [7] Clinical Institute of Laboratory Diagnostics, University Hospital Osijek, Osijek, Croatia, [8] Department of Pharmacology, Faculty of Medicine Osijek, Josip Juraj Strossmayer University of Osijek, Osijek, Croatia

OPEN ACCESS

Edited by:
Peter S. Steyger, Creighton University, United States

Reviewed by:
Andrew MacLean, Tulane University, United States
Simone Di Giovanni, Imperial College London, United Kingdom

***Correspondence:**
Matija Fenrich
mfenrich@mefos.hr
Marija Heffer
mheffer@mefos.hr

Specialty section:
This article was submitted to Cellular Neuropathology, a section of the journal Frontiers in Cellular Neuroscience

Received: *18 April 2020*
Accepted: *30 June 2020*
Published: *05 August 2020*

Citation:
Fenrich M, Mrdenovic S, Balog M, Tomic S, Zjalic M, Roncevic A, Mandic D, Debeljak Z and Heffer M (2020) SARS-CoV-2 Dissemination Through Peripheral Nerves Explains Multiple Organ Injury. Front. Cell. Neurosci. 14:229. doi: 10.3389/fncel.2020.00229

Coronavirus disease (CoVID-19), caused by recently identified severe acute respiratory distress syndrome coronavirus 2 (SARS-CoV-2), is characterized by inconsistent clinical presentations. While many infected individuals remain asymptomatic or show mild respiratory symptoms, others develop severe pneumonia or even respiratory distress syndrome. SARS-CoV-2 is reported to be able to infect the lungs, the intestines, blood vessels, the bile ducts, the conjunctiva, macrophages, T lymphocytes, the heart, liver, kidneys, and brain. More than a third of cases displayed neurological involvement, and many severely ill patients developed multiple organ infection and injury. However, less than 1% of patients had a detectable level of SARS-CoV-2 in the blood, raising a question of how the virus spreads throughout the body. We propose that nerve terminals in the orofacial mucosa, eyes, and olfactory neuroepithelium act as entry points for the brain invasion, allowing SARS-CoV-2 to infect the brainstem. By exploiting the subcellular membrane compartments of infected cells, a feature common to all coronaviruses, SARS-CoV-2 is capable to disseminate from the brain to periphery via vesicular axonal transport and passive diffusion through axonal endoplasmic reticula, causing multiple organ injury independently of an underlying respiratory infection. The proposed model clarifies a wide range of clinically observed phenomena in CoVID-19 patients, such as neurological symptoms unassociated with lung pathology, protracted presence of the virus in samples obtained from recovered patients, exaggerated immune response, and multiple organ failure in severe cases with variable course and dynamics of the disease. We believe that this model can provide novel insights into CoVID-19 and its long-term sequelae, and establish a framework for further research.

Keywords: SARS-CoV-2, neurotropic infection, axonal transport, peripheral nerves, neurological symptoms, multiple organ failure

INTRODUCTION

The ongoing pandemic of coronavirus disease (CoVID-19) has profoundly affected many aspects of our lives. The disease is caused by severe acute respiratory distress syndrome coronavirus 2 (SARS-CoV-2), a positive-sense single-stranded RNA beta-coronavirus that uses angiotensin converting enzyme 2 (ACE2) to invade host cells (Hoffmann et al., 2020a). CoVID-19 exhibits variable clinical presentations, ranging from mild respiratory and/or gastrointestinal symptoms to acute respiratory distress syndrome and multiple organ failure (Hani et al., 2020; Jiang et al., 2020; Lai et al., 2020; Pan et al., 2020). A significant number of apparently asymptomatic individuals were also reported (Day, 2020).

So far, SARS-CoV-2 was has been shown to infect bronchial, alveolar, and conjunctival epithelia, alveolar macrophages (Bao et al., 2020; Hui et al., 2020), T-lymphocytes (Wang et al., 2020c), neurons (Moriguchi et al., 2020; Paniz-Mondolfi et al., 2020), cholangiocytes (Zhao et al., 2020a), vascular endothelium (Varga et al., 2020), gastrointestinal mucosa (Xiao et al., 2020), the heart, liver, and kidneys (Puelles et al., 2020). It has been suggested that brain involvement might contribute to more complicated clinical presentations (Li et al., 2020; Steardo et al., 2020). According to initial reports, more than a third of hospitalized patients exhibited symptoms and signs of neuronal involvement (Mao et al., 2020), and speculations on neuroinvasive potential of the virus were promptly made (Toljan, 2020). We would like to propose that SARS-CoV-2, after infecting the targeted brain nuclei, might be capable of spreading to multiple organs through peripheral nerves, precipitating multiple organ failure independently of an underlying respiratory infection.

INTERNALIZATION OF ACE2 AS A DOMINANT ENTRY MECHANISM

S-glycoproteins, expressed on the surface of SARS-CoV-2 virions, engage the ACE2 on host cells, and invade the cells either by membrane fusion or endocytosis. In order to initiate the membrane fusion, S-glycoproteins need to undergo cleaving by endogenous proteases, which enables them to engage the ACE2 more avidly (Ou et al., 2020). This feature is absent in other coronaviruses, including SARS-CoV-1 (Jaimes et al., 2020). Some proteases involved in this process have already been identified, e.g., furin and TMPRSS2 (Hoffmann et al., 2020b; Walls et al., 2020), however, other proteases might be also involved. Additionally, the docking of SRAS-CoV-2 to the cell membrane is facilitated by heparan sulfate proteoglycans on the host cell, which interact with S-glycoproteins (Mycroft-West et al., 2020). In SARS-CoV-2 S-glycoprotein, three novel glycosaminoglycan-binding motifs have been recently described, one of which is located at S1/S2 cleavage site (Kim et al., 2020). This finding further implies involvement of host cell surface proteoglycans in the process of cell entry.

When the proteases are unavailable, membrane fusion cannot happen, and binding of SARS-CoV-2 to ACE2 would result in endocytosis instead. Moreover, even when the proteases are available, the virions still prefer entry via endocytosis (Ou et al., 2020). Endocytotic entry in *Coronaviridae* dependents on the localization of their receptors in membrane lipid rafts, since lipid rafts mediate this process. This mechanism shares the same activating principles with renin-angiotensin-aldosterone system, suggesting their common phylogenic origin (Chen et al., 2012). The initiation of ACE2-dependent endocytosis in SARS-CoV-2 was reported to be dependent on phosphatidylinositole biphosphate (Ou et al., 2020). The protease-independent and lipid-raft-mediated entry might mimic physiological activation of the receptor by angiotensin II, which results in its recruitment to the intracellular renin-angiotensin system (Escobales et al., 2019; Abassi et al., 2020). We still do not know much of this system, nonetheless, its involvement in the various aspects of metabolic regulation of subcellular compartments is gradually being elucidated (Villar-Cheda et al., 2017; Shi et al., 2018; Sotomayor-Flores et al., 2020).

After ACE2 endocytosis, lysosomal cathepsin L proteases are normally trafficked to the endosome. It has been recently demonstrated that cathepsin L is capable of cleaving S-glycoproteins, enabling virions to initiate fusion, escape endosomes and release their proteins and genetic material into cytosol (Mao et al., 2020). By preferably relying on endocytosis instead of membrane fusion, SARS-CoV-2 likely postpones its detection by the immune system, because in this way fewer antigenic viral proteins are left on the cell surface (Marsh and Helenius, 2006). The mechanisms of cell entry are summarized in the **Figure 1A**.

EXPLOITATION OF SUBCELLULAR MEMBRANE COMPARTMENTS AND INTRACELLULAR TRANSPORT

An important feature of coronaviruses is that their replication-transcription complexes are associated with double membrane vesicles built from modified Golgi apparatus and endoplasmic reticulum (Snijder et al., 2020). The viruses extensively remodel the membranes of subcellular compartments into organelle-like and web-like structures, known as reticulovesicular networks (Knoops et al., 2008). A recent preprint electron microscopy study confirmed the same for SARS-CoV-2 (Belhaouari et al., 2020). The viral replication-transcription domains and assembled virions were also reported in autophagosomes (Prentice et al., 2004) and secretory vesicles (Krijnse-Locker et al., 1994; Salanueva et al., 1999; Verheije et al., 2008), implying that assembly and transport of new virions might take place during vesicular trafficking. For their replication and neuronal dissemination, neuroinvasive viruses must express proteins that control vesicular traffic (Enquist, 2012). Angiotensin II increases and mediates neuronal vesicular trafficking (Wang et al., 2001; Aschrafi et al., 2019), and since the receptor binding site of S-glycoproteins in SARS-CoV-2 is structurally similar to angiotensin II, the virus might be capable of increasing and modulating the neuronal vesicular trafficking system in the same manner (see **Figure 1B**). Moreover, as coronaviruses modify and assembly inside of structures derived from endoplasmic

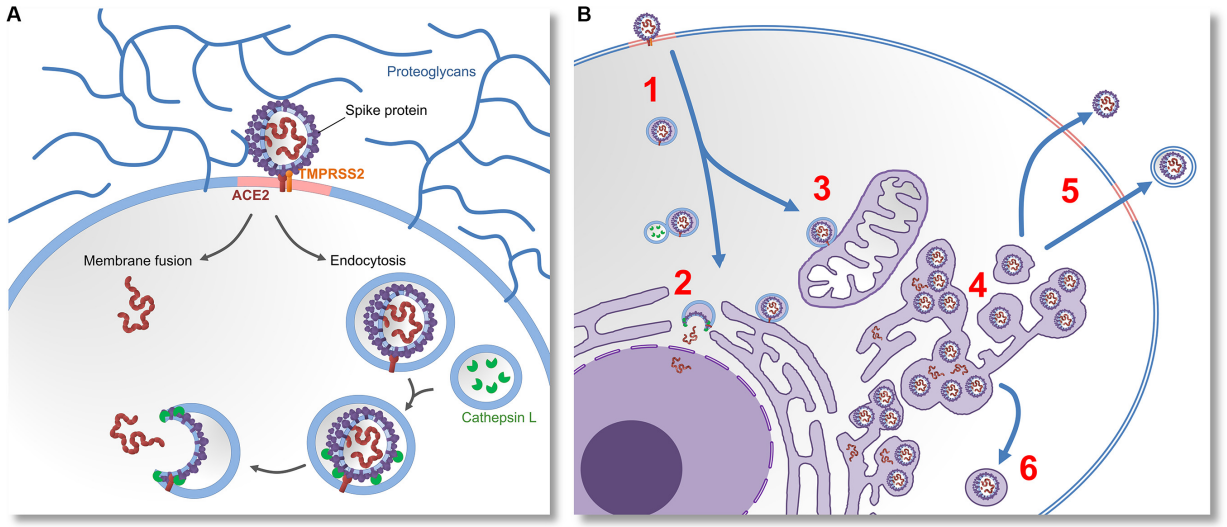


FIGURE 1 | Molecular mechanisms of cell entry, replication and egression of SARS-CoV-2. **(A)** The virus invades the cell by docking on the cell-surface proteoglycans and engaging the ACE2 receptor with "Spike" (S) glycoprotein. If S glycoprotein is cleaved by host proteases (TMPRSS2), entry by membrane fusion or endocytosis would happen. If the cleavage does not occur, the virus would invade the cell via receptor-mediated endocytosis. Lysosomal proteases (Cathepsin L) eventually cleave the S glycoproteins. This enables them to induce membrane fusion and release the viral proteins and RNA into the cytoplasm. **(B)** After the virus enters the cell (1) it releases its genetic material (2), and replicates in the cell nucleus. Virions that do not get their S glycoproteins primed by lysosomal proteases would be further trafficked to various subcellular membrane compartments (3), which possibly modulates their metabolism and changes their morphology. This results in the emergence of a membranous system called reticulovesicular network. Translation of viral messenger RNA, synthesis of viral proteins and assembly of new virions takes place inside of this network and other intracellular vesicles (4). New virions leave the infected cell by budding through lipid rafts, either by membrane-fusion-mediated egression or by exosomes (5). Intracellular cleavage of S glycoprotein by furin or TMPRSS2 proteases would enable the virions to induce membrane fusion. Alternatively, assembly of virions inside of secretory vesicles would allow them to be transported to the apical cell membrane (6) or presynaptic membrane (in the case of neurons).

reticulum, we further suggest that SARS-CoV-2 could also utilize continuous longitudinally spanning endoplasmic reticula, which were described in the myelinated axons, and which are likely a continuation of the somatic organelles (Gonzalez and Couve, 2014). Since SARS-CoV-2 is a neurotropic virus, we suggest that, by binding to ACE2, it is able to disseminate via both vesicular transport and passive diffusion through axonal endoplasmic reticulum over large distances and at a fast pace.

New virions that are assembled in a reticulovesicular network are not immediately released out of the infected cell. Instead, they are accumulating in dedicated areas of its lumen (Knoops et al., 2008). Their egression is most likely elicited by fusion of the vesicles derived from the reticulovesicular network and plasma membrane in a process that seems to be dependent on interaction with lipid rafts (Chazal and Gerlier, 2003; Baglivo et al., 2020; Fantini et al., 2020) and autophagosomal proteins (Tanida et al., 2009). Since the surfaces of lipid rafts are much smaller than the viral envelopes, egression has to happen on sites where many lipid rafts cluster into a lipid microdomain (Lorizate and Kräusslich, 2011). This egression mechanism might be crucial for the induction of syncytia. S-glycoproteins of SARS-CoV-2 induce syncytia by transcellular transfections dependent on TMPRSS2 proteolytic activity (Ou et al., 2020). Apparently, the virion cannot directly induce a syncytium without proteases, likely because membrane fusion cannot be initiated. In such cases the budding would likely result in an endocytic transfection, enabling the virus to spread in a cell-to-cell fashion. SARS-CoV-2 was reported to show superior *in vitro* cell-cell fusion capacity compared to SARS-CoV-1 (Xia et al., 2020). Additionally, in some coronaviruses, soluble S-glycoproteins are secreted out of the infected cell, and are shown to induce syncytia independently of transfection (Masters, 2006).

Axonal dissemination by vesicular transport and passive diffusion, syncytium induction and cell-to-cell spread could explain the unexpectedly low viral load in the blood – possibly less than 1% of PCR blood tests in CoVID-19 patients yield a positive result (Wang et al., 2020b; Wölfel et al., 2020; Yu et al., 2020), suggesting that viremia likely does not underlie the multi-organ dissemination.

BRAIN AS A HUB FOR FURTHER DISSEMINATION

ACE2 is expressed in neurons of many brain regions (Doobay et al., 2007). It can bind to integrins and modulate their signaling (Clarke et al., 2012). Integrins are transmembrane receptors responsible for signal transduction between a cell and extracellular matrix, and are abundantly expressed in synapses and terminals of sensory neurons that mediate pain (Dina et al., 2004), implying a possible colocalization with ACE2 at those sites. Furthermore, an integrin-binding motif in S-glycoprotein of SARS-CoV-2 was recently identified, suggesting that they might be alternative receptors for the

virus, and an ACE2-independent infection in integrin-expressing cells might be possible (Sigrist et al., 2020). The presence of SARS-CoV-2 in the cerebrospinal fluid was recently reported in a case of viral encephalitis (Moriguchi et al., 2020), and the virus was directly observed in the brain cells of deceased CoVID-19 patients (Paniz-Mondolfi et al., 2020), confirming its neurotropic nature. Based on these findings and recent reports (Cheema et al., 2020; Colavita et al., 2020), we propose that nerve terminals in the oral and nasal mucosa, conjunctiva and eyes, as well as the olfactory nerves, might be potential entry sites for SARS-CoV-2 neurotropic infections. *Post-mortem* MRI findings revealed asymmetric olfactory bulbs in four deceased CoVID-19 patients, further implying that olfactory neuroepithelium might be an entry point for the virus (Coolen et al., 2020).

CoVID-19 patients frequently present with hyposmia and dysguesia (Bagheri et al., 2020; Lechien et al., 2020), and both ACE2 and TMPRSS2 proteases are expressed in olfactory neuroepithelium (Fodoulian et al., 2020). Moreover, Dubé et al. (2018) directly observed propagation of a human coronavirus to the brainstems of mice following the intranasal and intralingual inoculations, suggesting that SARS-CoV-2 might be able to spread to the brainstem either directly via olfactory nerves, or alternatively, through orofacial nerve fibers via cranial ganglia. A non-peer-reviewed report demonstrated the presence of SARS-CoV-2 in the trigeminal ganglia, olfactory epithelium, olfactory bulbs, brainstem, uvula, conjunctiva and cornea in some deceased patients (Meinhardt et al., 2020). Olfactory inoculation likely involves propagation to the piriform cortex and amygdala, and further spreading through the medial forebrain bundle to the brainstem (see **Figure 2A**). Lateral fiber stream of the medial forebrain bundle projects caudally to the solitary tract and dorsal vagal nuclei (Holstege, 1987). Replication of the virus in the solitary tract neurons may also explain the reported dysgeusia. Spreading through the orofacial sensory fibers would be especially convenient for the virus, since their pseudounipolar somata, which reside in the cranial ganglia, could be plausible persistent infection sites or intermediary replication posts. This could facilitate either further brainstem invasion by axonal transport or allow for an exocytosis-endocytosis-mediated transfection of other fibers passing through the ganglia. Such virion-containing endocytes could establish membrane contact sites with axonal endoplasmic reticulum (Eden, 2016), enabling the virion to freely diffuse along the axon using the organelle lumen. Passive diffusion of coronavirions in axons was reported both *in vitro* and *in vivo* (Dubé et al., 2018). However, it is possible that vesicular transport might prevail *in vivo*. Although hematologic dissemination to the brain cannot be excluded, the observed discrepancy between a significant incidence of neurological manifestations (Mao et al., 2020) and a low yield of positive blood tests (Wang et al., 2020b; Wölfel et al., 2020; Yu et al., 2020) suggests

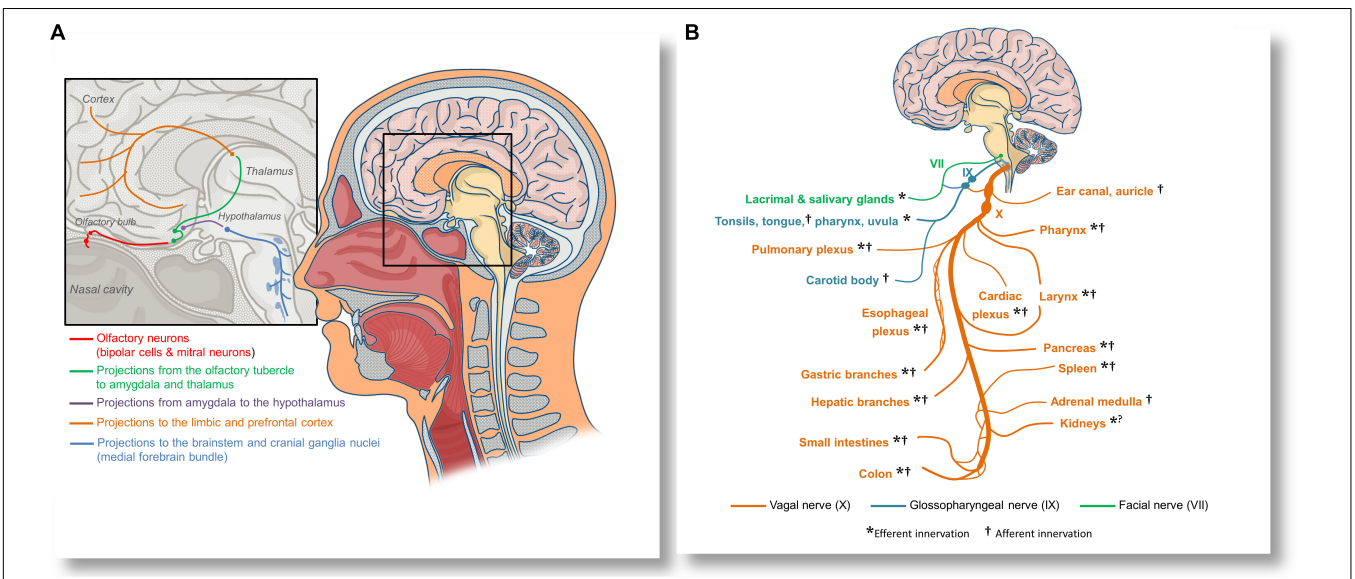


FIGURE 2 | Anatomical overview of the proposed olfactory inoculation and axonal dissemination pathways of SARS-CoV-2. **(A)** Olfactory neurons are only a synapse away from the central nervous system. SARS-CoV-2 has been reported to infect olfactory neuroepithelium and to invade the olfactory bulbs via cribriform plate. By exploiting the anterograde axonal transport in the olfactory tract, the virus could infect neurons of the olfactory tubercle and spread to the amygdala and thalamus, from where it might further invade the cingular and orbitofrontal cortex. By exploiting the axonal transport in fibers projecting into the hypothalamus, the virus may infect cranial ganglia nuceli via the medial forebrain bundle. **(B)** SARS-CoV-2 could also disseminate to various organs and tissues by axonal transport in the vagal nerve (X). Immediately after leaving the skull, the vagus establishes anastomoses (connections) with the glossopharyngeal nerve (IX), allowing the virus to spread to the oropharyngeal mucosa, or alternatively, to use the same route for neuroinvasion. Glossopharyngeal fibers that cross to the facial nerve (VII) could be an additional pathway for dissemination or neuroinvasion. The vagal nerve innervates many tissues and organs that can be affected in CoVID-19, including the pharynx, larynx, lungs, the heart, esophagus, stomach, liver, gallbladder, pancreas, spleen, adrenal medulla, kidneys, muscles, and glands of a part of the intestines, as well as lymphatic tissue in the correspondent intestinal mucosa. By disrupting the vagal innervation, SARS-CoV-2 could also impair the activity of the cholinergic inflammatory reflex, and precipitate dysregulated immune responses in many organs.

that viremia is unlikely to be a major contributor to the brain infection.

Viral penetration into the central nervous system through peripheral fibers is a multi-step process. In order to reach neuronal soma from the periphery, the virus needs to exploit the retrograde axonal transport machinery. SARS-CoV-2 uses ACE2-mediated endocytotic pathway for internalization and intracellular transport, and in the case of SARS-CoV-1 infection, endosomes containing virion/ACE2 complexes are trafficked to the perinuclear area (Wang et al., 2008). The virus might use this intrinsic clathrin-independent intracellular ACE2 endocytic transport to reach the perikaryon. However, for a successful further invasion, it would also need to be able to cross synaptic membranes. Another beta-coronavirus was shown to be capable of trans-synaptic propagation by presynaptic exocytosis and postsynaptic endocytosis (Li et al., 2013), which suggests that SARS-CoV-2 could use the same mechanism. Anterograde axonal transport is mediated by kinesin molecular motors, and allows for trafficking of vesicles and organelles from the soma to the axon and synaptic terminals (Berth et al., 2009). Since the virus replicates and assembles inside of vesicles derived from the endoplasmic reticulum and Golgi apparatus, it could also exploit the already present kinesin-mediated anterograde transport to propagate further along the axons. Lateral transfections, i.e., cell-to-cell or axo-axonal spreading via exocytosis, could be also possible. Exosomal pathways are hypothesized to contribute to viral dissemination (Khan et al., 2017), and it was demonstrated that ACE2 trafficking could involve exosome-mediated cell-to-cell transfer (Wang et al., 2020a). Arguably, this mechanism could allow the infection to spread from neurons to cerebrovascular endothelial cells, and *vice versa*. The ways the virus might exploit intracellular vesicular trafficking in neurons are summarized in **Figure 3**.

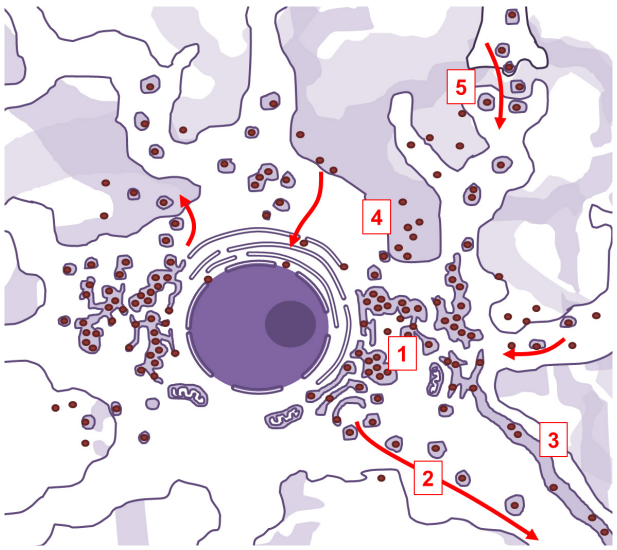


FIGURE 3 | Aspects of intracellular vesicular trafficking that may be exploited by SARS-CoV-2 in infected neurons. Neurons are polarized cells with abundance of intracellular endocytic pathways. Life cycle of SARS-CoV-2 is compatible with the possibility of exploiting those pathways. The virus extensively modifies subcellular organelles into a reticulovesicular network, a structure where viral membrane-bound replication-transcription complexes are situated and where new virions are being assembled (1). This elaborate network is connected to secretory Golgi compartments, allowing the newly assembled virions to be trafficked to the synapse via kinesin-mediated anterograde axonal transport (2). The reticulovesicular network is also continuous with endoplasmic reticulum. In myelinated projection neurons, endoplasmic reticulum extends along the axon, which might enable the virions to freely diffuse inside its lumen (3). Newly assembled virions can also directly leave the infected neurons by membrane-fusion or by exosomes (4), and infect the nearby cells. Trans-synaptic spreading is confirmed in some beta-coronaviruses, and could be possible in SARS-CoV-2 as well (5).

Once the virus has reached the brainstem and spinal cord, it could access practically every organ system in the body. By infecting the vagal nuclei alone, the virus may be capable of dissemination to the lungs, heart, liver, intestines and kidneys, as well as of impairing the vagal activity (see **Figure 2B**). This might precipitate multiple organ injury independently of an underlying respiratory pathology. In a murine model of neuronal infection with human coronavirus OC43, the viral RNA was detected in the livers of three out of nine animals in spite of undetectable viral loads in the blood (Dubé et al., 2018). This finding supports the possibility of dissemination through vagal fibers. Additionally, viral shedding at the periphery could also be associated with activation of the integrin signalization on peripheral nerve terminals, which could enable the virus to attenuate local algesic and inflammatory response, hindering the immune reaction to its shedding (Dina et al., 2004; Moon et al., 2009; Hu et al., 2016). Alternatively, the virus may establish a persistent neuronal infection, and stay dormant for a certain period until eventual reactivation. This is a common strategy in some neuroinvasive viruses (Koyuncu et al., 2013).

Other manifestations that are considered atypical for a respiratory infection, such as coagulopathy (Iba et al., 2020), thrombosis (Helms et al., 2020; Leisman et al., 2020), vasculitis (Castelnovo et al., 2020; Sachdeva et al., 2020; Verdoni et al., 2020) and dysregulated inflammatory responses (Blanco-Melo et al., 2020; Leisman et al., 2020) were also reported in CoVID-19 patients. Previous studies showed that vagal activity is an important factor in anti-inflammatory modulation and inhibition of prothrombotic events in the innervated tissues (de Jonge et al., 2005; Westerloo et al., 2006; Koopman et al., 2016; Li et al., 2016; Cacho et al., 2020), and SARS-CoV-2 could be capable of hijacking axonal transport in the vagal nerves, impairing their signaling in the cholinergic anti-inflammatory pathway (Johnston and Webster, 2009; Pavlov and Tracey, 2012). We propose that vagal dysfunction might significantly contribute to exaggerated immune responses and thromboembolic incidents in some CoVID-19 patients. Interestingly, vagal neuropathies due to upper-respiratory viral infections are already clinically recognized as contributors to various para-infectious and post-infectious sequelae (Amin and Koufman, 2001; Rees et al., 2009; Chung et al., 2013; Niimi and Chung, 2015).

Due to the dynamics of the active transport and passive diffusion in axons, the brain infection might develop weeks after the virus exposure or development of primary respiratory infection, giving rise to the possibility that patients with severe clinical presentation and multiple organ affection might have

contracted the virus earlier than assumed. The exact time needed for the virus to invade the brain in humans is unknown, and it certainly depends on the entry route and inocculation dose. In mice, a strain of human coronavirus was detected in the olfactory bulbs as early as 2 days after intranasal inoculation, in the cortex and brainstem 3 days after inoculation, and in the spinal cord 5 days after inoculation (Dubé et al., 2018).

IMPLICATIONS AND PERSPECTIVES

Based on the presented concept, we would like to suggest that respiratory and neuronal types of CoVID-19 may be distinct clinical entities. These two types might present independently, as a respiratory infection without brain infection and *vice versa*, concomitantly or consecutively. Due to different entry routes, the two types would likely have different incubation periods and different occurrence rates of initial symptoms, which could explain the observed variability in both parameters (Day, 2020; Jiang et al., 2020; Wan et al., 2020). However, wide dispersion of reported values could be also due to limited sample sizes in the initial reports.

Increased susceptibility to a particular type of the disease might be driven by underlying conditions. ACE2 expression is increased in patients with morbidities associated with metabolic syndrome (Pinto et al., 2020), and those patients are also more likely to develop neurological manifestations (Mao et al., 2020). Patients with such conditions who develop CoVID-19 respiratory infections might be at risk of more serious CoVID-19 neuronal infections which could in turn result in the virus dissemination to multiple organs through peripheral nerves. Most patients, however, do not develop brain infection. It is important to note that the nasal mucosa possess mechanisms that efficiently prevent neuroinvasion via olfactory nerves, such as nasal secretion, mucus barrier formation, pathogen recognition receptors (Kalinke et al., 2011) and cyclic shedding and replacement of olfactory neurons with the new ones (Loseva et al., 2009). Another host protective response was reported to be apoptosis of olfactory neurons (Mori et al., 2004). Conditions that interfere with these mechanisms might compromise their protective roles against neuroinvasive infectious agents. Aging, diabetes, and hypertension are associated with less efficient nasal mucocilliary clearance (Selimoglu et al., 1999; Yue, 2007; Proença de Oliveira-Maul et al., 2013), and aging might also precipitate reduced olfactory nerve replenishment (Enwere et al., 2004; Brann and Firestein, 2014). This would additionally explain the observed higher incidence of neurological involvement in patients with these comorbidities. For most otherwise healthy and younger individuals, respiratory epithelium would be the primary and likely the only site of infection, whereas the aforementioned high-risk groups might be more susceptible to both neuronal and respiratory types of CoVID-19.

Theoretically, a primary lung infection could also progress to a brain or spinal cord infection via retrograde axonal transport through peripheral nerves. However, more aggressive immune responses to viral pathogens in peripheral tissues compared to the ones in the central nervous system would likely impede such a scenario. Due to irreplaceability of neurons, the immune reactions to viral infection in the brain do not include cytolytic responses, and are therefore less efficient in containing and clearing intracellular pathogens (Griffin, 2003). Olfactory neurons, although replaceable, are in an immediate proximity to the central nervous system, which makes them an anatomically and immunologically more plausible route for successful neuroinvasion. Nevertheless, a primary lung infection in some patients could still progress to acute respiratory distress syndrome without or independently of neuronal infection. Such lung injuries might be due to suboptimal host reaction to the infection, possibly characterized by a weak antiviral response and elevated expression of proinflammatory cytokines, as demonstrated by an *in vitro* study (Blanco-Melo et al., 2020). Still, many CoVID-19 patients who develop respiratory infection without neural involvement could have better clinical outcomes, whereas a combination of direct cytopathic effects, vagal neuropathy and centrally driven lung injuries could be associated with less favorable outcomes.

We propose that the original type of cell in which the virion assembly and budding took place could be identified based on the lipid profile of the viral particles. The lipid composition of retroviral envelopes corresponds to the lipid profile of the membrane lipid rafts at which the budding took place (Ono, 2010; Waheed and Freed, 2010). Since lipid rafts of the brain have a distinctive lipid profile rich in specific gangliosides (Vajn et al., 2013; Schnaar et al., 2014), by comparing it to the lipid profile of the virions, it could be possible to confirm the neuronal origin of SARS-CoV-2 in peripheral tissues.

A proportion of purportedly asymptomatic or oligosymptomatic carriers could suffer a less severe CoVID-19 neuronal infection, with subtle neuropsychiatric manifestations without respiratory involvement. RNA viruses are known to be able to persistently infiltrate CNS as well as to cause subacute psychiatric and neurological symptoms and post-infectious sequelae, such as cognitive impairment, seizures, ataxia, psychiatric illnesses, chronic fatigue syndrome, etc. (Klein et al., 2019; Bo et al., 2020). To the best of our knowledge, so far reported neurological manifestations in CoVID-19 patients include hyposmia, dysgeusia (Lechien et al., 2020), convulsions (Karimi et al., 2020), neurogenic syncope (Canetta et al., 2020), meningoencephalitis (Moriguchi et al., 2020), Guillain-Barré syndrome (Zhao et al., 2020b), intracerebral hemorrhage (Sharifi-Razavi et al., 2020), acute hemorrhagic necrotizing encephalopathy (Poyiadji et al., 2020), acute post-infectious myelitis (Zhao et al., 2020c), cerebrovascular diseases (Mao et al., 2020), vertigo, nausea, headaches (Mao et al., 2020; Nie et al., 2020), demyelination (Zanin et al., 2020), and cortical blindness (Kaya et al., 2020), but the causative or coincidental nature of these findings is yet to be determined. It is important to point out that some of the reported neurological symptoms could also be caused by hypoxia as a consequence of lung injury. However, not all CoVID-19 patients who developed neurological symptoms suffered pulmonary insufficiency, and the presence of subtle neuropsychiatric abnormalities in the subclinical cases might be actually underreported (Zhang et al., 2020b).

The fetus seems to be protected from the axonal invasion of SARS-CoV-2 from the infected mother by factors that inhibit nerve growth on the maternal side of the umbilicus and placenta (Marzioni et al., 2004). Both amniotic fluid and umbilical cord blood samples were reported to test negative to SARS-CoV-2, and no vertical transmission was reported (Chen et al., 2020a), except for a recent report of three cases of neonatal CoVID-19, in which vertical transmission could not be ruled out (Zeng et al., 2020). Since ACE2 is expressed in the uterus and placenta (Valdes et al., 2013), a possibility of viral interference with expression of the factors that mediate nerve growth inhibition must not be dismissed. In addition, CoVID-19-related thromboembolic placental injuries were recently described (Baergen and Heller, 2020).

Development of neuronal CoVID-19 infection might explain a growing number of positive PCR tests in recovered patients even weeks after hospital discharge (Lan et al., 2020; Xing et al., 2020; Zhang et al., 2020c). Viral shedding at nerve terminals of pulmonary epithelium and nasopharyngeal mucosa could explain the sustained presence of SARS-CoV-2 in throat and nasal swabs, implying that a carrier state could persist over a significant timespan. Although prolonged positivity could theoretically be explained by presence of remnants of unviable viral RNA, we believe this is an unlikely explanation. Physiological nasopharyngeal washing and, possibly, activity of certain canonical ribonucleases in the respiratory mucosa (Koczera et al., 2016) would not allow for a sustained presence of the viral RNA weeks after recovery. By analogy, viral shedding may be also possible on the enteric nerve terminals, maintaining the detectability of the virus in enterocytes and stool even after apparent recovery. Hu et al. (2020) have recently reported that SARS-CoV-2 can persist in stool samples longer than in the respiratory tract in recovered patients who were previously without gastrointestinal symptoms.

The damage to multiple organs in some patients may as well be explained by hypoxia and cytokine storm (Bonow et al., 2020; Mehta et al., 2020; Pei et al., 2020; Yang et al., 2020). Even so, hypoxia and cytokine storm do not accompany all cases of organ damage (Kochi et al., 2020; Zhang et al., 2020a), and the correlation of incidence of hypercytokinemia and presence of viral RNA in blood (Chen et al., 2020b), in spite of practically non-existent viremia, suggests that cytokine storm might be preceded and driven by organ damage and subsequent release of viral antigens from necrotic cells. As a matter of fact, the virus presence was confirmed in vascular endothelial cells (Varga et al., 2020) and multiple organs in deceased patients (Puelles et al., 2020), and different mechanisms of organ failure do not necessarily exclude each other. Detrimental pro-thrombotic and pro-inflammatory state could also be driven by hypothesized SARS-CoV-2-induced vagal neuropathy (Li et al., 2011; Huston, 2012), and eventual development of neurogenic pulmonary edema secondary to an infection-related cerebrovascular event might contribute to the ultimate cardiopulmonary failure (Davison et al., 2012).

It was also suggested that possible fecal-oral transmission may explain the gastrointestinal symptoms in CoVID-19 (Cha et al., 2020; Steardo et al., 2020; Tian et al., 2020), even though SARS-CoV-2 is not stable in the media with pH <3 (Chin et al., 2020). Nonetheless, SARS-CoV-2 was still detected in stool and gastrointestinal mucosa (Xiao et al., 2020), but stool tested positive even in patients who did not have gastrointestinal symptoms (Zhang et al., 2020c). Still, the proposed fecal-oral route does not exclude the possibility of axonal dissemination of SARS-CoV-2 to gastrointestinal tract via vagal fibers and spinal nerves. Another possibility might be an infection of the gallbladder or biliary ducts (Zhao et al., 2020a), in which case the virus in stool would be of biliary origin.

Finally, pharmacologic approaches that would hinder the exploitation of the neuronal endocytic trafficking by SARS-CoV-2 could be an effective treatment for the infection. Chloroquine and its derivatives disrupt endocytosis and vesicular trafficking by endosomal alkalization and inhibition of autophagy, also interfering with terminal glycosylation in ACE2, which hinders its interaction with S-glycoproteins (Liu et al., 2020). These medications are already being clinically used in CoVID-19 patients. Other autophagy inhibitors, such as azithromycin are also commonly used (Gautret et al., 2020). Therefore, we suggest that the treatment of CoVID-19, due to its neuroinvasive properties, should focus on interfering with viral hijacking of the cellular endocytic trafficking system and axonal transport. A study of rat primary superior cervical ganglia culture revealed that emetine (translation elongation inhibitor) may be used as inhibitory modulator of rabies virus axonal transport (MacGibeny et al., 2018), implying a possible therapeutic approach for SARS-CoV-2. In the case of poliomyelitis virus infection in rats, vinblastine (inhibitor of tubulin polymerization) was shown to hinder retrograde axonal transport of the virus when applied topically to infected peripheral nerves (Ohka et al., 2004). Microtubule-associated inhibitors, such as vinblastine, vincristine, paclitaxel, colchicine, nocodazole and other inhibitors of retrograde axonal transport, such as macrolide drug mycalolide B (Cavolo et al., 2015), could be used to investigate the mechanisms underlying retrograde axonal transport of SARS-CoV-2 *in vivo*. However, these drugs do not alter the redistribution and abundance of viral proteins, and do not influence the viral replication (Wu et al., 2019). Moreover, treatment with these agents was reported to induce reactivation of varicella-zoster virus infection along with their neurotoxic effects. HSP90 inhibitor geldanamycin is suggested as a potential drug in the treatment of CoVID-19 (Sultan et al., 2020), and SARS-CoV-2 proteases inhibitor quercetine is being studied as a prophylaxis and treatment option (Onal and Semerci, 2020). It also affects the cytoskeletal signaling by inhibiting protein kinase C. Another potential treatment option for CoVID-19 are rho-kinase inhibitors, such as fasudil, ripasudil, and netarsudil (Abedi et al., 2020; Calò et al., 2020). Interestingly, all these compounds share a quinoline backbone moiety. Additionally, since neurotropic viruses have to propagate across the synapses, neutralizing antibodies could be used to stop them from spreading from neuron to neuron, as it was demonstrated in animal models of West Nile virus neuronal infection (Oliphant et al., 2005; Samuel et al., 2007). Another group of potential axonal transport modulators could be bioactive compounds isolated from marine organisms. Some of them are reported to

inhibit molecular motors underlying anterograde or retrograde axonal transport (kinesin and dynein, respectively), and several compounds are proposed to interfere with autophagosomal pathways in neurons (White et al., 2016).

The model we put forward clarifies a wide range of clinically observed phenomena in CoVID-19 patients (see **Supplementary Table S1**). Detection of viral particles in peripheral nerves, together with recent findings of brainstem and cranial ganglia infection, as well as other findings summarized in this paper, could confirm the axonal dissemination of SARS-CoV-2. If correct, this would significantly affect our understanding of this novel disease and its potential long-term sequelae. This would warrant modifications in many aspects of diagnostics, treatment and follow-up of CoVID-19 patients. The proposed model could also be utilized by many other viruses – chronic persistence in the host's nervous system and eventual reactivations with shedding in the respiratory or gastrointestinal mucosa could be an effective survival and spreading strategy for a virus. Finally, the presence of antibodies to other coronaviruses in the cerebrospinal fluid of patients with Parkinson's disease and some psychiatric disorders (Fazzini et al., 1992; Severance et al., 2009; Okusaga et al., 2011) points to the possibility that these and similar pathologies might be triggered by viral infections. Vagal atrophy observed in patients with Parkinson's disease (Walter et al., 2018), might also be secondary to bulbar lesions caused by a coronavirus infection. The proposed model of axonal dissemination and vagal dysfunction could give us novel insights not only into CoVID-19, but also into hypothesized common viral etiology of certain neurodegenerative and psychiatric disorders and their systemic manifestations. Therefore, we believe this idea merits further investigation.

As a closing remark, it is important to add that most individuals diagnosed with CoVID-19 will likely convalesce without developing neuronal infection. Moreover, the sole presence of proviral genomes in the brain does not imply a definite corresponding clinical correlate. Many viruses have already left their genetic imprints in our DNA, and thus became a part of our evolutionary heritage, and a part of us.

DATA AVAILABILITY STATEMENT

All datasets generated for this study are included in the article/**Supplementary Material**.

AUTHOR CONTRIBUTIONS

MF, SM, and MH devised the main conceptual ideas. MF drafted the initial manuscript. MF, SM, MB, ST, MZ, AR, DM, ZD, and MH reviewed and revised the manuscript, and expanded the original concept. All authors contributed to the article and approved the submitted version.

FUNDING

This study was funded by the European Union through the European Regional Development Fund, Operational Programme Competitiveness and Cohesion, Grant Agreement No. KK.01.1.1.01.0007, the CoRE – Neuro, and by the Croatian Science Foundation (HRZZ IP-2014-09-2324).

SUPPLEMENTARY MATERIAL

The Supplementary Material for this article can be found online at: https://www.frontiersin.org/articles/10.3389/fncel.2020.00229/full#supplementary-material

REFERENCES

Abassi, Z., Assady, S., Khoury, E. E., and Heyman, S. N. (2020). Letter to the editor: angiotensin-converting enzyme 2: an ally or a Trojan horse? Implications to SARS-CoV-2-related cardiovascular complications. *Am. J. Physiol. Heart Circul. Physiol.* 318, H1080–H1083.

Abedi, F., Rezaee, R., and Karimi, G. (2020). Plausibility of therapeutic effects of rho kinase inhibitors against severe acute respiratory syndrome coronavirus 2 (COVID-19). *Pharmacol. Res.* 156:104808. doi: 10.1016/j.phrs.2020.104808

Amin, M. R., and Koufman, J. A. (2001). Vagal neuropathy after upper respiratory infection: a viral etiology? *Am. J. Otolaryngol.* 22, 251–256. doi: 10.1053/ajot.2001.24823

Aschrafi, A., Berndt, A., Kowalak, J. A., Gale, J. R., Gioio, A. E., and Kaplan, B. B. (2019). Angiotensin II mediates the axonal trafficking of tyrosine hydroxylase and dopamine beta-hydroxylase mRNAs and enhances norepinephrine synthesis in primary sympathetic neurons. *J. Neurochem.* 150, 666–677. doi: 10.1111/jnc.14821

Baergen, R. N., and Heller, D. S. (2020). Placental pathology in covid-19 positive mothers: preliminary findings. *Pediatr. Dev. Pathol.* 23, 177–180. doi: 10.1177/1093526620925569

Bagheri, S. H. R., Asghari, A. M., Farhadi, M., Shamshiri, A. R., Kabir, A., Kamrava, S. K., et al. (2020). Coincidence of COVID-19 epidemic and olfactory dysfunction outbreak. *medRxiv [Preprint]* doi: 10.1101/2020.03.23.20041889

Baglivo, M., Baronio, M., Natalini, G., Beccari, T., Chiurazzi, P., Fulcheri, E., et al. (2020). Natural small molecules as inhibitors of coronavirus lipid-dependent attachment to host cells: a possible strategy for reducing SARS-COV-2 infectivity? SARS-COV-2 lipid-dependent attachment to host cells. *Acta Bio Med. Atenei Parmensis* 91, 161–164.

Bao, L., Deng, W., Huang, B., Gao, H., Liu, J., Ren, L., et al. (2020). The pathogenicity of SARS-CoV-2 in hACE2 transgenic mice. *Nature* [Epub ahead of print].

Belhaouari, D. B., Fontanini, A., Baudoin, J.-P., Haddad, G., Le Bideau, M., Bou Khalil, J. Y., et al. (2020). *The Strengths of Scanning Electron Microscopy in Deciphering SARSCoV-2 Infectious Cycle*. Marseille: HU pre-publication site on COVID-19.

Berth, S. H., Leopold, P. L., and Morfini, G. N. (2009). Virus-induced neuronal dysfunction and degeneration. *Front. Biosci. (Landmark Ed.)* 14, 5239–5259.

Blanco-Melo, D., Nilsson-Payant, B. E., Liu, W. C., Uhl, S., Hoagland, D., Møller, R., et al. (2020). Imbalanced host response to SARS-CoV-2 drives development of COVID-19. *Cell* 181, 1036.e9–1045.e9.

Bo, H. X., Li, W., Yang, Y., Wang, Y., Zhang, Q., Cheung, T., et al. (2020). Posttraumatic stress symptoms and attitude toward crisis mental health services among clinically stable patients with COVID-19 in China. *Psychol. Med.* [Epub ahead of print].

Bonow, R. O., Fonarow, G. C., O'Gara, P. T., and Yancy, C. W. (2020). Association of coronavirus disease 2019 (COVID-19) with myocardial injury and mortality. *JAMA Cardiol.* [Epub ahead of print].

Brann, J. H., and Firestein, S. J. (2014). A lifetime of neurogenesis in the olfactory system. *Front. Neurosci.* 8:182. doi: 10.3389/fnins.2014.00182

Cacho, B., Abdala, J., and Wilson, C. G. (2020). Anti-inflammatory effects of vagus nerve simulation in a newborn rat model of acute inflammation. *FASEB J.* 34:1. doi: 10.1096/fasebj.2020.34.s1.03202

Calò, L. A., Bertoldi, G., and Davis, P. A. (2020). Rho kinase inhibitors for SARS-CoV-2 induced acute respiratory distress syndrome: Support from Bartter's and Gitelman's syndrome patients. *Pharmacol. Res.* 158:104903. doi: 10.1016/j.phrs.2020.104903

Canetta, C., Accordino, S., Buscarini, E., Benelli, G., La Piana, G., Scartabellati, A., et al. (2020). Syncope at SARS-CoV-2 onset due to impaired baroreflex response. *medRxiv [Preprint]* doi: 10.1101/2020.05.29.20114751

Castelnovo, L., Capelli, F., Tamburello, A., Faggioli, P. M., and Mazzone, A. (2020). Symmetric cutaneous vasculitis in COVID-19 pneumonia. *J. Eur. Acad. Dermatol. Venereol.* doi: 10.1111/jdv.16589 [Epub ahead of print].

Cavolo, S. L., Zhou, C., Ketcham, S. A., Suzuki, M. M., Ukalovic, K., Silverman, M. A., et al. (2015). Mycalolide B dissociates dynactin and abolishes retrograde axonal transport of dense-core vesicles. *Mol. Biol. Cell* 26, 2664–2672. doi: 10.1091/mbc.e14-11-1564

Cha, M. H., Regueiro, M., and Sandhu, D. S. (2020). Gastrointestinal and hepatic manifestations of COVID-19: a comprehensive review. *World J. Gastroenterol.* 26, 2323–2332.

Chazal, N., and Gerlier, D. (2003). Virus entry, assembly, budding, and membrane rafts. *Microbiol. Mol. Biol. Rev.* 67, 226–237. doi: 10.1128/mmbr.67.2.226-237.2003

Cheema, M., Aghazadeh, H., Nazarali, S., Ting, A., Hodges, J., McFarlane, A., et al. (2020). Keratoconjunctivitis as the initial medical presentation of the novel coronavirus disease 2019 (COVID-19). *Can. J. Ophthalmol.* [Epub ahead of print].

Chen, H., Guo, J., Wang, C., Luo, F., Yu, X., Zhang, W., et al. (2020a). Clinical characteristics and intrauterine vertical transmission potential of COVID-19 infection in nine pregnant women: a retrospective review of medical records. *Lancet (London, England)* 395, 809–815. doi: 10.1016/s0140-6736(20)30360-3

Chen, X., Zhao, B., Qu, Y., Chen, Y., Xiong, J., Feng, Y., et al. (2020b). Detectable serum SARS-CoV-2 viral load (RNAaemia) is closely associated with drastically elevated interleukin 6 (IL-6) level in critically ill COVID-19 patients. *Clin. Infect. Dis.* 17:ciaa449. doi: 10.1093/cid/ciaa449 [Epub ahead of print].

Chen, L., Lin, Y.-L., Peng, G., and Li, F. (2012). Structural basis for multifunctional roles of mammalian aminopeptidase N. *Proc. Natl. Acad. Sci. U.S.A.* 109, 17966–17971. doi: 10.1073/pnas.1210123109

Chin, A., Chu, J., Perera, M., Hui, K., Yen, H.-L., Chan, M., et al. (2020). Stability of SARS-CoV-2 in different environmental conditions. *medRxiv [Preprint]* doi: 10.1101/2020.03.15.20036673

Chung, K. F., McGarvey, L., and Mazzone, S. B. (2013). Chronic cough as a neuropathic disorder. *Lancet Respir. Med.* 1, 414–422. doi: 10.1016/s2213-2600(13)70043-2

Clarke, N. E., Fisher, M. J., Porter, K. E., Lambert, D. W., and Turner, A. J. (2012). Angiotensin converting enzyme (ACE) and ACE2 bind integrins and ACE2 regulates integrin signalling. *PLoS ONE* 7:e34747. doi: 10.1371/journal.pone.0034747

Colavita, F., Lapa, D., Carletti, F., Lalle, E., Bordi, L., Marsella, P., et al. (2020). SARS-CoV-2 isolation from ocular secretions of a patient with COVID-19 in Italy with prolonged viral RNA detection. *Ann. Int. Med.* M20–M1176.

Coolen, T., Lolli, V., Sadeghi, N., Rovai, A., Trotta, N., Taccone, F. S., et al. (2020). Early postmortem brain MRI findings in COVID-19 non-survivors. *medRxiv [Preprint]* doi: 10.1101/2020.05.04.20090316

Davison, D. L., Terek, M., and Chawla, L. S. (2012). Neurogenic pulmonary edema. *Crit Care.* 16:212.

Day, M. (2020). Covid-19: four fifths of cases are asymptomatic, China figures indicate. *BMJ* 369:m1375. doi: 10.1136/bmj.m1375

de Jonge, W. J., van der Zanden, E. P., The, F. O., Bijlsma, M. F., van Westerloo, D. J., Bennink, R. J., et al. (2005). Stimulation of the vagus nerve attenuates macrophage activation by activating the Jak2-STAT3 signaling pathway. *Nat. Immunol.* 6, 844–851. doi: 10.1038/ni1229

Dina, O. A., Parada, C. A., Yeh, J., Chen, X., McCarter, G. C., and Levine, J. D. (2004). Integrin signaling in inflammatory and neuropathic pain in the rat. *Eur. J. Neurosci.* 19, 634–642. doi: 10.1111/j.1460-9568.2004.03169.x

Doobay, M. F., Talman, L. S., Obr, T. D., Tian, X., Davisson, R. L., and Lazartigues, E. (2007). Differential expression of neuronal ACE2 in transgenic mice with overexpression of the brain renin-angiotensin system. *Am. J. physiol. Regul. Integr. Compar. Physiol.* 292, R373–R381.

Dubé, M., Le Coupanec, A., Wong, A. H. M., Rini, J. M., Desforges, M., and Talbot, P. J. (2018). Axonal transport enables neuron-to-neuron propagation of human coronavirus OC43. *J. Virol.* 92, JVI.404–JVI.418. doi: 10.1128/JVI.00404-18

Eden, E. R. (2016). The formation and function of ER-endosome membrane contact sites. *Biochim. Biophys. Acta (BBA)* 1861, 874–879. doi: 10.1016/j.bbalip.2016.01.020

Enquist, L. W. (2012). Five questions about viral trafficking in neurons. *PLoS Pathog.* 8:e1002472. doi: 10.1371/journal.ppat.1002472

Enwere, E., Shingo, T., Gregg, C., Fujikawa, H., Ohta, S., and Weiss, S. (2004). Aging results in reduced epidermal growth factor receptor signaling, diminished olfactory neurogenesis, and deficits in fine olfactory discrimination. *J. Neurosci.* 24, 8354–8365. doi: 10.1523/jneurosci.2751-04.2004

Escobales, N., Nunez, R. E., and Javadov, S. (2019). Mitochondrial angiotensin receptors and cardioprotective pathways. *Am. J. physiol. Heart Circul. Physiol.* 316, H1426–H1438.

Fantini, J., Di Scala, C., Chahinian, H., and Yahi, N. (2020). Structural and molecular modelling studies reveal a new mechanism of action of chloroquine and hydroxychloroquine against SARS-CoV-2 infection. *Int. J. Antimicrob Agents* 55:105960. doi: 10.1016/j.ijantimicag.2020.105960

Fazzini, E., Fleming, J., and Fahn, S. (1992). Cerebrospinal fluid antibodies to coronavirus in patients with Parkinson's disease. *Movement Disord.* 7, 153–158. doi: 10.1002/mds.870070210

Fodoulian, L., Tuberosa, J., Rossier, D., Landis, B. N., Carleton, A., and Rodriguez, I. (2020). SARS-CoV-2 receptor and entry genes are expressed by sustentacular cells in the human olfactory neuroepithelium. *bioRxiv [Preprint]* doi: 10.1101/2020.03.31.013268

Gautret, P., Lagier, J.-C., Parola, P., Hoang, V. T., Meddeb, L., Mailhe, M., et al. (2020). Hydroxychloroquine and azithromycin as a treatment of COVID-19: results of an open-label non-randomized clinical trial. *Int J Antimicrob Agents*. 56:105949. doi: 10.1016/j.ijantimicag.2020.105949 [Epub ahead of print].

Gonzalez, C., and Couve, A. (2014). The axonal endoplasmic reticulum and protein trafficking: Cellular bootlegging south of the soma. *Semin. Cell Dev. Biol.* 27, 23–31. doi: 10.1016/j.semcdb.2013.12.004

Griffin, D. E. (2003). Immune responses to RNA-virus infections of the CNS. *Nature Reviews Immunology*. 3, 493–502. doi: 10.1038/nri1105

Hani, C., Trieu, N. H., Saab, I., Dangeard, S., Bennani, S., Chassagnon, G., et al. (2020). COVID-19 pneumonia: a review of typical CT findings and differential diagnosis. *Diagn Interv. Imaging.* 101, 263–268. doi: 10.1016/j.diii.2020.03.014

Helms, J., Tacquard, C., Severac, F., Leonard-Lorant, I., Ohana, M., Delabranche, X., et al. (2020). High risk of thrombosis in patients with severe SARS-CoV-2 infection: a multicenter prospective cohort study. *Intens. Care Med.* [Epub ahead of print].

Hoffmann, M., Kleine-Weber, H., Krüger, N., Müller, M., Drosten, C., and Pöhlmann, S. (2020a). The novel coronavirus 2019 (2019-nCoV) uses the SARS-coronavirus receptor ACE2 and the cellular protease TMPRSS2 for entry into target cells. *bioRxiv [Preprint]* doi: 10.1101/2020.01.31.929042

Hoffmann, M., Kleine-Weber, H., Schroeder, S., Krüger, N., Herrler, T., Erichsen, S., et al. (2020b). SARS-CoV-2 cell entry depends on ACE2 and TMPRSS2 and is blocked by a clinically proven protease inhibitor. *Cell* 181, 271–280.e8. doi: 10.1016/j.cell.2020.02.052

Holstege, G. (1987). Some anatomical observations on the projections from the hypothalamus to brainstem and spinal cord: an HRP and autoradiographic tracing study in the cat. *J. Compar. Neurol.* 260, 98–126. doi: 10.1002/cne.902600109

Hu, X., Han, C., Jin, J., Qin, K., Zhang, H., Li, T., et al. (2016). Integrin CD11b attenuates colitis by strengthening Src-Akt pathway to polarize anti-inflammatory IL-10 expression. *Sci. Rep.* 6:26252.

Hu, Y., Shen, L., Xu, Z., Zhou, J., and Zhou, H. (2020). SARS-CoV-2 may persist in digestive tract longer than respiratory tract. [Preprint]. doi: 10.20944/preprints202002.0354.v1

Hui, K., Cheung, M.-C., Perera, R. A. P. M., Ng, K.-C., Bui, C., Ho, J., et al. (2020). Tropism of the novel coronavirus SARS-CoV-2 in human respiratory tract: an analysis in ex vivo and in vitro cultures. *SSRN Electron. J.* 1:e10.

Huston, J. M. (2012). The vagus nerve and the inflammatory reflex: wandering on a new treatment paradigm for systemic inflammation and sepsis. *Surg. Infect.* 13, 187–193. doi: 10.1089/sur.2012.126

Iba, T., Levy, J. H., Levi, M., Connors, J. M., and Thachil, J. (2020). Coagulopathy of coronavirus disease 2019. *Crit. Care Med.* [Preprint]. doi: 10.1097/CCM.0000000000004458

Jaimes, J. A., André, N. M., Millet, J. K., and Whittaker, G. R. (2020). Structural modeling of 2019-novel coronavirus (nCoV) spike protein reveals a proteolytically-sensitive activation loop as a distinguishing feature compared to SARS-CoV and related SARS-like coronaviruses. *bioRxiv [Preprint]* doi: 10.1101/2020.02.10.942185

Jiang, F., Deng, L., Zhang, L., Cai, Y., Cheung, C. W., and Xia, Z. (2020). Review of the clinical characteristics of coronavirus disease 2019 (COVID-19). *J. General Int. Med.* 35, 1545–1549.

Johnston, G. R., and Webster, N. R. (2009). Cytokines and the immunomodulatory function of the vagus nerve. *Br. J. Anaesth.* 102, 453–462. doi: 10.1093/bja/aep037

Kalinke, U., Bechmann, I., and Detje, C. N. (2011). Host strategies against virus entry via the olfactory system. *Virulence* 2, 367–370. doi: 10.4161/viru.2.4.16138

Karimi, N., Sharifi Razavi, A., and Rouhani, N. (2020). Frequent convulsive seizures in an adult patient with COVID-19: a case report. *Iran. Red. Crescent Med. J.* 22:e102828.

Kaya, Y., Kara, S., Akinci, C., and Kocaman, A. S. (2020). Transient cortical blindness in COVID-19 pneumonia; a PRES-like syndrome: case report. *J. Neurol. Sci.* 413:116858. doi: 10.1016/j.jns.2020.116858

Khan, G., Ahmed, W., and Rony, P. (2017). Exosomes and their role in viral infections. *Open Virol. J.* 12, 134–148.

Kim, S. Y., Jin, W., Sood, A., Montgomery, D. W., Grant, O. C., Fuster, M. M., et al. (2020). Glycosaminoglycan binding motif at S1/S2 proteolytic cleavage site on spike glycoprotein may facilitate novel coronavirus (SARS-CoV-2) host cell entry. *bioRxiv [Preprint]* doi: 10.1101/2020.04.14.041459

Klein, R. S., Garber, C., Funk, K. E., Salimi, H., Soung, A., Kanmogne, M., et al. (2019). Neuroinflammation During RNA Viral Infections. *Annu. Rev. Immunol.* 37, 73–95. doi: 10.1146/annurev-immunol-042718-041417

Knoops, K., Kikkert, M., Worm, S. H., Zevenhoven-Dobbe, J. C., van der Meer, Y., Koster, A. J., et al. (2008). SARS-coronavirus replication is supported by a reticulovesicular network of modified endoplasmic reticulum. *PLoS Biol.* 6:e226. doi: 10.1371/journal.pbio.0060226

Kochi, A. N., Tagliari, A. P., Forleo, G. B., Fassini, G. M., and Tondo, C. (2020). Cardiac and arrhythmic complications in patients with COVID-19. *J. Cardiovasc. Electrophysiol.* 31, 1003–1008. doi: 10.1111/jce.14479

Koczera, P., Martin, L., Marx, G., and Schuerholz, T. (2016). The ribonuclease A superfamily in humans: canonical rnases as the buttress of innate immunity. *Int. J. Mol. Sci.* 17:1278. doi: 10.3390/ijms17081278

Koopman, F. A., Chavan, S. S., Miljko, S., Grazio, S., Sokolovic, S., Schuurman, P. R., et al. (2016). Vagus nerve stimulation inhibits cytokine production and attenuates disease severity in rheumatoid arthritis. *Proc. Natl. Acad. Sci. U.S.A.* 113, 8284–8289. doi: 10.1073/pnas.1605635113

Koyuncu, O. O., Hogue, I. B., and Enquist, L. W. (2013). Virus infections in the nervous system. *Cell Host Microbe.* 13, 379–393.

Krijnse-Locker, J., Ericsson, M., Rottier, P. J., and Griffiths, G. (1994). Characterization of the budding compartment of mouse hepatitis virus: evidence that transport from the RER to the Golgi complex requires only one vesicular transport step. *J. Cell Biol.* 124, 55–70. doi: 10.1083/jcb.124.1.55

Lai, C.-C., Shih, T.-P., Ko, W.-C., Tang, H.-J., and Hsueh, P.-R. (2020). Severe acute respiratory syndrome coronavirus 2 (SARS-CoV-2) and coronavirus disease-2019 (COVID-19): The epidemic and the challenges. *Int. J. Antimicrob. Agents* 55:105924. doi: 10.1016/j.ijantimicag.2020.105924

Lan, L., Xu, D., Ye, G., Xia, C., Wang, S., Li, Y., et al. (2020). Positive RT-PCR test results in patients recovered from COVID-19. *JAMA* 323, 1502–1503.

Lechien, J. R., Chiesa-Estomba, C. M., De Siati, D. R., Horoi, M., Le Bon, S. D., Rodriguez, A., et al. (2020). Olfactory and gustatory dysfunctions as a clinical presentation of mild-to-moderate forms of the coronavirus disease (COVID-19): a multicenter European study. *Eur. Arch. Otorhinolaryngol.* 277, 2251–2261. doi: 10.1007/s00405-020-05965-1

Leisman, D. E., Deutschman, C. S., and Legrand, M. (2020). Facing COVID-19 in the ICU: vascular dysfunction, thrombosis, and dysregulated inflammation. *Inten. Care Med.* 46, 1105–1108. doi: 10.1007/s00134-020-06059-6

Li, D.-J., Evans, R., Yang, Z.-W., Song, S.-W., Wang, P., Ma, X.-J., et al. (2011). Dysfunction of the cholinergic anti-inflammatory pathway mediates organ damage in hypertension. *Hypertension (Dallas, Tex:* 1979) 57, 298–307. doi: 10.1161/hypertensionaha.110.160077

Li, P., Liu, H., Sun, P., Wang, X., Wang, C., Wang, L., et al. (2016). Chronic vagus nerve stimulation attenuates vascular endothelial impairments and reduces the inflammatory profile via inhibition of the NF-κB signaling pathway in ovariectomized rats. *Exp. Gerontol.* 74, 43–55. doi: 10.1016/j.exger.2015.12.005

Li, Y. C., Bai, W. Z., and Hashikawa, T. (2020). The neuroinvasive potential of SARS-CoV2 may play a role in the respiratory failure of COVID-19 patients. *J. Med. Virol.* [Epub ahead of print].

Li, Y. C., Bai, W. Z., Hirano, N., Hayashida, T., Taniguchi, T., Sugita, Y., et al. (2013). Neurotropic virus tracing suggests a membranous-coating-mediated mechanism for transsynaptic communication. *J. Compar. Neurol.* 521, 203–212. doi: 10.1002/cne.23171

Liu, J., Cao, R., Xu, M., Wang, X., Zhang, H., Hu, H., et al. (2020). Hydroxychloroquine, a less toxic derivative of chloroquine, is effective in inhibiting SARS-CoV-2 infection in vitro. *Cell Discov.* 6:16.

Lorizate, M., and Kräusslich, H.-G. (2011). Role of lipids in virus replication. *Cold Spring Harb. Perspect. Biol.* 3:a004820–a.

Loseva, E., Yuan, T.-F., and Karnup, S. (2009). Neurogliogenesis in the mature olfactory system: a possible protective role against infection and toxic dust. *Brain Res. Rev.* 59, 374–387. doi: 10.1016/j.brainresrev.2008.10.004

MacGibeny, M. A., Koyuncu, O. O., Wirblich, C., Schnell, M. J., and Enquist, L. W. (2018). Retrograde axonal transport of rabies virus is unaffected by interferon treatment but blocked by emetine locally in axons. *PLoS Pathog.* 14:e1007188. doi: 10.1371/journal.ppat.1007188

Mao, L., Jin, H., Wang, M., Hu, Y., Chen, S., He, Q., et al. (2020). Neurologic manifestations of hospitalized patients with coronavirus disease 2019 in Wuhan, China. *JAMA Neurol.* 77, 683–690.

Marsh, M., and Helenius, A. (2006). Virus entry: open sesame. *Cell* 124, 729–740. doi: 10.1016/j.cell.2006.02.007

Marzioni, D., Tamagnone, L., Capparuccia, L., Marchini, C., Amici, A., Todros, T., et al. (2004). Restricted innervation of uterus and placenta during pregnancy: evidence for a role of the repelling signal Semaphorin 3A. *Dev. Dynam.* 231, 839–848. doi: 10.1002/dvdy.20178

Masters, P. S. (2006). The molecular biology of coronaviruses. *Adv. Virus Res.* 66, 193–292. doi: 10.1016/s0065-3527(06)66005-3

Mehta, P., McAuley, D. F., Brown, M., Sanchez, E., Tattersall, R. S., and Manson, J. J. (2020). COVID-19: consider cytokine storm syndromes and immunosuppression. *Lancet (Lond. Engl).* 395, 1033–1034. doi: 10.1016/s0140-6736(20)30628-0

Meinhardt, J., Radke, J., Dittmayer, C., Mothes, R., Franz, J., Laue, M., et al. (2020). Olfactory transmucosal SARS-CoV-2 invasion as port of central nervous system entry in COVID-19 patients. *bioRxiv [Preprint]* doi: 10.1101/2020.06.04.135012

Moon, C., Han, J. R., Park, H. J., Hah, J. S., and Kang, J. L. (2009). Synthetic RGDS peptide attenuates lipopolysaccharide-induced pulmonary inflammation by inhibiting integrin signaled MAP kinase pathways. *Respir. Res.* 10:18.

Mori, I., Nishiyama, Y., Yokochi, T., and Kimura, Y. (2004). Virus-induced neuronal apoptosis as pathological and protective responses of the host. *Rev. Med. Virol.* 14, 209–216. doi: 10.1002/rmv.426

Moriguchi, T., Harii, N., Goto, J., Harada, D., Sugawara, H., Takamino, J., et al. (2020). A first case of meningitis/encephalitis associated with SARS-Coronavirus-2. *Int. J. Infect. Dis.* 4, 55–58.

Mycroft-West, C., Su, D., Elli, S., Guimond, S., Miller, G., Turnbull, J., et al. (2020). The 2019 coronavirus (SARS-CoV-2) surface protein (Spike) S1 Receptor Binding Domain undergoes conformational change upon heparin binding. *bioRxiv [Preprint]* doi: 10.1101/2020.02.29.971093

Nie, S., Zhao, X., Zhao, K., Zhang, Z., Zhang, Z., and Zhang, Z. (2020). Metabolic disturbances and inflammatory dysfunction predict severity of coronavirus disease 2019 (COVID-19): a retrospective study. *medRxiv [Preprint]* doi: 10.1101/2020.03.24.20042283

Niimi, A., and Chung, K. F. (2015). Evidence for neuropathic processes in chronic cough. *Pulmon. Pharmacol. Therap.* 35, 100–104. doi: 10.1016/j.pupt.2015.10.004

Ohka, S., Matsuda, N., Tohyama, K., Oda, T., Morikawa, M., Kuge, S., et al. (2004). Receptor (CD155)-dependent endocytosis of poliovirus and retrograde axonal

transport of the endosome. *J. Virol.* 78, 7186–7198. doi: 10.1128/jvi.78.13.7186-7198.2004

Okusaga, O., Yolken, R. H., Langenberg, P., Lapidus, M., Arling, T. A., Dickerson, F. B., et al. (2011). Association of seropositivity for influenza and coronaviruses with history of mood disorders and suicide attempts. *J. Affect. Disord.* 130, 220–225. doi: 10.1016/j.jad.2010.09.029

Oliphant, T., Engle, M., Nybakken, G. E., Doane, C., Johnson, S., Huang, L., et al. (2005). Development of a humanized monoclonal antibody with therapeutic potential against West Nile virus. *Nat. Med.* 11, 522–530. doi: 10.1038/nm1240

Onal, H., and Semerci, S. Y. (2020). *Effect of Quercetin on Prophylaxis and Treatment of COVID-19: Kanuni Sultan Suleyman Training and Research Hospital* Available online at: https://clinicaltrials.gov/ct2/show/NCT04377789 (accessed March 20, 2020).

Ono, A. (2010). Relationships between plasma membrane microdomains and HIV-1 assembly. *Biol. Cell.* 102, 335–350. doi: 10.1042/bc20090165

Ou, X., Liu, Y., Lei, X., Li, P., Mi, D., Ren, L., et al. (2020). Characterization of spike glycoprotein of SARS-CoV-2 on virus entry and its immune cross-reactivity with SARS-CoV. *Nat. Commun.* 11:1620.

Pan, C., Chen, L., Lu, C., Zhang, W., Xia, J.-A., Sklar, M. C., et al. (2020). Lung recruitability in COVID-19-associated acute respiratory distress syndrome: a single-center observational study. *Am. J. Respir. Crit. Care Med.* 201, 1294–1297. doi: 10.1164/rccm.202003-0527le

Paniz-Mondolfi, A., Bryce, C., Grimes, Z., Gordon, R. E., Reidy, J., Lednicky, J., et al. (2020). Central nervous system involvement by severe acute respiratory syndrome coronavirus -2 (SARS-CoV-2). *J. Med. Virol.* 92, 699–702. doi: 10.1002/jmv.25915

Pavlov, V. A., and Tracey, K. J. (2012). The vagus nerve and the inflammatory reflex–linking immunity and metabolism. *Nat. Rev. Endocrinol.* 8, 743–754. doi: 10.1038/nrendo.2012.189

Pei, G., Zhang, Z., Peng, J., Liu, L., Zhang, C., Yu, C., et al. (2020). Renal involvement and early prognosis in patients with COVID-19 pneumonia. *J. Am. Soc. Nephrol.* 31, 1157–1165. doi: 10.1681/asn.2020030276

Pinto, B. G., Oliveira, A. E., Singh, Y., Jimenez, L., Goncalves, A. N., Ogava, R. L., et al. (2020). ACE2 expression is increased in the lungs of patients with comorbidities associated with severe COVID-19. *medRxiv [Preprint]*. doi: 10.1101/2020.03.21.20040261.

Poyiadji, N., Shahin, G., Noujaim, D., Stone, M., Patel, S., and Griffith, B. (2020). COVID-19-associated acute hemorrhagic necrotizing encephalopathy: CT and MRI features. *Radiology* 296:201187.

Prentice, E., McAuliffe, J., Lu, X., Subbarao, K., and Denison, M. R. (2004). Identification and characterization of severe acute respiratory syndrome coronavirus replicase proteins. *J. Virol.* 78, 9977–9986. doi: 10.1128/jvi.78.18.9977-9986.2004

Proença de Oliveira-Maul, J., Barbosa, de Carvalho, H., Goto, D. M., Maia, R. M., et al. (2013). Aging, diabetes, and hypertension are associated with decreased nasal mucociliary clearance. *Chest* 143, 1091–1097. doi: 10.1378/chest.12-1183

Puelles, V. G., Lütgehetmann, M., Lindenmeyer, M. T., Sperhake, J. P., Wong, M. N., Allweiss, L., et al. (2020). Multiorgan and renal tropism of SARS-CoV-2. *N. Engl. J. Med.* doi: 10.1056/NEJMc2011400 [Epub ahead of print].

Rees, C. J., Henderson, A. H., and Belafsky, P. C. (2009). Postviral vagal neuropathy. *Ann. Otol. Rhinol. Laryngol.* 118, 247–252. doi: 10.1177/000348940911800402

Sachdeva, M., Gianotti, R., Shah, M., Lucia, B., Tosi, D., Veraldi, S., et al. (2020). Cutaneous manifestations of COVID-19: report of three cases and a review of literature. *J. Dermatol. Sci.* 98, 75–81. doi: 10.1016/j.jdermsci.2020.04.011

Salanueva, I. J., Carrascosa, J. L., and Risco, C. (1999). Structural maturation of the transmissible gastroenteritis coronavirus. *J. Virol.* 73, 7952–7964. doi: 10.1128/jvi.73.10.7952-7964.1999

Samuel, M. A., Wang, H., Siddharthan, V., Morrey, J. D., and Diamond, M. S. (2007). Axonal transport mediates West Nile virus entry into the central nervous system and induces acute flaccid paralysis. *Proc. Natl. Acad. Sci. U.S.A.* 104, 17140–17145. doi: 10.1073/pnas.0705837104

Schnaar, R. L., Gerardy-Schahn, R., and Hildebrandt, H. (2014). Sialic acids in the brain: gangliosides and polysialic acid in nervous system development, stability, disease, and regeneration. *Physiol. Rev.* 94, 461–518. doi: 10.1152/physrev.00033.2013

Selimoglu, M. A., Selimoglu, E., and Kurt, A. (1999). Nasal mucociliary clearance and nasal and oral pH in patients with insulin-dependent diabetes. *Ear Nose Throat J.* 78, 585–590. doi: 10.1177/014556139907800814

Severance, E., Dickerson, F., Bossis, Y., Stallings, C., Origoni, A., Sullens, A., et al. (2009). Coronavirus immunoreactivity in individuals with a recent onset of psychotic symptoms. *Schizophr. Bull.* 37, 101–107. doi: 10.1093/schbul/sbp052

Sharifi-Razavi, A., Karimi, N., and Rouhani, N. (2020). COVID 19 and Intra cerebral hemorrhage: causative or coincidental. *New Microbes New Infect.* 35:100669. doi: 10.1016/j.nmni.2020.100669

Shi, T.-T., Yang, F.-Y., Liu, C., Cao, X., Lu, J., Zhang, X.-L., et al. (2018). Angiotensin-converting enzyme 2 regulates mitochondrial function in pancreatic β-cells. *Biochem. Biophys. Res. Commun.* 495, 860–866. doi: 10.1016/j.bbrc.2017.11.055

Sigrist, C. J., Bridge, A., and Le Mercier, P. (2020). A potential role for integrins in host cell entry by SARS-CoV-2. *Antiv. Res.* 177:104759. doi: 10.1016/j.antiviral.2020.104759

Snijder, E. J., Limpens, R. W. A. L., de Wilde, A. H., de Jong, A. W. M., Zevenhoven-Dobbe, J. C., Maier, H. J., et al. (2020). A unifying structural and functional model of the coronavirus replication organelle: tracking down RNA synthesis. *bioRxiv [Preprint]* doi: 10.1101/2020.03.24.005298

Sotomayor-Flores, C., Rivera-Mejias, P., Vasquez-Trincado, C., Lopez-Crisosto, C., Morales, P. E., Pennanen, C., et al. (2020). Angiotensin-(1-9) prevents cardiomyocyte hypertrophy by controlling mitochondrial dynamics via miR-129-3p/PKIA pathway. *Cell Death Diff.* [Epub ahead of print].

Steardo, L., Steardo, L. Jr., Zorec, R., and Verkhratsky, A. (2020). Neuroinfection may contribute to pathophysiology and clinical manifestations of COVID-19. *Acta Physiol. (Oxf. Engl.)* 229:e13473.

Sultan, I., Howard, S., and Tbakhi, A. (2020). Drug repositioning suggests a role for the heat shock protein 90 inhibitor geldanamycin in treating COVID-19 infection. *Res. Square* [Preprint]. doi: 10.21203/rs.3.rs-18714/v1

Tanida, I., Fukasawa, M., Ueno, T., Kominami, E., Wakita, T., and Hanada, K. (2009). Knockdown of autophagy-related gene decreases the production of infectious hepatitis C virus particles. *Autophagy* 5, 937–945. doi: 10.4161/auto.5.7.9243

Tian, Y., Rong, L., Nian, W., and He, Y. (2020). Review article: gastrointestinal features in COVID-19 and the possibility of faecal transmission. *Aliment Pharmacol. Ther.* 51, 843–851. doi: 10.1111/apt.15731

Toljan, K. (2020). Letter to the editor regarding the viewpoint Evidence of the COVID-19 virus targeting the CNS: tissue distribution, host-virus interaction, and proposed neurotropic mechanism. *ACS Chem. Neurosci.* 11, 1192–1194. doi: 10.1021/acschemneuro.0c00174

Vajn, K., Viljetic, B., Degmecic, I. V., Schnaar, R. L., and Heffer, M. (2013). Differential distribution of major brain gangliosides in the adult mouse central nervous system. *PLoS ONE* 8:e75720. doi: 10.1371/journal.pone.0075720

Valdes, G., Corthorn, J., Bharadwaj, M. S., Joyner, J., Schneider, D., and Brosnihan, K. B. (2013). Utero-placental expression of angiotensin-(1-7) and ACE2 in the pregnant guinea-pig. *Reproduct. Biol. Endocrinol.* 11:5. doi: 10.1186/1477-7827-11-5

Varga, Z., Flammer, A. J., Steiger, P., Haberecker, M., Andermatt, R., Zinkernagel, A. S., et al. (2020). Endothelial cell infection and endotheliitis in COVID-19. *Lancet (London, England)* 395, 1417–1418. doi: 10.1016/s0140-6736(20)30937-5

Verdoni, L., Mazza, A., Gervasoni, A., Martelli, L., Ruggeri, M., Ciuffreda, M., et al. (2020). An outbreak of severe Kawasaki-like disease at the Italian epicentre of the SARS-CoV-2 epidemic: an observational cohort study. *Lancet (London, Engl.)* 395, 1771–1778. doi: 10.1016/s0140-6736(20)31103-x

Verheije, M. H., Raaben, M., Mari, M., Te Lintelo, E. G., Reggiori, F., van Kuppeveld, F. J., et al. (2008). Mouse hepatitis coronavirus RNA replication depends on GBF1-mediated ARF1 activation. *PLoS Pathog.* 4:e1000088. doi: 10.1371/journal.ppat.1000088

Villar-Cheda, B., Costa-Besada, M. A., Valenzuela, R., Perez-Costas, E., Melendez-Ferro, M., and Labandeira-Garcia, J. L. (2017). The intracellular angiotensin system buffers deleterious effects of the extracellular paracrine system. *Cell Death Dis.* 8:e3044. doi: 10.1038/cddis.2017.439

Waheed, A. A., and Freed, E. O. (2010). The role of lipids in retrovirus replication. *Viruses* 2, 1146–1180. doi: 10.3390/v2051146

Walls, A. C., Park, Y. J., Tortorici, M. A., Wall, A., McGuire, A. T., and Veesler, D. (2020). Structure, function, and antigenicity of the SARS-CoV-2 spike glycoprotein. *Cell* 181, 281–292.e6. doi: 10.1016/j.cell.2020.02.058

Walter, U., Tsiberidou, P., Kersten, M., Storch, A., and Lohle, M. (2018). Atrophy of the vagus nerve in Parkinson's disease revealed by high-resolution ultrasonography. *Front. Neurol.* 9:805.

Wan, S., Xiang, Y., Fang, W., Zheng, Y., Li, B., Hu, Y., et al. (2020). Clinical features and treatment of COVID-19 patients in northeast Chongqing. *J. Med. Virol.* 92, 797–806. doi: 10.1002/jmv.25783

Wang, H., Yang, P., Liu, K., Guo, F., Zhang, Y., Zhang, G., et al. (2008). SARS coronavirus entry into host cells through a novel clathrin- and caveolae-independent endocytic pathway. *Cell Res.* 18, 290–301. doi: 10.1038/cr.2008.15

Wang, J., Chen, S., and Bihl, J. (2020a). Exosome-mediated transfer of ACE2 (angiotensin-converting enzyme 2) from endothelial progenitor cells promotes survival and function of endothelial cell. *Oxidat. Med. Cell. Long.* 2020: 4213541.

Wang, W., Xu, Y., Gao, R., Lu, R., Han, K., Wu, G., et al. (2020b). Detection of SARS-CoV-2 in different types of clinical specimens. *JAMA* 323, 1843–1844. doi: 10.1001/jama.2020.3786

Wang, X., Xu, W., Hu, G., Xia, S., Sun, Z., Liu, Z., et al. (2020c). SARS-CoV-2 infects T lymphocytes through its spike protein-mediated membrane fusion. *Cell. Mol. Immunol.* [Epub ahead of print].

Wang, X., Yang, H., and Raizada, M. K. (2001). Angiotensin II increases vesicular trafficking in brain neurons. *Hypertension (Dallas Tex:* 1979) 37(2 Pt 2), 677–682. doi: 10.1161/01.hyp.37.2.677

Westerloo, D., Giebelen, I., Meijers, J., Daalhuisen, J., Vos, A., Levi, M., et al. (2006). Vagus nerve stimulation inhibits activation of coagulation and fibrinolysis during endotoxemia in rats. *J. Thrombos. Haemostas.* 4, 1997–2002. doi: 10.1111/j.1538-7836.2006.02112.x

White, J. A., Banerjee, R., and Gunawardena, S. (2016). Axonal Transport and neurodegeneration: how marine drugs can be used for the development of therapeutics. *Mar. Drugs* 14:102. doi: 10.3390/md14050102

Wölfel, R., Corman, V. M., Guggemos, W., Seilmaier, M., Zange, S., Müller, M. A., et al. (2020). Virological assessment of hospitalized patients with COVID-2019. *Nature* 581, 465–469. doi: 10.1038/s41586-020-2196-x

Wu, Y., Wei, F., Tang, L., Liao, Q., Wang, H., Shi, L., et al. (2019). Herpesvirus acts with the cytoskeleton and promotes cancer progression. *J. Cancer* 10, 2185–2193. doi: 10.7150/jca.30222

Xia, S., Liu, M., Wang, C., Xu, W., Lan, Q., Feng, S., et al. (2020). Inhibition of SARS-CoV-2 (previously 2019-nCoV) infection by a highly potent pan-coronavirus fusion inhibitor targeting its spike protein that harbors a high capacity to mediate membrane fusion. *Cell Res.* 30, 343–355. doi: 10.1038/s41422-020-0305-x

Xiao, F., Tang, M., Zheng, X., Li, C., He, J., Hong, Z., et al. (2020). Evidence for gastrointestinal infection of SARS-CoV-2. *Gastroenterology* 158, 1831–1833.e3. doi: 10.1053/j.gastro.2020.02.055

Xing, Y., Mo, P., Xiao, Y., Zhao, O., Zhang, Y., and Wang, F. (2020). Post-discharge surveillance and positive virus detection in two medical staff recovered from coronavirus disease 2019 (COVID-19), China. *Euro Surveill.* 25:2000191.

Yang, Y., Shen, C., Li, J., Yuan, J., Yang, M., Wang, F., et al. (2020). Exuberant elevation of IP-10, MCP-3 and IL-1ra during SARS-CoV-2 infection is associated with disease severity and fatal outcome. *medRxiv [Preprint]* doi: 10.1101/2020.03.02.20029975

Yu, F., Yan, L., Wang, N., Yang, S., Wang, L., Tang, Y., et al. (2020). Quantitative detection and viral load analysis of SARS-CoV-2 in infected patients. *Clin. Infect. Dis.* [Epub ahead of print]. doi: 10.1093/cid/ciaa345

Yue, W. L. (2007). Nasal mucociliary clearance in patients with diabetes mellitus. *J. Laryngol. Otol.* 103, 853–855. doi: 10.1017/s0022215100110291

Zanin, L., Saraceno, G., Panciani, P. P., Renisi, G., Signorini, L., Migliorati, K., et al. (2020). SARS-CoV-2 can induce brain and spine demyelinating lesions. *Acta Neurochirurg.* [Epub ahead of print].

Zeng, L., Xia, S., Yuan, W., Yan, K., Xiao, F., Shao, J., et al. (2020). Neonatal early-onset infection with SARS-CoV-2 in 33 neonates born to mothers with COVID-19 in Wuhan, China. *JAMA Pediatr.*

Zhang, C., Shi, L., and Wang, F. S. (2020a). Liver injury in COVID-19: management and challenges. *Lancet Gastroenterol. Hepatol.* 5, 428–430. doi: 10.1016/s2468-1253(20)30057-1

Zhang, J., Lu, H., Zeng, H., Zhang, S., Du, Q., Jiang, T., et al. (2020b). The differential psychological distress of populations affected by the COVID-19 pandemic. *Brain Behav. Immun.* 87, 49–50. doi: 10.1016/j.bbi.2020.04.031

Zhang, J., Yan, K., Ye, H., Lin, J., Zheng, J., and Cai, T. (2020c). SARS-CoV-2 turned positive in a discharged patient with COVID-19 arouses concern regarding the present standard for discharge. *Int. J. Infect. Dis.* 97, 212–214. doi: 10.1016/j.ijid.2020.03.007

Zhao, B., Ni, C., Gao, R., Wang, Y., Yang, L., Wei, J., et al. (2020a). Recapitulation of SARS-CoV-2 infection and cholangiocyte damage with human liver organoids. *Protein Cell* [Epub ahead of print].

Zhao, H., Shen, D., Zhou, H., Liu, J., and Chen, S. (2020b). Guillain-barre syndrome associated with SARS-CoV-2 infection: causality or coincidence? *Lancet Neurol.* 19, 383–384. doi: 10.1016/s1474-4422(20)30109-5

Zhao, K., Huang, J., Dai, D., Feng, Y., Liu, L., and Nie, S. (2020c). Acute myelitis after SARS-CoV-2 infection: a case report. *medRxiv [Preprint]* doi: 10.1101/2020.03.16.20035105

Conflict of Interest: The authors declare that the research was conducted in the absence of any commercial or financial relationships that could be construed as a potential conflict of interest.

Copyright © 2020 Fenrich, Mrdenovic, Balog, Tomic, Zjalic, Roncevic, Mandic, Debeljak and Heffer. This is an open-access article distributed under the terms of the Creative Commons Attribution License (CC BY). The use, distribution or reproduction in other forums is permitted, provided the original author(s) and the copyright owner(s) are credited and that the original publication in this journal is cited, in accordance with accepted academic practice. No use, distribution or reproduction is permitted which does not comply with these terms.

frontiers in Cellular Neuroscience

ORIGINAL RESEARCH
published: 10 December 2020
doi: 10.3389/fncel.2020.601176

Mesenchymal Stromal Cell-Derived Extracellular Vesicles Reduce Neuroinflammation, Promote Neural Cell Proliferation and Improve Oligodendrocyte Maturation in Neonatal Hypoxic-Ischemic Brain Injury

Nicole Kaminski[1†], Christian Köster[1†], Yanis Mouloud[2], Verena Börger[2], Ursula Felderhoff-Müser[1], Ivo Bendix[1], Bernd Giebel[2] and Josephine Herz[1]*

[1] Department of Pediatrics I, Neonatology and Experimental Perinatal Neurosciences, University Hospital Essen, University Duisburg-Essen, Essen, Germany, [2] Institute for Transfusion Medicine, University Hospital Essen, University Duisburg-Essen, Essen, Germany

OPEN ACCESS

Edited by:
Daniel Alonso-Alconada, University of the Basque Country, Spain

Reviewed by:
Marta Fumagalli, University of Milan, Italy
Lauren Jantzie, Johns Hopkins University, United States

***Correspondence:**
Josephine Herz
josephine.herz@uk-essen.de

[†] These authors have contributed equally to this work

Specialty section:
This article was submitted to Cellular Neuropathology, a section of the journal Frontiers in Cellular Neuroscience

Received: 31 August 2020
Accepted: 19 November 2020
Published: 10 December 2020

Citation:
Kaminski N, Köster C, Mouloud Y, Börger V, Felderhoff-Müser U, Bendix I, Giebel B and Herz J (2020) Mesenchymal Stromal Cell-Derived Extracellular Vesicles Reduce Neuroinflammation, Promote Neural Cell Proliferation and Improve Oligodendrocyte Maturation in Neonatal Hypoxic-Ischemic Brain Injury.
Front. Cell. Neurosci. 14:601176.
doi: 10.3389/fncel.2020.601176

Background: Neonatal encephalopathy caused by hypoxia-ischemia (HI) is a major cause of childhood mortality and disability. Stem cell-based regenerative therapies seem promising to prevent long-term neurological deficits. Our previous work in neonatal HI revealed an unexpected interaction between mesenchymal stem/stromal cells (MSCs) and the brains' microenvironment leading to an altered therapeutic efficiency. MSCs are supposed to mediate most of their therapeutic effects in a paracrine mode via extracellular vesicles (EVs), which might be an alternative to cell therapy. In the present study, we investigated the impact of MSC-EVs on neonatal HI-induced brain injury.

Methods: Nine-day-old C57BL/6 mice were exposed to HI through ligation of the right common carotid artery followed by 1 h hypoxia (10% oxygen). MSC-EVs were injected intraperitoneally 1, 3, and 5 days after HI. One week after HI, brain injury was evaluated by regional neuropathological scoring, atrophy measurements and immunohistochemistry to assess effects on neuronal, oligodendrocyte and vessel densities, proliferation, oligodendrocyte maturation, myelination, astro-, and microglia activation. Immunohistochemistry analyses were complemented by mRNA expression analyses for a broad set of M1/M2- and A1/A2-associated molecules and neural growth factors.

Results: While total neuropathological scores and tissue atrophy were not changed, MSC-EVs significantly protected from HI-induced striatal tissue loss and decreased micro- and astroglia activation. MSC-EVs lead to a significant downregulation of the pro-inflammatory cytokine TNFa, accompanied by a significant upregulation of the M2 marker YM-1 and the anti-inflammatory cytokine TGFb. MSC-EVs significantly decreased astrocytic expression of the A1 marker C3, concomitant with an increased

expression of neural growth factors (i.e., BDNF, VEGF, and EGF). These alterations were associated with an increased neuronal and vessel density, coinciding with a significant increase of proliferating cells in the neurogenic sub-ventricular zone juxtaposed to the striatum. MSC-EV-mediated neuroprotection went along with a significant improvement of oligodendrocyte maturation and myelination.

Conclusion: The present study demonstrates that MSC-EVs mediate anti-inflammatory effects, promote regenerative responses and improve key developmental processes in the injured neonatal brain. The present results suggest different cellular target mechanisms of MSC-EVs, preventing secondary HI-induced brain injury. MSC-EV treatment may be a promising alternative to risk-associated cell therapies in neonatal brain injury.

Keywords: mesenchymal stem/stromal cells (MSC), extracellular vesicles (EV), MSC-EV, neonatal hypoxia-ischemia, oligodendrocyte maturation, neuroregeneration, neuroinflammation

INTRODUCTION

Neonatal brain injury caused by hypoxia-ischemia (HI) is a leading cause of childhood mortality and neurodevelopmental morbidity, associated with cerebral palsy, epilepsy, and visual impairment as well as cognitive and motor deficits in later life (Ahearne et al., 2016). To date, the only clinically recommended and established therapeutic intervention is a hypothermia (HT) treatment initiated within the first 6 h of life. However, 40–50% of cooled infants still suffer from major neurological problems (Azzopardi et al., 2014). Thus, new and/or additional treatment strategies aiming at the attenuation of injury and the enhancement of repair mechanisms are urgently required.

Taking into account that acute neuroprotective treatment options like HT are significantly limited, regenerative therapies to promote endogenous repair by the use of mesenchymal stem/stromal cells (MSC) have gained major interest in the past. Transplantation of bone marrow-derived MSCs in a variety of animal models, including murine models of adult and neonatal ischemic brain injury has been shown to improve neurobehavioral deficits involving anti-apoptotic, pro-regenerative and immunomodulatory effects (Yasuhara et al., 2008; van Velthoven et al., 2010; Jellema et al., 2013; Doeppner et al., 2015; Herz et al., 2018b). However, MSCs still harbor unforeseen risks such as modulation of MSC function by an altered *in vivo* microenvironment caused by HT (Herz et al., 2018b). Therefore, new concepts circumventing potential risks associated with the cells' plasticity after release into complex *in vivo* systems are needed. Increasing evidence suggests that therapeutically relevant effects are mediated by MSC-derived extracellular vesicles (MSC-EVs) (Lener et al., 2015; Borger et al., 2017; Witwer et al., 2019). Containing lipids, proteins and RNA, MSC-EVs participate in complex intercellular communication processes in a variety of physiological and pathophysiological processes (Ludwig and Giebel, 2012; Lener et al., 2015; Borger et al., 2017; Witwer et al., 2019). MSC-EVs provide important advantages over cellular therapeutics, because they are not self-replicating, can be well-characterized *in vitro* and can be sterilized by filtration. Furthermore, unlike cells, EVs hardly sense environmental conditions and therefore do not change their function in a context-dependent manner (Lener et al., 2015).

Neuroprotective, neuroregenerative, and immunomodulatory effects of MSC-EVs have been demonstrated in different models of adult and neonatal brain injury (Doeppner et al., 2015; Drommelschmidt et al., 2016; Ophelders et al., 2016; Gussenhoven et al., 2019; Sisa et al., 2019; Wang et al., 2020). In a model of adult brain ischemia, we demonstrated that MSC-EVs improve neuro-angiogenesis and associated functional recovery, which was accompanied by immunomodulatory effects in the periphery and the brain (Doeppner et al., 2015; Wang et al., 2020). To evaluate the therapeutic potential of MSC-EVs in perinatal brain injury we further analyzed effects of systemically administered MSC-EVs in a model of inflammation-induced preterm brain injury revealing anti-apoptotic effects, enhanced myelination, and reduced astro- and microgliosis, resulting in improved cognitive function in later life (Drommelschmidt et al., 2016). Even though our previous studies (Doeppner et al., 2015; Drommelschmidt et al., 2016) hold great promise for a successful outcome in neonatal HI-induced brain injury, EVs' target mechanisms most probably depend on the underlying pathology. Due to different developmental stages and different pathologies, findings in the previously investigated models cannot be extrapolated unequivocally. For instance, in a fetal ovine model of HI, MSC-EV administration did not significantly modulate microglia activation and myelination in spite of improved functional outcome (Ophelders et al., 2016). In contrast to this report, a recent study in a rodent term-equivalent model of HI demonstrated reduced microglia activation after intranasal MSC-EV administration (Sisa et al., 2019). Common to both studies is the focus on short-term outcome. The impact on sub-acute inflammatory responses, regenerative processes, initiated in the delayed disease phase, and potential modulation of developmental processes like oligodendrocyte proliferation and differentiation remain unknown.

In the present study, we investigated effects of systemically administered MSC-EVs on delayed structural brain tissue injury and cellular responses for a broad variety of cells including neurons, oligodendrocytes, endothelial cells, astrocytes, and

microglia to get deeper insight into MSC-EVs' target mechanisms in neonatal HI-induced brain injury.

MATERIALS AND METHODS

Animal Care and Allocation

Experiments were performed in accordance to the Animal Research Reporting of *In Vivo* Experiments (ARRIVE) guidelines with government approval by the State Agency for Nature, Environment and Consumer Protection North Rhine-Westphalia. C57BL/6J mice were bred in house and kept under a 12 h light/dark cycle with food and water *ad libitum*. Bodyweight of pups was recorded at postnatal day 9 (P9), P10, P11, and P12. A total of 43 C57BL/6 mice ($n = 20$ female and $n = 23$ male) derived from 6 litters were enrolled. A pilot study with a small cohort of animals [1 litter, $n = 7$, 3 sham (2 female, 1 male), 4 HI (1 female, 3 male)] was performed to characterize the general impact of HI on major cellular and molecular mechanisms, investigated the present study (**Supplementary Figure 1**). Data from analysis of MSC-EV treatment effects in HI-injured animals were derived from two independent experiments (with 2 and 3 litters, respectively). For all analyses, animals per litter and experiment were randomly assigned to 3 experimental groups [vehicle $n = 14$, platelet-derived EVs (PL-EV) $n = 8$, MSC-EV $n = 14$] prior to intervention. To control the potential influence of weight and sex, a stratified randomization was performed followed by simple randomization within each block to assign pups to individual groups. Individuals involved in data analysis knew the animals' designation but were blinded to group assignment. In total, 5 animals [13.3%, 2 female (1 vehicle, 1 PL-EV) and 3 male (2 MSC-EV, 1 vehicle)] died. No group differences were observed for weight gain.

MSC-EV Production and Characterization

MSC-EVs were prepared and characterized as described previously (Kordelas et al., 2014; Doeppner et al., 2015). Briefly, MSCs were raised from human bone marrow aspirates from healthy donors following informed consent according to the Declaration of Helsinki and as approved by the local ethics commission (12-5295-BO). MSCs were propagated in low glucose Dulbecco's Modified Eagle Medium (DMEM) (PAN Biotech), supplemented with self-produced 10% human platelet lysate (PL), 100 U/ ml penicillin-streptomycin-glutamine (Thermo Fisher Scientific, Germany) and 5 IU/ ml Heparin (Ratiopharm, Germany) at 37°C in a 5% CO_2 atmosphere. MSC-conditioned media (MSC-CM) were harvested from cultures with 50 and 90% confluence, every 48 h. After harvesting, MSC-CMs were spun at 2,000 × g for 15 min (Avanti centrifuge and JS-5.3 rotor; Beckman Coulter). Supernatants were stored at −20°C until further processing. After thawing, debris and larger EVs were removed by 45 min centrifugation at 6,800 × g (Avanti J-26 XP centrifuge using the swing-out rotor JS-5.3; Beckman Coulter) and subsequent filtration of the supernatant through 0.22 µm Nalgene filters (Thermo Fisher Scientific). EVs were enriched by 10% polyethylene glycol 6000 (PEG) precipitation in 75 mM sodium chloride (NaCl). Following overnight incubation at 4°C, samples were spun at 1,500 × g and 4°C for 30 min (Avanti J-26 XP centrifuge with the JS-5.3 rotor) (Ludwig et al., 2018). EV containing pellets were solved in 0.9% NaCl (Braun, Melsungen, Germany). The content of co-precipitated molecules of PEG were reduced by a washing step with 0.9% NaCl and subsequent ultracentrifugation (XPN-80 ultracentrifuge using the tight angle rotor Ti45, Beckmann Coulter; 110,000 × g for 130 min, k-factor: 133). Obtained pellets were solved in NaCl-HEPES buffer (Thermo Fisher Scientific) to a concentration of 4 x 10^7 MSC equivalents per ml. Fresh PL supplemented media was processed exactly the same to obtain PL-EV control samples. Prepared samples were stored at −80°C until usage. All obtained EV samples were characterized according to the Minimal Information for Studies of Extracellular Vesicles (MISEV) 2018 criteria (Thery et al., 2018), i.e., NTA analyses, western blot and transmission electron microscopy. Using the same MSC-EV samples (line 41.5) as in our previous studies (Doeppner et al., 2015; Drommelschmidt et al., 2016; Wang et al., 2020), we like to refer to Wang et al. for the results of all quality control analyses (Wang et al., 2020).

Neonatal Hypoxia-Ischemia and MSC-EV Treatment

Hypoxic-ischemic (HI) brain injury was induced in 9-day-old animals as previously described (Reinboth et al., 2016; Herz et al., 2018a,b). Briefly, the right common carotid artery was occluded through cauterization (high temperature cauter, 1,200°C, Bovie, USA) under isoflurane anesthesia (1.5–4 Vol%, total duration of surgery: 5–7 min) followed by 1 h hypoxia (10% O_2) in an air-tight oxygen chamber (OxyCycler, Biospherix, USA) after 1 h recovery with their dams. Animals were placed on a warming mat (Harvard Apparatus, USA) to maintain nesting temperature during hypoxia (Reinboth et al., 2016). Sham animals were subjected to anesthesia and neck incision only. Perioperative analgesia was ensured by subcutaneous administration of 0.1 mg/kg Buprenorphine. According to our previous study, MSC-EVs (1×10^5 cell equivalents/g bodyweight) or the corresponding amount of PL-EVs were administered intraperitoneally in 10 µl/g body weight 24, 72, and 120 h post-HI (Doeppner et al., 2015). Vehicle treated control animals received the same volume of 0.9% NaCl at the same time points.

Tissue Preparation, Histology, and Immunohistochemistry

Seven days after HI, mice were deeply anesthetized with chloral-hydrate and transcardially perfused with ice-cold PBS. Brains were removed and snap frozen on dry ice. Tissue injury was assessed and scored on cresyl violet stained 20 µm cryostat sections as previously described (Sheldon et al., 1998; Reinboth et al., 2016). Briefly, 9 regions were scored: the anterior, middle and posterior cortex, CA1, CA2, CA3 and dentate gyrus of the hippocampus and the striatum. Each region was given a rating from 0 to 3 (0—no detectable cell loss, 1—small focal areas of neuronal cell loss, 2—columnar damage in the cortex or moderate to severe cell loss in the other regions, 3—cystic infarction and gliosis). The sum score from different regions was calculated for each animal resulting in a total maximum

score of 24. Tissue atrophy was determined by measurement of intact areas in ipsi- and contra-lateral hemispheres at a distance of 400 μm using Image J software (NIH, USA). Volumes were calculated for the total hemisphere and cortex between +1 and −2.6 mm from bregma, for the striatum between +1 and −0.6 mm from bregma and for the hippocampus between −0.6 and −2.6 mm from bregma. Tissue loss was determined by comparison with contralateral volumes according to the following equation: 1– (volume ratio (left vs. right)) × 100.

For analysis of neuronal, oligodendrocyte and vessel densities cryostat sections taken at the level of +0.2 to +0.3 mm from bregma were stained for neuronal nuclei (NeuN), oligodendrocyte transcription factor 2 (Olig2) and cluster of differentiation 31 (CD31), respectively. Proliferative responses, neural precursor cells, oligodendrocyte maturation, myelination, astrogliosis, and microglia were evaluated by staining of Ki67, doublecortin (DCX), adenomatous polyposis coli, clone CC1 positive (referred as CC1), O4, myelin basic protein (MBP), glial fibrillary acidic protein (GFAP), and ionized calcium-binding adaptor protein-1 (Iba-1), respectively. Micro- and astroglia were further analyzed for co-expression of typical M1/M2 and A1/A2 markers, in the following co-staining: Iba-1/CD206 (M2), GFAP/complement C3 (A1), GFAP/pentraxin 3 (PTX3) (A2). Since CD86 (M1) staining with commonly suggested antibodies (i.e., abcam: ab119857, eBioscience: 14-0862-81) did not work together with Iba-1 staining in native tissue sections, microglia were identified by CD11b expression. To exclude contamination with $CD11b^+$ peripheral leukocytes, CD45 was included in this co-staining. Detailed information on primary and secondary antibodies used, is provided in **Supplementary Table 1**. Immunohistochemistry was performed according to our previous studies (Drommelschmidt et al., 2016; Reinboth et al., 2016; Serdar et al., 2016; Herz et al., 2018b) with minor modifications. Briefly, tissue sections were thawed at 37°C for 15 min followed by fixation in 4% paraformaldehyde (PFA) for 5 min [NeuN, Olig2, CD31, Ki67, CC1, MBP, O4, GFAP (host: mouse) C3] or ice cold aceton/methanol [GFAP (host: rat), PTX3, CD45, CD11b, CD86, DCX] for 5 min. For Iba-1 staining, sections were incubated with 4% PFA overnight followed by antigen retrieval in sodium citrate buffer at 100°C for 20 min followed by incubation with 5% normal goat serum (NGS), 0.2% Tween 20 in phosphate buffered saline (PBS) for 30 min at room temperature. For CD45/CD11b/CD86 co-staining, tissue sections were incubated with 2% NGS, 1% bovine serum albumin (BSA) in 0.2% Tween in PBS for 30 min followed by anti-CD45 antibody incubation overnight at 4°C. For the other staining, unspecific antibody binding was blocked by incubation with 1% BSA, 0.3% cold fish skin gelatin (Sigma Aldrich, Germany), 0.2% Tween in PBS for 1 h at room temperature followed by primary antibody incubation overnight at 4°C. Antibody binding was visualized by incubation with appropriate anti-rat/mouse/rabbit/goat Alexa Flour 488, Alexa Flour 555 or Alexa Flour 647 conjugated secondary antibodies (all:1:500, Thermo Scientific, Germany) for 2 h at room temperature. For CD45/CD11b/CD86 co-staining, secondary antibody incubation (for CD45) was combined with fluorescein isothiocyanate (FITC)-conjugated anti-mouse CD11b and phycoerythrin (PE)-conjugated anti-mouse CD86 for 3 h. Nuclei were counterstained with 4′,6-Diamidin-2-phenylindol (DAPI, 100 ng/ml; Molecular Probes, USA).

Confocal imaging with the perfect focus system module (A1plus, Eclipse Ti, with NIS Elements AR software, Nikon, Germany) was performed to generate large scale images (stitching) of the complete striatum of NeuN-, Olig2-, CD31-, Ki67-, GFAP-, and Iba-1-stained tissue sections. Using the 20x objective z-stacks of 12 μm thickness (3 μm focal plane distance) were acquired in 7 × 6 overlapping regions (15% overlap). Images were converted into maximal intensity projections for automated software-based quantification using the NIS Elements AR software. Analysis was performed in entire striatum and the sub-ventricular zone (SVZ), which were demarcated on the basis of nuclei staining (DAPI) prior to measurement. Unbiased software based object detection was used to determine the number of $NeuN^+$, $Olig2^+$, $Ki67^+$ cells, and $CD31^+$ vessels. For assessment of oligodendrocyte maturation 2 defined non-overlapping regions of interest (ROIs) in the external capsule (each 135370 μm^2) and 3 ROIs in the striatum (each 2,15,000 μm^2) were analyzed to determine the number of Olig2/CC1, Olig2/O4 double, and Olig2 single positive cells. Myelination was quantified in the aforementioned ROIs by measurement of MBP-positive areas. Single object counting was not possible for Iba-1 and GFAP staining due to intensive local accumulation of microglia and glial scar formation by astrocytes in severely injured regions and animals (**Figure 4**). Therefore, positively stained areas and mean fluorescence intensities were quantified as a measure of cell density and activation, respectively (Pekny and Nilsson, 2005; Kozlowski and Weimer, 2012). To determine the expression level of typical A1/A2 markers, GFAP-positively-stained areas were automatically identified with the binary tool of the NIS Elements AR software followed by measurement of mean fluorescence intensities of C3 and PTX3 immunostaining on $GFAP^+$ areas. Using the same approach, CD86 immunostaining was quantified on CD11b positive and CD45 negative/low areas to exclude confounding effects by peripheral immune cells. While CD86 immunostaining was predominantly found in regions of dense microglia accumulation/severe tissue injury, not allowing single cell analysis, CD206 was expressed on distinct cells mainly at the border of injured areas (**Figure 4B**). For quantification, CD206/Iba-1 double positive cells were counted manually. For quantification of A1/A2 and M1/M2 marker expression, 4 non-overlapping ROIs (each 390.600 μm^2) were analyzed for each animal.

mRNA Expression Analysis

For mRNA expression analyses in ipsi- and contralateral tissue parts, one 160 μm thick tissue section/animal were collected at the striatal level (0.5 mm to 0 mm from bregma). Total RNA was isolated with the RNeasy Micro Kit (Qiagen Germany) according to the manufactures recommendations. First strand complementary DNA was synthesized using 0.6 μg of total RNA and TaqMan reverse transcription reagents (Applied Biosystems/Thermo Fisher Scientific). Polymerase chain reaction (PCR) was performed in duplicates in 96 well-optical reaction plates for 40 cycles with each cycle at 94°C for 15 s and 60°C for 1 min using the StepOnePlus

Real Time PCR system (Applied Biosystems/Thermo Fisher Scientific). PCR products were quantified using assay on demand primers and fluorogenic reporter oligonucleotide probes (Applied Biosystems/Thermo Fisher Scientific, **Supplementary Table 2**). CT values were normalized for the housekeeping gene beta-2-microglobulin [ΔCT = CT (target gene)-CT (beta-2-microglobulin)] and related to the mean of either sham-operated (**Supplementary Figure 1**) or vehicle-treated animals (**Figures 4**, **5**) using the $\Delta\Delta$CT formula [$\Delta\Delta$CT = ΔCT (sham/vehicle)-ΔCT (MSC-EV)]. Fold change values were calculated.

Statistical Analysis

All results are expressed as box plots with individual data points including median values, the 25% and the 75% percentile. For statistical analysis, the GraphPad Prism 6.0 software package (GraphPad Software) was used. Data were tested for Gaussian distribution and analyzed either by ordinal 1-way ANOVA or by Kruskal-Wallis (non-parametric) with *post-hoc* Sidak's or Dunn's multiple comparison tests, respectively. When 2 groups were compared, unpaired, two-tailed Student *t*-test or Mann Whitney test (non-parametric) were applied. In all analyses, $p < 0.05$ was considered statistically significant. Exploratory pilot data (**Supplementary Figure 1**) are presented as scatter plots (immunohistochemistry) or box plots (mRNA expression). *P*-values derived from unpaired, two-tailed Student *t*-test (immunohistochemistry) or one sample *t*-test (mRNA expression) are depicted in the graphs.

RESULTS

MSC-EVs Reduce HI-Induced Subacute Striatal Tissue Injury

To evaluate the impact of MSC-EVs on HI-induced brain injury we analyzed histopathological changes (**Figures 1A,B**) and brain atrophy (**Figures 1A,C**) in cresyl violet stained tissue sections (**Figure 1A**) 1 week after HI. In addition to vehicle control (Veh, 0.9% NaCl), we included EVs isolated from human platelet lysate (PL-EV), because our human MSCs were cultured in medium supplemented with platelet lysate, a rich source of EVs (Hemeda et al., 2014). While total neuropathological changes and atrophy were not modulated by MSC-EVs and PL-EVs, MSC-EVs but not PL-EVs significantly decreased pathological changes and tissue atrophy in the striatum (**Figures 1B,C**).

MSC-EVs Increase Neuronal and Endothelial Cell Densities

Neuropathological assessment and volumetric measurements in cresyl-violet stained sections provide a rough estimate of global HI-induced brain injury. However, cellular responses differ, e.g., while HI induces a significant reduction in neuronal and vessel densities; the number of oligodendrocytes increases (**Supplementary Figure 1A**; Reinboth et al., 2016). To get deeper insight, which cell types have been protected by MSC-EVs, we quantified neuronal (**Figure 2A**), vessel (**Figure 2B**), and oligodendrocyte (**Figure 2C**) densities in the striatum. Since potential confounding effects by PL-EVs in MSC-EV preparations could be excluded (**Figure 1**), we focused on the comparison between MSC-EV- and vehicle-treated animals. MSC-EVs lead to a significant increase in neuronal (**Figure 2A**) and vessel density (**Figure 2B**), while the amount of oligodendrocytes was not modulated (**Figure 2C**).

MSC-EVs Enhance Cell Proliferation in the Neurogenic Sub-ventricular Zone (SVZ)

According to the selective protection of the striatum, juxtaposed to the neurogenic niche of the SVZ, we next investigated neuroregenerative responses, differentiating between the striatum and the SVZ. Quantification of cellular proliferation via immunohistochemistry for the pan proliferation marker Ki67 demonstrated that HI induces an endogenous reparative response with an increased amount of proliferating cells in the striatum but not in the neurogenic SVZ (**Supplementary Figure 1B**). However, MSC-EV treatment lead to a significant increase of proliferating cells in the SVZ (**Figures 3A,B**). To identify proliferating cells we performed co-staining with the pan endothelial marker CD31 (**Figure 3C**) and the pan oligodendrocyte marker Olig2 (**Figure 3D** and **Supplementary Figure 1B**). To correct for the differences in overall Ki67$^+$ cell density (**Figures 3A,B** and **Supplementary Figure 1B**), we quantified the percentage of CD31$^+$ and Olig2$^+$ cells of Ki67$^+$ cells in the respective regions. Though total proliferating cells in striatum of HI-injured animals were increased compared to sham-animals, the percentage of CD31$^+$ cells of all proliferating cells was reduced, coinciding with the observed decreased vessel density (**Supplementary Figure 1A**). Interestingly, increased vessel densities in the striatum of MSC-EV-treated animals (**Figure 2B**) were associated with a significantly increased frequency of proliferating CD31$^+$ cells (**Figure 3C**). The proportion of oligodendrocytes in the total population of proliferating cells was not modulated, neither by HI nor by MSC-EV treatment (**Figure 3D** and **Supplementary Figure 1B**). To determine the contribution of neural precursor cell proliferation to the overall increase in cell proliferation in the striatum and the SVZ, we performed co-labeling with the neural precursor cell marker doublecortin (DCX). However, none of the DCX positive cells was labeled with Ki67. Furthermore, except of a slight increase of DCX$^+$ cells in the SVZ following HI (**Supplementary Figure 1B**), the amount of DCX$^+$ cells was not significantly modulated by MSC-EV-treatment (**Figure 3E**).

MSC-EVs Decrease Astro- and Microgliosis and Modulate Inflammatory Cytokine and Neural Growth Factor Expression

In addition to regenerative capacities, MSC-EVs have been suggested to reduce neuroinflammatory responses in different models of adult and perinatal brain injury (Drommelschmidt et al., 2016; Sisa et al., 2019; Wang et al., 2020; Xin et al., 2020). A major hallmark of HI-induced neuroinflammation is the activation of astrocytes and microglia, associated

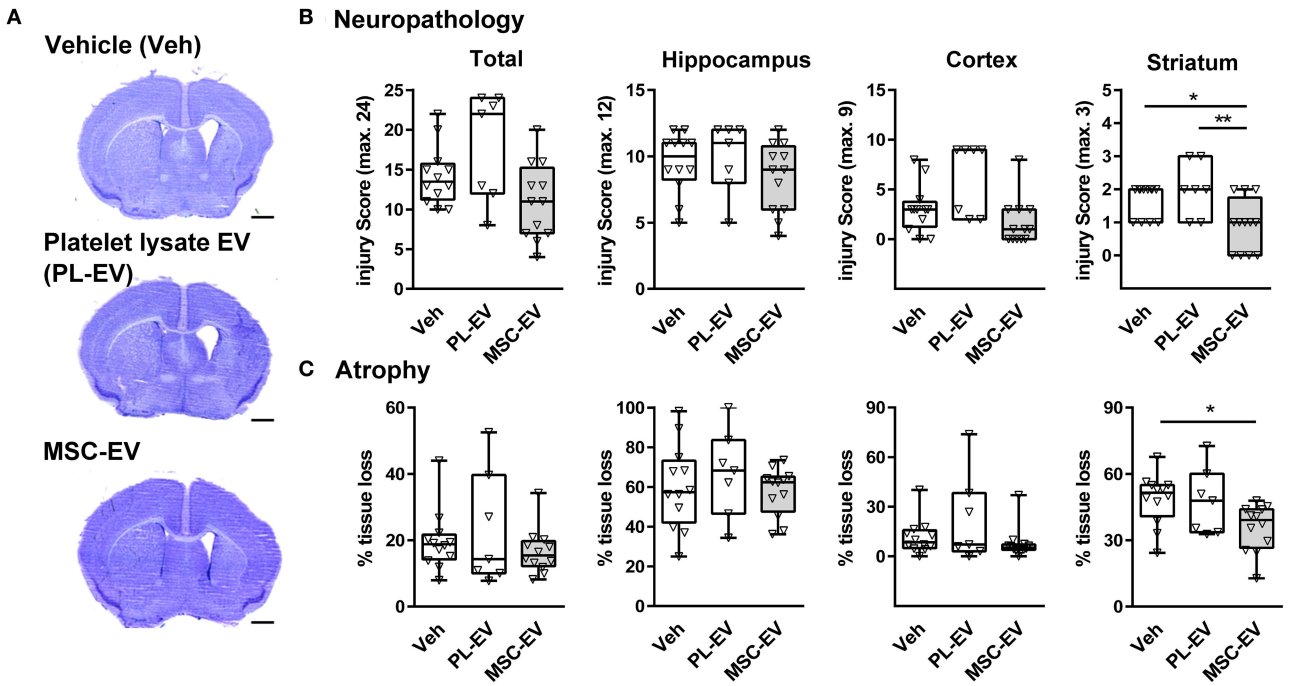


FIGURE 1 | MSC-EVs reduce HI-induced striatal tissue injury. Histological brain injury was determined on cresyl violet stained 20 μm cryostat sections 7 days after HI, performed in 9-day-old C57BL/6 mice. Vehicle (0.9% NaCl, Veh), platelet-derived EVs (PL-EV), and MSC-EVs were administered i.p. 24, 72, and 120 h after HI. **(A)** Representative images of injured hemispheres for each experimental group are shown (scale bar: 1 mm). **(B)** Injury scores were assessed in different brain regions (cortex, hippocampus, and striatum) resulting in a sum score (total) quantified for each animal. **(C)** Brain atrophy was analyzed by measurement of intact areas on tissue sections at a distance of 400 μm between + 1 mm and – 2.6 mm from bregma. Volumes were calculated for total hemispheres and the indicated brain regions. Tissue loss was expressed as the percentage of volume reduction compared to intact contralateral volumes. $^{*}p < 0.05$, $^{**}p < 0.01$, $n = 12$ (Veh), $n = 7$ (PL-EV), $n = 12$ (MSC-EV).

with modulation of their phenotype and alterations in the release of major effector molecules, i.e., cytokines and growth factors (**Supplementary Figures 1C–I**). Analysis of astroglia and microglia activation by immunohistochemistry for GFAP and Iba-1, respectively, demonstrated that HI induces an increase in micro- and astroglia densities accompanied by increased expression of Iba-1 and GFAP, as a measure of cellular activation (Pekny and Nilsson, 2005; Kozlowski and Weimer, 2012) (**Supplementary Figures 1C,F**). MSC-EV treatment significantly reduced the GFAP^{+} and Iba-1^{+} area and Iba-1 expression intensity (**Figure 4A**).

Microglia and astrocytes can acquire different activation states and exert many functions, contributing to both, brain damage and repair mechanisms (Ransohoff and Perry, 2009; Sofroniew, 2015; Liddelow and Barres, 2017). Being aware about the difficulty of terminology to describe the different activation states (Murray et al., 2014; Liddelow and Barres, 2017), we refer to the commonly used nomenclature of M1/M2 and A1/A2. M1/A1 cells are supposed to mediate pro-inflammatory/neurotoxic effects, while M2/A2 cells are supposed to reveal an anti-inflammatory and pro-regenerative phenotype (Ransohoff and Perry, 2009; Sofroniew, 2015; Liddelow and Barres, 2017). Immunohistochemistry analyses revealed that neonatal HI leads to an upregulation of the M1-cell surface marker CD86 on microglia cells, while no differences were observed for the amount CD206^{+} microglia compared to sham-operated animals (**Supplementary Figure 1D**). MSC-EV treatment did not modulate expression of both markers (**Figure 4B**). To quantify a broader set of typical M1/M2 molecules, we performed mRNA expression analyses in brain tissues obtained from the striatal level. These analyses demonstrated a strong upregulation of the pro-inflammatory cytokines tumor necrosis factor α (TNFα) and interleukin 1β (IL-1β) in HI-injured animals compared to sham controls (**Supplementary Figure 1E**). Of note, we also observed an upregulation of typical M2 markers, i.e., chitinase-like 3 protein (YM-1) and arginase-1 (Arg1) accompanied by reduced expression of typical M1 markers, i.e., inducible nitric oxide synthase (iNos) and cyclooxygenase 2 (Cox2) (**Supplementary Figure 1E**). Interestingly, HI-induced increase of TNFα expression and decreased iNos and Cox2 expression were reversed by MSC-EV therapy (**Figure 4C**). Furthermore, MSC-EV treatment lead to a significant elevation of the pro-inflammatory cytokine IL-18 and a further increase of the M2 marker YM-1 and the anti-inflammatory cytokine transforming growth factor β (TGFβ) (**Figures 4C,D**).

To characterize astrocytes more specifically, expression of the A1 protein complement C3 (C3) and the A2 protein pentraxin 3 (PTX3) were analyzed via immunohistochemistry.

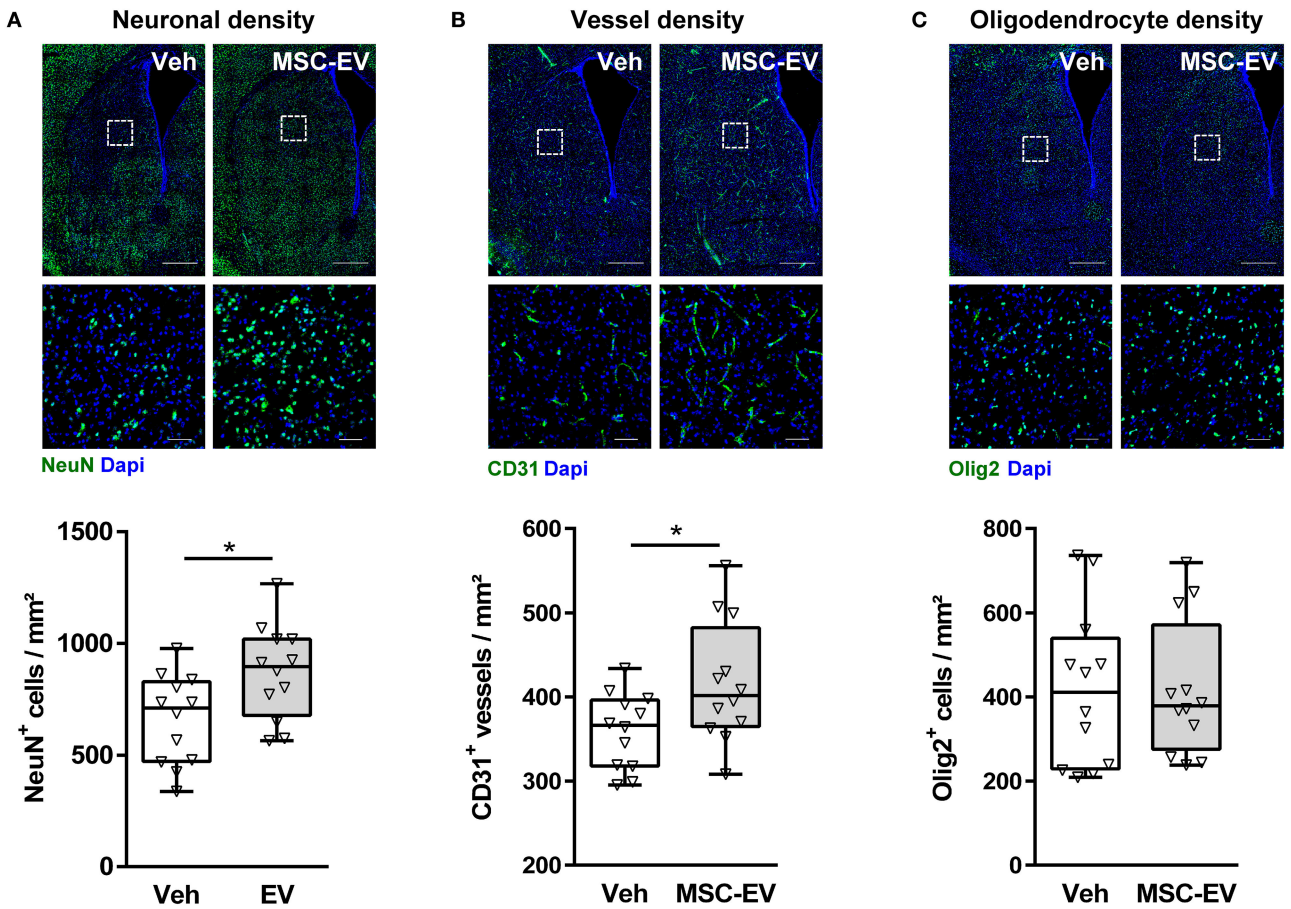


FIGURE 2 | MSC-EVs increase neuronal and vessel densities 1 week after HI. Neuronal **(A)**, vessel **(B)**, and oligodendrocyte **(C)** densities were analyzed via immunohistochemistry for NeuN, CD31, and Olig2, respectively. Analysis was carried out in stitched large scale confocal images of the striatum obtained from brain sections of 16-day-old C57BL/6 mice that were exposed to HI on postnatal day 9. Vehicle (0.9% NaCl, Veh) and MSC-EVs were administered i.p. 24, 72, and 120 h after HI. White squares in large scale representative images (scale bar: 500 μm) indicate the location of high resolution images (scale bar: 50 μm) shown below. Cellular densities were quantified by unbiased automated software-based object detection. $^*p < 0.05$, $n = 12$/group.

Neonatal HI lead to a strong but also moderate upregulation of C3 and PTX3, respectively (**Supplementary Figure 1G**). HI-induced upregulation of astrocytic C3 expression was significantly reduced in MSC-EV-treated animals, while PTX3 expression was not modulated (**Figure 4F**). To analyze further typical A1/A2 markers and prominent effector molecules of astrocytes (i.e., regenerative growth factors), mRNA expression analyses were performed. In line with results obtained from immunohistochemistry, both C3 and PTX3 mRNA expression were strongly upregulated, while the other two selected markers Serping 1 (A1) and S100 Calcium Binding Protein A10 [S100A10, (A2)] were not modulated by HI (**Supplementary Figure 1H**). Confirming results of astrocyte-specific protein expression analyses (**Figure 4F**), HI-induced increase in C3 expression was reversed by MSC-EV therapy and PTX3 expression was not altered (**Figure 4G**). Furthermore, the expression of the A2 marker S110A10 was significantly upregulated in MSC-EV-treated animals. As expected, neonatal HI lead to a significant reduction of important growth factors like brain derived growth factor (BDNF), vascular endothelial growth factor (VEGF) and epidermal growth factor (EGF) (**Supplementary Figure 1I**). Importantly, MSC-EV therapy significantly enhanced mRNA expression of these molecules including insulin like growth factor (IGF-1) (**Figure 4H**).

MSC-EVs Promote Oligodendrocyte Differentiation and Myelination

Disruption of developmental processes by HI plays an important role in neonatal brain injury. A major contributor to neurodevelopmental outcome is myelination. Besides oligodendrocyte proliferation, oligodendrocyte maturation is essential for brain development and function. Therefore, we determined the number of immature $O4^+$ (**Figure 5A** and **Supplementary Figure 1J**) and mature $CC1^+$ (**Figure 5B** and **Supplementary Figure 1K**) oligodendrocytes in the striatum and the adjacent white matter in the external capsule. Myelination was evaluated via immunohistochemistry for MBP (**Figure 5C** and **Supplementary Figure 1L**). In line with our previous

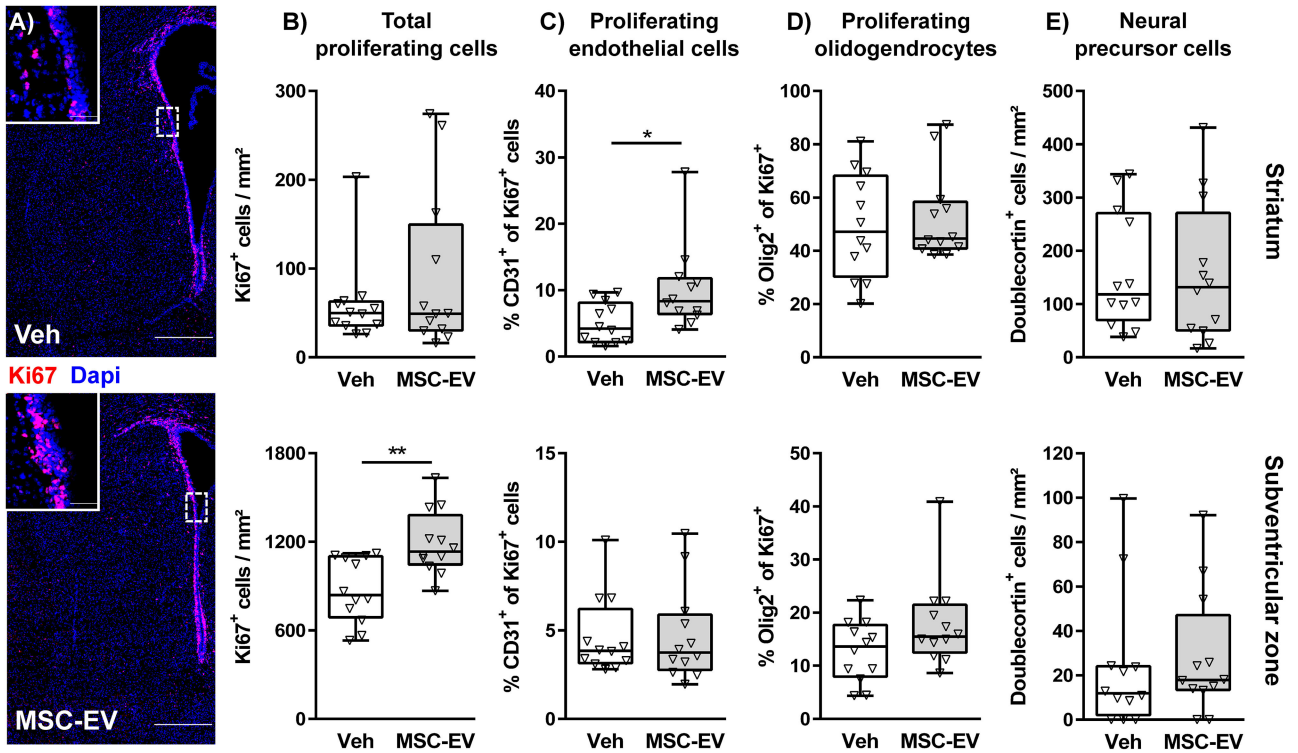


FIGURE 3 | MSC-EVs increase regenerative proliferation. Cell proliferation was analyzed 7 days after HI in C57BL/6 mice exposed to HI on postnatal day 9. Vehicle (0.9% NaCl, Veh) and MSC-EVs were i.p. injected 24, 72, and 120 h after HI. The amount of proliferating cells was determined via immunohistochemistry for the proliferation marker Ki67 in the striatum and the subventricular zone **(A,B)**. The percentage of proliferating endothelial cells **(C)** and oligodendrocytes **(D)** from all proliferating cells was quantified in tissue sections co-labeled for the endothelial cell marker CD31 and the oligodendrocyte marker Olig2, respectively. No co-labeling could be detected in co-staining of the neural precursor cell marker doublecortin and Ki67. Therefore, the absolute amount of DCX positive cells was quantified **(E)**. $^{*}p < 0.05$, $^{**}p < 0.01$, $n = 12$/group, scale bar in **(A)**: 500 μm (inset: 50 μm).

indications for an impaired oligodendrocyte maturation and disturbed myelination following neonatal HI (Reinboth et al., 2016), we detected a significantly reduced proportion of mature oligodendrocytes and reduced myelination in the white matter coinciding with a significant increase in immature oligodendrocytes (**Supplementary Figures 1J,L**). Of note, MSC-EVs significantly reduced the amount of immature $O4^+$ oligodendrocytes in the white matter (**Figure 5A**), which was accompanied by a significant increase of differentiated $CC1^+$ cells (**Figure 5B**) and enhanced MBP expression (**Figure 5C**). Results obtained from immunohistochemistry analysis were confirmed by mRNA expression analysis for CC1, MBP and 2′,3′-cyclic-nucleotide 3′-phosphodiesterase (CNPase) in brain tissues derived from the striatal level, revealing a strong reduction by neonatal HI compared to uninjured sham-operated animals for all investigated analytes (**Supplementary Figure 1L**). Importantly, these HI-induced deficits were significantly improved after MSC-EV therapy (**Figure 5D**).

DISCUSSION

The neuroprotective potential of MSC-EVs has been shown in different models of adult and neonatal brain injury (Doeppner et al., 2015; Drommelschmidt et al., 2016; Sisa et al., 2019; Wang et al., 2020). However, for neonatal HI, only limited data are available with partially discrepant study results (e.g., microglia activation; Ophelders et al., 2016; Sisa et al., 2019; Xin et al., 2020). Furthermore, common to the majority of studies was a major focus on the early phase after injury. In the present study, we investigated the impact of MSC-EVs in the subacute disease phase, when inflammatory processes, delayed cell death but also endogenous regenerative processes are overlapping (Ferriero, 2004). We demonstrate that MSC-EVs protect from HI-induced striatal tissue loss, associated with an increased neuronal and vessel density and a significant increase of proliferating cells in the neurogenic sub-ventricular zone juxtaposed to the striatum. Furthermore, MSC-EV treatment reduced astroglia and microglia activation and increased endothelial cell proliferation and oligodendrocyte maturation.

Regional differences in vulnerability to HI-induced brain injury and therapeutic interventions are well-known (Northington et al., 2011; Reinboth et al., 2016; Sisa et al., 2019). With regard to therapeutic effects of MSC-EVs, Sisa et al. observed significant protection from apoptosis and volume loss in the cortex, external capsule and thalamus (Sisa et al., 2019). We also observed regional differences, with major protection from brain injury in the striatum, but not

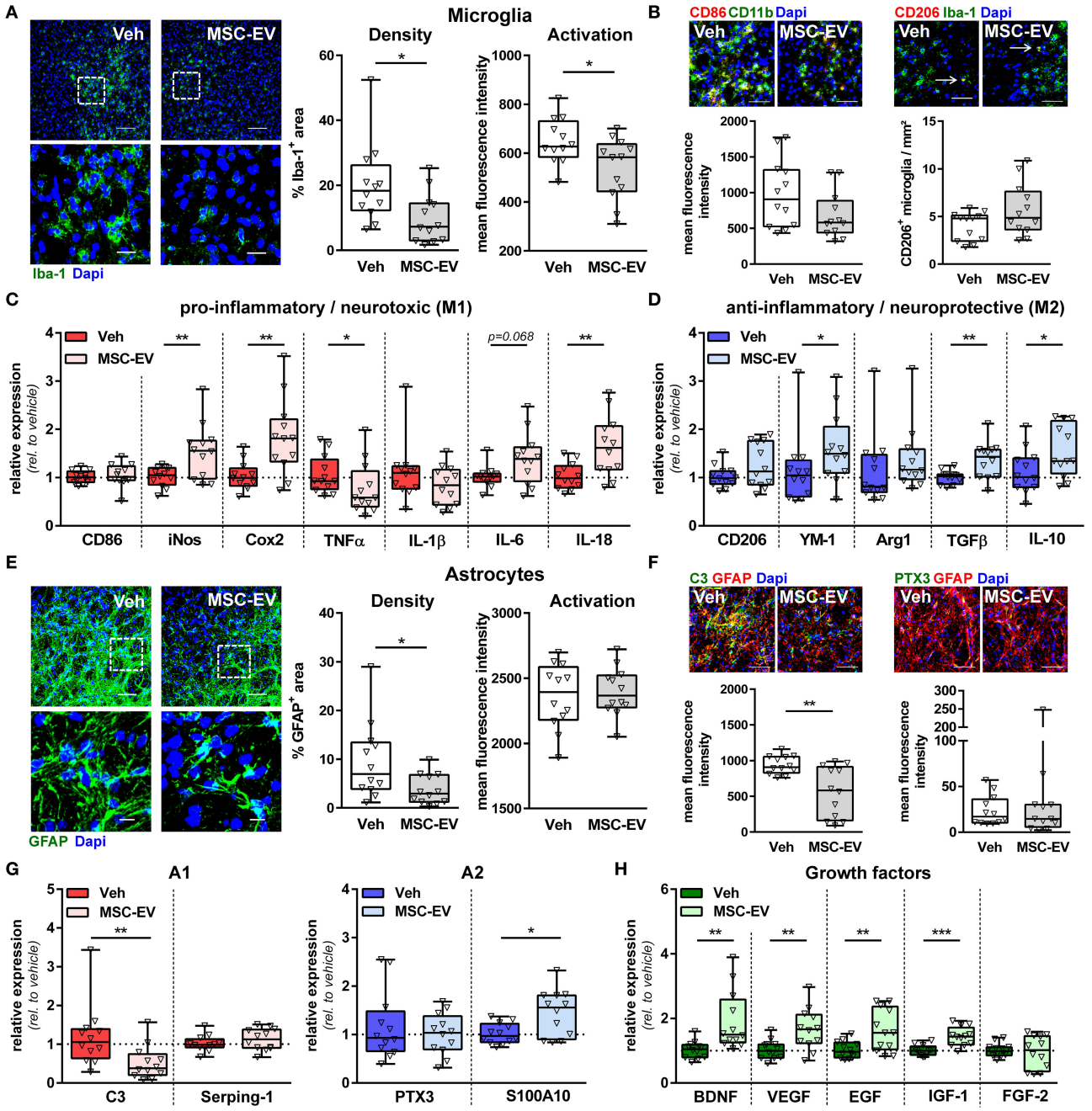


FIGURE 4 | MSC-EVs reduce astro- and microglia activation and improve oligodendrocyte maturation. Nine-day-old C57BL/6 mice were exposed to HI followed by i.p. injection of MSC-EVs or vehicle (0.9% NaCl, Veh) 24, 72, and 120 h post-HI. Microglia density and activation was analyzed in stitched large scale confocal images of the striatum, obtained from brain sections stained for the microglia marker Iba-1 **(A)**. Low magnification images (scale bar: 100 μm) reveal maximal intensity projections of 12 μm z-stacks (plane distance 3 μm). To demonstrate morphology, high magnification images (scale bar: 20 μm) were acquired at a single plane in the white square, depicted in low magnification images. Iba-1 immunoreactivity, as a measure of microglia activation, was quantified by measurement of positively stained areas and fluorescence intensities in positively stained areas **(A)**. Expression of typical M1 (CD86) and M2 (CD206) markers was analyzed in CD11b (green)/CD86 (red) and Iba-1 (green)/CD206 (red) staining (**B**, scale bar: 50 μm). CD45-staining (not shown) was included in CD11b/CD86 co-staining to exclude confounding effects by peripheral immune cells, i.e., CD86 expression was only quantified on $CD11b^+$ $CD45^-$ areas. While CD86 was found predominantly in regions of dense microglia accumulation, $CD206^+$ microglia were mainly found at the border region, which could be identified as discrete double positive cells (arrows, **B**). A broad set of pro-inflammatory M1-phenotype-associated **(C)** and anti-inflammatory M2-phenotype-associated **(D)** molecule expression was analyzed via real-time PCR in brain tissues (160 μm thickness) obtained from the striatal level (0.5–0 mm from bregma). Beta-2-microglobulin served as housekeeping gene and fold change values compared to vehicle-treated control animals were calculated. Astrocyte density and activation was analyzed in GFAP-stained brain tissue sections **(E)**. Analyses and acquisition of representative images was performed as described for microglia **(A)**. Expression of typical A1 (C3, green) and A2 (PTX3, green) markers was analyzed in co-staining with GFAP (red, **F**, scale bar: 50 μm). Immunohistochemistry results were confirmed by mRNA expression analysis as described for microglia including further typical A1 (Serping-1) and A2 (S100A10) markers **(G)** and essential neural growth factors **(H)**. $^*p < 0.05$, $^{**}p < 0.01$, $^{***}p < 0.001$, $n = 12$/group.

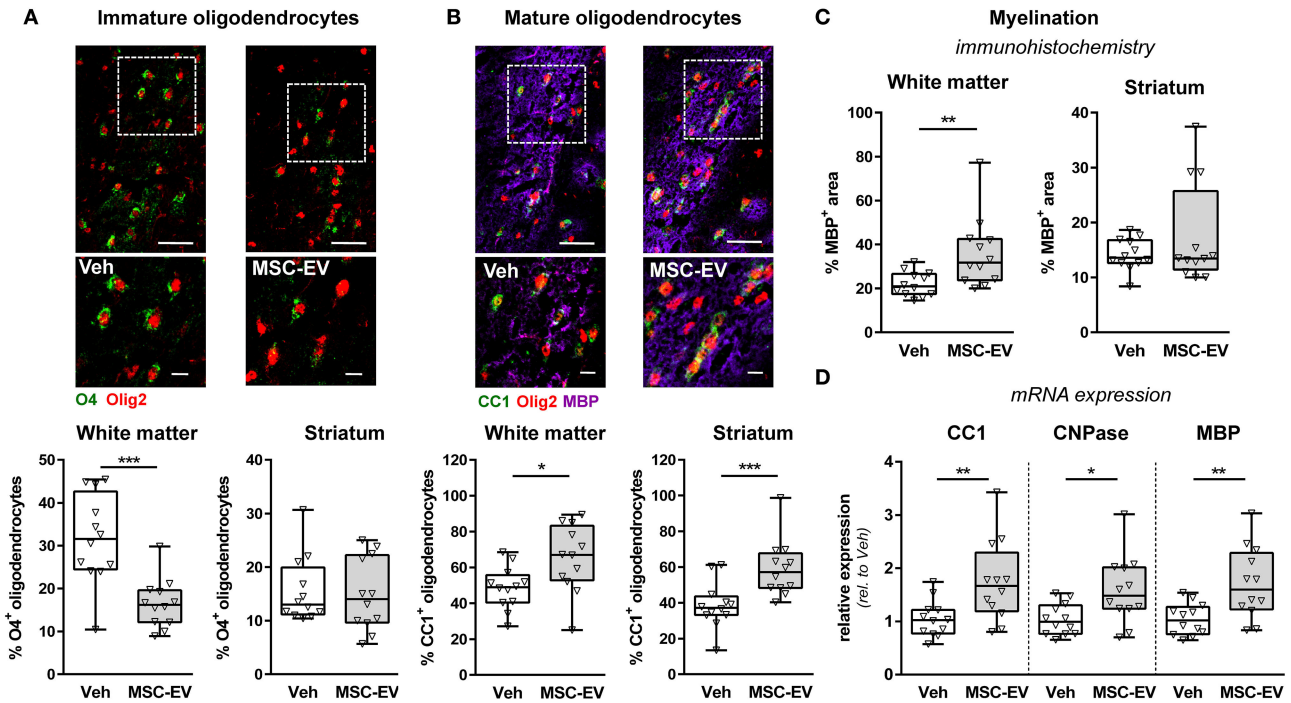


FIGURE 5 | MSC-EVs improve oligodendrocyte maturation and myelination. Oligodendrocyte maturation and myelination was investigated in the white matter (external capsule) and the striatum via immunohistochemistry in co-staining for the pan-oligodendrocyte marker Olig2 (red, **A,B**) and either O4, labeling immature oligodendrocyte precursor cells (green, **A**) or CC1, labeling mature oligodendrocytes (green, **B**). Myelination was assessed by co-staining against MBP (violet, **B,C**). Representative images are obtained from the external capsule. Low magnification images (scale bar: 40 μm) reveal maximal intensity projections of 10 μm z-stacks (plane distance 2 μm). To demonstrate morphology, high magnification images (scale bar: 10 μm) were acquired at a single plane in the white square, depicted in low magnification images. The percentage of double positive cells from total oligodendrocytes was quantified **(A,B)**. Myelination was quantified by measurement of MBP^+ areas **(C)**. Immunohistochemistry analyses were confirmed by mRNA expression analyses of CC1, CNPase and MBP in brain tissues (160 μm thickness) obtained from the striatal level (0.5 mm to 0 mm from bregma). Beta-2-microglobulin served as housekeeping gene and fold change values compared to vehicle-treated control animals were calculated **(D)** $^*p < 0.05$, $^{**}p < 0.01$, $^{***}p < 0.001$, $n = 12$/group.

in the cortex. Discrepancy in protected brain regions might not only be explained by differences in administration route (intranasal vs. intraperitoneal), but also by different time points of intervention and analysis (intervention: 0 vs. 24, 72, and 120 h; analysis: 2 vs. 7 days). Indeed, our previous study provided evidence for a spatial–temporal regulation of pathophysiological processes during the evolution of HI and for different therapeutic time windows in individual brain structures (Reinboth et al., 2016). In the present study, particularly the striatum was protected, which might be explained by the close proximity to the neurogenic sub-ventricular zone, where MSC-EVs promoted regenerative proliferation. Nevertheless, further in depth analysis of other brain structures, e.g., the neurogenic sub-granular zone at the level of the hippocampus may fully uncover the neuro-regenerative potential of MSC-EV therapy. Furthermore, whether protection in the striatum may lead to subsequent protection from thalamic injury and/or of striatal-thalamic projections needs to be analyzed in future studies.

Regenerative processes in the sub-acute disease phase include neurogenesis and angiogenesis. Similarly as in adult ischemic brain injury (Doeppner et al., 2015), we observed an increased proliferative response in neurogenic niches of the brain after MSC-EV-therapy. Increased proliferation in the sub-ventricular zone juxtaposed to the striatum may explain higher neuronal and vessel densities detected in the striatum. However, with our co-labeling strategies for oligodendrocytes, endothelial cells and neural precursor cells we could only assign 15% of total proliferating cells to a specific cell type. The amount of doublecortin positive cells, a major neural precursor cell marker, was not modulated by MSC-EV treatment. These results indicate that increased neuronal cell numbers in the striatum may be rather attributed to increased neuronal survival than to generation of new neurons. Further work investigating a broader set of markers for neuronal precursor cell types is needed to fully elucidate the impact of MSC-EVs on neurogenesis in neonatal HI. Nevertheless, in the present study we also show that MSC-EVs induce striatal angiogenesis, an important hallmark of post-ischemic neuroregeneration and neuronal network formation during brain development (Coelho-Santos and Shih, 2020; Hatakeyama et al., 2020). Thus, increased striatal angiogenesis after MSC-EV treatment might contribute to overall increased tissue recovery.

In addition to angiogenesis, myelination is key to the functional activity of axons, allowing them to connect to neurons and strengthen circuitry throughout nervous system development. Clinical and our preclinical studies revealed a strong association between oligodendrocyte maturation and long-term motor-cognitive neurodevelopment in preterm birth-related brain injury (Counsell et al., 2008; Drommelschmidt et al., 2016; Serdar et al., 2016). In the context of HI at term-equivalent age, we have previously shown that HI induces oligodendrocyte proliferation, which however fails to improve myelination (Reinboth et al., 2016). This is confirmed by the present results, demonstrating an overall increase of oligodendrocytes, most likely due to enhanced proliferation. However, this endogenous regenerative response is limited, as these newly arising oligodendrocytes do not differentiate into mature oligodendrocytes to promote myelination. Importantly, MSC-EVs significantly improve oligodendrocyte maturation and myelination. Since the amount of total oligodendrocytes was not altered by MSC-EVs, effects on oligodendrocyte cell death and/or proliferation seem unlikely. MSC-EVs may rather modulate the maturity level of oligodendrocytes, promoting oligodendrocyte differentiation. This is reflected by a reduction of immature oligodendrocytes and a simultaneous increase of differentiated cells and an increased expression of typical myelin markers (e.g., MBP, CNPase). These data suggest that MSC-EVs may overcome HI-induced disturbance of neurodevelopmental processes, i.e., oligodendrocyte maturation and myelination, which is supported by the study of Sisa et al. demonstrating protective effects by MSC-EVs in the white matter (i.e., external capsule) in the early post-hypoxic disease phase.

In line with Sisa et al. and own previous work in inflammation-induced preterm-related brain injury (Drommelschmidt et al., 2016; Sisa et al., 2019), astro- and microgliosis were reduced following MSC-EV treatment. While the former studies focused on the acute phase after the injurious stimulus, we here demonstrate that also secondary inflammatory processes are modulated by MSC-EVs, thereby probably facilitating an environment for enhanced regeneration and thus improved long-term recovery (Giebel and Hermann, 2019). Nevertheless, Iba-1 and GFAP immunoreactivity provide only limited information about astro- and microglia phenotype and function. Recent work indicates that MSC-EVs modulate the ratio of typical pro-inflammatory/neurotoxic M1 and anti-inflammatory/neuroprotective M2 markers (Xin et al., 2020). Here, we demonstrate that HI-related alterations of typical M1/M2 markers was counter-regulated by MSC-EV therapy. For instance, HI-induced upregulation of the pro-inflammatory cytokine TNFα was significantly reduced after MSC-EV treatment, while expression of the anti-inflammatory cytokine TGFβ and the M2 marker YM-1 was significantly increased. These results suggest that MSC-EVs modulate microglia to promote anti-inflammatory and protective effects. However, in line with previous reports (Hellstrom Erkenstam et al., 2016), this strict M1/M2 classification concept based on single molecule expression might oversimplify the complexity of cellular responses *in vivo*. Indeed, in the present study, we detected a reduction of the typical M1 molecules iNos and Cox2, which were associated with increased neuroinflammatory and degenerative responses, particularly in the acute phase after ischemic brain injury (del Zoppo et al., 2000; Willmot et al., 2005). Nevertheless, our present results are in line with previous work demonstrating a trend to reduced expression of iNos and Cox2 at delayed time points after perinatal brain injury (i.e., 5–7 days after injury; Hellstrom Erkenstam et al., 2016; Chhor et al., 2017). Considering the important function of both enzymes and their products in physiological brain development (Hickey et al., 2007; Angelis et al., 2020), HI-induced reductions of iNos and Cox2 1 week after injury, may lead to a delay of neurodevelopmental processes. This is supported by our observations that tissue-protective effects of an MSC-EV therapy were associated with a significantly increased expression of iNos and Cox2.

Analysis of astrocyte responses revealed similar difficulties for a strict phenotype classification. HI induced a significant increase of both, A1-associated C3 and A2-assoicated PTX3, expression. While MSC-EV treatment significantly reduced C3 expression, PTX3 was not modulated. However, the regenerative capacity of MSC-EVs was demonstrated by an elevated expression of major astrocytic effector molecules, i.e., neural growth factors. Interestingly, increased BDNF expression after MSC-EV therapy coincided with an upregulation of the pro-inflammatory cytokine IL-18. This might be explained by the double-edged function of IL-18, which does not only promote neurodegeneration (Felderhoff-Mueser et al., 2005a,b), but also enhances BDNF production and neuronal survival upon *in vitro* hypoxic-ischemic injury (Zhou et al., 2014). In addition to BDNF, growth factors involved in angiogenesis, i.e., VEGF and EGF were significantly upregulated after MSC-EV therapy. These findings provide a plausible link to the observed increase in vascular density and endothelial proliferation after MSC-EV treatment.

The present study suggests that MSC-EVs modulate micro- and astroglia phenotypes, facilitating an anti-inflammatory and reparative/regenerative tissue environment for protection from HI-induced secondary brain injury and associated neurodevelopmental complications. Nevertheless, data need to be interpreted with caution, since mRNA expression was analyzed in total tissue lysates, not allowing conclusions about the cellular source of cytokines and growth factors. Furthermore, previous work in adult and neonatal brain injury demonstrated co-expression of different category markers (Vogel et al., 2013; Hellstrom Erkenstam et al., 2016), which cannot be determined in the present study. Another issue, which warrants further investigation, is to distinguish cause and consequence, i.e., to identify direct cellular targets of MSC-EVs in neonatal HI. Considering that TNFα released from activated microglia is one of the strongest A1 inducers (Liddelow et al., 2017), our observations of a simultaneous downregulation of TNFα and C3 indicate that MSC-EVs modulated microglia with a consequent modulation of astrocyte phenotype and function. In contrast, MSC-EVs may directly affect both, micro- and astroglia, involving similar molecular mechanisms, e.g., through miRNAs targeting astrocytes (Xin et al., 2013, 2017) and microglia (Xin et al., 2020). To differentiate between direct in indirect effects of MSC-EVs, appropriate *in vitro* models with

purified cells, but also *in vivo* tracking analyses of systemically administered EVs will be indispensable. So far, the majority of studies, addressing this issue, applied EVs intravenously with most frequent accumulation in the liver, lung and spleen (Yi et al., 2020). However, bio-distribution depends on many different factors, including the kind of injury and the cellular source of EVs (Yi et al., 2020). With regard to intraperitoneal injection of MSC-EVs, as applied in the present study, data about bio-distribution are sparse. In a model of pancreatic cancer, it was demonstrated that MSC-EVs accumulated in the pancreas, liver, spleen and lung (Mendt et al., 2018). Though peripheral effects of EVs seem likely, HI-induced modulation of the blood brain barrier may facilitate increased accumulation of systemically administered MSC-EVs in the injured brain. Nevertheless, considering limitations of currently available labeling techniques due to potential modulation of EV function and labeling artifacts (Thery et al., 2018), additional work is needed, to identify direct cellular targets of MSC-EVs.

Taken together, the present results suggest that MSC-EVs increase neuronal survival and/or neurogenesis through modulation of micro- and astroglial cell responses and promotion of neurodevelopmental processes (i.e., myelination). We partially confirmed observations made in other models of brain injury, which may help to identify common cellular targets in the CNS (e.g., glial cells, endothelial cells). Nevertheless, comparisons between different studies are limited not only due to different pathologies and developmental stages, but also due to the well-known EV heterogeneity. Major contributors to MSC-EV heterogeneity are differences in MSC donors, MSC culture conditions and EV preparation (Lener et al., 2015; Borger et al., 2017; Witwer et al., 2019; Wang et al., 2020). In our previous study, we observed different therapeutic activities between MSC-EV preparations, although they were prepared with the same protocol (Wang et al., 2020). Since we administered MSC-EVs prepared from one single donor, our study results need to be confirmed with other EV preparations in future studies. In addition to donor differences, methods of MSC cultivation for EV preparation differ between laboratories, e.g., media supplements (Witwer et al., 2019). We used human platelet lysate (PL) as substitute for fetal calf serum. Since PL is a rich source of EVs (Hemeda et al., 2014), which co-purifies with MSC-EVs, PL-EVs may contribute to or confound therapeutic effects of MSC-EVs. While this control was not included in previous studies, our present results demonstrate that PL-EVs do not mediate therapeutic effects, at least in this specific experimental setting. Therefore, observed protective and supportive effects of MSC-EVs in our study can be attributed to EVs derived from MSCs.

Our study provides important new information to the field, because we have shown that MSC-EV therapy can be applied within a delayed therapeutic window and therefore, in principle, allows combination with the standard clinical care HT. This is particularly important since HT is less effective in improvement of white matter injury compared to MSCs (Herz et al., 2018b). Therefore, MSC-EVs combined with HT may not only overcome risks associated with cell therapy but also limitations of HT, which needs to be proven in future studies.

DATA AVAILABILITY STATEMENT

The original contributions presented in the study are included in the article/**Supplementary Materials**, further inquiries can be directed to the corresponding author/s.

ETHICS STATEMENT

This animal study was reviewed and approved by State Agency for Nature, Environment and Consumer Protection North Rhine-Westphalia.

AUTHOR CONTRIBUTIONS

JH, BG, and IB conceptualized the study and designed the project. NK, CK, and JH performed experiments, analyzed, and interpreted data. YM, VB, UF-M, IB, and BG provided critical comments and suggestions during the drafting of the manuscript. JH wrote the manuscript. All authors contributed to the article and approved the submitted version.

FUNDING

This work was supported by the C. D.-Stiftung, the Karl-Heinz-Frenzen-Stiftung, the Else-Kröner-Fresenius-Stiftung (2018_A113), the LeitmarktAgentur.NRW, the European Union [European Regional Development Fund 2014–2020 and Horizon 2020 (PREMSTEM)], and ERA-NET EuroTransBio. We acknowledge support by the Open Access Publication Fund of the University of Duisburg-Essen.

SUPPLEMENTARY MATERIAL

The Supplementary Material for this article can be found online at: https://www.frontiersin.org/articles/10.3389/fncel.2020.601176/full#supplementary-material

REFERENCES

Ahearne, C. E., Boylan, G. B., and Murray, D. M. (2016). Short and long term prognosis in perinatal asphyxia: an update. *World J. Clin. Pediatr.* 5, 67–74. doi: 10.5409/wjcp.v5.i1.67

Angelis, D., Savani, R., and Chalak, L. (2020). Nitric oxide and the brain. Part 1: Mechanisms of regulation, transport and effects on the developing brain. *Pediatr Res*. doi: 10.1038/s41390-020-1017-0

Azzopardi, D., Strohm, B., Marlow, N., Brocklehurst, P., Deierl, A., Eddama, O., et al. (2014). Effects of hypothermia for perinatal asphyxia on childhood outcomes. *N. Engl. J. Med.* 371, 140–149. doi: 10.1056/NEJMoa1315788

Borger, V., Bremer, M., Ferrer-Tur, R., Gockeln, L., Stambouli, O., Becic, A., et al. (2017). Mesenchymal stem/stromal cell-derived extracellular vesicles and their potential as novel immunomodulatory therapeutic agents. *Int. J. Mol. Sci.* 18:1450. doi: 10.3390/ijms18071450

Chhor, V., Moretti, R., Le Charpentier, T., Sigaut, S., Lebon, S., Schwendimann, L., et al. (2017). Role of microglia in a mouse model of paediatric traumatic brain injury. *Brain Behav. Immun.* 63, 197–209. doi: 10.1016/j.bbi.2016.11.001

Coelho-Santos, V., and Shih, A. Y. (2020). Postnatal development of cerebrovascular structure and the neurogliovascular unit. *Wiley Interdiscip. Rev. Dev. Biol.* 9:e363. doi: 10.1002/wdev.363

Counsell, S. J., Edwards, A. D., Chew, A. T., Anjari, M., Dyet, L. E., Srinivasan, L., et al. (2008). Specific relations between neurodevelopmental abilities and white matter microstructure in children born preterm. *Brain 131(Pt* 12), 3201–3208. doi: 10.1093/brain/awn268

del Zoppo, G., Ginis, I., Hallenbeck, J. M., Iadecola, C., Wang, X., and Feuerstein, G. Z. (2000). Inflammation and stroke: putative role for cytokines, adhesion molecules and iNOS in brain response to ischemia. *Brain Pathol.* 10, 95–112. doi: 10.1111/j.1750-3639.2000.tb00247.x

Doeppner, T. R., Herz, J., Gorgens, A., Schlechter, J., Ludwig, A. K., Radtke, S., et al. (2015). Extracellular vesicles improve post-stroke neuroregeneration and prevent postischemic immunosuppression. *Stem Cells Transl. Med.* 4, 1131–1143. doi: 10.5966/sctm.2015-0078

Drommelschmidt, K., Serdar, M., Bendix, I., Herz, J., Bertling, F., Prager, S., et al. (2016). Mesenchymal stem cell-derived extracellular vesicles ameliorate inflammation-induced preterm brain injury. *Brain Behav. Immun.*60, 220–232. doi: 10.1016/j.bbi.2016.11.011

Felderhoff-Mueser, U., Schmidt, O. I., Oberholzer, A., Buhrer, C., and Stahel, P. F. (2005a). IL-18: a key player in neuroinflammation and neurodegeneration? *Trends Neurosci.* 28, 487–493. doi: 10.1016/j.tins.2005.06.008

Felderhoff-Mueser, U., Sifringer, M., Polley, O., Dzietko, M., Leineweber, B., Mahler, L., et al. (2005b). Caspase-1-processed interleukins in hyperoxia-induced cell death in the developing brain. *Ann. Neurol.* 57, 50–59. doi: 10.1002/ana.20322

Ferriero, D. M. (2004). Neonatal brain injury. *N. Engl. J. Med.* 351, 1985–1995. doi: 10.1056/NEJMra041996

Giebel, B., and Hermann, D. M. (2019). Identification of the right cell sources for the production of therapeutically active extracellular vesicles in ischemic stroke. *Ann. Transl. Med.* 7:188. doi: 10.21037/atm.2019.03.49

Gussenhoven, R., Klein, L., Ophelders, D., Habets, D. H. J., Giebel, B., Kramer, B. W., et al. (2019). Annexin A1 as neuroprotective determinant for blood-brain barrier integrity in neonatal hypoxic-ischemic encephalopathy. *J. Clin. Med.* 8:137. doi: 10.3390/jcm8020137

Hatakeyama, M., Ninomiya, I., and Kanazawa, M. (2020). Angiogenesis and neuronal remodeling after ischemic stroke. *Neural Regen. Res.* 15, 16–19. doi: 10.4103/1673-5374.264442

Hellstrom Erkenstam, N., Smith, P. L., Fleiss, B., Nair, S., Svedin, P., Wang, W., et al. (2016). Temporal characterization of microglia/macrophage phenotypes in a mouse model of neonatal hypoxic-ischemic brain injury. *Front. Cell. Neurosci.* 10:286. doi: 10.3389/fncel.2016.00286

Hemeda, H., Giebel, B., and Wagner, W. (2014). Evaluation of human platelet lysate versus fetal bovine serum for culture of mesenchymal stromal cells. *Cytotherapy* 16, 170–180. doi: 10.1016/j.jcyt.2013.11.004

Herz, J., Koster, C., Crasmoller, M., Abberger, H., Hansen, W., Felderhoff-Muser, U., et al. (2018a). Peripheral T cell depletion by FTY720 exacerbates hypoxic-ischemic brain injury in neonatal mice. *Front. Immunol.* 9:1696. doi: 10.3389/fimmu.2018.01696

Herz, J., Koster, C., Reinboth, B. S., Dzietko, M., Hansen, W., Sabir, H., et al. (2018b). Interaction between hypothermia and delayed mesenchymal stem cell therapy in neonatal hypoxic-ischemic brain injury. *Brain Behav. Immun.* 70, 118–130. doi: 10.1016/j.bbi.2018.02.006

Hickey, R. W., Adelson, P. D., Johnnides, M. J., Davis, D. S., Yu, Z., Rose, M. E., et al. (2007). Cyclooxygenase-2 activity following traumatic brain injury in the developing rat. *Pediatr. Res.* 62, 271–276. doi: 10.1203/PDR.0b013e3180db2902

Jellema, R. K., Wolfs, T. G., Lima Passos, V., Zwanenburg, A., Ophelders, D. R., Kuypers, E., et al. (2013). Mesenchymal stem cells induce T-cell tolerance and protect the preterm brain after global hypoxia-ischemia. *PLoS ONE* 8:e73031. doi: 10.1371/journal.pone.0073031

Kordelas, L., Rebmann, V., Ludwig, A. K., Radtke, S., Ruesing, J., Doeppner, T. R., et al. (2014). MSC-derived exosomes: a novel tool to treat therapy-refractory graft-versus-host disease. *Leukemia* 28, 970–973. doi: 10.1038/leu.2014.41

Kozlowski, C., and Weimer, R. M. (2012). An automated method to quantify microglia morphology and application to monitor activation state longitudinally *in vivo*. *PLoS ONE* 7:e31814. doi: 10.1371/journal.pone.0031814

Lener, T., Gimona, M., Aigner, L., Borger, V., Buzas, E., Camussi, G., et al. (2015). Applying extracellular vesicles based therapeutics in clinical trials - an ISEV position paper. *J. Extracell Vesicles* 4:30087. doi: 10.3402/jev.v4.30087

Liddelow, S. A., and Barres, B. A. (2017). Reactive astrocytes: production, function, and therapeutic potential. *Immunity* 46, 957–967. doi: 10.1016/j.immuni.2017.06.006

Liddelow, S. A., Guttenplan, K. A., Clarke, L. E., Bennett, F. C., Bohlen, C. J., Schirmer, L., et al. (2017). Neurotoxic reactive astrocytes are induced by activated microglia. *Nature* 541, 481–487. doi: 10.1038/nature21029

Ludwig, A. K., De Miroschedji, K., Doeppner, T. R., Borger, V., Ruesing, J., Rebmann, V., et al. (2018). Precipitation with polyethylene glycol followed by washing and pelleting by ultracentrifugation enriches extracellular vesicles from tissue culture supernatants in small and large scales. *J. Extracell Vesicles* 7:1528109. doi: 10.1080/20013078.2018.1528109

Ludwig, A. K., and Giebel, B. (2012). Exosomes: small vesicles participating in intercellular communication. *Int. J. Biochem. Cell Biol.* 44, 11–15. doi: 10.1016/j.biocel.2011.10.005

Mendt, M., Kamerkar, S., Sugimoto, H., McAndrews, K. M., Wu, C. C., Gagea, M., et al. (2018). Generation and testing of clinical-grade exosomes for pancreatic cancer. *JCI Insight* 3:e99263. doi: 10.1172/jci.insight.99263

Murray, P. J., Allen, J. E., Biswas, S. K., Fisher, E. A., Gilroy, D. W., Goerdt, S., et al. (2014). Macrophage activation and polarization: nomenclature and experimental guidelines. *Immunity* 41, 14–20. doi: 10.1016/j.immuni.2014.06.008

Northington, F. J., Chavez-Valdez, R., and Martin, L. J. (2011). Neuronal cell death in neonatal hypoxia-ischemia. *Ann. Neurol.* 69, 743–758. doi: 10.1002/ana.22419

Ophelders, D. R., Wolfs, T. G., Jellema, R. K., Zwanenburg, A., Andriessen, P., Delhaas, T., et al. (2016). Mesenchymal stromal cell-derived extracellular vesicles protect the fetal brain after hypoxia-ischemia. *Stem Cells Transl. Med.* 5, 754–763. doi: 10.5966/sctm.2015-0197

Pekny, M., and Nilsson, M. (2005). Astrocyte activation and reactive gliosis. *Glia* 50, 427–434. doi: 10.1002/glia.20207

Ransohoff, R. M., and Perry, V. H. (2009). Microglial physiology: unique stimuli, specialized responses. *Annu. Rev. Immunol.* 27, 119–145. doi: 10.1146/annurev.immunol.021908.132528

Reinboth, B. S., Koster, C., Abberger, H., Prager, S., Bendix, I., Felderhoff-Muser, U., et al. (2016). Endogenous hypothermic response to hypoxia reduces brain injury: implications for modeling hypoxic-ischemic encephalopathy and therapeutic hypothermia in neonatal mice. *Exp. Neurol.* 283(Pt A), 264–275. doi: 10.1016/j.expneurol.2016.06.024

Serdar, M., Herz, J., Kempe, K., Lumpe, K., Reinboth, B. S., Sizonenko, S. V., et al. (2016). Fingolimod protects against neonatal white matter damage and long-term cognitive deficits caused by hyperoxia. *Brain Behav. Immun.* 52, 106–119. doi: 10.1016/j.bbi.2015.10.004

Sheldon, R. A., Sedik, C., and Ferriero, D. M. (1998). Strain-related brain injury in neonatal mice subjected to hypoxia-ischemia. *Brain Res.* 810, 114–122. doi: 10.1016/S0006-8993(98)00892-0

Sisa, C., Kholia, S., Naylor, J., Herrera Sanchez, M. B., Bruno, S., Deregibus, M. C., et al. (2019). Mesenchymal stromal cell derived extracellular vesicles reduce hypoxia-ischaemia induced perinatal brain injury. *Front. Physiol.* 10:282. doi: 10.3389/fphys.2019.00282

Sofroniew, M. V. (2015). Astrocyte barriers to neurotoxic inflammation. *Nat. Rev. Neurosci.* 16, 249–263. doi: 10.1038/nrn3898

Thery, C., Witwer, K. W., Aikawa, E., Alcaraz, M. J., Anderson, J. D., Andriantsitohaina, R., et al. (2018). Minimal information for studies of extracellular vesicles 2018 (MISEV2018): a position statement of the International society for extracellular vesicles and update of the MISEV2014 guidelines. *J. Extracell Vesicles* 7:1535750. doi: 10.1080/20013078.2018.1535750

van Velthoven, C. T., Kavelaars, A., van Bel, F., and Heijnen, C. J. (2010). Mesenchymal stem cell treatment after neonatal hypoxic-ischemic brain injury improves behavioral outcome and induces neuronal and oligodendrocyte regeneration. *Brain Behav. Immun.* 24, 387–393. doi: 10.1016/j.bbi.2009.10.017

Vogel, D. Y., Vereyken, E. J., Glim, J. E., Heijnen, P. D., Moeton, M., van der Valk, P., et al. (2013). Macrophages in inflammatory multiple sclerosis

lesions have an intermediate activation status. *J. Neuroinflammation* 10:35. doi: 10.1186/1742-2094-10-35

Wang, C., Borger, V., Sardari, M., Murke, F., Skuljec, J., Pul, R., et al. (2020). Mesenchymal stromal cell-derived small extracellular vesicles induce ischemic neuroprotection by modulating leukocytes and specifically neutrophils. *Stroke* 51, 1825–1834. doi: 10.1161/STROKEAHA.119.028012

Willmot, M., Gibson, C., Gray, L., Murphy, S., and Bath, P. (2005). Nitric oxide synthase inhibitors in experimental ischemic stroke and their effects on infarct size and cerebral blood flow: a systematic review. *Free Radic. Biol. Med.* 39, 412–425. doi: 10.1016/j.freeradbiomed.2005.03.028

Witwer, K. W., van Balkom, B. W. M., Bruno, S., Choo, A., Dominici, M., Gimona, M., et al. (2019). Defining mesenchymal stromal cell (MSC)-derived small extracellular vesicles for therapeutic applications. *J. Extracell Vesicles* 8:1609206. doi: 10.1080/20013078.2019.1609206

Xin, D., Li, T., Chu, X., Ke, H., Yu, Z., Cao, L., et al. (2020). Mesenchymal stromal cell-derived extracellular vesicles modulate microglia/macrophage polarization and protect the brain against hypoxia-ischemic injury in neonatal mice by targeting delivery of miR-21a-5p. *Acta Biomater.* 113, 597–613. doi: 10.1016/j.actbio.2020.06.037

Xin, H., Li, Y., Liu, Z., Wang, X., Shang, X., Cui, Y., et al. (2013). MiR-133b promotes neural plasticity and functional recovery after treatment of stroke with multipotent mesenchymal stromal cells in rats via transfer of exosome-enriched extracellular particles. *Stem Cells* 31, 2737–2746. doi: 10.1002/stem.1409

Xin, H., Wang, F., Li, Y., Lu, Q. E., Cheung, W. L., Zhang, Y., et al. (2017). Secondary release of exosomes from astrocytes contributes to the increase in neural plasticity and improvement of functional recovery after stroke in rats treated with exosomes harvested from microRNA 133b-overexpressing multipotent mesenchymal stromal cells. *Cell Transplant* 26, 243–257. doi: 10.3727/096368916X693031

Yasuhara, T., Hara, K., Maki, M., Mays, R. W., Deans, R. J., Hess, D. C., et al. (2008). Intravenous grafts recapitulate the neurorestoration afforded by intracerebrally delivered multipotent adult progenitor cells in neonatal hypoxic-ischemic rats. *J. Cereb. Blood Flow Metab.* 28, 1804–1810. doi: 10.1038/jcbfm.2008.68

Yi, Y. W., Lee, J. H., Kim, S. Y., Pack, C. G., Ha, D. H., Park, S. R., et al. (2020). Advances in analysis of biodistribution of exosomes by molecular imaging. *Int. J. Mol. Sci.* 21:665. doi: 10.3390/ijms21020665

Zhou, J., Ping, F. F., Lv, W. T., Feng, J. Y., and Shang, J. (2014). Interleukin-18 directly protects cortical neurons by activating PI3K/AKT/NF-kappaB/CREB pathways. *Cytokine* 69, 29–38. doi: 10.1016/j.cyto.2014.05.003

Conflict of Interest: The authors declare that the research was conducted in the absence of any commercial or financial relationships that could be construed as a potential conflict of interest. However, BG is scientific board member of Evox Therapeutics and Innovex Therapeutics SL.

Copyright © 2020 Kaminski, Köster, Mouloud, Börger, Felderhoff-Müser, Bendix, Giebel and Herz. This is an open-access article distributed under the terms of the Creative Commons Attribution License (CC BY). The use, distribution or reproduction in other forums is permitted, provided the original author(s) and the copyright owner(s) are credited and that the original publication in this journal is cited, in accordance with accepted academic practice. No use, distribution or reproduction is permitted which does not comply with these terms.

Advantages of publishing in Frontiers

OPEN ACCESS
Articles are free to read for greatest visibility and readership

FAST PUBLICATION
Around 90 days from submission to decision

HIGH QUALITY PEER-REVIEW
Rigorous, collaborative, and constructive peer-review

TRANSPARENT PEER-REVIEW
Editors and reviewers acknowledged by name on published articles

Frontiers
Avenue du Tribunal-Fédéral 34
1005 Lausanne | Switzerland

Visit us: www.frontiersin.org
Contact us: frontiersin.org/about/contact

REPRODUCIBILITY OF RESEARCH
Support open data and methods to enhance research reproducibility

DIGITAL PUBLISHING
Articles designed for optimal readership across devices

FOLLOW US
@frontiersin

IMPACT METRICS
Advanced article metrics track visibility across digital media

EXTENSIVE PROMOTION
Marketing and promotion of impactful research

LOOP RESEARCH NETWORK
Our network increases your article's readership